

Rui Tamura · Mikiji Miyata *Editors*

# Advances in Organic Crystal Chemistry

Comprehensive Reviews 2015

 Springer

# Advances in Organic Crystal Chemistry



Rui Tamura • Mikiji Miyata  
Editors

# Advances in Organic Crystal Chemistry

Comprehensive Reviews 2015

 Springer

*Editors*

Rui Tamura  
Graduate School of Human  
and Environmental Studies  
Kyoto University  
Kyoto, Japan

Mikiji Miyata  
The Institute of Scientific  
and Industrial Research  
Osaka University  
Osaka, Japan

ISBN 978-4-431-55554-4

ISBN 978-4-431-55555-1 (eBook)

DOI 10.1007/978-4-431-55555-1

Library of Congress Control Number: 2015947134

Springer Tokyo Heidelberg New York Dordrecht London

© Springer Japan 2015

This work is subject to copyright. All rights are reserved by the Publisher, whether the whole or part of the material is concerned, specifically the rights of translation, reprinting, reuse of illustrations, recitation, broadcasting, reproduction on microfilms or in any other physical way, and transmission or information storage and retrieval, electronic adaptation, computer software, or by similar or dissimilar methodology now known or hereafter developed.

The use of general descriptive names, registered names, trademarks, service marks, etc. in this publication does not imply, even in the absence of a specific statement, that such names are exempt from the relevant protective laws and regulations and therefore free for general use.

The publisher, the authors and the editors are safe to assume that the advice and information in this book are believed to be true and accurate at the date of publication. Neither the publisher nor the authors or the editors give a warranty, express or implied, with respect to the material contained herein or for any errors or omissions that may have been made.

Printed on acid-free paper

Springer Japan KK is part of Springer Science+Business Media ([www.springer.com](http://www.springer.com))

# Preface

For the last decade, the topics of organic crystal chemistry have become diversified, and each topic has been substantially advanced in concert with the rapid development of various analytical and measurement techniques for solid-state organic materials. The aim of this book is to systematically summarize and record the recent notable advances in various topics of organic crystal chemistry involving liquid crystals and organic–inorganic hybrid materials that have been achieved mainly in the last 5 years or so. The summaries and records contained herein are by invited members of the Division of Organic Crystals in the Chemical Society of Japan (CSJ) and prominent invited authors from abroad. In this first volume, most of the authors were plenary or invited speakers at the Joint Congress of the 11th International Workshop on the Crystal Growth of Organic Materials (CGOM 11) and the Asian Crystallization Technology Symposium 2014 (ACTS-2014) held in Nara, Japan, 17–20 June 2014. The 35 papers contributed to this volume are roughly classified into eight categories: (1) Nucleation and Crystal Growth, (2) Crystal Structure Determination and Molecular Orbital Calculation, (3) Crystal Structure, (4) Polymorphism, (5) Chirality, (6) Solid-State Reaction, (7) Photo-induced Behavior, and (8) Electric and Magnetic Properties.

The Division of Organic Crystals was founded in CSJ in 1997 as a stimulus for research in organic crystal chemistry in Japan. The first president was the late Professor Fumio Toda, who performed a great service in establishing the division. Today's activities consist of two annual domestic conferences (the Symposium on Organic Crystals in the autumn and the Annual Spring Meeting of CSJ at the end of March) and biannual publication of the *Organic Crystals Division News Letter*. We hope that this edited volume will be published periodically, at least every 5 years, as one of the division's activities through contributions by prominent authors in Japan and from abroad.

Finally, we editors would like to express our sincerest gratitude to all authors for their great contributions to *Advances in Organic Crystal Chemistry: Comprehensive Reviews 2015*.

Kyoto, Japan  
Suita, Japan  
February 2015

Rui Tamura  
Mikiji Miyata

# Contents

## Part I Nucleation and Crystal Growth

- 1 **Photochemically Induced Crystallization of Protein** ..... 3  
Tetsuo Okutsu
- 2 **Ultrasonication-Forced Amyloid Fibrillation of Proteins** ..... 15  
Masatomo So, Yuichi Yoshimura, and Yuji Goto
- 3 **In Situ Solid-State NMR Studies of Crystallization Processes** ..... 31  
Kenneth D.M. Harris, Colan E. Hughes,  
and P. Andrew Williams
- 4 **Nucleation and Crystal Growth in Limited Crystallization Field** ..... 55  
Hiroshi Takiyama
- 5 **Particle Engineering with CO<sub>2</sub>-Expanded Solvents: The  
DELOS Platform** ..... 73  
Paula E. Rojas, Santi Sala, Elisa Elizondo, Jaume Veciana,  
and Nora Ventosa
- 6 **Addressing the Stochasticity of Nucleation: Practical Approaches** ... 95  
Nadine Candoni, Zoubida Hammadi, Romain Grossier,  
Manuel Ildefonso, Shuheng Zhang, Roger Morin,  
and Stéphane Veesler
- 7 **Metastability of Supersaturated Solution and Nucleation** ..... 115  
Noriaki Kubota, Masanori Kobari, and Izumi Hirasawa

## Part II Crystal Structure Determination and MO Calculation

- 8 **Structure Determination of Organic Molecular Solids  
from Powder X-Ray Diffraction Data: Current  
Opportunities and State of the Art** ..... 141  
Kenneth D.M. Harris and P. Andrew Williams

<b>9</b>	<b>Magnetically Oriented Microcrystal Arrays and Suspensions: Application to Diffraction Methods and Solid-State NMR Spectroscopy</b> .....	167
	Tsunehisa Kimura	
<b>10</b>	<b>Analysis of Intermolecular Interactions by Ab Initio Molecular Orbital Calculations: Importance for Studying Organic Crystals</b> .....	187
	Seiji Tsuzuki	
<b>Part III Crystal Structure</b>		
<b>11</b>	<b>Construction of Aromatic Folding Architecture: Utilization of Ureylene and Iminodicarbonyl Linkers</b> .....	203
	Shigeo Kohmoto	
<b>12</b>	<b>Crystal Engineering of Coordination Networks Using Multi-interactive Ligands</b> .....	223
	Yumi Yakiyama, Tatsuhiko Kojima, and Masaki Kawano	
<b>13</b>	<b>Azacalixarene: An Ever-Growing Class in the Calixarene Family</b> ....	241
	Hirohito Tsue and Ryusei Oketani	
<b>Part IV Polymorphism</b>		
<b>14</b>	<b>Polymorphism in Molecular Crystals and Cocrystals</b> .....	265
	Srinivasulu Aitipamula	
<b>15</b>	<b>Hydration/Dehydration Phase Transition Mechanism in Organic Crystals Investigated by Ab Initio Crystal Structure Determination from Powder Diffraction Data</b> .....	299
	Kotaro Fujii and Hidehiro Uekusa	
<b>16</b>	<b>Characteristics of Crystal Transitions Among Pseudopolymorphs</b> ...	317
	Yoko Sugawara	
<b>17</b>	<b>Anomalous Formation Properties of Nicotinamide Co-crystals</b> .....	337
	Si-Wei Zhang and Lian Yu	
<b>18</b>	<b>Isothermal Crystallization of Pharmaceutical Glasses: Toward Prediction of Physical Stability of Amorphous Dosage Forms</b> .....	355
	Kohsaku Kawakami	
<b>Part V Chirality</b>		
<b>19</b>	<b>Twofold Helical Molecular Assemblies in Organic Crystals: Chirality Generation and Handedness Determination</b> .....	371
	Mikiji Miyata and Ichiro Hisaki	

<b>20 Chiral Discrimination in the Solid State: Applications to Resolution and Deracemization</b> .....	393
G�rard Coquerel	
<b>21 How to Use Pasteur’s Tweezers</b> .....	421
Richard M. Kellogg	
<b>22 Total Resolution of Racemates by Dynamic Preferential Crystallization</b> .....	445
Masami Sakamoto and Takashi Mino	
<b>23 Chiral Recognition by Inclusion Crystals of Amino-Acid Derivatives Having Trityl Groups</b> .....	463
Motohiro Akazome	
<b>Part VI Solid-State Reaction</b>	
<b>24 Reactions and Orientational Control of Organic Nanocrystals</b> .....	485
Shuji Okada and Hidetoshi Oikawa	
<b>25 Topochemical Polymerization of Amino Acid <i>N</i>-Carboxy Anhydrides in Crystalline State</b> .....	503
Hitoshi Kanazawa	
<b>26 Topochemical Polymerizations and Crystal Cross-Linking of Metal Organic Frameworks</b> .....	517
Kazuki Sada, Takumi Ishiwata, and Kenta Kokado	
<b>Part VII Photoinduced Behavior</b>	
<b>27 Photoinduced Mechanical Motion of Photochromic Crystalline Materials</b> .....	533
Seiya Kobatake and Daichi Kitagawa	
<b>28 Photoinduced Reversible Topographical Changes on Photochromic Microcrystalline Surfaces</b> .....	549
Kingo Uchida	
<b>29 Luminescence Modulation of Organic Crystals by a Supramolecular Approach</b> .....	569
Norimitsu Tohnai	
<b>30 Solid-State Circularly Polarized Luminescence of Chiral Supramolecular Organic Fluorophore</b> .....	587
Yoshitane Imai	
<b>Part VIII Electric and Magnetic Properties</b>	
<b>31 Relationship Between the Crystal Structures and Transistor Performance of Organic Semiconductors</b> .....	607
Yoshiro Yamashita	

<b>32 Photocurrent Action Spectra of Organic Semiconductors</b> .....	627
Richard Murdey and Naoki Sato	
<b>33 Electro-Responsive Columnar Liquid Crystal Phases Generated by Achiral Molecules</b> .....	653
Keiki Kishikawa	
<b>34 Crystal Engineering Approach Toward Molecule-Based Magnetic Materials</b> .....	669
Naoki Yoshioka	
<b>35 Observation of Magnetoelectric Effect in All-Organic Ferromagnetic and Ferroelectric Liquid Crystals in an Applied Magnetic Field</b> .....	689
Rui Tamura, Yoshiaki Uchida, and Katsuaki Suzuki	
<b>Erratum</b> .....	E1

**Part I**  
**Nucleation and Crystal Growth**

# Chapter 1

## Photochemically Induced Crystallization of Protein

Tetsuo Okutsu

**Abstract** A photochemical reaction of protein triggers crystal growth. Residual Trp or Tyr radical intermediates are produced by photochemical reactions. The intermediates collide with other proteins to form protein dimers, and some of the dimers grow larger than the critical radius to form crystal nuclei; however, not all dimers grow into nuclei. It appears that, in order to grow into a nucleus, a dimer needs to have the same configuration as two adjacent molecules in the crystal. Molecules that have such configurations are called template molecules. In the case of lysozyme, a dimer combined at Tyr<sup>53</sup>-Tyr<sup>53</sup> residuals was considered a template molecule. It was also found that not all the dimers produced always grew to template molecules; thus, we examined a strategy to produce template molecules.

**Keywords** Protein crystallization • Photochemical reaction • Photo-induced crystallization

### 1.1 Introduction

We have discovered a phenomenon of photo-induced crystallization in which crystals were produced easily by irradiating protein solution with ultraviolet light to induce a photochemical reaction and have researched its mechanism [1–13]. In this chapter, we explain its experimental technique, consider a relationship between photochemical reactions of protein and crystallization, examine photochemical reactions at an amino acid level, and describe the crystallization mechanism. Crystallization of protein is an important technique to realize genome-based drug discovery, and a further development of the technology is expected [14]. Although it is said that crystallization of protein depends largely on experiences and intuitions of researchers, we hope our study contributes to the development of genome-based drug discovery by observing phenomena related to crystal growth and by developing a method that guides crystallization logically.

---

T. Okutsu (✉)

Applied Chemistry/Biochemistry, Graduate School of Engineering, Gunma University, 1-5-1 Tenjin-cho, Kiryu-shi, Gunma-ken 376-8515, Japan

e-mail: [okutsu@gunma-u.ac.jp](mailto:okutsu@gunma-u.ac.jp)

© Springer Japan 2015

R. Tamura, M. Miyata (eds.), *Advances in Organic Crystal Chemistry*,

DOI 10.1007/978-4-431-55555-1\_1

## 1.2 Mechanism of Photo-Induced Crystallization

Sazaki et al. shows that although protein is a biomolecule, the mechanism of its crystal growth can be explained by a mechanism similar to that of the crystal growth of ordinary inorganic or organic compounds [15]. First, we explain why a photochemical reaction of protein triggers crystallization. Figure 1.1 shows a model of the initial stage of crystal growth. Molecules first come in contact and are combined by an intermolecular force to form a bimolecular cluster. Since this cluster has the minimum combined stabilization energy, its lifespan is generally short. A third molecule collides with the bimolecular cluster during its lifespan to form a three-molecular cluster, which dissociates again or grows into a four-molecular cluster. At this initial stage, there is a region in which a small cluster is unstable, even if the solution is supersaturated, and does not grow into a bulk crystal.

Suppose that a stable bimolecular cluster is added to such a solution. Although bimolecular clusters have been known to be unstable and do not grow easily into a three-molecular cluster, however, starting with a stable bimolecular cluster would enable easier formation of a critical nucleus. A method of protein crystallization triggered by a photochemical reaction produces a stable dimer of protein or a stable cluster in the system that induces nucleus formation.

This does not mean, however, that production of a stable dimer always starts crystal nucleus formation. We assumed that a dimer which grows into a crystal should have configurations which construct part of the crystal. In other words, having similar configurations as the two adjacent molecules in crystal is considered a necessary condition. Such a molecule is called a template molecule. We believe that it is possible to explain the configurations of a dimer produced by the reaction intermediates of radicalized amino acid protein by photoexciting the protein. By

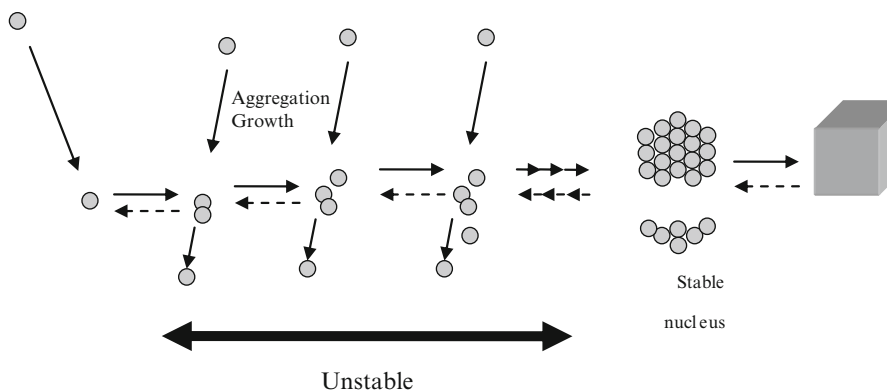


**Fig. 1.1** A model illustrating photo-induced crystallization. Although a dimer formed initially is most unstable, a stable covalent dimer is formed by photochemical reaction and a nucleus is easily formed

following photochemical reactions at an amino acid level, we have been conducting a study to clarify the dimer configurations, which is described below.

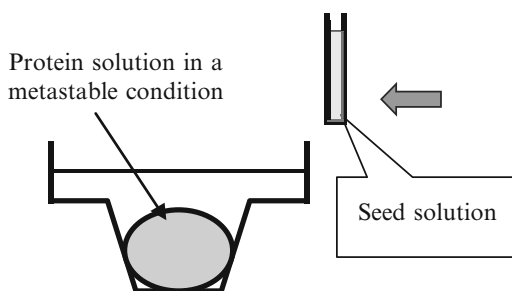
### 1.3 Experiment on Photo-Induced Crystallization of Protein

Here, we explain a method of photo-induced crystallization experiment. For crystallization, we used a light source with a radiation spectrum at 280 nm to excite amino acids of protein such as Trp, Tyr, and Phe. We mainly used ultraviolet portion of Xe lamp light. To analyze reaction intermediates, we also used a YAG laser of 266 nm as a light source to excite protein.

We performed crystal growth by salting out. A representative example of crystallization is a hanging drop vapor diffusion method [16, 17]. When a mixed solution of protein and salt as well as a reservoir solution of concentrated salt are placed together in a sealed container, the solvent vaporizes eventually so that the salt concentrations become equal, condensing the protein solution beyond the solubility and leading to crystal formation. Since unsaturated protein solution initially prepared gradually becomes supersaturated, crystallization is expected. The vapor diffusion method is used as a main method for practical protein crystallization. On the other hand, when the crystal growth of protein and nucleus formation mechanism are discussed, a batch method may be used, in which a supersaturated solution is prepared from the beginning and the concentration of salt in the solution is not changed. In order to determine whether a crystal appears, we conducted a seed crystal method. In this method, a metastable protein solution was prepared at the point of crystal formation, and crystal nuclei formed by photochemical reaction were added to this solution. Figure 1.2 shows a schematic of the photo-induced crystallization experiment performed in this study. We first prepared two types of protein solutions. One was a protein solution in which nuclei were formed by light irradiation. The other was a solution in a metastable condition for nucleus growth. These two solutions were blended and left to rest. Then, the crystals that appeared a few days later in the well were observed with a microscope.

Figure 1.3 shows typical results of the crystallization experiment. These photographs were taken a day after 5  $\mu$ l of lysozyme solution was dropped onto a

**Fig. 1.2** Experiment on photo-induced crystallization of protein. We conducted this experiment by a seed crystal method using a solution in which a nucleus was formed by photochemical reaction and a metastable solution in which a crystal grows



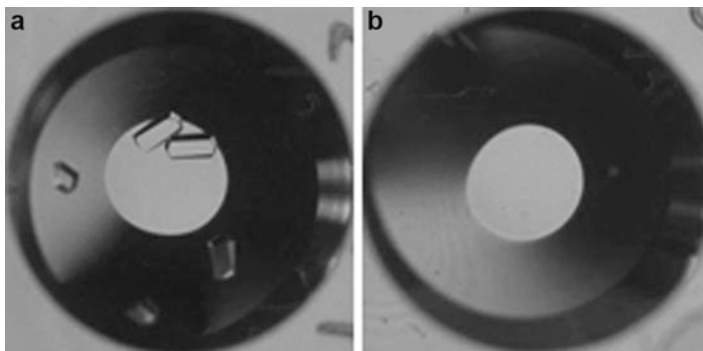


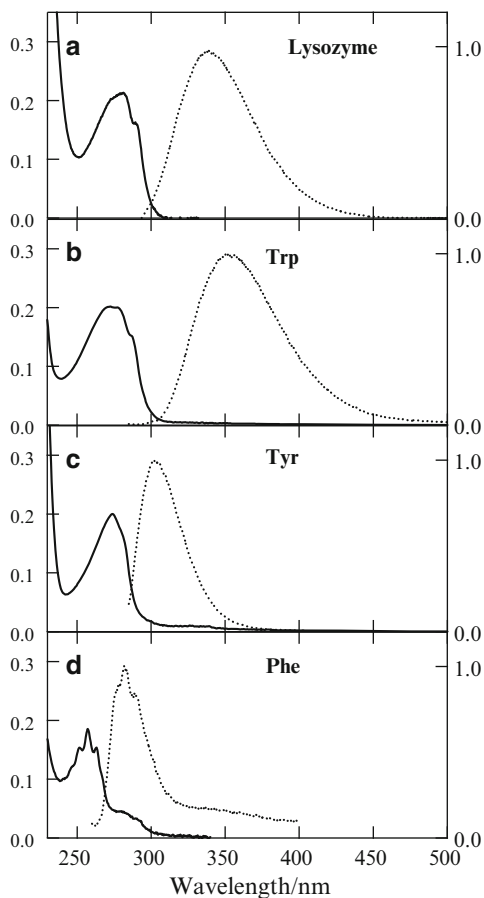
**Fig. 1.3** Typical results of photo-induced crystallization. (a) After being irradiated with UV light for 60 s, a lysozyme solution was added to a growing solution, and (b) the solution was not irradiated with light

micro-batch plate and irradiated with light, and equal quantity of the growing protein solution was blended and left at 20 °C. Figure 1.3a is the solution that was blended with a solution irradiated with light for 1 min, and Fig. 1.3b is the solution in which the drops not irradiated with light were added as the control experiment. Lysozyme crystals appeared in the well in which the solution irradiated with light was mixed. However, the accuracy of this experiment is poor since handling of solution is subject to a scale of  $\mu\text{l}$ . To solve this problem, we conducted many experiments simultaneously and studied the statistical significance. Alternatively, we handled solution in a scale of ml to improve accuracy.

## 1.4 Photochemical Reaction of Protein

In this section, we describe photochemical properties of protein. Since protein consists of amino acids, its absorption spectrum is an overlapped absorption spectrum of amino acids. Here, we describe the photochemistry of hen egg-white lysozyme, a typical protein. Among the amino acids that make up lysozyme, those that have the  $\pi$ -electron system and are involved in photochemical reaction are Trp, Tyr, and Phe. Figure 1.4a–d shows absorption and fluorescence spectra of lysozyme and these amino acids at a steady state. Lysozyme contains six Trp, four Tyr, and two Phe. The absorption spectrum of lysozyme is overlapped absorption spectra of these amino acids. On the other hand, the fluorescence spectrum of lysozyme is almost the same as that of the Trp. This was explained by photochemical studies in the 1970s. When amino acid residuals of Tyr and Phe cause optical absorption, excitation energy transfer occurs efficiently in lysozyme molecules, an excited state of Trp with the lowest excited state energy is established, and fluorescence is generated [18–21]. That is, although a protein consists of various amino acids, the most likely phenomenon is the eventual appearance of an excited state of Trp, and an excited state of protein can be considered as an excited state of residual Trp.

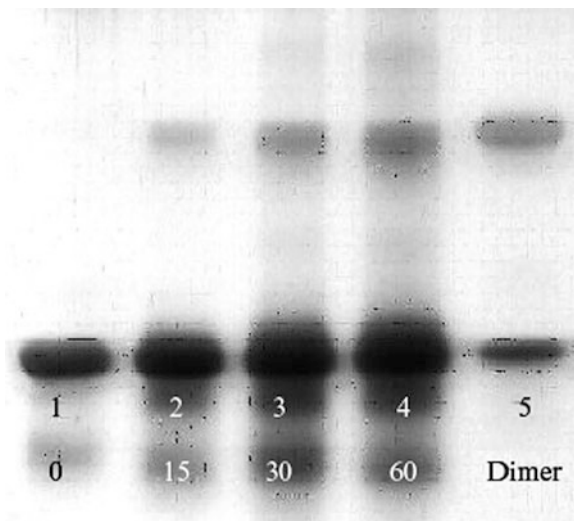
**Fig. 1.4** Absorption spectra and fluorescence spectra of lysozyme and amino acids involved in photochemical reaction. Absorption spectra of protein can be explained by a sum of absorption spectra of amino acids. Fluorescence spectra are emissions from residual Trp. This is because when amino acids such as Tyr and Phe absorb light, energy transfer occurs efficiently in protein molecules and an excited state of Trp appears eventually



Next, we describe what occurs in a photochemical reaction. For this, we used transient absorption measurement. Transient absorption measurement is a method that uses pulsed lasers to simultaneously excite a sample with a large amount of photon, producing reaction intermediates at high density ( $10^{-6}$  M) to measure absorption. At the initial stage of photochemical reaction of lysozyme, reaction intermediate radicals of Trp are observed. It is known that reaction intermediates of residual Trp indicate that another residual Trp reacts with a radicalized lysozyme or with lysozyme in a ground state. Although reaction intermediates of phenol group radicals of residual Tyr are also expected to be produced, these intermediates are masked by intermediates of residual Trp and are not observed clearly. However, fluorescence derived from dityrosine, a combined Tyr-Tyr, is observed in lysozyme solution irradiated with light [22]. This shows that the residual Tyr also gets involved in photochemical reaction.

Proteins of radicalized amino acids produce covalent protein dimers. Figure 1.5 shows the result of the electrophoresis experiment before and after irradiation of

**Fig. 1.5** Experimental results of electrophoresis of protein after photochemical reaction. Lanes 1–4 are lysozyme irradiated with light. Production amount of dimers increased as irradiation time increased. Lane 5 is electrophoresis of purified dimer sample



lysozyme. Reaction intermediates are protein of residual amino acid radicals, and, with time, they are expected to react with other proteins to form oligomers and become crystal nuclei. We conducted an experiment to confirm that dimers were produced by electrophoresis. Lane 1 is a lysozyme before irradiation, Lanes 2–4 are irradiated lysozyme solution, and Lane 5 is a lysozyme dimer produced chemically by repetition of freezing and heating [23, 24]. Irradiation lasted 0, 15, 30, and 60 min. When irradiated, a spot at the position of double the molecular weight of a parent molecule became clear. In an SDS-PAGE method, a van der Waals assembly that is not in covalent bonding dissociates and is observed as a monomer. This experimental result shows that a covalent dimer is formed by irradiation. As expected from the experimental result of transient absorption, it was confirmed by the electrophoresis experiment that two molecules of reaction intermediate radicals of protein were combined to form a dimer.

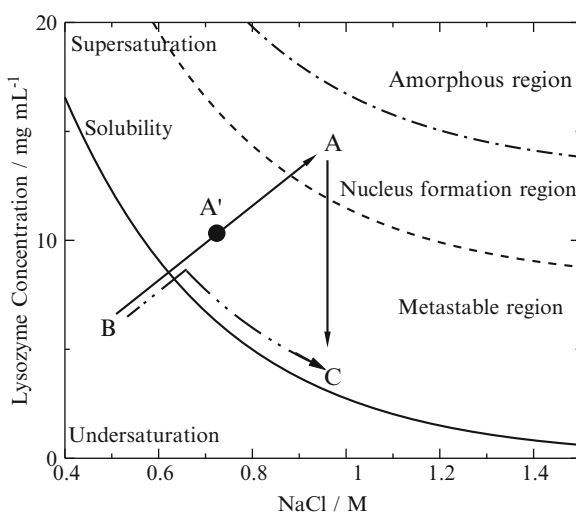
We investigated whether dimer formation could be a mechanism of photo-induced crystallization. As a function of the volume of a cluster, bulk free energy changes in the direction of stabilization as molecules aggregate. On the other hand, surface free energy disadvantage is proportional to a surface area and changes in the unstable direction. Crystal nucleus formation is expressed as a sum of bulk free energy and surface free energy disadvantage, and it is understood that as the nuclear radius exceeds the maximum value ( $r^*$ ) and increases, free energy change turns to minus and nucleus formation starts spontaneously. In some cases, proteins may dissolve dozens more times than the solubility. The causes for this are considered to be the following: the protein has large anisotropy and a crystal nucleus with proper orientation is difficult to be formed, and the intermolecular force to form a crystal is small compared to the size of a molecule. That is, since a cluster larger than  $r^*$  is not formed even in a supersaturated condition, spontaneous crystallization does not occur.

We studied how much the wall of free energy (to exceed the critical radius  $r^*$ ) dropped between two cases where the nucleus formation process started from a monomer and a dimer. Vekilov et al. estimated nucleus formation frequency under the actual condition of lysozyme crystallization and reported that in our experimental conditions (protein concentration, salt concentration, buffer, and temperature), the critical size was a cluster of 4 molecules [25]. As a result, it was estimated that free energy required from the start of a stable dimer to the formation of a critical nucleus made of four molecules dropped to  $2/3$  and that nucleus formation frequency became  $10^7$  times larger than that in the case where the nucleus formation process started from a monomer.

Then, we conducted an experiment in which we added a dimer in supersaturated solution to confirm that crystallization was accelerated. We also conducted another experiment in which a dimer was added in unsaturated solution. The solution was condensed gradually to supersaturation to see if crystallization was accelerated. We show the concept of the experiment using a solubility curve. Figure 1.6 shows the solubility curve of lysozyme, a region where nucleus formation occurs spontaneously, a region where it does not occur, and an amorphous region. Then, a solution was prepared in which nucleus formation, shown as A in the figure, occurs spontaneously. In this solution, nucleus formation occurs, a crystal grows, degree of supersaturation drops, and concentration in the solution changes to C. If a dimer is added at point A, the number of crystals should increase since the dimer grows into a crystal.

Another experiment was conducted in which we prepared unsaturated solution, shown as B in the figure, and condensed it gradually by the vapor diffusion method to form a crystal. When the solution is condensed to the nucleus formation region, nucleus formation begins, and crystallization proceeds toward C. When the solution stays in a metastable condition due to poor condensation at A', however, a

**Fig. 1.6** Solubility curve of lysozyme. In high supersaturation (amorphous region), aggregation occurs and nucleus formation does not occur. In medium supersaturation (nucleus formation region), nucleus formation occurs spontaneously. In low supersaturation (metastable region), nucleus formation does not occur but a nucleus grows



crystal does not appear. If the solution contains a cluster that grows into a crystal, crystallization starts when the solution exceeds the solubility curve, and crystal growth proceeds along the chain line in the figure.

We conducted an experiment to confirm that a covalent dimer forms a crystal in the process, as discussed above. We used hen egg-white lysozyme as protein and a covalent dimer—isolated as impurity contained in a lysozyme monomer—as a lysozyme dimer. A batch method was used in which a dimer was added in a solution having a degree of supersaturation 7, corresponding to A in the figure, and a dimer was added in unsaturated solution (degree of supersaturation 0.6), corresponding to B in the figure, and condensed it by vapor diffusion. We then compared them with cases in which the dimer was not added. The number of molecules of the dimer added was a ratio of  $5 \times 10^{-6}$  to that of monomer molecules contained in the solution. We prepared the solution and observed it 1 week later. At the same time, we used eight wells and a hanging drop method to carry out an experiment under the same conditions.

The results are shown in Fig. 1.7. Figures (a) and (b) are experiment results by the batch method, and (c) and (d) are average experiment results by the vapor diffusion

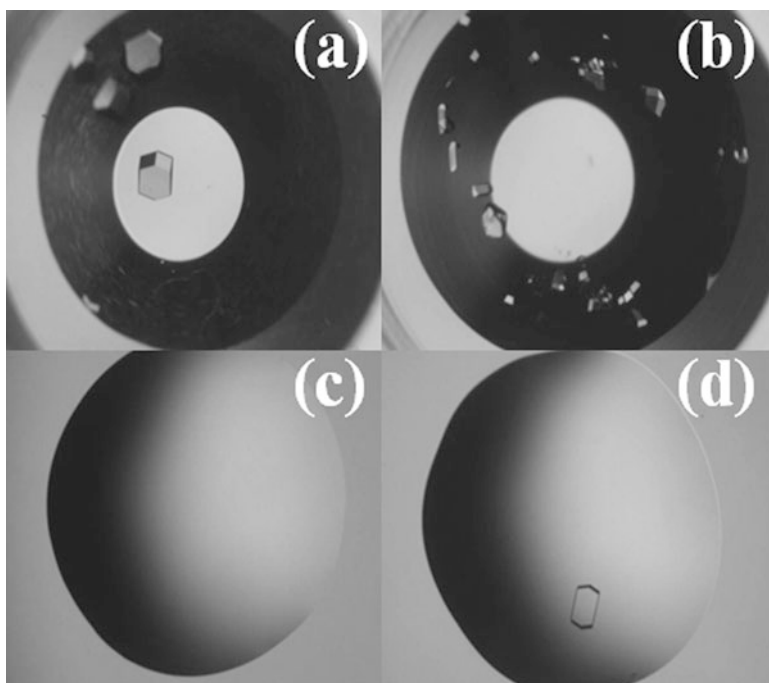


**Fig. 1.7** Photographs of metastable solution in which a dimer was added. They were taken 7 days after addition. (a) and (b) are experiment results by the batch method. (a) is the well in which a dimer was not added, and (b) is the well in which a dimer was added. (c) and (d) are experiment results by the vapor diffusion method. (c) is the well in which a dimer was not added, and (d) is the well in which a dimer was added

method. In the batch method experiment, (a) shows the result of the control solution in which a dimer was not added, and (b) shows the result of a solution in which a dimer was added. In the control solution, on average, five crystals appeared in one well. In the wells in which a dimer was added, 20 crystals appeared on average. Since spontaneous nucleus formation is possible in the control, crystals do appear. But the fact that the number of crystals increased with additional dimer can be explained by dimers growing into crystals.

On the other hand, in the vapor diffusion method experiment, in the well of (c) in which a dimer was not added as control, crystals did not appear. This is because the condensed solution did not reach the nucleus formation region. In (d), in which a dimer was added, a crystal appeared in each of the four wells among eight wells. The frequency of appearance of crystal was 0.5. In this experiment, it appeared that when the solution was condensed and the solubility was exceeded, a nucleus that could grow into a crystal started to grow. And since the solution changed along the solubility curve while maintaining a low degree of supersaturation, new nucleus formation did not occur, and only a minimum number of crystals appeared. These experimental results show that a dimer grows into a crystal.

## 1.5 Dimer as a Template Molecule that Grows into a Crystal

Finally, we studied what properties a dimer should have as a molecule that grows into a crystal. For a dimer to grow into a crystal, the dimer should function as a template molecule. This template molecule is considered to be a “molecule having the same configurations as the two adjacent molecules in a crystal.” The dimer used in the dimer addition experiment described above is a dimer isolated and purified from a lysozyme monomer. It appears at the position of about double of the molecular weight by electrophoresis and it also has enzyme activity, but its configurations are not known. The number of dimers added in one well was approximately  $10^{11}$ , but only a few dimers grew to crystals. Therefore, not all dimers grow into crystals, and it seems that some natural dimers grow into crystals while others do not.

On the converse, since the reactive sites in the structure of a dimer molecule formed by photochemical reaction are limited, its configuration types can be defined. We investigated whether a molecule formed by reaction could be a template molecule and found that intermediates formed by photochemical reaction of lysozyme are 52nd residual Trp radicals and any of the 20th, 23rd, and 53rd residual Tyr radicals on the surface of the molecule. Although the details of the experimental methods are omitted here, the protein of 62nd residual Trp radicals reacts with other protein of residual Trp radicals at the same site to form a dimer. Figure 1.8a shows the configuration of a dimer formed at the site. A dimer such as this is formed under conditions where radical density increases, for example, where photon density of excitation light is increased with a pulsed laser. Some experimental results showed that when dimers were formed efficiently with a pulsed

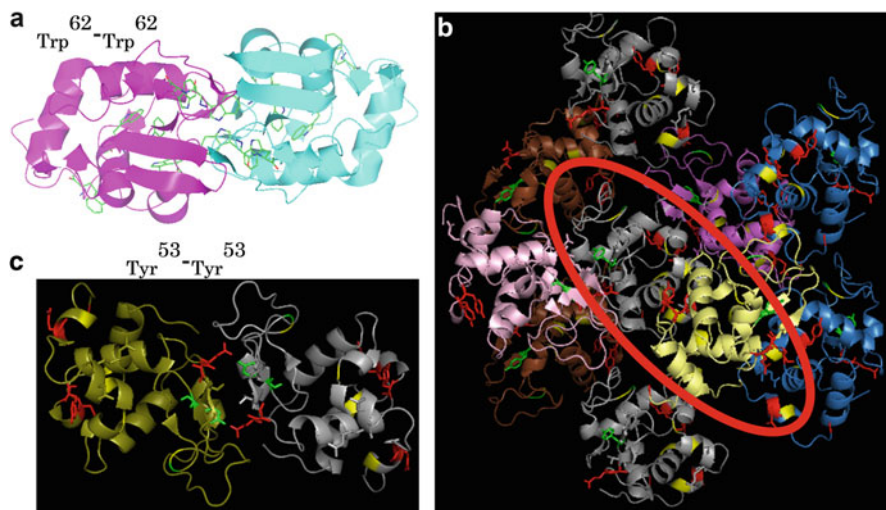


**Fig. 1.8** (a) Configurations of a dimer expected to be formed by photochemical reaction when excited with high-density photon. (b) Unit lattice of lysozyme. (c) Configurations of a dimer in covalent bond at Tyr53-Tyr53

laser, crystallization was not accelerated, and it was considered that a dimer having these configurations could not grow into a nucleus. It is also known that protein of the residual Trp radicals reacts with residual Trp of other protein and that reaction with other amino acids is slow and negligible.

Some experiment showed that protein of residual Tyr radicals reacted with other residual Tyr on the surface of lysozyme. Since lysozyme has three residual Tyr on the surface, there are six possible combinations. Figure 1.8b shows the unit lattice of lysozyme. A dimer combined at Tyr<sup>53</sup>-Tyr<sup>53</sup> shown in Fig. 1.8c has configurations similar to two adjacent molecules in the unit lattice. This showed that a template molecule was formed among some of the formed dimers.

From the above discussion, we can infer that a formed dimer does not always have the configurations of a template molecule. That is, since reactive sites are limited by positions of residual Trp and Tyr, configurations of a formed dimer are limited, but it does not always have the same configurations as two adjacent molecules in crystal. We have succeeded so far in photo-induced crystallization of some proteins, but there is a possibility that formation of the template molecule was only a coincidence.

If this method was to be applied for other types of proteins in order to facilitate crystallization, it is not promising to form a template molecule by a method of exciting protein directly to produce radicals of specific amino acid in the protein and reacting the radicals with other proteins to form a dimer. This is because the configuration of a formed dimer is limited by the configuration of the amino acid on the surface of the protein. To overcome this problem, it is necessary to form

dimers with diverse configurations without depending on the individual properties of a protein and to cause reaction in which one of these configurations functions as a template molecule.

We are currently working on a method to create such a reaction by using photochemical reactions. We are hopeful that we will be reporting on the results in the near future.

## 1.6 Conclusion

A photochemical reaction of protein triggers crystal growth. Residual Trp or Tyr radical intermediates are produced by photochemical reactions. The intermediates collide with other proteins to form protein dimers, and some of the dimers grow larger than the critical radius to form crystal nuclei; however, not all dimers grow into nuclei. It appears that, in order to grow into a nucleus, a dimer needs to have the same configuration as two adjacent molecules in the crystal. Molecules that have such configurations are called template molecules. In the case of lysozyme, a dimer combined at Tyr53-Tyr53 residuals was considered a template molecule. It was also found that not all the dimers produced always grew to template molecules; thus, we examined a strategy to produce template molecules.

**Acknowledgments** This study was conducted by Strategic Basic Research Programs of National Institute of Japan Science and Technology Agency: PRESTO project “Innovative Use of Light and Materials/Life.”

## References

1. T. Okutsu, T. Terao, H. Hiratsuka et al., *Cryst. Growth Des.* **5**, 1393 (2005)
2. S. Veessler, K. Furuta, H. Horiuchi et al., *Cryst. Growth Des.* **6**, 1631 (2006)
3. T. Okutsu, *J. Photochem. Photobiol. C Photochem. Rev.* **8**, 143 (2007)
4. T. Okutsu, M. Sato, K. Furuta et al., *Chem. Lett.* **36**, 338 (2007)
5. T. Okutsu, K. Sugiyama, K. Furuta et al., *J. Photochem. Photobiol. A Chem.* **190**, 88 (2007)
6. K. Furuta, T. Okutsu, G. Sazaki et al., *Chem. Lett.* **36**, 714 (2007)
7. K. Furuta, H. Horiuchi, H. Hiratsuka et al., *Cryst. Growth Des.* **8**, 1886 (2008)
8. H. Hiratsuka, T. Okutsu, *J. Jpn. Assoc. Cryst. Growth* **33**, 366 (2006)
9. T. Okutsu, *J. Photochem. Photobiol. C Photochem. Rev.* **8**, 143 (2008)
10. T. Okutsu, *Photochemistry* **40**(1), 26 (2009)
11. Forefront of Light Science Research (sharing), ed. “Forefront of Light Science Research” Editorial Committee, Japan Intense Light Field Science Society (2005)
12. Forefront of Light Science Research II (sharing), ed. “Forefront of Light Science Research” Editorial Committee, Japan Intense Light Field Science Society (2009)
13. S. Haruta, H. Misawa, K. Ueno et al., *J. Photochem. Photobiol. A Chem.* **221**, 268 (2011)
14. N. Sakabe, M. Aihara (eds.), *Crystallization of Protein* (Kyoto University Press, Kyoto, 2005)
15. G. Sazaki, K. Sato (ed.), *Chapter 4. In: Crystallization from Solution* (Kyoritsu Shuppan, 2002)
16. N. Hirayama, *Organic Compound Crystallization Handbook* (Maruzen, Tokyo, 2001)

17. S. Oba, S. Yano, *X-Ray Crystal Structure Analysis* (Publishing, Asakura, 1999)
18. F. Tanaka, *Kagaku Sosetsu* **26**, 253 (1980)
19. N. Mataga, H. Masuhara, T. Kobayashi, *Kagaku Sosetsu* **24**, 253 (1979)
20. L.I. Grossweiner, A.G. Kaluskar, J.F. Baugher, *Int. J. Radiat. Biol.* **29**, 1 (1976)
21. L.I. Grossweiner, Y. Usui, *Photochem. Photobiol.* **13**, 195 (1971)
22. S. Hashimoto, *Int. J. Radiat. Biol.* **41**, 303 (1982)
23. Y. Iimura, Y. Yoshizaki, H. Nakamura et al., *Cryst. Growth Des.* **5**, 301 (2005)
24. Yoshizaki I, Rong L, Adachi S et al., *JAXA Research and Development Report JAXA-RR-04-051* (2005)
25. O. Galkin, P. Vekilov, *J. Am. Chem. Soc.* **122**, 156 (2000)

# Chapter 2

## Ultrasonication-Forced Amyloid Fibrillation of Proteins

Masatomo So, Yuichi Yoshimura, and Yuji Goto

**Abstract** Amyloid fibrils are self-assemblies of proteins with an ordered cross- $\beta$  architecture and are associated with serious disorders. Amyloid fibrillation is similar to the crystallization of solutes from a supersaturated solution. We found that ultrasonication triggers the spontaneous formation of fibrils in solutions of monomeric amyloidogenic proteins. Cavitation microbubbles are likely to play a key role in effectively converting the metastable state of supersaturation to the labile state, leading to spontaneous fibrillation. With a newly constructed instrument, a HANdai Amyloid Burst Inducer (HANABI), the ultrasonication-forced fibrillation of proteins can be automatically and rapidly analyzed. The results with hen egg-white lysozyme suggested that the large fluctuation observed in the lag time for amyloid fibrillation originated from a process associated with a common amyloidogenic intermediate. The HANABI system will also be useful for studying the mechanism of crystallization of proteins because proteins form crystals by the same mechanism as amyloid fibrils under supersaturation.

**Keywords** Amyloid fibrils • High-throughput analysis • Protein aggregation • Solubility and supersaturation • Ultrasonication

### Abbreviations

$\beta_2$ -m	$\beta_2$ -microglobulin
AFM	Atomic force microscopy
CV	Coefficient of variation
HANABI	HANdai Amyloid Burst Inducer
SD	Standard deviation
SDS	Sodium dodecyl sulfate
ThT	Thioflavin T

---

M. So • Y. Yoshimura • Y. Goto (✉)  
Institute for Protein Research, Osaka University, 3-2 Yamadaoka, Suita, Osaka 565-0871, Japan  
e-mail: [ygoto@protein.osaka-u.ac.jp](mailto:ygoto@protein.osaka-u.ac.jp)

## 2.1 Introduction

Amyloid fibrils are linear self-assemblies of proteins with an ordered cross- $\beta$  structure in which the  $\beta$ -strands are arranged perpendicular to the long fibril axis [1–4]. As seen from Fig. 2.1, amyloid fibrils are around 10 nm in diameter and several  $\mu\text{m}$  in length. Formation of amyloid fibrils (hereinafter referred to as “amyloid fibrillation”) is thought to be a result of protein misfolding because their deposition is associated with the pathology of more than 20 serious disorders such as Alzheimer’s disease, Parkinson’s disease, type II diabetes, and dialysis-related amyloidosis [5, 6]. On the other hand, amyloid-like structures are also utilized for beneficial purposes in nature, known as functional amyloids [7–9]. Because many structurally unrelated proteins can form amyloid fibrils, amyloid fibrillation is likely to be a general property of polypeptide chains [4].

Human  $\beta_2$ -microglobulin ( $\beta_2$ -m), a protein responsible for dialysis-related amyloidosis, is one of the most extensively studied proteins [10–18]. Dialysis-related amyloidosis is a common and serious complication in patients receiving hemodialysis for more than 10 years [14, 19].  $\beta_2$ -m, a typical immunoglobulin domain made of 99 amino acid residues, is present as the non-polymorphic light chain of the class I major histocompatibility complex (MHC-I) [20]. Renal failure disrupts the clearance of  $\beta_2$ -m from the serum, and  $\beta_2$ -m does not pass through the dialysis membrane, resulting in an increase in the  $\beta_2$ -m concentration by up to 50-fold in the blood circulation [14, 21].  $\beta_2$ -m then self-associates to form amyloid

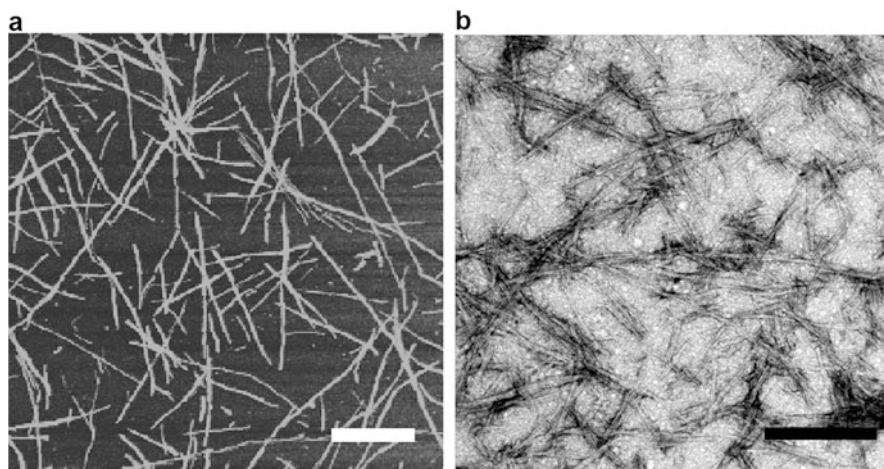


**Fig. 2.1** Morphology of amyloid fibrils. **(a)** AFM image of amyloid fibrils of  $\beta_2$ -m. The scale bar indicates 500 nm. **(b)** Electron microscopic image of amyloid fibrils of hen egg-white lysozyme. The scale bar indicates 200 nm

fibrils. Although the details are still unclear, it is evident that an increase in the concentration of  $\beta_2$ -m in the blood is one of the most important risk factors for the disease.

Hen egg-white lysozyme is also extensively used to study amyloid fibrillation [22, 23]. Although lysozyme in the native state does not easily form amyloid fibrils, destabilization of the native structure by guanidine hydrochloride (Gdn-HCl) and alcohols induces amyloid fibrillation [24–26].

Amyloid fibrillation consists of nucleation and growth [27–29]. The nucleation process, in which a number of monomers associate to form a minimal fibril unit, does not readily occur. Once a nucleus is formed, however, subsequent growth of fibrils proceeds rapidly via the incorporation of the monomers into seed fibrils. These characteristics are similar to those of the crystal growth of solute substances, where agitation of the solution often accelerates the nucleation process. Indeed, shaking and stirring of solutions have been used widely to promote amyloid fibrillation [30]. While  $\beta_2$ -m does not readily form amyloid fibrils at pH 2.5 under the quiescent conditions, agitation induces amyloid fibrillation. Recent studies have focused on the accelerating effects of ultrasonic irradiation on amyloid fibrillation of  $\beta_2$ -m [31–34].

## 2.2 Ultrasonication-Induced Amyloid Fibrillation

Ultrasonication has been routinely used for preparing seeds from preformed fibrils, where long fibrils are fragmented to produce short fibrils [28]. Because the ends of fibrils act as the templates of subsequent growth, ultrasonic treatment is effective to maximize the seeding potential of preformed fibrils. The same effects have been applied to the amplification of infectious prion proteins [35, 36]. Considering the strong mechanical impacts of ultrasonication on the preformed fibrils, ultrasonic irradiation is another type of agitation for accelerating the nucleation process. Stathopoulos et al. [37] showed that for various proteins (i.e., bovine serum albumin, horse heart myoglobin, hen egg-white lysozyme, Tm0979, recombinant hisactophilin, and human cytosolic Cu/Zn superoxide dismutase), ultrasonication results in the formation of amyloid-like aggregates.

Ohhashi et al. [31] studied in detail the effects of ultrasonication on  $\beta_2$ -m. After the reaction mixture (i.e., 0.3 mg/mL  $\beta_2$ -m monomer at pH 2.5 containing 0.1 M NaCl) was prepared in an Eppendorf tube, ultrasonic treatment was started with the tube placed in a water bath-type ultrasonicator (ELESTEIN 070-GOT, Elekon) at 37 °C. The effects of ultrasonication were monitored by fluorometric analysis with thioflavin T (ThT), a specific dye for amyloid fibrils [38]. Repeated ultrasonication induced a sudden and remarkable increase of ThT fluorescence after a lag time of about 2 h. The fibrils were confirmed by atomic force microscopy (AFM) and acted as seeds for subsequent growth.

## 2.3 Developing a High-Throughput Assay System

### 2.3.1 Combined Use of Ultrasonication and a Microplate Reader

It is likely that a large proportion of proteins have the potential to cause amyloidosis [39]. Potential amyloidogenicity argues the necessity for a genome-wide search for the amyloidogenicity of proteins. A high-throughput assay system for screening acceleratory and inhibitory factors is also important for developing therapeutic strategies. Giehm and Otzen [30] proposed a high-throughput screening assay of amyloid fibrillation with a microplate reader, in which the orbital shaking of each well with glass beads was employed to increase reproducibility.

So et al. [33] combined the use of ultrasonication and a microplate reader, taking advantage of the marked effects of ultrasonication. As illustrated in Fig. 2.2a, a microplate (6 cm × 10 cm with 8 × 12 wells) was set at the center of the water bath,

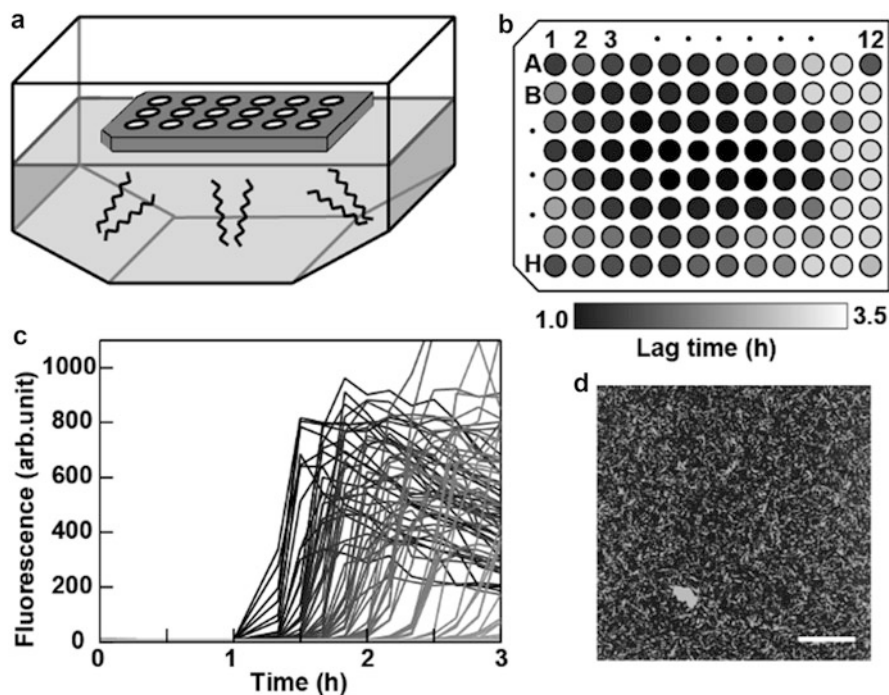


**Fig. 2.2** High-speed assay of amyloid fibrillation using ultrasonication and a microplate reader. (a) Illustration of the experimental procedure. The microplate was set at the *center* of a water bath-type ultrasonicator. The formation of fibrils was monitored by measuring ThT fluorescence with a microplate reader. (b) Distribution of the lag time on the microplate defined by the *gray scale bar*. (c) Time course of the formation of fibrils in 96 wells monitored by measuring ThT fluorescence. *Lines* of different colors represent the kinetics in different wells, shown with the same color as defined in (b). (d) AFM image of the fibrils. The scale bar represents 1  $\mu\text{m}$  (The figures were reproduced from So et al. [33] with permission)

and ultrasonic pulses (19 kHz) from three directions were applied to the microplate. In a standard experiment, the wells were filled with the sample solutions of  $\beta_2$ -m (0.2 mL each at 0.3 mg/mL at pH 2.5) containing 0.1 M NaCl and 5  $\mu$ M ThT. The plate was subjected to ultrasonic irradiation. After the ultrasonication treatment, the plate was set on the microplate reader to assay the ThT fluorescence. The process was repeated during the incubation period.

The microplate was subjected to cycles of ultrasonication for 1 min followed by 9-min quiescence and 37 °C. Many wells exhibited an increase in ThT fluorescence after a lag period (Fig. 2.2b, c). The increase was much faster than that on agitating the microplate by shaking. No increase in fluorescence occurred for 2 days under quiescent conditions. The AFM image showed many short fibrils (Fig. 2.2d). However, the lag time for fibrillation varied significantly depending on the location in the microplate due to the relatively wide microplate, and the final fluorescence intensity also varied, indicating that the amyloid fibrillation is predominantly determined by the ultrasonication power.

Although So et al. [33] developed the method of the use of a 96-well microplate for simultaneous assays of ultrasonication-forced amyloid fibrillation, the microplate has to be moved manually from the ultrasonicator to the microplate reader after each ultrasonic irradiation. In order to analyze the ultrasonication-forced amyloid fibrillation of proteins automatically, Umemoto et al. [40] constructed an instrument, HANdai Amyloid Burst Inducer (HANABI, see Fig. 2.3). With the

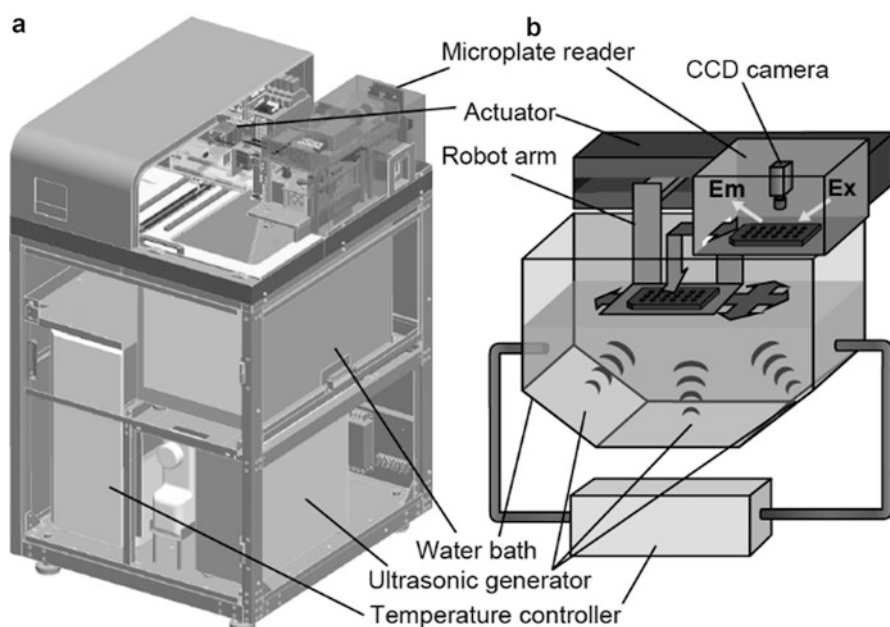


**Fig. 2.3** Overview (a) and schematic illustration (b) of HANABI. HANABI combines a water bath-type ultrasonicator and a fluorescence microplate reader (The figure was reproduced from Umemoto et al. [40] with permission)

HANABI system, ultrasonic irradiation was performed in a water bath, the plate was then moved to the microplate reader, and ThT fluorescence was monitored; these three processes were repeated automatically under programmed time schedules. In order to irradiate all the sample solutions as evenly as possible, the microplate can be moved horizontally during ultrasonication periods (see below).

### 2.3.2 Measurements of Ultrasonic Power

To understand the variation of fibrillation depending on the location, So et al. [33] monitored the ultrasonic amplitude (or pressure) of each well using a lead zirconate titanate (PZT) detector. The ultrasonic amplitude varied depending on the position of the well (Fig. 2.4a), and the variation was similar to that for lag time (Fig. 2.2b), suggesting that the amyloid fibrillation depends critically on the ultrasonic amplitude. The lag times were plotted against ultrasonic amplitude, obtaining a correlation coefficient value of 0.5 (Fig. 2.4b). Although scattering of the data is significant, a linear correlation between the lag time and ultrasonic amplitude confirms that the amyloid fibrillation is predominantly determined by ultrasonic amplitude. The apparent scattering is likely to be caused by both the difficulty in accurately measuring the ultrasonic amplitude and the intrinsic fluctuation of the lag time even under the same ultrasonic amplitude.

There are several additional methods to quantitatively determine ultrasonic power [41]. Calorimetry is often used to specify the ultrasonic power dissipated into a solution, where the initial rate of temperature increase is measured upon irradiation of the solution with ultrasonic pulses. With the calorimetric method, ultrasonic power ( $Q$ ) is calculated using the equation  $Q = (dT/dt) c_p M$ , where  $c_p$

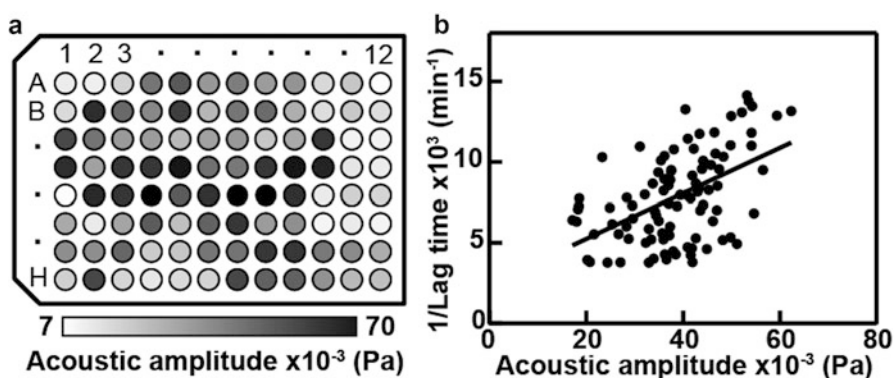


**Fig. 2.4** Correlation of the lag time with ultrasonic amplitude. (a) Distribution of ultrasonic amplitude on the microplate measured with a PZT detector. (b) Correlation of the lag time as shown in Fig. 2.2b with ultrasonic amplitude (The figures were reproduced from So et al. [33] with permission)

is the heat capacity of water ( $4.2 \text{ J g}^{-1} \text{ K}^{-1}$ ) and  $M$  is the mass of water (g).  $(dT/dt)$  is the increase in temperature per second. Yamaguchi et al. [42] investigated the position dependence of the ultrasonic power of a water bath-type ultrasonic transmitter (ELESTEIN 070-GOT, Elekon) using the calorimetric method, showing that the ultrasonic power ranged from 0.3 to 2.7 W.

Chemical dosimetries have also been proposed for the calibration of ultrasonic power [41]. Chemical dosimetry gives sonochemical efficiency in a whole reaction solution, based on oxidation and/or reduction reactions occurring in an aqueous solution. A conventional system is the generation of the triiodide ( $\text{I}_3^-$ ) ion from an aqueous potassium iodide (KI) solution by ultrasonic irradiation, known as KI oxidation. When ultrasound is irradiated into the KI solution,  $\text{I}^-$  ions are oxidized to give diatomic molecules ( $\text{I}_2$ ). When excess  $\text{I}^-$  ions are present in solutions,  $\text{I}_2$  reacts with the excess  $\text{I}^-$  ions to form  $\text{I}_3^-$  ions. The amount of  $\text{I}_3^-$  ions produced after an adequate duration of sonication, which can be estimated by measuring the absorbance of  $\text{I}_3^-$  at 355 nm, is regarded as a relative measure of ultrasonic power. Yamaguchi et al. [42] investigated the position dependence of the amount of  $\text{I}_3^-$  ions produced by a water bath-type ultrasonic transmitter (ELESTEIN 070-GOT, Elekon) and revealed that the ultrasonic strength determined by KI oxidation was in agreement with that determined by calorimetry. Therefore, KI oxidation would also be useful for evaluating the position dependence of amyloid fibrillation.

### 2.3.3 *Minimizing the Well-Dependent Variation*

For high-throughput screening assays, the well-dependent variation in ultrasonic amplitude should be minimized for comparing the amyloidogenicity of various samples. So et al. [33] rotated the microplate horizontally at the center of the plate so as to apply power evenly to all the wells. Rotation of the microplate led to a significant improvement in synchronized amyloid fibrillation as well as a slight shortening of the lag time. The mean  $\pm$  standard deviation (SD) values of 96 wells with and without rotation were  $69.0 \text{ min} \pm 11.0 \text{ min}$  and  $107.2 \text{ min} \pm 26.4 \text{ min}$ , respectively (Fig. 2.5). Although the lag time was still scattering, the results suggest a promising approach to achieving a uniform distribution of ultrasonic energy.

By constructing a HANdai Amyloid Burst Inducer (HANABI), which combines the use of a water bath-type ultrasonicator and microplate reader (Fig. 2.3), Umemoto et al. [40] examined the effects of plate movements by monitoring the oxidation of KI. The plate was horizontally translated during the ultrasonication periods. The mean, standard deviation (SD), and coefficient of variation (CV) for the KI oxidation rate in the 96 wells were obtained in the presence and absence of plate movements. Here, the CV value, defined as the ratio of the SD to the mean, indicates a degree of relative variation. Without plate movements, the rate of KI oxidation was low in many wells and varied significantly depending on the well. These variations were attributed to fluctuations in the ultrasonic power, even

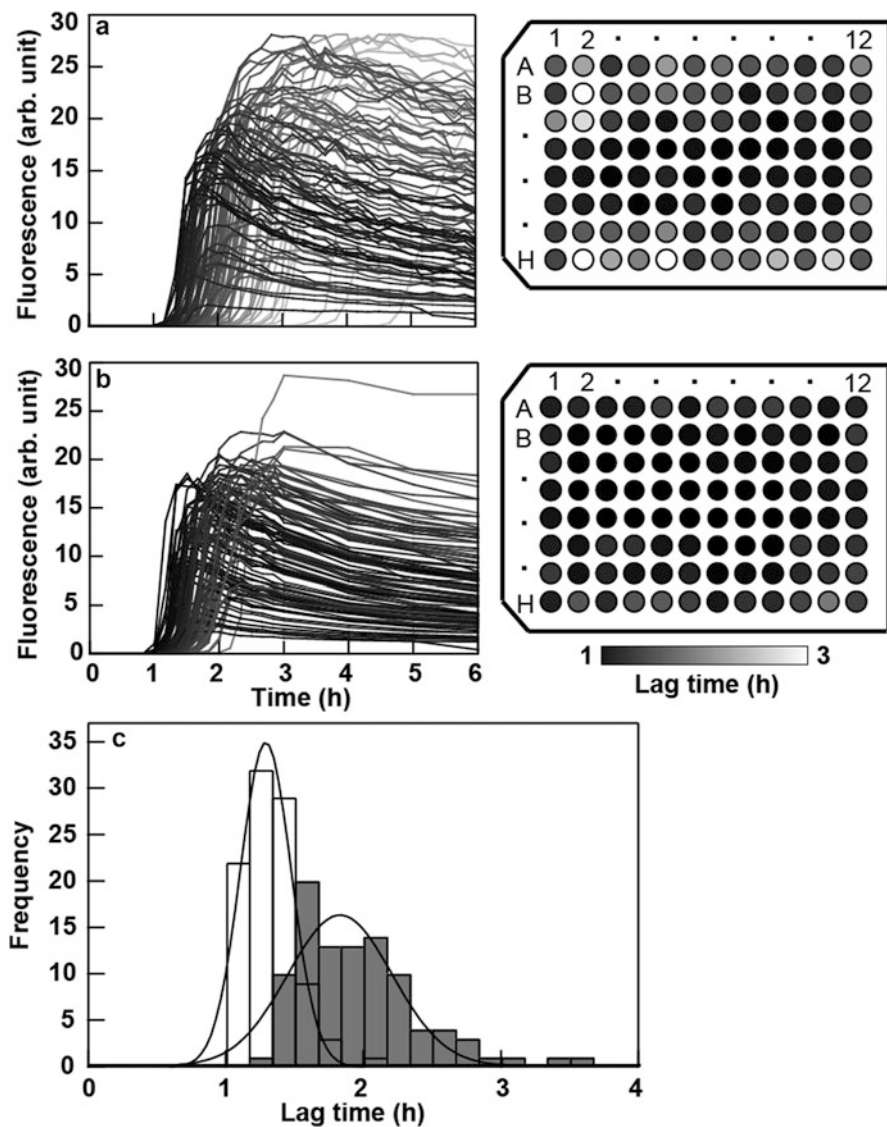


**Fig. 2.5** Effects of the rotation of the microplate on the fibrillation of  $\beta_2$ -m. **(a and b)** Time course of the formation of amyloid fibrils without **(a)** and with **(b)** rotation at 6 rpm. The gradient of colors was used in terms of the lag time, as defined by the *gray scale bar*. The distribution of the lag time on the microplate wells is also shown with the same colors. **(c)** The distribution of the lag time with *(white)* or without *(gray)* rotation. The *lines* were obtained by Gaussian curve fittings (The figure was reproduced from So et al. [33] with permission)

though the 3 ultrasonic transducers were set to maximize the ultrasonic intensity at the location of the plate. Upon moving the microplate, on the other hand, the oxidation rate increased and the variation in the KI oxidation rate was significantly suppressed. The CV values in the absence and presence of the plate movements were 1.4 and 0.2, respectively. Because KI oxidation is a simple reaction that is directly proportional to the ultrasonic energy, it was assumed that the observed variations in the KI oxidation rate represented the basic performance of the HANABI system. The ultrasonication-dependent KI oxidation experiments were repeated three times in the presence and absence of the plate movement. The CV values were constant in the three experiments, which suggested that fluctuations between the experiments were minimal.

### ***2.3.4 High-Throughput Analysis of Amyloid Fibrillation with HANABI***

The HANABI system makes it possible to perform the fibrillation experiments with many samples efficiently, providing extensive understanding of amyloidogenicity. Umemoto et al. [40] performed the experiments using hen egg-white lysozyme at various concentrations of Gdn-HCl. The lysozyme solutions were incubated at 37 °C with the plate movements during cycles of ultrasonication for 3 min at 7-min intervals, and the fibrillation was monitored by measuring ThT fluorescence. Figure 2.6 represents the distribution of lag times at various concentrations of Gdn-HCl. The fibrillation experiments were repeated three times. At 1.0 M Gdn-HCl, fibrillation occurred with a significant variation in the lag time from 1 to 11 h depending on the wells. Fibrillation was the fastest in the presence of 3.0 M Gdn-HCl, with a lag time of less than 1.5 h for most of the wells. At 5.0 M Gdn-HCl, fibrillation became slow with apparently scattered lag times. The results provided an important insight into the mechanism underlying amyloid fibrillation. At 1.0 M Gdn-HCl, the concentration at which lysozyme dominantly assumes its native structure, the protein had to unfold to form fibrils. At 5.0 M Gdn-HCl, highly disordered proteins returned to the amyloidogenic conformation with some degree of compaction. The lag time of the fibrillation showed a minimum at 3.0 M Gdn-HCl, where amyloidogenic conformation was stably populated.

The mean, SD, and CV of the lag time were obtained for each of the experiments at various Gdn-HCl concentrations (Fig. 2.6f, g). The mean and SD depended on the concentration of Gdn-HCl. Scattering of the lag time at the lower and higher Gdn-HCl concentrations was larger than that at 2.0–4.0 M Gdn-HCl. However, the CV was constant at a value of 0.4, independent of the Gdn-HCl concentration. The larger CV value for the fibrillation than KI oxidation with the CV value of 0.2

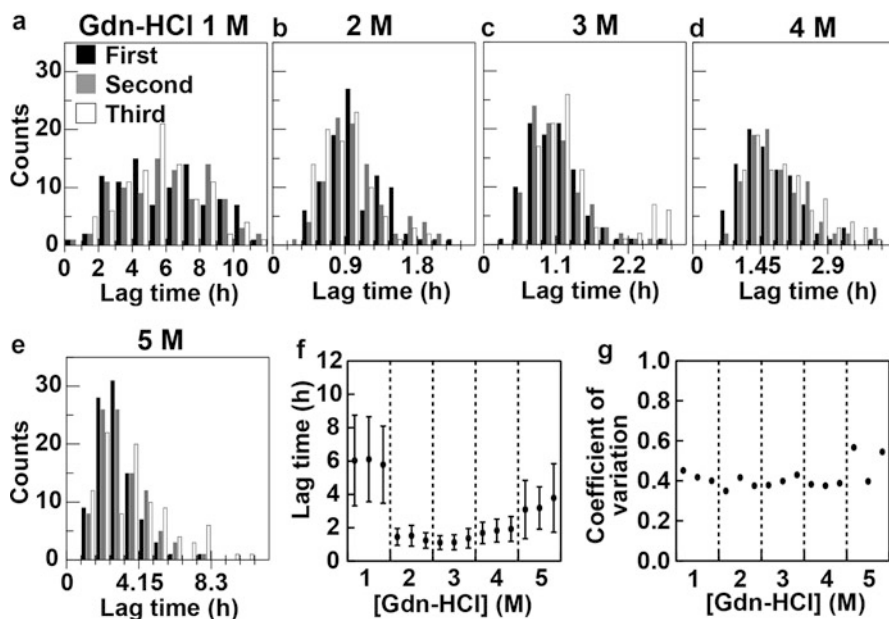


**Fig. 2.6** Dependence of the lag time of lysozyme fibrillation on the Gdn-HCl concentration on the basis of “whole plate analysis.” (a–e) Histograms of the lag time at various Gdn-HCl concentrations. (f, g) The average lag times with the standard deviations (f) and coefficients of variation (g) at various Gdn-HCl concentrations. The results of three experiments are shown (The figure was reproduced from Umemoto et al. [40] with permission)

represents a complicated mechanism of amyloid nucleation. Although the factors that produce a high CV value have yet to be determined, the HANABI system has the potential to address these factors by advancing the high-throughput analysis of the forced fibrillation of proteins.

## 2.4 Ultrasonication-Dependent Crystallization of Lysozyme

Ultrasonication was previously shown to be useful for accelerating the crystallization of proteins [43, 44]. Umemoto et al. [40] installed a CCD camera to the HANABI system in order to rapidly and automatically monitor the crystallization of hen egg-white lysozyme at a concentration of 20 mg/mL, pH 4.8, and 25 °C, as described previously [43]. No crystals were observed after 1-day incubation at 1.0 M NaCl in the absence of agitation (Fig. 2.7a). However, when the solution was subjected to ultrasonication for 5 min, crystals appeared at 10 h and grew in size by 30 h (Fig. 2.7b). These results indicated that the supersaturated protein solution can no longer be kept metastable upon ultrasonic irradiation, leading to protein crystallization.

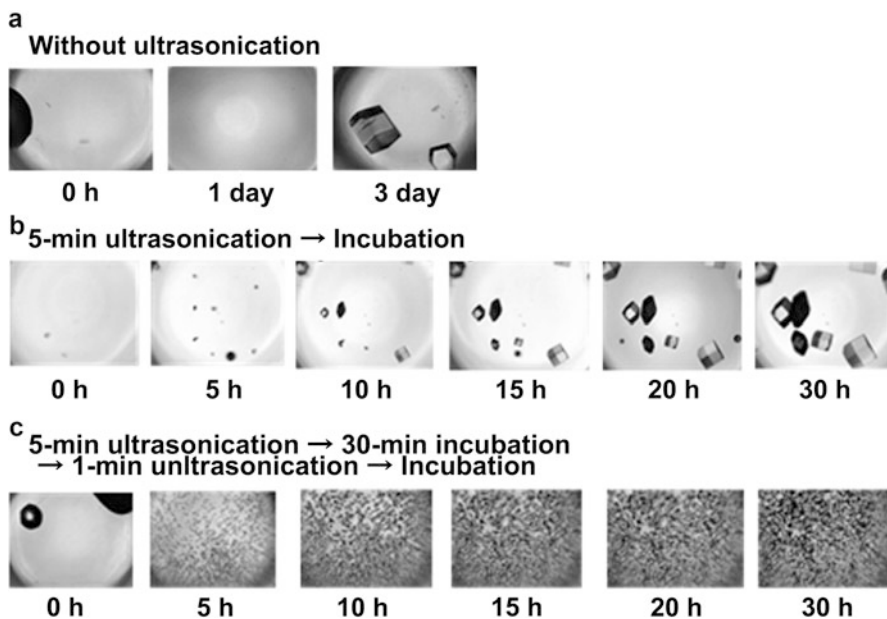


**Fig. 2.7** Monitoring the crystallization of lysozyme. (a) Crystallization without ultrasonication. (b) Crystallization with 5-min ultrasonication followed by quiescence. (c) Crystallization with 5-min ultrasonication followed by 30-min quiescence, 1-min ultrasonication, and quiescence. Sizes of images were 3 mm × 4 mm (The figure was reproduced from Umemoto et al. [40] with permission)

Ultrasonication has been shown to exert opposing effects on amyloid fibrils: the induction of monomers to form fibrils and the breakdown of preformed fibrils into smaller fibrils [32, 45]. This also appears to be true for protein crystals based on the finding that ultrasonication-induced crystals were relatively homogeneous and small in size [43]. A smaller number of ultrasonic pulses followed by incubation without agitation were useful for obtaining a smaller number of larger crystals [43]. Thus, the size and homogeneity of protein crystals can be regulated by manipulating ultrasonic pulses. Extensive ultrasonication, which was achieved by repeated pulses, resulted in a large number of small and homogeneous crystals (Fig. 2.7c).

## 2.5 Mechanism of Ultrasonication-Forced Fibrillation

Ultrasonication has become an important approach to inducing amyloid fibrillation in apparently monomeric protein solutions. Then, what are the mechanisms of the ultrasonication-forced amyloid fibrillation (Fig. 2.8)? Generally, irradiation of an aqueous solution with ultrasonic waves produces cavitation microbubbles, which repeatedly grow and collapse in synchrony with the driving acoustic pressure (or

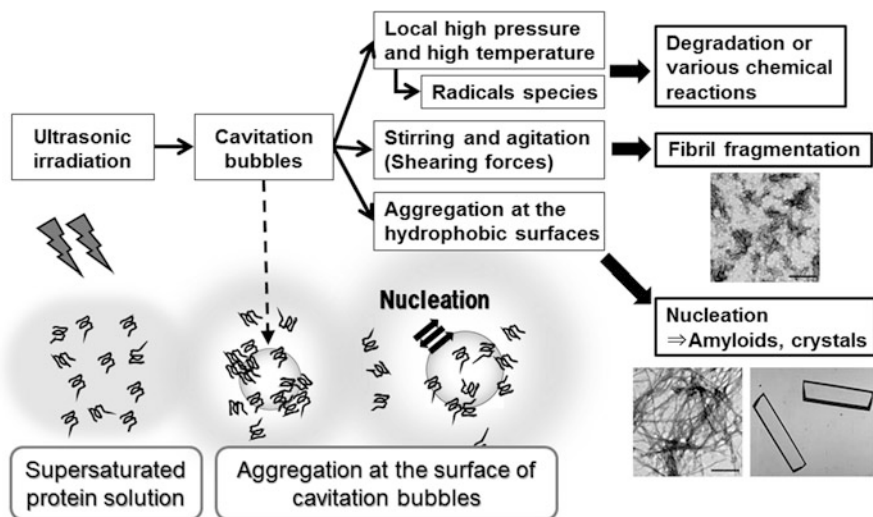


**Fig. 2.8** The mechanism of ultrasonication-induced amyloid fibrillation (The figure was reproduced from Yoshimura et al. [55] with permission. Copyright (2013) The Japan Society of Applied Physics)

ultrasonic amplitude) [46]. When the microbubbles collapse, the temperature inside drastically increases because of isothermal compression effects, providing hot spots and free radical species [47, 48]. These decompose organic compounds in the solution, that is, a sonochemical reaction [49–51]. The sonochemical reactions occur most effectively in focused regions with a high-amplitude acoustic resonant mode where the ultrasonic amplitude is much higher than the standard amplitude [46].

However, because  $\beta_2$ -m is intact even after extensive ultrasonication [31, 32], sonochemical reactions do not seem to be the main mechanisms responsible for the breakdown and formation of the fibrils. On the other hand, the repeated growth and collapse of cavitation bubbles and concomitant large shearing forces [52–54] seem to be directly linked to triggering of the amyloid nucleation in supersaturated monomeric solutions. One possible mechanism of ultrasonication-forced nucleation is the formation of glassy (i.e., amorphous) aggregates at the hydrophobic liquid-gas interface of cavitation bubbles. Development of the nucleus-competent conformation in the glassy aggregates triggers the growth of crystal-like amyloid fibrils in the supersaturated metastable region. Large shearing forces, breaking the growing fibrils and thus increasing the number of nuclei (i.e., secondary nucleation), further accelerate spontaneous fibrillation. Moreover, ultrasonication is likely to induce denaturation of the native proteins at the hydrophobic liquid-gas interface, leading to the acceleration of their fibrillation. Clarifying the physical nature of these effects is the next challenge for advancing the general mechanism of amyloid fibrillation in supersaturated solutions.

## 2.6 Conclusion

Amyloid fibrils form in supersaturated solutions of precursor proteins by a nucleation and growth mechanism characterized by a lag time. We have shown that ultrasonication dramatically accelerates the formation of amyloid fibrils by breaking supersaturation. We suggest that cavitation microbubbles play a key role in effectively converting the metastable state of supersaturation to the labile state, leading to spontaneous fibrillation. A HANABI system, which combines the use of a water bath-type ultrasonicator and microplate reader, enables a high-throughput analysis of the amyloid fibrillation. The HANABI system will also be useful for analyzing crystallization of proteins because proteins form crystals by the same mechanism as amyloid fibrils under supersaturation. Moreover, supersaturation-limited reactions are common to various natural phenomena including supercooling of water and polymerization of actins and microtubules. Ultrasonication and thus HANABI will become an important approach for addressing the mechanism of various supersaturation-limited phase transitions.

**Acknowledgments** We would like to thank Profs. Hisashi Yagi, Hironobu Naiki, and Hirotsugu Ogi for discussion. This work was supported by the Japanese Ministry of Education, Culture, Sports, Science and Technology and Kansai Bureau of Economy, Trade and Industry.

## References

1. M. Sunde, C.C. Blake, From the globular to the fibrous state: protein structure and structural conversion in amyloid formation. *Q. Rev. Biophys.* **31**, 1–39 (1998)
2. F.E. Cohen, J.W. Kelly, Therapeutic approaches to protein-misfolding diseases. *Nature* **426**, 905–909 (2003)
3. V.N. Uversky, A.L. Fink, Conformational constraints for amyloid fibrillation: the importance of being unfolded. *Biochim. Biophys. Acta* **1698**, 131–153 (2004)
4. F. Chiti, C.M. Dobson, Protein misfolding, functional amyloid, and human disease. *Annu. Rev. Biochem.* **75**, 333–366 (2006)
5. C.M. Dobson, Protein folding and misfolding. *Nature* **426**, 884–890 (2003)
6. P. Westermark, M.D. Benson, J.N. Buxbaum et al., A primer of amyloid nomenclature. *Amyloid* **14**, 179–183 (2007)
7. D.M. Fowler, A.V. Koulov, W.E. Balch et al., Functional amyloid – from bacteria to humans. *Trends Biochem. Sci.* **32**, 217–224 (2007)
8. C. Wasmer, A. Lange, H. Van Melckebeke et al., Amyloid fibrils of the HET-s(218–289) prion form a beta solenoid with a triangular hydrophobic core. *Science* **319**, 1523–1526 (2008)
9. S.K. Maji, M.H. Perrin, M.R. Sawaya et al., Functional amyloids as natural storage of peptide hormones in pituitary secretory granules. *Science* **325**, 328–332 (2009)
10. V.J. McParland, N.M. Kad, A.P. Kalverda et al., Partially unfolded states of  $\beta_2$ -microglobulin and amyloid formation in vitro. *Biochemistry* **39**, 8735–8746 (2000)
11. M. Hoshino, H. Katou, Y. Hagihara et al., Mapping the core of the  $\beta_2$ -microglobulin amyloid fibril by H/D exchange. *Nat. Struct. Biol.* **9**, 332–336 (2002)
12. M.I. Ivanova, M.R. Sawaya, M. Gingery et al., An amyloid-forming segment of  $\beta_2$ -microglobulin suggests a molecular model for the fibril. *Proc. Natl. Acad. Sci. U. S. A.* **101**, 10584–10589 (2004)

13. A. Corazza, F. Pettirossi, P. Viglino et al., Properties of some variants of human  $\beta_2$ -microglobulin and amyloidogenesis. *J. Biol. Chem.* **279**, 9176–9189 (2004)
14. S. Yamamoto, F. Gejyo, Historical background and clinical treatment of dialysis-related amyloidosis. *Biochim. Biophys. Acta* **1753**, 4–10 (2005)
15. E. Chatani, Y. Goto, Structural stability of amyloid fibrils of  $\beta_2$ -microglobulin in comparison with its native fold. *Biochim. Biophys. Acta* **1753**, 64–75 (2005)
16. D. Ozawa, H. Yagi, T. Ban et al., Destruction of amyloid fibrils of a  $\beta_2$ -microglobulin fragment by laser beam irradiation. *J. Biol. Chem.* **284**, 1009–1017 (2009)
17. T. Eichner, S.E. Radford, Understanding the complex mechanisms of  $\beta_2$ -microglobulin amyloid assembly. *FEBS J.* **278**, 3868–3883 (2011)
18. Y.H. Lee, Y. Goto, Kinetic intermediates of amyloid fibrillation studied by hydrogen exchange methods with nuclear magnetic resonance. *Biochim. Biophys. Acta* **1824**, 1307–1323 (2012)
19. F. Gejyo, T. Yamada, S. Odani et al., A new form of amyloid protein associated with chronic hemodialysis was identified as  $\beta_2$ -microglobulin. *Biochem. Biophys. Res. Commun.* **129**, 701–706 (1985)
20. P.J. Bjorkman, M.A. Saper, B. Samraoui et al., Structure of the human class I histocompatibility antigen, HLA-A2. *Nature* **329**, 506–512 (1987)
21. J. Floege, G. Ehlerding,  $\beta_2$ -microglobulin-associated amyloidosis. *Nephron* **72**, 9–26 (1996)
22. K. Sasahara, H. Yagi, H. Naiki et al., Heat-induced conversion of  $\beta_2$ -microglobulin and hen egg-white lysozyme into amyloid fibrils. *J. Mol. Biol.* **372**, 981–991 (2007)
23. S.-Y. Ow, D.E. Dunstan, The effect of concentration, temperature and stirring on hen egg white lysozyme amyloid formation. *Soft Matter* **9**, 9692–9701 (2013)
24. S. Goda, K. Takano, Y. Yamagata et al., Amyloid protofilament formation of hen egg lysozyme in highly concentrated ethanol solution. *Protein Sci.* **9**, 369–375 (2000)
25. B.A. Vernaglia, J. Huang, E.D. Clark, Guanidine hydrochloride can induce amyloid fibril formation from hen egg-white lysozyme. *Biomacromolecules* **5**, 1362–1370 (2004)
26. Y.X. Lin, Y.H. Lee, Y. Yoshimura et al., Solubility and supersaturation-dependent protein misfolding revealed by ultrasonication. *Langmuir* **30**, 1845–1854 (2014)
27. J.T. Jarrett, P.T. Lansbury Jr., Seeding “one-dimensional crystallization” of amyloid: a pathogenic mechanism in Alzheimer’s disease and scrapie? *Cell* **73**, 1055–1058 (1993)
28. H. Naiki, S. Hashimoto, H. Suzuki et al., Establishment of a kinetic model of dialysis-related amyloid fibril extension *in vitro*. *Amyloid* **4**, 223–232 (1997)
29. T. Ban, K. Yamaguchi, Y. Goto, Direct observation of amyloid fibril growth, propagation, and adaptation. *Acc. Chem. Res.* **39**, 663–670 (2006)
30. L. Giehm, D.E. Otzen, Strategies to increase the reproducibility of protein fibrillation in plate reader assays. *Anal. Biochem.* **400**, 270–281 (2010)
31. Y. Ohhashi, M. Kihara, H. Naiki et al., Ultrasonication-induced amyloid fibril formation of  $\beta_2$ -microglobulin. *J. Biol. Chem.* **280**, 32843–32848 (2005)
32. E. Chatani, Y.H. Lee, H. Yagi et al., Ultrasonication-dependent production and breakdown lead to minimum-sized amyloid fibrils. *Proc. Natl. Acad. Sci. U. S. A.* **106**, 11119–11124 (2009)
33. M. So, H. Yagi, K. Sakurai et al., Ultrasonication-dependent acceleration of amyloid fibril formation. *J. Mol. Biol.* **412**, 568–577 (2011)
34. Y. Yoshimura, Y. Lin, H. Yagi et al., Distinguishing crystal-like amyloid fibrils and glass-like amorphous aggregates from their kinetics of formation. *Proc. Natl. Acad. Sci. U. S. A.* **109**, 14446–14451 (2012)
35. G.P. Saborio, B. Permanne, C. Soto, Sensitive detection of pathological prion protein by cyclic amplification of protein misfolding. *Nature* **411**, 810–813 (2001)
36. P. Saa, J. Castilla, C. Soto, Ultra-efficient replication of infectious prions by automated protein misfolding cyclic amplification. *J. Biol. Chem.* **281**, 35245–35252 (2006)
37. P.B. Stathopoulos, G.A. Scholz, Y.M. Hwang et al., Sonication of proteins causes formation of aggregates that resemble amyloid. *Protein Sci.* **13**, 3017–3027 (2004)
38. H. Naiki, K. Higuchi, M. Hosokawa et al., Fluorometric determination of amyloid fibrils *in vitro* using the fluorescent dye, thioflavin T. *Anal. Biochem.* **177**, 244–249 (1989)

39. L. Goldschmidt, P.K. Teng, R. Riek et al., Identifying the amyloids, proteins capable of forming amyloid-like fibrils. *Proc. Natl. Acad. Sci. U. S. A.* **107**, 3487–3492 (2010)
40. A. Umemoto, H. Yagi, M. So et al., High-throughput analysis of ultrasonication-forced amyloid fibrillation reveals the mechanism underlying the large fluctuation in the lag time. *J. Biol. Chem.* **289**, 27290–27299 (2014)
41. S. Koda, T. Kimura, T. Kondo et al., A standard method to calibrate sonochemical efficiency of an individual reaction system. *Ultrason. Sonochem.* **10**, 149–156 (2003)
42. K. Yamaguchi, T. Matsumoto, K. Kuwata, Proper calibration of ultrasonic power enabled the quantitative analysis of the ultrasonication-induced amyloid formation process. *Protein Sci.* **21**, 38–49 (2012)
43. H. Kitayama, Y. Yoshimura, M. So et al., A common mechanism underlying amyloid fibrillation and protein crystallization revealed by the effects of ultrasonication. *Biochim. Biophys. Acta* **1834**, 2640–2646 (2013)
44. R. Crespo, P.M. Martins, L. Gales et al., Potential use of ultrasound to promote protein crystallization. *J. Appl. Crystallogr.* **43**, 1419–1425 (2010)
45. Y. Yoshimura, K. Sakurai, Y.H. Lee et al., Direct observation of minimum-sized amyloid fibrils using solution NMR spectroscopy. *Protein Sci.* **19**, 2347–2355 (2010)
46. H. Ogi, Y. Tomiyama, Y. Shoji et al., Effects of dissolved and ambient gases on sonochemical degradation of methylene blue in high-amplitude resonant mode. *Jpn. J. Appl. Phys.* **45**, 4678–4683 (2006)
47. J. Dewulf, H. Van Langenhove, A. De Visscher et al., Ultrasonic degradation of trichloroethylene and chlorobenzene at micromolar concentrations: kinetics and modelling. *Ultrason. Sonochem.* **8**, 143–150 (2001)
48. L. Rong, K. Yasuda, Y. Bando et al., Ultrasonic decomposition of a mixture of phenol and p-chlorophenol in aqueous solution. *Jpn. J. Appl. Phys.* **41**, 3272–3276 (2002)
49. T.J. Mason, Sonochemistry and sonoprocessing: the link, the trends and (probably) the future. *Ultrason. Sonochem.* **10**, 175–179 (2003)
50. T. Yu, Z. Wang, T.J. Mason, A review of research into the uses of low level ultrasound in cancer therapy. *Ultrason. Sonochem.* **11**, 95–103 (2004)
51. M.N. Gupta, I. Roy, Enzymes in organic media. Forms, functions and applications. *Eur. J. Biochem.* **271**, 2575–2583 (2004)
52. J.R. Thomas, Sonic degradation of high polymers in solution. *J. Phys. Chem.* **63**, 1725–1729 (1959)
53. E. Webster, Cavitation. *Ultrasonics* **1**, 39–48 (1963)
54. E.K. Hill, B. Krebs, D.G. Goodall et al., Shear flow induces amyloid fibril formation. *Biomacromolecules* **7**, 10–13 (2006)
55. Y. Yoshimura, M. So, H. Yagi et al., Ultrasonication: an efficient agitation for accelerating the supersaturation-limited amyloid fibrillation of proteins. *Jpn. J. Appl. Phys.* **52**, 07HA01 (2013)

# Chapter 3

## In Situ Solid-State NMR Studies of Crystallization Processes

Kenneth D.M. Harris, Colan E. Hughes, and P. Andrew Williams

**Abstract** While solid-state NMR spectroscopy is a versatile technique for studying structural and dynamic properties of solids, adaptation of this technique for in situ monitoring of chemical processes is often associated with technical challenges. In this regard, it is only very recently that an in situ solid-state NMR strategy for monitoring the evolution of crystallization processes has been developed. The early results from the application of this strategy suggest that it is a powerful approach both for identifying the sequence of polymorphic forms (or other solid forms) present as a function of time during crystallization from solution and for discovering new polymorphs. Furthermore, the latest development of this in situ technique (called “CLASSIC NMR”) allows the simultaneous measurement of *both* liquid-state *and* solid-state NMR spectra as a function of time during crystallization, yielding complementary information on the evolution of both the solid and liquid phases. This article describes the foundations of these techniques and presents several examples of applications that highlight the potential of in situ solid-state NMR to deepen our understanding of crystallization processes.

**Keywords** In situ NMR • Crystallization • Polymorphism

### 3.1 Introduction

In the present day, the experimentalist interested in the study of organic crystal chemistry is blessed with the availability of a vast array of experimental techniques that may be exploited to reveal insights into specific aspects of the material of interest. While each individual technique can reveal different (and in many cases unique) information about the properties of the material, solid-state NMR spectroscopy [1, 2] is perhaps the most versatile technique in terms of the wide variety of different types of knowledge that can be obtained, including information on local structural properties, internuclear interactions and dynamic processes

---

K.D.M. Harris (✉) • C.E. Hughes • P.A. Williams  
School of Chemistry, Cardiff University, Park Place, Cardiff, Wales CF10 3AT, UK  
e-mail: [HarrisKDM@cardiff.ac.uk](mailto:HarrisKDM@cardiff.ac.uk)

occurring across a broad range of characteristic timescales. Furthermore, as each NMR-active isotope has a unique set of NMR properties, solid-state NMR studies of different nuclei within a given material give access to different types of NMR experiment and different types of NMR phenomenon, yielding potentially a vast amount of complementary information about the structural and dynamic properties of the material.

However, although solid-state NMR is a powerful and versatile technique for the physico-chemical characterization of solids, adaptation of this technique for in situ studies of chemical processes is often associated with technical challenges. These challenges include the fact that high-resolution solid-state NMR spectra are usually recorded under conditions of rapid sample spinning (at frequencies typically around 10,000 revolutions per second; see Sect. 2) and the fact that the sample is located in a sealed rotor within a confined and relatively inaccessible space inside the magnet of the solid-state NMR spectrometer. For these reasons, the development of in situ solid-state NMR techniques has tended to lag behind the advances that have been made in other in situ experimental strategies (e.g. those based on diffraction, other spectroscopies and microscopy).

Among the various types of chemical process for which the potential advantages of deploying experimental techniques for in situ investigations have been recognized, the study of crystallization processes from solution poses particular challenges as such systems intrinsically comprise two phases (liquid and solid). Crystal growth processes [3, 4] are encountered in many different fields of scientific endeavour and are crucially important in many aspects of chemical, pharmaceutical and biological sciences. Progress towards improving our understanding of crystallization processes has important practical implications, not least the importance of improving our ability to exert control over the polymorphic form of crystals produced in industrial applications. Deepening our fundamental physico-chemical understanding of crystallization relies significantly on the development and application of new experimental strategies, particularly those that allow direct in situ monitoring of the process. In general, crystallization processes are governed by kinetic factors, and metastable polymorphs are often produced rather than the thermodynamically stable polymorph (in this context, polymorphs [5–12] are defined as crystalline materials that have identical chemical composition but different crystal structures). Furthermore, crystallization processes often evolve through a sequence of different solid forms before reaching the final crystallization product, and details of the time evolution of the process can depend critically on the exact conditions of the crystallization experiment. In order to optimize and control crystallization in such situations, it is essential to understand the sequence of events involved in the evolution of the solid form, rather than simply characterizing the final crystalline phase collected at the end of the process. In this regard, exploitation of experimental strategies that allow direct in situ monitoring of crystallization processes is clearly essential. A wide variety of in situ techniques have been used to study crystallization [13], including scattering techniques [e.g. X-ray diffraction (either in energy-dispersive or angular-dispersive mode), small-angle X-ray scattering, neutron diffraction and small-angle neutron scattering],

spectroscopic methods (e.g. infrared, Raman and X-ray absorption spectroscopies) and microscopy (e.g. atomic force microscopy). Until now, however, solid-state NMR spectroscopy has not been used extensively in this regard, presumably as a consequence of the technical challenges discussed above.

In order to make progress to address this issue, our recent research on fundamental aspects of crystallization processes has explored the development of a new in situ solid-state NMR technique [14, 15] for monitoring the evolution of the solid phase during crystallization from solution. This technique has the potential to yield new insights on several issues relating to crystallization processes, particularly concerning the evolution of different polymorphic forms (and interconversion between polymorphs) as a function of time during crystallization. Very recently [16], we further extended this methodology by proposing and demonstrating a strategy for in situ studies of crystallization involving combined liquid-state and solid-state NMR measurements, allowing the evolution of *both* the solid phase *and* the liquid phase to be probed as a function of time during the same crystallization experiment.

This chapter presents an overview of all these recent developments in the in situ monitoring of crystallization processes using NMR spectroscopy.

## 3.2 Essential Background to High-Resolution Solid-State NMR

A basic premise underlying the development of solid-state NMR for in situ studies of crystallization processes is the well-established fact that high-resolution solid-state NMR can be utilized for the identification of different polymorphic forms [11, 17, 18]. In the case of organic solids, for example, the high-resolution solid-state  $^{13}\text{C}$  NMR spectrum should contain one peak for each crystallographically distinguishable carbon atom in the crystal structure (although, in practice, the actual number of *observed* peaks may be less than this number as a consequence of accidental peak overlap). The peak positions (i.e. the isotropic chemical shifts) in the high-resolution solid-state  $^{13}\text{C}$  NMR spectrum depend both on the environment of the  $^{13}\text{C}$  nucleus within the molecule and also on the local environment surrounding the  $^{13}\text{C}$  nucleus within the crystal structure. As a consequence, for a given  $^{13}\text{C}$  site within an organic molecule, the peak positions in high-resolution solid-state  $^{13}\text{C}$  NMR spectra can typically differ within a range of about  $\pm 5$  ppm between different polymorphs (or other solid forms) due to the dependence of the isotropic chemical shift on the crystal structure. Of course, larger differences in peak positions may arise between polymorphs that contain significantly different conformations or different tautomeric forms of the molecule. In the present context, we give only a brief introduction to the experimental methods for measuring high-resolution solid-state NMR spectra of powder samples, which nowadays can be applied relatively routinely on dedicated solid-state NMR spectrometers.

In the case of high-resolution solid-state  $^{13}\text{C}$  NMR of organic solids (at natural isotopic abundance), the primary contributions to line broadening arise from chemical shift anisotropy and from direct  $^{13}\text{C}$ – $^1\text{H}$  dipole–dipole interactions. The line broadening can be effectively eliminated (resulting in high-resolution  $^{13}\text{C}$  NMR spectra) by a combination of rapid magic-angle sample spinning (MAS), typically at spinning frequencies of around 10 kHz, and high-power  $^1\text{H}$  decoupling.

Another experimental technique that is commonly applied in the measurement of high-resolution solid-state  $^{13}\text{C}$  NMR spectra of organic materials is  $^1\text{H} \rightarrow ^{13}\text{C}$  cross polarization (CP) [1, 2, 11]. In this technique, rather than directly exciting the  $^{13}\text{C}$  nuclei followed by detection of the  $^{13}\text{C}$  NMR signal, the procedure is to excite the  $^1\text{H}$  nuclei, followed by transfer of magnetization from the  $^1\text{H}$  nuclei to the  $^{13}\text{C}$  nuclei (i.e. the “cross-polarization” process) and detection of the resulting  $^{13}\text{C}$  NMR signal. In the measurement of high-resolution solid-state  $^{13}\text{C}$  NMR spectra of powder samples, the major benefit of using  $^1\text{H} \rightarrow ^{13}\text{C}$  CP is that it gives a significant enhancement of signal intensity compared to normal  $^{13}\text{C}$  direct excitation. However, as discussed in Sect. 3, in the context of applying high-resolution solid-state  $^{13}\text{C}$  NMR for in situ studies of crystallization from solution, the use of  $^1\text{H} \rightarrow ^{13}\text{C}$  CP has the critical benefit of allowing selective detection of the  $^{13}\text{C}$  NMR signal *only* from the solid component of the heterogeneous solid/liquid system that exists during the crystallization process.

More details of these techniques and other technical aspects of solid-state NMR spectroscopy can be found elsewhere [1, 2].

### 3.3 Experimental Aspects of In Situ Solid-State NMR Studies of Crystallization Processes

Until recently, the prospect of using solid-state NMR for in situ studies of crystallization from solution was limited by the difficulty of securely sealing a fluid phase inside an NMR rotor such that MAS could be carried out at several kHz without problems arising from leakage of the liquid from the rotor. Recently, suitable rotor technology has been developed (Fig. 3.1) for sealing solutions inside NMR rotors for MAS experiments, and this technical development paved the way for the types of experiment described here.

In the in situ solid-state NMR strategy that we have developed for monitoring crystallization processes, a homogeneous (undersaturated) solution is initially prepared inside the NMR rotor at elevated temperature, and crystallization is then induced by decreasing the temperature rapidly to a specific target temperature at which the solution is supersaturated (Fig. 3.2). Crystallization is thermodynamically favoured at the target temperature, and the time dependence of the crystallization process is monitored by repeatedly recording high-resolution solid-state NMR

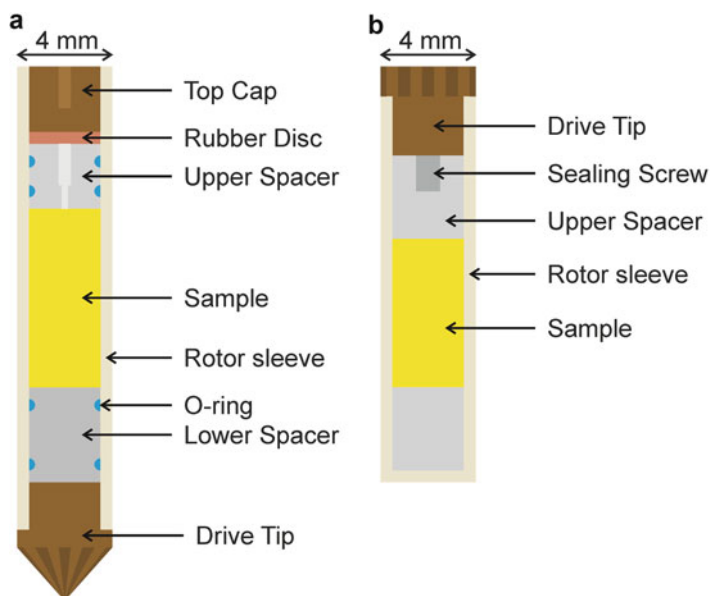


**Fig. 3.1** Examples of designs that have overcome the challenges of sealing liquid-containing samples inside NMR rotors for use in rapid MAS experiments, as required for in situ solid-state NMR studies of crystallization from solution. The rotor designs shown represent schematics of sealing systems used by Varian (*left*) and Bruker (*right*)

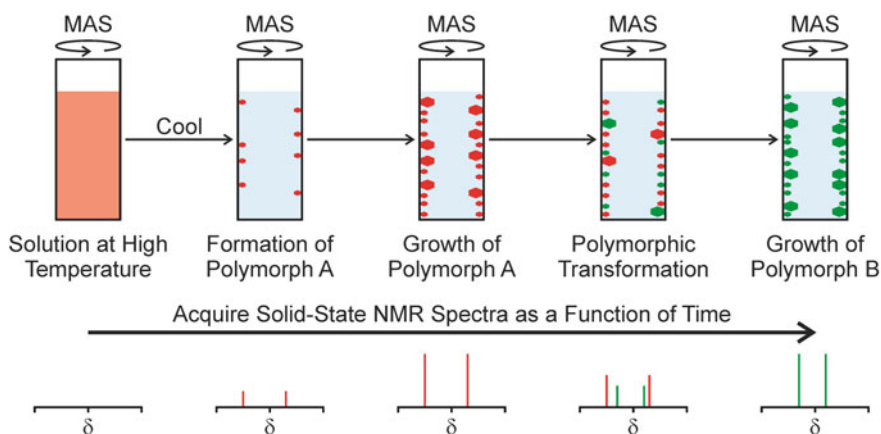


**Fig. 3.2** Schematic of the strategy for in situ solid-state NMR studies of crystallization processes, illustrated by the case of a system in which the crystallization process initially produces a metastable polymorph A (*red*) followed by a polymorphic transformation to produce a more stable polymorph B (*green*). The corresponding changes in the measured solid-state NMR spectrum as a function of time are shown at the bottom

spectra as a function of time. Clearly, the time resolution of the in situ monitoring of the crystallization process depends on the time required to record an individual NMR spectrum of adequate quality to identify and distinguish the different solid forms present during the evolution of the system. As discussed in Sect. 2, sufficiently good spectral resolution is also required in order to identify and assign the solid phases present at different stages of the crystallization process. Clearly, it is desirable to be able to detect and identify the first solid particles produced in the crystallization process, at which stage the amount of solid in the system is generally very low. Thus, optimization of the sensitivity of the measurement is also important, allowing solid-state NMR spectra of adequate quality to be recorded in the shortest possible time. In order to maximize the sensitivity, isotopic labelling of the material to be crystallized is desirable (although not always essential and/or feasible), and carrying out the experiments at high applied magnetic field is clearly also advantageous. For this reason, much of our recent research on the application of the techniques described here has been carried out at the UK National High-Field (850 MHz) Solid-State NMR Facility.

A key feature of our solid-state NMR strategy for in situ studies of crystallization processes is that it exploits the opportunity afforded by NMR of complete selectivity in detecting *only* the solid component in the crystallization system, such that the dissolved solute and solvent remain undetected in the measurement. In the case of organic materials, such discrimination between solid and solution phases may be achieved by recording  $^{13}\text{C}$  NMR spectra under conditions of  $^1\text{H} \rightarrow ^{13}\text{C}$  cross polarization (CP). As a consequence of the differences in the dynamic behaviour of molecules in the solid state and the solution state, measurements under normal conditions for  $^1\text{H} \rightarrow ^{13}\text{C}$  CP give rise to a signal *only* from the solid phase. Thus, even if only a small fraction of the solute has crystallized (e.g. in the early stages of the crystallization experiment), it is only the solid particles that contribute to the measured NMR spectrum, while the dissolved solute molecules (present in much higher amount in the early stages of the crystallization process) are “invisible” to the measurement.

In contrast, for in situ studies of crystallization processes based on X-ray or neutron scattering techniques, scattering occurs *both* from the crystalline solid particles (giving rise to Bragg diffraction peaks) *and* from the solution phase (giving rise to a broad background scattering). As a result, the scattering data may be dominated by the contribution from the solution phase, particularly in the early stages of the crystallization process when the amount of the solid phase is low. Furthermore, it is important to emphasize that, in the in situ solid-state NMR experiment, essentially the entire crystallization system (i.e. the sample inside the NMR rotor) is studied. In the case of in situ X-ray or neutron scattering experiments, on the other hand, a finely focused incident beam is usually used, which interrogates only a fraction of the sample inside the in situ cell.

### 3.4 Applications of In Situ Solid-State NMR to Study Polymorphic Evolution During Crystallization

The first applications of our in situ solid-state NMR technique focused on the crystallization of glycine ( $\text{H}_3^+\text{NCH}_2\text{CO}_2^-$ ) from different solvents. As crystallization of glycine has been very widely studied [19–37], it has acquired the status of a prototypical system in polymorphism research. Under ambient conditions, three polymorphs of glycine (denoted  $\alpha$ ,  $\beta$  and  $\gamma$ ) are known [19–23]. The  $\gamma$  polymorph is the thermodynamically stable form, while the  $\beta$  polymorph is the least stable form [28, 38]. The consensus in the literature is that crystallization from water at neutral pH produces the metastable  $\alpha$  polymorph. However, it was suggested in an early publication [21] that crystallization from deuterated water may promote the formation of the  $\gamma$  polymorph, although systematic studies of this isotope effect were only reported very recently [33, 35], in which it was demonstrated inter alia that deuteration (even at levels as low as 1 %) does indeed lead to a significant increase in the probability of obtaining the  $\gamma$  polymorph. In high-resolution solid-state  $^{13}\text{C}$  NMR spectra, the isotropic peaks for the carboxylate group in the  $\alpha$ ,  $\beta$  and  $\gamma$  polymorphs of glycine are at 176.5, 175.5 and 174.5 ppm, respectively [30], and these peaks are sufficiently well resolved to allow the three polymorphs to be readily distinguished. In contrast, the peaks for the  $\text{CH}_2$  group are not sufficiently well resolved.

Our first demonstration of the in situ solid-state NMR strategy [14] involved crystallization of glycine (for a sample with  $^{13}\text{C}$  labelling in both carbon environments) from water with natural isotopic abundance (Fig. 3.3a). At the earliest

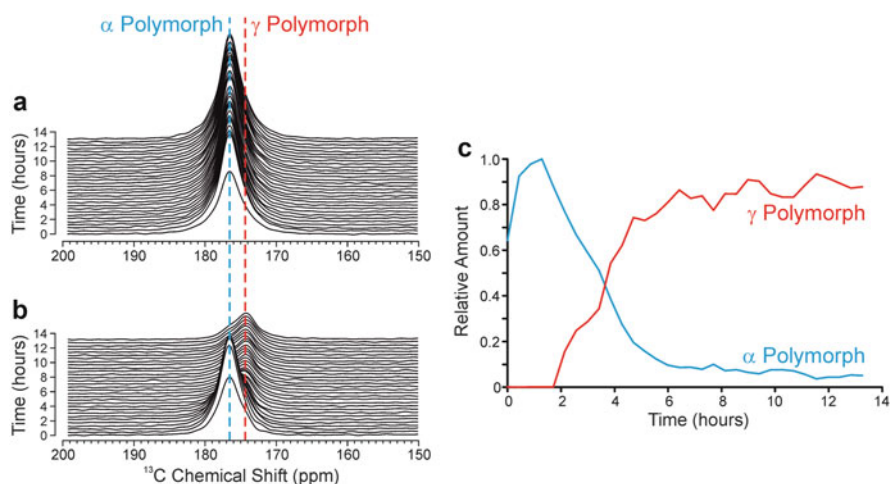


**Fig. 3.3** In situ solid-state  $^{13}\text{C}$  NMR spectra (showing only the carboxylate region) recorded as a function of time during crystallization of glycine from (a)  $\text{H}_2\text{O}$  and (b)  $\text{D}_2\text{O}$ . (c) The relative amounts of the  $\alpha$  (blue) and  $\gamma$  (red) polymorphs of glycine as a function of time during crystallization from  $\text{D}_2\text{O}$ , established from the in situ solid-state  $^{13}\text{C}$  NMR data shown in (b)

stages of the crystallization process, a peak emerges at 176.5 ppm and the intensity increases as a function of time. From the chemical shift, this solid phase is assigned as the  $\alpha$  polymorph. These observations indicate that formation and growth of the  $\alpha$  polymorph occur under these conditions, with no detectable amounts of the  $\beta$  polymorph or  $\gamma$  polymorph observed throughout the duration (13 h) of the experiment.

To explore the isotope effect discussed above, a separate in situ solid-state NMR experiment (Fig. 3.3b) investigated the crystallization of glycine (again for a sample with  $^{13}\text{C}$  labelling in both carbon environments) from deuterated water. In this experiment, the total level of deuteration of all exchangeable hydrogen sites in the system (i.e. the water molecules and the  $\text{NH}_3^+$  group of the zwitterionic glycine molecules) was 86 %. Our in situ solid-state  $^{13}\text{C}$  NMR results indicate that the  $\alpha$  polymorph is again the first solid form produced in the crystallization process, suggesting that the same nucleation pathway is followed in both  $\text{H}_2\text{O}$  and  $\text{D}_2\text{O}$ . The amount of the  $\alpha$  polymorph continues to increase during the first *ca.* 1.5 h of the crystallization process. However, at this time, a new peak emerges in the solid-state  $^{13}\text{C}$  NMR spectrum at 174.5 ppm, characteristic of the  $\gamma$  polymorph. The intensity of this new peak then increases as a function of time, while the intensity of the peak due to the  $\alpha$  polymorph exhibits a concomitant decrease. The relative amounts of the  $\alpha$  and  $\gamma$  polymorphs present as a function of time, established from integrated peak intensities (corrected to allow for the different cross-polarization efficiencies of the  $\alpha$  and  $\gamma$  polymorphs), are shown in Fig. 3.3c. There is no evidence for the presence of any intermediate solid phase in the transformation from the  $\alpha$  polymorph to the  $\gamma$  polymorph, consistent with the rate of increase in the amount of the  $\gamma$  polymorph mirroring the rate of decrease in the amount of the  $\alpha$  polymorph (Fig. 3.3c). Throughout the period after *ca.* 1.5 h, the total amount of solid glycine remains approximately constant. The polymorphic transformation is assigned as a solution-mediated process rather than a direct solid-state phase transition [based, in part, on the observation that a “dry” powder sample of the  $\alpha$  polymorph (i.e. not in contact with a liquid phase) under ambient conditions transforms to the  $\gamma$  polymorph only over a much longer timescale than the duration of the in situ solid-state NMR study]. For each of the two isotopomeric systems, the final polymorph obtained at the end of the in situ solid-state NMR study (i.e. the  $\alpha$  polymorph in the natural abundance system and the  $\gamma$  polymorph in the deuterated system) is consistent with the preferred polymorphic outcome observed in conventional (*ex situ*) laboratory crystallization experiments [35] carried out under the same conditions and over the same total period of time.

Next, we consider the application of the in situ solid-state  $^{13}\text{C}$  NMR strategy to study crystallization of glycine under conditions (from methanol/water) that are anticipated [31] to promote the formation of the  $\beta$  polymorph. The in situ solid-state  $^{13}\text{C}$  NMR spectra recorded as a function of time in this experiment [15] are shown in Fig. 3.4 and selected spectra are shown in Fig. 3.5. In these experiments, the glycine was  $^{13}\text{C}$  labelled only in the carboxylate group, thus eliminating the line broadening due to unresolved  $^{13}\text{C}\cdots^{13}\text{C}$  J-coupling in the double  $^{13}\text{C}$ -labelled sample of glycine used in the experiments described above (thus, the linewidths

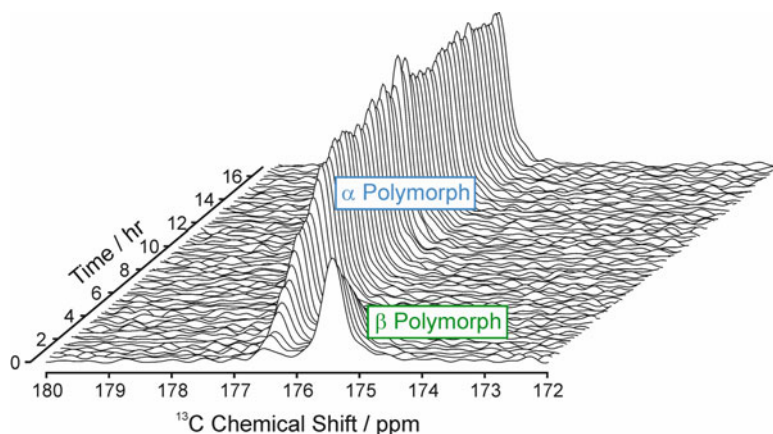


**Fig. 3.4** In situ solid-state  $^{13}\text{C}$  NMR spectra (showing the carboxylate region) recorded as a function of time during crystallization of glycine from water/methanol

in Figs. 3.4 and 3.5 are significantly narrower than those in Fig. 3.3). In the first spectrum recorded (Fig. 3.5a), the solid phase is identified as a virtually pure sample of the  $\beta$  polymorph (with a very small amount of the  $\alpha$  polymorph also present). Thus, it is clear that the very early stages of crystallization yield a significant excess of the  $\beta$  polymorph in this system. Further experiments [15], including ex situ studies to characterize the crystallization products by powder X-ray diffraction, confirmed that a pure sample of the  $\beta$  polymorph is formed immediately on adding methanol to an aqueous solution of glycine. Thus, we can deduce that the low-intensity signal from the  $\alpha$  polymorph observed in the first spectrum in the in situ solid-state NMR study (Fig. 3.5a) emerges *after* the initial crystallization event (but still within the time taken to record the first spectrum in the in situ solid-state  $^{13}\text{C}$  NMR study). The transformation from the  $\beta$  polymorph to the  $\alpha$  polymorph is again assigned as a solution-mediated transformation. Importantly, the results from our in situ solid-state  $^{13}\text{C}$  NMR study allow the timescale of the transformation from the  $\beta$  polymorph to the  $\alpha$  polymorph to be established and indicate that a viable strategy for isolating the  $\beta$  polymorph would be to stop the crystallization experiment at the stage of the initial crystallization product, within only a few minutes of triggering the crystallization process.

Another example of the application of the in situ solid-state NMR strategy to explore polymorphic evolution during crystallization concerns crystallization of *m*-aminobenzoic acid (*m*-ABA) from methanol. Five polymorphs of *m*-ABA have been reported [39, 40]. The crystal structures of four polymorphs (Forms II, III, IV and V) are known, while the crystal structure of Form I has not yet been determined. Interestingly, in Forms I, III and IV, the *m*-ABA molecules exist as zwitterions, whereas in Forms II and V, the *m*-ABA molecules are non-zwitterionic. As shown in Fig. 3.6, each polymorph is uniquely distinguished by its high-resolution solid-state  $^{13}\text{C}$  NMR spectrum, which enables the polymorphs present during the in situ

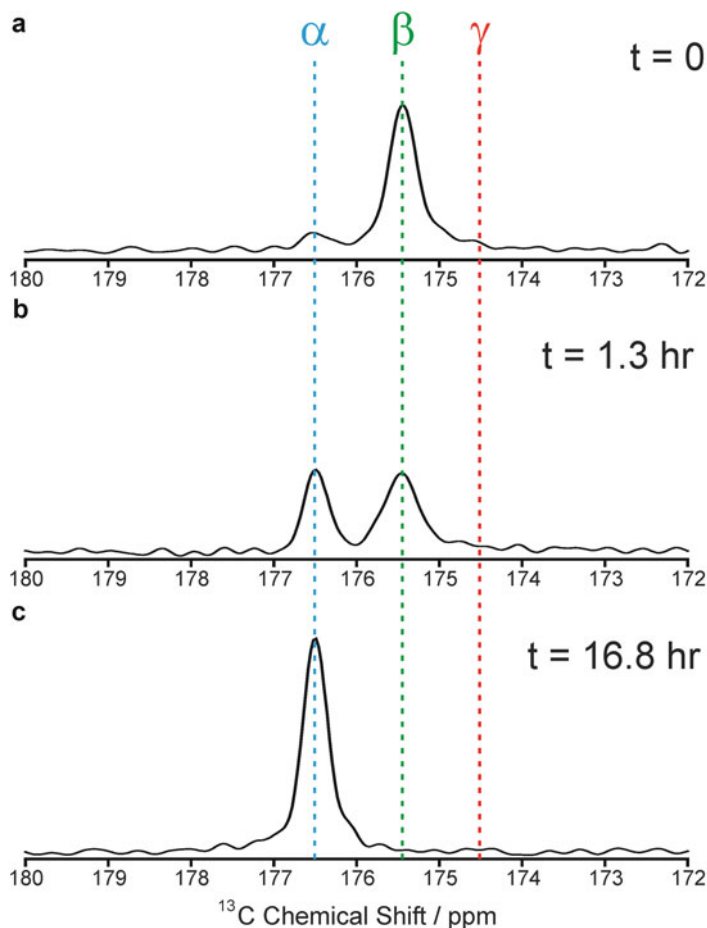


**Fig. 3.5** Selected solid-state  $^{13}\text{C}$  NMR spectra from Fig. 3.4. Dashed lines represent the position of the isotropic peak for the carboxylate group in each of the  $\alpha$ ,  $\beta$  and  $\gamma$  polymorphs

crystallization experiments to be identified [16]. The results from the in situ solid-state  $^{13}\text{C}$  NMR study of crystallization of *m*-ABA from methanol are shown in Fig. 3.7 (left) (focusing on the region of the spectrum for the carboxylate/carboxylic acid group of *m*-ABA) and in Fig. 3.7 (right) (focusing on the region of the spectrum for the aromatic carbons). It is clear from the peak assignments that the first solid form produced during the crystallization process is Form I of *m*-ABA (black dashed lines in Fig. 3.7). Subsequently, a polymorphic transformation occurs to produce Form III (green dashed lines in Fig. 3.7). From *ca.* 9 h after commencing the experiment, the crystallization product is a monophasic sample of Form III.

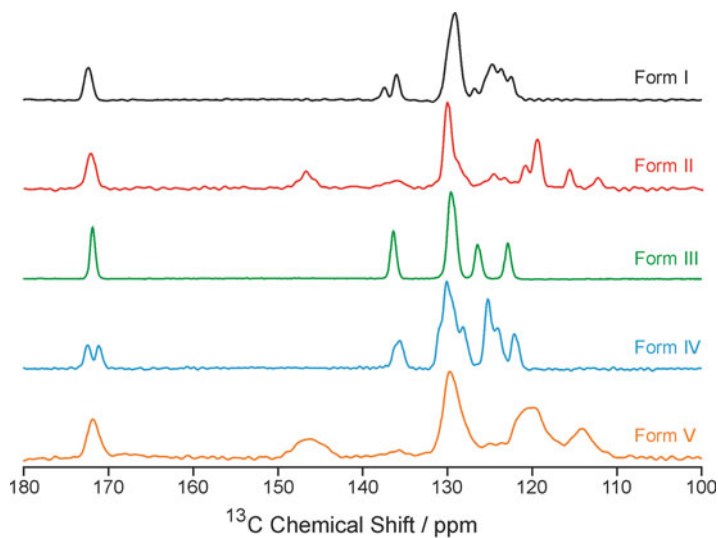


**Fig. 3.6** High-resolution solid-state  $^{13}\text{C}$  NMR spectra recorded for powder samples of the five polymorphs of *m*-ABA

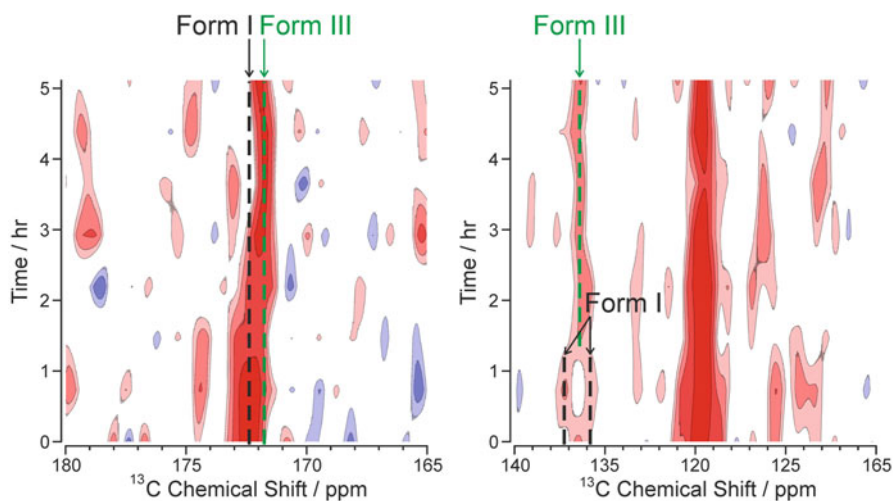


**Fig. 3.7** In situ solid-state  $^{13}\text{C}$  NMR spectra recorded as a function of time during crystallization of *m*-ABA from methanol. *Left*: the region of the spectrum containing the peak for the carboxylate group (the known peak positions for the carboxylate groups in Form I and Form III are highlighted by *dashed lines*). *Right*: the region of the spectrum containing the peaks for the aromatic ring (the known peak positions for C3, the carbon directly bonded to the  $\text{NH}_3^+$  group, in Form I and Form III are highlighted by *dashed lines*). Intensity contour intervals are defined on a logarithmic scale, with the same scale used both for contours of positive intensity (*red shades*) and contours of negative intensity (*blue shades*)

### 3.5 Applications of In Situ Solid-State NMR for Polymorph Discovery

The examples discussed in the previous section demonstrated the capability of the in situ solid-state NMR strategy to observe transient polymorphic forms on the pathway to the final crystallization product in cases for which the transient polymorphs were already *known* and well characterized. Clearly, the in situ solid-state NMR technique also affords the opportunity to reveal the existence of new (previously unknown) polymorphs, and the technique therefore has the potential to have an impact within the domain of polymorph discovery [41]. Furthermore, in such cases, the results from in situ solid-state NMR studies provide insights on the specific crystallization parameters required to produce each new polymorph observed, including the appropriate “time window” during which a specific new polymorph is present.

As an example, we consider hydrogen-bonded co-crystals formed between even-chain  $\alpha,\omega$ -dihydroxyalkanes and urea (in 1:2 molar ratio). These co-crystals have been reported previously [42] for  $\alpha,\omega$ -dihydroxyalkanes  $\text{HO}(\text{CH}_2)_n\text{OH}$  with  $n = 6, 8, 10, 12, 14$  and  $16$ . The crystal structures (Fig. 3.8) contain double-stranded, hydrogen-bonded ribbons of urea molecules. Adjacent ribbons are linked by hydrogen bonding to the  $\alpha,\omega$ -dihydroxyalkane molecules, resulting in a ladderlike arrangement. The observed crystal structures can be subdivided into three well-defined structure types (Fig. 3.8) characterized by the following features: (1) the two strands of the hydrogen-bonded urea ribbon are either *parallel* [observed only for 1,8-dihydroxyoctane-(urea)<sub>2</sub>] or *antiparallel* [observed for all other  $\alpha,\omega$ -dihydroxyalkane-(urea)<sub>2</sub> co-crystals studied], and (2) the angle between the axis of the  $\alpha,\omega$ -dihydroxyalkane molecule and the positive direction of the urea strand is either *acute* [observed for 1,6-dihydroxyhexane-(urea)<sub>2</sub> and 1,8-dihydroxyoctane-(urea)<sub>2</sub>] or *obtuse* [observed for all other  $\alpha,\omega$ -dihydroxyalkane-(urea)<sub>2</sub> co-crystals studied]. In spite of the structural diversity exhibited by this family of materials, however, no polymorphism has been observed for any member of the family. Thus, for a given  $\alpha,\omega$ -dihydroxyalkane, only *one* of the three structure types of  $\alpha,\omega$ -dihydroxyalkane-(urea)<sub>2</sub> co-crystals has been observed.

Here we focus on crystallization of the 1,10-dihydroxydecane/urea system. Our in situ solid-state <sup>13</sup>C NMR study [41] of the co-crystallization of urea and 1,10-dihydroxydecane from methanol was carried out under conditions known to promote the formation of the 1:2 co-crystal rather than the conventional urea inclusion compound [43–49] (in which the 1,10-dihydroxydecane molecules are located as “guests” inside the one-dimensional tunnels in a hydrogen-bonded urea “host” structure). In these experiments, <sup>13</sup>C-labelled urea was used in order to enhance the sensitivity of the measurement. The time resolution of the in situ study, dictated by the time taken to record a single <sup>13</sup>C NMR spectrum, was 2.67 min.

The results of the in situ solid-state <sup>13</sup>C NMR study are shown in Fig. 3.9, focusing on the region of the solid-state <sup>13</sup>C NMR spectrum containing the peak for the <sup>13</sup>C site in urea (we note that, in high-resolution solid-state <sup>13</sup>C NMR studies

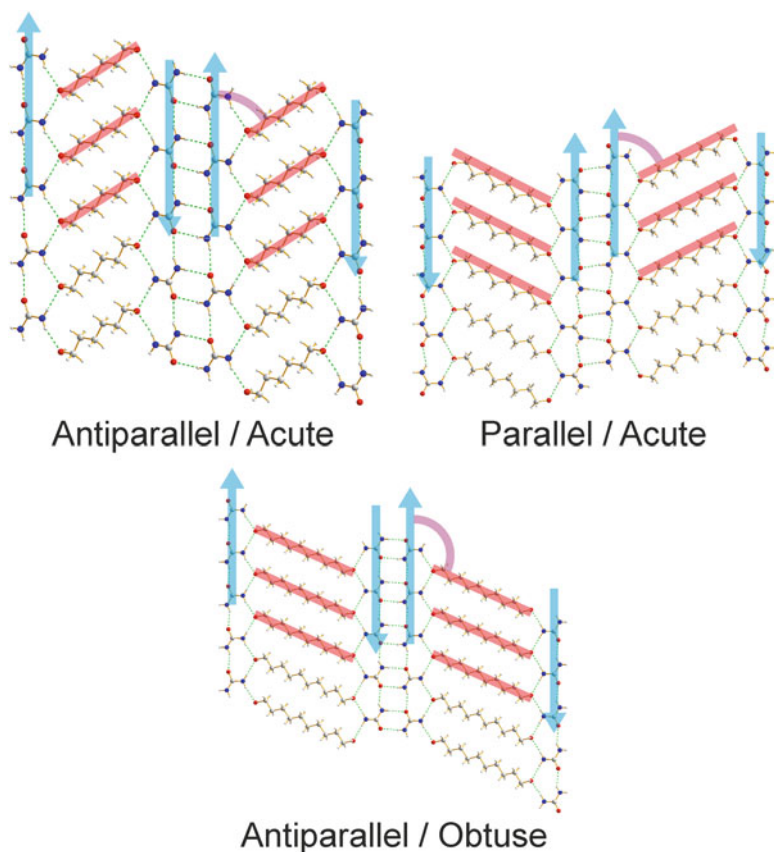


**Fig. 3.8** Examples of the three structure types observed for co-crystals of urea and  $\alpha,\omega$ -dihydroxyalkanes, illustrated by 1,6-dihydroxyhexane-(urea)<sub>2</sub> (*antiparallel/acute*, top left), 1,8-dihydroxyoctane-(urea)<sub>2</sub> (*parallel/acute*, top right), and 1,10-dihydroxydecane-(urea)<sub>2</sub> (*antiparallel/obtuse*, bottom)

of materials containing urea, the peak for the  $^{13}\text{C}$  site in urea often exhibits an asymmetric line shape as a consequence of second-order quadrupolar effects [50] from the directly bonded  $^{14}\text{N}$  nuclei). The first spectrum recorded has a single isotropic peak at 164.12 ppm, which grows in intensity during the subsequent 40 min. At this stage, a new peak at 164.58 ppm appears suddenly and then grows rapidly in intensity. The new peak corresponds to the known 1,10-dihydroxydecane-(urea)<sub>2</sub> co-crystal, which has the *antiparallel/obtuse* structure type. After the peak due to the known co-crystal phase appears, the peak due to the initially observed solid phase cannot be monitored because these peaks overlap significantly and because the intensity of the peak for the known co-crystal increases very rapidly. At the end of the in situ crystallization experiment (11.4 h), only the peak at 164.58 ppm is present. Ex situ powder X-ray diffraction analysis of the solid phase

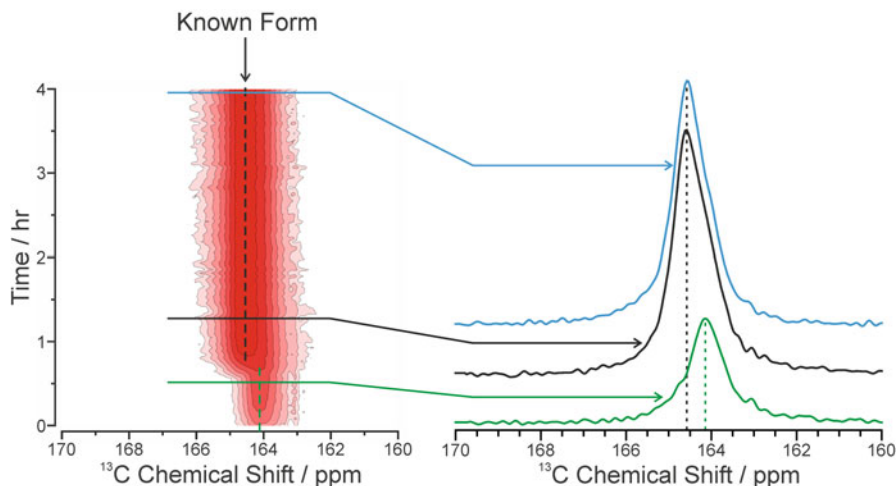


**Fig. 3.9** In situ solid-state  $^{13}\text{C}$  NMR spectra (showing the region of the spectrum containing the peak for urea) recorded as a function of time during co-crystallization of 1,10-dihydroxydecane and  $^{13}\text{C}$ -labelled urea from methanol. Intensity contour intervals are defined on a logarithmic scale

collected at the end of the in situ solid-state NMR experiment confirms that the final crystallization product (corresponding to the peak at 164.58 ppm) is indeed a monophasic sample of the known 1,10-dihydroxydecane-(urea) $_2$  co-crystal phase with the *antiparallel/obtuse* structure type.

The in situ solid-state  $^{13}\text{C}$  NMR results reveal clearly that a transient solid form is present in the early stages of crystallization, preceding the formation of the known 1,10-dihydroxydecane-(urea) $_2$  co-crystal phase, and it is clear that the transient solid form contains urea. In these experiments, the  $^{13}\text{C}$  NMR spectrum is dominated by the contribution from  $^{13}\text{C}$ -labelled urea, and the conditions of the measurement were not optimized for detecting the substantially weaker contribution from the unlabelled 1,10-dihydroxydecane. Significantly, however, summation of all solid-state  $^{13}\text{C}$  NMR spectra recorded during the first 40 min of the experiment shows a weak (but unambiguous) set of peaks characteristic of 1,10-dihydroxydecane, suggesting that the transient solid form contains both urea and 1,10-dihydroxydecane. Comparison of the measured  $^{13}\text{C}$  chemical shift (164.12 ppm) for urea in the transient solid form with the  $^{13}\text{C}$  chemical shifts for urea in different materials provides further insights into the identity of the transient solid form. First, the possibility that the transient solid form is either the conventional 1,10-dihydroxydecane/urea inclusion compound (165.05 ppm) or pure solid urea (162.9 ppm) can be ruled out. Second, as discussed above, the family of  $\alpha,\omega$ -dihydroxyalkane-(urea) $_2$  co-crystals can be subdivided into three structure types. The isotropic  $^{13}\text{C}$  chemical shifts for urea in representative examples of each of the three structure types are *antiparallel/acute*, 164.29 ppm [1,6-dihydroxyhexane-(urea) $_2$ ]; *parallel/acute*, 164.06 ppm [1,8-dihydroxyoctane-(urea) $_2$ ]; and *antiparallel/obtuse*, 164.58 ppm

[1,10-dihydroxydecane-(urea)<sub>2</sub>]. Significantly, the isotropic <sup>13</sup>C chemical shift for urea in the transient solid form observed in the early stages of crystallization in the 1,10-dihydroxydecane/urea system (164.12 ppm) closely matches the isotropic <sup>13</sup>C chemical shift for urea in the 1,8-dihydroxyoctane-(urea)<sub>2</sub> co-crystal (164.06 ppm), from which we may suggest that the transient solid form present in the early stages of the crystallization process may be a 1,10-dihydroxydecane-(urea)<sub>2</sub> co-crystal with the *parallel/acute* structure type.

As a second example of polymorph discovery, we consider an in situ solid-state <sup>31</sup>P NMR study of crystallization of methyldiphenylphosphine oxide (MDPPO, Fig. 3.10) from toluene. Initially, we note that only one crystal structure of MDPPO has been reported in the literature [51]. In the in situ study, <sup>31</sup>P NMR spectra were recorded using <sup>1</sup>H → <sup>31</sup>P CP (allowing selective detection of the solid phase in the crystallization process) and high-power <sup>1</sup>H decoupling. The high-resolution solid-state <sup>31</sup>P NMR spectrum of a powder sample of the known solid form of MDPPO has a single peak at 30.78 ppm. The in situ solid-state <sup>31</sup>P NMR study of crystallization from toluene involved the measurement of 327 spectra consecutively over 17.4 h (3.2 min per spectrum). As shown in Fig. 3.10, it is advantageous to focus on the time evolution of the first-order spinning sideband at higher chemical shift than the isotropic peak, as this spinning sideband is the most intense peak of the spinning sideband manifold. From Fig. 3.10 (which shows the first 16 spectra recorded in the experiment), it is clear that crystallization had already commenced by the time of recording the first spectrum and all spectra are dominated by the intense peak (at 65.6 ppm) corresponding to the known solid form of MDPPO. However, careful inspection of the spectra reveals that two additional peaks of much lower intensity are also present in the spectrum in the early stages of the crystallization process, with first-order spinning sidebands at 63.7 ppm and 64.5 ppm (corresponding to isotropic peaks at 28.8 ppm and 29.6 ppm, respectively). As only one crystalline

**Fig. 3.10** In situ solid-state <sup>31</sup>P NMR spectra recorded as a function of time during crystallization of MDPPO from toluene, showing the first spinning sidebands at higher chemical shift than the isotropic peaks. Intensity contour intervals are defined on a logarithmic scale

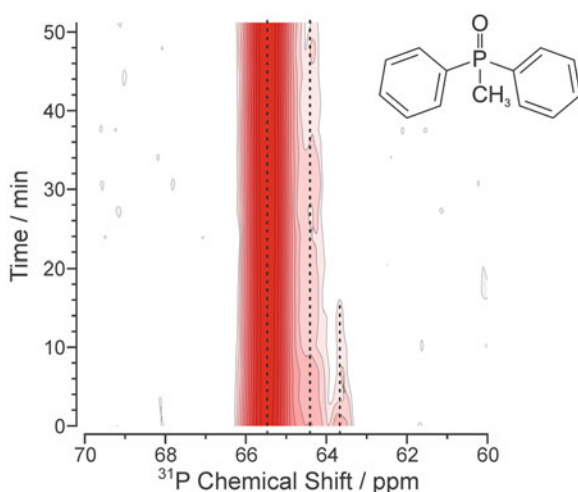
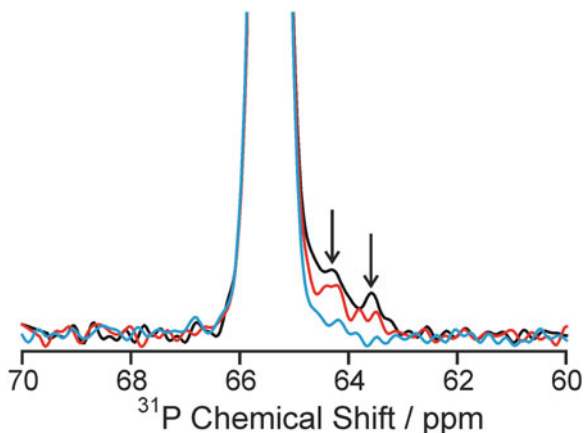


**Fig. 3.11** Individual solid-state  $^{31}\text{P}$  NMR spectra recorded during crystallization of MDPPO from toluene, showing the first spinning sidebands at higher chemical shift than the isotropic peaks. The spectra were recorded after 9.6 min (black), 35 min (red) and 16 h (blue). Arrows indicate the two peaks due to new solid forms



phase of MDPPO has been reported, these two peaks must clearly represent new solid forms of MDPPO produced at a very early stage of the crystallization process. The intensity of the new peaks is highest in the first spectrum recorded and then diminishes as a function of time (see Fig. 3.11). The assignment that these two peaks represent *different* solid forms (rather than a single solid phase with two distinguishable  $^{31}\text{P}$  environments) is inferred from the fact that the intensities of these peaks decay at significantly different rates. Thus, the peak at 63.7 ppm becomes indiscernible after *ca.* 16 min, whereas the peak at 64.5 ppm is observed until *ca.* 6 h. From the  $^{31}\text{P}$  NMR results, we cannot rule out the possibility that one or both of these new solid forms could be a toluene solvate of MDPPO (however, it is noted that no toluene solvate of MDPPO has been reported previously).

In addition to revealing the existence of new solid forms of MDPPO, the results of the in situ solid-state  $^{31}\text{P}$  NMR study also indicate the conditions (particularly the time window) under which each of these new solid forms exists during the crystallization process. In principle, this information may be used to design experimental protocols in which crystallization is arrested at a specific time to allow crystals of the new solid forms to be collected. However, in the case of MDPPO, this task is challenging as the two new solid forms always exist concomitantly with the known polymorph and in substantially smaller amounts than the known polymorph.

### 3.6 Combined Liquid- and Solid-State In Situ Crystallization NMR: “CLASSIC NMR”

The in situ solid-state NMR strategy described above has been shown to be a powerful approach for establishing the sequence of solid phases produced during crystallization (inter alia, indicating the time period in which each transient solid phase is present) and for the discovery of new polymorphs. Our most recent

development of the in situ NMR technique, which has the potential to yield significantly deeper insights into crystallization processes than the version described above, exploits the fact that NMR spectroscopy is able to study *both* the liquid phase *and* the solid phase in a heterogeneous solid/liquid system *using the same instrument*, simply by changing the pulse sequence used to record the NMR data. Specifically, by alternating between two different pulse sequences in an in situ NMR study of crystallization, alternate solid-state NMR and liquid-state NMR spectra are recorded, yielding essentially simultaneous information on the time evolution of *both* the solid phase *and* the liquid phase during the crystallization process (Fig. 3.12). This strategy is called “CLASSIC NMR” (Combined Liquid-And Solid-State In situ Crystallization NMR). Significantly, the CLASSIC NMR experiment can be carried out on any standard solid-state NMR spectrometer, without requiring modification of the instrumentation.

The aim of the CLASSIC NMR experiment is to elucidate the complementary changes that occur in the solid phase and in the liquid phase as a function of time during the crystallization process. The time evolution of the crystallization in terms of both the amount and the polymorphic identity of the solid phase present is established from the solid-state NMR spectra. Concomitantly, the solution phase becomes more dilute as crystallization proceeds, and the changes in the solution-state speciation and the modes of molecular aggregation in solution are monitored from the time evolution of the liquid-state NMR spectrum.

In the CLASSIC NMR experiment, spectra are recorded using an alternating cycle of two pulse sequences (Fig. 3.12). The key requirement is that one pulse sequence is selective for detecting a signal from the solid phase (ideally with

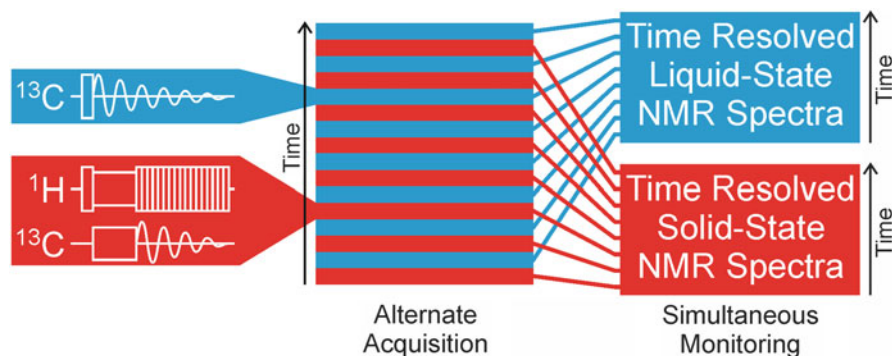


**Fig. 3.12** Schematic of the CLASSIC NMR experiment, in which NMR spectra are recorded in situ as a function of time during the crystallization process using two alternating pulse sequences. One pulse sequence (*red*) detects the solid phase selectively and the other pulse sequence (*blue*) detects the liquid phase selectively. After completion of the experiment, the two sets of data are separated to give a time-resolved set of solid-state NMR spectra (*red*) and a time-resolved set of liquid-state NMR spectra (*blue*). Thus, the CLASSIC NMR experiment effectively allows simultaneous monitoring of the evolution of *both* the solid phase *and* the liquid phase as a function of time during the crystallization process

the liquid phase “invisible” to the measurement) and the other pulse sequence is selective for detecting a signal from the liquid phase (ideally with the solid phase “invisible” to the measurement). Clearly, the details of the specific pulse sequences selected for the solid-state and liquid-state measurements may depend on the specific system under investigation.

The advantages of the CLASSIC NMR strategy have been demonstrated [16] in a  $^{13}\text{C}$  NMR study of crystallization of *m*-aminobenzoic acid (*m*-ABA) from dimethyl sulfoxide (DMSO). As described in Sect. 4, there are five known polymorphs of *m*-ABA. Each polymorph of *m*-ABA is uniquely distinguished by its high-resolution solid-state  $^{13}\text{C}$  NMR spectrum (see Fig. 3.6), enabling the polymorphs present in in situ crystallization experiments to be identified.

In the CLASSIC NMR study of crystallization of *m*-ABA from DMSO, the high-resolution solid-state  $^{13}\text{C}$  NMR spectrum was recorded using  $^1\text{H} \rightarrow ^{13}\text{C}$  CP with high-power  $^1\text{H}$  decoupling, allowing selective detection of the signal only from the solid phase. To record the liquid-state  $^{13}\text{C}$  NMR spectrum, a direct-excitation  $^{13}\text{C}$  NMR pulse sequence was used, with no  $^1\text{H}$  decoupling and with a relatively short recycle delay (of the magnitude typically used to record liquid-state NMR spectra). The absence of  $^1\text{H}$  decoupling and the short recycle delay ensure that no significant signal is detected from the solid phase. The solution of *m*-ABA in DMSO was initially held at 120 °C for 1 h to ensure complete dissolution and then cooled to 33 °C over *ca.* 15 min. The CLASSIC NMR strategy was then applied for a total time of 15 h. The time to record each solid-state  $^{13}\text{C}$  NMR spectrum was 38.4 min, and the time to record each liquid-state  $^{13}\text{C}$  NMR spectrum was 6.4 min. Thus, the effective time resolution for the CLASSIC NMR study was 44.8 min. In extensive *ex situ* tests of crystallization of *m*-ABA from DMSO under normal laboratory conditions, only Form I was observed as the final crystallization product.

The evolution of the solid-state  $^{13}\text{C}$  NMR spectrum in the CLASSIC NMR experiment is shown in Fig. 3.13. The first solid-state signal emerged *ca.* 2 h after commencing the experiment, signifying the start of crystallization. From the  $^{13}\text{C}$  chemical shifts, the solid phase is assigned as Form I of *m*-ABA. The total integrated intensity of the solid-state  $^{13}\text{C}$  NMR spectrum then increased monotonically with time (Fig. 3.14), indicating an increase in the amount of solid, levelling off at *ca.* 8 h. No change in  $^{13}\text{C}$  chemical shifts was observed with time, indicating that only Form I was present during the crystallization process and no polymorphic transformation was observed within the duration of the experiment.

The liquid-state  $^{13}\text{C}$  NMR spectra recorded in the CLASSIC NMR experiment contain sharp peaks for each of the seven  $^{13}\text{C}$  environments in the *m*-ABA molecule, and only the J-coupling to directly bonded  $^1\text{H}$  nuclei is resolved. Time-dependent changes in the concentration of *m*-ABA in the solution phase can be monitored from the total integral of the liquid-state  $^{13}\text{C}$  NMR spectrum. As shown in Fig. 3.14, this integral is constant until the time (*ca.* 2 h) at which the first signal was observed in the solid-state  $^{13}\text{C}$  NMR spectrum. The total integral then decreases with time, before reaching a constant value at *ca.* 8 h.

Significantly, the results from both the solid-state and liquid-state components of the CLASSIC NMR data are in excellent agreement, concurring that crystallization

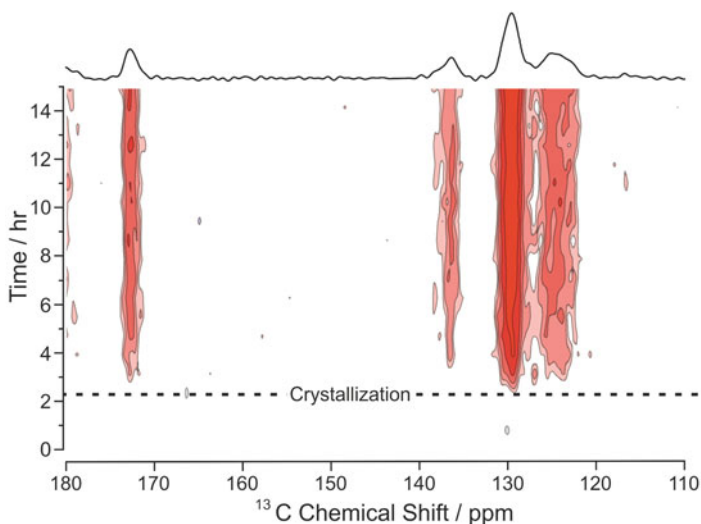
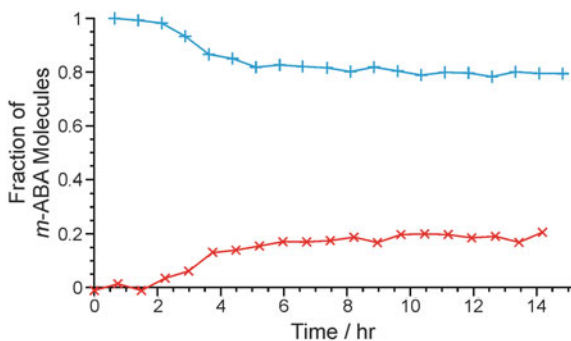


**Fig. 3.13** Solid-state component of the CLASSIC  $^{13}\text{C}$  NMR data recorded for crystallization of *m*-ABA from DMSO. The sum of all spectra (shown at top) is identified as Form I of *m*-ABA, with no evidence that any other polymorph was present during the crystallization process

**Fig. 3.14** Fraction of *m*-ABA molecules in the liquid (blue, + marks) and solid (red, × marks) phases as a function of time, established from the integrals of the liquid-state and solid-state components of the CLASSIC NMR data, respectively



commenced *ca.* 2 h after the start of the experiment. Crystal growth then continued for the next *ca.* 6 h. Thereafter, the total amounts of *m*-ABA in the liquid and solid phases showed no further evolution with time suggesting that, by this stage, the system comprised an equilibrium saturated solution.

A more detailed interpretation of the changes in the liquid phase during the crystallization process can be gained from analysis of changes in the peak positions in the liquid-state  $^{13}\text{C}$  NMR spectrum as a function of time. Figure 3.15 shows the  $^{13}\text{C}$  chemical shift for each  $^{13}\text{C}$  site in the *m*-ABA molecule as a function of time relative to the corresponding value at the start of the CLASSIC NMR measurement. At the start of the measurement, the system is a supersaturated solution. After crystallization begins, the supersaturation decreases with time, and by the end of the crystallization process, the system is an equilibrium saturated solution. It is

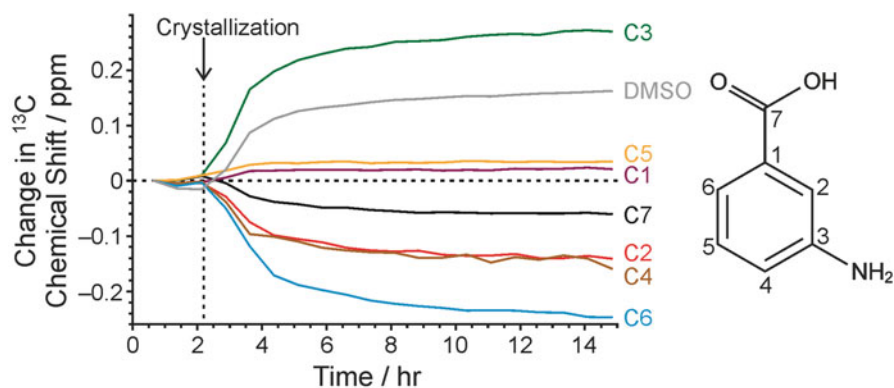


**Fig. 3.15** Evolution of  $^{13}\text{C}$  chemical shifts in the liquid-state component of the CLASSIC  $^{13}\text{C}$  NMR data recorded for crystallization of *m*-ABA from DMSO. The vertical dashed line indicates the time at which crystallization commenced (see also Fig. 3.13)

known from independent studies [52] that, in an equilibrium saturated solution of *m*-ABA in DMSO, the *m*-ABA molecules exist in the non-zwitterionic form. From this knowledge, and by rationalizing the change in the  $^{13}\text{C}$  chemical shift for each  $^{13}\text{C}$  site in *m*-ABA observed as a function of time during the CLASSIC NMR experiment, significant insights can be gained on the nature of the supersaturated solution that exists at the start of the crystallization experiment.

As discussed in detail in the original paper [16], the observed changes in  $^{13}\text{C}$  chemical shifts as a function of time during the crystallization process are consistent with the supersaturated solution of *m*-ABA in DMSO at the start of the crystallization experiment having (a) a higher proportion of zwitterionic *m*-ABA molecules and/or (b) a higher proportion of non-zwitterionic *m*-ABA molecules present in hydrogen-bonded aggregates, relative to a saturated solution of *m*-ABA in DMSO. Both scenarios (a) and (b) represent an increased degree of protonation of the  $\text{NH}_2$  group of *m*-ABA, leading to increased positive charge on the N atom and promoting the specific changes in  $^{13}\text{C}$  chemical shifts observed. Although the crystal structure of Form I of *m*-ABA has not yet been determined, the *m*-ABA molecules are known [from N(1 s) XPS studies] to be zwitterionic [40] and clearly either situation (a) or situation (b) is a plausible solution-state precursor to the  $\text{O}^- \cdots \text{H}-\text{N}^+$  hydrogen bonds that must exist between *m*-ABA zwitterions in the crystal structure of Form I. Although it is not possible from the available evidence to distinguish whether situation (a) or situation (b) is predominant, the results nevertheless give clear insights into the nature of the speciation and interactions that exist in the supersaturated pre-nucleation solution of *m*-ABA in DMSO prior to crystallization, relative to those in the saturated solution at the end of the crystallization process.

Furthermore, the change in the  $^{13}\text{C}$  chemical shift for the solvent DMSO as a function of time in the liquid-state component of the CLASSIC NMR data

(Fig. 3.15) can be rationalized straightforwardly. As DMSO has no hydrogen-bond donor group, the only strong hydrogen bonds that DMSO can form in the *m*-ABA/DMSO solution are hydrogen bonds involving *m*-ABA molecules as the donor and DMSO molecules as the acceptor. As the concentration of *m*-ABA decreases during the crystallization process, there must be a corresponding decrease in the proportion of DMSO molecules engaged as the acceptor in hydrogen bonds with *m*-ABA molecules, resulting in the observed  $^{13}\text{C}$  chemical shift of DMSO becoming progressively more positive as a function of time.

### 3.7 Future Prospects

The results from the applications of the in situ solid-state NMR strategy described in this chapter suggest that the technique has considerable scope and potential for characterizing the evolution of the solid phase during crystallization processes, including the capability to observe the formation and transformation of transient polymorphs and to enable the discovery of new polymorphs. This technique offers new opportunities for directly monitoring the time evolution of crystallization processes, yielding new fundamental insights that could not be gained from ex situ analysis of the final solid product recovered from the crystallization experiment. Importantly, the in situ solid-state NMR technique gives insights not only on the crystallization conditions required to produce new solid forms but also yields knowledge of the specific time window during which each new solid form is present during the crystallization process. Furthermore, the recently developed CLASSIC NMR experiment extends significantly the scope and capability of in situ monitoring of crystallization processes, as it is unique in providing simultaneous and complementary information on the time evolution of *both* the solid phase *and* the liquid phase. We fully anticipate that the advantages of the CLASSIC NMR strategy will yield significant new insights on a wide range of crystallization systems in the future.

**Acknowledgements** We are grateful to the UK 850 MHz Solid-State NMR Facility for the award of significant amounts of time for in situ NMR studies of crystallization processes. This facility is funded by EPSRC, BBSRC and the University of Warwick, including part funding through Birmingham Science City Advanced Materials Projects 1 and 2 supported by Advantage West Midlands and the European Regional Development Fund. We particularly appreciate the assistance of the Facility Manager, Dr Dinu Iuga.

### References

1. D.C. Apperley, R.K. Harris, P. Hodgkinson, *Solid State NMR: Basic Principles & Practice* (Momentum Press LLC, New York, 2012)

2. M.J. Duer, *Introduction to Solid-State NMR Spectroscopy* (Blackwell Publishing Ltd., Oxford, 2004)
3. B. Kahr, J.M. McBride, *Angew. Chem. Int. Ed.* **31**, 1–26 (1992)
4. *Crystal Growth and Nucleation*, Faraday Discuss., Vol. 136 (RSC Publishing, 2007)
5. J.D. Dunitz, *Pure Appl. Chem.* **63**, 177–185 (1991)
6. J. Bernstein, *Polymorphism in Molecular Crystals*. IUCr Monographs on Crystallography (Oxford University Press, Oxford, 2002)
7. R.J. Davey, *Chem. Commun.*, 1463–1467 (2003)
8. J. Bernstein, *Chem. Commun.*, 5007–5012 (2005)
9. S. Chen, H. Xi, L. Yu, *J. Am. Chem. Soc.* **127**, 17439–17444 (2005)
10. S. Ahn, F. Guo, B.M. Kariuki, K.D.M. Harris, *J. Am. Chem. Soc.* **128**, 8441–8452 (2006)
11. R.K. Harris, *Analyst* **131**, 351–373 (2006)
12. S.L. Price, *Acc. Chem. Res.* **42**, 117–126 (2008)
13. N. Pienack, W. Bensch, *Angew. Chem. Int. Ed.* **50**, 2014–2034 (2011)
14. C.E. Hughes, K.D.M. Harris, *J. Phys. Chem. A* **112**, 6808–6810 (2008)
15. C.E. Hughes, K.D.M. Harris, *Chem. Commun.* **46**, 4982–4984 (2010)
16. C.E. Hughes, P.A. Williams, K.D.M. Harris, *Angew. Chem. Int. Ed.* **53**, 8939–8943 (2014)
17. G.E. Balimann, C.J. Groombridge, R.K. Harris, K.J. Packer, B.J. Say, S.F. Tanner, *Philos. Trans. R. Soc. A* **299**, 643–663 (1981)
18. K.D.M. Harris, J.M. Thomas, *J. Solid State Chem.* **94**, 197–205 (1991)
19. G. Albrecht, R.B. Corey, *J. Am. Chem. Soc.* **61**, 1087–1103 (1939)
20. Y. Iitaka, *Acta Crystallogr.* **13**, 35–45 (1960)
21. Y. Iitaka, *Acta Crystallogr.* **14**, 1–10 (1961)
22. P.-G. Jönsson, Å. Kvik, *Acta Crystallogr. Sect. B* **28**, 1827–1833 (1972)
23. Å. Kvik, W.M. Canning, T.F. Koetzle, G.J.B. Williams, *Acta Crystallogr. Sect. B* **36**, 115–120 (1980)
24. B.A. Garetz, J. Matic, A.S. Myerson, *Phys. Rev. Lett.* **89**, 175501 (2002)
25. V.A. Drebuschak, E.V. Boldyreva, T.N. Drebuschak, E.S. Shutova, *J. Cryst. Growth* **241**, 266–268 (2002)
26. T.N. Drebuschak, E.V. Boldyreva, E.S. Shutova, *Acta Crystallogr. Sect. E* **58**, o634–o636 (2002)
27. E.S. Ferrari, R.J. Davey, W.I. Cross, A.L. Gillon, C.S. Towler, *Cryst. Growth Des.* **3**, 53–60 (2003)
28. E.V. Boldyreva, V.A. Drebuschak, T.N. Drebuschak, I.E. Paukov, Y.A. Kovalevskaya, E.S. Shutova, *J. Therm. Anal. Calorim.* **73**, 409–418 (2003)
29. C.S. Towler, R.J. Davey, R.W. Lancaster, C.J. Price, *J. Am. Chem. Soc.* **126**, 13347–13353 (2004)
30. R.A. Taylor, *Concepts Magn. Reson.* **22A**, 79–89 (2004)
31. I. Weissbuch, V.Y. Torbeev, L. Leiserowitz, M. Lahav, *Angew. Chem. Int. Ed.* **44**, 3226–3229 (2005)
32. M. Xu, K.D.M. Harris, *J. Phys. Chem. B* **111**, 8705–8707 (2007)
33. C.E. Hughes, S. Hamad, K.D.M. Harris, C.R.A. Catlow, P.C. Griffiths, *Faraday Discuss.* **136**, 71–89 (2007)
34. S.K. Poornachary, P.S. Chow, R.B.H. Tan, *Cryst. Growth Des.* **8**, 179–185 (2007)
35. C.E. Hughes, K.D.M. Harris, *New J. Chem.* **33**, 713–716 (2009)
36. C. Chen, O. Cook, C.E. Nicholson, S.J. Cooper, *Cryst. Growth Des.* **11**, 2228–2237 (2011)
37. G.J. Han, S. Thirunahari, P.S. Chow, R.B.H. Tan, *CrystEngComm* **15**, 1218–1224 (2013)
38. G.L. Perlovich, L.K. Hansen, A. Bauer-Brandl, *J. Therm. Anal. Calorim.* **66**, 699–715 (2001)
39. A. Théorêt, *Spectrochim. Acta, Part A* **27**, 11–18 (1971)
40. P.A. Williams, C.E. Hughes, G.K. Lim, B.M. Kariuki, K.D.M. Harris, *Cryst. Growth Des.* **12**, 3104–3113 (2012)
41. C.E. Hughes, P.A. Williams, T.R. Peskett, K.D.M. Harris, *J. Phys. Chem. Lett.* **3**, 3176–3181 (2012)

42. J. Martí-Rujas, B.M. Kariuki, C.E. Hughes, A. Morte-Ródenas, F. Guo, Z. Glavcheva-Laleva, K. Taştēmür, L.-L. Ooi, L. Yeo, K.D.M. Harris, *New J. Chem.* **35**, 1515–1521 (2011)
43. L.C. Fetterly, *Non-Stoichiometric Compounds* (Academic, New York, 1964), pp. 491–567
44. K.D.M. Harris, *J. Solid State Chem.* **106**, 83–98 (1993)
45. K.D.M. Harris, *J. Mol. Struct.* **374**, 241–250 (1996)
46. K.D.M. Harris, *Chem. Soc. Rev.* **26**, 279–289 (1997)
47. F. Guillaume, *J. Chim. Phys. (Paris)* **96**, 1295–1315 (1999)
48. M.D. Hollingsworth, *Science* **295**, 2410–2413 (2002)
49. K.D.M. Harris, *Supramol. Chem.* **19**, 47–53 (2007)
50. R.K. Harris, A.C. Olivieri, *Prog. Nucl. Magn. Reson. Spectrosc.* **24**, 435–456 (1992)
51. F. Dornhaus, M. Bolte, H.-W. Lerner, M. Wagner, *Eur. J. Inorg. Chem.* 5138–5147 (2006)
52. L. Van Blaricom, E.F. Gilbert, *J. Am. Chem. Soc.* **61**, 3238–3239 (1939)

# Chapter 4

## Nucleation and Crystal Growth in Limited Crystallization Field

Hiroshi Takiyama

**Abstract** The crystallization operation is widely used in chemical processes and is one of the unit operations which deals with crystallization phenomena. The purposes of crystallization are to separate desired component and to produce crystalline particles. However, phenomena of crystallization are not simple and the relationships between operation conditions and product specification are complicated. The driving force of crystallization is supersaturation in nonequilibrium process. So the operation strategy for designing supersaturation is important to keep the high quality of size distribution and crystal morphology. In the general crystallizer, nucleation and growth occur in the same location and at the same time, because the driving force of both phenomena is only supersaturation. However, if the location and start period of nucleation and growth can be limited separately, it becomes easy to control the quality of crystalline particles. In this chapter, the examples which controlled the quality of crystalline particles by designing both nucleation and growth phenomena in a limited crystallization field are introduced.

**Keywords** Industrial crystallization • Templated crystallization • Anti-solvent crystallization

### 4.1 Introduction

Crystallization is widely used in various chemical industries such as pharmaceuticals and the food field. Crystallization is the unit operation with the nonequilibrium crystallization phenomenon of which driving force is supersaturation. A crystal is the solid form which the molecule and the ion arranged orderly, and crystallization is used not only as separation but as purification operation. In the case of solution-suspended crystallization, crystallization operation is also used for manufacturing crystalline particles. Thus, crystallization operation is the method to realize “separation and purification” and “crystalline particle production.” However, demand

---

H. Takiyama (✉)

Department of Chemical Engineering, Tokyo University of Agriculture and Technology (TUAT), Tokyo, Japan

e-mail: [htakiyam@cc.tuat.ac.jp](mailto:htakiyam@cc.tuat.ac.jp)

© Springer Japan 2015

R. Tamura, M. Miyata (eds.), *Advances in Organic Crystal Chemistry*,

DOI 10.1007/978-4-431-55555-1\_4

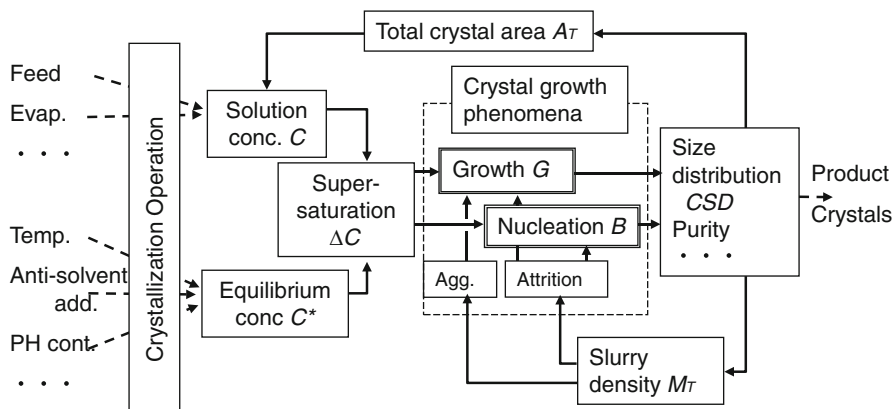


Fig. 4.1 Relationships among crystallization phenomena

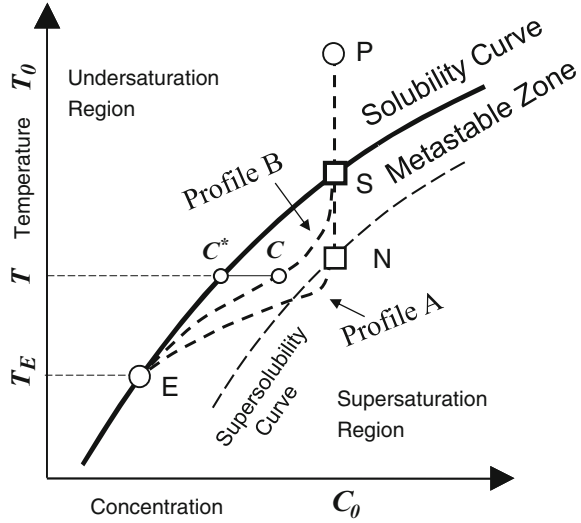
to crystalline qualities has been getting severe recently. The strategy of operation design to manufacture the crystalline particles with high quality is important.

The generation of supersaturation is essential to crystallization, because it is the driving force for nucleation and crystal growth. When crystalline particles are manufactured, particle size distribution is determined by the suspended crystallizer. In batch crystallization operation, as crystal growth proceeds, solution concentration changes. Accordingly, the subsequent nucleation and crystal growth processes are influenced by reduced supersaturation (Fig. 4.1). It is the characteristic of crystallization to have feedback structure in such processes. And the product quality of crystals is decided through these phenomena. Especially, when industrial productivity is taken into consideration, it is necessary to control the crystal size distribution. When the research target is extended to the field which deals with the nucleation and growth by the driving force of supersaturation, the application range of crystallization becomes wide. There are many contact points with crystallization operation in the field of solid-state material production of nanomaterial development. This chapter focuses on the solution crystallization operation in which the characteristics of crystalline particles are observed.

## 4.2 Supersaturation in Crystallization Operation

In order to deposit crystals, the temperature must be lowered than the solubility curve, or the concentration must be higher than the solubility curve. If the clear solution (point P of Fig. 4.2) is cooled, this solution is saturated when solution states cross the solubility curve (point S). If the solution is cooled continuously, the solution reaches the supersaturation condition. If the solution temperature further decreases, nucleation occurs (point N) and the solution concentration begins to decrease because crystal growth begins. Since the supersaturation condition can be

**Fig. 4.2** Solution concentration profile during cooling crystallization (phase diagram)



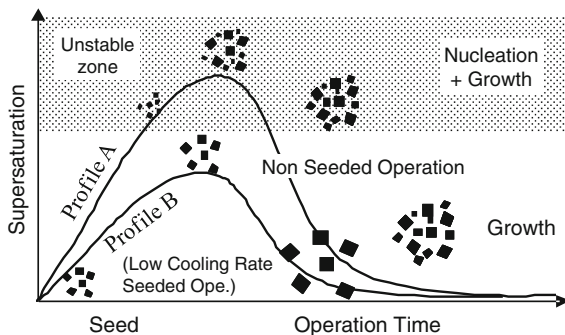
maintained whenever cooling operation continues, crystalline particles continue to grow. If the cooling operation stops, the solution concentration reaches the saturated concentration at this temperature (point E), and crystal growth stops. The driving force of crystallization is the supersaturation which is defined by Eq. (4.1) and is expressed as  $\ln S$  and/or  $\sigma$ .

$$\frac{\Delta\mu}{kT} \cong \ln\left(\frac{C}{C^*}\right) = \ln S = \ln\left(1 + \frac{\Delta C}{C^*}\right) = \ln(1 + \sigma) \cong \sigma \quad (4.1)$$

The growth rate and the nucleation rate are required to decide a production rate and to estimate the number of crystals which is generated during operation, respectively. Therefore, it is important to estimate a degree of supersaturation. The growth phenomena are dominant if an operation point is in the region near the solubility curve. The nucleation becomes dominant if an operation point is more distant from the solubility curve. In cooling crystallization, the operation is carried out in a metastable zone [18] so that a nucleation may not become dominant [15].

Figure 4.3 is the time profile for the change in the solution concentration shown in Fig. 4.2. If an operating point exceeds a metastable zone, a nucleation occurs frequently. Therefore, the crystalline particles with undesired particle size distribution are obtained (Profile A). On the other hand, if a supersaturation peak is reduced, growth phenomenon becomes dominant and can control nucleation. For example, if sufficient quantity of seed crystals is introduced at the early stages of cooling, the consumption rate of solute becomes high and the peak of supersaturation decreases. Moreover, even if the cooling rate decreases at an early time, there is a possibility that the peak of supersaturation decreases (Profile B). In this way, it is important how the trajectory of supersaturation is designed in crystallization operation [21].

**Fig. 4.3** Solution concentration profile during cooling crystallization (changes in supersaturation)



### 4.3 Quality of Crystalline Particles

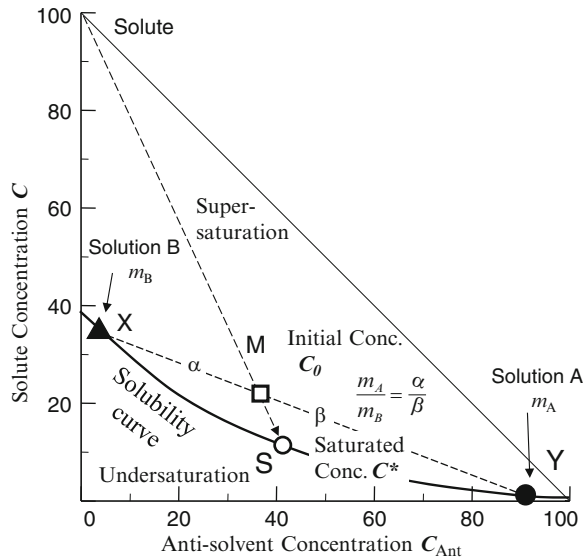
Since pharmaceuticals are life-related substances, severe qualities of crystalline particles are required. In pharmaceutical production, the suspended-type crystallizer of batch process is often used. “Cooling crystallization” which deposits crystals by cooling, “anti-solvent addition method” which adds the solvent whose target pharmaceuticals do not dissolve, and “concentrating method” which removes the solvent by evaporation are used. Of course, there is also a crystallization method which combined these methods [16]. In addition to the high purity, the particle size distribution, polymorphism, and morphology which are required in industrial crystallization, bioavailability, solubility, and stability are important in pharmaceuticals production. Moreover, from the viewpoint of a pharmaceutical preparation process, the quality of compressibility, flowability, plasticity, and mixing nature are important. Such qualities are deeply concerned with particle size distribution and crystal morphology. It is necessary to carry out the operation in which various crystalline qualities are satisfied simultaneously. However, as shown in Fig. 4.1, there are few operational parameters, and most of those qualities are dependent on the supersaturation described earlier. That is, the generation method and generation rate of supersaturation are very important for the determination of crystalline qualities. And if the location and start period of nucleation and growth processes can be limited, it becomes easy to control the quality of crystalline particles.

## 4.4 Milli-segmented Flow Crystallizer

### 4.4.1 Anti-Solvent Crystallization

A grinding process is commonly used for producing fine crystalline particles. However, there are problems such as the difficulties in crystal size distribution and crystal shape control, improvement in energy efficiency, and treatment free of contamination. In the pharmaceutical industry, the denaturation behavior of

**Fig. 4.4** Definition of supersaturation in anti-solvent crystallization



materials by mechanical and thermal energy is also an important problem. The demands for manufacturing fine crystalline particles by solution crystallization are also growing for simplification of the pharmaceutical preparation process.

Anti-solvent crystallization (crystallization by mixing two solutions) is one of the techniques for producing crystalline particles. This crystallization process consists of three steps: (1) mixing of a feed solution and an anti-solvent, (2) nucleation from the mixed solution, and (3) crystal growth. In particular, supersaturation is achieved by mixing the feed solution and the anti-solvent, and then nucleation and crystal growth occur.

The generation method of the supersaturation of anti-solvent crystallization is illustrated on the phase diagram (Fig. 4.4). If solution B (point X) and solution A (anti-solvent, point Y) are mixed, the initial apparent concentration is point M. This solution is supersaturated, since crystallization occurs and the solution concentration reduces to give the saturated condition (point S). There is an operational merit that temperature operation is unnecessary, and it is possible to generate various supersaturation only by changing the mixing ratio.

If the number of crystal generation is controlled and crystal growth can be restricted, it can be expected that fine crystalline particles having monodispersed CSD (crystal size distribution) will be produced. In a stirred tank crystallizer, it takes a certain time period to mix a solution, since the crystallization field is large. Therefore, concentration distribution arises in the stirred tank. The existence of a concentration distribution has been clarified by a simulation [5]. Furthermore, it is difficult to control not only mixing but also nucleation because of the large crystallization field. Therefore, it is difficult for the stirred tank crystallizer to produce fine crystalline particles having monodispersed CSD.

A new crystallization method which produces fine crystals using a micro-reactor has been studied. The aim of this method is the restriction of crystal growth. For example, there are studies using a tubular crystallizer ([8]). The research of fine crystalline particle production using a micro-reactor has been reviewed by Zhao et al. [27]. The improvement in solution mixing behavior by using a segmented flow tubular reactor (SFTR) [6] has been studied. Solution volume is limited by segmented flow, which consists of the feed solution and anti-solvent joined at a mixer by immiscible fluid. The residence time of each segment in the tubular reactor is maintained constant if the flow rate of each fluid is controlled. However, in general, the crystallization using a micro-reactor also has a disadvantage in that the flow channel becomes clogged because of rapid crystal growth. On the other hand, in batch cooling crystallization, temperature profiles to produce crystals having a monodispersed CSD have been studied [14]. Takiyama et al. [20] reported that it is possible to make crystals with improved CSD by modulating the cooling program with heating operation (undersaturation operation) in the non-seeding operation.

If these approaches are applied and integrated with anti-solvent crystallization, it is expected that the CSD of fine crystals will be improved. For example, the nucleation zone can be introduced to a part of the segment flow in a milli-sized tube flow. There is a possibility of a further improvement in CSD by introducing temperature-modulated operation at the part of flow channel after nucleation. Furthermore, it is possible to prevent the flow channel clogging by introducing modulated operation. Thus, if each operating zone of a tubular crystallizer with milli-sized segmented flow has a crystallization function, it is expected to produce crystals which have a monodispersed CSD.

#### 4.4.2 Nucleation Control

The nucleation control method was carried out for producing fine particles. The experiment was performed with the tubular-type crystallizer shown in Fig. 4.5. A taurine (solute) – water (solvent) – EtOH (anti-solvent) system was used. The

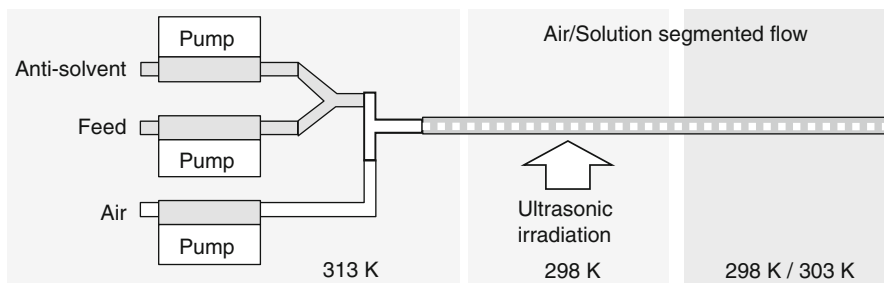


Fig. 4.5 Schematic diagram of the experimental apparatus

feed solution and anti-solvent were a saturated taurine aqueous solution and pure ethanol, respectively. The tube flow crystallizer consisted of a Y-connector, T-connector, flexible connection tube, and metal tube ([10]). The metal tube was used for enhancement of nucleation by ultrasound irradiation. The Y-connector and T-connector were used as a mixer and a segmenter.

### 4.4.3 Production of Fine Crystals

The experimental conditions and obtained crystal qualities are shown in Table 4.1. An SEM image for the samples of Run X and Run D is shown in Fig. 4.6.

Based on Table 4.1, the effect of nucleation is not observed only under the cooling operation condition. On the other hand, ultrasound irradiation is effective in inducing nucleation. In addition, it was observed that the nucleation was enhanced by integrating ultrasound irradiation and temperature modulation. For Run D and Run X, each number-based CSD is shown in Fig. 4.7.

While the CSD became wide and the mean size of crystals also became larger in the early stage in the case of Run X, which was carried out as a batch crystallization, fine crystalline particles which have monodispersed and comparatively narrow CSD were obtained in Run D. From these results, it became clear that the

**Table 4.1** Experimental conditions and crystal quality

Run no.	Type	Temperature modulation	Ultrasonic irradiation	Crystal quality
X	Tank	–	–	Rod crystals
A	Tube	–	–	Nearly no crystals
B		○	–	Nearly no crystals
C		–	○	Needle and rod crystals
D		○	○	Numerous rod crystals

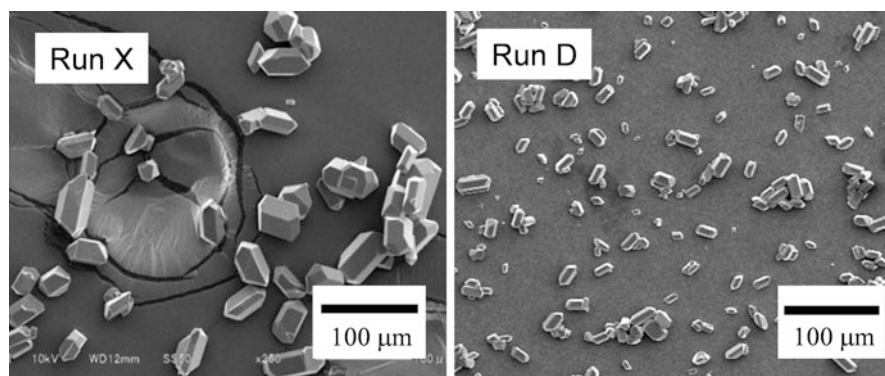
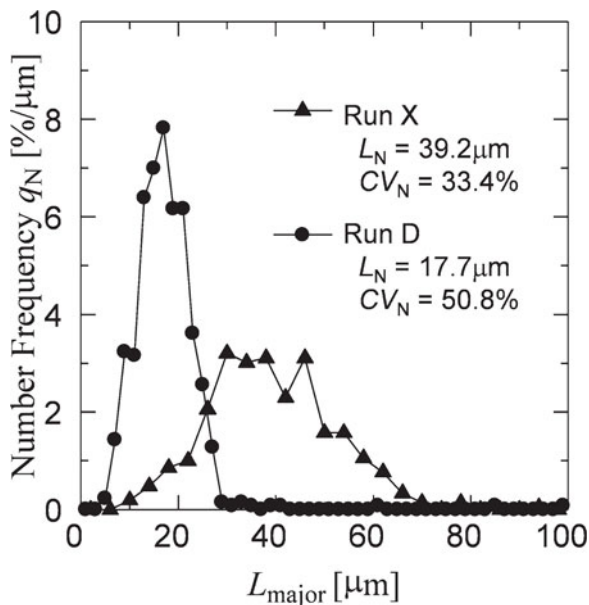


**Fig. 4.6** SEM photomicrographs for samples of Run X and Run D

**Fig. 4.7** CSDs for samples of Run X and Run D



integration method of ultrasound irradiation and temperature modulation in milli-sized segmented flow is capable of controlling nucleation, and fine particles with monodispersed CSD were produced.

Based on these results, an operation strategy could be proposed. This strategy is the adjustment of slurry concentration by controlling the anti-solvent composition and flow rate of each fluid. It was confirmed that the integration of ultrasound irradiation and temperature modulation in a milli-sized segmented flow is effective in producing organic fine crystalline particles having monodispersed and narrow CSD.

## 4.5 Templated Crystallization

### 4.5.1 Nucleation at the Interface

Fine monomodal crystalline particles are required in many fields such as pharmaceuticals and fine chemicals. The production of crystals with well-controlled size distribution facilitates improvement of dissolution rate. The inhaled drug delivery systems require particle size between 1 and 6  $\mu\text{m}$  for maximum efficiency [23]. Control of nucleation is essential technology to produce fine monomodal crystalline particles. The effects of operations for nucleation control were investigated in many studies. The templated crystallization is a method which can constrain nucleation field. Templated crystallization by using organic molecular assembly that can

control molecular arrangement and constrain crystallization field has been also investigated in various studies. Since templated crystallization can control molecular arrangement directly, this method is investigated to control polymorphism [11, 1, 17, 13]. This method is used to investigate for mimicking biomineralization processes [12, 2, 3]. One of key features of templated crystallization is preferential appearance of crystals at template interface by interaction of template molecules and objective molecules. This characteristic nature at the template interface has advantageous field for crystallization.

In this section, the effect of template at the air/solution interface on the nucleation phenomena was introduced. If the timing of nucleation can be controlled by using template effects, monomodal crystalline particles can also be produced. Moreover, if crystalline particles after nucleation can be collected immediately, fine monomodal crystalline particles can be produced.

### 4.5.2 Templated Crystallization

There are some studies of templated crystallization that used glycine and L-leucine [24, 25, 4]. It was understood that L-leucine molecules were arranged in air/solution interface and glycine crystals grow at the interface. Then air bubble was inserted into the solution (this time was  $\theta_{\text{Air-in}}$ ), and glycine crystals were observed at the air bubble/solution interface by using optical microscope ([26]).

Figure 4.8 shows the crystal growth at the template interface ( $\theta_{\text{Air-in}} = 458$  s) in bubble insert experiment. The crystals at the interface had the same pyramid-like morphology and the same size, and these crystals are deposited selectively on the air/solution interface. These crystals were similarly grown and uniformed.

Figure 4.9 shows crystal growth curves (crystal a and b in Fig. 4.8). The key of inverted triangle showed the timing when the bubble was inserted and the template interface was created. According to these growth curves, timings of nucleation were

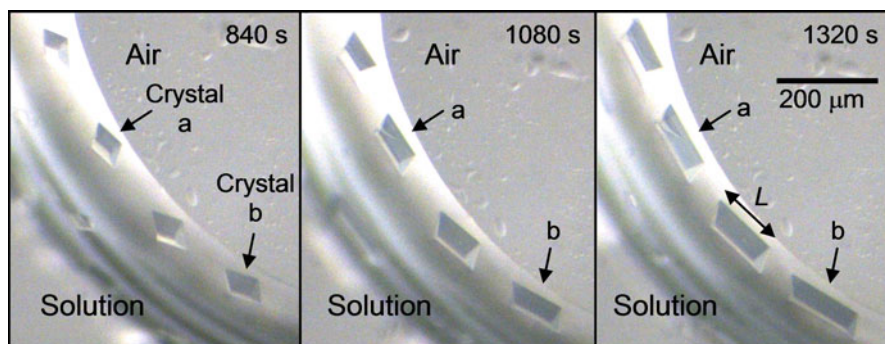
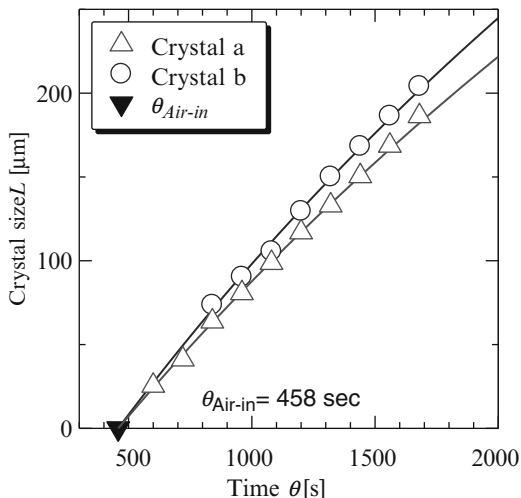
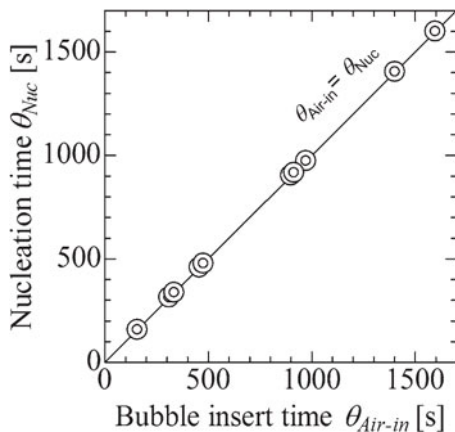


Fig. 4.8 Glycine crystals grown at the air bubble/solution interface ( $\theta_{\text{Air-in}} = 458$  s)

**Fig. 4.9** Glycine crystal growth curves of crystal a and crystal b ( $\theta_{Air-in} = 458$  s)



**Fig. 4.10** The relationships between the template interface formation timing  $\theta_{Air-in}$  and the nucleation timing  $\theta_{Nuc}$



estimated. When growth curves were extrapolated  $L = 0$ , the value of  $\theta$  was the nucleation time,  $\theta_{Nuc}$ . The  $\theta_{Nuc}$  values of crystal a and crystal b were identical 458 s. This result indicated that crystal nucleation was induced immediately after insert of the bubble into the supersaturated solution.

This experiment was carried out under the conditions of several air bubble insert times ( $\theta_{Air-in}$ ). Figure 4.10 shows the relationships between  $\theta_{Air-in}$  and  $\theta_{Nuc}$ . All plots were located on a diagonal line. These experimental results indicated that the timings of air bubble insert  $\theta_{Air-in}$  and the timings of nucleation  $\theta_{Nuc}$  were very close, even if the air bubbles were inserted at any timing. The repeatability of nucleation phenomena often becomes a problem. However, this result indicated that crystal nucleation was able to be induced immediately after insert of the bubble into the supersaturated solution. Consequently, formation of air/solution interface into the supersaturated solution acted as the nucleation trigger.

### 4.5.3 Nucleation Trigger

In order to produce fine monomodal crystalline particles, the experiment was carried out to collect crystals just after nucleation by using nucleation trigger. The experimental apparatus is shown in Fig. 4.11. This apparatus produced segmented flow of air bubbles and solution by pumping water and solution. The production timing of the air bubble in segmented flow was able to act as the nucleation trigger. So, fine monomodal crystalline particles were able to be produced by collecting immediately after using the nucleation trigger. Based on this operation strategy, the experiment was carried out ([26]).

Under the certain condition, the fine crystalline particles (number-based mean size  $L_N = 0.62 \mu\text{m}$ , coefficient of variation  $CV_N = 56 \%$ ) were obtained (Fig. 4.12). The glycine crystals had well-defined crystal face and pyramid-like morphology. It means that these fine crystals were generated on the air/solution interface. In

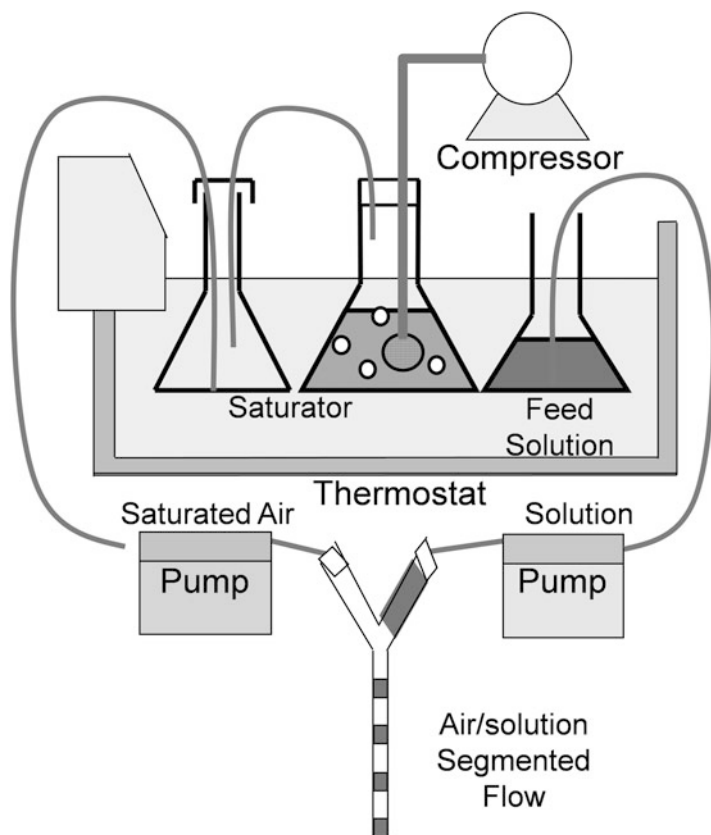
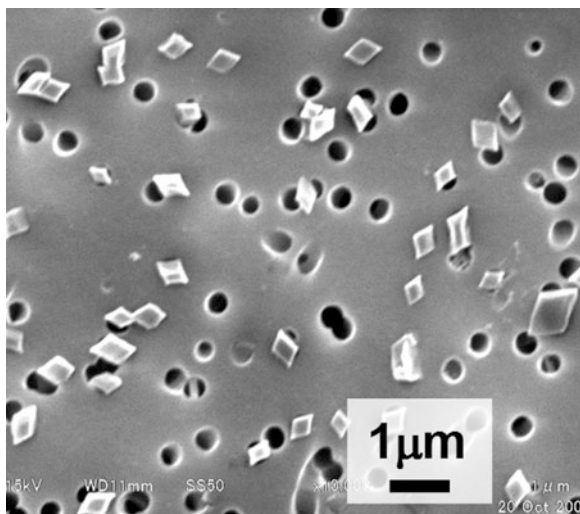


**Fig. 4.11** Experimental apparatus for application of microcrystal generation by using the nucleation trigger

**Fig. 4.12** Obtained glycine microcrystals by using the nucleation trigger



these ways, by collecting crystalline particles immediately after nucleation was induced by nucleation trigger, submicron-order particles were obtained. Moreover, this operation method by using the nucleation trigger has the potential to produce fine crystalline particles with desirable size.

## 4.6 Liquid-Liquid Interface in Emulsion

### 4.6.1 *Liquid-Liquid Interface*

An anti-solvent crystallization method is the operation which adds the anti-solvent for reducing the solubility of the object solute and can be operated at ambient temperatures. This crystallization operation is used for the production of many pharmaceuticals. However, there are problems such as the difficulty of control of crystal morphology and size and generation of agglomerated crystals [19, 7]. In the previous report of the anti-solvent crystallization method, it becomes clear that a supersaturation ratio influences crystal size and morphology [19]. However, if local fluctuation of the supersaturation exists at the time of anti-solvent addition, various crystal sizes and morphologies would be deposited during desupersaturation.

In original anti-solvent crystallization, the supersaturation is generated by mixing a good solvent and an anti-solvent. And the contact area of these solvents is not controlled. It is considered that high local fluctuation of the supersaturation is produced in the case that the contact interface area between a good solvent and an anti-solvent is insufficient or in the case of slow solvent diffusion rate. Therefore, the following method can be proposed. First, rich contact surface area is built up in a solution, and then the crystallization is carried out at this limited interface.

Specifically, a rich contact interface is generated by preparing an emulsion with an immiscible good solvent and anti-solvent. Next, a solvent diffusion rate is adjusted by adding the coupled solvent which can mingle with each solution. If the solvent diffusion rate in the liquid-liquid interface of an emulsion is controllable, it is possible to reduce high local fluctuation of the supersaturation.

There is a spherical crystallization method as an example of crystallization using an emulsion interface [9]. A spherical crystallization method generates the emulsion drop of uniform size, and supersaturation is supplied by temperature operation or anti-solvent addition. The crystallization occurred in an emulsion drop and the spherical agglomeration crystals of uniform size are obtained. There is a research of particle size distribution control of agglomeration crystals; however, there are very few discussions with the objective of crystallization engineering such as relationships between supersaturation and crystallization. In this session, the establishment of operating conditions of crystallization to produce fine crystals with desired size and shape in an anti-solvent crystallization with emulsion is introduced.

## ***4.6.2 Production of Particles by Using Liquid-Liquid Interface***

### **4.6.2.1 Observation of Crystallization at Liquid-Liquid Interface**

The taurine-saturated aqueous ethanol solution (Liquid A), the taurine-saturated hexane solution (Liquid B), and the taurine-saturated aqueous ethanol solution (Liquid C) of arbitrary concentration were prepared. A crystallization target is taurine. Quaternary system of taurine (crystalline material), water (original solvent), hexane (anti-solvent), and ethanol (coupled solvent) was considered.

A single small droplet of Liquid A was prepared in Liquid B by using microsyringe between two glass plates. Liquid-liquid interface was observed by using an optical microscope. After predetermined period, Liquid C (coupled solvent) was added. The crystallization phenomenon near the place of liquid-liquid interface was observed ([22]).

Figure 4.13 shows the observation of crystallization near the interface. Figure 4.13a shows the liquid-liquid interface of Liquid A and Liquid B. After addition of coupled solvent Liquid C, crystallization was stated at the place of liquid-liquid interface (Fig. 4.13b). The supersaturation was generated by adding the coupled solvent which can be mixed with Liquid A and Liquid B. So it can be confirmed that the liquid-liquid interface should act as the limited crystallization field. In the case of original conventional anti-solvent crystallization, the supersaturation was generated by the direct mixture to a good solvent and an anti-solvent. However, by using this method, the direct mixture is avoided and it is expected that the solvent diffusion rate can be adjusted by the coupled solvent conditions. Furthermore, the influence of local supersaturation fluctuation can be reduced by increasing the liquid-liquid surface area with emulsification.

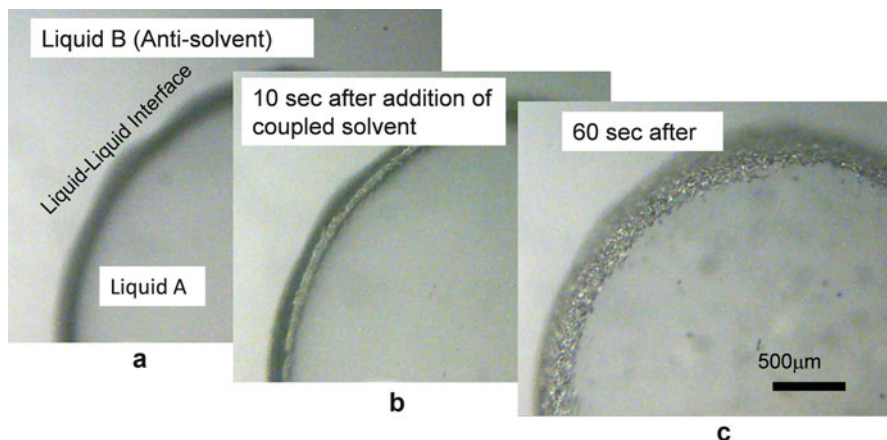


Fig. 4.13 Photomicrographs of crystallization phenomena near the liquid-liquid interface

#### 4.6.2.2 Production of Particles by Using Liquid-Liquid Interface in Emulsion

The capacity of the crystallizer equipped with a jacket and homogenizer was 100 mL. A predetermined amount of Liquid A and Liquid B was physically emulsified at 14,500 rpm by the mechanical shearing force by homogenizer, and the crystallization field was prepared. The obtained crystal morphologies, mass-based mean crystal size of major length ( $L_M$ ), and coefficient of variation ( $CV$ ) changed depending on the operating conditions. In order to consider the relationships between crystal morphology and an operating condition in detail, categorization of crystal morphology was attempted by the supersaturation. In order to calculate a supersaturation ratio, the quaternary phase diagram was determined (Fig. 4.14). This phase diagram is indicated by the triangular pyramid coordinate. The curve on the x-y plane shows the liquid-liquid equilibrium. The curve on the y-z plane indicates the liquid/solid equilibrium.

The degree of supersaturation  $\Delta C$  and supersaturation ratio  $\ln S$  was calculated by applying the lever rule to this quaternary phase diagram. The relationship between supersaturation and crystal morphology was shown in Figs. 4.15 and 4.16.

In Fig. 4.15, the horizontal axis means equilibrium concentration, the vertical axis means a degree of supersaturation, and the slope of straight line means the supersaturation  $S-1$ . As a result, it became clear that a taurine crystal becomes rod-like under the low supersaturation condition and becomes needlelike under the high supersaturation condition. When the result of the proposed crystallization method is compared with that of the conventional anti-solvent crystallization method, it is characteristic that the region where different kinds of crystal morphologies coexist is narrow. In the conventional anti-solvent crystallization, diffusion of the solute occurs only from the local point where the anti-solvent was added. Therefore,

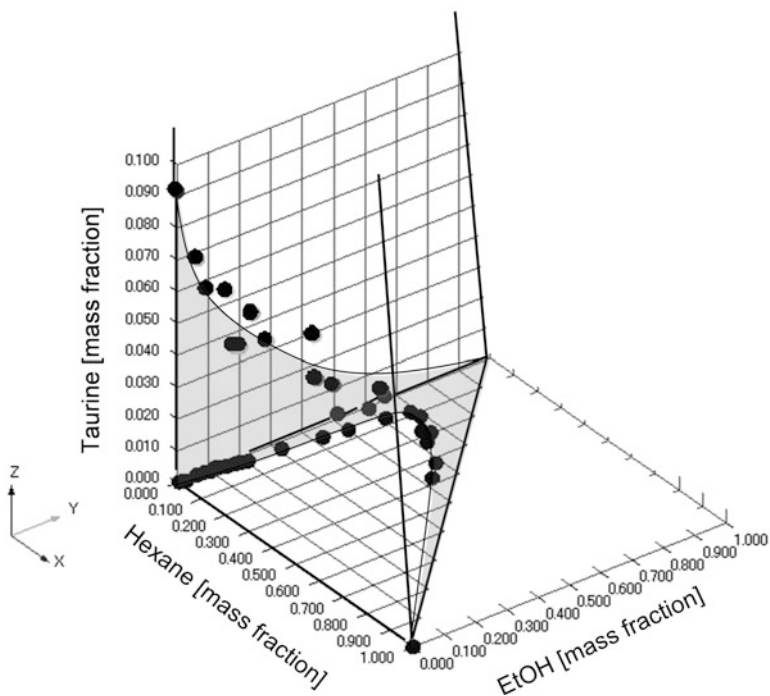
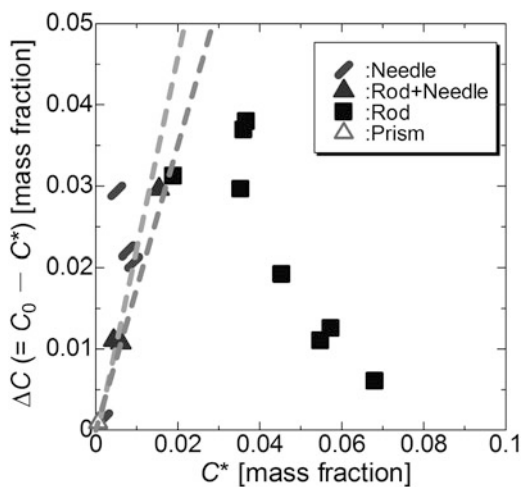
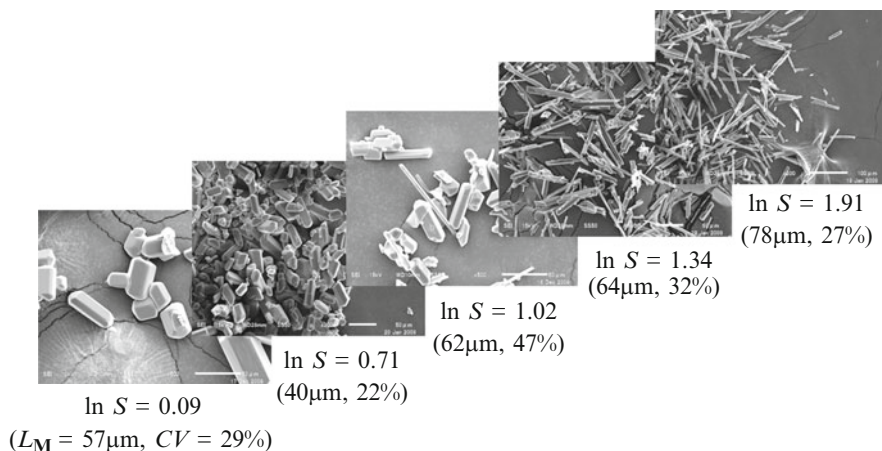


Fig. 4.14 Quaternary phase diagram of taurine, water, hexane, and ethanol

Fig. 4.15 Relationships between crystal shapes and operating conditions in anti-solvent crystallization with emulsion



the difference in the solute concentration between an anti-solvent and a good solvent is large in an addition position. On the other hand, the difference of solute concentrations becomes small in the area distant from the anti-solvent addition position. Thus, the supersaturation distribution arises depending on the location in



**Fig. 4.16** Relationships between crystal shapes and supersaturation ratio in anti-solvent

a solution. Since there is high local supersaturation fluctuation in an anti-solvent addition position, it is easy to generate a needlelike crystal. More than two kinds of crystal morphologies deposit easily because supersaturation distribution arises in a solution. In the case of emulsion conditions, supersaturation is not generated directly by addition of an anti-solvent, but supersaturation generates on a rich liquid-liquid interface after solvent diffusion. Therefore, local fluctuation of the supersaturation is not produced, but supersaturation is homogeneous in a solution. And the crystallization region of a needlelike crystal was limited, and there were few cases that more than two kinds of crystal morphologies were intermingled in the case of emulsion. The liquid-liquid interface area is used effectively for uniformed crystallization by dispersion of local supersaturation.

In the crystallization of an emulsion application, the relationships between supersaturation ratio and crystal morphology were correlated by estimating the quaternary phase diagram and analyzing supersaturation in equilibrium theory. Moreover, high local supersaturation fluctuation has been reduced by using a liquid-liquid interface as a crystallization field. Therefore, the method using the limited crystallization field such as liquid-liquid interface is useful for controlling the crystal size distribution and morphology in an anti-solvent crystallization.

## 4.7 Conclusions

The driving force of both nucleation and growth phenomena is supersaturation, so these phenomena occur in the same location at the same time. This is the reason why control of the quality of crystalline particles is not easy. Therefore, the operation design has been investigated to separate the location of nucleation

and growth and the start period of these phenomena. If both phenomena can be limited separately, the quality of crystalline particles can be improved. The research topics are introduced to control the quality by designing both nucleation and growth phenomena in the limited crystallization field. The examples of the limited crystallization field are the air/solution interface of the segmented flow and the liquid-liquid interface of the emulsion. From the experimental results, the crystallization method using the limited crystallization field is useful for controlling the crystal size distribution and morphology. The advanced study on the limited crystallization field will further improve the quality of crystalline particles.

## References

1. J. Aizenberg, A.J. Black, G.M. Whitesides, Oriented growth of calcite controlled by self-assembled monolayers of functionalized alkanethiols supported on gold and silver. *J. Am. Chem. Soc.* **121**, 4500–4509 (1999)
2. J. Aizenberg, A.J. Black, G.M. Whitesides, Control of crystal nucleation by patterned self-assembled monolayers. *Nature* **398**, 495–498 (1999)
3. J. Aizenberg, Patterned crystallization of calcite in vivo and in vitro. *J. Cryst. Growth* **211**, 143–148 (2000)
4. B.D. Chen, J.J. Cilliers, R.D. Davey, J. Garside, E.T. Woodburn, Templated nucleation in a dynamic environment: crystallization in foam lamellae. *J. Am. Chem. Soc.* **120**, 1625–1626 (1998)
5. A. Jones, S. Rigopoulos, R. Zauner, Crystallization and precipitation engineering. *Comput. Chem. Eng.* **29**, 1159–1166 (2005)
6. N. Jongen et al., Development of a continuous segmented flow tubular reactor and the “scale-out” concept – in search of perfect powders. *Chem. Eng. Technol.* **26**, 303–305 (2003)
7. S. Kaneko, Y. Yamagami, H. Tochiwara, I. Hirasawa, Effect of supersaturation on crystallization phenomena in antisolvent crystallization of sodium chloride. *Bull. Soc. Sea Water Sci. Jpn.* **57**, 22–26 (2003)
8. M. Kawase, K. Miura, Fine particle synthesis by continuous precipitation using a tubular reactor. *Adv. Powder Technol.* **18**, 725–738 (2007)
9. Y. Kawashima, C. Fude, H. Takeuchi, T. Niwa, T. Hino, K. Kihara, Agglomeration behaviour and modification of spherical crystallization process of pharmaceuticals by the emulsion-solvent-diffusion method and proposed closed-circuit batch system. *J. Pharm. Soc. Jpn.* **111**, 451–462 (1991)
10. S. Kudo, H. Takiyama, Production of fine organic crystalline particles by using milli segmented flow crystallizer. *J. Chem. Eng. Jpn.* **45**, 305–309 (2012)
11. J. Küther, G. Nelles, R. Seshadri, M. Schaub, H. Butt, W. Tremel, Templated crystallisation of calcium and strontium carbonates on centred rectangular self-assembled monolayer substrates. *Chem. Eur. J.* **4**, 1834–1842 (1998)
12. A.L. Litvin, S. Valiyaveetil, D.L. Kaplan, S. Mann, Template-directed synthesis of aragonite under supramolecular hydrogen-bonded langmuir monolayers. *Adv. Mater.* **9**, 124–127 (1997)
13. L. Lu, G. Zhou, H.J. Zhai, Y. Wang, H. Wang, Nucleation and growth of glycine crystals with controllable sizes and polymorphs on langmuir–blodgett films. *Cryst. Growth Des.* **7**, 2654–2657 (2007)
14. M. Moscasa-Santillán, O. Bals, H. Fauduet, C. Porte, A. Delacroix, Study of batch crystallization and determination of an alternative temperature-time profile by on-line turbidity analysis—application to glycine crystallization. *Chem. Eng. Sci.* **55**, 3759–3770 (2000)
15. J.W. Mullin, *Crystallization*, 4th edn. (Butterworth-Heinemann, Oxford, 2001), pp. 201–205

16. Z.K. Nagy, M. Fujiwara, R.D. Braatz, Modelling and control of combined cooling and antisolvent crystallization processes. *J. Process Control* **18**, 856–864 (2008)
17. F. Quist, A. Kakkar, Self-assembled monolayers: influence of complementarity between chemisorbed and crystallizing molecules in polymorph selection. *J. Colloid Interface Sci.* **313**, 378–382 (2007)
18. K. Sangwal, Recent developments in understanding of the metastable zone width of different solute-solvent systems. *J. Cryst. Growth* **318**, 103–109 (2011)
19. H. Takiyama, T. Otsuhata, M. Matsuoka, Morphology on NaCl crystals in drowning-out precipitation operations. *Chem. Eng. Res. Des.* **76**, 809–814 (1998)
20. H. Takiyama, K. Shindo, M. Matsuoka, Effects of undersaturation on crystal size distribution in cooling type batch crystallization. *J. Chem. Eng. Jpn.* **35**, 1072–1077 (2002)
21. H. Takiyama, Supersaturation operation for quality control of crystalline particles in solution crystallization. *Adv. Powder Technol.* **23**, 273–278 (2012)
22. H. Takiyama, K. Ito, Production of organic fine-crystalline particles by using the liquid-liquid interface in an emulsion. *Chem. Eng. Technol.* **35**, 991–994 (2012)
23. M.P. Timsina, G.P. Martin, C. Marriott, D. Ganderton, M. Yianneskis, Drug delivery to the respiratory tract using dry powder inhalers. *Int. J. Pharm.* **101**, 1–13 (1994)
24. I. Weissbuch, L. Addadi, Z. Berkovitch-Yellin, E. Gati, M. Lahav, L. Leiserowitz, Spontaneous generation and amplification of optical activity in  $\alpha$ -amino acids by enantioselective occlusion into centrosymmetric crystals of glycine. *Nature* **310**, 161–164 (1984)
25. I. Weissbuch, F. Frolov, L. Addadi, M. Lahav, L. Leiserowitz, Oriented crystallization as a tool for detecting ordered aggregates of water-soluble hydrophobic  $\alpha$ -amino acids at the air-solution interface. *J. Am. Chem. Soc.* **112**, 7718–7724 (1990)
26. H. Yamamoto, H. Takiyama, Production of organic micro-crystals by using templated crystallization as nucleation trigger. *J. Cryst. Growth* **373**, 69–72 (2013)
27. C.X. Zhao, L. He, S.Z. Qiao, A.P.J. Middelberg, Nanoparticle synthesis in microreactors. *Chem. Eng. Sci.* **66**, 1413–1479 (2011)

# Chapter 5

## Particle Engineering with CO<sub>2</sub>-Expanded Solvents: The DELOS Platform

Paula E. Rojas, Santi Sala, Elisa Elizondo, Jaume Veciana, and Nora Ventosa

**Abstract** Compressed fluids and especially CO<sub>2</sub>-expanded solvents (a mixed solvent composed of CO<sub>2</sub> dissolved in an organic solvent) present unique properties for the eco-efficient production of active pharmaceutical ingredients (APIs) with an exceptional control of the operational variables that allow tuning the final properties of the active compounds. The pharmaceutical industry nowadays is facing several challenges, as nearly 40 % of the newly discovered drugs are poorly soluble in water and, hence, present low bioavailability. In addition, there is a huge necessity to move to a more environmentally friendly way of product manufacturing. Therefore, the use of compressed fluid-based technology is a promising solution for the pharmaceutical industry. This chapter provides a general overview covering the properties of compressed fluids (CF), the most used CF-based processes, and a more comprehensive summary of the application of CO<sub>2</sub>-expanded solvents for the tailored crystallization of active compounds.

**Keywords** Compressed fluids • Microparticles • APIs • Polymorphism • Supercritical CO<sub>2</sub> • CO<sub>2</sub>-expanded solvents • DELOS

### 5.1 Introduction

The product quality of materials including explosives, catalysts, pigments, and pharmaceuticals can be strongly influenced by physical properties such as particle size distribution and morphology [1]. For example, in laser printers, dependency of the photoelectric properties of organic xerographic photoreceptors with particle size is of utmost importance for the successful technical development of copying process [2]. Regarding the pharmaceutical industry, specific characteristics of particles such

---

P.E. Rojas • S. Sala • E. Elizondo • J. Veciana • N. Ventosa (✉)

Department of Molecular Nanoscience and Organic Materials, Institut de Ciència de Materials de Barcelona (ICMAB-CSIC), Campus de la Universitat Autònoma de Barcelona (UAB), 08193 Bellaterra, Spain

Networking Research Center on Bioengineering, Biomaterials and Nanomedicine (CIBER-BBN), Madrid, Spain

e-mail: [ventosa@icmab.es](mailto:ventosa@icmab.es)

as size, surface, crystal structure, and morphology are among the most important factors to control biopharmaceutical properties of drug products [3]. Therefore, the control of particle size and shape is of vital relevance as they influence a large variety of important physical properties, manufacturing processability, and quality attributes [4].

Hence, the reproducible preparation of organic crystals in a specifically custom-made form and size is a major aspect that must be tackled. Moreover, regulatory authorities in the pharmaceutical industry also emphasize the importance of solid-state and crystallographic purity in addition to careful monitoring of the polymorphism of drugs and excipients [5].

Polymorphic purity is an important parameter to take into account in soft materials. Polymorphism is the ability of a molecule to adopt more than one crystal form. Each crystal form has a unique set of physicochemical properties such as melting point, solubility, hygroscopicity, etc. In the fat-based food products, for instance, the melting point and melting behavior, external appearance, taste, stability, etc., are to a great extent influenced by the structure of the solid-fat phase. In the pharmaceutical industry, it is also a relevant aspect, since solubility and bioavailability depend on the crystalline structure. For this reason, regulatory authorities have long acknowledged the necessity for limiting polymorphic impurities in active pharmaceutical ingredients (APIs) [3].

The control of particle size, morphology, polymorphism, crystallinity, and purity is essential for developing more effective pharmaceutical formulations.

Techniques used to produce particles with a controlled particle size can be categorized into two major classes: top-down and bottom-up technologies. Top-down approaches mainly comprise mechanical comminution (crushing, grinding, and milling) and high-pressure homogenization. Although these techniques are widely used, their limitations include long preparation time, difficulty in achieving a narrow size distribution, high energy input, contamination, and adverse effects of the high shear and temperature on the chemical and physical stability of the active compounds. Bottom-up procedures such as recrystallization from solution using liquid anti solvents, freeze drying, and spray drying also have some shortcomings: thermal and chemical degradation of products, trace residues, inter-batch particle size variability, and excessive solvent use and disposal [6]. Regarding to this, the pharmaceutical industry is one of the industrialized sectors that uses more kg of organic solvent per kg of product produced [7].

Therefore, the production of contaminant-free particles with tailored particle size and desired product qualities in an environmentally friendly manner continues to be a major challenge in industry. In the case of pharmaceutical industry, requirements for high-quality products and society concerns about health and environments make the implementation of new efficient and environmentally respectful technologies for the preparation of APIs with tailored properties an urgent necessity.

In the following section, a general overview covering different CF-based process and the fundamentals of compressed fluids will be presented. A more comprehensive explanation is given to *Depressurization of an Expanded Liquid Organic Solution* (DELLOS) method, where CO<sub>2</sub>-expanded solvents are used as crystallization media.

## 5.2 Compressed Fluids (CF): Green Solvents for Particle Engineering

The application of CF technology covers various processes, including nutraceutical manufacturing, the petroleum industry, chromatography, and pigment production as well as pharmaceutical development [8]. This technology is rapidly evolving, as reflected by the number of new processes reported since its beginning [7]. Among the most successful applications of CFs, particle engineering of pharmaceutical actives seems to be at the moment, the area with the highest blooming [3, 9].

In contrast to conventional particle formation methods, where larger particles are originally formed and then milled to the desired size, CF technology involves growing particles in a tailored manner to reach the desired final physical properties. This means that the solid particle, once formed, does not have to undergo any thermal nor mechanical stresses, as happens in conventional techniques. This feature makes supercritical and compressed fluid technology amenable to produce biomolecules and other sensitive compounds in their native pure state.

The phase when both critical pressure and temperature have either been reached or exceeded possesses unique characteristics. Substances in this phase are called supercritical fluids. A supercritical fluid can behave as either a liquid or a gas, but is actually neither. Figure 5.1 depicts the phase diagram of compressed CO<sub>2</sub>, and Table 5.1 shows the physicochemical properties of a supercritical fluid (SCF) compared with those of liquid and gas. The density, viscosity, diffusion coefficient, and heat conductivity values are between those for liquid and gas. The density of a SCF is either the same or close to that of a liquid, which enhances the solubility

**Fig. 5.1** Phase diagram of compressed CO<sub>2</sub>

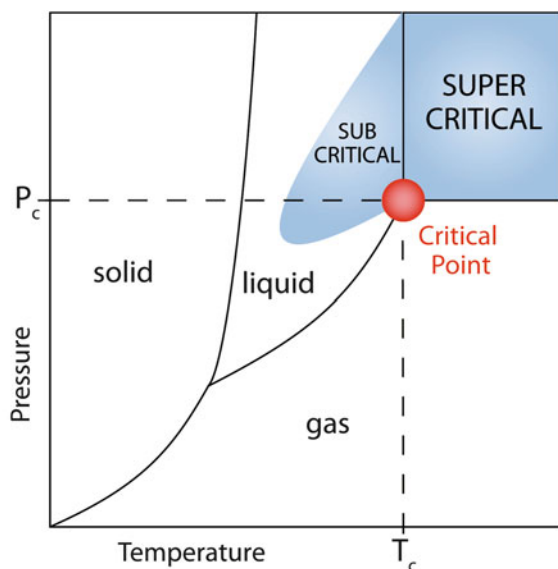


**Table 5.1** Characteristics of supercritical fluids compared to those of liquids and gases

	Liquid	SCF	Gas
Density (kg/m <sup>3</sup> )	1,000	200–900	0.6 <sup>-1</sup>
Viscosity (μPa s)	10 <sup>-3</sup>	10 <sup>-5</sup> –10 <sup>-4</sup>	10 <sup>-5</sup>
Diffusion coefficient (m <sup>2</sup> /s)	<10 <sup>-9</sup>	10 <sup>-7</sup> –10 <sup>-8</sup>	10 <sup>-5</sup>
Heat conductivity (W/mK)	<10 <sup>-1</sup>	10 <sup>-3</sup> –10 <sup>-1</sup>	10 <sup>-3</sup>

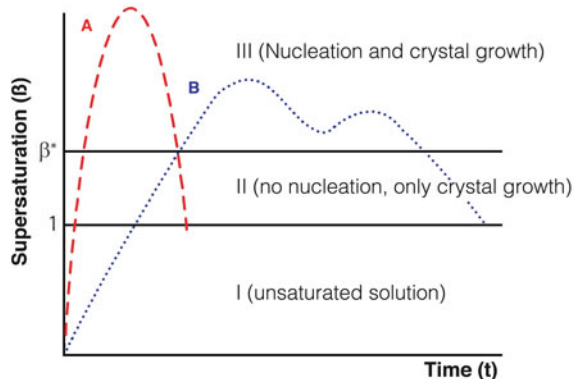
of compounds in SCF in comparison with that in gases. In contrast, because its diffusion coefficient is close to that of a gas, the viscosity of SCF is much lower than that of liquids. In addition, these physical properties of an SCF, such as density, viscosity, diffusion coefficient, and heat conductivity values, can be varied by slightly changing the temperature and pressure around critical point. These higher diffusivities, lower viscosities, and lower surface tension enhance reaction rates. Moreover, the tunability of the density and transport properties of the supercritical fluid not only allows the easy manipulation of reactions but also helps in product separation [10]. Residual solvent removal by SCF exploits the great diffusivity of the compressed gas as well as the easy evaporation of organic solvent into the supercritical phase.

Two of the main advantages of CF technology are the avoidance of the excessive use of organic solvents and high temperature to produce particles. Other benefits are its high versatility, the flexibility in offering various processing approaches and the ability to reach unique processing conditions, which are not possible to obtain in traditional process. In addition, the considerable reduced complexity of supercritical process due to a decrease in the number of steps, is an important factor to bear in mind.

CF-based precipitation process occurs in a non-oxidizing atmosphere and without applying high shear forces, which makes this technology very suitable for thermally, chemically, or physically unstable materials, such as biological compounds, chemical intermediates and pharmaceuticals.

Precipitation or crystallization is a transient nonequilibrium process associated with a phase change leading to crystal formation. The driving force for this process is supersaturation. In the area above the supersaturation boundary, the crystallization process, which makes reference to the simultaneous occurrence of nucleation, crystal growth, and agglomeration, takes place [5]. A high degree of supersaturation increases the nucleation rate and reduces the growth rate (see Fig. 5.2). The degree of supersaturation is the ratio of the drug concentration in the solution to its solubility in that solution at that particular condition. If the degree of supersaturation is low and achieved slowly (in case of poor mixing), then nucleation rate is slow and it takes a longer time for the system to cross the metastable zone, favoring particle growth over nucleation. On the other hand, if supersaturation is high and is attained very fast, then nucleation rate would be very high and it would take less time to cross the metastable zone. This hinders particle growth, and thereby the particle size obtained is comparatively smaller. However, a high supersaturation also increases the mass transfer gradient and can enhance particle growth [11–13].

**Fig. 5.2** Qualitative supersaturation profiles corresponding to a crystallization process where nucleation phenomena are dominant over crystal growth (trace A) or crystal growth is dominant over nucleation (trace B).  $\beta$  is the ratio between the actual concentration ( $C$ ) and the saturation concentration, or solubility, ( $C_s$ ), of the solute to crystallize



Crystallization is governed by both thermodynamic and kinetic factors, which are often difficult to control as there are several operative conditions that can be modified: temperature range, cooling/heating rates, choice of solvents, and variation of solute concentration (which depends on the temperature). Additional factors such as impurity level, mixing regime, vessel design, and cooling profiles can deeply impact the size, number, and shape of the crystals produced.

Traditional crystallization methods include sublimation, crystallization from solutions, evaporation, thermal treatment, desolvation, or grinding/milling. Classical crystallization processes are based on temperature variation where the thermal conductivity is the rate-limiting step [14]. In conventional crystallization, efficient stirring systems are required to transmit the temperature changes efficiently through the whole solution. In large-scale applications, stirring efficiencies are usually very poor, and as a consequence very low and heterogeneous supersaturation profiles are obtained. Hence, very large particles are obtained in industry and down-stream operations are required (see Fig. 5.3).

However, in SCF process, the advantage is literally the millisecond timescale for pressure reduction or admixing solvents. The use of SCFs also takes advantage of other unique conditions such as high rate of solvent evaporation and fine-tuning of the density. The kinetics of the crystallization process is mainly driven by diffusion, which is strongly related to the density of the solvent. Additionally, the possibility of modulating the rate of solvent evaporation deeply influences the kinetics of the process [5].

If large levels of supersaturation are attained rapidly and there is homogeneity of this supersaturation profile through the bulk solution, nucleation phenomena will dominate crystal growth, and very small and mono disperse particles will be produced (see Fig. 5.4). When using CFs as solvents or cosolvents, large levels of supersaturation all over the system can be obtained and, as a consequence, uniform micro- and nanoparticulate materials are produced in a single step.

Summarizing, the most noticeable process parameters that differentiate SCF technologies from conventional methods are the high compressibility and diffusivity of the supercritical fluid and the possibility of fine-tuning pressure and solvent

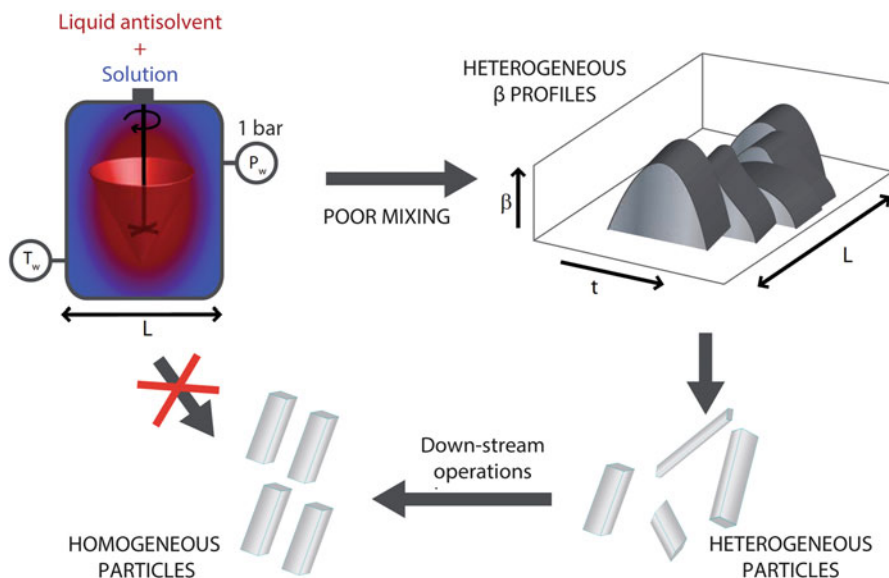


**Fig. 5.3** Schematic representation of a conventional precipitation process based on composition changes, in which poor mixing between solvent and antisolvent promotes low and heterogeneous supersaturation ( $\beta$ ) degrees, generating large and heterogeneous particles that need further processing.  $\beta$ , supersaturation; L, distance; t, time

evaporation rate. These parameters provide additional dimensions for process control and the possibility of easy tailoring the final properties of the active compounds. A unique advantage that should be underlined is the almost instantaneous pressure variation in supercritical processes, which leads to uniform conditions in the whole solution [15]. Furthermore, supercritical fluid-based technology is a promising green alternative, since regulatory requirements in the pharmaceutical industry are becoming more and more restrictive in the use and residual content of volatile organic solvents in drug products [5].

The most widely used CF is  $\text{CO}_2$  because it is nontoxic, nonflammable, cheap, and easy recyclable. Hence, the physicochemical properties of  $\text{CO}_2$  are key factors in particle design. In particular, solubility in  $\text{CO}_2$  is the major prerequisite for designing particles using this CF, that is, the applicability of the technology is dependent on this solubility. When  $\text{CO}_2$  is used as a solvent, size distribution and morphology of the particles produced are a function of the concentration of the materials in  $\text{CO}_2$  and the subsequent expansion conditions. In contrast,  $\text{CO}_2$  antisolvent processes are based on the change in the solubilization power of the solvent as a result of the addition of  $\text{CO}_2$  [8].

To choose a process for particle design, the first thing to consider is the solubility of the substance in the supercritical fluid. The choice between different methods will then be made considering the desired particle size, shape and structure, processing costs, and production scale [14]. The study of phase behavior of the drug in pure

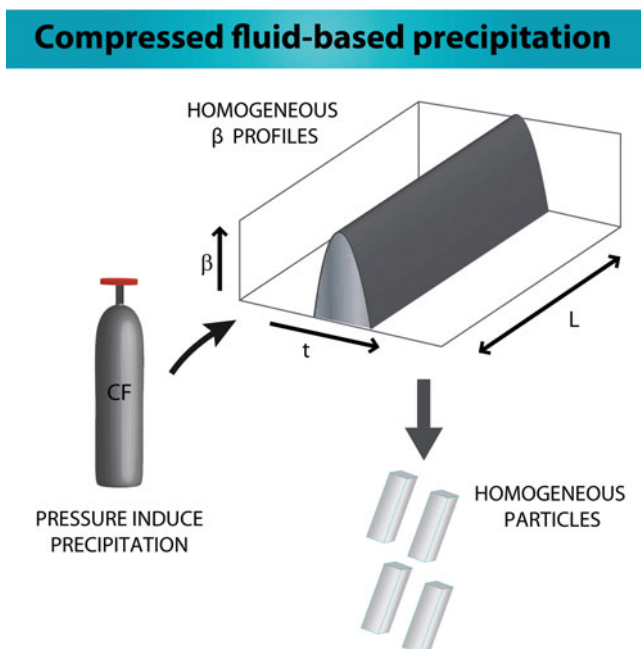


**Fig. 5.4** Schematic representation of the homogeneous supersaturation ( $\beta$ ) profiles usually achieved by CF-based methods, which result in uniform particles in a single step (Adapted with permission from [14])

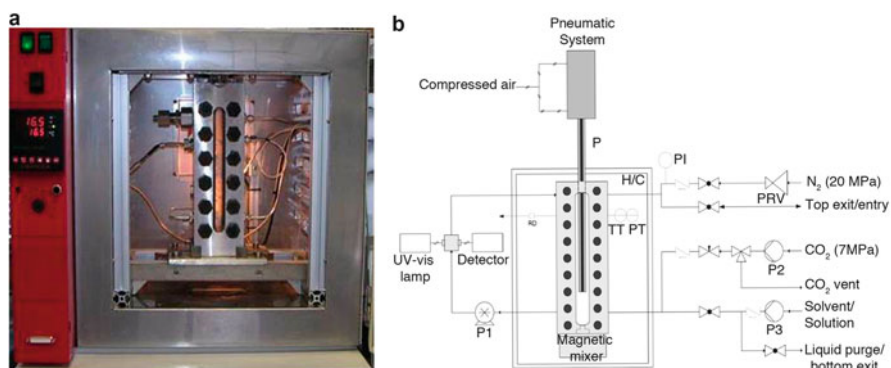


**Fig. 5.5** (a) Image and (b) Schematic representation of the variable volume cell

CO<sub>2</sub> or CO<sub>2</sub>-expanded solvents becomes crucial, and it is an important step toward successful election of the most suitable methodology to process the active compound. One of the most effective methods for conducting solubility measurements implies the use of a high-pressure phase analyzer equipped with windows that allow visualization of its interior (Fig. 5.5). Solubility measurements aid to avoid

time and economic expenses derived from trial-and-error procedures. There are well-documented examples of the use of high-pressure analyzers for studying the solubility behavior of different drugs, lipids, and biodegradable polymers in  $\text{CO}_2$ -expanded solvents [16–20].

As one of the main objectives of using CFs is to avoid the use of organic solvents during processing of the APIs, the study of the phase behavior in pure  $\text{CO}_2$  is the first step in solubility studies.

A certain amount of the compound of interest is introduced inside the high-pressure phase analyzer under the working conditions of temperature and pressure. The addition of  $\text{CO}_2$  into the cell could lead to three different scenarios: the progressive dissolution of the solid in  $\text{CO}_2$ , the swelling of the CF inside the compound, or neither situation. This last case is the most common behavior for the majority of drugs, polymers, and polar substances. In the latter, further studies in mixtures of organic solvents and  $\text{CO}_2$  would be required. In order to get the solubility curve of a compound in the mixture of organic solvent and  $\text{CO}_2$ , the solubility of the compound in the pure organic solvent and in pure  $\text{CO}_2$  needs to be measured, as well as the solubility of the compound in the mixture of organic solvent/ $\text{CO}_2$  at different concentrations of  $\text{CO}_2$ . The method to calculate the solubility of the compound in the expanded mixture is called the vanishing point method, and it is explained in detail in the [Appendix](#). Examples of solubility curves are depicted in Fig. 5.6, which shows the very different behaviors that can

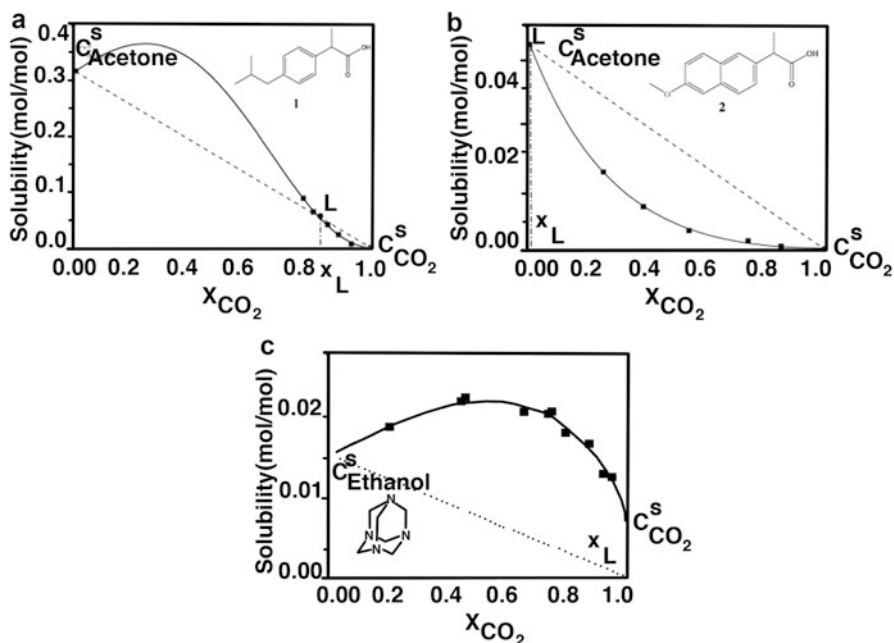


**Fig. 5.6** Solubility curve of (a) ibuprofen, (b) naproxen in  $\text{CO}_2$ -expanded acetone at 10 MPa and 298 K, and (c) hexamethylenetetramine in  $\text{CO}_2$ -expanded ethanol at 10 MPa and 313 K (*dashed lines* represent the ideal dilution behavior)

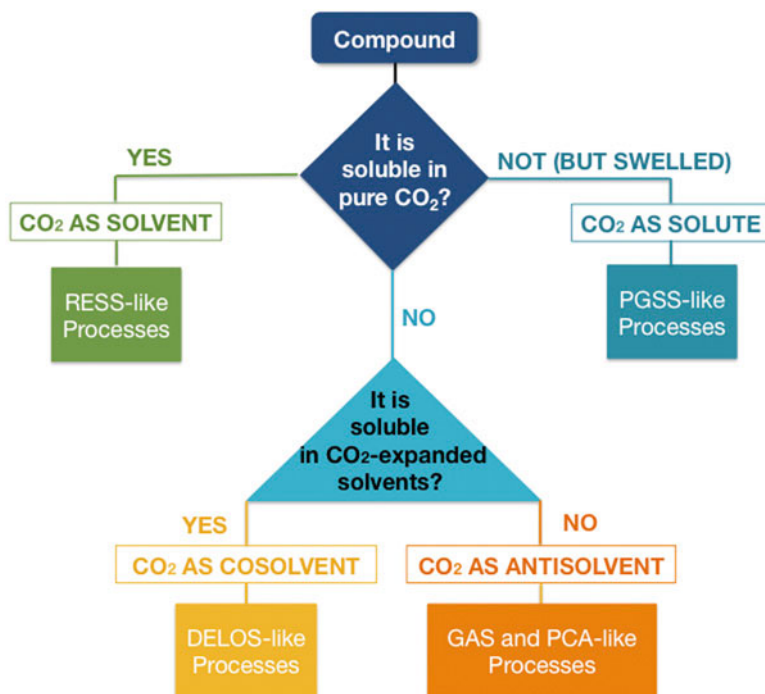


Fig. 5.7 Different CF-based technologies (Adapted with permission from [14])

be attained when CO<sub>2</sub> is added to a solution of a compound in an organic solvent. The behavior is defined by the minimum composition from which the CO<sub>2</sub> starts to provoke the precipitation of the compound, which can be calculated from the intersection of the solubility curve with the ideal dilution line of the compound in the organic solvent/CO<sub>2</sub> mixture. In the case of ibuprofen in CO<sub>2</sub>-expanded acetone, CO<sub>2</sub> acts as a cosolvent until molar fractions of 0.82 (Fig. 5.6a), whereas in the case of naproxen (Fig. 5.6b), the addition of CO<sub>2</sub> over the solution of the solid in acetone provokes the precipitation of the drug, revealing the antisolvent character of the CO<sub>2</sub> [16]. Moreover, CO<sub>2</sub> can show a synergic behavior with the organic solvents, as was observed for the hexamethylenetetramine in CO<sub>2</sub>-expanded ethanol (Fig. 5.6c) [18].

CF-based precipitation processes can be classified into different groups depending on whether the CF, usually CO<sub>2</sub>, acts as a solvent, solute, cosolvent, or antisolvent with respect to the material to precipitate (Fig. 5.7).

### 5.2.1 CF as a Solvent: Rapid Expansion of Supercritical Solution (RESS)

In this process, the solute is first solubilized in the supercritical fluid. The solution is then expanded across a nozzle or capillary at supersonic velocities. The rapid expansion leads to supersaturation of the solute and subsequent precipitation of

micro- and submicron particles. The RESS process has been demonstrated to produce contaminant-free microparticles ranging from a few microns to several hundred microns, but some examples in the literature report nanometric particles using appropriate nozzles. [21, 22]. The RESS process has also been applied for coprecipitation of solutes [10].

The facts that affect particle size and morphology in the RESS process include the length/diameter ratio of the expansion device, the RESS time scale determined by the expansion trajectory from the preheater, and the particle agglomeration during free-jet expansion.

A major limitation of the RESS process is that, at moderate temperatures and pressures (<60 °C and 300bars), solubilities of compounds in CO<sub>2</sub> are in the order of 0.01 wt% or less. Indeed, the high temperatures that are often required make it unsuitable for labile polymers and drugs. To circumvent this problem, small percentages of organic cosolvents are normally used.

### 5.2.2 *CF as an Antisolvent*

The relatively low solubilities of pharmaceutical compounds and polymers in CO<sub>2</sub> are exploited in this type of processes, where the active compound is first dissolved in a conventional solvent to form a solution and the CO<sub>2</sub>, which behaves as an antisolvent for this solution, is added to provoke solute precipitation. The ideal situation is that the solute is insoluble in compressed CO<sub>2</sub> (cCO<sub>2</sub>), and at the same time, the organic solvent is completely miscible with cCO<sub>2</sub> at the working temperature and pressure [23, 24].

The advantage of processes using CO<sub>2</sub> as an antisolvent in comparison with conventional precipitation techniques is that powders may be produced at ambient temperatures, in a low-shear environment and with a low level of oxygen exposure. All these considerations are relevant for the production of drug and protein powders. It also has the advantages of having a higher solute throughput and flexibility of solvent choice.

Antisolvent techniques are probably the most used for micronization of pure active drugs and polymers, and particle sizes ranging from nanometers to microns can be obtained.

The solute can be recrystallized in two ways:

- In the GAS (gas antisolvent) process, a solution is expanded several fold by its mixing with compressed CO<sub>2</sub> in a vessel. Because CO<sub>2</sub> expanded solvent has a lower solvent strength in comparison with the pure solvent, the mixtures become supersaturated, forcing the solute to precipitate or crystallize as micro particles [25, 26].
- The PCA (precipitation with a compressed antisolvent) process, which is semi-continuous, involves spraying the solution through a nozzle as fine droplets into compressed CO<sub>2</sub> [27–29]. Using PCA-like methods, precipitates with a high

residual solvent content are generally achieved and long drying periods are therefore required, which often leads to particle agglomeration and aggregation. This can be overcome by enhancing mass transfer between the supercritical antisolvent and the solution during the spraying, which can be achieved by favoring the mixing between both fluids, for example, using an ultrasonic nozzle.

### **5.2.3 CF as a Solute: Particles from Gas-Saturated Solutions (PGSS)**

As the solubilities of compressed gases in liquids and solid like polymers are usually high and much higher than the solubilities of such liquids and solids in the compressed gas phase, the process consists in the solubilization of supercritical CO<sub>2</sub> in melted or liquid-suspended substances, leading to a so-called gas-saturated solution/suspension. When this solution is rapidly depressurized through a nozzle, microparticles are formed due to a reduction in temperature and atomization experienced by the gas-saturated solution during the expansion. Advantages of PGSS process include the lack of necessity for the solute to be soluble in CO<sub>2</sub> and the absence of solvents. However, its main limitation is the melting of the compound, which can be problematic for heat-sensitive molecules. In order to tackle this problem, some drugs have been processed with polyethylene glycol 4,000, which dissolves the drugs lowering their melting point and, hence, allowing their precipitation at milder conditions [30–33].

### **5.3 CF as a Cosolvent: DELOS (Depressurization of an Expanded Liquid Organic Solution)**

In contrast to antisolvent techniques, DELOS process takes advantage of the cosolvent behavior that some CFs present over solutions of compounds in certain organic solvents. In this method, the CF is added to an organic solution of the compound to precipitate, resulting in a new pressurized solution, usually at pressures lower than 10 MPa, in which the solvent medium is formed by the mixture of “organic solvent/CF.” As usual, the most common CF used is CO<sub>2</sub>. The DELOS process, which is described in Fig. 5.8, is a crystallization technique based on the use of CO<sub>2</sub>-expanded solutions.

The crystallization driving force in this process is the large, abrupt and extremely homogeneous temperature decrease produced by the rapid evaporation of CO<sub>2</sub>, which was dissolved at a given pressure ( $P_w$ ) and temperature ( $T_w$ ) in an organic liquid solution containing the compound to be crystallized. This abrupt and homogeneous temperature reduction produced during depressurization of the CO<sub>2</sub>-expanded solution generates a pronounced and very homogeneous increase of the

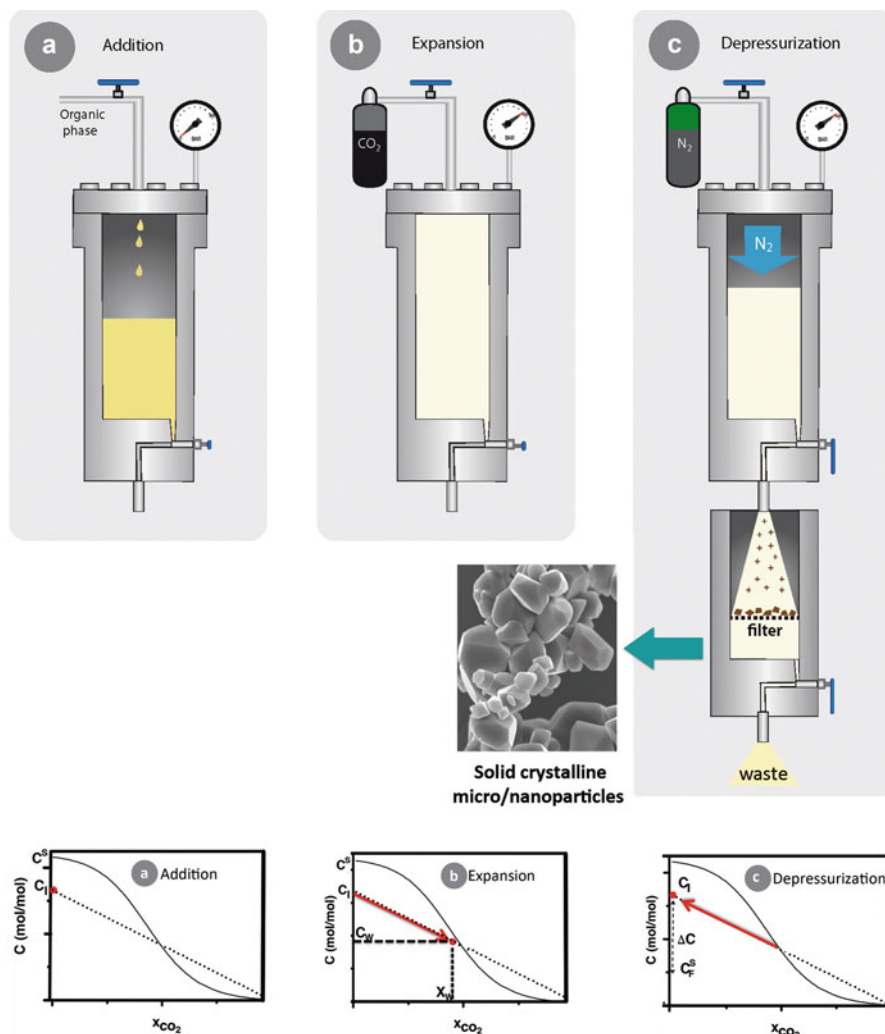


**Fig. 5.8** Stages of the DELOS process

supersaturation in every point of the solution, which favors nucleation rather than crystal growth, and promotes the formation of micro- or submicron-sized particles with narrow particle size distributions and unique supramolecular structural homogeneity.

In DELOS process, it can be assumed that the final temperature reached after depressurization is attained before primary nucleation takes place, and therefore, as schematized in Fig. 5.8, the initial solute concentration is reestablish ( $C_F = C_1$ ).

As mentioned, the abrupt and homogenous decrease in temperature experienced by the CO<sub>2</sub>-expanded solution is what generates the supersaturation; hence, the

magnitude of the temperature decrease ( $\Delta T = T_F - T_W$ ) is what determines the yield and characteristics of the crystalline particles produced.

It has been demonstrated that changes in the flow rate through the depressurization valve and in the working pressure ( $P_w$ ) keeping the molar fraction of CO<sub>2</sub> constant ( $x_w$ ), do not affect  $\Delta T$ . This result is very relevant from a practical point of view since it allows to work at much lower  $P_w$  than those used in other high-pressure crystallization techniques, without influencing neither the yield nor the final characteristics of the precipitate. The  $\Delta T$  is determined by the nature of the solvent employed in the process and the CO<sub>2</sub> content ( $x_w$ ) of the expanded solution. During depressurization of the expanded solution, CO<sub>2</sub> goes from the liquid state at  $P_w$  to the vapor state at atmospheric pressure, and, since DELOS is an adiabatic process, the heat required for the CO<sub>2</sub> vaporization must be extracted from the liquid solution, and as a consequence, the solution experiences the large, abrupt, and homogenous decrease of temperature [34].

In DELOS crystallization, it could be considered that the difference between the initial concentration ( $C_i$ ) of the compound in the organic solution and the solute solubility ( $C_F^S$ ) in the organic solvent at the final temperature reached after depressurization,  $\Delta C$  ( $\Delta C = C_i - C_F^S$ ), is the maximum supersaturation achieved and the supersaturation ratio ( $S$ ) can be calculated as  $S = C_i/C_F^S$ . Thus, the higher the  $\Delta C$ , the higher the maximum supersaturation attained, and the more favored is the nucleation on the crystal growth. As a consequence, small particles are crystallized.

The supersaturation expressed as mass difference,  $\Delta C$ , is influenced by the initial concentration of the compound in the organic solvent ( $C_i$ ) and the CO<sub>2</sub> content ( $x_w$ ), as the amount of CO<sub>2</sub> determines the final temperature achieved after depressurization, and this value will define the solute solubility in the organic solvent at that final temperature  $C_F^S$ . The higher the  $x_w$  and  $C_i$ , the higher the supersaturation attained, and as a consequence, the smaller the particles produced. However, except when the addition of CO<sub>2</sub> provokes a synergistic enhancement of the solubility in the CO<sub>2</sub>-expanded mixture,  $x_w$  and  $C_i$  cannot be increased unlimitedly, since the drug solubility behavior in the CO<sub>2</sub>-expanded solvent limits the operation conditions as can be seen in Fig. 5.6.

Through DELOS process, it has been possible to obtain micron-sized particles of 1,1-bis-(*n*-butylamino)-9,10-anthraquinone (colorant solvent blue [35]) with a high degree of crystallinity. Particle size was reduced two orders of magnitude in comparison with that presented by particles produced through conventional cooling crystallization from methanol solutions [34].

The feasibility of DELOS to process active pharmaceutical ingredients such as ibuprofen, cholesterol, aspirin, and naproxen as finely divided powders with narrow size distribution, high crystallinity degree, high polymorphic purity, and with a minimum solvent content below the permitted by the regulation has been demonstrated. Figure 5.9 depicts the SEM images of the processed drugs.

It has been mentioned that polymorph control is paramount in pharmaceutical development. Different polymorphs can have different bioavailability, activity, and

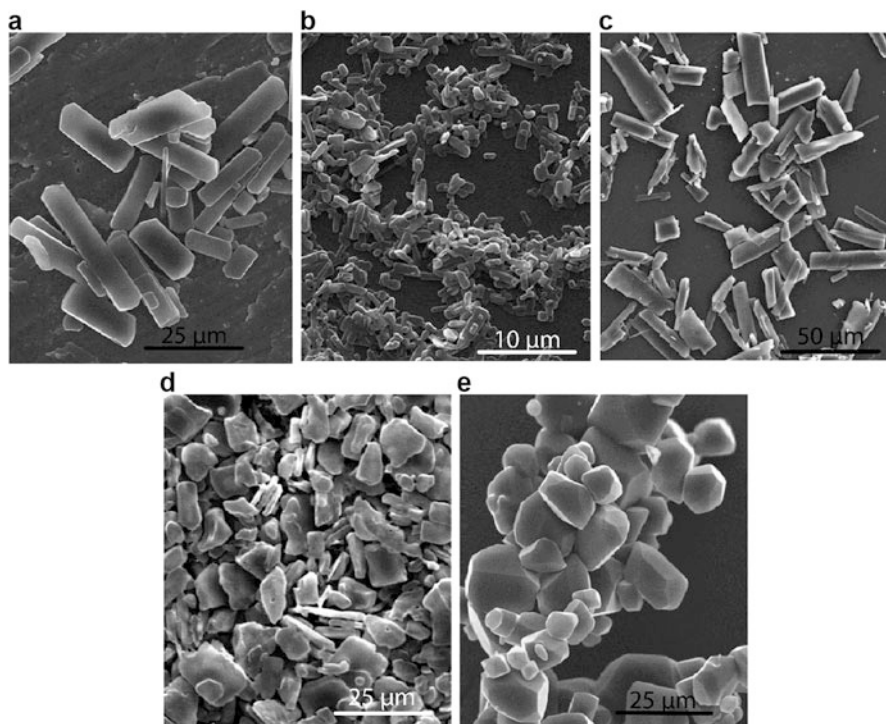
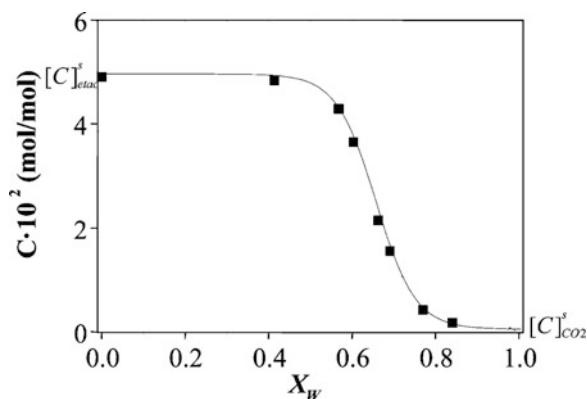


**Fig. 5.9** SEM images of DELOS processed drugs. *Top images*, from left to right: aspirin, cholesterol, naproxen. *Bottom images*, from left to right: ibuprofen and acetaminophen [37]

even toxicity and can have pronounced effects on shelf life, formulation, and processing of a drug [36].

Another advantage of introducing pressure as a new degree in freedom when using a CF-based process is that pressure influences not only the kinetics and the thermodynamics of the process, but also the occurrence of different polymorphic forms of the crystallized compound. Stearic acid was chosen as a model molecule of long alkyl chain compounds because it is extremely rich in polymorphic forms. Five polymorphic phases of stearic acid have been reported: two triclinic forms belonging to what is called the A-form, the  $A_2$  and  $A_3$  forms whose structures are still not known, and three monoclinic forms having an orthorhombic subcell, called B, C, and E polymorphs. B and E polymorphs show the phenomenon called polytypism that corresponds to a higher-order structural difference caused by the different stacking sequences of the layers. In both B and E forms, there are two distinct polytypes: one showing a single-layered structure with a monoclinic space symmetry ( $E_m$ ) and another exhibiting a double-layered structure with orthorhombic space symmetry ( $E_o$ ). Regarding the thermodynamic stability of these polymorphs, it is established that B and C forms are stable below and above 305 K, respectively, while the A and E forms are considered as metastable phases in the whole

**Fig. 5.10** Solubility of stearic acid in CO<sub>2</sub>-expanded ethyl acetate at 6 MPa and 293 K



temperature region. It is proven that usually stearic acid crystallizes predominantly into the E<sub>m</sub> form with traces of E<sub>o</sub> and C forms from rapid crystallization experiments. From slow crystallization conditions, forms A<sub>2</sub>, B<sub>o</sub>, B<sub>m</sub>, E<sub>m</sub>, and C are obtained. A<sub>2</sub> form is mainly obtained from isooctane at room temperature, B<sub>m</sub> form is mainly obtained from toluene at 273 K, and finally, B<sub>o</sub> form with traces of B<sub>m</sub> is obtained from toluene at 298 K. On heating, the low-temperature phases (A, E, B) experience an irreversible first-order solid–solid transition into the C form. The C form melts and it is recovered from the melt on cooling, remaining metastable. However, the pure E<sub>m</sub> form has never been achieved using conventional crystallization methods.

Figure 5.10 shows the solubility data of stearic acid in CO<sub>2</sub>-expanded ethyl acetate at 293 K and 6 MPa at different CO<sub>2</sub> compositions, showing that CO<sub>2</sub> acts as a cosolvent in a wide range of molar fractions, from 0.00 to 0.80. This solubility behavior suggests that DELOS method is the most appropriate one in order to crystallize stearic acid with high yields.

When precipitating stearic acid through DELOS, only the monoclinic E form is produced [37]. If stearic acid is precipitated using conventional cooling crystallization experienced the same  $\Delta T$  as in the DELOS process, a mixture of the monoclinic E form and the C form is obtained. Such difference can be attributed to the much slower cooling rate and the less homogenous supersaturation rate occurring over all the solution in the conventional cooling process than that experienced in a DELOS crystallization. The C form is thermodynamically enhanced over the E form. At lower temperatures, such as the ones reached in the DELOS process, the E form may become thermodynamically enhanced in relation to the C form. However, in this type of process, the thermodynamic balance is less important in the polymorphic production than the kinetic control due to the high supersaturation rates that are obtained in DELOS crystallizations.

GAS crystallizations of stearic acid give the thermodynamic-enhanced C form because of the low influence of kinetic aspects on this process.

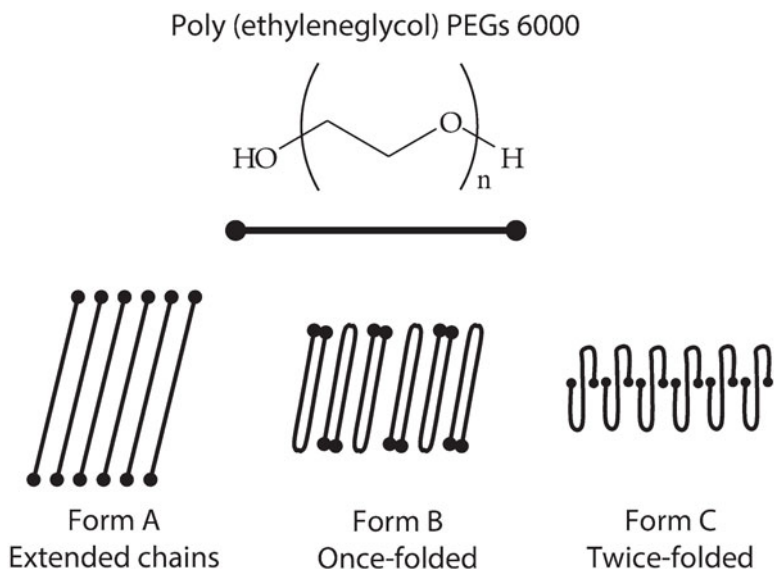


**Fig. 5.11** Different crystal phases of PEG6000

Hence, DELOS process is a kinetically controlled crystallization in which high supersaturation levels are rapidly achieved. This process is especially indicated for obtaining kinetically controlled polymorphs of exceptional polymorphic purity.

Similar results have been obtained when precipitating polyethulene glycols (PEGs) through DELOS process. These polymers are self-organizing polymers, which have the ability to form different functional structural hierarchies, such as micelles and lyotropic phases. PEGs are very promising candidates for thermal energy storage materials and also have relevant biomedical and biotechnological applications. The polymer chain folding can be modified depending on the crystallization/precipitation method. In particular, PEG6000 can crystallize into three different forms: with polymer chains extended, folded once or folded twice (Fig. 5.11).

The melting behavior of these polymers has been studied in detail [38, 39]. It was revealed that the most thermodynamically stable phase is the extended chain phase, and the folded ones are metastable phases, being the twice-folded metastable in comparison with the once folded. It has been demonstrated that by choosing the appropriate experimental process variables, a kinetically enhanced pure phase can be obtained by DELOS as can be ascertained from Fig. 5.12 [40].

Recently, a new polymorph of  $\beta$ -sitosterol has been discovered, which is more crystalline than the native form, through its precipitation by DELOS process [41]. In addition, particle size was reduced by an order of magnitude.  $\beta$ -sitosterol is a common phytosterol, an ingredient used in functional food and nutraceutical products to address cholesterol reduction. Phytosterols are not synthesized by the

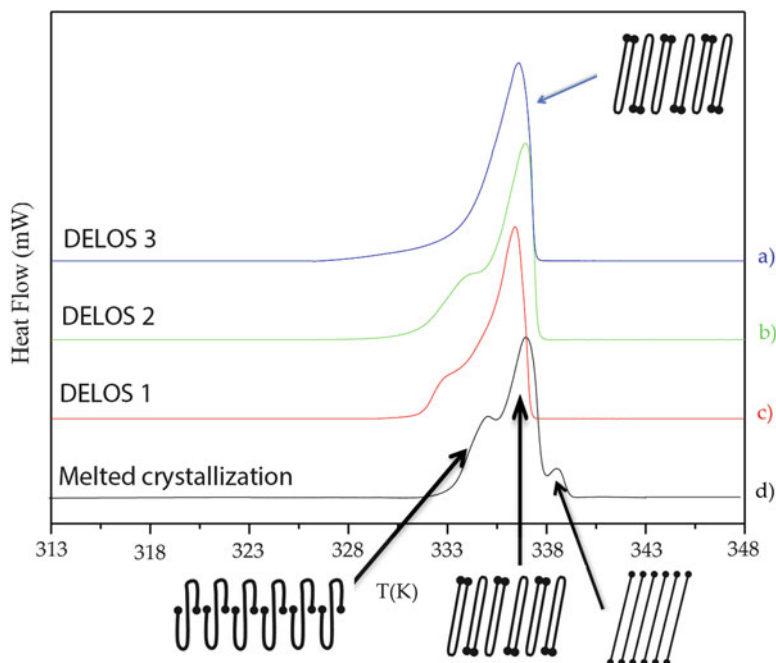


**Fig. 5.12** DSC analysis of PEG6000 solids obtained by DELOS process (a, b, c) and by a conventional cooling method from the melted solid (d)

human body and, hence, have to be incorporated in the diet. Phytosterols are isolated commercially from vegetable oil deodorizer distillates or tall oil in the form of a mixture of sterol components, and its separation presents a major challenge. A lot of effort has been put in the obtaining of small crystals of unbond sterols. Different approaches have been investigated for this objective, ranging from micronization of crystals to the formation of emulsions and liposomes. Supercritical carbon dioxide technology has been applied for the recovery of phytosterols from different sources; however, the use of supercritical fluid technologies for phytosterol particle engineering has been scarce, and although some processes have produced particles with very small size (aggregates of 50 nm particles), the main shortcoming is scaling up the process as phytosterol presents a very low solubility in scCO<sub>2</sub>. The behavior of phytosterol–ethanol–CO<sub>2</sub> mixtures was studied, and the data revealed that CO<sub>2</sub> acts as a cosolvent for a wide range of concentrations [42], highlighting that DELOS process has a huge potential to precipitate phytosterols. The precipitation of phytosterols by DELOS yielded a new and highly crystalline polymorph of phytosterols in the form of fine powder with a mean particle size diameter of 6.5  $\mu\text{m}$  and narrow particle size distribution. This new phase presents a higher chemical purity and higher crystallinity than the native mixture; it is stable at room temperature at least for 2 years and can be converted into the native form by heating it above 368 K.

This last observation reveals the exceptional ability of CF precipitation techniques to reach unique processing conditions, otherwise impossible to obtain in traditional processes.

In DELOS, CO<sub>2</sub> acts as a cosolvent, which allows to work with more concentrated solutions than in technologies using pure CO<sub>2</sub>. This makes possible to precipitate higher amounts of polar and high-molecular-weight compounds than in RESS process, working at lower pressures. In addition, this method is suitable for drugs with low melting point or for polymers that are not able to absorb high quantities of CO<sub>2</sub>. In comparison with other CF crystallization techniques, like RESS and PCA, DELOS process requires mild working pressure, which is a crucial parameter in the economical evaluation of the process for industrial applications.

## 5.4 Scale-Up of the DELOS Process

The formation of drug particles using CO<sub>2</sub> as a green solvent holds immense appeal for large-scale application in pharmaceutical industry [10]. Although large-scale commercial use of SCF technology has been used successfully to decaffeinate coffee and tea, as well as extract spices, hops, and flavoring, it has not yet become the first-choice technology for particle design in the pharmaceutical industry. The reason may be the cost of installing GMP-compliant equipment and the relatively limited experience actual manufacturers have with commercial production of CF-based technology. Although CO<sub>2</sub> is inexpensive and can be recycled, the capital investment and running cost for CO<sub>2</sub>-based technology processes are at least as much as those for other multipurpose processes, such as fluidized-bed granulation spray drying and freeze drying. However, recently, a study on scale-up for particle formulation that launches a positive scenario has been revealed: the study publishes evidence of the successful implementation of industrial-scale CF-based facilities for pharmaceutical particle design [8].

The price of large-capacity plants, with optimized design and operation, is of the very same order of magnitude as those related to conventional processes with similar restrictions in terms of environmental and health issues [43].

DELOS process was successfully scaled-up by sevenfold from laboratory (300 mL vessel volume) to pilot-plant scale (2,000 mL vessel volume). The results showed an extremely high reproducibility, regarding particle size and yields. The scale-up design was easily done by geometrical factors. In crystallizations from liquid solvents, the common scale-up troubles are related to effective mixing, since the bigger the vessel, the bigger the gradient temperature, yielding very heterogeneous supersaturation profiles and poor reproducibility. In DELOS, stirring is only needed to ensure a homogenous mixture between the organic solutions of the solid and CO<sub>2</sub>, and it is not relevant during depressurization step, where precipitation takes place; therefore, the final characteristics of the particles do not depend on stirring efficiency.

In addition, feasibility of DELOS process for industrial applications has been evaluated. The design turned out to be perfectly viable according to GMP's rules. Compared to conventional multistep procedures, decreasing process units also simplifies the related quality documentation. Evaluation of the environmental sustainability of this process, compared again to conventional techniques, showed very interesting results: sustainability indexes, which account for the required amount of materials, energy, water, and contamination emitted for kg of produced product, were significantly lower than the corresponding index of conventional process. This reveals that DELOS is a greener and more environmentally friendly precipitation technique than conventional pharmaceutical procedures.

## 5.5 Conclusions

CF-based processes are promising technologies for the production of APIs with precise physical properties such as size, shape, supramolecular organization, and crystalline purity, unattainable by conventional methodologies. In particular, DELOS platform emerges as a powerful alternative for commercial-scale plants. Here, it has been summarized the unique properties of supercritical fluids, as well as the most important CF-based processes. The feasibility of DELOS platform for the preparation in a single step of micron-sized particulate APIs has been proved with several examples. In addition, it was shown that DELOS platform is a suitable technology for obtaining highly pure polymorphic phases. Summarizing, CF-based technologies are cost-effective procedures that entail a high potential for the one-step preparation of particles with the desired particle size and morphology. In light of the actual requirements of the pharmaceutical industry, CF-based processes are very promising eco-efficient solutions.

## Annexes: Vanishing Point Method

The vanishing point method is based on the observation of the progressive redissolution of a solute C until a complete transparent solution is formed. Such solid is in equilibrium with a saturated phase of itself in a homogeneous mixture between two fluids A and B. The increase of the solvating capacity of A/B binary mixture through the change of its composition provokes the progressive redissolution of the solute, which is completed at what is called *the vanishing point*. The vanishing point method is an adequate procedure for performing solubility studies either at atmospheric pressure, where A and B are both conventional solvents, or at high pressure, where A and B can be a conventional solvent and a compressed fluid (CF), such as CO<sub>2</sub>, respectively (Wubbolts, F.E., *Supercritical crystallisation: volatile components as antisolvents*, Ph. D. Thesis, Technical UniG.M., *Measurement and*

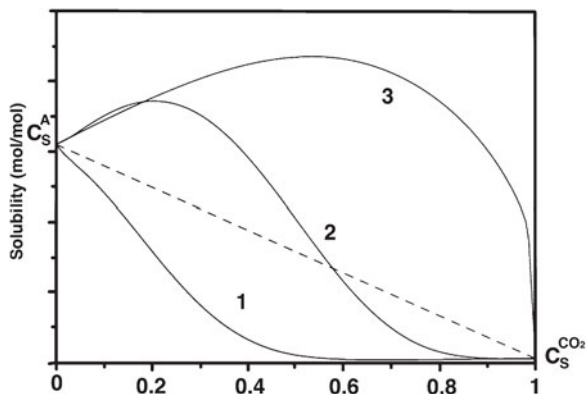


**Fig. 5.A.1** Possible solubility curves of a solute C in an organic solvent/ $\text{CO}_2$  mixture of different compositions at constant pressure and temperature. Curve 1: antisolvent behavior of  $\text{CO}_2$ , curve 2: cosolvent behavior of  $\text{CO}_2$ , curve 3: synergistic behavior between  $\text{CO}_2$  and the organic solvent. The *dashed line* represents the ideal solubility variation with respect to solvent compositions.  $C_s$  = saturation concentration

*modelling of the solubility of solids in mixtures of common solvents and compressed gases*, Journal of Supercritical Fluids, 32 (2004) 79–87.).

The high-pressure phase analyzer enables to obtain solubility curves of a solute in organic solvent/ $\text{CO}_2$  mixtures like those depicted in Fig. 5.A.1, where the CF can present different behaviors with respect to the solution of the solute C in the organic solvent A. Thus, the CF can act as antisolvent (curve 1), cosolvent (curve 2) or can have a synergic behavior with the organic solvent augmenting, as a consequence, the solvating capacity of the mixture organic solvent/ $\text{CO}_2$  with respect to the pure solvents (curve 3) [7].

In curve 1, the addition of  $\text{CO}_2$ , at constant pressure ( $P_w$ ) and temperature ( $T_w$ ), over a saturated solution of the compound C in the organic solvent A provokes the precipitation of such compound presenting, therefore, an antisolvent behavior. In curve 2, there is a range of  $x_{\text{CO}_2}$  in which the CF acts as a cosolvent, preventing the precipitation of the solute. This range is defined by the intersection point between the ideal dilution line and the curve corresponding to the real variation of compound C solubility with the composition of the binary mixture organic solvent/ $\text{CO}_2$ . In the case of curve 3, the addition of  $\text{CO}_2$  generates a binary system with a superior solvating power than the organic solvent A due to a synergic effect of the CF and the organic solvent in a range of  $x_{\text{CO}_2}$ .

## References

1. A. Zeinolabedini Hezave, F. Esmailzadeh, *J. Disper. Sci. Technol.* **33**(8), 1106 (2012)
2. D. Horn, J. Rieger, *Angew. Chem. Int. Ed.* **40**(23), 4330 (2001)
3. I. Pasquali, R. Bettini, F. Giordano, *Eur. J. Pharm. Sci.* **27**(4), 299 (2006)

4. B. Shekunov, P. Chattopadhyay, H. Tong, A. Chow, *Pharm. Res.* **24**(2), 203 (2007)
5. I. Pasquali, R. Bettini, F. Giordano, *Adv. Drug Deliv. Rev.* **60**(3), 399 (2008)
6. B.Y. Shekunov, P. Chattopadhyay, J. Seitzinger, R. Huff, *Pharm. Res.* **23**(1), 196 (2006)
7. C. Vemavarapu, M.J. Mollan, M. Lodaya, T.E. Needham, *Int. J. Pharm.* **292**(1), 2 (2005)
8. T. Yasuji, H. Takeuchi, Y. Kawashima, *Adv. Drug Deliv. Rev.* **60**(3), 388 (2008)
9. K. Moribe, Y. Tozuka, K. Yamamoto, *Adv. Drug Deliv. Rev.* **60**(3), 328 (2008)
10. B. Subramaniam, R.A. Rajewski, K. Snavelly, *J. Pharm. Sci.* **86**(8), 885 (1997)
11. I. Pasquali, R. Bettini, *Int. J. Pharm.* **364**(2), 176 (2008)
12. M. Löffelmann, A. Mersmann, *Chem. Eng. Sci.* **57**(20), 4301 (2002)
13. N. Variankaval, A. Cote, M. Doherty, *AIChE J.* **54**(7), 1682 (2008)
14. E. Elizondo, J. Veciana, N. Ventosa, *Nanomedicine* **7**(9), 1391 (2012)
15. J. Jung, M. Perrut, *J. Supercrit. Fluids* **20**(3), 179 (2001)
16. M. Muntó, N. Ventosa, S. Sala, J. Veciana, *J. Supercrit. Fluids* **47**(2), 147 (2008)
17. M. Muntó, J. Gómez-Segura, J. Campo, M. Nakano, N. Ventosa, D. Ruiz-Molina, J. Veciana, *J. Mater. Chem.* **16**(26), 2612 (2006)
18. S. Sala, N. Ventosa, T. Tassaing, M. Cano, Y. Danten, M. Besnard, J. Veciana, *ChemPhysChem* **6**(4), 587 (2005)
19. M. Cano-Sarabia, N. Ventosa, S. Sala, C. Patino, R. Arranz, J. Veciana, *Langmuir* **24**(6), 2433 (2008)
20. M. Turk, P. Hils, B. Helfgen, K. Schaber, H. Martin, M. Wahl, *J. Supercrit. Fluids* **22**(1), 75 (2002)
21. C. Domingo, E. Berends, G. Van Rosmalen, *J. Supercrit. Fluids* **10**(1), 39 (1997)
22. S. Cihlar, M. Tuerk, K. Schaber, *J. Aerosol Sci.* **30**(1), 355 (1999)
23. S. Kim, S. Lee, H.-S. Kim, Y.-W. Lee, J. Lee, *Comput. Aided Chem. Eng.* **31**, 135 (2012)
24. J. Cai, Z. Zhou, X. Deng, *Chin. J. Chem. Eng.* **9**(3), 258 (2001)
25. F. Fusaro, M. Mazzotti, G. Muhrer, *Cryst. Growth Des.* **4**(5), 881 (2004)
26. G. Muhrer, M. Mazzotti, M. Müller, *J. Supercrit. Fluids* **27**(2), 195 (2003)
27. D.J. Dixon, K.P. Johnston, R.A. Bodmeier, *AIChE J.* **39**(1), 127 (1993)
28. W. Schmitt, M. Salada, G. Shook, S. Speaker III, *AIChE J.* **41**(11), 2476 (1995)
29. S. Mawson, S. Kanakia, K. Johnston, *J. Appl. Polym. Sci.* **64**(11), 2105 (1997)
30. D. Perinelli, G. Bonacucina, M. Cespi, A. Naylor, M. Whitaker, G. Palmieri, G. Giorgioni, L. Casettari, *Int. J. Pharmaceut.* **468**(1–2), 250 (2014)
31. M. Fraile, A. Martin, H.,D. Deodato, S. Rodriguez-Rojo, I. Nogueira, A. Simplicio, M. Cocero, C. Duarte, *J. Supercrit. Fluids* **81**, 226 (2013)
32. J. Li, H. Matos, E. De Azevedo, *J. Supercrit. Fluids* **32**(1–3), 275 (2004)
33. M. Brion, S. Jaspert, L. Perrone, G. Piel, B. Evrard, *J. Supercrit. Fluids* **51**(1), 50 (2009)
34. N. Ventosa, S. Sala, J. Veciana, *J. Supercrit. Fluids* **26**(1), 33 (2003)
35. N. Ventosa, S. Sala, J. Veciana, J. Torres, *J. Llibre, Cryst. Growth Des.* **1**(4), 299 (2001)
36. S. Sala, A. Cordoba, E. Moreno-Calvo, E. Elizondo, M. Munto, P.E. Rojas, M.A.A. Larrayoz, N. Ventosa, J. Veciana, *Cryst. Growth Des.* **12**(4), 1717 (2012)
37. S. Sala, E. Elizondo, E. Moreno, T. Calvet, M.A. Cuevas-Diarte, N. Ventosa, J. Veciana, *Cryst. Growth Des.* **10**(3), 1226 (2010)
38. *Non-ionic Surfactants: Polyoxyalkylene Block Copolymers.* (Marcel Dekker, New York, 1996), vol 5, p. 185
39. S. Moghimi, A. Hunter, *Trends Biotechnol.* **18**(10), 412 (2000)
40. PhD Thesis, M. Muntó, *Micro- i nanoestructuracio de materials moleculars funcionals amb fluids comprimits: Desenvolupament de metodologies de preparacio i estudis fisicoquimics*, UAB, 2009
41. E. Moreno-Calvo, F. Temelli, A. Cordoba, N. Masciocchi, J. Veciana, N. Ventosa, *Cryst. Growth Des.* **14**(1), 58 (2014)
42. F. Temelli, A. Cordoba, E. Elizondo, M. Cano-Sarabia, J. Veciana, N. Ventosa, *J. Supercrit. Fluids* **63**, 59 (2012)
43. M. Perrut, *Ind. Eng. Chem. Res.* **39**(12), 4531 (2000)

# Chapter 6

## Addressing the Stochasticity of Nucleation: Practical Approaches

Nadine Candoni, Zoubida Hammadi, Romain Grossier, Manuel Ildefonso, Shuheng Zhang, Roger Morin, and Stéphane Veessler

**Abstract** This chapter presents different practical ways to address nucleation stochasticity. The methods use either statistical studies on spontaneous nucleation or local control of nucleation. Techniques developed in our laboratory are described: droplet-based microfluidics, microinjectors in oil, and external electrical or mechanical fields in confined systems. Results of nucleation kinetics obtained on various molecules are presented in terms of metastable zone, critical supersaturation, nucleation rate, induction time, interfacial energy of the critical nucleus, polymorphism, and detection of the critical nucleus. These practical approaches show considerable potential to increase understanding and control of the nucleation mechanism.

**Keywords** Spontaneous nucleation • Induced nucleation • Microfluidics • Confinement • External fields

### 6.1 Introduction

In crystallization of materials such as pharmaceuticals, proteins, or nanomaterials, the most important properties are crystal morphology, habit, size distribution, and phases. The control of these properties demands an understanding of the mechanisms governing the successive steps of nucleation and growth. Although a great deal is known about crystal growth, considerably less is known about crystal nucleation because of the difficulty of directly observing the nuclei. Indeed, the first nuclei are defined by Kashiev as randomly generated nanoscopic new phases “that have the ability for irreversible overgrowth to macroscopic size” [1]. Hence, nucleation is a stochastic phenomenon and the probability of observing the first nuclei is very low, for spatial and temporal reasons.

---

N. Candoni (✉) • Z. Hammadi • R. Grossier • S. Zhang • R. Morin • S. Veessler  
Aix-Marseille Université, CNRS, CINaM UMR 7325, 13288 Marseille, France  
e-mail: [candoni@cinam.univ-mrs.fr](mailto:candoni@cinam.univ-mrs.fr)

M. Ildefonso  
Université de Pau et des Pays de l'Adour, CNRS, LFC-R UMR 5150, 64012 Pau, France

In this chapter we present practical ways of addressing the stochasticity of nucleation [2]. The first idea consists in performing many spontaneous nucleation experiments and hoping that the law of large numbers permits us to obtain a sharper picture of nucleation. Observation is enhanced by reducing the volume of crystallization [3] and hence the number of crystals. The techniques presented here are droplet-based microfluidics [4–9] and microinjection in oil [10–13]. The second idea consists in inducing nucleation where and when we choose controlling nucleation, which is no longer spontaneous. In this case, the techniques combine confinement of nucleation with localized external fields, such as electrical [14, 15] and mechanical fields [16].

The purpose of this chapter is to show what these techniques currently offer in terms of nucleation kinetics measurements and detection of the critical nucleus. The main questions are what are the factors that influence nucleation and how they are revealed by these techniques? Since we explore nucleation from a purely practical point of view, we do not consider any a priori assumption on the nucleation mechanism. We will present practical examples with mineral, organic, and biological molecules, confirming that nucleation mechanisms are identical for all molecules [17].

## 6.2 Theoretical Background

The following is a brief reminder of nucleation theory and experimental parameters, introducing all the properties accessible with our techniques.

### 6.2.1 Critical Nucleus

Until recently, solution nucleation has been described solely by the classical nucleation theory (CNT), a theory derived from nucleation of droplets in the bulk of pure supersaturated vapors [18]. It considers that once a cluster has reached a critical size, nucleation starts. Hence, the first nucleus is called the critical nucleus. In this model, the critical nucleus appears by densification of molecules and nucleation of a solid phase at the same time. Therefore, the transition from the liquid phase to the solid phase is described by one order parameter, i.e., density. According to CNT, the critical size  $r^*$  is given by the Gibbs–Thomson equation:

$$r^* = \frac{2\Omega\gamma}{kT \ln \beta} \quad (6.1)$$

with  $\Omega$  ( $\text{m}^3$ ) the volume of a molecule inside the crystal,  $\gamma$  ( $\text{J} \cdot \text{m}^{-2}$ ) the interfacial energy of the critical nucleus,  $k$  the Boltzmann constant ( $\text{J} \cdot \text{K}^{-1}$ ),  $T$  the temperature (K), and  $\beta$  the supersaturation ( $C/C_s$ ).  $C$  is the concentration of the solute in solution and  $C_s$  the equilibrium concentration. Hence, if  $\beta > 1$ , the crystal grows; if  $\beta < 1$ , the crystal dissolves; and if  $\beta = 1$ , the crystals and solution are at equilibrium.

While this theory has the advantage of simplicity, some discrepancies (in predicting nucleation frequencies) have been observed with experiments [3, 19–22]. Consequently, a more complicated two-step mechanism was proposed: first, formation of a dense phase of clusters on the model of a liquid–liquid phase separation and, second, organization of these clusters into structured clusters [23–25]. This theory is based on two order parameters, density and structure [26]. Subsequently, a third nucleation theory was proposed linked to biomineralization, consisting of a nucleation via stable prenucleation clusters [27]. For reviews, see Refs. [28] and [29]. Concerning experimental discrepancies, different explanations are proposed. For instance, Knezic et al. [30] suggested that macromolecules take longer to rearrange themselves into crystalline nuclei than smaller molecules (this rearrangement step is not directly taken into account in CNT). Hence, the limiting step, densification or structuration, will depend on the solute.

It must be pointed out that experimental observations and interpretations are influenced by the fact that the location, the nature, and the lifetime of the dense phase and/or the critical nucleus are currently unknown.

## 6.2.2 Nucleation Kinetics

In this chapter we are looking at primary nucleation, i.e., the appearance of crystals in a solution which contains no crystals of that phase. The nucleation kinetics is commonly described by the nucleation rate  $J$ , which is the number of nuclei that form in the supersaturated solution per unit of volume and per unit of time [1, 31–33]. Theoretically, the nucleation rate  $J$  is determined by CNT derived from the Gibbs treatment of droplet nucleation [18]. The general equation for primary nucleation is expressed as Eq. (6.2) [34]:

$$J = K_0 \exp\left(\frac{\Delta G^*}{kT}\right) \quad (6.2)$$

with  $K_0$  the kinetic factor ( $\text{m}^{-3} \cdot \text{s}^{-1}$ ) and  $\Delta G^*$  the activation free energy (J).

CNT assumes a spherical form for the critical nucleus as mentioned by Fletcher [35]. In the general case of heterogeneous or homogeneous nucleation, a constant shape for the cluster (here spherical) is assumed, which depends on the possible presence of foreign substances: foreign molecules or particles, bubbles, crystallizer walls, and liquid–liquid or liquid–air interfaces. Hence, the value of  $\Delta G^*$  depends on surface interactions, which are taken into account by introducing an effective interfacial energy  $\gamma_{ef}$  of the critical nucleus, and  $J$  is given by Eq. (6.3) [4]:

$$J = K_0 \exp\left(-\frac{16\pi}{3} \frac{\Omega^2 \gamma_{ef}^3}{(kT)^3 \ln^2 \beta}\right) \quad (6.3)$$

### 6.2.3 Critical Supersaturation

According to Eq. (6.3), there is a zone in the supersaturated region ( $\beta > 1$ ) where no nucleation occurs for a given time in a given volume. This is the metastable zone [36], which is delimited by the critical supersaturation (CS) for a given temperature or the temperature of metastable zone (TMZ) for a given concentration (Fig. 6.1).

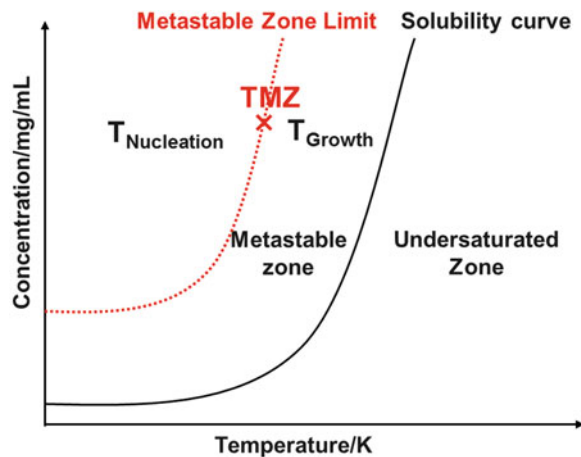
In the nucleation zone or zone of spontaneous nucleation, nucleation (i.e., the appearance of crystals) is promoted; in the metastable zone, growth (i.e., the subsequent expansion of the crystal) is promoted.

### 6.2.4 Experimental Considerations

In practice, the two usual methods used to determine the nucleation rate  $J$  are:

- *Measurement of the induction time*, i.e., the time it takes to form a detectable amount of the new crystalline phase after a given supersaturation  $\beta$  is established. However, nuclei must grow to a minimum size before they are observable; thus, the induction time includes the nucleation time and the time required for growth to a detectable size. The supersaturation range over which the experiment can be performed is rather limited due to the metastable zone. When  $\beta$  is too small, heterogeneous nucleation may replace homogeneous nucleation. When  $\beta$  is too large, induction times are difficult to measure because they are too short. In practice, we are able to measure the induction time in the vicinity of the metastable zone limit and we could reasonably assume that the growing period can be considered negligible compared to the nucleation period.

**Fig. 6.1** Phase diagram of supersaturation vs. temperature, with the solubility curve and the metastable zone



- *The double-pulse technique (DPT)*, which permits nucleation and growth to be separated [37–39]. At the beginning of a run, the solution is loaded at a temperature chosen to prevent nucleation of crystals. Then the temperature is lowered (respectively raised if the solubility is reverse with T) to a selected  $T_1$  at which nucleation occurs. After a period of  $\Delta t_1$  (nucleation time), the temperature is raised (respectively lowered if the solubility is reverse with T) from the nucleation temperature  $T_1$  to the growth temperature  $T_2$  in the metastable zone. At  $T_2$ , crystals already formed can grow to detectable dimensions. The nucleation rate, at given concentration  $C$  and temperature, is given by the variation of the amount of crystals nucleated as a function of nucleation time.

### 6.3 Studying Nucleation: An Unpredictable Phenomenon

As we have seen above, nucleation plays a fundamental role in the physical properties of crystals. However, the unpredictability of the spatial and temporal location of the critical nucleus makes its study difficult. In this part we address the problem of the stochasticity of nucleation in two ways: first, by carrying out statistical studies on single crystals spontaneously nucleated and, second, by inducing nucleation.

#### 6.3.1 Statistical Studies of Spontaneous Nucleation

For statistical studies, a large number of samples in the same condition are required. In large volumes, it is difficult to accurately detect crystals as they are formed, so sample volumes need to be limited. Therefore, the idea is to reduce the volume of nucleation to the nL–pL range. Hence, the number of crystals nucleating and the zone of observation are reduced, thus increasing the resolution of the detection. Moreover, this has the advantage of decreasing the quantity of molecules while speeding up heat and mass transfer [40]. Volume reduction to nL is realized using droplet-based microfluidics. Then pL–fL volumes are obtained by microinjection methods.

##### 6.3.1.1 Nucleation in Nanoliter Droplets

Droplet-based microfluidics permits series of nanoliter droplets to be generated by injecting the crystallization solution in a nonmiscible continuous phase and without using surfactant. Droplets are monodisperse (in size, composition, frequency) nanocrystallizers isolated from each other and in which crystallization can occur independently. Hundreds of droplets can be generated per condition, leading to a large number of samples for statistical studies while consuming only small quantities of material.

- *Microfluidic devices*: (1) molded in PDMS and adapted from Salmon [41–43] and (2) composed of Teflon tubing with junctions in PEEK (Fig. 6.2a, b). The continuous phase is silicon or fluorinated oil according to the solvent of crystallization (discontinuous phase). The crystallization solvent is water in PDMS systems. This microfluidic system thus becomes compatible with almost all solvents, since Teflon tubing is used instead of PDMS chips (Fig. 6.2c). Crystals of various organic molecules obtained in aqueous and organic solvents are presented in Figs 6.2d–h [6].

The microfluidic setup [7] in Fig. 6.3 allows us to determine the properties of nucleation described above theoretically: metastable zone width, nucleation rate  $J$ , effective interfacial energy  $\gamma_{ef}$  of the critical nucleus, and polymorphism.

- *Metastable zone width*: evaluated from measurements of the temperature of the metastable zone (TMZ) illustrated in Fig. 6.1. This is the maximum temperature above which the supersaturated solution does not lose its metastability over a given time [36]. For a given concentration, TMZ is determined by storing solutions at given temperatures for a given time (here 20 h). During this time if  $T < TMZ$ , crystals nucleate, and if  $T > TMZ$ , no crystal appears. Hence, TMZ at which there is no crystal is extrapolated (interpolation) from a plot of the average number of crystals versus temperature. Moreover a rapid screening of the solubility diagram (black curve of Fig. 6.4) can be carried out as shown by Laval et al. [41, 42].
- *Nucleation rate*: determined by using the double-pulse technique (DPT), based on the phase diagram of Fig. 6.4. Crystals are nucleated at a  $T_{\text{Nucleation}}$  outside the metastable zone (below TMZ) and for a given nucleation time  $\Delta t$ ; then, the crystals are stored at  $T_{\text{Growth}}$  in the metastable zone, where the crystals already formed grow to detectable dimensions and are counted. From the variation of the

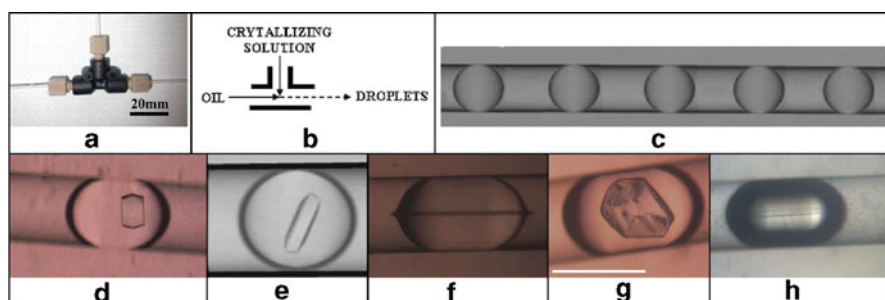


**Fig. 6.2** (a) Photo and (b) scheme of a T-junction made of PEEK, (c) photo of isolated droplets of 60 nL volume of crystallization solution separated by fluorinated oil in Teflon tubing of 500  $\mu\text{m}$  diameter, (d) lysozyme crystals in aqueous droplets, (e) rasburicase crystal in a viscous medium, (f) caffeine crystals in ethanol droplets, (g) isonicotinamide crystal in an ethanol droplet, and (h) isonicotinamide crystals in nitrobenzene droplets in Teflon tubing of 500  $\mu\text{m}$  diameter [6] (Copyright 2012 American Chemical Society)

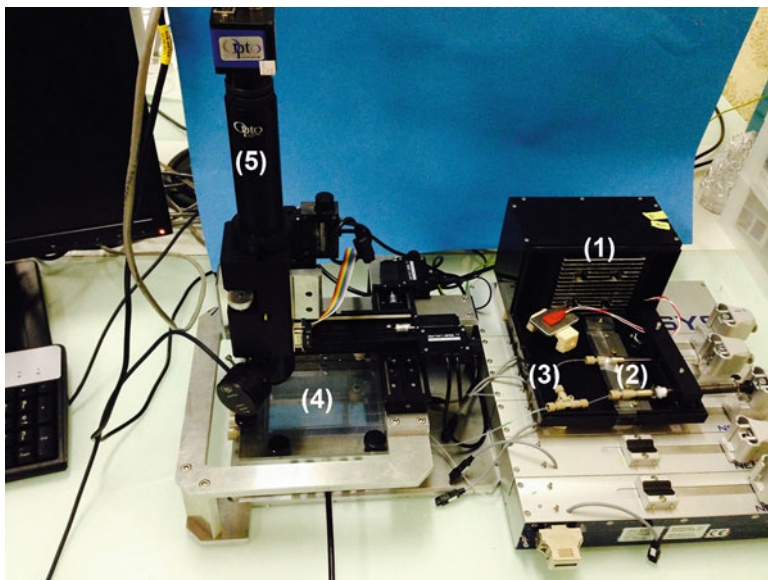
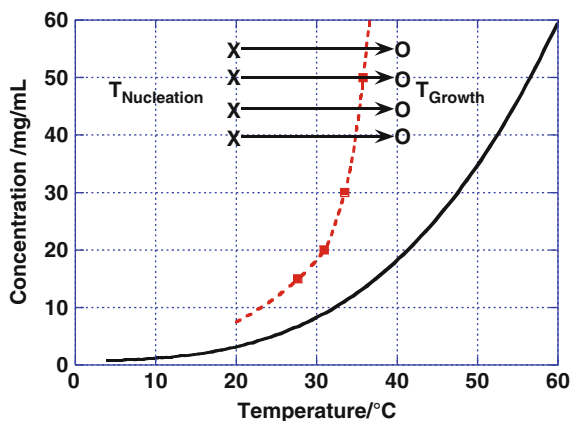


**Fig. 6.3** The microfluidics setup: (1) and (2) thermostated syringe pumps, (3) T-junction, (4) thermostated sample holder, (5) camera + zoom on XYZ stage

**Fig. 6.4** Metastable zone [5] and solubility curve [44] of tetragonal lysozyme (0.7 M NaCl, pH = 4.5); lines improve legibility (Copyright 2011 American Chemical Society)



average number of crystals nucleated as a function of  $\Delta t$ , the steady-state primary nucleation rate  $J$  is determined for given temperature and concentration. Our results obtained in nucleation volumes of 250 nL of lysozyme are summarized in Fig. 6.5.

As shown in Fig. 6.5, our kinetic data are in good agreement with the data of Galkin and Vekilov [21, 22] obtained for the same NaCl concentration at 12.6 °C, using droplets of 1  $\mu\text{L}$  suspended in Teflon wells. Moreover, the supersaturation

**Fig. 6.5** Lysozyme nucleation rate vs. supersaturation: data come from our study at 20 °C [5] and data from Galkin and Vekilov at 12.6 °C [21, 22] (Copyright 2011 American Chemical Society)

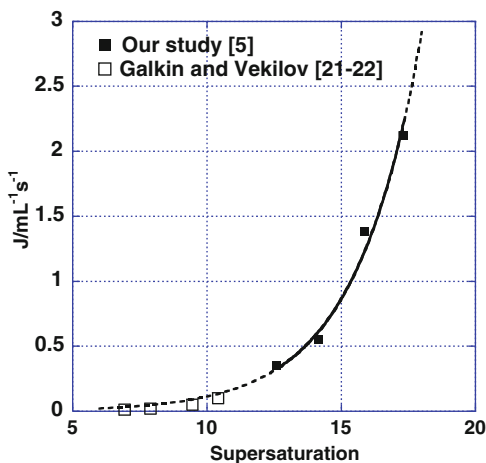


**Table 6.1** Effective interfacial energy  $\gamma_{ef}$  of the critical nucleus determined for oils of different chemical natures, by different authors

	Ildefonso et al. [5]	Vekilov group [21, 22]	Ildefonso et al. [4]	Fraden group [20]
Device	PDMS	Teflon wells	Teflon	PDMS
Oil	Silicon	Silicon	Fluorinated	Fluorinated
$\gamma_{ef}$ (mJ/m <sup>2</sup> )	0.62 (0.13)	0.56	0.88 (0.05)	0.91

The deviation in absolute is given in parentheses; errors are not available in Refs. [20–22]

range experimentally accessible when reducing the volume of nucleation to the nL–pL range is increased for kinetic [5] and thermodynamic [14] reasons (see part 3.2.).

- *Effective interfacial energy*  $\gamma_{ef}$  computed from Eq. (6.3) shows that primary nucleation is not influenced by the container material (Fig. 6.5). Indeed, the oil creates a “containerless” environment, as pointed out by Chayen [45]. However,  $\gamma_{ef}$  determined in fluorinated oil and in silicon oil (Table. 6.1) demonstrates the influence of the droplet–oil interface in droplet-based microfluidics [4].
- *Polymorphism*: droplet-based microfluidics is adapted for detection of new phases for statistical reasons. For instance, different polymorphs can nucleate and the most stable polymorph corresponds to the minimal free energy of the system. Moreover, according to Ostwald’s rule of states [46], a chemical system does not tend directly toward the most stable state, but rather tends toward the closest metastable state. Hence, performing many spontaneous nucleation experiments increases the probability of observing an event. In the case of lysozyme, we observed a metastable phase, the sea urchin-like phase, in 6 droplets out of 237 (Fig. 6.6) [8]. It was already known [47, 48], but is not easy to observe in mL crystallizers. Moreover, because of mononuclear nucleation, the nucleated crystal of the metastable phase cannot easily follow a solution-mediated phase transition to a more stable phase. Thus, small volumes of droplets seem to

**Fig. 6.6** Droplets of lysozyme solutions (20 mg/mL, 0.7 M NaCl, pH 4.5) in Teflon tubing of 500  $\mu\text{m}$  diameter, observed at 20 °C after storage for 20 h at 6 °C: the tetragonal form *top left* and the sea urchin-like form *bottom right* [8]

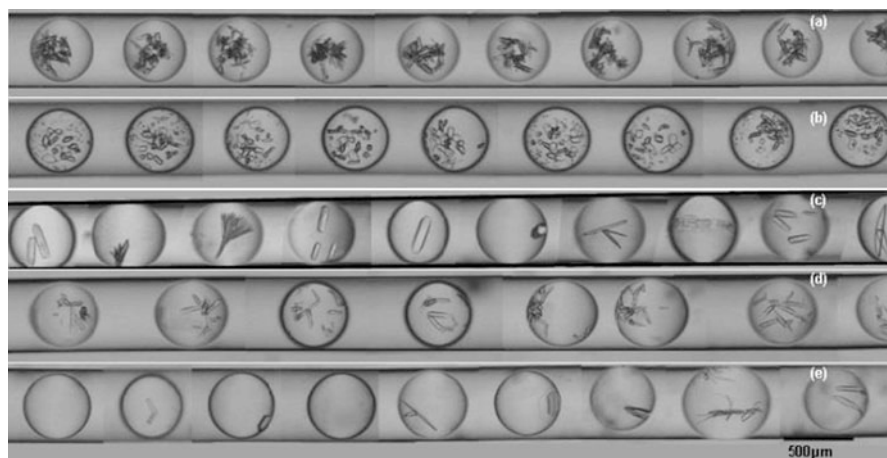
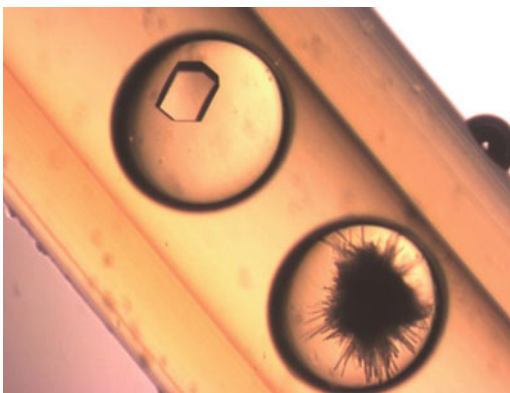


**Fig. 6.7** Photos of crystals of rasburicase obtained in 65 nL droplets: each line corresponds to the same crystallization conditions (a) 10 % PEG, 10  $\mu\text{g}/\mu\text{L}$  rasburicase, at 5 °C. (b) 10 % PEG, 10  $\mu\text{g}/\mu\text{L}$  rasburicase, at 20 °C. (c) 5 % PEG, 10  $\mu\text{g}/\mu\text{L}$  rasburicase, at 5 °C. (d) 7.5 % PEG, 5  $\mu\text{g}/\mu\text{L}$  rasburicase, at 5 °C. (e) 7.5 % de PEG, 5  $\mu\text{g}/\mu\text{L}$  rasburicase, at 20 °C [9] (Copyright 2015 American Chemical Society (paper submitted))

“freeze” the metastable phase [49]. Lastly, the higher supersaturations reached in microfluidics due to volume reduction increase the probability of nucleating a metastable phase [50].

In screening the crystallization conditions of rasburicase, the same experimental conditions produce different crystal habits and phases. Moreover, the two polymorphs known for rasburicase [51] appear simultaneously in droplets (Fig. 6.7) [9]. This concomitant nucleation occurs mainly because the difference between their solubilities is weak.

Figures 6.6 and 6.7 highlight the importance of performing statistical studies through a large number of experiments per condition because of the stochasticity of

nucleation. Statistically each crystallization condition should be tested from 50 to 100 times in order to decide whether the result (obtaining crystals, targeted polymorph(s)) is positive or negative. This is the main problem with the conventional crystallization robots, where typically a few hundred different conditions are tested only 1–5 times each, leading often to non-reproducible results.

To summarize, droplet-based microfluidics is an accurate method for studying nucleation kinetics due to statistical approach, exploring one experimental condition in hundreds of identical droplets. Moreover, as droplet volumes are nanoliter, this statistical approach requires only a few milligrams of molecules.

### 6.3.1.2 Nucleation in Picoliter to Femtoliter Droplets

Small-droplet generation with micropipettes or microinjectors renders microdroplets accessible and makes the size range easier to control compared to microfluidics, which is limited by channel size (hardware limitation). However, statistical analysis cannot be carried out with single micro-droplet injection [40, 52, 53].

- *The fluidic device developed in our laboratory* [10] (Fig. 6.8a) generates arrayed aqueous phase micro-droplets through a layer of inert oil (sessile geometry), without using surfactant. Up to thousands of micro-droplets can be generated, with volumes ranging from nanoliter to femtoliter (Fig. 6.8b), thus allowing statistical studies of nucleation.

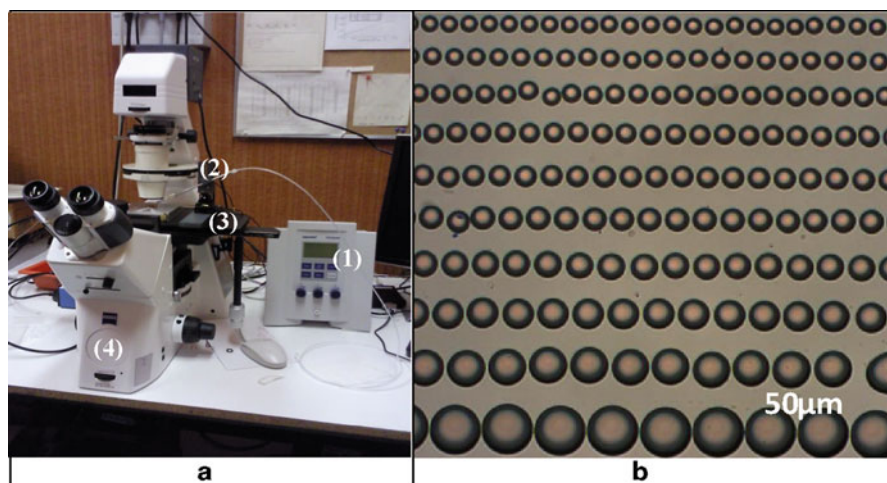


**Fig. 6.8** (a) The microinjector in oil setup: (1) injector, (2) glass micropipette, (3) XYZ miniature translation stages for injector, and (4) microscope. (b) Array of monodisperse water droplets with volumes ranging from nanoliter to femtoliter [10]. (a) Copyright 2010 Elsevier and (b) with permission from [10] (Copyright 2011 AIP Publishing LLC)

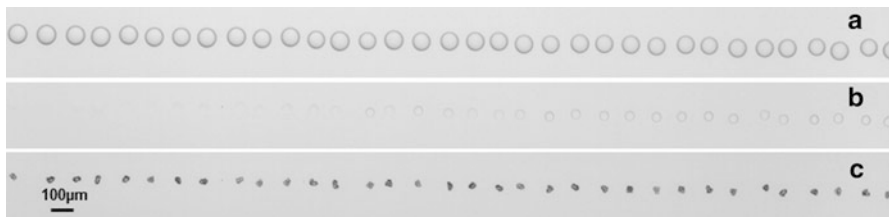
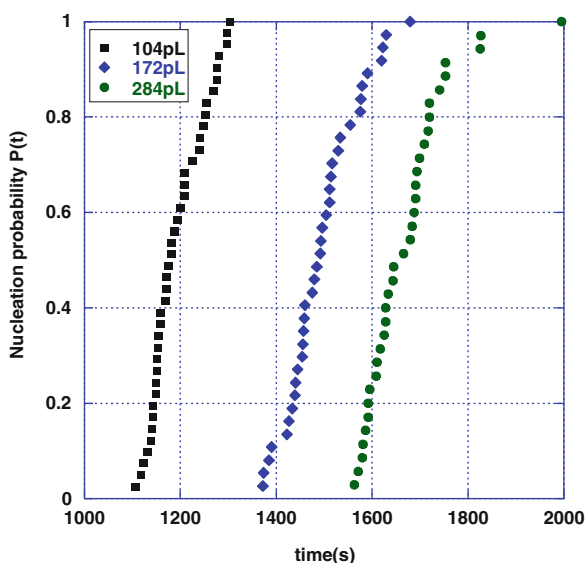


**Fig. 6.9** (a) Array of droplets (300pL) of NaCl solutions at  $\beta = 0.1$  generated through a layer of inert DMS oil. (b) Contraction of droplets due to evaporation of aqueous phase in oil. (c) Nucleation of single crystals in every droplet [16]

**Fig. 6.10** Nucleation probability  $P(t)$  vs. time.  $P(t)$  represents the normalized fraction of nucleated micro-droplets for droplet volumes of 104 pL, 172 pL, and 284 pL [16] (Reproduced from Ref. [16] with permission from the Royal Society of Chemistry)



- *The droplet-contraction method* is used to generate supersaturation and thus to create crystals, as we can see with picoliter droplets of NaCl solution in Fig. 6.9a [16]. Indeed, at this scale, droplets slowly evaporate, linearly decreasing the volume (Fig. 6.9b) [11]. Hence, the concentration, which is given by the refractive index [12], increases until it exceeds the critical supersaturation, i.e., the supersaturation required to nucleate a new phase [54]. Then single crystals nucleate (Fig. 6.9c).
- *The induction time* can be measured with the droplet-contraction method because the growth rate is so fast that the time required for the newly formed nuclei to grow to a detectable size is negligible with regard to the induction time [13]. Thus, the time before a detectable crystal is observed can be considered as the induction time. Moreover, the smaller the volume, the faster the evaporation rate and the faster the nucleation (Fig. 6.10) [16].

To summarize, this technique of droplet microinjection in oil combines the advantage of channeled microfluidic techniques, generating thousands of droplets, with the advantage of micropipette techniques: control over size, micro-droplet accessibility, and contraction of droplets in oil to increase supersaturation. Both of these techniques involve easy-to-build devices and are easy to use. Moreover, it must be noted that they require no surfactant that might affect crystallization.

### 6.3.2 *Influence of Volume on Nucleation*

Reducing the volume of crystallization raises several questions: How do kinetic parameters such as the metastable zone and the critical supersaturation vary? Does CNT, which supposes an infinite reservoir of molecules, i.e., a constant supersaturation during the nucleation event, remain valid in small volumes? What are the limitations of small volumes and how small?

- *A kinetic limitation* in small volumes arises from nucleation rate  $J$  (number of nucleus per unit of volume and per unit of time).  $J$  is an intensive property (does not vary with volume). However,  $J$  is inversely proportional to volume and proportional to induction time. Hence, the smaller the volume, the longer the induction time. For instance, an induction time of 1 s in a volume of 1 mL becomes 11 days in a volume of 1 nL.
- *A thermodynamic limitation* appears because the critical size and energy barrier required for nucleation increase when the crystallization volume decreases [55]. When the volume decreases, the concentration in solution can no longer be considered constant during the nucleation process but is decreasing. In practice, this means that the reservoir of molecules is finite, in contradiction with CNT. Hence, the critical supersaturation, where no nucleation can occur, increases with confinement (Fig. 6.11), widening the metastable zone [13, 55]. Thus, “scale-down” requires creation of sufficient supersaturation within each droplet to ensure nucleation, with a risk of unwanted nucleation before droplet formation. In practice there is a “thermodynamic” influence of volume on nucleation from picoliter range down.

To summarize, two effects occur depending on droplet volume: (1) for nL range droplets, a kinetic effect increases the induction time; (2) for pL–fL range droplets, the same kinetic effect is accompanied by a thermodynamic effect. In both cases these effects widen the metastable zone, hence requiring higher supersaturation for nucleation. However, these effects stabilize high-supersaturated solutions, permitting critical clusters and nucleation to be controlled.

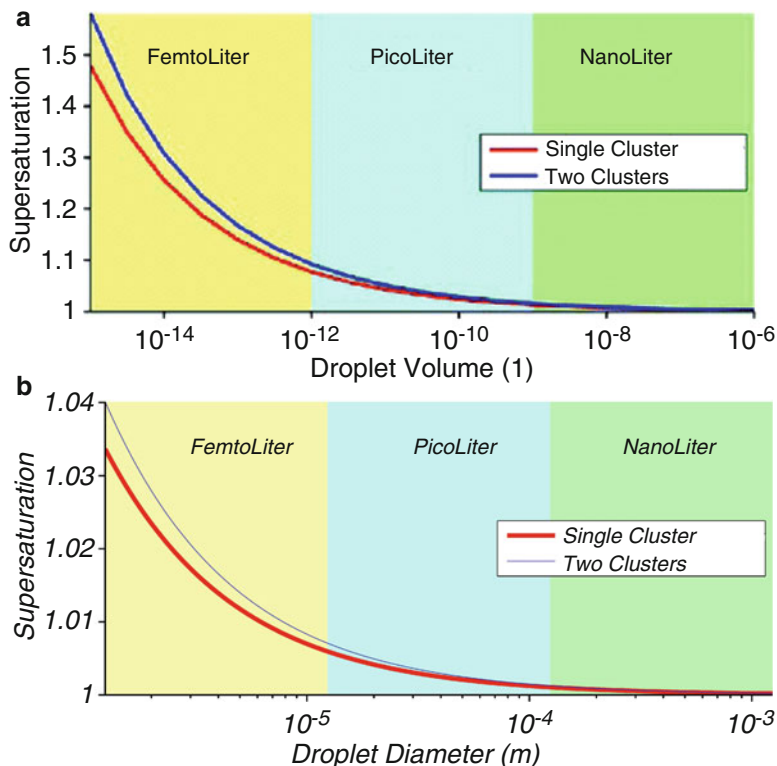


**Fig. 6.11** Critical supersaturation (below which no nucleation can occur) vs. droplet size, the *red curve* for a single nucleation event, and the *blue curve* for a second event: (a) for lysozyme in NaCl solution [55], (b) for NaCl [13]. (a) Copyright 2009 American Chemical Society and (b) Copyright 2010 Elsevier

### 6.3.3 Predictive Study of Induced Nucleation

Nucleation can even be induced in the metastable zone, thus becoming predictive. In other words, we determine where and when it will occur. Nucleation is induced using an external field, the implications of which were highlighted by Voss [56], Oxtoby [57], and Revalor [58]. Two effects on the supersaturated solution are expected: molecular orientation and density fluctuation. As a general rule, any disturbance triggers nucleation once a highly supersaturated metastable state has been achieved [59]. First, localization in time is achieved by triggering nucleation in a metastable solution with a localized mechanical contact or a localized electrical field. Then localization in space is achieved by either confining the nucleation volume or by controlling fluxes in non-convective gel medium.

### 6.3.3.1 Mechanical Action and Confinement by Volume

- *Coupling a mechanical action using a sharp tip with volume confinement by microinjector triggers nucleation, as previously shown. A structural transformation is thereby induced in a dense supersaturated droplet at precisely determined points and times (Fig. 6.12). Then the crystal grows at a rate greater than  $200 \mu\text{m/s}$  for the first 20 ms [16].*
- *The induction time is shorter than 5 ms, corresponding to the time between tip contact and observation of nucleation (Figs. 6.12a–b). However, the droplet is repeatedly tapped with the tip during the generation of supersaturation by water diffusion in order to launch nucleation. The crystal nucleated is rough and transition to a faceted crystal is observed in less than 1 s, i.e., the transition between the nucleation form and the equilibrium form. In practice, the tip position being controlled with micromanipulators, the position of the critical nucleus can be determined with an accuracy of 16 nm.*
- *This method is suitable for a binary crystallization medium, with a solute and a solvent. The solute concentrates during droplet contraction and reaches high supersaturation. Then the solute nucleates due to the mechanical action. When the crystallization medium is ternary containing a solvent, a solute, and a crys-*

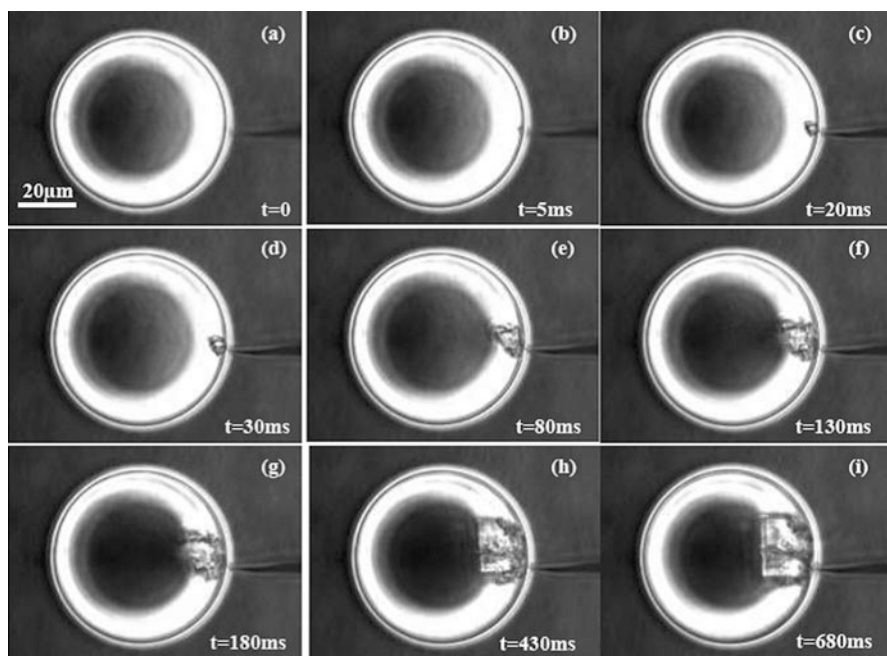


**Fig. 6.12** Time sequence showing nucleation induced by a sharp tip touching a 95 pL droplet of NaCl ( $\beta > 1.24$ ) and growth of NaCl in paraffin oil: (a) to (b) nucleation in less than 5 ms, (c) to (i) growth [16] (Reproduced from Ref. [16] with permission from the Royal Society of Chemistry)

tallization agent, e.g., protein crystallization, both the solute and crystallization agent concentrate during droplet contraction and reach high supersaturation. Hence, for kinetic reasons [60], the crystallization agent often nucleates first, before solute nucleation. Therefore, supersaturation must be achieved via a method other than droplet contraction.

### 6.3.3.2 Electrical Field and Confinement by Gel

- *Coupling a localized electric field generated by a sharp-tip electrode with a gel eliminating convection* in a supersaturated metastable solution increases supersaturation at the tip apex and induces nucleation. A large electrical field [61] and large field gradients are created near the tip at low DC voltage, due to its nanometer size (Fig. 6.13).

The electrical field induces high current density inside the solution close to the region of high curvature [14]. The resulting flux accumulates molecules at a precise point in the vicinity of the tip apex [15] and the concentration gradient in solution tends to be counteracted by convection. However, the solution being in a gel, convection is eliminated and the confinement is kept in the vicinity of the tip until the critical supersaturation is reached. Then the crystal nucleates near the electrode tip [16].

- *Induction time* is measured by optical observation and by the evolution of the current in the solution. An example of nucleation induction in a supersaturated metastable solution of lysozyme in agarose gel is shown in Fig. 6.14.

The optical observation of nucleation gives an induction time shorter than 600 s. The nucleated crystal is rough, due to high local supersaturation encountered during

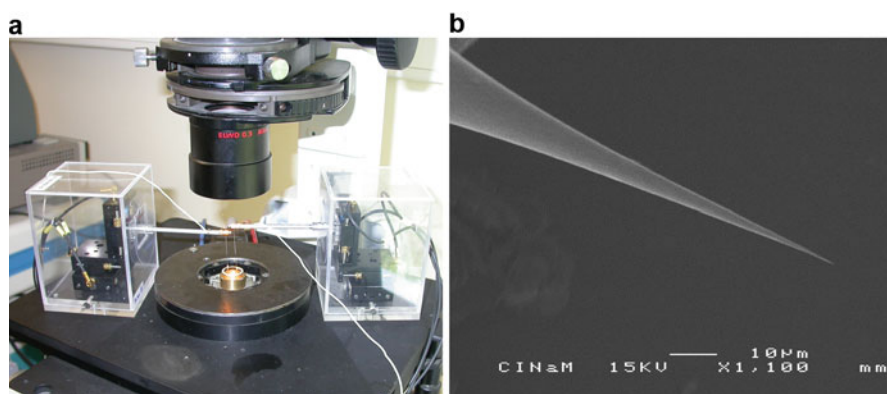


**Fig. 6.13** (a) Temperature-controlled crystallization cell with 2 micromanipulators and (b) SEM image of a W-tip [2] (Reproduced from Ref. [16] with permission from the Royal Society of Chemistry)

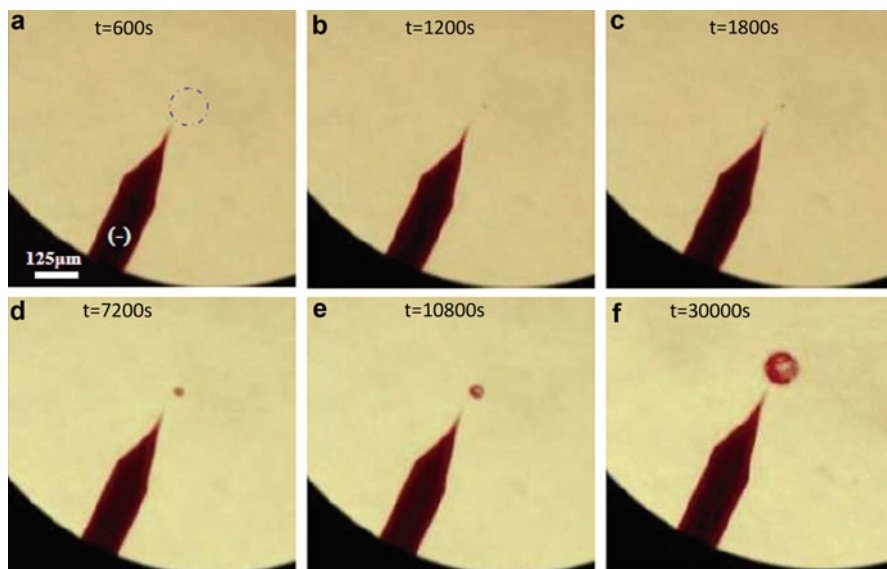


**Fig. 6.14** Time sequence in a supersaturated metastable solution of lysozyme 20 mg/mL (NaCl 0.7 M). Nucleation is induced by an external localized electric field with a sharp-tip electrode and in agarose gel 1 % [16] (Reproduced from Ref. [16] with permission from the Royal Society of Chemistry)

nucleation and growth. Growth rate (between 600 and 10,800 s) is  $15 \mu\text{m/h}$  in agreement with the growth rate obtained by Durbin et al. [62] at high supersaturation for lysozyme. Compared to optical determination of the induction time, the measures of the current during the experiment are clearly more sensitive (Fig. 6.15) [16]. Indeed, the induction time is given by the modification in the slope at 300 s.

To summarize, these techniques of inducing nucleation with fluxes confer a predictive nature on nucleation. Thus, the nucleation mechanism can be studied directly on one crystal.

## 6.4 Conclusion

Faced with the stochasticity of nucleation, different experimental approaches have been developed to study nucleation. In the first approach, nucleation is allowed to proceed spontaneously and the stochastic nature of results is addressed by statistical studies. Thus, the volume is reduced to droplets of nL to fL volume that are generated in large numbers. Droplet-based microfluidics and microinjectors in oil are used. These are compatible with many solvents and involve easy-to-use and material-saving techniques. In the second approach, nucleation is controlled by external electrical or mechanical fields in confined systems. Hence, nucleation

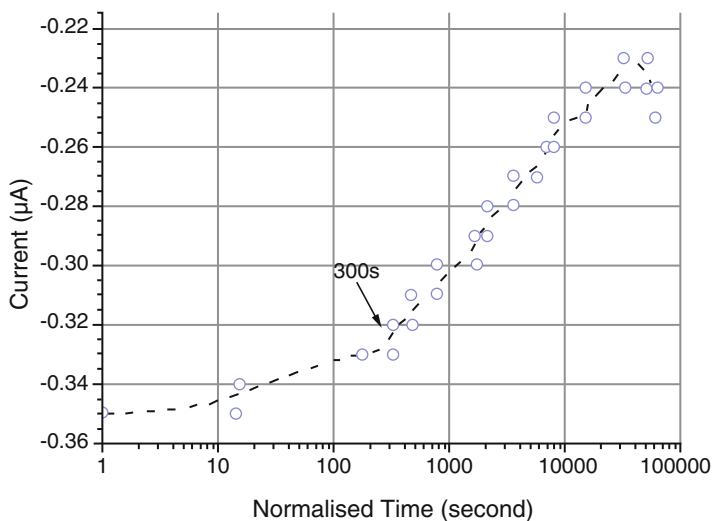


**Fig. 6.15** Evolution of current over time during the experiment, semilog scale. Line is a guide for the eye (Reproduced from Ref. [16] with permission from the Royal Society of Chemistry)

becomes predictive, triggering nucleation for molecules that are not easy to crystallize, nucleating one crystal per crystallizer, and localizing nucleation in space and in time for measurements on the critical nucleus.

All of these methods approach nucleation kinetics through the induction time or the nucleation rate. Moreover, factors affecting the nucleation process (confinement, complexity of solution) are brought to light. These practical approaches show considerable potential to increase understanding and control of the nucleation mechanism.

**Acknowledgments** We thank N. Ferté for protein characterization and fruitful discussions. We thank M. Sweetko for the English revision.

## References

1. D. Kashchiev, *Nucleation: Basic Theory with Applications* (Butterworth-Heinemann, Oxford, 2000)
2. N. Candoni, Z. Hammadi, R. Grossier, M. Ildefonso, E. Revalor, N. Ferté, T. Okutsu, R. Morin, S. Veessler, *Int. J. Nanotechnol.* **9**(3–7), 439–459 (2012)
3. Z. Hammadi, N. Candoni, R. Grossier, M. Ildefonso, R. Morin, S. Veessler, *C. R. Phys* **14**, 192–198 (2013)
4. M. Ildefonso, N. Candoni, S. Veessler, *Cryst. Growth Des.* **13**, 2107–2110 (2013)
5. M. Ildefonso, N. Candoni, S. Veessler, *Cryst. Growth Des.* **11**(5), 1527–1530 (2011)
6. M. Ildefonso, N. Candoni, S. Veessler, *Org. Process Res. Dev.* **16**, 556–560 (2012)

7. S. Zhang, C. Guivier-Curien, S. Veessler, N. Candoni, Chem. Eng. Sci., CES-D-14-02096 (submitted) (2014)
8. M. Idefonso, E. Revalor, P. Punniyam, J.B. Salmon, N. Candoni, S. Veessler, J. Cryst. Growth **342**(1), 9–12 (2012)
9. S. Zhang, N. Ferté, N. Candoni, S. Veessler, Org. Process Res. Dev. (submitted)
10. R. Grossier, Z. Hammadi, R. Morin, A. Magnaldo, S. Veessler, Appl. Phys. Lett. **98**, 091916–091913 (2011)
11. I. Rodríguez-Ruiz, Z. Hammadi, R. Grossier, J. Gómez-Morales, S. Veessler, Langmuir **29**, 12628–12632 (2013)
12. R. Grossier, Z. Hammadi, R. Morin, S. Veessler, Phys. Rev. Lett. **107**, 025504 (2011)
13. R. Grossier, A. Magnaldo, S. Veessler, J. Cryst. Growth **312**, 487–489 (2010)
14. Z. Hammadi, R. Morin, J. Olives, Appl. Phys. Lett. **103**, 223106 (2013)
15. Z. Hammadi, J.P. Astier, R. Morin, S. Veessler, Cryst. Growth Des. **7**, 1476–1482 (2007)
16. Z. Hammadi, R. Grossier, A. Ikn, N. Candoni, R. Morin, S. Veessler, Faraday Discuss. (2015)
17. A.A. Chernov, J. Mater. Sci. Mater. Electron. **12**, 437–449 (2001)
18. J. Gibbs, *The Collected Works. Vol. 1. Thermodynamics*, vol. 1 (Yale University Press, New Haven, 1948)
19. N.M. Dixit, A.M. Kulkarni, C.F. Zukoski, Colloids Surf. A Physicochem. Eng. Asp. **190**, 47–60 (2001)
20. S. Selimovic, Y. Jia, S. Fraden, Cryst. Growth Des. **9**(4), 1806–1810 (2009)
21. O. Galkin, P.G. Vekilov, J. Phys. Chem. B **103**, 10965–10971 (1999)
22. O. Galkin, P.G. Vekilov, J. Am. Chem. Soc. **122**, 156–163 (2000)
23. H.N.W. Lekkerkerker, Physica A **244**, 227–237 (1997)
24. P.R. Ten Wolde, D. Frenkel, Science **277**, 1975–1978 (1997)
25. V.J. Anderson, H.N.W. Lekkerkerker, Nature **416**, 811–815 (2002)
26. D. Erdemir, A.Y. Lee, A.S. Myerson, Chem. Res. **42**(5), 621–629 (2009)
27. D. Gebauer, H. Cölfen, Nano Today **6**, 564–584 (2011)
28. P.G. Vekilov, Cryst. Growth Des. **4**, 671–685 (2004)
29. D. Erdemir, A.Y. Lee, A.S. Myerson, Account Chem. Res. **42**, 621–629 (2009)
30. D. Knezic, J. Zaccaro, A.S. Myerson, J. Phys. Chem. B **108**, 10672–10677 (2004)
31. A.C. Zettlemoyer, *Nucleation* (Marcel Dekker, New York, 1969)
32. F.F. Abraham, *Homogeneous nucleation theory* (Academic, Amsterdam, 1974), p. 263
33. S. Toschev, Homogeneous nucleation, in *Crystal growth: an introduction*, ed. by P. Hartman (North Holland, Amsterdam, 1973), pp. 1–49
34. R. Boistelle, J.P. Astier, J. Cryst. Growth **90**, 14–30 (1988)
35. N.H. Fletcher, J. Chem. Phys. **29**(3), 572–576 (1958)
36. D. Kashchiev, D. Verdoes, G.M. Van Rosmalen, J. Cryst. Growth **110**, 373–380 (1991)
37. D. Tsekova, S. Dimitrova, C.N. Nanev, J. Cryst. Growth **196**(2–4), 226–233 (1999)
38. O. Galkin, P.G. Vekilov, J. Phys. Chem. B **103**(3), 10965–10971 (1999)
39. G.Z. Tammann, Phys. Chem. **25**, 441–479 (1898)
40. S. Lee, J. Wiener, J. Chem. Educ. **88**, 151–157 (2010)
41. P. Laval, N. Lisai, J.-B. Salmon, M. Joanicot, Lab Chip **7**, 829–834 (2007)
42. J. Leng, J.-B. Salmon, Lab Chip **9**, 24–34 (2009)
43. P. Laval, J.-B. Salmon, M. Joanicot, J. Cryst. Growth **303**, 622–628 (2007)
44. E. Cacioppo, M.L. Pusey, J. Cryst. Growth **114**, 286–292 (1991)
45. N.E. Chayen, Protein Eng. **9**(10), 927–929 (1996)
46. W.Z. Ostwald, Phys. Chem. **22**, 289 (1897)
47. M. Ataka, M. Asai, J. Cryst. Growth **90**, 86–93 (1988)
48. L. Legrand, M. Ries-Kautt, M.-C. Robert, Acta Crystallogr. D **58**, 1564–1567 (2002)
49. A.Y. Lee, I.S. Lee, A.S. Myerson, Chem. Eng. Technol. **29**, 281–285 (2006)
50. D. Mangin, F. Puel, S. Veessler, Org. Process Res. Dev. **13**, 1241–1253 (2009)
51. D. Vivares, S. Veessler, J.P. Astier, F. Bonneté, Cryst. Growth Des. **6**, 287–292 (2006)
52. P.B. Duncan, D. Needham, Langmuir **22**, 4190–4197 (2006)
53. K. Allain, R. Bebaee, S. Lee, Cryst. Growth Des. **9**, 3183–3190 (2009)

54. D. Kashchiev, *J Chem Phys* **134**, 196102–196102 (2011)
55. R. Grossier, S. Veessler, *Cryst. Growth Des.* **9**, 1917–1922 (2009)
56. D. Voss, *Science* **274**, 1325 (1996)
57. D.W. Oxtoby, *Nature* **420**, 277–278 (2002)
58. E. Revalor, Z. Hammadi, J.P. Astier, R. Grossier, E. Garcia, C. Hoff, K. Furuta, T. Okutsu, R. Morin, S. Veessler, *J. Cryst. Growth* **312**, 939–946 (2010)
59. D. Vivares, E.W. Kalera, A.M. Lenhoff, *Acta Crystallogr. D* **61**, 819–825 (2005)
60. A. A. Chernov, I.M. Lifshitz and condensed matter theory. *Phys. Rep.* **288**, 61–75 (1997)
61. R. Gomer, *Field emission and field ionization* (Harvard University press, Cambridge, 1961)
62. S.D. Durbin, G. Feher, *J. Cryst. Growth* **76**, 583–592 (1986)

# Chapter 7

## Metastability of Supersaturated Solution and Nucleation

Noriaki Kubota, Masanori Kobari, and Izumi Hirasawa

**Abstract** A certain time may elapse for the occurrence of a first nucleation after a solution is made supersaturated. Thus, the supersaturated solution looks as if it could be in a metastable state though in a limited time. Such metastability of a supersaturated solution has been evaluated (rather technically) by the magnitude of the metastable zone width (MSZW), *i.e.*, the supercooling at which a first nucleation event is detected when supersaturation is increased by cooling, or the induction time, *i.e.*, the time elapsed until a first nucleation event is detected at a constant temperature. The larger these values are, the higher the metastability is. Surprisingly, however, these two nucleation-related quantities are not clearly understood. There is still much confusion. This chapter provides an overview of recent understandings of the MSZW and induction time with focus on the problems of (1) stochastic and deterministic aspects, (2) time-dependent change of solution structure, (3) role of nucleation, and (4) relevance to the operation of an industrial batch crystallizer.

**Keywords** Nucleation • Metastable zone width • Induction time • Crystallization • Population balance model

---

N. Kubota (✉)

Department of Chemistry and Bioengineering, Iwate University, Morioka, Japan  
e-mail: [nkubota@iwate-u.ac.jp](mailto:nkubota@iwate-u.ac.jp)

M. Kobari

EN Technology Center, JGC Corporation, Yokohama, Japan

Department of Applied Chemistry, School of Science and Engineering, Waseda University, Tokyo, Japan

e-mail: [kobari.masanori@jgc.com](mailto:kobari.masanori@jgc.com)

I. Hirasawa

Department of Applied Chemistry, School of Science and Engineering, Waseda University, Tokyo, Japan

e-mail: [izumih@waseda.jp](mailto:izumih@waseda.jp)

## 7.1 Introduction

The metastability of a supersaturated solution is judged by the magnitude of metastable zone width (MSZW) or the induction time. The MSZW and induction are usually defined, respectively, as the supercooling at which first crystals are detected when the solution is cooled at a constant rate and as the time elapsed from the instance of achievement of supersaturation until the detection of first crystals under the condition of a constant supercooling [1]. The MSZW and the induction time are both considered to be related to nucleation kinetics. And these two quantities are used as a measure of the metastability of a supersaturated solution with respect to nucleation. If a solution exhibits a larger MSZW or a larger induction time, the metastability of the solution is judged to be higher.

The concept of metastable zone was proposed and expressed first more than 100 years ago by Ostwald in 1897 [2], and later its industrial importance as the region within which batch crystallizers should be operated was pointed out by Griffiths in 1925 [3]. Thus, the concept of metastability of supersaturated solution has a long history. Nevertheless, the physical meanings both of MSZW and induction time are not clearly understood, and there is still much confusion in the interpretation. Typical questions are as follows. (1) Why do the measured values of MSZW and induction time exhibit stochastic nature only when the volume of solution is reduced? (2) Do the MSZW and induction time change with changing the volume of the solution used for the measurements? (3) Does the structure of a solution (cluster size distribution) change gradually with time after the achievement of supersaturation during the measurements of MSZW and induction time? (4) Is the MSZW the region within which a batch crystallizer can be operated safely without nucleation?

In this chapter, we review previous published work on the MSZW and induction time, and we also summarize the authors' own work on the metastability of supersaturated solution. In summary, the metastable state or time-dependent nonequilibrium state of a supersaturated solution is not considered to exist for solutions encountered in ordinary crystallization processes. And either the MSZW or the induction time is only an indication of apparently observed metastable state. We do not have any direct experimental evidence supporting this view, but it enables us to treat the MSZW, induction time, and batch crystallization processes in a unified manner.

## 7.2 Stochastic or Deterministic

Nucleation is stochastic by nature, because it is a process that a cluster of molecules (or ions) will reach and then surpass the critical size by thermal fluctuation. However, the stochastic aspect of nucleation is not always observed in actual experiments. The stochastic nature appears only when nucleation occurs in a small sample solution with a relatively high supersaturation. In a large sample, nucleation is observed generally to occur in a deterministic way.

### 7.2.1 *Experiments by Kadam et al.*

Recently, Kadam et al. [4] reported MSZW data measured on different sample volumes for primary nucleation of paracetamol from stirred aqueous solution using the polythermal (increasing supersaturation by cooling) method. The MSZWs obtained on small samples (1 mL) were not reproducible and distributed very widely, reflecting the stochastic nature of nucleation. For these small samples, the MSZW was determined as the supercooling at which crystals were detected by the decrease in transmission of light through the sample cell. This decrease in light transmission was caused by the burst of crystals that is induced with secondary nucleation from a grown first single nucleus. The burst occurred immediately after the appearance of a first single crystal (about 5 s later). The period of 5 s was negligibly small compared to the time elapsed from the start of cooling or the start of the measurement of MSZW, which ranged roughly from  $8 \times 10^2$  to  $4 \times 10^3$  s. Therefore, this burst was treated as an indication of the appearance of a first crystal; this was called as single nucleus mechanism [4]. Kadam et al. [4] also measured MSZWs, in the same study, on a large vessel of 1 L for the same paracetamol solution by detecting crystals (not a single crystal) with an in situ camera. This detection point did not correspond to the abovementioned burst of crystals but the moment when the crystals accumulated until a value specific to the detector used. The MSZW obtained on 1 L samples was reproducible and deterministic.

It must be noted that the MSZW was defined, though unintentionally, in two different ways in the work of Kadam et al., depending on the range of sample volume. For 1 mL samples, the MSZW was defined as the supercooling at which a first nucleus was detected (though indirectly), while, for 1 L samples, it was defined as the supercooling at which the number density of accumulated crystals reached the detector sensitivity  $(N/V)_{\text{det}}$ .

### 7.2.2 *Why Is Nucleation Stochastic Only When Sample Volume Is Small?*

The metastable zone width or the induction time could be observed as a stochastic quantity if the rate of nucleation per sample  $BV$  (not per unit volume) is very low or the average time interval of nucleation  $t_n$ , which would be given as  $1/BV$ , is very long compared to the observation time  $t_{\text{ob}}$ , which ranges roughly several minutes to several hours in ordinary laboratories. When the average time interval of nucleation  $t_n$  is relatively long, say  $t_n/t_{\text{ob}} \approx 0.1$ –1, the MSZW or the induction time would be observed as a stochastic quantity.

Such low nucleation rate per sample can be realized by reducing the sample volume  $V$ . Such low nucleation rate per sample  $BV$  is one requirement for stochastic nucleation to be observed. Another requirement is the capability of detecting a first single nucleus just at the moment of nucleation. However, strictly speaking, it is

impossible to detect a nucleus just at formation, since the nucleus is very small and invisible. Accordingly, indirect detection techniques have been employed. The experiment of Kadam et al. [4], illustrated above, is such an example where the burst of secondary nucleus-grown crystals was seen immediately after the formation of an invisible first nucleation. High supersaturation, which induces rapid crystal growth, is a necessary condition for these indirect techniques. These techniques have been used widely by many researchers [5–11]).

Even for large sample volume  $V$ , nucleation rate per sample  $BV$  can be low if supersaturation is lowered enough. Such low supersaturation is always encountered at early stage in the measurement of MSZW where supersaturation is continuously increased by cooling. And it can be realized in the measurement of induction time by setting supersaturation at low levels. Under such condition, the MSZW and induction time should be stochastic, respectively. However, no experimental data of stochastic MSZW and induction time have been reported for large samples, because a first single crystal can be never detected.

Instead, for large samples, a large number of accumulated nucleus-grown crystals (not a single crystal) are detected, where the average time interval of nucleation is much smaller than the observation time, say  $t_n/t_{ob} \ll 1$ . The measurement has been made by using a variety of detectors: an FBRM (focused beam reflectance measurement) probe [12–14]), a turbidity meter [15, 16]), a spectrometer [13]), naked eyes [17]), and an electric conductivity meter [18]. The MSZW and induction time measured with these detectors are not stochastic any more, but deterministic. These detectors do not detect the total number of crystals per crystallizer  $N$  (extensive variable) but a quantity relating to the number density of crystals or the number of crystals per unit volume  $N/V$  (intensive variable).

### 7.2.3 *Effect of Sample Volume on MSZW and Induction Time*

The MSZW measured for small samples decreases with an increase of sample volume [5, 19], while that measured for large volume samples does not [20]. Why is the volume effect on the experimental MSZW different depending on the volume range of the sample used for the measurement? It will be shown below that this variation in the volume effect is only apparent, but it is caused by how the MSZW (the induction time also) is measured. It is not a problem caused by the sample volume itself.

We consider first the case that a single first nucleus is detected as the point at which the MSZW or the induction time is reached. The probability of appearance of a single nucleus per sample is proportional to the sample volume  $V$ . A first nucleus appears earlier in a larger sample, because nucleation occurs in a spatially uniform manner, and then the MSZW and induction time become smaller. This view holds regardless of the range of sample volume.

While in the case that the MSZW and the induction time are determined on the basis of the number density of crystals  $N/V$  as described in the preceding section,

the experimental values of MSZW and induction time do not depend on the sample volume. This is because the number density  $N/V$ , which is an intensive variable, remains unchanged, while the absolute number of crystals  $N$  increases in proportion to  $V$ . Therefore, if the MSZW and induction time are determined on the basis of the absolute number of crystals  $N$  (instead of  $N/V$ ), the value of MSZW and induction time decreases with an increase of sample volume. It is simply because  $N$ , which is an extensive variable, reaches earlier the fixed detection limit  $N_{\text{det}}$ . Thus, the variation in the volume effect is not a problem caused by the sample volume itself, but it is a problem of which of intensive ( $N/V$ ) and extensive ( $N$ ) variables is used for the determination of MSZW and induction time. It must be noted that this problem on the variation in the volume effect was briefly treated earlier by Harano et al. [21].

Below in Sect. 7.5.1, the effect of solvent mass (instead of sample volume) on the MSZW and induction time will be explained mathematically, where only heterogeneous primary nucleation was assumed to occur with no concentration depletion due to crystallization.

Kashchiev et al. [22] proposed a mathematical model explaining the effect of sample volume on the induction time. The induction time was defined by them, for small samples, as the time at which a single nucleus was detected. It was stochastic. For large samples, it was defined by Kashchiev et al. [22] as the time at which the volume fraction of total nucleus-grown crystals reached a detection limit  $\alpha_{\text{det}}$ . It was deterministic. The average of the former stochastic values was denoted as  $t_{\text{MN}}$  and the latter deterministic value  $t_{\text{PN}}$  (Kashchiev et al. [22]). The induction time  $t_{\text{MN}}$  decreases with an increase in sample volume, while  $t_{\text{PN}}$  remains unchanged even when the sample volume is changed. Kashchiev et al. [22] combined these two differently defined induction times as  $t_{\text{ind}} = t_{\text{MN}} + t_{\text{PN}}$ . We think this summation is unacceptable, simply because the induction times  $t_{\text{MN}}$  and  $t_{\text{PN}}$  are defined differently.

## 7.3 What Is Happening Before MSZW and Induction Time Are Reached?

### 7.3.1 Relaxation Time

Garside et al. [23] wrote as follows: “If the state of the solution changes, so also does the aggregation of particles. This change occurs, however, at a limited rate so it may be delayed in comparison with the change of state of the system. So it is clear that the width of the metastable zone (or induction time) necessary for the clusters to reach the critical size depends on many factors such as temperature, cooling rate, agitation, thermal history of solution, presence of solid particles and of admixtures.” Mullin also wrote in his book [1] that “. . . , a certain “relaxation time”,  $t_r$ , is required for this system to achieve a quasi-steady state distribution of molecular clusters. Time is also required for the formation of a stable nucleus,  $t_n$ , and then the nucleus to grow to a detectable size  $t_g$ .” As seen in these statements, the MSZW and the induction

time are regarded as the region and the time, respectively, needed for the system to reach a quasi-steady-state distribution of molecular clusters. Nucleation seems to occur progressively after the MSZW and the induction time are reached.

Igarashi et al. [24] reported a long induction time of about 20 h for a NaCl-added lysozyme solution, of which pH was adjusted to 4.65. They considered this induction time as the time needed for first amorphous aggregates of lysozyme molecules to change to ordered aggregates. Saito et al. [25] also reported long induction times ranging few hours to several tens of hours for chloroform solutions of *p*-acetanisidide. They concluded that the induction time was the time needed for the structure of randomly arrayed aggregates to transform to that of orderly arrayed aggregates (or crystal nuclei). Thus, Igarashi et al. and Saito et al. both considered that long induction times they observed should be attributed to slow structure change of aggregates. They seem to consider that nucleation occurs continuously after the MSZW and the induction time are reached.

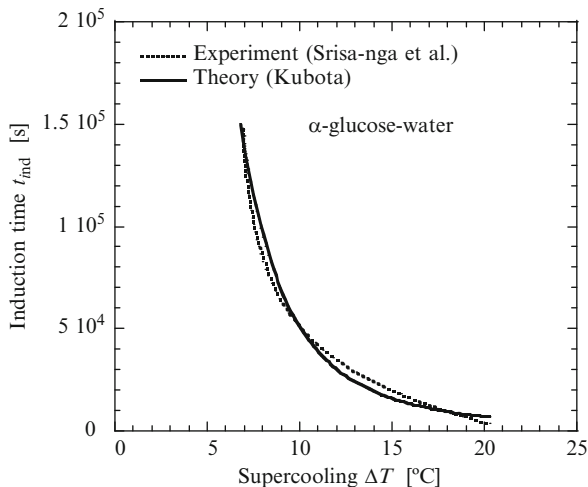
Contrarily, Söhnel and Mullin [26] estimated that the relaxation time  $t_r$  was very short, *i.e.*, in the order of  $10^{-7}$  s for sparingly soluble inorganic electrolyte in aqueous solutions. And they wrote that “in very highly viscous systems (or glass-forming systems),  $t_r$  can be very long and measurable.” We support the view of Söhnel and Mullin [26]. The relaxation time could be very short in ordinary (nonviscous) solutions that are dealt with in ordinary crystallization. See below Sects. 7.5.1 and 7.5.2 where the models based on the idea assuming very short relaxation time are outlined.

### 7.3.2 *Is MSZW Dependent on Induction Time?*

This subtitle may sound strange slightly to the readers. However, some researchers have discussed on the effect of induction time on MSZW. Srisa-nga et al. [27] and Wantha and Flood [28] determined induction times at specified different supersaturations for  $\alpha$ -glucose monohydrate and  $\gamma$ -DL-methionine, respectively, both in seeded aqueous solution. It must be stressed that what they determined was the induction time (not MSZW). Nevertheless, they claimed in reverse that what they measured was MSZWs (not induction times). This claim is very strange and unacceptable, because, in their experiments, the supersaturation (they called this MSZW) was clearly an operating variable that was chosen arbitrarily and the induction time was a dependent variable that was obtained as a result. However, they considered that the MSZW in terms of supersaturation (they called this the secondary nucleation threshold, SNT) was affected by the induction time.

Threlfall et al. [29] also determined induction times at different supersaturations for acetanilides and propionanilides in seeded aqueous ethanol solutions and interpreted the results in the same way as that made by Srisa-nga et al. [27] and Wantha and Flood [28]. The same view was reported earlier for seeded aqueous solutions of potassium dichromate by Janse and de Jong [30] and for unseeded

**Fig. 7.1** Induction time as a function of supercooling. The *solid line* is the experimental value reported by Srisa-nga et al. [27], and the *dotted line* is a best fit of a theoretical equation. This graph was taken from Kubota [32]



aqueous solutions of potassium dihydrogen phosphate, ammonium dihydrogen phosphate, and potassium dichromate by Söhnel and Mullin [31].

The above-described view, which seems to be grounded on the idea that the structure of a solution changes gradually upon supersaturating the solution, may be wrong. Instead, we consider simply that the induction time is affected by supersaturation or supercooling at which it is measured. In fact, Kubota [32] explained successfully the experimental data reported in the above-cited paper [27] (see Fig. 7.1), by assuming the stationary secondary nucleation (*i.e.*, neglecting transient time) with no concentration change. This success seems to corroborate the validity of the idea that MSZW is not affected by time but in reverse the view that induction time depends on supersaturation.

### 7.3.3 Effect of Thermal History

It has been widely known that the thermal history (temperature and time before cooling) of a solution has an effect on MSZW and induction time. There is an overall tendency in the experiments for the solution to exhibit a larger MSZW (*i.e.*, lower nucleation rate) if it is heated for a longer time at a higher temperature above the saturation temperature. Recently, Nordström et al. [33] studied the effect of thermal history on MSZW for *m*-hydroxybenzoic acid in ethyl acetate. The effect of thermal history was observed though it was not very strong. Nordström et al. [33] explained this thermal effect on MSZW by assuming that clusters of solute molecules lose some degree of structure taken from dissolved crystals. Hussain et al. [34] also studied the effect of thermal history on MSZW of vanillin and ethyl vanillin in water-mixed solvents of each of ethanol, 2-propanol, ethylene glycol,

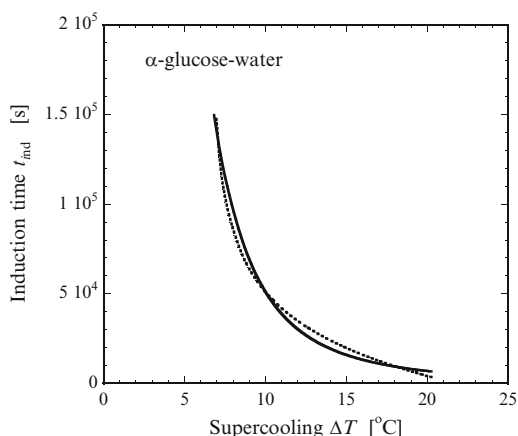
and acetonitrile. The MSZW increased with an increase in the heating temperature above the saturation temperature. They concluded that this is an indication of a preservation of structure “memory” on dissolution of the precipitate. Threlfall et al. [29] support this view and wrote that “Solutions undoubtedly possess structure, and such structure can be altered or broken down by maintenance for long periods at temperatures above the dissolution point. If sufficient change of these conditions occurred, then it would be expected that the MSZW might vary.” On the other hand, Kubota and Fujisawa [19] explained the thermal effect by assuming that heterogeneous solid impurities present in the solution catalyzing primary nucleation heterogeneously are deactivated by heating for a prolonged time. In the above-cited paper of Nordström et al. [33], a brief review on the problem of the thermal history is also presented, which will be useful for the readers.

We support the view proposed by Kubota and Fujisawa [19] because primary nucleation realized both in laboratory and industry is almost all heterogeneous and the structural memory within the solution (cluster size distribution) is hardly to last for a long period of time and it is likely to be lost immediately (the relaxation time needed for the system to achieve a quasi-steady-state size distribution of clusters is very short in ordinary nonviscous solutions).

### 7.3.4 Effect of Agitation

It is known that the MSZW and induction time both decrease with increasing agitation speed. Matsui and Harano [35] studied the effect of agitation on MSZW for the potassium bromate-water system and reported that the MSZW decreased (nucleation rate increases) with increasing agitation speed (see Fig. 7.2). After the work of Matsui and Harano [35], there have been some experimental studies on the effect of agitation on MSZW [36, 37]. These studies exhibit the same experimental

**Fig. 7.2** The effect of agitation speed on MSZW for the potassium bromate-water system (Data were taken from Matsui and Harano [35])

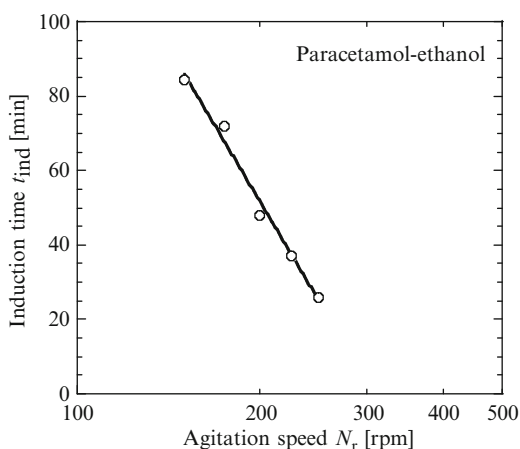


results as those reported by Matsui and Harano [35] in that the agitation reduces the MSZW.

As for the induction time, Liu and Rasmuson [9] reported recently that it decreased (nucleation rate increased) with an increase of agitation speed for an ethanol solution of butyl paraben. They wrote that “Shear-induced molecular alignment and in particular agitation-enhanced cluster aggregation are mechanisms that appear to deserve further attention.” The effect of agitation on induction time has been also studied by other researchers [38–44]). Almost all of these studies show the same results in that the induction time decreases with an increase in agitation speed. In Fig. 7.3, the data reported by Mitchell et al. [44] are shown as such an example. Mitchell et al. ([44] speculated that the agitation effect was caused by an increase in primary nucleation rate. Barata and Serrano [41] attributed the effect of agitation to a reduction in the barrier to the homogeneous primary nucleation processes at the molecular level. Thus, the effect of agitation has been explained, more or less, by assuming a change in clustering process leading to primary nucleation. However, Veintemillas-Verdaguer et al. [42] proposed a different (though qualitative) mechanism in which the effect of agitation is attributed to secondary nucleation caused by grown nuclei.

Incidentally, it is widely known that homogeneous chemical reaction in nonviscous liquid like aqueous solution is not affected by agitation. This suggests that molecular motion in liquid phase and hence collisions between molecules are never affected by agitation. Therefore, it would be reasonable to consider that primary nucleation, which is a molecular-level clustering process, is not influenced by agitation in nonviscous solutions encountered in ordinary crystallization processes. The effect of agitation on MSZW and induction time will be explained later more in detail in Sect. 7.5.3.

**Fig. 7.3** Induction time as a function of agitation speed (Mitchell et al. [44])



## 7.4 Relation of Nucleation to MSZW and Induction Time

### 7.4.1 Nývlt's Model

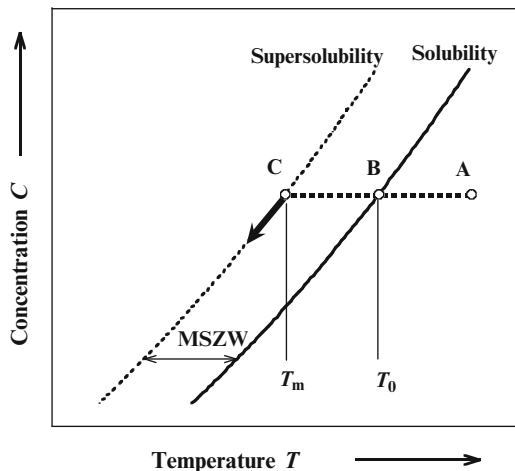
Nývlt [45] proposed a model relating primary nucleation rate with the MSZW. It was such a first attempt. If an undersaturated solution at point A is cooled (see a dotted line in Fig. 7.4), nuclei do not appear immediately after the moment when the solution enters the supersaturated region at point B ( $T = T_0$ ). Nuclei look as if they first appeared afterward at point C ( $T = T_m$ ). Nývlt [45] assumed that the nucleation rate (mass basis) at point C is equal to the “supersaturation rate” or the rate of supersaturation generation by cooling. He also assumed that no nucleation occurred before the point C, *i.e.*, in the region of metastable zone. These two assumptions made by Nývlt [45] are unrealistic and unacceptable. He might have considered that the aggregation of particles (or cluster formation) in solution is delayed in comparison with the change of the state of the solution by cooling.

Nývlt's equation [45] fits well experimental linear relationship of  $\log \Delta T_m$  vs.  $\log R$  (where  $\Delta T_m = \text{MSZW}$ ,  $R = \text{cooling rate}$ ). And the nucleation parameters have been deduced for many material systems by fitting Nývlt's equation to experimental data. However, the fitting is only superficial, and the parameters obtained by fitting are questionable. No constructive discussion on crystallization has been made by using those parameters obtained.

### 7.4.2 Sangwal's Model

Recently, a new model was proposed by Sangwal [46, 47]. His model is basically the same as Nývlt's in that the rate of crystal generation at point C in Fig. 7.4 is equal to the generation rate of supersaturation. Sangwal used the nucleation rate in

**Fig. 7.4** Supersolubility, solubility, and MSZW. A dotted line (A to C) with an arrow was inserted for explaining Nývlt's model [45]; when solution A is cooled at a constant rate, nuclei appear “first” at point C, where the concentration  $C$  begins to decrease in a direction parallel with the solubility curve



a number basis of particle or cluster (opposed to mass basis in Nývlt's model [45]). As same as Nývlt [45], he might have considered that the aggregation of particles is delayed in comparison with the change of the state of the solution by cooling. Sangwal's model can be considered to be improved in that nucleation rate is written in a number basis. However, the basic assumption is still questionable.

Sangwal [46, 47] (and Nývlt [45] also) did not mention anything about the induction time, though it is another nucleation-related physical quantity. The basic assumptions they made cannot be extended to the analysis of induction time.

### 7.4.3 Model of Kashchiev et al.

Kashchiev et al. [48] proposed a different model of MSZW: they defined the MSZW as the supercooling at which the volume fraction of total nucleus-grown crystals reached the detection limit  $\alpha_{\text{det}}$ . In their model, it was assumed that new crystals in the solution are continuously nucleated among the already growing ones with the steady-state (or progressive) homogeneous nucleation mechanism. The homogeneous nucleation rate  $B_{\text{hom}}$  is given by Eq. (7.1) [1]) as

$$B_{\text{hom}} = A \exp \left[ -\frac{16\pi\sigma^3 v^2}{3k^3 T^3 (\ln S)^2} \right] \quad (7.1)$$

where  $A$  is the pre-exponential term (constant),  $\sigma$  is interfacial energy,  $v$  is the molecular volume of crystal (volume per molecule),  $k$  is the Boltzmann constant,  $S$  ( $= C/C_s$ ) is supersaturation ratio, and  $T$  is temperature (in Kelvin). Kashchiev et al. [48] named the MSZW thus defined as the critical undercooling for crystallization. Using this model, they discussed the effect of cooling rate on MSZW.

About 20 years before the abovementioned study of MSZW, Kashchiev et al. [22] also defined similarly the induction time as the time elapsed from the instance of establishment of supersaturation to the time when the volume fraction of nucleus-grown crystals reached the fraction of  $\alpha_{\text{det}}$ . They analyzed the effect of sample volume on induction time, as already described above. It must be noted that Kashchiev et al. [22, 48] and Kashchiev and Rosmalen [49] did not assume the existence of relaxation time as opposed to Mullin [1], Garside et al. [23], and Threlfall et al. [29] (see above Sect. 7.3).

### 7.4.4 Model of Harano et al.

Harano et al. [21] and Harano and Oota [50] defined the induction time as the time elapsed at a constant supercooling from the moment of creation of supersaturation to the time needed for the total number of crystals  $N$  to reach the number-based detection limit  $N_{\text{obs}}$ . In the same way, Harano and coworkers [35, 51] defined the

MSZW as the supercooling at which the total number of crystals  $N$  in a crystallizer reached  $N_{\text{obs}}$  when the solution temperature is lowered linearly. As same as in the model of Kashchiev et al. [22, 48], Harano et al. [21, 35, 50, 51] assumed that new crystals in the solution are continuously nucleated among the already growing ones with the steady-state (or progressive) homogeneous nucleation mechanism. Harano et al. deduced the nucleation parameters from experimental data of MSZW [51] and induction time [21, 50]. They also discussed the effect of agitation on MSZW [35]. It must be noted that the model of Harano et al. is the same as that of Kubota [32, 52, 53], Kubota et al. [54, 55], and Kobari et al. [56–58] in that the MSZW and induction time are both defined on the basis of number-based detection limit. The model of Kubota et al. [32, [52–58]] will be introduced below in Sects. 7.5.1 and 7.5.2.

### 7.4.5 Surface Energy Deduced from Induction Time Data

Surface energy or interfacial tension of nucleus in solution has been deduced by many researchers from induction time data for a variety of substances. The induction time  $t_{\text{ind}}$  is given as a function of  $S$  by Eq. (7.2), which is obtained by combining the relation of  $t_{\text{ind}} \propto 1/B_{\text{hom}}$  and the homogeneous nucleation rate given by Eq. (7.1):

$$t_{\text{ind}} \propto \frac{1}{B_{\text{hom}}} = A \exp \left[ \frac{16\pi\sigma^3 v^2}{3k^3 T^3 (\ln S)^2} \right]. \quad (7.2)$$

As indicated by Eq. (7.2), the relationship between  $\ln t_{\text{ind}}$  and  $1/(\ln S)^2$  is linear with the slope of  $16\pi\sigma^3 v^2/3k^3 T^3$ , from which the value of interfacial energy  $\sigma$  can be calculated. The interfacial energy deduced from induction time was pointed out to be unreliable by Kubota et al. [55]. One reason for that is that homogenous nucleation is unlikely to occur in ordinary experiments [6, 59].

## 7.5 Model of Kubota et al.

### 7.5.1 Analytical Solution of MSZW and Induction Time: A Limiting Case

Nucleation rate is related here to MSZW and induction time for a limiting case where only steady-state heterogeneous primary nucleation is assumed to occur with no concentration change during the measurements of MSZW and induction time.

As described in a previous section entitled “Effect of Sample Volume on MSZW and Induction Time,” the stochastic MSZW and induction time could be realized experimentally only when sample volume was small. This was due to an experimental problem concerning the detection of a first single nucleus. That

is, “whether nucleation is stochastic or deterministic” is not a problem of sample volume essentially, but it is basically a problem of how large the rate of nucleation per sample is.

In the case that the rate of nucleation per sample  $B_1M$  ( $B_1$ , nucleation rate per unit solvent mass;  $M$ , solvent mass) is very low, nucleation occurs randomly in a stochastic manner. For such a case, MSZW and induction time are determined by detecting a first single nucleus. The average MSZW  $\Delta T_{10}$  and induction time  $t_{10}$  are calculated [53], respectively, as

$$\Delta T_{10} = \Gamma \left( \frac{b1 + 2}{b1 + 1} \right) \left[ \frac{(b1 + 1)}{k_{b1}M} \right]^{\frac{1}{b1+1}} R^{\frac{1}{b1+1}} \quad (7.3)$$

and

$$t_{10} = \left( \frac{1}{k_{b1}M} \right) \Delta T^{-b1} \quad (7.4)$$

where  $\Gamma(x)$  is the complete gamma function of  $x$ , which is defined as  $\Gamma(x) = \int_0^\infty t^{x-1} \exp(-t) dt$ ,  $R$  is cooling rate,  $\Delta T$  is supercooling at which the measurement of induction time was made, and  $k_{b1}$  and  $b1$  are the parameters of heterogeneous primary nucleation rate equation shown as

$$B_1 = k_{b1} \Delta T^{b1}. \quad (7.5)$$

In the case that the nucleation rate per sample is not so low, the MSZW and induction time are determined by detecting the point at which the number density of crystals  $N/M$ , which does not mean ( $N$  divided by  $M$ ) reaches the detector sensitivity  $(N/M)_{\text{det}}$ . In such case, the MSZW  $\Delta T_m$  and induction time  $t_{\text{ind}}$  are both deterministic and given [52–58]), respectively, as

$$\Delta T_m = \left[ \frac{(N/M)_{\text{det}} (b1 + 1)}{k_{b1}} \right]^{\frac{1}{b1+1}} R^{\frac{1}{b1+1}} \quad (7.6)$$

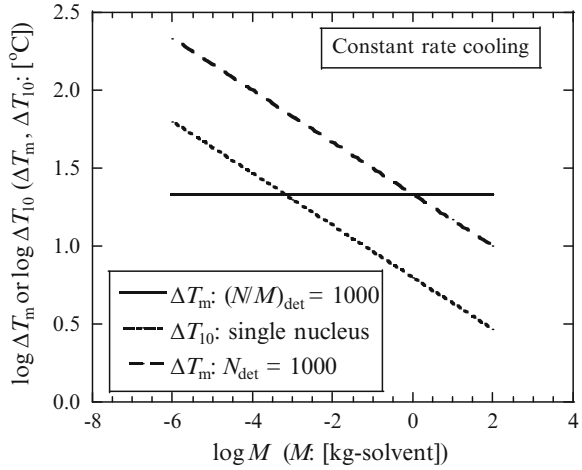
and

$$t_{\text{ind}} = \left[ \frac{(N/M)_{\text{det}}}{k_{b1}} \right] \Delta T^{-b1}. \quad (7.7)$$

Alternatively, if the MSZW and induction time are both determined on the basis of the extensive variable  $N$  (not  $N/M$ ), the following equations are obtained:

$$\Delta T_m = \left[ \frac{N_{\text{det}} (b1 + 1)}{k_{b1}} \right]^{\frac{1}{b1+1}} \left( \frac{1}{M} \right)^{\frac{1}{b1+1}} R^{\frac{1}{b1+1}} \quad (7.8)$$

**Fig. 7.5** The effect of solvent mass on MSZW. The line based on the intensive detection limit  $(N/M)_{\text{det}}$  does not depend on  $M$ , but the line based on the extensive detection limit  $N_{\text{det}}$  and the line based on the single nucleus mechanism decrease with an increase in  $M$ . (Kubota [53])



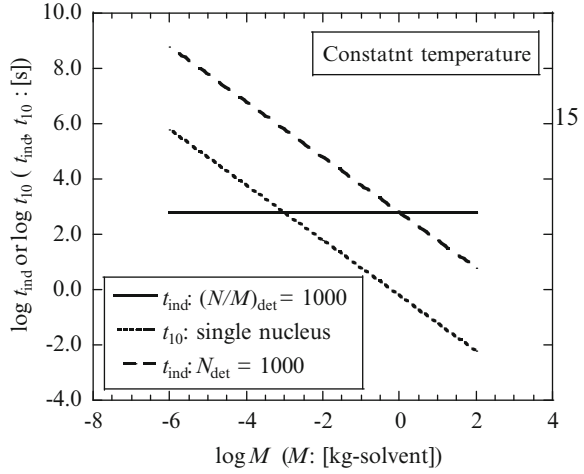
$$t_{\text{ind}} = \left( \frac{N_{\text{det}}}{k_{b1}} \right) \left( \frac{1}{M} \right) \Delta T^{-b1} \quad (7.9)$$

where  $N_{\text{det}}$  is another detector sensitivity. If  $N_{\text{det}} = 1$ , Eq. (7.9) reduces to Eq. (7.4), *i.e.*,  $t_{\text{ind}}$  coincides with  $t_{10}$ . The MSZWs calculated with Eqs. (7.3) and (7.6) are shown in Fig. 7.5. As seen in Fig. 7.5, the deterministic MSZW calculated on the basis of the intensive variable  $N/M$  does not change over a wide range of solvent mass  $M$ ; however, the MSZW calculated on the basis of the extensive variable  $N$  and the average stochastic MSZW  $\Delta T_{10}$  decrease linearly with an increase in  $\log M$ . An experimental linear relation between  $\Delta T_{10}$  and  $\log V$  (sample volume) was reported by Melia and Moffitt [5] for ammonium chloride aqueous solution. Similarly, the deterministic induction time based on the intensive variable  $N/M$  does not change with  $M$ , while the deterministic induction time based on the extensive variable  $N$  and the average stochastic induction time  $t_{10}$  decrease as the solvent mass is increased (see Fig. 7.6). The calculated results shown in Fig. 7.5 and Fig. 7.6 corroborate the qualitative discussion on the effect of sample volume on MSZW and induction time described above.

### 7.5.2 Numerical Analysis of MSZW and Induction Time: A General Case

Kubota et al. [54, 55]) and Kobari et al. [56–58] analyzed the MSZW and induction time for a general case that steady-state heterogeneous primary nucleation as well as steady-state secondary nucleation was assumed to occur. And concentration depletion due to crystallization was also considered. For this general case, analytical solutions described above cannot be applied to. Using the population balance model,

**Fig. 7.6** The effect of solvent mass on induction time. The line based on the intensive detection limit  $(N/M)_{\text{det}}$  does not depend on  $M$ , but the line based on the extensive detection limit  $N_{\text{det}}$  and the line based on single nucleus mechanism decrease with an increase in  $M$ . (Kubota [53])



Kubota et al. [54, 55]) and Kobari et al. [56–58] determined numerically the MSZW and induction time. This is such a first attempt. However, the population balance model itself is not new, which has been widely applied to the analysis of crystallization processes. It consists of the population balance equation and the mass balance equation, which are shown, respectively, as

$$\frac{\partial n(L, t)}{\partial t} + G \frac{\partial n(L, t)}{\partial L} = (B_1 + B_2) \delta(L - L_0) \quad (7.10)$$

and

$$\frac{dC}{dt} = -3\rho_c k_v G \mu_2 - \rho_c k_v (B_1 + B_2) L_0^3 \quad (7.11)$$

where  $B_1$  and  $B_2$  are heterogeneous primary nucleation and secondary nucleation rates, respectively,  $G$  is the linear growth rate  $dL/dt$ ,  $n(L, t)$  is the population density function of crystals,  $L$  is the size of crystal,  $t$  is the time,  $C$  is the concentration of solution,  $\rho_c$  is the density of crystal,  $k_v$  is the volume shape factor of a crystal,  $L_0$  is the size of a nucleus born with either primary or secondary nucleation mechanism,  $\mu_2$  is the second moment of crystal size distribution, and  $\delta(x)$  is the Dirac delta function of  $x$ . The heterogeneous nucleation rate  $B_1$  and secondary nucleation rate  $B_2$  and the growth rate  $G$  are given by the power laws of supercooling  $(T_{\text{sat}} - T)$ , respectively, as

$$B_1 = k_{b1} (T_{\text{sat}} - T)^{b1} \quad (7.12)$$

$$B_2 = k_{b2} (T_{\text{sat}} - T)^{b2} \mu_3 \quad (7.13)$$

$$G = k_g (T_{\text{sat}} - T)^g \quad (7.14)$$

where  $k_{b1}$ ,  $k_{b2}$ ,  $b1$ ,  $b2$ , and  $g$  are empirical constants.  $\mu_3$  is the third moment of crystal size distribution, with which the effect of suspension density of crystals on secondary nucleation is considered.  $T_{\text{sat}}$  is the saturation temperature of a solution of concentration  $C$  at a temperature  $T$ . The supercooling ( $T_{\text{sat}} - T$ ) is not merely a temperature difference. It indirectly considers a solution concentration through  $T_{\text{sat}}$ . When  $C$  remains unchanged and it is equal to the initial concentration  $C_0$ ,  $T_{\text{sat}}$  is always equal to the initial saturation temperature  $T_0$  and then  $(T_{\text{sat}} - T)$  is  $(T_0 - T)$ , which is  $\Delta T$  in the abovementioned analytical solutions. The true driving force for crystal growth and nucleation is the difference in chemical potential  $\Delta\mu$ , which is equal to  $kT\ln S$  ( $k$ , Boltzmann factor;  $S$ , supersaturation ratio). In the model of the group of Kubota et al. [32, 52–58], however, growth rate and nucleation rate were expressed as a power function of supercooling  $\Delta T$  or  $(T_{\text{sat}} - T)$  as described above. These rate expressions are considered to be acceptable as a practical approximation. Alternatively, the rate expression using the chemical potential can be used in the abovementioned numerical analysis with basically no modification of the model.

The population and mass balance equations were solved simultaneously with an initial condition of no crystals and  $C = C_0$  by using the moment method by Kubota et al. [54, 55] and Kobari et al. [56–58]). The MSZW and induction time were determined, respectively, as the supercooling and the time at which the numerically obtained number density of total crystals  $N/M$  reached the detector sensitivity  $(N/M)_{\text{det}}$  (see Fig. 7.7).

MSZWs obtained by the simulation are shown in Fig. 7.8. As seen in Fig. 7.8, the MSZW increases as cooling rate  $R$  is increased, while it decreases as the detector sensitivity is increased (the value of  $(N/M)_{\text{det}}$  is decreased). These tendencies match well with experimental data reported in the literature (see Mullin and Jančić [17], Kobari et al. [56]). The effect of secondary nucleation on MSZW by nucleus-grown crystals becomes significant (the solid lines deviate lower) in the range of low cooling rates in Fig. 7.8. This was named the secondary nucleation-mediated mechanism [55, 57, 58]. At high cooling rates or at high sensitivities (low values

**Fig. 7.7** Crystal number density  $N/M$  vs. time. The number density  $N/M$  reaches the detector sensitivity  $(N/M)_{\text{det}}$  at the time  $t_m$  (○). The MSZW is given with  $\Delta T_m = R \times t_m$  (This graph was taken from Kobari et al. [56] with a minor modification)

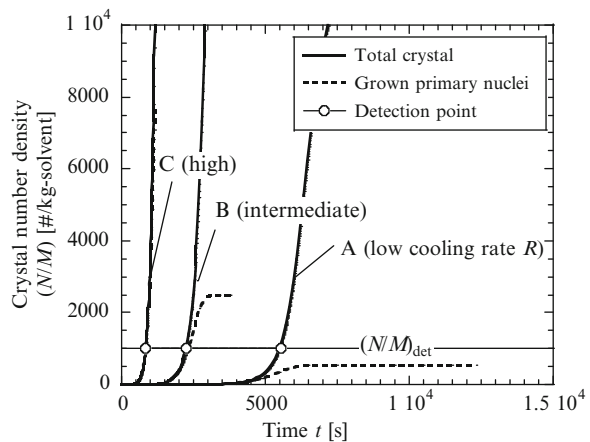
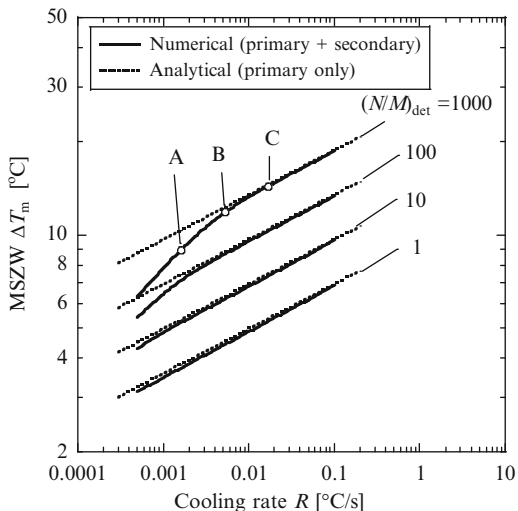


**Fig. 7.8** Effect of detection sensitivity on the relation of MSZW vs. cooling rate  $R$ . Small value of  $(N/M)_{det}$  means high detector sensitivity (Kobari et al. [56]). Open circles A, B, and C correspond, respectively, to those cooling rates shown in Fig. 7.7



of  $(N/M)_{det}$ ), the effect of secondary nucleation on MSZW vanishes, where the numerical solutions coincide with the analytical solutions.

In the simulation of induction time [57], it was shown that the induction time decreases with an increase of detector sensitivity (a decrease of the value of  $(N/M)_{det}$ ), and it also decreases with an increase of agitation speed. The secondary nucleation-mediated mechanism was significantly effective at low supercoolings, while, at high supercoolings, it is not effective and the simulated induction times coincide with the analytical solutions [57]).

### 7.5.3 Explanation of the Agitation Effect by Secondary Nucleation-Mediated Mechanism

In the previous section entitled “Effect of Agitation,” we briefly reviewed the literatures dealing with the effect of agitation on MSZW and induction time. It was shown that almost all previous studies, except for that of Veintemillas-Verdaguer et al. [42], explained the agitation effect by assuming a change in clustering process leading to primary nucleation. And we pointed out that this mechanism was unlikely to be acceptable.

The simulated MSZW is shown in Fig. 7.9 as a function of the kinetic constant  $k_{b2}$  with cooling rate  $R$  as parameter. The simulated MSZW decreases with an increase in the kinetic constant  $k_{b2}$ . In the range of low  $k_{b2}$ , it approaches the analytical MSZW calculated by Eq. (7.6) assuming no secondary nucleation. Therefore, the MSZW can be said to decrease with an increase in agitation speed, because the kinetic constant  $k_{b2}$  in the secondary nucleation rate equation, Eq. (7.13), increases with an increase in agitation speed  $N_r$ , as described as  $k_{b2} \propto N_r^j$  (Garside and

**Fig. 7.9** Effect of the kinetic constant of secondary nucleation  $k_{b2}$  on MSZW.

This effect can be regarded as the effect of stirrer speed  $N_r$ , since  $k_{b2}$  is proportional to  $N_r^j$  (secondary nucleation-mediated effect of stirrer speed) (Kobari et al. [56]). Open circles A, B, and C correspond, respectively, to those cooling rates shown in Fig. 7.7

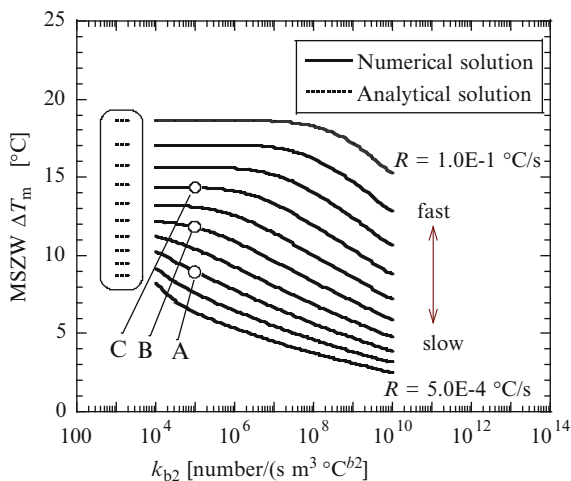
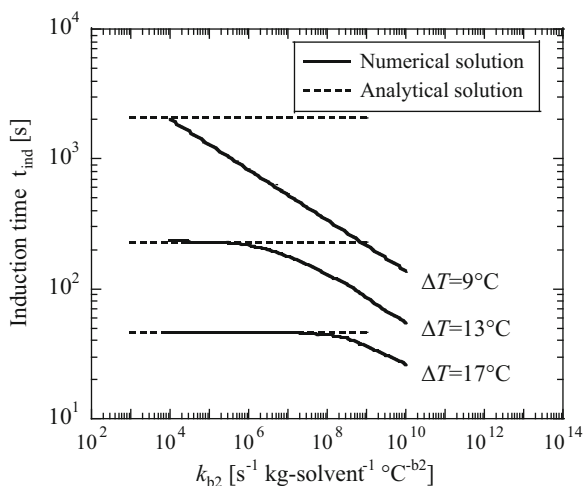


**Fig. 7.10** Effect of the kinetic constant of secondary nucleation  $k_{b2}$  on induction time. This effect can be regarded as the effect of stirrer speed  $N_r$ , since  $k_{b2}$  is proportional to  $N_r^j$  (secondary nucleation-mediated effect of stirrer speed) (Kobari et al. [57])



Davey, [60]). This is an explanation of the agitation effect on induction time by the secondary nucleation-mediated mechanism (Kobari et al. [56]). In the simulation of induction time (Kobari et al. [57]), the simulated induction time decreases with an increase of the secondary nucleation constant  $k_{b2}$ , as seen in Fig. 7.10. As  $k_{b2} \propto N_r^j$ , this indicates that the induction time decreases with an increase in agitation speed. The secondary nucleation-mediated mechanism thus explains also the experimental effect of agitation on induction time (shown in Fig. 7.3).

## 7.6 Relevance to Industrial Crystallization

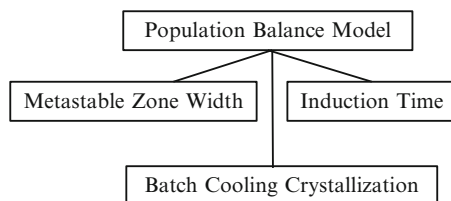
### 7.6.1 *Is MSZW the Region Where Spontaneous Nucleation Is Avoided?*

It has been long and widely believed that the metastable zone is the supersaturated region within which spontaneous nucleation can be avoided and a crystallizer can be operated safely in a controlled manner. Fujiwara et al. [61] wrote that “The vast majority of pharmaceutical crystallization processes are designed so that the desired operation is within the metastable zone.” Price [62] also wrote that “The metastable zone represents the region within which the supersaturation needs to be maintained for the crystallization to be controlled.” The industrial importance of the metastable zone was first drawn attention about 90 years ago by Griffiths [3], though the concept of metastable zone was expressed much earlier by Ostwald [2].

As described above, the MSZW is only a kinetic property which depends on many factors such as cooling rate, agitation speed, and the technique used for detection of nucleation event. It would be never a criterion governing the stability of batch crystallization with respect to nucleation. To our knowledge, there have been no successful industrial applications of this concept. From academic side, however, some research papers have been published concerning this concept. Mullin and Nývlt [63] proposed a very simple expression of the so-called controlled cooling policy. They claimed that, by using this cooling policy, the supersaturation could be controlled within the metastable zone during seeded batch cooling crystallization and then nucleation could be avoided. However, the crystal size distribution presented in their original paper [63], in which a large amount of small nucleus-grown crystals are included, indicates that nucleation occurred significantly in their experiment. This suggests that the controlled cooling policy was not successful. Yu et al. [64] studied the effect of supersaturation feedback control (within the MSZW) on the crystal size distribution for anti-solvent crystallization of paracetamol in the mixed solvent of acetone and water. The supersaturation control was successful only when seed crystals were added adequately. The amount of seeds seems to play a key role for avoiding nucleation. Control of supersaturation seems to have a minor effect. The failure of crystal size distribution control in the controlled cooling method may be due to the inadequate amount of seed crystals. It was pointed out by Doki et al. [65, 66], Kubota et al. [67, 68], and Kubota and Onosawa [69] that enough seeding can suppress nucleation in batch cooling crystallization.

The metastable zone is not the supersaturation region that guarantees safe batch crystallization operation with no nucleation. The MSZW is not a thermodynamic equilibrium value, but it is only a kinetic one, which depends on many factors described above.

**Fig. 7.11** Metastable zone width, induction time, and batch cooling crystallization can be all simulated with a single population balance model



### 7.6.2 *A Unified Understanding of MSZW, Induction Time, and Batch Crystallization Operation*

As already described above, the MSZW (and also the induction time) is a nucleation-related kinetic quantity. It was simulated by using the population balance model, where quasi-steady-state heterogeneous primary nucleation as well as quasi-steady-state secondary nucleation was assumed to occur. The population balance model itself used in the simulation is not a special one, but it is known to have been used successfully for the simulation and analysis of batch crystallization processes as summarized in a recent review paper [70]. It can be said, therefore, that the MSZW (and also induction time) and batch crystallization processes could be treated in a unified manner by using the population balance model (see Fig. 7.11). A set of experimental data of MSZW and induction time and data of time-dependent concentration, temperature, and crystal size distribution in batch crystallization, obtained in a laboratory, could be all utilized for the estimation of kinetic parameters of primary nucleation, secondary nucleation, and crystal growth. These parameters may be used successfully for the process design of batch crystallization.

This methodology using the population balance model for MSZW and induction time is much more useful for the design and operation of an industrial crystallizer than the method based on the concept that the MSZW is the region for the stable operation of a crystallizer.

## 7.7 Conclusions

Nucleation is stochastic by nature. The MSZW and induction time are observed as a stochastic variable for small sample volume but not for large one. These are experimental facts. When sample volume  $V$  is small, the nucleation rate per sample  $BV$  could be small due to small  $V$ . In theory, the nucleation rate  $BV$  can be reduced even for large sample volume  $V$  if the nucleation rate per unit volume  $B$  is lowered by reducing supersaturation, and the nucleation should be stochastic. But this situation cannot be realized in experiment due to a lack of detection technique of nucleation event. Whether the MSZW and induction time are dependent on the sample volume or not is related to what is detected as nucleation event. If an extensive variable (*e.g.*, absolute number of crystals  $N$ ) is detected, these should

depend on the sample volume, while if an intensive variable (*e.g.*, number of crystals per sample  $N/V$ ) is detected, the MSZW and induction time should not depend on the sample volume.

The relaxation time for the system to achieve a quasi-steady-state distribution of molecular clusters after the solution is made supersaturated can be negligibly small. The metastable state or time-dependent nonequilibrium state of a supersaturated solution should not be considered to exist for solutions encountered in ordinary crystallization processes. The effect of thermal history should be explained with deactivation mechanism of hetero-nuclei that induce nucleation. The effect of agitation on the MSZW and induction time can be explained by the mechanism based on the secondary nucleation caused by nucleus-grown crystals.

Published models relating nucleation rate to MSZW and induction time are briefly reviewed. The models of Sangwal [46, 47]) and Nývlt [45], both of which seem to assume the existence of time-dependent nonequilibrium state before nucleation, are plausible. Different models for MSZW (Kashchiev et al. [48]) and induction time (Kashchiev et al. [22]) look reasonable. They assumed the steady-state progressive homogeneous nucleation. Harano et al. analyzed MSZWs [51] and induction times [21, 50] using their original models based on the number-based detection limit. The interfacial energy deduced from induction time was pointed out to be unreliable. Analytical solutions of MSZW and induction time were presented, which were derived by Kubota [52, 53]) both for stochastic and deterministic circumstances. The effects of cooling rate, supercooling, and sample volume were mathematically explained for a limiting case of no secondary nucleation and no concentration depletion due to crystallization. For a general case that secondary nucleation caused by grown nuclei and the concentration depletion are considered, numerical calculation using the population balance model was presented. The effect of agitation was explained by using the secondary nucleation-mediated mechanism.

Finally, the relevance of MSZW and induction time to batch crystallization was discussed. The existing view that the metastable zone is the region within which crystallization is guaranteed to proceed safely without nucleation was criticized. Instead, the methodology using the population balance model was recommended. It is useful to understand in a unified manner the MSZW, the induction time, and the design and operation of an industrial crystallizer.

## References

1. J.W. Mullin, *Crystallization*, 4th edn. (Butterworth-Heinemann, Oxford, 2001)
2. W. Ostwald, Studien über die Bildung und Umwandlung fester Körper. *Z. Phys. Chem.* **22**, 289–330 (1987)
3. H. Griffiths, Mechanical crystallization. *J. Soc. Chem. Ind.* **44**, 7T–18T (1925)
4. S.S. Kadam, H.J.M. Kramer, J.H. ter Hoost, Combination of a single primary nucleation event and secondary nucleation in crystallization processes. *Cryst. Growth Des.* **11**, 1271–1277 (2011)

5. T.P. Melia, W.P. Moffitt, Crystallization from aqueous solution. *J. Colloid Sci.* **19**, 433–447 (1964)
6. N. Kubota, T. Kawakami, T. Tadaki, Calculation of supercooling temperature for primary nucleation of potassium nitrate from aqueous solution by the two-kind active site model. *J. Cryst. Growth* **74**, 259–274 (1986)
7. L. Goh, K. Chen, V. Bhamidi, G. He, N.C.S. Kee, P.J.A. Kenis, C.F.Z. III, R.D. Braatz, A stochastic model for nucleation kinetics determination in droplet-based microfluidic systems. *Cryst. Growth Des.* **10**, 2515–2521 (2010)
8. D. Knezic, J. Zaccaro, A.S. Myerson, Nucleation induction time in levitated droplets. *J. Phys. Chem. B* **108**, 10672–10677 (2004)
9. J. Liu, Å.C. Rasmuson, Influence of agitation and fluid shear on primary nucleation in solution. *Cryst. Growth Des.* **13**, 4385–4394 (2013)
10. S. Teychene, B. Biscans, Crystal nucleation in a droplet based microfluidic crystallizer. *Chem. Eng. Sci.* **77**, 242–248 (2012)
11. S.A. Kulkarni, S.S. Kadam, H. Meekes, A.I. Stankiewicz, J.H. ter Horst, Crystal Nucleation kinetics from induction times and metastable zone widths. *Cryst. Growth Des.* **13**, 2435–2440 (2013)
12. P. Barrett, B. Glennon, Characterizing the metastable zone width and solubility curve using Lasentec FBRM and PVM. *Trans. IChem.* **80A**, 799–805 (2002)
13. D. O’Grady, M. Barrett, E. Casey, B. Glennon, The effect of mixing on the metastable zone width and nucleation kinetics in the anti-solvent crystallization of benzoic acid. *Chem. Eng. Res Des* **85**, 945–952 (2007)
14. L.L. Simon, Z.K. Nagy, K. Hugerbuhler, Comparison of external bulk video imaging with focused beam reflectance measurement and ultra-violet visible spectroscopy for metastable zone identification in food and pharmaceutical crystallization processes. *Chem. Eng. Sci.* **64**, 3344–3351 (2009)
15. A.R. Parsons, S.N. Black, R. Colling, Automated measurement of metastable zones for pharmaceutical compounds. *Trans. IChemE.* **81**, 700–704 (2003)
16. C.J. Brown, Y.C. Lee, Z.K. Nagy, X. Ni, Evaluation of crystallization kinetics of adipic acid in an oscillatory baffled crystallizer. *CrystEngComm* **16**, 8008–8014 (2014)
17. J.W. Mullin, S.J. Jančić, Interpretation of metastable zone widths. *Trans. IChemE.* **57**, 188–193 (1979)
18. N. Lyczko, F. Espitalie, O. Louisnard, J. Schwartzentruber, Effect of ultrasound on the induction time and the metastable zone widths of potassium sulphate. *Chem. Eng. J.* **86**, 233–241 (2002)
19. N. Kubota, Y. Fujisawa, Effects of filtration and thermal history on primary nucleation of potassium bromate from aqueous solution, in *Proceedings of the 9th symposium on industrial crystallization* (1984), pp. 259–262
20. S.S. Kadam, S.A. Kulkarni, R.C. Ribera, A.I. Staniewicz, J.H. ter Horst, A new view on the metastable zone width during cooling crystallization. *Chem. Eng. Sci.* **72**, 10–19 (2012)
21. Y. Harano, K. Nakano, M. Saito, T. Imoto, Nucleation rate of potassium chlorate from quiescent supersaturated aqueous solution. *J. Chem. Eng. Jpn.* **9**, 373–377 (1976)
22. D. Kashchiev, D. Verdoes, G.M. van Rosmalen, Induction time and metastability limit in new phase formation. *J. Cryst. Growth* **110**, 373–380 (1991)
23. J. Garside, A. Mersmann, J. Nývlt (eds.), *Measurement of Crystal Growth and Nucleation Rates*. IChemE (Institution of Chemical Engineers, Rugby), pp. 157–158 (2002)
24. K. Igarashi, M. Azuma, J. Kato, H. Ooshima, The initial stage of crystallization of lysozyme: a differential scanning calorimetric (DSC) study. *J. Cryst. Growth* **204**, 191–200 (1999)
25. A. Saito, K. Igarashi, M. Azuma, H. Ooshima, Aggregation of p-acetanisidide molecules in the under-and super-saturated solution and its effect on crystallization. *J. Chm. Eng. Jpn.* **35**, 1133–1139 (2002)
26. O. Söhnel, J.W. Mullin, Interpretation of crystallization induction periods. *J. Colloid Interface Sci.* **123**, 43–50 (1988)

27. S. Srisa-nga, A.W. Flood, E.T. White, The secondary nucleation threshold and crystal growth of  $\alpha$ -glucose monohydrate in aqueous solution. *Cryst. Growth Des.* **3**, 795–801 (2006)
28. L. Wantha, A.W. Flood, Crystal growth rates and secondary nucleation threshold for  $\gamma$ -DL-methionine in aqueous solution. *J. Cryst. Growth* **318**, 117–121 (2011)
29. T.L. Threlfall, R.W. De'Ath, S.J. Coles, Metastable zone widths, conformational multiplicity, and seeding. *Org. Process Res. Dev.* **17**, 578–584 (2013)
30. A.H. Janse, E.J. de Jong, On the width of the metastable zone. *Trans. Inst. Chem. Eng.* **56**, 187–193 (1978)
31. O. Söhnel, J.W. Mullin, The role of time in metastable zone width determination. *Chem. Eng. Res. Des.* **66**, 537–540 (1988)
32. N. Kubota, A unified interpretation of metastable zone widths and induction times measured for seeded solutions. *J. Cryst. Growth* **312**, 548–554 (2010)
33. F.L. Nordström, M. Svard, B. Malmberg, A.C. Rasmuson, Influence of solution thermal and structural history on the nucleation of m-hydroxybenzoic acid polymorphs. *Cryst. Growth Des.* **12**, 4340–4348 (2012)
34. K. Hussain, G. Thorsen, D. Malthe-Sorensen, Nucleation and metastability in crystallization of vanillin and ethyl vanillin. *Chem. Eng. Sci.* **56**, 2295–2304 (2001)
35. T. Matsui, Y. Harano, Effect of agitation on nucleation of  $\text{KBrO}_3$  from unseeded aqueous solution. *Kagaku Kogaku Ronbunshu* **11**, 198–202 (1985)
36. K. Liang, G. White, D. Wilkinson, L.J. Ford, K.J. Roberts, W.M.L. Wood, Examination of the process scale dependence of L-glutamic acid batch crystallized from supersaturated aqueous solutions in relation to reactor hydrodynamics. *Ind. Eng. Chem. Res.* **43**, 1227–1234 (2004)
37. M. Akrap, N. Kuzmanic, J. Prlic-Kardum, Effect of mixing on the crystal size distribution of borax decahydrate in a batch cooling crystallizer. *J. Cryst. Growth* **312**, 3603–3608 (2010)
38. M.S. Joshi, A.V. Antony, Nucleation in supersaturated potassium dihydrogen orthophosphate solutions. *J. Cryst. Growth* **6**, 7–9 (1979)
39. J.W. Mullin, S. Zacek, The precipitation of potassium aluminum sulphate from aqueous solution. *J. Cryst. Growth* **53**, 515–518 (1981)
40. J. Mydlarz, A.G. Jones, Crystallization and agglomeration kinetics during the batch drowning-out precipitation of potash alum with aqueous acetone. *Powder Technol.* **65**, 187–194 (1991)
41. P.A. Barata, M.L. Serrano, Salting-out precipitation of potassium dihydrogen phosphate (KDP) II. Influence of agitation intensity. *J. Cryst. Growth* **163**, 426–433 (1996)
42. S. Veintemillas-Verdaguer, S.O. Esteban, M.A. Herrero, The effect of stirring on sodium chlorate crystallization under symmetry breaking conditions. *J. Cryst. Growth* **303**, 562–567 (2007)
43. S. Machefer, K. Schnitzlein, Experimental study on the effect of polyol admixtures on the interfacial tension of potassium dihydrogen phosphate in aqueous solutions: induction time experiments versus drop shape analysis. *Ind. Eng. Chem. Res.* **48**, 2659–2670 (2009)
44. N.A. Mitchell, P.J. Frawley, C.T. Ó'Ciardhá, Nucleation kinetics of paracetamol–ethanol solutions from induction time experiments using Lasentec FBRM. *J. Cryst. Growth* **321**, 91–99 (2011)
45. J. Nývlt, Kinetics of nucleation in solutions. *J. Cryst. Growth* **3/4**, 377–383 (1968)
46. K. Sangwal, A novel self-consistent Nývlt-like equation for metastable zone width determined by the polythermal method. *Cryst. Res. Technol.* **44**, 231–247 (2009)
47. K. Sangwal, Novel approach to analyze metastable zone width determined by the polythermal method: physical interpretation of various parameters. *Cryst. Growth Des.* **9**, 942–950 (2009)
48. D. Kashchiev, A. Borissova, R.B. Hammond, K.J. Roberts, Effect of cooling rate on the critical undercooling for crystallization. *J. Cryst. Growth* **312**, 698–704 (2010)
49. D. Kashchiev, G.M. van Rosmalen, Review: nucleation in solutions revisited. *Cryst. Res. Technol.* **38**, 555–574 (2003)
50. Y. Harano, K. Oota, Measurement of crystallization of potassium bromate from its quiescent aqueous solution by differential scanning calorimeter – homogeneous nucleation rate. *J. Chem. Eng. Jpn.* **11**, 159–161 (1978)

51. Y. Harano, H. Yamamoto, T. Miura, Non-isothermal analysis of nucleation of  $\text{KBrO}_3$ . *J. Chem. Eng. Jpn.* **14**, 439–444 (1981)
52. N. Kubota, A new interpretation of metastable zone widths measured for unseeded solutions. *J. Cryst. Growth* **310**, 629–634 (2008)
53. N. Kubota, Effect of sample volume on metastable zone width and induction time. *J. Cryst. Growth* **345**, 27–33 (2011)
54. N. Kubota, M. Kobari, I. Hirasawa, Analytical and numerical study of detector sensitivity and resolution effects on metastable zone width. *CrystEngComm* **15**, 2091–2098 (2013)
55. N. Kubota, M. Kobari, I. Hirasawa, Effects of detector sensitivity and resolution on induction time reading. *CrystEngComm* **16**, 1103–1112 (2014)
56. M. Kobari, N. Kubota, I. Hirasawa, Computer simulation of metastable zone width for unseeded potassium sulfate aqueous solution. *J. Cryst. Growth* **317**, 64–69 (2011)
57. M. Kobari, N. Kubota, I. Hirasawa, Secondary nucleation-mediated effects of stirrer speed and growth rate on induction time for unseeded solution. *CrystEngComm* **14**, 5255–5261 (2012)
58. M. Kobari, N. Kubota, I. Hirasawa, Deducing primary nucleation parameters from metastable zone width and induction time data determined with simulation. *CrystEngComm* **15**, 1199–1209 (2013)
59. N. Kubota, Y. Fujisawa, T. Tadaki, Effect of volume on the supercooling temperature for primary nucleation of potassium nitrate from aqueous solution. *J. Cryst. Growth* **89**, 545–552 (1988)
60. J. Garside, R. Davey, Invited review secondary contact nucleation: kinetics, growth and scale-up. *Chem. Eng. Commun.* **4**, 393–3424 (1980)
61. M. Fujiwara, Z.K. Nagy, J.W. Chew, R.D. Braatz, First-principles and direct design approaches for the control of pharmaceutical crystallization. *J. Process Control* **15**, 493–504 (2005)
62. C.J. Price, Take some solid steps to improve crystallization. *Chem. Eng. Prog.* **93**, 34–43 (1997)
63. J.W. Mullin, J. Nývlt, Programmed cooling of batch crystallizers. *Chem. Eng. Sci.* **26**, 369–377 (1971)
64. Z.Q. Yu, P.S. Chow, R.B.H. Tan, Application of attenuated total reflectance-Fourier transform infrared (ATR-FTIR) technique in the monitoring and control of anti-solvent crystallization. *Ind. Eng. Chem. Res.* **45**, 438–444 (2006)
65. N. Doki, N. Kubota, A. Sato, M. Yokota, O. Hamada, F. Masumi, Scaleup experiments on seeded batch cooling crystallization of potassium alum. *AIChE J.* **45**, 2527–2533 (1999)
66. N. Doki, N. Kubota, A. Sato, M. Yokota, Effect of cooling mode on product crystal size in seeded batch crystallization of potassium alum. *Chem. Eng. J.* **81**, 313–316 (2001)
67. N. Kubota, N. Doki, M. Yokota, D. Jagadesh, Seeding effect on product crystal size in batch crystallization. *J. Chem. Eng. Jpn.* **35**, 1063–1071 (2002)
68. N. Kubota, N. Doki, M. Yokota, A. Sato, Seeding policy in batch cooling crystallization. *Powder Technology* **121**, 31–38 (2001)
69. N. Kubota, M. Onosawa, Seeded batch crystallization of ammonium aluminum sulfate from aqueous solution. *J. Cryst. Growth* **311**, 4525–4529 (2009)
70. Z.K. Nagy, G. Févotte, H. Kramer, L.L. Simon, Recent advances in the monitoring, modelling and control of crystallization systems. *Chem. Eng. Res. Des.* **91**, 1903–1922 (2013)

**Part II**  
**Crystal Structure Determination and MO**  
**Calculation**

# Chapter 8

## Structure Determination of Organic Molecular Solids from Powder X-Ray Diffraction Data: Current Opportunities and State of the Art

Kenneth D.M. Harris and P. Andrew Williams

**Abstract** Knowledge of crystal structure is a prerequisite for understanding fundamental properties and developing applications of crystalline materials. Although single-crystal X-ray diffraction (XRD) is the most powerful experimental technique for determining crystal structures, the requirement for a single-crystal specimen can impose severe limitations on the scope of this technique. For materials that cannot be grown as suitable single crystals, structure determination must be tackled instead using *powder* XRD data. However, the task of carrying out structure determination from powder XRD data is significantly more challenging than from single-crystal XRD data, particularly for organic materials. As recently as the early 1990s, no organic molecular crystal structure had ever been solved directly from powder XRD data, as such materials present significant challenges for the application of traditional structure-solution techniques. However, since that time, the direct-space strategy for structure solution has transformed the field, such that structure determination of organic crystal structures of moderate complexity from powder XRD data is now relatively routine. This chapter gives an overview of the current opportunities for carrying out structure determination of organic materials directly from powder XRD data. Results from the application of the direct-space strategy are presented, with examples from several different fields within chemical, materials and biological sciences.

**Keywords** Powder X-ray diffraction • Structure solution • Direct-space strategy

### 8.1 Introduction

Single-crystal X-ray diffraction (XRD) is the most powerful and routine technique for determining structural information at the atomic level [1–3], and many crucially important advances in chemical, biological, physical and materials sciences have

---

K.D.M. Harris (✉) • P.A. Williams  
School of Chemistry, Cardiff University, Park Place, Cardiff, Wales CF10 3AT, UK  
e-mail: [HarrisKDM@cardiff.ac.uk](mailto:HarrisKDM@cardiff.ac.uk)

resulted from the application of this technique during the past 100 years. Nevertheless, the requirement for a single-crystal specimen of appropriate size and quality imposes a limitation on the scope of the single-crystal XRD technique. Indeed, many crystalline solids can be prepared *only* as microcrystalline powders and therefore cannot be studied using single-crystal XRD. To understand the structural properties of such materials, the most suitable approach is to use powder XRD data. However, the process of carrying out structure determination from powder XRD data [4] is significantly more challenging than structure determination from single-crystal XRD data. Although single-crystal XRD patterns and powder XRD patterns contain essentially the same information, the diffraction data are distributed in three-dimensional space in the case of single-crystal XRD but are “compressed” into one dimension in the case of a powder XRD measurement (Fig. 8.1). Consequently, there is usually considerable peak overlap in the powder XRD pattern (Fig. 8.2), which obscures information on the positions and intensities of the peaks and can therefore impede or prohibit the process of crystal structure determination. As crystalline organic molecular solids typically have large unit cells and low symmetry, the problem of peak overlap is often particularly severe, and structure determination from powder XRD data can be particularly challenging for such materials. Indeed, it is only since the early 1990s that it has been possible

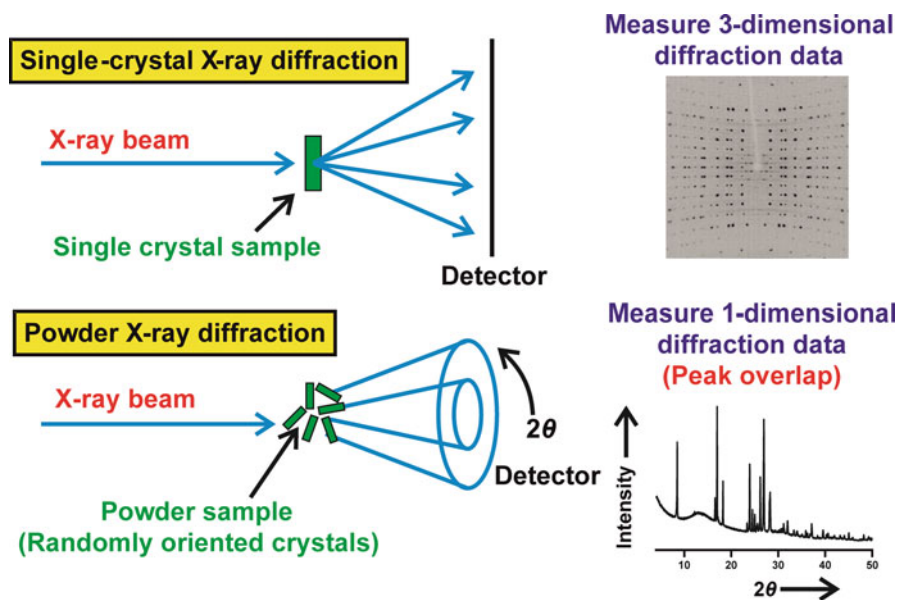


**Fig. 8.1** Comparison of single-crystal XRD and powder XRD measurements. In powder XRD, the diffraction phenomenon for each individual crystallite in the powder is the same as the diffraction phenomenon in single-crystal XRD. However, the powder comprises a large collection of crystallites with (in principle) a random distribution of crystallite orientations. Consequently, in the powder XRD measurement, the three-dimensional diffraction data are effectively compressed into one dimension (intensity *versus* diffraction angle  $2\theta$ )

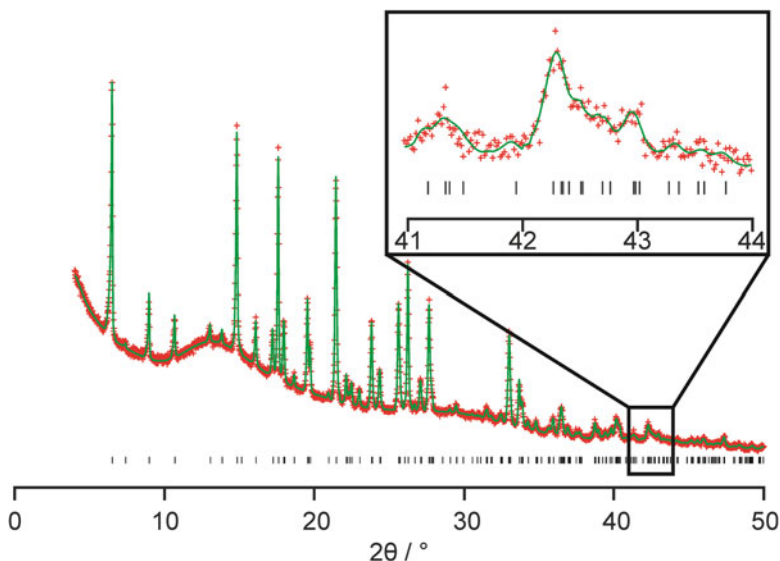


**Fig. 8.2** The powder XRD pattern of L-phenylalanine hemihydrate. The tick marks at the bottom indicate the  $2\theta$  values of individual “peaks”. The inset highlights a typical region with substantial peak overlap. Note that the density of peaks (i.e. the number of peaks within a given  $2\theta$  range) increases significantly at higher  $2\theta$  values and that the overall intensity decreases at higher  $2\theta$  values

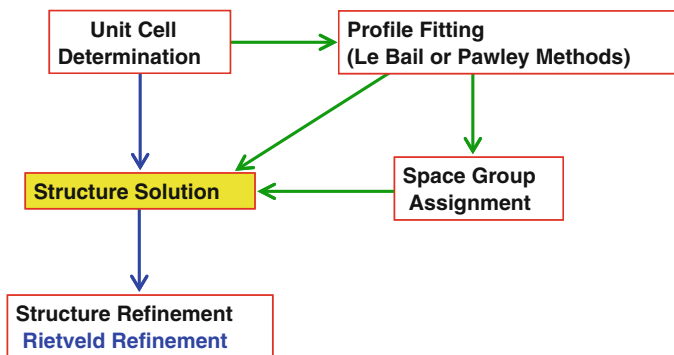


**Fig. 8.3** The sequence of stages involved in crystal structure determination from powder XRD data

to determine the crystal structures of organic molecular materials directly from powder XRD data [5–19]. In the intervening time, considerable research efforts have been devoted to the development and application of new techniques in this field, leading to significant advances in the scope and potential for carrying out structure determination of organic materials directly from powder XRD data.

Crystal structure determination from XRD data involves three stages (Fig. 8.3): (i) unit cell determination and space group assignment, (ii) structure solution and

(iii) structure refinement. The aim of *structure solution* is to obtain a sufficiently good approximation to the crystal structure, using the unit cell and space group determined in stage (i) but starting with no knowledge of the actual arrangement of atoms or molecules within the unit cell. If a sufficiently good structure solution is obtained, a high-quality description of the structure is then obtained by *structure refinement*. For powder XRD data, structure refinement is carried out routinely using the Rietveld profile refinement technique [20–22].

Techniques for carrying out structure solution from powder XRD data can be subdivided into two different strategies: the *traditional* structure-solution strategy and the *direct-space* structure-solution strategy. In the case of organic molecular solids, the vast majority of reported examples of structure determination from powder XRD data have been carried out using the direct-space strategy for structure solution, although there have also been several reports of successful structure solution of such materials using the traditional strategy.

The traditional strategy for structure solution follows a close analogy to the analysis of single-crystal XRD data. In this strategy, the integrated intensities of individual diffraction maxima are extracted directly from the powder XRD pattern to generate a single-crystal-like  $I(hkl)$  dataset, which is then used in the types of structure-solution calculation that are used for single-crystal XRD data. However, as discussed above, peak overlap in the powder XRD pattern can limit the reliability of the extracted intensities  $I(hkl)$  and can therefore lead to difficulties in attempts to carry out structure solution using these intensity data. Such problems may be particularly severe when there is substantial peak overlap in the powder XRD pattern, as encountered for most organic molecular solids.

In the direct-space strategy, the structure-solution process is handled as a global optimization problem, as discussed in more detail in Sect. 8.2. The dramatic upsurge of activity in the last 20 years in structure determination of organic materials from powder XRD data was catalysed by the development of the direct-space strategy for structure solution, and the direct-space strategy is now adopted as the standard methodology for structure solution in this field.

This article provides an overview of the *direct-space* strategy for structure solution from powder XRD data. A wide range of examples are given to illustrate the state of the art for applications of this technique, focusing in particular on organic (and organometallic) materials, with examples taken from a range of fields of research.

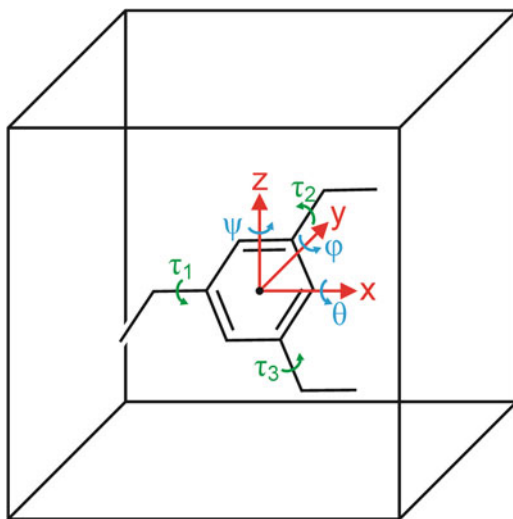
## 8.2 The Direct-Space Strategy for Structure Solution from Powder XRD Data

In the present day, most reported structure determination of organic molecular solids from powder XRD data uses the direct-space strategy [23] for structure solution, in which structure solution is handled as a problem of global optimization. In the direct-space strategy, trial structures are generated in direct space, independently of

the experimental powder XRD data. The quality of each trial structure is assessed by direct comparison between the powder XRD pattern calculated for the trial structure and the experimental powder XRD pattern. An appropriate figure-of-merit is used to quantify the level of agreement between the calculated and experimental powder XRD patterns. The figure-of-merit used in our implementations of the direct-space strategy is the weighted powder profile  $R$ -factor  $R_{wp}$  (the  $R$ -factor normally used in Rietveld refinement). In the definition of  $R_{wp}$ , the entire digitized intensity profile is considered point-by-point rather than the integrated intensities of individual diffraction maxima.

Each trial structure is defined by a set (denoted  $\Gamma$ ) of structural variables, which represent the position, orientation and intramolecular geometry of each molecule in the asymmetric unit. The position of the molecule is defined by the coordinates  $\{x, y, z\}$  of the centre of mass or a selected atom, and the orientation of the molecule is defined by rotation angles  $\{\theta, \varphi, \psi\}$  around a set of orthogonal axes. An important feature underlying the success of the direct-space strategy is that it incorporates reliable prior knowledge of molecular geometry (i.e. bond lengths, bond angles, geometries of rigid moieties such as aromatic rings) directly within the structure-solution calculation. In general, the bond lengths and bond angles are fixed (either using standard values for the type of molecule under investigation or using the known geometry of a similar molecule), and the intramolecular geometry is specified by a set of variable torsion angles  $\{\tau_1, \tau_2, \dots, \tau_n\}$  that define the molecular conformation. Thus, in general, for each molecule in the asymmetric unit, there are  $6 + n$  variables (Fig. 8.4),  $\Gamma = \{x, y, z, \theta, \varphi, \psi, \tau_1, \tau_2, \dots, \tau_n\}$ . Other definitions of variable space in direct-space structure solution of organic molecular materials have been explored and may be advantageous in certain cases [24] (e.g. for molecules with a high degree of conformational flexibility).

**Fig. 8.4** Schematic illustration of the structural variables used in direct-space structure solution from powder XRD data: positional variables  $\{x, y, z\}$ , orientational variables  $\{\theta, \varphi, \psi\}$  and torsion-angle variables  $\{\tau_1, \tau_2, \tau_3\}$ . The bond lengths, bond angles and the geometry of the aromatic ring are fixed at standard values



The direct-space strategy aims to find the trial structure corresponding to the lowest value of  $R_{wp}$  and is equivalent to exploring a hypersurface  $R_{wp}(\mathbf{\Gamma})$  to find the set of variables  $\mathbf{\Gamma}$  corresponding to the global minimum in  $R_{wp}(\mathbf{\Gamma})$ . In principle, any technique for global optimization may be used to find the lowest point on the  $R_{wp}(\mathbf{\Gamma})$  hypersurface, and much success has been achieved using Monte Carlo, simulated annealing and genetic algorithm techniques in this field. In addition, grid search and differential evolution techniques have also been employed.

The remainder of this chapter is focused on presenting applications of structure determination of organic materials directly from powder XRD data, illustrating the current scope for applying state-of-the-art powder XRD methodologies within the domain of organic solid-state chemistry.

### **8.3 Examples of Structure Determination from Powder XRD Data in Organic Solid-State Chemistry**

For many organic materials, conventional techniques for crystallization from solution do not produce single crystals of suitable size and quality for single-crystal XRD studies, and instead yield only microcrystalline powders. In such cases, structure determination from powder XRD data provides a viable route for understanding the structural properties of the materials obtained.

In other cases, certain solid phases cannot be obtained at all (even as microcrystalline powders) by conventional crystallization experiments, but instead can be produced only by other types of preparation procedure. However, many procedures for materials preparation commonly yield microcrystalline products, including (a) preparation of materials directly by solid-state chemical reactions, (b) preparation of materials by desolvation of a solvate material (e.g. dehydration of a crystalline hydrate), (c) preparation of materials by solid-state grinding (mechanochemical) processes, and (d) preparation of materials directly by rapid precipitation from solution (as distinct from slow crystallization procedures). Given the microcrystalline nature of the product phases typically obtained from these processes, structure determination from powder XRD data may represent the only opportunity for elucidating the structural properties of new solid phases obtained by such processes.

#### ***8.3.1 Structure Determination of Materials that Are Difficult to Prepare as Single Crystals Under Conventional Crystallization Conditions***

##### **8.3.1.1 Oligopeptides**

Knowledge of the conformational properties and interactions in model peptide systems can yield important insights concerning the structural properties of polypeptide

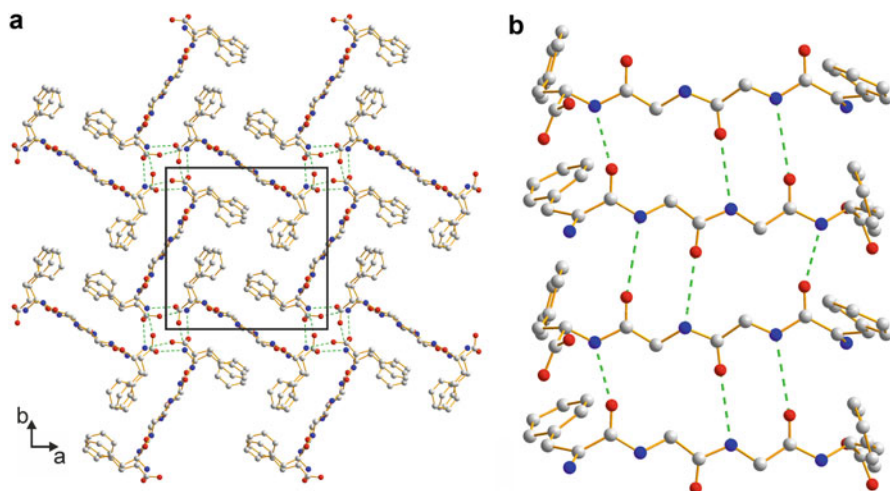
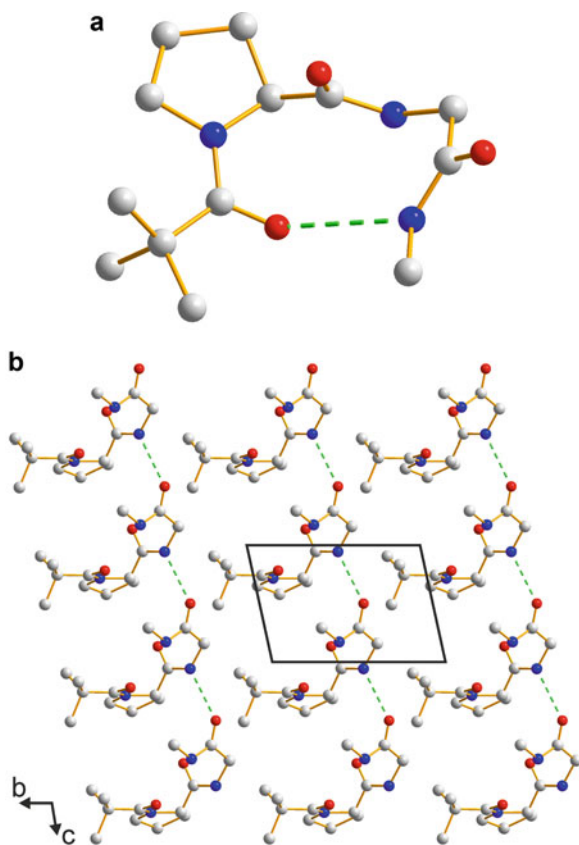


**Fig. 8.5** (a) Crystal structure of Phe-Gly-Gly-Phe viewed along the *c*-axis. (b) Interactions between adjacent molecules in the crystal structure of Phe-Gly-Gly-Phe (viewed perpendicular to the *c*-axis) illustrating the formation of an antiparallel  $\beta$ -sheet arrangement. Hydrogen atoms are omitted for clarity

sequences in proteins. However, in many cases, peptide crystallization does not readily yield single crystals of suitable size and quality for structure determination using single-crystal XRD, and in such cases, there is considerable potential to exploit powder XRD methodologies. Indeed, the crystal structures of several oligopeptides have been determined from powder XRD data using the direct-space strategy for structure solution. The first published example was Phe-Gly-Gly-Phe [25]. In the structure-solution calculation, which used the genetic algorithm technique, the molecule was defined by 11 variable torsion angles, with the peptide groups constrained to be planar with the O-C-N-H torsion angle fixed at  $180^\circ$ . The crystal structure (space group  $P4_1$ ) comprises hydrogen-bonded ribbons (Fig. 8.5) that run along the *c*-axis; adjacent molecules in these ribbons interact through three N-H $\cdots$ O hydrogen bonds in a manner directly analogous to an antiparallel  $\beta$ -sheet. Intermolecular N-H $\cdots$ O hydrogen bonds involving the end groups of the oligopeptide chains give rise to two intertwined helical chains that run along the  $4_1$  screw axis.

The crystal structures of the peptides Piv-L-Pro-Gly-NHMe [26] and Piv-L-Pro- $\gamma$ -Abu-NHMe [27] have also been determined using the direct-space genetic algorithm technique for structure solution, motivated by interest in the potential for these molecules to form  $\beta$ -turn conformations (structural features that allow polypeptide chain reversals in proteins). In the structure of Piv-L-Pro-Gly-NHMe, a type-II  $\beta$ -turn conformation is found (Fig. 8.6), involving an intramolecular  $4 \rightarrow 1$  hydrogen bond between the C=O group of the Piv residue and the methylamide N-H group. In the crystal structure of Piv-L-Pro- $\gamma$ -Abu-NHMe, a folded confor-

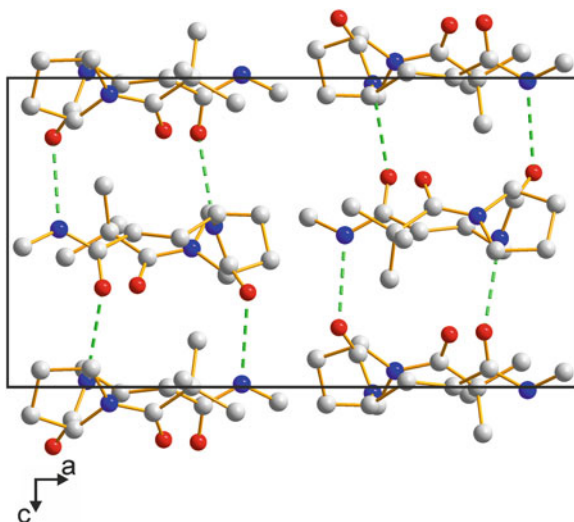
**Fig. 8.6** (a) Molecular geometry of Piv-<sup>L</sup>Pro-Gly-NHMe in the crystal structure with the intramolecular hydrogen bond shown as a *dashed line*. (b) Crystal structure of Piv-<sup>L</sup>Pro-Gly-NHMe viewed along the *a*-axis with N-H···O hydrogen bonds shown as *dashed lines*. Hydrogen atoms are omitted for clarity



mation is also observed (Fig. 8.7), with a short C-H···O interaction between an H atom of the methylene group of  $\gamma$ -Abu and the C=O group of the Piv residue. This C-H···O interaction defines an intramolecular cyclic 10-atom motif, similar to the classical  $\beta$ -turn involving an intramolecular N-H···O=C hydrogen bond (as observed for Piv-<sup>L</sup>Pro-Gly-NHMe).

Another example from the oligopeptide field is the structure determination of the 5-residue peptide acetyl-Tyr-Glu-Gln-Gly-Leu-amide [28]. This pentapeptide motif has a known biological role as a trafficking motif in the C-terminus of mammalian P2X<sub>4</sub> receptors. Comparison of the crystal structure of acetyl-Tyr-Glu-Gln-Gly-Leu-amide (Fig. 8.8), determined directly from powder XRD data, and that of a complex formed with the  $\mu$ 2 subunit of the clathrin adaptor protein complex AP2 reported previously from single-crystal XRD data [29] reveals differences in conformational properties although with similarities in aspects of the hydrogen-bonding arrangement and the hydrophobic environment of the Leu side chain.

**Fig. 8.7** Crystal structure of Piv-<sup>L</sup>Pro- $\gamma$ -Abu-NHMe illustrating the one-dimensional columns of hydrogen-bonded molecules along the *c*-axis. Hydrogen atoms are omitted for clarity



With regard to future applications of powder XRD in structural biology, an ultimate goal is to achieve *ab initio* structure solution of proteins, circumventing the need to grow single crystals of sufficient size for conventional protein crystallography. In this regard, progress has been made in several aspects of the study of proteins by powder XRD [30], including optimization of the conditions for recording high-quality powder XRD data using synchrotron radiation sources. In favourable cases, the data quality has been shown to be adequate for successful indexing and structure refinement (with refinement starting from a known structural model, including the application of “molecular replacement” strategies to define the starting model) [31–36]. Although complete *ab initio* structure solution of a protein structure from powder XRD data has not yet been reported, continued progress in the development of methodology for structure solution from powder XRD data promises to pave the way to achieve this goal in the future.

### 8.3.1.2 An Early-Generation Dendrimeric Material

Dendrimers are large, highly branched molecules composed of a core moiety and radiating functionality. The highly branched architecture can lead to spatially well-defined voids within the dendrimer, which is a crucial feature underlying many of the expanding range of applications of these materials. However, dendrimeric materials are often difficult to grow as single crystals suitable for single-crystal XRD, and in such cases structure determination from powder XRD data may represent the only viable opportunity for structural characterization. The first structure determination of a dendrimeric material directly from powder XRD data [37] was for

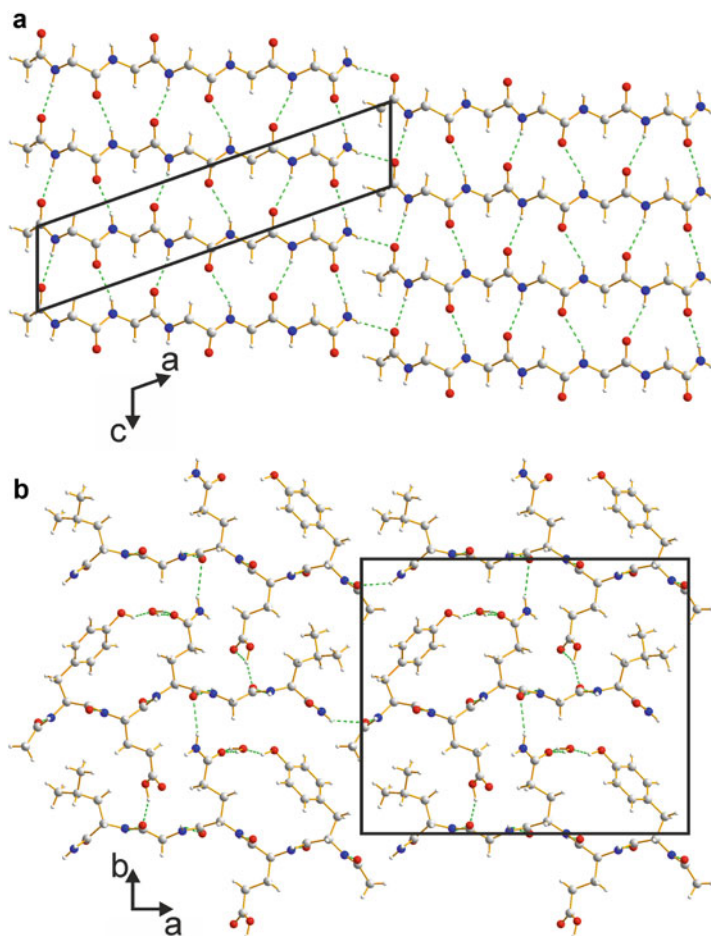


**Fig. 8.8** Crystal structure of acetyl-Tyr-Glu-Gln-Gly-Leu-amide viewed (a) along the *b*-axis (showing only the backbone of the peptide) and (b) along the *c*-axis showing the whole of the peptide and the water molecules present in the crystal structure

the early-generation dendrimer tetrakis[(3,5-dimethoxybenzyloxy)methyl]methane (TDMM), using the direct-space strategy for structure solution. The space group was assigned as *Fdd2* and density considerations, together with results from high-resolution solid-state  $^{13}\text{C}$  NMR, suggested that the asymmetric unit is half the TDMM molecule (the central carbon atom is located on a twofold rotation axis). In the crystallographically independent half-molecule, there are 12 variable torsion angles. Structure solution was carried out using the direct-space genetic algorithm technique followed by Rietveld refinement. In the crystal structure (Fig. 8.9), the two independent branches that radiate from the core differ significantly both in the conformation of the  $\text{C}-\text{CH}_2-\text{O}-\text{CH}_2-\text{Ph}$  chain and in the conformation of the two methoxy substituents on the benzyloxy ring.

**Fig. 8.9** Crystal structure of TDMM viewed along the *c*-axis. Hydrogen atoms are omitted for clarity

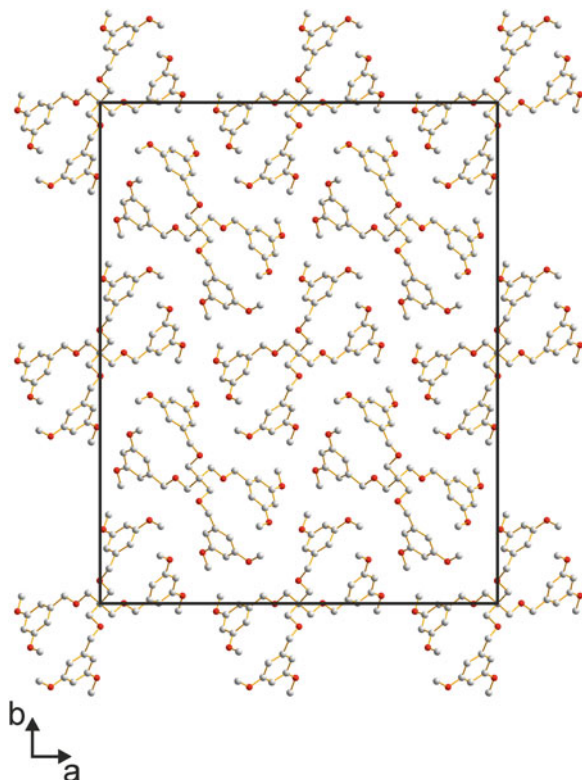
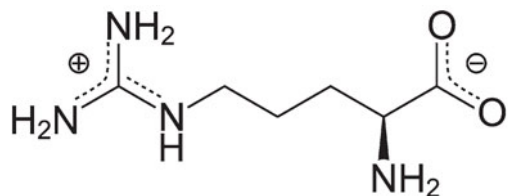


**Fig. 8.10** Molecular structure of L-arginine



### 8.3.1.3 Amino Acids

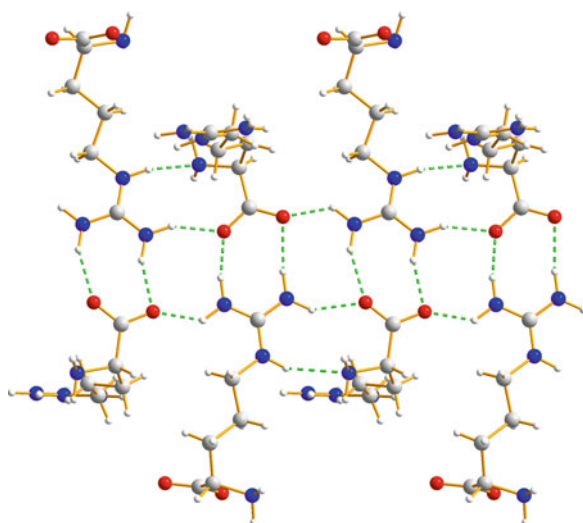
Of the 20 directly encoded proteinogenic amino acids (i.e. those that are encoded directly by the codons of the standard genetic code), L-arginine (Fig. 8.10) was, until recently, one of only very few cases for which the crystal structure of the pure (non-solvate) crystalline form had not been reported. The absence of a reported crystal structure was due to difficulties in obtaining crystals of sufficient size and quality for single-crystal XRD studies. Indeed, attempts to crystallize L-arginine from several different solvents and under a variety of experimental conditions failed to produce any crystals suitable for single-crystal XRD. For this reason, the crystal structure of L-arginine was determined directly from powder XRD data [38], using the direct-

space genetic algorithm technique for structure solution followed by Rietveld refinement. It is important to note that, as L-arginine is susceptible to hydration under an ambient atmosphere, careful experimental protocols must be followed to ensure that the powder XRD data can be recorded for the anhydrous polycrystalline phase.

The crystal structure of L-arginine [38] (space group  $P2_1$ ) has  $Z' = 2$ , fully consistent with results from high-resolution solid-state  $^{13}\text{C}$  NMR spectroscopy. In the direct-space structure-solution calculation, each trial structure was defined by 25 variables. For one molecule, the position along the  $b$ -axis can be fixed arbitrarily for space group  $P2_1$ , so only two positional variables are required, while three positional variables are required for the other molecule. In addition, for each of the two independent molecules, three orientational variables and seven torsion-angle variables are required.

In the final refined crystal structure of L-arginine (Fig. 8.11), the two independent molecules (denoted A and B) have very similar conformations. Along the  $b$ -axis, the molecules are arranged in two distinct “sinusoidal” chains: one chain involves only molecules of type A and the other chain involves only molecules of type B. In each chain, the molecules are arranged in a head-to-tail manner, and adjacent molecules are linked by two  $\text{N-H}\cdots\text{O}$  hydrogen bonds between the guanidinium (tail) group of one molecule and the carboxylate (head) group of the adjacent molecule. Adjacent chains are linked by  $\text{N-H}\cdots\text{O}$  hydrogen bonds between the guanidinium moiety of a molecule in one chain and the carboxylate groups of molecules in the two neighbouring chains, giving rise to a ribbon motif that extends along the  $a$ -axis. The overall crystal structure is described in terms of severely puckered sheets with an average plane parallel to the  $ab$ -plane. The severe puckering arises from the sinusoidal topology of hydrogen-bonded chains that run parallel to the  $b$ -axis. All hydrogen bonding in the structure occurs within these sheets, and stacking of the sheets along the  $c$ -axis involves only van der Waals interactions.

**Fig. 8.11** Crystal structure of L-arginine, viewed perpendicular to the (041) plane, showing the hydrogen-bonded ribbon motif along the  $a$ -axis (horizontal)



### 8.3.1.4 Pharmaceutical Materials

Many drug substances are administered as polycrystalline powders (e.g. as compressed tablets). In such cases, in addition to the intrinsic pharmacological activity of the drug molecule itself, knowledge of the crystal structure is crucial in order to fully understand and optimize the pharmaceutical performance of the drug. Relevant aspects in this regard include understanding and controlling the solubility, bioavailability and the conditions for handling and administration. Importantly, a given drug substance administered in different polymorphic forms may lead to very different results. For all these reasons, knowledge of the crystal structures of pharmaceutical materials is of considerable importance, and in many cases, powder XRD provides the only possible route towards accessing this information. Furthermore, the quest to produce and fully characterize all accessible polymorphs of a given drug substance has become an area of intense activity within the pharmaceuticals industry in recent years (motivated, in part, by patenting, registration and litigation issues), and powder XRD also plays a crucial role in this regard.

An early example of the application of powder XRD in pharmaceutical research concerns structure determination of a new polymorph of fluticasone propionate (FP) [39]. FP is a steroid of pharmaceutical importance as an anti-inflammatory agent which suppresses inflammation of the bronchial passages in the lungs. When formulated as an inhaled product, the anti-inflammatory action of FP treats the underlying inflammatory component of asthma. The FP molecule can exist in two different polymorphic forms. Form 1 is readily obtained by recrystallization from a variety of solvents, and the crystal structure of this polymorph was determined previously from single-crystal XRD. On the other hand, attempts to control the size and shape of the crystals by crystallization in a supercritical fluid medium were found to result in a new polymorph (Form 2). As Form 2 was prepared as a microcrystalline powder, the crystal structure (Fig. 8.12) was determined directly from powder XRD data [39]. There are interesting similarities and contrasts between the crystal structures of Forms 1 and 2 of FP, with both structures containing similar hydrogen-bonded chains, but differing in the structural relationship between adjacent chains.

Another example of pharmaceutical relevance concerns acrinol (2-ethoxy-6,9-diaminoacridine monolactate), which is used extensively as an antibacterial agent. Acrinol forms a monohydrate phase (denoted H) on crystallization from water, but two polymorphs of anhydrous acrinol, denoted form I (AI) and form II (AII), have also been discovered. Polymorph AI is obtained directly on heating phase H, by a solid-state dehydration process, and polymorph AII is obtained subsequently from form AI by a polymorphic transformation. The crystal structures of both forms AI and AII have been determined directly from powder XRD data [40], using the direct-space genetic algorithm technique for structure solution followed by Rietveld refinement. From the structural properties of forms AI and AII, mechanistic aspects of the dehydration process and the polymorphic transformation have been established. On the basis of measured dissolution rates and enthalpies of dissolution, the thermodynamically stable polymorph is assigned as form AII (with a monotropic

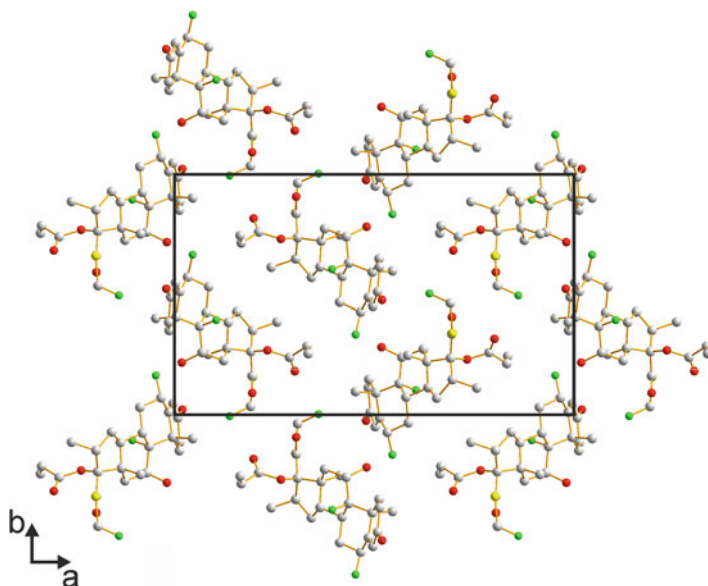


**Fig. 8.12** Crystal structure of form 2 of fluticasone propionate viewed along the  $c$ -axis. Hydrogen atoms are omitted for clarity

relationship between forms AI and AII). Interestingly, the hydration properties of forms AI and AII contrast significantly; form AI is found to hydrate more readily than form AII, with hydration occurring at substantially lower relative humidity.

### 8.3.2 *Structure Determination of New Materials Prepared by Solid-State Mechanochemical Processes*

Many novel solid materials can be prepared only by mechanochemical procedures [41] in which two (or more) solid phases are ground together to generate a new product phase. However, materials prepared by solid-state mechanochemistry are virtually always microcrystalline powders and are not suitable for structure determination by single-crystal XRD. Thus, powder XRD serves a crucial role in the structural characterization of new materials prepared by solid-state mechanochemical procedures.

The first reported [42] application of powder XRD to determine the structure of a molecular co-crystal prepared by solid-state grinding was for the three-component co-crystal material containing racemic *bis*- $\beta$ -naphthol (BN), benzoquinone (BQ) and anthracene (AN). Grinding the pure crystalline phases of BN, BQ and AN together produces a polycrystalline material with reddish purple colour (in contrast, crystallization of the same components from solution gives a different co-crystal

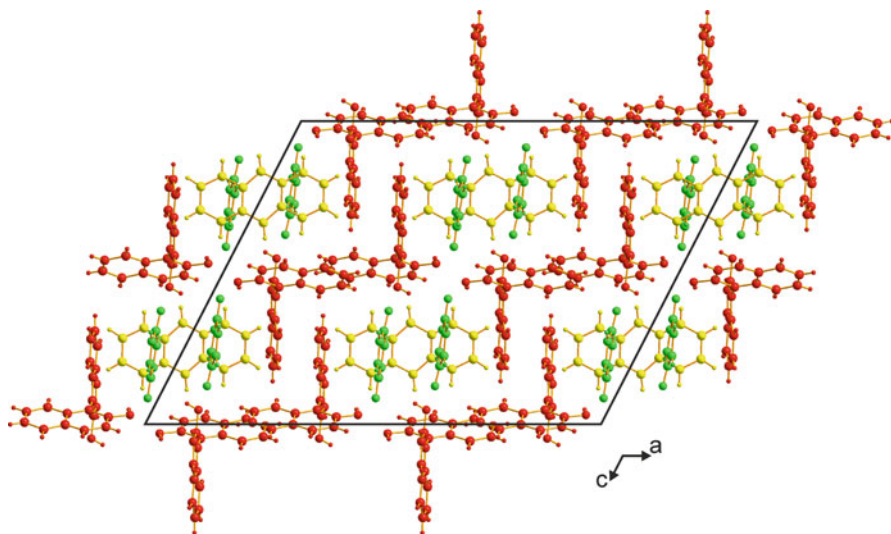


**Fig. 8.13** Crystal structure of the BN/BQ/AN co-crystal material prepared by solid-state grinding viewed along the *b*-axis (BN molecules shown in red; BQ molecules shown in green; AN molecules shown in yellow)

with bluish black colour). The contents of the asymmetric unit in the new co-crystal phase (confirmed by high-resolution solid-state  $^{13}\text{C}$  NMR) comprise one BN molecule, one BQ molecule and one half AN molecule (which is located on a crystallographic twofold rotation axis). The structure was solved using the direct-space genetic algorithm technique, involving a total of 17 structural variables. The crystal structure (Fig. 8.13) is rationalized in terms of three different interaction motifs: edge-to-face interactions between BQ (edge) and AN (face) molecules, face-to-face interactions between BQ and BN molecules, and chains of  $\text{O}-\text{H}\cdots\text{O}$  hydrogen bonds involving BN and BQ molecules.

Another material prepared by solid-state mechanochemistry for which the structure has been determined directly from powder XRD data [43] is a porous interpenetrated mixed-ligand metal-organic-framework material with composition  $\text{Zn}_2(\text{fma})_2(\text{bipy})$  prepared by mechanochemical milling of  $\text{Zn}(\text{OAc})_2 \cdot 2\text{H}_2\text{O}$ , fumaric acid ( $\text{H}_2\text{fma}$ ), and 4,4'-bipyridine (bipy). The crystal structure (Fig. 8.14) determined from powder XRD data has some resemblance to the structure of a DMF solvate  $\text{Zn}_2(\text{fma})_2(\text{bipy})(\text{DMF})_{0.5}$  prepared by solvothermal synthesis, for which the structure was determined by single-crystal XRD [44]. However, there are important structural differences between these materials, including the fact that the bipy ligands in the DMF solvate lie in a crystallographic mirror plane and are therefore strictly planar. In contrast, the dihedral angle between the two rings of the bipy ligand in the mechanochemically prepared material is  $53.2^\circ$ . Interestingly, desolvation of the DMF solvate yields a material identical to that prepared by the mechanochemical synthesis.

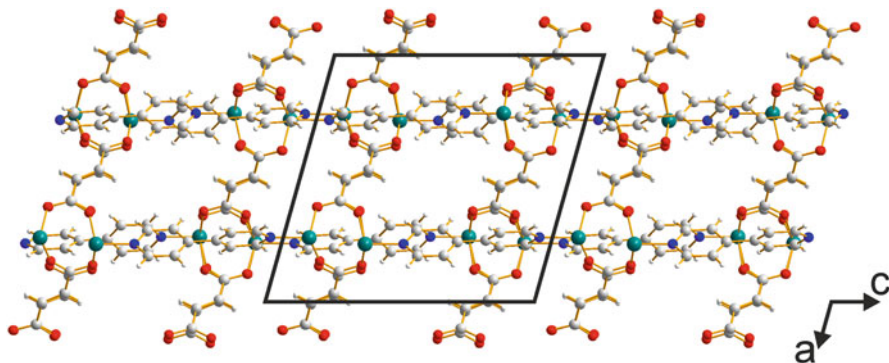


**Fig. 8.14** The crystal structure of  $\text{Zn}_2(\text{fma})_2(\text{bipy})$  viewed along the  $b$ -axis

The crystal structures of several other materials prepared by mechanochemical routes have been determined from powder XRD data, including (1) a metal-organic framework material  $\text{Co}(\text{dibenzoylmethanate})_2(\text{nicotinamide})_2$  obtained by thermal desolvation of the corresponding acetone solvate prepared by liquid-assisted grinding [45]; (2) a hydrate co-crystal of 5-methyl-2-pyridone and trimesic acid, prepared by grinding a methanol solvate co-crystal of the same components under an ambient atmosphere [46]; and (3) the 1:1 co-crystals of theobromine with trifluoroacetic acid and theobromine with malonic acid, each prepared by liquid-assisted grinding [47].

In another example [48], a novel acetic acid solvate of the organic light-emitting diode material  $\text{Alq}_3$  ( $q = 8$ -hydroxyquinolate) was prepared by ball milling a mixture of basic aluminium(III) diacetate  $[\text{Al}(\text{OAc})_2(\text{OH})]$  and 8-hydroxyquinoline. The powder XRD pattern of the resultant microcrystalline powder was different from that of any known solvate or polymorph of  $\text{Alq}_3$ . From the combined results of microanalysis, thermogravimetric analysis and solution-state  $^1\text{H}$  NMR, the material was identified as a 1:1 solvate of  $\text{Alq}_3$  and acetic acid. The crystal structure was solved from powder XRD data using the direct-space genetic algorithm technique, followed by Rietveld refinement, giving the structure shown in Fig. 8.15.

Finally, we consider the structure determination of a new chiral anhydrous phase of  $\text{Ru}(\text{bipy})_3(\text{ClO}_4)_2$  ( $\text{bipy} = 2,2'$ -bipyridine) [49]. The new phase is prepared by mechanical grinding followed by annealing of the known chiral hydrate phase of this material (and can also be obtained by solid-state dehydration of the chiral hydrate phase at high temperature). As the new chiral anhydrous phase is obtained as a microcrystalline powder, structure determination of this material exploited the capabilities of modern powder XRD techniques, using the direct-space genetic algorithm technique for structure solution followed by Rietveld refinement. The crystal structure of the chiral anhydrous phase is found to share several features in common with the chiral hydrate phase concerning the spatial arrangements of the  $\text{Ru}(\text{bipy})_3^{2+}$  cations and  $\text{ClO}_4^-$  anions, with only relatively small differences in the relative positions and orientations of these components in the two structures. As a consequence, interconversion between the hydrate and anhydrous phases by means

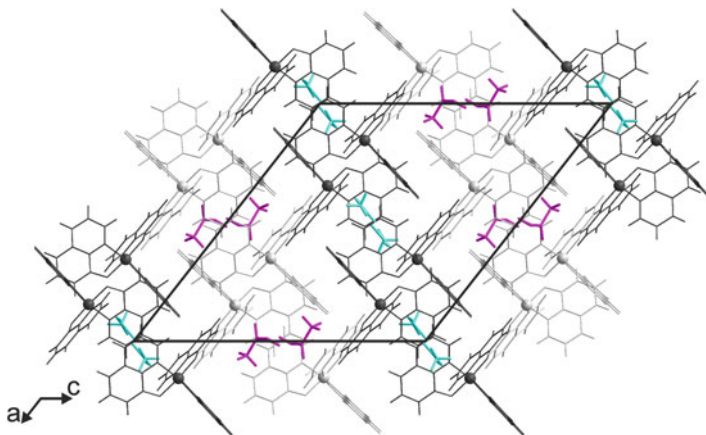


**Fig. 8.15** The crystal structure of the mechanochemically synthesized acetic acid solvate of Alq<sub>3</sub>, determined directly from powder XRD data, containing two independent molecules of Alq<sub>3</sub> and two independent molecules of acetic acid (viewed along the *b*-axis)

of hydration and dehydration processes requires comparatively little reorganization of the crystal structure. Indeed, it is observed (and confirmed by powder XRD analysis) that the chiral anhydrous phase undergoes a facile transformation to the chiral hydrate phase under an ambient atmosphere. We note that this work [49] exploited instrumentation that allows the *simultaneous* measurement of powder XRD data and differential scanning calorimetry (DSC) data, leading to a detailed understanding of the process of dehydration of the chiral hydrate phase.

### 8.3.3 Structure Determination of Materials Prepared by Solid-State Dehydration/Desolvation Processes

For many organic compounds, preparation of a “pure” (non-solvate) crystalline phase by crystal growth from solution is difficult due to the facile formation of solvate crystals. In such cases, a viable route to obtain the “pure” phase is to desolvate the solvate phase at elevated temperature and/or reduced pressure. However, desolvation processes of this type are often associated with loss of crystal integrity, such that single crystals of the solvate phase yield a microcrystalline powder following desolvation. Clearly, in such cases, powder XRD is essential for structure determination of the “pure” desolvated product phase.

As an example, benzene-1,2,3-tricarboxylic acid (BTCA) has a strong tendency to form solvate structures upon crystallization from solution, such as the dihydrate BTCA(H<sub>2</sub>O)<sub>2</sub>. The “pure” (non-solvate) phase of BTCA is obtained by dehydration of the dihydrate at elevated temperature, but as a microcrystalline powder. The crystal structure of the “pure” phase of BTCA was solved directly from powder XRD data [50] using the direct-space genetic algorithm technique for structure solution,

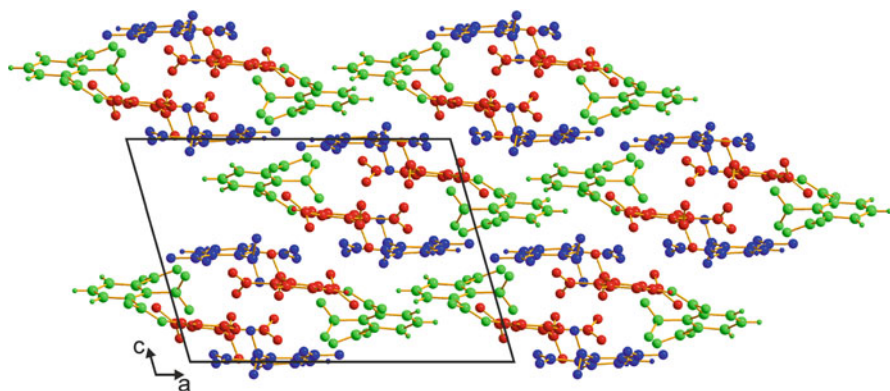


**Fig. 8.16** The crystal structure of BTCA viewed along the  $b$ -axis (the three independent molecules are shown in *red, green and blue*)

followed by Rietveld refinement. There are three independent BTCA molecules in the asymmetric unit, and trial structures in the direct-space structure-solution calculation were defined by a total of 27 structural variables. In the crystal structure (Fig. 8.16), all carboxylic acid groups are engaged in intermolecular hydrogen bonding to other carboxylic acid groups *via* the double  $\text{O}-\text{H}\cdots\text{O}$  hydrogen-bonded motif characteristic of carboxylic acid “dimers”. The structure of the “pure” phase of BTCA differs substantially from that of BTCA dihydrate. Given the substantial structural reorganization associated with the transformation from the dihydrate to the “pure” phase, it is not surprising that large high-quality single crystals of the dihydrate transform into a polycrystalline product phase in the solid-state dehydration process.

Another material with a strong propensity to form solvate structures in crystallization experiments is trithiocyanuric acid (TTCA), and the “pure” (non-solvate) crystalline phase is obtained by desolvation of a solvate phase. In this case, the structure of “pure” TTCA was again determined directly from powder XRD data [51] and presents interesting contrasts in comparison with the crystal structure of the oxygen analogue cyanuric acid.

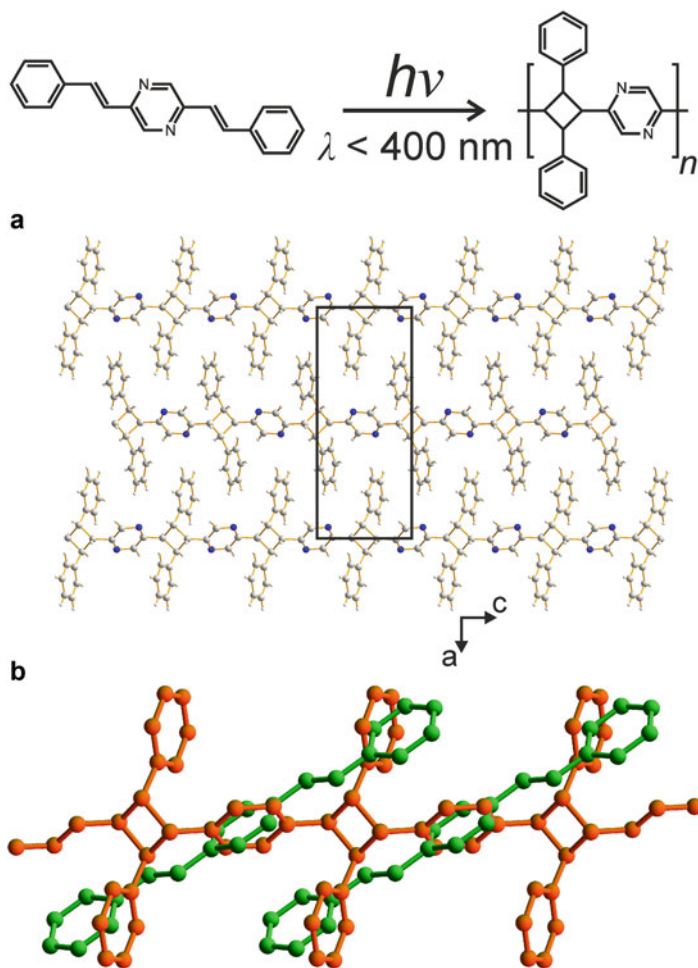
Another example concerns dehydration of the crystalline hydrate of chloroquine bis-(dihydrogen phosphate) [denoted  $\text{CQ}(\text{DHP})_2$ ] to form anhydrous  $\text{CQ}(\text{DHP})_2$  as a microcrystalline powder. The structure of the anhydrous phase was determined directly from powder XRD data [52]. The crystal structure displays several contrasting features compared to the structure of the parent hydrate phase, particularly with regard to the topology of hydrogen-bonded chains of DHP anions. In the hydrate phase, these chains are linear, whereas the chains in the anhydrous phase have a zigzag topology as a result of changes in the mode of hydrogen bonding of the DHP anions within the chain. Given the substantial structural reorganization that occurs on dehydration, it is not surprising that the anhydrous phase is formed as a microcrystalline powder.

### 8.3.4 Structure Determination of Products from Solid-State Reactions

Many crystalline solids undergo chemical transformations induced by incident radiation, heat or other stimuli. In order to understand mechanistic aspects of such solid-state reactions, it is essential to know the structural properties of the product phase obtained *directly* from the reaction, allowing the structural relationships between the product and reactant phases to be elucidated. In many cases, the product phase produced directly from the solid-state reaction is a microcrystalline powder, which does not contain single crystals suitable for single-crystal XRD. In such cases, structure determination from powder XRD data provides the only opportunity to establish the structural properties of the product phase.

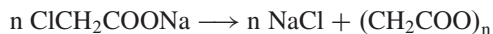
As an example, photopolymerization of 2,5-distyrylpyrazine (DSP) occurs *via* intermolecular [2 + 2] photocyclization reactions at each end of the monomer molecule (Fig. 8.17). This reaction was studied extensively in the 1970s [53, 54] and is regarded as a classic solid-state reaction, but structure determination of the polymeric product phase was only carried out recently [55], exploiting the opportunities afforded by modern techniques for structure determination from powder XRD data. In the crystal structure (Fig. 8.17a), polymer chains are aligned along the *c*-axis, and the distance (3.71 Å) between the centres of adjacent cyclobutane and pyrazine rings is half the *c*-axis repeat of the unit cell. An overlay of the monomer and polymer structures (Fig. 8.17b) demonstrates that the solid-state reaction is associated with only very small atomic displacements at the site of the [2 + 2] photocyclization reaction (displacement of the carbon atoms of the C = C double bonds of monomer molecules on forming the cyclobutane ring of the polymer is only *ca.* 0.8 Å for one pair of carbon atoms and *ca.* 1.6 Å for the other pair). Small atomic movements of this type are consistent with the assignment of the reaction as a topochemical transformation [56–59].

Recently, a solid-state chemical transformation has been exploited [60] to generate the previously unknown tetrahalide dianion  $[\text{I}_2\text{Br}_2]^{2-}$ . The procedure involved the initial formation of the material  $\text{HMET}^{2+} \cdot 2\text{Br}^- \cdot 2\text{I}_2$ , where  $\text{HMET}^{2+}$  denotes the 1,6-bis(trimethylammonium)hexane cation  $(\text{CH}_3)_3\text{N}^+(\text{CH}_2)_6\text{N}^+(\text{CH}_3)_3$ . This material contains pairs of adjacent  $[\text{I}_2\text{Br}]^-$  anions located within a cavity in a framework formed by the  $\text{HMET}^{2+}$  cations. Heating the material to sufficiently high temperature leads to the loss of  $\text{I}_2$  and formation of  $\text{HMET}^{2+} \cdot [\text{I}_2\text{Br}_2]^{2-}$ , containing  $[\text{I}_2\text{Br}_2]^{2-}$  anions trapped within the  $\text{HMET}^{2+}$  framework. As the product phase  $\text{HMET}^{2+} \cdot [\text{I}_2\text{Br}_2]^{2-}$  was obtained as a microcrystalline powder, crystal structure determination was carried out directly from powder XRD data, leading to the first direct structural evidence of a discrete  $[\text{I}_2\text{Br}_2]^{2-}$  dianion (Fig. 8.18). A similar procedure, starting from the material  $\text{HMET}^{2+} \cdot 2\text{Cl}^- \cdot 2\text{I}_2$ , yielded  $\text{HMET}^{2+} \cdot [\text{I}_2\text{Cl}_2]^{2-}$  as the product, again obtained as a microcrystalline powder. Structure determination from powder XRD data revealed the presence of  $[\text{I}_2\text{Cl}_2]^{2-}$  in the product phase, representing only the second report of this tetrahalide dianion.



**Fig. 8.17** The solid-state photopolymerization reaction of DSP (shown at top). (a) Crystal structure of the polymeric product phase obtained directly from the solid-state photopolymerization reaction of DSP, viewed along the  $b$ -axis (for clarity, only half the unit cell is shown along the direction of view), and (b) overlay of the monomer (green) and polymer (orange) in their crystal structures

Rationalization of chemical reactivity of solids also relies heavily on knowledge of the structural properties of the reactant phase, and therefore crystal structure determination of reactive materials is also crucial for understanding solid-state reactions. Solid sodium chloroacetate has been known [61, 62] since the 1850s to undergo a polymerization reaction at elevated temperature to produce polyglycolide and sodium chloride:



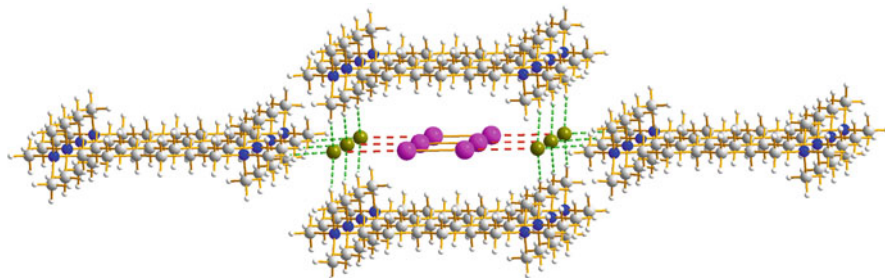
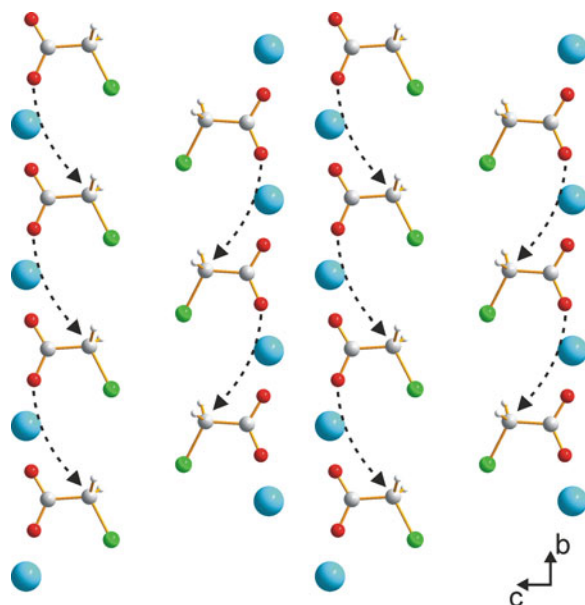


**Fig. 8.18** The crystal structure of  $\text{HMET}^{2+} \cdot [\text{I}_2\text{Br}_2]^{2-}$  showing a column of  $[\text{I}_2\text{Br}_2]^{2-}$  dianions located within the framework of  $\text{HMET}^{2+}$  cations

**Fig. 8.19** Crystal structure of sodium chloroacetate determined directly from powder XRD data (viewed along the  $a$ -axis). Within the linear arrays of chloroacetate anions (which run vertically in the figure), the *arrows* indicate the direction of attack of each anion on its neighbour, leading to the formation of polyglycolide (and sodium chloride) as the reaction product



However, sodium chloroacetate is a microcrystalline material and is unsuitable for investigation by single-crystal XRD. However, in the absence of knowledge of the crystal structure, it is not possible to gain insights on mechanistic aspects of the polymerization reaction. Fortunately, the direct-space strategy for structure solution from powder XRD data allowed the crystal structure of sodium chloroacetate to be determined [63]. The crystal structure (Fig. 8.19) contains rows of chloroacetate anions within which one of the two oxygen atoms of the carboxylate group is ideally positioned to attack the  $\alpha$ -carbon atom of a neighbouring chloroacetate anion, expelling a  $\text{Cl}^-$  anion. Propagation of this intermolecular attack along the row of chloroacetate anions in the crystal structure results in polymerization to

produce polyglycolide. Thus, from knowledge of the crystal structure of sodium chloroacetate, the formation of polyglycolide is rationalized directly in terms of a topochemical reaction pathway.

### 8.3.5 *Structure Determination of Materials Produced by Rapid Precipitation from Solution*

According to conventional wisdom, carrying out crystallization processes from solution in a manner that is as slow as realistically possible is conducive to the formation of large, high-quality crystals. The aim is to ensure that changes in the degree of (super)saturation of the solution during the crystallization process occur as slowly as possible. Typical procedures, for example, involve slow cooling of a solution starting from a high temperature at which the solution is slightly undersaturated, or slow evaporation of solvent from a solution that is initially undersaturated. For some systems, however, the identity (e.g. the polymorphic form) of the resulting solid phase may depend on the rate of the crystallization process, and some solid phases can be obtained only by procedures that involve rapid precipitation. In general, rapid precipitation leads to microcrystalline products that do not contain crystals of suitable size or quality for single-crystal XRD. In such circumstances, structure determination from powder XRD data is essential.

The reaction of  $[\text{Co}(\text{H}_2\text{O})_2\{(\text{OH})_2\text{Co}(\text{en})_2\}_2](\text{SO}_4)_2$  with  $\text{NH}_4\text{Br}$  to give the chiral complex  $\text{cis}-[\text{CoBr}(\text{NH}_3)(\text{en})_2]\text{Br}_2$  has been studied widely in relation to phenomena such as chiral symmetry breaking, spontaneous resolution and chiral amplification. This reaction is historically important as  $\text{cis}-[\text{CoBr}(\text{NH}_3)(\text{en})_2]\text{Br}_2$  was one of the first octahedral metal complexes to be resolved into  $\Delta$  and  $\Lambda$  stereoisomers, some years after Werner predicted that octahedral ions  $\text{M}(\text{en})_2\text{XY}$  should exist as enantiomeric pairs. As the reaction product  $\text{cis}-[\text{CoBr}(\text{NH}_3)(\text{en})_2]\text{Br}_2$  precipitates rapidly from the reaction solution, it is obtained as a microcrystalline powder. From powder XRD studies, the product obtained directly from the reaction was confirmed to be a new solid phase of  $\text{cis}-[\text{CoBr}(\text{NH}_3)(\text{en})_2]\text{Br}_2$ . Structure determination was carried out [64] directly from powder XRD data using the direct-space genetic algorithm technique for structure solution followed by Rietveld refinement. In the crystal structure (Fig. 8.20), the  $\text{cis}-[\text{CoBr}(\text{NH}_3)(\text{en})_2]^{2+}$  complexes are arranged in two different types of chain, propagating along the  $a$ -axis and  $b$ -axis, respectively, with neighbouring complexes in each type of chain linked by  $\text{N}-\text{H}\cdots\text{Br}\cdots\text{H}-\text{N}$  interactions. Along the  $a$ -axis, neighbouring repeat units are related by translation, and the chain is relatively straight; along the  $b$ -axis, neighbouring repeat units are related by the  $2_1$  screw axis and the chain is helical. Importantly, the material has a racemic crystal structure (non-chiral space group  $\text{P}2_1/n$  with one formula unit in the asymmetric unit). Studies of the reaction under a wide range of experimental conditions consistently produced this new racemic phase of  $\text{cis}-[\text{CoBr}(\text{NH}_3)(\text{en})_2]\text{Br}_2$  and

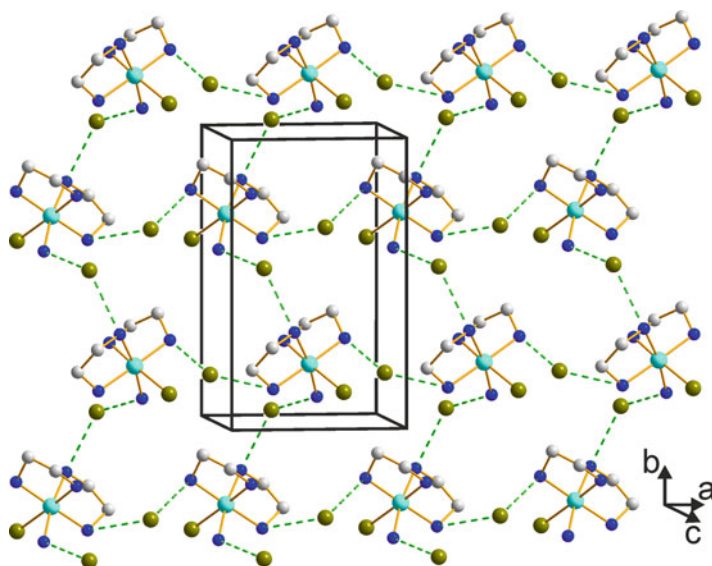


**Fig. 8.20** The crystal structure of *cis*-[CoBr(NH<sub>3</sub>)(en)<sub>2</sub>]Br<sub>2</sub> viewed nearly along the *c*-axis, showing the straight and helical chains that run along the *a*-axis and *b*-axis respectively. Hydrogen atoms are omitted for clarity

conglomerate phases were never obtained. The implications of this result in relation to previous reports of spontaneous induction of chirality in this system are discussed elsewhere [64].

## 8.4 Concluding Remarks

In concluding, it is relevant to reflect on the quality of the structural information that can be obtained from structure determination by powder XRD *versus* single-crystal XRD. In general, the final structural parameters obtained from powder XRD data are not as accurate or precise as those that could be determined for the same material from single-crystal XRD (if single crystals were available). Nevertheless, a properly refined crystal structure from powder XRD data provides reliable information on the arrangement of atoms and molecules in the structure and allows an understanding of most aspects of the structure that are of interest to chemists and materials scientists, such as details of the molecular packing arrangement and identification of the intermolecular interactions.

As illustrated by the examples presented in this chapter, the opportunity to carry out complete crystal structure determination of organic materials *directly* from powder XRD data is now a very real prospect, which unfortunately remains underexploited within the chemical and materials science communities. While

significant advances have been made since the early 1990s in the development and application of new techniques in this field, there is nevertheless considerable scope for the further development of new techniques and strategies to facilitate the routine determination of crystal structures that are more complex and more challenging than those that represent the current state of the art. Extrapolating from the progress achieved during the last 20 years, the field of structure determination from powder XRD data has a very promising outlook, and we predict that the future will yield considerable new structural information on a wide range of important materials that are not amenable to investigation by single-crystal XRD techniques.

## References

1. J.P. Glusker, K.N. Trueblood, *Crystal Structure Analysis – A Primer* (Oxford University Press, Oxford, 1985)
2. J.D. Dunitz, *X-ray Analysis and the Structures of Organic Molecules* (Verlag Helvetica Chimica Acta, Basel, 1995)
3. G.M. Sheldrick, *Acta Crystallogr. Sect. A* **64**, 112–122 (2008)
4. K.D.M. Harris, P.A. Williams, in *Structure from Diffraction Methods*, ed. by D.W. Bruce, D. O'Hare, R.I. Walton (Wiley, Chichester, 2014), pp. 1–81
5. K.D.M. Harris, M. Tremayne, *Chem. Mater.* **8**, 2554–2570 (1996)
6. D.M. Poojary, A. Clearfield, *Acc. Chem. Res.* **30**, 414–422 (1997)
7. A. Meden, *Croat. Chem. Acta* **71**, 615–633 (1998)
8. K.D.M. Harris, M. Tremayne, B.M. Kariuki, *Angew. Chem. Int. Ed.* **40**, 1626–1651 (2001)
9. V.V. Chernyshev, *Russ. Chem. Bull.* **50**, 2273–2292 (2001)
10. W.I.F. David, K. Shankland, L.B. McCusker, C. Baerlocher (eds.), *Structure Determination from Powder Diffraction Data* (IUCr/OUP, Oxford, 2002)
11. K.D.M. Harris, *Cryst. Growth Des.* **3**, 887–895 (2003)
12. K.D.M. Harris, E.Y. Cheung, *Chem. Soc. Rev.* **33**, 526–538 (2004)
13. M. Tremayne, *Philos. Trans. R. Soc. Lond. Ser. A* **362**, 2691–2707 (2004)
14. A. Altomare, R. Caliandro, M. Camalli, C. Cuocci, C. Giacovazzo, A.G.G. Moliterni, R. Rizzi, R. Spagna, J. Gonzalez-Platas, *Z. Kristallogr.* **219**, 833–837 (2004)
15. R. Černý, *Croat. Chem. Acta* **79**, 319–326 (2006)
16. H. Tsue, M. Horiguchi, R. Tamura, K. Fujii, H. Uekusa, *J. Synth. Org. Chem. Jpn.* **65**, 1203–1212 (2007)
17. W.I.F. David, K. Shankland, *Acta Crystallogr. Sect. A* **64**, 52–64 (2008)
18. K.D.M. Harris, *Mater. Manuf. Process.* **24**, 293–302 (2009)
19. K.D.M. Harris, *Top. Curr. Chem.* **315**, 133–177 (2012)
20. H.M. Rietveld, *J. Appl. Crystallogr.* **2**, 65–71 (1969)
21. R.A. Young (ed.), *The Rietveld Method* (International Union of Crystallography, Oxford, 1993)
22. L.B. McCusker, R.B. Von Dreele, D.E. Cox, D. Louër, P. Scardi, *J. Appl. Crystallogr.* **32**, 36–50 (1999)
23. K.D.M. Harris, M. Tremayne, P. Lightfoot, P.G. Bruce, *J. Am. Chem. Soc.* **116**, 3543–3547 (1994)
24. Z. Zhou, V. Sieglér, E.Y. Cheung, S. Habershon, K.D.M. Harris, R.L. Johnston, *ChemPhysChem* **8**, 650–653 (2007)
25. E. Tedesco, G.W. Turner, K.D.M. Harris, R.L. Johnston, B.M. Kariuki, *Angew. Chem. Int. Ed.* **39**, 4488–4491 (2000)

26. E. Tedesco, K.D.M. Harris, R.L. Johnston, G.W. Turner, K.M.P. Raja, P. Balaram, *Chem. Commun.* 1460–1461 (2001)
27. E.Y. Cheung, E.E. McCabe, K.D.M. Harris, R.L. Johnston, E. Tedesco, K.M.P. Raja, P. Balaram, *Angew. Chem. Int. Ed.* **41**, 494–496 (2002)
28. K. Fujii, M.T. Young, K.D.M. Harris, *J. Struct. Biol.* **174**, 461–467 (2011)
29. S.J. Royle, O.S. Qureshi, L.K. Bobanovic, P.R. Evans, D.J. Owen, R.D. Murrell-Lagnado, *J. Cell Sci.* **118**, 3073–3080 (2005)
30. I. Margiolaki, J.P. Wright, *Acta Crystallogr. Sect. A* **64**, 169–180 (2008)
31. R.B. Von Dreele, *J. Appl. Crystallogr.* **32**, 1084–1089 (1999)
32. R.B. Von Dreele, *Acta Crystallogr. Sect. D* **57**, 1836–1842 (2001)
33. S. Basso, A.N. Fitch, G.C. Fox, I. Margiolaki, J.P. Wright, *Acta Crystallogr. Sect. D* **61**, 1612–1625 (2005)
34. I. Margiolaki, J.P. Wright, A.N. Fitch, G.C. Fox, R.B. von Dreele, *Acta Crystallogr. Sect. D* **61**, 423–432 (2005)
35. R.B. Von Dreele, P.L. Lee, Y. Zhang, *Z. Kristallogr. Supp.* **23**, 3–8 (2006)
36. I. Margiolaki, J.P. Wright, M. Wilmanns, A.N. Fitch, N. Pinotsis, *J. Am. Chem. Soc.* **129**, 11865–11871 (2007)
37. Z. Pan, E.Y. Cheung, K.D.M. Harris, E.C. Constable, C.E. Housecroft, *Cryst. Growth Des.* **4**, 451–455 (2004)
38. E. Courvoisier, P.A. Williams, G.K. Lim, C.E. Hughes, K.D.M. Harris, *Chem. Commun.* **48**, 2761–2763 (2012)
39. B.M. Kariuki, K. Psallidas, K.D.M. Harris, R.L. Johnston, R.W. Lancaster, S.E. Staniforth, S.M. Cooper, *Chem. Commun.* 1677–1678 (1999)
40. K. Fujii, H. Uekusa, N. Itoda, G. Hasegawa, E. Yonemochi, K. Terada, Z. Pan, K.D.M. Harris, *J. Phys. Chem. C* **114**, 580–586 (2010)
41. S.L. James, C.J. Adams, C. Bolm, D. Braga, P. Collier, T. Frišćić, F. Grepioni, K.D.M. Harris, G. Hyett, W. Jones, A. Krebs, J. Mack, L. Maini, A.G. Orpen, I.P. Parkin, W.C. Shearouse, J.W. Steed, D.C. Waddell, *Chem. Soc. Rev.* **41**, 413–447 (2012)
42. E.Y. Cheung, S.J. Kitchin, K.D.M. Harris, Y. Imai, N. Tajima, R. Kuroda, *J. Am. Chem. Soc.* **125**, 14658–14659 (2003)
43. K. Fujii, A.L. Garay, J. Hill, E. Sbircea, Z. Pan, M. Xu, D.C. Apperley, S.L. James, K.D.M. Harris, *Chem. Commun.* **46**, 7572–7574 (2010)
44. B.Q. Ma, K.L. Mulfort, J.T. Hupp, *Inorg. Chem.* **44**, 4912–4914 (2005)
45. T. Frišćić, E. Meštrović, D.Š. Šamec, B. Kaitner, L. Fábíán, *Chem. Eur. J.* **15**, 12644–12652 (2009)
46. K. Fujii, Y. Ashida, H. Uekusa, S. Hirano, S. Toyota, F. Toda, Z. Pan, K.D.M. Harris, *Cryst. Growth Des.* **9**, 1201–1207 (2009)
47. S. Karki, L. Fábíán, T. Frišćić, W. Jones, *Org. Lett.* **9**, 3133–3136 (2007)
48. X.H. Ma, G.K. Lim, K.D.M. Harris, D.C. Apperley, P.N. Horton, M.B. Hursthouse, S.L. James, *Cryst. Growth Des.* **12**, 5869–5872 (2012)
49. E.Y. Cheung, K. Fujii, F. Guo, K.D.M. Harris, S. Hasebe, R. Kuroda, *Cryst. Growth Des.* **11**, 3313–3317 (2011)
50. F. Guo, K.D.M. Harris, *J. Am. Chem. Soc.* **127**, 7314–7315 (2005)
51. F. Guo, E.Y. Cheung, K.D.M. Harris, V.R. Pedireddi, *Cryst. Growth Des.* **6**, 846–848 (2006)
52. D. Albesa-Jové, Z. Pan, K.D.M. Harris, H. Uekusa, *Cryst. Growth Des.* **8**, 3641–3645 (2008)
53. H. Nakanishi, N. Nakano, M. Hasegawa, *J. Polym. Sci. B: Polym. Lett.* **8**, 755–760 (1970)
54. Y. Sasada, H. Shimanouchi, H. Nakanishi, M. Hasegawa, *Bull. Chem. Soc. Jpn.* **44**, 1262–1270 (1971)
55. F. Guo, J. Martí-Rujas, Z. Pan, C.E. Hughes, K.D.M. Harris, *J. Phys. Chem. C* **112**, 19793–19796 (2008)
56. G.M.J. Schmidt, *Pure Appl. Chem.* **27**, 647–678 (1971)
57. M.D. Cohen, G.M.J. Schmidt, *J. Chem. Soc.* 1996–2000 (1964)
58. J.M. Thomas, *Philos. Trans. R. Soc. Lond. A* **277**, 251–286 (1974)
59. J.M. Thomas, *Nature* **289**, 633–634 (1981)

60. J. Martí-Rujas, L. Meazza, G.K. Lim, G. Terraneo, T. Pilati, K.D.M. Harris, P. Metrangolo, G. Resnati, *Angew. Chem. Int. Ed.* **52**, 13444–13448 (2013)
61. R. Hoffmann, *Liebigs Ann. Chem.* **102**, 1–20 (1857)
62. A. Kekulé, *Liebigs Ann. Chem.* **105**, 288 (1858)
63. L. Elizabé, B.M. Kariuki, K.D.M. Harris, M. Tremayne, M. Epple, J.M. Thomas, *J. Phys. Chem. B* **101**, 8827–8831 (1997)
64. F. Guo, M. Casadesus, E.Y. Cheung, M.P. Coogan, K.D.M. Harris, *Chem. Commun.* 1854–1856 (2006)

# Chapter 9

## Magnetically Oriented Microcrystal Arrays and Suspensions: Application to Diffraction Methods and Solid-State NMR Spectroscopy

Tsunehisa Kimura

**Abstract** Crystal structure determination is a first and important step in understanding the physical, chemical, and biological functions of crystals in their final use. Single-crystal diffractometry and spectroscopy are the most commonly used and reliable methods for this purpose. However, there are many circumstances where only a microcrystalline powder is formed, which hinders the use of these methods. In this chapter, we describe a novel technique that enables to convert a microcrystalline powder to a large “single” crystal by means of magnetic alignment. The obtained “single” crystal gives rise to diffractions and spectra equivalent to those obtained from a corresponding real single crystal. Basic concepts of the magnetic alignment are described, followed by crystal structure determinations of some organic crystals.

**Keywords** X-ray diffraction • Solid-state NMR • Magnetic orientation • Microcrystalline powder

### 9.1 Introduction

Crystal structure determination is a first and important step in understanding the physical, chemical, and biological functions of crystals in their final use. X-ray diffraction (XRD) is the most commonly used method for this purpose. If a single crystal that is large enough is available, single-crystal XRD may be the best characterization method because it provides the most reliable results [1]. However, there are many circumstances where it takes a long time to produce a large crystal, or only a microcrystalline powder is formed. In such cases, powder diffraction [2] is widely used. However, the results obtained are sometimes less reliable than those from the single-crystal method, so validation of the results is needed.

Most inorganic, organic, biological, metallic, and organometallic materials are diamagnetic; a minority is paramagnetic or ferromagnetic. Diamagnetic materials

---

T. Kimura (✉)  
Graduate School of Agriculture, Kyoto University, Kyoto, Japan  
e-mail: [tkimura@kais.kyoto-u.ac.jp](mailto:tkimura@kais.kyoto-u.ac.jp)

can orient if well-defined magnetic conditions are present, although their response to magnetic fields is generally very weak. The orientation occurs because of the diamagnetic anisotropy that originates mainly from anisotropic electron distribution, such as that in chemical bonds. Therefore, organic materials are rich in magnetic anisotropy. Diamagnetism of organic materials was intensively studied some years ago [3–5]. Crystals, liquid crystals, fibers, and polymers all have potential to undergo magnetic alignment [6–8].

Magnetic orientation in a static magnetic field is simple; the easy magnetization axis of a crystal aligns parallel to the direction of the applied field. In contrast, under a rotating magnetic field, the hard magnetization axis aligns perpendicular to the plane of magnetic rotation. It is known that a combination of these two types of magnetic fields can induce biaxial alignment of the magnetic axes [9, 10]. Because the magnetic axes are embedded in the crystal lattice, the crystal can align accordingly.

In this chapter, we describe the basic concept of the magnetic technique to align crystals. Then, we show its application to the diffraction and spectroscopic analyses of crystals. This magnetic technique is useful when one wants to perform single-crystal analyses but has a powder sample rather than a single crystal.

## 9.2 Magnetic Orientation of Crystals

Magnetic alignment of a crystal subjected to various types of applied magnetic fields is systematically studied in terms of the anisotropic magnetic energy. The parameters concerning the orientation of a crystal are the type of applied magnetic fields (static, rotating, etc.) and the physical properties of the crystal, including its magnetic anisotropy, size, and shape.

### 9.2.1 Magnetic Susceptibility of Diamagnetic Crystals

When a magnetic field is applied to a diamagnetic crystal, a magnetization is induced that is proportional to the intensity of the applied field. The proportionality constant is referred to as magnetic susceptibility. Magnetic susceptibility is a scalar if the crystal is isotropic and a tensor if the crystal is uniaxial or biaxial. The magnetic susceptibility tensor  $\chi$  which is expressed by a  $3 \times 3$  symmetric matrix is characterized by three principal values ( $\chi_1$ ,  $\chi_2$ , and  $\chi_3$ ) and corresponding principal magnetic axes. We define  $\chi_3 \leq \chi_2 \leq \chi_1 < 0$ . The  $\chi_1$  and  $\chi_3$  axes are referred to as easy and hard magnetization axes, respectively.

In isotropic crystals, all three  $\chi$  values are equal and there is no magnetic anisotropy. In uniaxial crystals, two  $\chi$  values are equal ( $\chi_3 = \chi_2 < \chi_1$  or  $\chi_3 < \chi_2 = \chi_1$ ). The  $\chi_1$  or  $\chi_3$  axis corresponds to the four-, six-, or threefold crystallographic axis for the tetragonal, hexagonal, or trigonal system, respectively.

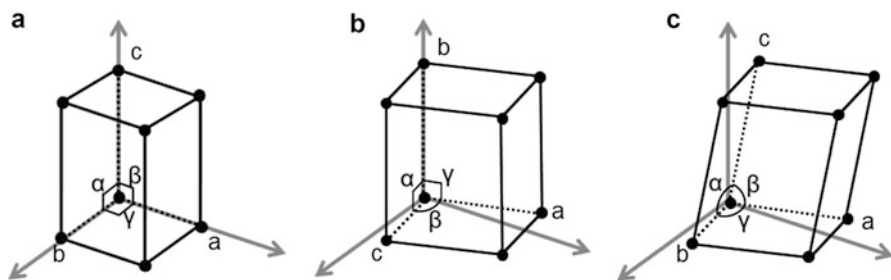


**Fig. 9.1** Relationships between magnetic and crystallographic axes for biaxial crystals: (a) orthorhombic, (b) monoclinic, and (c) triclinic systems. *Arrows* indicate the magnetic axes that are mutually orthogonal

In biaxial crystals, all three  $\chi$  values are different. In the orthorhombic system, the three  $\chi$  axes coincide with the crystallographic  $a$ ,  $b$ , and  $c$  axes. In the monoclinic system, one of the three  $\chi$  values coincides with the twofold (rotation or inversion) axis. In the triclinic system, there is no relation to crystallographic axes. The relation between magnetic and crystallographic axes for biaxial crystals is depicted schematically in Fig. 9.1.

The diamagnetic anisotropy of a molecule originates from the electron distribution of chemical bonds. The magnetic anisotropy of several chemical bonds has been reported [6]. The anisotropy is defined as  $\chi_{\parallel} - \chi_{\perp}$ , where the parallel indicates the bond direction. Double bonds exhibit positive values and thus correspond to the easy magnetization axis. This means that double bonds tend to align parallel to a magnetic field. In contrast, single bonds have negative values, so they tend to align perpendicular to a magnetic field. Anisotropy is especially high for aromatic structures, which is usually attributed to the ring current induced by  $\pi$  electrons. The direction perpendicular to the aromatic ring coincides with the hard magnetization axis. The packing of the molecules in a crystal determines the final magnetic anisotropy of the crystal. Classical and quantum mechanical theories of diamagnetic susceptibility can be found in the literature [4, 5]. Both theories give the same result.

Several terms for magnetic susceptibility are used in the literature, including molar susceptibility  $\chi_m$  ( $\text{cm}^3 \text{mol}^{-1}$ ), gram susceptibility  $\chi_g$  ( $\text{cm}^3 \text{g}^{-1}$ ), and volume susceptibility  $\chi$  (dimensionless). These terms are related by the equations  $\chi_m = \chi V_{\text{mol}}$  and  $\chi_g = \chi / \rho$ , where  $V_{\text{mol}}$  and  $\rho$  are molar volume and density, respectively. In addition, both emu and SI units for electromagnetic properties are used in the literature. A unit in SI is equal to the unit in emu multiplied by  $4\pi$ . When using susceptibility values, it is important to identify which unit is used. Volume susceptibility in SI is used throughout this chapter. In this unit, the magnetic susceptibility of water is  $-9.04 \times 10^{-6}$ .

The magnetic susceptibility values of organic crystals are available in reference [11]. In this reference, molar susceptibility is used. Figure 9.2a presents a plot of  $\chi_{m,2} - \chi_{m,3}$  versus  $\chi_{m,1} - \chi_{m,2}$ . It is difficult to find clear correlations between these

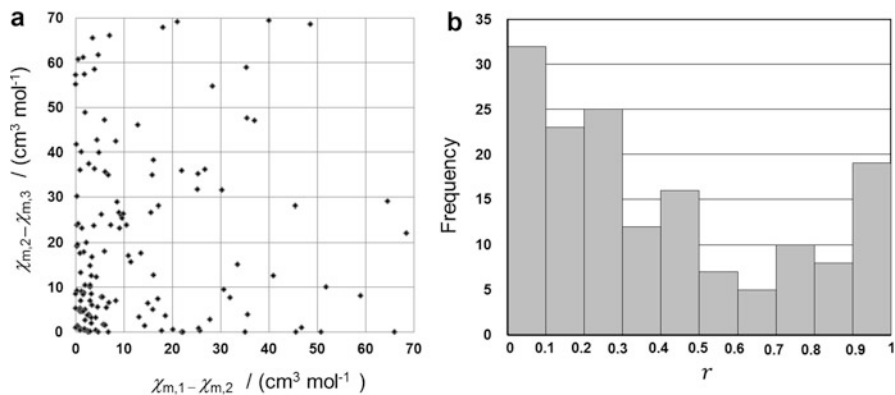


**Fig. 9.2** (a) Relationship between  $\chi_{m,2} - \chi_{m,3}$  and  $\chi_{m,1} - \chi_{m,2}$  for various organic crystals tabulated in reference [11] and (b) histogram for the ratio  $r = (\chi_{m,1} - \chi_{m,2}) / (\chi_{m,1} - \chi_{m,3})$

quantities. Figure 9.2b shows a histogram for the ratio  $r = (\chi_{m,1} - \chi_{m,2}) / (\chi_{m,1} - \chi_{m,3})$ .  $r = 0$  and 1 correspond to uniaxial crystal. There is no peculiar distribution of  $r$ .

## 9.2.2 Anisotropic Magnetic Energy

The anisotropic magnetic energy of a crystal with volume  $V$  [ $\text{m}^3$ ] that is subjected to an external magnetic field is expressed by [10]

$$E = \frac{-V}{2\mu_0} {}^t\mathbf{B} ({}^t\mathbf{A}\boldsymbol{\chi}\mathbf{A}) \mathbf{B}, \quad (9.1)$$

where  $\mu_0 = 4\pi \times 10^{-7}$  [ $\text{Wb}/(\text{A m})$ ] is the magnetic permeability of vacuum,  $\mathbf{B}$  [T] is the magnetic field, and  $\boldsymbol{\chi}$  (dimensionless) is the magnetic susceptibility tensor expressed with respect to the principal axes coordinates: it is diagonal with the components of  $\chi_1$ ,  $\chi_2$ , and  $\chi_3$ . With these units, the energy  $E$  is expressed in the unit of J (joule). The matrix  $\mathbf{A}$  is used to transform  $\boldsymbol{\chi}$  into laboratory coordinates. It can be expressed, for example, by using Eulerian angles [12]. The superscript  $t$  indicates the transpose.

### 9.2.2.1 Under a Static Field

Mathematical expression of Eq. 9.1 is complicated in most cases. However, a simple expression can be obtained for some specific examples: if the magnetic field is static and  $\chi_3 = \chi_2 < \chi_1$ , then the anisotropic magnetic energy  $E_a$  is expressed as [8]

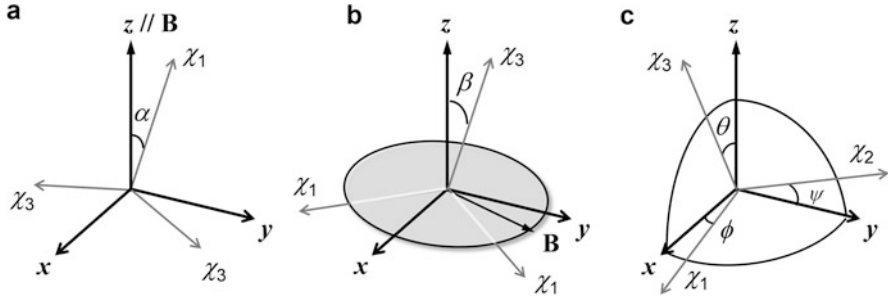


**Fig. 9.3** Magnetic orientations of (a)  $\chi_1$  axis under a static field; (b)  $\chi_3$  axis under a rotating field; and (c)  $\chi_1$ ,  $\chi_2$ , and  $\chi_3$  axes under a modulated rotating field. Angles  $\phi$ ,  $\theta$ , and  $\psi$  are assumed to be small

$$E_a = -\frac{VB^2}{2\mu_0} (\chi_1 - \chi_3) \cos^2\alpha, \tag{9.2}$$

where  $\alpha$  is the angle between the magnetic field and  $\chi_1$  axis. Here, the isotropic term is neglected.  $E_a$  has a minimum at  $\alpha = 0$ ; that is,  $\chi_1 \parallel \mathbf{B}$  (Fig. 9.3a).

### 9.2.2.2 Under a Rotating Field

If a magnetic field that rotates at frequency  $\omega$  is applied, we have three kinetically different regimes depending on the time constant  $\tau$ . This constant is related to the time required to align under a given condition including the field intensity, viscosity of the surrounding medium, and shape of the crystal. When the magnetic rotation is extremely high ( $\omega\tau \gg 1/2$ , which we refer to as the rapid rotation regime (RRR) [13]), a crystal cannot follow the rotation. In such a situation, the magnetic energy shown in Eq. 9.1 can be time averaged over one revolution (this is discussed in detail in Sect. 9.2.4.2).

When a magnetic field  $\mathbf{B} = (B \cos\omega t, B \sin\omega t, 0)$  ( $t$  is time) that is rotating in the  $xy$  plane at frequency  $\omega$  is applied to a crystal with  $\chi_3 < \chi_2 = \chi_1$ , the time-averaged magnetic energy can be expressed as

$$\langle E_a \rangle = -\frac{B^2V}{4\mu_0} (\chi_1 - \chi_3) \cos^2\beta, \tag{9.3}$$

if the conditions for RRR are satisfied. Here,  $\beta$  is the angle between the laboratory  $z$  axis and  $\chi_3$  axis.  $\langle E_a \rangle$  has a minimum at  $\beta = 0$ ; that is,  $\chi_3 \parallel z$  (the direction normal to the rotation plane) (Fig. 9.3b). It should be noted that the curvature around the minimum is half of that for the static case; the constraining effect is smaller in the rotating case.

### 9.2.2.3 Under a Modulated Rotating Field

For three-dimensional (3D) orientation of the magnetic axes, we need to use much more complicated time-dependent magnetic fields [14] such as  $\mathbf{B} = (B_x \cos \omega t, B_y \sin \omega t, 0)$  where  $B_x > B_y$  [10]. With this type of magnetic field and RRR conditions, we obtain [15]

$$\langle E_a \rangle = C_x \psi^2 + C_y \theta^2 + C_z \varphi^2, \quad (9.4)$$

where the coefficients  $C_x$ ,  $C_y$ , and  $C_z$  are the functions of  $B_x$ ,  $B_y$ , volume  $V$ , and three  $\chi$  values ( $C_x \propto \chi_2 - \chi_3$ ,  $C_y \propto \chi_1 - \chi_3$ ,  $C_z \propto \chi_1 - \chi_2$ ). Here, the isotropic and higher terms of the Eulerian angles  $\phi$ ,  $\theta$ , and  $\psi$  are truncated. This energy has a minimum at  $\phi = \theta = \psi = 0$  (Fig. 9.3c), indicating that the  $\chi_1$ ,  $\chi_2$ , and  $\chi_3$  axes are confined in the  $x$ ,  $y$ , and  $z$  directions, respectively, by the harmonic potentials.

## 9.2.3 Thermal Fluctuation

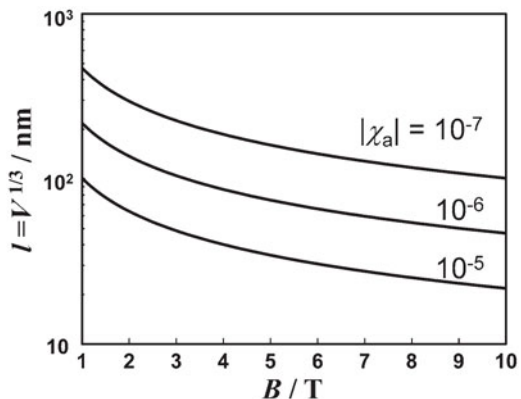
### 9.2.3.1 Size Dependence

Magnetic orientation competes with thermal fluctuation. As a result, magnetic orientation fluctuates because of thermal agitation. The orientation distribution of magnetic axes is described by the Boltzmann factor,  $\exp(-E_a/kT)$ . To observe a significant orientation, it may be required that

$$VB^2 |\chi_a| / (2\mu_0) \gg kT. \quad (9.5)$$

Here, orientation under a static field is assumed, and  $\chi_a = \chi_1 - \chi_3$  is the difference between two  $\chi$  values that may be chosen depending on the orientation of a certain axis. Figure 9.4 shows the volume of a crystal plotted as a function of a magnetic

**Fig. 9.4** Minimum crystal size required for magnetic orientation at  $T = 298$  K plotted as a function of applied magnetic field. Typical values of anisotropic magnetic susceptibility  $\chi_a$  are indicated in the figure (Ref. [8])



field where the left- and right-side quantities are equal. The anisotropic values  $\chi_a$  used here are typical of organic crystals. We find that nanosized crystals can be aligned if a magnetic field as high as 10 T is used.

### 9.2.3.2 Anisotropy of Fluctuations

The mean square fluctuation in the orientation angle is proportional to the inverse of the curvature around the energy minimum. For example, in the case of orientation in a static field (Eq. 9.2), we obtain

$$\langle \alpha^2 \rangle \propto \frac{2\mu_0}{VB^2(\chi_1 - \chi_3)}. \tag{9.6}$$

This fluctuation is related to the half width of XRD spots. In the case of 3D alignment, which is discussed in Sect. 9.2.2.3, the orientation fluctuations are anisotropic because the values of curvatures  $C_x \propto \chi_2 - \chi_3$ ,  $C_y \propto \chi_1 - \chi_3$ , and  $C_z \propto \chi_1 - \chi_2$  are different. Accordingly, the mean square fluctuations,  $\langle \psi^2 \rangle$ ,  $\langle \theta^2 \rangle$ , and  $\langle \phi^2 \rangle$ , are different. Generally,  $C_y$  is the largest term, so  $\langle \theta^2 \rangle$  is the smallest.

It should be noted that the 3D orientation of the magnetic axes does not necessarily indicate the 3D orientation of the crystallographic axes. This can occur for biaxial crystals. For example, let us consider a crystal whose point group is (9.2) (monoclinic system). One of the magnetic axes (say the  $\chi_1$  axis) coincides with the twofold axis (say the  $b$  axis). The other two magnetic axes are located in the  $ac$  plane, but do not coincide with the  $a$  and  $c$  axes. The orientations produced by a  $\pi$  rotation about each magnetic axis have the same magnetic energies, so these orientations are allowed in a magnetically oriented sample. As a result, we have two different orientations, as shown in Fig. 9.5. The number of possible orientations depending on the point group of a crystal is summarized in Table 9.1 [16].

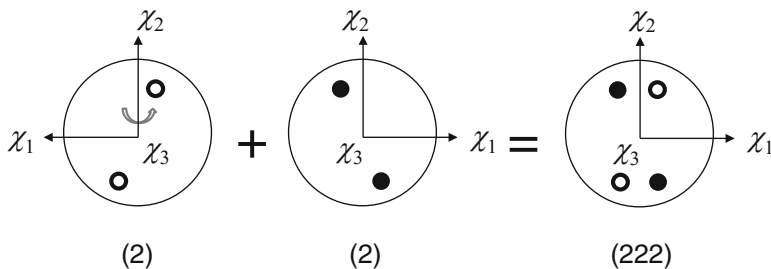


**Fig. 9.5** Twin structure in magnetically oriented crystals with point group (9.2). The probabilities for these two orientations are the same because they have an equal anisotropic magnetic energy

**Table 9.1** Number of possible orientations and the point group exhibited by an assembly of magnetically oriented biaxial crystals

Crystal system	Point group of single crystal	Number of orientations	Point group of PSC
Triclinic	1	4	222
	$\bar{1}$	4	<i>mmm</i>
Monoclinic	2	2	222
	<i>m</i>	4	<i>mmm</i>
	2/ <i>m</i>	2	<i>mmm</i>
Orthorhombic	222	1	222
	<i>mm</i> 2	2	<i>mmm</i>
	<i>mmm</i>	1	<i>mmm</i>

Ref. [16]

### 9.2.4 Orientation Kinetics

Experimentally, magnetic alignment is performed on microcrystals suspended in a liquid medium. Therefore, the viscosity of the medium and shape of the microcrystals are important parameters affecting the orientation kinetics. The equation of motion is expressed by the balance of the magnetic torque  $\mathbf{N}$  and the hydrodynamic torque  $\mathbf{M}$  [17, 18]:

$$\mathbf{N} + \mathbf{M} = 0 \quad (9.7)$$

The inertia term is neglected because it is far smaller than the viscous term. The magnetic torque is obtained by taking a derivative of anisotropic magnetic energy with respect to the angles describing the orientation of a crystal:

$$\mathbf{N} = \mu_0^{-1} V (\chi \mathbf{B}) \times \mathbf{B}. \quad (9.8)$$

Conversely, the hydrodynamic torque is expressed as:

$$\mathbf{M} = -\eta \mathbf{L} \boldsymbol{\Omega} \quad (9.9)$$

where  $\eta$  is the viscosity of the suspending fluid,  $\boldsymbol{\Omega}$  is the rotation vector, and  $\mathbf{L}$  is the hydrodynamic tensor. Inserting  $\mathbf{N}$  and  $\mathbf{M}$  into Eq. 9.7, we obtain a differential equation for the time course of the orientation angles. In the case of a spherical crystal with radius  $a$ , the tensor  $\mathbf{L}$  becomes a scalar expressed as  $8\pi a^3$ . Because both the magnetic torque and hydrodynamic torque are proportional to the volume of the crystal, Eq. 9.7 does not include the volume. As a result, the orientation speed does not depend on the volume.

### 9.2.4.1 Orientation Kinetics of a Rod-Shaped Particle

The orientation kinetics of a magnetically uniaxial rod subjected to a static field is simple. The temporal change in orientation angle  $\theta$  between the rod axis ( $||\chi_1$ ) and the direction of the magnetic field is expressed as [19]:

$$\tan \theta = \tan \theta_0 \exp(-t/\tau). \tag{9.10}$$

Here,  $\theta_0$  is the initial angle and  $\tau$  is the time constant expressed as:

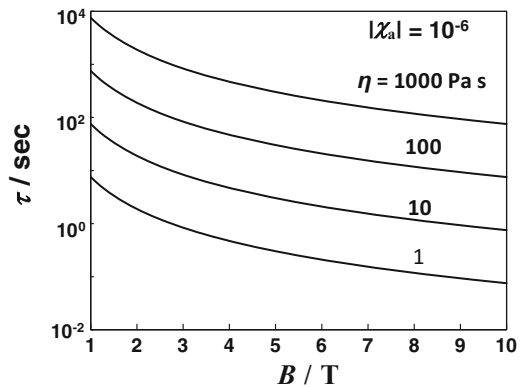
$$\tau^{-1} = F(D)\chi_a B^2(6\mu_0\eta)^{-1}, \tag{9.11}$$

where  $\chi_a = \chi_{||} - \chi_{\perp}$  (rod axis is assumed parallel).  $F(D)$  is a rapidly decreasing function of the aspect ratio  $D$  of the rod (for a sphere  $F(1) = 1$ ), indicating that the higher the aspect ratio, the slower the orientation. Figure 9.6 shows a plot of  $\tau$  as a function of  $B$ .

### 9.2.4.2 Three Regimes of Orientation Kinetics

Crystal orientation under a magnetic field rotating at a frequency  $\omega$  is classified into three regimes [13]. There is an intrinsic time constant  $\tau$ , expressed by Eq. 9.11, associated with orientation of a crystal under a static magnetic field. If the rotation speed is slow enough compared to  $\tau^{-1}$ , the crystal is regarded as being in a static field. Then, the crystal can follow the rotation of the magnetic field in phase. This circumstance is specified by  $\omega\tau < 1/2$  and referred to as the synchronous rotation regime (SRR). With an increase in  $\omega$ , the motion of the crystal becomes out of phase with that of the magnetic field. This occurs at  $\omega\tau > 1/2$  and is referred to as the asynchronous rotation regime (ARR). With further increase in  $\omega$ , the

**Fig. 9.6** Time required for the magnetic orientation of a crystal as a function of the magnetic field, where Eq. 9.11 is used with  $F(D) = 1$  and for various viscosities. Ref. [8]



crystal becomes completely unable to follow the rotation of the magnetic field. This happens at  $\omega\tau \gg 1/2$ , which is the RRR. Under RRR conditions, the magnetic energy of Eq. 9.1 can be time averaged over one revolution to give time-averaged magnetic energies, as shown in Eqs. 9.3 and 9.4.

### 9.3 Single-Crystal XRD Analyses from a Powder

Three-dimensionally oriented microcrystals can produce X-ray and neutron diffractions similar to those obtained from a real large single crystal, which enables single-crystal diffraction analyses of powder samples. Therefore, this magnetic technique can increase the applicability of conventional diffraction methods including single-crystal, fiber, and powder diffraction. Magnetic alignment is useful when only a powder sample is available. It is especially useful for single-crystal neutron measurements because they require a large single crystal of millimeter order. Figure 9.7 illustrates this magnetic alignment technique.

#### 9.3.1 Magnetic Orientation of Microcrystalline Powders

Magnetically oriented microcrystals can be used in two different forms for the purpose of single-crystal diffraction analyses. (1) For polymer composites: the oriented microcrystals in suspension are fixed by consolidation of the suspending fluid by photopolymerization, thermosetting, or gelation. Such composites are called magnetically oriented microcrystal arrays (MOMAs) or pseudo-single crystals. A MOMA (powder content of 10–30 %) can be as large as the centimeter scale. (2) For suspensions: in this case, the suspension of oriented microcrystals is subjected to in situ diffraction measurement. These suspensions are termed magnetically oriented microcrystal suspensions (MOMSs). The orientation can be uniaxial or biaxial depending on the magnetic nature of the crystal and the magnetic field used. We differentiate these two types of magnetic ordering by referring to the type and dimensions, such as 1D MOMA, 3D MOMS, etc.

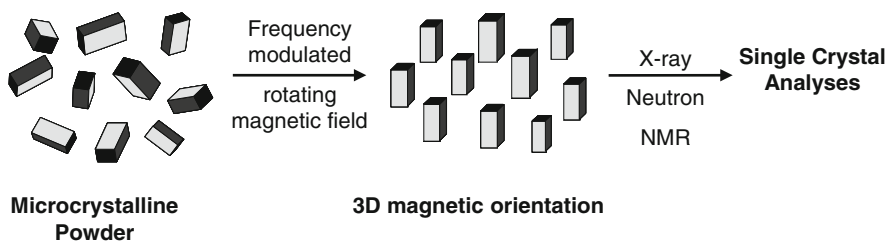


Fig. 9.7 Schematic diagram of the magnetic technique applied to a microcrystalline powder

### 9.3.1.1 Suspending Fluids and Microcrystals

Suspending fluids need to satisfy several requirements. They should be inert to the microcrystals and disperse them perfectly. Aggregation of microcrystals may deteriorate their alignment. In most cases, the aggregates cannot be disintegrated by the magnetic process. In the case of MOMAs, the suspending liquid should be solidified after magnetic orientation. The viscosity of the suspending fluid strongly affects the orientation kinetics. The viscosity is selected so that RRR conditions ( $\omega\tau \gg 1/2$ ) are satisfied. In general, a higher viscosity is needed when the applied magnetic field is strong.

The suspending liquid must not contain heavy atoms such as chlorine to minimize the background diffraction. In the case of MOMAs, the fluid should be solidified after magnetic orientation. Usually, photopolymerizable monomers, thermosetting resins, and sols are used. Solidifying the liquid by cooling may also work. In any case, care should be taken during the solidification process not to deteriorate the achieved orientation. For neutron measurements, use of deuterated liquid is favored to reduce the background diffraction.

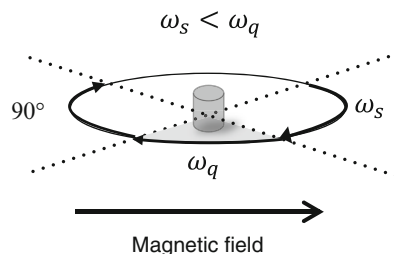
For magnetic orientation, each microcrystal should be a single crystal. Polycrystalline particles do not have sufficient magnetic anisotropy to be aligned to a desired degree. If the magnetic anisotropy and crystal size are known, the required experimental conditions can be predicted theoretically [14, 15]. The magnetic anisotropy of microcrystals can be determined experimentally. Superconducting quantum interference device (SQUID) measurements of 1D MOMAs prepared under static and rotating magnetic fields, in addition to the powder measurements, can provide the values of  $\chi_1$ ,  $\chi_3$ , and  $(\chi_1 + \chi_2 + \chi_3) / 3$ . From these values, the anisotropic magnetic susceptibilities used in magnetic energy (Eq. 9.4) can be calculated, enabling the determination of experimental conditions necessary to prepare 3D MOMAs.

### 9.3.1.2 Magnetic Fields

A MOMA is prepared *ex situ* by using strong magnetic fields (10 T or more) generated by superconducting magnets, so it is suitable for nanosized crystals and crystals with small magnetic anisotropy. Magnets available for MOMS experiments are limited because they should be compact to allow attachment to a conventional diffractometer. We usually use neodymium magnets (ca. 1 T).

Rotating and modulated rotating magnetic fields as defined theoretically in Sects. 9.2.2.2 and 9.2.2.3 are difficult to realize and even impossible in the case of superconducting magnets. Instead, in experiments, the suspension is subjected to a simple rotation or modulated rotation in a static magnetic field, which are considered to represent rotating and modulated rotating magnetic fields, respectively. Hereafter, these two terminologies are used interchangeably. In addition, an amplitude-modulated (AM) field, as described in Sect. 9.2.2.3, cannot be realized by sample

**Fig. 9.8** Schematic diagram of a frequency-modulated rotating magnetic field (Ref. [20])



rotation. Instead, we employ frequency modulation (FM) in which the rotation frequency is switched between  $\omega_s$  and  $\omega_q$  ( $>\omega_s$ ) every  $90^\circ$ s (Fig. 9.8).

### 9.3.2 Single-Crystal X-Ray Diffraction Analyses Using 3D MOMAs

In this section, we demonstrate single-crystal XRD analyses of organic crystals using 3D MOMAs. For demonstration purposes, we used compounds whose crystal structures are known: L-alanine, cellobiose, and 1,3,5-triphenyl benzene (TPB) [20]. We have also reported similar analyses for sucrose [21], lysozyme [22], and  $\text{LiCoPO}_4$  [23], although they are not described here.

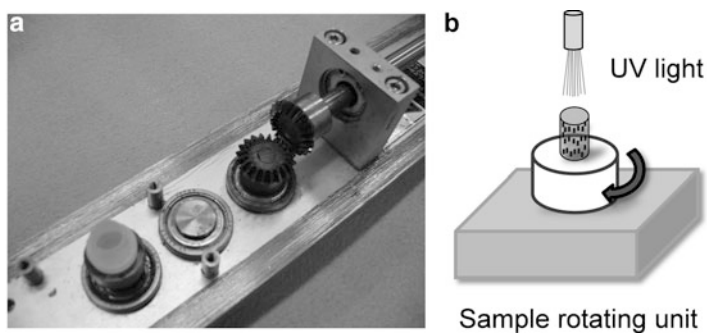
#### 9.3.2.1 Preparation and XRD Measurement of 3D MOMAs

Each as-received crystal sample was pulverized in a mortar and mixed with a UV-curable monomer to prepare a suspension. The concentration of microcrystals, viscosity of the suspending fluid, magnetic field intensity, FM-type rotation frequency ( $\omega_s/\omega_q$ ), and duration of magnetic exposure were 10 wt%, 1.2 Pa s, 5 T, 5/25 rpm, and 2 h, respectively, for L-alanine, 15 wt%, 2.0 Pa s, 2 T, 20/100 rpm, and 5 min, respectively, for TPB, and 12 Pa s, 8 T, 10/80 rpm, and 1 h, respectively, for cellobiose. About 0.1 mL of each suspension was used to prepare a MOMA. Figure 9.9a shows the apparatus for sample rotation working in a superconducting magnet generating a horizontal magnetic field.

UV light was irradiated onto the rotating sample and the magnetic exposure was maintained (Fig. 9.9b). Each MOMA was cut into a cube of less than  $1 \text{ mm}^3$  and subjected to XRD measurements using a conventional diffractometer (Cu  $K\alpha$  radiation).

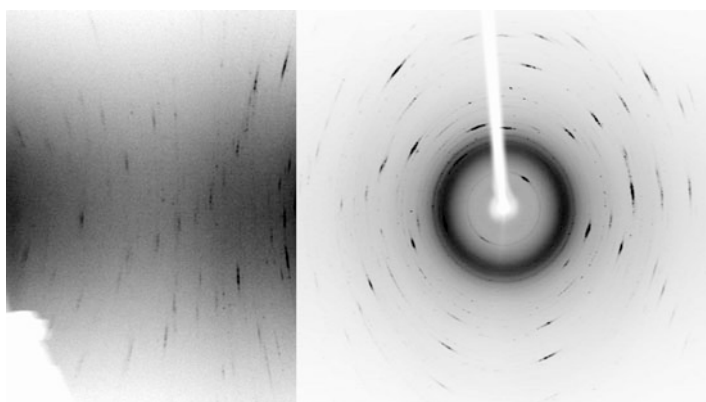
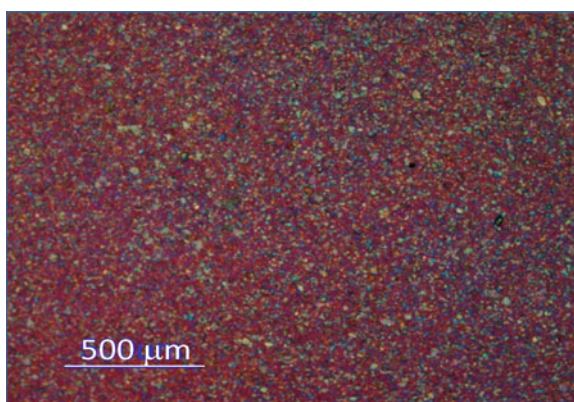
#### 9.3.2.2 Results

A micrograph of the suspension of cellobiose is shown in Fig. 9.10. The microcrystals with sizes of less than ca.  $50 \mu\text{m}$  are well dispersed. Figure 9.11 depicts a diffraction image obtained for the 3D MOMA of cellobiose. Well-separated spots are observed at larger  $2\theta$  values.



**Fig. 9.9** (a) Apparatus used to generate a frequency-modulated rotation of the sample in a superconducting magnet and (b) UV light irradiation to consolidate the orientation (b) (Ref. [16, 20, 22])

**Fig. 9.10** Micrograph of a suspension of cellobiose microcrystals (Ref. [20])

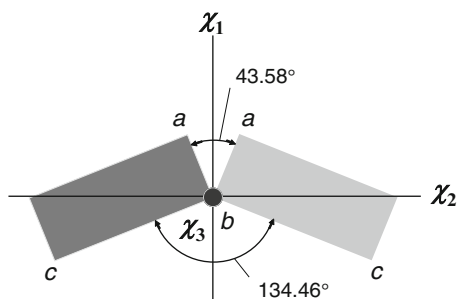


**Fig. 9.11** XRD image of a cellobiose 3D MOMA. Contrasts of the left and right halves are different (Ref. [20])

**Table 9.2** Crystallographic data obtained from MOMAs and single crystals

Sample	L-alanine MOMA	L-alanine	TPB MOMA	TPB	Cellobiose MOMA	Cellobiose
Crystal system	Orthorhombic	Orthorhombic	Orthorhombic	Orthorhombic	Monoclinic	Monoclinic
Space group	$P2_12_12_1$	$P2_12_12_1$	$Pna\ 2_1$	$Pna\ 2_1$	$P2_1$	$P2_1$
Temperature	293.1	295(2)	296	293	296	173.0(1)
$a$ (Å)	5.7837(3)	5.7762(9)	7.5958(2)	7.620(1)	5.0868(3)	5.0633(2)
$b$ (Å)	6.0328(3)	6.0345(10)	19.7480(14)	11.265(1)	13.0628(8)	13.0170(5)
$c$ (Å)	12.3406(6)	12.361(3)	11.2510(3)	19.772(5)	10.9758(7)	10.9499(4)
$\alpha$ (°)	90.0000	90.00	90.0000	90.00	90.0000	90.000
$\beta$ (°)	90.0000	90.00	90.0000	90.00	90.990(7)	90.811(2)
$\gamma$ (°)	90.0000	90.00	90.0000	90.00	90.0000	90.000
$V$ (Å <sup>3</sup> )	430.59(4)	430.86(14)	1,687.68(13)	1,697.349	729.21(8)	721.62(5)
$Z$	4	4	4	4	2	2
$\theta_{\max}$ (X-ray source)	68.2 (Cu)	26.37 (Mo)	136.4 (Cu)	24.99(Mo)	68.25 (Cu)	27.103 (Mo)
$R_1$	0.0662	0.0378	0.0993	0.0397	0.1062	0.0391
$wR_2$ [all data]	0.1718	0.0754	0.3082	0.909	0.3323	0.0841
GOF	1.018	1.044	1.031	1.000	1.146	1.049
CCDC No.	970,543	756,484	970,545	867,818	970,544	673,203

Ref. [20]

**Fig. 9.12** Twin distribution of cellobiose microcrystals in a 3D MOMA (Ref.[20])

The structure of cellobiose was solved by direct methods. Table 9.2 summarizes the crystallographic data obtained from MOMAs along with the reference data for single crystals. The data obtained for the MOMAs agrees well with those obtained for single crystals.

As shown in Table 9.1, crystals with point group (9.2) (monoclinic system) exhibit two different crystal orientations; that is, twin structures exist in a MOMA. Cellobiose belongs to space group  $P2_1$ . Because only the point group is relevant, the MOMA of cellobiose crystals exhibits a twin structure. The diffractions from the cellobiose 3D MOMA were analyzed using a conventional computer program. Figure 9.12 shows the results obtained for the twin structure. The  $\chi_3$  axis corresponds to the  $b$  axis, and the  $a$  and  $c$  axes are located in the  $\chi_1\chi_2$  plane, making

an angle of  $21.79^\circ$  between the  $\chi_1$  and  $a$  axes. Because the angle between the  $a$  and  $c$  axes is close to  $90^\circ$  ( $\beta = 90.99^\circ$ ), the cellobiose crystals are close to orthorhombic metric symmetry. However, this does not necessarily mean that the magnetic axes are close to the crystallographic axes.

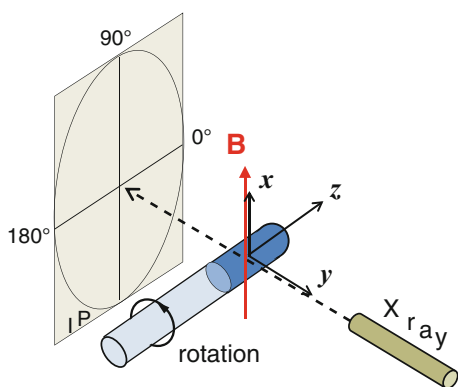
### 9.3.3 XRD of 1D MOMSs

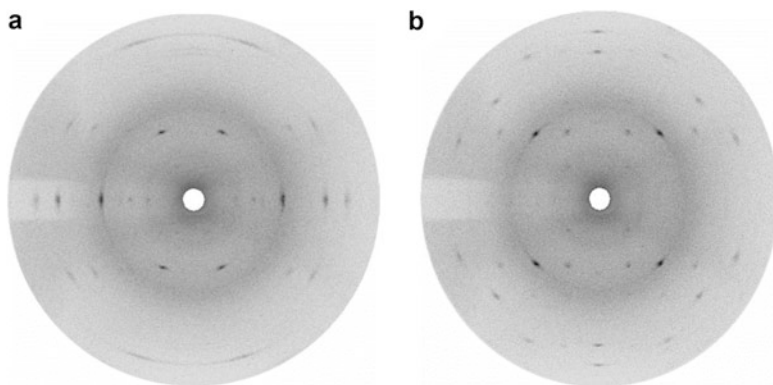
To maintain the 3D alignment of a MOMS, it should be rotated in an FM mode in a static magnetic field. Therefore, if diffraction images of MOMSs are measured in situ, they will look like a fiber pattern, and the 3D information is lost. We need a device to solve this problem. In contrast, simple, uniform rotation of the suspension gives a 1D MOMS that exhibits a fiber diffraction image. We have two fiber diffraction images that are obtained with and without sample rotation. These images might be analyzed in a similar manner to that used for single-crystal analyses. These topics are being studied now and will be reported elsewhere. Figure 9.13 shows a schematic diagram of the attachment used for the in situ diffraction measurement.

Figure 9.14a, b illustrates the diffraction images of L-alanine (space group  $P2_12_12_1$ ) 1D MOMS taken with and without rotation, respectively [24]. Both images show layer lines. From the line spacing of the image in Fig. 9.14a, the lattice parameter, say  $c$ , is determined, and from the line spacing of the image in Fig. 9.14b, the lattice parameter, say  $b$ , is determined. Thus, the lattice parameters  $b$  and  $c$  are determined from the 1D MOMS obtained with and without rotation. The distribution of the spots on each layer line is reflected by the lattice parameter  $a$ , so the value of  $a$  is determined. The relationship between the magnetic and crystallographic axes of L-alanine is now determined as  $\chi_1||c$ ,  $\chi_2||a$ , and  $\chi_3||b$ . Furthermore, the systematic absence of diffraction spots (extinction rule) provides information about the space group. In the case of L-alanine, the space group  $P2_12_12_1$  is uniquely determined. This information provided by powder diffraction might be of great use as a first step. Of course, if a 3D MOMA is available, 1D MOMS

**Fig. 9.13** Schematic diagram of in situ XRD measurement.

**B:** magnetic field, **IP:** imaging plate. Measurement is conducted with or without sample rotation (Ref. [24])





**Fig. 9.14** In situ diffraction images of an L-alanine 1D MOMS measured under 1 T without (a) and with (b) sample rotation (20 rpm) (Ref. [24])

seems less useful. However, considering that 1D MOMS experiments are easier than 3D MOMS and the recent advancement and large number of users of powder diffraction analyses, the 1D MOMS technique can be useful if combined with the powder method. The combination of 1D MOMS and the analytical procedures of fiber diffraction techniques might be also useful.

## 9.4 Single-Crystal Solid-State NMR Spectroscopy

The electron distribution around a nucleus in a molecule is affected by the chemical bonds by which the nucleus is connected to surrounding nuclei. If an external magnetic field is applied, an electric current and the resultant magnetic field opposite to the applied field are induced around the nucleus. As a result, the applied field is shielded to some extent. The ratio of the induced magnetic field to the applied field is about  $10^{-6}$  (ppm). The order of this value is close to that of the diamagnetic susceptibility  $\chi$ . This is not coincidental because both quantities are governed by the same physical phenomenon; that is, the induced current. The shielding effect is not uniform because the electron distribution is not homogeneous; the electron density is higher in the direction of the chemical bonds. The anisotropy in the shielding effect is described by the chemical shift tensor (CST) and provides important information about electron distribution around the nucleus. CSTs are determined by NMR spectroscopy.

Solid-state FT-NMR spectroscopy is widely used for analyses of solid substances. It has advantages over liquid FT-NMR spectroscopy because it can be applied to substances that exhibit physical properties of interest only in solid states or to those that do not dissolve. For organic compounds,  $^{13}\text{C}$  nuclei are most frequently measured. The sample may be a single crystal, a microcrystalline powder,

or amorphous solid. For powder samples, magic angle spinning (MAS) is essential to obtain a sharp resonance peak that gives the average of principal values of CST. Without MAS, broad peaks representing the three principal values of CST are observed, but usually, it is difficult to identify individual peaks because of the overlap with peaks from other  $^{13}\text{C}$  nuclei. There are pulse techniques to determine the principal values of CST, but the principal axes with respect to the crystal frame can only be determined by using a single-crystal sample.

When a single crystal is used, we can obtain full information of CSTs, including principal values and principal axes. The bottleneck here is that a large single crystal is required. Same as for diffractometry, MOMAs are a powerful tool for single-crystal NMR spectroscopy.

### 9.4.1 Single-Crystal NMR Spectroscopy Using MOMAs

#### 9.4.1.1 CST of Crystals

The goal of single-crystal NMR spectroscopy is to determine the CST of a crystal. The CST expressed with respect to the principal axis frame is denoted by  $\sigma_{\text{P}}$  whose diagonal values are  $\sigma_{11}$ ,  $\sigma_{22}$ , and  $\sigma_{33}$ . This tensor is transformed into  $\sigma_{\text{C}} = {}^t\mathbf{R}_1\sigma_{\text{P}}\mathbf{R}_1$  with respect to the crystallographic axis frame using the transformation matrix  $\mathbf{R}_1$ . Then,  $\sigma_{\text{C}}$  is further transformed into  $\sigma_{\text{L}} = {}^t\mathbf{R}_2\sigma_{\text{C}}\mathbf{R}_2$  with respect to the laboratory  $xyz$  frame. The  $zz$  component of  $\sigma_{\text{L}}$  is the chemical shift value observed in NMR experiments (magnetic field parallel to the laboratory  $z$  axis). Based on a series of chemical shift values obtained by changing the mutual orientation of  $\sigma_{\text{P}}$  with respect to the laboratory frame, the principal values ( $\sigma_{11}$ ,  $\sigma_{22}$ , and  $\sigma_{33}$ ) are determined. At the same time, the direction cosines of the principal axes are also determined from the transformation matrix  $\mathbf{R}_1$ .

For L-alanine crystals, for example, there are four conformationally equivalent molecules in the unit cell. Because their orientations with respect to the NMR magnetic field differ from one molecule to another, the peak positions for these four molecules are also different. As a result, we observe four peaks from crystallographically equivalent but magnetically nonequivalent  $^{13}\text{C}$  nuclei.

#### 9.4.1.2 Single-Crystal NMR Analyses of an L-Alanine MOMA [25]

A 3D MOMA sample for NMR measurements was prepared in a similar manner to that used for X-ray measurements. Here, the experimental conditions were 1.7 Pa s, 8 T, 30/140 rpm, and 50 min. The 3D MOMA has a diameter of ca. 2 mm and height of 12 mm, as shown in Fig. 9.15a. The 3D alignment of microcrystals was confirmed by XRD measurements.

A gonioprobe is usually used for single-crystal NMR measurements. A MAS probe can also be used, although the data processing becomes complicated. The

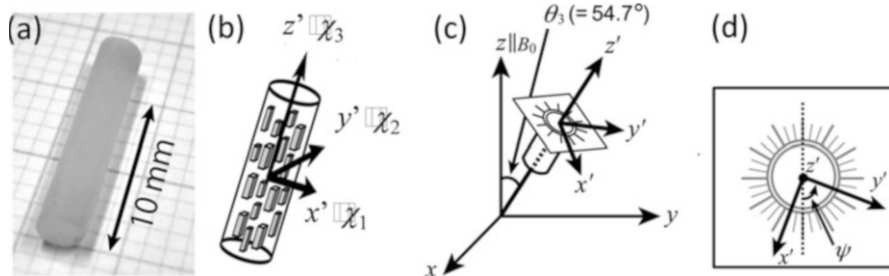
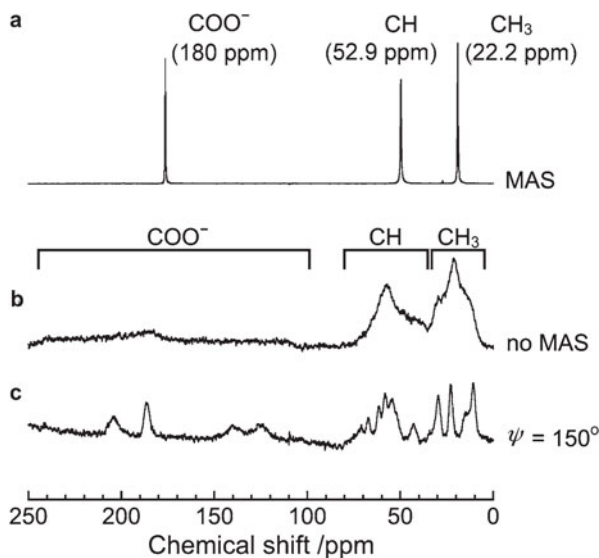


**Fig. 9.15** A photo of a 3D MOMA (a). The long axis ( $z'$  axis), which is parallel to the  $\chi_3$  axis (b), was inserted into a MAS probe at an angle of  $54.7^\circ$  (MAS angle) (c), where the sample was rotated by the angle  $\psi$  about the  $z'$  axis (d). Ref. [25]

**Fig. 9.16** NMR spectrum of L-alanine: a powder (a) with MAS and (b) without MAS and (c) MOMA measured at  $\psi = 150^\circ$ . The baseline from the matrix polymer is subtracted in the case of the MOMA (Ref. [25])



sample was inserted in a conventional MAS rotor and placed in an NMR system operated at a  $^{13}\text{C}$  resonance frequency of 100 MHz. The setting of a MOMA in the NMR spectrometer is illustrated schematically in Fig. 9.15b, c.

By changing the angle  $\psi$  as shown in Fig. 9.15d, a series of spectra were obtained. Figure 9.16 shows the spectrum measured at  $\psi = 150^\circ$ . We find four peaks attributable to carboxyl carbons in the region between 100 and 250 ppm. Plotting these four chemical shift values as a function of  $\psi$ , we obtain Fig. 9.17. The curves in this figure were simulated by using appropriate values for  $\sigma_{11}$ ,  $\sigma_{22}$ ,  $\sigma_{33}$ , and the nine components of the transformation matrix  $\mathbf{R}_1$  (the actual procedure is described in reference [25]). The results obtained are summarized in Table 9.3.

To perform single-crystal NMR spectroscopy, knowledge of the crystallographic structure of the crystal under investigation is a prerequisite. If a large single crystal

**Fig. 9.17** Curve fitting of the measured chemical shift values (Ref. [25])

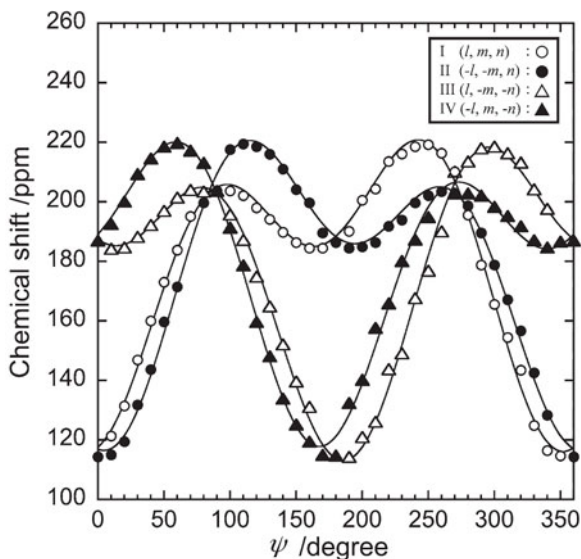


**Table 9.3** Comparison between the results for L-alanine chemical shift tensors obtained from a MOMA and from the real single crystal reported in reference [26]

Carbon	Principal values		Direction cosines		
			<i>a</i>	<i>b</i>	<i>c</i>
COO <sup>-</sup> [26]	$\sigma_{11}$	242.76 <sup>a</sup>	0.2005	-0.0719	0.9771
	$\sigma_{22}$	183.36 <sup>a</sup>	-0.7737	0.6025	0.2029
	$\sigma_{33}$	106.56 <sup>a</sup>	-0.6011	-0.7966	0.0648
COO <sup>-</sup>	$\sigma_{11}$	241	0.225	-0.095	0.969
	$\sigma_{22}$	184	-0.745	0.624	0.235
	$\sigma_{33}$	111	-0.627	-0.775	0.069

Ref. [25]

<sup>a</sup>Converted to ppm with respect to ADM

is unavailable, XRD cannot be performed and neither can single-crystal NMR spectroscopy. Even if single-crystal diffraction measurements are possible for a piece of single crystal, it may not be large enough for NMR spectroscopy. Therefore, the 3D MOMA technique is essential when one wishes to know the CST of a microcrystalline powder sample.

## 9.5 Conclusions

In this chapter, the magnetic orientation of crystals of weakly magnetic (mainly diamagnetic) materials is described, followed by the application of this phenomenon to XRD and solid-state NMR spectroscopy. Although the history of magnetic

orientation itself is rather long, its application to diffraction and spectroscopic methods is quite recent. Using the magnetic technique described in this chapter, a microcrystalline powder is converted to a “single crystal”-like composite. Single-crystal XRD and single-crystal solid-state NMR spectroscopy, which are techniques only suitable for real single crystals, are successfully performed on this composite.

**Acknowledgment** The author’s special thanks go to among many students and colleagues at Tokyo Metropolitan University and Kyoto University, Dr. F. Kimura for most of the topics throughout this chapter, Prof. M. Yamato for 1D alignment, M. Yoshino for 3D alignment, Dr. K. Matsumoto for 1D-MOMS, Drs. K. Aburaya and M. Maeyama for XRD analyses of MOMAs, and Dr. R. Kusumi for single-crystal NMR of L-alanine MOMA.

## References

1. G.H. Stout, L.H. Jensen, *X-Ray Structure Determination* (Wiley, Hoboken, 1989)
2. K.D.M. Harris, M. Tremayne, B.M. Kariuki, *Angew. Chem. Int. Ed.* **40**, 1626 (2001)
3. L. Pauling, *J. Chem. Phys.* **4**, 673 (1936)
4. J.H. Van Vleck, *The Theory of Electric and Magnetic Susceptibilities* (Oxford University Press, Oxford, 1932)
5. A. Weiss, H. Witte, *Magnetochemie* (Verlag Chemie GmbH, Weinheim, 1973)
6. Maret, G.; Dransfeld, K, in *Topics in Applied Physics*, ed. by F. Herlach (Springer, Berlin, 1985), *57*, chapter 4
7. “*Jikikagaku*”, (in Japanese), ed. by K. Kitazawa, S. Ozeki, Y. Tanimoto, M. Yamaguchi (IPC, Tokyo, 2002)
8. T. Kimura, *Polym. J.* **35**, 843 (2003)
9. J.-Y. Genoud, M. Staines, A. Mawdsley, V. Manojlovic, W. Quinton, *Supercond. Sci. Technol.* **12**, 663 (1999)
10. T. Kimura, M. Yoshino, *Langmuir* **21**, 4805 (2005)
11. Gupta, R.R. in *Landolt-Bornstein*, ed. H.-H. Hellwege, A.W. Hellwege (Springer, Berlin, 1986), vol.II/16, Chapter 8
12. H. Goldstein, C. P. Poole, J. L. Safko (eds.), *Classical Mechanics*, 3rd edn. Addisonwesley (2001)
13. T. Kimura, *Jpn. J. Appl. Phys.* **48**, 020217 (2009)
14. M. Yamaguchi, I. Yamamoto, T. Kimura, *Jpn. J. Appl. Phys.* **52**, 098003 (2013)
15. T. Kimura, T. Tanaka, G. Song, K. Matsumoto, K. Fujita, F. Kimura, *Cryst. Growth Des.* **13**, 1815 (2013)
16. F. Kimura, T. Kimura, K. Matsumoto, N. Metoki, *Cryst. Growth Des.* **10**, 48 (2010)
17. T. Kimura, M. Yoshino, T. Yamane, M. Yamato, M. Tobita, *Langmuir* **20**, 5669 (2004)
18. S. Tsukui, T. Kimura, *Jpn. J. Appl. Phys.* **51**, 057301 (2012)
19. T. Kimura, M. Yamato, W. Koshimizu, M. Koike, T. Kawai, *Langmuir* **16**, 858 (2000)
20. F. Kimura, W. Oshima, H. Matsumoto, H. Uekusa, K. Aburaya, M. Maeyama, T. Kimura, *CrystEngComm* **16**, 6630 (2014)
21. F. Kimura, T. Kimura, W. Oshima, M. Maeyama, K. Aburaya, *J. Appl. Cryst.* **43**, 151 (2010)
22. F. Kimura, K. Mizutani, B. Mikami, T. Kimura, *Cryst. Growth Des.* **11**, 12 (2011)
23. T. Kimura, C. Chang, F. Kimura, M. Maeyama, *J. Appl. Cryst.* **42**, 535 (2009)
24. K. Matsumoto, F. Kimura, S. Tsukui, T. Kimura, *Cryst. Growth Des.* **11**, 945 (2011)
25. R. Kusumi, F. Kimura, G. Song, T. Kimura, *J. Magn. Reson.* **223**, 68 (2012)
26. A. Naito, S. Ganapathy, K. Akasaka, C.A. McDowell, *J. Chem. Phys.* **74**, 3190 (1981)

# Chapter 10

## Analysis of Intermolecular Interactions by Ab Initio Molecular Orbital Calculations: Importance for Studying Organic Crystals

Seiji Tsuzuki

**Abstract** Ab initio molecular orbital calculation is becoming a powerful method for studying intermolecular interactions. The analysis of the nature of intermolecular interactions by ab initio calculation is important for studying the roles of intermolecular interactions in determining crystal structures, although the intermolecular interactions have been discussed mainly based on crystal structures. It is often dangerous to judge the nature of intermolecular interactions solely on crystal structures. For example, it is sometimes claimed that the CH/ $\pi$  interaction is weak hydrogen bond, and the CH/ $\pi$  interaction is important for determining crystal structures probably due to the similarity of the structures of CH/ $\pi$  interaction and  $\pi$  hydrogen bond. But ab initio molecular orbital calculations show that the nature of the CH/ $\pi$  interaction is completely different from that of  $\pi$  hydrogen bond. The hydrogen bond is strong and directional, and therefore, the hydrogen bond is important in determining orientation of molecules in crystals. On the other hand, the CH/ $\pi$  interaction is weak, and the directionality is negligible in general, which suggests that most of the CH/ $\pi$  interaction cannot play important roles in determining orientation of molecules in crystals.

**Keywords** Intermolecular interaction • Ab initio calculation • CH/ $\pi$  interaction • Cation/ $\pi$  interaction • Directionality

### 10.1 Introduction

Intermolecular interactions are important for understanding structures and properties of organic crystals, as intermolecular interaction controls orientation of molecules in organic crystals and determines their physicochemical properties. Due

---

S. Tsuzuki (✉)

National Institute of Advanced Industrial Science and Technology, Tsukuba, Ibaraki 305-8568, Japan

e-mail: [s.tsuzuki@aist.go.jp](mailto:s.tsuzuki@aist.go.jp)

to this reason, detailed information on intermolecular interactions is often needed for studying organic crystals.

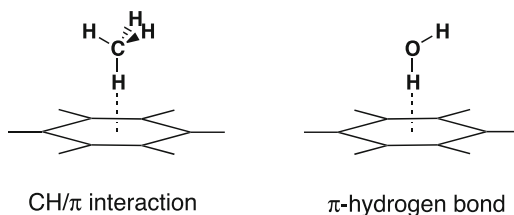
Although we can obtain information on intermolecular interactions by several experimental methods, it is still difficult to reveal the details of intermolecular interaction only by experimental measurements. Crystal structure analysis shows us the position of potential energy minimum (equilibrium intermolecular distance). But the crystal structure analysis does not provide direct information on the magnitude of the attraction between molecules. Measurements of heat of vaporization and heat of sublimation show us the magnitude of averaged intermolecular interactions in liquids and in crystals. But these measurements do not show the magnitude of the interactions between specific molecules and the orientation dependence of the interaction.

On the other hand, we can obtain detailed information on intermolecular interactions easily by *ab initio* molecular orbital calculations. We can evaluate magnitude of the attraction by calculating the intermolecular interaction energy. The directionality of the interaction can be evaluated by rotating a molecule when we calculate the interaction energy. The contribution of each intermolecular force (electrostatic, induction, dispersion, exchange repulsion, etc.) to the interaction energy can be evaluated separately by *ab initio* molecular orbital calculations. These calculations can be done using a desk-side personal computer at present, including the calculations shown in the later part of this chapter, although such calculations required a very large computer in a computer center 20 years ago. I believe that *ab initio* calculation is becoming a powerful and practical method for studying intermolecular interactions.

The nature of intermolecular interactions is important for understanding their roles in controlling orientation of molecules in organic crystals. For example, the hydrogen bond is well known as an important interaction in determining structures of organic crystals, as the hydrogen bond is sufficiently strong and sufficiently directional [1]. *Ab initio* molecular orbital calculation is useful for understanding the nature (magnitude of the attraction, directionality and origin of attraction) of the intermolecular interactions.

On the other hand, intermolecular interactions in organic crystals have been discussed based mainly on crystal structures. Although crystal structures provide useful information for intermolecular interactions, recent *ab initio* calculations of intermolecular interactions show that the discussion on the nature of the intermolecular interactions solely on crystal structures is sometimes misleading. *Ab initio* molecular orbital calculations show that the nature of the intermolecular interactions is quite different in many cases, even if the structures of interacting molecules are similar. For example, the nature of CH/ $\pi$  interaction is completely different from the nature of the  $\pi$  hydrogen bond (OH/ $\pi$  and NH/ $\pi$  interactions) [2], although the structures of these two interactions are similar (Fig. 10.1). We will show some other examples where the nature of the interactions is different, although the structures of interacting molecules are similar. These examples show that the analysis of the nature of the intermolecular interaction by *ab initio* molecular

**Fig. 10.1** Structures of CH/ $\pi$  interaction and  $\pi$  hydrogen bond



orbital calculation is important for understanding the roles of the intermolecular interactions in determining the structures of organic crystals.

## 10.2 Ab Initio Calculation of Intermolecular Interaction

Ab initio molecular orbital calculation is an approximation, although it does not use any empirical parameter based on experimental measurements. The level of approximation is mainly determined by the choice of basis set and electron correlation correction procedure used for the calculation. Molecular orbital is described as a linear combination of gauss orbitals located on atoms of the molecule in ab initio molecular orbital calculation. The set of gauss orbitals (basis function) is called as basis set. The accuracy of the calculation depends on the number and the angular flexibility of gauss orbitals used for the calculation.

The calculated interaction energy depends strongly on the choice of basis set and electron correlation correction procedure. Figure 10.2 shows the basis set dependence of the calculated interaction energy of the benzene dimer with the electron correlation correction by the second-order Møller-Plesset perturbation (MP2) method. The size of basis set increases in the order of 6-31G\* < cc-pVDZ < cc-pVTZ < cc-pVQZ. The small 6-31G\* basis set underestimates the attraction significantly compared with large cc-pVQZ basis set. The dispersion interaction, which is the major source of the attraction in the benzene dimer, has its origin in the polarization of molecules. Small basis set underestimates the molecular polarizability and therefore underestimates the dispersion interaction [3]. Figure 10.3 shows the effects of electron correlation correction. The interaction energy potential calculated by the Hartree-Fock (HF) method does not have a potential minimum, as the HF method cannot evaluate the dispersion interaction, which has its origin in electron correlation. The MP2 method overestimates the attraction greatly compared with the more reliable coupled cluster calculations with single, double, and triple excitations (CCSD(T)). These results show that a large basis set near saturation and CCSD(T)-level electron correlation correction is necessary for an accurate evaluation of the interaction energy of the benzene dimer [3].

Generally, we can evaluate intermolecular interaction energy very accurately, if a very large basis set is used and electron correlation is corrected by the CCSD(T)

**Fig. 10.2** Effects of basis set on the calculated interaction energy of the benzene dimer

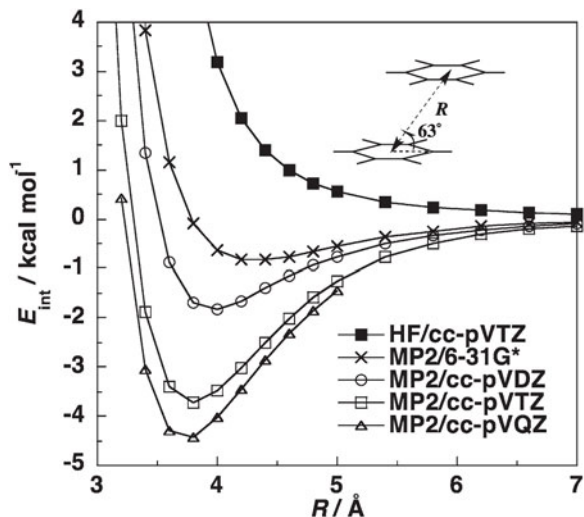
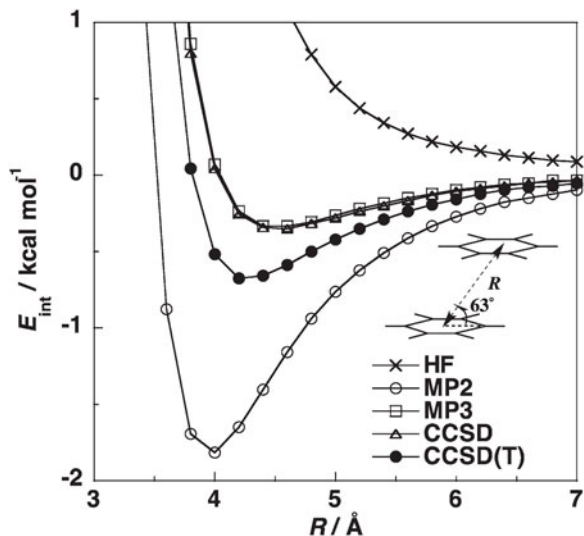


**Fig. 10.3** Effects of electron correlation correction on the calculated interaction energy of the benzene dimer using cc-pVDZ basis set



method. The calculated CCSD(T)-level interaction energies for molecular clusters using very large basis sets well reproduce the experimental interaction energies in the gas phase [4]. The CCSD(T)-level interaction energy at the basis set limit ( $E_{\text{CCSD(T)}(\text{limit})}$ ) is often estimated for an accurate evaluation of the intermolecular interaction energy [3]. The basis set limit is the limit where the size of the basis set is infinite.

The MP2-level interaction energy at the basis set limit ( $E_{\text{MP2}(\text{limit})}$ ) can be estimated from the calculated MP2-level interaction energies using the Dunning's cc-pVXZ or aug-cc-pVXZ ( $X = D, T, Q$ , etc.) basis sets by extrapolation using

the method proposed by Feller [5] or by the method of Helgaker et al. [6]. The  $E_{\text{CCSD(T)}(\text{limit})}$  is obtained as the sum of  $E_{\text{MP2}(\text{limit})}$  and CCSD(T) correction term ( $\Delta\text{CCSD(T)}$ ) according to Eq. (10.1):

$$E_{\text{CCSD(T)}(\text{limit})} = E_{\text{MP2}(\text{limit})} + \Delta\text{CCSD(T)}. \quad (10.1)$$

The  $\Delta\text{CCSD(T)}$  is the difference between the calculated CCSD(T)- and MP2-level interaction energies ( $E_{\text{CCSD(T)}}$  and  $E_{\text{MP2}}$ ) as Eq. (10.2):

$$\Delta\text{CCSD(T)} = E_{\text{CCSD(T)}} - E_{\text{MP2}}. \quad (10.2)$$

The basis set dependence of  $\Delta\text{CCSD(T)}$  is weak. We can calculate the  $\Delta\text{CCSD(T)}$  sufficiently accurately using a medium-size basis set.

The interaction energies of hydrogen-bonding clusters can be evaluated sufficiently accurately by MP2-level calculations using a large basis set [7]. The MP2 calculation requires less CPU time compared with the CCSD(T) calculation. The interaction energy of ions can be evaluated by HF or by density functional (DFT) methods with sufficient accuracy [8, 9], as the contribution of the dispersion interaction is relatively small due to the very strong electrostatic and induction interactions. The HF and DFT calculations do not need large CPU time as in the cases of the CCSD(T) and MP2 calculations.

The MP2-level interaction energies calculated for hydrogen-bonding clusters well reproduce the experimental interaction energies measured in the gas phase, if a sufficiently large basis set is used for the calculations [7] as shown in Table 10.1. CCSD(T)-level interaction energies calculated for the aromatic clusters (benzene dimer, benzene-methane, benzene-ammonia, and benzene-water clusters) agree well with gas-phase interaction energies [3, 10–12] as shown in Table 10.2.

The cost of computation depends on the number of basis functions and the choice of electron correlation correction procedure. The CPU time required for HF level calculation is approximately proportional to the forth power of the number of basis functions used for the calculations. The CPU time for MP2 and CCSD(T)-level calculations is proportional to the 5th and 7th power of the number of basis functions, respectively. Therefore, the calculations with electron correlation

**Table 10.1** Calculated and experimental interaction energies of hydrogen-bonded clusters<sup>a</sup>

	Calc <sup>b</sup>	Exp <sup>c</sup>
H <sub>2</sub> O – H <sub>2</sub> O	–4.9	–5.0
MeOH – MeOH	–5.6	–4.6 ~ –5.9
HCOOH – HCOOH	–13.8	–13.2
HF – HF	–4.4	–4.6 ± 0.3
HCN – HF	–7.4	–6.9

<sup>a</sup>Energy in kcal/mol

<sup>b</sup>MP2-level interaction energy at the basis set limit ( $E_{\text{MP2}(\text{limit})}$ ). See text

<sup>c</sup>Reference [7] and references therein

**Table 10.2** Calculated and experimental interaction energies of benzene dimer and benzene clusters with methane, ammonia, and water<sup>a</sup>

	Calc <sup>b</sup>	Exp <sup>c</sup>
C <sub>6</sub> H <sub>6</sub> – C <sub>6</sub> H <sub>6</sub>	–2.5	–2.8 ± 0.4, –2.0 ± 0.2
C <sub>6</sub> H <sub>6</sub> – CH <sub>4</sub>	–1.4	–1.3 ~ –1.4
C <sub>6</sub> H <sub>6</sub> – NH <sub>3</sub>	–2.2	–2.0
C <sub>6</sub> H <sub>6</sub> – H <sub>2</sub> O	–3.0	–3.3 ± 0.3, –3.4 ± 0.1

<sup>a</sup>Energy in kcal/mol

<sup>b</sup>CCSD(T)-level interaction energy at the basis set limit ( $E_{\text{CCSD(T)}(\text{limit})}$ ). See text

<sup>c</sup>References [3, 10–12] and references therein

correction by the MP2 and CCSD(T) methods require large CPU time compared with the HF calculation. The CPU time for DFT calculation is proportional to the cubes of the number of basis functions. Therefore, DFT calculations are often used for large systems. DFT calculation includes the effects of electron correlation. But DFT calculations with commonly used BLYP, B3LYP, and PBE functionals cannot accurately evaluate the dispersion interaction [7], which is sometimes the major source of attraction between organic molecules [3, 10, 11].

The contributions of the electrostatic and induction interactions to the interaction energy ( $E_{\text{es}}$  and  $E_{\text{ind}}$ ) can be evaluated using distributed multipole analysis [13, 14]. The effect of electron correlation correction on the calculated interaction energy ( $E_{\text{corr}}$ ) is the difference between the interaction energy calculated with electron correlation correction ( $E_{\text{int}}$ ) and that calculated at the HF level ( $E_{\text{HF}}$ ) as Eq. (10.3):

$$E_{\text{corr}} = E_{\text{int}} - E_{\text{HF}}. \quad (10.3)$$

The  $E_{\text{corr}}$  calculated for the interaction between neutral molecules is mainly dispersion energy [3]. Therefore, the contribution of the dispersion interaction can be discussed based on the size of  $E_{\text{corr}}$ . The contribution of the electrostatic, induction, and dispersion interactions can also be evaluated using symmetry-adapted intermolecular perturbation theory [15]. But this method requires large CPU time for calculating a large system using a large basis set. The  $E_{\text{HF}}$  is mainly the contribution of the electrostatic, induction, and short-range orbital-orbital (exchange repulsion and charge transfer) interactions. Therefore, the contributions of the orbital-orbital interactions ( $E_{\text{short}}$ ) can be estimated by subtracting  $E_{\text{es}}$  and  $E_{\text{ind}}$  from  $E_{\text{HF}}$  [16] as Eq. (10.4):

$$E_{\text{short}} = E_{\text{HF}} - E_{\text{es}} - E_{\text{ind}} \quad (10.4)$$

The total interaction energy ( $E_{\text{int}}$ ) is divided into four terms as Eq. (10.5):

$$\begin{aligned} E_{\text{int}} &= E_{\text{HF}} + E_{\text{corr}} \\ &= E_{\text{es}} + E_{\text{ind}} + E_{\text{short}} + E_{\text{corr}}. \end{aligned} \quad (10.5)$$

### 10.3 CH/ $\pi$ Interaction

The contacts between C-H bond and aromatic ring are frequently observed in organic crystals [17]. The attraction between the C-H bond and aromatic ring is called as CH/ $\pi$  interaction [18]. The structure of the CH/ $\pi$  interaction is similar to that of  $\pi$  hydrogen bond (OH/ $\pi$  and NH/ $\pi$  interactions) as shown in Fig. 10.1. It is sometimes claimed that the CH/ $\pi$  interaction is the weakest hydrogen bond, and the CH/ $\pi$  interaction is playing important roles in controlling crystal structures as in the case of the hydrogen bond [18] probably due to the structural similarity of the CH/ $\pi$  interaction and  $\pi$  hydrogen bond.

However, the nature of the CH/ $\pi$  interaction is completely different from the nature of the hydrogen bond in most cases [2]. The CH/ $\pi$  interaction is weak and the directionality of CH/ $\pi$  interaction is negligible. On the other hand, the hydrogen bond is strong and directional. The hydrogen bond is important in controlling the orientation of molecules in crystals, as it is sufficiently strong and sufficiently directional [1]. The weak attraction and negligible directionality of the CH/ $\pi$  interaction suggest that most of the CH/ $\pi$  interaction cannot play important roles in determining orientation of molecules in organic crystals.

The contribution of electrostatic interaction to the attraction is significant in conventional hydrogen bond such as the hydrogen bond of the water dimer [2]. Conventional hydrogen bonds have strong directionality due to the large contribution of the electrostatic interaction to the attraction. The electrostatic interaction between neutral molecules is highly orientation dependent, as the highly directional dipole-dipole or the quadrupole-quadrupole interaction is the leading term of the electrostatic interaction between neutral molecules.

Molecules have their charges around atoms of molecules. The electrostatic interaction between molecules (the Coulombic interaction between static charges of molecules) can be expressed approximately as the sum of the interactions between multipoles located on the centers of gravity of molecules [19]. The dipole-dipole or the quadrupole-quadrupole interaction is the leading term of the electrostatic interaction between neutral molecules, as the charge-charge interaction and other interactions of molecular charge with multipoles are zero. On the other hand, the isotropic charge-charge interaction is the leading term in the electrostatic interaction between cation and anion. Therefore, the directionality of the interaction between cation and anion is weak.

The major source of the attraction in the CH/ $\pi$  interaction is the dispersion interaction in contrast to the hydrogen bond [2, 10, 11]. The contribution of the electrostatic interaction to the attraction in the CH/ $\pi$  interaction is small. Due to the small contribution of the electrostatic interaction to the attraction, the CH/ $\pi$  interaction is weak and the directionality of the CH/ $\pi$  interaction is negligible [2].

High-level ab initio calculations show that the magnitude of the attraction of the CH/ $\pi$  interaction is substantially weaker than the hydrogen bond. The intermolecular interaction energies ( $E_{\text{int}}$ ) calculated for the benzene-methane and benzene-ethylene clusters (CH/ $\pi$  interactions) are compared with those calculated

for the water dimer and benzene-water cluster (hydrogen bonds) [2] as summarized in Table 10.3. The  $E_{\text{int}}$  calculated for the benzene-methane and benzene-ethylene clusters are  $-1.47$  and  $-2.17$  kcal/mol, respectively. While those for the water dimer and the benzene-water cluster are  $-4.80$  and  $-3.02$  kcal/mol, respectively.

The electrostatic energy ( $E_{\text{es}}$ ) and the contribution of electron correlation ( $E_{\text{corr}}$ ) for the benzene-methane and benzene-ethylene clusters are compared with those for the water dimer and benzene-water cluster [2] as summarized in Table 10.3. The  $E_{\text{es}}$  calculated for the benzene-methane and benzene-ethylene clusters is very small. The large  $E_{\text{corr}}$  values show that the dispersion is the major source of the attraction in the CH/ $\pi$  interaction. On the other hand, the contribution of the electrostatic interaction to the attraction is significant in hydrogen bonds.

The distance dependence of the total interaction energy and each energy term calculated for benzene-methane cluster is shown in Fig. 10.4. The size of total

**Table 10.3** Total interaction energy and contribution of each energy term calculated for CH/ $\pi$  interactions and hydrogen bonds<sup>a</sup>

	$E_{\text{int}}^{\text{b}}$	$E_{\text{es}}^{\text{c}}$	$E_{\text{short}}^{\text{d}}$	$E_{\text{corr}}^{\text{e}}$
$\text{C}_6\text{H}_6 - \text{CH}_4$	-1.47	-0.19	1.21	-2.50
$\text{C}_6\text{H}_6 - \text{C}_2\text{H}_4$	-2.17	-0.38	1.80	-3.58
$\text{H}_2\text{O} - \text{H}_2\text{O}$	-4.80	-6.65	3.20	-1.35
$\text{C}_6\text{H}_6 - \text{H}_2\text{O}$	-3.02	-1.86	1.07	-2.23

<sup>a</sup>Energy in kcal/mol

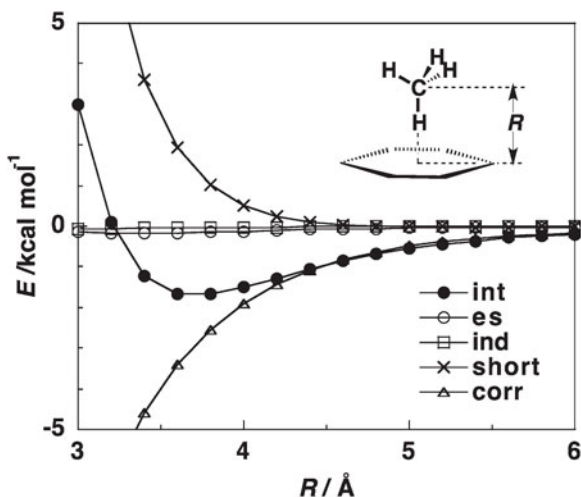
<sup>b</sup>Total interaction energy. CCSD(T)-level interaction energy at the basis set limit ( $E_{\text{CCSD(T)}(\text{limit})}$ ). See text

<sup>c</sup>Electrostatic energy

<sup>d</sup>Contribution of short-range orbital-orbital interaction.  $E_{\text{short}} = E_{\text{int}} - E_{\text{es}}$ . The small  $E_{\text{ind}}$  is included in  $E_{\text{short}}$

<sup>e</sup>Contribution of electron correlation. Mainly dispersion interaction

**Fig. 10.4** Distance dependence of total interaction energy ( $E_{\text{int}}$ ) calculated for the benzene-methane cluster and contribution of each energy term.  $E_{\text{int}}$  was calculated at the MP2/aug-cc-pVTZ level



interaction energy decreases slowly with distance, which clearly shows that the long-range interactions (electrostatic, induction, and dispersion interaction) are the major source of the attraction in the benzene-methane cluster. The long-range interactions have their origin in Coulombic interaction. Therefore, the energy of long-range interaction is proportional to some inverse power of the distance. The energy of long-range interactions decreases slowly, while the short-range orbital-orbital interactions (exchange-repulsion and charge-transfer interactions) have their origin in the overlap of molecular orbitals. Therefore, the energy of short-range interactions is approximately proportional to the overlap integral. The energy of short-range interaction decreases exponentially with distance. The short-range interactions are negligible when molecules are well separated.

Figure 10.4 shows that the dispersion interaction ( $E_{\text{corr}}$ ) is the major source of the attraction in the benzene-methane cluster. The contributions of electrostatic ( $E_{\text{es}}$ ) and induction ( $E_{\text{ind}}$ ) interactions are very weak. The short-range orbital-orbital interaction ( $E_{\text{short}}$ ) is repulsive, although the orbital-orbital interaction (charge-transfer interaction) was sometimes claimed as the origin of the attraction in the CH/ $\pi$  interaction [18].

Ab initio calculations show that the directionality of the CH/ $\pi$  interaction is very weak. The orientation dependence of the interaction energies of the CH/ $\pi$  interactions (the interactions of benzene-methane and benzene-acetylene clusters) is compared with the orientation dependence of the interaction energies of the hydrogen bonds (the interactions of the water dimer and benzene-water cluster). The changes of the interaction energies by the rotation of molecules from equilibrium geometries ( $\Delta E_{\text{int}}$ ) [2] are shown in Fig. 10.5. The hydrogen bond of the water dimer has strong directionality. The  $\pi$  hydrogen bond (the interaction between benzene and water) has weak directionality. On the other hand, the directionality of the CH/ $\pi$  interaction is very weak. The directionality of the interaction between benzene and acetylene is weaker than that of the interaction of the benzene-water cluster. The

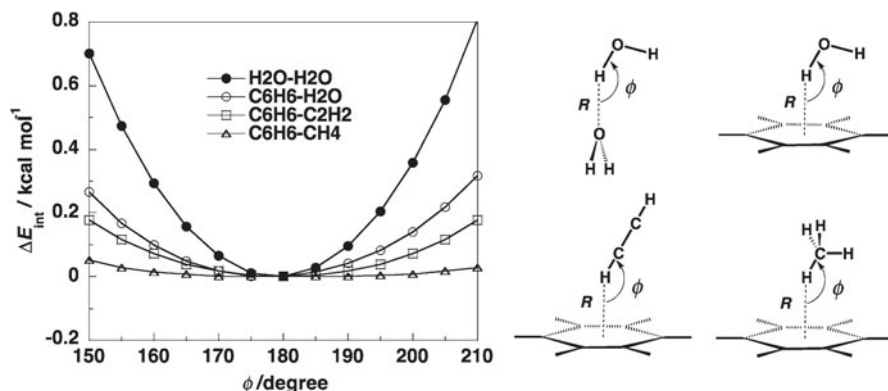


Fig. 10.5 Directionality of CH/ $\pi$  interaction and hydrogen bond

directionality of the interaction between benzene and methane is negligible. The change of the interaction energy is less than 0.05 kcal/mol, even if  $\phi$  changes  $30^\circ$  from the potential minimum.

The small contribution of the electrostatic interaction to the attraction is the cause of the negligible directionality of the interaction between benzene and methane. The dispersion interaction is the major source of the attraction in the CH/ $\pi$  interactions. The electrostatic interaction in the CH/ $\pi$  interactions is very weak, if few exceptions are excluded. The weak electrostatic interactions in the CH/ $\pi$  interactions show that the directionality of the CH/ $\pi$  interaction is very weak in general. The CH/ $\pi$  interactions of acetylene and chloroform are exceptional, where the electrostatic interaction is not weak due to the large positive charge on the hydrogen atom of interacting C-H bond [2].

The shifts of C-H vibrational frequency suggest that the nature of CH/ $\pi$  interaction is not close to that of hydrogen bond but close to the interactions in van der Waals clusters. A low-frequency shift of an X-H stretch band is a well-known marker of hydrogen bond formation. The O-H stretch band has a strong low-frequency shift ( $-106\text{ cm}^{-1}$ ) in the water dimer [20]. On the other hand, low-frequency shifts associated with the CH/ $\pi$  interaction are very small [21], or sometimes, unconventional high-frequency shifts are observed [22]. The observed low-frequency shifts in the methane clusters with benzene, toluene, *p*-xylene, mesitylene, and naphthalene are  $-5$  to  $-12\text{ cm}^{-1}$  [21].

The shifts of electronic spectra also suggest that the nature of the CH/ $\pi$  interaction is close to the interactions in van der Waals clusters. The high-frequency shifts of the  $S_1$ - $S_0$  vibronic transition are generally seen associated with the formation of  $\pi$  hydrogen bond clusters, while the low-frequency shifts are observed in van der Waals clusters. The shifts in the benzene-water and benzene-argon clusters are  $+50$  and  $-21\text{ cm}^{-1}$ , respectively [23, 24]. Low-frequency shifts ( $-11$  to  $-56\text{ cm}^{-1}$ ) were observed in the methane clusters with benzene, toluene, *p*-xylene, mesitylene, and naphthalene [21]. The low-frequency shifts show that the nature of the interactions in the methane clusters (the CH/ $\pi$  interaction) is not close to that of  $\pi$  hydrogen bond, but close to that of van der Waals clusters.

The nature of the CH/ $\pi$  interaction is completely different from that of hydrogen bond, although the structure of the CH/ $\pi$  interaction is similar to  $\pi$  hydrogen bond. These results show that it is often dangerous to judge the roles of the intermolecular interaction in determining the structures of organic crystals solely by the structures of interacting molecules.

## 10.4 Cation/ $\pi$ Interaction of Aromatic Cations

There exists strong attraction between a nitrogen-containing aromatic cation (pyridinium and imidazolium) and a neutral  $\pi$  system (Fig. 10.6) [25]. This interaction is sometimes called as  $\pi/\pi$  interaction probably due to the structural similarity

**Fig. 10.6** Interactions between nitrogen-containing aromatic cation and benzene

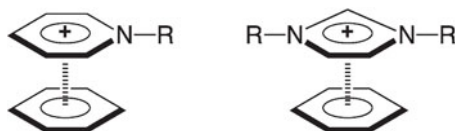


**Table 10.4** Total interaction energy and contribution of each energy term calculated for benzene dimer, benzene clusters with *N*-methylpyridinium and  $K^+$ <sup>a</sup>

	$E_{\text{int}}^{\text{b}}$	$E_{\text{es}}^{\text{c}}$	$E_{\text{ind}}^{\text{d}}$	$E_{\text{short}}^{\text{e}}$	$E_{\text{corr}}^{\text{f}}$
$C_6H_6 - C_6H_6$	-2.48	0.90	-0.25	3.01	-6.14
$C_6H_6 - C_6H_5NCH_3^+$	-9.36	-4.05	-3.52	5.79	-7.58
$C_6H_6 - K^+$	-17.2	-11.9	-12.8	11.8	-4.4

<sup>a</sup>Energy in kcal/mol

<sup>b</sup>Total interaction energy. CCSD(T)-level interaction energy at the basis set limit ( $E_{\text{CCSD(T)}(\text{limit})}$ ). See text

<sup>c</sup>Electrostatic energy

<sup>d</sup>Induction energy

<sup>e</sup>Contribution of short-range orbital-orbital interaction

<sup>f</sup>Contribution of electron correlation. Mainly dispersion interaction

with the  $\pi/\pi$  interactions of neutral aromatic molecules. However, the nature of the interaction is completely different from the  $\pi/\pi$  interactions of neutral aromatic molecules [26].

High-level ab initio calculations show that the magnitude of the attraction between a nitrogen-containing aromatic cation and neutral benzene is stronger than the interaction in the neutral benzene dimer significantly. The intermolecular interaction energy ( $E_{\text{int}}$ ) calculated for the benzene cluster with *N*-methylpyridinium is  $-9.36$  kcal/mol, while  $E_{\text{int}}$  for the benzene dimer is  $-2.48$  kcal/mol [26] as shown in Table 10.4.

The electrostatic and induction (attraction by induced polarization) interactions ( $E_{\text{es}}$  and  $E_{\text{ind}}$ ) are mainly responsible for the strong attraction in the benzene cluster with *N*-methylpyridinium, while the dispersion interaction ( $E_{\text{corr}}$ ) is the major source of the attraction in the neutral benzene dimer. The contributions of the electrostatic and induction interactions to the attraction are small in the benzene dimer. The  $E_{\text{es}}$ ,  $E_{\text{ind}}$ , and  $E_{\text{corr}}$  calculated for the benzene cluster with *N*-methylpyridinium and the benzene dimer [26] are compared in Table 10.4.

The comparison of the interaction in the benzene cluster with *N*-methylpyridinium and that in the benzene dimer also shows that it is dangerous to judge the nature of the intermolecular interaction solely by structure of interacting molecules. The nature of the interaction in the benzene cluster with *N*-methylpyridinium is similar to that of the cation/ $\pi$  interaction between benzene and alkali metal cation, where the electrostatic and induction interactions are the major source of the attraction [8] as shown in Table 10.4.

## 10.5 Interactions of Ammonium and Alkyl Ammonium with Benzene

The interactions of benzene with ammonium and alkyl ammonium cations (Fig. 10.7) are sometimes called as strong NH/ $\pi$  and CH/ $\pi$  interactions, respectively, due to the contact of the N-H and C-H bonds with benzene. However, the nature of these interactions is different from the nature of the NH/ $\pi$  and CH/ $\pi$  interactions of neutral molecules [2].

High-level ab initio calculations show that the interactions of benzene with ammonium and alkyl ammonium cations are significantly stronger than the NH/ $\pi$  and CH/ $\pi$  interactions of neutral molecules. The intermolecular interaction energies ( $E_{\text{int}}$ ) calculated for the benzene clusters with ammonium and tetramethylammonium cations are  $-19.30$  and  $-9.66$  kcal/mol, respectively, while those for the benzene clusters with ammonia and methane are  $-2.22$  and  $-1.47$  kcal/mol, respectively [2], as shown in Table 10.5.

The electrostatic and induction interactions ( $E_{\text{es}}$  and  $E_{\text{ind}}$ ) are mainly responsible for the strong attraction in the benzene clusters with the ammonium and tetramethylammonium cations. On the other hand, the electrostatic interactions are small in

**Fig. 10.7** Interactions of benzene with ammonium and tetramethylammonium cations

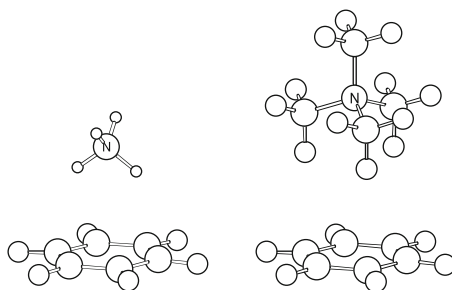


**Table 10.5** Total interaction energy and contributions of each energy term calculated for benzene clusters with ammonium, tetramethylammonium, ammonia, and methane<sup>a</sup>

	$E_{\text{int}}^{\text{b}}$	$E_{\text{es}}^{\text{c}}$	$E_{\text{ind}}^{\text{d}}$	$E_{\text{short}}^{\text{e}}$	$E_{\text{corr}}^{\text{f}}$
$\text{C}_6\text{H}_6 - \text{NH}_4^+$	$-19.30$	$-11.04$	$-13.58$	$9.58$	$-4.26$
$\text{C}_6\text{H}_6 - \text{NMe}_4^+$	$-9.66$	$-5.27$	$-3.80$	$4.27$	$-4.85$
$\text{C}_6\text{H}_6 - \text{NH}_3$	$-2.22$	$-1.01$	–	$1.14^{\text{g}}$	$-2.36$
$\text{C}_6\text{H}_6 - \text{CH}_4$	$-1.47$	$-0.19$	–	$1.21^{\text{g}}$	$-2.50$

<sup>a</sup>Energy in kcal/mol

<sup>b</sup>Total interaction energy. CCSD(T)-level interaction energy at the basis set limit ( $E_{\text{CCSD(T)}(\text{limit})}$ ). See text

<sup>c</sup>Electrostatic energy

<sup>d</sup>Induction energy

<sup>e</sup>Contribution of short-range orbital-orbital interaction

<sup>f</sup>Contribution of electron correlation. Mainly dispersion interaction

<sup>g</sup> $E_{\text{short}} = E_{\text{int}} - E_{\text{es}}$ . The small  $E_{\text{ind}}$  is included in  $E_{\text{short}}$

the benzene cluster with ammonia and methane. The dispersion interaction ( $E_{\text{corr}}$ ) is the major source of the attraction in the benzene cluster with ammonia and methane. The  $E_{\text{es}}$ ,  $E_{\text{ind}}$ , and  $E_{\text{corr}}$  calculated for these clusters are summarized in Table 10.5 [2].

The comparison of the interactions of benzene with ammonium and alkyl ammonium cations with the NH/ $\pi$  and CH/ $\pi$  interactions of neutral molecules is another example that the nature of the interactions cannot be judged solely by structures of interacting molecules.

## 10.6 Summary

Ab initio molecular orbital calculation is becoming a powerful method for studying intermolecular interactions, which provides detailed information on intermolecular interactions (magnitude of attraction, directionality and origin of attraction). Ab initio calculations show that the nature of the intermolecular interactions is often completely different, even if structures of interacting molecules are similar. For example, the structures of the CH/ $\pi$  interaction are similar to the  $\pi$  hydrogen bond, while the nature of the two interactions is completely different. The nature of the intermolecular interaction is important for understanding their roles in controlling the structure of organic crystals. The hydrogen bond is strong and directional, while the CH/ $\pi$  interaction is weak and the directionality is very weak in general. The hydrogen bond is an important interaction for controlling structures of organic crystals, as the hydrogen bond is sufficiently strong and sufficiently directional. On the other hand, CH/ $\pi$  interaction is weak and the directionality is very weak in general. Therefore, most of the CH/ $\pi$  interaction cannot play important roles in determining orientations of molecules in organic crystals. Two other examples (the cation/ $\pi$  interaction of aromatic cation and the interactions of ammonium and alkyl ammonium cations with benzene) also show that the nature of the interactions is different, even if the structures of interacting molecules are similar. These results show that it is often dangerous to discuss the roles of intermolecular interactions in determining the structures of organic crystals solely by the crystal structures and that analysis of intermolecular interactions by ab initio molecular orbital calculation is important.

## References

1. G.R. Desiraju, T. Steiner, *The Weak Hydrogen Bond* (Oxford University Press, New York, 1999)
2. S. Tsuzuki, A. Fujii, *Phys. Chem. Chem. Phys.* **10**, 2584 (2008)
3. S. Tsuzuki, K. Honda, T. Uchamaru, M. Mikami, K. Tanabe, *J. Am. Chem. Soc.* **124**, 104 (2002)
4. T.H. Dunning Jr., *J. Phys. Chem. A* **104**, 9062 (2000)

5. D. Feller, *J. Chem. Phys.* **96**, 6104 (1992)
6. T. Helgaker, W. Klopper, H. Koch, J. Noga, *J. Chem. Phys.* **106**, 9639 (1997)
7. S. Tsuzuki, H.P. Luthi, *J. Chem. Phys.* **114**, 3949 (2001)
8. S. Tsuzuki, M. Yoshida, T. Uchimaru, M. Mikami, *J. Phys. Chem. A* **105**, 769 (2001)
9. S. Tsuzuki, H. Tokuda, K. Hayamizu, M. Watanabe, *J. Phys. Chem. B* **109**, 16474 (2005)
10. S. Tsuzuki, K. Honda, T. Uchimaru, M. Mikami, K. Tanabe, *J. Am. Chem. Soc.* **122**, 3746 (2000)
11. K. Shibasaki, A. Fujii, N. Mikami, S. Tsuzuki, *J. Phys. Chem. A* **110**, 4397 (2006)
12. S. Tsuzuki, K. Honda, T. Uchimaru, M. Mikami, K. Tanabe, *J. Am. Chem. Soc.* **122**, 11450 (2000)
13. A.J. Stone, M. Alderton, *Mol. Phys.* **56**, 1047 (1985)
14. A. Stone, *J. Mol. Phys.* **56**, 1065 (1985)
15. A.J. Misquitta, A.J. Stone, S.L. Price, *J. Chem. Theory Comput.* **4**, 19 (2008)
16. S. Tsuzuki, N. Sato, *J. Phys. Chem. B* **117**, 6849 (2013)
17. Y. Umezawa, S. Tsuboyama, K. Honda, J. Uzawa, M. Nishio, *Bull. Chem. Soc. Jpn.* **71**, 1207 (1998)
18. M. Nishio, M. Hirota, Y. Umezawa, *The CH/ $\pi$  Interaction* (Wiley-VCH, New York, 1998)
19. A.J. Stone, *The Theory of Intermolecular Forces* (Clarendon Press, Oxford, 1996)
20. U. Buck, F. Huisken, *Chem. Rev.* **100**, 3863 (2000)
21. S. Morita, A. Fujii, N. Mikami, S. Tsuzuki, *J. Phys. Chem. A* **110**, 10583 (2006)
22. P. Hobza, V. Spirko, Z. Havlas, K. Buchhold, B. Reimann, H.-D. Barth, B. Brutschy, *Chem. Phys. Lett.* **299**, 180 (1999)
23. A.J. Gotch, T.S. Zwier, *J. Chem. Phys.* **96**, 3388 (1992)
24. T. Weber, A. von Bargaen, E. Riedle, H.J. Neusser, *J. Chem. Phys.* **92**, 90 (1990)
25. M.A. Petti, T.J. Shepodd, R.E. Barrans Jr., D.A. Dougherty, *J. Am. Chem. Soc.* **110**, 6825 (1988)
26. S. Tsuzuki, M. Mikami, S. Yamada, *J. Am. Chem. Soc.* **129**, 8656 (2007)

**Part III**  
**Crystal Structure**

# Chapter 11

## Construction of Aromatic Folding Architecture: Utilization of Ureylene and Iminodicarbonyl Linkers

Shigeo Kohmoto

**Abstract** This review discusses the creation of aromatic folded structures in a zigzag way in crystalline state. A pillar-like columnar array of aromatic rings by folding can be constructed by using U-shaped linkers to connect the aromatic rings. As such linkers, ureylene and iminodicarbonyl groups have been utilized. Physical and spectroscopic properties of aromatic foldamers created in this fashion are affected considerably with increasing numbers of aromatic rings involved. To create folding networks by hydrogen bonding in crystal structures, U-shaped urea building blocks were developed. A variety of folded structures have been generated in the cocrystals by hydrogen bonding between the building blocks and hydrogen-bonding acceptor molecules. Interesting examples of stacked zigzag ribbon-type aromatic folding architectures are also presented.

**Keywords** Foldamers • Aromatic ureas • Aromatic acyclic imides • Hydrogen bonding

### 11.1 Introduction

Folding attracted many chemists for decades. Folding patterns of biological macromolecules like peptides and proteins are strictly controlled by the combination of noncovalent forces, such as hydrogen bonding, hydrophobic and electrostatic interactions, and van der Waals force. The resulting secondary and/or tertiary structures are highly optimized for their biological operations in a sophisticated manner. Chemists have been actively mimicking their functions by inducing folded or helical conformations with assistance of noncovalent forces. The molecules which possess folded structures are generally named foldamers. The word “foldamer” was coined by Gellman in 1996 [1]. Foldamers are defined as any polymers with a

---

S. Kohmoto (✉)

Department of Applied Chemistry, Graduate School of Engineering, Chiba University, Chiba  
263-8522, Japan

e-mail: [kohmoto@faculty.chiba-u.jp](mailto:kohmoto@faculty.chiba-u.jp)

© Springer Japan 2015

R. Tamura, M. Miyata (eds.), *Advances in Organic Crystal Chemistry*,  
DOI 10.1007/978-4-431-55555-1\_11

203

strong tendency to adopt a specific compact conformation [2]; as sequence-specific oligomers akin to peptide, proteins, and oligonucleotides that fold into well-defined three-dimensional structures [3]; and also as artificial folded molecular architectures inspired by the structures and functions of biopolymers [4].

Foldamers are classified into several types by their secondary structures [5]. Up to now, a variety of artificial foldamers with oligomeric and polymeric backbones have been synthesized. Except some examples, a majority of artificial foldamers possess folding conformations such as canonical helices, linear strands, turns, and sheetlike structures, typical folding patterns observed in biopolymers [6]. The most common aromatic foldamers are the helices derived from oligoamides [7]. Their high potentialities mimicking this secondary structure of biopolymers originate in the restricted rotation of aryl–amide bond through specific attractive and repulsive interactions between the amide and the other functional groups at the *ortho* position on the aryl moiety. The sequence of this conformational restriction results in the curvature of the oligomeric strand [8]. As another class of artificial aromatic foldamers creating helices, *m*-phenyleneethynylene oligomers have been developed [9]. They are potentially suitable for piling up aromatics. Their helical structures are formed solvophobicly or by inclusion of guest molecules [10]. Because of their flexible structures, folding and unfolding of them can be driven dynamically [11]. An attempt was made to use them as reactive sieving for mimicking enzyme behavior [12]. Aromatic foldamers other than the helical type, the zigzag type, are known. In this type, aromatic rings are connected with U-shaped linkers to create a columnar array of aromatic rings.

Therefore, the linkers to connect aromatic rings are important. Conformational regulations are required by the linkers to place the connected aromatic rings in a position facing each other. Urea-[13], guanidine- and guanidium- [14], and imide [15]-derived linkers are the suitable ones for this purpose. Some aromatic oligoureas, oligoguanidiniums, and oligoimides form stacked arrangement by using the combinations of aromatic stacking interactions and the preferred conformations of backbones by steric hindrance and/or by electrostatic repulsion. They are stacked in a zigzag fashion to create a pillar-like columnar array of aromatic rings.

In this chapter, folded architectures, such as pillars, stacked ribbons, and helices created in the crystalline state by stacks of aromatic rings in a zigzag way, are discussed. The piling of aromatic rings by folding is interesting from the viewpoints of enhanced physical and spectroscopic properties induced by stacking.

## 11.2 Foldamers Based on Ureylene Linker

### 11.2.1 *U-Shaped Conformation of $N,N'$ -Disubstituted Aromatic Ureas*

In the early 1970s, conformations of *N*-substituted arylureas were examined to possess U-shaped conformations in which two phenyl rings aligned parallel to each other both in crystal structure [16] and in solution [17]. Recently, the origin

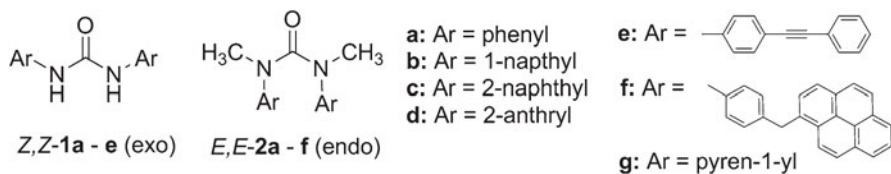


**Fig. 11.1** Chemical structures of diarylurea derivatives with unfolded and folded conformations

of conformational preference of *N,N'*-diaryl-*N,N'*-dimethylureas was intensively studied by electronic structure calculations using density functional (M06-2X) and a DFT approach (DFT-D) [18]. The calculations predicted that the *exo* conformer of *N,N'*-diphenylurea (**1a**) is favored over the corresponding *endo* conformer by  $9.0 \text{ kJ mol}^{-1}$ . On the contrary, the *endo* ( $\pi$ -stacked) conformer of *N,N'*-dimethylated diphenylurea (**2a**) becomes favored by  $15.1 \text{ kJ mol}^{-1}$  than the *exo* conformer (Fig. 11.1). There are some confusions on the nomenclature of urea conformations. In this review, their conformations are classified according to the nomenclature by Clayden and Lewis. It is clear that the steric repulsion between the methyl groups and the ortho hydrogens of the phenyl groups in the *exo* conformer is responsible for this reversal in stability. It is noted that the *endo* conformer is not symmetrical. The phenyl rings are displaced with respect to each other.

Such conformational changes induced by *N,N'*-dimethylation caused the alteration of emission of fluorescent diarylureas from monomer to excimer emission. It is known that the trimethylene is the optimal length as the linkers to connect polynuclear aromatic hydrocarbons for the formation of intramolecular fluorescent excimers. A strain-free geometry suitable for a face-to-face interaction of aromatic moieties can be created with this linker. 1,3-Diarylalkanes, such as naphthalene [19], anthracene [20], and pyrene [21] derivatives, were examined. This concept was first applied to tertiary *N,N'*-diarylureas by Lewis et al. The secondary diarylureas, **1c** and **1d**, were strongly fluorescent, whereas tertiary ones, **2c**, **2d**, and **2g**, showed broad and red-shifted fluorescence [22]. The crystal structures and solution NMR spectra of the secondary and tertiary di-1-naphthylureas, **1b** and **2b**, established that they adopted extended (*Z,Z*) and folded (*E,E*) structures, respectively, both in the solid state and in solution [23]. The tertiary urea **2b** exhibited blue-shifted absorption and red-shifted emission in contrast to the typical naphthalene-like monomer absorption and fluorescence spectra of the secondary one **1a**. The unfolded phenylacetylene-substituted urea **1e** showed its fluorescence maximum wavelength at 348 nm while that of folded **2e** appeared at 454 nm. The fluorescence quantum yield of **2e** was one fortieth of **1e** [24]. Conformational change from unfolded to folded by *N*-methylation was visualized via fluorescence change in the pyrene derivatives **1g** and **2g** [25].

The stacking of multiple aromatic rings by connecting with ureylene linkers was first achieved with the *N*-methylated pentaphenyl urea **3** [13]. Its crystal structure showed that it had five-layered folded structure in which all four ureylene linkers possessed (*E,E*) conformation (Fig. 11.2a). The distances between aromatic carbon

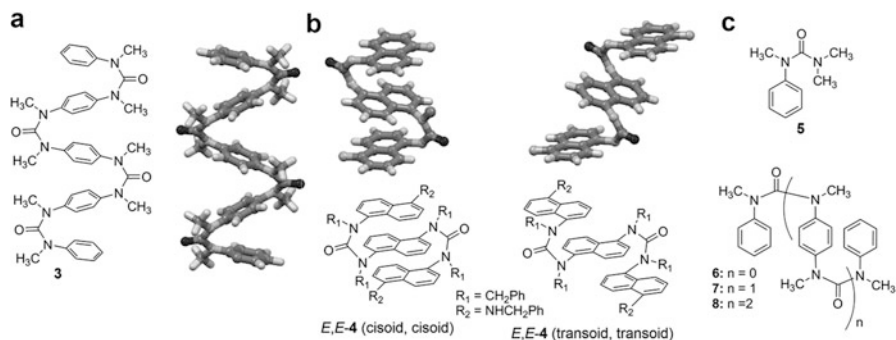


**Fig. 11.2** Chemical structures of tertiary oligoarylureas with folded conformations (a–c) and crystal structures of (a) for **3** and (b) for **4**. Benzyl groups are omitted in the crystal structure of **4** for clarity

atoms bearing a nitrogen atom are 3.31 Å (the first and second) and 2.96 Å (the second and third), which indicates that the molecule has a well-folded structure. Its solution stereochemistry is considered to be quite similar to that in crystal structure based on the NMR chemical shifts. Similar *N*-benzylated oligomers of 1,4-diureidobenzenes and 1,5-diureidonaphthalenes were prepared up to their 9-mers [26]. Two conformers were observed in the crystal structure of the trimer of 1,5-diureidonaphthalenes **4** (Fig. 11.2b). In both conformers the ureylene linkage takes (*E,E*) conformation. However, the orientation of the naphthalene rings in respect to each other is different. The cisoid/cisoid and transoid/transoid conformations existed.

The effect of the degrees of the stacking of aromatic rings on the physical properties of *N*-methylated tertiary oligo(arylureas) has been intensively studied by Lewis et al. [27–29]. The NMR chemical shifts, absorption and emission maxima, and electrochemical oxidation potentials of a series of oligomeric *N*-methylated tertiary oligoarylureas possessing one to five phenyl rings, **3**, **5–8** (Fig. 11.2c), were all dependent on the number of phenyl rings. ZINDO calculations showed that the frontier orbitals of the ureas with one to three phenyl rings were localized on a single phenyl ring, whereas those of the higher oligomers were delocalized over two phenyl rings [27]. Arylurea oligomers were applied to the generation of polyaryl anion radicals by reductive elimination of the urea linkages with alkali metal [28]. Molecular wirelike behavior of them was demonstrated by oligo(arylureas) bearing a hole donor and hole acceptor as capping groups separated by phenylene linkages [29].

The way of connection of benzene rings in aromatic multilayered oligophenyleneureas was found to be important to induce helical structures in solution. Crystal structure of five-layered oligoarylureas of *m*-phenylenediamine **9** showed that it had  $\pi$ -stacked helical structure [30]. Similar helical conformations of unsymmetrical *N*-substituted oligoarylurea foldamers based on a *m*-phenylenediamine monomer possessing up to eight ureylene linkers were examined both in solid

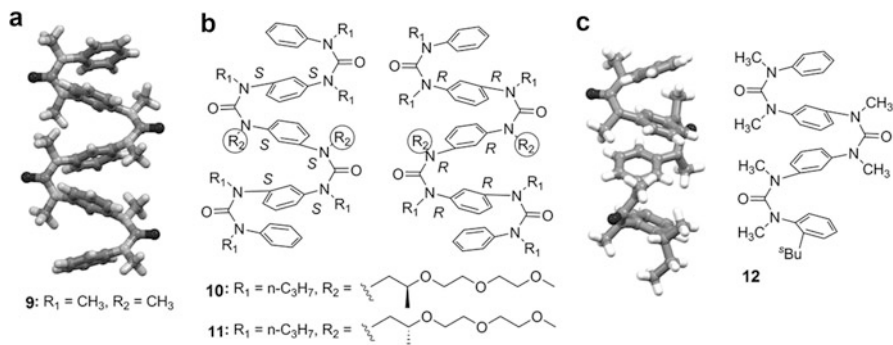


**Fig. 11.3** (a) Crystal structure of *m*-substituted oligourea **9**, (b) chemical structures of **10** and **11**, and (c) crystal structure of unsymmetrical *m*-substituted oligourea **12**

state and solution. Ring-stacked conformations observed in X-ray crystal structure persisted in solution indicated by  $^1\text{H}$  NMR study [31]. Figure 11.3c shows the crystal structure of four-layered unsymmetrical oligourea **12**.

An attempt was made to control its dynamic helical structure (all-*R* or all-*S* axis chirality) in solution by introducing chiral *N*-substituents. Oligoureas **10** and **11** possessing two chiral *N*-2-(methoxyethoxyethoxy)propyl groups were prepared, and their CD and vibrational CD (VCD) were examined [32]. Observation of the CD and VCD spectra of **10** as mirror images of those of **11** indicated the induction of handedness in the helical structure. Helix persistence and breakdown in oligourea foldamers were investigated by Clayden et al. [33] Oligomeric ureas derived from *m*-phenylenediamine with chain lengths of up to seven ureylene linkages bearing a terminal chiral sulfinyl or amide group were examined to show that the transmission of chirality in these systems was limited to about 24 bond lengths. The oligoureas of short lengths adopt a defined helical secondary structure in solution, but the helicity breakdown occurs in longer oligomers.

### 11.2.2 Hydrogen-Bonding Approach Using U-Shaped Ureadicarboxylic Acids as Building Blocks

Among the linkers to connect aromatic rings in a U-shaped fashion for the creation of pillar-like columnar structures, the ureylene linker seems to be the most effective one. Considering this point, the novel U-shaped aromatic urea molecule appended with hydrogen-bonding (H-bonding) sites, *N,N'*-dimethyl-*N,N'*-diphenylureadicarboxylic acid **13**, was prepared as an efficient folded building block for the construction of a variety of aromatic folded structures in the crystalline state via H-bonding [34]. *N,N'*-Dimethylation ensures a face-to-face conformation. Single-crystal X-ray structure of **13** shows it has a U-shaped folding structure

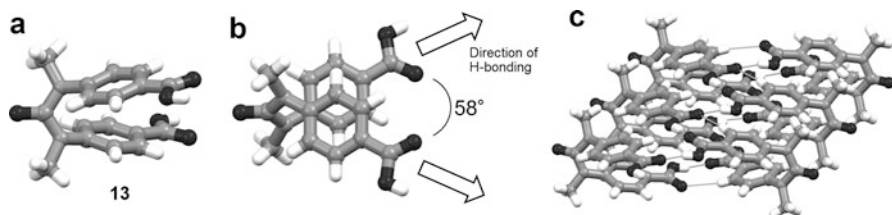


**Fig. 11.4** Crystal structures of ureadicarboxylic acid **13**. (a) Side and (b) top views and (c) the double catemeric structure created by H-bonding networks

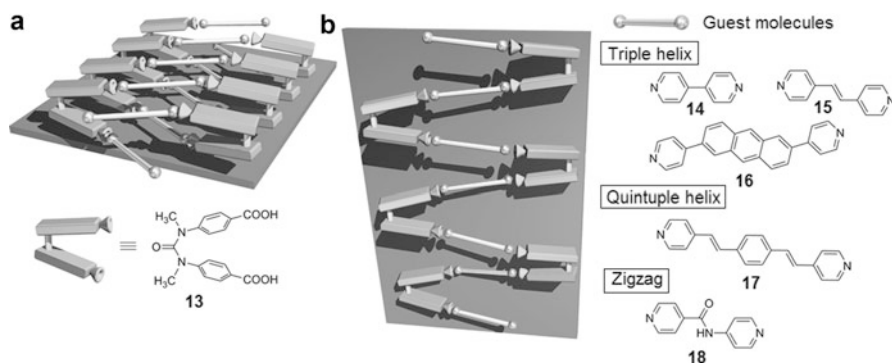


**Fig. 11.5** Schematic representation of two types of assemblies derived from the U-shaped building block **13** with H-bonding acceptor molecules. (a) Helical and (b) zigzag architectures

(Fig. 11.4a). The molecule is twisted with the torsion angle of  $58^\circ$  between the two phenyl groups (Fig. 11.4b). It means that **13** can create H-bonding with two molecules of H-bonding acceptors to settle them with this angle. Because of this torsion, no dimeric type H-bonding between two carboxy groups was observed. The infinite H-bonding in a helical way afforded double catemeric structure resulting in the formation of a rodlike structure with almost no cavity inside (Fig. 11.4c). The interesting feature of this building block is that it can make cocrystals with H-bonding acceptor molecules possessing two H-bonding sites in two ways of infinite H-bonding to construct helical and zigzag architectures. This is schematically represented in Fig. 11.5.

Several dipyriddy derivatives were subjected to cocrystallization with **13**. Carboxylic acids and pyridine derivatives are well-known pairs forming H-bonding [35]. Pyridine derivatives, **14–18**, afforded cocrystals with **13**. Triple helices were observed in the cocrystals of **13** with **14**, **15**, and **16**. The crystal structures of triple helices observed in the cocrystal of **13** with **14** are shown in Fig. 11.6. Triple helices of the same type were constructed with **15** and **16**. The pitch of the triple helix is ca. 20 Å for the three of them. Almost the same width of the included dipyriddy derivatives but with a different length afforded the triple helices with the same pitch with a different width. However, the unique quintuple helix was

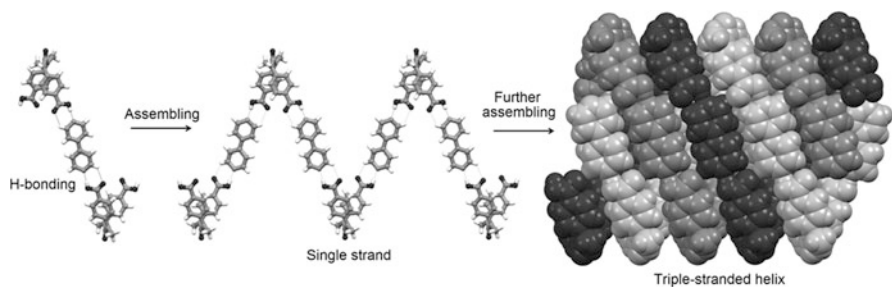


**Fig. 11.6** Crystal structure of triple helix observed in the cocrystal of **13** with **14** in a space-filling model. Strands are colored with three different colors to distinguish each strand

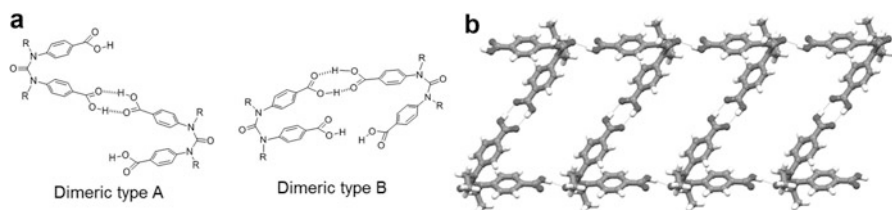


**Fig. 11.7** (a) Two types of the dimeric H-bonding of ureadicarboxylic acids. (b) Ladder-type H-bonding network in the crystal structure of *N,N'*-diethylureadicarboxylic acid

created recently in the cocrystal of **13** with **17**, although the molecular width of **17** is almost the same to other bipyridyl derivatives [36]. The stacking between the strands affected the fluorescence of **16**. It showed excimer emission in the solid state as cocrystals in contrast to the observation of monomer emission in solution. Since the pioneering work by Lehn, many examples of metal complexes of triple-stranded helicates have been reported [37]. However, a triple helix without an assistance of metal coordination has been hardly reported [38]. In contrast to the helix formation, a zigzag architecture was created in the cocrystal of **13** with **18**. Spontaneous chiral induction afforded chiral cocrystals from achiral molecules. Formation of enantiomeric cocrystals was confirmed by the observation of their mirror-image CD spectra. The crystal structure of the cocrystals showed that the folding unit **13** had the unidirectional torsion, which furnished a chirally twisted zigzag tape.

Versatility of the ureadicarboxylic acid building block has been further demonstrated for the construction of ladders, channels [39], and cyclic heterotetramers [40]. *N,N'*-Diethyl- and diallyl-substituted ureadicarboxylic acids gave ladder-type networks in their cocrystals with bipyridine. Figure 11.7a shows two types of dimeric H-bonding type, A and B, depending on the orientation of ureadicarboxylic acids. The type A is the dimeric H-bonding created among the upper carboxyls of the neighboring ureadicarboxylic acids. The dimeric type B involves H-bonding among upper carboxyls or bottom carboxyls. Ladder-type structures are created by using one of the carboxyls in the dimeric type A for H-bonding with the carbonyl of the ureylene moiety. When linear H-bonding acceptor molecules are inserted

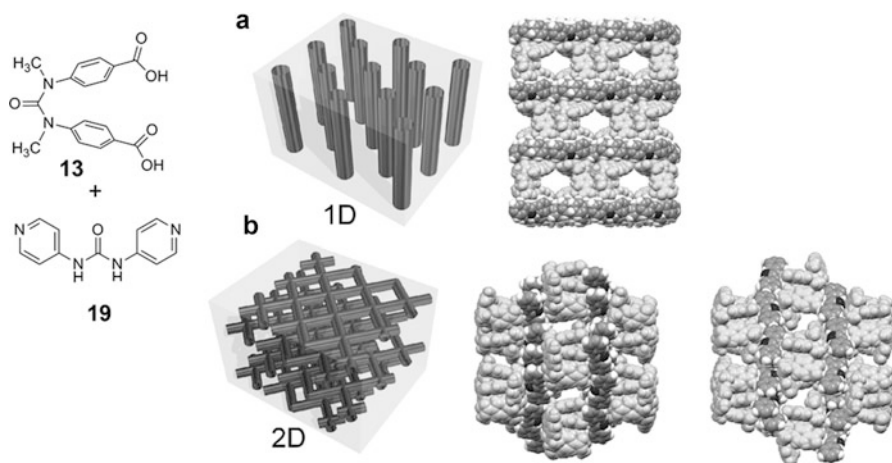


**Fig. 11.8** A schematic representation and crystal structure (a space-filling model) of channels created in the cocrystals of **13** and **19**. (a) A schematic representation of one-dimensional channel and the crystal structure viewed along the crystallographic  $c$ -axis. (b) A schematic representation of two-dimensional channel and the crystal structure viewed from the direction of  $[110]$  (left) and  $[-1-10]$  (right). Two conformations of **13** with different tone colors in the channel are omitted for clarity

in the dimeric type A H-bonding network, zigzag architectures will be created. On the contrary, in the insertion of H-bonding acceptor molecules in the dimeric type B H-bonding network, helical structures can be created. Unique channel structures, namely, one-dimensional and two-dimensional channels, were formed in the cocrystals of ureadicarboxylic acid **13** with dipyridylurea **19**, a combination of the U-shaped urea and the linear-type urea. It was reported that **19** could assemble linearly in the presence of dicarboxylic acids [41]. A pyridinium generated by the protonation with carboxylic acids creates a H-bond with the remaining pyridyl moiety. Linear array of **19** is afforded by the sequential H-bonding. Carboxylates generated after protonation interact with the urea moiety by H-bonding to give channels. Two carboxylates of the U-shaped building block connect the two straight scaffolds. Crystal structure of methanol-solvated cocrystal of **13** with **19** (molar ratio; **13**:**19**: MeOH = 2:3:4) showed a channel structure in which methanol and water molecules were included. Figure 11.8a shows the channels viewed along the crystallographic  $c$ -axis in which included methanol and water molecules are omitted for clarity. Two conformations of **13**, ( $E, E$ ) and ( $E, Z$ ), existed in the crystal structure. They are presented with different tone colors. In contrast to this one-dimensional channel, unique fishnet-type two-dimensional channel was constructed when the solvent for recrystallization was changed from methanol to ethanol (Fig. 11.8b).

The folding nature of ureadicarboxylic acid was applied to cyclic assembly [40]. A torsional angle of  $58^\circ$  between two phenyl moieties in **13** is close to an ideal angle  $60^\circ$  for cyclic assembly. It can pursue cyclic assembly with organic bases

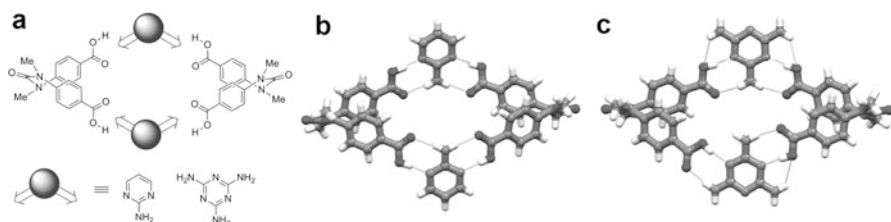


**Fig. 11.9** Crystal structures of cyclic heterotetramers. (a) A schematic representation of cyclic assembly of **13** with aromatic bases and cyclic heterotetramers with (b) 2-aminopyrimidine and (c) melamine

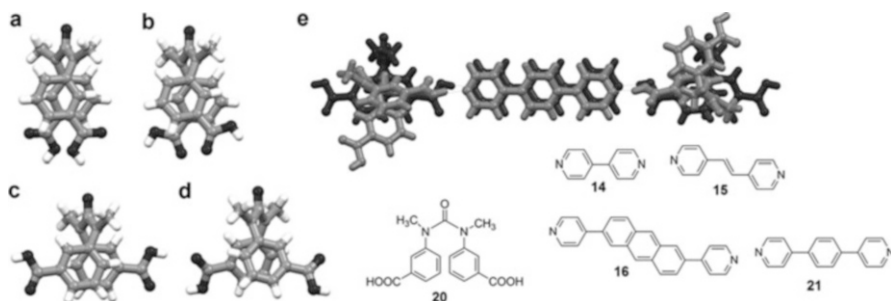


**Fig. 11.10** Comparison of the conformations of **20** (top views) found in the crystal structures of (a) **20**, (b) **20**•**14**•(H<sub>2</sub>O)<sub>3</sub>, (c) **20**•**21**•CH<sub>3</sub>OH, and (d) **20**•**21** and (e) superimposed image of the way of H-bonding of **21** in both cocrystals in which the structures of **20**•**21**•CH<sub>3</sub>OH and **20**•**21** are colored with different tone. The same types of conformations as (b) and (d) were observed for **20**•**15** and **20**•**16**, respectively

possessing two H-bonding sites located with an angle of 120° with respect to each other (Fig. 11.9a). Cyclic heterotetramer motifs of rhombus shapes were created as a 2:2 mixture of **13** and 2-aminopyrimidine (Fig. 11.9b) and melamine (Fig. 11.9c). The H-bonded eight-membered-ring R<sub>2</sub><sup>2</sup>(8) heterosynthon is responsible for the cyclic heterotetramer formation. This heterosynthon is involved in the 2:1 cocrystal formation of carboxylic acid with 2-aminopyrimidine [42].

The effects of the positions of carboxy groups on the folding architecture created by U-shaped urea building blocks have been investigated by employing *meta*-substituted ureadicarboxylic acid **20** as a folded building block [43]. Because of the flexible conformation of the molecular framework of *meta*-substituted ureadicarboxylic acids, many U-shaped conformations can be generated. There are three possible geometrical relations of two carboxy moieties in them. In each geometrical relation, three possible orientations of carboxy moieties exist. Therefore, a total of nine U-shaped conformations can possibly be taken instead of a single U-shaped conformation in *para*-substituted one. Cocrystals of **20** were prepared with four bipyridyl derivatives. Out of six crystal structures including **20**, four types of U-shaped conformations were found. Figure 11.10 shows crystal structures of these four U-shaped conformations. The direction of H-bonding was regulated by these

conformations. Triple helices with one-dimensional water channels were created in the cocrystals with **14**. Infinite crossbelt structures and steplike structures were observed in the cocrystals with **15**, **16**, and **21**. Pseudo-polymorphic cocrystals of **20** and **21** were obtained with and without inclusion of methanol molecules. They have different U-shaped conformations of **20**. They are shown as a superimposed image in Fig. 11.10e.

### 11.2.3 S-Shaped Aromatic Ureadicarboxylic Acid

To diversify the folding architectures, S-shaped ureadicarboxylic acid building blocks **22**, **23**, and **24** were prepared [44]. Because of their flexible molecular framework, two types of conformations, meso and helical, possibly exist. However, crystal structures of them showed that they were all meso conformers. Their conformations are similar to that of S-shaped bisurea without a carboxy group. Figure 11.11b shows the crystal structure of DMF solvate of **22** as a representative example. Two DMF molecules are inserted between the carboxy groups via H-bonding, and the zigzag H-bonding network is created. Single crystals of **23** and **24** were obtained as solvent-free crystals. Unique cocrystals of **22** and **23** with melamine were obtained. Both cocrystals showed almost the same crystal

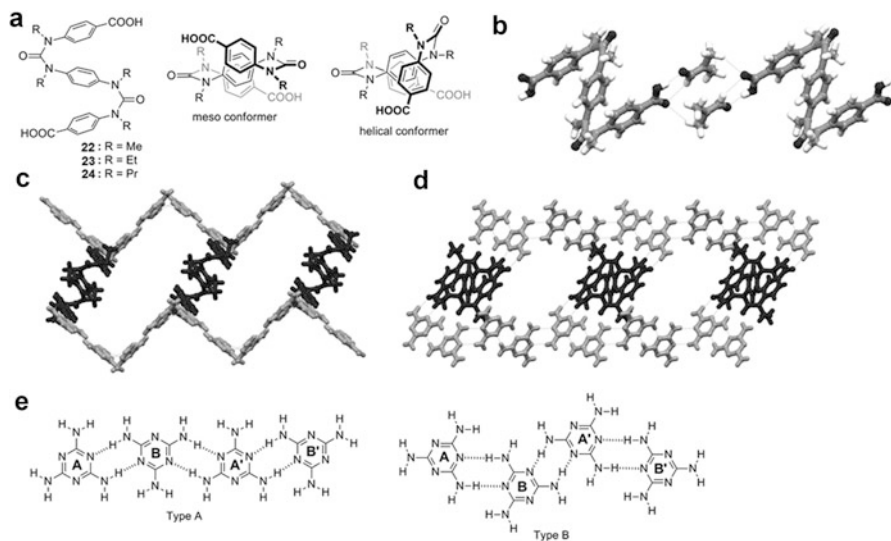


**Fig. 11.11** Crystal structures of S-shaped ureadicarboxylic acids and cocrystals with melamine. (a) Chemical structures and possible conformations of them, (b) the crystal structure of DMF solvate of **22**, (c) and (d) the crystal structures of the cocrystal of **23** with melamine viewed along the crystallographic *a*- and *b*-axes, respectively, in which the molecules of **23** and melamine are colored with different tone, and (e) two common patterns of H-bonding networks of melamine

structures in which unusual zigzag tapes of H-bonding network of melamine molecules were created. The zigzag tapes were connected with S-shaped ureas by H-bonding to furnish interpenetrated fishnet-type crystal structure. Figure 11.11c, d shows the fishnet structures in the cocrystal of **23** and melamine viewed along the crystallographic *a*- and *b*-axes, respectively. Two common patterns of H-bonding networks of melamine, type A and B, with graph set  $R^2_2(8)$  are presented in Fig. 11.11e. Type B H-bonding pattern is observed in the crystal structures of the cocrystals of **23** and **24** with melamine. A Cambridge Structural Database (CSD) search for the H-bonding network of melamine and melaminium showed that the type B network had almost a flat structure. For example, a melamine sheet structure was reported in which six molecules of melamine were assembled in a cyclic way to give a hexagonal unit [45]. In contrast to the known type B flat network, the cocrystals of S-shaped ureadicarboxylic acids and melamine possess H-bonding networks of melamine as zigzag tapes.

## 11.3 Foldamers Based on Iminodicarbonyl Linker

### 11.3.1 U-Shaped Aromatic Acyclic Imides

Some aromatic acyclic imides are also known to adopt their molecular structures to be U-shapes in their crystal structures. Examples of the U-shaped molecular structures of them determined by X-ray crystallographic analyses are shown in Fig. 11.12. Diastereoselective and enantioselective [4 + 4] photocycloaddition reactions of **25** [46] and **26** [47], respectively, were examined in solid state. Compound **26** was obtained as chiral crystals with space group  $P2_1$ . The solid-state photoreaction of **26** gave the corresponding cycloadduct with almost 100% ee. The solid-state [4 + 4] photocycloaddition of 2-pyridone derivative **27** [48] proceeded efficiently with high stereoselectivity. The concaved nature of an iminodicarbonyl linker was utilized for the design of liquid crystalline dimers consisting of two

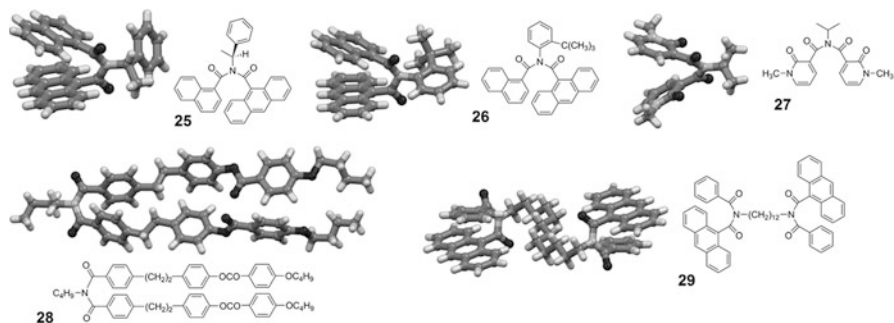
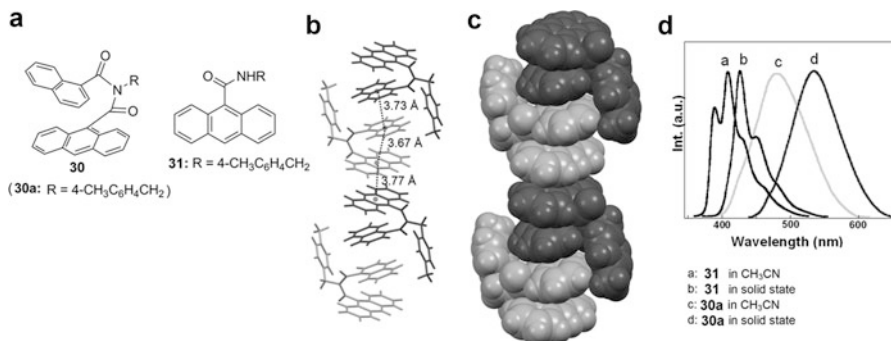


Fig. 11.12 Crystal structures of acyclic aromatic imides with U-shaped molecular structures



**Fig. 11.13** Crystal structures and fluorescence spectra of U-shaped imides possessing naphthyl and anthryl moieties. (a) Chemical structures, (b) and (c) columnar packing of **30a** in stick- and space-filling models, respectively, and (d) fluorescence spectra of **30a** and **31**. The distances between the centroids of the adjacent aromatic rings are indicated in (b)

mesogenic units in parallel conformation. In compound **28** [49], two mesogenic cores were connected by an imidodicarbonyl moiety. The crystal structure of **29** [50] in which two U-shaped acyclic imides were connected with a 12 methylene chain was reported. The structure contained two *s*-cisoid connections to have a compact crystal packing.

The relation between the crystal packing of U-shaped aromatic acyclic imides and their fluorescence in solid state was examined [51]. A series of compounds **30** (ten compounds with different N-substituents) showed their fluorescence emission maxima at 480–486 nm in  $\text{CH}_3\text{CN}$ , whereas they ranged from 459 to 535 nm in solid state. They were affected by the way of crystal packing. The longest emission maximum wavelength, 535 nm, was observed for **30a**. Its packing structures are shown in Fig. 11.13b, c in stick- and space-filling models, respectively. The molecules of **30a** are piled up via  $\pi$ – $\pi$  stacking to create a columnar array of naphthalene and anthracene rings. Compounds with the packing structures similar to **30a** showed similar fluorescence to it. The compounds that exhibit shorter emission maxima (459–473 nm) lack the stacking between the anthracene moieties. Therefore, the longer fluorescence wavelengths of the U-shaped aromatic acyclic imides originate in the efficient overlapping between the two neighboring anthracene rings. Figure 11.13d shows the comparison of the fluorescence spectra of **30a** and amide **30b** in solution and solid state.

In order to examine the conformational stability of U-shaped acyclic aromatic imides in solution, CD spectra of chiral imides **26** and **32** were examined in solid state and  $\text{CHCl}_3$  [52]. Although **26** and **32** have no chiral center, they gave enantiomeric chiral crystals spontaneously upon recrystallization. Bulkiness of the N-substituents could play a crucial role in displaying CD in solution. Without the aid of steric hindrance by the bulky N-substituents, immediate racemization or epimerization occurs after dissolving to result in the observation of no CD signal.

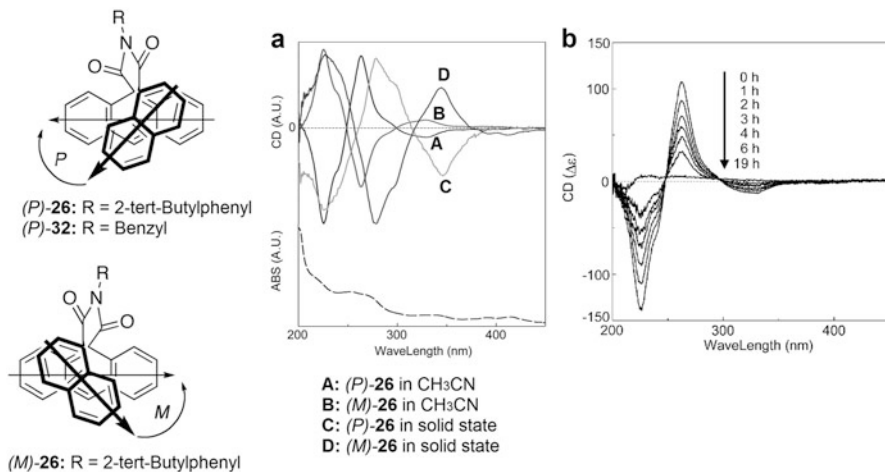


**Fig. 11.14** CD spectra of chiral U-shaped acyclic aromatic imides **26**. **(a)** CD spectra of (*P*)-**26** and (*M*)-**26** in solution (CH<sub>3</sub>CN) and in the solid state (KBr). Absorption spectrum of **26** in the solid state (KBr) is indicated by *dashed lines*. **(b)** CD spectral change of (*P*)-**26** heated at 70 °C in CH<sub>3</sub>CN

Indeed, no CD signal was observed for **32** in solution. In contrast, enantiomeric chiral crystals of (*P*)-**26** and (*M*)-**26** gave CD signals of mirror images in solution as well as in the solid state (Fig. 11.14a). Induced CD signal that appeared for **26** in the region between 315 and 400 nm is due to the exciton coupling between the anthryl and naphthyl chromophores [53]. Identical signs of Cotton effect and the similar shape of the spectra to those in the solid state were observed after dissolving, which indicated that their folded conformations in crystals were retained even in solution. To examine the thermal stability of **26**, the time-dependent CD spectrum of (*P*)-**26** was measured at 70 °C in CH<sub>3</sub>CN (Fig. 11.14b). The activation energy of the racemization was calculated to be 27.9 kcal/mol.

### 11.3.2 Chiral Photochromic System Based on Reversible [4 + 4] Photocycloaddition of S-Shaped Iminodicarbonyl-Based Foldamers

Conformationally stable photoreactive chiral *S*-shaped iminodicarbonyl-based foldamers possessing anthracene and naphthalene moieties were studied as reversible chiral photochromic system [52]. Figure 11.15a shows a schematic representation of a chiral T-type photochromic system. A CD active form becomes a CD inactive form after a cycloaddition reaction. In the [4 + 4] cycloadduct, the exciton coupling between the anthracene and naphthalene moieties no longer exists.

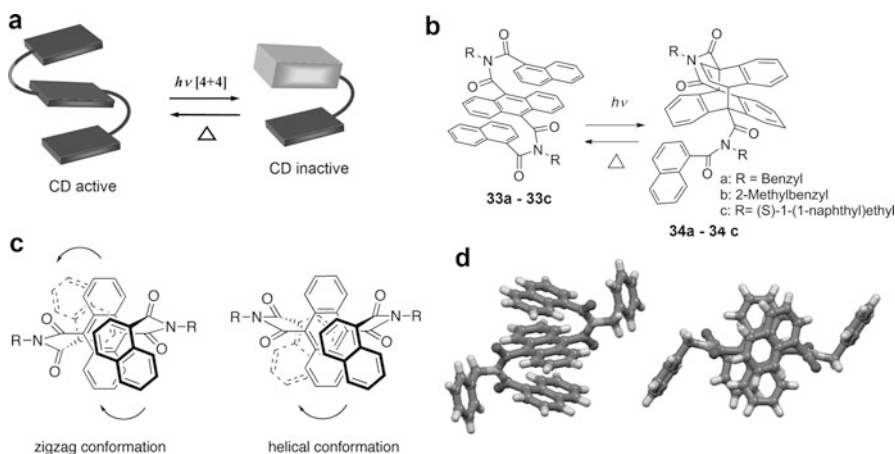


**Fig. 11.15** (a) A schematic representation of a reversible T-type chiral photochromic system, (b) S-shaped imide foldamers for the [4 + 4] photocycloaddition and their thermal retro-cycloaddition reactions, (c) two possible folding patterns of S-shaped foldamers, and (d) side and top views of single-crystal X-ray structures of **33a** with zigzag conformation

Therefore, the cycloadduct is a CD inactive form (Fig. 11.15b). Out of two possible conformations, zigzag and helical, the helical conformation is the desirable one for induced CD (Fig. 11.15c). Crystal structures of **33a** (Fig. 11.15d) and **33b** showed that they had zigzag conformations. Cycloadditions proceeded in  $\text{CHCl}_3$  in a quantitative yield. The most bulky compound **33c** showed the shortest half-life of cycloreversion (8.5 h at ca. 25 °C). Some sterically constrained molecules have been known to undergo ring opening. The norbornadiene–quadricyclane cycle is a good example of a ring-strain-driven T-type photochromic system [54]. The driving force for the cycloreversion of the cycloadducts of S-shaped foldamers is similar to this, the steric constraint generated by cycloaddition. The bi-planemer [55]-type adduct thrusts its planes up- and downward to cause steric compression on the remaining naphthoyl moiety. Due to this steric constraint, the cycloreversion occurs to release the steric energy.

The S-shaped foldamer **33c** showed induced CD in  $\text{CHCl}_3$ , which indicated that it had helical conformation in solution. Figure 11.16a, b shows the CD spectral changes of **33c** during irradiation and the subsequent thermal cycloreversion, respectively. After the completion of the photocycloaddition, almost no CD signal was observed. Recovery of the CD signal was observed after heating. This indicated that the original helical conformation of **33c** was regenerated completely after thermal cycloreversion. Irradiation and heating were carried out alternately to show the effectiveness of the system.

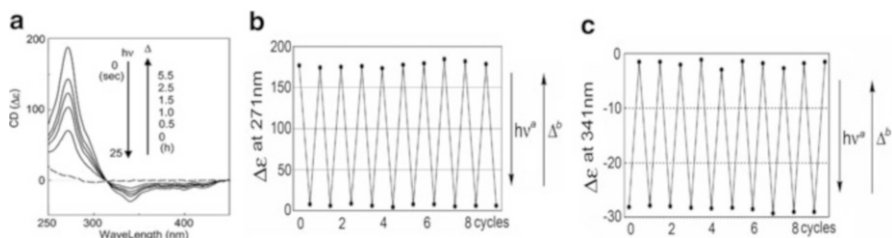


**Fig. 11.16** (a) CD spectral changes of **33c** to **34c** after irradiation (>290 nm), changes from *top* to *bottom*, and thermal recovery of **34c**, changes from *bottom* to *top*, at ambient temperature (ca. 25 °C) in  $\text{CHCl}_3$ . CD spectral changes ( $\Delta\varepsilon$ ) observed in (b) and (c), irradiation<sup>a</sup> was carried out with a high-pressure mercury lamp for 25s and heating<sup>b</sup> was carried out for 20 min at 60 °C

### 11.3.3 Chirality Amplification

Aromatic imides possessing one, two, three, and five naphthalene rings connected at their  $\alpha$ -position with iminodicarbonyl linkers were examined to elucidate the effect of folding on their physical properties, especially chirality amplification [15]. Single crystals were obtained for trimers **35a–35e**, while powders were done for pentamers. Molecular structures of all five trimers obtained by single-crystal X-ray analysis are similar. Figure 11.17 shows the molecular structure of **35a** as a representative example. The main chain has a zigzag-type structure. Three naphthalene rings in a main chain are stacked on each other with neighboring naphthalene rings and spread out radially. The molecule has a helically zigzag conformation. In all five crystal structures, the distances between the naphthalene rings are in the range of 3.5–3.9 Å, which is the typical distance for  $\pi$ – $\pi$  stacking [56]. The average values of 134–139° for the torsion angles between the naphthalene rings mean that roughly three naphthalene rings are expected to exist per pitch in longer oligomers. The folding conformations of these molecules in solution were confirmed by the upfield shift of the protons at the  $\alpha$ -position of the central naphthalene rings in their  $^1\text{H}$  NMR spectra and also attested by the observation of NOE between the protons of the two neighboring naphthalene rings.

To examine chirality amplification in foldamers [57], the CD spectra of the series of compounds with different numbers of naphthalene rings possessing chiral auxiliaries, (*S*)-1-phenylethyl and (*S*)-1-(1-naphthyl)ethyl, were measured (Fig. 11.18a). In the (*S*)-1-phenylethyl series, only marginal CD signals were observed both in solution and solid state even for the five-storied foldamer. Switching of chiral induction using solid-state–solution-state equilibrium was known in helical oligoamides [58]. The equilibrium inclined to a stable diastereomer in solution when crystals composed of two diastereomers of helical oligoamides were dissolved, which resulted in induction of handedness. The *N*-substituent, the (*S*)-1-phenylethyl group, is not bulky enough to incline the equilibrium to one of the diastereomers to induce handedness. Nearly equivalent amount of two diastereomeric folded forms

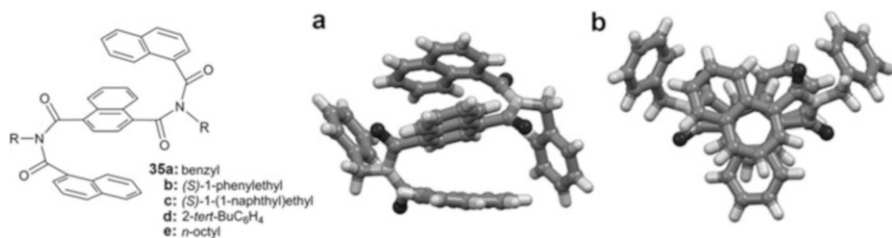


**Fig. 11.17** Crystal structures of **35a**. (a) Side and (b) top views

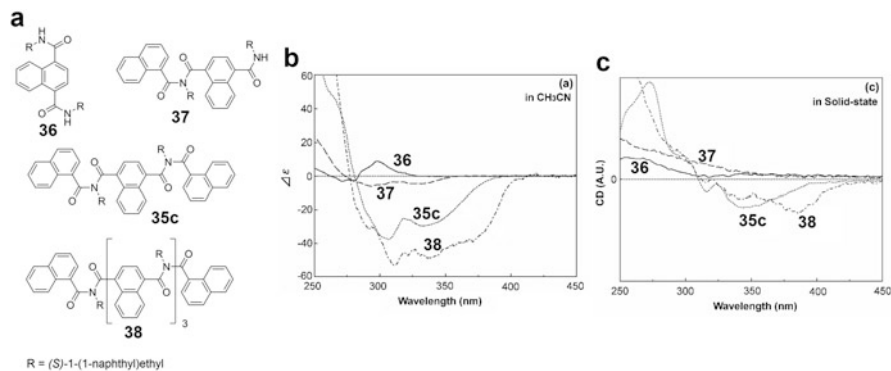


**Fig. 11.18** CD spectra of **36**, **37**, **35c**, and **38**. (a) Chemical structures (b) in CH<sub>3</sub>CN (20 μM) and (c) in solid state

exists in solution. In contrast, (*S*)-1-(1-naphthyl)ethyl series showed induced CD both in solution and solid state. Comparing with **36** and **37**, intense CD signals were observed for **35c** and **38**, the compounds with three and five naphthalene moieties, respectively (Fig. 11.18b, c). These CD signals correspond to the band caused by  $\pi$ - $\pi$  interactions between naphthalene moieties in the UV-vis absorption spectra [53]. The compound **38** showed an extra negative Cotton effect in a longer wavelength region than that of **35c**. The results were consistent with the UV-vis spectral behavior of **38**, whose absorption band shifted 25 nm compared that of **35c** at a longer wavelength.

It is plausible that the observed conformation in the crystal structure is the stable conformation of it in solution. The same sign of Cotton effect for **35c** and **38** indicates that both compounds have the same helicity. However, it is not always unambiguous to determine the secondary structure by comparing the similarity of CD signals [59]. It is difficult to predict which conformation, zigzag or helical, will be the preferable folding conformation even in simple S-shaped molecules. An introduction of a chiral group tends to create a helical one. This tendency was observed in the crystal structures of the S-shaped aromatic imide foldamers in which three aromatic rings are connected with imidodicarbonyl linkers in a sequence anthracene-phenylene-anthracene [60].

## 11.4 Stacked Ribbon-Type Foldamers

At the end of the chapter, it is noteworthy to mention about the recent development in stacked ribbon-type foldamers as extended zigzag-folding architectures. Sheetlike structures have less frequently been observed comparing with helical synthetic foldamers [4]. It is explained that the removal of sheets from the context of a tertiary structure as found in proteins is difficult because of their tendency to aggregate and precipitate. To avoid aggregation, an effort was made to design the molecular structures of aromatic oligoamides in which noncovalent interactions occur preferentially in an intramolecular fashion. Following this idea, Huc et al. reported synthesis and structural characterization of discrete aromatic oligoamide  $\beta$ -sheet foldamers by using rigid turn units and short linear strands [6]. Figure 11.19 shows the crystal structure of heptadecamer **39** with the five-stranded conformation. The xylyl groups are perpendicular to the dinitrophenyl moieties. The layer distance between a face-to-face stacked terephthalamide groups is ca. 3.5 Å. The aryl-aryl distance between the xylyl groups imparted by the dinitrobenzene unit is 4.8 Å. This indicates the attractive interactions between stacked linear segments. Two-stranded sheets with less rigid turn units and longer linear strands were also reported [61]. The usefulness of the 4,6-dinitro-1,3-diaminophenyl moiety as rigid turn unit was also demonstrated in oligo-*m*-aniline foldamers. They gave a snake-shape folding structure in the crystalline state [62].

Anthracene-stacked oligomers and polymers were synthesized using xanthene skeleton as the scaffold [63]. Very rigid turn units were created by the xanthene with ethynyl linkers at its 4 and 5 positions. Figure 11.20 shows the chemical

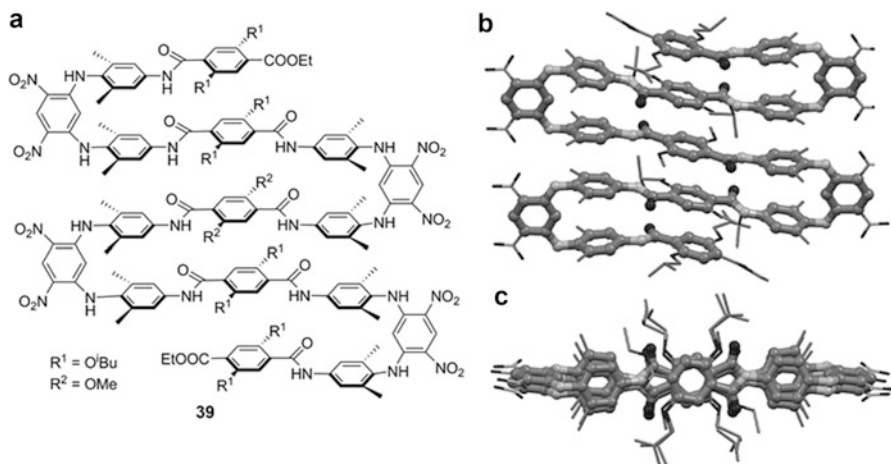


**Fig. 11.19** (a) Chemical structure of heptadecamer **39** as a four-turn  $\beta$ -sheet foldamer and (b) top and (c) side views of the crystal structures of **39**. Hydrogen atoms and included solvent molecules are omitted and a backbone structure is emphasized with *bold sticks*

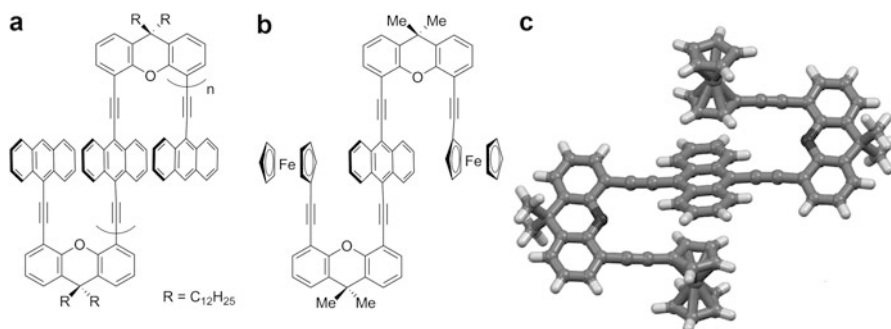


**Fig. 11.20** (a) and (b) chemical structures of anthracene-stacked oligomers with xanthene turn units **40** and a model compound **41**, respectively, and (c) crystal structure of **41**

structures of the oligomers and the S-shaped crystal structure of the model compound with terminal ferrocene units. Intramolecular  $\pi$ - $\pi$  stacking of the anthracene rings in the ground and excited state was observed. Similar anthracene-stacked oligomers were prepared with 1,8-anthrylene-ethynylene as the turn unit. Their folding and unfolding were controlled by [4 + 4] photochemical cycloaddition and thermal cycloreversion, respectively [64]. The 1,8-naphthalenediol-derived linker was utilized as a C-shaped linker to create folded columnar superstructure [65]. This linker was applied to delineate overcrowded benzene-1,3,5-tricarboxamides.

## 11.5 Conclusion

In this chapter, some of the attempts to create aromatic folding architectures in crystalline state are highlighted. The choice of the linkers to connect aromatic moieties is highly important to furnish folding structures. Ureylene and imidodicarbonyl linkers are useful for this purpose. Zigzag folding structures are also created by utilizing U-shaped building blocks as H-bonding donor together with H-bonding acceptor molecules. Substitution positions of the linkers could influence on the folding patterns either straight zigzag or helically zigzag. In these zigzag-folding structures, the closest packing of aromatic moieties is facile, which furnishes  $\pi$ -stacked aromatic columns. The stacking affects their physical properties: absorption, fluorescence, and CD spectra. The degree of influence depends on the number of aromatic layers involved. Special emphasis is placed on the helically zigzag-folding aromatic structures. A column of chiral aromatic chromophores could be potentially useful for chiral photochromic systems and circularly polarized luminescence which are of current interests.

## References

1. D.H. Appella, L.A. Christianson, I.L. Karle, D.R. Powell, S.H. Gellman, *J. Am. Chem. Soc.* **118**, 13071–13072 (1996)
2. S.H. Gellman, *Acc. Chem. Res.* **31**, 173–180 (1998)
3. C.M. Goodman, S. Choi, W.F. DeGrado, *Nat. Chem. Biol.* **3**, 252–262 (2007)
4. G. Guichard, I. Huc, *Chem. Commun.* **47**, 5933–5941 (2011)
5. D.J. Hill, M.J. Mio, R.B. Prince, T.S. Hughes, J.S. Moore, *Chem. Soc. Rev.* **101**, 3893–4011 (2001)
6. L. Sebaoun, V. Marizot, T. Granier, B. Kauffmann, I. Huc, *J. Am. Chem. Soc.* **136**, 2168–2174 (2014)
7. D.-W. Zhang, X. Zhao, J.-L. Hou, Z.-T. Li, *Chem. Rev.* **112**, 5271–5316 (2012)
8. I. Huc, *Eur. J. Org. Chem.*, 17–29 (2004)
9. J.C. Nelson, J.G. Saven, J.S. Moore, P.G. Wolynes, *Science* **277**, 1793–1796 (1997)
10. M.T. Stone, J.M. Heemstra, J.S. Moore, *Acc. Chem. Res.* **39**, 11–20 (2006)
11. A. Khan, C. Kaiser, S. Hecht, *Angew. Chem. Int. Ed.* **45**, 1878–1881 (2006)
12. R.A. Smaldone, J.S. Moore, *Chem. Eur. J.* **14**, 2650–2657 (2008)
13. K. Yamaguchi, G. Matsumura, H. Kagechika, I. Azumaya, Y. Ito, A. Itai, K. Shudo, *J. Am. Chem. Soc.* **113**, 5474–5475 (1991)
14. A. Tanatani, H. Kagechika, I. Azumaya, K. Yamaguchi, K. Shudo, *Chem. Pharm. Bull.* **44**, 1135–1137 (1996)
15. H. Masu, M. Sakai, K. Kishikawa, M. Yamamoto, K. Yamaguchi, S. Kohmoto, *J. Org. Chem.* **70**, 1423–1431 (2005)
16. P. Gains, G. Avitabile, E. Benedetti, C. Pedone, M. Goodman, *Proc. Natl. Acad. Sci.* **67**, 426–433 (1970)
17. G. Lepore, S. Migdal, D.E. Blagdon, M. Goodman, *J. Org. Chem.* **38**, 2590–2594 (1973)
18. J. Clayden, U. Hennecke, M.A. Vincent, I.H. Hikkier, M. Helliwell, *Phys. Chem. Chem. Phys.* **12**, 15056–15064 (2010)
19. E.A. Chandross, C.J. Dempster, *J. Am. Chem. Soc.* **92**, 3586–3593 (1970)
20. T. Hayashi, N. Mataga, Y. Sakata, S. Misumi, M. Morita, J. Tanaka, *J. Am. Chem. Soc.* **98**, 5910–5913 (1976)
21. A. Tsuchida, T. Ikawa, T. Tomie, M. Yamamoto, *J. Phys. Chem.* **99**, 8169–8199 (1995)
22. F.D. Lewis, T.L. Kurth, W. Liu, *Photochem. Photobiol. Sci.* **1**, 30–37 (2002)
23. T.L. Kurth, F.F. Lewis, *J. Am. Chem. Soc.* **125**, 13760–13767 (2003)
24. H.L. Ricks, L.S. Shimizu, M.D. Smith, U.H.F. Bunz, K.D. Shimizu, *Tetrahedron Lett.* **45**, 3229–3232 (2004)
25. T. Hirano, T. Osaki, S. Fujii, D. Komatsu, I. Azumaya, A. Tanatani, H. Kagechika, *Tetrahedron Lett.* **50**, 488–491 (2009)
26. F.C. Krebs, M. Jørgensen, *J. Org. Chem.* **67**, 7511–7518 (2002)
27. F.D. Lewis, T.L. Kurth, G.B.D. Santos, *J. Phys. Chem. B* **109**, 4893–4899 (2005)
28. F.D. Lewis, T.L. Kurth, C.M. Hattan, R.C. Reiter, C.D. Stevenson, *Org. Lett.* **6**, 1605–1608 (2004)
29. T.A. Zeidan, Q. Wang, T. Fiebig, F.D. Lewis, *J. Am. Chem. Soc.* **129**, 9848–9849 (2007)
30. A. Tanatani, H. Kagechika, I. Azumaya, R. Fukutomi, Y. Ito, K. Yamaguchi, K. Shudo, *Tetrahedron Lett.* **38**, 4425–4428 (1997)
31. J. Clayden, L. Lemiégre, M. Helliwell, *J. Org. Chem.* **72**, 2302–2308 (2007)
32. M. Kudo, T. Hanashima, A. Muranaka, H. Sato, M. Uchiyama, I. Azumaya, T. Hirano, H. Kagechika, A. Tanatani, *J. Org. Chem.* **74**, 8154–8163 (2009)
33. J. Clayden, L. Lemiégre, G.A. Morris, M. Pickworth, T.J. Snape, L.H. Jones, *J. Am. Chem. Soc.* **130**, 15193–15202 (2008)
34. S. Hisamatsu, H. Masu, I. Azumaya, M. Takahashi, K. Kishikawa, S. Kohmoto, *Cryst. Growth Des.* **11**, 1453–1457 (2011)

35. P. Gilli, L. Pretto, V. Bertolasi, G. Gilli, *Acc. Chem. Res.* **42**, 33–44 (2009)
36. S. Hisamatsu, H. Masu, M. Takahashi, M. Kishikawa, S. Kohmoto, (unpublished work)
37. R. Krämer, J.-M. Lehn, A. DeCian, J. Fischer, *Angew. Chem. Int. Ed. Engl.* **32**, 703–706 (1993)
38. P. Dapporto, P. Paoli, S. Roelens, *J. Org. Chem.* **66**, 4930–4933 (2001)
39. S. Hisamatsu, H. Masu, I. Azumaya, M. Takahashi, K. Kishikawa, S. Kohmoto, *Cryst. Growth Des.* **11**, 5387 (2011)
40. S. Hisamatsu, H. Masu, M. Takahashi, K. Kishikawa, S. Kohmoto, *Tetrahedron Lett.* **53**, 3903–3906 (2012)
41. N.N. Adarsh, D.K. Kumar, P. Dastidar, *Tetrahedron* **63**, 7386–7396 (2007)
42. M.C. Etter, D.A. Admond, *J. Chem. Soc. Chem. Commun.*, 589–591 (1990)
43. S. Hisamatsu, H. Masu, M. Takahashi, K. Kishikawa, *Cryst. Growth Des.* **13**, 2327–2334 (2013)
44. S. Kohmoto, S. Sekizawa, S. Hisamatsu, H. Masu, M. Takahashi, K. Kishikawa, *Cryst. Growth Des.* **14**, 2209–2217 (2014)
45. N.E. Braml, A. Sattler, W. Schnick, *Chem. Eur. J.* **18**, 1811–1819 (2012)
46. S. Kohmoto, H. Masu, C. Tatsuno, K. Kishikawa, M. Yamamoto, K. Yamaguchi, *J. Chem. Soc. Perkin Trans.* **1**, 4464–4468 (2000)
47. S. Kohmoto, Y. Ono, H. Masu, K. Yamaguchi, K. Kishikawa, M. Yamamoto, *Org. Lett.* **3**, 4153–4155 (2001)
48. H. Masu, K. Ohmori, K. Kishikawa, M. Yamamoto, K. Yamaguchi, S. Kohmoto, *Bull. Chem. Soc. Jpn.* **78**, 1127–1131 (2005)
49. K. Kishikawa, Y. Miwa, T. Kurosaki, S. Kohmoto, M. Yamamoto, K. Yamaguchi, *Chem. Mater.* **13**, 2468–2471 (2001)
50. H. Masu, K. Ohmori, K. Kishikawa, M. Yamamoto, K. Yamaguchi, S. Kohmoto, *Anal. Sci.* **21**, x33–x34 (2005)
51. H. Masu, I. Mizutani, Y. Ono, K. Kishikawa, I. Azumaya, K. Yamaguchi, S. Kohmoto, *Cryst. Growth Des.* **6**, 2086–2091 (2006)
52. H. Masu, I. Mizutani, T. Kato, I. Azumaya, K. Yamaguchi, K. Kishikawa, S. Kohmoto, *J. Org. Chem.* **71**, 8037–8044 (2006)
53. G. Snatzke, *Angew. Chem. Int. Ed. Engl.* **18**, 363–377 (1979)
54. F. Franceschi, M. Guardigli, E. Solari, C. Floriani, A. Chiesi-Villa, C. Rizzoli, *Inorg. Chem.* **36**, 4099–4107 (1997)
55. M. Kimura, K. Sirasu, H. Okamoto, K. Satake, S. Morosawa, *Tetrahedron Lett.* **33**, 697–6978 (1992)
56. S. Aravinda, N. Shamala, C. Das, A. Sriranjini, I.L. Karle, P. Balaram, *J. Am. Chem. Soc.* **125**, 5308–5315 (2003)
57. (a) Y. Inai, Y. Ishida, K. Tagawa, A. Takasu, T. Hirabayashi, *J. Am. Chem. Soc.* **124**, 2466–2473 (2002). (b) H. Fenniri, B.-L. Deng, A.E. Ribbe, *J. Am. Chem. Soc.* **124**, 11064–11072 (2002)
58. H. Jiang, C. Dolain, J.-M. Léger, H. Gornitzka, I. Huc, *J. Am. Chem. Soc.* **126**, 1034–1035 (2004)
59. A. Gättli, X. Daura, D. Seebach, W.F. van Gunstern, *J. Am. Chem. Soc.* **124**, 12972–12978 (2002)
60. S. Kohmoto, H. Takeichi, K. Kishikawa, H. Masu, I. Azumaya, *Tetrahedron Lett.* **49**, 1223–1227 (2008)
61. L. Sebaoun, B. Kauffmann, T. Delclos, V. Maurizot, I. Huc, *Org. Lett.* **16**, 2326–2329 (2014)
62. S. Li, D.-X. Wang, M.-X. Wang, *Tetrahedron Lett.* **53**, 6426–6429 (2012)
63. Y. Morisaki, T. Sawamura, T. Murakami, Y. Chujo, *Org. Lett.* **12**, 3188–3191 (2010)
64. S. Toyota, M. Kug, A. Takatsu, M. Goichi, T. Iwanaga, *Chem. Commun.*, 1323–1325 (2008)
65. W. Zhang, D. Horoszewski, J. Decatur, C. Nuckolls, *J. Am. Chem. Soc.* **125**, 4870–4873 (2003)

# Chapter 12

## Crystal Engineering of Coordination Networks Using Multi-interactive Ligands

Yumi Yakiyama, Tatsuhiro Kojima, and Masaki Kawano

**Abstract** During molecular assembly processes, weak intermolecular interactions have important functions by precise molecular recognition and stabilization of key metastable intermediates in various kinds of reactions. Introducing these features of weak intermolecular interactions into the confined spaces of porous materials enables selective molecular trapping of metastable species and control of chemical reactions. However, such interactive sites often react with each other or with metal ions during the self-assembly process, thereby resulting in non-interactive stable forms. In this chapter, we describe the potential of using multi-interactive molecules to prepare coordination polymers that possess interactive pores. The multi-interactive  $\pi$ -planar organic ligand, tri(4-pyridyl)hexaazaphenylene, enables the formation of interactive pores by dynamic and selective networking which can be readily controlled by adjusting the reaction conditions. As a result, various porous coordination networks can be prepared from the same starting materials. Furthermore, it enables the formation of kinetic network which can be transformed to thermally more stable one by addition of outer stimuli.

**Keywords** Intermolecular interaction • Coordination network • Kinetic networking • Multi-interactivity • Network diversity

### 12.1 Introduction

#### 12.1.1 General Backgrounds

Weak intermolecular interactions (e.g., hydrogen bonds (H bond),  $\pi$ - $\pi$  interactions, halogen-halogen interactions, and cation/anion- $\pi$  interactions) make important contributions to supramolecular chemistry. Indeed, their directionality like complementary H bonds between nucleic acids realizes the construction of specific

---

Y. Yakiyama • T. Kojima • M. Kawano (✉)

Division of Advanced Materials Science, Pohang University of Science and Technology (POSTECH), 77 Cheongam-ro, Nam-gu, Pohang, Gyeongbuk 790-784, South Korea  
e-mail: [mkawano@postech.ac.kr](mailto:mkawano@postech.ac.kr)

structures such as the double helix of DNA and the quadruplex of guanine. In supramolecular systems, their polarized nature also contributes to providing positively or negatively charged moieties which enable selective molecular recognition. In addition, it is also very important that weak intermolecular interactions stabilize key metastable states in biological reactions. Although each interaction formed in this process is very weak, it is crucial to perform biological reactions with the best efficiency. Depending on environmental conditions such as temperature, pressure, concentration, and additives, the stabilizing effect of weak intermolecular interactions can realize the formation of a variety of networks from the same components.

Research of porous coordination networks has exploited such features of weak intermolecular interactions to achieve desired functions, especially by host–guest interactions in pores [1–8]. As a result, many applications that use their unique encapsulation ability have been proposed, such as gas storage [9–15], molecular separation [13, 16–20], sensing [21, 22], reaction catalysis [23–27], and proton conductors [28–31]. To achieve these functions, methods to construct interactive pores are essential. To prepare such networks, researchers have generally focused on hydro-/solvothermal syntheses which usually need high temperature or slow crystallization by layer diffusion in organic solvents; these methods tend to yield thermally favorable species. However, making pores that have interactive sites is difficult because thermodynamic effect often causes conventional methods to consume these sites and reduce the pore size to stabilize the network (Fig. 12.1). One way

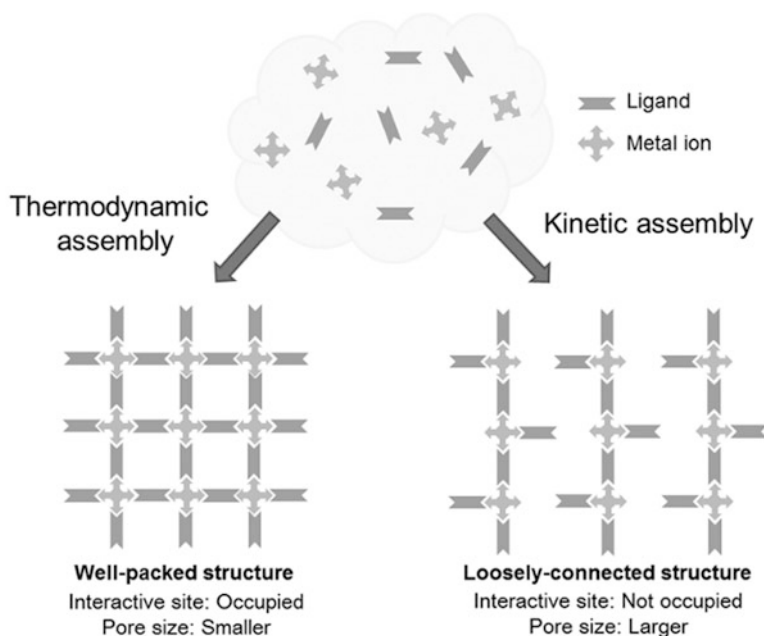


**Fig. 12.1** Schematic model of the features of thermodynamically and kinetically prepared porous coordination networks

to construct interactive porous coordination networks is to use metastable (kinetic) states that have fewer weak intermolecular interactions than thermodynamic ones. Furthermore, the addition of outer stimuli such as heat, light, and pressure to kinetic networks may induce transformation into other structures that cannot be obtained with conventional methods. Despite this great potential of kinetic networks, their preparation and structure determination are not always trivial. Only a few reports about kinetic networks are available [32, 33].

In this chapter, we show our strategy to construct interactive pores by formation of kinetic networks. We first describe our previous approach to kinetic network formation called *instant synthesis* [34, 35]. Then we show the formation of various coordination networks based on the multi-interactive ligand, tri(4-pyridyl)hexaazaphenylene (TPHAP), using weak intermolecular interaction [36, 37].

### 12.1.2 *Instant Synthesis*

In the chemistry of molecular self-assembly, kinetic control in the synthesis of porous coordination networks is potentially very important because it can provide networks which cannot be fabricated using conventional methods. However, this process encounters two difficulties: (1) usually kinetic products (metastable product) are not uniform because of high reactivity and (2) the products are often obtained as microcrystalline powder, so single crystal determination of structure is difficult. We have overcome these difficulties by developing *instant synthesis* (i.e., crystallization with ca. 30 s) [34, 35]. This method enables us to obtain selectively formed homogeneous kinetic products by simply adding a metal solution instantaneously to a vigorously stirred saturated solution of ligand. This method immediately produces a microcrystalline kinetic product that has a structure different from that of a thermodynamic network prepared by slow-crystallization techniques.

Fast addition of a methanol solution of  $\text{ZnBr}_2$  to a vigorously stirred nitrobenzene/methanol solution of 2,4,6-tri(4-pyridyl)triazine (TPT) resulted in microcrystals within 30 s. Ab initio X-ray powder diffraction (XRPD) analysis revealed an interpenetrating structure with large channels containing nitrobenzene (Fig. 12.2).

The channels are interconnected in two directions to yield a two-dimensional (2D) channel network with a ca. 50 % free volume of the unit cell. In contrast, slow crystallization by the layer diffusion method using exactly the same stoichiometric ratio of starting reagents gave a non-interpenetrating structure of thermodynamic product that has large 1D pores encapsulating nitrobenzene. On the basis of these results, further network formation having still-larger and more complex porous coordination structures could be achieved by using *instant synthesis* and *template synthesis* with the addition of a large template molecule such as triphenylene [38–40]. The crystalline-to-amorphous-to-crystalline phase transition also could be induced by heating the crystalline powder of  $\text{ZnX}_2$ -TPT ( $X = \text{I}, \text{Br}, \text{Cl}$ ) network to give a thermally stable network [41, 42]. Especially,  $\text{ZnI}_2$ -TPT system produces a highly thermally stable porous network that has a stacking structure of 1D “saddle-

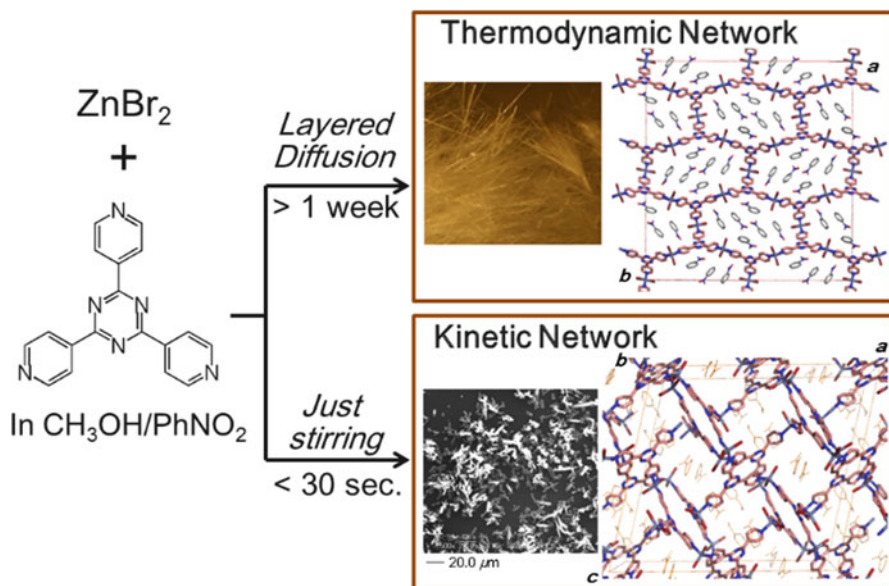


**Fig. 12.2** Selective formation of thermodynamic and kinetic networks composed of TPT and  $\text{Zn}^{2+}$  ion

type” units composed of two TPTs connected by three  $\text{ZnI}_2$  [41]. This network showed the novel ability to encapsulate small reactive sulfur allotropes [43].

Kinetic products prepared by *instant synthesis* generally possess larger pores than do products prepared by thermodynamic synthesis. In addition, kinetic products have more interactive sites than do thermodynamic ones. These features indicate that the weak intermolecular interaction among components, especially the solvent effect, is the key to selective trapping of kinetic species and formation of interactive pores during the self-assembly process. This phenomenon is exemplified in biological systems which are composed of multi-interactive components. For example, enzymatic reaction involves the formation of many intermediate states stabilized by weak intermolecular interactions and changes their energy potentials depending on the amount of water [44]. These facts stimulated the idea of introducing multipoint weak intermolecular interaction sites into new ligand design for selective trapping of porous coordination networks that have interactive and large pores.

## 12.2 Network Formation Using Multi-interactive TPHAP

### 12.2.1 TPHAP: The Multi-interactive Ligand

To design a multi-interactive ligand, we considered a hexaazaphenalene (HAP) skeleton (Fig. 12.3) [45, 46]. HAP has a planar  $\pi$ -system with  $D_{3h}$  symmetry

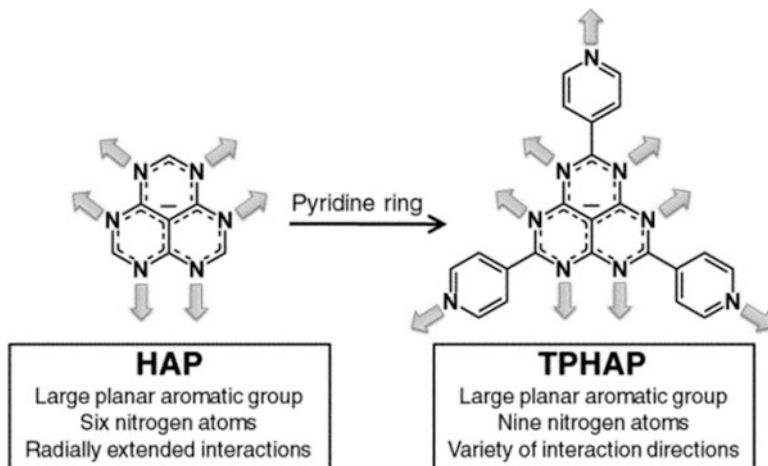


Fig. 12.3 Molecular design of TPHAP based on HAP

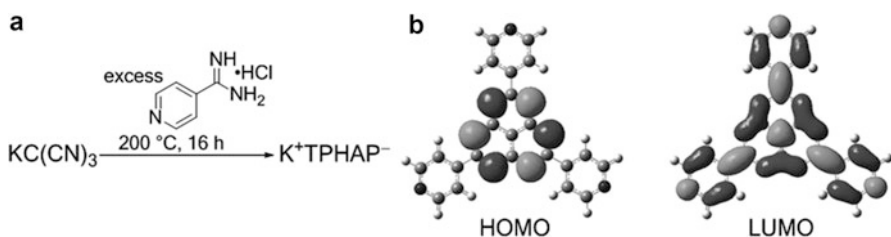
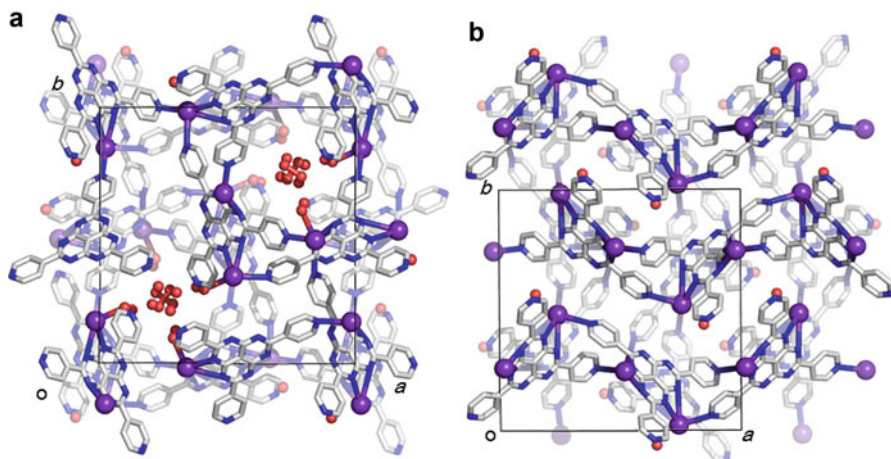


Fig. 12.4 Preparation and property of  $\text{TPHAP}^-$ . (a) Synthetic scheme of  $\text{K}^+\text{TPHAP}^-$ . (b) HOMO and LUMO drawings of  $\text{TPHAP}^-$

and shows radially extended H-bonding interactions, metal coordination, and  $\pi$ - $\pi$  stacking interaction in the single-crystal structures of  $\text{K}^+$  salt and  $\text{Cu}^{2+}$  complex,  $[\text{Cu}(\text{HAP}^-)_2(\text{NH}_3)_4]$  [45]. A HAP anion is exceptionally stable among phenalenyl [47–50] anions because of its low HOMO energy level.

We chose a pyridine group as the additional interaction/coordination site for further functionalization of HAP to design a new multi-interactive ligand, TPHAP (Fig. 12.3) [36]. TPHAP can be obtained as a potassium salt ( $\text{K}^+\text{TPHAP}^-$ , Fig. 12.4a) from commercially available tricyanomethanide and 4-amidinopyridine hydrochloride in moderate yield (62 %) on gram scale by using a procedure modified from that in reference [46].

The salient features of TPHAP are as follows: (a) a large aromatic plane which enables easy formation of  $\pi$ -stacks, (b) nine nitrogen atoms which can be involved in H bonds or coordination bond formation, and (c) a delocalized negative charge over the central HAP skeleton which contributes to the high stability of the anion form (Fig. 12.4b). Such a multi-interactive ligand with a radially extended mode is quite rare in porous coordination networks. Additionally,  $\text{K}^+\text{TPHAP}^-$  is



**Fig. 12.5** Crystal structures of  $\text{K}^+\text{TPHAP}^-$  before and after desolvation. (a) Crystal structure before desolvation. (b) Crystal structure after desolvation at  $500\text{ }^\circ\text{C}$ . Gray, C; blue, N; red, O; purple, K. Hydrogen atoms are omitted for clarity

remarkably thermally stable. Even after heating a single crystal of  $\text{K}^+\text{TPHAP}^-$  at  $500\text{ }^\circ\text{C}$  under a nitrogen atmosphere, the crystallinity remained intact with some molecular rearrangement (Fig. 12.5).

### 12.2.2 Trapping of Kinetic Network by Utilization of Multi-interactivity of TPHAP

The formation of networks with transition metals was affected by the multi-interactive nature of TPHAP. Using  $\text{K}^+\text{TPHAP}^-$  and  $\text{Co}^{2+}$  or  $\text{Cd}^{2+}$  ions, we succeeded in trapping crystals of kinetic networks,  $[\text{Co}(\text{TPHAP}^-)_2(\text{CH}_3\text{OH})_2(\text{H}_2\text{O})] \cdot 3\text{C}_6\text{H}_5\text{NO}_2 \cdot \text{HNO}_3 \cdot 5\text{H}_2\text{O}$  (**1**) and  $[\text{Cd}(\text{TPHAP}^-)_2(\text{CH}_3\text{OH})_2(\text{H}_2\text{O})] \cdot 2\text{C}_6\text{H}_5\text{NO}_2 \cdot n\text{CH}_3\text{OH}$  (**2**). The crystal structures were determined by synchrotron X-ray diffraction. The layering diffusion of a methanol solution of  $\text{Co}(\text{NO}_3)_2 \cdot 6\text{H}_2\text{O}$  or  $\text{Cd}(\text{NO}_3)_2 \cdot 4\text{H}_2\text{O}$  into a methanol–nitrobenzene solution of  $\text{K}^+\text{TPHAP}^-$  at  $14\text{ }^\circ\text{C}$  for 1 day produced single crystals of **1** and **2**. These crystals have isostructures and are organized by H bonds and  $\pi$ – $\pi$  interactions of 1D chains composed of monodentate and bidentate TPHAP<sup>−</sup>s (Fig. 12.6). Both  $\text{Co}^{2+}$  and  $\text{Cd}^{2+}$  metal centers have octahedral geometry coordinated by a monodentate- and two bidentate TPHAP<sup>−</sup> moieties, two methanol molecules, and one water molecule.

Within a few days after the formation of **1**, the crystal started to shrink and instead new dark red crystals grew on the crystal surface (Fig. 12.7). Synchrotron X-ray analysis of the new crystals grown on the initial crystal surface revealed that those crystals are uniform and that the crystal structure is a porous coordination network of

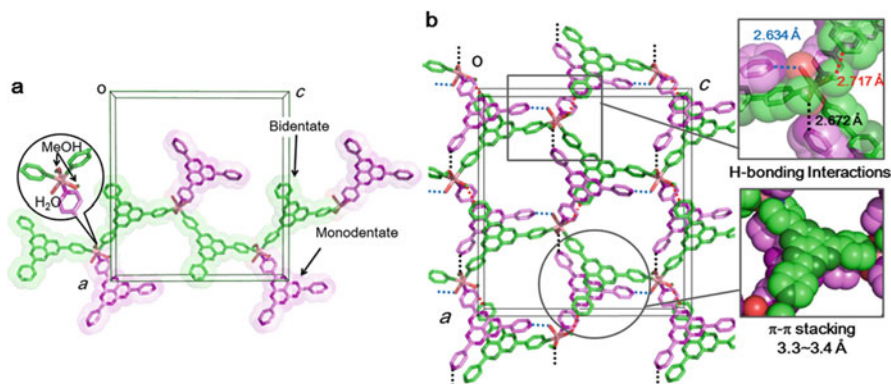


**Fig. 12.6** (a) 1D chain structure in **1**. The *inset* figures show the coordination environments around  $\text{Co}^{2+}$  ion (soft pink). (b) Porous network structure of **1** viewed from the *b* axis. Broken lines show the  $\text{N} \cdots \text{HO}$  type H-bonding interactions. Magenta, monodentate TPHAP<sup>-</sup>; green, bidentate TPHAP<sup>-</sup>. Hydrogen atoms and solvent molecules are omitted for clarity

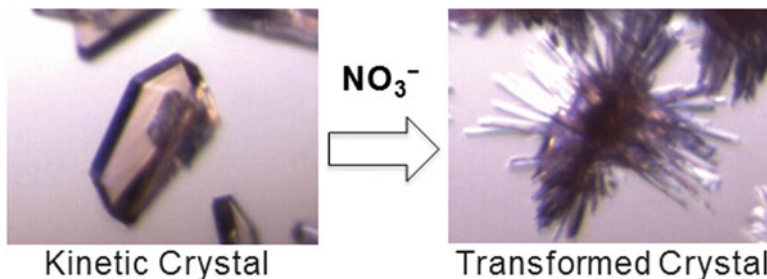


**Fig. 12.7** Photos of kinetically obtained crystals **1** and the transformed crystals **3**

$[\text{Co}(\text{NO}_3^-)(\text{TPHAP}^-)(\text{CH}_3\text{OH})_2] \cdot \text{CH}_3\text{OH} \cdot \text{C}_6\text{H}_5\text{NO}_2 \cdot 2\text{HNO}_3 \cdot \text{H}_2\text{O}$  (**3**) which is composed of 1D chains of  $\text{Co}^{2+}$  and bidentate TPHAP<sup>-</sup>s (Fig. 12.8). In this crystal, ligand exchange of monodentate TPHAP<sup>-</sup> and water around  $\text{Co}^{2+}$  with bidentate  $\text{NO}_3^-$  occurred. Crystal **3** showed no further transformation, indicating that **3** was a thermodynamically more stable product formed from kinetically prepared **1**. The transformation was accelerated when the concentration of  $\text{NO}_3^-$  around the crystals was increased by shaking the crystallization tube. Furthermore, when the crystals of **1** were immersed in a solution in the absence of  $\text{NO}_3^-$ , the structure transformation did not occur. These results indicate that the structure transformation was caused by reaction with  $\text{NO}_3^-$ . Also in crystal **2**, the same crystal shrinkage/new crystal formation was observed as in crystal **1**, but the newly formed crystal was too small to obtain enough X-ray diffraction data to identify its structure.

The structure transformation mechanism from **1** to **3** can be explained by the ligand exchange reaction triggered by reaction between small  $\text{NO}_3^-$  from the  $(-4 - 1 0)$  plane and a  $\text{Co}^{2+}$  center, followed by dissociation of a monodentate TPHAP anion and a water molecule (Fig. 12.9). The structure transformations

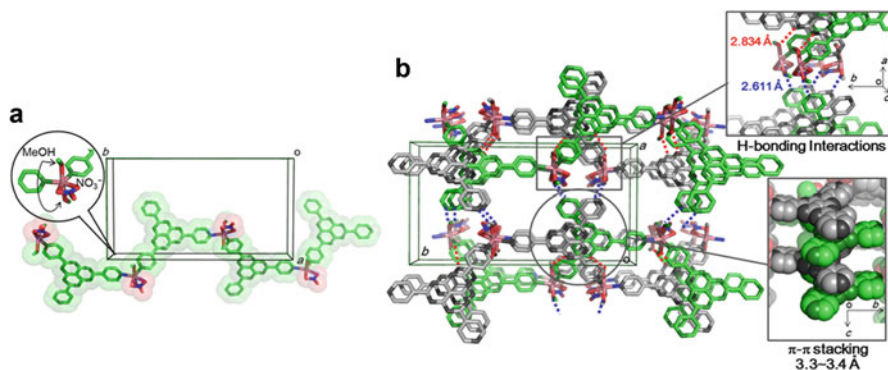


**Fig. 12.8** (a) 1D chain structure in **3**. The *inset* figures show the coordination environments around  $\text{Co}^{2+}$  ion. (b) The porous network structure of **3** viewed from the *c* axis. *Broken lines* show the  $\text{N}\cdots\text{HO}$  type H-bonding interactions. Hydrogen atoms and solvent molecules are omitted for clarity

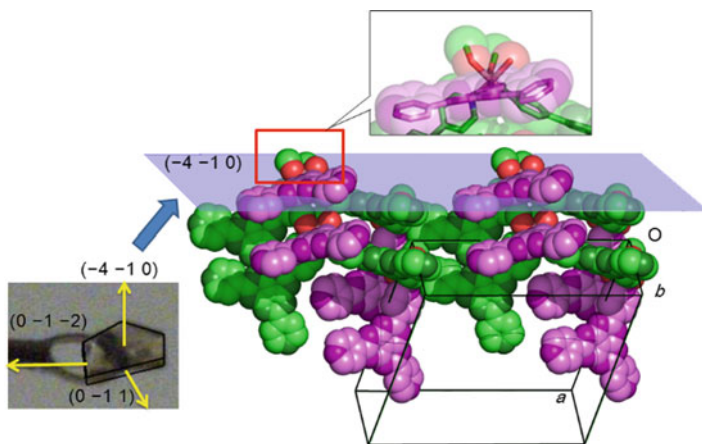


**Fig. 12.9** Face index of the single crystal of **1** and the  $(-4 -1 0)$  plane in the crystal structure. *Magenta*, monodentate  $\text{TPHAP}^-$ ; *green*, bidentate  $\text{TPHAP}^-$

occurred in the two other planes ( $(0-1-2)$  and  $(0-1 1)$ ). Their mechanism can be explained in the same way. Eventually, after dissociation of the monodentate  $\text{TPHAP}^-$  anions and water molecules, reconstruction of a thermodynamically stable network **3** is induced by H-bond formation and  $\pi-\pi$  stacking interaction among 1D chains. During formation of the network, weak intermolecular interactions associated with  $\text{TPHAP}^-$  have important functions in the stabilization of the systems. Such a structure transformation of the open-framework network on the crystal surface triggered by the ligand exchange has been rarely reported, although single-crystal-to-single-crystal transformations in open-framework networks are relatively common.

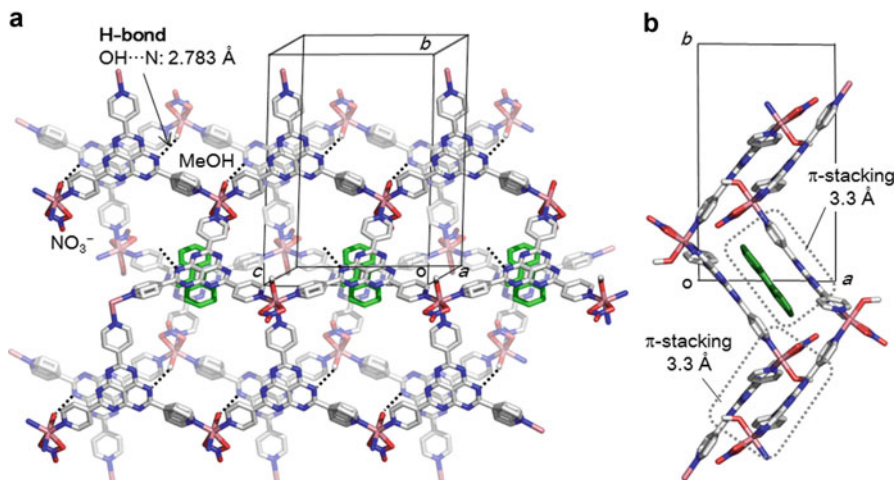


**Fig. 12.10** (a) H-bonding interactions in **4**. (b) The view from the *c* axis showing  $\pi$ - $\pi$  interactions between TPHAP<sup>-</sup>s and nitrobenzene. Gray, C; blue, N; red, O; soft pink, Co. The green color molecule is a disordered nitrobenzene. Hydrogen atoms and solvent molecules are omitted for clarity

Increasing the temperature also affects the network formation. When the crystallization temperature changed from 14 °C to 25 °C during synthesis of **1**, another coordination network, [Co(NO<sub>3</sub><sup>-</sup>)(TPHAP<sup>-</sup>)(CH<sub>3</sub>OH)] · CH<sub>3</sub>OH · 2.5C<sub>6</sub>H<sub>5</sub>NO<sub>2</sub> · H<sub>2</sub>O (**4**), was obtained in addition to **1**. **4** is a dark red block crystal. Unlike crystals **1** and **3**, all TPHAP<sup>-</sup> moieties in **4** work as a tridentate ligands to form a 2D layered structure (Fig. 12.10). **4** includes two kinds of  $\pi$ - $\pi$  interaction and OH $\cdots$ N-type H bonds between HAP skeleton and coordinating methanol. These weak interactions largely contribute to stabilizing the whole structure. This network also has pores along the *c* axis in which nitrobenzene is severely disordered.

In situ X-ray powder diffraction analysis using a capillary sample of dozens of single crystals of **1** in the presence of a mother solution for crystallization at 25 °C confirmed that crystals of **3** were generated only through the kinetic network of **1**, but that **4** was not generated through **1** nor **3**. Although, in addition to anisotropic crystal growth, the number of crystals was not sufficient for statistically quantitative intensity analysis, in situ diffraction data indicated structure transformation from **1** to **3** but not to **4** in the bulk state (Fig. 12.11). Even at temperatures >40 °C, formation of **4** was not observed. Obviously **4** was generated through a reaction pathway different from that of **1** and **3**.

The temperature effect is also crucial for Cd(NO<sub>3</sub>)<sub>2</sub>-TPHAP<sup>-</sup> system. When the crystallization temperature was decreased to 4 °C, a highly symmetrical kinetic network of [Cd(TPHAP<sup>-</sup>)<sub>2</sub>] · solvents (**5**) was obtained within a day as a colorless block crystal. In the crystal structure, all TPHAP<sup>-</sup> moieties work as tridentate ligand and coordinate to Cd<sup>2+</sup> ions that have octahedral geometry (Fig. 12.12). Neither solvent molecules nor counterions coordinate to Cd<sup>2+</sup> ion. This network has large

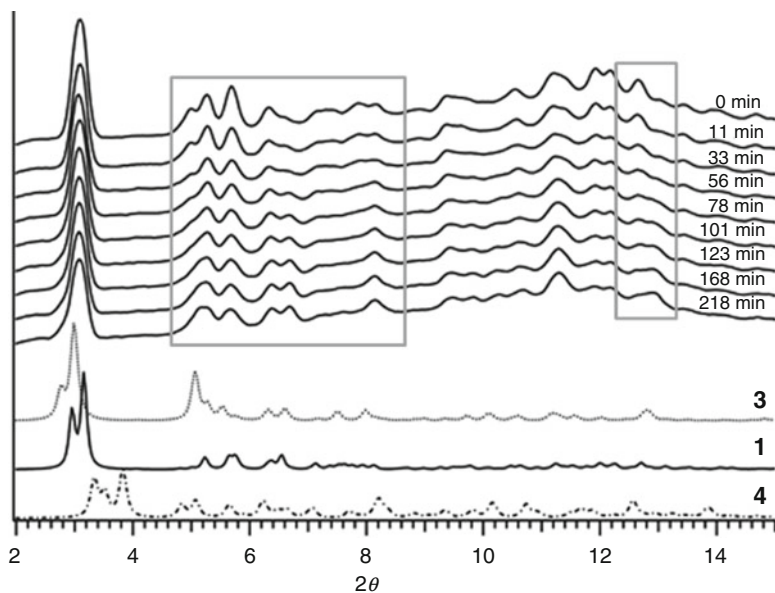


**Fig. 12.11** In situ X-ray powder diffraction of single crystals of **1**. The powder plots were obtained by integration of 2D image data. The *gray squares* show the regions in which large peak shifts were observed. Simulated powder diffraction: *solid line*, **1**; *gray line*, **3**; *dotted line*, **4**

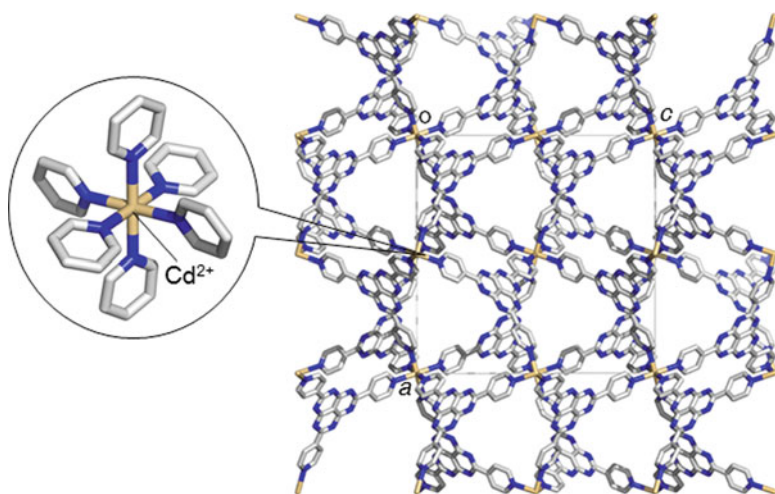


**Fig. 12.12** Crystal structure of porous network **5**. *Yellow*, Cd. Hydrogen atoms and solvent molecules are omitted for clarity

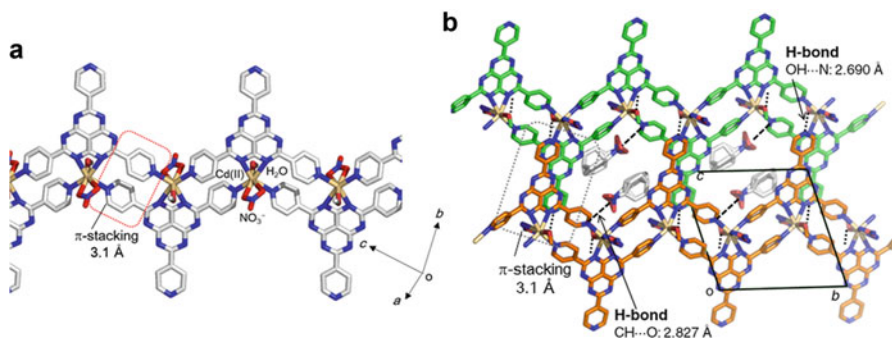


**Fig. 12.13** (a) 1D chain structure in **6**. (b) Porous network structure of **6** viewed from the *b* axis. Broken lines show the N···HO type H-bonding interactions. Hydrogen atoms and solvent molecules are omitted for clarity

pores; we assume that the solvent molecules of CH<sub>3</sub>OH, H<sub>2</sub>O, and nitrobenzene are encapsulated. However, because of random residual electron density peaks, the solvent positions could not be determined. In addition, neither H bonds nor π–π interactions between TPHAP<sup>-</sup> moieties are formed. Therefore, crystal **5** was unstable even when kept in a crystallization tube at 4 °C and disappeared within 2 or 3 days to give single crystals of **2**. This lability and large pore size are typical features of kinetic products.

In contrast, when the crystallization temperature was increased to 40 °C, which is higher than the crystallization temperature of **2**, the thermodynamic product, [Cd(NO<sub>3</sub><sup>-</sup>)(TPHAP<sup>-</sup>)(CH<sub>3</sub>OH)]·CH<sub>3</sub>OH·C<sub>6</sub>H<sub>5</sub>NO<sub>2</sub> (**6**), was obtained as a pale yellow block crystal (Fig. 12.13). The clear difference of **6** from the others is that not only three pyridyl groups but also two nitrogen atoms on the HAP skeleton coordinate to the Cd<sup>2+</sup> ion. The formation of a large number of coordination bonds clearly shows that **6** is the thermodynamic product. This unique coordination mode forms a 1D chain that has strong π–π interaction between two pyridine rings (Fig. 12.13a). The 1D chains interact with each other through H bonds and π–π stacking interactions to give a porous network structure that encapsulates nitrobenzene.

### 12.3 Effects of Solvent Additives on the Network Formation Using Multi-interactive Ligand

The multi-interactive ligand, TPHAP<sup>-</sup>, forms various kinds of kinetic and thermodynamic porous networks selectively depending on crystallization temperature (Sect. 12.2). Furthermore, the obtained kinetic network is transformed into a thermally more stable state by addition of NO<sub>3</sub><sup>-</sup> ion. These results support our claim that kinetic states can be trapped by weak intermolecular interactions that can deepen local minimum potential energy funnels.

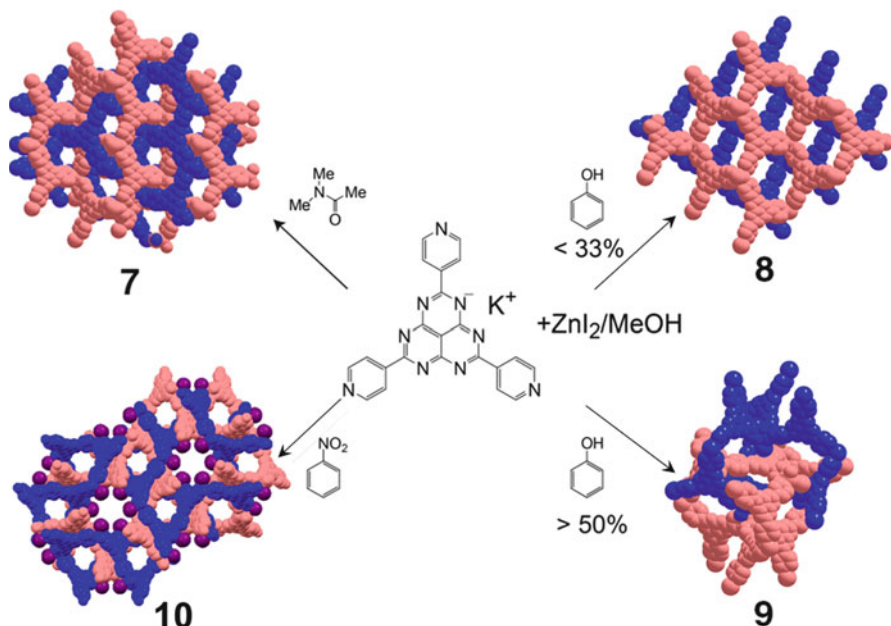


Fig. 12.14 Diversity of Zn<sup>2+</sup>-TPHAP<sup>-</sup> networks

We direct our attention to the solvent effect on the network formation using TPHAP. Although the effect of solvents has been discussed in crystal engineering for a long time, it is still controversial [51–54]. Investigation of the sensitivity of TPHAP to weak intermolecular interaction, i.e., the solvent effect, will give an important knowledge for crystal engineering. Here, we examine the diversity of the resulting networks composed of Zn<sup>2+</sup> and TPHAP<sup>-</sup> to show how the solvent affects network formation. By changing solvents used for crystallization, four types of networks were obtained depending on the solvent systems (Fig. 12.14). Precise structure analysis revealed the correlations between network formation and weak intermolecular interaction, especially  $\pi$ - $\pi$  interactions and H bonds.

One of the significant features of TPHAP<sup>-</sup> is the large aromatic plane which can introduce  $\pi$ - $\pi$  interaction into self-assembly. Indeed, except for **5**, all products discussed in the previous section have  $\pi$ - $\pi$  stacking structures between TPHAP skeletons and aromatic guest molecules such as nitrobenzene. This result indicates the importance of  $\pi$ - $\pi$  interaction in networking. In this section, we describe the structural details of the four networks and focus on whether the solvents have an aromatic ring.

### 12.3.1 Crystallization from Nonaromatic Solvents

All single crystals grew from a triple-layered solution consisting of methanol solution of ZnI<sub>2</sub> as the top layer, methanol as the middle layer, and additive/methanol

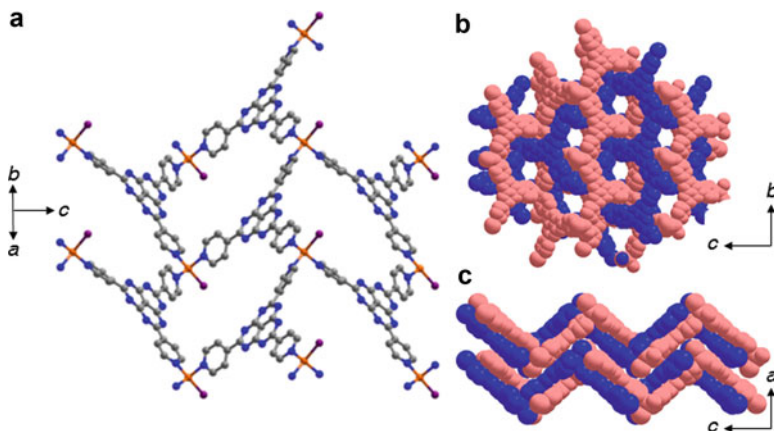


**Fig. 12.15** Crystal structure of **7**. (a) An undulating  $6^3\text{-hcb}$  sheet structure composed of  $\text{Zn}(\text{I}^-)(\text{TPHAP}^-)$ .  $\text{Zn}^{2+}$  ion acts as a trident junction. Orange, Zn; purple, I. (b) Interpenetrating sheet structure viewed from the  $a$  axis, showing 1D porous channels. (c) Interpenetrating sheet structure viewed from the  $b$  axis, showing no space for guest encapsulation between  $\text{TPHAP}^-$ s. Hydrogen atoms and solvent molecules are omitted for clarity

solution of  $\text{K}^+\text{TPHAP}^-$  as the bottom layer at  $14^\circ\text{C}$ . When nonaromatic solvents such as dimethylacetamide (DMA), dimethyl sulfoxide (DMSO), 1,4-dioxane, and tetrahydrofuran (THF) were used as additive solvents, single crystals of  $[\text{Zn}(\text{I}^-)(\text{TPHAP}^-)] \cdot 3.5\text{CH}_3\text{OH}$  (**7**) grew. **7** has an undulating sheet structure composed of  $\text{Zn}^{2+}$ ,  $\text{I}^-$ , and  $\text{TPHAP}^-$  (Fig. 12.15). This structure is assigned as a  $6^3\text{-hcb}$  net according to the RCSR (Reticular Chemistry Structure Resource) database [55–61]. The  $\text{Zn}^{2+}$  center has a tetrahedral geometry coordinated by three tridentate  $\text{TPHAP}^-$ s and  $\text{I}^-$ . Because of nonaromatic solvents,  $\pi$ – $\pi$  interaction may dominate intermolecular interactions within only  $\text{TPHAP}^-$  molecules, thereby forming interpenetrating network and  $\pi$ – $\pi$  stacking layer [62, 63]. No additive solvents are encapsulated in **7** because both the additive solvents and  $\text{TPHAP}^-$  have only H-bond acceptor sites which cannot interact with each other. This result indicates that the weak molecular interaction between the additive solvents and  $\text{TPHAP}^-$  is strongly correlated with guest encapsulation as well as with network formation.

### 12.3.2 Crystallization from Aromatic Solvents

Here, phenol and nitrobenzene were used as an additional aromatic solvent. Phenol has an H-bond donating OH group that can interact with  $\text{TPHAP}^-$ ; nitrobenzene has an H-bond accepting  $\text{NO}_2$  group. Therefore, these two solvents are good targets for demonstrating the multi-interactivity of  $\text{TPHAP}^-$ .

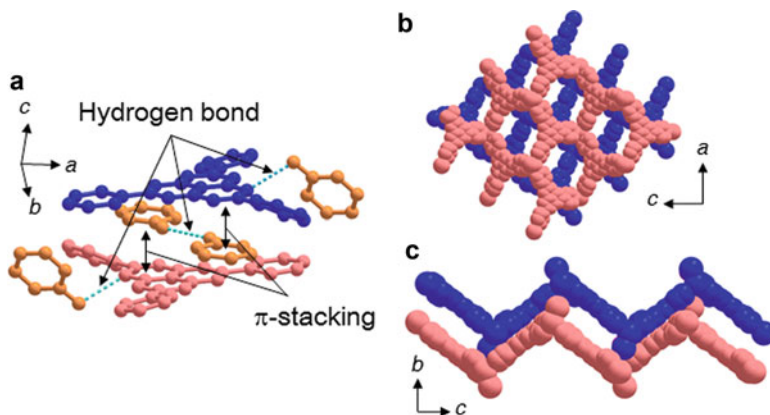


**Fig. 12.16** Crystal structure of **8**. (a) Encapsulation of phenols (*orange*) via  $\pi$ - $\pi$  interaction and a H bond. (b) Non-interpenetrating sheet stacking structure viewed from the *b* axis. (c) Non-interpenetrating sheet stacking structure viewed from the *a* axis. Hydrogen atoms and solvent molecules are omitted for clarity

By replacing DMA with phenol, two kinds of guest encapsulating networks were obtained. When the phenol/methanol ratio (v:v) was 1:2, the product was  $[\text{Zn}(\text{I}^-)(\text{TPHAP}^-)] \cdot 3\text{CH}_3\text{OH} \cdot 3\text{C}_6\text{H}_5\text{OH}$  (**8**). When this ratio was 1:1 or 2:1, the product was  $[\text{Zn}(\text{I}^-)(\text{TPHAP}^-)] \cdot 2.5\text{CH}_3\text{OH} \cdot 5\text{C}_6\text{H}_5\text{OH}$  (**9**), which has an undulating 6<sup>3</sup>-**hcb** sheet structure composed of  $\text{Zn}^{2+}$ ,  $\text{I}^-$ , and  $\text{TPHAP}^-$ , and is a non-interpenetrating version of **7** (Fig. 12.16). **8** accommodates two groups of phenol molecules in the pore. One group interacts with the large aromatic plane of  $\text{TPHAP}^-$  via  $\pi$ - $\pi$  interaction, and the other group interacts with the central HAP nitrogen through H bonds, thereby demonstrating clearly the multi-interactivity of  $\text{TPHAP}^-$ . Encapsulation of phenols by  $\pi$ - $\pi$  interaction causes formation of a non-interpenetrating stacking layer structure rather than an interpenetrating one. In contrast, **9** has the same  $\text{Zn}(\text{I}^-)(\text{TPHAP}^-)$  component as **8**, but **9** forms an interpenetrating 10<sup>3</sup>-**srs** 3D network which is totally different from **8** (Fig. 12.17).

The crucial difference between **8** and **9** is whether  $\text{TPHAP}^-$  moieties form a dimer; **8** includes a  $\text{TPHAP}^-$  dimer unit which tends to form 2D stacking sheet structure, but **9** does not. In **9**, a phenol is sandwiched between two  $\text{TPHAP}^-$ s by  $\pi$ - $\pi$  interaction, and as a result, a 3D network is formed rather than a 2D network. Another important feature is that four phenols form H bonds with nitrogen atoms on two central  $\text{TPHAP}^-$  skeletons. The network **9** obtained from phenol-rich solution (the phenol/methanol ratio (v:v) was 1:1 or 2:1) includes a larger number of solvents through H bonds than does **8**. Phenol may form H bonds more readily than  $\pi$ - $\pi$  interactions; if this is true, then  $\text{TPHAP}^-$  dimer formation would be impeded. Most importantly, **8** and **9** were obtained selectively from the same solvent system (phenol/methanol) with different ratios of phenol. This fact indicates that even very slight differences of weak intermolecular interactions can affect the reactions by  $\text{TPHAP}^-$ .

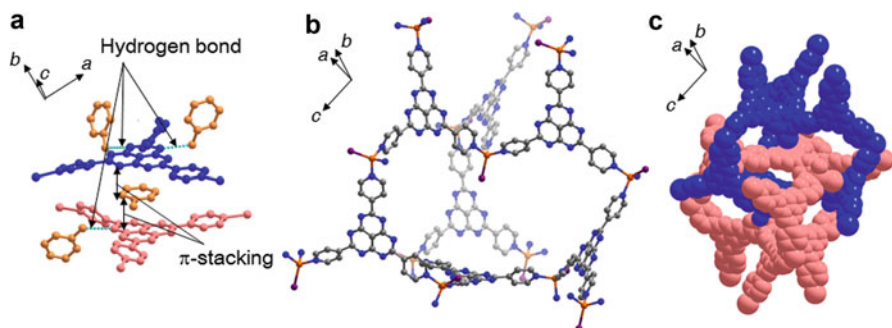


**Fig. 12.17** Crystal structure of **9**. (a) Encapsulation of one phenol sandwiched between two TPHAP<sup>-</sup>s via π-π interaction and four phenols through H bond with TPHAP<sup>-</sup>s. (b) 10<sup>3</sup>-srs 3D network composed of Zn(I<sup>-</sup>)(TPHAP<sup>-</sup>). (c) Interpenetrating 10<sup>3</sup>-srs 3D network. Hydrogen atoms and solvent molecules are omitted for clarity

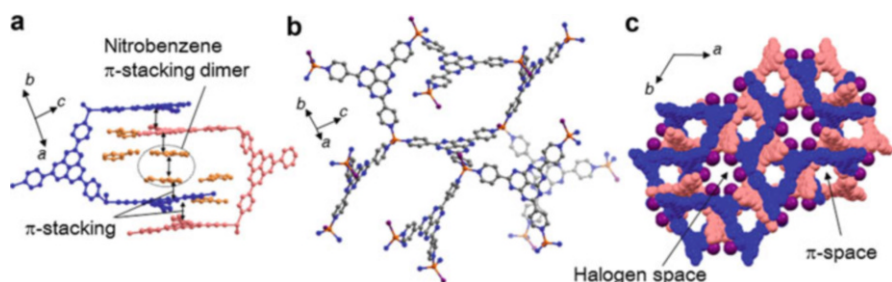


**Fig. 12.18** Crystal structure of **10**. (a) Encapsulation of nitrobenzene (*orange*) dimer between TPHAP<sup>-</sup>s via π-π interaction. (b) 8<sup>3</sup>-etf 3D network composed of Zn(I<sup>-</sup>)(TPHAP<sup>-</sup>). (c) Interpenetrating biporous 3D network, showing two kinds of 1D porous channels which are surrounded by π-planes and iodine atoms. Hydrogen atoms and solvent molecules are omitted for clarity

When nitrobenzene was used as an additive solvent, an unexpected 3D network  $[\text{ZnI}^-(\text{TPHAP}^-)] \cdot 2\text{PhNO}_2 \cdot 6\text{CH}_3\text{OH}$  (**10**) was formed. Although the components of this network are the same as those of **7**, **8**, and **9**, the topology is an interpenetrating 8<sup>3</sup>-etf net which is very rare and totally different from those of **7**, **8**, and **9**. **10** has two kinds of 1D porous channels along the *c* axis, so-called biporous structure (Fig. 12.18). Each channel is surrounded by different characteristic environments, halogen space (surrounded by coordinating I<sup>-</sup>s), and π-space (surrounded by π-planes of TPHAP<sup>-</sup> moieties). Indeed, the π-space accommodates aromatic nitrobenzene by π-π interaction with TPHAP<sup>-</sup>. Furthermore, nitrobenzene forms π-stacking dimers. Therefore, a quadruple π-stacking structure forms; it consists of two TPHAP<sup>-</sup>s and two nitrobenzenes (TPHAP<sup>-</sup>/nitrobenzene/nitrobenzene/TPHAP<sup>-</sup>). Because of the nitrobenzene dimer and the 1D channel, this network has a large pore which can exchange guest molecules smoothly.

TPHAP<sup>-</sup> and Zn<sup>2+</sup> produced four types of network topologies composed of Zn(I<sup>-</sup>)(TPHAP<sup>-</sup>) depending on the nature of the solvent. The structural features of each network are explained by focusing on the weak intermolecular interactions between TPHAP<sup>-</sup> and guest molecules. Especially, the results proved that the multi-interactivity of TPHAP<sup>-</sup> is strongly affected by even very slight differences in weak intermolecular interactions; therefore, TPHAP<sup>-</sup> can be an excellent probe for weak intermolecular interactions and is useful for trapping kinetic state networks.

## 12.4 Summary

Weak intermolecular interaction has long been an important concept in the field of supramolecular chemistry. These interactions are actively used for obtaining specific desired structures by reducing the flexibility of the system rather than by introducing diversity. In this study, we demonstrated that our strategy focusing on multi-interactivity can be used to control the formation of diverse networks which are composed of the same components. On the basis of structural features of the HAP skeleton, we designed and synthesized a multi-interactive tripyridyl ligand, TPHAP. The multi-interactivity of TPHAP successfully traps the kinetic porous coordination network as seen in enzymatic reactions. This network shows structure transformation to a thermally more stable network by ligand exchange reaction that is caused by change in ion concentration. Temperature change also affected the network formation paths to give totally different networks with the different coordination modes of TPHAP. Furthermore, addition of other components realized diverse network formation which can be controlled precisely by selecting the molecular structure of additives and adjusting their amount. Most of the obtained networks possessed interactive pores that can be effective sites for molecular recognition and reaction. These interactive pores can be applied not only for the conventional applications of porous materials but also for trapping metastable species such as unstable small allotropes. The unique chemical reactions caused by pore effects can potentially be exploited to give unexpected reaction products selectively. Ligand functionalization by introducing redox-active moieties may also expand the potential of multi-interactive networks as solid devices that have dynamic physical properties. We believe that multi-interactivity and its control are important keys to developing a new class of materials.

## References

1. R. Robson, *Dalton Trans.* **38**, 5101–5248 (2008)
2. M. Eddaoudi, D.B. Moler, H. Li, B. Chen, T.M. Reineke, M. O’Keeffe, O.M. Yaghi, *Acc. Chem. Res.* **34**, 319–330 (2001)
3. H. Furukawa, K.E. Cordova, M. O’Keeffe, O.M. Yaghi, *Science* **341**, 1230444 (2013)

4. S. Kitagawa, R. Kitaura, S.-I. Noro, *Angew. Chem. Int. Ed.* **43**, 2334–2375 (2004)
5. G. Férey, *Chem. Soc. Rev.* **37**, 191–214 (2008)
6. A. Bétard, R.A. Fischer, *Chem. Rev.* **112**, 1055–1083 (2012)
7. O.K. Farha, J.T. Hupp, *Acc. Chem. Res.* **43**, 1166–1175 (2010)
8. T.R. Cook, Y.-R. Zheng, P.J. Stang, *Chem. Rev.* **113**, 734–777 (2013)
9. M. Kondo, T. Yoshitomi, H. Matsuzaka, S. Kitagawa, K. Seki, *Angew. Chem. Int. Ed. Engl.* **36**, 1725–1727 (1997)
10. D.N. Dybtsev, H. Chun, S.H. Yoon, D. Kim, K. Kim, *J. Am. Chem. Soc.* **126**, 32–33 (2004)
11. J.L.C. Rowsell, O.M. Yaghi, *Angew. Chem. Int. Ed.* **44**, 4670–4679 (2005)
12. R. Matsuda, R. Kitaura, S. Kitagawa, Y. Kubota, R.V. Belosludov, T.C. Kobayashi, H. Sakamoto, T. Chiba, M. Takata, Y. Kawazoe, Y. Mita, *Nature* **436**, 238–241 (2005)
13. J.-R. Li, R.J. Kuppler, H.-C. Zhou, *Chem. Soc. Rev.* **38**, 1477–1504 (2009)
14. L.J. Murray, M. Dincă, J.R. Long, *Chem. Soc. Rev.* **38**, 1294–1314 (2009)
15. K. Sumida, D.L. Rogow, J.A. Mason, T.M. McDonald, E.D. Bloch, Z.R. Herm, T.H. Bae, J.R. Long, *Chem. Rev.* **112**, 724–781 (2012)
16. M. Eddaoudi, J. Kim, N. Rosi, D. Vodak, J. Wachter, M. O’Keeffe, O.M. Yaghi, *Science* **295**, 469–472 (2002)
17. H. Hayashi, A.P. Côté, H. Furukawa, M. O’Keeffe, O.M. Yaghi, *Nat. Mater.* **6**, 501–506 (2007)
18. D. Britt, H. Furukawa, B. Wang, T.G. Glover, O.M. Yaghi, *Proc. Natl. Acad. Sci. U.S.A.* **106**, 20637–20640 (2009)
19. A. Demessence, D.M. D’Alessandro, M.L. Foo, J.R. Long, *J. Am. Chem. Soc.* **131**, 8784–8786 (2009)
20. J.-R. Li, J. Sculley, H.-C. Zhou, *Chem. Rev.* **112**, 869–932 (2012)
21. B. Chen, S. Xiang, G. Qian, *Acc. Chem. Res.* **43**, 1115–1124 (2010)
22. L.E. Kreno, K. Leong, O.K. Farha, M. Allendorf, R.P. Van Duyne, J.T. Hupp, *Chem. Rev.* **112**, 1105–1125 (2012)
23. J. Lee, O.K. Farha, J. Roberts, K.A. Scheidt, S.T. Nguyen, J.T. Hupp, *Chem. Soc. Rev.* **38**, 1450–1459 (2009)
24. J.S. Seo, D. Whang, H. Lee, S.I. Jun, J. Oh, Y.J. Jeon, K. Kim, *Nature* **44**, 982–986 (2000)
25. L. Ma, C. Abney, W. Lin, *Chem. Soc. Rev.* **38**, 1248–1256 (2009)
26. D. Farrusseng, S. Aguado, C. Pinel, *Angew. Chem. Int. Ed.* **48**, 7502–7513 (2009)
27. A. Corma, H. García, I. Llabrés, F.X. Xamena, *Chem. Rev.* **110**, 4606–4655 (2010)
28. S. Bureekaew, S. Horike, M. Higuchi, M. Mizuno, T. Kawamura, D. Tanaka, N. Yanai, S. Kitagawa, *Nat. Mater.* **8**, 831–836 (2009)
29. J.A. Hurd, R. Vaidhyanathan, V. Thangadurai, C.I. Ratcliffe, I.L. Moudra-kovski, G.K.H. Shimizu, *Nat. Chem.* **1**, 705–710 (2009)
30. M. Sadakiyo, T. Yamada, H. Kitagawa, *J. Am. Chem. Soc.* **131**, 9906–9907 (2009)
31. M. Yoon, K. Suh, S. Natarajan, K. Kim, *Angew. Chem. Int. Ed.* **52**, 2688–2700 (2013)
32. P. Mahata, M. Prabu, S. Natarajan, *Inorg. Chem.* **47**, 8451–8463 (2008)
33. A.K. Cheetham, C.N.R. Rao, R.K. Feller, *Chem. Commun.* **46**, 4780–4795 (2006)
34. M. Kawano, T. Haneda, D. Hashizume, F. Izumi, M. Fujita, *Angew. Chem. Int. Ed.* **47**, 1269–1271 (2008)
35. J. Martí-Rujas, M. Kawano, *Acc. Chem. Res.* **46**, 493–505 (2013)
36. Y. Yakiyama, A. Ueda, Y. Morita, M. Kawano, *Chem. Commun.* **48**, 10651–10653 (2012)
37. T. Kojima, T. Yamada, Y. Yakiyama, E. Ishikawa, Y. Morita, M. Ebihara, M. Kawano, *CrystEngComm* **16**, 6335–6344 (2014)
38. M. Kawano, T. Kawamichi, T. Haneda, T. Kojima, M. Fujita, *J. Am. Chem. Soc.* **129**, 15418–15419 (2007)
39. T. Haneda, M. Kawano, T. Kawamichi, M. Fujita, *J. Am. Chem. Soc.* **130**, 1578–1579 (2008)
40. J. Martí-Rujas, N. Islam, D. Hashizume, F. Izumi, M. Fujita, H.J. Song, H.C. Choi, M. Kawano, *Angew. Chem. Int. Ed.* **50**, 6105–6108 (2011)
41. K. Ohara, J. Martí-Rujas, T. Haneda, M. Kawano, D. Hashizume, F. Izumi, M. Fujita, *J. Am. Chem. Soc.* **131**, 3860–3861 (2009)

42. J. Martí-Rujas, N. Islam, D. Hashizume, F. Izumi, M. Fujita, M. Kawano, *J. Am. Chem. Soc.* **133**, 5853–5860 (2011)
43. H. Ohtsu, W. Choi, N. Islam, Y. Matsushita, M. Kawano, *J. Am. Chem. Soc.* **135**, 11449–11452 (2013)
44. M. Chaplin, *Nat. Rev. Mol. Cell Biol.* **7**, 861–866 (2006)
45. S. Suzuki, Y. Morita, K. Fukui, K. Sato, D. Shiomi, T. Takui, K. Nakasuji, *Inorg. Chem.* **44**, 8197–8199 (2005)
46. S. Suzuki, K. Fukui, A. Fuyuhiko, K. Sato, T. Takui, K. Nakasuji, Y. Morita, *Org. Lett.* **12**, 5036–5039 (2010)
47. Y. Morita, S. Nishida, Chapter 3: Phenalenyls, cyclopentadienyls, and other carbon-centered radicals, in *Stable Radicals: Fundamentals and Applied Aspects of Odd-Electron Compounds*, ed. by R. Hicks (Wiley, Chichester, 2010), pp. 81–145
48. Y. Morita, S. Suzuki, K. Fukui, S. Nakazawa, H. Kitagawa, H. Kishida, H. Okamoto, A. Naito, A. Sekine, Y. Ohashi, M. Shiro, K. Sasaki, D. Shiomi, K. Sato, T. Takui, K. Nakasuji, *Nat. Mater.* **7**, 48–51 (2008)
49. Y. Morita, S. Suzuki, K. Sato, T. Takui, *Nat. Chem.* **3**, 197–204 (2011)
50. Y. Morita, S. Nishida, M. Murata, M. Moriguchi, A. Ueda, M. Satoh, K. Arifuku, K. Sato, T. Takui, *Nat. Mater.* **10**, 947–951 (2011)
51. G.R. Desiraju, *Angew. Chem. Int. Ed.* **46**, 8342–8356 (2007)
52. C.-P. Li, M. Du, *Chem. Commun.* **47**, 5958–5972 (2011)
53. S. Chen, I.A. Guzei, L. Yu, *J. Am. Chem. Soc.* **127**, 9881–9885 (2005)
54. V. López-Mejías, J.W. Kampf, A.J.J. Matzger, *Am. Chem. Soc.* **134**, 9872–9875 (2012)
55. Analyzed by TOPOS, V.A. Blatov, *Crystallogr. Rev.* **10**, 249–318 (2004)
56. V.A. Blatov, *IUCr CompComm. Newsl.* **7**, 4–38 (2006)
57. O. Delgado-Friedrichs, M. O’Keeffe, O.M. Yaghi, *Acta Crystallogr. Sect. A: Found. Crystallogr.* **59**, 22–27 (2003)
58. V.A. Blatov, L. Carlucci, G. Ciani, D.M. Proserpio, *CrystEngComm* **6**, 378–395 (2004)
59. I.A. Baburin, V.A. Blatov, L. Carlucci, G. Ciani, D.M.J. Proserpio, *Solid State Chem.* **178**, 2452–2474 (2005)
60. M. O’Keeffe, M.A. Peskov, S.J. Ramsden, O.M. Yaghi, *Acc. Chem. Res.* **41**, 1782–1789 (2008)
61. E.V. Alexandrov, V.A. Blatov, A.V. Kochetkov, D.M. Proserpio, *CrystEngComm* **13**, 3947–3958 (2011)
62. L. Carlucci, G. Ciani, D.M. Proserpio, *Coord. Chem. Rev.* **246**, 247–289 (2003)
63. D.M. Proserpio, *Nat. Chem.* **2**, 435–436 (2010)

# Chapter 13

## Azacalixarene: An Ever-Growing Class in the Calixarene Family

Hirohito Tsue and Ryusei Oketani

**Abstract** The chemistry of azacalixarenes, in which the aromatic rings are linked by nitrogen bridges, has been growing steadily and attracting much attention as a new class in the calixarene family ever since our previous review of azacalixarenes was published in 2008. In the years that have followed, an increasing variety of azacalixarene derivatives have been reported to date. Although the diversity is still limited as compared to carbon- and sulfur-bridged calixarenes, the intriguing chemistry of azacalixarenes on the basis of the introduction of nitrogen atoms as the bridging units has thus far been disclosed. Particularly encouraging progress in the azacalixarene chemistry since 2008 has been made in the synthetic chemistry as well as the host–guest chemistry in the solid state, as revealed by recent studies. This review covers the papers published in the last 6 years, especially concentrating on the preparations and complexation properties of this new calixarene family.

**Keywords** Azacalixarene • Synthesis • Complexation • Crystal structure

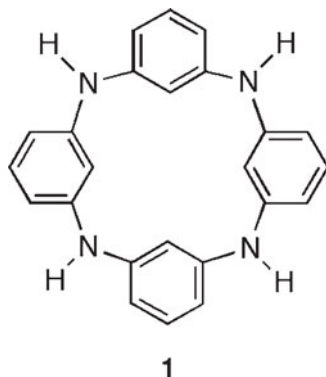
### 13.1 Introduction

“Azacalixarene” is a general term coined for nitrogen-bridged calixarene analogues that have recently emerged as a new calixarene family [1–6] by breaking a long silence that persisted since the first paper was published in 1963 on the X-ray crystallographic analysis of **1** (Fig. 13.1) [7]. Owing to the structural and electronic nature of the nitrogen bridges that allow to impart novel properties and functions to molecules, the intriguing chemistry of azacalixarenes on the basis of the introduction of nitrogen atoms as the bridging units has thus far been disclosed. To summarize the accumulated knowledge since 1963 as to their syntheses, unique molecular structures, and versatile complexation properties, we had published a review relating to the topics in 2008 [3], at which time only less than 20 papers had appeared in the chemical literature. In the years that have followed, almost all

---

H. Tsue (✉) • R. Oketani  
Graduate School of Human and Environmental Studies, Kyoto University,  
Yoshida-nihonmatsu, Sakyo-ku, Kyoto 606-8501, Japan  
e-mail: [tsue@orgmater.h.kyoto-u.ac.jp](mailto:tsue@orgmater.h.kyoto-u.ac.jp)

**Fig. 13.1** The first azacalix[4]arene reported by Smith in 1963 [7]



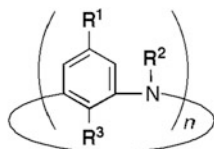
of the researchers already committed in 2008 have greatly expanded their studies, and other new researchers have entered this field. As an outcome, the 6 years after 2008 have shown great advances in the chemistry of azacalixarenes. In fact, about 40 papers have been published only in the last 6 years, during which a variety of azacalixarene derivatives have been reported and are enumerated in Fig. 13.2 and Table 13.1. Particularly encouraging progress in the azacalixarene chemistry since 2008 has been made in the synthetic chemistry as well as the host–guest chemistry in the solid state, as revealed by recent studies summarized in the following sections. This review covers the papers published from the middle of 2008 to the third-quarter of 2014, especially concentrating on the preparations and complexation properties of this new calixarene family with a  $[1_n]$ metacyclophane framework.

## 13.2 Synthetic Chemistry

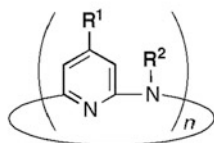
As described in our previous review published in 2008 [3], three typical synthetic strategies are generally applied to the synthesis of azacalixarenes, i.e., (1) single-step synthesis, (2) non-convergent stepwise synthesis, and (3) convergent fragment-coupling synthesis. The 6 years after 2008 have shown much progress in the synthesis of azacalixarene frameworks. In the following subsections, the preparations and post-functionalization methods of azacalixarenes are described.

### 13.2.1 Single-Step Synthesis

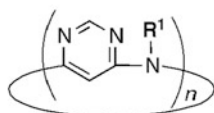
A single-step synthesis is the most efficient approach to azacalixarenes composed of one single type of aromatic unit. A typical example is the synthesis of azacalix[3]pyridine **9** reported by Kanbara and coworkers [16]. As shown in Scheme 13.1, Ullmann coupling reaction of **73** afforded **9** as a HBr salt in 92 %



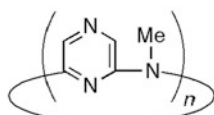
- 2:  $R^1 = R^3 = H, R^2 = Me, n = 6$   
 3:  $R^1 = t\text{-Bu}, R^2 = H, R^3 = OMe, n = 4$   
 4:  $R^1 = t\text{-Bu}, R^2 = H, R^3 = OMe, n = 5$   
 5:  $R^1 = t\text{-Bu}, R^2 = H, R^3 = OMe, n = 6$   
 6:  $R^1 = t\text{-Bu}, R^2 = H, R^3 = OMe, n = 7$   
 7:  $R^1 = Cl, R^2 = H, R^3 = OMe, n = 5$   
 8:  $R^1 = t\text{-Bu}, R^2 = Me, R^3 = OMe, n = 6$



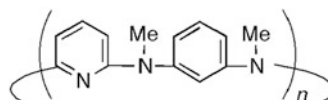
- 9:  $R^1 = H, R^2 = Toly, n = 3$   
 10:  $R^1 = Pyrrolidino, R^2 = Toly, n = 3$   
 11:  $R^1 = Pyrrolidino, R^2 = Anisyl, n = 3$   
 12:  $R^1 = Pyperidino, R^2 = Toly, n = 3$   
 13:  $R^1 = H, R^2 = Toly, n = 4$   
 14:  $R^1 = Pyrrolidino, R^2 = Toly, n = 4$   
 15:  $R^1 = Pyrrolidino, R^2 = Anisyl, n = 4$   
 16:  $R^1 = H, R^2 = Me, n = 4$   
 17:  $R^1 = H, R^2 = Me, n = 6$   
 18:  $R^1 = H, R^2 = Me, n = 7$   
 19:  $R^1 = H, R^2 = Me, n = 8$   
 20:  $R^1 = H, R^2 = Me, n = 9$



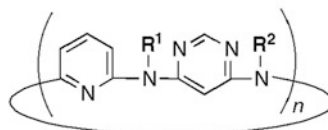
- 21:  $R^1 = Me, n = 4$   
 22:  $R^1 = Bu, n = 4$   
 23:  $R^1 = allyl, n = 4$   
 24:  $R^1 = Bn, n = 4$   
 25:  $R^1 = PMB, n = 4$   
 26:  $R^1 = Et, n = 6$



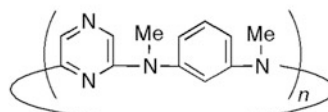
- 27:  $n = 4$   
 28:  $n = 8$



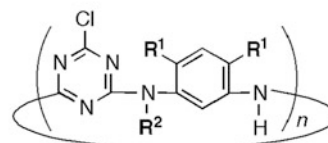
- 29:  $n = 2$   
 30:  $n = 3$



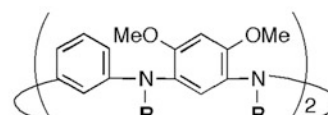
- 31:  $R^1 = R^2 = Me, n = 3$   
 32:  $R^1 = Me, R^2 = Allyl, n = 3$   
 33:  $R^1 = Me, R^2 = Bn, n = 3$   
 34:  $R^1 = Me, R^2 = 2\text{-Naphthylmethyl}, n = 3$   
 35:  $R^1 = Me, R^2 = 1\text{-Naphthylmethyl}, n = 3$   
 36:  $R^1 = Me, R^2 = 1\text{-Pyrenylmethyl}, n = 3$   
 37:  $R^1 = Me, R^2 = PhCH_2CH_2, n = 3$   
 38:  $R^1 = Me, R^2 = 4\text{-Cyanobenzyl}, n = 3$   
 39:  $R^1 = Me, R^2 = PMB, n = 3$   
 40:  $R^1 = R^2 = Allyl, n = 3$   
 41:  $R^1 = R^2 = Bn, n = 3$



- 42:  $n = 2$   
 43:  $n = 4$

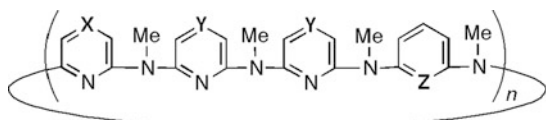


- 44:  $R^1 = R^2 = H, n = 2$   
 45:  $R^1 = H, R^2 = Me, n = 2$

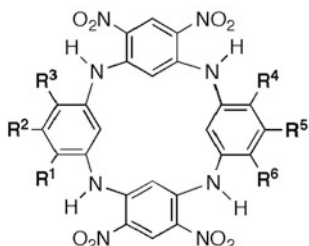


- 46:  $R = H$   
 47:  $R = 4\text{-(N,N-Dianisylamino)phenyl}$

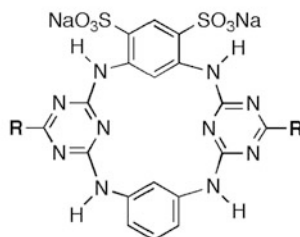
Fig. 13.2 Azacalixarenes reported from the middle of 2008 to the third-quarter of 2014. Compounds 94, 104–106, and 108–110 reported in this period are shown in Schemes 13.6, 13.11, and 13.12, respectively



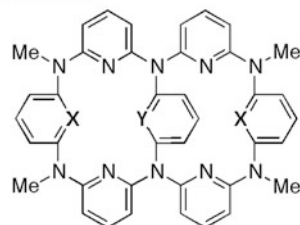
- 48: X = Y = Z = N, n = 1  
 49: X = Y = Z = N, n = 2  
 50: X = Z = N, Y = CH, n = 1  
 51: X = Z = N, Y = CH, n = 2  
 52: X = Y = Z = CH, n = 1



- 53: R<sup>1</sup> = R<sup>2</sup> = R<sup>3</sup> = R<sup>4</sup> = R<sup>5</sup> = R<sup>6</sup> = H  
 54: R<sup>1</sup> = R<sup>3</sup> = R<sup>4</sup> = R<sup>6</sup> = *i*-Pr, R<sup>2</sup> = R<sup>5</sup> = H  
 55: R<sup>1</sup> = R<sup>4</sup> = Me, R<sup>2</sup> = R<sup>3</sup> = R<sup>5</sup> = R<sup>6</sup> = H  
 56: R<sup>1</sup> = R<sup>6</sup> = Me, R<sup>2</sup> = R<sup>3</sup> = R<sup>4</sup> = R<sup>5</sup> = H  
 57: R<sup>1</sup> = R<sup>4</sup> = OMe, R<sup>2</sup> = R<sup>3</sup> = R<sup>5</sup> = R<sup>6</sup> = H  
 58: R<sup>1</sup> = R<sup>4</sup> = NHPH, R<sup>2</sup> = R<sup>3</sup> = R<sup>5</sup> = R<sup>6</sup> = H  
 59: R<sup>1</sup> = OMe, R<sup>2</sup> = R<sup>3</sup> = R<sup>4</sup> = R<sup>6</sup> = H, R<sup>5</sup> = CO<sub>2</sub>Me  
 60: R<sup>1</sup> = NHPH, R<sup>2</sup> = R<sup>3</sup> = R<sup>4</sup> = R<sup>6</sup> = H, R<sup>5</sup> = CO<sub>2</sub>Me  
 61: R<sup>1</sup> = R<sup>3</sup> = R<sup>4</sup> = R<sup>6</sup> = H, R<sup>2</sup> = R<sup>5</sup> = CO<sub>2</sub>Me  
 62: R<sup>1</sup> = R<sup>3</sup> = R<sup>4</sup> = R<sup>6</sup> = H, R<sup>2</sup> = R<sup>5</sup> = CH<sub>2</sub>OH  
 63: R<sup>1</sup> = R<sup>3</sup> = R<sup>4</sup> = R<sup>6</sup> = H, R<sup>2</sup> = CO<sub>2</sub>Me, R<sup>4</sup> = Me



- 64: R = NH*t*-Bu  
 65: R = NHBn  
 66: R = NHCH<sub>2</sub>CH<sub>2</sub>SCH<sub>2</sub>CH<sub>2</sub>OH  
 67: R = Cl



- 68: X = Y = N  
 69: X = N, Y = CH  
 70: X = Y = CH

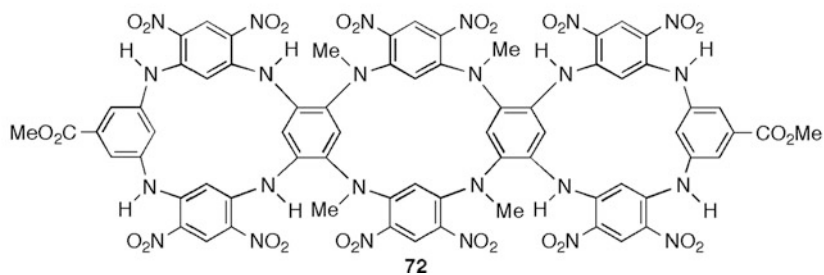
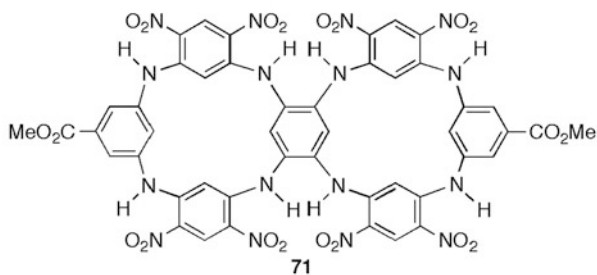


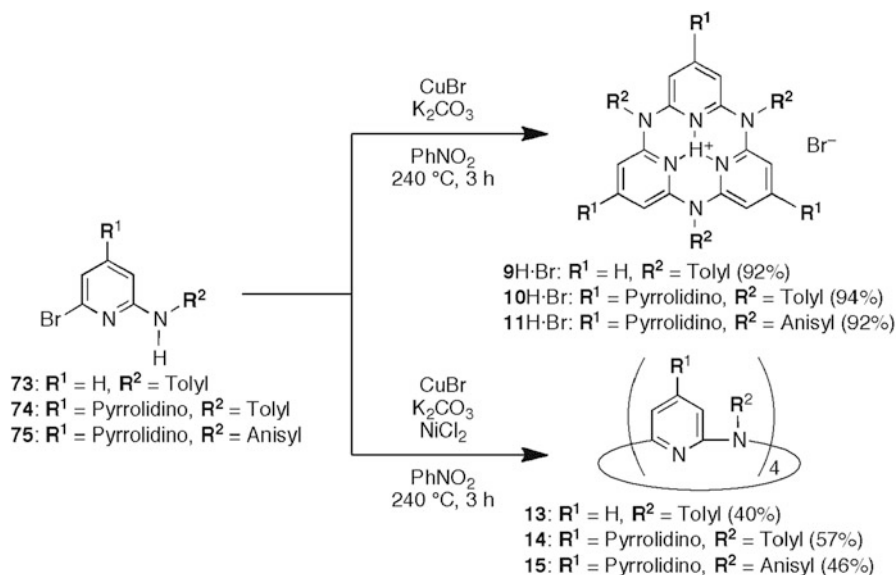
Fig. 13.2 (continued)

**Table 13.1** A list of references for all the azacalixarenes shown in Fig. 13.2

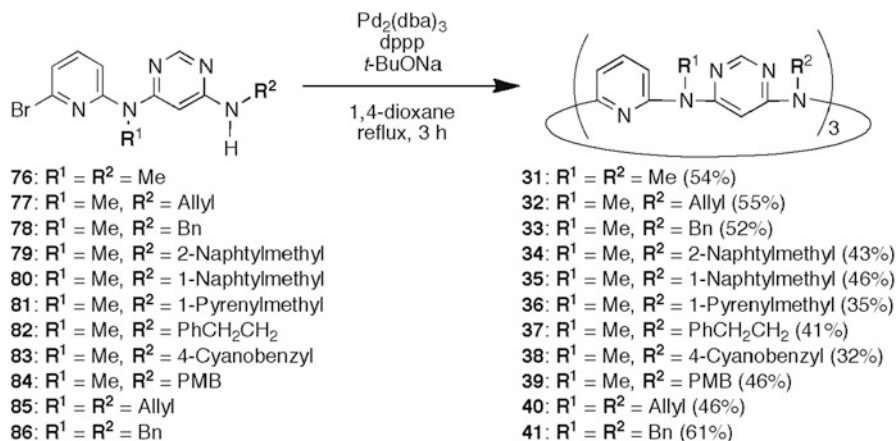
Cmpnd	Ref	Cmpnd	Ref	Cmpnd	Ref
2	[8]	26	[8]	50	[31]
3	[9–11]	27	[29]	51	[31]
4	[9–11]	28	[29]	52	[35]
5	[10–12]	29	[20]	53	[36]
6	[10, 11, 13]	30	[8]	54	[37, 38]
7	[14]	31	[8, 30]	55	[39, 40]
8	[15]	32	[8]	56	[40]
9	[16–18]	33	[8]	57	[39]
10	[16, 17]	34	[8]	58	[39]
11	[16, 17]	35	[8]	59	[39]
12	[17]	36	[8]	60	[39]
13	[16, 18]	37	[8]	61	[36, 40]
14	[16]	38	[8]	62	[40]
15	[16]	39	[8]	63	[40]
16	[19–21]	40	[8]	64	[32, 41]
17	[8, 19, 22–25]	41	[8]	65	[32, 41]
18	[19]	42	[31]	66	[32, 41]
19	[19, 26]	43	[31]	67	[41]
20	[19]	44	[32, 33]	68	[42]
21	[27, 28]	45	[32]	69	[42]
22	[27]	46	[34]	70	[42]
23	[27]	47	[34]	71	[43]
24	[27]	48	[31]	72	[43]
25	[27]	49	[31]		

yield; hydrogen bromide was formed in situ as a by-product. Interestingly, the proton adduct of **9** was obtained in 88 % yield even under high concentration conditions of 1 mol dm<sup>-3</sup>. The excellent yields of **9** clearly indicate that the template effect of proton is operative in the synthesis of a **9H**·Br salt because neutral **9** behaves as an organic superbase ( $pK_{BH^+} = 23.1$  in MeCN) far basic than proton sponge ( $pK_{BH^+} = 18.2$  in MeCN) [18]. In a similar manner, the HBr salts of azacalix[3]pyridines **10** and **11** were also synthesized in excellent yields (94 and 92 %, respectively) owing to the same template effect.

Furthermore, Kanbara and coworkers reported another template effect using nickel(II) ion in the synthesis of azacalix[4]pyridines **13–15** [16]. In the absence of nickel(II) ion, azacalix[3]pyridine **9** rather than azacalix[4]pyridine **13** was obtained in 80 % yield because of the template effect of proton mentioned above. In contrast, azacalix[4]pyridines **13–15** were successfully formed in 40–57 % yields in the presence of nickel(II) chloride, as shown in Scheme 13.1. This template effect was strongly supported by the X-ray crystallographic analysis of the nickel(II) complex of **13** (see Sect. 13.3.1).

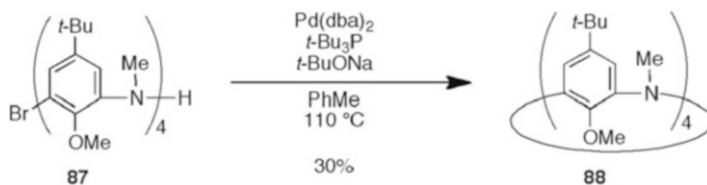


**Scheme 13.1** Single-step approach to azacalix[3]pyridine HBr salts **9H·Br**–**11H·Br** and azacalix[4]pyridines **13–15** [16]

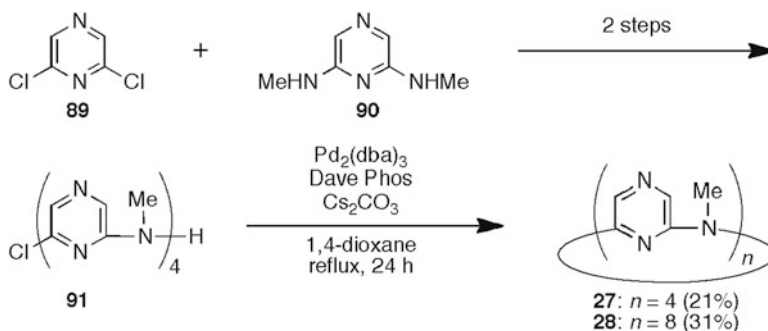


**Scheme 13.2** Single-step synthesis of azacalix[3]pyridine[3]pyrimidines **31–41** [8]

Another interesting application of the single-step procedure was made by Wang et al., who utilized palladium(0)-catalyzed Buchwald–Hartwig aryl amination reaction for preparing “mixed” azacalix[6]arenes **31–41** designated as azacalix[3]pyridine[3]pyrimidines, in which pyridine and pyrimidine rings were alternately linked by nitrogen bridges [8] (Scheme 13.2).



**Scheme 13.3** Stepwise approach to azacalix[4]arene **88** [46]



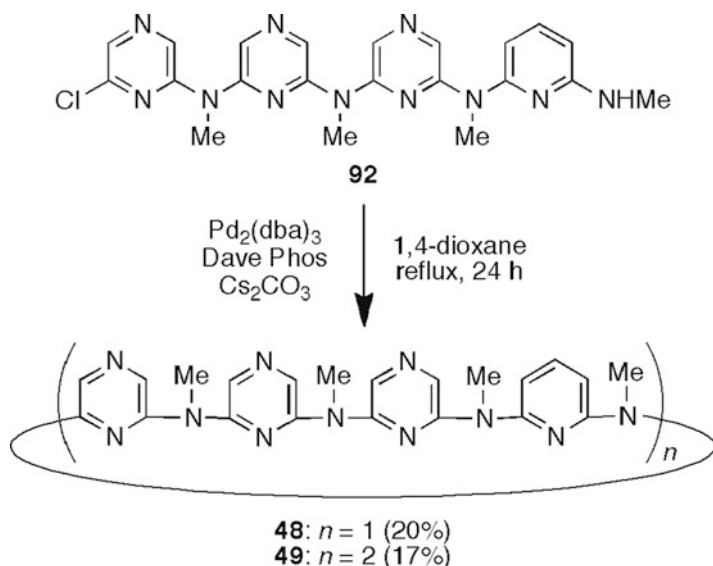
**Scheme 13.4** Stepwise synthesis of azacalixpyrazines **27** and **28** [29]

### 13.2.2 Non-convergent Stepwise Synthesis

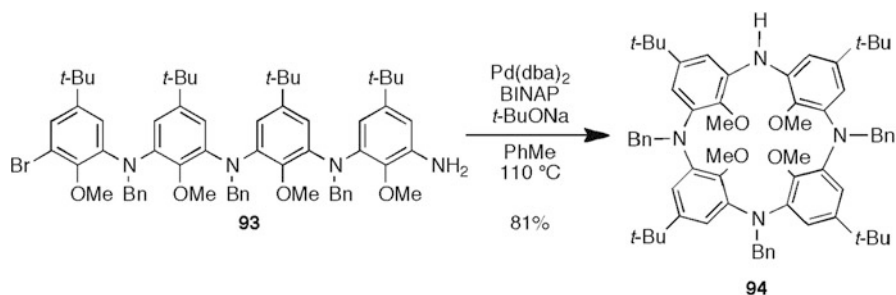
Historically, non-convergent stepwise strategy was first devised by Hayes et al. in 1956 to synthesize carbon-bridged calixarenes from linear phenol oligomers [44, 45]. Before our previous review was published in 2008 [3], only one application was reported for the non-convergent stepwise synthesis of azacalixarene; Tsue and coworkers prepared exhaustively methylated azacalix[4]arene **88** [46] by applying Buchwald–Hartwig aryl amination reaction to the intramolecular cyclization of linear tetramer **87** (Scheme 13.3).

In 2012, Wang and coworkers successfully applied a non-convergent stepwise strategy to the synthesis of azacalixpyrazines **27** and **28** [29], which were obtained by the Buchwald–Hartwig aryl amination reaction of linear pyrazine tetramer **91** prepared from monomers **89** and **90** in two steps, as shown in Scheme 13.4.

In principle, the non-convergent stepwise strategy provides a versatile synthetic approach to azacalixarenes. Recently, this was clearly demonstrated by Wang and coworkers [31], who used Buchwald–Hartwig aryl amination reaction for preparing “mixed” azacalixarenes **48** and **49** called azacalix[3*n*]pyridine[*n*]pyrazines in which pyridine rings were regioselectively placed in the macrocyclic frameworks mainly made of pyrazine rings (Scheme 13.5).

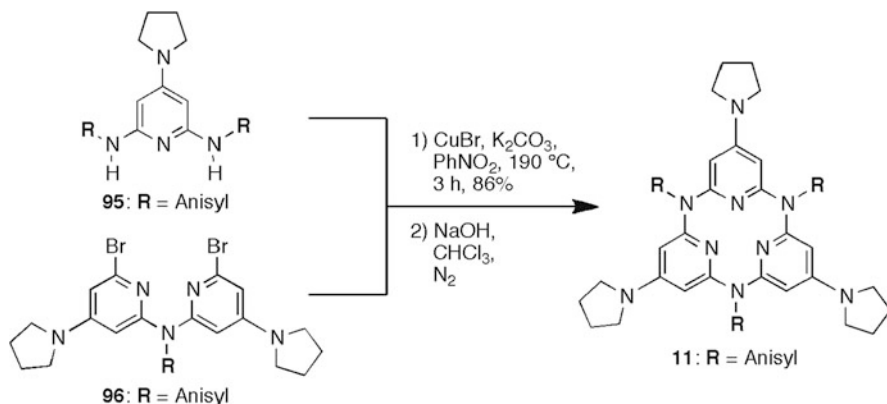


**Scheme 13.5** Stepwise synthesis of azacalix[3*n*]pyridine[*n*]pyrazines **48** and **49** [31]



**Scheme 13.6** Stepwise synthesis of inherently chiral azacalix[4]arene **94** [47]

An interesting application of the non-convergent stepwise procedure was made by Tsue and coworkers, who reported the first example of inherently chiral azacalix[4]arene **94** [47], a synthetic precursor of **3** [9] (Scheme 13.6). *N,N,N'*-tribenzylated **94** adopts a frozen 1,3-alternate conformation with pseudo *C*<sub>2</sub> symmetry, and both enantiomers are separated by a chiral stationary phase column. The inherent chirality of **94** was confirmed unambiguously by the circular dichroism spectra of the (+)- and (–)-enantiomers. In a similar manner, Tsue and coworkers also succeeded in the non-convergent stepwise synthesis of azacalix[5]arenes **4** and **7** [9, 14].



**Scheme 13.7** Fragment-coupling approach to azacalix[3]pyridine **11** [17]

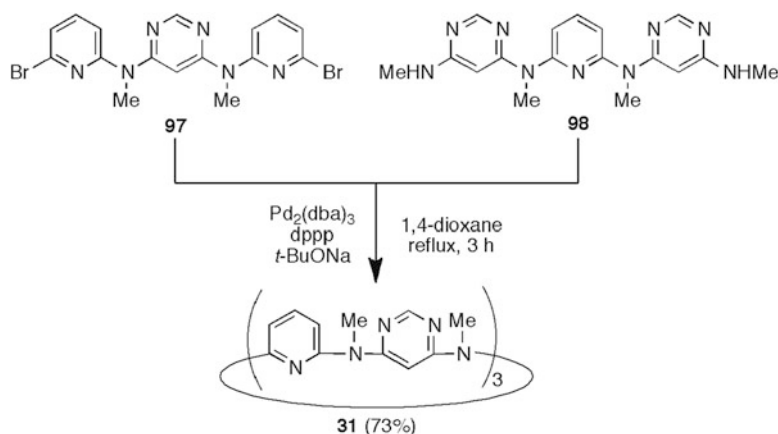
### 13.2.3 Convergent Fragment-Coupling Synthesis

In 1979, Böhmer et al. devised a convergent fragment-coupling strategy in which two different molecules were coupled in the cyclization step to synthesize carbon-bridged calixarenes [48]. This strategy also provides a flexible synthetic approach to azacalixarenes, as the non-convergent stepwise method does (Sect. 13.2.2). In fact, a wide variety of azacalixarenes have been prepared by applying this strategy.

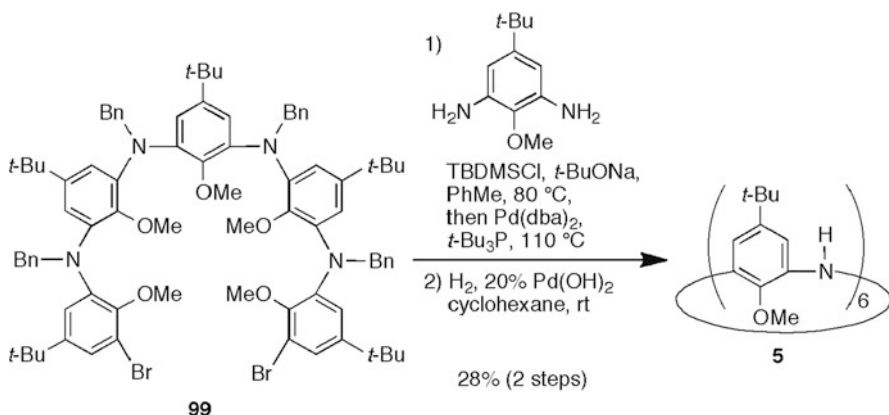
As mentioned in Sect. 13.2.1, azacalix[3]pyridine **11** was prepared by using the single-step procedure (see Scheme 13.1). Kanbara and coworkers further examined the convergent fragment-coupling procedure [17], by which azacalix[3]pyridine **11** was prepared via the copper(I)-catalyzed Ullmann coupling reaction of two component monomers **95** and **96**, followed by neutralization with NaOH, as shown in Scheme 13.7.

Wang and coworkers also examined the convergent fragment-coupling synthesis of azacalix[3]pyridine[3]pyrimidine **31** [30] which was synthesizable by applying the single-step procedure (see Scheme 13.2). As shown in Scheme 13.8, the Buchwald–Hartwig aryl amination reaction of two component trimers **97** and **98** afforded **31** in 73 % yield that was slightly higher than 54 % yield observed in the single-step procedure. In a similar manner, Wang and coworkers prepared azacalix[6]arene **2** [8], azacalix[6]pyridines **17–20** [19], azacalix[3]arene[3]pyridine **30** [8], and internally 1,3-arylene-bridged azacalix[6]arenes **68–70** by using this strategy [42].

To suppress an undesirable  $\beta$ -elimination reaction in the Buchwald–Hartwig aryl amination reaction, “a temporal *N*-silylation protocol” was devised by Tsue and coworkers [49]. The protocol involves a smooth in situ *N*-silylation before aryl amination reaction, followed by spontaneous cleavage of the N–Si bond in the usual workup process, to furnish secondary aromatic amines as the cross-coupled product



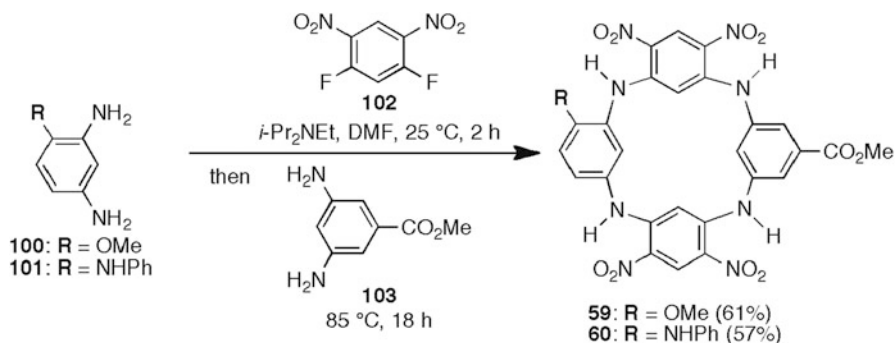
**Scheme 13.8** Fragment-coupling synthesis of azacalix[3]pyridine[3]pyrimidine **31** [30]



**Scheme 13.9** Fragment-coupling synthesis of azacalix[6]arene **5** by applying a temporal *N*-silylation protocol [12]

with no silyl group on the nitrogen atom. By applying this protocol, azacalix[6]arene **5** was successfully prepared in two steps, as shown in Scheme 13.9 [12]. In a similar manner, azacalixarenes **6** and **8** were also prepared by Tsue and coworkers [13, 15].

In addition to the transition metal-catalyzed synthesis described above, “metal-free” synthesis was also applied to the convergent fragment-coupling strategy on the basis of aromatic nucleophilic substitution reaction ( $\text{S}_{\text{N}}\text{Ar}$ ). As a typical example, Katz and coworkers carried out the  $\text{S}_{\text{N}}\text{Ar}$  reactions of **100** or **101** with monomer **102** and then with another monomer **103** to prepare three-component azacalix[4]arenes **59** and **60** [39] (Scheme 13.10). Azacalixpyrimidines **21–25** [27], azacalix[2]arene[2]triazines **44** and **45** [32], and azacalix[4]arenes **53–58** and **61–63** [36–40] were also synthesized in a similar manner. Very recently, Siri and coworkers



**Scheme 13.10** Fragment-coupling synthesis of three-component azacalix[4]arenes **59** and **60** [39]

succeeded in preparing “fused” azacalix[4]arenes **71** and **72** in which two and three azacalix[4]arene frameworks were merged, respectively [43].

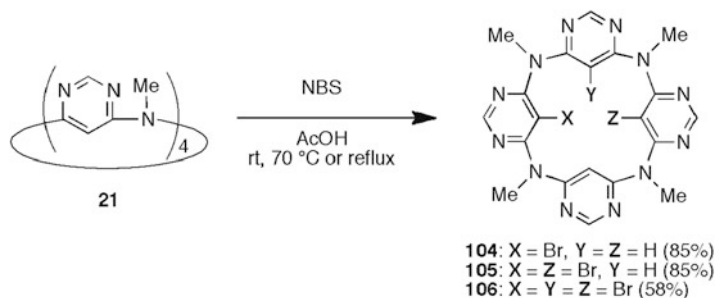
### 13.2.4 Post-Functionalization

In the carbon-bridged calixarene chemistry, a variety of post-functionalization methods were reported to modify the upper and lower rims [50–53]. In contrast, before our previous review was published in 2008 [3], the post-functionalizations of azacalixarene frameworks were only limited to four literature reported independently by Graubaum and Wang [54–57]. Graubaum and coworkers reported the amination of azacalix[2]arene[4]triazine, while Wang and coworkers carried out the amination of azacalix[2]arene[2]triazine **44**, followed by *N*-arylation of the nitrogen bridges.

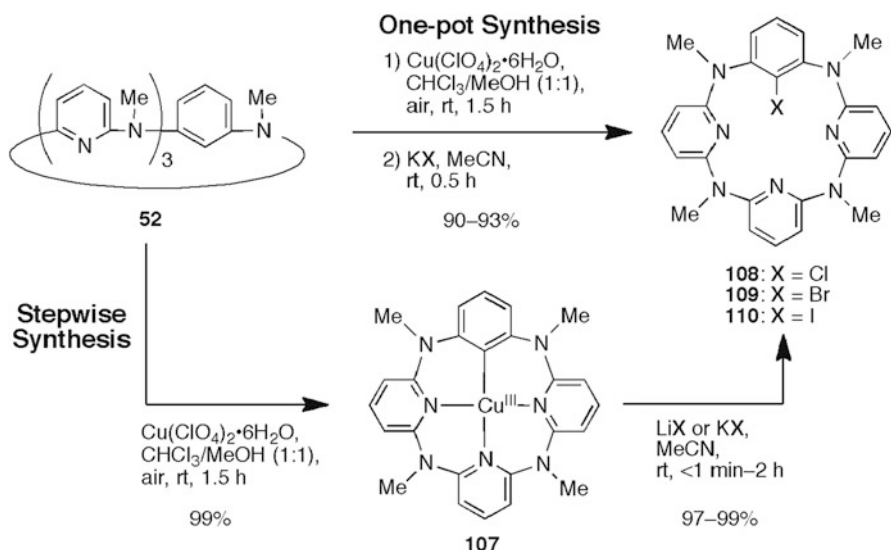
These types of post-functionalizations have been conducted ever since 2008. Moiteriro and Félix reported the *N*-alkylation of **44** [33], and Ito and coworkers carried out the *N*-arylation of **46** to prepare **47**, of which the dicationic and tetracationic species exhibited spin-triplet and spin-quintet states, respectively [34].

In 2010, Wang and coworkers introduced a new post-functionalization method, namely, the bromination of azacalixarene framework [27]. As shown in Scheme 13.11, azacalix[4]pyrimidine **21** was treated with NBS under controlled reaction conditions to selectively produce brominated products **104–106** in good yields. Afterward, Wang and coworkers continued their extensive studies to make the regioselective fluorination, chlorination, bromination, and deuteration of **21** possible [27, 28].

A more interesting post-halogenation method was recently devised by Wang and coworkers [35]. As shown in the bottom of Scheme 13.12, azacalix[1]arene[3]pyridine **52** was treated with  $\text{Cu}(\text{ClO}_4)_2$  under mild aerobic conditions to quantitatively give a stable aryl–Cu(III) complex **107**, which was able to react with a variety of alkali metal halides to give the corresponding



**Scheme 13.11** Selective bromination of azacalix[4]pyrimidine **21** [27]



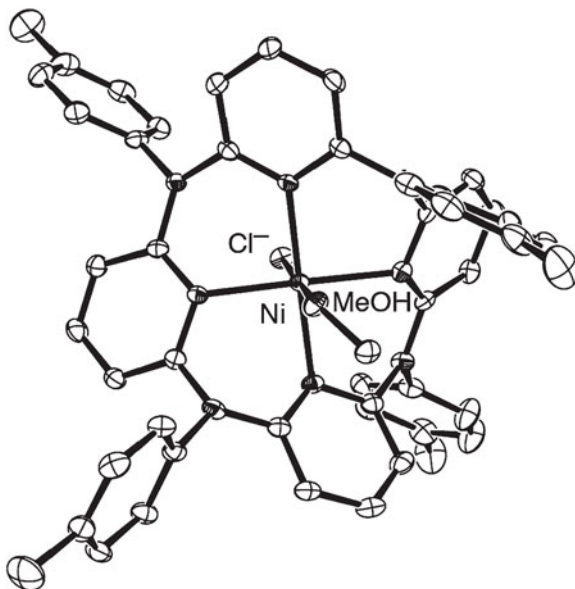
**Scheme 13.12** One-pot and stepwise syntheses of monohalogenated azacalix[1]arene[3]pyridines **108–110** [35]

monohalogenated products **108–110** in 97–99 % yields. It is worth noting that convenient one-pot syntheses of **108–110** are also feasible at ambient temperature in excellent yields (90–93 %), as shown in the top of Scheme 13.12. The aryl–Cu(III) complex **107**, a key intermediate in the post-halogenation reactions, was fully characterized by means of X-ray crystallographic analysis (see Sect. 13.3.1).

### 13.3 Host–Guest Chemistry in the Solid State

As described in our previous review published in 2008 [3], azacalixarenes act as versatile complexation agents, contributing greatly to the growth of the azacalixarene chemistry. Before 2008, however, only seven papers on the host–guest chemistry

**Fig. 13.3** ORTEP drawing of the nickel(II) complex of **13** [16]



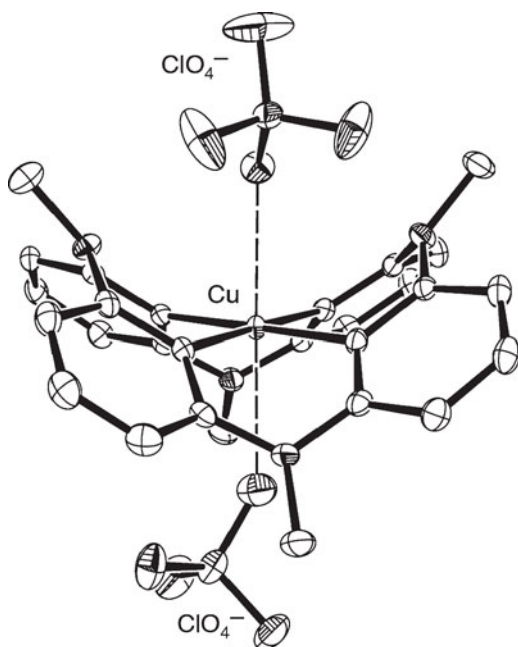
of azacalixarenes had appeared in the chemical literature. The last 6 years have shown much progress especially in the host–guest chemistry in the solid state. In the following subsections, three fascinating topics such as (1) metal ion complexation, (2) fullerene complexation, and (3) gas sorption in the solid state are described.

### 13.3.1 Metal Ion Complexation

As mentioned in Sect. 13.2.1, Kanbara and coworkers reported that nickel(II) ion promoted the formation of azacalix[4]pyridines **13–15** by the template effect [16]. To explain this effect, they performed the X-ray crystallographic analysis of the nickel(II) complex of **13** [16]. As shown in Fig. 13.3, a nickel(II) ion is embedded in the cavity of **13**. The nickel center adopts an octahedral geometry and is coordinated by the four pyridine nitrogen atoms of **13**, a counter chloride anion, and one molecule of methanol. Because the nickel center nicely fits the cavity of **13**, the crystal structure strongly supports that a nickel(II) ion serves as the template for preferentially affording azacalix[4]pyridines **13–15**.

Wang and coworkers succeeded in characterizing aryl–Cu(III) complex **107**, a key intermediate in the post-halogenation reactions (Sect. 13.2.4), by means of X-ray crystallographic analysis [21]. As shown in Fig. 13.4, a copper(III) ion is accommodated in the cavity of **29**. The macrocyclic aryl–Cu(III) complex **107** adopts a saddle conformation, and the copper(III) ion is coordinated by three pyridine nitrogen atoms and one carbon atom of the benzene in a planar square geometry. It is interesting to note that azacalix[4]pyridine **52** undergoes an efficient

**Fig. 13.4** ORTEP drawing of aryl–Cu(III) complex **107** [21]



aerobic C–H activation at room temperature to form stable aryl–Cu(III) complex **107**, which is converted highly efficiently to monohalogenated products **108–110** upon treatment with various nucleophiles under very mild conditions (see Scheme 13.12) [35].

Wang and Zhao studied the metal-binding property of internally 1,3-arylene-bridged azacalix[6]pyridine **68**. In the solid state, azacalix[6]pyridine **68** formed a 1:1 or 1:2 complex with transition metal ions. As shown in Fig. 13.5, a nickel(II) ion is embedded in the one cavity of **68** with a similar geometry to that of the nickel(II) complex of **13** (see Fig. 13.3). On the other hand, two cadmium(II) ions were accommodated in each cavity of **68** because of the large ionic radius of cadmium(II) ion as compared to nickel(II) ion. Wang and Zhao further studied the 1:1 complexation behavior of **68** with cadmium(II) ion in solution. Very interestingly, NMR titration experiments provided an evidence for a dynamic hopping motion by which a cadmium(II) ion moved from one side of the cavity of **68** to another side in solution.

Recently, Wang and Zhao reported the interesting stabilization of reactive polynuclear silver carbide cluster through the encapsulation within azacalix[6]pyridine **17** [25]. As shown in Fig. 13.6b, two molecules of **17** form a closed silver cage with a  $C \equiv C^{2-}$  anion trapped inside. In the cage of **17**, the silver carbide cluster is composed of two disordered parts,  $C_2@Ag_5$  and  $C_2@Ag_6$ . As shown in Fig. 13.6a, four silver atoms (Ag1, Ag2, Ag3, and Ag4) share their positions in both two cluster aggregates, whereas three remaining silver

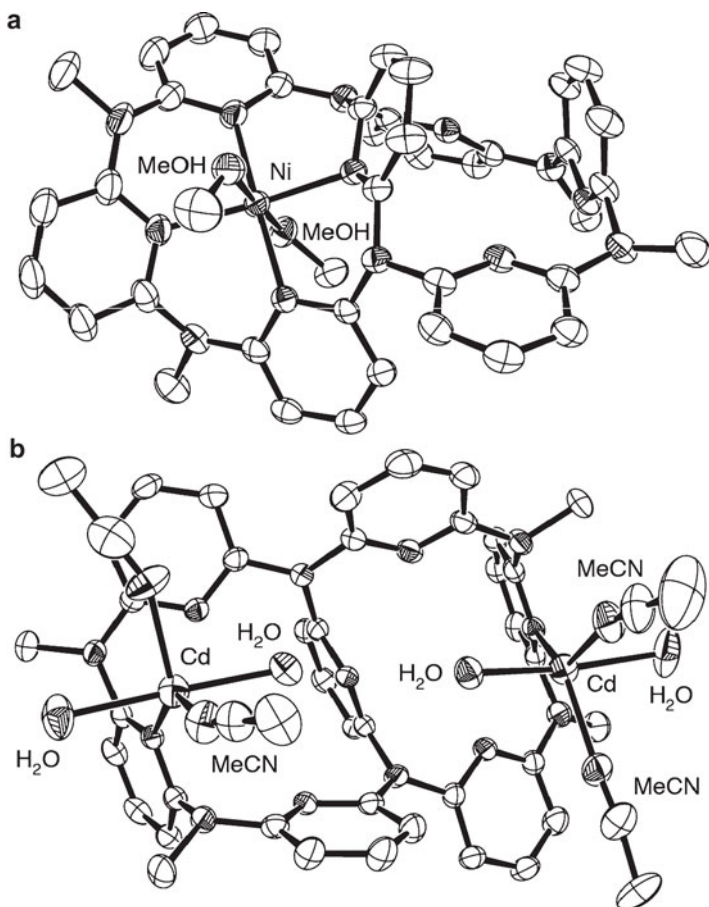


**Fig. 13.5** ORTEP drawing of the (a) Ni(II) and (b) Cd(II) complexes of internally 1,3-arylene-bridged azacalix[6]arene **68** [42]

atoms (Ag5 and the Ag5A–Ag5B) are disordered with a site-occupancy ratio of 0.70 and 0.30, respectively. Thus, the formula of the complex is expressed as  $(\text{Ag}_5(\text{C}\equiv\text{C})\mathbf{17}_2)_{0.7}(\text{Ag}_6(\text{C}\equiv\text{C})\mathbf{17}_2)_{0.3}$ . The silver carbide cluster is encapsulated by two bowl-shaped **17** in the complex through the Ag–N coordination and the cation/ $\pi$  interactions. A similar encapsulation of silver carbide cluster by azacalix[8]pyridine **19** was also reported by Wang and Zhao [26]. Because silver carbides are highly explosive in the dry state when subjected to heating or mechanical shock, the supramolecular capsule of **17** and **19** serves as a new class of container molecule for the storage of unstable silver carbide clusters.

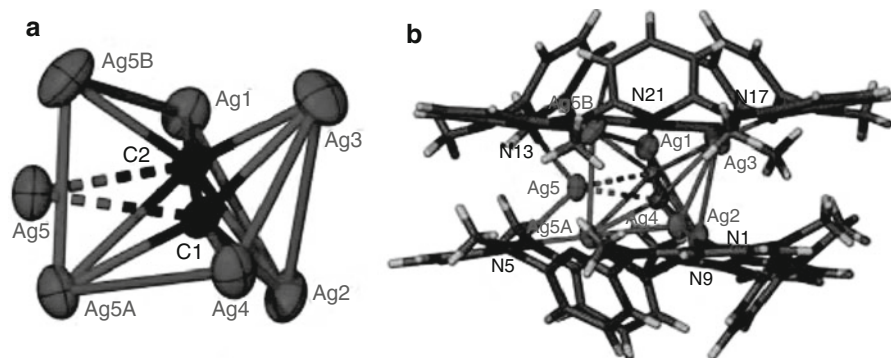


**Fig. 13.6** (a) Two components of silver-acetylide cluster aggregates, C<sub>2</sub>@Ag<sub>5</sub> and C<sub>2</sub>@Ag<sub>6</sub>, in complex (Ag<sub>5</sub>(C≡C)**17**<sub>2</sub>)<sub>0.7</sub>(Ag<sub>6</sub>(C≡C)**17**<sub>2</sub>)<sub>0.3</sub>. (b) Supramolecular capsule encapsulating a silver carbide cluster by two molecules of **17** (Reprinted with permission from Ref. [25] (Wang and Zhao's group). Copyright 2012 American Chemical Society)

### 13.3.2 Fullerene Complexation

As described in our previous review [3], Wang and coworkers reported that azacalix[*n*]pyridines (*n* = 5, 8, 10) and azacalix[4]arene[4]pyridine strongly interacted with fullerenes C<sub>60</sub> and C<sub>70</sub> in toluene with much higher stability constants than those obtained for the complexation of fullerenes with other mono-macrocyclic receptors [58–60].

Since this finding, Wang and coworkers continued their extensive study and very recently succeeded in elucidating the crystal structures of the fullerene complexes of azacalix[3]pyridine[3]pyrimidine **40** [8]. From fluorescence titration experiments in toluene, large association constants of  $(6.29 \pm 0.07) \times 10^4$  and  $(6.72 \pm 0.10) \times 10^4 \text{ mol}^{-1} \text{ dm}^3$  were observed for the 1:1 complexation of **40** with C<sub>60</sub> and C<sub>70</sub>, respectively. High-quality single crystals of the complex of **40** with fullerenes C<sub>60</sub> and C<sub>70</sub> were prepared by controlled slow mutual diffusion of fullerene solution in toluene and the solution of **40** in chloroform at ambient temperature. As shown in Fig. 13.7, azacalix[3]pyridine[3]pyrimidine **40** forms a 2:1 complex with C<sub>60</sub> in the solid state, and the encapsulated C<sub>60</sub> is sandwiched by two capsule-like molecules of **40**. Each pyrimidine ring of **40** interacts with six-membered ring of C<sub>60</sub>, while each pyridine ring points toward the five-membered ring of C<sub>60</sub>. Besides, three methylene units connected to the bridging nitrogen atoms also interact with C<sub>60</sub> through CH/π interactions. Azacalix[3]pyridine[3]pyrimidine **40** also forms a 2:1 complex with C<sub>70</sub> through essentially the same intermolecular interactions [8]. From the additional crystal structure determinations of the fullerene complexes with **30**, **31**, **32**, and **36** [8], Wang and coworkers concluded that multiple π/π and CH/π interactions between concave azacalix[3]pyridine[3]pyrimidines and convex fullerenes contributed a driving force to the formation of the host-guest complexes.

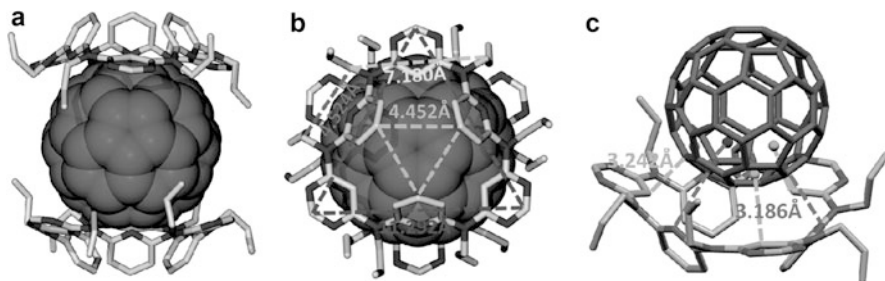


**Fig. 13.7** X-ray crystal structure of  $C_{60}@40$ . (a) Side and (b) top views and (c)  $\pi/\pi$  interactions between  $C_{60}$  and one molecule of **40** (Reprinted with permission from Ref. [8] (Wang's group). Copyright 2014 American Chemical Society)

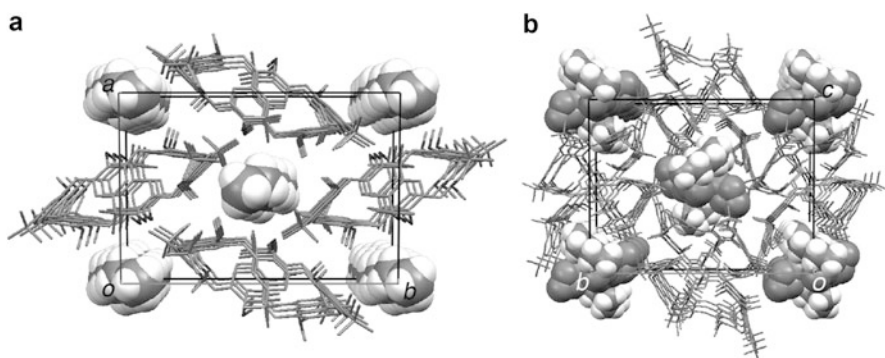


**Fig. 13.8** Crystal structures of the hexane clathrates of azacalixarenes (a) **5** and (b) **6** with one-dimensional channel crystal architecture. Molecules of azacalixarene and hexane are represented by stick and space-filling models, respectively [12, 13]

### 13.3.3 Gas Sorption

As described above, X-ray crystallographic analysis was widely used to investigate the “static” structures of azacalixarenes and the complexes in the solid state. However, there was no precedent for the “dynamic” complexation studies of azacalixarenes in the solid state before 2008, when our previous review [3] was published.

Recently, Tsue and coworkers reported that the single crystals of **3** as well as the crystalline powders of **4**, **5**, and **6** were capable of rapidly and selectively sorbing  $CO_2$  among four main atmospheric components such as  $N_2$ ,  $O_2$ , Ar, and  $CO_2$ .

As shown in Fig. 13.8, azacalix[6]arene **5** [12] and azacalix[7]arene **6** [13] form single crystals of 1:1 and 1:2 hexane clathrates with one-dimensional (1D) channel crystal architecture, respectively. Although the single crystals lost the single crystallinity upon heating for the sake of desolvation, powder X-ray diffraction (PXRD) and IR measurements demonstrated that the resulting solvent-free crys-

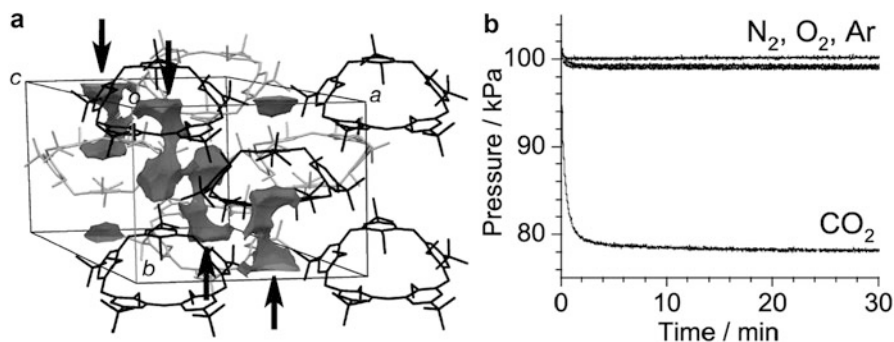


**Fig. 13.9** (a) Crystal structure of the solvent-free crystalline powders of azacalix[5]arene **4** with seemingly nonporous crystal architecture. Molecules of **4** are represented by stick model, and *arrows* indicate the isolated lattice voids. (b) Gas sorption isotherms of the crystalline powders of **4** for N<sub>2</sub>, O<sub>2</sub>, Ar, and CO<sub>2</sub> at 293 K [9]

talline powders of **5** and **6** kept essentially the same crystal structure as those of the single crystals. In other words, upon heating the single crystals of the hexane clathrates of **5** and **6**, the molecules of hexane escape through the 1D channel. By applying the crystalline powders of **5** and **6** to adsorbents, their gas sorption behavior was examined using N<sub>2</sub>, O<sub>2</sub>, Ar, and CO<sub>2</sub> as adsorbates. As a result, the rapid and selective uptake of CO<sub>2</sub> was observed by the crystalline powders of **5** and **6** at a low temperature.

More interesting gas sorption behavior was reported for azacalix[5]arene **4** by Tsue and coworkers [9]. The crystal structure of the solvent-free crystalline powders of **4** was successfully solved by means of *ab initio* PXRD analysis using the synchrotron X-ray diffraction data. Interestingly, the crystal structure was characterized as seemingly nonporous crystal architecture with no channels interconnecting voids in the crystal, as shown in Fig. 13.9a. Nevertheless, the crystalline powders of **4** exhibited the rapid and selective uptake of CO<sub>2</sub> under ambient conditions, as shown in Fig. 13.9b. The observed high selectivity of **4** for CO<sub>2</sub> was superior to those of activated carbon and molecular sieve 5A, and these noteworthy experimental results were applied for a patent [61, 62].

More recently, Tsue and coworkers succeeded in analyzing the CO<sub>2</sub> sorption state of azacalix[4]arene **3** at an atomic level [11]. Unlike **4**, **5**, and **6** mentioned above, azacalix[4]arene **3** afforded a non-clathrated single crystal with seemingly nonporous crystal architecture, as shown in Fig. 13.10a. Gas sorption experiments clearly revealed that the single crystals of **3** exhibited the highly selective uptake of CO<sub>2</sub> at a low temperature. Very interestingly, single crystal X-ray crystallography successfully permitted the atomic level analysis of the CO<sub>2</sub> sorption state (Fig. 13.10b), clearly indicating that the molecules of CO<sub>2</sub> could penetrate and diffuse even into the seemingly nonporous crystals of **3**. A Kitaura–Morokuma energy decomposition analysis demonstrated that the CO<sub>2</sub> uptake was induced by intermolecular CH/O interactions in which a dispersion force was found to play a major role.

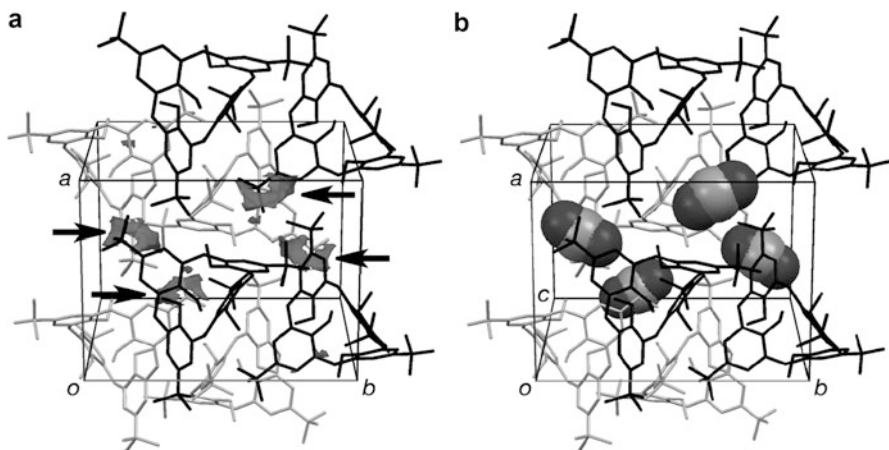


**Fig. 13.10** Crystal structures of (a) azacalix[4]arene **3** with seemingly nonporous crystal architecture and of (b) the CO<sub>2</sub> sorption state of **3**. In Fig. 13.10a, molecules of **3** are represented by stick model, and arrows indicate the isolated lattice voids. In Fig. 13.10b, molecules of CO<sub>2</sub> are represented by space-filling model [11]

### 13.4 Concluding Remarks

In the last 6 years, a wide variety of azacalixarene derivatives have been prepared by applying the three synthetic strategies. Although the diversity is still limited as compared to carbon- and sulfur-bridged calixarenes, the intriguing chemistry of azacalixarenes on the basis of the introduction of nitrogen atoms as the bridging units has thus far been disclosed especially through the studies on the host–guest chemistry in the solid state. In addition to the topics described in this review, an increasing variety of functions have been reported for azacalixarenes in the last 6 years, i.e., (1) catalysis [17], (2) redox [15, 34, 63], (3) inherent chirality [28, 39, 47], (4) nanosheet formation [24], (5) delayed fluorescence [18], (6) protonation and deprotonation [40, 43, 64], and (7) complexation with metal ion [20, 26, 42], fullerene [8, 30], and nucleotide [22, 23, 47] in solution. As clearly revealed by these studies, the chemistry of azacalixarenes has been growing steadily and greatly. For the further exciting progress of the chemistry, however, a broader knowledge of this new calixarene family has to be accumulated and organized as the history of carbon- and sulfur-bridged calixarenes demonstrates us.

**Acknowledgments** The author's work was supported by Grants-in-Aids for Scientific Research (C) (Nos. 19550037, 23550052) from Japan Society for the Promotion of Science (JSPS). The author's synchrotron radiation experiments were performed at the BL02B2 beamline of the SPring-8 with the approval of Japan Synchrotron Radiation Research Institute (JASRI) (Proposal Nos. 2009A1425, 2010A1346, 2010B1496, 2011B1303, and 2013B1160).

## References

1. B. König, M.H. Fonseca, *Eur. J. Inorg. Chem.* **2303** (2000)
2. M. Vysotsky, M. Saadioui, V. Böhmer, in *Calixarenes 2001*, ed. by Z. Asfari, V. Böhmer, J. Harrowfield, J. Vicens, M. Saadioui (Kluwer, Dordrecht, 2001), pp. 250–265
3. H. Tsue, K. Ishibashi, R. Tamura, in *Heterocyclic Supramolecules I*, ed. by K. Matsumoto. Topics in Heterocyclic Chemistry, vol. 17 (Springer, Berlin/Heidelberg, 2008), pp. 73–96
4. M.-X. Wang, *Chem. Commun.* **4541** (2008)
5. H. Tsue, K. Ishibashi, R. Tamura, *J. Synth. Org. Chem. Jpn.* **67**, 898 (2009)
6. M.-X. Wang, *Acc. Chem. Res.* **45**, 182 (2012)
7. G.W. Smith, *Nature* **198**, 879 (1963)
8. S.-X. Fa, L.-X. Wang, D.-X. Wang, L. Zhao, M.-X. Wang, *J. Org. Chem.* **79**, 3559 (2014)
9. H. Tsue, K. Ono, S. Tokita, K. Ishibashi, K. Matsui, H. Takahashi, K. Miyata, D. Takahashi, R. Tamura, *Org. Lett.* **13**, 490 (2011)
10. H. Tsue, K. Ono, S. Tokita, H. Takahashi, R. Tamura, *CrystEngComm* **15**, 1536 (2013)
11. H. Tsue, H. Takahashi, K. Ishibashi, R. Inoue, S. Shimizu, D. Takahashi, R. Tamura, *CrystEngComm* **14**, 1021 (2012)
12. H. Tsue, K. Ishibashi, S. Tokita, H. Takahashi, K. Matsui, R. Tamura, *Chem. Eur. J.* **14**, 6125 (2008)
13. H. Tsue, K. Matsui, K. Ishibashi, H. Takahashi, S. Tokita, K. Ono, R. Tamura, *J. Org. Chem.* **73**, 7748 (2008)
14. H. Tsue, K. Miyata, D. Takahashi, H. Takahashi, K. Sasaki, R. Tamura, *Heterocycles* **86**, 159 (2012)
15. K. Ishibashi, H. Tsue, H. Takahashi, S. Tokita, K. Matsui, R. Tamura, *Heterocycles* **76**, 541 (2008)
16. N. Uchida, R. Zhi, J. Kuwabara, T. Kanbara, *Tetrahedron Lett.* **55**, 3070 (2014)
17. N. Uchida, J. Kuwabara, A. Taketoshi, T. Kanbara, *J. Org. Chem.* **77**, 10631 (2012)
18. N. Uchida, T. Sato, J. Kuwabara, Y. Nishimura, T. Kanbara, *Chem. Lett.* **43**, 459 (2014)
19. E.-X. Zhang, D.-X. Wang, Q.-Y. Zheng, M.-X. Wang, *Org. Lett.* **10**, 2565 (2008)
20. H.-Y. Gong, D.-X. Wang, Q.-Y. Zheng, M.-X. Wang, *Tetrahedron* **65**, 87–92 (2009)
21. B. Yao, D.-X. Wang, Z.-T. Huang, M.-X. Wang, *Chem. Commun.* 2899 (2009)
22. A.-J. Guan, E.-X. Zhang, J.-F. Xiang, Q. Li, Q.-F. Yang, L. Li, Y.-L. Tang, M.-X. Wang, *J. Phys. Chem. B* **115**, 12584 (2011)
23. A.-J. Guan, E.-X. Zhang, J.-F. Xiang, Q.-F. Yang, Q. Li, H.-X. Sun, D.-X. Wang, Q.-Y. Zheng, G.-Z. Xu, Y.-L. Tang, *J. Phys. Chem. Lett.* **3**, 131 (2012)
24. Y. Yi, S. Fa, W. Cao, L. Zeng, M. Wang, H. Xu, X. Zhang, *Chem. Commun.* **48**, 7495 (2012)
25. C.-Y. Gao, L. Zhao, M.-X. Wang, *J. Am. Chem. Soc.* **134**, 824 (2012)
26. C.-Y. Gao, L. Zhao, M.-X. Wang, *J. Am. Chem. Soc.* **133**, 8448 (2011)
27. L.-X. Wang, D.-X. Wang, Z.-T. Huang, M.-X. Wang, *J. Org. Chem.* **75**, 741 (2010)
28. J.-T. Li, L.-X. Wang, D.-X. Wang, L. Zhao, M.-X. Wang, *J. Org. Chem.* **79**, 2178 (2014)
29. J.-C. Wu, L. Zhao, D.-X. Wang, M.-X. Wang, *Inorg. Chem.* **51**, 3860 (2012)
30. L.-X. Wang, L. Zhao, D.-X. Wang, M.-X. Wang, *Chem. Commun.* **47**, 9690 (2011)
31. J. Wu, L. Zhao, D. Wang, M. Wang, *Chin. J. Chem.* **31**, 589 (2013)
32. J. Clayden, S.J.M. Rowbottom, W.J. Ebenezer, M.G. Hutchings, *Org. Biomol. Chem.* **7**, 4871 (2009)
33. J.M. Caio, T. Esteves, S. Carvalho, C. Moiteiro, V. Félix, *Org. Biomol. Chem.* **12**, 589 (2014)
34. A. Ito, S. Inoue, Y. Hirao, K. Furukawa, T. Kato, K. Tanaka, *Chem. Commun.* 3242 (2008)
35. B. Yao, Z.-L. Wang, H. Zhang, D.-X. Wang, L. Zhao, M.-X. Wang, *J. Org. Chem.* **77**, 3336 (2012)
36. M. Touil, M. Lachkar, O. Siri, *Tetrahedron Lett.* **49**, 7250 (2008)
37. H. Konishi, S. Hashimoto, T. Sakakibara, S. Matsubara, Y. Yasukawa, O. Morikawa, K. Kobayashi, *Tetrahedron Lett.* **50**, 620 (2009)
38. Y. Yasukawa, K. Kobayashi, H. Konishi, *Tetrahedron Lett.* **50**, 5130 (2009)

39. J.L. Katz, B.A. Tschaen, *Org. Lett.* **12**, 4300 (2010)
40. M. Touil, M. Elhabiri, M. Lachkar, O. Siri, *Eur. J. Org. Chem.* 1914 (2011)
41. J. Clayden, S.J.M. Rowbottom, M.G. Hutchings, W.J. Ebenezer, *Tetrahedron Lett.* **50**, 3923 (2009)
42. Y.-X. Fang, L. Zhao, D.-X. Wang, M.-X. Wang, *J. Org. Chem.* **77**, 10073 (2012)
43. R. Haddoub, M. Touil, Z. Chen, J.-M. Raimundo, P. Marsal, M. Elhabiri, O. Siri, *Eur. J. Org. Chem.* 745 (2014)
44. B.T. Hayes, R.F. Hunter, *Chem. Ind.* 193 (1956)
45. B.T. Hayes, R.F. Hunter, *J. Appl. Chem.* **8**, 743 (1958)
46. H. Tsue, K. Ishibashi, H. Takahashi, R. Tamura, *Org. Lett.* **7**, 2165 (2005)
47. K. Ishibashi, H. Tsue, H. Takahashi, R. Tamura, *Tetrahedron Asymmetry* **20**, 375 (2009)
48. V. Böhmer, P. Chhim, H. Kämmerer, *Makromol. Chem.* **180**, 2503 (1979)
49. K. Ishibashi, H. Tsue, S. Tokita, K. Matsui, H. Takahashi, R. Tamura, *Org. Lett.* **8**, 5991 (2006)
50. C.D. Gutsche, in *Calixarenes*, ed. by J.F. Stoddart (Royal Society of Chemistry, Cambridge, 1989), pp. 127–148
51. C.D. Gutsche, in *Calixarenes: A Versatile Class of Macrocyclic Compounds*, ed. by J. Vicens, V. Böhmer (Kluwer, Dordrecht, 1991), pp. 12–26
52. C.D. Gutsche, in *Calixarenes Revisited*, ed. by J.F. Stoddart (Royal Society of Chemistry, Cambridge, 1998), pp. 79–145
53. I. Thondorf, A. Shivanyuk, V. Böhmer, in *Calixarenes 2001*, ed. by Z. Asfari, V. Böhmer, J. Harrowfield, J. Vicens, M. Saadioui (Kluwer, Dordrecht, 2001), pp. 26–53
54. H. Graubaum, G. Lutze, B.J. Costisella, *J. Prakt. Chem./Chem.-Ztg.* **339**, 266 (1997)
55. H. Graubaum, G. Lutze, B.J. Costisella, *J. Prakt. Chem./Chem.-Ztg.* **339**, 672 (1997)
56. M.-X. Wang, H.-B. Yang, *J. Am. Chem. Soc.* **126**, 15412 (2004)
57. Q.-Q. Wang, D.-X. Wang, H.-W. Ma, M.-X. Wang, *Org. Lett.* **8**, 5967 (2006)
58. M.-X. Wang, X.-H. Zhang, Q.-Y. Zheng, *Angew. Chem. Int. Ed. Engl.* **43**, 838 (2004)
59. H.-Y. Gong, X.-H. Zhang, D.-X. Wang, H.-W. Ma, Q.-Y. Zheng, M.-X. Wang, *Chem. Eur. J.* **12**, 9262 (2006)
60. E.-X. Zhang, D.-X. Wang, Q.-Y. Zheng, M.-X. Wang, *Org. Lett.* **10**, 2565 (2008)
61. H. Tsue, K. Ishibashi, S. Tokita, K. Sakai, *Jpn. Pat. Appl.* 2009–21511
62. H. Tsue, K. Ishibashi, S. Tokita, K. Sakai, *Jpn. Unexam. Pat. Appl. Publ.* 2010–174002
63. K. Ishibashi, H. Tsue, N. Sakai, S. Tokita, K. Matsui, J. Yamauchi, R. Tamura, *Chem. Commun.* 2812 (2008)
64. I. Despotović, Z.B. Maksić, *Tetrahedron Lett.* **52**, 6263 (2011)

# **Part IV**

## **Polymorphism**

# Chapter 14

## Polymorphism in Molecular Crystals and Cocrystals

Srinivasulu Aitipamula

**Abstract** Polymorphism refers to a compound's ability to exist in more than one crystalline modification through variations in the solid-state structures. Over the years, polymorphism has received extensive academic and industrial attention because of its impact on physical and chemical properties of active pharmaceutical ingredients and materials. It is preferable to develop the most stable polymorph to avoid unwanted phase transformation during processing and manufacturing. Therefore, a thorough polymorph screening and complete characterization of all the polymorphs are vital for understanding stability and phase transformations among different polymorphs. Recent advances in screening methodologies and analytical techniques paved ways for successful identification of potential polymorphs. While polymorphism in active pharmaceutical ingredients and single-component crystals is widely studied, such studies in multicomponent crystals such as cocrystals have received significant attention only in recent years. This chapter highlights some recent polymorphic systems of molecular crystals and cocrystals and emphasizes the potential implications of polymorphism in pharmaceutical and materials science. A brief history of polymorphism, factors that control the crystallization of polymorphs, thermodynamic aspects, and recent advances in screening methodologies and analytical techniques are also covered.

**Keywords** Polymorphism • Cocrystal • Crystallization • Crystal structure • Physicochemical properties

---

S. Aitipamula (✉)

Crystallization and Particle Science, Institute of Chemical and Engineering Sciences, A\*STAR (Agency for Science, Technology and Research), 1 Pesek Road, Jurong Island, 627833 Singapore  
e-mail: [srinivasulu\\_aitipamula@ices.a-star.edu.sg](mailto:srinivasulu_aitipamula@ices.a-star.edu.sg)

## 14.1 Introduction

### 14.1.1 *Scope of the Book Chapter*

Crystal is an ensemble of molecules connected via intermolecular interactions such as hydrogen bonds, ionic or electrostatic bonds, metal–ligand bonds, and heteroatom- and halogen-based and van der Waals interactions. Crystals are generally obtained by a process of crystallization when solutions of compounds reach a certain level of supersaturation. The delicate nature of crystallization under different experimental conditions leads to various solid forms as the final outcome of crystallization. Polymorphs are formed when a substance crystallizes in two or more crystal structures [1]. Polymorphism significantly impacts on physicochemical properties of materials such as stability, density, melting point, solubility, bioavailability, etc. Hence, the characterization of all possible polymorphs, identification of the stable polymorph, and design of reliable process for consistent production are critical in modern-day development of pharmaceuticals and materials. The current chapter aims to highlight some recent examples of polymorphs in organic molecular crystals and cocrystals. Special emphasis will be made on polymorphism in cocrystals which are being actively developed as potential solid forms for improving the physicochemical properties of the parent compounds.

### 14.1.2 *Different Solid Forms*

Crystallization is a key experimental technique for the purification and separation of organic compounds. Aggregation of molecules into energetically favorable packing motifs through intermolecular interactions is the key step in the crystallization pathway [2]. The process of crystallization is determined by several external factors such as temperature, pressure, supersaturation, etc. Therefore, depending on the experimental conditions, the outcome of crystallization could be various alternative forms such as amorphous, solvates, hydrates, polymorphs, salts, cocrystals, solid solutions, eutectic mixtures, etc. Figure 14.1 summarizes the various solid-state materials. As mentioned before, polymorphs are formed when a substance crystallizes in two or more crystal structures. Solvates are crystalline solids that contain solvent molecules within the crystal lattice [3]. If the included solvent is water, they are termed hydrates. Salts are generally formed when proton transfer from an acid to the conjugate base occurs during crystallization [4]. Cocrystals belong to multicomponent solids that are molecular complexes of two or more compounds which are solids at ambient conditions [5]. Cocrystal structures were reported in the 1990s, but they were referred to as molecular complexes or molecular compounds in the older literature. Their potential utility in pharmaceutical applications, with the so-called pharmaceutical cocrystals, has emerged only recently [6]. A solid solution is a variable stoichiometry multicomponent crystalline solid formed by substitutional incorporation of a component in the lattice of another component

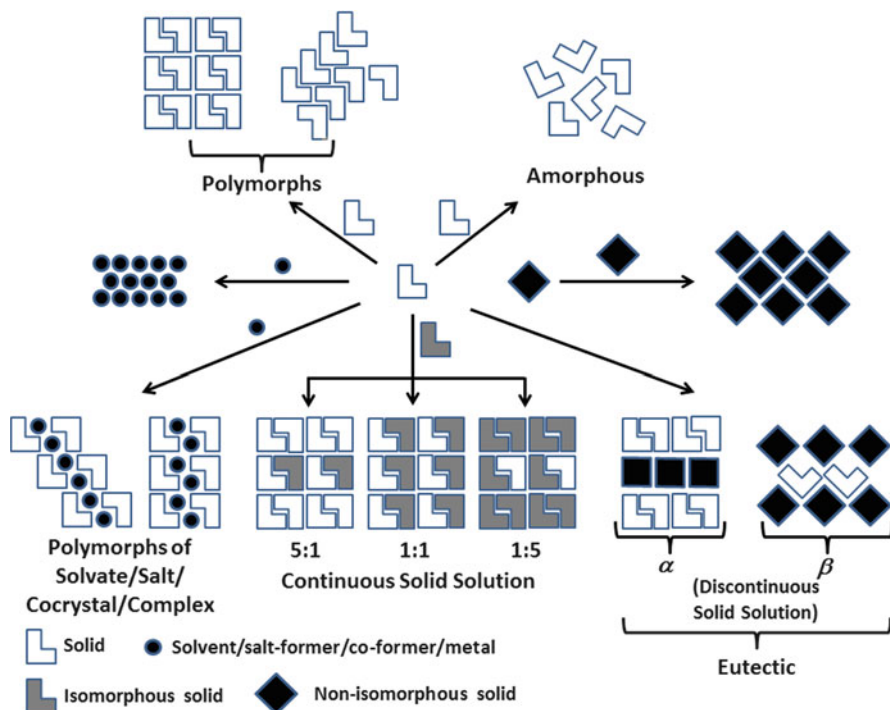


**Fig. 14.1** Schematic representation of different solid-state forms. Multicomponent crystals such as solvates, hydrates, salts, and cocrystals can also exist in polymorphic forms (Adapted from Ref. [8] with permission from The Royal Society of Chemistry)

[7]. Eutectics are conglomerates of solid solutions or conglomerates of lattice structures of different materials [8]. Amorphous materials are distinct from the abovementioned solids, which lack long-range molecular order and relatively high energy materials compared to their crystalline counterparts [9].

### 14.1.3 Significance of Polymorphism in Pharmaceuticals

Selection of a right polymorph is critical during formulation of pharmaceutical materials [1]. This is due to the fact that polymorphs exhibit different physical properties, such as stability, solubility, melting point, bioavailability, etc. Therefore, it is possible that properties of the active pharmaceutical ingredients (APIs) could be optimized by a suitable polymorph. For example, better tableability of  $\alpha$ -form of indomethacin over its  $\gamma$ -form is due to differences in solid-state structures [10]:  $\gamma$ -form contains slip planes that offer increased compressibility and deformation; on the other hand,  $\alpha$ -form showed greater compactibility due to closer molecular packing (Fig. 14.2). The impact of polymorphism on various pharmaceutical properties has been highlighted with representative examples in the later sections.

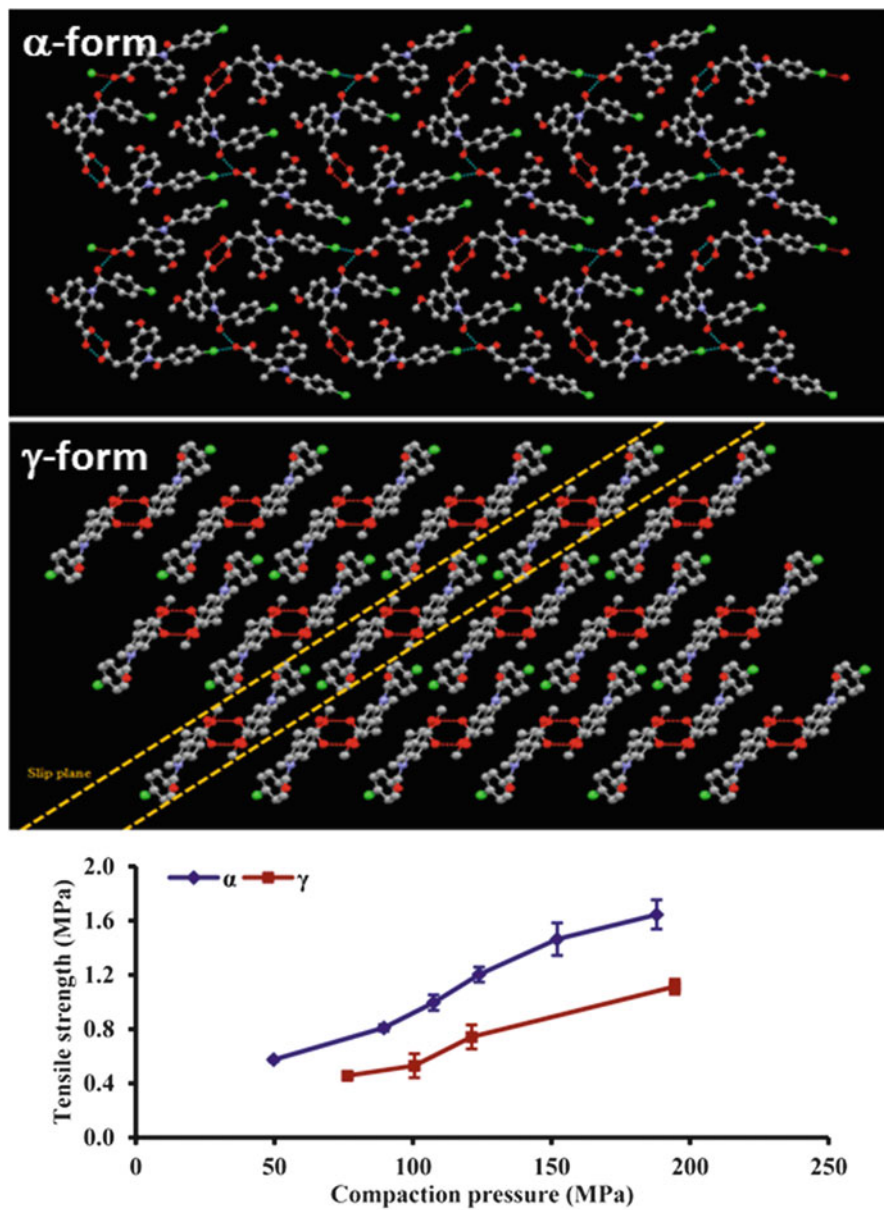


**Fig. 14.2** Indomethacin polymorphs showing differences in crystal packing and compaction properties. Notice that  $\gamma$ -form shows slip planes that promote deformation, whereas  $\alpha$ -form is a close-packed structure with greater stability (Adapted with permission from Ref. [10]. Copyright 2013, The American Chemical Society)

## 14.2 Polymorphism: Historical to Present

The observation of same composition of matter forming different crystal structures dates back to the late seventeenth century when Klaproth discovered the same chemical composition of  $\text{CaCO}_3$  for calcite and aragonite [11]. However, the first use of the term polymorphism has been credited to Mitscherlich for his series of observations on several distinct structures of complex arsenate and phosphate salts,  $\text{NaH}_2\text{PO}_4 \cdot \text{H}_2\text{O}/\text{NaH}_2\text{AsO}_4 \cdot \text{H}_2\text{O}$  and  $\text{Na}_2\text{HPO}_4 \cdot \text{H}_2\text{O}/\text{Na}_2\text{HAsO}_4 \cdot \text{H}_2\text{O}$  [12]. Mitscherlich experiments on the polymorphs of  $\text{CaCO}_3$  revealed that the interfacial angles in the case of calcite varied with temperature. He also observed similar variation in the case of crystals of various elements. This was led, in 1825, to the discovery of allotropic crystals which are known to expand unequally in the direction of dissimilar axes when heated [12]. The importance of allotropism in elements such as carbon, phosphorous, and sulfur can be easily understood by the differences in their physical properties. For example, diamond is the hardest natural mineral and it is an insulator, whereas graphite is a soft material and an electrical conductor. Major milestones in the field of polymorphism in the last 200 years are listed in Table 14.1 [13].

The late eighteenth century was considered as an important era in the history of polymorphism that witnessed discovery of phase transformations in crystal forms

**Table 14.1** Important milestones in polymorphism research during the last 200 years

1798	Klaproth concluded that calcite and aragonite have the same chemical composition $\text{CaCO}_3$
1822	Mitscherlich identified different crystal forms of arsenate and phosphate
1844	Amici discovered polarizing microscope for visual characterization of solids
1876	Millard considered geometrical and structural basis in growing different forms of the same substance
1891	Lehmann observed phase transformation in crystal forms
1897	Ostwald's famous "rule of steps" on relative stability of polymorphs
1906–1919	Organic crystal polymorphism in Groth's five-volume collection
1926	Tammann's work on thermodynamic stability and relationships of polymorphs
1937	Bloom and Burger's fundamental property changes in polymorphs
1956–1969	McCrone's work on pharmaceutical and drug polymorphism
1973	Corradini coined the term conformational polymorphism
1996	Glaxo vs. Novopharm litigation on Form I and II of ranitidine hydrochloride (Zantac)
1998	Unexpected appearance of stable, less soluble Form II of ritonavir (Norvir) at Abbott
2000–present	Several books, monographs, and reviews on polymorphism. Special issues of journals on crystallization, polymorphism, and its industrial significance
2005	First article that raises the question whether cocrystals are less or more prone to polymorphism
2014	Comprehensive review on polymorphic cocrystals

by Lehmann and formulation of “rule of steps” by Ostwald. Lehmann characterized polymorphic systems as two different types, monotropic and enantiotropic, in 1891 [14]. Monotropic involves two polymorphs in which one undergoes an irreversible phase change to the second form, and in enantiotropic polymorphs, two polymorphs can undergo a reversible phase transition. The pioneering work on the relative stability of different polymorphs by Ostwald in 1897 has led him to formulate the “rule of steps” or “Law of Successive Reactions,” which states that “. . . that on leaving any state, and passing into a more stable one, that which is selected is not the most stable one under the existing conditions, but the nearest” [15].

Interest in polymorphism continued to grow rapidly in the nineteenth century. Gustav Tammann demonstrated the use of thermodynamic measures to explain the relative stability of polymorphs. A series of rules have been formulated for understanding the relative thermodynamic stabilities of polymorphs [16]. These rules help to determine whether a polymorphic system belongs to the monotropic or the enantiotropic category. Tammann was the first to develop these rules in the 1920s, and they were later extended by Burger and Ramberger who applied these rules to several polymorphic systems [17]. Most common of these rules include heat of transition rule, heat of fusion rule, entropy of fusion rule, density rule, and infrared rule. Thermodynamic principles behind each of these rules and their application in understanding polymorphic systems are explained in the following sections.

With the advent of X-ray diffraction techniques, nineteenth century witnessed a rapid understanding of the phenomenon of polymorphism. Based on the observation of polymorphism in several organic compounds, McCrone stated in 1965 that “every compound has different polymorphic forms and that, in general, the number of forms known for a given compound is proportional to the time and money spent in research on that compound” [18], which appears to be still valid. The implication from this famous statement is that every compound should exist in different polymorphic forms, provided that the stability attributes of polymorphs are achieved by the external experimental conditions applied. However, on the contrary, a caveat to these statements is that some well-known organic compounds, e.g., benzoic acid and naphthalene, have never shown evidence of polymorphism despite repeated crystallizations over the years.

Patenting and a thorough identification of all the solid forms of an API is a rigorous exercise in pharmaceutical companies for safeguarding their intellectual property. Different polymorphic forms are patentable because of their novelty, nonobviousness, and utility. Sudden appearance of an unknown polymorph leading to dramatic changes in physicochemical properties of drug substances could be highlighted by the famous case of a HIV-I protease inhibitor, ritonavir (Norvir) [19]. Only one form was known until 1995 (Form I) and marketed as oral solution or soft gelatin capsules. In early 1998, some batches of ritonavir capsules failed the dissolution test because a new less-soluble form had precipitated. This new polymorph had reduced bioavailability, resulting in the withdrawal of the drug from the market in 1998, and Abbott had to develop a new gel capsule formulation for Norvir using the stable polymorph.

In contrast to the single-component crystals and APIs, studies concerning polymorphism in cocrystals are not so widely reported, and there were only a very few studies devoted to identifying novel polymorphs of cocrystals. Furthermore, it was once thought that cocrystals could be a means to prevent polymorphism, but many recent examples of cocrystal polymorphs have been discovered and reported. This is due to the increased interest in the development of cocrystals as potential solid forms for modifying the physicochemical properties of materials, the number of polymorphic cocrystals being reported has significantly increased in recent years [20].

### 14.3 Theoretical Aspects of Polymorphism

The primary goal of crystallization is to generate particles with the desired size, shape, crystal form, and chemical purity in a reproducible manner. This is because these characteristics can significantly impact the physical and chemical properties of the solids. In the case of polymorphs, the above characteristics vary from one polymorph to the other. Therefore, understanding the origin of polymorphism requires a thorough knowledge of thermodynamic and kinetic factors that affect the crystallization process.

#### 14.3.1 *Thermodynamic Relationships in Polymorphs*

Phase transition from one polymorph to the other may occur by changing the temperature. If such a phase transition is reversible, the two polymorphs are said to be enantiotropes and the energy of transition on heating is endothermic. When the phase transition is irreversible, the two polymorphs are termed as monotropes, in which case only one form is stable whatever the temperature, and the transformation of the metastable form to the stable one is exothermic.

The thermodynamic stability between polymorphs is conveniently represented in energy–temperature diagrams (E–T diagrams) [21]. Schematic E–T diagrams for enantiotropic and monotropic polymorphs are shown in Fig. 14.3.

A series of rules have been formulated for understanding the relative thermodynamic stabilities of polymorphs. These rules also help to determine whether a polymorphic system belongs to the monotropic or the enantiotropic category.

##### 14.3.1.1 Heat of Transition Rule

The rule states that if an endothermic phase transition is observed at a particular temperature, the thermodynamic transition point lies below that temperature, and the two polymorphs are said to be enantiotropically related. Two polymorphs are related

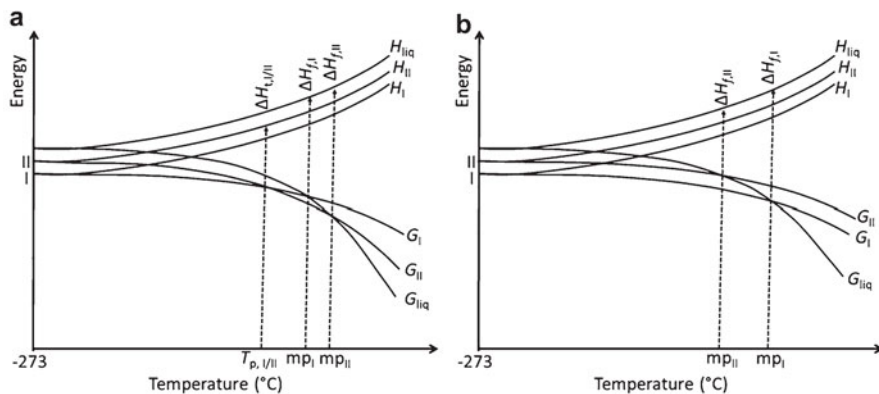


**Fig. 14.3** Energy vs. temperature ( $E$ - $T$ ) diagram of a dimorphic system: (a) enantiotropic (the two polymorphs undergo reversible solid–solid phase transformation at a transition point ( $T_p$ )) and (b) monotropic system (the free-energy curves do not intersect).  $G$  Gibbs free energy,  $H$  enthalpy, *liq* liquid phase, and  $T_p$  transition point of two polymorphs (Reproduced with permission of Elsevier, Ref. [21])

monotropically if an exothermic phase transition is observed at a particular temperature, and there is no thermodynamic transition point below this temperature. The same situation can also occur when the two polymorphs are enantiotropically related and in addition have a thermodynamic transition temperature that is higher than the experimentally observed transition temperature. As the endothermic and exothermic phase transitions are easily determined by differential scanning calorimetry (DSC), the heat of transition rule for polymorphs is frequently applied to establish the relationship between polymorphs [17].

#### 14.3.1.2 Heat of Fusion Rule

According to this rule, if the higher melting polymorph has the lower heat of fusion, then the two polymorphs are enantiotropic; if the higher melting polymorph has the higher heat of fusion, the two polymorphs are related monotropically [21]. The application of this rule is based on the assumption that the heat of transition can be approximated by the difference between the heats of fusion of the polymorphs.

#### 14.3.1.3 Entropy of Fusion Rule

As the entropy of fusion can be measured by DSC, the enthalpy of fusion and the melting point of a crystal can be obtained in one experiment ( $\Delta S_f = \Delta H_f / \Delta T_f$ ). The entropy of fusion rule states that if the modification with the higher melting point has the lower entropy of fusion, the two forms are enantiotropic. The monotropic relationship arises when the lower melting form shows the lower entropy of fusion [17].

#### 14.3.1.4 Density Rule

The density rule states that two polymorphs are related monotropically if the higher melting form has the higher density; otherwise, they are enantiotropically related. It is apparent that exceptions to the density rule are possible, because energetically favorable hydrogen bonds may overcome the packing efficiency and also compensate for the loss of van der Waals energy and thus stabilize the polymorph having a lower density.

#### 14.3.1.5 Infrared Rule

In general, the formation of strong hydrogen bonds results in a reduction in entropy and an increase in the frequency of the vibrational modes of the same hydrogen bonds. For polymorphic structures which contain strong hydrogen bonds, the infrared rule states that the polymorph with the higher bond stretching frequency may be assumed to have the greater entropy and should belong to the most stable form. One of the problems associated with the application of this rule is that if a molecule forms more than one type of hydrogen bond, then it is difficult to correlate the frequencies observed with a particular polymorphic form. In such cases, other rules described thus far help to understand the relative stabilities of polymorphs.

### 14.4 Polymorph Screening and Characterization: Conventional Methods and Recent Trends

Successful preparation of a desired polymorph depends on the selection of a suitable experimental method. It is generally believed that the chances of finding new polymorphs increase with increasing experimental efforts. Therefore, it is important to perform crystallization experiments under diverse experimental conditions. A wide variety of methods are currently being used for this purpose. In addition to the conventional methods such as solvent evaporative crystallization, additive- and pressure-induced crystallization, and pH- or supersaturation-controlled crystallization, methods such as laser-induced crystallization; polymer-induced heteronucleation; capillary growth, supercritical, and high-throughput techniques; and cocrystallization route are gaining more attention in the recent times for polymorph screening. This section gives a brief overview of some of these techniques.

#### 14.4.1 *Crystallization from Solvents*

Crystallization from solution is the most common method for polymorph screening because it generally yields single crystal that can be analyzed by single-crystal X-ray diffraction. The choice of solvent will have a profound effect on the resulting poly-

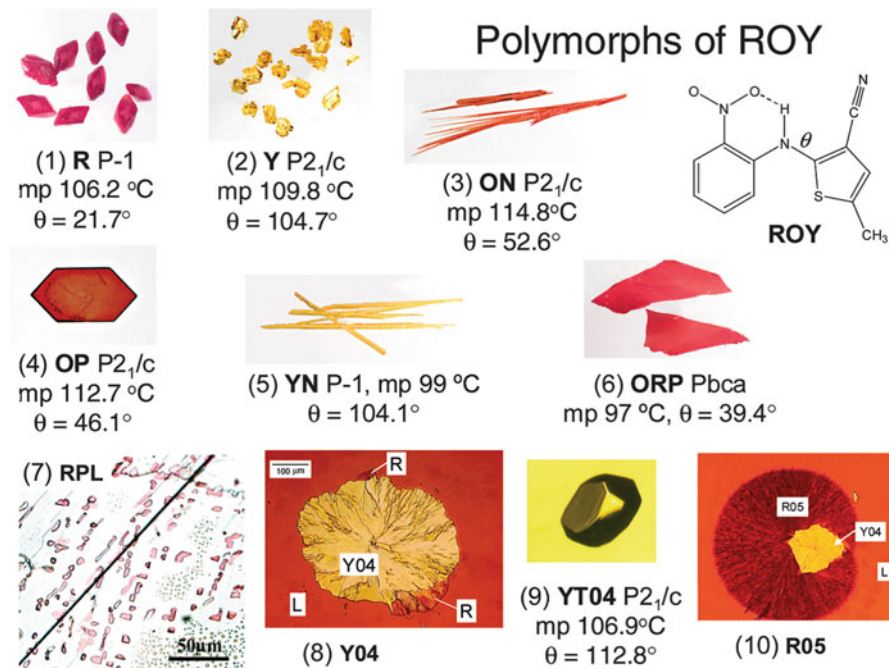


**Fig. 14.4** Polymorphs of ROY. The number 1–10 indicates the order of discovery. The polymorphs have different colors, melting points, and molecular conformations (most pronounced in the torsional angle  $\theta$ ) (Reprinted with permission from Ref. [22]. Copyright 2010, The American Chemical Society)

morph and morphology. For example, rich polymorphism of an organic substance, [5-methyl-2-[(2-nitrophenyl) amino]-3-thiophenecarbonitrile (also known as ROY for its red, orange, and yellow polymorphs), represents an ideal case of the use of solvent-based technique for polymorph screening [22]. ROY has been reported to form at least ten polymorphs, among which seven have been structurally characterized (Fig. 14.4). Remarkably, all the polymorphs of ROY have been prepared near ambient conditions and many can even crystallize simultaneously from the same liquid. Cocrystallization is often conducted in solution phase for the preparation of crystalline samples for structural analysis. Therefore, most of the cocrystal polymorphs thus far reported have been obtained from solvent-based techniques [20]. For example, of the five polymorphs reported for a cocrystal involving a loop diuretic drug, furosemide, and nicotinamide (NCT), four polymorphs were obtained by cocrystallization experiments from solvents of different polarities [23]. However, the selection of a suitable solvent in which the constituents of the cocrystal dissolve is crucial in the preparation of cocrystals and their polymorphs.

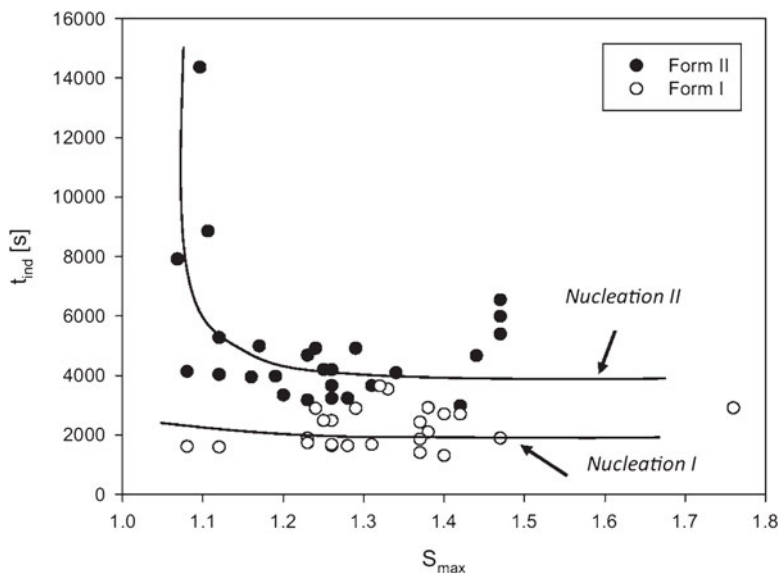


**Fig. 14.5** Comparison between induction time and maximum supersaturation ratio of Form I (seeded) and II (unseeded) of clopidogrel hydrogen sulfate (Reproduced from Ref. [24] with permission from Wiley-VCH)

#### 14.4.1.1 The Role of Supersaturation

Supersaturation is an important parameter which is also the driving force of the crystallization and influences the kinetics of crystal nucleation and growth. In general, the degree of supersaturation can be defined as the ratio of the concentration of a solution to that of the saturated solution. In general, as the degree of supersaturation increases at a given temperature, the rates of nucleation and crystal growth increase. This means that at a given temperature, a particular polymorph can be grown by controlling the supersaturation. For example, Jim and Kim recently studied the role of supersaturation on the polymorph nucleation of an antithrombotic drug, clopidogrel hydrogen sulfate [24]. They found that the induction time decreases with increasing supersaturation for both polymorphs (Forms I and II); however, the induction time for metastable Form I is lower than that of the stable Form II at the same supersaturation levels (Fig. 14.5).

#### 14.4.1.2 The Role of Temperature

The effect of temperature on the crystallization of polymorphic compounds has both thermodynamic and kinetic significance, because the solubility of a particular compound changes as a function of temperature. In general, crystallization of poly-

morphic compounds can result in different polymorphs at different temperatures. For example, the effect of different heating/cooling rates on the low-temperature polymorphic behavior of 3-amino-1-propanol has been investigated by Fausto and coworkers [25]. It was found that faster cooling rates produce an amorphous phase that upon heating crystallizes into the metastable Form II. On the other hand, at higher temperatures, the metastable phase converts into the stable Form I, and slow cooling rates were always found to favor formation of the stable polymorph.

#### 14.4.1.3 The Role of Pressure

Applications of high pressure in exploring new polymorphs have been elegantly reviewed recently by Pulham and coworkers [26]. From a thermodynamic perspective, the polymorph obtained at a low pressure will be less dense, and this means that the application of high pressure to metastable polymorphs can induce phase transformation to a more stable polymorph. Pulham and coworkers have recently shown that new polymorphs of simple molecular organic and inorganic compounds, such as ketones, alcohols, and mineral acids, are readily obtained by cooling the liquid compound contained within a diamond-anvil cell under conditions of high pressure. The authors have grown single crystals of novel solid forms of phenanthrene, paracetamol, and piracetam from their corresponding solutions at high pressure [27]. Successful application of high pressure on these systems revealed novel polymorphs of phenanthrene and piracetam and a novel dihydrate of paracetamol from water at a pressure of 1.1 GPa. Furthermore, it was also found that the metastable polymorph of paracetamol under which it is stable at ambient conditions can also be selectively prepared from ethanol at a pressure of 1.1 GPa.

#### 14.4.2 *Anti-solvent Crystallization*

Controlling the supersaturation is an effective way to prepare a desired polymorph. This can be sometimes aided by means of the addition of a second solvent, that is, an anti-solvent, which decreases the solubility of the solutes. Thus, supersaturation levels can be controlled by varying the amount of anti-solvent added. An added advantage with the anti-solvent crystallization is that the crystallization experiments can be carried out at room temperature and high yields of crystals can be expected. The effect of anti-solvent crystallization on the polymorphic behavior of L-histidine has been studied by Profio and coworkers who used porous membrane for the gradual dosing of the anti-solvent in the vapor phase [28]. Ethanol was used as anti-solvent for an aqueous solution of L-histidine. When the amount of anti-solvent added is low, only the elongated crystals of Form A (thermodynamic form) were observed. As the amount of anti-solvent increases, nucleation of Form A was followed by the nucleation of Form B. In this case, the utilization of porous membrane helps to gradually adjust the nucleation and growth rates and thereby results in the crystallization of a specific polymorph.

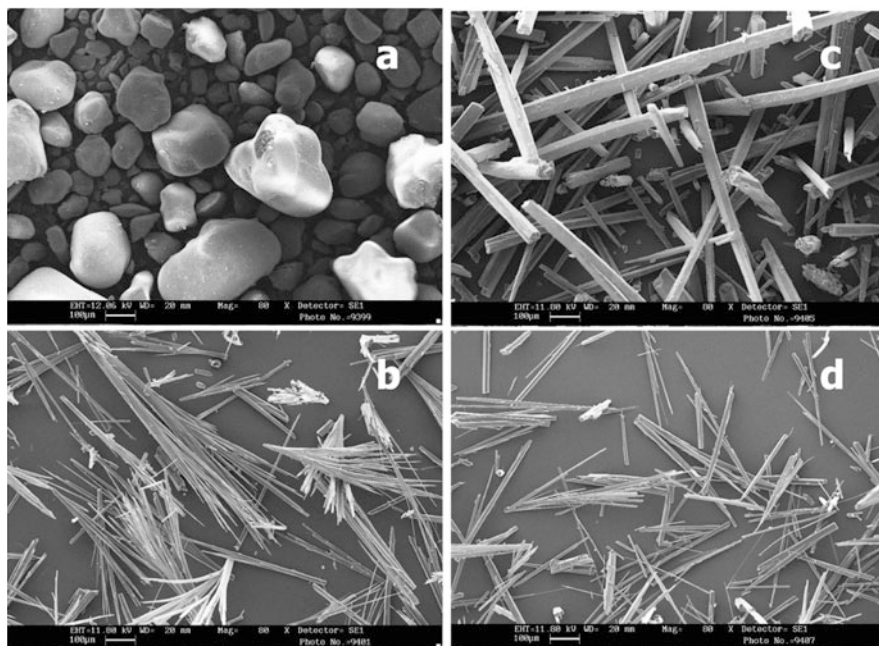


**Fig. 14.6** SEM images of (a) commercial sample of CBZ, (b) CBZ- $\text{CO}_2$  processed with acetone, (c) CBZ- $\text{CO}_2$  processed with dichloromethane, and (d) CBZ- $\text{CO}_2$  processed with ethyl acetate (Reprinted with permission from Ref. [31]. Copyright 2003, Elsevier)

### 14.4.3 Polymorph Control by Supercritical Fluids

The use of supercritical carbon dioxide ( $\text{CO}_2$ ) as processing medium in pharmaceutical applications has received significant interest in the recent times [29]. This is because the critical pressure and temperature of  $\text{CO}_2$  are easily accessible ( $T_c = 31.1^\circ\text{C}$ ,  $P_c = 74\text{ bar}$ ), and it is cheap, nonflammable, nontoxic, recyclable, and “generally regarded as safe (GRAS).” In general, supercritical  $\text{CO}_2$  is used to reduce the solubility of the solute in the dissolved solvent so that the solute particles precipitate. Crystallization experiments aided by supercritical  $\text{CO}_2$  have been proved to be successful in the identification of a novel polymorph of anti-HIV agent, didanosine by Bettini and coworkers [30]. Moneghini and coworkers used supercritical  $\text{CO}_2$  as an anti-solvent for investigating the polymorphism of carbamazepine (CBZ) [31]. The authors tested the effect of supercritical  $\text{CO}_2$  on the CBZ in three different solvents: acetone, ethyl acetate, or dichloromethane. In all the solvents, the supercritical  $\text{CO}_2$  treatment helped to convert Form III into Form I with improved dissolution rate which was attributed to the change in crystal size and morphology (Fig. 14.6).

#### ***14.4.4 Additive-Induced Polymorph Nucleation***

Additives play a major role in selective crystallization of polymorphic materials. It is believed that the additive molecules adsorb selectively to particular faces of the growing crystal and hinder the growth of the affected faces while the crystal continues to grow in the other directions. The role of additives in controlled crystallization has recently been elegantly reviewed by Song and Cölfen [32]. Additive-induced polymorph preparation is a widespread approach. For example, a metastable polymorph of the antibacterial drug sulfamerazine was selectively crystallized in the presence of structurally related sulfonamide drugs such as additives, e.g., sulfamethazine, sulfadiazine, and N<sup>4</sup>-acetylsulfamerazine [33]. It was noted that a trace amount of N<sup>4</sup>-acetylsulfamerazine as impurity prevented solution-mediated phase transformation from Form I to Form II even after suspension for 2 weeks in acetonitrile.

#### ***14.4.5 Grinding-Assisted Polymorph Screening***

Solid-state grinding has been extensively used for cocrystal screening, and it has also been proved to be effective in polymorph screening of cocrystals. For example, a second polymorph of a 1:1 cocrystal of ethenzamide with ethylmalonic acid was first observed by grinding [34]. Polymorphic outcome of a cocrystallization experiment could also be controlled by using different grinding methods as demonstrated by Trask et al. on a 1:1 cocrystal of caffeine and glutaric acid [35]. While Forms I and II of 1:1 caffeine–glutaric acid crystallized concomitantly from evaporative crystallization, Form I could be obtained by neat grinding or grinding with a few drops of nonpolar solvents and Form II could be obtained by grinding with a few drops of polar solvents (Fig. 14.7). This observation has been rationalized on the fact that Form I has a nonpolar cleavage plane between the stacks of ribbons formed by caffeine and glutaric acid and that nonpolar solvents may preferentially stabilize this exposed plane. In the case of single-component crystals, grinding-assisted phase transformation from metastable polymorph to the stable polymorph has been reported in several polymorphic systems. For example, famotidine, cimetidine, indomethacin, clarithromycin, and ranitidine hydrochloride all undergo polymorphic phase transformation upon solid-state grinding.

#### ***14.4.6 Polymer-Induced Heteronucleation***

Polymer-induced heteronucleation (PIHn) is a relatively new technique used for selective crystallization of polymorphic forms. In this method, compounds are crystallized in the presence of a wide variety of polymers using routine crystallization techniques. For example, a novel polymorph of 6-amino-2-phenylsulfonylimino-1,2-dihydropyridine was found when polymers were used to induce the crystal-

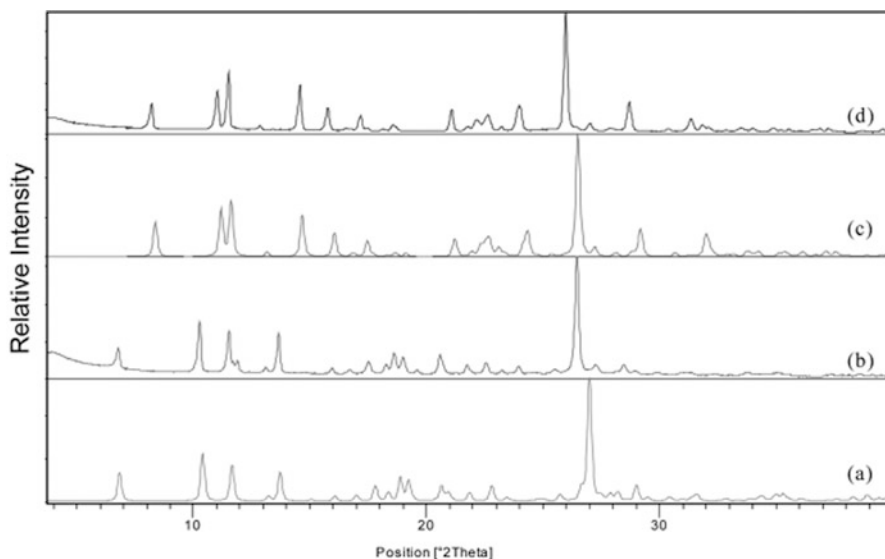


**Fig. 14.7** Powder X-ray diffraction pattern of the polymorphs of 1:1 cocrystal of caffeine and glutaric acid, (a) simulated pattern from single-crystal structure of Form I, (b) result of solvent-drop grinding of caffeine and GA with cyclohexane, (c) simulated pattern from single-crystal structure of Form II, (d) result of solvent-drop grinding of caffeine and GA with chloroform (Reproduced from Ref. [35]. Copyright Royal Society of Chemistry, 2004)

lization [36]. Crystallization of this compound from ethanol using benzyloxy-4-bromobenzene-modified polystyrene as heteronuclei resulted in concomitant crystallization of a novel polymorph together with the two known polymorphs of this molecule. Not only for single-component crystals, PIHn has also shown promise in polymorph screening of cocrystals. For example, despite a thorough investigation using high-throughput screening, neat grinding, and solvent-drop grinding with several solvents, there was no evidence of polymorphism in the cocrystals of CBZ with saccharin and NCT. However, a novel polymorph of the cocrystals was found when functionalized cross-linked polymers were utilized as heteronuclei for crystal growth (Fig. 14.8) [37]. The findings reiterate the fact that a successful polymorph screen should involve diverse nucleation conditions for comprehensive understanding of the polymorphic behavior of cocrystals.

#### 14.4.7 Kinetic Methods: Rotavap and Spray-Drying Techniques

In addition to the methods described above, fast evaporation of the solvent from a crystallization batch by rotavap or by spray-drying techniques showed applications in the polymorph screening of single-component crystals and cocrystals. The

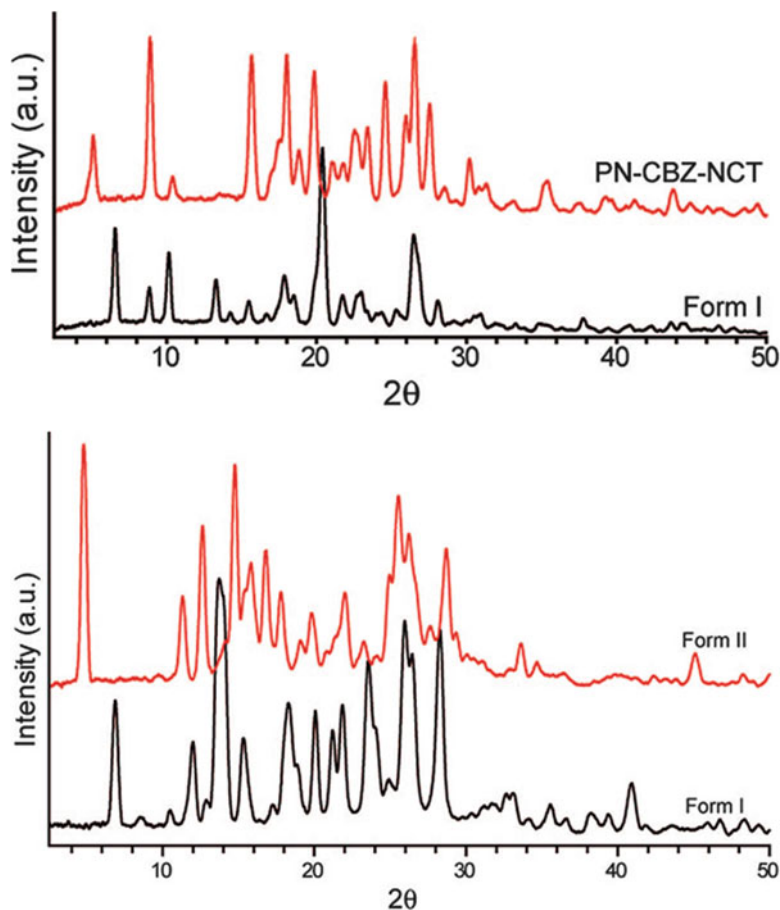


**Fig. 14.8** Powder X-ray diffraction patterns of the new polymorphs of the cocrystals of CBZ with NCT (*top*) and SAC (*bottom*). The PXRD patterns represented in *red* correspond to the results from cocrystallization experiments using cross-linked polymers as heteronuclei (Reprinted with permission from Ref. [37]. Copyright 2008, The American Chemical Society)

advantage with these kinetic methods is that the polymorphic forms that crystallize first from the solvent do not get an opportunity to transform to the more stable polymorphs because of the fast removal of the solvent. Hence, the crystallization solutions are maintained at high supersaturation levels and promote the formation of metastable polymorphs. For example, metastable Form II of the aspirin, which has a tendency to grow within the crystals of long-known Form I as intergrowths, has been selectively prepared by fast evaporation of dichloromethane containing the aspirin [38a]. The method has also been found to be useful for the polymorph screening of the cocrystals. For example, as described in the previous section, the second polymorph of the cocrystal that contains CBZ and saccharin has been recently

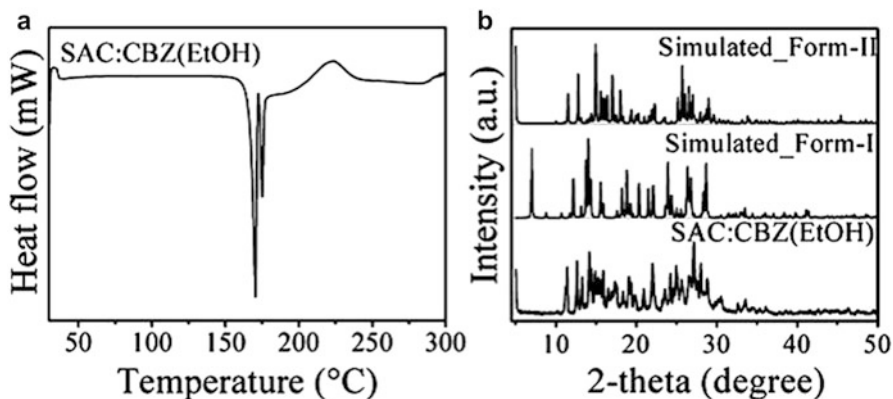


**Fig. 14.9** Dimorphic SAC:CBZ (1:1). (a) The DSC and (b) PXRD patterns of the solids obtained by the rotavap method confirm the simultaneous presence of the two reported cocrystal forms I (175 °C) and II (168 °C) (Reproduced from Ref. [38b]. Copyright Royal Society of Chemistry, 2011)

found when functionalized polymers were used as heteronuclei for crystallization. Cocrystallization by the rotavap method in ethanol resulted in the metastable Form II along with the trace amounts of Form I in the mixture, thus suggesting efficacy of the rotavap method in polymorph screening of cocrystals (Fig. 14.9) [38b].

A similar method of kinetically controlled cocrystallization using spray drying has been demonstrated by Alhalaweh and Velaga. The authors found that spray drying of an ethanol solution of 1:1 molar ratio of caffeine and glutaric acid selectively produces the metastable polymorph (form I) of the cocrystal (Fig. 14.10) [39].

### 14.4.8 High-Throughput Screening

A very recent technique that utilizes fully automated robotic systems is high-throughput screening (HTS), which is capable of performing thousands of crystallization experiments per week with only a few grams of the API [9]. The compounds obtained from these experiments are analyzed by X-ray powder diffraction and Raman microscopy and then systematically classified (e.g., as polymorph, cocrystal, salt, solvate, hydrate, etc.). One of the key aspects of HTS is that the choice of solvent and solvent mixtures should normally be different for every substance, taking into account solubilities of the compounds used for screening, possible chemical reactions, and also solvent–solute interactions. In general, the data obtained from HTS provide valuable information on the existence of multiple forms of a given substance. Thus, the method demonstrates the suitability for discovering polymorphs and identifying the conditions under which they can be produced.

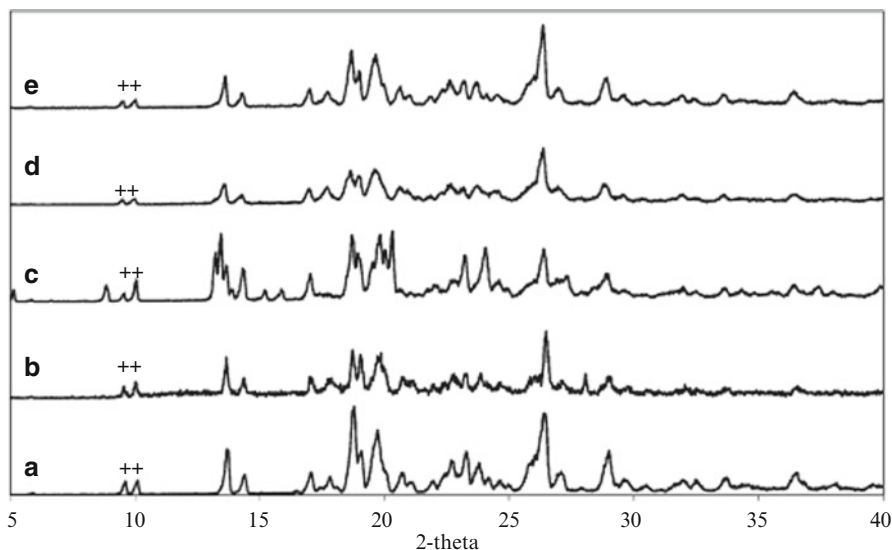


**Fig. 14.10** PXRD patterns of (a) reference cocrystalline material of CBZ–GLT and solid phases resulting by subjecting stoichiometric solutions of CBZ–GLT to solvent evaporation under (b) a congruently saturating condition (ethyl acetate) and (c) an incongruently saturating condition (ethanol) and to spray drying under (d) a congruently saturating condition (ethyl acetate) and (e) an incongruently saturating condition. Observe the additional peaks in pattern c (Reprinted with permission from Ref. [39]. Copyright 2010, The American Chemical Society)

## 14.5 Characterization of Polymorphs

Characterization of all the polymorphs is prerequisite for precise understanding of the polymorphic behavior of a compound, the stability relationships, and their interconversions. Over the years, a number of novel techniques have been developed for polymorph characterization. Some of these will be discussed in this section.

X-ray diffraction techniques, such as powder X-ray diffraction (PXRD) and single-crystal X-ray diffraction (SCXRD), are invaluable methods for the unambiguous quantification of polymorph structure, because each polymorph results in its own characteristic diffraction pattern. If single crystals suitable for SCXRD are difficult to grow, PXRD is the most reliable method for distinguishing polymorphs. One of the added advantages of the diffraction technique is that experiments can be carried out at different temperatures, pressures, and humidities to identify phase stability, phase transformations, transition temperature, and hydration states. The use of X-ray diffraction in the characterization of polymorphs can be exemplified by the polymorphs of the muscle relaxant, metaxalone, which exists in two polymorphic forms. The crystal structure analysis revealed a distinct hydrogen-bonding interaction, and PXRD shows unique diffraction patterns for the polymorphs (Fig. 14.11) [40].

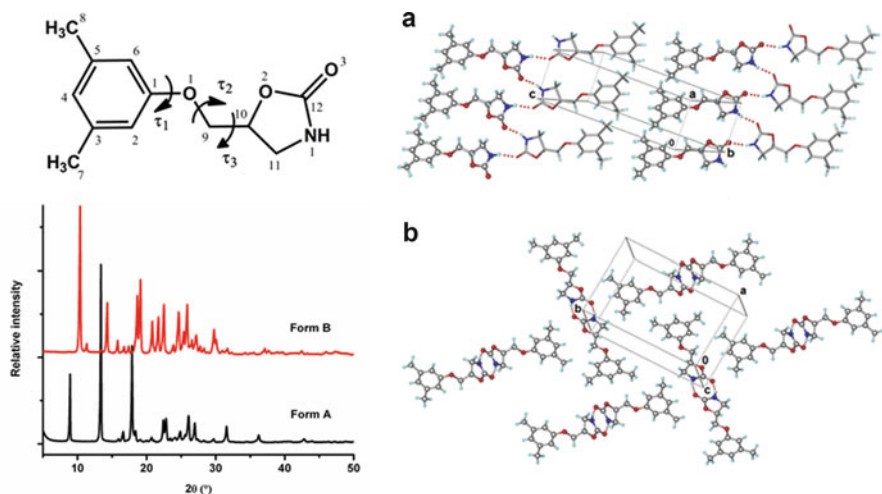


**Fig. 14.11** Metaxalone, a flexible molecule, forms two polymorphs with distinct crystal structures, form A (a), form B (b) (Reprinted with permission from Ref. [40]. Copyright 2011, The American Chemical Society)

Differential scanning calorimetry (DSC) is one of the most commonly used thermal techniques for accurate measurement of thermal behavior of polymorphs. For example, DSC thermograms appear as endotherms for the thermal events in which heat is absorbed, such as solvent loss, phase transitions, or melting. The exotherms represent processes such as crystallization or chemical reactions where heat is evolved. The area under the curve proportional to the heat change involved. Therefore, the data obtained from DSC such as enthalpy of fusion, phase transformation, and melting behavior can be used to understand thermodynamic relationships by applying Burger's rules [17]. Over the years, DSC has been instrumental in the characterization of several polymorphic systems including pharmaceuticals. For example, thermodynamic relationship among various polymorphs of the antidiabetic drug, tolbutamide, has recently been deduced by DSC (Fig. 14.12) [41]. Polymorphic phase transformations from Form I<sup>L</sup> to Form I<sup>H</sup> and Form III to Form I<sup>H</sup> were observed as endothermic transitions, whereas Form IV undergoes an exothermic transition. Form II, which was found to be the thermodynamic form at ambient conditions, shows an endothermic peak at 117 °C for melting followed by an exotherm for recrystallization to Form I<sup>H</sup>.

The use of microscope plays a significant role in the characterization of polymorphs. Observation of morphological differences by the use of microscope helps to identify new polymorphs more precisely. A microscope coupled with a hot stage facilitates the identification of phase transformations, monotropic and enantiotropic relationships, crystalline to amorphous phase, the appearance of kinetic and thermodynamic polymorphs, sublimation, melting, and chemical reactions. Potential uses of hot-state microscope (HSM) in the characterization of

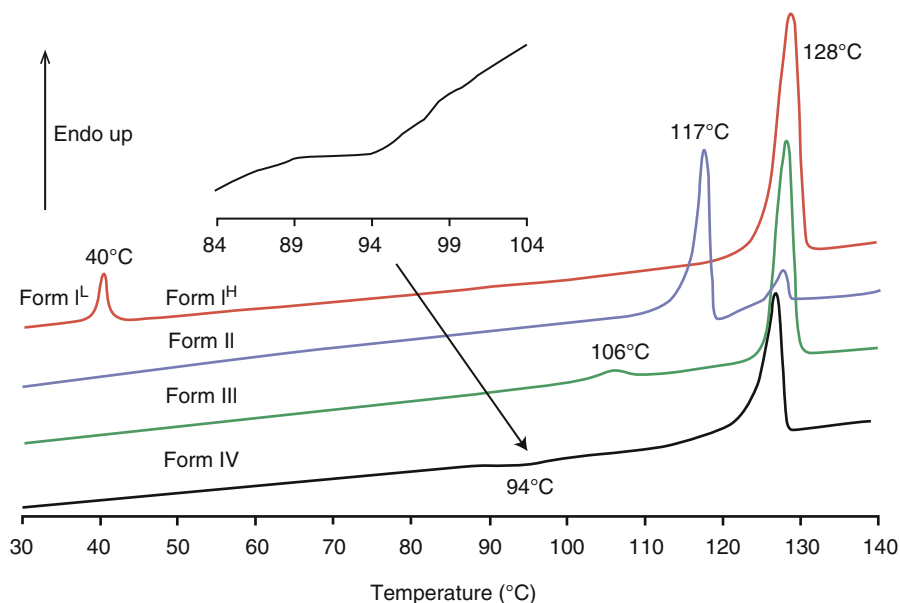


**Fig. 14.12** DSC thermograms of tolbutamide polymorphs (Reproduced with permission from Ref. [41]. Copyright 2010 Wiley-Liss, Inc.)

polymorphic systems have been vastly reported. For example, we have recently used the HSM to evaluate phase transformation behavior of a cocrystal involving NCT and pimelic acid, which forms two polymorphs in 1:1 molar ratio [42]. As shown in Fig. 14.13, Form 1 crystal showed partial opaqueness for phase transition before it melted at 110 °C. In contrast, Form 2 crystal directly melted at 110 °C. This observation confirms the phase transition from Form 1 to Form 2 and supports the conclusions drawn from stability experiments.

Since polymorphs have different solid-state structures, the chemical environment of at least a few of the atoms will differ from one structure to another. Therefore, techniques such as FT-IR, Raman, and solid-state NMR spectroscopy are frequently used for the characterization of polymorphs. These techniques are used to identify differences in molecular conformation and hydrogen bonding in the solid state. A major advantage of Raman and NIR is that they can be used to analyze tablets and capsules intact without sample preparation. An advantage with the solid-state NMR is that it provides valuable crystallographic information, such as the number of crystallographically independent molecules in the crystal structure due to doubled peaks for the same carbon atom.

Atomic force microscopy (AFM) is a type of scanning probe microscopy which has emerged as the method of choice for characterizing the surface structure of crystals. AFM has been successfully used to distinguish polymorphs of many organic molecules and APIs. For example, morphological differences in surface

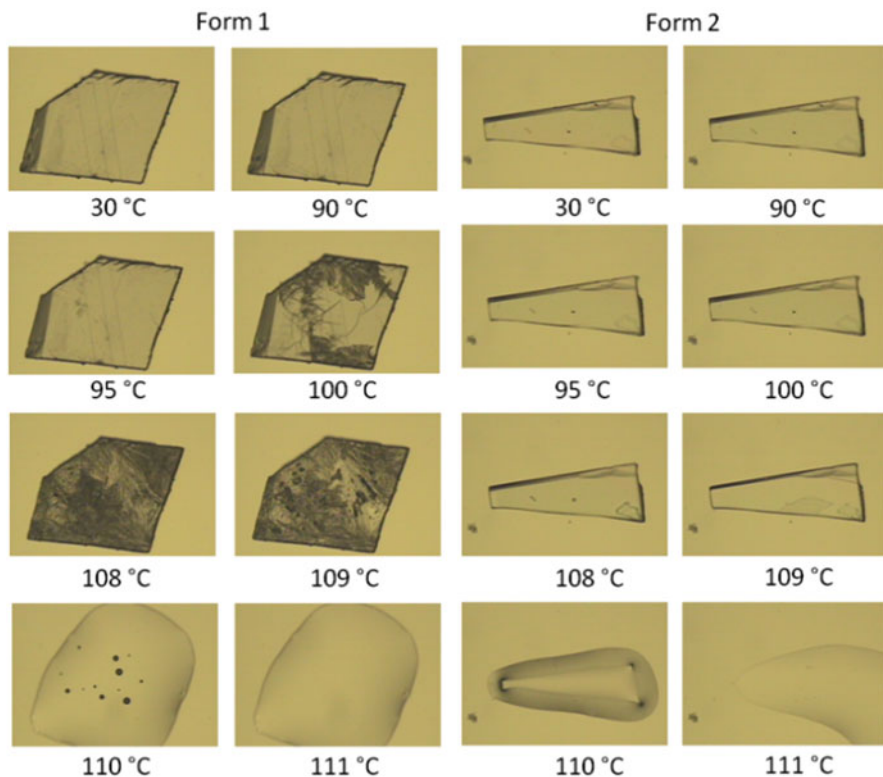


**Fig. 14.13** Photomicrographs of Forms 1 and 2 crystals of 1:1 NCT–pimelic acid cocrystal at various temperatures in the HSM experiment. Notice that Form 1 crystal undergoes phase transition before melting at 110 °C (Reproduced from Ref. [42])

characteristics of the polymorphs of sulfamerazine, cimetidine, etc. have been thoroughly evaluated by the AFM technique. AFM has also been used for the characterization and monitoring of phase changes of cocrystal polymorphs. For example, Jones and coworkers used AFM to monitor changes at the crystal surfaces during the phase transformation of the caffeine–glutaric acid cocrystal [43]. The cocrystal exists in two polymorphic forms, and crystal structures of both the polymorphs feature a similar hydrogen-bonded linear tapes mediated by  $O-H\cdots O$  hydrogen bonds. The only difference between the packing of two forms is the conformation of the alkyl chain of the glutaric acid molecule. Using the intermittent contact mode AFM, phase transformation of Form I, which was stored at ambient temperature and 70 % relative humidity (RH), was monitored continuously in situ. Significant surface rearrangement which was accompanied by change in the spacing between the layers of molecules was evident during the phase transformation to Form II, which not only helps to distinguish the two polymorphs but also understand the mechanism of phase transformation (Fig. 14.14).

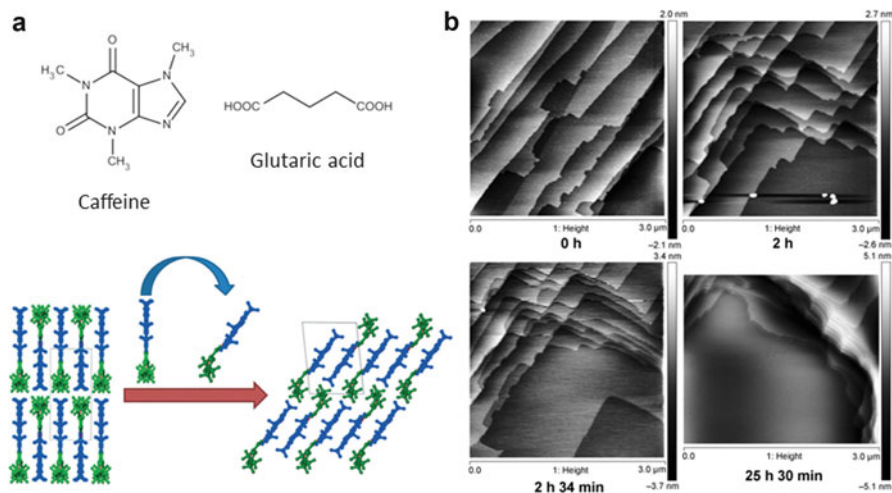


**Fig. 14.14** An example for AFM applications in polymorph characterization; (a) phase transformation of Form I to Form II involves tilting of the layers by  $38^\circ$  in a concerted manner resulting in a decrease in step height by  $2.5 \text{ \AA}$  and (b) real time in situ IC-AFM images of the movement of layers at the surface of a caffeine–glutaric acid cocrystal undergoing a phase change from Form I to Form II at ambient temperature and 70 % RH. Images were recorded over a 26 h period, with the phase change occurring in all surface layers at the 2 h 34 min time point (Reproduced with permission from Ref. [43]. Copyright © 2013 WILEY-VCH Verlag GmbH & Co. KGaA, Weinheim)

## 14.6 Classification of Polymorphs

Polymorphs can be classified into different types based on the nature of their appearance from the crystallization and on the structural differences. The advantage with these classifications is that the differences between the polymorphic forms can be easily identified and helps to convey the information pertaining to the origin of polymorphism. It should be cautioned that polymorphs may belong to one or more of the different classifications, and hence, these classifications cannot be applied in the strictest sense.

### 14.6.1 Classifications Based on Structural Differences

Crystal structural analysis is the ultimate tool for precise identification of structural differences in polymorphs, and hence, polymorphs can be classified based on their structural differences. A brief overview of these different classes is provided in this section.

### 14.6.1.1 Conformational Polymorphs

Conformational polymorphism is the existence of different conformers of the same molecule in different polymorphic forms [44]. Conformational polymorphism is more frequently observed in molecules with several degrees of freedom such that the differences in conformation will arise from one or more significant differences in the torsion angles. In general, APIs are predisposed with multiple functional groups and substituents, and hence, conformational polymorphism is frequently observed in this class of molecules. ROY represents one of the best representative examples for conformational polymorphism, for which as many as seven polymorphs have been characterized by single-crystal X-ray diffraction, and adopts significantly different conformations in the polymorphs (Fig. 14.15) [22]. Conformational polymorphs are also more frequently reported in cocrystals. As we have noted from a recent review of the reported examples of polymorphic cocrystals, majority of the cocrystals feature different conformations of one or more of the cocrystal components [20]. Conformational polymorphs provide ideal systems for studying structure-property relationships, since the number of chemical variables is reduced to zero and the polymorphic structures differ in their molecular structure due to differences in crystal environment.

### 14.6.1.2 Synthons or Hydrogen-Bond Polymorphism

Polymorphs that differ by their primary hydrogen-bond motifs or synthons can be classified as synthon polymorphs. Polymorphs of tetrolic acid represent a classic example in single-component crystals:  $\alpha$ -form contains the acid–acid dimer synthon and the  $\beta$ -form contains a catemer synthon [45]. Many well-known polymorphic compounds such as metaxalone, furosemide, temozolomide, and CBZ show differences in their hydrogen-bond synthons and can be classified as synthon polymorphs. Synthon polymorphism arising from different hydrogen-bond synthons has also been reported in cocrystals. For example, polymorphs of a cocrystal involving ethenzamide and 3,5-dinitrobenzoic acid represent the synthon polymorphs [46]. Form I is sustained by an acid–amide heterosynthon, whereas Form II is sustained by an amide–amide homosynthon (Fig. 14.16).

### 14.6.1.3 Packing Polymorphs

Polymorphs can be classified as packing polymorphs when they differ by their overall three-dimensional crystal packing. Although there is no clear distinction between packing polymorphs and other classes of polymorphs, the former is more common for totally rigid molecules or molecules with weak conformational flexibility. For example, p-nitrophenol, chlordiazepoxide, and sulfathiazole all show

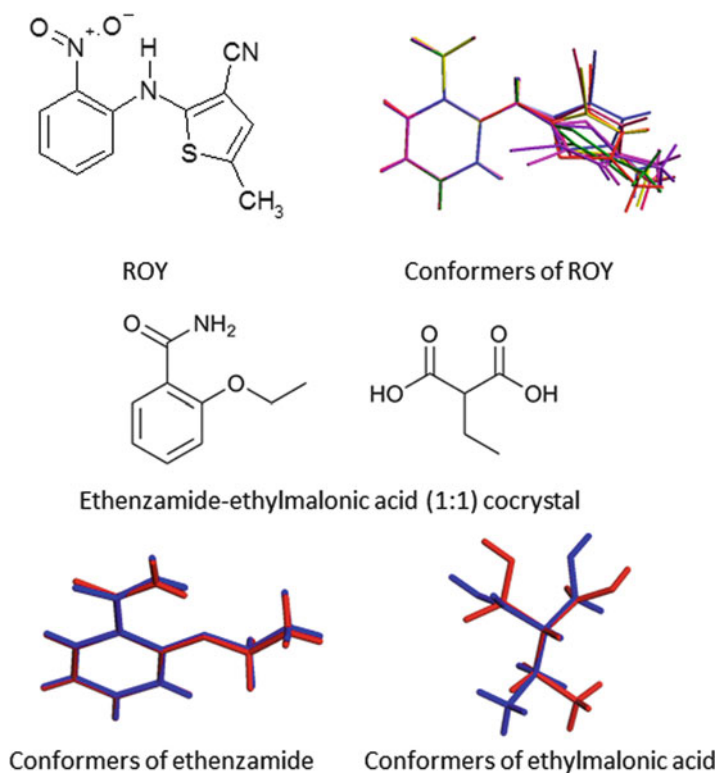


**Fig. 14.15** Examples of conformational polymorphs in a molecular crystal and cocrystal (Part of the figure was reproduced from Ref. [34])

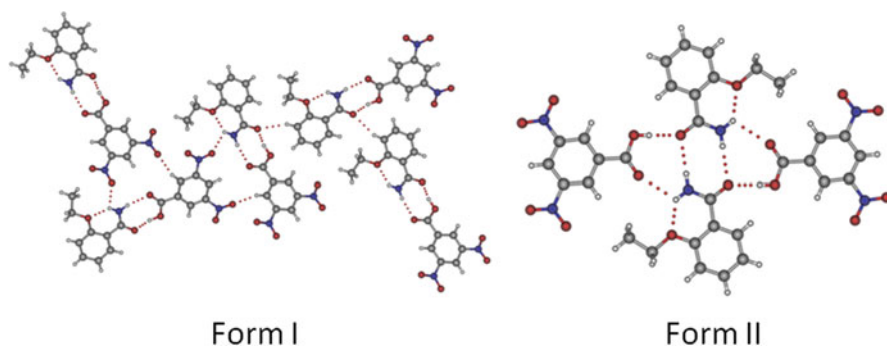


**Fig. 14.16** Synthon polymorphs of ethenzamide-3,5-dinitrobenzoic acid (1:1) cocrystal (Reprinted with permission from Ref. [46]. Copyright 2010, The American Chemical Society)

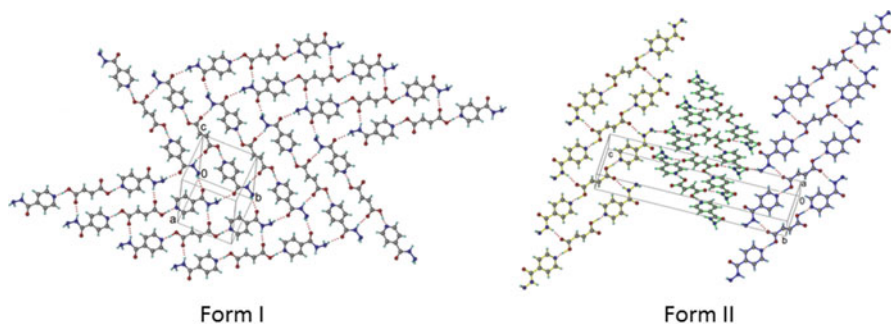


**Fig. 14.17** Comparison of the crystal packing of the polymorphs of the 1:0.5 cocrystal involving isoniazid and fumaric acid (Reproduced from Ref. [47])

minor differences in their conformations but show significant differences in their overall crystal packing. Packing polymorphism in cocrystals has also been observed in many polymorphic systems. For example, dimorphs (Form I and II) of a 1:0.5 cocrystal involving the anti-tuberculosis drug, isoniazid, and fumaric acid represent packing polymorphism [47]. Both the polymorphs crystallize concomitantly from common organic solvents with different morphologies. In both the polymorphs, isoniazid and fumaric acid molecules interact via acid–pyridine synthon and N–H (secondary amine of isoniazid)···O (carbonyl of fumaric acid) hydrogen bond to produce a hydrogen-bonded ladder. However, as shown in Fig. 14.17, the overall packing of the ladders in the polymorphs is different. While Form I features a planar two-dimensional sheet structure, Form II is a corrugated sheet composed of the ladder networks related by a glide plane.

#### 14.6.1.4 Tautomeric Polymorphs

When different tautomers of a compound crystallize in different crystal forms, they are termed as tautomeric polymorphs. In general, tautomerism occurs when the constitutional isomers of different hydrogen-atom connectivity are in dynamic equilibrium with one another. Tautomers that interconvert in solution or in the melt are considered to be the same chemical compound, and hence, the crystal forms that contain these tautomers can be classified as polymorphs. In contrast to other previously described classes of polymorphs, tautomeric polymorphs are rare. A very few examples of these have been reported. For example, APIs such as omeprazole, sulfasalazine, and triclabendazole have been reported to contain different tautomers in their polymorphic forms. Tautomeric polymorphs are very rare in cocrystals. There is only one reported example of a configurational polymorph which features a nonsteroidal anti-inflammatory drug, piroxicam, and 4-hydroxybenzoic acid in 1:1 molar ratio [48]. One of the polymorphs contains the piroxicam molecule as zwitterion tautomer, whereas the other contains piroxicam molecule as the

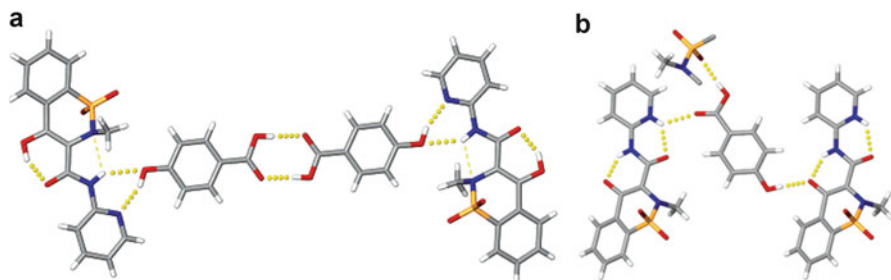


**Fig. 14.18** Tautomeric polymorphs of a 1:1 cocrystal of piroxicam and 4HBA. Notice that piroxicam exists as neutral form in (a) and as zwitterion form in (b). Only the sulfonamide group that is accepting a hydrogen bond from the carboxylic acid of the 4HBA is shown in (b) (Reprinted with permission from Ref. [48]. Copyright 2007, The American Chemical Society)

non-ionized tautomer. As shown in Fig. 14.18, the polymorph that contains the non-ionized tautomer features acid–acid dimer synthon and phenol–pyridine synthons, whereas the polymorph that contains the zwitterion tautomer features acid–sulfonyl and phenol–enolate oxygen synthons.

## 14.6.2 Classifications Based on Appearance from Crystallization Experiments

Control over crystallization process is very important for selective preparation of a particular polymorph. Hence, crystallization experiments are designed such that only a specific polymorph is produced selectively. However, despite wise selection of crystallization conditions, there are instances where two or more polymorphs appear simultaneously and some polymorphs difficult to prepare after a certain period of time. These two cases are termed as concomitant polymorphs and disappearing polymorphs, respectively.

### 14.6.2.1 Concomitant Polymorphs

Concomitant polymorphs are those that crystallize simultaneously from the same crystallization batch under identical crystallization conditions. In general, polymorphs crystallize together when there are two or more local minima on the free-energy curve with relatively equal energies. Concomitant polymorphs that are grown from and remain in contact with solution will most possibly undergo phase transformation such that the metastable polymorph undergoes a complete dissolution and the most stable thermodynamic form recrystallizes from the solution. Concomitant polymorphism in several organic, inorganic, and protein samples has been reviewed by Bernstein et al., and the thermodynamic and kinetic factors that govern competitive and concomitant crystallization of polymorphs were highlighted [49]. Interestingly, the earliest reported organic compound to show

**Table 14.2** A list of cocrystals that form concomitant polymorphs

S. No.	Cocrystal (molar ratio)
1.	4-Cyanopyridine + 4,4'-bipyridylethane (1:1)
2.	4-Cyanopyridine + 4,4'-biphenol (1:0.5)
3.	Trimesic acid + 4,4'-bipyridylethylene (2:3)
4.	4,4'-Dihydroxybenzophenone + 4,4'-bipyridylethane (1:1)
5.	Sulfamethazine + 4-hydroxybenzamide (1:1)
6.	Gallic acid + acetamide (ACT) (1:1)
7.	Triphenylsilanol + 4,4-bipyridine (4:1)
8.	Isoniazid + 4-hydroxybenzoic acid + water (1:1:1)
9.	Isoniazid + fumaric acid (1:0.5)
10.	4-Hydroxybenzoic acid + 4,4'-bipyridine (2:1)
11.	Caffeine + glutaric acid (1:1)
12.	Caffeine + 4-chloro-3-nitrobenzoic acid (1:1)
13.	Theophylline + p-coumaric acid (1:1)
14.	1-Iodo-3,5-dinitrobenzoic acid + 1,4-diazabicyclo[2.2.2]octane (1:1)
15.	1,3-Adamantanedicarboxylic acid + 1,7-phenanthroline (1:2)
16.	2,4-Dihydroxybenzoic acid + NCT (1:1)
17.	Malonic acid + NCT (1:2)

Reprinted from Ref. [20]

polymorphism, benzamide, crystallizes as two concomitant polymorphs from a hot saturated aqueous solution as featherlike needles and blocks. Literature on polymorphic materials contains several examples of concomitant polymorphs. For example, metaxalone, m-nitrophenol, diphenylcarbamide, acetone tosylhydrazone, alprazolam, 3-acetylcoumarin, 2,4-diaminobenzenesulfonic acid, cinchomeric acid, butoxycaine hydrochloride, progesterone, and nitrofurantoin monohydrate all form the polymorphs concomitantly.

Concomitant polymorphism is also not uncommon in cocrystals, and several such polymorphic cocrystals have been reported in the recent literature [20]. Some examples of concomitant polymorphs in cocrystals are listed in Table 14.2.

#### 14.6.2.2 Disappearing Polymorphs

Lack of control over crystallization process often leads to undesirable crystallization outcomes. In some cases, after nucleation of a more stable crystal form, a previously obtained polymorph becomes unobtainable. These polymorphs are often classified as disappearing polymorphs [50]. While in some cases the original form can no longer be isolated, in some other cases, the polymorph can be isolated under extreme measures free from the seeds of the new more stable polymorph. The occurrence and difficulty in reproducing a disappearing polymorph often question the reproducibility of the crystallization processes. However, there are several reported examples of disappearing polymorphs that draw a significant attention from crystallization and pharmaceutical perspective. For example, the well-known case of ritonavir polymorphs could be the best example for disappearing polymorphs

[19]. As it was briefly mentioned in Sect. 14.2, once more stable and poorly soluble Form II emerged, it was difficult to make the unstable Form I. Some examples of disappearing polymorphs include sulfathiazole, 1,2,3,5-tetra-O-acetyl- $\beta$ -D-ribofuranose, xylitol, benzocaine picrate, 3-aminobenzenesulfonic acid, and benzylidene-dl-piperitone.

## 14.7 Impact of Polymorphism on the Physicochemical Properties

By definition, polymorphs refer to distinct solid-state entities of a given compound. Since bulk properties of a material depend on its solid-state structure, it is expected that the polymorphs possess distinct physicochemical properties. As such, polymorphism is well known to impact properties such as solubility, dissolution rate, stability, bioavailability, mechanical properties, etc. This section highlights some polymorphic systems that demonstrate differences in the properties of the materials; this also includes the polymorphs of cocrystals that show distinct properties.

### 14.7.1 Solubility and Dissolution Rate

Solubility and dissolution rate are two important parameters that determine the bioavailability of a drug substance. Polymorphs with distinct solid-state structures confer different properties to the drug substance. As discussed in the previous section, the well-known case of ritonavir emphasizes the potential impact of polymorphism on the solubility and dissolution rate of drugs [19]. The impact of polymorphism on the solubility and dissolution rate of cocrystals has also been demonstrated recently. For example, Goud and Nangia recently reported two polymorphs of a cocrystal of a sulfonamide antibiotic, SACT, with ACT [51]. Crystal structure analysis revealed that the two polymorphs can be distinguished by  $N-H \cdots O_{\text{sulfonamide}}$  and  $N-H \cdots O_{\text{carbonyl}}$  hydrogen bonds and thus can be classified as synthon polymorphs. Dissolution studies suggest that the dissolution rates of the metastable Form I and stable Form II of SACT–ACT are 1.6 times and 1.3 times, respectively, faster than the dissolution rate of SACT (2.18 (mg/cm<sup>2</sup>)/min) in aqueous pH 7 buffer medium (Fig. 14.19).

### 14.7.2 Bioavailability

Bioavailability refers to the extent and rate at which a drug absorbed into the living system. As the solubility and dissolution rate are directly correlated with the absorption, different polymorphs of a drug show different bioavailability. For

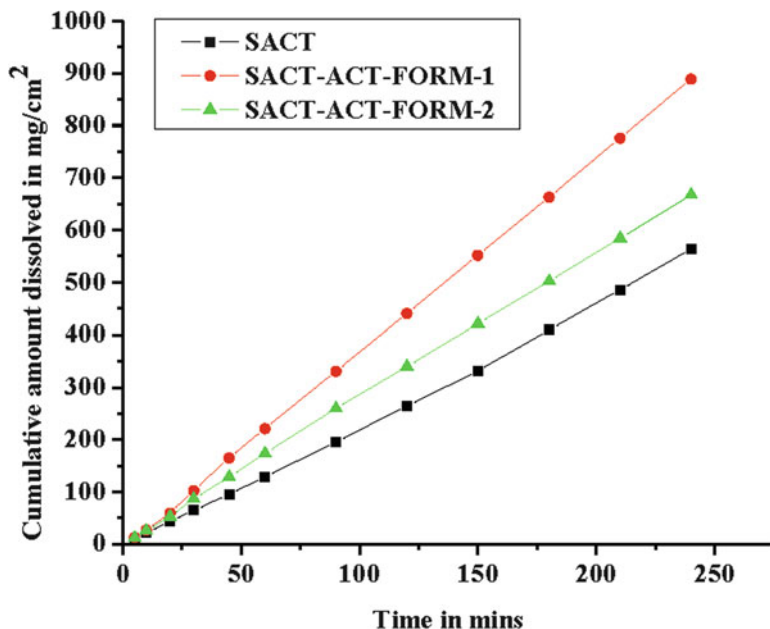


**Fig. 14.19** Comparison of intrinsic dissolution rate curves of SACT and SACT–ACT polymorphs in pH 7 buffer medium (Reproduced with from Ref. [51]. Copyright Royal Society of Chemistry, 2013)

example, Du et al. recently reported differences in the bioavailability of three polymorphs of an antidepressant drug, agomelatine [52]. The authors studied the bioavailability by oral administration on dogs under fasted conditions and found that the bioavailability of the polymorphs was in the order of Form III > Form II > Form I (Fig. 14.20). The poor bioavailability of Form II was attributed to the lowest solubility and dissolution rate.

### 14.7.3 Photoreactivity

Polymorphs of cocrystals that show distinct photoreactivity have been reported recently. For example, MacGillivray and coworkers have found that the polymorphs of a cocrystal involving resorcinol and 1,2-bis(4-pyridyl)ethane show differences in their photoreactivity [53]. The olefinic double bonds in the second polymorph are separated by 4.6 Å and therefore lie outside the range required for photoreaction. As expected, the second polymorph is photostable, but the first polymorph undergoes complete transformation to the cocrystal involving res and rctt-tetrakis(4-pyridyl)cyclobutane.

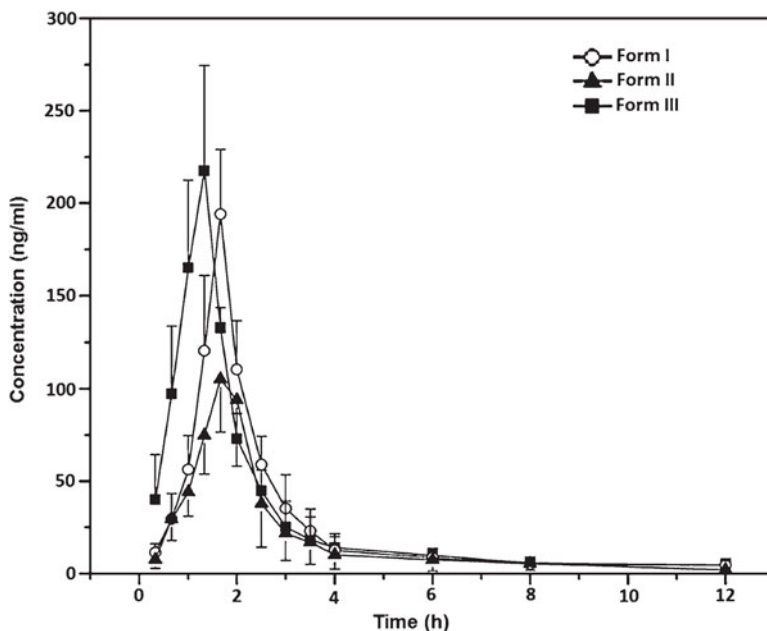


**Fig. 14.20** Mean plasma concentration–time curves of agomelatine polymorphs in beagle dog plasma following administration of single oral tablet with a dose of 6.8 mg/kg under fasting conditions (Reproduced from Ref. [52])

#### 14.7.4 Stability

It is a prerequisite that the stability of a drug substance has to be thoroughly investigated before it is marketed as a medicine. Polymorphs are well known to possess differences in their stability. In general, at a given experimental condition, only one polymorph is stable and all other polymorphs tend to convert to the most stable polymorph. APIs such as CBZ, furosemide, and enalapril maleate all show differences in the chemical and thermal/photochemical stability. The variations in the stability of polymorphs of a cocrystal have also been demonstrated in the case of a 1:1 cocrystal of caffeine and glutaric acid: Form I transforms to Form II within 24 h at high humidity, but Form II is stable for over 3 days under these conditions before undergoing conversion to caffeine hydrate [54].

### 14.8 Statistical Analysis of Polymorphs

Polymorphism is a widespread phenomenon in pharmaceutical solids, and approximately more than 50 % of drug molecules are estimated to be polymorphic. However, the number of reported polymorphic systems in the Cambridge Structural

Database (CSD) is only minimal compared to the total crystal structures reported in the CSD. Recent database studies estimated that about 4–5 % organic compounds and 2 % coordination compounds exist in polymorphic forms. The recent emergence of novel experimental techniques for polymorph screening and automated techniques such as high-throughput screening further facilitated the discovery of novel polymorphs.

Compared to the single-component crystals, polymorphism in the cocrystals is not well documented, and there are only 114 polymorphic cocrystals in the literature at the end of September 2013 [20]. However, our recent analysis of the crystal structures deposited into the CSD revealed that the percentage of polymorphic cocrystals is comparable to the percentage of single-component polymorphic structures [46]. The database analysis further revealed an increasing number of polymorphic cocrystals that are being reported. This could be mainly due to the recent interest in the development of cocrystals for applications in pharmaceutical and material sciences.

Statistical analyses are often subjective and depend on the criteria used for data acquisition; therefore, it is not appropriate to strictly rely on the statistics when dealing with polymorphism of a particular compound. As presented in the previous sections, finding a novel polymorph of a compound solely relies on our ability to find the right experimental conditions.

## 14.9 Conclusions

Polymorphs of a material represent solid states with distinct crystal structures. Differences in solid-state structures mean that the polymorphs exhibit different physical and chemical properties. Therefore, prior knowledge on polymorphism of a material is valuable for its successful development. A thorough characterization of all the polymorphs and studies concerning phase transitions are essential for determination of the most stable polymorph and subsequent production of the desired polymorph in bulk. Although polymorphism studies in single-component crystals and active pharmaceutical ingredients are widely reported, such studies in cocrystals are only being reported in the current decade. This is mainly due to the recent interest in pharmaceutical cocrystals for development of drug formulations. While most of the reported cocrystal polymorphs have been discovered serendipitously during cocrystallization experiments, development of systematic screening methods to discover new polymorphs of cocrystal is an emerging activity. The current chapter provides a brief history of polymorphism and highlights potential significance of polymorphism in pharmaceutical and materials science. The thermodynamic rules that govern the polymorphs, different classifications, and potential impact of polymorphism on the physicochemical properties are emphasized with representative examples.

**Acknowledgments** SA thanks Prof. Reginald B. H. Tan and Dr. Pui Shan Chow of the Institute of Chemical and Engineering Sciences for encouragement and support and the Science and Engineering Research Council of A\*STAR, Singapore, for research funding.

## References

1. J. Bernstein, *Polymorphism in Molecular Crystals* (Clarendon, Oxford, 2002)
2. G.M. Frankenbach, M.C. Etter, Relationship between symmetry in hydrogen-bonded benzoic acids and the formation of acentric crystal structures. *Chem. Mater.* **4**, 272–278 (1992)
3. D.D. MacNicol, F. Toda, R. Bishop, Comprehensive supramolecular chemistry, solid-state supramolecular chemistry, in *Crystal Engineering*, vol. 6 (Pergamon Press, Oxford, 1996)
4. P.H. Stahl, C.G. Wermuth, *Handbook of Pharmaceutical Salt Properties, Selection and Use* (Wiley-VCH, Weinheim/New York, 2002)
5. F.H. Herstein, *Crystalline Molecular Complexes and Compounds*. IUCr Monograph (Oxford University, Oxford, 2005)
6. Ö. Almarsson, M.J. Zawortko, Crystal engineering of the composition of pharmaceutical phases. Do pharmaceutical co-crystals represent a new path to improved medicines? *Chem. Commun.* 1889–1896 (2004)
7. M.A. Oliveira, M.L. Peterson, D. Klein, Continuously substituted solid solutions of organic cocrystals. *Cryst. Growth Des.* **8**, 4487–4493 (2008)
8. S. Cherukuvada, A. Nangia, Eutectics as improved pharmaceutical materials: design, properties and characterization. *Chem. Commun.* **50**, 906–923 (2014)
9. S.L. Morissette, Ö. Almarsson, M.L. Peterson, J.F. Remenar, M.J. Read, A.V. Lemmo, S. Ellis, M.J. Cima, C.R. Gardner, High-throughput crystallization: polymorphs, salts, co-crystals and solvates of pharmaceutical solids. *Adv. Drug Deliv. Rev.* **56**, 275–300 (2004)
10. K.S. Khomane, P.K. More, G. Raghavendra, A.K. Bansal, Molecular understanding of the compaction behavior of indomethacin polymorphs. *Mol. Pharm.* **10**, 631–639 (2013)
11. M.H. Klaproth, *J. Bergmannisch.* **I**, 294–299 (1798)
12. E. Mitscherlich, Über die Körper, welche in zwei verschiedenen krystallisieren Formen. *Abhl. Akad. Berlin.* **1822–1823**, 43–48
13. A. Nangia, Conformational polymorphs, multi Z' crystal structures and phase transformations. *J. Indian Inst. Sci.* **87**, 133–147 (2007)
14. O. Lehmann, *Die Kristallanalyse oder die chemische Analyse durch Beobachtung der Krystallbildung mit Hilfe des Mikroskops* (Wilhelm Engelmann, Leipzig, 1891)
15. W.F. Ostwald, Studien über die bildung und umwandlung feöter körper. Studies on formation and transformation of solid materials. *Z. Phys. Chem.* **22**, 289–330 (1897)
16. G. Tamman, *The States of Aggregation* (trans. FF Mehl) (Constable and Company, Ltd., London, 1926), pp. 116–157
17. (a) A. Burger, R. Ramberger, On the polymorphism of pharmaceuticals and other molecular crystals. I. Theory of thermodynamic rules. *Mikrochim. Acta.* **II**, 259–272 (1979), (b) A. Burger, R. Ramberger, On the polymorphism of pharmaceuticals and other molecular crystals. *Mikrochim. Acta.* **II**, 273–316 (1979)
18. W.C. McCrone, in *Physics and Chemistry of the Organic Solid State*, ed. by D. Fox, M.M. Labes, A. Weissberger, vol. 2 (Interscience, London, 1965), pp. 725–767
19. S.R. Chemburkar, J. Bauer, K. Deming, H. Spiwek, K. Patel, J. Morris, R. Henry, S. Spanton, W. Dziki, W. Porter, J. Quick, P. Bauer, J. Donaubauber, B.A. Narayanan, M. Soldani, D. Riley, K. McFarland, Dealing with the impact of ritonavir polymorphs on the late stages of bulk drug process development. *Org. Process Res. Dev.* **4**, 413–417 (2000)
20. S. Aitipamula, P.S. Chow, R.B.H. Tan, Polymorphism in cocrystals: a review and assessment of its significance. *CrystEngComm* **16**, 3451–3465 (2014)

21. A. Grunenberg, J.-O. Henck, H.W. Siesler, Theoretical derivation and practical application of energy/temperature diagrams as an instrument in preformulation studies of polymorphic drug substances. *Int. J. Pharm.* **129**, 147–158 (1996)
22. L. Yu, Polymorphism in molecular solids: an extraordinary system of red, orange, and yellow crystals. *Acc. Chem. Res.* **43**, 1257–1266 (2010)
23. T. Ueto, N. Takata, N. Muroyama, A. Nedu, A. Sasaki, S. Tanida, K. Terada, Polymorphs and a hydrate of furosemide-nicotinamide 1:1 cocrystal. *Cryst. Growth Des.* **12**, 485–494 (2012)
24. M. Jim, K.-J. Kim, Effect of supersaturation on polymorphs of clopidogrel hydrogen sulfate in drawing-out crystallization. *Chem. Eng. Technol.* **35**, 995–1002 (2012)
25. C. Cacula, A. Baudot, M.L. Duarte, A.M. Matos-Beja, M.R. Silva, J.A. Paixão, R. Fausto, Low temperature polymorphism in 3-amino-1-propanol. *J. Mol. Struct.* **649**, 143–153 (2003)
26. F.P.A. Fabbiani, D.R. Allan, W.I.F. David, S.A. Moggach, S. Parsons, C.R. Pulham, High-pressure recrystallization—a route to new polymorphs and solvates. *CrystEngComm* **6**, 504–511 (2004)
27. F.P.A. Fabbiani, D.R. Allan, S. Parsons, C.R. Pulham, An exploration of the polymorphism of piracetam using high pressure. *CrystEngComm* **7**, 179–186 (2005)
28. G.D. Profio, A. Caridi, R. Caliandro, A. Guagliardi, E. Curcio, E. Drioli, Fine dosage of anti-solvent in the crystallization of L-histidine: effect on polymorphism. *Cryst. Growth Des.* **10**, 449–455 (2010)
29. B. Subramaniam, R.A. Rajewski, K. Snavely, Pharmaceutical processing with supercritical carbon dioxide. *J. Pharm. Sci.* **86**, 885–890 (1997)
30. R. Bettini, R. Menabeni, R. Tozzi, M.B. Prazo, I. Pasquali, M.R. Chierott, R. Gobetto, L. Pellegrino, Didanosine polymorphism in a supercritical antisolvent process. *J. Pharm. Sci.* **99**, 1855–1870 (2010)
31. M. Moneghini, I. Kikic, D. Voinovich, B. Perissutti, P. Alessi, A. Cortesi, F. Princivalle, D. Solinas, Study of the solid state of carbamazepine after processing with gas anti-solvent technique. *Eur. J. Pharm. Biopharm.* **56**, 281–289 (2003)
32. R.-Q. Song, H. Cölfen, Additive controlled crystallization. *CrystEngComm* **13**, 1249–1276 (2011)
33. Y. Gong, B.M. Colliman, S.M. Mehrens, E. Lu, J.M. Miller, A. Blackburn, D.J. Grant, Stable-form screening: overcoming trace impurities that inhibit solution-mediated phase transformation to the stable polymorph of sulfamerazine. *J. Pharm. Sci.* **97**, 2130–2144 (2008)
34. S. Aitipamula, P.S. Chow, R.B.H. Tan, Conformational and enantiotropic polymorphism of a 1:1 cocrystal involving ethenzamide and ethylmalonic acid. *CrystEngComm* **12**, 3691–3697 (2010)
35. A.V. Trask, W.D.S. Motherwell, W. Jones, Solvent-drop grinding: green polymorph control of cocrystallization. *Chem. Commun.* 890–891 (2004)
36. S. Roy, A.J. Matzger, Unmasking a third polymorph of a benchmark crystal-structure-prediction compound. *Angew. Chem. Int. Ed.* **48**, 8505–8508 (2009)
37. W.W. Porter III, S.C. Elie, A.J. Matzger, Polymorphism in carbamazepine cocrystals. *Cryst. Growth Des.* **8**, 14–16 (2008)
38. (a) P.P. Bag, C.M. Reddy, Screening and selective preparation of polymorphs by fast evaporation method: a case study of aspirin, anthranilic acid, and niflumic acid. *Cryst. Growth Des.* **12**, 2740–2743 (2012), (b) P.P. Bag, M. Patni, C.M. Reddy, A kinetically controlled crystallization process for identifying new co-crystal forms: fast evaporation of solvent from solutions to dryness. *CrystEngComm* **13**, 5650–5652 (2011)
39. A. Alhalaweh, S.P. Velaga, Formation of cocrystals from stoichiometric solutions of incongruently saturating systems by spray drying. *Cryst. Growth Des.* **10**, 3302–3305 (2010)
40. S. Aitipamula, P.S. Chow, R.B.H. Tan, Conformational polymorphs of a muscle relaxant, metaxalone. *Cryst. Growth Des.* **11**, 4101–4109 (2011)
41. S. Thirunahari, S. Aitipamula, P.S. Chow, R.B.H. Tan, Conformational polymorphism of tolbutamide: a structural, spectroscopic, and thermodynamic characterization of Burger's forms I–IV. *J. Pharm. Sci.* **99**, 2975–2990 (2010)

42. S. Aitipamula, A.B.H. Wong, P.S. Chow, R.B.H. Tan, Polymorphism and phase transformations of a cocrystal of nicotinamide and pimelic acid. *CrystEngComm* **14**, 8193–8198 (2012)
43. R. Thakuria, M.D. Eddleston, E.H.H. Chow, G.O. Lloyd, B.J. Aldous, J.F. Krzyzaniak, A.D. Bond, W. Jones, Use of in situ atomic force microscopy to follow phase changes at crystal surfaces in real time. *Angew. Chem. Int. Ed.* **52**, 10541–10544 (2013)
44. A. Nangia, Conformational polymorphism in organic crystals. *Acc. Chem. Res.* **41**, 595–604 (2008)
45. S. Parveen, R.J. Davey, G. Dent, R.G. Pritchard, Linking solution chemistry to crystal nucleation: the case of tetrolic acid. *Chem. Commun.* 1531–1533 (2005)
46. S. Aitipamula, P.S. Chow, R.B.H. Tan, Polymorphs and solvates of a cocrystal involving an analgesic drug, ethenzamide, and 3,5-dinitrobenzoic acid. *Cryst. Growth Des.* **10**, 2229–2238 (2010)
47. S. Aitipamula, A.B.H. Wong, P.S. Chow, R.B.H. Tan, Novel solid forms of the anti-tuberculosis drug, isoniazid: ternary and polymorphic cocrystals. *CrystEngComm* **15**, 5877–5887 (2013)
48. S.L. Childs, K.I. Hardcastle, Cocrystals of piroxicam with carboxylic acids. *Cryst. Growth Des.* **7**, 1291–1304 (2007)
49. J. Bernstein, R.J. Davey, J.-O. Henck, Concomitant polymorphs. *Angew. Chem. Int. Ed.* **38**, 3440–3461 (1999)
50. J.D. Dunitz, J. Bernstein, Disappearing polymorphs. *Acc. Chem. Res.* **28**, 193–200 (1995)
51. N.R. Goud, A. Nangia, Synthon polymorphs of sulfacetamide-acetamide cocrystal based on  $N-H\cdots O=S$  and  $N-H\cdots O=C$  hydrogen bonding. *CrystEngComm* **15**, 7456–7461 (2013)
52. W. Du, Y. Zhou, Y. Gong, C. Zhao, Investigation of physicochemical properties and in-vitro in-vivo evaluation of agomelatine polymorphs. *Asian J. Pharm. Sci.* **8**, 181–190 (2013)
53. T. Friščić, L.R. MacGillivray, Engineering cocrystal and polymorph architecture via pseudoseeding. *Chem. Commun.* 773–775 (2009)
54. A.V. Trask, W.D.S. Motherwell, W. Jones, Pharmaceutical cocrystallization: engineering a remedy for caffeine hydration. *Cryst. Growth Des.* **5**, 1013–1021 (2005)

# Chapter 15

## Hydration/Dehydration Phase Transition Mechanism in Organic Crystals Investigated by Ab Initio Crystal Structure Determination from Powder Diffraction Data

Kotaro Fujii and Hidehiro Uekusa

**Abstract** The study of organic crystals is a very active field. Molecules in a crystal are responsive to environmental changes, such as temperature, humidity, and irradiation. The motion of these molecules in response to the external stimuli may result in chemical reactions, in addition to altering their arrangement in the crystal. Such structural rearrangements can only be understood by crystal structure comparison before and after the change. However, disintegration of crystal order due to the molecular motion may make structural investigation difficult. Recently, by using the structure determination from powder diffraction data (SDPD) technique, the study of dynamic structural phenomena is possible using X-rays. In this chapter, three such crystal structure rearrangements, which can only be revealed by the SDPD technique, are reviewed. They are the dehydration and hydration mechanism of pharmaceutical crystals, organic vapor-induced dehydration and polymorphic structure change, and photochemical reaction in organic crystal.

**Keywords** Crystal structure • Pharmaceutical crystal • Dehydration • Photochemical reaction • Powder structure analysis

### 15.1 Introduction

An organic crystal can be considered as the solid-state environment where molecules exhibit various behaviors and properties which arise from the constraints of neighboring molecules. Knowledge of the precise crystal structure is therefore essential in rationalizing any changes to the molecule or its crystal. However, if large structural changes occur from external stimuli, single crystals usually lose their long range order and are no longer amenable to single-crystal X-ray structure

---

K. Fujii • H. Uekusa (✉)

Department of Chemistry and Materials Science, Tokyo Institute of Technology, Tokyo, Japan

e-mail: [kfujii@cms.titech.ac.jp](mailto:kfujii@cms.titech.ac.jp); [uekusa@cms.titech.ac.jp](mailto:uekusa@cms.titech.ac.jp)

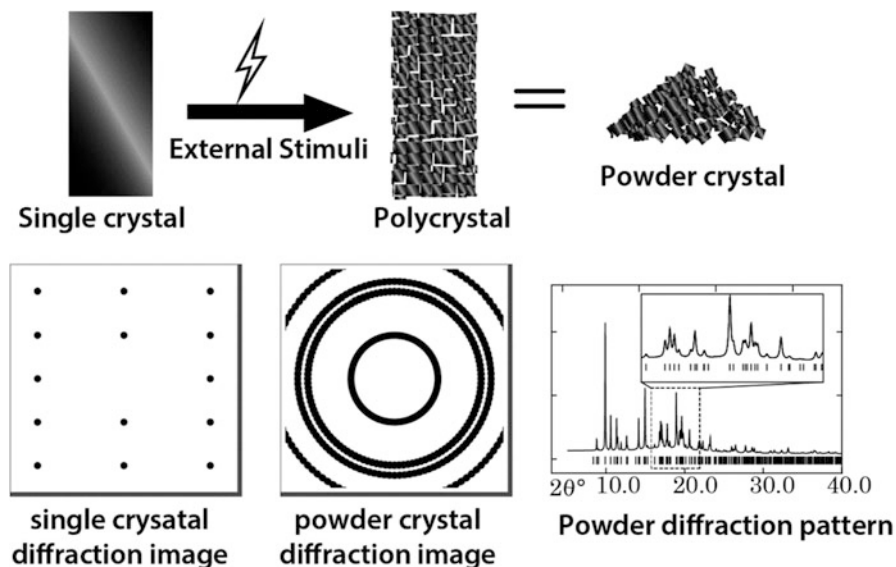


**Fig. 15.1** Schematic illustration of the disintegration of single crystal by the external stimuli (*upper*) and the resulting diffraction change (*lower*)

determination (Fig. 15.1). For this reason, precise mechanistic investigations of the dynamic phenomena in organic crystals were limited to those cases in which the structure of the molecular solid was known before and after the action of the external stimuli. In situations where single crystallinity was lost after the external stimuli, the resulting powder can still be recrystallized into single crystals for structural analysis. However, it is apparent that the crystal structure obtained from the recrystallized crystal could be different from that of the powder.

In the 1990s, the first example of *ab initio* structure determination from powder diffraction data (SDPD) of an organic molecule was demonstrated [1–15]. This breakthrough opened up structural investigations of dynamic phenomena in polycrystalline materials. The SDPD technique is discussed elsewhere in this book, so no further explanation is needed here. In this chapter, several dynamic phenomena in organic crystals are presented.

The first case study is that of stoichiometric and nonstoichiometric dehydration and hydration phenomena of crystals of active pharmaceutical ingredients (APIs) acrinol and erythromycin A. Understanding of the dehydration and hydration of APIs such as erythromycin A is highly valued in the pharmaceutical industry. The impact of the dehydration and hydration on the structure is discussed, as well as the differences in physicochemical properties before and after the structural transition.

In the second case study, the dehydration phenomena caused by organic vapor are explored. Several distinct polymorphic and pseudo-polymorphic phases are obtained and analyzed. Structural changes arising from exposure to vapor are particularly intriguing because they are less reported in the literature.

In the final case study, photochemical reactions in the crystalline state are discussed. Chemical reactions in the crystalline state attract a lot of interest because of their ability to access compounds which are difficult to achieve using conventional synthetic chemistry.

## 15.2 Dehydration/Hydration Transformations of Pharmaceuticals

Organic molecules often exist in several different crystalline forms, such as polymorphs, hydrates, and solvates. These different crystalline forms are important research targets, particularly in the pharmaceutical industry, because they commonly have different physical or chemical solid-state properties, such as solubility, dissolution rate, stability, and bioavailability [16, 17]. Another important aspect of these materials is the solid-state transformations between different forms induced by environmental changes, e.g., temperature, humidity, and pressure. These may occur during the drug manufacturing processes or storage of the drug in bulk or in the dosage form. In many cases, the dehydration/hydration transformations of pharmaceutical solids due to environmental changes are accompanied by disintegration of single crystals, resulting in polycrystalline products. In such cases, SDPD can reveal the mechanism of these dehydration/hydration transformations. There have been several reports that the crystalline dehydration/hydration phenomena in pharmaceutical materials have been revealed by SDPD [18–22]. These examples gave new insights into the mechanistic aspects of the dehydration/hydration behaviors of pharmaceutical materials.

In the case of acrinol (2-ethoxy-6,9-diaminoacridine monolactate; Fig. 15.2a) [19], two different anhydrous forms were found by heating and both structures were revealed by SDPD. Acrinol is a 1:1 co-crystal comprising ethacridinium cations and lactate anions, which is used as an antibacterial agent. The crystal structure of the monohydrate form of acrinol (**AcH**) had been reported, although the thermal behavior of **AcH** and the structural changes associated with dehydration of **AcH** had not been reported previously. Simultaneous PXRD and DSC measurements (XRD-DSC, Fig. 15.2b), recorded on heating a sample of **AcH** from ambient temperature, show that **AcH** transforms to a crystalline anhydrous form at ca. 110–120 °C, which is assigned as anhydrous form **AcAI** from its powder X-ray diffraction (PXRD) pattern. Upon further heating, **AcAI** transforms to anhydrous form **AcAII** at ca. 190–200 °C by a polymorphic transformation (the characteristic PXRD pattern of **AcAII** is indicated in Fig. 15.2b). While handling the anhydrous phases in an ambient atmosphere, a significant difference in the ease of hydration of **AcAI** and **AcAII** was observed, with hydration occurring much more readily for **AcAI** than for **AcAII**. For this reason, the hydration behavior of **AcAI** and **AcAII** was investigated in more detail by dynamic vapor sorption measurements (Fig. 15.2c). It is found that, while hydration of **AcAI** occurs at a relative humidity of ca. 10 %, **AcAII**

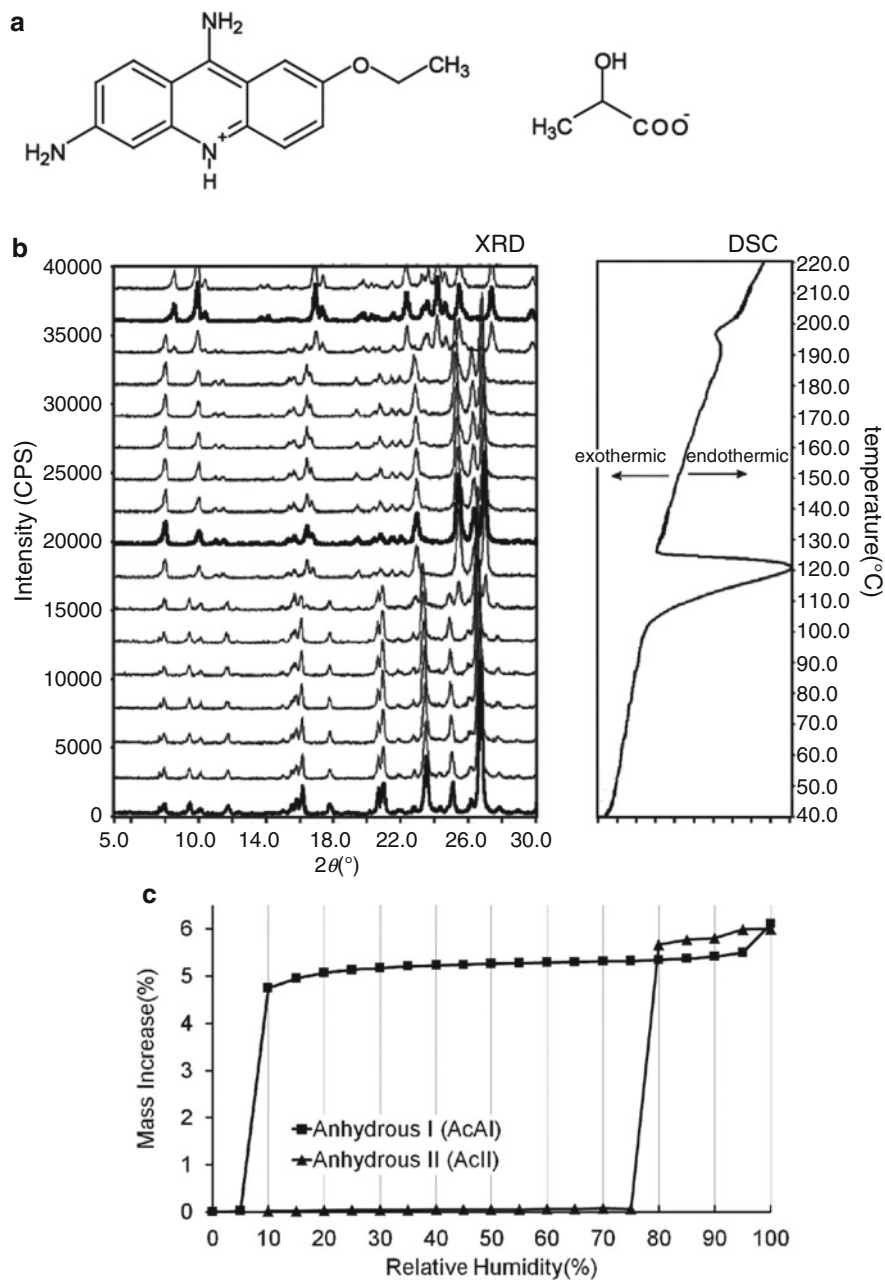


**Fig. 15.2** (a) Molecular structures of the components in acrinol. (b) Simultaneous powder X-ray diffraction and DSC results obtained on heating a powder sample of **AcH** (left side, powder X-ray diffraction; right side, DSC). (c) The result of dynamic vapor sorption measurements for the anhydrous phases (a) **AcAI** and (b) **AcAII**

undergoes hydration only when the relative humidity reaches ca. 80 %. Thus, **AcAII** is substantially more resistant to hydration than **AcAI**.

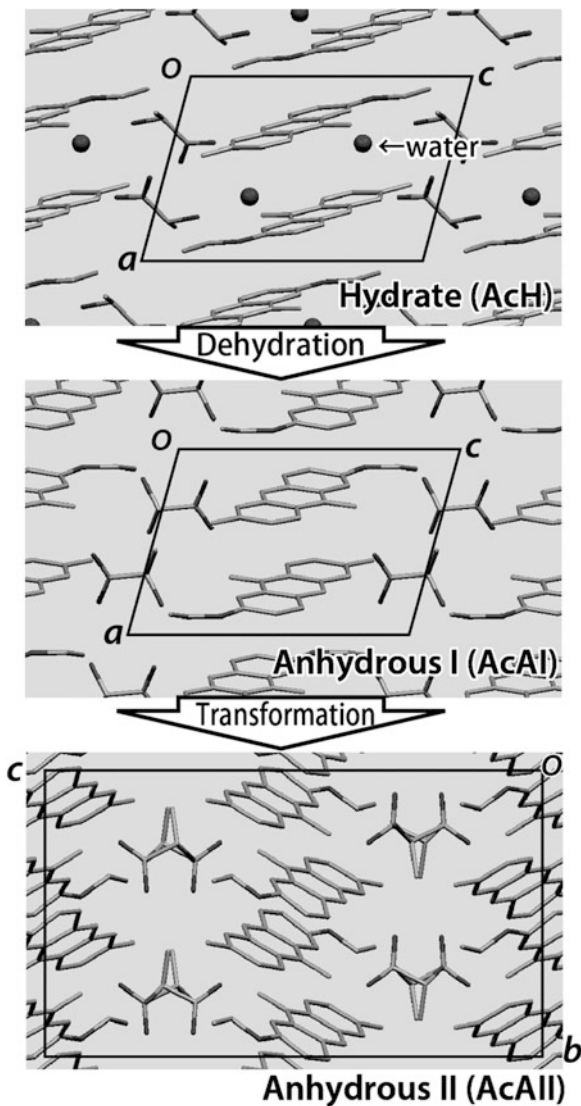
Structure determination of **AcAI** and **AcAII** by single-crystal X-ray diffraction is not viable, because dehydration of a single crystal of **AcH** is associated with loss of crystal integrity to form a polycrystalline sample of **AcAI**. Clearly, **AcAII** formed in the subsequent polymorphic transformation from **AcAI** is also polycrystalline. For these reasons, the crystal structures of **AcAI** and **AcAII** were determined directly from PXRD data. Structural analysis was carried out based on the synchrotron PXRD data for **AcAI** and the laboratory PXRD data (CuK $\alpha$ 1 radiation) for **AcAII**. The data were analyzed in the following process: (1) indexing (DICVOL04), (2) whole profile fitting by Le Bail method (GSAS), (3) structure solution by the direct-space genetic algorithm (EAGER), and (4) structure refinement by Rietveld method (GSAS). The final results of the Rietveld analysis showed good agreement between the observed and calculated PXRD patterns.

The crystal structures of **AcH**, **AcAI**, and **AcAII** are shown in Fig. 15.3. The crystal structure of **AcH** comprises stacking of ethacridinium cations and lactate anions along the *a*-axis. The water molecules are arranged along the *a*-axis forming a water channel. The crystal structure of **AcAI** retains several of the structural features present in the parent hydrate phase **AcH** and contains similar stacks of ethacridinium cations and lactate anions. Although the ethacridinium cations retain their molecular conformation during the transformation from **AcH** to **AcAI**, they undergo slight displacements into the vacant space created by removal of the water molecules from **AcH**. In addition, the positions and orientations of the lactate anions undergo some adjustment, resulting in a modified hydrogen-bonding network. From such structural comparison, the dehydration process of **AcH** or hydration process of **AcAI** accompanies small structural rearrangement. Thus, the hydration of **AcAI** (observed in DVS plot) easily occurred even at the low humidity condition.

On the other hand, the crystal structure of **AcAII** is completely different from that of **AcAI** (or **AcH**). Given the significant differences between the crystal structures of **AcAI** and **AcAII**, substantial molecular movements are implicated in the polymorphic transformation between **AI** and **AII**, involving essentially complete reconstruction of the crystal structure and significant changes in the hydrogen-bonding arrangement. The fact that **AcAII** does not readily rehydrate to produce **AcH** can be understood on the basis of the substantial differences in structure between **AcAII** and **AcH**, and thus hydration of **AcAII** to produce **AcH** requires significant structural reorganization. The stability with respect to hydration is a desirable property for pharmaceutical applications, as facile hydration of a drug substance can represent a significant problem in processing or storage. Thus, our observation that anhydrous polymorph **AII** of acrinol is relatively resistant to hydration may be an important consideration in future applications.

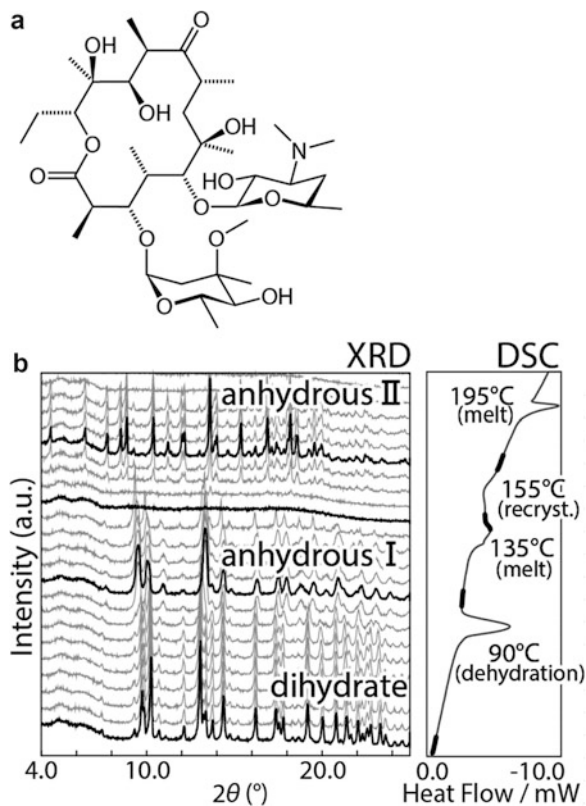
The dehydration/hydration behavior of erythromycin A was also revealed by SDPD and was found to show interesting dehydration/hydration behaviors [22]. Erythromycin A (Fig. 15.4a) is a widely used macrolide antibiotic and is known to form a dihydrate in the crystalline phase (**EDH**) when recrystallized from aqueous solution. Crystals of **EDH** undergo dehydration upon heating to give an anhydrous phase (anhydrous phase I, **EAI**), which transforms into another anhydrous phase

**Fig. 15.3** Crystal structures of **AcH**, **AcAI**, and **AcAII**. **AcH** transforms to **AcAI** followed by the transformation to **AcAII** by heating



(anhydrous phase II, **EAI**) after a melt process on further heating. This process was clearly observed by XRD-DSC measurement (Fig. 15.4b). The change in the PXRD during the dehydration process of **EDH** is small, and **EAI** was already known to be a dehydrated hydrate, which is also referred to as an isomorphic desolvate [23]. These terms “dehydrated hydrate” and “isomorphic desolvate” mean that the dehydrated (or desolvated) crystalline phase retains the molecular packing of the parent hydrate (or solvate) after dehydration (or desolvation).

**Fig. 15.4** (a) The molecular structure of erythromycin A. (b) Simultaneous XRD-DSC results obtained on heating a powder sample of **EDH** (left side, powder X-ray diffraction; right side, DSC)



The hydration and dehydration of **EAI** and **EAI** showed interesting behaviors that were observed by dynamic vapor sorption (DVS) measurements. As shown in Fig. 15.5a, **EAI** underwent hydration at a relative humidity (RH) of 5% with a mass increase corresponding to two water molecules, and no significant mass change was observed with further humidification. The hydrated phase was confirmed as **EDH** by powder XRD (PXRD). The dehydration of **EDH** only occurred at RH < 5% (the desorption process in Fig. 15.5a), suggesting **EDH** is stable through this process. Because the number of incorporated water molecules is stoichiometric for both **EDH** (two) and **EAI** (zero), the dehydration and hydration processes between **EDH** and **EAI** are stoichiometric dehydration and hydration processes. On the other hand, **EAI** showed nonstoichiometric hydration and dehydration (Fig. 15.5b). In both processes, the mass gradually changed depending on the humidity, and thus the number of incorporated water molecules was not stoichiometric. Here, we call this hydrated phase of **EAI** a nonstoichiometric hydrate phase (**ENSH**). The maximum number of incorporated water molecules in the **ENSH** was estimated to be about 1.3 water molecules per erythromycin A molecule from the dynamic vapor DVS plot. Even though the **ENSH** incorporates some water, the PXRD patterns of **EAI** and **ENSH** are similar (Fig. 15.5c), which clearly indicates that the crystal

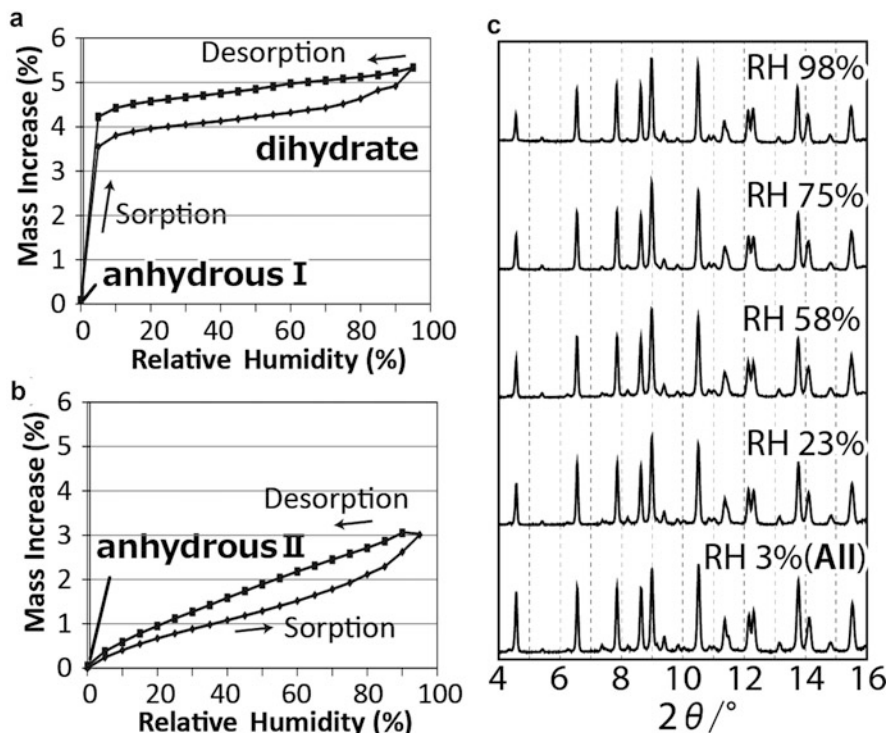


**Fig. 15.5** DVS plots of the erythromycin A anhydrous phases (a) I (EAI) and (b) II (EAI) and (c) the changes in the XRD pattern of erythromycin A anhydrous phase II (EAI) in response to humidity

structure of **EAI** is also a dehydrated hydrate of **ENSH** (or the **ENSH** is an isomorphous hydrate of **EAI**). This is interesting as one polymorph shows stoichiometric hydration/dehydration behavior and the other shows nonstoichiometric hydration/dehydration behavior. Because these two polymorphs consist of the same molecule, the different hydration/dehydration behavior must be due to differences in the crystal structures. Therefore, the crystal structures of these two anhydrous phases should provide important information about the mechanism of the stoichiometric or nonstoichiometric hydration/dehydration processes.

Because the dehydration process is accompanied by the disintegration of the single crystalline form of **EDH**, the samples of **EAI** and **EAI** were only obtainable as powders. For this reason, the crystal structures of **EAI** and **EAI** were determined directly from the PXRD data measured using synchrotron radiation. The erythromycin A molecule contains a 14-membered lactone ring that can adopt several different conformations. However, the conformations of the 14-membered lactone rings are the same in all the different crystal structures, such as the **DH** [23], the zinc complex solvate of erythromycin A [24], erythromycin B [23], and clarithromycin [23, 25, 26]. Thus, the conformation of the 14-membered lactone

ring was fixed during the structure solution calculations. It is worth to note that **EAI** has two independent molecules in the unit cell and the total structural variables, which should be determined in the structure solution process, was 26. Even such large number of parameters, the structure determination was succeeded.

The crystal structures of **EDH** [23], **EAI**, and **EAI** are shown in Fig. 15.6. In the crystal structure of **EDH** (top of Fig. 15.6), two independent water molecules are arranged along the *a*-axis forming a water channel. These water molecules bridge erythromycin A molecules by hydrogen bonds. The crystal structure of **EAI** (middle of Fig. 15.6) has a similar molecular packing to **EDH**, and thus these two crystalline phases are isostructural. By loss of the water molecules, the water-mediated hydrogen bonds in **EDH** switch to inter- and intramolecular hydrogen bonds between erythromycin A molecules. The crystal structure of **EAI** also contains significant voids, as shown by the translucent spheres in Fig. 15.6. There are two independent voids in **EAI** with volumes of about 10 and 15 Å<sup>3</sup>. The positions of the voids in **EAI** and the positions of the water molecules in **EDH** are almost the same, and therefore, the voids are created by the loss of the water molecules. The sum of the volumes of the two voids observed in **EAI** (25 Å<sup>3</sup>) is less than the volume the two water molecules occupy in **EDH** (54 Å<sup>3</sup>). Therefore, the voids created by the removal of water do not remain, and structural relaxation occurs to reduce the void volume. Given that incorporation of water molecules into the voids will give the stable crystalline state **EDH** without large structural reconstruction, it is natural that the crystals of **EAI** readily transform back to **EDH**. Both the water molecules in **EDH** and the voids in **EAI** form channels along the *a*-axis. Therefore, the loss and incorporation of water molecules in the dehydration and hydration processes could proceed through this channel with only small structural changes.

The crystal structure of **EAI** (bottom of Fig. 15.6) has a completely different molecular packing from **EDH** and **EAI**. The erythromycin A molecules aggregate to form a tetramer via intermolecular hydrogen bonds and the tetramer units are arranged in a herringbone pattern. There are no hydrogen bonds (*D*⋯*A* distances of less than 3.2 Å) between the tetramer units, and all but one of the hydroxyl groups point toward the center of the tetramer unit; the remaining hydroxyl group forms an intramolecular hydrogen bond. Interestingly, as observed in **EAI**, the crystal structure of **EAI** also has voids around the tetramer units, shown as translucent spheres in Fig. 15.6. There are four independent void spaces, which have volumes of 48, 24, 22, and 17 Å<sup>3</sup>. Because there are no hydrophilic groups around these void spaces, they can be considered hydrophobic voids, whereas the voids observed in **EAI** are hydrophilic. The hydrophobic nature of the voids may be the reason for the nonstoichiometric hydration behavior of **EAI**. The voids incorporate water molecules, but no energetic stabilization by hydrogen bonds is possible because the water molecule cannot form hydrogen bonds. However, the volumes of the voids are large enough to incorporate water molecules, and it enables nonstoichiometric incorporation of water molecules without major structural changes. Structural analysis of **ENSH** at RH = 98 % was also carried out, although the positions of the water molecules could not be determined. Considering that the PXRD patterns

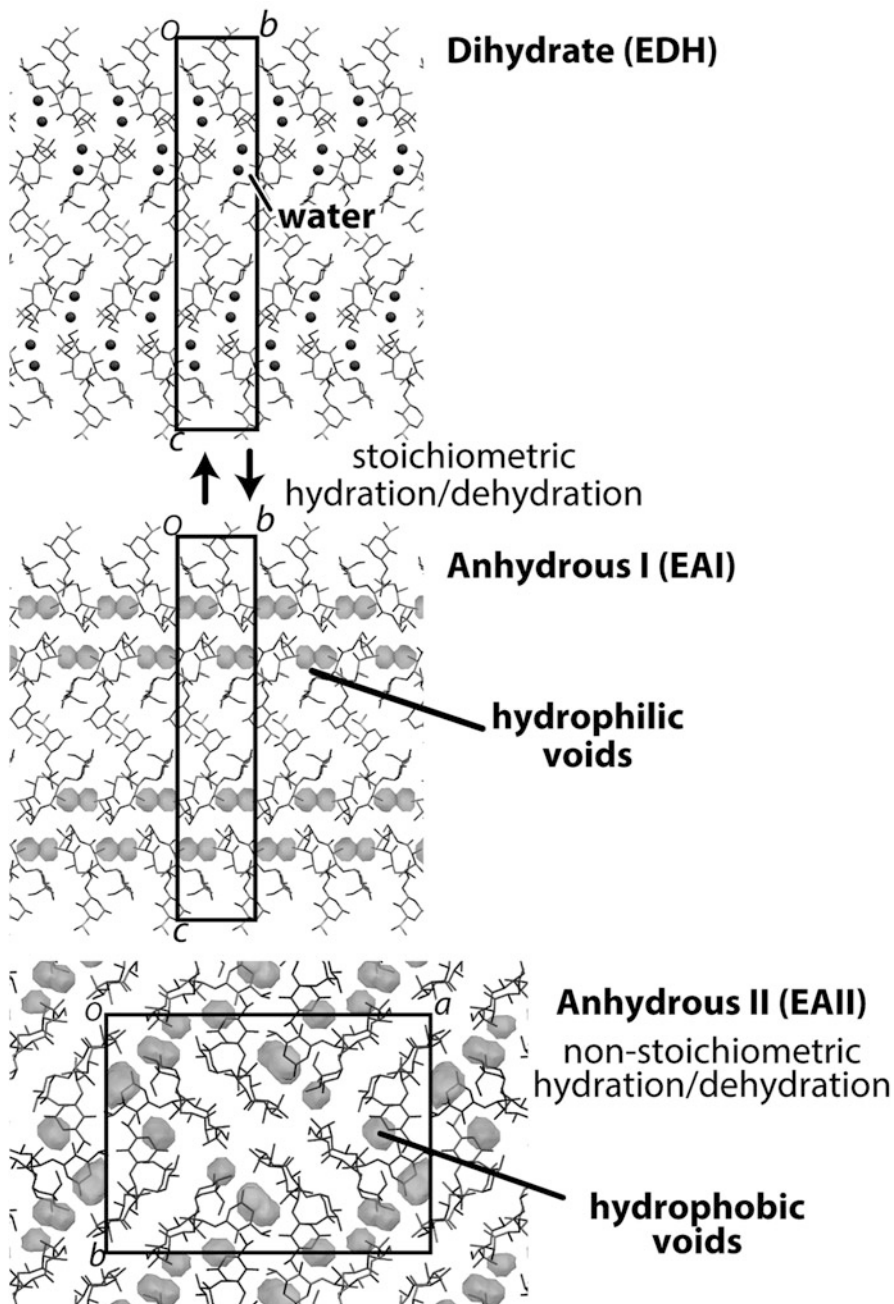


**Fig. 15.6** Crystal structure of erythromycin A dihydrate phase (EDH, *top*), anhydrous phase I (EAI, *middle*), and anhydrous phase II (EAIi, *bottom*)

measured at low and high humidity are quite similar, the water molecules are most likely highly disordered in the voids in the crystal structure of **ENSH**, and the incorporation of the water molecules would not greatly contribute to the diffraction intensities.

The dehydration/hydration behaviors of organic crystals including pharmaceutical materials are still not clear. However, as shown in this example, the crystal structures of the hydrated or dehydrated phases can aid in understanding the dehydration/hydration process. Further systematic understanding will proceed by further research using SDPD.

### 15.3 Vapor-Induced Crystalline Transformations

Solvent molecules are often incorporated in crystal structures to form solvate crystals that are also known as pseudopolymorphs [27–29], which include non-solvated crystalline phases. (There have been some arguments about the usage of the term *pseudopolymorph*, and its usage is not universal. However, here the term *pseudopolymorph* is straightforward and is used to represent both the solvated and non-solvated crystals.) Pseudopolymorphism is of interest in many aspects of solid-state chemistry, because significantly different crystalline phases can have different solid-state properties even when they consist of almost the same components [16, 27–32]. Recrystallization using different solvents and/or in different conditions is frequently used and is the most useful strategy for exploring the pseudopolymorphs of an organic compound. Alternatively, solvent vapor exposure of target crystalline materials also leads to pseudopolymorphs and is a simpler approach compared with the recrystallization.

A co-crystal that consists of a 1:1 mixture of 5-methyl-2-pyridone and trimesic acid (Fig. 15.7a) shows interesting crystalline transformations on exposure to vapors [33, 34]. This co-crystal was studied as part of an investigation on the photoreactivity of 2-pyridone derivatives in co-crystals. Three pseudopolymorphs were found in this system, which were a methanol solvate (**M**), a hydrate (**H**), and an unsolvated phase (**U**). First, **M** was found to transform into **H** by grinding in an ambient atmosphere, which indicates the presence of water vapor would lead to the solvent exchange (methanol to water) transformation. Thus, transformations among these phases were investigated by exposing to several different solvent vapors. The results are shown in Fig. 15.7b. Solvation transformations from **U** to **M** or **H** were observed by exposing **U** to methanol or water vapor, and solvent exchange transformations between **M** and **H** were observed by exposing **H** to methanol vapor or **M** to water vapor. Furthermore, exposure of **M** and **H** to acetonitrile, acetone, or ethanol vapor gave rise to desolvation transformations to produce **U**. The crystals of **M**, **H**, and **U** are insoluble in acetonitrile, acetone, and ethanol, so it is unlikely that partial dissolution of these materials can explain this observation. The desolvation process did not occur on exposure to hexane vapor, drying, or exposure to vacuum. Therefore, it is deduced that the crystalline solvate molecule would leave from

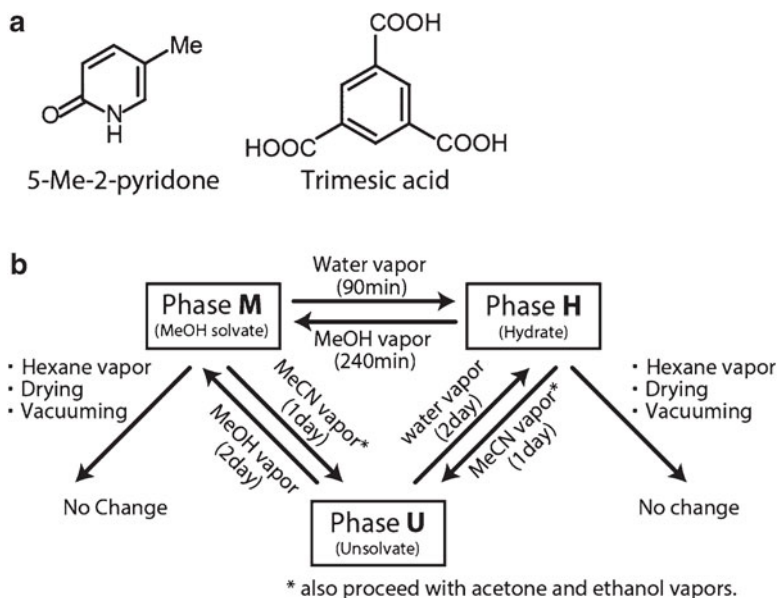


**Fig. 15.7** (a) Molecular structures of 5-methyl-2-pyridone and trimesic acid. (b) Summary of the results of experiments involving exposure of the materials to solvent vapor, drying, and exposure to vacuum

the crystal lattice only when the molecule has an affinity with the organic vapor molecule which is applied to the crystal. This deduction may explain why the crystalline solvate molecule of methanol (**M**) and water (**H**) desolvates by MeCN, acetone, and ethanol vapor, but does not by hexane vapor.

Another interesting aspect of these experiments is the time required for the transformations to occur on exposure to solvent vapors. The solvent exchange transformation from **M** to **H** is complete in a few hours. However, the transformations of **U** to form the solvate structures **M** or **H** on exposure to methanol and water vapors required about 2 days. To understand the structural changes in these pseudopolymorph transformations by vapors, the crystal structures of **M**, **H**, and **U** were determined. The crystal structures of **H** and **U** had to be determined from PXRD data because these phases could only be obtained via transformations that caused the disintegration of the single crystalline forms.

The crystal structures of **M**, **H**, and **U** are shown in Fig. 15.8. Although the space groups of **M** ( $P2_1/n$ ) and **H** ( $P\bar{1}$ ) are different, there are structural similarities between these two crystal structures. As shown in Fig. 15.8, both **M** and **H** have similar hydrogen-bonding units that consist of two 5-methyl-2-pyridone, two trimesic acid, and two solvents (methanol for **M** and water for **H**). These units are stacked along the same directions, giving solvent channels in both crystal structures. From the structural similarities between **M** and **H**, it is expected that solvent exchange might occur through the solvent channel, with preservation of the

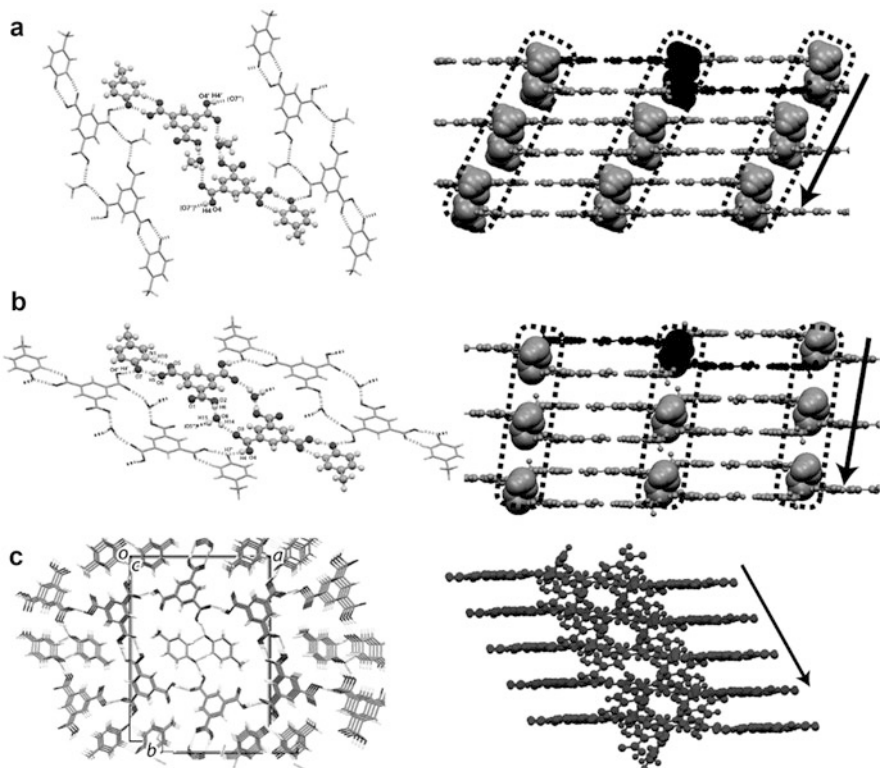


**Fig. 15.8** The crystal structures of the co-crystal (5-methyl-2-pyridone and trimesic acid) (a) methanol solvate (**M**), (b) hydrate (**H**), and (c) unsolvated phase (**U**)

hydrogen-bonding unit, thus promoting the facile transformations between **M** and **H**. On the other hand, the crystal structure of **U** ( $P2_1/a$ ) has a completely different hydrogen-bonding network. Thus, the solvation or desolvation transformations require large structural changes, requiring longer times when compared with the solvent exchange transformations.

Although the crystal structures of **M** and **H** are significantly different from **U**, the exposure of **M** or **H** to acetonitrile, acetone, or ethanol vapor easily causes the desolvation transformations which completed within one day at ambient temperature. Further investigations have been carried out, and similar vapor-induced desolvation (dehydration) was found for the hemihydrate of 5-aminoisophthalic acid [35]. In this case, exposing the hemihydrate of 5-aminoisophthalic acid to acetonitrile, methanol, or ethanol vapor led to dehydration and gave the anhydrous phase of 5-aminoisophthalic acid. Interestingly, this process is accompanied by a color change from pale pink in the hemihydrate to yellow in the anhydrous crystal. The anhydrous phase returns to the hemihydrate on exposure to water vapor, giving a reversible color change caused by solvent vapors. As shown in this example, solvent vapor-induced transformations can lead to interesting and useful behaviors.

## 15.4 Solid-State Photoreaction in Organic Crystal

Solid-state photoreactions have attracted considerable attention because of their potential to achieve high reaction selectivity, stereoselectivity, and high yield [36–39]. These advantages come from the restriction of molecular motion in the reacting crystals, and the photoreaction properties can be explained by the topochemical postulate and the concept of reaction cavities [40–42]. In special cases, the solid-state photoreaction proceeds in a single-crystal-to-single-crystal (SCSC) manner, and these photoreaction processes can be followed using single-crystal X-ray analysis. However, in many cases, solid-state photoreactions induce the destruction of the crystalline form of the parent crystal. This severely limits the use of X-ray analysis to trace the structural changes during a photoreaction. Thus, subsequent recrystallizations of the polycrystalline photoproduct phase are usually carried out to obtain single crystals of the photoproduct. However, these recrystallizations do not always give the same crystalline phase as obtained directly from the solid-state photoreaction.

In the case of the crystalline state photoreaction of 2-(2,4,6-triisopropylbenzoyl)((*S*)-1-phenylethyl)benzamide (**1**), it undergoes a diastereospecific Norrish type II photocyclization under UV irradiation, producing (*R,S*)-cyclobutenol (**2**) (Fig. 15.9a) [43]. The initial crystalline phase of **1** transforms into the crystalline product phase **2A** upon UV irradiation with disintegration of the initial single crystalline form. Subsequent recrystallizations always gave a different crystalline product phase **2B**, but never the original **2A**. Furthermore, the photoreaction could not proceed in the SCSC manner even using absorption edge irradiation. Therefore, the mechanistic aspects of the photoreaction should be discussed indirectly using the crystal structures of **1** (initial crystal) and **2B** (product crystal obtained by subsequent recrystallization), which has a significantly different PXRD pattern from both **2A** and the parent phase **1**. This may mean there is still a lack of understanding in the structural changes during the photoreaction process. Therefore, the crystal structure of the metastable polymorphic form **2A** was determined from the PXRD data.

A powder sample of **2A** was prepared by photo-irradiation of a powder sample of **1**. The reaction was monitored by PXRD, and the UV irradiation was continued until no further changes were observed in the diffraction pattern. The crystal structure was then analyzed based on the synchrotron PXRD via the simulated annealing method to give the structure solution followed by Rietveld structural refinement.

The crystal structures of **1** (before photoreaction), **2A** (after photoreaction), and **2B** (after recrystallization of **2** from the solution) are shown in Fig. 15.9b, c, and d. Comparing the crystal structure of **1** and **2A**, the crystal packing has been retained during the photoreaction process. Considering from the molecular formula, (*S,S*)-cyclobutenol may also be the photoreaction product. However, detailed structural consideration, such as molecular conformation and reaction cavity, clearly indicates that (*R,S*)-cyclobutenol is much more favored than (*S,S*)-cyclobutenol when the photoreaction proceeds in the crystal structure of **1**.

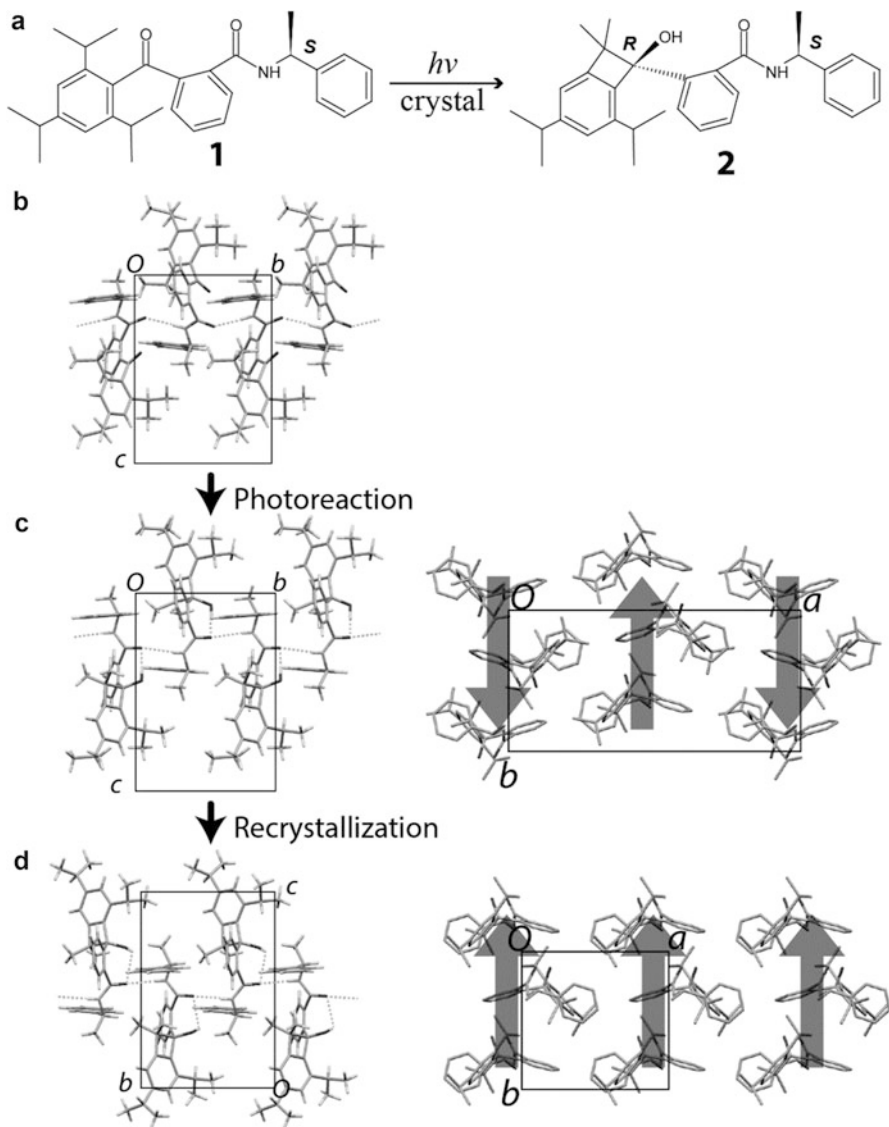


**Fig. 15.9** (a) Reaction scheme of the solid-state photoreaction of 2-(2,4,6-triisopropylbenzoyl)((*S*)-1-phenylethyl)benzamide (**1**). Crystal structures of (b) **1** (before photoreaction), (c) after photoreaction (**2A**), and (d) after the recrystallization of **2** (**2B**)

The space group of **2B** ( $P2_1$ ) is different from that of **2A** ( $P2_12_12_1$ ) and has half-size unit cell volume of **2A**. However, interestingly, the hydrogen bonds observed in **2A** and **2B** are almost the same. Both structures have one intramolecular  $\text{O}-\text{H}\cdots\text{O}$  hydrogen bond and one intermolecular  $\text{N}-\text{H}\cdots\text{O}$  hydrogen bond. The

intermolecular hydrogen bond forms a one-dimensional chain. The most important difference between the crystal structures of **2A** and **2B** is in the arrangement of this chain. Although adjacent chains are arranged in opposite directions in **2A** (Fig. 15.9d), they run in the same direction in **2B**. This causes a difference in the crystal densities. The densities are calculated to be  $1.12 \text{ g cm}^{-3}$  (at 300 K) for **2A** and  $1.13 \text{ g cm}^{-3}$  (at 296 K) for **2B**. The difference is small but **2B** has a more dense crystal packing arrangement than **2A**. According to the density rule introduced by Burger and Ramberger [44, 45], the less stable polymorph will tend to have a lower density, and therefore the **2A** phase is expected to be less stable than **2B**, as is observed.

As the density difference was too small to reach a conclusion, lattice energy calculations were carried out for these two crystals to evaluate the energetic relationship between **2A** and **2B**. The lattice energy calculations were carried out for the crystal structures of **2A** and **2B** using the Forcite module in Material Studio 4.0 software from Accelrys [46]. For all force fields used in the calculations (COMPASS [47], Dreiding [48], and Universal [49]), **2B** has a lower lattice energy than **2A** by 6.6–10.2 kcal mol<sup>-1</sup>, which indicates that **2B** is more stable than **2A**. The energy differences in the molecular conformation (intramolecular energy) between **2A** and **2B** are less than 2.0 kcal mol<sup>-1</sup>, so the intermolecular energy differences (6.3–10.7 kcal mol<sup>-1</sup>) have a much larger contribution to the total lattice energy difference. Thus, the stability of **2B** mostly comes from the intermolecular interactions such as van der Waals and electrostatic interactions. Hydrogen bonds are also included in the intermolecular interactions; however, the hydrogen bonds are similar in these two phases, as described above. Thus, the energetic difference is not due to the hydrogen bonds but to the other intermolecular interactions, i.e., omnidirectional interactions. For a complete picture of the crystallization processes, entropies (the Gibbs free energy) and/or the kinetic factors must be considered as well as the lattice energy. However, the lattice energy difference is one of the reasons why **2B** is always crystallized from solution instead of **2A**. This type of energetic evaluation is only possible when the crystal structure is known. In this case, the SDPD of the crystal structure of **2A** was necessary to achieve the discussion.

## 15.5 Summary

As shown in this chapter, structure determination from powder diffraction data (SDPD) enables us to understand many interesting dynamic phenomena that occur in organic crystals, such as dehydration/hydration transformations, solvent vapor-induced transformations, and solid-state photoreaction process. Because these investigations were based on the crystal structures and changes in those crystal structures, our understanding of the phenomena is enhanced at the atomic or molecular level. For more details and systematic understanding of the behavior of organic crystals, the SDPD will continue to help the chemical crystallographer.

## References

1. K.D.M. Harris, M. Tremayne, *Chem. Mater.* **8**, 2554 (1996)
2. K.D.M. Harris, M. Tremayne, B.M. Kariuki, *Angew. Chem. Int. Ed.* **40**, 1626 (2001)
3. V.V. Chernyshev, *Russian Chem. Bull.* **50**, 2273 (2001)
4. W.I.F. David, K. Shankland, L.B. McCusker, C. Baerlocher (eds.), *Structure Determination from Powder Diffraction Data* (OUP/IUCr, Oxford/New York, 2002)
5. A. Huq, P.W. Stephens, *J. Pharm. Sci.* **92**, 244 (2003)
6. K.D.M. Harris, E.Y. Cheung, *Chem. Soc. Rev.* **33**, 526 (2004)
7. M. Tremayne, *Philos. Trans. R. Soc.* **362**, 2691 (2004)
8. V. Favre-Nicolin, R. Cerny, *Z. Kristallogr.* **219**, 847 (2004)
9. K. Shankland, A.J. Markvardsen, W.I.F. David, *Z. Kristallogr.* **219**, 857 (2004)
10. V. Brodski, R. Peschar, H. Schenk, *J. Appl. Crystallogr.* **38**, 688 (2005)
11. S. Karki, L. Fabian, T. Friscic, W. Jones, *Org. Lett.* **9**, 3133 (2007)
12. H. Tsue, M. Horiguchi, R. Tamura, K. Fujii, H. Uekusa, *J. Synth. Org. Chem. Jpn.* **65**, 1203 (2007)
13. W.I.F. David, K. Shankland, *Acta Crystallogr. Sect: A* **64**, 52 (2008)
14. K.D.M. Harris, M. Tremayne, P. Lightfoot, P.G. Bruce, *J. Am. Chem. Soc.* **116**, 3543 (1994)
15. F.H. Allen, *Acta Crystallogr. Sect: B* **58**, 380 (2002)
16. J.K. Haleblan, *J. Pharm. Sci.* **64**, 1269 (1975)
17. S. Data, D.J.W. Grant, *Nat. Rev.* **3**, 42 (2004)
18. K. Sugimoto, R.E. Dinnebier, M. Zakrzewski, *J. Pharm. Sci.* **96**, 3316 (2007)
19. K. Fujii, H. Uekusa, N. Itoda, G. Hasegawa, E. Yonemochi, K. Terada, Z. Pan, K.D.M. Harris, *J. Phys. Chem. C* **114**, 580 (2010)
20. I. Halasz, R.E. Dinnebier, *J. Pharm. Sci.* **99**, 871 (2010)
21. K. Fujii, H. Uekusa, N. Itoda, E. Yonemochi, K. Terada, *Cryst. Growth Des.* **12**, 6165 (2012)
22. K. Fujii, M. Aoki, H. Uekusa, *Cryst. Growth Des.* **13**, 2060 (2013)
23. G.A. Stephenson, E.G. Groleau, R.L. Kleemann, W. Xu, D.R. Rigsbee, *J. Pharm. Sci.* **87**, 536 (1998)
24. J.D. Oliver, L.C. Strickland, *Acta Crystallogr. Sect: C* **42**, 952 (1986)
25. J. Tian, P.K. Thallapally, S.J. Dalgarno, J.L. Atwood, *J. Am. Chem. Soc.* **131**, 13216 (2009)
26. J. Tian, S.J. Dalgarno, J.L. Atwood, *J. Am. Chem. Soc.* **133**, 1399 (2011)
27. W.C. McCrone, in *Physics and Chemistry of the Organic Solid State*, ed. by D. Fox, M.M. Labes, A. Weissberger, vol. 2 (Wiley-Interscience, New York, 1965)
28. S.R. Byrn, *Solid State Chemistry of Drugs* (Academic, New York, 1982)
29. J. Bernstein, *Polymorphism in Molecular Crystals* (Oxford University Press, Oxford, 2002)
30. S. Byrn, R. Pfeiffer, M. Ganey, C. Hoiberg, G. Poochikian, *Pharm. Res.* **12**, 945 (1995)
31. S.R. Vippagunta, H.G. Brittain, D.J.W. Grant, *Adv. Drug Deliv. Rev.* **48**, 3 (2001)
32. K.R. Morris, U.J. Griesser, C.J. Eckhardt, J.G. Stowell, *Adv. Drug Deliv. Rev.* **48**, 91 (2001)
33. S. Hirano, S. Toyota, F. Toda, K. Fujii, H. Uekusa, *Angew. Chem. Int. Ed.* **45**, 6013 (2006)
34. K. Fujii, Y. Ashida, H. Uekusa, S. Hirano, S. Toyota, F. Toda, Z. Pan, K.D.M. Harris, *Cryst. Growth Des.* **9**, 1201 (2009)
35. K. Fujii, A. Sakon, A. Sekine, H. Uekusa, *Cryst. Growth Des.* **11**, 4305 (2011)
36. V. Ramamurthy, K. Venkatesan, *Chem. Rev.* **87**, 433 (1987)
37. F. Toda, *Acc. Chem. Res.* **28**, 480 (1995)
38. K. Tanaka, F. Toda, *Chem. Rev.* **100**, 1025 (2000)
39. G. Kaupp, *Curr. Opin. Solid State Mater. Sci.* **6**, 131 (2002)
40. M.D. Cohen, G.M.J. Schmidt, *J. Chem. Soc.* **383**, 1996 (1964)
41. G.M.J. Schmidt, *Pure Appl. Chem.* **27**, 647 (1971)
42. M.D. Cohen, *Angew. Chem. Int. Ed.* **14**, 386 (1975)
43. H. Koshima, M. Fukano, H. Uekusa, *J. Org. Chem.* **72**, 6786 (2007)
44. A. Burger, R. Ramberger, *Mikrochimica Acta* **2**, 259 (1979)
45. A. Burger, R. Ramberger, *Mikrochimica Acta* **2**, 273 (1979)

46. Material Studio, Packages: Discover and Forcite, Version 4.0. (Accelrys, Inc, San Diego)
47. H. Sun, *J. Phys. Chem. B* **102**, 7338 (1998)
48. S.L. Mayo, B.D. Olafson, W.A. Goddard III, *J. Phys. Chem.* **94**, 8897 (1990)
49. A.K. Rappe, C.J. Casewit, K.S. Colwell, W.A. Goddard III, W.M. Skiff, *J. Am. Chem. Soc.* **114**, 10024 (1992)

# Chapter 16

## Characteristics of Crystal Transitions Among Pseudopolymorphs

Yoko Sugawara

**Abstract** Reversible phase transitions among the pseudopolymorphs of nucleoside and nucleotide hydrates were induced by humidity (vapor pressure of water) and temperature conditions. A single crystal state at a high frequency was retained after these transitions, and the original, the final, and in some cases the intermediate crystal structures were determined. On the basis of the determined structures and information from complementary methods (e.g., Raman spectroscopy and molecular dynamics simulation), the characteristics of the transitions (i.e., conformational changes, sliding of molecular layers, and cyclic and bifurcated transitions) were revealed. The transition schemes and mechanisms are discussed.

**Keywords** Pseudopolymorphs • Hydrates • Nucleotides • Nucleosides • Humidity-induced phase transition • Single crystal transition scheme and mechanism

### 16.1 Introduction

Polymorphs are a group of crystals made of the same components with different crystal structures. Polymorphs include inorganic, organic, and biomolecular crystals [1–3]. In the case of organic crystals, several classifications have been proposed, e.g., conformational polymorphs [4, 5] and synthon polymorphism [6]. Polymorphs are not defined by a difference in crystal morphology. There are many crystals with different morphologies but the same crystal structure, because the crystallization conditions often affect the morphology. Polymorphism has attracted much attention in the pharmaceutical and optical nonlinear material fields, because the physical properties of polymorphs are generally different. In the case of drugs, a difference in solubility might affect bioavailability.

---

Y. Sugawara (✉)

School of Science, Kitasato University, Sagamihara, Kanagawa 252-0373, Japan

e-mail: [sugawara@sci.kitasato-u.ac.jp](mailto:sugawara@sci.kitasato-u.ac.jp)

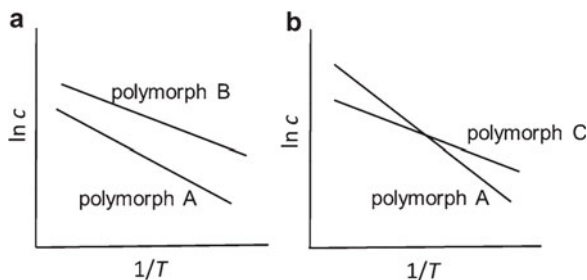
© Springer Japan 2015

R. Tamura, M. Miyata (eds.), *Advances in Organic Crystal Chemistry*,

DOI 10.1007/978-4-431-55555-1\_16

317

**Fig. 16.1** Plots of natural logarithms of concentration vs.  $T$  inverse of two types of polymorphs



The term pseudopolymorph is usually used for a group of crystals made of the same substance with different amounts or types of solvate molecules [7]. One of representative examples is the hydrates of copper sulfate. As in the cases of polymorphs, the physical properties, e.g., stability and dissolution rate of pseudopolymorphs, are generally different. Solvent contents of pseudopolymorphs have a tendency to change depending on mechanical processing and physical conditions of temperature and vapor pressure. Therefore, pseudopolymorph is an important subject, in particular, from the pharmaceutical point of view.

The origin of polymorphs is understood on the basis of thermodynamics. The situation is nearly the same for pseudopolymorphs. If some physical condition is defined, there is only one stable form, and other forms are metastable.

Polymorphs are classified into two types: those with monotropism and enantiotropism [3]. In the case of monotropic polymorphs, one crystal form is stable below the melting point of a compound. On the other hand, if the stability switches between two forms depending on the temperature, the term enantiotropic polymorph is used. In the case of crystallization from solutions, we can also distinguish two types, where the solubility of one form is lower than those of other forms at any temperature, and the solubility curves of two forms cross each other at some temperature (Fig. 16.1). In the former case, only one form appears in the cooling process of a solution (polymorph A in Fig. 16.1a). In the latter case, one form (polymorph C in Fig. 16.1b) reaches a saturation condition first, and crystals appear. If the temperature continues to decrease, the other form (polymorph A in Fig. 16.1b) appears, and the crystals of the second form take the place of the form that first appeared. If the solubilities of the two forms are similar, and the change rate between the first and second forms is slow compared with the cooling rate, both forms appear in the same solution [3]. We occasionally find such a phenomenon. In situ observation of crystal transformations offers noteworthy information on the transitions of polymorphs. A stable form often appears on the surface of an unstable form and sometimes at an inner site of a crystal [8].

The situation is similar in the case of pseudopolymorphs. If a hydrate with low water content is obtained in the high-temperature region and one with high water content is obtained in the low-temperature region, we can obtain both crystals separately and determine their crystal structures using crystallographic analysis. On the other hand, there are many pseudopolymorphs that are obtained by the exchange of solvates or the desorption/absorption processes for solvates depending on the

temperature and/or vapor pressure conditions of the solvate around the crystals after harvesting from the mother liquid. In such cases, the crystallinity is often lowered during the transition, and crystal structure analysis becomes difficult. Examinations using thermal analysis, infrared and Raman spectroscopies, and powder X-ray analysis are usually carried out. Of course, these analyses offer valuable information on the pseudopolymorphs (see Sect. 16.5). However, without knowledge of the crystal structures, a discussion on transition schemes would remain at the qualitative level. In recent years, the *ab initio* structure determination method based on powder diffraction data has successfully been developed, and further information has become available [9].

In the case of the structure transitions of pseudopolymorphs of nucleoside and nucleotide hydrates, the transitions often proceed while maintaining a single crystal state. Therefore, the crystal structures before and after transitions could be determined, and we could discuss the transformation of the structure and the origin of the transformation at an atomic resolution. We have been carrying out such systematic examinations. The characteristics of the transitions are described, and their mechanisms are discussed in the following sections.

## 16.2 Overview of Structure Transitions Among Pseudopolymorphs of Nucleoside and Nucleotide Hydrates

Nucleotides and nucleosides usually crystallize as hydrates. The humidity-induced transformation between A-DNA and B-DNA is well known [10]. At the same time, it had been reported that the hydration numbers of nucleosides and nucleotides, which are the components of DNA and RNA, were reversibly changed depending on relative humidity (RH) on the basis of a gravimetric analysis [11].

In a systematic analysis, we found that the humidity-induced structure transitions of nucleoside and nucleotide hydrates often proceed while maintaining a single crystal state (Fig. 16.2). In the crystals, the base moieties are stacked to form molecular layers. Water molecules and hydrated counterions exist between these molecular layers. The crystal structure of disodium cytidine 5'-monophosphate ( $\text{Na}_2\text{CMP}$ ) nonhydrate is shown in Fig. 16.3a, as a typical example [12]. The molecular layer is supported by successive hydrogen bonds among the oxygen atoms of phosphate moieties and hydroxyl groups of riboses (Fig. 16.3b). The interlayer distances enlarge or shorten in a hydration or dehydration process, and networks in inorganic regions of water and cations are reconstructed.

In most cases, transitions are reversible. However, a large or small hysteresis is usually observed. For example, the humidity-dependent transition from form I to form II of  $\text{Na}_2\text{CMP}$  proceeds at around 40 %RH, but the inverse transition proceeds at around 70 %RH (Fig. 16.4). In Sects. 16.3.1, 16.3.2, 16.3.3, and 16.3.4, the characteristics of the transitions will be explained using several examples.

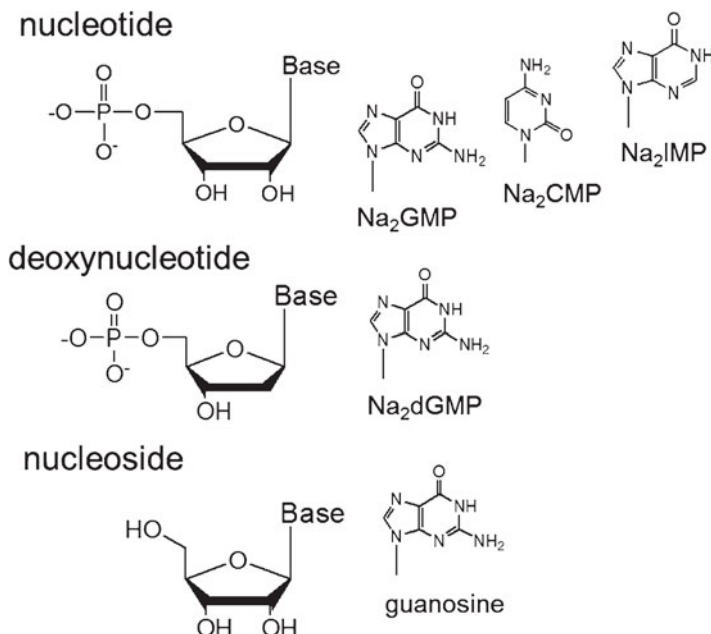


**Fig. 16.2** Examples of nucleosides and nucleotides that crystallized as hydrates and their humidity- or temperature-governed phase transitions proceeded while retaining single crystal states.  $\text{Na}_2\text{GMP}$ ,  $\text{Na}_2\text{CMP}$ ,  $\text{Na}_2\text{IMP}$ , and  $\text{Na}_2\text{dGMP}$  are disodium salts of guanosine 5'-monophosphate, cytidine 5'-monophosphate, inosine 5'-monophosphate, and 2'-deoxyguanosine 5'-monophosphate, respectively

Coupled with the transitions, conformational changes in the nucleoside and nucleotide molecules, and the reconstruction of hydrogen-bonding networks and cation coordination schemes, are induced (Sect. 16.3.1). The sliding of molecular layers is occasionally observed (Sect. 16.3.2). In some cases, the intermediate phases that appear in the hydration and dehydration processes are different. We define this type of transition as cyclic (Sect. 16.3.3). In the case of  $\text{Na}_2\text{dGMP}$ , two different anhydrides appear, depending on the temperature and humidity conditions, and we call this type a bifurcate transition (Sect. 16.3.4). Their mechanisms are discussed in Sect. 16.4 on the basis of the observed characteristics.

## 16.3 Characteristics of Transition Illustrated by Examples

### 16.3.1 Transitions Associated with Prominent Conformational Changes

The transitions among the pseudopolymorphs of nucleosides and nucleotides hydrates often accompany conformational changes in the molecules on a large or

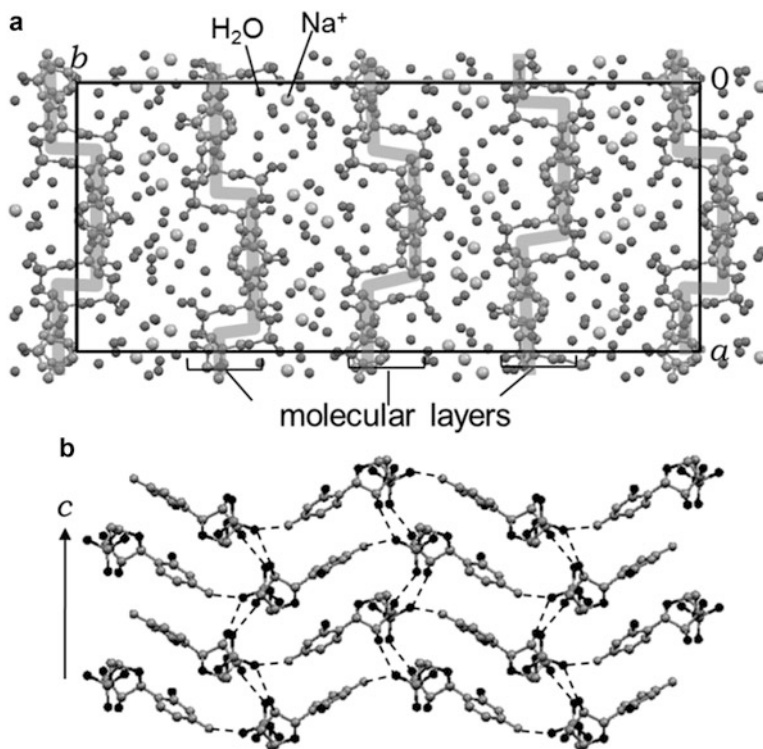


**Fig. 16.3** Crystal structure of disodium cytidine 5'-monophosphate nonahydrate. Projection along c axis (a) and interactions within molecular layer (b). Hydrogen bonds are indicated by *dashed lines*

small scale. The conformational flexibilities of nucleosides and nucleotides have been thoroughly classified [10]. The conformations around a glycosidic bond  $\chi$  are classified as *anti* and *syn*, and *anti* is usually stable in cases of non-substituted bases. The conformation of ribose is known as pseudorotation. Although the energy difference along the pseudorotation phase angles,  $P$ , is very small, C2'-*endo* and C3'-*endo* are slightly stable, and O4'-*endo* and O4'-*exo* are unstable. The conformations around a C4'-C5' bond are classified into three types: *gg* (*gauche-gauche*), *gt* (*gauche-trans*), and *tg* (*trans-gauche*) on the basis of torsional angles of O4'-C4'-C5'-O5' and C3'-C4'-C5'-O5' (Fig. 16.5). According to a statistical analysis of nucleoside and nucleotide crystal structures, *gg* is observed with high frequency.

The transition of disodium adenosine 5'-triphosphate (Na<sub>2</sub>ATP) between dihydrate and trihydrate [13] is a typical example, which is accompanied by prominent conformational changes. Na<sub>2</sub>ATP crystallizes as the trihydrate [14, 15]. On the basis of gravimetric analysis, powder diffraction data, and Raman spectra, the four phases D (monohydrate), M1 (dihydrate), M2 (trihydrate), and W (approximate)

**Fig. 16.4** Humidity dependence of hydration numbers of disodium cytidine 5'-monophosphate nonahydrate

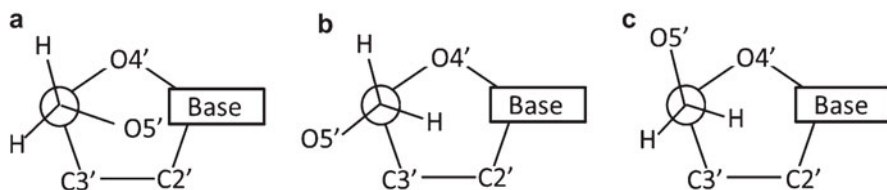
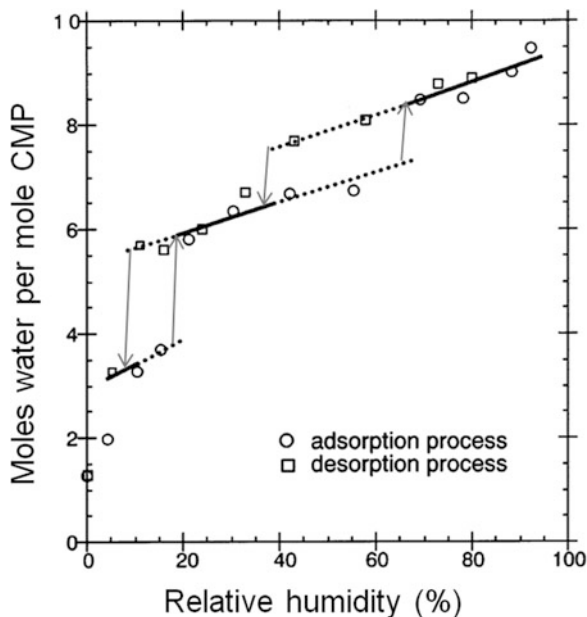


**Fig. 16.5** Conformations around a  $C4'-C5'$  bond, *gg* (a), *tg* (b), and *gt* (c)

mately tetrahydrate) are distinguished (Fig. 16.6) [16]. Among these, the trihydrate and dihydrate crystal structures were determined (Fig. 16.7) [13]. The trihydrate reversibly changes to dihydrate in the range of 10–50 %RH, while maintaining a single crystal state. There are two ATPs and four sodium ions in an asymmetric unit. Adenine bases stack in a parallel fashion (Fig. 16.7), and the triphosphate linkages form a pseudo-helical structure parallel to the stacking direction (Fig. 16.8). Two of the four sodium ions bridge oxygen atoms of the phosphate groups.

In the trihydrate, two ATP molecules belonging to the neighboring layers are bridged by water molecules (Fig. 16.7b). In the dihydrate, a portion of the water molecules are lost, and direct hydrogen bonds are formed between two ATPs (Fig. 16.7a). The conformation of the ribose moiety ATP changes from  $C2'-endo-C3'-exo$  in the trihydrate to  $C4'-endo$  in the dihydrate. At the same time, the conformation around the  $C4'-C5'$  bond changes from *gg* to *tg*, and the dihedral angle around the  $O5'-P$  bond changes from  $-45^\circ$  to  $75^\circ$  (Fig. 16.9). The structural changes could be interpreted as follows: coupled with the loss of two water

**Fig. 16.6** Humidity dependence of hydration numbers of disodium adenosine 5'-triphosphate nonahydrate

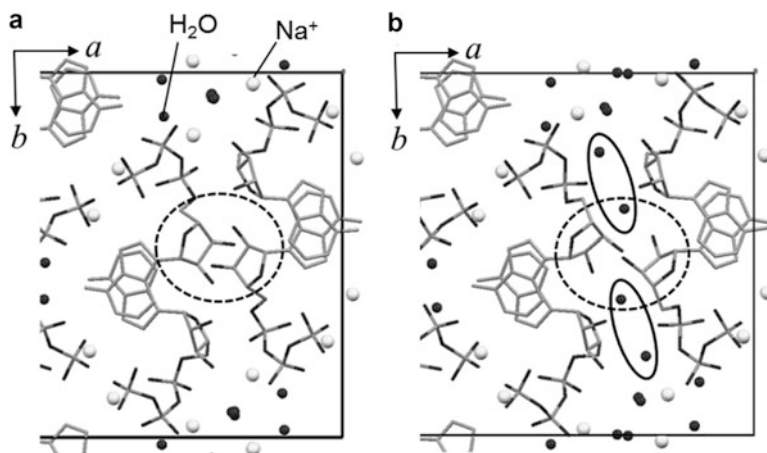
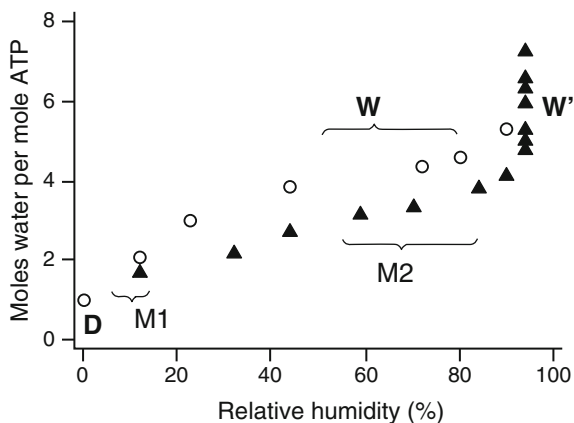


**Fig. 16.7** Structural changes coupled with transition of disodium adenosine 5'-triphosphate from dihydrate (a) to trihydrate (b). Water molecules in the trihydrate enclosed in the ellipses are lost in the dihydrate, and the conformations of the ribose moieties enclosed in the dashed ellipses are transformed, coupled with the transition

molecules, the molecular layers approach each other while avoiding conflict and form new interlayer interactions. The conformational changes of the riboses realize the direct interactions between ATP molecules belonging to the neighboring layers. While concerted changes of the two torsional angles around C4'-C5' and O5'-P simultaneously maintain the stacking of the bases and the helical structure of the triphosphates.

In the transition of guanosine dihydrate, a drastic conformational change occurs between *syn* and *anti* around the glycosidic bond  $\chi$ . The details are described in Sect. 16.3.3 from the viewpoint of the cyclic phase transition.

**Fig. 16.8** Helix-like structure made by triphosphate moieties of ATP and  $\text{Na}^+$ . Base moieties are not shown. Coordination around sodium ions is indicated by *dashed lines*, and estimated hydrogen bonds between  $\text{P}\alpha\text{-O}^-$  and  $\text{P}\gamma\text{-OH}$  are indicated by *dotted lines*

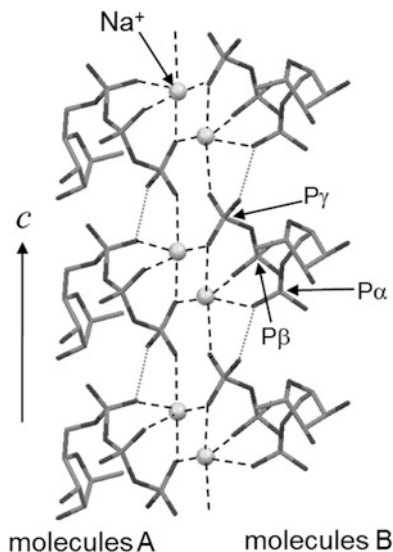
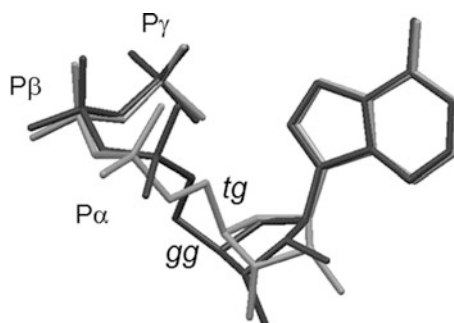


**Fig. 16.9** ATP molecules superimposed on dihydrate (*light gray*) and trihydrate (*deep gray*)



### 16.3.2 Transitions Accompanied by Sliding of Molecular Layers

The crystal structure of disodium cytidine 5'-monophosphate ( $\text{Na}_2\text{CMP}$ ) nonahydrate and the humidity dependence of the hydration numbers were described in Sect. 16.2 as one typical example of the crystal structure transitions of nucleotides.  $\text{Na}_2\text{CMP}$  crystallizes as a nonahydrate from an aqueous solution, and the humidity-induced transition between this nonahydrate and the 1.3 hydrate proceeds through the octahydrate and hexahemihydrate in the 0–80 %RH region at room temperature (Fig. 16.4) [12]. The crystal structures of the nona-, octa-, and hexahemihydrates were determined (Fig. 16.10). The molecular layer structure of the nucleotides was maintained throughout the transitions.

The conformational changes are rather small in the case of the phase transition of the  $\text{Na}_2\text{CMP}$  hydrate. However, the relative positions of the neighboring molecular layers slide together with the transition from the octahydrate to the hexahemihydrate.

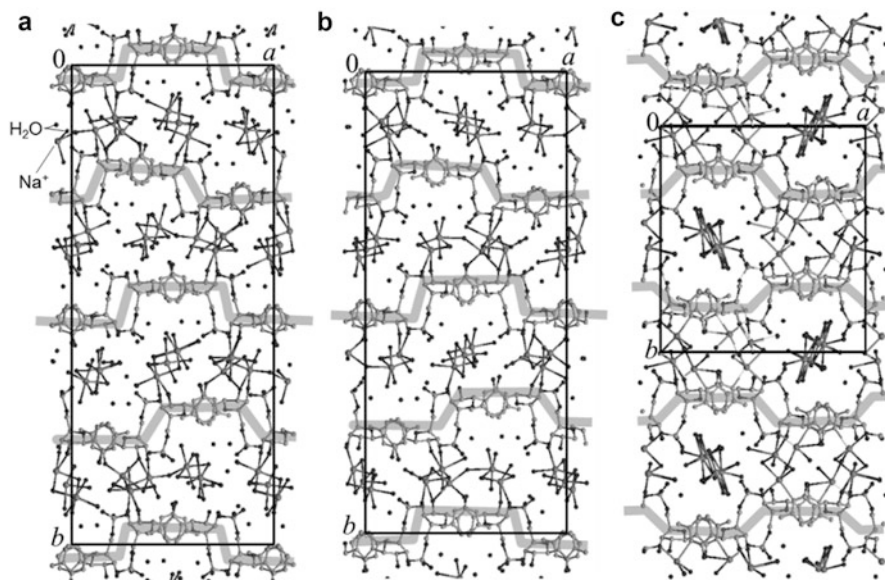


**Fig. 16.10** Crystal structures of disodium cytidine 5'-monophosphate nonahydrate (a), octahydrate (b), and hexahemihydrate (c). The gray bent lines indicate the molecules to make it easy to compare the relative positions of the successive molecular layers in each structure

The crystal structure of the octahydrate is similar to that of the nonahydrate, although the water and counterion sites rearrange (Fig. 16.10a, b). On the other hand, the longest axis  $b$  of the hexahemihydrate is one half of that of the octahydrate (Fig. 16.10c). This change is caused by the sliding of the molecular layers. The origin of this sliding could be explained as follows (Fig. 16.11). In hexahemihydrate, the hydrophilic regions of the neighboring layers face each other. Positively charged sodium ions, negatively charged phosphates, and polarized atoms are gathered in one region and are separated by a monolayer of water molecules, i.e., a small amount of water molecules effectively shield the electrostatic repulsion.

It is rather curious that such a drastic change proceeds while retaining the single crystal state. Mnyukh proposed a mechanism of epitaxial (oriented) nucleation and growth in a layered crystal [17].

### 16.3.3 Cyclic Transitions

Guanosine crystallizes as dihydrate from an aqueous solution (Fig. 16.12) [18]. A structural transition occurs between the dihydrate (phase H) and anhydride (phase A) in the region of 20–0 %RH [16, 19]. The change in the number of crystal water molecules determined by gravimetric measurements and the X-ray powder

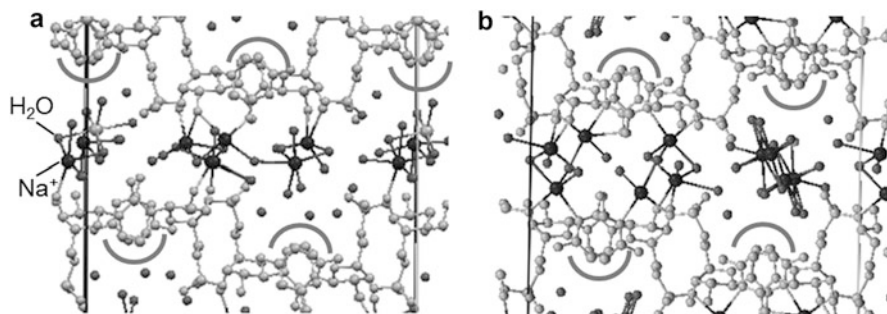


**Fig. 16.11** Crystal structures of disodium cytidine 5'-monophosphate octahydrate (a) and hexahemihydrate (b). The curved lines indicate the hydrophobic surfaces of molecular layers, and the large black circles and dark gray circles are sodium ions and the oxygen atoms of water molecules, respectively

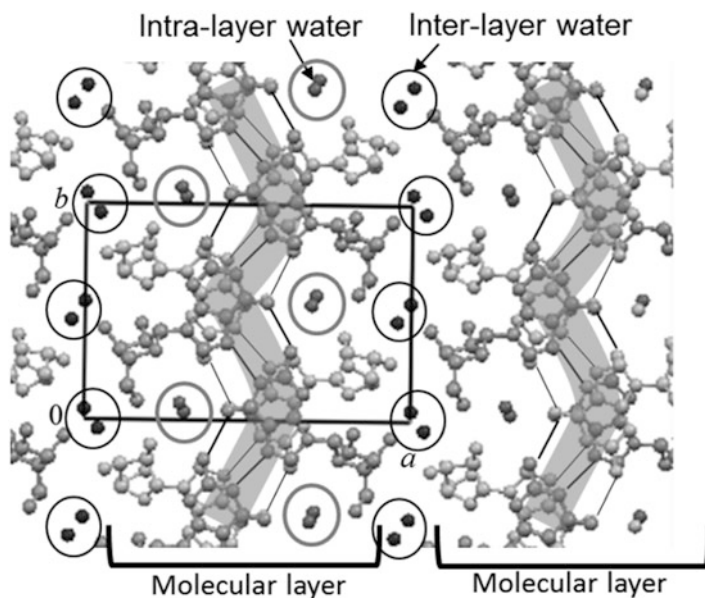


**Fig. 16.12** Crystal structure of guanosine dihydrate (crystal data: monoclinic, space group  $P2_1$ ,  $a = 17.518$ ,  $b = 11.278$ ,  $c = 6.658$  Å,  $\beta = 98.17^\circ$ , and  $Z = 4$ )

patterns are shown in Fig. 16.13a, b, respectively. Phase H transforms into phase A through two intermediate phases, H' and A'. The reverse transition from phase A to phase H proceeds through two intermediate phases, A' and M. The X-ray diffraction patterns indicated that the crystal structures of phases H' and M were quite different (Fig. 16.13b). Phase H' appears only in the dehydration process, and phase M only in the hydration process. We defined this type of transition as cyclic.

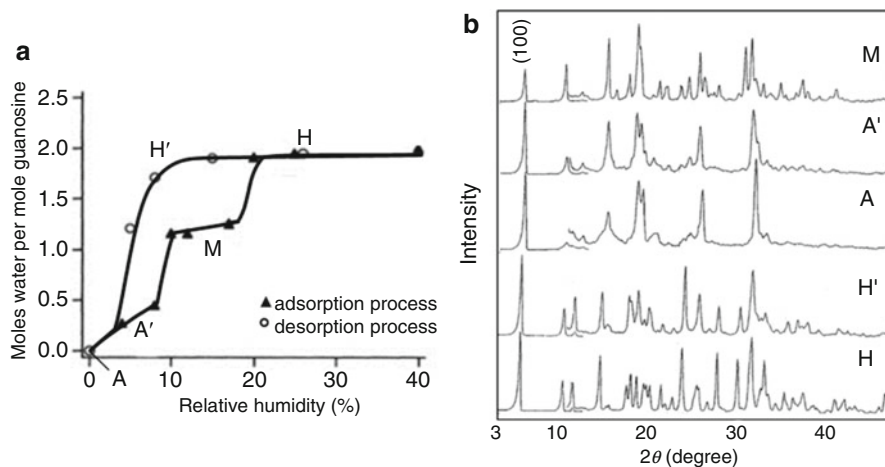


**Fig. 16.13** Humidity dependence of hydration numbers (a) and changes in powder diffraction patterns (b) coupled with structure transitions of guanosine dihydrate

Guanine bases are known to form hydrogen bonds among themselves. The tetramer formation is famous. In guanosine dihydrate, base moieties stack in parallel and form hydrogen-bonding chains along the twofold screw axis, which is perpendicular to the stacking direction. As a result, a molecular layer is formed (Fig. 16.12). There are four symmetrically independent water molecules, and these are classified into two groups. Two are in a columnar space surrounded by guanosine molecules (intra-layer water). The other water molecules exist between two molecular layers and bridge them by hydrogen bonds (interlayer water).

The distance between the (100) planes,  $d_{100}$ , reflects the interlayer distance. The values of  $d_{100}$  in phase H and phase H' are close to 17.3 Å. On the other hand, those of phases A', A, and M are close to 16.3 Å. Therefore, it was speculated that the interlayer water molecules still exist in H' and are lost in the A, A', and M phases.

Among the two types of water sites, it seems that intra-layer water is easy to absorb/desorb because it is in a columnar space. On the other hand, the interlayer water molecules tightly bridge the riboses of guanosine molecules belonging to the neighboring layers and seem to be hard to desorb.

The crystal structure of phase M was also determined [20]. The conformational change around the glycosidic bond between *anti* and *syn* occurs during the transition from phase M to H (Fig. 16.14). In the hydration process, water occupies the columnar space of the intra-layer sites first. The intermediate water sites appear and also occupied in phase M. At the last stage of the transition from phase M to phase H, a portion of the water molecules shift to the interlayer sites, coupled by the widening of the interlayer space. The conformational change around the glycosidic bond from *syn* to *anti* isolates the inter- and intra-layer water sites. In the dehydration process

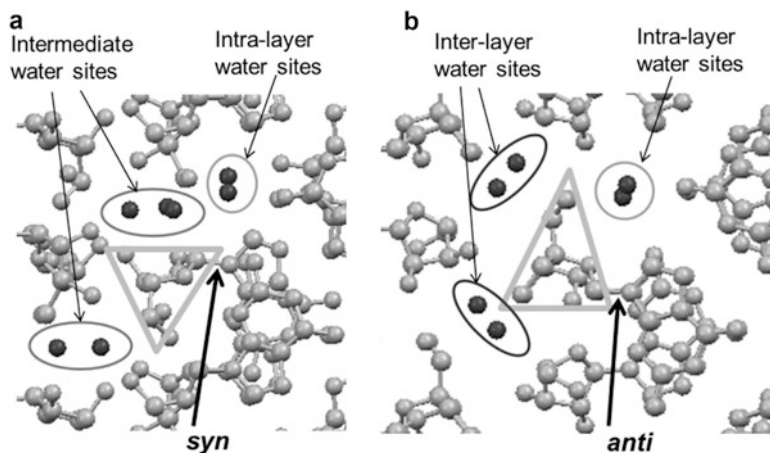


**Fig. 16.14** Water sites and conformations of guanosine in phase M (a) and phase H (b)

from phase H' to phase A', a conformational change from *anti* to *syn* would occur. The *syn* conformation opens the channels between the inter- and intra-layer sites, and the interlayer water molecule escapes from the crystal.

### 16.3.4 Bifurcation of Transitions Depending on Physical Conditions

Disodium 2'-deoxyguanosine 5'-monophosphate ( $\text{Na}_2\text{dGMP}$ ) crystallizes as tetrahydrate (phase H) (Fig. 16.15a) [21]. Depending on the physical temperature and humidity conditions, the dehydration process yields two different anhydrides [22]. The tetrahydrate changes to an anhydride (phase A) at 40 °C (Fig. 16.15b) and a water vapor pressure of 0 kPa (0 %RH). On the other hand, the same tetrahydrate mainly changes to another anhydrous form (phase B) at 80 °C and 1.5–2.0 kPa (Fig. 16.15c). Phases A and B are polymorphs, and we call this phenomenon a bifurcated transition. The amount of anhydrous phases A and B depends upon the vapor pressure of the water: the ratios of A to B are 100:0 at 0 kPa, 50:50 at 1 kPa, and 20:80 at 2 kPa. The notable difference among the crystal structures of phases H, A, and B is the conformation around the C4'–C5' bond. The conformation around C4'–C5' is *gt* in phases H and A and *tg* in phase B.

Bifurcation could be explained on the basis of their crystal structures as follows. In the transition from phase H to phase A at low temperature, dGMP molecules merely approach each other while retaining their conformations. At high temperature, dGMP is mobile. In the transition from phase H to phase B, dGMP molecules approach each other and change their conformation to reconstruct the interaction and fill the space occupied by water molecules in phase H.

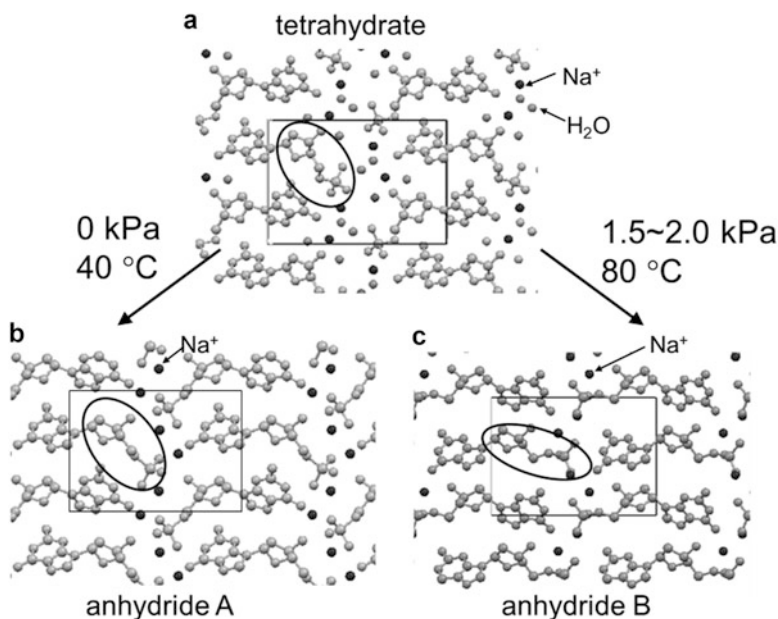


**Fig. 16.15** Crystal structures of disodium deoxyguanosine 5'-phosphates of tetrahydrate (a), anhydride A (b), and anhydride B (c). The moieties including C4'-C5' bonds are enclosed in ellipses

## 16.4 Mechanisms of Transition Among Hydrates

Now, we will consider the mechanism of the transitions whose characteristics were described in the previous section. First, it should be mentioned that the rigidity of the layer structure could be attributed to single crystal–single crystal transitions. In the case of Na<sub>2</sub>ATP, the base stacking structure and continued helical structure made of triphosphate linkages play a role in maintaining the crystal lattice (Figs. 16.7 and 16.8). In guanosine hydrates, guanine bases are stacked, and the hydrogen-bonding chains among them are formed along the twofold screw axis (Fig. 16.12). At the same time, conformational flexibility is an important factor to reconstruct the interaction networks (Figs. 16.9 and 16.15).

Rigidity of the layer structure also contributes to the reversibility of the transitions. One of the opposite examples is inosine dihydrate [18]. Its crystal structure highly resembles that of guanosine dihydrate (Fig. 16.12). However, inosine lacks an amino group at the 2 position of the base, and the number of hydrogen bonds between the bases, which successively continue along the twofold screw axis, is less than that in guanosine dihydrate. Inosine dihydrate slowly loses crystal water molecules and irreversibly transforms into the  $\alpha$ -form of anhydride [23] if it is removed from the mother liquid.

Next, let us consider the origin of the cyclic and bifurcate transitions. Hydration or dehydration transition is classified as the first-order phase transition, and an

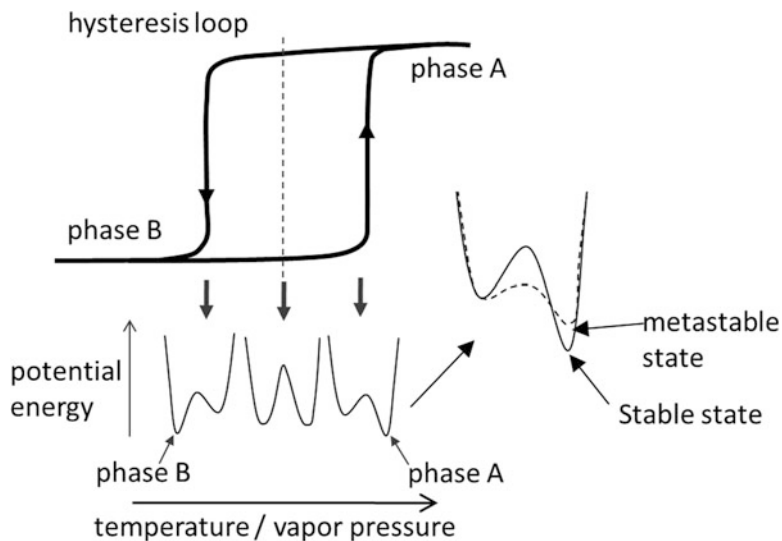


**Fig. 16.16** Hysteresis loop and schematic energy diagrams of first-order transition

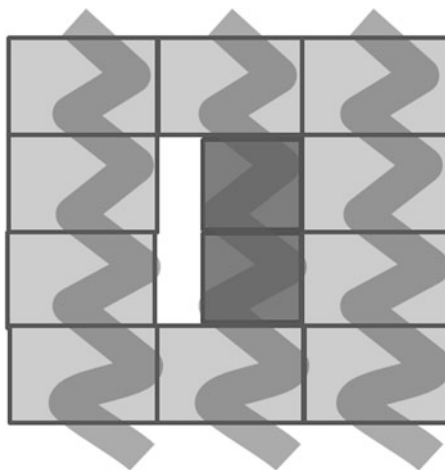
energy barrier exists at the transition point (Fig. 16.16). The dehydration (or hydration) transitions accompany a shortening (or lengthening) of the crystal axis by 5–10 %. Therefore, the nucleation of the dehydrated (or hydrated) phase in the hydrated (or dehydrated) phase produces a large strain in the lattices at the interface (Fig. 16.17), and the critical nucleation radius would generally be large, i.e., the energy barrier at the transition point is fairly high. If there is a metastable state whose crystal structure is similar to the original one, the energy barrier between the original and metastable states would be low, and the metastable state would easily appear (Fig. 16.16). The transition proceeds under kinetic control instead of by an energetic one [3].

It should be noted that there is a question about which water molecules disappear first. It is difficult to determine which water molecules in the original crystal structure disappear first because the position of the lost water is often filled by the remaining water in order to compensate for lost interactions. There is a tendency for the water molecules around ions to remain because of large electrostatic interactions. In addition, it seems that water molecules whose interactions are easily compensated by remaining molecules can be easily lost.

## 16.5 Use of Complementary Methods

The crystallographic structure determination of each phase that appears, together with the progress of the transitions, makes it possible to discuss structural transformation at an atomic resolution. At the same time, the complementary use of other

**Fig. 16.17** Model of transition state from phase A (hydrated state) with large unit cell to phase B (dehydrated state) with small unit cell. The *dark gray* bent bands indicate molecular layers in crystals retained during the transition. *Dark gray* cells are an embryo of phase B. Interaction in phase A is lost and new interaction in phase B are not constructed in the *white* region



methods is very important to deepen our insight into the transitions. One typical example is the structure transition of guanosine hydrates, which was described in Sect. 16.3.3. We examined this transition using not only X-ray analysis but also Raman spectroscopy and molecular dynamics simulation [16, 19, 24].

In general, the Raman peaks observed between 200 and 4,000  $\text{cm}^{-1}$  are used to identify polymorphs. On the other hand, we gave attention to the low-frequency modes that appear below 200  $\text{cm}^{-1}$ . There is one characteristic band at around 20  $\text{cm}^{-1}$ . This mode is assigned to the collective motion of stacked bases [25], and the origin would be common with that of the mode observed in the Raman spectra of DNA [26]. Its frequency is known to shift coupled with the transition between A-DNA and B-DNA.

In the case of guanosine dihydrate, the frequency of the corresponding peak changed within the range of 21–32  $\text{cm}^{-1}$ , coupled with the transition (Fig. 16.18) [16]. In phases A and A', the mode shifted to the low side compared with that of phase H, which indicates that the molecular layer is retained, but the interactions among bases are weakened. On the other hand, in phase M, it shifted to the upper side and split, which could be attributed to the fact that the unit cell is doubled, and guanine bases are tilted.

The motive force of the transitions is attributed to the hydration or dehydration of crystal water. Therefore, the mobility of water molecules caught our attention. We carried out a molecular dynamics (MD) simulation of guanosine dehydrate, paying attention to the mobility of crystal water molecules [24]. The mean square deviations of atoms obtained by MD simulations showed good correspondence with the X-ray atomic displacement parameters (temperature factors). MD calculations indicated that the intra-layer water molecules, which were surrounded by several hydrogen acceptor sites, frequently switched their hydrogen-bond sites (Fig. 16.19). In addition, the translocation of one water molecule from the interlayer site to the intra-layer site occurred within an MD calculation time of 1 ns (Fig. 16.20).

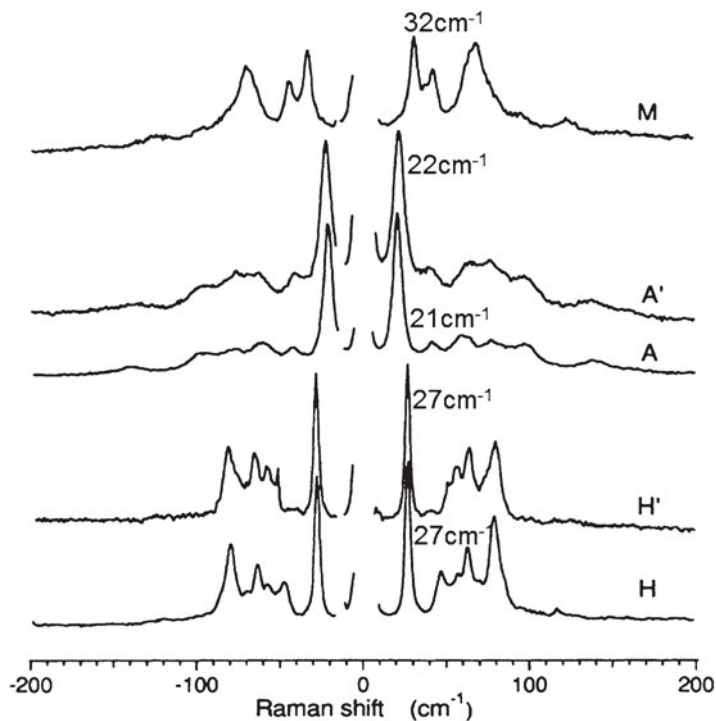


**Fig. 16.18** Low-frequency Raman spectrum of guanosine for each phase in the transition between the dihydrate and anhydride

The interlayer sites are isolated from the intra-layer sites by the ribose moieties of guanosine. However, the width of the junction that isolates the inter- and intra-layer water sites narrows or widens coupled with the fluctuation of guanosine molecules (Fig. 16.21). The translocation that occurred in the MD simulation would indicate a possible dehydration pass of the interlayer water molecules during the transition from phase H to phase H'. The MD results are reminiscent of the crystal structure of phase M (Sect. 16.3.3). In phase M, whose crystal structure was determined by X-ray analysis, the conformation around the glycosidic bond  $\chi$  is *syn*, i.e., the gate between the inter- and intra-layer sites is fixed in the open form.

## 16.6 Concluding Remarks

The characteristics of the humidity- and temperature-governed structure transitions of nucleoside and nucleotide hydrates were described. The coexistence of rigid parts made of molecular layers and flexible parts consisting of molecular conformations were found to be a key factor for reversible transition. The structural characteristics

**Fig. 16.19** Snapshot during MD simulation indicating fluctuation of intra-layer water molecules

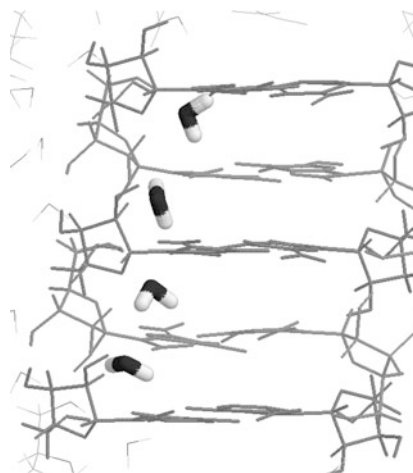
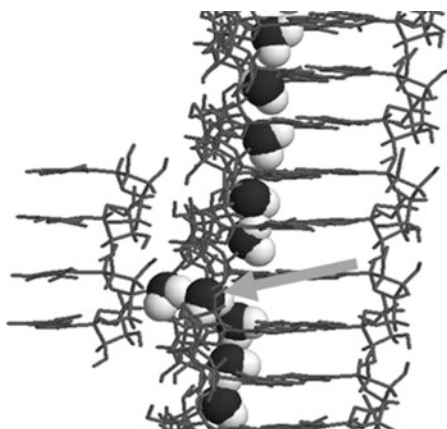


**Fig. 16.20** Snapshot when one interlayer water molecule, as indicated by *arrow*, translocates into intra-layer site



would also be linked to a high probability of single crystal–single crystal transitions. In addition, because of the high-energy barrier at a transition point, metastable states can easily appear, and cyclic or bifurcated phase transitions would proceed. Understanding these characteristics will guide us to a method to control the transitions among the pseudopolymorphs of hydrates. In addition, the cyclic and bifurcated transitions suggest a new control method for physical properties.

The development of a two-dimensional CCD detector makes it possible to precisely monitor the course of the hydration–dehydration process using X-ray analysis. In the case of the hydration–dehydration transition of disodium guanosine 5′-monophosphate ( $\text{Na}_2\text{GMP}$ ) heptahydrate, it was found that the transition proceeded through multiple steps and the cell volume of the first-to-appear intermediate phase (the pentahydrate) was around three times that of the initial phase (the heptahydrate) (Fig. 16.22) [27]. The determination of such an intermediate structure will unveil the precise transition scheme and aid in our further understanding of structure transitions among pseudopolymorphs.

**Fig. 16.21** Cavities in one snapshot clipped by planes orthogonal to *b* axis. *Dark gray* regions are cavities which are surrounded by solvent accessible surface of guanosine molecules drawn with a wire model. Widths of bottlenecks connecting inter- and intra-layer water sites are correlated with fluctuations of guanine molecules

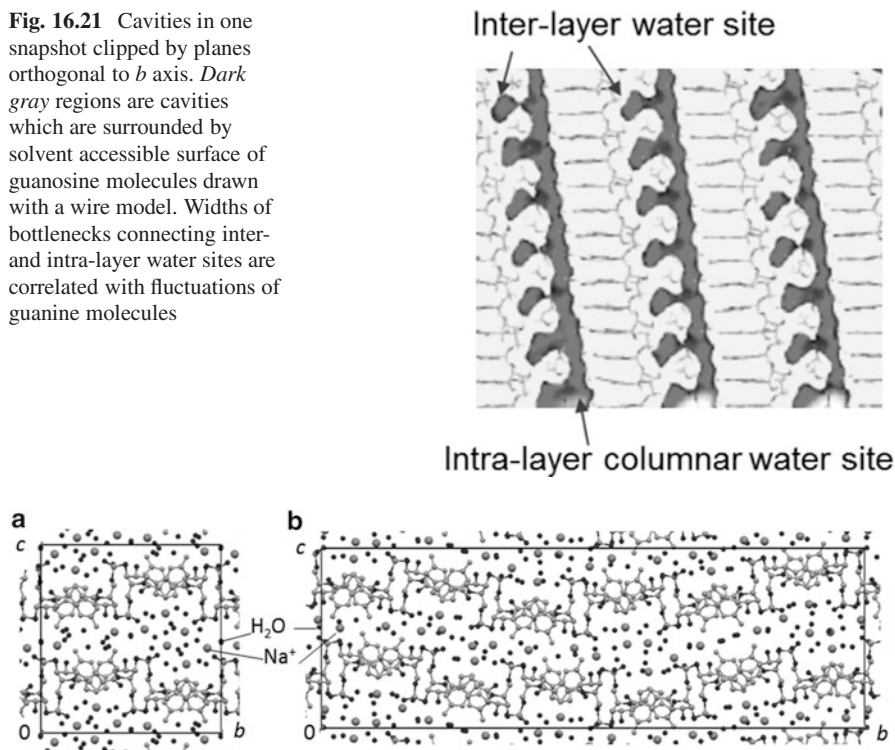


**Fig. 16.22** Crystal structures of disodium guanosine 5'-monophosphate heptahydrate (a) and pentahydrate (b)

## References

1. J.K. Haleblan, *J. Pharm. Sci.* **64**, 1269–1288 (1975)
2. S. Byrn, R. Pfeiffer, M. Ganey, C. Hoiberg, G. Poochikian, *Pharm. Res.* **12**, 945–954 (1995)
3. J. Bernstein, *Polymorphism in Molecular Crystals* (Clarendon, Oxford, 2002)
4. J. Bernstein, A.T. Hagler, *J. Am. Chem. Soc.* **100**, 673–681 (1978)
5. A. Nangia, *Acc. Chem. Res.* **41**, 595–604 (2008)
6. G.R. Desirau, *Angew. Chem. Int. Ed. Eng.* **34**, 2311–2327 (1995)
7. A. Nangia, *Cryst. Growth Des.* **6**, 2–4 (2006)
8. J. Bernstein, R.J. Davey, J.-O. Henck, *Angew. Chem. Int. Ed.* **38**, 3440–3461 (1999)
9. R. Černý, V. Favre-Nicolin, *Z. Kristallogr.* **222**, 105–113 (2007)
10. W. Saenger, *Principles of Nucleic Acid Structure* (Springer, New York/Berlin, 1983)
11. M. Falk, *Can. J. Chem.* **43**, 314–318 (1965)
12. Y. Sugawara, A. Nakamura, Y. Iimura, K. Kobayashi, H. Urabe, *J. Phys. Chem. B* **106**, 10363–10368 (2002)
13. Y. Sugawara, N. Kamiya, H. Iwasaki, T. Ito, Y. Satow, *J. Am. Chem. Soc.* **113**, 5440–5445 (1991)
14. O. Kennard, N.W. Isaacs, W.D.S. Motherwell, J.C. Coppola, D.L. Wampler, A.C. Larson, D.G. Watson, *Proc. R. Soc. Lond. A* **A325**, 401–436 (1971)
15. A.C. Larson, *Acta Cryst. B* **34**, 3601–3604 (1978)

16. H. Urabe, Y. Sugawara, T. Kasuya, *Phys. Rev. B* **51**, 5666–5672 (1995)
17. Y.V. Mnyukh, *Mol. Cryst. Liq. Cryst.* **52**, 163–200 (1979)
18. U. Thewalt, C.E. Bugg, R.E. Marsh, *Acta Crystallogr. B* **26**, 1089–1101 (1970)
19. Y. Sugawara, Y. Iimura, H. Iwasaki, H. Urabe, H. Saito, *J. Biomol. Struct. Dyn.* **11**, 721–729 (1994)
20. Y. Sugawara, S. Yamamura, S. Yoneda, K. Osaka, K. Miura, Abstracts of Joint Congress of ACTS-2014 and CGOM11, OC-CGOM-35, Nara (2014)
21. D.W. Young, P. Tollin, H.R. Wilson, *Acta Crystallogr. B* **30**, 2012–2018 (1974)
22. S. Yamamura, T. Moriguchi, S. Yoneda, Y. Sugawara, *Acta Crystallogr. A* **61**, C326–C327 (2005)
23. E. Subramanian, *Cryst. Struct. Commun.* **8**, 777–785 (1979)
24. S. Yoneda, Y. Sugawara, H. Urabe, *J. Phys. Chem. B* **109**, 1304–1312 (2005)
25. H. Urabe, Y. Sugawara, M. Tsukakoshi, T. Kasuya, *J. Chem. Phys.* **95**, 5519–5523 (1991)
26. H. Urabe, Y. Tominaga, *Biopolymers* **21**, 2477–2481 (1982)
27. M. Tsubonoya, Master Thesis, Graduate School of Science, Kitasato University, Kanagawa, Japan, 2015

# Chapter 17

## Anomalous Formation Properties of Nicotinamide Co-crystals

Si-Wei Zhang and Lian Yu

**Abstract** Co-crystals provide an opportunity to improve the properties of organic materials. We report that co-crystals containing nicotinamide (NIC) are anomalous as their formation generally decreases energy but expands volume. This conclusion is demonstrated first for an extraordinary system of co-crystals of NIC and (*R*)-mandelic acid (RMA) and then for all NIC co-crystals in general. The volume expansion is evaluated using the crystallographic densities of the co-crystals and their component crystals. The energy decrease upon co-crystallization is demonstrated using experimental data on four co-crystals of NIC and RMA and then generalized for all NIC co-crystals using computed values from a dispersion-corrected DFT model, after validating the model on the experiment. The anticorrelation between energy and volume on the formation of NIC co-crystals is in contrast to most physical processes, but similar to water freezing. As in the case of water freezing, the co-crystallization with NIC leads to stronger hydrogen bonds and looser molecular packing, a combination that is likely responsible for the anomalous formation properties. NIC has two conformers 4 kJ/mol apart in energy and both can form co-crystals, with the resulting structures having comparable formation energies and volumes. These results are relevant for understanding the nature of co-crystallization and why NIC is a prolific co-crystal former.

**Keywords** Co-crystal • Thermodynamics • Nicotinamide • Formation energy • Formation volume • Enthalpy-volume correlation

### 17.1 Introduction

A co-crystal is a solid phase that contains multiple chemical components [1]. Interest in organic co-crystals has grown in recent years, driven in part by their applications in engineering pharmaceutical solids [2] and other molecular materials [3]. Pharmaceutical co-crystals have been studied to expand the number of solid

---

S.-W. Zhang • L. Yu (✉)

School of Pharmacy and Department of Chemistry, University of Wisconsin – Madison, Madison, WI, USA

e-mail: [lyu@pharmacy.wisc.edu](mailto:lyu@pharmacy.wisc.edu)

© Springer Japan 2015

R. Tamura, M. Miyata (eds.), *Advances in Organic Crystal Chemistry*,

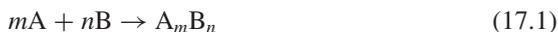
DOI 10.1007/978-4-431-55555-1\_17

337

forms available for an active pharmaceutical ingredient (API) and to improve solubility and dissolution rate [4–7], bioavailability [8], mechanical properties [9, 10], and physical stability [11, 12].

Despite the growing interest in co-crystals, the nature of co-crystallization remains inadequately understood. Many studies have focused on the discovery and structures of co-crystals, while less is known about their thermodynamics and structure–property relations – both of which are essential for understanding a solid-state phenomenon. It remains a mystery why some molecules (e.g., nicotinamide [13–16]) are prolific co-crystal formers and to what extent this tendency is linked to their molecular attributes (e.g., conformational flexibility and ability to form hydrogen bonds). The formation of racemic compounds – a special class of co-crystals containing the opposite enantiomers – is typically associated with energy decrease and volume reduction in reference to their components [17, 18], but it is unclear whether the conclusions apply to other co-crystals. Answering these questions helps advance the science of co-crystallization to technological benefits.

To understand the nature of co-crystallization, a valuable approach is to compare the properties of co-crystals and their component crystals. It is standard to make this comparison on the basis of *formation properties*, as defined in reference to the following reaction:

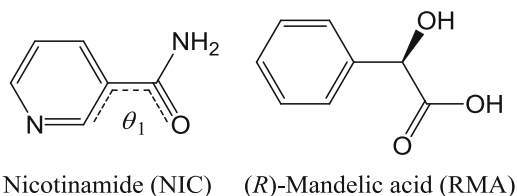


where A, B, and  $A_mB_n$  are the crystal of component A, the crystal of component B, and the co-crystal of A and B, respectively. A formation property can be defined for any thermodynamic property – energy, volume, and others – and reports the change of that property upon co-crystallization. The formation properties of co-crystals are the foundation for understanding how physical properties change as a consequence of forming co-crystals.

To study the structure–property relationship in co-crystallization, it is valuable to have many distinct co-crystal structures that are composed of the same chemical components. This advantage is similar to the benefit of having many polymorphs of the same molecule as one seeks the structural origin of the different properties of crystal polymorphs [19]. In both cases, fixing the molecule(s) and expanding the number of solid structures allow the variation of properties to be traced to the difference in molecular packing, without complications from changes of molecular species.

In the following sections, we describe an extraordinary system of co-crystals containing nicotinamide (NIC) and (*R*)-mandelic acid (RMA, Scheme 17.1) in many stoichiometric ratios (4:1, 1:1 in two polymorphs, and 1:2) [16]. The NIC-RMA co-crystals are remarkable as their formation from the component crystals lowers energy but expands volume, which stands in contrast to the positive energy–volume correlation in most physical processes, but is analogous to water freezing. This phenomenon proves to be general for all NIC co-crystals: they tend to have positive formation volumes ( $+3.9 \text{ \AA}^3$  or  $+17 \text{ cm}^3/\text{kg}$  on average, corresponding to a 2 % expansion) [16] and negative formation energies [20, 21]. We demonstrate the

**Scheme 17.1** Structures of nicotinamide (NIC) and (*R*)-mandelic acid (RMA).  $\theta_1$  indicates the angle of torsion in NIC



negative formation energies using both experimental data and computational results from a dispersion-corrected density functional theory (DFT-D) model. As in the case of water freezing, we attribute the anomalous formation properties of NIC co-crystals to the formation of stronger hydrogen bonds. The last section is concerned with the conformational flexibility of NIC and its role in co-crystallization. We show that the two conformers of NIC, 4 kJ/mol apart in energy [15], form co-crystals of comparable formation energies and volumes [21]. These results are relevant for understanding the formation of organic co-crystals and why NIC is a prolific co-crystal former.

## 17.2 An Extraordinary System of Co-crystals NIC-RMA and Its Anomalous Formation Properties

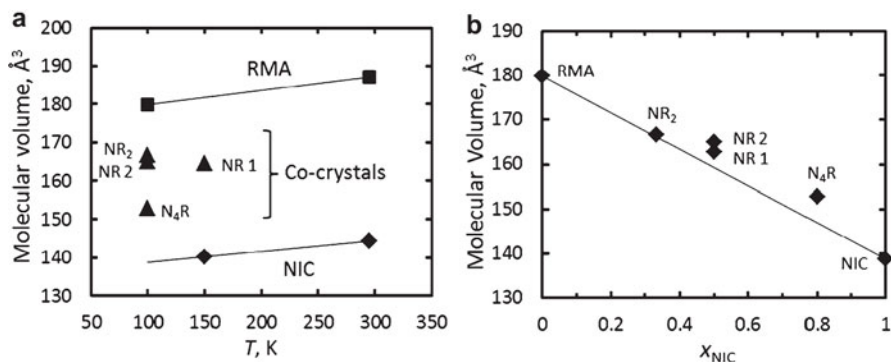
### 17.2.1 Discovery of NIC-RMA Co-crystals in Many Stoichiometric Ratios

The co-crystallization of NIC and RMA produces a remarkable number of structures of different stoichiometries. In addition to the 1:1 co-crystal of Frišćić and Jones (hereafter NR Form 1) [13], we discovered a polymorph of the 1:1 co-crystal (NR Form 2) [22], a 4:1 co-crystal (N<sub>4</sub>R), and a 1:2 co-crystal (NR<sub>2</sub>) [16]. Table 17.1 shows the structural parameters of NIC-RMA co-crystals and their component crystals. It is rare for two organic molecules to co-crystallize in so many ratios [23].

It is noteworthy that our discovery of new NIC-RMA co-crystals relied on melt crystallization, without use of solvents. In this method, a mixture of NIC and RMA in a chosen ratio is melted together and allowed to crystallize. The resulting crystals were analyzed by X-ray diffraction and Raman spectroscopy for new crystalline phases. Seeds acquired from melt crystallization were used for growing high-quality crystals from solution for structural solution. This method is also effective for discovering polymorphs in single-component systems, as is the experience of chemical microscopists and illustrated for the especially rich system ROY [19]. It is not suggested that this method generally outperforms others in discovering new solid forms. The special merit of the method, however, appears to be the ability to form metastable structures at large driving forces and protect them against solvent-mediated transformation (since solvents are absent).

**Table 17.1** Crystal structures of NIC, RMA, and NIC-RMA co-crystals

	RMA [16]	NR <sub>2</sub> [16]	NR Form 1 [13]	NR Form 2 [22]	N <sub>4</sub> R [16]	NIC [24]
<i>T</i> , K	100	100	150	100	100	295
Crystal system	Monoclinic	Triclinic	Monoclinic	Monoclinic	Monoclinic	Monoclinic
Space group	<i>P</i> 2 <sub>1</sub>	<i>P</i> 1	<i>C</i> 2	<i>P</i> 2 <sub>1</sub>	<i>P</i> 2 <sub>1</sub>	<i>P</i> 2 <sub>1</sub> / <i>c</i>
<i>a</i> , Å	8.377	6.5020	32.6557	5.2406	6.0810	3.975
<i>b</i> , Å	5.859	7.5220	5.475	10.0477	34.245	15.632
<i>c</i> , Å	15.047	20.6532	14.9264	12.6006	7.4405	9.422
$\alpha$ , deg	90	97.770	90	90	90	90
$\beta$ , deg	103.08	91.964	99.400	95.678	99.280	99.03
$\gamma$ , deg	90	90.557	90		90	90
<i>V</i> , Å <sup>3</sup>	719.4	1,000.1	2,632.9	660.24	1,529.2	578.2
<i>Z</i>	4	2	8	2	2	4
$\rho$ , g cm <sup>-3</sup>	1.405	1.416	1.384	1.380	1.391	1.403

**Fig. 17.1** Molecular volumes in the crystals of NIC and RMA and in their co-crystals plotted against temperature (a) and at 100 K (b). The lines in (a) correspond to  $\alpha_V = 2.1 \times 10^{-4} \text{ K}^{-1}$ 

### 17.2.2 Formation Volumes of NIC-RMA Co-crystals: Co-crystallization of NIC and RMA Expands Volume

A remarkable property of NIC-RMA co-crystals is their looser molecular packing relative to the component crystals. We demonstrate this conclusion with the data in Fig. 17.1. Figure 17.1a shows the volume of one molecule in the crystals of NIC and RMA and in their co-crystals, all calculated from crystallographic data using  $V = V_{\text{cell}}/Z$ , where  $V_{\text{cell}}$  is the volume of the unit cell and  $Z$  the number of molecules therein. One “molecule” in a co-crystal  $A_mB_n$  consists of  $m/(m+n)$  of A and  $n/(m+n)$  of B. The  $V$  thus obtained is the volume occupied by one molecule in a crystal including void space. For NIC and RMA,  $V$  is known at different temperatures (NIC at 150 K and 295 K [24]; RMA at 295 K [25] and at 100 K

[16]), yielding a thermal expansion coefficient ( $\alpha_V$ ) of  $2.1 \times 10^{-4} \text{ K}^{-1}$  for both systems [ $\alpha_V = d(\ln V)/dT$ ]. This  $\alpha_V$  value is typical for organic solids and allows the calculation of  $V$  at different temperatures.

Figure 17.1b shows the molecular volumes at 100 K in the crystals of NIC and RMA and their co-crystals. Most are experimental data determined at 100 K; the value for NIC is obtained by extrapolating the data at 150 K and 295 K (Fig. 17.1a); the value for NR Form 1 is obtained from the data at 150 K and  $\alpha_V = 2.1 \times 10^{-4} \text{ K}^{-1}$ . Given that NIC and RMA have identical  $\alpha_V$ , we assume the value for their co-crystals to be similar. Figure 17.1b shows that every NIC-RMA co-crystal has a molecular volume larger than the weighted average of the values of the component crystals (the line). In other words, the co-crystals have positive volumes of formation, defined as

$$\Delta V_f = V_{cc} - [m/(m+n)V_A + n/(m+n)V_B] \quad (17.2)$$

In Fig. 17.1b,  $\Delta V_f$  is the vertical distance from a co-crystal point to the line between NIC and RMA:  $\Delta V_f (\text{\AA}^3/\text{molecule}) = +0.5 (\text{NR}_2)$ ,  $+3.6 (\text{NR Form 1})$ ,  $+5.8 (\text{NR Form 2})$ , and  $+5.9 (\text{N}_4\text{R})$ . In  $\text{cm}^3/\text{kg}$ , we find  $\Delta V_f (\text{cm}^3/\text{kg}) = +2.3 (\text{NR}_2)$ ,  $+15.6 (\text{NR Form 1})$ ,  $+25.3 (\text{NR Form 2})$ , and  $+28.0 (\text{N}_4\text{R})$ . Though evaluated at 100 K, these values are expected to be insensitive to temperature change given the similar thermal expansion coefficients of NIC and RMA. The positive formation volumes of the NIC-RMA co-crystals are surprising because as we discuss below, they have *negative* enthalpies of formation. Furthermore, the mixing of acids and bases in the liquid state is known to *reduce* volume [26].

### 17.2.3 Formation Enthalpies of NIC-RMA Co-crystals: Co-crystallization of NIC and RMA Decreases Enthalpy

The formation enthalpy of a NIC-RMA co-crystal ( $A_mB_n$ ) can be calculated from the corresponding melting enthalpies of the co-crystal and the physical mixture of component crystals ( $A + B$ ) [22]:

$$\Delta H_f = \Delta H_{m(A+B)}(T_S \rightarrow T_L) - \Delta H_{mAB}(T_S \rightarrow T_L) \quad (17.3)$$

where  $T_S$  is a temperature at which the co-crystal and the physical mixture of component crystals are solid and at which  $\Delta H_f$  is evaluated,  $T_L$  is a temperature at which the co-crystal and the physical mixture are both melted to the same liquid, and  $\Delta H_{m(A+B)}(T_S \rightarrow T_L)$  and  $\Delta H_{mAB}(T_S \rightarrow T_L)$  are the corresponding enthalpies of melting (properly scaled to reflect the stoichiometry of the co-crystal).

Similarly, the mixing enthalpy of a liquid of component A (NIC) and a liquid of component B (RMA) can be determined by eq. (17.4) [22]

$$\Delta H_{\text{mix}} = \Delta H_{m(A+B)}(T_S \rightarrow T_L) - \Delta H_{mA}(T_S \rightarrow T_L) - \Delta H_{mB}(T_S \rightarrow T_L) \quad (17.4)$$

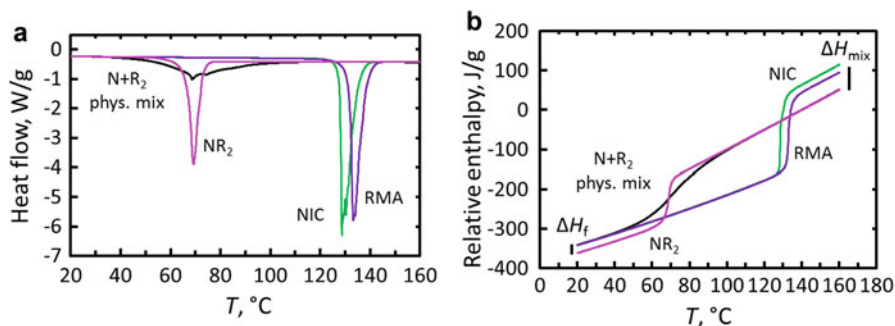


**Fig. 17.2** (a) Melting endotherms of the NR<sub>2</sub>, NIC, RMA, and a physical mixture of NIC and RMA at 1:2 molar ratio. (b) Relative enthalpies between NR<sub>2</sub>, NIC, RMA, and the N + R<sub>2</sub> physical mixture.  $\Delta H_f$  is the formation enthalpy of NR<sub>2</sub>.  $\Delta H_{\text{mix}}$  is the mixing enthalpy of NIC and RMA in the liquid state

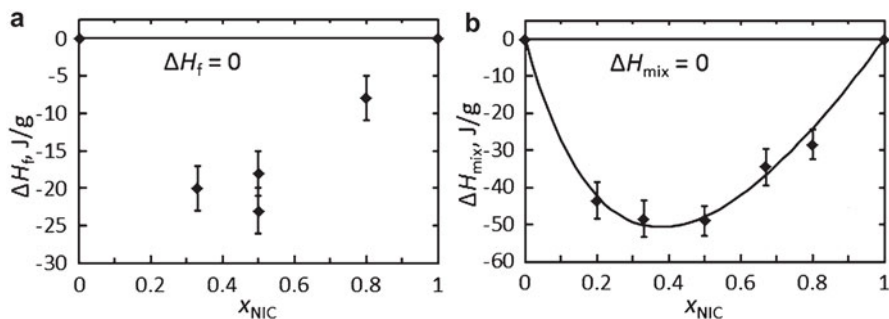
where  $T_S$  is a temperature at which NIC, RMA, and their physical mixture are all solids,  $T_L$  is a temperature at which the three materials are all melted and at which  $\Delta H_{\text{mix}}$  is evaluated, and  $\Delta H_{\text{mA}}(T_S \rightarrow T_L)$ ,  $\Delta H_{\text{mB}}(T_S \rightarrow T_L)$ , and  $\Delta H_{\text{m(A+B)}}(T_S \rightarrow T_L)$  are the corresponding enthalpies of melting (properly scaled to reflect the solution composition).

Figure 17.2 illustrates the determination of the  $\Delta H_f$  of NIC-RMA co-crystals and the  $\Delta H_{\text{mix}}$  of NIC and RMA in the liquid state. To obtain  $\Delta H_f$ , the heat-flow data of a co-crystal (NR<sub>2</sub> in this case) and the corresponding physical mixture of the component crystals (Fig. 17.2a) are integrated from a common liquid-state temperature (140 °C) down to a common solid-state temperature (30 °C). The enthalpy of the co-crystal relative to the physical mixture is its  $\Delta H_f$  (Fig. 17.2b). Similarly, to obtain  $\Delta H_{\text{mix}}$ , the melting endotherms of crystalline NIC, crystalline RMA, and their physical mixture are integrated from a common solid-state temperature (20 °C) to a common liquid-state temperature (160 °C). Assuming the enthalpy of mixing is negligible in the crystalline state,  $\Delta H_{\text{mix}}$  is obtained from the enthalpy of the solution relative to the pure liquids (Fig. 17.2b).

Figure 17.3 compares the  $\Delta H_f$  and  $\Delta H_{\text{mix}}$  data for the NIC-RMA system. For this system,  $\Delta H_f$  and  $\Delta H_{\text{mix}}$  are both negative (reactions are exothermic), indicating the mixed state has lower energy than the separated state. The larger  $\Delta H_f$  in the solid state approximately correlates with larger  $\Delta H_{\text{mix}}$  in the liquid state. These negative enthalpy changes are expected for mixing a base (NIC) and an acid (RMA) and consistent with stronger intermolecular interactions in the mixed state.

Note that at 1 bar, the formation enthalpies of NIC-RMA co-crystals ( $\Delta H_f$ ) are approximately the same as their formation energies ( $\Delta E_f$ ), because the difference  $\Delta H_f - \Delta E_f = P\Delta V_f$  is small. For a typical NIC-RMA co-crystal,  $\Delta V_f = +20 \text{ cm}^3/\text{kg}$ ; at  $P = 1 \text{ bar}$ ,  $P\Delta V_f$  is 2 mJ/g, which is much smaller than the typical magnitude of  $\Delta H_f$  ( $\sim 20 \text{ J/g}$ ). From here on,  $\Delta H_f$  and  $\Delta E_f$  shall not be distinguished.

Table 17.2 summarizes the formation properties of NIC-RMA co-crystals. The key finding is that the formation of NIC-RMA co-crystals from their components



**Fig. 17.3** The formation enthalpies of NIC-RMA co-crystals and the mixing enthalpies of NIC and RMA liquids. Table 17.2 gives the values of  $\Delta H_f$ .  $\Delta H_{\text{mix}} = -28(4)$ ,  $-34(5)$ ,  $-49(4)$ ,  $-48(5)$ , and  $-44(5)$  J/g for mixing liquid NIC and RMA at 4:1, 2:1, 1: 1, 1:2, and 1:4 molar ratios ( $T = 160$  °C)

**Table 17.2** Experimental and calculated formation properties of NIC-RMA co-crystals<sup>a</sup>

	$M$ , g/mol	$\Delta V_{f \text{ expt}}$ , cm <sup>3</sup> /kg	$\Delta V_{f \text{ calc}}$ , cm <sup>3</sup> /kg	$\Delta H_{f \text{ expt}}$ , J/g	$\Delta E_{f \text{ calc}}$ , J/g
RMA	152.15	0	0	0	0
NR <sub>2</sub>	142.14	2.3	-6.5	-20 (3)	-36.8
NR Form 1	137.14	15.8	11.8	-23 (3)	-48.0
NR Form 2	137.14	25.3	17.6	-18 (3)	-49.7
N <sub>4</sub> R	128.13	28.0	22.0	-8 (3)	-18.3
NIC	122.12	0	0	0	0

<sup>a</sup>One mole of co-crystal  $A_mB_n$  is defined as containing  $m/(m+n)$  mole of A and  $n/(m+n)$  mole of B. The calculated values are obtained with a dispersion-corrected DFT model [21]

lowers energy ( $\Delta H_f < 0$ ) but expands volume ( $\Delta V_f > 0$ ). The energy decrease upon co-crystallization is expected for a base (NIC) reacting with an acid (RMA); indeed, the two components mix exothermically in the liquid state ( $\Delta H_{\text{mix}} < 0$ ; Fig. 17.3b), as do other similar acids and bases [27]. The expansion of volume, however, is unexpected given the observation that acid–base mixing in the liquid state reduces volume [26]. In the next section, the data shows that the anticorrelation between energy and volume is general for the formation of NIC co-crystals.

## 17.3 Anomalous Formation Properties of NIC Co-crystals

### 17.3.1 NIC Co-crystals Generally Have Positive Formation Volumes

To test the generality of our observation on four NIC-RMA co-crystals, we examined all the co-crystals containing NIC in the CSD [28] (Table 17.3).  $\Delta V_f$  was evaluated according to Eq. (17.2) at the temperature  $T_{cc}$  at which the co-crystal

**Table 17.3** Experimental formation volumes  $\Delta V_f$  and calculated formation energies  $\Delta E_f$  of co-crystals containing NIC<sup>a</sup>

Co-former B	<i>m:n</i>	<i>T</i> <sub>cc</sub> , K	$\theta_1$ , °	$\Delta V_f$ , Å <sup>3</sup>	$\Delta V_f$ , cm <sup>3</sup> /kg	$\Delta E_f$ calc, J/g
3-hydroxy-2-naphthoic acid	1:1	293	±143.7	−6	−23.4	
Citric acid	2:1	293	±44.5, ±172.2	0.8	3.4	
Succinic acid	2:1	120	±26.7, ±152.3	3.2	16.2	−53.8
5-methyl-benzene-1,3-diol	4:1	150	±169.9, ±158.4, ±164.8, ±165.5	1.9	9.6	−23.7
Flufenamic acid	1:1	100	±33.7	3.5	10.5	
Margaric acid	1:1	293	±25.4	−4	−12.3	−21.6
Baicalein	1:1	100	±150.3	2.6	8.1	
Ethyl paraben	1:1	113	±163.4	−0.8	−3.3	−23.5
Indole-3-acetic acid	1:1	295	±29.3	1.2	4.8	−33.9
Palmitic acid	1:1	298	±23.1	5.9	18.8	−14.6
( <i>R</i> )-mandelic acid	1:1	150	35.3, 12.0	3.6	15.8	−48.0
( <i>R</i> )-mandelic acid	1:1	100	−28.8	5.8	25.3	−49.7
( <i>R</i> )-mandelic acid	4:1	100	−162.6, 162.8, −167.1, 164.2	5.9	28	−18.3
( <i>R</i> )-mandelic acid	1:2	100	−17.7, −20.1	0.5	2.3	−36.8
Malonic acid	2:1	180	±25.2, ±24.2	7.1	36.7	
Fumaric acid	1:1	293	±4.6	5.8	29.4	−57.1
Fumaric acid	2:1	295	±15.5	10.8	54.3	
Glutaric acid	1:1	180	±177.5	−1.3	−5.9	−58.8
Adipic acid	1:1	180	±22.8	2.4	11	−34.1
Adipic acid	2:1	180	±25.8	2	9.1	−51.2
Pimelic acid	1:1	110	±175.3	3	13	−29.2
Pimelic acid	1:1	110	±14.2	13.6	58.2	
Suberic acid	1:1	180	±7.9	8.2	33.4	−40.3
Suberic acid	2:1	180	±25.3	2	8.8	−36.8
Azelaic acid	1:1	180	±8.2	13.6	52.8	−21.0
Sebacic acid	2:1	180	±25.3	2.1	8.4	−38.5
4-hydroxy-3-methoxybenzaldehyde	1:1	100	±146.1	−0.7	−3.3	
Octadecanoic acid	1:1	295	±25.2	9.5	28.2	−8.2
4-hydroxy-benzoic acid	1:1	293	±165.6	3.6	16.7	−90.2
( <i>RS</i> )-ibuprofen	1:1	120	±171.8, ±172.5	8.5	31	−13.6
Salicylic acid	1:1	120	±144.9	7.5	34.8	−52.0
( <i>S</i> )-ibuprofen	1:1	120	170.2, −169.9, 170.5, −170.6	5.2	19.1	−18.5
2-chloro-4-nitrobenzoic acid	1:1	293	±20.5	3	11.1	
Lauric acid	1:1	298	±26.1	6.7	25.2	−18.1

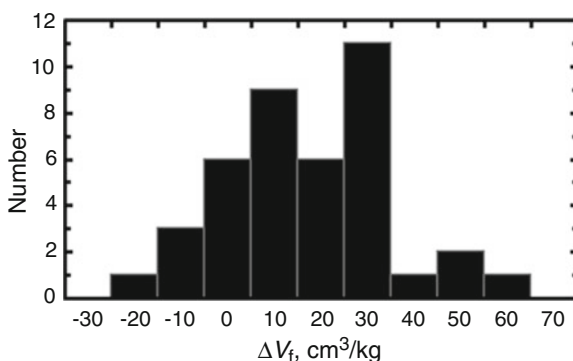
(continued)

**Table 17.3** (continued)

Co-former B	$m:n$	$T_{cc}$ , K	$\theta_1$ , °	$\Delta V_f$ , Å <sup>3</sup>	$\Delta V_f$ , cm <sup>3</sup> /kg	$\Delta E_{f,calc}$ , J/g
Isonicotinamide	1:1	100	$\pm 4.1, \pm 11.6$	5.2	25.4	
Carbamazepine	1:1	200	$\pm 25.3$	5.5	18.6	-1.8
3-hydroxy-benzoic acid	1:1	100	$\pm 171.1$	5.9	27.4	-59.7
Benzene-1,2,3-triol	1:2	100	$\pm 170.6$	0.3	1.3	
( <i>S</i> )-naproxen	1:2	223	-10	-3.2	-9.9	
2,5-dihydroxy-benzoic acid	1:1	295	-158.5	5.9	25.9	

<sup>a</sup> $m$  and  $n$  describe the stoichiometry of co-crystal  $A_mB_n$  ( $A = \text{NIC}$ ,  $B = \text{co-former}$ ).  $T_{cc}$  is the temperature at which co-crystal structure is determined and  $\Delta V_f$  is evaluated. Error in  $\Delta V_f$  is  $0.5 \text{ \AA}^3$  or  $2 \text{ cm}^3/\text{kg}$

**Fig. 17.4** Formation volumes  $\Delta V_f$  of NIC-containing co-crystals in the CSD ( $n = 40$ )



structure is determined. The molecular volumes of NIC and co-former B were temperature-corrected as illustrated in Fig. 17.1a if necessary [16].

Figure 17.4 and Table 17.3 show that most co-crystals containing NIC (34 of 40) have positive  $\Delta V_f$  values, with an average value of  $+3.9 \text{ \AA}^3/\text{molecule}$  or  $+17 \text{ cm}^3/\text{kg}$ . These values are similar to those for the subgroup NIC-RMA, suggesting the subgroup well represents the entire set of NIC co-crystals. These data indicate that, in all NIC co-crystals for which there are data, the average molecule occupies a volume 2 % larger than that in the individual component crystals.  $\Delta V_f$  is not significantly dependent on the temperature at which it is evaluated or on the molecular volume of co-former B. As we discuss later, the expansion reflects the formation of more open structures containing stronger hydrogen bonds.

It is of interest to compare the volume change upon forming NIC co-crystals with that of other processes. van de Streek and Motherwell compared the molecular volumes in hydrated and anhydrous crystals and concluded that the volume expands 1.2 % upon the hydration of an anhydrous crystal [29]. Their analysis is different from ours – since water is a liquid at their experimental temperature (298 K), the volume of water ( $V_w$ ) is given a value estimated from the average atomic volumes in organic crystals, which does not reflect water–water hydrogen bonding.

Their analysis would be formally equivalent to ours if  $V_w$  were extrapolated from the density of ice to 298 K, which would increase the  $V_w$  value and decrease the 1.2 % volume expansion upon hydrate formation. Price et al. compared the packing efficiencies of solvated and solvent-free crystals for several prolific solvate-forming molecules and reported that space is more or less efficiently filled in solvated crystals [30]. Their study differs from ours in that the pure solvent phase is not included in the reference state (roughly equivalent to our comparing a co-crystal's packing efficiency with that of only one component crystal). It is also worth noting that our analysis is based entirely on experimental densities obtained from crystal structures (Table 17.3), whereas these two studies make model-dependent assumptions about molecular volumes; for example, van der Waals volumes are used for calculating packing efficiencies [30]. It would be valuable to apply a consistent analysis to various systems of interest to understand the nature of molecular packing in single- and multiple-component crystals.

### 17.3.2 *Most NIC Co-crystals Have Negative Formation Energies*

To evaluate that whether NIC co-crystals have lower energies than the corresponding component crystals, we complement our calorimetric measurements with the computational results of Chan et al. [20]. They applied a dispersion-corrected density functional theory (DFT-D) method to calculate ab initio the formation energies of NIC co-crystals, according to Eq. (17.5):

$$\Delta E_f = E_{cc} - (mE_A + nE_B) \quad (17.5)$$

where  $E_{cc}$ ,  $E_A$ , and  $E_B$  are the energies of the co-crystal, the component crystal A, and the component crystal B, respectively. Each calculated energy is the total energy of the crystal, including intramolecular and intermolecular contributions. Before calculating its energy, the experimental crystal structure is optimized [31].

To validate the DFT-D model, the computed  $\Delta E_f$  of the NIC-RMA co-crystals was compared with the experimental value [21]. (As noted earlier, for NIC co-crystals at 1 bar,  $\Delta H_f$  is approximately the same as  $\Delta E_f$ , because the difference  $P\Delta V_f$  is small.) Table 17.2 shows that there is a reasonable agreement between theory and experiment. By experiment, the NIC-RMA co-crystals were found to have negative  $\Delta E_f$  and positive  $\Delta V_f$ . The DFT-D calculations yielded negative  $\Delta E_f$  for all four co-crystals and positive  $\Delta V_f$  for three of the four co-crystals. The one outlier corresponds to NR<sub>2</sub> whose experimental  $\Delta V_f$  is a small positive value and the calculated  $\Delta V_f$  a small negative one. Overall, the agreement is gratifying given the small differences being studied. It is noteworthy that the NIC-RMA co-crystals are the first system for which a comparison has been made between experimental and calculated formation properties.

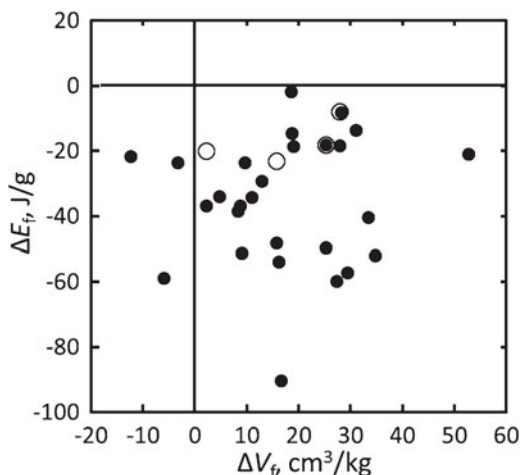
Table 17.3 (last column) collects the DFT-D formation energies of NIC co-crystals [21]. These values are generally negative, indicating the formation of NIC co-crystals generally lowers energy. These results demonstrate the generality of the conclusion previously reached for a subset of NIC co-crystals (those with RMA) and now enable a more extensive evaluation of the anomalous formation properties first revealed by the NIC-RMA co-crystals, as we describe next.

### 17.3.3 The Formation of NIC Co-crystals Generally Lowers Energy But Expands Volume, in Contrast to Most Physical Processes

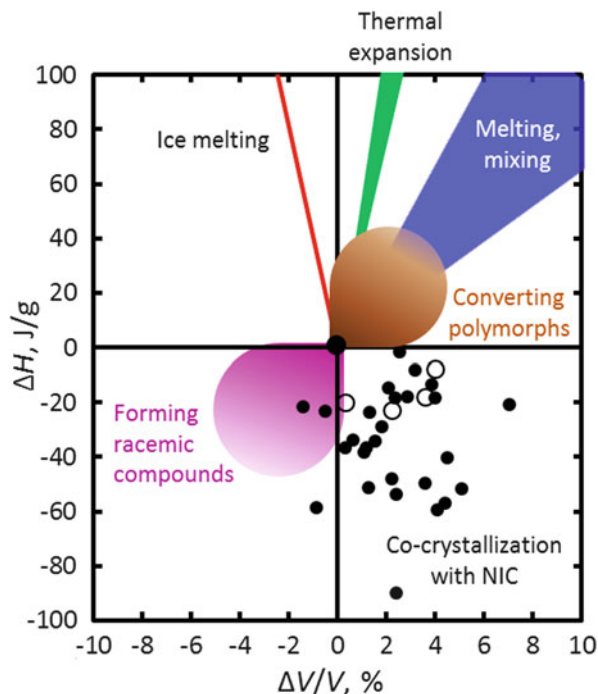
Table 17.3 collects the formation volumes  $\Delta V_f$  of NIC co-crystals and, when available, their formation energies  $\Delta E_f$ . These two properties are plotted against each other in Fig. 17.5. It is evident that the negative  $\Delta E_f$  are generally correlated with the positive  $\Delta V_f$ . It is therefore a general property for the co-crystallization of NIC with a second component that energy decreases but volume increases in reference to the component crystals. While this point was proposed on the ground of experimental  $\Delta H_f$  of NIC-RMA co-crystals, the calculated data of all NIC co-crystals substantiate that conclusion.

Figure 17.6 compares the enthalpy–volume correlation for the formation of NIC co-crystals with that for other physical processes [21]. Most processes summarized in Fig. 17.6 feature simultaneous increases or decreases of enthalpy and volume (positive correlation): (1) heating organic solids at 1 bar,  $\Delta H/(\Delta V/V) = C_p/\alpha_V \approx 50$  J/g/(1 % expansion); (2) melting crystals,  $\Delta H/(\Delta V/V) \approx 10$  J/g/(1 %) [32]; (3) mixing organic liquids,  $\Delta H/(\Delta V/V) \approx 10$  J/g/(1 %) [33]; (4) forming racemic compounds from opposite enantiomorphs,

**Fig. 17.5** Correlation between the energies and volumes of formation of NIC co-crystals. The  $\Delta V_f$  values are from crystallographic data; the  $\Delta E_f$  values are both experimental (*open circles*,  $T = 303$  K) and calculated (*solid circles*,  $T = 0$  K)



**Fig. 17.6** Enthalpy–volume correlation for co-crystallization with NIC and for other physical processes. For the co-crystals, the volume data are from crystallography; the enthalpy data are from experiment (*open circles*,  $T = 303$  K) and DFT-D (*solid circles*,  $T = 0$  K). The co-crystallization reduces enthalpy but expands volume, in contrast to many physical processes, but analogous to water freezing (the ice melting line extended to the opposite quadrant)



$\Delta H \approx -20$  J/g [17] and  $\Delta V/V \approx -2$  % [18]; and (5) converting low-temperature to high-temperature polymorphs,  $\Delta H \approx 20$  J/g and  $\Delta V/V \approx 2$  % [34, 35]. In contrast to the processes just described, the formation of NIC co-crystals exhibits a negative correlation between enthalpy and volume. Such negative correlation, however, is in common with ice melting ( $\Delta H = 335$  J/g and  $\Delta V/V = -8$  %) and water freezing.

## 17.4 Shorter and Stronger Hydrogen Bonds Are the Likely Cause for the Anomalous Formation Properties of NIC Co-crystals

The simultaneous volume expansion and energy decrease as water freezes is attributed to the formation of stronger hydrogen bonds and the frustration of close molecular packing. Given that NIC (a weak base) typically co-crystallizes with a weak acid, the co-crystal is expected to have stronger hydrogen bonds. It is possible that the anomalous formation properties of NIC co-crystals share the same structural origin as those of ice. To test this idea, we calculated the change of hydrogen-bond length upon co-crystallization as follows [16]

$$\Delta R_{\text{HB}} = \langle R_{\text{HB}} \rangle_{\text{cc}} - [m/(m+n) \langle R_{\text{HB}} \rangle_{\text{A}} + n/(m+n) \langle R_{\text{HB}} \rangle_{\text{B}}] \quad (17.6)$$

where  $\langle R_{\text{HB}} \rangle_{\text{cc}}$ ,  $\langle R_{\text{HB}} \rangle_{\text{A}}$ , and  $\langle R_{\text{HB}} \rangle_{\text{B}}$  are, respectively, the average heavy-atom-to-heavy-atom distances for all hydrogen bonds in the co-crystal  $A_mB_n$ , component crystal A, and component crystal B.

This analysis found that the formation of NIC co-crystals generally shortens the hydrogen bonds ( $\Delta R_{\text{HB}} < 0$ ). Moreover, the shortening of hydrogen bonds upon co-crystallization broadly correlates with the accompanying volume expansion (Fig. 17.7a) and energy decrease (Fig. 17.7b). These results argue that NIC co-crystals contain stronger hydrogen bonds than their component crystals and, as a result, have lower energies but fail to simultaneously achieve efficient molecular packing. The stronger hydrogen bonding is consistent with the co-crystallization of a weak base (NIC) and a weak acid (the typical co-former): on average, their hydrogen bonding should be stronger than that between the acid molecules or between the base molecules. The correlation between the lowering of crystal energy and the shortening of hydrogen bonds (Fig. 17.7b) argues that the energy decrease upon forming stronger hydrogen bonds offsets the energy increase upon forming lower-density crystals. Thus, among the various intermolecular interactions, hydrogen bonding appears to make the largest contribution to the decrease of crystal energy upon co-crystallization.

In summary, the anomalous formation properties of NIC co-crystals ( $\Delta E_f < 0$  and  $\Delta V_f > 0$ ) may result from their stronger hydrogen bonding, which lowers energy but hinders efficient molecular packing. In this respect, the formation of NIC co-crystals is analogous to other processes with negative energy–volume correlation, for example, the freezing of water and the transformation of  $\beta$ -resorcinol to  $\alpha$ -resorcinol [36]. It would be of interest to ascertain whether the same holds for other families of co-crystals (e.g., those of isonicotinamide [37]).

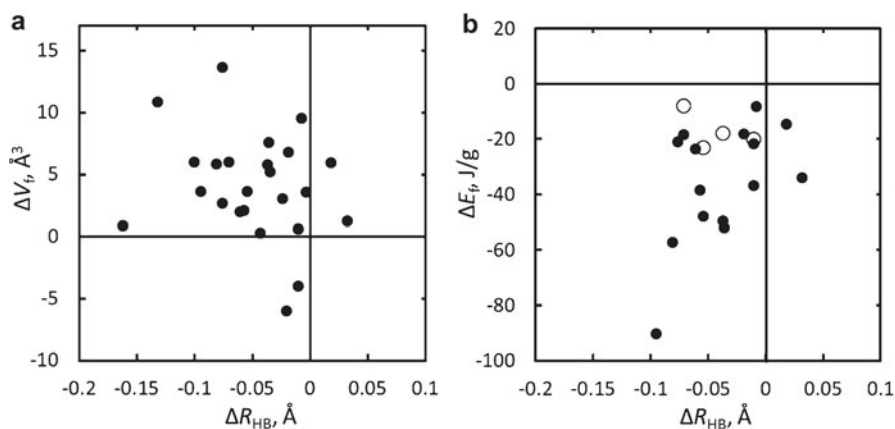


**Fig. 17.7** Correlation between  $\Delta V_f$  and  $\Delta R_{\text{HB}}$  (a) and between  $\Delta E_f$  and  $\Delta R_{\text{HB}}$  (b) of NIC co-crystals. The  $\Delta E_f$  values are both experimental (open circles,  $T = 293$  K) and calculated (solid circles,  $T = 0$  K)

## 17.5 Different Conformers of NIC Can Form Co-crystals of Comparable Stability

NIC is flexible with respect to the amide torsion relative to the pyridine ring ( $\theta_1$  in Scheme 17.1); its potential energy vs.  $\theta_1$  curve has two distinct minima: one at  $\theta_1 = \pm 160^\circ$  (Conformer 1) and the other at  $\pm 20^\circ$  (Conformer 2), with Conformer 2 being +4 kJ/mol higher in energy [15]. It is of interest to expand the study of the formation properties of NIC co-crystals and inquire whether different conformers of NIC can be used to build co-crystals and whether the resulting co-crystals have different formation properties.

Although the crystals of pure NIC (two polymorphs of known structure) contain Conformer 1 [24, 38], the co-crystals of NIC can contain both conformers (see Table 17.3 for the values of  $\theta_1$ ). The NIC conformers in co-crystals observed to date are similar to the two lowest-energy conformers in the gas phase. A given co-crystal usually contains either Conformer 1 or Conformer 2 of NIC, and only rarely are both conformers present in the same lattice [39, 40]. For the four NIC-RMA co-crystals, N<sub>4</sub>R contains Conformer 1, but the others contain Conformer 2 (Table 17.3).

In Fig. 17.8, we plot the available data to assess whether the construction of co-crystals with different NIC conformers can systematically alter their formation properties. The solid circles in Fig. 17.8 correspond to crystals in achiral space groups, which contain NIC molecules of both hands ( $+\theta_1$  and  $-\theta_1$ ) and the open circles to crystals in chiral space groups, which contain NIC molecules of one chirality ( $\theta_1$  adopts a single positive or negative value). Figure 17.8 shows that despite their different energies, the two conformers of NIC produce co-crystals of comparable formation energies and volumes. Given that Conformer 2 is 4 kJ/mol higher in energy than Conformer 1, the independence of a co-crystal's formation energy on the NIC conformation implies that the intermolecular energy (total crystal

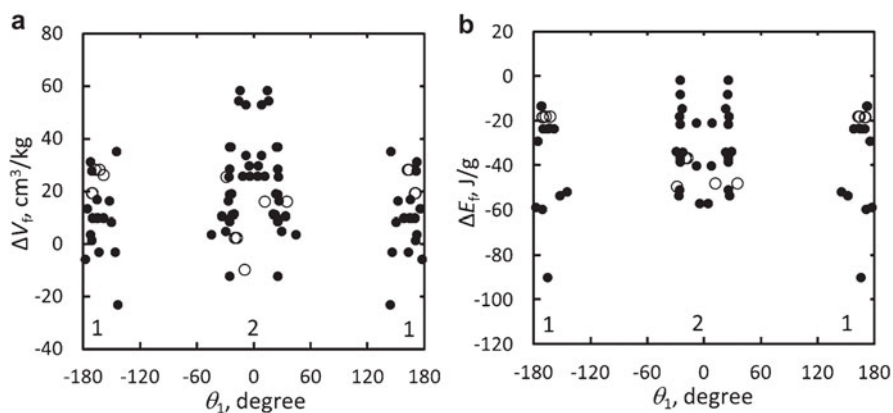


**Fig. 17.8** The effect of NIC conformation on the formation volume (a) and the formation energy (b) of NIC co-crystals. *Open circles* indicate crystals in chiral space groups

energy minus conformational energy) is in fact more negative for the co-crystals that contain the higher-energy Conformer 2 than those containing Conformer 1. The possibility of building crystals of comparable energy with a higher-energy conformer indicates the versatility of NIC in forming co-crystals and may contribute to its ability to form many co-crystals.

## 17.6 Conclusion

This study has shown that the co-crystallization of nicotinamide with a second component generally lowers energy, expands volume, and shortens hydrogen bonds. The energy decrease was experimentally determined from the melting enthalpies or computed with a dispersion-corrected DFT model, with a reasonable agreement seen between the two where comparison is possible. The volume expansion and the change of hydrogen bonds were evaluated using crystallographic data. The simultaneous expansion of volume and reduction of energy upon forming NIC co-crystals is anomalous because the two properties are positively correlated in most physical processes. We speculate that as NIC co-crystallizes with another component (often a weak acid), the resulting structure may be optimized for hydrogen bonding but fail to simultaneously achieve efficient molecular packing, in analogy with the freezing of water and the polymorphic transformation of resorcinol.

NIC is conformationally flexible, and although its own crystals are composed of the lowest-energy conformer, many NIC co-crystals contain a high-energy conformer. Despite their higher conformational energies, however, these co-crystals have comparable formation energies and volumes as those constructed with the stable conformer. This versatility of NIC to make conformational adjustments in crystallization may be partially responsible for its proficiency to form many co-crystals. It would be of interest to extend the present study to other prolific co-crystal formers.

**Acknowledgements** We thank Pfizer, the National Institute for Pharmaceutical Technology and Education (NIPTE), and the National Science Foundation (DMR 0804786, 1234320) for supporting this work. We thank our coauthors in some of the papers on which this chapter is based: Michelle Harasimowicz, Ilia Guzei, Melgardt de Villiers, Joseph Krzyzaniak, John Kendrick, and Frank Leusen.

## References

1. A. Findlay, A.N. Campbell, N.O. Smith, *Phase Rule and Its applications* (Dover Publications, Mineola, 1951)
2. C.C. Sun, Cocrystallization for successful drug delivery. *Expert Opin. Drug Deliv.* **10**, 201–213 (2013)

- O. Bolton, A.J. Matzger, Improved stability and smart-material functionality realized in an energetic cocrystal. *Angew. Chem. Int. Ed.* **50**, 8960–8963 (2011)
- D.J. Good, N. Rodríguez-Hornedo, Solubility advantage of pharmaceutical cocrystals. *Cryst. Growth Des.* **9**, 2252–2264 (2009)
- J.F. Remenar, S.L. Morissette, M.L. Peterson, B. Moulton, J.M. MacPhee, H.R. Guzman, O. Almarsson, Crystal engineering of novel cocrystals of a triazole drug with 1,4-dicarboxylic acids. *J. Am. Chem. Soc.* **125**, 8456–8457 (2003)
- S.L. Childs, L.J. Chyall, J.T. Dunlap, V.N. Smolenskaya, B.C. Stahly, G.P. Stahly, Crystal engineering approach to forming cocrystals of amine hydrochlorides with organic acids. Molecular complexes of fluoxetine hydrochloride with benzoic, succinic, and fumaric acids. *J. Am. Chem. Soc.* **126**, 13335–13342 (2004)
- S. Basavoju, D. Bostrom, S.P. Velaga, Indomethacin-saccharin cocrystal: design, synthesis and preliminary pharmaceutical characterization. *Pharm. Res.* **25**, 530–541 (2008)
- D.P. McNamara, S.L. Childs, J. Giordano, A. Iarriccio, J. Cassidy, M.S. Shet, R. Mannion, E. O'Donnell, A. Park, Use of a glutaric acid cocrystal to improve oral bioavailability of a low solubility API. *Pharm. Res.* **23**, 1888–1897 (2006)
- S. Karki, T. Friščić, L. Fabian, P.R. Laity, G.M. Day, W. Jones, Improving mechanical properties of crystalline solids by cocrystal formation: new compressible forms of paracetamol. *Adv. Mater.* **21**, 3905–3909 (2009)
- S. Chattoraj, L. Shi, C.C. Sun, Understanding the relationship between crystal structure, plasticity and compaction behaviour of theophylline, methyl gallate, and their 1:1 co-crystal. *CrystEngComm* **12**, 2466–2472 (2010)
- A.V. Trask, W.D.S. Motherwell, W. Jones, Pharmaceutical cocrystallization: engineering a remedy for caffeine hydration. *Cryst. Growth Des.* **5**, 1013–1021 (2005)
- A.V. Trask, W.D.S. Motherwell, W. Jones, Physical stability enhancement of theophylline via cocrystallization. *Int. J. Pharm.* **320**, 114–123 (2006)
- T. Friščić, W. Jones, Cocrystal architecture and properties: design and building of chiral and racemic structures by solid-solid reactions. *Faraday Discuss.* **136**, 167–178 (2007)
- D.J. Berry, C.C. Seaton, W. Clegg, R.W. Harrington, S.J. Coles, P.N. Horton, M.B. Hursthouse, R. Storey, W. Jones, T. Friščić, N. Blagden, Applying hot-stage microscopy to co-crystal screening: a study of nicotinamide with seven active pharmaceutical ingredients. *Cryst. Growth Des.* **8**, 1697–1712 (2008)
- A. Lemmerer, C. Esterhuysen, J. Bernstein, Synthesis, characterization, and molecular modeling of a pharmaceutical co-crystal: (2-chloro-4-nitrobenzoic acid)–(nicotinamide). *J. Pharm. Sci.* **99**, 4054–4071 (2010)
- S.W. Zhang, M.T. Harasimowicz, M.M. de Villiers, L. Yu, Cocrystals of nicotinamide and (*R*)-mandelic acid in many ratios with anomalous formation properties. *J. Am. Chem. Soc.* **135**, 18981–18989 (2013)
- J. Jacques, A. Collet, S.H. Wilen, *Enantiomers, Racemates, and Resolutions* (Krieger Publishing Company, Malabar, 1991)
- C.P. Brock, W.B. Schweizer, J.D. Dunitz, On the validity of Wallach's rule: on the density and stability of racemic crystals compared with their chiral counterparts. *J. Am. Chem. Soc.* **113**, 9811–9820 (1991)
- L. Yu, Polymorphism in molecular solids: an extraordinary system of red, orange, and yellow crystals. *Acc. Chem. Res.* **43**, 1257–1266 (2010)
- H.C.S. Chan, J. Kendrick, M.A. Neumann, F.J.J. Leusen, Towards ab initio screening of co-crystal formation through lattice energy calculations and crystal structure prediction of nicotinamide, isonicotinamide, picolinamide and paracetamol multi-component crystals. *CrystEngComm* **15**, 3799–3807 (2013)
- S.W. Zhang, J. Kendrick, F.J.J. Leusen, L. Yu, Cocrystallization with nicotinamide in two conformations lowers energy but expands volume. *J. Pharm. Sci.* **103**(9), 2896–2903 (2014)
- S.W. Zhang, I.A. Guzei, M.M. de Villiers, L. Yu, J.F. Krzyzaniak, Formation enthalpies and polymorphs of nicotinamide – *R*-mandelic acid co-crystals. *Cryst. Growth Des.* **12**, 4090–4097 (2012)

23. S. Aitipamula, P.S. Chow, R.B.H. Tan, Polymorphism in cocrystals: a review and assessment of its significance. *CrystEngComm* **16**, 3451–3465 (2014)
24. Y. Miwa, T. Mizuno, K. Tsuchida, T. Taga, Y. Iwata, Experimental charge density and electrostatic potential in nicotinamide. *Acta Crystallogr. B* **55**, 78–84 (1999)
25. A.O. Patil, W.T. Pennington, I.C. Paul, D.Y. Curtin, C.E. Dykstra, Reactions of crystalline (*R*)-(–)-mandelic and (*S*)-(+)-mandelic acid with amines – crystal-structure and dipole-moment of (*S*)-mandelic acid – a method of determining absolute-configuration of chiral crystals. *J. Am. Chem. Soc.* **109**, 1529–1535 (1987)
26. Y.P. Handa, G.C. Benson, Volume changes on mixing 2 liquids – review of the experimental-techniques and the literature data. *Fluid Phase Equilib.* **3**, 185–249 (1979)
27. A.K. Nandi, S.N. Bhattacharyya, Excess-enthalpies of mixing and excess heat-capacities of binary-mixtures of formic-acid and pyridine at 30 °C. *J. Chem. Eng. Data* **38**, 358–360 (1993)
28. I.J. Bruno, J.C. Cole, P.R. Edgington, M. Kessler, C.F. Macrae, P. McCabe, J. Pearson, R. Taylor, New software for searching the Cambridge Structural Database and visualizing crystal structures. *Acta Crystallogr. B* **58**, 389–397 (2002). The version used for this work is 5.34 (November 2012) with the Feb 2013 and May 2013 updates
29. J. van de Streek, S. Motherwell, New software for searching the Cambridge Structural Database for solvated and unsolvated crystal structures applied to hydrates. *CrystEngComm* **9**, 55–64 (2007)
30. C.P. Price, G.D. Glick, A.J. Matzger, Dissecting the behavior of a promiscuous solvate former. *Angew. Chem. Int. Ed.* **45**, 2062–2066 (2006)
31. M.A. Neumann, M.A. Perrin, Energy ranking of molecular crystals using density functional theory calculations and an empirical van der Waals correction. *J. Phys. Chem. B* **109**, 15531–15541 (2005)
32. A.A.K. Al-Mahdi, A.R. Ubbelohde, Melting and crystal structure. The onset of “rotation” on melting. *Proc. R. Soc. A* **220**, 143–156 (1953)
33. A.R. Hansen, C.A. Eckert, A relationship between excess volumes and enthalpies. *Fluid Phase Equilib.* **60**, 59–80 (1990)
34. A. Gavezzotti, G. Fillippini, Polymorphic forms of organic crystals at room conditions: thermodynamic and structural implications. *J. Am. Chem. Soc.* **117**, 12299–12305 (1995)
35. A. Burger, R. Ramberger, Polymorphism of pharmaceuticals and other molecular-crystals. 1. Theory of thermodynamic rules. *Mikrochimica Acta* **2**, 259–271 (1979)
36. J.M. Robertson, A.R. Ubbelohde, New form of resorcinol. I. Structure. II. Thermodynamic properties. *Proc. R. Soc. A-Math Phys* **167**, 122–147 (1938)
37. N.B. Buthori, A. Lemmerer, G.A. Venter, S.A. Bourne, M.R. Caira, Pharmaceutical co-crystals with isonicotinamide-vitamin B3, clofibric acid, and diclofenac-and two isonicotinamide hydrates. *Cryst. Growth Des.* **11**, 75–87 (2011)
38. J.J. Li, S.A. Bourne, M.R. Caira, New polymorphs of isonicotinamide and nicotinamide. *Chem. Commun.* **47**, 1530–1532 (2011)
39. A. Lemmerer, J. Bernstein, The co-crystal of two GRAS substances: (citric acid)–(nicotinamide). Formation of four hydrogen bonding heterosynthons in one co-crystal. *CrystEngComm* **12**, 2029–2033 (2010)
40. L.J. Thompson, R.S. Voguri, A. Cowell, L. Male, M. Tremayne, The co-crystal nicotinamide-succinic acid (2/1). *Acta Crystallogr. C* **66**, o421–o424 (2010)

# Chapter 18

## Isothermal Crystallization of Pharmaceutical Glasses: Toward Prediction of Physical Stability of Amorphous Dosage Forms

Kohsaku Kawakami

**Abstract** Difficulty in predicting physical stability of drug molecules during long-term storage is one of the most important issues inhibiting the wide use of amorphous solid dispersions in the pharmaceutical industry. This chapter discusses the isothermal crystallization behavior of pharmaceutical glasses. Although the crystallization time of the different compounds appears to vary widely, initiation time for crystallization can be generalized as a function of  $T_g/T$ , where  $T_g$  and  $T$  are the glass transition temperature and storage temperature, respectively, if the crystallization is governed by temperature. Compounds, in which crystallization is inhibited by a large energy barrier, exhibit better stability. For these compounds, crystallization is likely to be dominated by local pressure, and stochastic nucleation plays an important role for initiating crystallization. An example, in which an increase in the surface area and adsorption of moisture on the surface changes the dominant factor from pressure to temperature, is also presented. The dominance of either temperature or pressure is related with the nucleation mechanism. This observation should help prediction of the physical stability of amorphous pharmaceuticals and enhance the effective use of amorphous solid dispersions for poorly soluble drugs.

**Keywords** Crystallization • Physical stability • Glass transition • Surface effect

### 18.1 Introduction

Recent drug candidates are prone to have low aqueous solubility. It may be difficult to develop such compounds using conventional formulation technologies. Amorphous solid dispersion is one of the most important formulation technologies for poorly soluble drugs because it can improve their bioavailability by aiding the

---

K. Kawakami (✉)

International Center for Materials Nanoarchitectonics, National Institute for Materials Science,  
1-1 Namiki, Tsukuba, Ibaraki 305-0044, Japan

e-mail: [kawakami.kohsaku@nims.go.jp](mailto:kawakami.kohsaku@nims.go.jp)

© Springer Japan 2015

R. Tamura, M. Miyata (eds.), *Advances in Organic Crystal Chemistry*,

DOI 10.1007/978-4-431-55555-1\_18

355

**Table 18.1** Properties of good glass formers

Chemical structure	Physicochemical property
Large molecular weight	Large melting enthalpy/entropy
Few benzene rings	High melting temperature
Low symmetry	Large crystal/amorphous energy difference
Many rotatable bonds	Large fragility
Many branches	Large $T_g/T_m$
Many electronegative atoms	Large viscosity above $T_g$
Strong molecular interaction	Low molecular mobility

$T_g$  Glass transition temperature,  $T_m$  Melting temperature

dissolution process [1–3]. However, while their effectiveness is widely recognized by industrial researchers, the number of marketed oral amorphous formulations is still limited. A major issue for the use of amorphous dosage forms is the concern about their physical/chemical stability [3]. Because the amorphous solids are in an energetically higher state than crystalline solids, their chemical reactivity is also higher. In addition, their physical transformation to the crystalline solids must be prevented for assuring efficacy of the amorphous solids. However, a methodology for evaluating their long-term storage stability has not been established yet, and this can be a serious issue during developmental study of amorphous dosage forms [3, 4]. Therefore, a deeper understanding of the crystallization of organic compounds is required to widen the use of amorphous solid dispersion technology in the pharmaceutical industry.

Many attempts have been made to find a general rule that can describe the crystallization tendencies of various organic compounds. Table 18.1 lists the suggested characteristics of good glass formers, that is, the compounds that can easily be transformed to the amorphous state. Requirements for chemical structures of good glass formers include a large molecular weight, low number of benzene rings, low level of molecular symmetry, many rotatable bonds, branched carbon skeletons, and many electronegative atoms [5–7]. Also, the physicochemical characteristics of good glass formers include a large melting enthalpy/entropy, large free-energy difference between the crystalline and amorphous states, and high melting temperature [6]. Fragility may be another factor influencing the crystallization ability of compounds [6, 8]. However, even with this information, quantitative prediction of the crystallization behavior of a specific compound is not possible. Moreover, much of the information as presented above has been obtained by observing crystallization during cooling from the melt (i.e., hot crystallization); this behavior is completely different from the isothermal crystallization behavior, which is of great interest to formulators.

The crystallization is a process still full of mysteries. However, at least the constituent molecules need to diffuse and/or orient for inducing the nucleation, which is followed by the crystal growth. Both thermal energy and molecular packing, which are governed by temperature and local pressure, respectively,

influence the dynamics of molecules in the glassy state [9, 10]. During cooling from the melt, both of these factors continuously change, whereas during isothermal crystallization, fluctuations in the local energy required to overcome the energy barrier for crystallization are important. The isothermal crystallization behavior of pharmaceutical compounds is discussed below, with a focus on the derivation of a general rule to predict crystallization time of pharmaceutical compounds.

## 18.2 Temperature- and Pressure-Controlled Crystallization

Amorphous state is thermodynamically unstable and tends to transform to a stable, crystalline state. Nucleation is the first step in this transformation. If the energy barrier for nucleation can be ignored because of little steric hindrance, the crystallization behavior should be dominated by the free-energy difference between the crystalline and amorphous states, which can be described as a function of temperature only under ambient pressure conditions. This is a situation where the system is temperature controlled. In this case, if the melt is cooled from the melting temperature, crystallization should occur at the same temperature, regardless of the cooling rate. Nucleation is expected to proceed homogeneously because no templates are required. Figure 18.1a shows differential scanning calorimetry (DSC) cooling curves for haloperidol [11]. Crystallization always occurred at 100 °C, regardless of the cooling rate, and thus was clearly a temperature-controlled process. Figure 18.1b shows cooling curves for tolbutamide (TLB) [11], in which the crystallization temperature was determined based on the competition of thermodynamic (temperature) and kinetic (cooling rate) factors. In this case, the influence of the energy barrier to crystallization cannot be ignored. A higher energy barrier inhibits crystallization during the cooling process, as shown in Fig. 18.1c. Acetaminophen (AAP) did not crystallize during the cooling process; however, crystallization was observed during subsequent reheating. In the case of loratadine (LTD) (Fig. 18.1d), crystallization was not observed even during reheating, for which local pressure seemed to dominate the crystallization behavior. Thus, the crystallization behaviors appear to depend significantly on the compound species.

Taylor et al. proposed a classification system for crystallization tendencies after observing crystallization behaviors during the cooling and reheating of various compounds in the DSC measurements [6, 12]. In their classification system, the crystallization behaviors presented in Fig. 18.1a–d are classified as classes Ia, Ib, II, and III, respectively. Although the original purpose of the system was discrimination of the crystallization tendencies during cooling/heating processes, this classification system also appears to be useful for evaluating whether temperature or pressure is the dominant factor influencing the crystallization process. Particularly, class Ia molecules can be regarded as temperature-controlled compounds, whereas class III compounds are classified as pressure-controlled ones. The behaviors of classes Ib and II compounds are caused by the competition between temperature and pressure

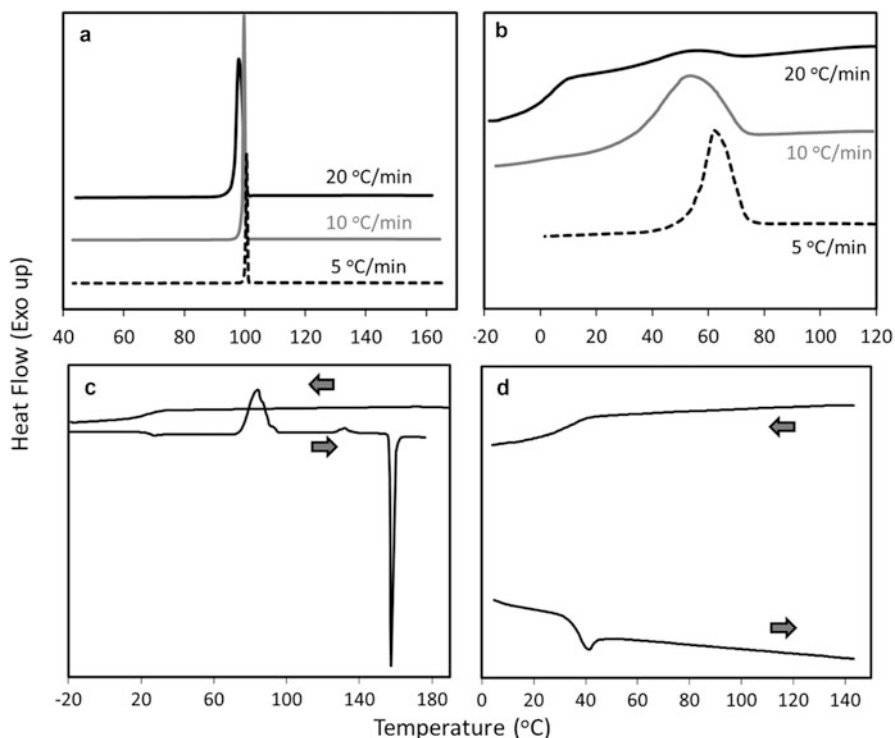


**Fig. 18.1** DSC cooling/heating curves for (a) haloperidol (HPD), (b) tolbutamide (TLB), (c) acetaminophen (AAP), and (d) loratadine (LTD). For HPD and TLB, only the cooling curves after melting are presented. Cooling rates are indicated in the figure. For AAP and LTD, the heating and subsequent cooling curves (10 °C/min) are presented

factors. The relative importance of temperature and pressure should be the same for isothermal crystallization of a given compound.

## 18.3 Isothermal Crystallization Without Surface Effects

### 18.3.1 Experimental Protocol

It is frequently reported that surfaces play an important role in crystallization behavior. Thus, the surface areas of the amorphous samples used in the following experiments were minimized using quenched samples in DSC [13]. Briefly, the crystalline samples were melted by heating them above their glass transition temperatures, followed by rapid cooling at 50 °C/min. The obtained samples were stored in sealed DSC pans at various temperatures under dried conditions. Crimped pans were used for nifedipine (NDP), because its crystallization behavior is highly

sensitive to residual/atmosphere moisture. Annealing was performed in DSC for the storage period of less than 48 h, and temperature-controlled ovens were used for storage periods greater than 48 h.

### 18.3.2 Determination of Crystallinity

The crystallinities of the stored samples, which can crystallize during the heating process of the DSC measurements, were determined from the crystallization enthalpies. Figure 18.2 shows the DSC heating curves for TLB. The quenched TLB (initial sample) crystallized as form IV at ca. 50 °C during heating with an exothermic enthalpy of ca. 72 J/g. The crystal form was revealed by the x-ray powder diffraction (XRPD) analysis. During the isothermal storage at 30 °C, the TLB glass gradually crystallized to the same crystal form, form IV. The heating curve of the TLB stored at 30 °C for 45 min is also shown in Fig. 18.2. A small exothermic peak can be seen at ca. 40 °C due to crystallization of the remaining

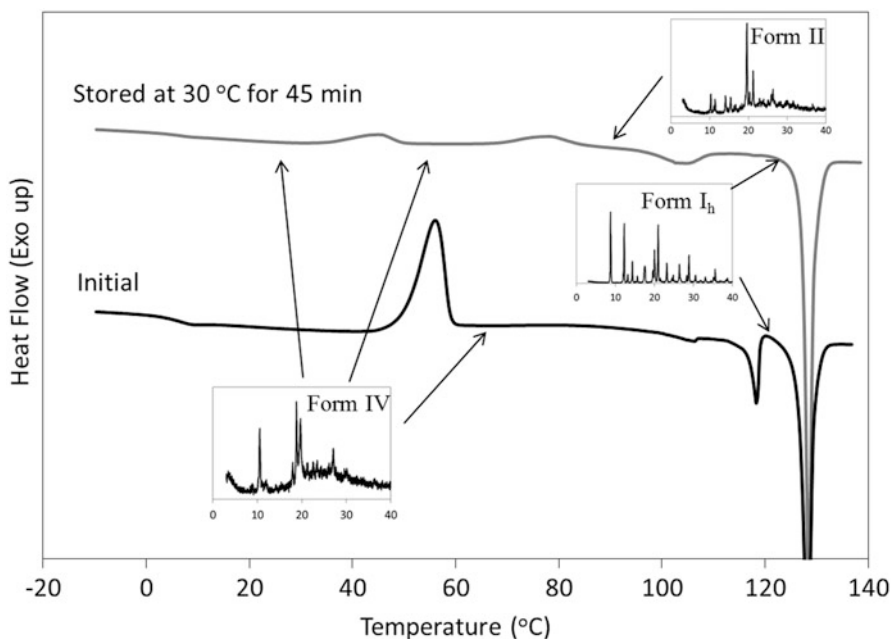


**Fig. 18.2** DSC heating curves (10 °C/min) for quenched (denoted as initial) and annealed (stored) TLB. The quench was performed in the DSC at a rate of 50 °C/min. The annealing was also achieved in the DSC at 30 °C for 45 min. XRPD patterns of the samples at the indicated points are also presented in the figure

amorphous part as form IV. The crystallinity,  $X$ , of the stored amorphous sample was calculated using the following equation:

$$X (\%) = 100 \left\{ \frac{\Delta H}{\Delta H_q - \int_T^{T_q} \Delta C_p} \right\}, \quad (18.1)$$

where  $\Delta H$  and  $\Delta H_q$  are the crystallization enthalpies of the stored and initial samples, respectively,  $T$  and  $T_q$  are their corresponding crystallization temperatures, and  $\Delta C_p$  is the difference in heat capacities of the amorphous and crystalline forms. Note that powder samples did not produce reproducible heat capacity values, presumably due to gas phases in the powders that can influence the measured heat capacities and thermal homogeneity in the samples [14]. Thus, the quenched glasses were used to determine the heat capacities of the amorphous states. Crystalline samples were prepared by partially melting the crystalline powders at just below the melting temperature and then allowing recrystallization using the residual crystal as a template. The crystallinities of TLB, chlorpropamide (CPA), and AAP were evaluated by this procedure.

NDP exhibited polymorphic transformation immediately after crystallization, and its exothermic peak overlapped with the crystallization peak, preventing precise determination of its crystallization enthalpy. In this case, a shift in the baseline due to partial crystallization could be used to estimate the crystallinity:

$$X (\%) = 100 (W - W_a) / \Delta W, \quad (18.2)$$

where  $W$  is the heat flow of the stored sample obtained by the heating and  $W_a$  is that of the amorphous reference obtained during subsequent reheating. Due to partial crystallization, the heat capacity of the annealed sample ranged between those of the crystalline and amorphous samples, depending on the crystallinity.  $\Delta W$  is the difference in the heat flows of the amorphous and crystalline samples.

For compounds that do not undergo crystallization and exhibit only melting behavior, crystallinity was calculated from the melting enthalpy. This procedure was applicable to ritonavir (RTV) and loratadine (LTD). The crystallinity,  $X$ , was calculated using the following equation:

$$X (\%) = 100 \left( \frac{H_m}{H_{mi}} \right) \left( \frac{H_{m-m}}{H_{m-s}} \right), \quad (18.3)$$

where  $H_m$ ,  $H_{mi}$ ,  $H_{m-m}$ , and  $H_{m-s}$  are the melting enthalpy of the stored sample, that of the sample before quenching, the theoretical melting enthalpy of the observed crystal form, and that of the initial crystalline form. In the case of quenched RTV, the initial crystalline powder was of form II, and the quenched glass crystallized as form IV. LTD crystallized to a stable form below 30 °C and to a metastable form above 50 °C.

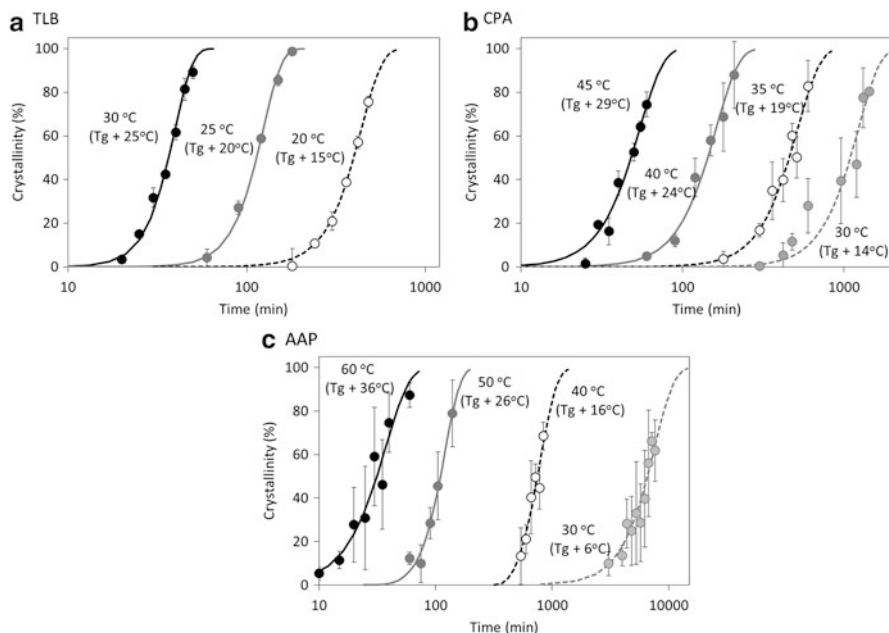


**Fig. 18.3** Evolution of the crystallinity of quenched TLB, CPA, and AAP as a function of time at the indicated temperatures. Each data point represents the average of at least three measurements, and the *error bars* indicate the standard deviations. The fitting lines were drawn using the Avrami-Erofeev equation

### 18.3.3 Analysis of the Crystallization Process

The isothermal crystallization process was analyzed using the Avrami-Erofeev equation as shown below:

$$X(\%) = 100 [1 - \exp \{-k(t - d)^n\}], \quad (18.4)$$

where  $k$  and  $d$  are the crystallization rate and induction time, respectively, and  $n$  is the Avrami exponent determined by the dimension of the crystal growth and nucleation mechanism. Figure 18.3 shows the crystallization curves for TLB, CPA, and AAP at various temperatures. In all cases, evolution of the crystallinity was explained well using the Avrami-Erofeev equation. Figure 18.4 shows the time when crystallinity reached 10 %,  $t_{10}$ , as a function of the reduced temperature,  $T_g/T$ . The parameter  $t_{10}$  is referred to as the initiation time hereafter. Note that the induction time,  $d$ , is a more reasonable parameter for describing the time when crystallization begins; however, the reliability of  $d$  obtained from fitting of the Avrami equation is generally problematic because of the shape of the logarithmic function. In addition

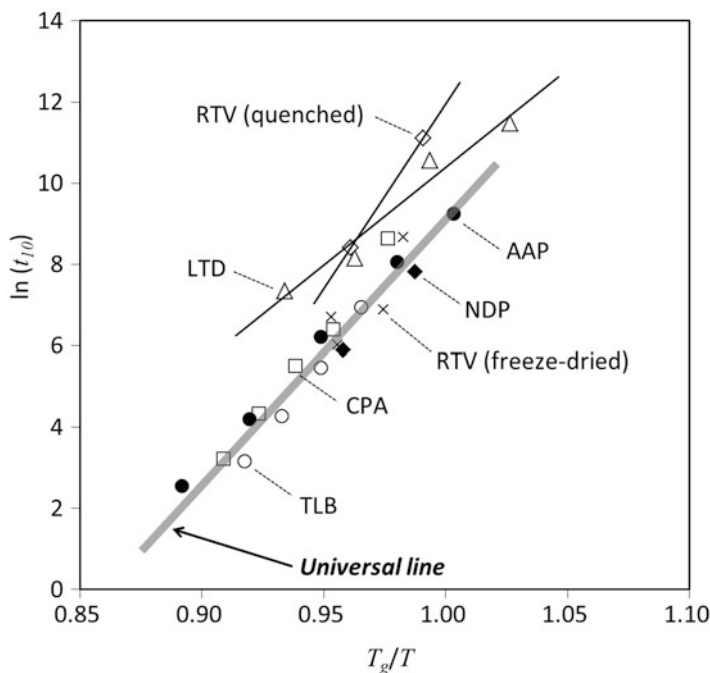


**Fig. 18.4** Ten percent crystallization time (initiation time, min) as a function of  $T_g/T$  for various model compounds [13, 19]. The fitting line (“universal line”) was drawn for TLB (○), CPA (□), AAP (●), and NDP (◆), which exhibited temperature-dominated crystallization

to its higher reliability, the advantage of using  $t_{10}$  values is that their validity can easily be judged by interpolation of the experimental data around 10 % crystallinity.

The  $t_{10}$  data for the compounds exhibiting temperature-controlled crystallization behavior fell on the same line (denoted as the “universal line”), at least above their  $T_g$  values. Thus, the initiation time for these compounds can be described as a function of  $T_g$  only. The line passes through approximately  $\ln(t_{10}) = 9$  at  $T_g/T = 1$ , indicating that compounds exhibiting temperature-controlled crystallization should begin crystallizing in 6 days at their  $T_g$ . Although this value has a deviation of approximately one order, there is demonstrable universality in the initiation time, regardless of the compound species. The initiation times for RTV and LTD were significantly longer. Because crystallization of both compounds was dominated by pressure, their slow crystallization can be explained in terms of large energy barriers due to structural frustration. In addition, the Avrami exponents for the compounds with temperature-controlled crystallization were generally larger than those for pressure-controlled compounds [13]. This fact suggested that nucleation of the temperature-controlled compounds tended to occur homogeneously, whereas that of the pressure-controlled compounds is initiated heterogeneously. As the relatively low reproducibility in crystallization of the latter compounds suggested

that the crystallization should have been initiated by stochastic nucleation, the heterogeneous nucleation seems to be reasonable mechanism.

## 18.4 Influence of Surface Effects on Crystallization Behavior

### 18.4.1 Role of Surface in Crystallization Behavior

In the above investigation, the surface areas of the glasses were minimized, and their contact with moisture was avoided. However, there have been many examples in which surface have played an important role in crystallization behavior. Generally, a decrease in the particle size enhances crystallization due to an increase in the surface area [15, 16]. Conversely, the presence of a surface coating is known to effectively inhibit crystallization [17, 18]. Thus, surface effects must be considered for predicting the crystallization behavior of practical formulations. In the following study, a pharmaceutical glass was prepared via freeze drying [19], which typically produces glasses with surface areas much greater than 1 m<sup>2</sup>/g.

### 18.4.2 Experimental Protocol

RTV was used as a model compound for observing the surface effects. It was dissolved in *t*-butyl alcohol, followed by freezing at  $-20\text{ }^{\circ}\text{C}$ , and then subjected to primary drying at ambient temperature for 24 h. Secondary drying was subsequently performed at  $40\text{ }^{\circ}\text{C}$  for 30 min. The samples were stored under both dry and two levels of relative humidity (RH) conditions that were achieved using desiccators with silica gel at  $50\text{ }^{\circ}\text{C}$ , saturated potassium acetate solution (23 %RH), and saturated magnesium nitrate solution (48 %RH). The chemical stability during the storage was confirmed to be negligible. The crystallinity was evaluated in the same manner as that for the quenched glasses.

### 18.4.3 Analysis of Crystallization Process

The  $T_g$  of the quenched RTV was approximately  $47.0\text{ }^{\circ}\text{C}$  (onset temperature), whereas that for the freeze-dried glass decreased to  $44.4\text{ }^{\circ}\text{C}$ . Because the moisture was removed prior to the DSC measurements, this decrease in the  $T_g$  value should be caused by surface molecules with high molecular mobility and/or less condensed structure. After storage of the freeze-dried glass at 22 % and 48 % RH,  $T_g$  further decreased to  $41.8$  and  $35.7\text{ }^{\circ}\text{C}$ , respectively. Figure 18.5 shows a comparison of the crystallization behavior of the quenched and freeze-dried glasses. It can

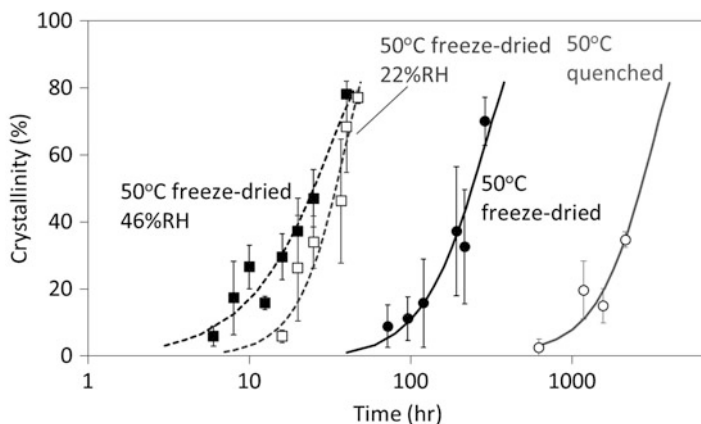


**Fig. 18.5** Evolution of the crystallinity of quenched and freeze-dried RTV as a function of time at the indicated temperatures and humidities [19]

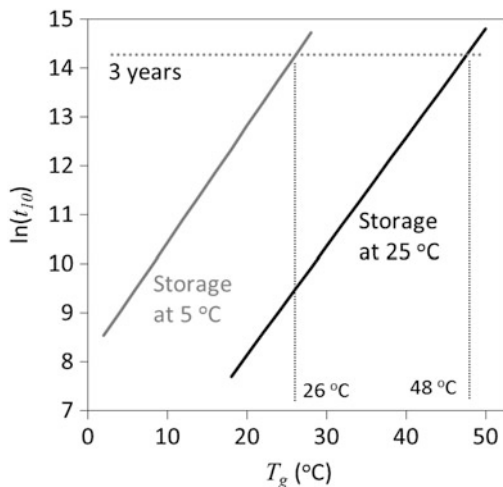
be observed that the freeze-dried samples began crystallizing more rapidly than the quenched samples. The crystallization became faster as the storage humidity increased. Therefore, it is obvious that the decrease in the  $T_g$  values of the samples led to shortening of the initiation period.

The  $t_{10}$  values for the freeze-dried samples are also plotted in Fig. 18.4. Despite the slower crystallization of the quenched RTV compared to the temperature-controlled compounds, the  $t_{10}$  values for the freeze-dried RTV samples fell on the universal line. These results indicate that the increase in mobility of the surface molecules resulted in overcoming the energy barrier inhibiting the temperature-controlled crystallization. Furthermore, these results support the existence of a universal line that should be applicable for crystallizations in which the energy barrier for nucleation is assumed to be small.

## 18.5 Prediction of the Physical Stability of Pharmaceutical Glasses

If a trace amount of crystals exists in an amorphous formulation, it significantly enhances crystallization after dispersion to the aqueous medium. Thus, the presence of 10 % crystalline material is sufficient to ruin the advantage of an amorphous dosage form. The results of the present investigation provided a general idea for quantitatively predicting the initiation time of crystallization of an amorphous solid. Figure 18.6 shows the initiation times as a function of  $T_g$  for the compounds wherein crystallization is dominated by temperature. From the graph, it can be stated that  $T_g$  must be higher than 48 or 26 °C for successful storage at 25 or 5 °C for 3 years, respectively. The differences between the critical  $T_g$  and storage temperatures are

**Fig. 18.6** Initiation time for temperature-controlled crystallization as a function of glass transition temperature. The universal line in Fig. 18.4 was used for the calculations, assuming storage at 5 °C or 25 °C [13]



23 and 21 °C, respectively. Amorphous materials have been considered to be stable if stored below  $T_g - 50$  °C [2, 3] which is roughly consistent with the Kauzmann temperature. Our calculations provide more concrete and optimistic idea compared to this rule. For pressure-controlled compounds, greater stability may be expected. The initiation time for temperature-controlled compounds can be regarded as the worst case for pressure-controlled compounds. It should be noted that the “universal line” was basically drawn using the data obtained at temperatures above  $T_g$ . The validity of its extrapolation to lower temperatures requires further investigation.

## 18.6 Relevance to Formulation Stability

The formulation stability of amorphous solid dispersions should be much greater than that of the glass compounds. In this chapter, only the crystallization of the glass compounds was discussed which can be regarded as the worst case for formulation stability. The miscibility of a drug substance with excipients is a property of greater importance that influences the formulation stability and can basically be predicted using the Flory-Huggins equation shown below.

$$\frac{\Delta G_i}{kT} = \phi_d^i \ln \phi_d^i + \frac{\phi_p^i}{N} \ln \phi_p^i + \chi \phi_d^i \phi_p^i \quad (18.5)$$

where  $\Delta G_i$ ,  $\phi_d^i$ , and  $\phi_p^i$  are the mixing free energy, drug fraction, and excipient (polymer in many cases) fraction of phase  $i$ , respectively.  $\chi$  is the interaction parameter between the drug and the polymer and is  $<0.5$  when they are miscible. However, the value for the combination of a poorly soluble drug and hydrophilic

polymer is likely to be  $>0.5$ . The parameters  $k$  and  $N$  are the Boltzmann constant and segment number of the polymer molecule, respectively. If phase separation occurs, the overall mixing free energy  $\Delta G$  can be calculated as follows:

$$\Delta G = x_d \Delta G_d + x_p \Delta G_p \quad (18.6)$$

where the subscripts  $d$  and  $p$  represent the drug- and polymer-rich phases, respectively.  $x$  represents the fraction of each phase. Generally, crystallization is considered to be initiated in the drug-rich phase. To avoid phase separation, the drug content is typically kept below 30 %. Note that the actual amorphous solid dispersion may not be in the metastable state expected based on thermodynamics. For example, phase separation may be enhanced in the case of spray-dried products due to freezing of the dynamic structure during evaporation of the solvent [20].

Although molecular-level mixing between drug and excipient molecules is expected for stable amorphous formulations, current analysis techniques only allow investigation of miscibility on larger scales. For example, DSC is typically evaluating miscibility on a 10–100 nm scale [20]. Solid-state nuclear magnetic resonance may evaluate smaller-scale miscibility; nevertheless, the lower limit remains a few nanometers. In addition, miscibility can change during storage and even during analysis [21]. If clusters of drug molecules that may have a size of nano-order exist in the formulation, the formulation stability may be nearly equal to that of the pure drug, which can be predicted as described above.

Despite the complicated nature of formulations, a deep understanding of the crystallization behavior of drug molecules identified for developmental study is important. Because amorphous solid dispersion is not the only option for the development of poorly soluble drugs, selection of the formulation type may be influenced by information about the crystallization behavior of the candidate molecule. Such knowledge of molecules should help improve the risk assessment of the storage stability of amorphous dosage forms. Thus, finding a general rule for isothermal crystallization should greatly enhance the development of poorly soluble drugs in the pharmaceutical industry.

## 18.7 Summary

To date, crystallization of pharmaceutical glasses has been discussed on a case-by-case basis. Herein, a general idea on isothermal crystallization behavior was presented. It was found that the initiation time for crystallization can be expressed as a function of  $T_g/T$  if the crystallization is dominated by temperature. Compounds for which crystallization is dominated by local pressure are expected to exhibit better stability. Surface effects, i.e., an increase in the surface area and adsorption of moisture on the surface, were found to change the dominant influencing factor for crystallization from pressure to temperature using the RTV glass as a model compound. The nucleation mechanism depended on whether temperature or

pressure dominated the crystallization process. These observations should make it easier to predict the physical stability of amorphous formulations, thus enhancing the effective use of amorphous solid dispersions for poorly soluble drugs.

**Acknowledgments** This work was in part supported by World Premier International Research Center (WPI) Initiative on Materials Nanoarchitectonics, MEXT, Japan.

## References

1. A.T.M. Serajuddin, Solid dispersion of poorly water-soluble drugs: early promises, subsequent problems, and recent breakthroughs. *J. Pharm. Sci.* **88**, 1058–1066 (1999)
2. L. Yu, Amorphous pharmaceutical solids: preparation, characterization and stabilization. *Adv. Drug Deliv. Rev.* **48**, 27–42 (2001)
3. K. Kawakami, Modification of physicochemical characteristics of active pharmaceutical ingredients and application of supersaturatable dosage forms for improving bioavailability of poorly absorbed drugs. *Adv. Drug Deliv. Rev.* **64**, 480–495 (2012)
4. C. Bhugra, M.J. Pikal, Role of thermodynamic, molecular, and kinetic factors in crystallization from the amorphous state. *J. Pharm. Sci.* **97**, 1329–1349 (2008)
5. T. Miyazaki, S. Yoshioka, Y. Aso, T. Kawanishi, Crystallization rate of amorphous nifedipine analogues unrelated to the glass transition temperature. *Int. J. Pharm.* **336**, 191–195 (2007)
6. J.A. Baird, B. van Eerdenbrugh, L.S. Taylor, A classification system to assess the crystallization tendency of organic molecules from undercooled melts. *J. Pharm. Sci.* **99**, 3787–3806 (2010)
7. D. Mahlin, S. Ponnambalam, M.H. Hockerfeit, C.A.S. Bergstrom, Toward in silico prediction of glass-forming ability from molecular structure alone: a screening tool in early drug development. *Mol. Pharm.* **8**, 498–506 (2011)
8. O.N. Senkov, Correlation between fragility and glass-forming ability of metallic alloys. *Phys. Rev. B* **76**, 104202 (2007)
9. K. Kawakami, M.J. Pikal, Calorimetric investigation of the structural relaxation of amorphous materials: evaluating validity of the methodologies. *J. Pharm. Sci.* **94**, 948–965 (2005)
10. A. Adjanowicz, A. Grzybowski, K. Kaminski, M. Paluch, Temperature and volume effect on the molecular dynamics of supercooled ibuprofen at ambient and elevated pressure. *Mol. Pharm.* **8**, 1975–1979 (2011)
11. K. Kawakami, T. Usui, M. Hattori, Understanding the glass-forming ability of active pharmaceutical ingredients for designing supersaturating dosage forms. *J. Pharm. Sci.* **101**, 3239–3248 (2012)
12. J.A. Baird, D. Santiago-Quinonez, C. Rinaldi, L.S. Taylor, Role of viscosity in influencing the glass-forming ability of organic molecules from the undercooled melt state. *Pharm. Res.* **29**, 271–284 (2012)
13. K. Kawakami, T. Harada, K. Miura, Y. Yoshihashi, E. Yonemochi, K. Terada, H. Moriyama, Relationship between crystallization tendencies during cooling from melt and isothermal storage: toward a general understanding of physical stability of pharmaceutical glasses. *Mol. Pharm.* **11**, 1835–1843 (2014)
14. T. Harada, K. Kawakami, Y. Yoshihashi, E. Yonemochi, K. Terada, H. Moriyama, Practical approach for measuring heat capacity of pharmaceutical crystals/glasses by modulated-temperature DSC. *Chem. Pharm. Bull.* **61**, 315–319 (2013)
15. K.J. Crowley, G. Zografis, The effect of low concentrations of molecularly dispersed poly(vinylpyrrolidone) on indomethacin crystallization from the amorphous state. *Pharm. Res.* **20**, 1417–1422 (2003)

16. T. Wu, L. Yu, Surface crystallization of indomethacin below T<sub>g</sub>. *Pharm. Res.* **23**, 2350–2355 (2006)
17. T. Wu, Y. Sun, N. Li, M.M. de Villiers, L. Yu, Inhibiting surface crystallization of amorphous indomethacin by nanocoating. *Langmuir* **23**, 5148–5153 (2007)
18. S. Zhang, K. Kawakami, M. Yamamoto, Y. Masaoka, M. Kataoka, S. Yamashita, S. Sakuma, Coaxial electrospray formulations for improving oral absorption of a poorly water-soluble drug. *Mol. Pharm.* **8**, 807–813 (2011)
19. K. Kawakami, Surface effect on crystallization of ritonavir glass. *J. Pharm. Sci.* **104**(1), 276–279 (2015)
20. K. Kawakami, Y. Hasegawa, K. Deguchi, S. Ohki, T. Shimizu, Y. Yoshihashi, E. Yonemochi, K. Terada, Competition of thermodynamic and dynamic factors during formation of multicomponent particles via spray drying. *J. Pharm. Sci.* **102**, 518–529 (2013)
21. K. Kawakami, Miscibility analysis of particulate solid dispersions prepared by electrospray deposition. *Int. J. Pharm.* **433**, 71–78 (2012)

**Part V**  
**Chirality**

# Chapter 19

## Twofold Helical Molecular Assemblies in Organic Crystals: Chirality Generation and Handedness Determination

Mikiji Miyata and Ichiro Hisaki

**Abstract** Conventionally, twofold helical molecular assemblies in organic crystals have been considered from space groups but not from space geometry, leading to an obscure understanding of their chirality generation. The reason is that identical twofold helical assemblies are obtained by twofold screw operations with clockwise or anticlockwise rotations by  $180^\circ$ , while enantiomeric twofold helical assemblies are observed even from achiral molecules. On the basis of three-dimensional space geometry, we succeeded in exposing chirality which has been hidden for a long time. The key for the success consists of the following two methods: one is multipoint approximation with lines and faces for representing materials and the other is tilt alignments along a helical axis for discriminating chirality and handedness. These methods proved generation of real chirality in twofold helical assemblies of organic molecules and further led us to the fact that the twofold helices exhibit three-axial chirality toward right-to-left, up-to-down, and in-to-out directions. Such helices are bundled together in various ways to provide crystals with the corresponding space groups. The bundling of only one-handed preferred helices affords one-handed crystals, explaining chiral crystallization of achiral molecules from a geometrical viewpoint.

**Keywords** Twofold helices • Chirality generation • Handedness determination • Three-axial chirality • Bundles • Chiral crystallization

---

M. Miyata (✉)

The Institute of Scientific and Industrial Research, Osaka University, 8-1 Mihogaoka, Ibaraki, Osaka 567-0047, Japan

e-mail: [miyata@mls.eng.osaka-u.ac.jp](mailto:miyata@mls.eng.osaka-u.ac.jp)

I. Hisaki

Department of Material and Life Science, Graduate School of Engineering, Osaka University, 2-1 Yamadaoka, Suita, Osaka 565-0871, Japan

e-mail: [hisaki@mls.eng.osaka-u.ac.jp](mailto:hisaki@mls.eng.osaka-u.ac.jp)

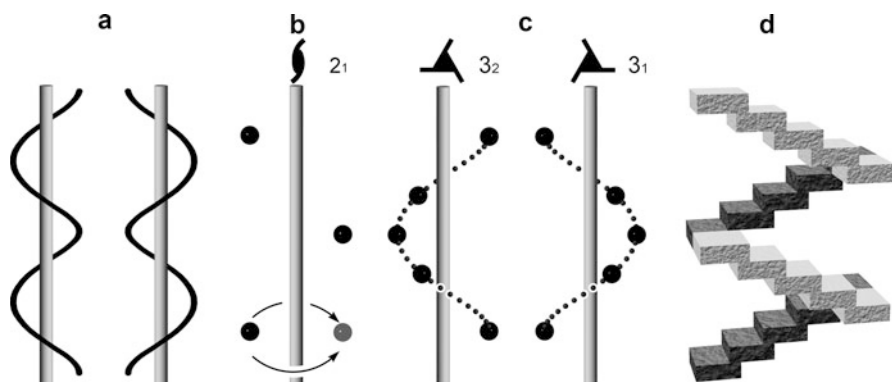


**Fig. 19.1** Handedness of helices: continuous helix (a), discontinuous twofold (b) and threefold (c) helical assemblies of points, and twofold helical stairs in daily life (d)

## 19.1 Introduction

In daily life, we see continuous helices with curved lines, such as helical stairs, springs, and vines [1]. At a molecular level, such helices are available in biopolymers, such as proteins, DNA, polysaccharides, as well as various synthetic polymers. Right- and left-handedness of these helices are clearly discriminated in appearance (Fig. 19.1a) [2]. On the other hand, discontinuous helices are defined by symmetry operations in mathematics. Such helices of materials seldom appear in daily life, but are fulfilled in supramolecules [3], especially in crystals at a nanometer level [4]. The organic crystals have regular molecular arrangements with repeated unit distances. Such arrangements are mathematically elucidated with symmetry operations in space groups [5]. Historically, crystallographic theory lists 230 space groups in the International Tables for Crystallography, Volume A: Space-Group Symmetry [6].

The Tables describe handedness of the discontinuous helices in crystals. A typical example is cited as follows: the twofold helix with rotations by  $180^\circ$  has only one notation,  $2_1$ , without handedness (Fig. 19.1b), while a threefold helix has a pair of notations,  $3_1$  for right-handedness and  $3_2$  for left-handedness (Fig. 19.1c) [7]. For this reason, many people believe that the twofold helices exhibit no handedness. On the other hand, three-dimensional space geometry has a clear method for generating chirality and determining handedness [8]. For example, stairs in daily life can be easily discriminated in handedness (Fig. 19.1d). Analogically, we determined handedness of twofold helical assemblies of benzene molecules [9, 10]. This analogy induced the idea that helical chirality should be ascertained by three-dimensional space geometry rather than the space group theory. If so, the other possible logic would become a beacon light as follows: the space group theory tells us only an existence of the twofold screw (or helix) symmetry operation, but does not mention

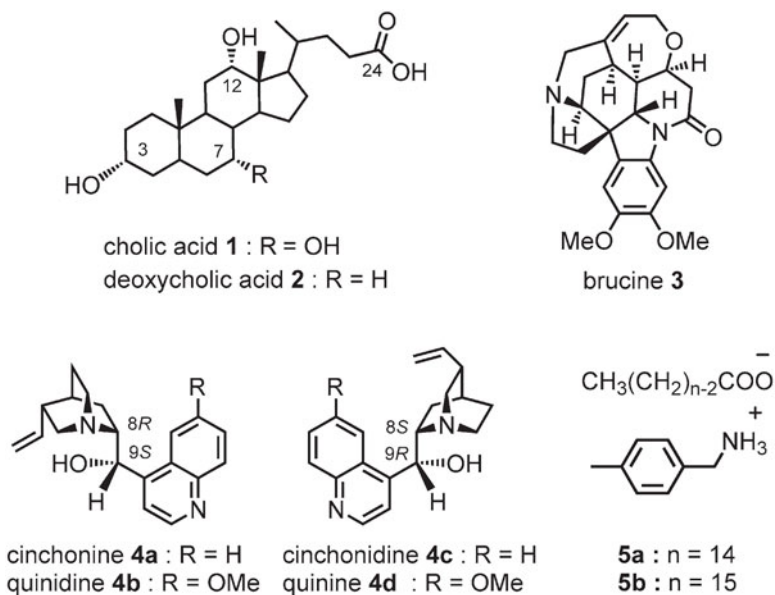
the handedness of the resulting twofold helical assemblies. Such assemblies may exhibit either handedness or non-handedness, depending on molecular arrangements.

As for the twofold helices, two important experimental things are well known, but still less well understood: one is that a vast amount of organic crystals include the twofold helices [11]. Actually, the Cambridge Structural Database involves over 600,000 data till January 2013 [12]. Over 70 % of them belong to space groups with twofold helices, such as  $P2_1/c$ ,  $P2_1$ ,  $P2_12_12_1$ . The other is that chiral crystals can be obtained from achiral molecules. Racemic molecules sometimes form chiral crystals, termed as racemic conglomerates, instead of racemic crystals [13]. Similarly, achiral molecules sometimes afford the conglomerates which exhibit the so-called mirror-image Cotton effects in circular dichroism (CD) spectra [14]. It is noteworthy that occurrence probability of the conglomerates amounts into about 8 % [15].

As mentioned above, the twofold helices embrace the contradiction regarding chirality generation and handedness determination. We have challenged to clarify the unsolved subject, focusing on space geometry rather than space group. This is because chirality belongs to a general subject in three-dimensional material world, rather than crystalline world. This chapter deals with dissolution of the lengthy unsolved problems of the twofold helices. As described below, the solution has come from multipoint approximation of materials as well as tilt alignments along a helical axis.

## 19.2 Development of Our Research for Twofold Helical Assemblies

Our primary study on twofold helices dates back to about 30 years ago, when we discovered inclusion compounds of cholic acid (Scheme 19.1–1) with a variety of organic substances [16, 17]. Their crystals have bilayered structures of the chiral hosts and one-dimensional arrays of guests in channels. These structures were compared with those of deoxycholic acid (Scheme 19.1–2). The formers mostly belong to space group  $P2_1$ , while the latter to  $P2_12_12_1$ . At that time, it fascinated us that only one oxygen atom causes the different space groups between the two host molecules, like DNA and RNA. Their twofold helical assemblies were examined from asymmetric molecular structures of the hosts [18, 19]. The steroidal molecules have facial structures with three-axial chirality toward the following three directions: head-to-tail, belly-to-back, and right-to-left (Fig. 19.2a). In addition, the resultant assemblies have tilt alignments to a helical axis, enabling us to determine right- or left-handedness of the twofold helical assemblies (Fig. 19.2b). The handedness determination gave rise to the idea that the helices also exhibit three-axial chirality toward the up-to-down, in-to-out, and right-to-left directions along the axis. In this way, three-axial chirality of the host molecules was linked to that of the



**Scheme 19.1** Molecular structures of cholic acid **1**, deoxycholic acid **2**, brucine **3**, four kinds of *Cinchona* alkaloids **4a–4d**, and organic salts of 4-methylbenzylamine with myristic acid **5a** as well as pentadecanoic acid **5b**

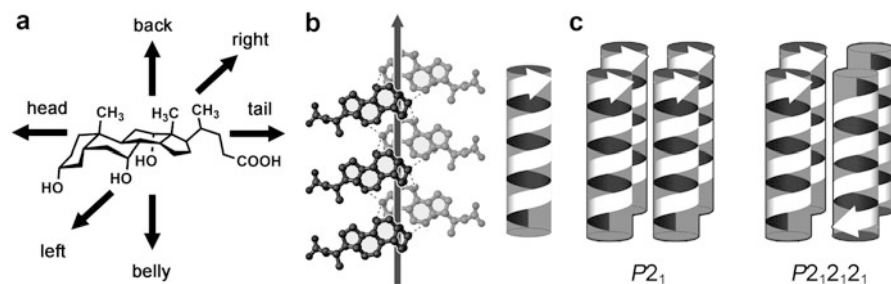


**Fig. 19.2** Three-axial chirality of a cholic acid molecule (**a**) as well as its twofold helical assembly (**b**) and bundles of the twofold helical assemblies for space groups  $P2_1$  (left) and  $P2_12_12_1$  (right) (**c**)

twofold helical assemblies [20–22]. This linkage between molecules and twofold helical assemblies was confirmed in the case of other natural compounds, such as brucine (Scheme 19.1–3) [23, 24], and *Cinchona* alkaloids, such as cinchonine (Scheme 19.1–4a), quinidine (Scheme 19.1–4b), cinchonidine (Scheme 19.1–4c), and quinine (Scheme 19.1–4d) [25–29]. Subsequently, the twofold helices with three-axial chirality are bundled in different ways, affording chiral crystals,  $P2_1$  and  $P2_12_12_1$  (Fig. 19.2c). Such a hierarchical method was extended to achiral organic salts of 4-methylbenzylamine with myristic acid (Scheme 19.1–5a) and

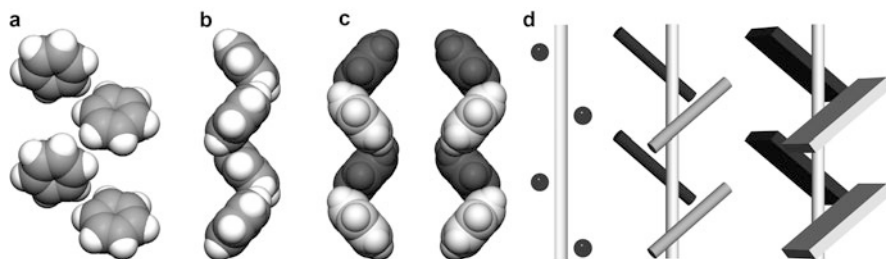


**Fig. 19.3** Twofold helical assembly of benzene molecules in a cholic acid channel (a), its special side view around a helical axis with a tilt alignment (b), an enantiomeric pair of helical assemblies with *right-* or *left-*tilt alignments (c), and twofold helical assemblies of points (*left*), lines (*middle*), and faces (*right*) by the multipoint approximation method for chirality generation as well as handedness determination (d)

pentadecanoic acid (Scheme 19.1–5b), resulting in the successful interpretation of chiral crystallization of achiral molecules [30].

With rapid development of personal computers, molecular graphics enabled us to freely construct and move molecular assemblies on display. During such a daily observation of the assemblies in 2006, we met a twofold helical assembly of benzene molecules in a channel of cholic acid inclusion crystals (Fig. 19.3a) [9]. This was responsible for an intuition that the assembly looked like stairs in daily life. Subsequently, we recognized a special side view (Fig. 19.3b), where faces of benzene molecules are viewed as lines during rotations around a twofold helical axis, reaching a conclusion that its handedness can be judged clearly. Thus, one can define that the twofold helical assembly is right-handed when the lines exhibit tilt alignment to the right along the twofold helical axis (and *vice versa*) (Fig. 19.3c). This method was applied to various channel-type inclusion crystals involving benzene derivatives [9] as well as crystals of benzene itself [10]. Based on such tilt alignments, we established a supramolecular-tilt-chirality method for determining right- or left-handedness of twofold helical assemblies [31, 32]. In the same way, a variety of organic molecules were ascertained to exhibit right- or left-handedness in their twofold helical assemblies [33, 34].

These abovementioned observations convinced us that both chiral and achiral molecules can afford the twofold helical assemblies with distinguishable handedness. This experimental fact, however, is inconsistent with symmetry theory that twofold helices are not discriminable in handedness. In other words, twofold screw operations form identical assemblies by clockwise and anticlockwise rotations, but enantiomers of twofold helical assemblies really exist in crystals. Such discrepancy confused us very much, leading us to the idea that chirality generation should be mathematically related to space geometry, rather than space groups. Namely, any other methods are necessary for linking between space groups and space geometry.

At last, we reached multipoint approximation for materials which are expressed by a line with two points, a face with three points, and so on instead of a point (Fig. 19.3d) [33, 34]. This approximation clarified both chirality generation and

handedness determination of twofold helical assemblies, and elucidated a linkage between molecular and supramolecular chirality [35]. Such multipoint approximation method has been comprehensively extended toward hidden supramolecular chirality of various materials [36].

## 19.3 Chirality Generation and Handedness of Twofold Helical Assemblies

### 19.3.1 Chirality Generation in Space Groups for Crystallography

Since the establishment of crystallographic theory in the first half of the last century, researchers have no doubt that the theory has complete consistency. Since original group theory is substantially abstract, a mathematical factor can represent every material. Simply, a material is approximated as a point, so that we can understand symmetry operations of both 73 point space groups and 230 space groups in crystallography.

According to the one-point approximation, symmetry operations provide assemblies of the points. For example, a screw operation with rotations and translations yields a helical assembly which is analyzed for determining its handedness. Thus, screw operations include only four kinds, namely, two-, three-, four-, and sixfold ones. A twofold screw operation yields a single helical assembly with only one notation,  $2_1$ . This is attributable to a rotation by 180 degrees around a helical axis. Both the right- and left-handed rotations produce an identical assembly without handedness (Fig. 19.1b). In contrast, a threefold screw operation always results in a pair of enantiomeric helical assemblies. Namely, the right- and left-handed rotations afford the corresponding right- and left-handed assemblies with the notations  $3_1$  and  $3_2$ , respectively (Fig. 19.1c). Similarly, fourfold screw operation yields three different assemblies. A mirror image has a pair of notations,  $4_1$  for right-handedness and  $4_3$  for left-handedness. An additional fourfold assembly has a notation,  $4_2$ , without handedness. Finally, sixfold screw operation provides five different helical assemblies: a pair of  $6_1$  and  $6_5$ , a pair of  $6_2$  and  $6_4$ , and in addition one notation  $6_3$ . In this manner, screw operations yield only four enantiomeric pairs of the helical assemblies and three non-enantiomeric assemblies.

The International Tables for Crystallography describes the following interesting sentence [6]: “In practical crystallography one wants to distinguish between right- and left-handed screws and does not want to change from a right-handed to a left-handed coordinate systems.” This sentence suggests that handedness determinations are practically performed without considering the other related mathematics. However, we have to evaluate chirality of materials from three-dimensional space geometry, rather than space groups. Namely, we consider a methodology for molecular chirality of organic substances, as mentioned below.

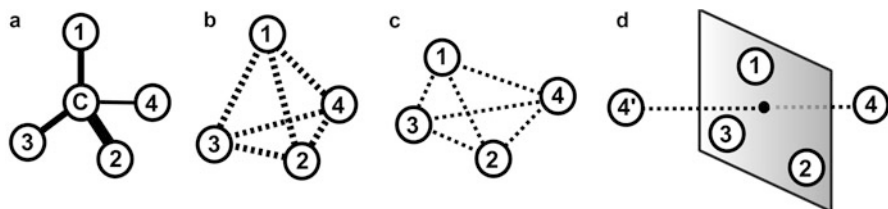


**Fig. 19.4** Four points necessary for chirality generation: a tetrahedral carbon with four different substituents (a), four points without the tetrahedral carbon (b), four points for an irregular tetrahedron (c), and chirality generation due to the fourth point separated from a plane consisting of the other three points (d)

## 19.3.2 Chirality Generation in Three-Dimensional Space Geometry

### 19.3.2.1 Four Points for Chirality Generation

From the nineteenth century, a vast amount of studies have been devoted to molecular chirality, including central, axial, and facial chirality of organic molecules. These studies discuss chirality generation from a viewpoint of three-dimensional space geometry. The representative comprises a tetrahedral carbon with four different substituents which have a priority sequence for determining handedness of an enantiomeric pair of organic molecules (Fig. 19.4a) [8]. Thus, according to the Cahn-Prelog-Ingold (CPI) priority rule, the first, second, and third substituents are located on the foreside, and the fourth substituent is done to the far side. The former three ones are arranged clockwise or anticlockwise to define the corresponding right- or left-handedness, respectively.

Hypothetically, we can remove the asymmetric carbon and four covalent bonds which connect among the carbon and the substituents (Fig. 19.4b). The four substituents are left in three-dimensional space and are expressed as points with numbers. Their relative location can be freely changed into irregular tetrahedrons (Fig. 19.4c). As a result, it can be seen from Fig. 19.4d that the three points form a plane which is separated from the fourth point. This proves that such four points are necessary for chirality generation.

In general, three-dimensional space geometry tells us that the four points take free locations each. Chirality generation takes place when the three points form a plane, from which the fourth point is separated. Two special cases do not generate chirality: one constitutes a single plane with all of the points and the other has inner enantiomeric mirrors among the four points, as in cases of regular tetrahedrons or their elongated ones.

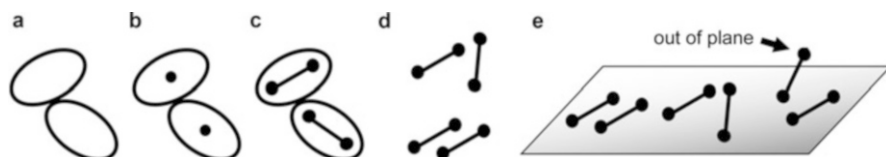


**Fig. 19.5** Chirality generation by the four points: a bimolecular assembly (a), its one-point approximation (b), two-point approximation yielding four points in total (c), two lines with parallel or antiparallel alignments (d), and chirality generation of antiparallel two lines with the fourth point separated from a face consisting of the other three points (e)

### 19.3.2.2 Multipoint Approximation for Chirality Generation

Such four points may be observed in molecular assemblies with intermolecular non-covalent bonds. At first, we consider various relative locations of a bimolecular assembly composed of the identical molecules (Fig. 19.5a). One-point approximation to each material results in only two points from the bimolecular assembly (Fig. 19.5b). This one-point approximation is reasonably applicable to inorganic sphere materials, such as atoms and ions, but is not always suitable for organic non-sphere molecules with diverse shapes.

On the other hand, two-point approximation can afford four points necessary for generating chirality in space geometry (Fig. 19.5c). The resulting two lines form either parallel or nonparallel alignment (Fig. 19.5d). The former always yields a plane with all of the points, while the latter does the following two cases (Fig. 19.5e): one is that the two lines are located on the same plane and the other forms a plane from which one point is separated for generating chirality. It is noteworthy that the two lines do not intersect on the plane from each other in the bimolecular assembly. These facts indicate that organic molecules should be approximated by at least two points in order to evaluate chirality.

The line method can be reasonably extended to the face method with at least three points. This face method employs a line in the special side view mentioned above (Fig. 19.3d), and the line is extended to the face. The resultant two faces form either parallel or nonparallel arrangements. The parallel faces yield a non-enantiomeric assembly while the nonparallel ones either an enantiomeric assembly or a non-enantiomeric one with inner enantiomeric mirrors.

### 19.3.2.3 Chirality Generation in Twofold Helical Assemblies of Lines and Faces

Next, we consider formation of an assembly through symmetry operations. Twofold screw operation produces twofold helical assemblies of points, lines, and faces along a helical axis. The points afford a non-enantiomeric helical assembly, because all of the points are located on a single plane involving the axis. In contrast, the lines and faces can provide an enantiomeric helical assembly with chirality, as described below.

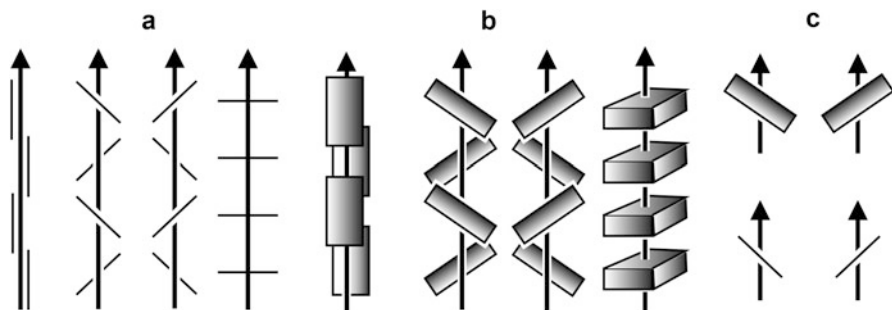


**Fig. 19.6** Alignments along twofold helical axes: lines (a) and faces (b) in parallel (*left*), with *left* or *right* tilt (*middle*) and perpendicular to the axes (*right*). The tilt alignments originate an enantiomeric pair of a line (*bottom*) or a face (*top*) with a helical axis (c). Twofold screw operations of the line or face yield an enantiomeric pair of twofold helical assemblies

The line method through the twofold screw operation results in three kinds of twofold helical assemblies: parallel, nonparallel, and perpendicular ones (Fig. 19.6a). The parallel assembly has a plane containing the axis and all of the lines, generating no chirality. The perpendicular assembly exhibits no chirality due to inner enantiomeric mirrors. The nonparallel assembly shows the following two types, like the bimolecular assembly. The one consists of the lines which are intersected with the helical axis, generating no chirality. In contrast, the other consists of the lines which are not intersected with the helical axis and exhibit tilt alignments along the helical axis. A combination of the lines through the tilt alignments generates an enantiomeric helical assembly.

Similarly, the face method through the twofold screw operation produces three kinds of twofold helical assemblies: parallel, nonparallel, and perpendicular ones (Fig. 19.6b). The parallel and perpendicular assemblies generate no chirality due to inner enantiomeric mirrors, while the nonparallel assembly yields a pair of enantiomeric tilt alignments, as in the case of the line method.

These results indicate that the helical axis apparently combines with a tilt line or face so as to form an enantiomeric associate. That is, there exists a pair of enantiomeric lines or faces along the helical axis before performing the twofold screw operations (Fig. 19.6c). It should be reminded that twofold screw operations themselves yield identical helical assemblies by using clockwise and anticlockwise rotations by 180 degrees. Instead, the enantiomeric associates with tilt alignments originate the enantiomeric twofold helical assemblies through the twofold screw operations. In this manner, these line and face methods clearly present chirality generation through twofold screw operations.

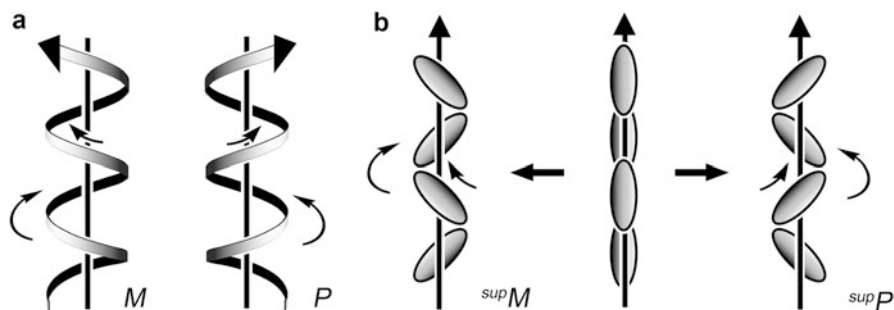


**Fig. 19.7** Handedness determination: continuous helices (a); twofold helical molecular assemblies by the supramolecular-tilt-chirality method (b)

### 19.3.3 Handedness Determination of Twofold Helical Assemblies

#### 19.3.3.1 Supramolecular Tilt Chirality for Handedness Determination

First, we briefly describe definition of handedness of continuous helices. As viewed from the one end to the other end, the helices have a forward transfer, accompanied by a clockwise or anticlockwise rotation around a helical axis. The right- or left-handed helix shows the clockwise or anticlockwise rotation, respectively (Fig. 19.7a). In addition, as viewed from its outside to inside, the right- or left-handed helix exhibits right- or left-tilt alignments along the helical axis, respectively. Such a definition indicates that the tilt alignments along a helical axis play a decisive role in determining handedness.

Therefore, even in the case of the discontinuous helices, handedness is determined from the tilt alignments of the lines or faces along the helical axis (Fig. 19.7b). A right- or left-handed helix consists of the right- or left-tilt alignments of lines or faces along a helical axis, accompanied by a forward transfer with a clockwise or anticlockwise rotation, respectively. We termed this chirality of supramolecular assemblies “supramolecular tilt chirality” [31–34]. The helices in molecular chirality are designated with symbols, *P* for right-handedness and *M* for left-handedness. Similarly, the helices in supramolecular chirality are done with symbols, <sup>sup</sup>*P* for right-handedness and <sup>sup</sup>*M* for left-handedness, where the superscript means supramolecules or supermolecules.

In this way, multipoint approximation methods have been established for chirality generation as well as handedness determination of twofold helical assemblies. It is noteworthy that the handedness of the assemblies depends on tilt alignments along a helical axis, but does not depend on the rotational directions of the twofold screw operations.

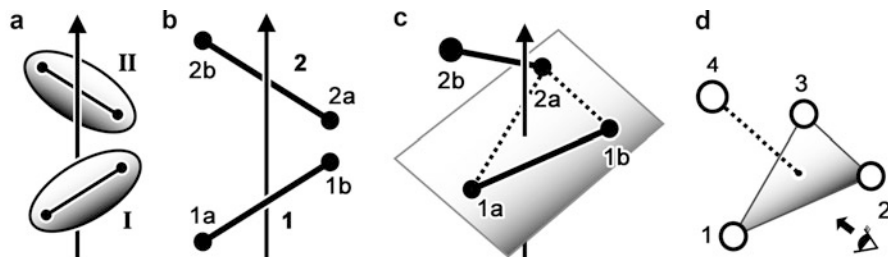


**Fig. 19.8** Comparison of handedness determination between molecular and supramolecular chirality: twofold helical assemblies of molecules along a helical axis (a), twofold helical assemblies of the lines by two-point approximation (b), handedness of four points on the basis of supramolecular chirality by tilt alignments (c), and handedness of four points on the basis of molecular chirality by the CPI rule (d)

### 19.3.3.2 Comparison Between Molecular and Supramolecular Chirality

The supramolecular-tilt-chirality method does not require the priority rule, such as the CPI rule in molecular chirality. Instead, the alignments of lines or faces along the helical axis play a key role in determining handedness. This is understood by a relation between the abovementioned four points and the helical assembly of lines. As schematically shown in Fig. 19.8, one can determine handedness of the twofold helical assemblies of the lines as follows. Molecule I is transferred forward along a helical axis with an arrow by the twofold screw operation to give the molecules II, III, etc. (Fig. 19.8a). Molecules I, II, III etc. are designated by the corresponding lines 1, 2, 3, etc. with point numbers 1a and 1b, 2a and 2b, 3a and 3b, etc., respectively (Fig. 19.8b). Lines 1 and 2 form four points which are arranged in a directional order of 1a, 1b, 2a, and 2b. In the case of a right-handed helix, the former three points (1a, 1b, and 2a) are clockwise located, as viewed from the downside to the upside in Fig. 19.8c. The fourth point 2b has a forward transfer along the helical axis. In this manner, the directional order of the four points along the axis serves as the effective method for determining the handedness. This is comparative to the priority order of the CPI rule in molecular chirality (Fig. 19.8d).

In this way, the multipoint approximation with lines and faces has clarified the following three important things: firstly, a twofold helical axis serves as a preferential hypothetical line, accompanied by a real line or face of a molecule; secondly, the line or face can have tilt alignment along the twofold helical axis, resulting in an enantiomeric associate of the axis and the line or face; and thirdly, the enantiomeric associate is subjected to twofold screw operation to generate a pair of enantiomeric twofold helical assemblies with right- or left-tilt alignment along the axis. Therefore, handedness of the twofold helical assemblies has nothing to do with right or left rotations of the twofold screw operation.

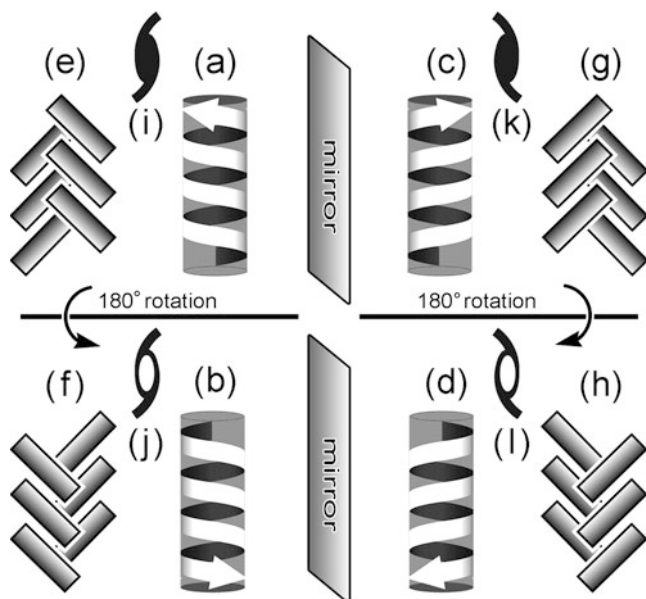


**Fig. 19.9** Symbols for displaying the twofold helices with three-axial chirality: graphical symbols for continuous left-handed helices (a, b) and right-handed helices (c, d), discontinuous left-handed helices (e, f) and right-handed helices (g, h), and symbols modified from that in crystallography for left-handed helices (i, j) and right-handed helices (k, l). The modified symbols proposed by us are used for understanding twofold helices with three-axial chirality

### 19.3.4 Three-Axial Chirality of Twofold Helical Assemblies

Polypeptide chains have a defined direction from amino group terminals till carboxylic group ones. This is connected with up-to-down directions of the resulting helices. The other right-to-left as well as in-to-out directions are briefly determined, as viewed along a helical axis. In general, an asymmetric sequential helical chain may have an asymmetric structure with three distinguishable directions: right to left, up to down, and in to out. This asymmetry of the helices is termed “three-axial chirality” and is illustrated by using four kinds of graphical symbols with an arrow (Fig. 19.9a–d). In these symbols, the in-to-out direction is self-evident.

Similarly, twofold helical assemblies may have such asymmetric structures. For example, one can remind a twofold helical assembly of benzene molecules in a channel of cholic acid (Fig. 19.3b). The in-to-out direction is self-evident, as viewed along the helical axis. The right-to-left direction of the helix is clear due to the supramolecular-tilt-chirality method. In this case, it is apparently difficult to discriminate the up-to-down direction due to edge-to-edge contact of benzene molecules. However, because of the edge-to-face or herringbone-type arrangement, it is easy to determine its direction. Figure 19.9e–h show the edge-to-face arrangement in crystals of benzene itself. In this case, we can discriminate two different

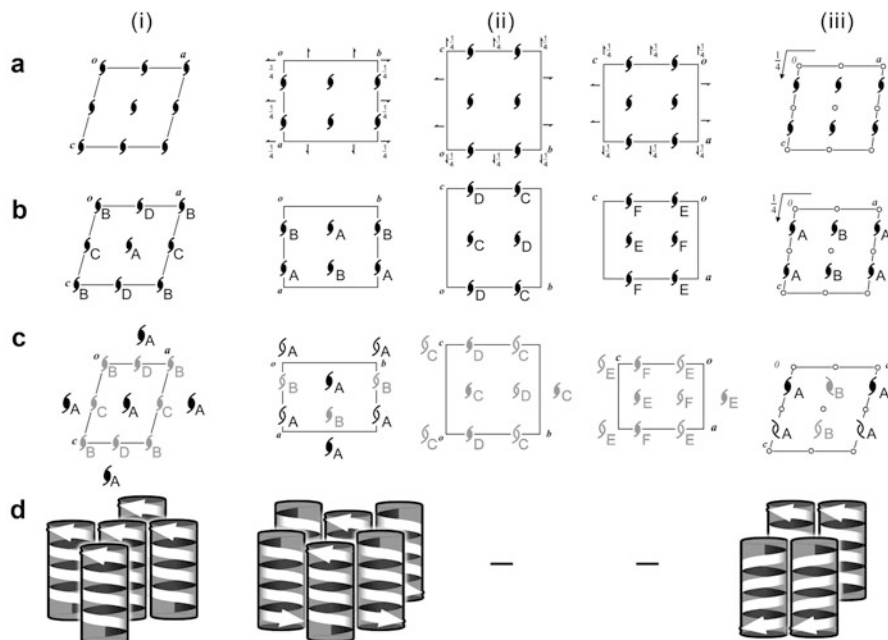


**Fig. 19.10** Bundles of twofold helices for space groups  $P2_1$  (i),  $P2_12_12_1$  (ii), and  $P2_1/c$  (iii): equal twofold helices for displaying twofold screw operations by using only one symbol in the International Tables for Crystallography (a); different twofold helices with alphabetical subscripts A–F (b); in real crystals, the different twofold helices are represented with the four modified symbols together with those in the surrounding units (c); bundles of only the preferred helices (As) with graphical helical symbols (d)

sides like a mountain: a closed summit side and an opened valley side. The former corresponds to the upside of the helix, while the latter does to the downside of the helix. Accordingly, the twofold helical assemblies exhibit three-axial chirality and are illustrated with the same four symbols as those of the polypeptide chains.

## 19.4 Chirality Generation in Bundles of Twofold Helical Assemblies

### 19.4.1 Symbols of Twofold Helical Assemblies with Three-Axial Chirality

The International Tables for Crystallography describes combinations of symmetry operations for every space group. In the Tables, twofold screw operation has only one symbol without three directions. For example, Fig. 19.10a(i–iii) show combinations of the symbols in space groups of  $P2_1$ ,  $P2_12_12_1$ , and  $P2_1/c$ , respectively.

These figures for symmetry operations may advance to those for twofold helical assemblies with three-axial chirality. This chirality demands modification of the symbol as follows. The outer part is used for right-to-left direction like a threefold helix, while the inner part is used for up-to-down direction. A closed or open symbol corresponds to a view from the upside or downside, respectively. The in-to-out direction is self-evident in these symbols, resulting in four different symbols (Fig. 19.9(i–l)). These modified symbols are effective for representing bundles of the twofold helical assemblies with three-axial chirality in organic crystals, as described in the subsequent section.

Such modified symbols are often used for drawing every helix on a projection, as viewed from a crystallographic axis. In comparison, the graphical helical symbols (Fig. 19.9a–d) are suitable for sterically showing the bundles of the selected helices.

### 19.4.2 *Combinations of Twofold Helical Assemblies with Three-Axial Chirality*

The International Tables for Crystallography represent combinations of equal twofold helices with only one symbol of twofold screw operation (Fig. 19.10a) [6]. However, there are different unequal helical assemblies, as exemplified in Fig. 19.10b, where different helices are designated with alphabetical subscripts, **A** to **F**. As shown in Fig. 19.10c, these helices in the real crystals are designated with the four modified symbols employed in Fig. 19.9i–l.

$P2_1$  crystal contains four different twofold helices along a crystallographic axis. An example deals with cholic acid crystal including benzene, where four different helices (**A**, **B**, **C**, **D**) are aligned along the crystallographic *b*-axis (Fig. 19.10c(i)). In contrast,  $P2_12_12_1$  crystal has two different helices along each crystallographic axis, totally six different helices (**A** to **F**). Figure 19.10c(ii) shows the corresponding twofold helices along the crystallographic *c*, *a*, and *b* axes in deoxycholic acid crystal, respectively.

On the other hand, a crystal structure of benzene belongs to achiral space group  $P2_1/c$ . The face method confirmed two enantiomeric pairs of two different twofold helical assemblies with three-axial chirality. One pair of the helices **A** has an edge-to-face contact, while the other pair of the helices **B** has an edge-to-edge contact. Figure 19.10c(iii) shows a combination of the assemblies with the symbols. It can be seen that the enantiomeric helices **A** align in parallel to form a layer and that the helices **B** are located between the layers. Namely, the resulting layers are inverted through glide operation.

### 19.4.3 Bundles of the Preferred Twofold Helices

As mentioned above, it was ascertained that multiple different twofold helices are combined together in unit cells, prompting us to select a preferable helix for simplification. This is because various non-covalent interactions construct helices and bridge between two helices. The well-known supramolecular synthons are highly effective for evaluating the different interactions in strength [37, 38].

For example, in the case of cholic acid crystal with  $P2_1$ , the hydrogen-bonding helix **A** consisting of head parts of cholic acid is preferable to the other three helices due to the strong hydrogen bonds. The preferred helices are located in the surrounding cells, as exemplified in Fig. 19.10c(i). In the case of deoxycholic acid crystal with  $P2_12_12_1$ , the preferable hydrogen-bonding helix **A** is selected among six different helices. The preferred helices are located in the surrounding cells along the crystallographic  $a$ -axis (Fig. 19.10c(ii)). In the benzene crystal with  $P2_1/c$ , the racemic helix **A** with face-to-edge contact is preferable to the racemic helix **B** with edge-to-edge contact due to their different intermolecular non-covalent bonds in strength. The preferred racemic helices **A** are located in the surrounding cells (Fig. 19.10c(iii)).

In order to draw the bundles three dimensionally, we use the graphical symbols of right- and left-handed helices with arrows toward up-to-down directions (Fig. 19.9a–d). The unit cells are extended along the preferred helices, enabling us to draw the bundles of the preferred helices. Figure 19.10d(i–iii) shows the bundles of the preferred helices in the corresponding crystals,  $P2_1$ ,  $P2_12_12_1$ , and  $P2_1/c$ , respectively.

### 19.4.4 Chirality Generation in Bundles of the Preferred Twofold Helices

The resulting bundles of the preferred and one-handed helices gave us an idea about crystal formation. Thus, the in-to-out direction is further divided into two different directions perpendicular to the helical axis. The crystal formation consists of the following three-stepwise and three-directional process. The first step corresponds to formation of the preferred and one-handed twofold helices along the helical axis. The second step comprises formation of chiral layers toward one direction among the divided in-to-out directions. The third step constructs three-dimensional crystals by stacking the layers toward the other direction among the divided directions.

For example, Fig. 19.11 shows the three-stepwise and three-directional process for crystals with space groups,  $P2_1$ ,  $P2_12_12_1$ , and  $P2_1/c$ . In the first step, a preferred and one-handed twofold helix is available (Fig. 19.11a). In the second step, the one-handed helices with the identical up-to-down direction align in parallel so as to produce chiral layers (Fig. 19.11b). In contrast, the subsequent third step for layer stacking is greatly different for each space group (Fig. 19.11c). The  $P2_1$

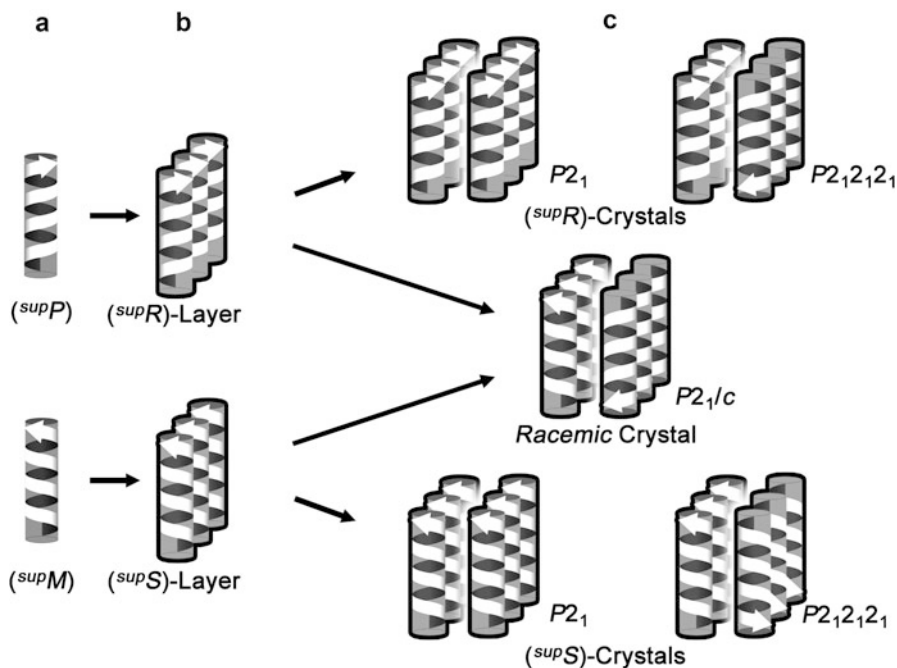


**Fig. 19.11** Crystal formation model through three-stepwise and three-directional processes by using preferred twofold helices: the first step for making a twofold helix (a), the second step for aligning the helices to make a layer (b), and the third step for stacking the layers to form crystals with space groups  $P2_1$  (left),  $P2_12_12_1$  (right), and  $P2_1/c$  (middle) (c)

crystal has a parallel stacking of the identical layers (Fig. 19.11c (left)) while the  $P2_12_12_1$  crystal an antiparallel stacking of them (Fig. 19.11c (right)). On the other hand, the  $P2_1/c$  crystal has an alternative antiparallel stacking of the enantiomeric layers (Fig. 19.11c (middle)). In this manner, the third step plays a decisive role in determining the space groups in these cases.

It was ascertained that supramolecular chirality lies in each step. The preferred twofold helices with three-axial chirality construct chiral layers, whose stacking can form chiral crystals. According to such a bundling method, chiral crystals are briefly defined as follows. Only right- or left-handed twofold helices are bundled to form the corresponding right- or left-handed crystals, respectively. Such right- and left-handed crystals are designated as  $(supR)$  and  $(supS)$  crystals, respectively. The representative chiral crystals, such as  $P2_1$  and  $P2_12_12_1$ , contain only one-handed twofold helices. This means that such chiral crystals consisting of achiral molecules are classified into the racemic conglomerates of  $(supR)$  and  $(supS)$  crystals.

## 19.5 Linkage Between Molecular Structures and Supramolecular Chirality

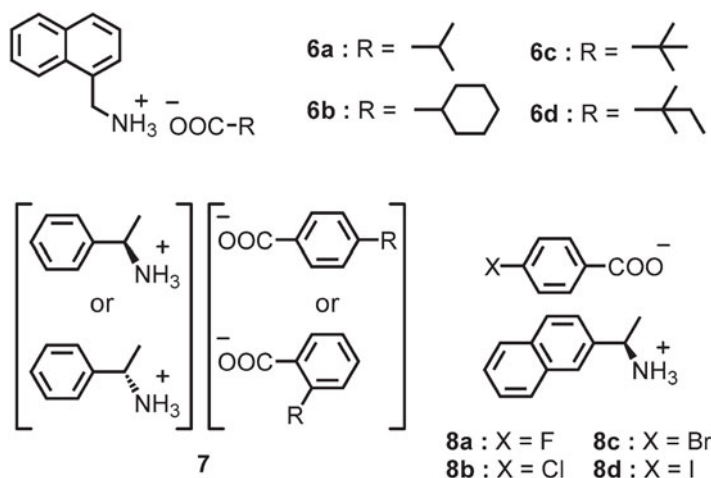
Organic crystals have molecular assemblies which depend on weak non-covalent interactions [39–42]. Therefore, molecular structures influence not only their twofold helical assemblies but also the bundles of the helices. In consequence, absolute configurations and conformations of organic molecules are connected with structures of the resulting supramolecules. The following two subjects are concerned with connections between molecular structures and supramolecular chirality through various weak interactions.

### 19.5.1 Chiral Crystallization of Achiral Molecules

The conventional method does not discriminate handedness of twofold helices, leading to the unclear interpretation of chiral crystals. A typical example is as follows. One can understand the formation of chiral crystals, termed “racemic conglomerates,” from racemic molecules. However, one cannot understand formation of the conglomerates from achiral molecules, termed “chiral crystallization of achiral molecules.” Previously, over thousands of achiral molecules underwent chiral crystallization, and the crystal engineering continues to search a relationship between molecular structures and their assembled structures [43–45].

Such an unsolved problem may be subjected to the concept of chirality generation in bundles of preferred twofold helices with three-axial chirality. As mentioned in Sect. 19.4.4, bundles of only right- or left-handed twofold helices can form the corresponding right- or left-handed crystals with chiral space groups, respectively.

We are searching for the chiral crystallization of many achiral molecules through the preferred twofold helices. An example is cited from our research with organic salts of 1-naphthylmethyl ammonium carboxylates. Remarkably, the salts of carboxylic acids with isopropyl group (Scheme 19.2–6a) or cyclohexyl group (Scheme 19.2–6b) form chiral crystals with  $P2_12_12_1$ , while the salts of those with *tert*-butyl group (Scheme 19.2–6c) or *tert*-amyl group (Scheme 19.2–6d) form achiral crystals with  $P2_1/n$  [46]. These crystals were analyzed with the three-stepwise and three-directional method for bundling preferred twofold helices. It was found that chiral crystallization is attributable to nonparallel contacts between the alkyl and aromatic groups in the third step for the layer stacking.



**Scheme 19.2** Molecular structures of organic salts **6–8**. Salts **6** of 1-naphthylmethylamine with isobutyric acid **6a**, cyclohexanecarboxylic acid **6b**, pivalic acid **6c**, and 2,2-dimethylbutyric acid **6d**. Salts **7** of (*R*)- or (*S*)- $\alpha$ -methylbenzylamine with *ortho*- or *para*-substituted benzoic acid derivatives. Salts **8** of (*R*)-1-(2-naphthyl)ethylamine of 4-halo-benzoic acids

### 19.5.2 Linkage Between Molecular and Supramolecular Chirality

It is well known that molecular structures of monomers link to helical handedness of macromolecules. For example, L- $\alpha$ -amino acids mainly form right-handed helices of their polypeptide chains. Similarly, molecular chirality may be connected to supramolecular chirality. We focus on twofold helical hydrogen-bonding networks of organic salts and introduce two examples below.

The one deals with chiral organic salts of (*R*)- $\alpha$ -methylbenzylamine with *ortho*- or *para*-substituted benzoic acids (Scheme 19.2–7) [35]. It was found that crystals of the salts belong to chiral space groups  $P2_12_12_1$  or  $C2$ . Chiral (*R*)-amine with *para*- or *ortho*-substituted benzoic acids forms chiral crystals with  $P2_12_12_1$  or  $C2$  space groups, linking to supramolecular chirality with  $^{sup}M$  or  $^{sup}P$  of the twofold helical hydrogen bonding networks, respectively. Remarkably, achiral elements of *para*- or *ortho*-isomers changed the linkage between molecular and supramolecular chirality. These results indicate that chiral molecules generally afford one-handed supramolecular assemblies and that a slight change of the molecules can produce the reverse one-handed assemblies.

The other deals with a control of chiral space groups through halogen bonds [47]. Such control was performed by using chiral organic salts of (*R*)-1-(2-naphthyl)ethylamine with *para*-halo-substituted benzoic acids. The compounds with fluorine (Scheme 19.2–8a), chlorine (Scheme 19.2–8b), or bromine

(Scheme 19.2–8c) form crystals with  $C_2$  space group, while the one with iodine (Scheme 19.2–8d) form crystals with  $P2_12_12_1$ . The  $C_2$  crystal has bundles of the twofold helices with the same up-to-down direction, similar to the  $P2_1$  crystal. In contrast, the iodine group brings about effective antiparallel stacking in the third step for bundling the preferred twofold helices.

## 19.6 Search for Hidden Supramolecular Chirality

A vast amount of researches have been conducted on molecular chirality through three-dimensional space geometry and reached complete well-known principles. In comparison, supramolecular chemistry developed drastically over the last few decades, but still includes undeveloped interdisciplinary fields, particularly supramolecular chirality of molecular assemblies in organic crystals. The conventional researches in this field are based on an obscure relation between space geometry and space groups, resulting in confusions for supramolecular chirality. Such a situation introduced a number of hidden supramolecular chirality in organic crystals.

### 19.6.1 Hidden Chirality in Space Groups

As mentioned in Sect. 19.3.1, screw operations construct only four pairs of enantiomeric helical assemblies. Based on the conventional method, rotation operations by 180, 120, 90, and 60 degrees afford the corresponding non-enantiomeric rotational assemblies with notations, 2, 3, 4, and 6. Translation operation yields an assembly without handedness with a notation 1. Totally, symmetry operations in space groups establish only four pairs of enantiomeric assemblies. These results are connected to 65 chiral space groups in crystallography. Among them, only 22 groups comprise 11 pairs of the enantiomeric ones, including  $3_1$  and  $3_2$ ,  $4_1$  and  $4_3$ ,  $6_1$  and  $6_5$ , and  $6_2$  and  $6_4$ . The remaining 43 groups contain the non-enantiomeric groups, resulting in comprehensive hidden chirality.

However, chirality generation should be considered from space geometry, rather than space groups. As mentioned above, the line and face approximation serves as a powerful method for exposing the hidden chirality. The previous sections describe chirality generation and handedness of only twofold helical assemblies in detail. The other rotational and translational assemblies still remain unexplored, meaning an existence of comprehensive assemblies with hidden supramolecular chirality.

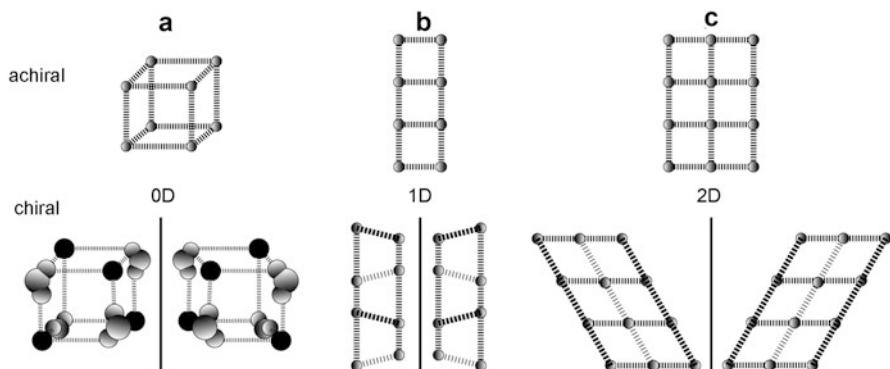


**Fig. 19.12** Hidden supramolecular chirality of hydrogen-bonding networks: zero-dimensional (0D) cubic (a), one-dimensional (1D) ladder (b), and two-dimensional (2D) sheet (c)

### 19.6.2 Hidden Chirality in Hydrogen-Bonding Networks

One of the hidden chirality lies in hydrogen-bonding networks. Graph set analysis functions as the powerful method for characterizing hydrogen-bonding supramolecular assemblies [48–50]. However, the conventional graph set analysis has tendency to lose symmetry information due to simplification, yielding hidden supramolecular chirality. Focusing on space geometry, we advanced the graph set analysis for exposing hidden chirality of hydrogen-bonding network [36].

The Cambridge Structural Database contains over 300 of crystal structures of primary ammonium carboxylates [51]. The hydrogen-bonding networks were mainly classified into three types: zero-dimensional (0D) cubic [52], one-dimensional (1D) ladder [53], and two-dimensional (2D) sheet type. We found that their networks mostly exhibit supramolecular chirality (Fig. 19.12). The 0D cubic networks involve nine topologically different subtypes. Their supramolecular chirality ( $^{sup}R$ ) and ( $^{sup}S$ ) were defined by ordering their faces. The 1D ladder networks are composed of twofold helical assemblies. Their ( $^{sup}P$ )-helicity and ( $^{sup}M$ )-helicity were distinguished by both advanced graph set analysis and supramolecular tilt chirality in common. Supramolecular chirality of the 2D sheet networks was also clarified by discriminating their prochiral faces.

### 19.6.3 Hidden Chirality of Polymeric Chains

The concept of twofold helices with three-axial chirality directed us to elucidate chirality generation on polymeric chains with *trans* and *gauche* conformations [54]. The multipoint approximation method with lines and faces has enabled us to discriminate handedness of twofold helical polymeric chains, such as  $\beta$ -chains of

polypeptides as well as cellulose. Especially, this methodology has exposed hidden chirality of various zigzag chains, which are achiral in appearance.

## 19.7 Conclusions and Perspectives

The multipoint and tilt alignment methods clarified a mechanism for chirality generation through symmetry screw operations. Consequently, the method exposed various hidden chirality of assemblies, including hydrogen-bonding networks, supramolecules, macromolecules, and so on. As a result, twofold helices with three-axial chirality link between molecular and crystal structures, opening a promising way for designing chiral crystals of achiral molecules. Another rotation and translation operations would contribute to the preparation of such chiral crystals.

Three-dimensional space geometry, rather than space groups, serves as the root for understanding chirality generation. Therefore, common principles are available among various kinds of materials, including molecules, supramolecules, macromolecules, crystals, living objects, artificial materials, architectures, and so on. Considering the screw and rotation axes at each level, the tilt-chirality method is expected to function as the powerful method for recognizing chirality generation and determining its handedness.

## References

1. M. Gardner, *The New Ambidextrous Universe* (W. H. Freeman and Company, New York, 1999)
2. R.A. Hegstrom, D.K. Kondepudi, The handedness of the universe. *Sci. Am.* **262**, 108 (1990)
3. J.-M. Lehn, *Supramolecular Chemistry: Concepts and Perspectives* (VCH, Weinheim, 1995)
4. G.R. Desiraju, *The Crystal as a Supramolecular Entity* (Wiley, Chichester, 1995)
5. J.P. Glusker, K.N. Trueblood, *Crystal Structure Analysis: A Primer*, 3rd edn. (Oxford University Press, Oxford, 2010)
6. T. Hahn, Edited. *International Tables for Crystallography*, vol A, Space-Group Symmetry (Kluwer Academic Publishers, London, 1983 (1st Ed), 2002 (5th Ed)).
7. D.W. Bennett, *Understanding Single-Crystal X-Ray Crystallography* (Wiley-VCH, Weinheim, 2010)
8. R.S. Cahn, C.K. Ingold, V. Prelog, *Angew. Chem. Int. Ed.* **5**, 385 (1966)
9. A. Tanaka, I. Hisaki, N. Tohnai, M. Miyata, *Chem. Asian. J.* **2**, 230 (2007)
10. I. Hisaki, T. Sasaki, K. Sakaguchi, W.T. Liu, N. Tohnai, M. Miyata, *Chem. Commun.* **48**, 2219 (2012)
11. A.I. Kitaigorodskii, *Molecular Crystals and Molecules* (Academic, New York, 1973)
12. Cambridge Structural Database, <http://www.ccdc.cam.ac.uk/products/csd/statistics/>
13. J. Jacques, A. Collet, S.H. Wilen, *Enantiomers, Racemates, and Resolutions* (Krieger, Malabar, 1991)
14. T. Matsuura, H. Koshima, *J. Synth. Org. Chem. Jpn.* **56**, 268/466 (1998)
15. T. Matsuura, H. Koshima, *J. Photochem. Photobiol. C, Photo. Rev.* **6**, 7 (2005)
16. K. Miki, A. Masui, N. Kasai, M. Miyata, M. Shibakami, K. Takemoto, *J. Am. Chem. Soc.* **110**, 6594 (1988)

17. M. Miyata, M. Shibakami, S. Chirachanchai, K. Takemoto, N. Kasai, K. Miki, *Nature* **343**, 446 (1990)
18. M. Miyata, K. Sada, “*Comprehensive Supramolecular Chemistry*”, vol 6, “*Solid State Supramolecular Chemistry: Crystal Engineering*”, ed. by J.-M. Lehn (Pergamon, Oxford, 1996), p. 147
19. M. Miyata, K. Sada, N. Yoswathananont, in *Encyclopedia of Supramolecular Chemistry*, ed. by J.L. Atwood, J.W. Steed, vol. 1 (Marcel Dekker, New York, 2004), p. 441
20. M. Miyata, N. Tohnai, I. Hisaki, *Molecules* **12**, 1973 (2007)
21. K. Nakano, K. Aburaya, I. Hisaki, N. Tohnai, M. Miyata, *Chem. Rec.* **9**, 124 (2009)
22. M. Miyata, K. Sada, K. Nakano, N. Tohnai, in *Bottom-Up Nanofabrication*, Chapter 79, eds. by H.S. Nalwa, K. Ariga, vol 3, Chapter 6 (American Scientific Publication, Stevenson Ranch, 2009), p. 147
23. T. Watabe, I. Hisaki, N. Tohnai, M. Miyata, *Chem. Lett.* **36**, 234 (2007)
24. T. Watabe, K. Kobayashi, I. Hisaki, N. Tohnai, M. Miyata, *Bull. Chem. Soc. Jpn.* **80**, 464 (2007)
25. T. Watabe, D. Yoshikawa, I. Hisaki, N. Tohnai, M. Miyata, *Chem. Lett.* **35**, 806 (2006)
26. I. Hisaki, T. Watabe, Y. Kogami, N. Tohnai, M. Miyata, *Chem. Lett.* **35**, 1274 (2006)
27. I. Hisaki, N. Shizuki, K. Aburaya, M. Katsuta, N. Tohnai, M. Miyata, *Cryst. Growth Des.* **9**, 1280 (2009)
28. I. Hisaki, N. Shizuki, T. Sasaki, Y. Ito, N. Tohnai, M. Miyata, *Cryst. Growth Des.* **10**, 5262 (2010)
29. T. Sasaki, N. Shizuki, E. Hiraishi, N. Tohnai, M. Miyata, *Org. Biomol. Chem.* **10**, 5985 (2012)
30. A. Tanaka, K. Inoue, I. Hisaki, N. Tohnai, M. Miyata, A. Matsumoto, *Angew. Chem. Int. Ed.* **45**, 4142 (2006)
31. M. Miyata, N. Tohnai, I. Hisaki, *Acc. Chem. Res.* **40**, 694 (2007)
32. I. Hisaki, N. Tohnai, M. Miyata, *Chirality* **20**, 330 (2008)
33. I. Hisaki, T. Sasaki, N. Tohnai, M. Miyata, *Chem. Eur. J. (Concept)* **18**, 10066 (2012)
34. I. Hisaki, T. Sasaki, N. Tohnai, M. Miyata, *J. Synth. Org. Chem. Jpn.* **70**, 908 (2012)
35. T. Sasaki, I. Hisaki, N. Miyano, N. Tohnai, K. Morimoto, H. Sato, S. Tsuzuki, M. Miyata, *Nat. Commun.* **4**, 1787/1–7 (2013). doi:[10.1038/ncomms2756](https://doi.org/10.1038/ncomms2756)
36. T. Sasaki, Y. Ida, I. Hisaki, T. Yuge, Y. Uchida, N. Tohnai, M. Miyata, *Chem. Eur. J.* **20**, 2478 (2014)
37. G.R. Desiraju, *Angew. Chem. Int. Ed.* **34**, 2311 (1995)
38. P. Ganguly, G.R. Desiraju, *CrystEngComm* **12**, 817 (2010)
39. G.R. Desiraju, T. Steiner, *The Weak Hydrogen Bond* (Oxford University Press, Oxford, 1999)
40. G. Gilla, P. Gilli, *The Nature of the Hydrogen Bond* (Oxford University Press, Oxford, 2009)
41. M. Nishio, M. Hirota, Y. Umezawa, *The CH/π Interaction – Evidence, Nature, and Consequences* (Wiley-VCH, New York, 1998)
42. E.R.T. Tiekink, J. Zukerman, *The Importance of Pi-Interactions in Crystal Engineering* (Wiley, Schpector, 2012)
43. G.R. Desiraju, *Crystal Engineering* (Elsevier, Amsterdam, 1989)
44. B. Moulton, M.J. Zaworotko, *Chem. Rev.* **101**, 1629 (2001)
45. D.B. Amabilino (ed.), *Chirality at the Nanoscale: Nanoparticles, Surfaces, Materials and More* (Wiley-VCH, Weinheim, 2009)
46. T. Sasaki, Y. Ida, A. Tanaka, I. Hisaki, N. Tohnai, M. Miyata, *CrystEngComm* **15**, 8237 (2013)
47. T. Sasaki, I. Hisaki, S. Tsuzuki, N. Tohnai, M. Miyata, *CrystEngComm* **14**, 5749 (2012)
48. M.C. Etter, *Acc. Chem. Res.* **23**, 120 (1990)
49. J. Bernstein, R.E. Davis, L. Shimoni, N.L. Chang, *Angew. Chem.* **1995**, 107 (1689), *Angew. Chem. Int. Ed.* **1995**, 34, 1555
50. J. Grell, J. Bernstein, G. Tinhofer, *Acta Crystallogr. Sect. B* **55**, 1030 (1999)
51. K. Sada, T. Tani, S. Shinkai, *Synlett* **15**, 2364 (2006)
52. T. Yuge, N. Tohnai, T. Fukuda, I. Hisaki, M. Miyata, *Chem. Eur. J.* **13**, 4163 (2007)
53. T. Yuge, T. Sakai, N. Kai, I. Hisaki, M. Miyata, N. Tohnai, *Chem. Eur. J.* **14**, 2984 (2008)
54. C.W. Bunn, *Proc. R. Soc.* **A180**, 67 (1942)

# Chapter 20

## Chiral Discrimination in the Solid State: Applications to Resolution and Deracemization

G rard Coquerel

**Abstract** Chiral discrimination in the solid state is addressed in several ways: (1) thermodynamics of equilibrium, (2) crystal packing, and (3) in a dynamic mode, by entrainment and deracemization. Based on several deviations from a pure even distribution, the hypothesis of clusters of conglomerates is put forward. For a chiral molecule, without any clear filiation from a known conglomerate, the question of prediction of full discrimination in the solid state remains open. Nevertheless, several avenues for new researches in that field are proposed. Progress on detection of conglomerates is detailed. New developments in preferential crystallization coupled or not with racemization in the liquid phase are detailed.

**Keywords** Chiral discrimination • Solid state • Preferential crystallization • Deracemization

### 20.1 Introduction

In 1848 Louis Pasteur found that the optically inactive tetrahydrated sodium ammonium tartrate is actually an equimolar mixture of (+) and (−) components. This is the landmark experiment which represents the birth of stereochemistry. In modern terms we will say that he found the first conglomerate: the first spontaneous chiral discrimination in the solid state. On top of that he could resolve this 50–50 mixture by recognition of the hemihedrism of the crystals enabling hand sorting. This chapter is devoted to the extension of that seminal work by considering in sequence the last developments of both the thermodynamic aspect and the crystallographic aspect. Then new resolution and deracemization processes based on crystallization will be detailed.

---

G. Coquerel (✉)

Normandie Universit , Crystal Genesis Unit EA3233 IMR 4114, Universit  de Rouen, F-76821  
Mont Saint Aignan CEDEX, France  
e-mail: [gerard.coquerel@univ-rouen.fr](mailto:gerard.coquerel@univ-rouen.fr)

## 20.2 What Is Chirality?

In an  $n$ -dimensional space, an object or a set of objects is chiral if it cannot be superimposed to its mirror image by movements in that space. For a mono-dimensional space (a straight line) three non-regularly distant objects make a chiral set. By moving the set  $A, B, C$  on line  $\Delta$  (Fig. 20.1), it is not possible to make it superimposed to  $A'B'C'$ . To ensure the superimposition it is enough to move in a bidimensional space (a rotation in a plane containing  $\Delta$ ) (Fig. 20.2).

Similarly, in a bidimensional space any scalene triangle is chiral because by translating and rotating this triangle in the plane  $P$ , it is not possible to make it superimposable to its image. An excursion in the three-dimensional space would be enough to turn over  $ABC$  to make it superimposed onto  $A'B'C'$ . In a three-dimensional space the same line of reasoning can be applied.  $ABCD$  being an irregular tetrahedron, it is not superimposable to its mirror image, but a voyage in the 4-dimensional space would be enough to convert it in  $A'B'C'D'$  with a zero energy process (Fig. 20.3)! The trouble is that so far, nobody has found the key to unlock the 4D world, and therefore, we need to rely on “conventional” methods in the 3D space to switch from one enantiomer to its antipode.

**Fig. 20.1** Illustration of 1D chirality

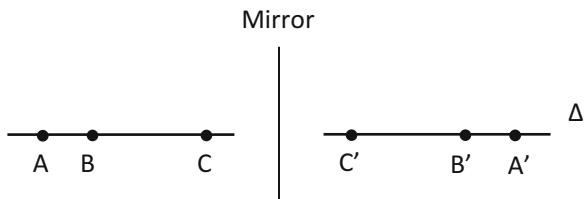


**Fig. 20.2** 2D chirality with two mirror-related scalene triangles

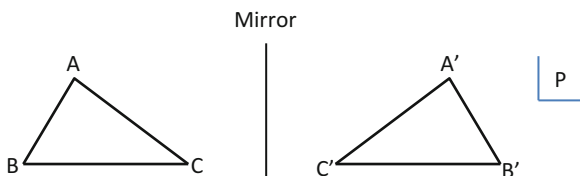
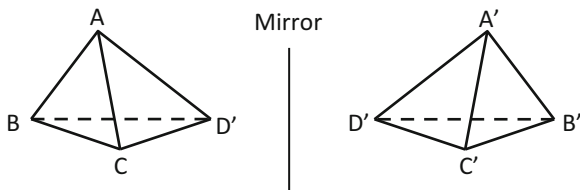


**Fig. 20.3** Schematic representation of chirality in a 3D space by using an irregular tetrahedron



## 20.3 The Thermodynamic Aspect of Chiral Discrimination

We need first to define properly the nature of the  $R$ - $S$  system. Two extreme situations can be distinguished:

1. The two enantiomers racemize rapidly in the liquid phase. The two components are not independent. The system is actually a unary system. This case will be treated later.
2. The two enantiomers are not able to racemize under the operating conditions and the time scale used. The system behaves like a symmetrical binary system. The symmetry comes from the exact equality between temperature of fusion,  $C_p$  versus  $T$ , enthalpy of fusion, density, hardness, etc.

### 20.3.1 Non-racemizable Enantiomers (Fig. 20.4)

Binary systems represented in Fig. 20.4 represent the most probable binary systems for a couple of non-racemizable enantiomers (and especially 4d to 4f with a probability of circa 90–95 %). In Fig. 20.4a the two enantiomers do not form any intermediate compound. There are just two liquidus lines more or less fitting with the simplified Schröder–Van Laar equation [2, 3]. A metastable  $\langle R-S \rangle$  compound cannot even be observed by contrast to Fig. 20.4b, c where a metastable racemic compound is becoming progressively less metastable. In Fig. 20.4c the metastable racemic compound  $\langle R-S \rangle$  is likely to be easily crystallized by a fast cooling of the molten racemic mixture down to a temperature below its metastable melting point. Systems depicted in Fig. 20.4a–c are called conglomerates and they represent a full spontaneous chiral discrimination in the solid state. Indeed every unitary particle should contain a single enantiomer only. According to several authors [4], they represent between 5 and 10 % of the total racemic mixtures.

In Fig. 20.4d, the racemic compound  $\langle R-S \rangle$  has changed its status because now it is a stable intermediate compound. The thermal stability of that  $\langle 1-1 \rangle$  stoichiometric compound increases from Fig. 20.4d–f. The Prigogine–Defay–Mausser equation [5] fits reasonably well with the liquidus of that intermediate compound. The horizontal tangent at the apex of the liquidus means that there is no specific  $R$ - $S$  association in the liquid state. The eutectic invariant between the two enantiomers has become metastable starting on the case depicted in Fig. 20.4d.

It is worth noting that due to shorter free migration path, the racemic compound whether stable or not has always a kinetic advantage over the conglomerate. In Fig. 20.4d–f, the metastable eutectic (i.e., conglomerate) is represented but probably difficult to observe.

It is also worth mentioning that discrete cases only are depicted from Fig. 20.4, but the readers have to conceive that there is actually a continuum.

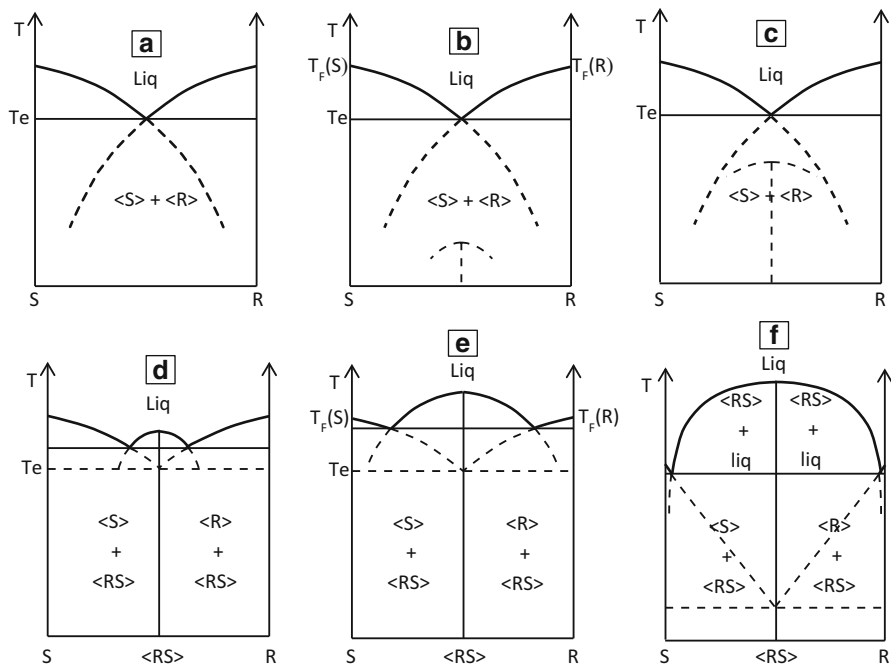


**Fig. 20.4** Progressive evolution of the thermal stability of the racemic compound  $\langle 1-1 \rangle$ . (a–c) correspond to a conglomerate-forming system; a metastable racemic compound appears in **b**, **c**. (d–f) correspond to racemic compound forming systems

### 20.3.2 What Are the Interests of Detecting a Stable Conglomerate?

- Recovering of the entire enantiomeric excess by a rationalized recrystallization

Figures 20.5, 20.6, and 20.7 show the enantiomeric purification of a mixture which was initially at 50 % e.e. In Fig. 20.5 the whole enantiomeric excess is recovered, the mother liquid is at 0 % e.e. at the end of the crystallization – filtration. In Fig. 20.6, one can see that at the end of the recrystallization, the mother liquor will contain ca. 30 % e.e. which shows the significant low yield of the purification by recrystallization.

In Fig. 20.7, it would not be possible to access to the pure enantiomer by simple recrystallization. Only the biphasic domain racemic compound and its saturated solution are accessible. Therefore, a partial purification can be completed up to 70 % e.e. Figure 20.7 corresponds more or less to Fig. 20.4e. If we consider now Fig. 20.4f, there is a high thermal stability of the racemic compound when compared to that of the enantiomers; this means a strong heterochiral recognition in the solid state. If now we consider an isotherm with this case (not represented), the doubly saturated solution (the equivalent of point J in Fig. 20.7) will certainly be shifted

**Fig. 20.5** Isothermal representation of a conglomerate at that temperature. The initial e.e. can be recovered as a pure  $\langle R \rangle$  in a quantitative way by adjusting the amount of solvent so that the overall synthetic mixture is represented by point K

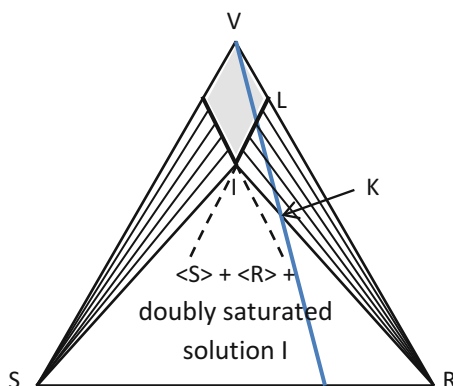


**Fig. 20.6** Isothermal representation of a racemic compound forming system with a small biphasic domain  $\langle RS \rangle$  plus its saturated solution. In order to access to the pure enantiomer, the purification of the initial mixture is possible, but the yield will be much lower than that described in Fig. 20.5

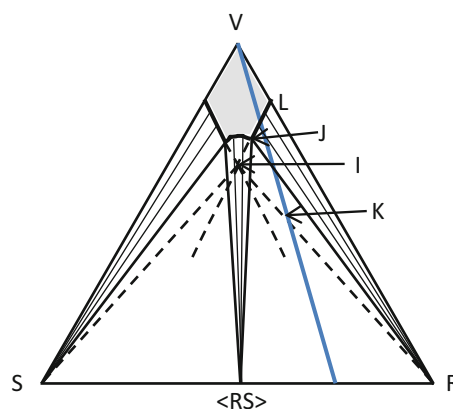
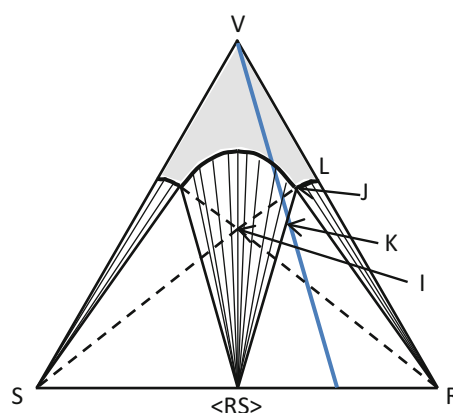


**Fig. 20.7** Isothermal representation of a racemic compound forming system with a large biphasic domain  $\langle RS \rangle$  plus its saturated solution. By considering stable equilibrium only, the access to the pure enantiomer by recrystallization from a (25 S-75 R, i.e., e.e. = 50 %) mixture in that solvent at that temperature is not possible



toward higher e.e. (>90 %). Then, the strong heterochiral recognition in the solid state leads to a high homochiral recognition in solution. This phenomenon is partly responsible for preferential enrichment.

- Quantitative resolution of the racemic mixture

If the so-called preferential crystallization is applicable, it is possible to resolve the racemic mixture without using any chiral auxiliary. This cost-effective process can be run at laboratory scale and in industry at tons scale. A new variant of the process will be detailed later.

- Induction of the preferential primary nucleation

In a supersaturated solution containing a racemic mixture of the enantiomers plus a small concentration of a structurally related chiral impurity, it is possible to initiate a stereoselective primary nucleation of one of the two enantiomers of the racemic mixture [6, 7].

- Deracemization by means of catalyst and a flux of energy (attrition, temperature cycling, temperature gradient, ultrasounds, etc.; see paragraph on racemizable enantiomers)

If crystallization and racemization can be combined under the same operating conditions, it is possible to “push” the system initially containing a racemic suspension, toward a suspension of a single enantiomer (see last paragraph in complement to Professor Richard Kellogg chapter in this book).

Figure 20.8a, b shows hybrid cases where the stability of the conglomerate and that of the racemic compound swap round according to temperature. In Fig. 20.8a, the conglomerate is stable at low temperature up to  $T_E$  where a eutectoid invariant [1] corresponds to the reversible formation of the racemic compound toward high

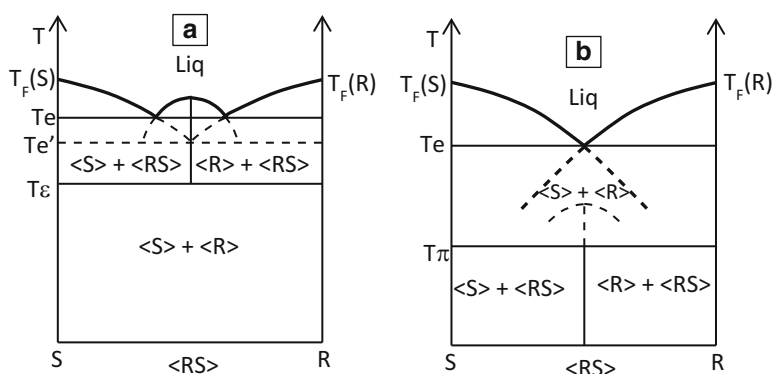


**Fig. 20.8** Inversion of the stability versus temperature between the conglomerate and the racemic compound. In (a) the conglomerate is stable at low temperature  $T < T_E$  and the racemic compound is stable for  $T > T_E$ . In (b) The racemic compound is stable up to  $T_\pi$ ; above that temperature the conglomerate is stable

temperature. In Fig. 20.8b, the stability of the conglomerate and that of the racemic compound are inverted. At low temperature for  $T < T\pi$ , the racemic compound is stable. But at  $T = T\pi$ , a peritectoid invariant corresponds to the reversible decomposition of this intermediate compound into its components  $\langle R \rangle$  and  $\langle S \rangle$  which are then stable up to the eutectic temperature  $T_e$ . The metastable liquid of the racemic compound is presented, but it might be difficult to observe. It is important to avoid confusion between those three phase invariants and polymorphism or any other solid–solid transitions. At  $T\pi$  and at  $T\varepsilon$ ,  $\Delta G = 0$  showing how close the competition in free energy between the racemic compound and the conglomerate could be.

Figure 20.9 is also a hybrid case: a conglomerate-forming system with symmetrical partial solid solutions [8–11]. The chiral discrimination is not total; a certain fraction of the antipode substitutes, at random, the major enantiomer to the benefit of the free enthalpy. These borderline cases are interesting, and they show the subtle interplay between density, chiral recognition,  $C_p$  versus  $T$ , entropy, etc.

In Fig. 20.10 at high temperature, there is a complete solid solution. Both enantiomers are randomly distributed in every particle. At low temperature the dashed-dotted line represents the possibility of an ordered racemic phase at low

**Fig. 20.9**  
Conglomerate-forming system with partial solid solutions on both ends in composition of the diagram

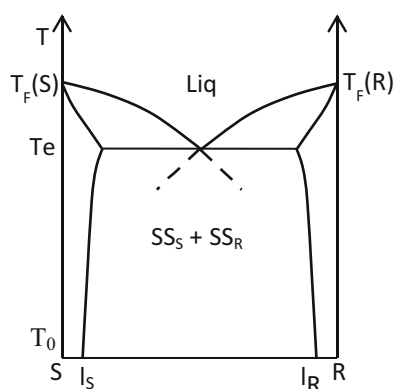


**Fig. 20.10** Complete solid solution by means of substitution (SSS) between the two enantiomers. The dashed-dotted line represents a possible ordered racemic phase at low temperature

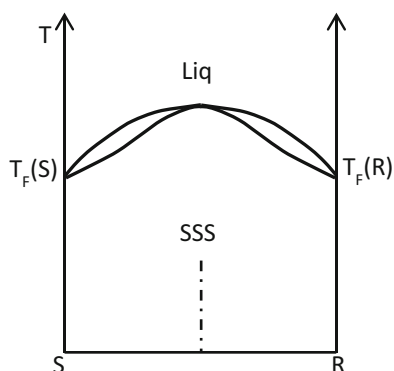


**Fig. 20.11** Isotherm corresponding to a conglomerate-forming system with partial solid solutions.  $L$  is the solubility of the pure enantiomer;  $I$  is the solubility of the racemic mixture. The tie line connects the composition of the solid solution with that of the corresponding saturated solution

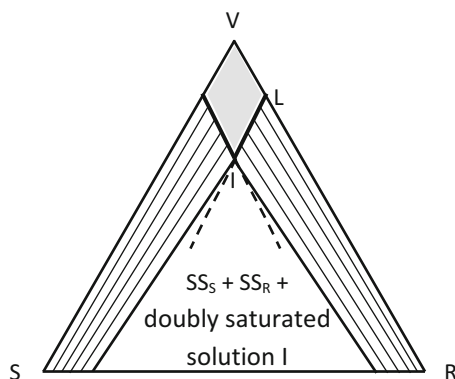
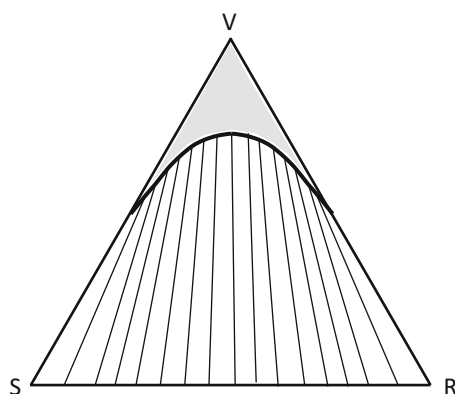


**Fig. 20.12** Complete solid solution between two enantiomers with a slight deviation from ideality because the tie lines connecting the compositions of the solid phase and the corresponding saturated solution do not converge to point V



temperature since the panel of space groups is bigger for the racemic composition (see later). There is barely any chiral discrimination in this case.

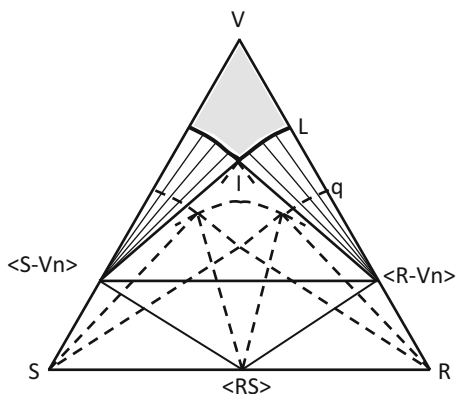
The conglomerate with partial solid solutions presented in Fig. 20.9 can lead to an isotherm such as the one presented in Fig. 20.11. Access to the pure enantiomer, although possible, is difficult in that case and will be at the expense of the yield.

Figure 20.12 corresponding to the situation depicted in Fig. 20.10 exemplifies the very poor chiral discrimination. The readers could check that the tie lines connecting the composition of the solid phase to that of the liquid phase have a very small deviation from ideality, i.e., the tie lines do not converge to point V.

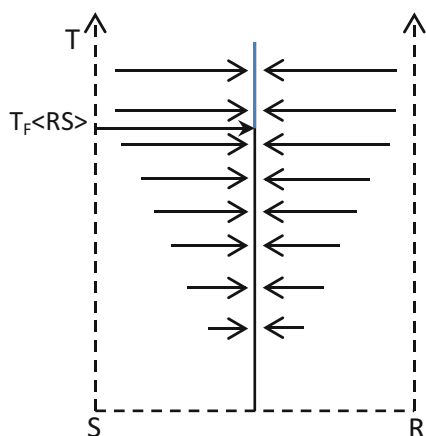
When seeking for a conglomerate, changing the partner of crystallization (for instance, salt screening) is not enough to maximize the chance of success. Indeed, there are numerous examples (some of them will be detailed in the next section on the structural aspect of chiral discrimination) for which the full chiral discrimination in the solid state is obtained when three partners of crystallization are put together: the enantiomer, the counter ion, and a solvent molecule. Figure 20.13 is a sketch representing this kind of situation: the conglomerate exists only for the mirror-imaged solvated phases.

**Fig. 20.13**

Conglomerate-forming system of solvated solids:  $\langle S-Vn \rangle$  and  $\langle R-Vn \rangle$ .  $L$  is the solubility of the pure solvated enantiomer  $R$ .  $I$  is the solubility of the conglomerate. Point  $q$  represents the metastable solubility of the non-solvated enantiomer. The tie lines connect the compositions of the saturated solutions and that of the pure enantiomers



**Fig. 20.14** Unary system of a couple of enantiomers crystallizing as a racemic compound. The *arrows* show the irreversible evolution of the system which will converge to the racemic composition. The length of the arrows is figurative of the conversion kinetics toward the racemic composition



### 20.3.3 Racemizable Enantiomers

In case of fast racemization in the liquid state and no racemization in the solid state, the binary and ternary systems are actually degenerated. In Fig. 20.14 a racemic compound exists as a stable phase; the only accessible state of the system is the median line: red for the solid phase and blue for the liquid phase. Note that by means of asymmetric synthesis, it might be possible to access to the pure enantiomer. If this enantiomer is stored at a temperature far from melting point, it is possible to construct in an appropriate solvent an out of equilibrium ternary isotherm such as that displayed in Figs. 20.6 and 20.7. If the temperature of the isotherm is too high and/or the solvent has also a catalytic effect, the ternary isotherm is reduced to the median line (Fig. 20.15).

If there is no stable heterochiral recognition (i.e., no formation of a racemic compound), then the system is ready for a spontaneous or induced break of symmetry depending on experimental conditions. Binary systems displayed on

**Fig. 20.15** Corresponding degenerated binary system of Fig. 20.14 in which the two enantiomers racemize easily in solution; temperature is fixed. Only racemic suspension and racemic solution are accessible for system in equilibrium. Point I represents the solubility of the racemic compound

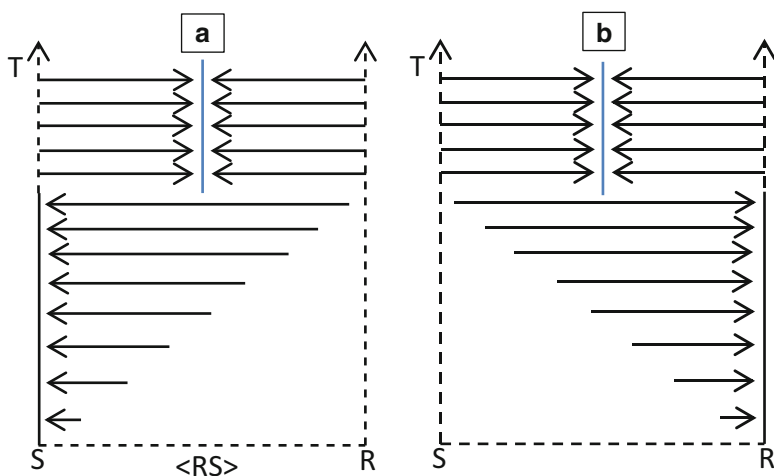
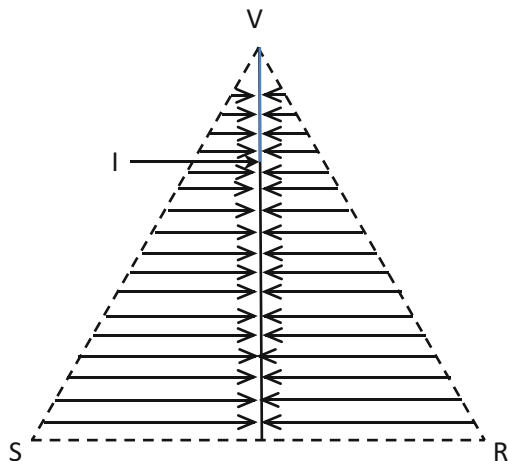


**Fig. 20.16** Degenerated unary system of a couple of enantiomers crystallizing as a conglomerate; i.e., in the solid state, when equilibrium is reached, only a single enantiomer can be present (spontaneous break of symmetry). In case a, senantiomer won the competition; in case b, renantiomer won the competition

Fig. 20.16 show that the system will evolve toward a pure enantiomer. The final evolution toward an intermediate e.e. has been predicted [12] and will correspond to the equivalent of partial solid solutions. This phenomenon has clear application in fundamental sciences such as how homochirality has emerged in some part of the universe. It has also important applications in deracemization of chiral substances [13]. Instead of asymmetric synthesis, one can shift the racemic mixture to the desired enantiomers by Viedma ripening or any other variant or even by second-order asymmetric synthesis (SOAT) [14]. The last part of this chapter is devoted to this kind of process (Fig. 20.17).

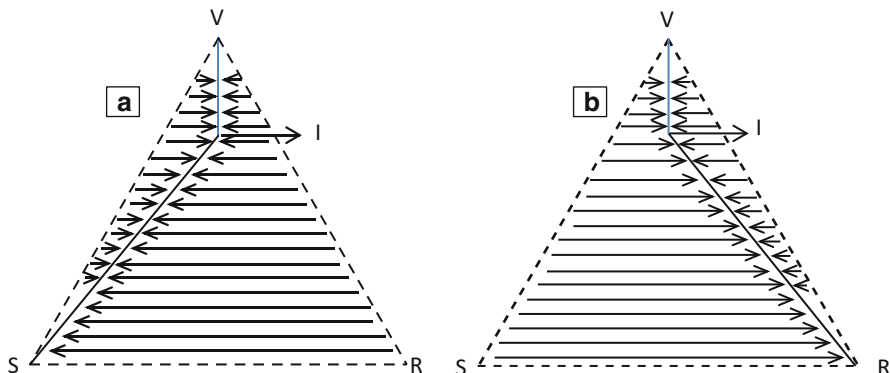


**Fig. 20.17** Degenerated ternary system of a couple of enantiomers crystallizing as a conglomerate in a solvent V in which fast racemization takes place, i.e., when equilibrium is reached only a single enantiomer can be present in the solid state and the saturated solution is racemic (spontaneous break of symmetry)

## 20.4 Structural Aspects of the Chiral Discrimination in the Solid State

### 20.4.1 Crystallographic Requirements for Homochirality

Starting from the 32 point groups which are compatible with 3 independent translations (the dogma for crystallized matter), it is possible to define 230 space groups by including microscopic translations associated with direct rotations (two-, three-, four-, and sixfold axes) and mirrors (i.e.,  $-2$  axis). The formers become screw axes  $\Lambda_n$ :  $2_1$ ,  $3_1$ ,  $3_2$ ,  $4_1$ ,  $4_2$ ,  $4_3$ ,  $6_1$ ,  $6_2$ ,  $6_3$ ,  $6_4$ , and  $6_5$ , with a translation of  $n/\Lambda$  for an elementary rotation  $2\pi/\Lambda$ , and the latter become glide mirrors,  $a$ ,  $b$ ,  $c$ ,  $n$ , and  $d$ , with translations,  $a/2$ ,  $b/2$ ,  $c/2$ ,  $(a+b)/2$  or  $(a+c)/2$  or  $(b+c)/2$ ,  $(a\pm b)/4$ ,  $(c\pm b)/4$ , and  $(a\pm c)/4$ , associated with the mirror operation, respectively.

The set of 230 space groups can be partitioned in three subsets (see Table 20.1):

- The 92 centrosymmetric space groups which contain a center of symmetry – labeled  $(-1)$  – at every origin of the lattice and at the center of the unit cell (sometimes more, for instance, in case of mode different from P). The crystal lattices corresponding to these space groups are compatible with racemic compounds. Small deviations from the pure  $R/S = 1$  stoichiometry cannot always be ruled out as appears in preferential enrichment [15]. In that case the genuine symmetry is actually  $(1)$ , but due to average and small deviation only, the X-ray diffraction method still sees only  $(-1)$ . Therefore, a pure enantiomer cannot crystallize with these 92 space groups of this class.
- The 65 chiral space groups. The symmetry operations are exclusively translations and direct rotations (if any). By contrast to the former subset, the pure enan-

**Table 20.1** Distribution of the centrosymmetric, chiral (i.e., Sohncke space groups) and non-centrosymmetric and non-chiral space groups among the seven systems

System	Centrosymmetric space groups	Chiral space groups	Non-centrosymmetric
			Non-chiral space groups
Triclinic	1	1	–
Monoclinic	6	3	4
Orthorhombic	28	9	22
Tetragonal	26	16	26
Cubic	17	13	6
Trigonal	8	11	6
Hexagonal	6	12	9
<b>Total</b>	<b>92</b>	<b>65</b>	<b>73</b>
<b>Frequency (in CSD 2014)</b>	<b>78 %</b>	<b>15.7 %</b>	<b>6.3 %</b>

tiomers can crystallize with these symmetries. In rather rare instances racemic compounds have also been observed to crystallize with these space groups. Of course, the two enantiomers are independent molecules in a crystallographic sense of the term. These two molecules can have different conformations in the solid state; let us define conformations: 1 and 2. Several crystal structures of “false conglomerates” [16] or “kryptoracemates” have been published so far [17, 18]. For instance, single crystals could contain either  $R_1S_2$  or  $R_2S_1$  within space group  $P2_12_12_1$ . The solid particles are therefore mirror related, but on dissolution every particle gives back a racemic solution.

- The 73 space groups which are not centrosymmetric but also not chiral. These crystal lattices contain the following symmetry operations: mirrors ( $-2$ ) or glide mirrors or inverted axes ( $-4$ ) and ( $-6$ ) which means that both enantiomers are in equal number in every particle. Therefore, once again these space groups are forbidden for the pure enantiomers but compatible with a racemic compound.

## 20.4.2 Statistical Aspects

If we look at the statistics on the frequency of these space groups (organic and metal organic compounds; see Tables 20.1 and 20.2), it is clear that there is a large deviation from an even distribution. Kitaigorodsky [19, 20] had long ago recognized that nature prefers to put a center of symmetry in organic crystals. According to figures in Table 20.2, it is more than three quarter of the molecules which crystallize in one of the centrosymmetric space groups. It is also important to say that these statistics are biased because the 92 centrosymmetric space groups (as the other 73 subsets of non-chiral non-centrosymmetric SG) are disqualified for the packing of pure chiral molecules.

**Table 20.2** Top 12 space group frequencies in the CSD 2014

Space group number	Space group	Frequency (%)	Frequency (%) among chiral space group
		Top 10 > 90 %	
14	P2 <sub>1</sub> /c	34.8	–
2	P-1	24.1	–
15	C2/c	8.3	–
19	P2 <sub>1</sub> 2 <sub>1</sub> 2 <sub>1</sub>	7.4	54.9–58.9
4	P2 <sub>1</sub>	5.2	28.5–29.8
61	P2 <sub>1</sub> /b2 <sub>1</sub> /c2 <sub>1</sub> /a	3.4	–
33	Pna2 <sub>1</sub>	1.4	–
62	P2 <sub>1</sub> /n2 <sub>1</sub> /m2 <sub>1</sub> /a	1.1	–
9	Cc	1.1	–
1	P1	0.9	4.0
60	P2 <sub>1</sub> /b2/c2 <sub>1</sub> /n	0.9	–
5	C2	0.7	3.5

After Ref. [47]

Pna2<sub>1</sub> and Cc are among the 73 members of their family, the two only non-centrosymmetric and non-chiral space groups appearing in the top twelve and not better ranked than (7–1.4 % and 9–1.1 %). If we neglect this set of non-centrosymmetric and non-chiral space groups with low occurrence, the dilemma of chiral discrimination in the solid state results from a competition between centrosymmetric and chiral space groups.

In Table 20.2, the four highlighted space groups account for circa 90 % of all “small” chiral organic molecules. For the rest, P2<sub>1</sub>2<sub>1</sub>2 and (P4<sub>1</sub>2<sub>1</sub>2–P4<sub>3</sub>2<sub>1</sub>2) are sometimes observed, and then, with a lower probability C222<sub>1</sub>, R3, (P4<sub>1</sub>–P4<sub>3</sub>), (P3<sub>1</sub>21–P3<sub>2</sub>21), (P3<sub>1</sub>–P3<sub>2</sub>), and P6<sub>3</sub> are in this order with a minor occurrence, etc. In other words, the number of crystal symmetries observed for chiral organic molecules is even lower than the number of crystal symmetries with a significant occurrence for other molecules in the whole set of space groups. Interestingly, the percentage of structure with several molecules in the asymmetric unit is higher for chiral space groups (ca. 15 %) than for the entire CSD (ca. 9 %) [21].

In Table 20.1, the chiral space groups account for circa 15.7 % of all crystals. In fact, for a given chiral molecule, there is not ca. 4 times more chance to have centrosymmetric space groups rather than chiral space groups for its racemic mixture. The statistics indicates 10–20 times more chance to have a centrosymmetric space group rather than a chiral space group (quasi exclusively corresponding to a conglomerate; the kryptoracemic compound being exceptional). The reason for that discrepancy comes from non-chiral molecules which could crystallize with a chiral space group. We will return to that question later.

### 20.4.3 On the Existence of Clusters of Conglomerates

As said in the previous paragraph, it is commonly accepted that the frequency of conglomerate is between 5 and 10 %. The validity of this estimation depends on the homogeneity of the distribution. Actually the author of this chapter is in the opinion that the conglomerates are not evenly distributed, and thus, the accepted occurrence – without being meaningless – is not very informative. The examples shown in Fig. 20.18 about a series of conglomerates evidence that there are in fact clusters of conglomerates. Thus, it is possible to have some substitutions on a conglomerate-forming molecule and to obtain other conglomerates. This is especially valid when the most energetic periodic bond chains (PBCs) between the molecules are not affected by the substitution. If, for instance, we take the 5-aryl-5-alkylhydantoin series, no less than 10 conglomerates have been spotted so far and probably several others exist. By considering an optimistic 10 % statistical chance to obtain a conglomerate, we understand that there is here “something” which deviates from a pure probabilistic aspect. Moreover, most of these derivatives have two polymorphs: one  $P2_12_12_1$  variety and one  $P2_1$  variety. All of them have the common  $6.23 \pm 0.02$  Å translation vector corresponding to the strong H-bonds network forming a flat ribbon involving every heteroatom of the hydantoin ring (O and N) (see next section Fig. 20.23). Preferential crystallization is efficient and easy to run on those derivatives. So far no metastable racemic compound has been spotted, except the efflorescent monohydrate of the derivative  $R2 = \text{Me}$  and  $R1 = \text{Et}$  [22].

Another striking example is (+) and (–) ethanolammonium mandelates (Fig. 20.18d) which crystallize as a conglomerate with partial solid solutions (see Figs. 20.9 and 20.11 [8]). As already said, so far a very limited number of examples

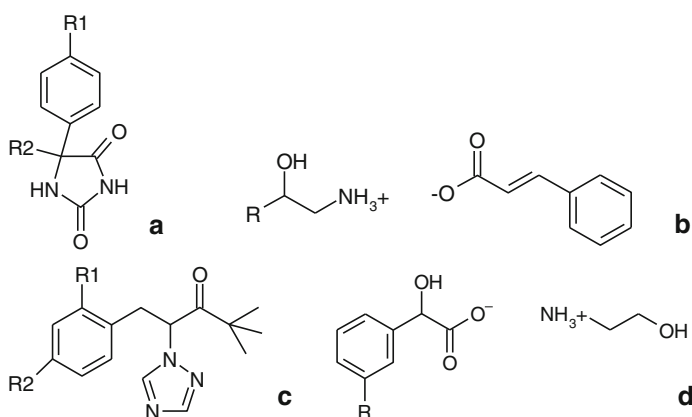


**Fig. 20.18** Series of conglomerates: (a) for  $R2 = \text{Me}$   $R = \text{H, Me, Et, MeO, Cl, Br, I}$ , for  $R2 = \text{Et}$ ,  $R1 = \text{H}$ , for  $R2 = \text{CF}_3$ ;  $R1 = \text{H}$  and  $\text{MeO}$ ; (b) for  $R = \text{Me, Et, Pr, iPr, But, IBut, and cHex}$  [45]; (c) for  $R1 = \text{H}$ ,  $R2 = \text{H, Me, Et, Cl, Br}$  and  $R2 = \text{F}$ ,  $R1 = \text{Cl}$ ; (d) for  $R = \text{H, Cl}$ , and possibly  $\text{Me, Br}$  because of positive SHG signals

of this behavior are known. Therefore, it was a sheer surprise to detect that the (+) and (-) ethanolammonium 3-chloro-mandelate gives also another conglomerate with partial solid solutions [9]. Ongoing researches [23] are devoted to test other derivatives of that family which could present the same unusual features. The “pocket” in position 3 of the phenyl ring – on this position only – may be submitted to various substitutions without impairing the partial homochiral recognition in the solid state.

There is then a new avenue for intense research which is to understand how far we can go in modulation of a given conglomerate-forming molecule to maintain the full chiral discrimination in the solid state.

#### 20.4.4 Importance of Solvates in Chiral Discrimination in the Solid State

A common screening of conglomerate involves a chiral molecule which has the possibility to form salts. If the molecule itself does not crystallize as a conglomerate, a combinatorial screen is usually initiated with simple mineral counter ions and in case of failures then come the organic counter ions from simple (often the cheapest) to more complicated. It is important not only to restrict the screening to the counter ions but also to extend the combinatorial approach to different solvent molecules or even mixtures of solvents. Some examples (Figs. 20.19, 20.20, 20.21, and 20.22) are designed to exemplify those facts for an enhanced probability to find a stable conglomerate. Figure 20.19 shows the connection between citric acid and

**Fig. 20.19** (a) View detailing how the water molecule acts as an electrostatic relay between the cation and the anion. (b) Projection showing how the water molecule is also involved in PBCs

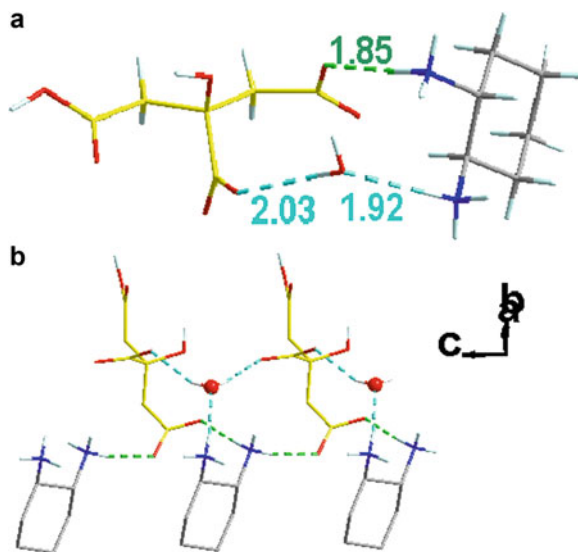


**Fig. 20.20** The ionic connection between  $K^+$  and the imidazole ring is bridged by the hydroxyl group of one of the two ethanol molecules

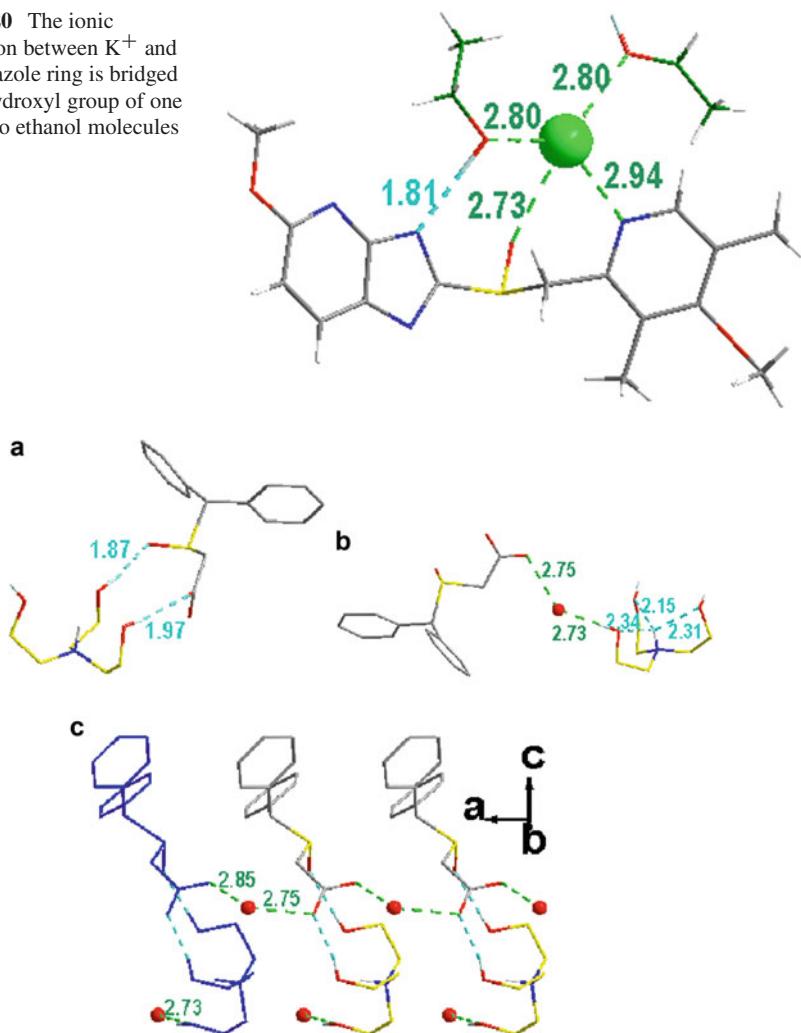


**Fig. 20.21** (a) Modafinilic acid and triethanol amine in a shape of a tulip. The carboxylic acid uses the hydroxyl group as an electrostatic relay to be linked to the ammonium group. (b) The water molecule is an intermediate in the double relay between the cation and the anion. (c) Role of the water molecules in the formation of PBCs triethanolammonium modafinate

*trans*-1,2-diaminocyclohexane of the monohydrated phase crystallizing as a stable conglomerate. The water molecule is very active in the formation of PBCs but also in bridging the cation and the anion of the second carboxylate.

Tenatoprazole crystallizes as conglomerate when the racemic mixture is mixed with an excess of potash in ethanol (Fig. 20.20). The two mirror-imaged solid phases which fully discriminate the two antipodes of this pharmaceutical drug are two diethanolate potassium salts. There is no direct link between the imidazole ring

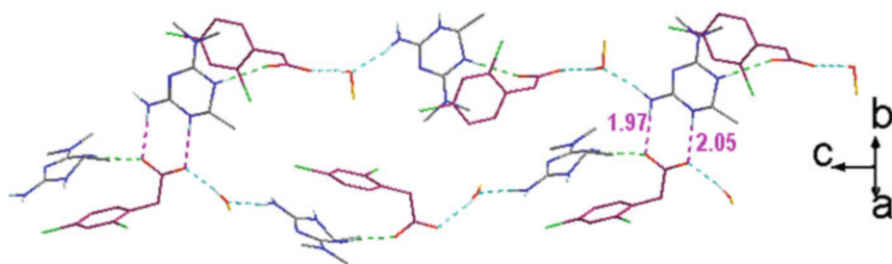


**Fig. 20.22** View along  $\langle 110 \rangle$  vector of the crystal structure of imegliminium 2,4-dichlorophenylacetate-methanol solvate. The H-bond between the carboxylic group and the hydroxyl group of the methanol molecule is 1.79 Å long; the H-bond between the oxygen of the methanol molecule and the imegliminium is 1.98 Å long

(bearing the negative charge) and  $K^+$ . One of the two ethanol molecules is acting as an electrostatic relay between the cation and the anion. The potassium is stabilized by four bonds: 2 ethanol molecules, the oxygen of the sulfoxide moiety, and the nitrogen of the pyridine ring.

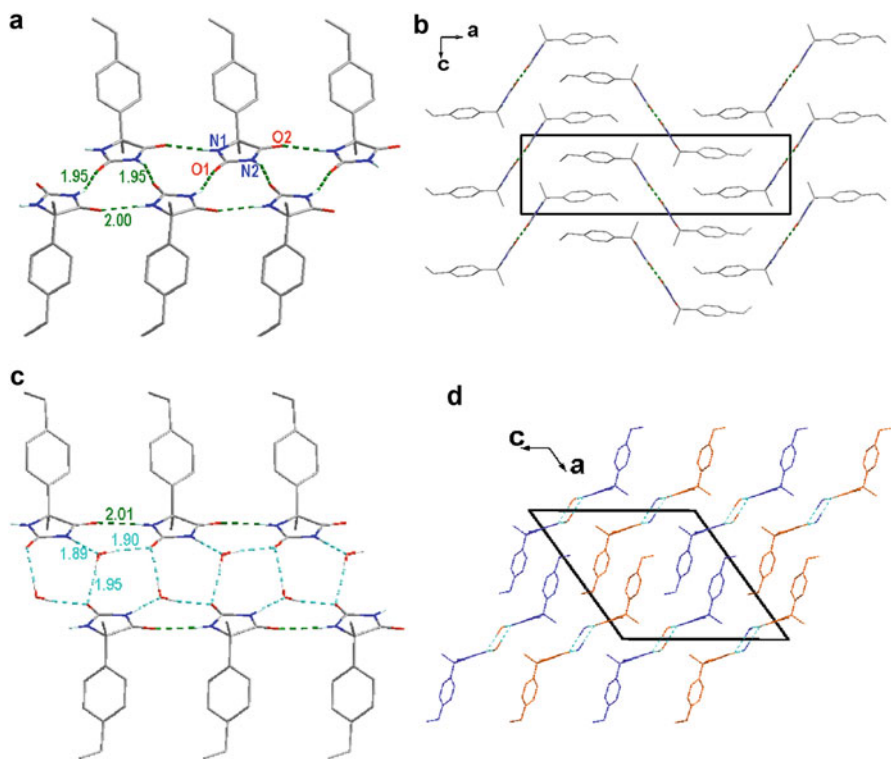
Because of steric hindrance, modafinate anion does not make a direct ionic bond with the triethanolammonium whose shape resembles that of a tulip. The crown of three hydroxyl groups stabilizes the ammonium; two of them are connected to the carboxylate anion and one via the water molecule. This water molecule is also participating in the PBCs via links with two oxygen atoms of two different  $COO^-$  groups (Fig. 20.21c)

Imegliminium 2,4-dichlorophenylacetate-methanol solvate is a highly efflorescent conglomerate at room temperature which is stable in methanolic solution. This conglomerate is suitable for a preparative resolution of  $(\pm)$  imeglimin [24]. The crystal structure reveals the unusual space groups  $P4_1$  and  $P4_3$  for the two enantiomers with a polar morphology. The methanol molecule combines the dual function of electrostatic relay and co-PBC builder (Fig. 20.22).

Of course finding solvates is not the panacea! One could find a racemic compound which is a solvate, whereas the non-solvated enantiomers make as a stable conglomerate or another solvate with a specific solvent molecule can be a conglomerate. More than 30 years of experience in the domain has convinced the author that when one solvate can be found, there are probably others to find.

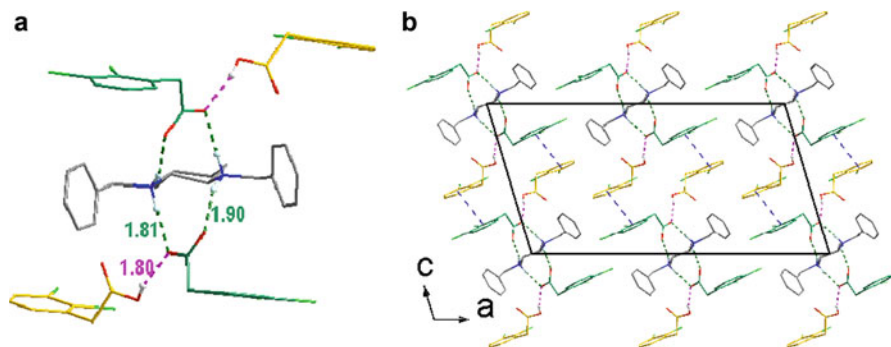
If a smooth and complete desolvation of the racemic solvate can be implemented below the glass transition of the non-solvated component and with the minimum residence time of the solvent molecules, a metastable racemic compound is likely to be formed [22]. It serves to assess the thermal stability difference between the conglomerate and the racemic compound for a given heating rate (see Sect. 20.3.1 and Fig. 20.4a–4)

Figure 20.23 illustrates this behavior for *5-(4-ethylphenyl)-5methylhydantoin*. Figure 20.23a, b shows the packing features of this stable anhydrous conglomerate (SG:  $P2_12_12_1$ ). The ribbon gathering all the strong H-bond appears totally flat



**Fig. 20.23** 5-(4-Ethylphenyl)-5methylhydantoin. Structure of the stable conglomerate in non-aqueous medium. (a) Perspective view of the 6.23 Å *b* axis which gathers the whole H-bonds. (b) Projection along *b* axis of the homochiral crystal packing. Structure of the efflorescent monohydrate. (c) Perspective view of the 6.23 *b* axis which gathers the whole H-bonds with the participation of the water molecule. (d) Projection along *b* axis of the heterochiral crystal packing (racemic compound)

on the projection along *b* axis. Figure 20.23c, d shows the same kind of view for the monohydrate. The two halves of the former homochiral ribbon are now slightly shifted apart and are connected via the water molecules through three H-bonds. The glide mirror *c* in this structure ( $SG = P2_1/c$ ) makes an alternation of (2 0–2) heterochiral slices. Below the glass transition ( $T_g$ ) of the anhydrous pure enantiomer, the kinetics of removal of the water molecules is critical to the nature of the anhydrous solid particles. Indeed, if the dehydration kinetics is fast in a dry environmental atmosphere, most of the structural information of the mother phase will be preserved and a metastable anhydrous racemic compound will be obtained. By contrast even if  $T < T_g$  but the amount of water molecules in the gas phase exceeds 30 % relative humidity at room temperature, the dehydration will proceed through a destructive–reconstructive process. This is perfectly in accordance with the Rouen-96 model of desolvation of molecular compounds [25]. When there is



**Fig. 20.24** (a) Detail of the association between the four equivalents of 2,3-dichlorophenylacetic acid. Two are deprotonated and two are protonated justifying the hybrid character: salt–cocrystal. (b) Projection along *b* axis showing the alternate stacking parallel to (001) of protonated layer of acid in between layers of “salt” associations

transmission of structural information, the departure of water molecule allows the two half ribbons to get closer and a sort of zip-on phenomenon recreates almost the same ribbon as that present in the pure enantiomer. But the heterochiral alternation of the (2 0–2) layer remains, and thus, this phase is a metastable anhydrous racemic compound.

This 5-aryl-5alkylhydantoin derivative is not particularly hygroscopic so that it is easy to work in a “dry” solvent and, for instance, to achieve the preparative resolution by preferential crystallization without any difficulty. In some other instances (e.g., a salt with a sulfonic acid), great care, to prevent uptake of water in the medium, will be necessary in order to avoid the crystallization of a racemic hydrate.

### 20.4.5 *Benefits of Exploring Odd Stoichiometries*

Chemists have always the reflex to test “normal” stoichiometries when dealing with salt formations. Unfortunately this is not necessarily the best way to find a conglomerate. A study on a derivative of (RR) and (SS) 1,4-transdiaminocyclohexane [26] has shown, by serendipity, the formation of a stable conglomerate with four equivalents of 2,3-dichlorophenylacetic acid. Figure 20.24 illustrates the main features of the crystal structure which can be classified as a hybrid salt – cocrystal. Moreover, the resolution by preferential crystallization is, in that case, unexpectedly very efficient: the selective crystallization can go beyond 20 % e.e. on both sides. Therefore, in addition to test a large variety of counter ions, each of them in different solvents, it is advisable to test various stoichiometries including those which seem “unnatural” for a chemist.

### 20.4.6 Detection of Conglomerates

There are numerous methods to detect conglomerates [27]. Owing to the difficulties to predict the existence of a conglomerate and the additional difficulty to know if it is suitable for preferential crystallization, a high-throughput prescreening method has been devised. Figure 20.25 represents the whole setup of this technique. Five nanosecond laser pulses (Nd:YAG; 1,064 nm) are generated at a frequency of 10 Hz. The beam is cleaned of every parasite photons and the energy is adjusted from 0 to 300 mJ. If the material is centrosymmetric, no emission of the second harmonic will be observed. If the material is crystallized and non-centrosymmetric, there will be an emission of a second harmonic that has to be differentiated from any fluorescence or any spurious light by a spectrometer analyzing around 532 nm the ratio intensity of the signal over noise. In practice the signal is valid for 1/100 of the intensity of quartz – a weak reference – whose crystal size distribution is narrow around 50  $\mu\text{m}$ . In case of positive response, further analyses need to be performed to confirm if it is indeed a conglomerate (it could be, for instance, a non-centrosymmetric and non-chiral space group such as  $\text{Pna}2_1\text{-Cc-Pca}2_1\text{-Pc-Fdd}2$  in this order of probability or more exceptionally a kryptoracemic compound; see above). The initial setup [28] has now been improved to be able to detect directly the SHG effect from the suspension, so that conglomerate of efflorescent solvates cannot be missed (e.g., imegliminium 2,4-dichlorophenylacetate-methanol solvate detailed above).

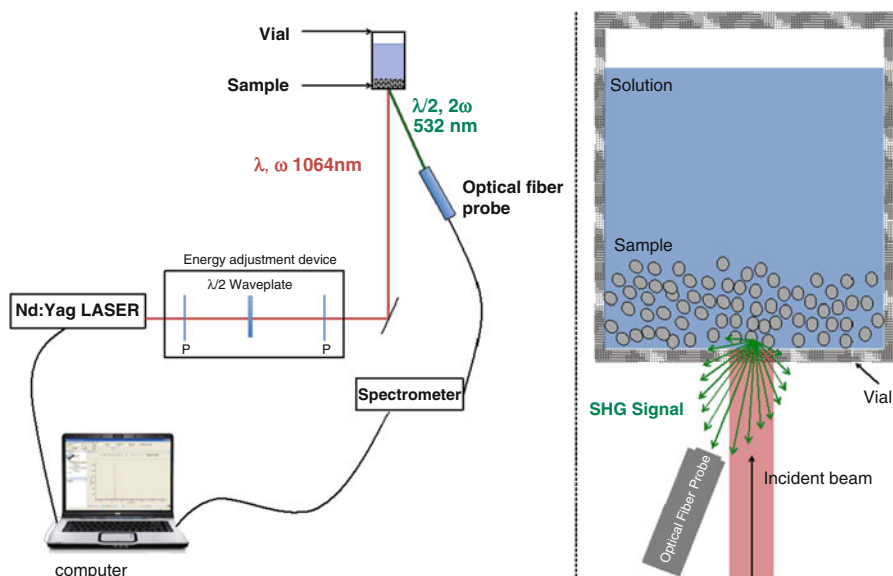


**Fig. 20.25** Scheme of the in situ detection of conglomerate (directly in suspension). This setup avoid to miss conglomerate-forming system of efflorescent solvates [46]

## 20.5 Preferential Crystallization

The reader could refer to reference [27] in which the subject of preferential crystallization induced by cooling has been thoroughly treated. During the last years other problems arose with, for instance, very poor variation of solubility versus temperature, chiral molecules sensitive to thermal treatment, conglomerates of solvates stable at relatively low temperature, etc., which prompt our laboratory to devise a new variant of preferential crystallization named Auto-Seeded *Preferential Crystallization Induced by Solvent Evaporation* (ASPreCISE). The principle is detailed below supposing an ideal mode.

The starting point of the process is a suspension containing an excess of  $\langle R \rangle$  with an initial saturated solution  $L_i$ ; the initial overall composition of the system is  $\Omega_i$  (see Fig. 20.26). The solvent is evaporated continuously; therefore, the overall composition of the system moves toward point E (not represented) receding from solvent V. Simultaneously, the composition of the liquid phase moves along the  $L_i$ – $L$ – $L_F$  trajectory. From  $L_i$  to  $L$ , this is the stable equilibrium, and thus, the genuine “entrainment” proceeds when the solution point goes from  $L$  to  $L_F$  on the metastable solubility curve of  $R$ . When reaching  $L_F$  the suspension is rapidly filtrated.

The recycling of this mother liquor is a two-stroke operation with addition of fine crystals of racemic mixture and solvent (Fig. 20.27) so that (1) the intermediate new overall synthetic mixture is point  $C'$  and (2) solvent is added so that  $\Omega_i'$  is obtained. This point is symmetrical to  $\Omega_i$  with reference to the “racemic line”  $V$ – $(\pm)$ . It is also the starting situation for the second auto-seeded preferential crystallization: for the  $S$  enantiomer. The suspension of  $\langle S \rangle$  with an overall concentration  $\Omega_i'$  and a mother liquor  $L_i'$  is submitted to an isothermal evaporation so that  $\Omega_i'$  moves toward  $\Omega_f'$  and simultaneously the liquid phase has its composition evolving along the  $L_i'$ – $L$ – $L_F'$  trajectory. At that latter point a swift filtration is performed and fine racemic particles are added to the mother liquor ( $L_F' \rightarrow C$ ) and a well-adjusted quantity of

**Fig. 20.26** Detail of an isothermal single ideal entrainment ( $R$  enantiomer) during an auto-seeded preferential crystallization induced by solvent evaporation. Starting from a suspension in equilibrium represented by the overall composition  $\Omega_i$  and the saturated solution  $L_i$ , the evaporation of the solvent moves these two points on  $\Omega_i$ – $\Omega_f$  and  $L_i$ – $L$ – $L_F$  trajectories, respectively

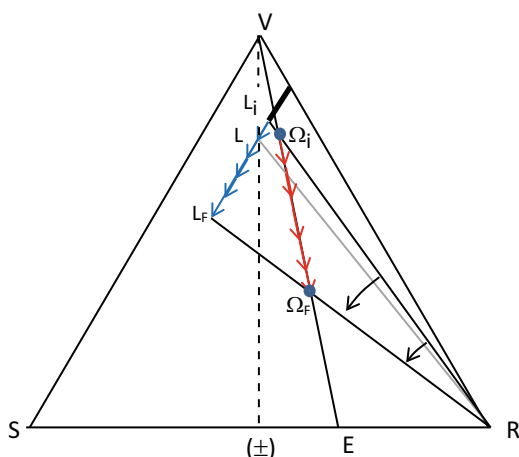
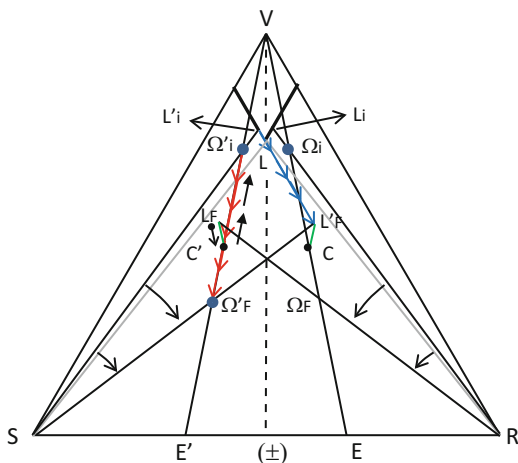


**Fig. 20.27** Full description of ASPreCISE process with a complete cycle of the operation

$V$  stands for a volatile solvent,  $L$  stands for the solubility of the racemic mixture

●→: evolution of the system by addition of ( $\pm$ ) crystals (green line: from LF to C')

→: evolution of the system by addition of solvent from C' to  $\Omega'i$



solvent  $V$  is added so that the composition of the whole system is  $\Omega'i$  again. After the necessary relaxation time to reach equilibrium so that  $S$  is completely dissolved, the saturated liquid phase of the suspension of  $\langle R \rangle$  crystals is back to  $L'i$  and the system is ready for another cycle which will deliver  $\langle R \rangle$  crystals. The sequence of operations is then repeated to give alternatively  $\langle S \rangle$ ,  $\langle R \rangle$ ,  $\langle S \rangle$ ,  $\langle R \rangle$ , etc.

### 20.5.1 Return to Chiral Discrimination in the Solid State

When preferential crystallization has been tested with different modes on 5-ethyl-5-methylhydantoin ( $R1 = Et$ ;  $R2 = Me$ ; 12H hereafter; c.f. Fig. 20.28a), the effect of entrainment has been observed, but the enantiomeric purities of the crude crops were not very good, but neither partial solid solution nor metastable racemic compound [29] could be detected and justify these poor results. The low concentration of the slurry could not be either an explanation. This question has been resolved when it appeared that this stable conglomerate has the ability to form multiepitaxy [30]. The crystal structure of this simple molecule is composed of near flat ribbons involving two nitrogen atoms and one oxygen atom (Fig. 20.28b) by contrast to the 5-alkyl-5-aryl hydantoin derivatives in which the flat ribbon of strong H-bond involves the 4 heteroatoms. The projections along  $b$  axis (Fig. 20.28c, d) show how the enantiomers can make a “magic” repeated epitaxial phenomenon along (101) and (10 $\bar{1}$ ) by means of antiparallel bundling of near flat ribbons with opposite handedness. Indeed, when a racemic solution in ethanol is left to crystallize in quiescent conditions, the shape of single particles is absolutely the same as that

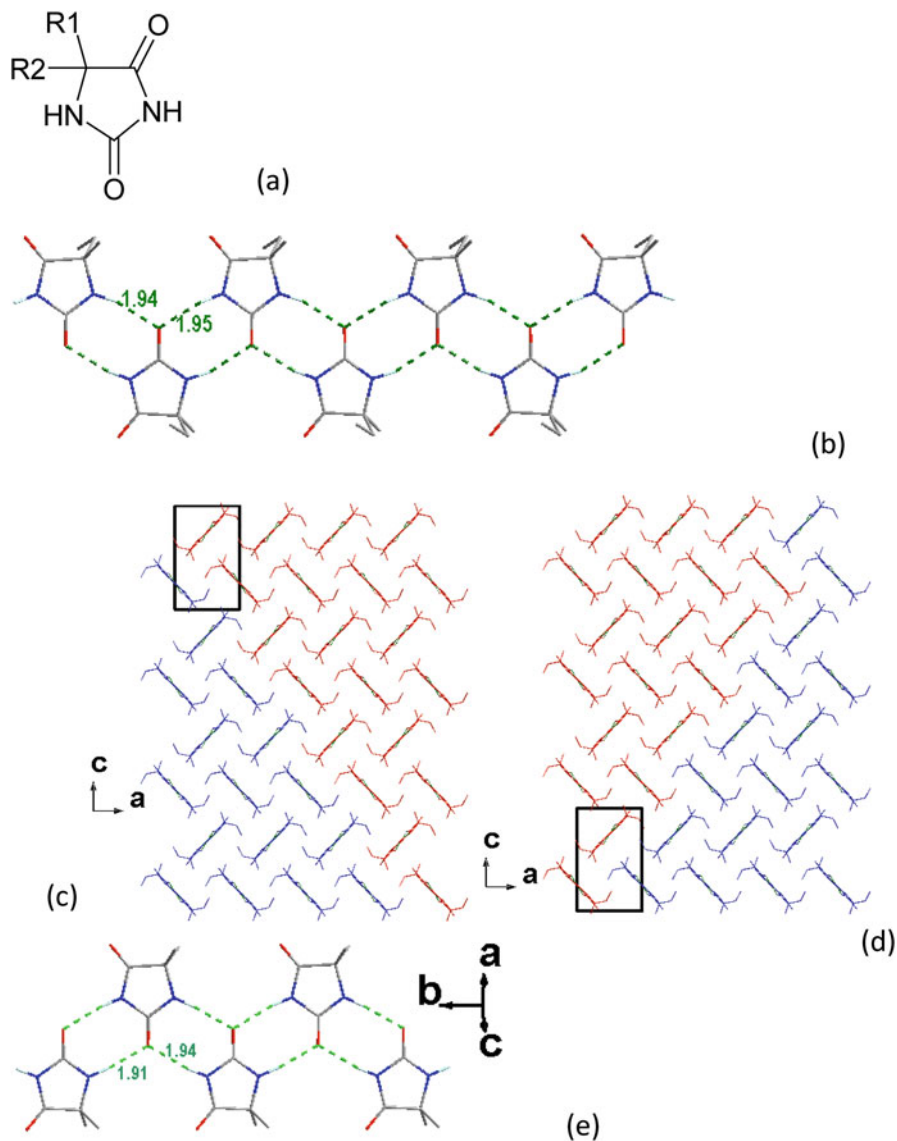


**Fig. 20.28** (a) Sketch of 5-5 derivatives of hydantoin. (b) Near flat H-bond network of 5-ethyl-5-methylhydantoin which crystallizes as a stable conglomerate SG  $P2_12_12_1$ . (c) and (d) projections along b axis showing the epitaxial interface between the two enantiomers along (101) and (10-1) planes, respectively. (e) Near flat H-bond network of the prochiral 5,5-dimethylhydantoin which crystallizes in chiral space group  $P2_12_12_1$

**Table 20.3** Crystallographic parameters of the prochiral 11H and the chiral derivative 12H

Symbol (REFCODE)	Space group	a (Å)	b (Å)	c (Å)
11H (BEPNIT)	P2 <sub>1</sub> 2 <sub>1</sub> 2 <sub>1</sub>	7.216	7.203	13.005
12H (ADUQOF)	P2 <sub>1</sub> 2 <sub>1</sub> 2 <sub>1</sub>	8.013	7.243	12.860

of a single crystal, but actually those particles consist of a stacking of homochiral lamellar fragments. Every interface of the two fragments can be considered as a bidimensional racemic compound. The reason why it does not expand in the third direction to give a “true” 3D racemic compound is unknown. The control of the thickness of those homochiral lamellae is challenging and possibly interesting for the tuning of optical and electronic devices. Several other examples have been published [31–34], but probably many more have been overlooked.

Interestingly the prochiral derivative 5,5-dimethylhydantoin  $R_1 = R_2 = \text{Me}$  (11 H hereafter; refcode: BEPNIT – Fig. 20.28a) crystallizes also in the same chiral space group as the chiral derivative 12H detailed above (refcode: ADUQOF). Moreover the crystallographic parameters are similar (see Table 20.3), and the near flat ribbons of strong H-bonds depicted in Fig. 20.28b, c look pretty similar. An analysis of the supramolecular tilt chirality around the 2<sub>1</sub> helical assemblies as promoted by Prof Miyata’s group [35, 36] reveals a slight asymmetry in the assemblies in the prochiral molecule as the hydantoin rings are not exactly parallel to the b axis. Several questions arise from these observations:

1. As epitaxy has been evidenced in 12H, is there any twinning by inversion in crystal of 11 H which, thus, would be more a patchwork of opposite supramolecular-tilt-chiral domains?
2. If a prochiral molecule spontaneously packs in a chiral space group with a supramolecular tilt chirality, is there any chance to find conglomerates for “close” derivatives which do not disrupt the strongest bond pattern of the structure. So far, in this series only 12H and the 5-vinyl-5-methylhydantoin [4] have been reported as conglomerate-forming systems. It is worth noting that the cluster can be rather “small” as the multiepitaxy detailed above being a sign of an ability to form racemic associations.
3. The putative “clusters” of conglomerates that we have exemplified by few cases above could have extensions on chiral assemblies of prochiral molecules, and vice versa, i.e., new clusters of conglomerate-forming systems could be found by derivatization of prochiral molecules crystallizing in chiral space groups with a supramolecular tilt chirality.

There are here once again interesting avenues for further researches and maybe ways to shed new light on the long-lasting problem of chiral discrimination in the solid state.

### 20.5.2 *Resolution of Racemic Mixture by Coupling Crystallization and In Situ Racemization in Solution*

When a resolution by crystallization is applied, the ideal yield cannot exceed 50 % if there is no recycling of the so-called distomer (by opposition to the eutomer which is the desired enantiomer). Sometimes, it is possible to racemize the distomer in a separate loop, but the problem of its economic benefit and addition of side products can be raised if several steps are necessary. When it works well, the racemized mixture is reinjected in the resolution process and so on. If the racemization can be operated under the same experimental conditions as the preferential crystallization, there are several variants for the access to the pure enantiomer in a single operation. Basically it is easy to distinguish two modes (scheme in Fig. 20.29): mode 1 close to equilibrium and mode 2 preferential crystallization initially far from equilibrium [37].

1. Starting from the suspension of the racemic mixture, a flux of energy will be applied to the system (Fig. 20.29a). This could be abrasion (Viedma ripening), temperature gradient, temperature cycling, ultrasound, etc. [13, 38–44]. The solution keeps the same racemic composition but also a concentration close to equilibrium all along the process of deracemization. Depending on the nature of energy which is injected in the system, the efficiency differs. The amount of energy injected per time unit is also a parameter which will govern the kinetics with which one of the two solid enantiomers will have completely disappeared.
2. At the beginning of the process (Fig. 20.29b), the system is composed of a supersaturated solution, and seeding triggers the crystallization coupled with deracemization toward the enantiomer of the same chirality as that of the seeds. The preferential crystallization proceeds, but by contrast to the mode without in situ racemization in the mother liquor, it keeps the enantiomeric excess of the mother liquor at 0. If there is a nucleation of the counter enantiomer, the flux of energy injected in the system will serve to suppress its growth and ultimately will induce its complete dissolution. Being initially far from equilibrium, the process ensures a fast and productive process.

In principle, mode 2 is faster than mode 1; it is also compatible with a continuous mode which is a real advantage for an industrial application. But optimization of mode 1 has led to substantial reduction of time and some hours now could be sufficient to deracemize near equilibrium.

## 20.6 Conclusion

The solid state is for sure the best way to ensure a chiral recognition between enantiomers by means of specific self-assemblies. Progress on fast detection has been made and is useful for extensive screens of conglomerate-forming systems.

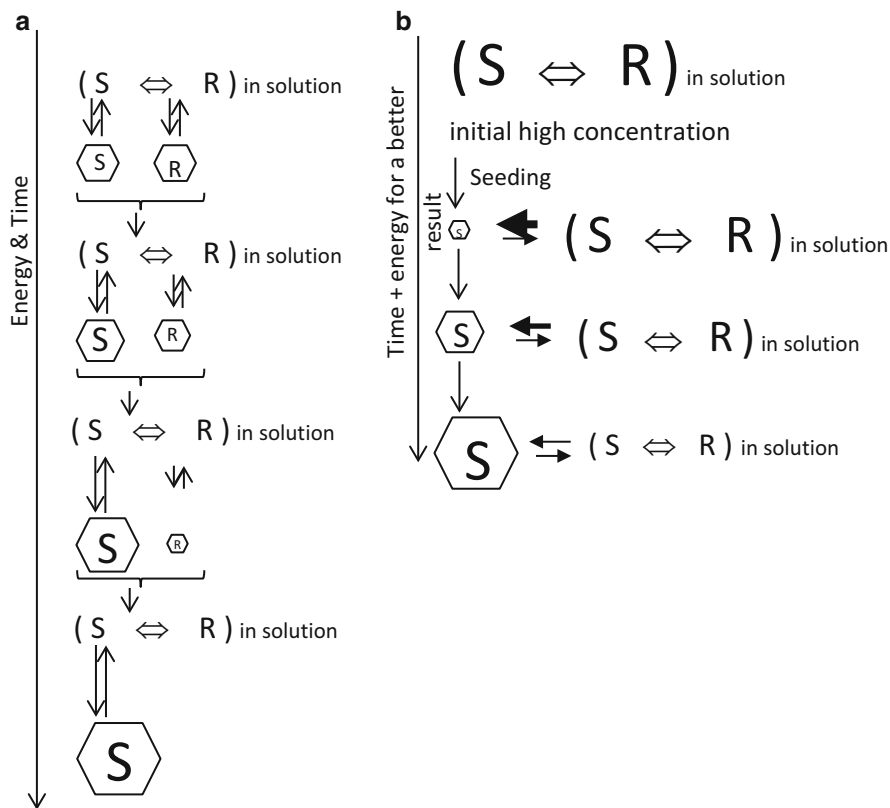


**Fig. 20.29** The two pathways to ensure deracemization: on the *left*, the process is run close to equilibrium – a flux of mechanical energy or temperature oscillations or temperature gradient or ultrasounds ensure the conversion into the suspension of a single enantiomer. On the *right* a preferential crystallization coupled with in situ racemization (also called second-order asymmetric transformation); if a flux of energy is also applied to the system, it will suppress the crystal growth of the counter enantiomer. In this latter case the preferential crystallization can be run safely far from equilibrium

Nevertheless, very little progress has been achieved in simply orienting the screens toward a better chance of success. Several avenues of research are proposed in this chapter which show that this domain deserves the interest of more scientists. New resolution and deracemization methods have now been applied to several examples showing the interest of an integrated interplay between fundamental and applied researches.

**Acknowledgments** The author is grateful to Dr. Marie-Noelle Delauney and Dr. Morgane Sanselme for their substantial help in the diagrams and the visualization of the structures, respectively. I thank Kyoto University for providing a position of visiting professor for 3 months in 2014.

## List of Symbols

V	Solvent
<RS>	Racemic compound
<R> and <S>	Solid phases of enantiomer <i>R</i> and of enantiomer <i>S</i>
< $\underline{S}$ - $Vn$ > and < $\underline{R}$ - $Vn$ >	Solvates of the pure enantiomers
Racemic composition	50–50 mixture of enantiomers
Racemic compound	Intermediate compound
SS <sub>S</sub> and SS <sub>R</sub>	Solid solutions with a majority of <i>S</i> and <i>R</i> , respectively
<i>T</i> <sub>g</sub>	Glass transition
PBC	Periodic bond chain

Gray zones in phase diagrams indicate undersaturated solutions.

Dashed lines represent metastable equilibria.

## References

1. G. Coquerel, *Enantiomer* **5**, 481 (2000)
2. I. Schroeder, *Z. Phys. Chem.* **11**, 449 (1893)
3. J.J. van Laar, *Arch. Neel.* **11**, 264 (1903)
4. J. Jacques, A. Collet, S.H. Wilen, *Enantiomers, Racemates and Resolutions* (Krieger Publishing Company, Malabar, 1994)
5. I. Prigogine, R. Defay, *Chemical Thermodynamics* (Longmans, London, 1954)
6. E. Ndzié, P. Cardinaël, M.-N. Petit, G. Coquerel, *Enantiomer* **4**, 97 (1999)
7. L. Addadi, J. van Mil, M. Lahav, *J. Am. Chem.* **103**, 1249 (1981)
8. N. Wermester, E. Aubin, M. Pauchet, S. Coste, G. Coquerel, *Tetrahedron Asymmetry* **18**, 821 (2007)
9. N.V. Taratin, H. Lorenz, E.N. Kotelnikova, A.E. Glikin, A. Galland, V. Dupray, G. Coquerel, A. Seidel-Morgenstern, *Cryst. Growth Des.* **12**, 5882 (2012)
10. L. Renou, T. Morelli, S. Coste, M.-N. Petit, B. Berton, J.-J. Malandain, G. Coquerel, *Cryst. Growth Des.* **7**, 1599 (2007)
11. A.A. Bredikhin, D.V. Zakharychev, A.T. Gubaidullin, R.R. Fayzullin, A.V. Pashagin, Z.A. Bredikhina, *Cryst. Growth Des.* **14**, 1676 (2014)
12. S. Gonella, G. Levilain, G. Coquerel, *J. Therm. Anal. Calorim.* **103**, 125 (2011)
13. W.L. Noorduin, E. Vlieg, R.M. Kellog, B. Kaptein, *Angew. Chem. Int. Ed.* **48**, 9600 (2009)
14. G. Levilain, G. Coquerel, *Process for the resolution of enantiomers by preferential evaporative crystallization*, WO2011/07330
15. R. Tamura, T. Ushio, in *Enantiomer Separation: Fundamentals and Practical Methods*, ed. by F. Toda (Kluwer, Dordrecht, 2004)
16. R. Bishop, M.L. Scudder, *Cryst. Growth Des.* **9**, 2890 (2009)
17. Y. Sunatsuki, K. Fujita, H. Maruyama, T. Suzuki, H. Ishida, M. Kojima, R. Glaser, *Cryst. Growth Des.* **14**, 3692 (2014)
18. N.G. Panina, M. Pauchet, F. Dufour, L. Lemiègre, P.M. Zorky, J. Maddaluno, G. Coquerel, *BIWIC* (France, Rouen, 2003), p. 329
19. A.I. Kitaigorodsky, *Organic Chemical Crystallography* (Springer, New York, 1961)
20. A. Kitaigorodsky, *Physical Chemistry*, vol. 29 (Elsevier, Amsterdam, 2012)
21. K.M. Anderson, K. Afarinkia, H. Yu, A.E. Goeta, J.W. Steed, *Cryst. Growth Des.* **6**, 2109 (2006)

22. Y. Amharar, S. Petit, M. Sanselme, Y. Cartigny, M.-N. Petit, G. Coquerel, *Cryst. Growth Des.* **11**, 2453 (2011)
23. Professor Terry Threlfall, University of Southampton, is thanked for the syntheses of those derivatives
24. S. Wacharine, G. Levilain, V. Dupray, G. Coquerel, *Org. Process Res. Dev.* **14**, 1358 (2010)
25. S. Petit, G. Coquerel, *Chem. Mater.* **8**, 2247 (1996)
26. J. Mahieux, S. Gonella, M. Sanselme, G. Coquerel, *CrystEngComm* **14**, 103 (2012)
27. G. Coquerel, 'Preferential crystallization', in *Topics in Current Chemistry. Novel Optical Resolution Technologies* (Springer GmbH, Heidelberg, 2007), p. 1
28. A. Galland, V. Dupray, B. Berton, S. Morin, M. Sanselme, H. Atmani, G. Coquerel, *Cryst. Growth Des.* **9**, 2713 (2009)
29. F. Dufour, G. Perez, G. Coquerel, *Bull. Chem. Soc. Jpn.* **77**, 79 (2004)
30. C. Gervais, S. Beilles, P. Cardinaël, S. Petit, G. Coquerel, *J. Phys. Chem. B* **106**, 646 (2002)
31. J. Mahieux, M. Sanselme, S. Harthong, C. Melan, C. Aronica, L. Guy, G. Coquerel, *Cryst. Growth Des.* **13**, 3621 (2013)
32. V.Y. Torbeev, K.A. Lyssenko, O.N. Kharybin, M.Y. Antipin, R.G. Kostyanovsky, *J. Phys. Chem. B* **107**, 13523 (2003)
33. J. van Eupen, R. Westheim, M. Deij, H. Meekes, P. Bennema, E. Vlieg, *Int. J. Pharm.* **368**, 146 (2009)
34. P.A. Levkin, V.Y. Torbeev, D.A. Lenev, R.G. Kostyanovsky, in *Topics in Stereochemistry*, ed. by J.S. Siegel, S.E. Denmark, vol. 25 (Wiley, Hoboken, 2006)
35. T. Sasaki, Y. Ida, A. Tanaka, I. Isaki, N. Tohnai, M. Miyata, *CrystEngComm* **15**, 8237 (2013)
36. T. Sasaki, I. Isaki, T. Miyano, N. Tohnai, K. Morimoto, H. Sato, S. Tsusuki, M. Miyata, *Nat. Commun.* **4**, 1787 (2013)
37. G. Levilain, G. Coquerel, *CrystEngComm* **12**, 1983 (2010)
38. C. Viedma, *Phys. Rev. Lett.* **94**, 065504 (2005)
39. W.L. Noorduin, T. Izumi, A. Millemaggi, M. Leeman, H. Meekes, W.J.P. Van Enckevort, R.M. Kellogg, B. Kaptein, E. Vlieg, D.G. Blackmond, *J. Am. Chem.* **130**, 1158 (2008)
40. J.M. McBride, J.C. Tully, *Nature* **452**, 161 (2008)
41. J.E. Hein, B.H. Cao, C. Viedma, R.M. Kellogg, D.G. Blackmond, *J. Am. Chem. Soc.* **134**, 12629 (2012)
42. D. Gherase, D. Conroy, O.K. Matar, D.G. Blackmond, *Cryst. Growth Des.* **14**, 928 (2014)
43. K. Suwannasang, A.E. Flood, C. Rougeot, G. Coquerel, *Cryst. Growth Des.* **13**, 3498 (2013)
44. C. Rougeot, F. Guillen, J.-C. Plaquevent, G. Coquerel, *Cryst. Growth Des.* doi: 10.1021/cg501765g (2015)
45. G. Coquerel, L. Catroux, Y. Combret, **WO1998/023559**
46. S. Clevers, Ph.D. dissertation, University of Rouen, 2014
47. <http://www.ccdc.cam.ac.uk/products/csd/statistics/>

# Chapter 21

## How to Use Pasteur's Tweezers

Richard M. Kellogg

**Abstract** Pasteur introduced two techniques to separate enantiomers. The common visual imagery is that of the first technique, which pertains to the use of tweezers to separate the mirror image crystals of a tartaric acid salt. A second method discovered thereafter, not restricted to the conglomerates necessary for the tweezer approach, is diastereomeric resolution. In this chapter, a short discussion is given of the basic principles of diastereomeric resolutions followed by short analysis of Dutch Resolution, a method based on the use of families of resolving agents. The role of specific nucleation inhibition is discussed. Attention is then turned to conglomerates. Preferential crystallisation is discussed briefly. Particular attention is paid to the discovery of near-equilibrium methods to separate (racemisable) conglomerates by employment of constant attrition of the growing crystals. This methodology has been extended to preparation of the chiral components of some major drugs, and the methodology has also been adapted to separation of non-racemisable conglomerates.

**Keywords** Conglomerates • Attrition • Racemisation • Enantiomers

### 21.1 Introduction

Although the visual image is part and parcel of the perception of chirality in chemistry, Pasteur's mechanical separation of mirror image crystals with tweezers has not lent itself, at least via this mechanical action, to broad (practical) application in organic chemistry [1–8].<sup>1,2</sup> It is too exacting and time consuming. Moreover,

---

<sup>1</sup>For cogent summaries of the Pasteur story, see [3, 4]. For a discussion of the behaviour of the Pasteur salt, see [5].

<sup>2</sup>A recently published organic textbook with an alternative approach continues to emphasise this story with enthusiasm [6]. As do more classical texts, see, for example, Vollhardt and Schore [7].

R.M. Kellogg (✉)

Syncom BV, Kadijk 3, Groningen 9747 AT, The Netherlands,

e-mail: [r.m.kellogg@syncom.nl](mailto:r.m.kellogg@syncom.nl)

Nature often does not provide enantiomeric crystals. Tartaric acid, as the sodium ammonium tetrahydrate salt studied by Pasteur, belongs to a significant minority of crystals that are enantiomorphous. Most crystals of chiral compounds are not. However, Pasteur, surely unaware both of his good fortune in choice of crystals and, indeed, of this difference, soon provided an alternative experimental approach that would allow chemists access to workable quantities of (reasonably) pure enantiomers obtained from racemates. There was no need for enantiomorphous crystals. The racemates needed only to possess acidic or basic properties and to form crystalline salts. This was the technique of diastereomeric resolution. For the case of tartaric acid itself, this involved formation of a salt with a (more or less) enantiomerically pure base, quinotoxine, and separation of the diastereomeric salts on the basis of solubility differences [1, 2]. This technique, based on simple acid-base chemistry, was applicable to many other racemates and provided chemists access to workable quantities of pure enantiomers obtained by separation of racemates.

Pasteur, with these experiments, opened an intellectual and experimental path through the forest of chirality. The further development of this discovery fell into the very capable hands of others. I will attempt here to give an overview, without excess detail, of various developments, particularly in the past two decades, for the separation of enantiomers using knowledge that stems in essence from Pasteur's tweezers.

We now know, of course, that Pasteur's keen visual recognition of the enantiomorphism of the crystals of the sodium ammonium hexahydrate salt of tartaric acid was only possible because Nature had taken the first step in separating the enantiomers. This particular salt, in the temperature range used in the Pasteur experiment, is a *conglomerate* (Fig. 21.1 right). The enantiomers of a conglomerate

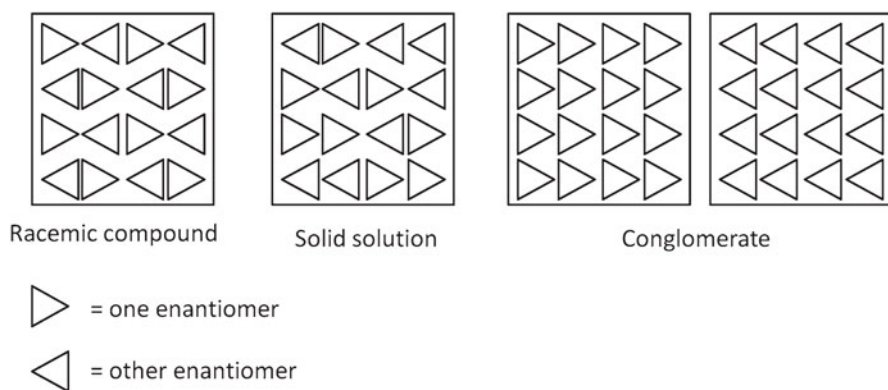


**Fig. 21.1** Cartoon representation of racemic crystal (*left*), solid (*centre*) and conglomerate (*right*)

---

For a discussion of the value of visual images in a modern historical different context, see Synder and Judt [8].

crystallise as separate phases. There is usually no centre of symmetry. Spontaneous formation of two separate phases occurs with a frequency, depending on type of compound, often estimated to be around 10 %. Conglomerates are thus a significant minority. However, most racemates of chiral organic compounds crystallise in a single phase as *racemic* crystals (Fig. 21.1 left).

For a conglomerate, Nature in effect performs a chiral separation of enantiomers during crystallisation but does not separate the phases. The frequency of appearance of conglomerates varies among classes of compounds [9]. For example, salts have a significantly higher incidence of conglomerate formation [10, 11].

Finally, there is a relatively small chance that a solid solution (Fig. 21.1 centre) may appear; in this case, the enantiomers have no particular arrangement relative to each other and the solid behaves as single phase although there may be local order.

Both in the literature and also in daily communication, the terms, *racemic* and *racemate*, are regularly used to describe 50:50 mixtures of enantiomers. This may lead to confusion because there is a difference. There are excellent general references that provide correct nomenclature [9].<sup>3</sup> Briefly, a *racemate* is an equimolar mixture of enantiomers. It may be a solid, liquid or gas. It does not rotate polarised light. A *racemic compound* is one with a particular crystal structure. The enantiomers are paired in the crystal, and there is usually a centre of symmetry. To illustrate with a simple example, a liquid racemate (50:50 mixture enantiomers) could crystallise either as a *racemic compound* (single phase with paired enantiomers in the crystal) or as a *conglomerate* (each enantiomer forms a separate phase).

## 21.2 Diastereomeric Resolutions<sup>3</sup>

Roughly a century and half after the Pasteur experiments, we are well aware that the apparent simplicity of the experimental procedures involved in diastereomeric resolution camouflages rather complex physics and chemistry involved in the phase changes intrinsic to the process. Although not often considered in the context of diastereomeric resolutions, the Gibbs-Thompson relationship (Eq. 21.1) provides an interesting starting point that couples well with the original Pasteur experiments as will become clear towards the end of this chapter [13]. Although long known, particularly in industry, the importance of this equation has only been recognised rather late by the organic chemistry community.

$$\ln [c(r)/c^*] = 2M\gamma/RT\rho r \quad (21.1)$$

---

<sup>3</sup>Undoubtedly, the best general discussion of diastereomeric resolutions and related matters including the history is that of Jacques et al. [12].

The equation deals with the solubility of crystals. As given here in oversimplified form [13], it applies to nonelectrolyte crystals in which the shape of the crystals is approximated as a sphere. The value  $c(r)$  is the solubility of an individual crystal of radius  $r$ ,  $c^*$  is the solubility at equilibrium,  $r$  is the radius of the (approximated) sphere,  $M$  is the molar mass of solid in solution,  $\gamma$  is the interfacial tension of the solid in contact with solution,  $\rho$  is the density of the solid,  $R$  is the gas constant and  $T$  is the temperature in degrees Kelvin.

A simple interpretation of Eq. 21.1 is that the solubilities of individual crystals depend inversely on their size expressed as radius of a sphere (by estimation). The greater the size, the lesser the solubility. Under crystallisation conditions, as the system proceeds towards equilibrium, larger crystals, which are less soluble, grow at the cost of more soluble smaller ones. The kinetics of growth will depend on various factors including how far the system is from equilibrium. The distance from equilibrium is often expressed as the degree of supersaturation; the greater the supersaturation, the greater the excess free energy. The supersaturation ratio at a given temperature is commonly expressed as Eq. 21.2

$$S = c/c^* \quad (21.2)$$

where  $c$  is actual concentration in solution and  $c^*$  the concentration at thermodynamic equilibrium.

This extremely simplified discussion does not include other effects such as polymorphism, a common complication. This effect of solubility dependent on crystal size lies behind “Ostwald ripening”, whereby crystal growth steadily proceeds towards larger and larger crystals.<sup>4</sup> This effect is well known in industrial applications where the size and shape of crystals must be rigidly controlled.

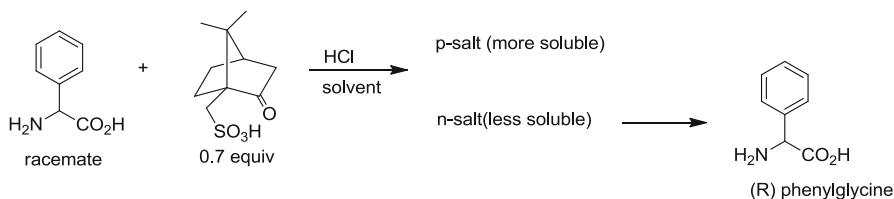
If crystal sizes are uneven, it will take time – kinetics – to achieve the final distribution – thermodynamics. In practice, the time scale turns out often to be one measured in manageable scales of minutes, hours or even days.<sup>5</sup> The interplay of kinetics and thermodynamics is the key to various techniques to be discussed in the following sections.

At first glance, a classical diastereomeric resolution is simplicity itself. Two industrial scale examples may be given. The first (Scheme 21.1) is the process used for resolution of the unnatural amino acid, phenylglycine, which is used often as a side chain of antibiotics [17]. In this highly optimised process, racemic phenylglycine is converted into the salt form using commercially available camphor

---

<sup>4</sup>For a brief and clear discussion of Ostwald ripening and the Gibbs-Thompson effect, see Mullin [13] and Ostwald Ripening [14]. The Ostwald rule of stages, namely, attainment of the final crystal form through a sequence of transient metastable states, is a related, but different, phenomenon; see also Mullin [13]; for a dramatic illustration of Ostwald ripening in the form of huge crystals, see [15], for information about the huge  $\text{CaSO}_4 \cdot 2\text{H}_2\text{O}$  crystals found in this cave in Mexico, which illustrate dramatically Ostwald ripening.

<sup>5</sup>For an extremely early report on the problem of reaching equilibrium during crystallisation, see van't Hoff [16].



**Scheme 21.1** Industrial example: DSM phenylglycine process

sulphonic acid as resolving agent. In theory, one needs only half an equivalent of resolving agent since only one diastereomeric salt will be isolated. In most resolutions, equivalent amounts or slight excesses of resolving agent are used. However, in this case slightly more than the theoretical amount of resolving agent is employed and HCl is used as achiral acid to convert all the racemate into the salt form. This modification using an achiral partner with the chiral resolving agent is known as the Pope-Peachey modification [18].

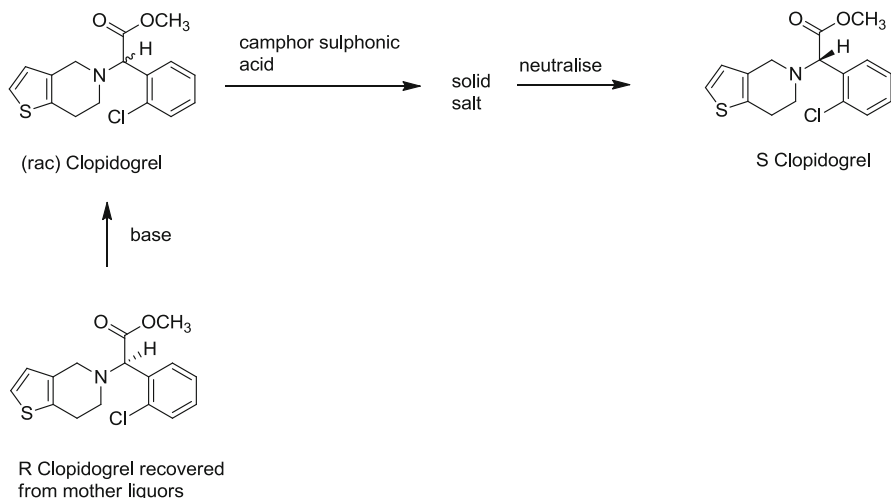
(R)-phenylglycine forms the least soluble salt (it is a common practice, although technically not entirely correct, to refer to the least soluble diastereomer as the n-salt and the more soluble diastereomer as the p-salt), which is isolated by precipitation. The more soluble (S) diastereomer is chiefly present as HCl salt and remains in solution from which it is isolated and subsequently subjected to racemisation to form new racemate. It is common to measure the efficiency of a resolution in terms of the S factor, which is defined by Eq. 21.3 [19].

$$S = 2 \bullet \text{yield} \bullet \text{enantiomeric excess} \quad (21.3)$$

The factor 2 is introduced to allow the scale to vary between 0 (no resolution) and 1 (maximum theoretical yield and absolute diastereomeric excess). The chemical yield of a single enantiomer from a racemate can never be more than 50 %. In the example shown,  $S = 0.9$ , which is very high. A value of 1.0 would be perfect.

A second example of industrial importance is the preparation of anti-platelet agent, clopidogrel (Plavix), which is active as the (S)-enantiomer. As shown in Scheme 21.2, racemic clopidogrel is resolved with commercially available levorotatory camphor sulphonic acid. The salt with (S)-clopidogrel is the least soluble and is isolated and neutralised. The (R)-clopidogrel is left in solution and is racemised with an alkoxide base, usually potassium t-butoxide, so that resolution can be performed again. The S factor is obviously high although it is difficult to calculate exactly from available literature data [20–23].

The above examples have been chosen for their industrial relevance and for the fact that the procedures have been optimised. Optimisation is not trivial. A great deal is known about diastereomeric resolutions and many companies have extensive in-house knowledge not available via the open literature. For bulk scale resolutions, the motivation to optimise the process with regard to solvent, time and temperature (as obvious parameters) is much greater for economic reasons. Smaller scale resolutions



**Scheme 21.2** Industrial process for the production of (S)-clopidogrel

are often not optimised; the main considerations are often speed, obtainment of resolution even at the cost of yield (“fast and dirty”) and simplicity of operation [24].<sup>6</sup> Many advances not discussed here have been made in recent years. The use of dielectric properties of solvents to influence resolutions is particularly interesting [25, 26]. Excellent practical hints have been given [27], and a wide ranging very recent review of all processes to separate enantiomers is available [28].

Despite their widespread use, diastereomeric resolutions have a chequered reputation. Until the past decade, success rates for first attempts at resolution of new racemates were distressingly low. It has been estimated that the success rate was only around 20 %. In my estimation, this percentage is probably a bit higher, perhaps 30 %, when carried out in a laboratory with experience and good facilities. Be that as it may, the chance of failure is high, although recent years certainly have brought improvement.<sup>6</sup>

### 21.3 Dutch Resolution

An examination of solvent-solid interplay, *under thermodynamic conditions*, is very useful in order to understand the details of diastereomeric resolutions. An effective way to do this is with a ternary phase diagram.<sup>7</sup>

<sup>6</sup>For a general discussion of this problem and resolutions in general, see Kellogg and Leeman [24].

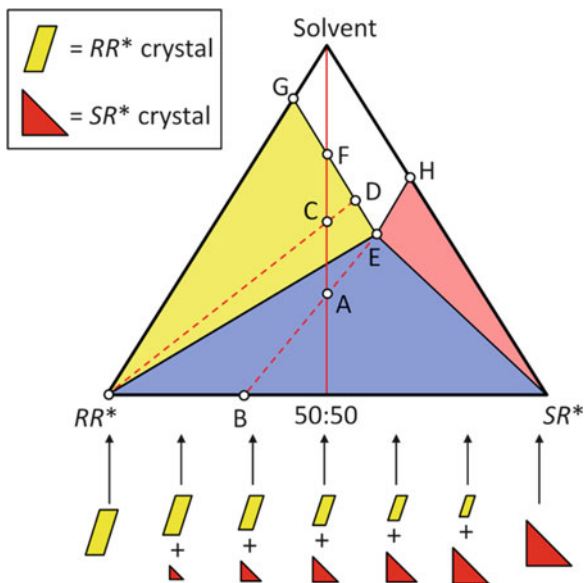
<sup>7</sup>For an excellent tutorial on use and significance of phase diagrams, see Coquerel [29]; for an older, but excellent, discussion of the basics of the use of phase diagrams, see Jacques et al. [12, 9]. A very detailed discussion of phase diagrams and manner of presentation is given [30].

As emphasised by Coquerel [29],<sup>7</sup> a phase diagram refers to thermodynamic equilibrium (although, with care, kinetic aspects can be superimposed). Fortunately such pictures can often provide suitable templates for understanding of the kinetic effects that ultimately lead to thermodynamic equilibrium. A ternary phase diagram for the primitive but illustrative purposes here will be an equilateral triangle. An idealised diagram ternary phase diagram for a diastereomeric resolution is shown in Fig. 21.2.

We assume that a racemate, RS (in principle, it makes no difference whether the racemate is a racemic compound or a conglomerate) has been allowed to undergo an acid-base (proton transfer) reaction with an enantiomerically pure resolving agent, R\*. For the sake of simplicity, assume that the equilibrium for this acid-base reaction lies entirely to the right. An example would be the resolution of a racemic amine by an acidic resolving agent. The system, under ideal conditions, consists of only two diastereomeric salts, RR\* and SR\* and solvent. As shown, pure RR\* is at the bottom left, pure SR\* at the bottom right corner of the triangle and pure solvent at the top. The composition of the salt varies along the base line. The composition of the salt formed from racemate is  $x = 0.5$  (equal quantities of diastereomers). The vertical line running from this point on the base line to the apex (solvent) is the dilution line. All the other points and lines shown in the diagram come from application of the *phase rule*. Excellent discussions of the phase rule are available and reader is referred to these. The operation of the phase rule is not intuitively obvious.

In simple terms, the resolution may be viewed as follows. For a successful resolution, the solubility of the salts, RR\* and SR\* are unequal. In Fig. 21.2, RR\* is less soluble. Point G reflects its solubility and point H the solubility of the more

**Fig. 21.2** Idealised phase diagram for a diastereomeric resolution



soluble diastereomer  $SR^*$ . It takes more solvent to dissolve  $RR^*$ . The solubility behaviour of the different compositions of diastereomers is given – roughly – by lines GE and HE (these lines can be calculated from theory and in practice are usually slightly curved instead of straight). Point E is the eutectic, the point of maximum solubility of the mixture of enantiomers. The mixture of diastereomeric salts could be diluted to, for example, point A. The phase rule now dictates that *at thermodynamic equilibrium*, the composition of the precipitated solid will be B (thus somewhat enriched in least soluble diastereomer relative to the 50:50 starting composition), and the mother liquor (solution) will have eutectic composition E on the line BE. The reader is directed to more advanced texts for discussion of the phase rule, the operation and predictions of which are not immediately obvious. To obtain diastereomerically pure  $RR^*$ , one must add enough solvent to go above the solubility line E- $RR^*$  and find a point within the triangle  $G \bullet E \bullet RR^*$ . The phase rule dictates that the solid will be pure  $RR^*$  and that the composition of the mother liquor will vary along the line GE. For a good crystallisation, one has to add enough solvent.

All is very simple. What could possibly go wrong? Lots of things. Although not illustrated, it often happens that as the composition of pure diastereomer is approached, solid solutions form because the growing crystals no longer recognise, perhaps owing to kinetics, the surrounding structures. Incomplete salt formation, insufficient or excessive solubility of the salts and simple failure to crystallise can frustrate a resolution. The kinetics of crystal growth, alluded to in the previous section, is also important and often not known. Another common problem is that the eutectic composition is not high enough. The eutecticum E should not be too close to the 50:50 dilution line with solvent (bisector of equilateral triangle). The greater the difference in solubility of the diastereomers, the higher the eutectic composition. In other words, the larger the size of the triangle  $G \bullet E \bullet RR^*$  for a given solvent and otherwise analogous conditions, the greater the operating room for a successful resolution.

Could one engineer a higher eutectic composition? At first sight, the answer is “no”. Solubilities determine eutectic compositions, and solubilities are thermodynamic quantities that in laboratory practice vary only with temperature.

More possibilities are opened if we recognise the possible interplay of thermodynamics and kinetics. If the precipitation of the more soluble diastereomer could be delayed, a kinetic effect, then within a “kinetic window” one might predict a “kinetic phase diagram” as shown in Fig. 21.3. If the precipitation of the more soluble diastereomer is delayed, this is effectively an increase in solubility, and one would expect a “kinetic eutectic” E' with a higher eutectic composition. The result is increase of the solubility window from the area denoted with (a + b) to the larger area now (a + b + c) in which precipitation of pure diastereomer (p-salt in the illustration) may be expected.

This is possible by the process of *nucleation inhibition*, a major effect now known to be behind the phenomenon known as Dutch Resolution [31–36].

Dutch Resolution was discovered in an attempt to address a major problem, mentioned previously, with diastereomeric resolutions, namely, the low success

**Fig. 21.3** The expected effect of “increase of solubility” of the more soluble diastereomer in a diastereomeric resolution

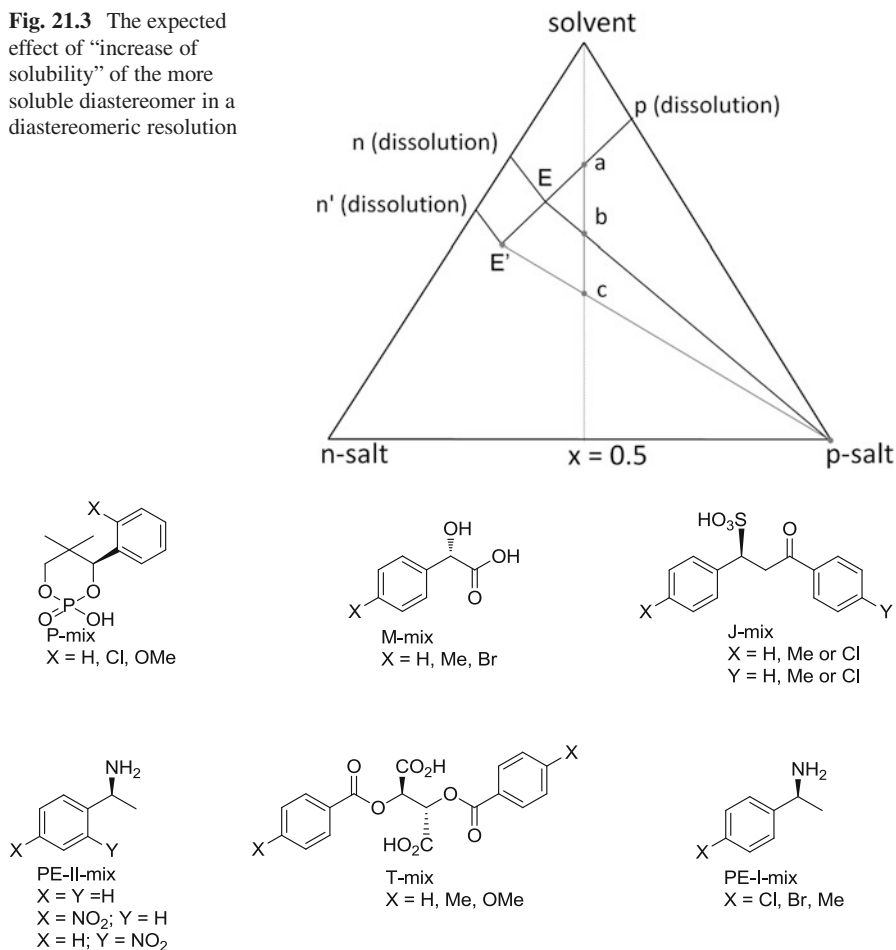


**Fig. 21.4** Some commonly used families for Dutch Resolution

rates especially with first-time resolutions. It was discovered that the success percentage for resolutions could be improved significantly by application of a counterintuitive approach. If the resolution is carried out with an equimolar mixture, usually three components, of a *family* of resolving agents, resolution often occurs quickly. “Family” refers to resolving agents that are structurally closely related to each other – simple variations in substitution patterns usually – and which are homochiral, that is to say that they all have the same absolute configurations (in terms of spatial comparison the R,S nomenclature system, which depends on priorities of groups and atoms, may be misleading). Typical examples of “families” are shown in Fig. 21.4.

For most cases, both enantiomeric sets of families are available. In a typical experiment, for example, resolution of a racemate of a chiral amine with the P

mix family, an equimolar amount of the racemate is mixed with the P family mixture as a 1:1:1 ratio. Diastereomeric salts precipitate usually in good to excellent diastereomeric excess. The salts contain a non-stoichiometric ratio of the resolving agents. For one well-investigated case, the salts are solid solutions indicative of the fact that the family members, probably owing to their structural similarity, do not recognise each other well [37]. This rather peculiar method of resolution has been subjected to extensive experimental test.

It is now known that for those cases investigated in detail, an interaction of kinetics and thermodynamics is involved in the success of this technique. One of the family members – we are unable to predict which one – acts as nucleation inhibitor. Structural similarity of the resolving agents appears to aid the nucleation inhibition. In the supersaturation zone that must be reached before precipitation can start, the rate of nucleation is slowed and this slowing is diastereomer specific. In fact, the nucleation inhibition is much greater for the more soluble diastereomer. Under kinetic conditions, the precipitation of the more soluble diastereomer is hindered thereby allowing the least soluble diastereomer – the one desired – to precipitate more selectively.

In essence, the situation portrayed in Fig. 21.3 has been achieved. A kinetic effect, nucleation inhibition, effectively increases the solubility of the more soluble diastereomer. In practice, there is also a kinetic effect on the least soluble diastereomer, but this is usually much smaller and not illustrated in Fig. 21.4. This may be explained in another manner. As mentioned above, if one could manipulate solubilities, it would also be possible to manipulate eutectic compositions. Solubilities, however, are thermodynamic quantities. Solubilities are, of course, temperature dependent, but it is not too likely that two structurally related diastereomeric salts would have significantly different solubility behaviour as function of temperature (for a successful resolution, the solubilities must be different, of course).<sup>8</sup>

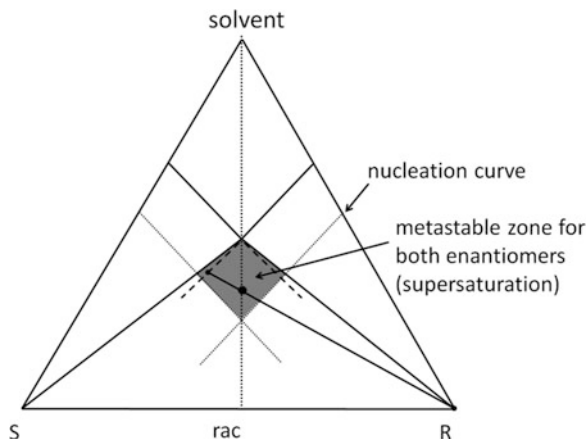
## 21.4 Preferential Crystallisation

Controlled interplay of kinetics and crystallisation is a key element in preferential crystallisation (entrainment), a method widely used to separate conglomerates. The details of this technique, which involves careful interplay of kinetic and thermodynamic effects, are discussed by Coquerel and co-workers in Chapter 18 of this volume.<sup>7</sup> The technique in its simplest form may be understood on the basis of the ternary phase diagram given in Fig. 21.5. The related, fascinating phenomenon of preferential enrichment as developed by Tamura and co-workers is also discussed in this chapter [39, 40].

---

<sup>8</sup>A particularly interesting new development is the Pasteurian resolution of trans-1,2-diaminocyclohexane on the surface of highly organised pyrolytic graphite (HOPG). It is clear that the concept of diastereomeric resolution can clearly be extended to two dimensional surfaces [38].

**Fig. 21.5** Resolution by preferential crystallisation



The phase diagram of Fig. 21.5 is that of a conglomerate. The shaded area is that of supersaturation. This area has to be carefully determined experimentally. Seeding in the supersaturation zone with, for example, S enantiomer allows precipitation of pure S enantiomer via the tie line. This precipitation must be stopped in a timely fashion to remain in the supersaturation zone. Racemate is then added to replace material and then seeding with R enantiomer is carried out. Providing that the experimental conditions are worked out carefully, this process can be repeated many times in the same solvent.

### 21.4.1 Conglomerates

The title of this chapter would not be possible were it not for conglomerate crystals. Conglomerates are indeed formed less frequently than racemic crystals, although at least 10 % and even higher within certain groups of compounds is a significant fraction. To make a comparison, the incidence of left handedness in the general population is around 10 % and also about 10 % of males suffer from red-green colour blindness.<sup>9</sup> These minorities are not usually referred to in terms of “rare”, and it is also inappropriate to consider conglomerates “rare”.

With regard to organic crystals, it is not possible to predict whether a particular racemate will deliver conglomerate or racemic crystals. If one has a library of ten structurally closely related crystalline compounds, the chances are very high that at least one and perhaps two will be conglomerates. Salts seem to have a higher tendency towards conglomerate formation [11, 12]. The incidence of conglomerate

<sup>9</sup>The left-handed and colour-blind author of this chapter confesses to bias with regard to this subject. These “significant minority” afflictions are frequently found together; see, for example, [41].

formation among helicenes is also rather high [42]. To the best of my knowledge, there are no reliable procedures to determine whether or not a given organic compound will crystallise as a conglomerate.

Note that the reflection symmetry breaking that lies at the heart of formation of crystalline conglomerates is by no means confined to crystals. Spontaneous separation into chiral phases – reflection symmetry breaking – is well known outside of the domain of crystals [43]. This phenomenon occurs quite frequently and is of much practical use in ferroelectric liquid crystals.<sup>10</sup> Recently, local chiral symmetry breaking has been described in the liquid crystalline phase for a remarkably simple system that consists of rigid, achiral triangular shapes formed from polymers [45].

On the basis of Monte Carlo calculations, it has been concluded that, independent of any particular chemical system, objects on a chiral surface subject to an attractive field – conditions used for the calculations – spontaneously may assemble into chiral structures [46, 47].

Gels can exhibit conglomerate formation [48], and at the solid-liquid interface, conglomerate formation readily occurs.<sup>11</sup> The causes are indeed the subject of much debate, but spontaneous reflection symmetry breaking occurs regularly in systems where molecules have the opportunity to aggregate together and via mutual interactions – recognition – form ordered structures.

### 21.4.2 *Nucleation*

What about nucleation? How do molecules come together in solution? What is the relationship between nucleation and formation of a racemic crystal or a conglomerate (not to mention nucleation leading to gels, for example)? Or is there any relationship? Dangerously little is known about this. In the usual type of experiments discussed here, nucleation will occur during supersaturation under nonequilibrium conditions. Is there recognition of chirality during nucleation? If so, how is it recognised? Current discussion on nucleation focusses essentially on two models [50, 51]. In the classical model (Fig. 21.6 lower), molecules associate together reversibly to form – in the simplest calculational version – a sphere (blocks are shown in the Figure). Once the radius becomes large enough that the internal stabilisation in free energy exceeds the destabilisation effective on the surface, the sphere will nucleate and grow into a crystal.

In contrast to this simple model, a high-level calculational approach was interpreted in terms of a two-step mechanism (Fig. 21.7) [52]. Meyerson et al. [50] and Davey et al. [51] have discussed this mechanism in considerable detail. The first step is formation of a dense liquid phase consisting of a fairly loosely organised cluster

---

<sup>10</sup>For a cogent discussion of reflection symmetry breaking in general and application to liquid crystals in particular, see Walba [44].

<sup>11</sup>For a recent reference and compilation of much earlier work, see Stöhr et al. [49].

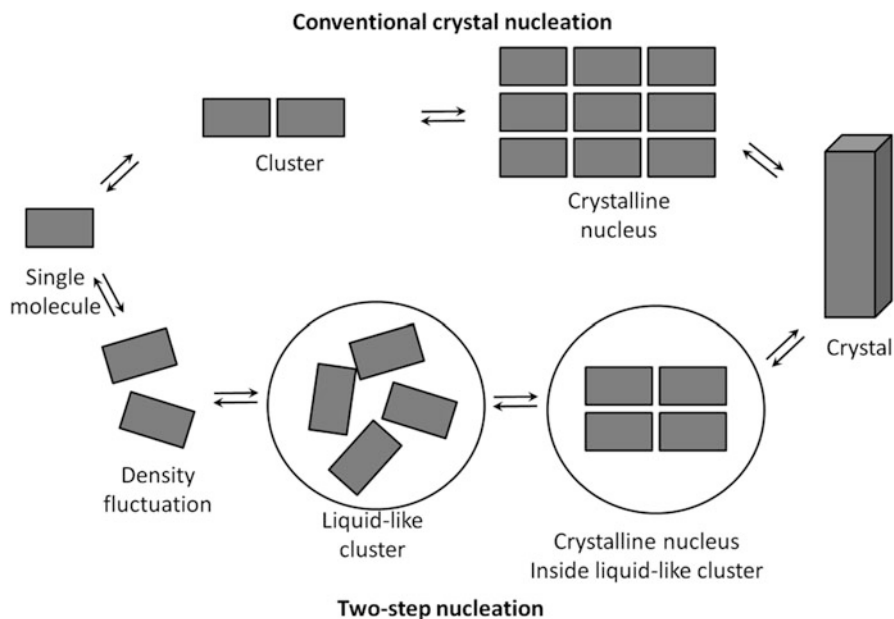


**Fig. 21.6** Models for nucleation in solution

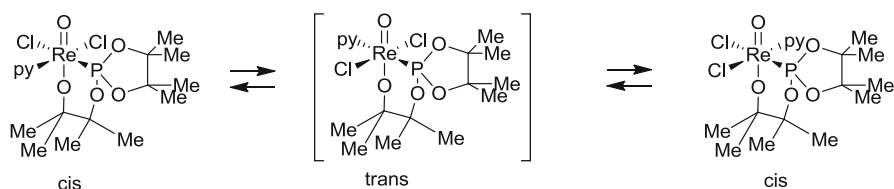


**Fig. 21.7** Thermally induced deracemisation of an inorganic complex

of molecules followed by a, often rate determining, reorganisation of the cluster into an ordered structure that either forms a crystal (primary nucleation) or attaches to a growing crystal (secondary nucleation) [53, 54]. Quite recently, molecular dynamics calculations on crystallisation in supersaturated  $\text{CaCO}_3$  solutions have been interpreted in terms of primary formation of a hydrated (water) cluster with about 26  $\text{CaCO}_3$  molecules at the maximum followed reorganisation towards the crystalline structure [55, 56]. The nucleation of  $\text{CaCO}_3$  has been followed in situ by transmission electron spectroscopy (TEM), and the results indicate that multiple pathways can be followed simultaneously [57].

Under these nonequilibrium conditions of crystallisation – supersaturation – one might intuitively expect more opportunity for influence of the chiral outcome of a crystallisation in a two-step mechanism. We note, for example, the profound nucleation inhibition effects observed in certain diastereomeric resolutions [34–36].

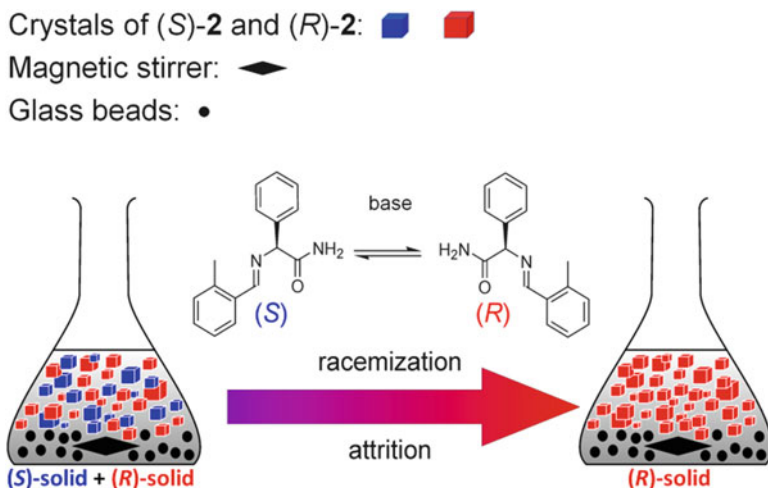


Fig. 21.8 Attrition-induced deracemisation of racemic 2

It is clear that there is still much to learn about the interface between crystallisation and nucleation. This has become a particularly serious area of discussion in the following development.

### 21.4.3 Attrition-Induced Deracemisation

In 2005, Viedma described the spontaneous deracemisation of  $\text{NaClO}_3$ , a conglomerate in the crystalline phase, simply by grinding of the partially dissolved crystals (liquid-solid system) with a stirring bar (attrition) under near-equilibrium conditions [58, 59]. The crystals were in contact with the saturated (not supersaturated) solution in which the chirality of the crystal is lost on dissolution. Shortly thereafter, a related deracemisation of rhenium complex 1 was demonstrated using attrition as the driving force. The racemisation process is probably the conversion in solution on warming to the achiral trans isomer as illustrated in Fig. 21.7 [60]. Spontaneous resolution of conglomerates of ligand-metal complexes is also relatively well known [61].

In 2008, Blackmond et al. demonstrated that deracemisation of an intrinsically chiral organic compound 2, the *o*-tolylimine of phenylglycyl amide that was a conglomerate and also subject to racemisation in solution by similar attrition, was also possible (Fig. 21.8) [62].

Subsequently, a demonstration was given that irradiation of 2 with circularly polarised light followed by attrition-induced grinding led to total deracemisation. The direction of deracemisation depended on the chirality of the circularly polarised light. Most likely the circularly polarised light induces the formation of a trace

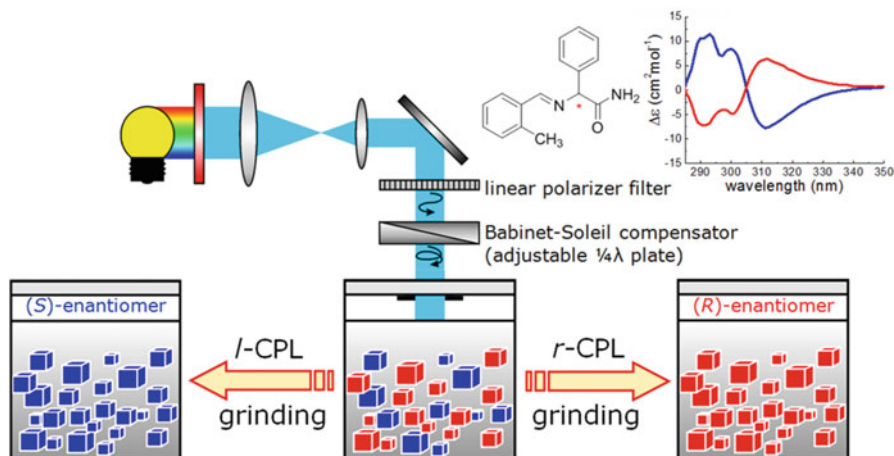


Fig. 21.9 Influence of circularly polarised light on attrition-induced deracemisation of 2

amount of an enantiomerically enriched impurity that then induced the further deracemisation on attrition grinding (Fig. 21.9) [63].

It was soon demonstrated that attrition-induced deracemisation of the methyl and ethyl esters of naproxen, both conglomerates, in the presence of base was possible (Fig. 21.10) [64].

Shortly thereafter, the attrition-induced deracemisation of 3, the benzaldehyde imine of 2-chloro-phenylglycylamide and a conglomerate, was reported together with conversion to the anti-platelet drug, clopidogrel (Fig. 21.11) [65, 66].

Attrition-induced deracemisation of 4, the 4-bromobenzaldehyde imine of 2-fluoro-phenylglycylamide, also a conglomerate, has been achieved [67]. Hydrolysis to the free amino acid proceeds cleanly without racemisation. This material is a possible building block for prasugrel, a market competitor of clopidogrel (Fig. 21.12) [68].<sup>12</sup>

The deracemisation of achiral molecules that form chiral crystals is by no means limited to  $\text{NaClO}_3$  and  $\text{NaBrO}_3$ . Cytosine, diphenyl disulphide, tetraphenylethylene and ninhydrin, just to give a limited number of examples, have been deracemised in the crystal by use of attrition [69].

Basic criteria for the success of attrition-induced deracemisation are (a) a conglomerate, (b) good crystallinity, (c) acceptable solubility in a solvent in which reversible racemisation may occur and (d) chemical stability under the conditions applied for deracemisation. Most applications described so far entail base-catalysed racemisation by means of deprotonation at the chiral centre. Suitably placed

<sup>12</sup>(S)-clopidogrel (Plavix) is a platelet aggregation inhibitor and is used for treatment of ischemic strokes, heart attacks and atherosclerosis as well as for prevention of thrombosis after placement of intracoronary artery stents. The market was reported to be \$9.3 billion in 2010.

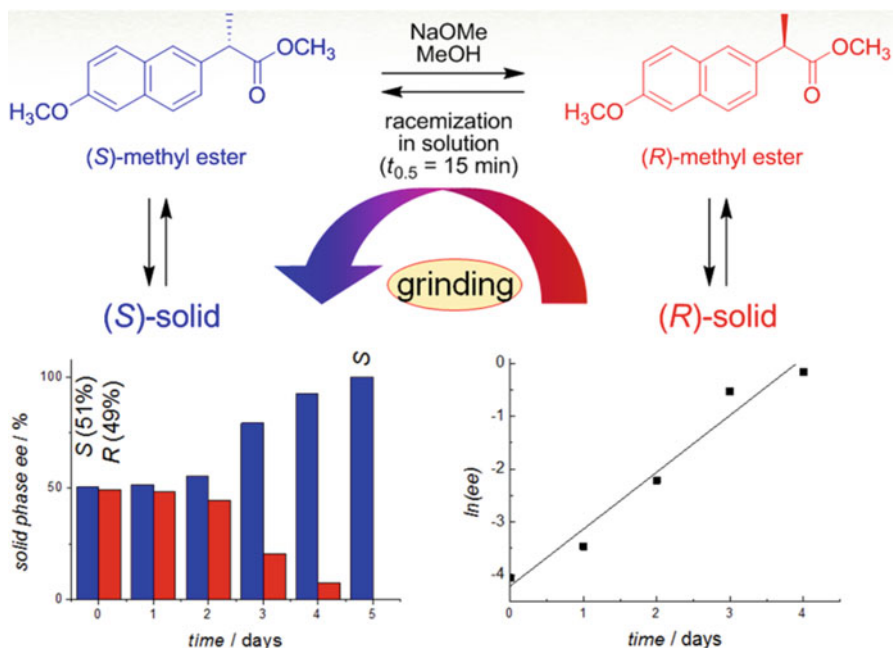


Fig. 21.10 Deracemization of naproxen methyl ester

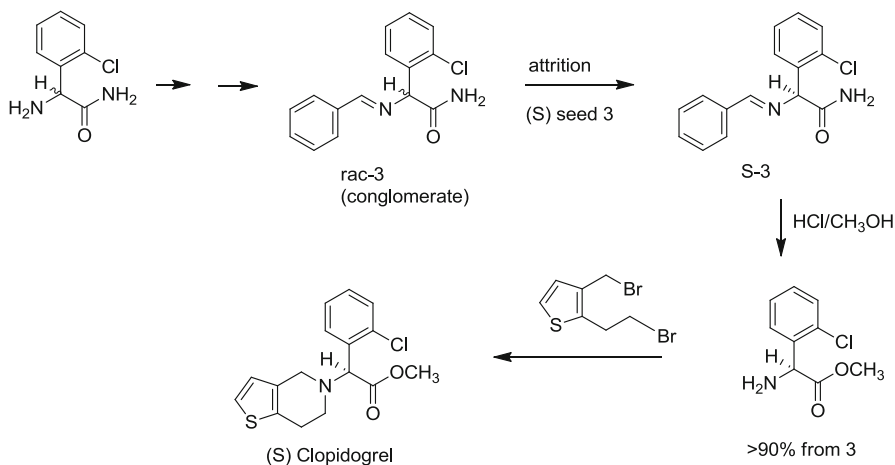
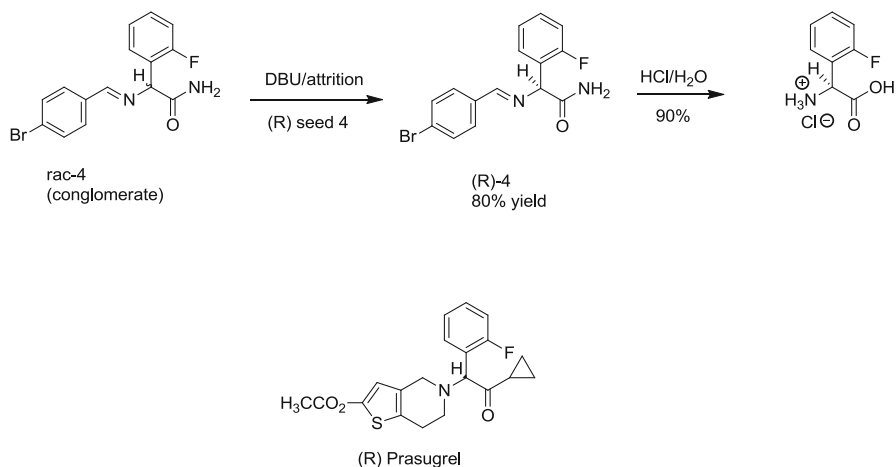


Fig. 21.11 Synthesis of (S)-clopidogrel via attrition-induced deracemisation

electron withdrawing substituents are required to stabilise the anion generated on deprotonation. For example, the deracemization of threonine in water-acetic acid under racemisation conditions – threonine is a conglomerate – has been described



**Fig. 21.12** Deracemisation of a conglomerate derivative of 2-F-phenylglycine

by Viedma and Blackmond [70]. Salicylaldehyde, a mimic of pyridoxal phosphate phosphate, forms an intermediate imine that is racemised.

Another approach is to start with achiral compounds that via reversible condensation reactions can provide chiral products. Application to the Mannich reaction has been described by Tsoogoeva et al. [71, 72] and to an aldol condensation by Bolm et al. [73]. Cuccia et al. have described a rather broad application of attrition-induced deracemisation to a remarkable range of conglomerate crystals of intrinsically achiral organic molecules [69]. Attempts by us to use various organometallic catalysts for racemisation on nonactivated alcohols and amines have been so far unsuccessful as have been attempts to deracemise conglomerate helicenes by thermal activation.

The mechanism of deracemisation by attrition-induced grinding has been the subject of much discussion and disagreement. An explanation based on Ostwald ripening remains easy to understand at least on the bulk scale [74].<sup>13</sup> The Gibbs-Thompson effect (Eq. 21.1) lies behind Ostwald ripening, which is the process whereby large crystals grow at the expense of smaller ones. This arises from the fact that smaller crystals are more soluble. A simplified explanation of attrition-induced deracemisation is that, under near-equilibrium conditions, primary nucleation is relatively slow. For a conglomerate, the first nucleation event will deliver one chirality or the other. Fragmentation of the first crystal followed by quite rapid secondary nucleation, whereby the same enantiomer is constantly incorporated, leads ultimately to complete conversion to that single enantiomer (rapid racemisation in solution occurs). This process is powered by the size-dependent difference solubility

<sup>13</sup>For a discussion of how Ostwald ripening could work and operate in attrition induced deracemisation, see McLaughlin et al. [74].

of crystals. It has been demonstrated that for compound **2** and aspartic acid, the kinetics of deracemisation is nicely compatible with operation of the “Meyerhoffer solubility rule”, which dictates that the solubility of racemic conglomerate is double that of the pure enantiomer [75–77]. This effect leads to an apparent effect of the amount of solid on the rate of deracemisation.

Various groups have argued that the Ostwald ripening mechanism by itself is insufficient to explain the sigmoidal kinetics of growth observed for the few systems that have been accurately studied [62]. Various agglomeration mechanisms in solution in the form of (chirality specific) clusters have been suggested and often convincingly modelled.<sup>14,15</sup> Surface-induced racemisation has also been suggested [71, 72]. The number of theoretical models considerably exceeds the supply of experimental studies. Qualitative observations in our laboratories suggest that deracemisation kinetics is often compound dependent and that phenomena such as polymorph formation can play a large role.<sup>16</sup>

A quite striking demonstration has been given that thermodynamic size-dependent solubility effects alone are sufficient to power a resolution of a conglomerate [87]. This is shown in Fig. 21.13.

A flask is filled with small crystals of racemic **2** (slide left, top). This is connected to a second flask that contains a relatively large seed crystal of enantiomerically pure *S*-**2**. The flasks are connected by a tube that allows liquid to pass but no solid. DBU is

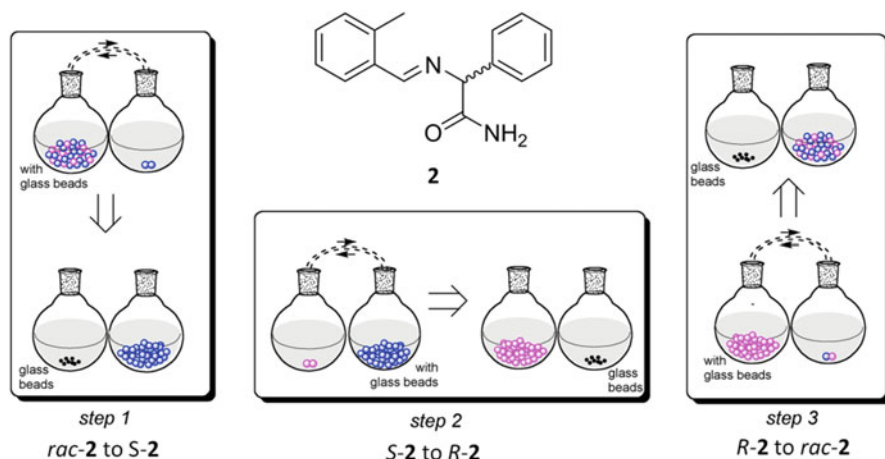


**Fig. 21.13** Cyclic process driven by Gibbs-Thompson effects. The racemate of **2** is converted to *S*-**2** (left diagram); *S*-**2** is converted to *R*-**2** (centre diagram); and *R*-**2** is converted back to the original racemate (right diagram)

<sup>14</sup>The following is a non-exhaustive list of articles on the possible mechanism of deracemisation whereby cluster forming is essential [77–83].

<sup>15</sup>For an opposing view, see [84, 85] and references contained therein.

<sup>16</sup>The mechanism of chiral growth of crystals of NaClO<sub>3</sub>, NaBrO<sub>3</sub> and threonine has recently been investigated by use of dyes [86].

added to the racemate to ensure racemisation. After attrition, all the material passes to the flask that contains S seed and is enantiomerically pure S. The middle slide illustrates conversion of the enantiomerically pure S-2 obtained from the left hand slide to R-2 by contact in the liquid phase via a filter that allows no solid material to pass with a seed of R-2 followed by attrition in the presence of DBU. The final slide on the right illustrates conversion of thus obtained R-2 back to racemate by use of a large seed crystal of racemate. This allows overall conversion in 88 % yield from racemate to S-2 and then to R-2 and finally back to the racemate of 2 all powered only by Gibbs-Thompson effects.

A non-racemisable conglomerate, threonine or Pasteur's salt, sodium ammonium tartrate tetrahydrate, can be spontaneously separated into enantiomers under near-equilibrium conditions by grinding the racemate (attrition) while allowing the solution to be in contact, via filters, with the pure enantiomers in separate flasks [87]. The crystals of the pure enantiomers used as seed are somewhat larger and thus less soluble. Attrition fragments the crystals of racemate into smaller, better soluble, fragments (Fig. 21.14). The larger crystals of pure enantiomer grow at the

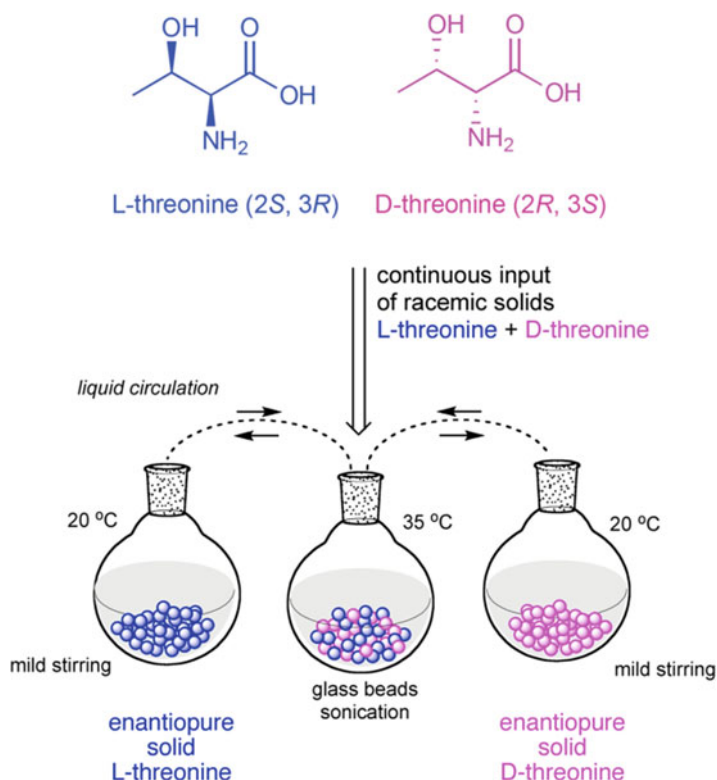


**Fig. 21.14** Deracemisation of non-racemisable conglomerates using attrition and the Gibbs-Thompson effect

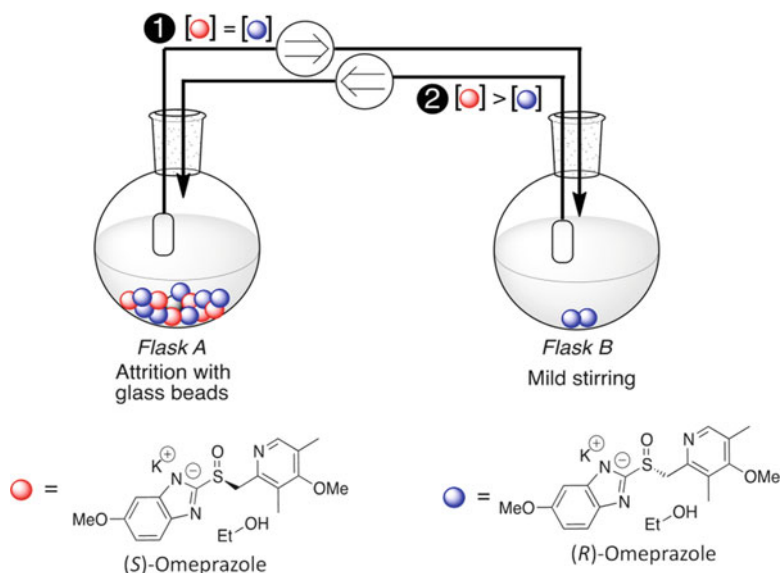


Fig. 21.15 Gibbs-Thompson-induced deracemisation of omeprazole potassium salt

cost of the smaller crystals of racemate, and complete resolution is achieved purely on the basis of solubility differences.

This same approach has been used to deracemise the extremely sensitive potassium ethanolate salt 5 of omeprazole as shown in Fig. 21.15 [88]. This salt has been shown by Coquerel et al. to be a conglomerate [89].

## 21.5 Conclusions

Although not used in practice as instrument, clearly the concept of Pasteur's tweezers has led to insights and applications. The kinetic action of manipulation of tweezers to separate solid and unchangeable (chiral) objects is a fitting metaphor for the interaction of kinetics and thermodynamics that lies at the heart of separation techniques for enantiomers. The next challenge? I suggest separation of racemic crystals using kinetics and solubility behaviour of crystals to effect the separation.

Since the submission of this chapter, several pertinent references with regard to attrition-induced deracemisation have appeared. The deracemisation of a metastable conglomerate of glutaric acid has been reported [90]. A report has appeared on salt formation with amino acids as a means to generate conglomerates suitable for deracemisation [91]. The deracemisation of isoindolinones by means of attrition has been described [92]. Attrition-induced deracemisation has been applied in a Mannich reaction [93] and represents another example of absolute asymmetric synthesis [94]. Temperature programming has been used as an aid in attrition-induced der-

acemisation to deracemise a conglomerate, 1-(4-chlorophenyl)-4,4-dimethyl-2-(1H-1,2,4-triazol-1-yl)pentan-3-ol [95]. A detailed discussion of the effect of crystal size and crystal growth on the deracemisation of **3** (Fig. 21.11) has appeared [85].

## References

1. L. Pasteur, C. R. Acad. Sci. **37**, 163 (1853)
2. L. Pasteur, Ann. Chim. (Paris), **3**, 38, 437 (1853)
3. D.M. Walba, *Topics in Stereochemistry*, **24**, 457–518, ref 18 (2003)
4. <http://www.foundersofscience.net/>
5. M.N. Petit, G. Coquerel, Mendeleev Commun. **13**, 95 (2003)
6. M.M. Green, *Organic Chemistry Principles in Context* (ScienceFromAway Publishing, New York, 2012), pp. 28–29
7. K.P.C. Vollhardt, N.E. Schore, *Organic Chemistry: Structure and Function*, 4th edn. (W.H. Freeman, New York, 2003), p. 183
8. T. Synder, T. Judt, *Thinking the Twentieth Century* (Vintage, London, 2013)
9. E.L. Eliel, S.H. Wilen, L.N. Mander (in part), *Stereochemistry of Organic Compounds* (John Wiley and Sons, New York, 1994), p. 1205
10. J. Jacques, M. Leclercq, M.J. Brienne, *Tetrahedron* **37**, 1727–1733 (1981)
11. R.A. Sheldon, *Industrial Synthesis of Optically Active Compounds* (M. Dekker, Inc., New York, 1993), pp. 173–204
12. J. Jacques, A. Collet, S.H. Wilen, *Enantiomers, Racemates, and Resolutions* (Krieger Publications, Malabar, 1994)
13. J.W. Mullin, *Crystallization*, 4th edn. (Elsevier, Amsterdam, 2001), p. 109
14. Ostwald Ripening, pp. 320–322, ref 13
15. [http://en.wikipedia.org/wiki/Cave\\_of\\_the\\_Crystals](http://en.wikipedia.org/wiki/Cave_of_the_Crystals)
16. J.H. van't Hoff, *Physical Chemistry in the Service of Science* (University Press, Chicago, 1903), p. 116; cited in ref. 7
17. R. Yoshioka, H. Hiramatsu, K. Okamura, I. Tsujioka, S.-I. Yamada, *J. Chem. Soc. Perkin Trans. 2*, 2121–2128 (2000)
18. W.J. Pope, S.J. Peachey, *J. Chem. Soc.* **101**, 1066 (1912)
19. E. Fogassy, A. Lopata, F. Faigl, F. Darvas, M. Ács, L. Toke, *Tetrahedron Lett.* **21**, 647 (1980)
20. L. Wang, J. Shen, Y. Tang, Y. Chen, W. Wang, Z. Cai, Z. Du, *Org. Process Res. Dev.* **11**, 487 (2007)
21. Teva Pharmaceutical Industries, U.S. Patent 6,800,759, 2004
22. Teva Pharmaceutical Industries, U.S. Patent 4,847,265, 1989
23. USV Ltd., U.S. Patent 6,074,242, 2006
24. R.M. Kellogg, M.S. Leeman, *Crystallization as a Tool in Industrial Applications of Asymmetric Synthesis, Comprehensive Chirality*, 1st edn, ed. by E.M. Carreira, H. Yamamoto (Elsevier, New York, 2012), 9.16, pp. 367–399
25. Y. Kitamoto, K. Suzuki, N. Morohashi, K. Sakai, T. Hattori, *J. Org. Chem.* **78**, 597–605 (2013)
26. M. Schmitt, D. Schollmeyer, S. Waldvogel, *Eur. J. Org. Chem.* doi:10.1002/ejoc.201301566
27. H. Lorenz, A. Seidel-Morgenstern, *Angew. Chem. Int. Ed.* **53**, 1218–1251 (2014)
28. X.-C. He, C.-Y. Qi, *Chin. J. Chem.* **25**, 583–586 (2007)
29. G. Coquerel, *Chem. Soc. Rev.* **43**, 2286–2300 (2014)
30. PhD thesis of F. Quenard, which is available via <http://tel.archives-ouvertes.fr/>
31. T. Vries, H. Wynberg, E. van Echten, J. Koek, W. ten Hoeve, R.M. Kellogg, Q.B. Broxterman, A. Minnaard, B. Kaptein, S. van der Sluis, L. Hulshof, J. Kooistra, *Angew. Chem. Int. Ed.* **37**, 2349 (1998)

32. R.M. Kellogg, J.W. Nieuwenhuijzen, K. Pouwer, T.R. Vries, Q.B. Broxterman, R.F.P. Grimbergen, B. Kaptein, R.M. La Crois, E. de Wever, K. Zwaagstra, A.C. van der Laan, *Synthesis* **10**, 1626 (2003)
33. R.M. Kellogg, B. Kaptein, T.R. Vries, *Top. Curr. Chem.* **269**, 159 (2007)
34. M. Leeman, G. Brasile, E. Gelens, T.R. Vries, B. Kaptein, R.M. Kellogg, *Angew. Chem. Int. Ed.* **47**, 1287 (2008)
35. J.W. Nieuwenhuijzen, R.F.P. Grimbergen, C. Koopman, R.M. Kellogg, T.R. Vries, K. Pouwer, E. van Echten, B. Kaptein, L.A. Hulshof, Q.B. Broxterman, *Angew. Chem. Int. Ed.* **41**, 4281 (2002)
36. J. Dalmolen, M. van der Sluis, J.W. Nieuwenhuijzen, M. van der Sluis, E. van Echten, T.R. Vries, B. Kaptein, Q.B. Broxterman, *Chem. Eur. J.* **11**, 5619 (2005)
37. C. Gervais, R.F.P. Grimbergen, I. Markovits, G.J.A. Ariaans, B. Kaptein, A. Bruggink, Q.B. Broxterman, *J. Am. Chem. Soc.* **126**, 655 (2004)
38. H. Xu, W.J. Saletta, P. Lavicoli, B. Van Averbeke, E. Ghijssens, K.S. Mali, A.P.H.J. Schenning, D. Beljonne, R. Lazzaroni, D.B. Amabilino, S. DeFeyter, *Angew. Chem. Int. Ed.* **51**, 11981–11985 (2012)
39. R. Tamura, H. Takahashi, D. Fujimoto, T. Ushio, *Top. Curr. Chem.* **269**, 53–82 (2007)
40. R.G. Gonnade, S. Iwama, R. Sujiwake, K. Manoj, H. Takahashi, H. Tsue, R. Tamura, *Chem. Commun.* **48**, 2791–2793 (2012)
41. <http://www.thomhartmann.com/users/natural-lefty/blog/2013/06/toward-more-balanced-world-instead-one-tilts-right>
42. Y. Shen, C.-F. Chen, *Chem. Rev.* **112**, 1463–1535 (2012)
43. D.R. Link, G. Natale, R. Shao, J.E. Maclellan, N.A. Clark, E. Körblová, D.M. Walba, *Science* **278**, 1924–1927 (1997)
44. D.M. Walba, *Top. Stereochem.* **24**, 457–518 (2003)
45. K. Zhao, R. Bruinsma, T.G. Mason, *Nat. Commun.* (2012). doi:10.1038/ncomms1803
46. B. Bergersen, D. Boal, P. Palffy-Muhoray, *J. Phys. A Math. Gen.* **27**, 2579–2586 (1994)
47. G.T. Pickett, M. Gross, H. Okuyama, *Phys. Rev. Lett.* **85**, 3652–3655 (2000)
48. J. Lin, Z. Guo, J. Plas, D.B. Amabilino, S. De Feyter, A.P.H. Schenning, *Chem. Commun.* **49**, 9320–9322 (2013)
49. M. Stöhr et al., *Angew. Chem. Int. Ed.* **50**, 9982–9986 (2011)
50. D. Erdemir, A.Y. Lee, A.S. Meyerson, *Acc. Chem. Res.* **42**, 621–629 (2009)
51. R.J. Davey, S.L.M. Schroeder, J.H. ter Horst, *Angew. Chem. Int. Ed.* **52**, 2166–2179 (2013)
52. P.R. ten Wolde, D. Frenkel, *Science* **277**, 1975–1978 (1997)
53. P.G. Vekilov, *Cryst. Growth Des.* **10**, 5007–5019 (2010)
54. S. Chattopadhyay, D. Erdemir, J.M.B. Evans, J. Ilavsky, H. Amenitsch, C.U. Segre, A.S. Myerson, *Cryst. Growth Des.* **5**, 523–527 (2005)
55. A.F. Wallace, L.O. Hedges, A. Fernandez-Martinez, P. Raiteri, J.D. Gale, G.A. Waychunas, S. Whitelam, J.F. Banfield, J.J. De Yoreo, *Science* **341**, 885–889 (2013)
56. A.S. Meyerson, B.L. Trout, *Science* **341**, 855–856 (2013)
57. M.H. Nielsen, S. Aloni, J.J. De Yoreo, *Science* **345**, 1158–1162 (2014)
58. C. Viedma, *Phys. Rev. Lett.* **94**, 065504 (2005)
59. C. Viedma, *Cryst. Growth Des.* **7**, 553–556 (2007)
60. W.K. Rybak, *Tetrahedron Asymmetry* **19**, 2234–2239 (2008)
61. T. Ezuhara, K. Endo, Y. Aoyama, *J. Am. Chem. Soc.* **121**, 3279–3283 (1999)
62. W.L. Noorduin, A. Izumi, M. Millemaggi, M. Leeman, H. Meekens, W.J.P. van Enkevort, R.M. Kellogg, B. Kaptein, E. Vlieg, D.G. Blackmond, *J. Am. Chem. Soc.* **130**, 1158–1159 (2008)
63. W.L. Noorduin, A.A.C. Bode, M. van der Meijden, H. Meekes, A.F. van Etteger, W.J.P. van Enkevort, P.C.M. Christianen, B. Kaptein, R.M. Kellogg, T. Rasing, E. Vlieg, *Nat. Chem.* **2**, 729 (2009)
64. W.L. Noorduin, B. Kaptein, H. Meekes, W.J.P. van Enkevort, R.M. Kellogg, E. Vlieg, *Angew. Chem. Int. Ed.* **48**, 4581–4583 (2009)

65. M.W. van der Meijden, M. Leeman, E. Gelens, W.L. Noorduyn, H. Meekes, W.J.P. van Enckevort, B. Kaptein, E. Vlieg, R.M. Kellogg, *Org. Process Res. Dev.* **13**, 1195 (2009)
66. W.L. van der Noorduyn, P. Asdonk, A.A.C. Bode, H. Meekes, W.J.P. van Enckevort, E. Vlieg, B. Kaptein, M.W. van der Meijden, R.M. Kellogg, G. Deroover, *Org. Process Res. Dev.* **14**, 908–911 (2010)
67. P. Wilmlink, C. Rougeot, K. Wurst, M. van der Meijden, W. Saletra, G. Coquerel, R.M. Kellogg, *Org. Process Res. Dev.* doi:[10.1021/op500352m](https://doi.org/10.1021/op500352m)
68. J.A. Jakubowski, C.D. Payne, J.T. Brandt, G.J. Weerakkody, N.A. Farid, D.S. Small, H. Naganuma, G.Y. Li, K.J. Winters, *J. Cardiovasc. Pharmacol.* **47**, 377–384 (2006)
69. D.T. McLaughlin, T.P.T. Nguyen, L. Mengnjo, C. Bian, Y.H. Leung, E. Goodellow, P. Ramrup, S. Woo, L.A. Cuccia, *Cryst. Growth Des.* **14**, 1067–1076 (2014)
70. C. Viedma, J.E. Ortiz, T. De Torres, T. Izumi, D.G. Blackmond, *J. Am. Chem. Soc.* **130**, 15274–15275 (2008)
71. S. Wei, M. Mauksch, S.B. Tsogoeva, *Chem. Eur. J.* **15**, 10255 (2009)
72. S.V. Tsogoeva, S. Wei, M. Freund, M. Mauksch, *Angew. Chem. Int. Ed.* **48**, 590–594 (2009)
73. A.M. Flock, C.M.M. Reucher, C. Bolm, *Chem. Eur. J.* **16**, 3918 (2010)
74. W.L. Noorduyn, E. Vlieg, R.M. Kellogg, B. Kaptein, *Angew. Chem. Int. Ed.* **48**, 9600–9606 (2009)
75. W. Meyerhoffer, *Ber. Dtsch. Chem. Ges.* **37**, 2604 (1904)
76. M. Klussmann, S.P. Mathew, H. Iwamura, D.H. Wells Jr., A. Armstrong, D.G. Blackmond, *Angew. Chem. Int. Ed.* **45**, 7989 (2006)
77. M. Klussmann, A.J.P. White, A. Armstrong, D.G. Blackmond et al., *Angew. Chem. Int. Ed.* **45**, 7985 (2006)
78. M. Uhawa, *J. Phys. Soc. Jpn.* **73**, 2601–2603 (2004)
79. M. Uwaha, K. Koyama, *J. Cryst. Growth* **312**, 1046–1054 (2010)
80. W.L. Noorduyn, W.J. van Enckevort, H. Meekes, B. Kaptein, R.M. Kellogg, J.C. Tully, J.M. McBride, E. Vlieg, *Angew. Chem. Int. Ed.* **49**, 8435–8438 (2010)
81. C. Blanco, J. Crusats, Z. El-Hachemi, A. Moyano, S. Veintemillas-Verdaguer, D. Hochberg, J. Ribó, *ChemPhysChem* **14**, 3982–3993 (2013)
82. M. Iggländ, M. Mazzotti, *Cryst. Growth Des.* **11**, 4611–4622 (2011)
83. F. Ricci, F.H. Stillinger, P.G. Debenedetti, *J. Chem. Phys.* **139**, 174503 (2013)
84. C. Viedma, B.J.V. Verhulij, J.E. Ortiz, T. de Torres, R.M. Kellogg, D.G. Blackmond, *Chem. Eur. J.* **16**, 4932–4937 (2010)
85. D. Gherase, D. Conroy, O.K. Matar, D.G. Blackmond, *Cryst. Growth Des.* **14**, 928–937 (2014)
86. C. Viedma, J.M. McBride, B. Kahr, P. Cintas, *Angew. Chem. Int. Ed.* **52**, 10545–10548 (2013)
87. J.E. Hein, B.H. Cao, C. Viedma, R.M. Kellogg, D.G. Blackmond, *J. Am. Chem. Soc.* **134**, 12629–12636 (2012)
88. J.E. Hein, B.H. Cao, M.W. van der Meijden, M. Leeman, R.M. Kellogg, *Org. Process Res. Dev.* **17**, 946–950 (2013)
89. G. Coquerel, M.N. Petit, G. Tauvel, U.S. Patent 2009/0124811 A1 (2009)
90. L. Spix, H. Meekes, R.H. Blauw, W.J.P. van Enckevort, E. Vlieg, *Cryst. Growth Des.* **12**, 5769–5799 (2012)
91. L. Spix, A. Alring, H. Meekes, W.J.P. van Enckevort, E. Vlieg, *Cryst. Growth Des.* [dx.doi.org/10.1021/cg4018882](https://doi.org/10.1021/cg4018882)
92. R.R.E. Steendam, M.C.T. Brouwer, E.M.E. Huijs, M.W. Kulka, H. Meekes, W.J.P. van Enckevort, J. Raap, F.P.J.T. Rutjes, E. Vlieg, *Chem. Eur. J.* **20**, 13527–13530 (2014)
93. I. Weissbuch, M. Lahav, *Chem. Rev.* **111**, 3236–3267 (2011)
94. R.R.E. Steendam, J.M.M. Verkade, T.J.B. van Benthem, H. Meekes, W.J.P. van Enckevort, J. Raap, F.P.J.T. Rutjes, E. Vlieg, *Nat. Comm.* doi:[10.1038/ncomms6543](https://doi.org/10.1038/ncomms6543)
95. K. Suwannasang, A.E. Flood, C. Rougeot, G. Coquerel, *Cryst. Growth Des.* **13**, 3498–3504 (2013)

# Chapter 22

## Total Resolution of Racemates by Dynamic Preferential Crystallization

Masami Sakamoto and Takashi Mino

**Abstract** Crystallization-induced asymmetric transformation (CIAT) of axially chiral materials is summarized on the basis of our studies. CIAT can be classified into two categories, Crystallization-Induced Enantiomer Transformation (CIET) and Crystallization-Induced Diastereomer Transformation (CIDT). Racemic mixtures or diastereomixtures that exist as a mixture of stereoisomers in solution converge on a single stereoisomer by dynamic crystallization. Many axially chiral materials, such as *N*-arylpyrimidine-2-(1*H*)-ones and -thiones, were crystallized as conglomerates, and total resolution was performed with high enantiomeric purities from the solution by CIET. Dynamic resolution of aromatic amides, such as 2-alkoxy-1-naphthamides, 2-quinolone-3-carboxamide, coumarin-3-carboxamide, and nicotinamides, was also successfully achieved by crystallization from the melt with high ees. Furthermore, optically active materials tend to crystallize in a chiral fashion, and CIDT is useful to obtain single diastereomers from a mixture of many diastereomers. Many types of aromatic amides with chiral auxiliaries were crystallized in a chiral fashion and were easily resolved by dynamic crystallization from the melt. Salt formation of oily racemic nicotinamides with enantiopure acid involving racemization during salt formation also gave diastereopure salts. The optical activity of the materials resolved by dynamic crystallization was effectively transferred to the products by many kinds of asymmetric reactions.

**Keywords** Chiral resolution • Dynamic crystallization • Preferential crystallization • Conglomerate • Racemization • Axial chirality • Enantiomer • Diastereomer • Asymmetric synthesis

---

M. Sakamoto (✉) • T. Mino

Department of Applied Chemistry and Biotechnology, Graduate School of Engineering,  
Chiba University, Yayoi, Inage, Chiba 263-8522, Japan

e-mail: [sakamotom@faculty.chiba-u.jp](mailto:sakamotom@faculty.chiba-u.jp)

© Springer Japan 2015

R. Tamura, M. Miyata (eds.), *Advances in Organic Crystal Chemistry*,  
DOI 10.1007/978-4-431-55555-1\_22

445

## 22.1 Introduction

Organic crystals have long been utilized by organic chemists to identify materials by comparing melting points with known compounds and to obtain pure materials by recrystallization. Since the latter half of the 1960s, many attractive aspects of crystals have been discovered. For example, crystals formed as a result of aggregation of organic molecules exhibit new properties, such as electric conductivity or nonlinear optics characteristics. In addition, chemistry using the key information recorded in the crystal has been developed. Molecular motion, which is cluttered with a variety of conformations in solution, is considerably more controlled in the crystal, and in many cases, molecules are arranged in a specific conformation depending on the closest-packing and molecular interactions. Therefore, a different molecular conformation will often be present in the crystal than in solution.

In some cases, information for chirality recorded in the crystal is particularly interesting [1]. Conglomerate crystals (a physical mixture of enantiomer crystals) obtained from racemates are also chiral crystals that can be used for preferential crystallization for resolution of racemates [2–5]. On the other hand, compounds with unstable axial chirality, even when achiral in solution, may provide axial chirality in a crystalline state where the molecular arrangement and molecular conformation are controlled. Using the chiral properties of the crystal, asymmetric synthesis without an external chiral source from achiral substrates has been studied by many research groups. This approach is also broadly recognized as an absolute asymmetric synthesis [6–13].

Here, we introduce “crystallization-induced asymmetric transformation” (CIAT), which is the combined methodology of dynamic stereoisomerization and preferential crystallization (Fig. 22.1). This is a practical methodology dynamically converging on a single stereoisomeric form from a mixture of stereoisomers by simultaneous crystallization and stereoisomerization in the system.

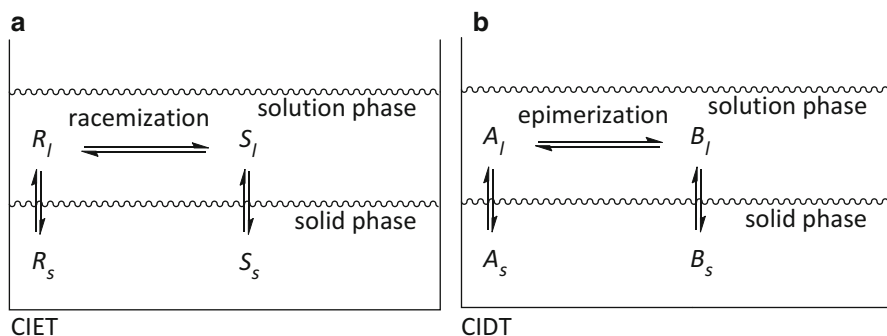


**Fig. 22.1** Crystallization-induced asymmetric transformation (CIAT). **(a)** Crystallization-Induced Enantiomer Transformation (CIET), *R* and *S* are enantiomers. **(b)** Crystallization-Induced Diastereomer Transformation (CIDT), *A* and *B* are diastereomers

CIAT is classified into two methodologies: one is CIDT (Crystallization-Induced Diastereomer Transformation), which is the dynamic crystallization of a diastereomixture involving epimerization (Fig. 22.1b), and the other is CIET (Crystallization-Induced Enantiomer Transformation), which can resolve each enantiomer from the racemates by dynamic crystallization (Fig. 22.1a) [14].

Resolution providing enantiopure materials from racemates or diastereomixtures is very important and eagerly desired in many fields, such as in pharmaceutical agents, agricultural chemicals, food products, and aroma chemicals. Furthermore, the development of the technique of obtaining enantiomers with high enantiomeric purity is also required in the field of electronics. The total resolution of racemates by dynamic preferential crystallization is a very effective methodology and can be applied on a large industrial scale.

## 22.2 Preferential Crystallization and Dynamic Preferential Crystallization

The crystal of a racemate can be classified into three categories: (1) the racemic compound is composed of an equivalent amount of both enantiomers, (2) each conglomerate consists of a single enantiomer, and (3) the racemic solid solution in which both enantiomers are arranged at random in a single crystal. All racemic materials studied crystallize as one of these three kinds of crystals. Preferential crystallization is not available for all the crystals of a racemate, and only a racemic conglomerate of the crystal (2) was utilized for resolution. However, most racemic materials crystallize as a type of racemic compound, and racemic conglomerates result in only about 10 % of the cases.

Irrespective of this situation, since the resolution by preferential crystallization does not require an external chiral reagent or resolving agent, it is very attractive and has been developed industrially as a resolution method for pharmaceutical agents.

A general preferential crystallization method is to add a crystal of a desired optically active substance to a supersaturated solution of a racemate as a seed crystal. Crystals of the same mirror image isomer as the added seed crystal will grow preferentially. It is possible to obtain both enantiomers in turn by adding racemate crystals and repeating the preferential crystallization. However, it is necessary to suppress the amount of crystals obtained from one-time crystallization to about 5–10 % to obtain a crystal with high enantiomeric purity. The technique to separate both enantiomers effectively is performed by adding additives in order to stabilize a supersaturated solution or create a difference in the nuclear generating speed between enantiomers. Since such preferential crystallization is described in many reports and general remarks, the explanation is omitted here [6–13].

CIET, the combined methodology of racemization and preferential crystallization, is a more effective method of resolution because the racemate can be totally transformed into a single enantiomer by one-time crystallization [14]. Enantiomor-

phic crystals are grown by seeding a desired crystal in a supersaturated solution under conditions in which fast racemization occurs. In the mother liquor, the racemization reaction prevents the mirror image isomer from crystallizing excessively. Crystal growth is promoted by reducing solubility by gradual condensation or by decreasing the temperature, and the racemate is converted to a single enantiomer. Furthermore, crystals with high enantiomeric purity can be efficiently obtained by a stirring effect during the crystallization. The stirring effect tears off microcrystals which grew from the seed crystal or the crystal surface formed in the beginning, and the crystals grow again based on this separated crystal.

The phenomenon in which an enantiomeric isomer increases nonlinearly is explained by “Ostwald ripening.” When the sizes of the particulates deposited from the supersaturated solution are different, a tiny particle disappears, and a large particle gradually becomes larger over time [15].

Successful examples of deracemization by dynamic preferential crystallization have been reported. Examples of applications to medical supplies are especially remarkable, and the resolution of amino acid derivatives and the synthetic process of the anti-inflammatory agent naproxen have been developed industrially [16]. Most of these examples involve racemization via an enolate anion generated by deprotonation from the  $\alpha$ -carbon of a carbonyl group [17–21]. In recent years, a phenomenon called Viedma’s ripening in which the whole crystal converges to one enantiomorphic crystal has also been reported by adding a glass bead to a little solvent and a racemization agent and by continuously stirring the mixture of racemate crystals with pulverization churning [22–28]. Some examples involving deracemization by atropisomerism and by an opening-and-closing ring process have also been developed. In this chapter, the CIAT process of atropisomers is summarized.

## 22.3 Total Resolution of Axially Chiral Materials by CIET

An attractive example of dynamic preferential crystallization accompanied by racemization of the asymmetric center at the  $\alpha$ -position of the carbonyl group has been reported. Furthermore, an interesting example of chiral amplification for atropisomers involving racemization by pivotal axial bond rotation has been developed.

Pincock reported the first example of chiral symmetry breaking of binaphthyl **1** from the melt (Fig. 22.2). When crystals of **1** were melted and solidified at 150 °C, an enantiomorphic crystal was obtained with high ee [29]. The activation free energy ( $\Delta G^\ddagger$ ) of binaphthyl is 23.5 kcal mol<sup>-1</sup> [30]. The half-life for racemization of binaphthyl in solution is 14.5 min at 50 °C, and it racemizes even at room temperature. This chiral amplification was successfully achieved on the basis of (1) that formed at 150 °C was the conglomerate and (2) that fast racemization occurred owing to bond rotation under crystallization conditions. When the melted sample was stirred during crystallization, crystals of high enantiomeric purity of more than 90 % ee were obtained with good reproducibility [31, 32].

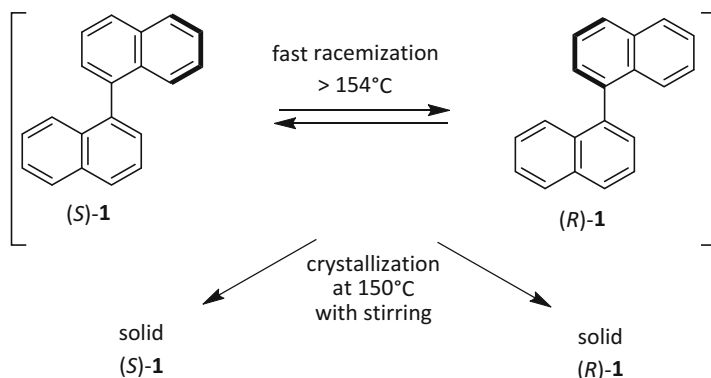
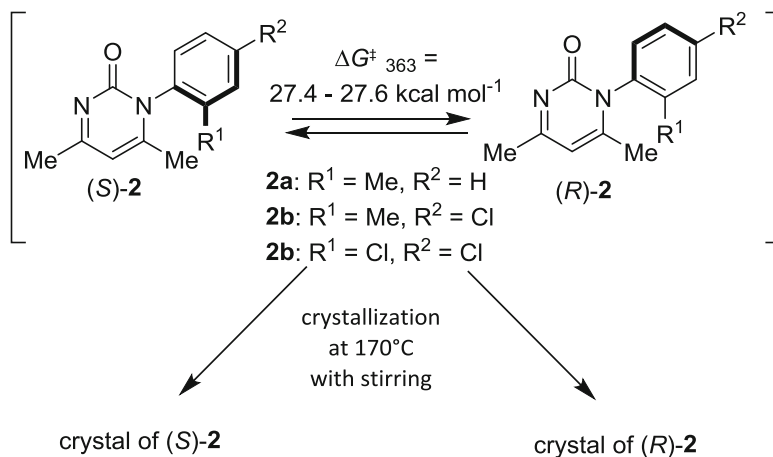


Fig. 22.2 Dynamic preferential crystallization of axially chiral binaphthyl

We found that several *N*-arylpyrimidin-2(1*H*)-ones, which are derivatives of pyrimidine nucleic acid bases, crystallized as conglomerates (Fig. 22.3) [33]. Moreover, these pyrimidinones have stable axial chirality when the C–N bond rotation corresponds to the racemization of these materials. When C–N bond rotation does not occur and the compounds have stable axial chirality at room temperature, unlike binaphthyl, then bond rotation can be promoted at high temperature. The free energy of activation of the racemization of **2a** at 90 °C was 27.9 kcal mol<sup>-1</sup> in xylene solution and those of **2b** and **2c** were 27.6 and 27.4 kcal mol<sup>-1</sup>, respectively. Their half-lives were 46 min, 31 min, and 24 min, respectively. Whereas the melting point of **2a** (mp 126–129 °C) was too low to achieve dynamic preferential crystallization at high temperature, the melting points of **2b** and **2c** exceeded 200 °C. Thus, after crystals of **2b** and **2c** were dissolved at 200 °C with minimal solvent, they crystallized after being cooled gradually to 170 °C. Enantiomeric crystals with high ee were obtained. The ee of the crystals was always more than 85 % ee, and the overall ee value in the batch including the racemic materials in the mother liquor was 70–73 % ee. Seeding the supersaturated solution and stirring during crystallization were effective for chiral symmetry breaking, and high ee of crystals was obtained with good reproducibility.

*N*-(1-Naphthyl) pyrimidine-2(1*H*)-thione **3** also gave a conglomerate crystal (Fig. 22.4) [34]. The rate of racemization of pyrimidinethione is faster than for the corresponding pyrimidinone. The  $\Delta G^\ddagger$  value for the racemization of **3** at 50 °C in xylene solution was 23.1 kcal mol<sup>-1</sup> and the half-life was only 4 min, whereas that of the corresponding pyrimidinone analog was 27.5 kcal mol<sup>-1</sup> and the half-life was 27 min at 90 °C. A toluene solution of pyrimidinethione **3** in a test tube was warmed to 90–100 °C with stirring; nitrogen was gradually introduced to the top of the test tube. The solvent was gently removed while evaporating at atmospheric pressure until all solvent was removed to solidify **3**. The enantiomeric excess of the remaining solid was analyzed by HPLC. When a small amount of seed crystals, i.e., a powdered single crystal obtained by standard recrystallization, was used during



**Fig. 22.3** Dynamic preferential crystallization of pyrimidinones

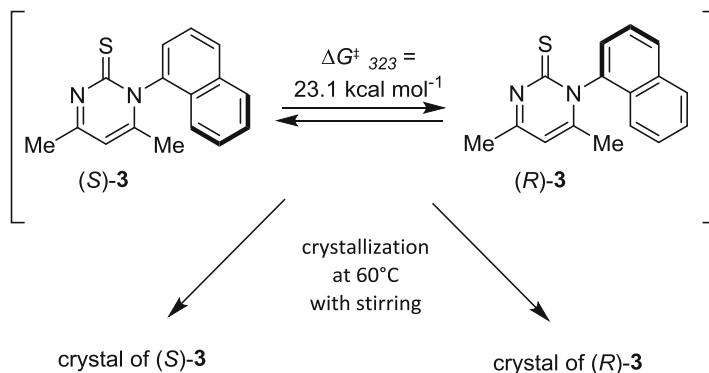


**Fig. 22.4** Dynamic preferential crystallization of pyrimidinethione

crystallization, chiral symmetry breaking of the solid was achieved up to 91 % ee. The effect of constant stirring during crystallization and seeding is needed to achieve CIET with reproducible high ees.

Aromatic amides **4a–b** also have axial chirality between the aromatic ring and amide plane (Fig. 22.5) [35]. 2-Alkoxy-1-naphthamides possessing piperidine and pyrrolidine groups gave conglomerate crystals. The  $\Delta G^{\ddagger}$  value for racemization of **4a** was  $21.1 \text{ kcal}^{-1}$  in THF, and the half-life was 11.8 min at 15 °C, which indicates slow racemization even at room temperature in nonpolar solvent. However, axial chirality was retained rather longer in MeOH/THF (50:50), where the half-life was 128 min at 15 °C. The free energy of activation in a polar solvent is higher than that in a nonpolar solvent. Furthermore, a protic solvent like methanol strongly controls racemization. Thus, polarity, hydrogen bonding, and solvation by alcohol are important factors that influence the rate of racemization. A nonpolar solvent

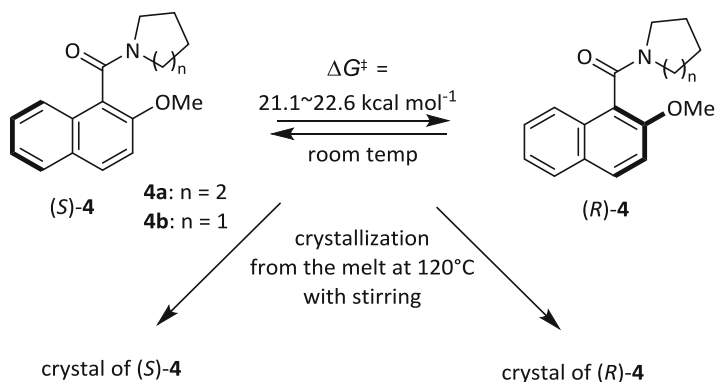


Fig. 22.5 Total resolution of axially chiral aromatic amides by dynamic preferential crystallization

lowers the  $\Delta G^\ddagger$  value by about 1.4 kcal mol<sup>-1</sup> relative to the value in a polar or protic solvent. For solvent effects, the solvent polarity may be attributable to the zwitterionic character of the amide group, and solvation by the hydrogen bond with protic solvent reduced the rate of bond rotation. Amide **4b** exhibits similar racemization behavior [36].

Chiral symmetry breaking by crystallization of **4** using the property of the conglomerate could be achieved. Racemic naphthamide **4a**, mp 110–112 °C, in a test tube was warmed to 120 °C until all crystals melted, then the melt was gradually cooled and solidified at 100 °C with stirring. Both enantiomers could be obtained randomly from many repeated crystallizations, and the desired enantiomeric crystals could be obtained on large scale by using the seeding method. When a small amount of seed crystals obtained from standard recrystallization was used during crystallization, chiral symmetry breaking was achieved with good reproducibility.

The axial chirality is retained long enough for subsequent asymmetric reaction (Fig. 22.6). For example, the axial chirality of **4a** was efficiently transferred to the photoproduct via 4 + 4 asymmetric photocycloaddition with 9-cyanoanthracene. When the solid was dissolved in cooled THF solution containing 9-cyanoanthracene and was irradiated with a 365 nm line at -20 °C, excited cyanoanthracene reacted from the vacant side of the amide oxygen atom, and 97 % ee in the adduct was obtained. This reaction provides a unique asymmetric synthesis using only the chirality of the crystal that was obtained by dynamic preferential crystallization. The molecular chirality in the crystal was also transferred to products via S<sub>N</sub>Ar reaction with *t*-BuLi [36], kinetic resolution of racemic amines [37], and asymmetric photocycloaddition with dienes [38].

4-Ethyl-*N,N*-diethylcoumarin-3-carboxamide **5** also afforded a conglomerate crystal (Fig. 22.7) [39]. The rate of racemization was measured according to the changes in the CD spectra using a cryostat apparatus, and the activation free energy and the half-life were calculated. The racemization of **5** in THF was too fast at room temperature to determine the rate. However, when the crystals of **5** were dissolved

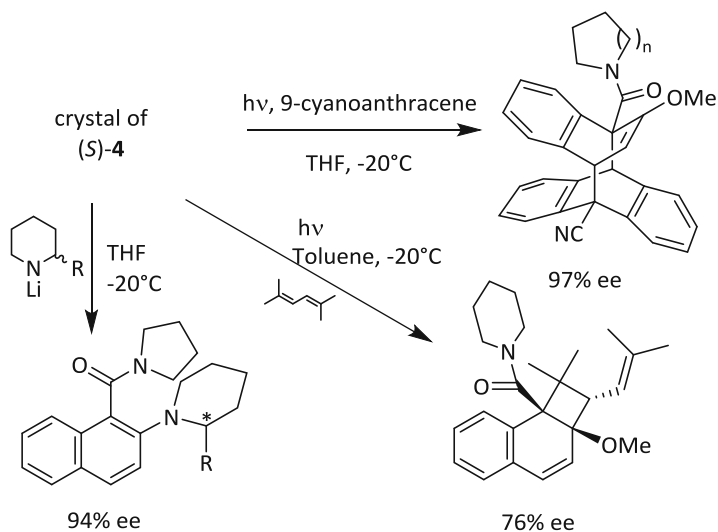


**Fig. 22.6** Asymmetric synthesis using the optically active crystals prepared by dynamic preferential crystallization of naphthamides

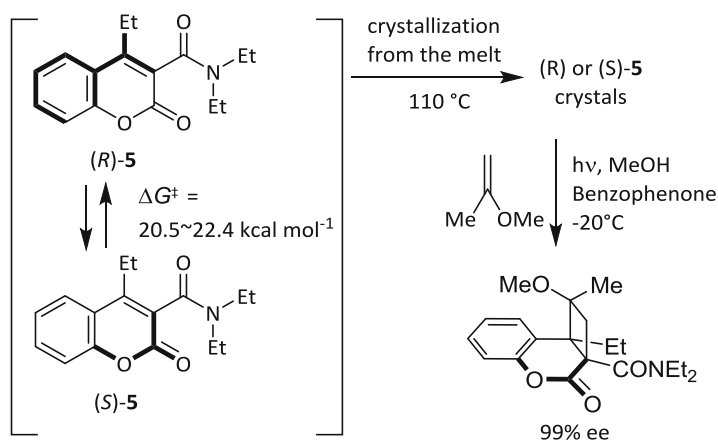


**Fig. 22.7** Dynamic preferential crystallization and subsequent asymmetric photoreaction

in THF at 5 °C, the half-life of racemization was 11.9 min. The half-life increased as the temperature was lowered, and  $t_{1/2}$  was 30.5 and 82.0 min at the temperatures of 0 °C and -5 °C, respectively. The activation free energy ( $\Delta G^\ddagger$ ) was calculated as 20.5–20.7 kcal mol<sup>-1</sup>. In the case of racemization in MeOH or DMF, there was a considerably lower activation free energy of 22.3–22.4 kcal mol<sup>-1</sup>, with  $t_{1/2}$  of 20.2 and 23.6 min at 25 °C, in MeOH and DMF, respectively. These results indicate that the racemization of **5** is too fast to resolve in the usual manner. However, the racemization can be controlled by lowering the temperature and selection of the solvent, and the lifetime becomes long enough for utilization in asymmetric synthesis.

Crystals of **5** were prepared by stirred crystallization at high temperature, in which the completely melted sample of **5** at 120 °C (mp: 114 °C) was cooled and solidified by lowering the temperature to 110 °C with stirring. A high level of reproducibility of both chiral crystallization and asymmetric photoreaction was achieved by this method. The chirality in the optically active crystals was utilized in a photosensitized 2 + 2 photocycloaddition with electron-rich alkenes, and optically active cyclobutanes were obtained up to 99 % ee. Optically active products were obtained derived from the chirality generated by dynamic preferential crystallization without an external chiral source.

*N,N*-Diallylquinolonamide **6** also afforded a conglomerate of a  $P2_1$  crystal system, and chiral symmetry breaking was easily achieved by crystallization from the melt (Fig. 22.8) [40]. The rate of racemization was determined on the basis of the changes of the optical rotation immediately after chiral crystals were dissolved in a solvent, and the activation free energies and half-lives were then calculated. The half-lives of racemization in toluene were 9.8, 2.8, and 1.1 min at temperatures of 20, 30, and 40 °C, respectively. The half-life for racemization of **6** increased as the temperature was lowered. In comparison with the rate of racemization in toluene, the rate was considerably suppressed in the polar protic solvent MeOH. The half-life of **6** in THF at 0 °C was estimated on the basis of the Arrhenius equation to be about 5 h. These results indicate that the racemization can be controlled by lowering the temperature and by the selection of the solvent and that the chiral conformation adopted in the crystal is retained long enough for application to subsequent asymmetric syntheses as a frozen molecular chirality. The molecular chirality in the crystal was retained after the crystals were dissolved in solvent at a low temperature, and the frozen molecular chirality was effectively transferred to the products by a two-step reaction involving hydrogenation and intermolecular photocycloaddition [41].

The  $\Delta G^\ddagger$  value for racemization of **7** was 22.4 kcal<sup>-1</sup> in toluene, and the half-life was 49 min at 20 °C, which indicates slow racemization even at room temperature in nonpolar solvent (Fig. 22.9) [42]. However, rather stable axial chirality was exhibited in MeOH, where the half-life was 343 min at 20 °C. The free energy of activation in a polar solvent is higher than that in a nonpolar solvent. Furthermore, a protic solvent like methanol strongly controls racemization. A nonpolar solvent lowers the  $\Delta G^\ddagger$  value by about 1.2 kcal mol<sup>-1</sup> relative to the value in a polar or protic solvent. We examined chiral symmetry breaking by crystallization of **7** using the property of the conglomerate. Racemic nicotinamide **7**, mp 147–148 °C, in a test tube was warmed to 160 °C until all crystals melted, and the melt was gradually cooled and then solidified at 125 °C with stirring. When a small amount of seed crystals from powdered single crystals (>99 % ee) obtained by standard recrystallization was used during crystallization, chiral symmetry breaking of the solid was achieved up to 92 % ee with good reproducibility.

Total resolution by CIET, in other words, dynamic preferential crystallization, is a powerful tool to obtain enantiomorphic crystals from racemates. This method does not need an external chiral source and easily achieves resolution by crystallizing materials under the conditions of fast racemization.

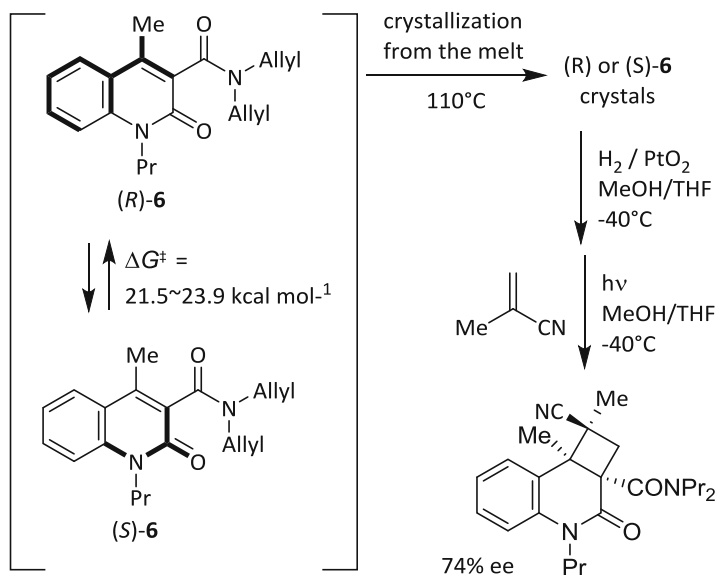


Fig. 22.8 Dynamic preferential crystallization and subsequent two-step asymmetric synthesis

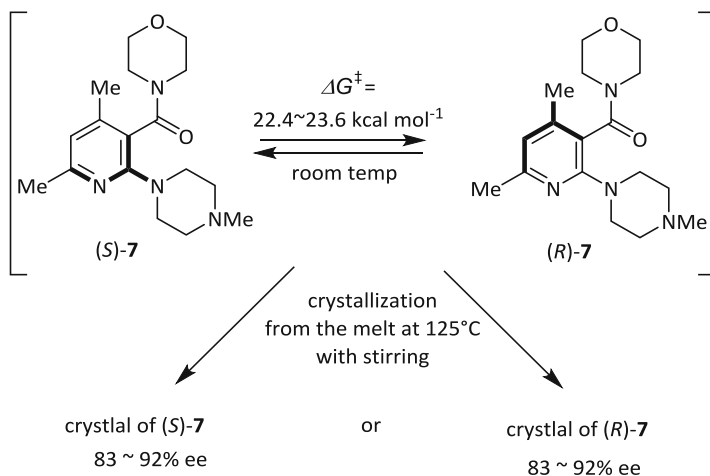
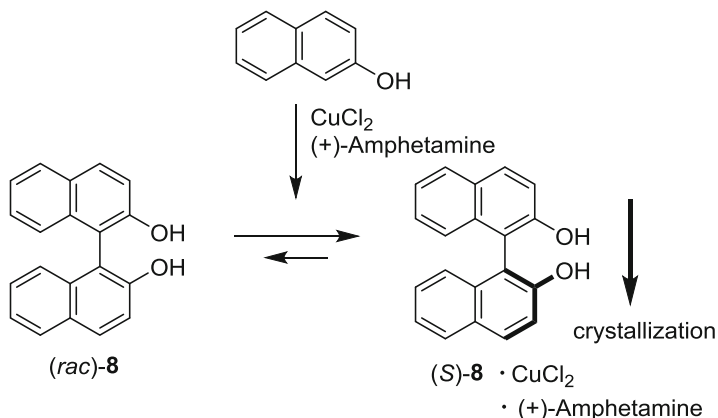


Fig. 22.9 Dynamic preferential crystallization of nicotinamide derivative

## 22.4 Dynamic Resolution of Axially Chiral Materials by CIDT

Optically active materials can be conveniently obtained by resolution via dynamic preferential crystallization; however, the methodology is not applicable to all crystalline materials, but is successful only in conglomerate crystals, which are formed



**Fig. 22.10** Resolution of BINOL by CIDT

at a rate of only 10 % in organic racemic materials. On the other hand, most optically active materials crystallize in a chiral fashion. Some methodologies have been developed in which racemic mixtures could be converted to diastereomers through the formation of chiral salts with enantiopure materials, making a metal complex with a chiral ligand or forming a chiral auxiliary intramolecularly, followed by resolution by dynamic crystallization involving epimerization [43]. Crystallization-Induced Diastereomer Transformation is particularly useful for the preparation of optically active amino acids, pharmaceutical reagents [44, 45], and axially chiral materials.

One of the pioneering successful examples of resolution using dynamic crystallization between diastereomers was reported in 1913 [46]. Recrystallization of a 1:1 salt of racemic indanone and brucine from acetone gave crystalline salts of (+)-indanone and brucine since the racemization of indanone took place simultaneously with the yield reaching 93 %. Since the  $\alpha$ -position of the carbonyl group is acidic, the racemization advanced easily, and diastereomeric salts converged on one crystalline diastereomer. Many examples of CIDT involve epimerization at the  $\alpha$ -position of a carbonyl group [20, 47–56].

CIDT is also used for the dynamic resolution of axially chiral compounds. For example, BINOL **8**, important as a ligand of asymmetric organometallic catalysis, was resolved by the oxidative coupling reaction of 2-naphthol by using copper chloride [57, 58]. In this case, making a crystalline (+)-amphetamine copper complex resulted in the dynamic resolution of 96 % de (Fig. 22.10). Moreover, the experiment that used (–)-sparteine instead of (+)-amphetamine has also been reported, and the de of the complex was 80 % [59].

Adams et al. reported that the crystallization of axially chiral cinnamic acid derivative **9** with an equimolar amount of quinine gave 76 % yield of the salt from acetone (Fig. 22.11) [60]. Moreover, Newman et al. obtained an optically active salt of phenanthrene acetic acid derivative **10** and brucine by recrystallization of

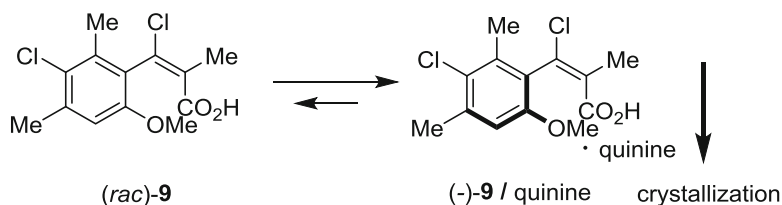


Fig. 22.11 Crystalline 1:1 salt of (-)-9 and quinine was obtained by CIDT

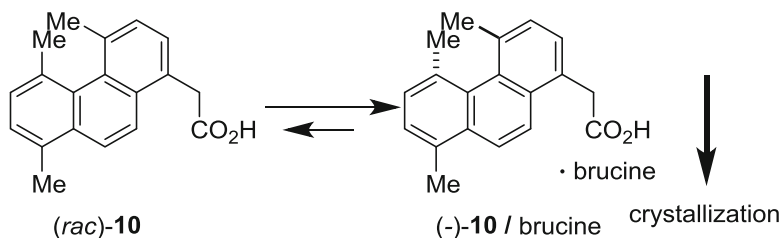


Fig. 22.12 Crystalline 1:1 salt of (-)-10 and brucine was obtained by CIDT

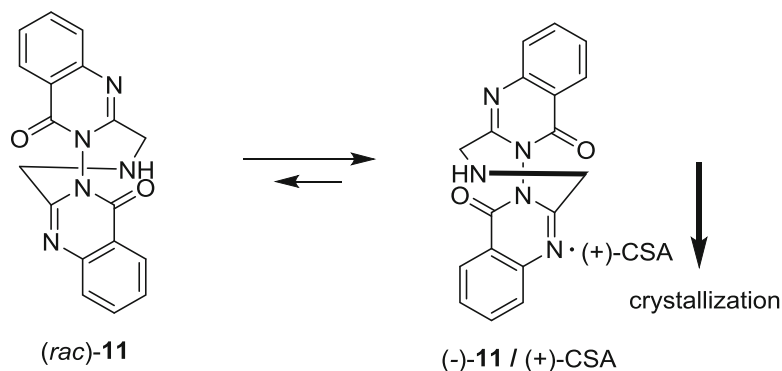
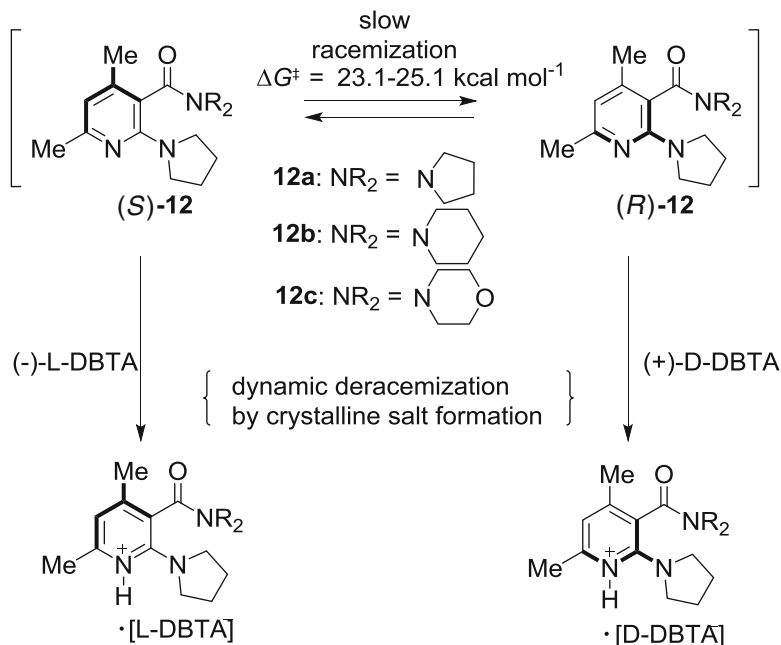


Fig. 22.13 Crystalline 1:1 salt of (-)-11 and (+)-CSA was obtained by CIDT

racemic **10** and brucine in 74 % yield from a mixed solution of ethanol and ethyl acetate (Fig. 22.12) [61]. Coogan et al. obtained 93 % ee of a 1:1 salt of N-N axially chiral **11** with (+)-camphorsulfonic acid in 82 % yield by heating racemic **11** in benzene (Fig. 22.13) [62].

Deracemization of oily racemic nicotinamides with a basic group was examined by dynamic salt formation with enantiopure dibenzoyltartaric acid (DBTA) (Fig. 22.14) [63]. Dynamic racemization through the formation of crystalline salts achieves effective deracemization of the racemic base to give optically active salts. Furthermore, the chiral acidic adjuvant can be easily removed by extraction under basic conditions.



**Fig. 22.14** Deracemization by dynamic salt formation of nicotinamides with enantiopure DBTA

The axial chirality of **12a–c** could not be controlled in the solution phase because the chiral acid in the salt was located far from the axial chiral auxiliary. In contrast, all of the amides formed crystalline salts with enantiopure DBTA by slow evaporation of the solvent. A chloroform solution of racemic **12a** and an equimolar amount of enantiopure L-DBTA in a test tube were warmed to 60 °C to accelerate the deracemization of **12a**, and removal of the solvent led to the formation of crystalline salts (from 60 to 67 % ee after removal of DBTA).

In the case of deracemization of **12b** by salt formation with L-DBTA, a better ee of (–)-**12b** was obtained (from 75 to 83 % ee). When enantiopure D-DBTA was used for salt formation, (+)-**12b** was obtained with almost the same ee value. Both enantiomers of **12b** could be easily prepared by selection of the appropriate enantiomeric DBTA.

Deracemization of **12c** by salt formation with L-DBTA was also successful, and a 51–60 % ee of **12c** was obtained, with (–) specific optical rotation, after removal of DBTA. Racemization of **12c** was slightly faster than that of **12a** and **12b**. Therefore, the ee value may have decreased during the workup process.

Dynamic resolution involving epimerization has also been performed for aromatic amides with a chiral auxiliary connected by a covalent bond. Axial chirality of various optically active aromatic amides was controlled by CIDT (Fig. 22.15). Naphthamide with a chiral prolyl group (*S*)-**13** has both an asymmetric center and axial chirality and exists as a mixture of two diastereomers in solution. By

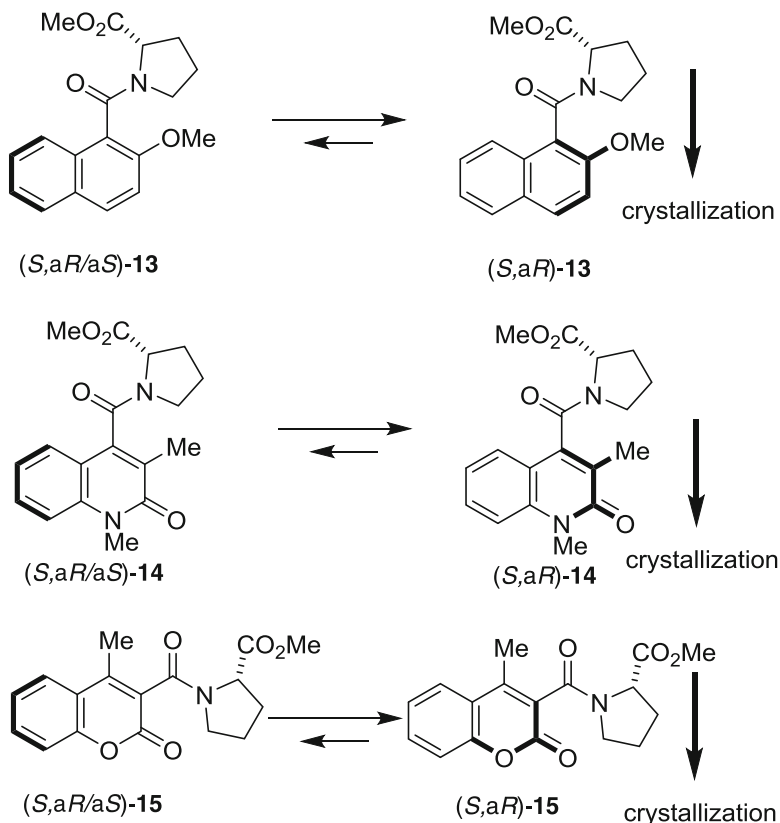


**Fig. 22.15** Resolution of aromatic amides with center and axial chirality by CIDT involving epimerization of axial chirality

crystallization of the mixture from the melt, the diastereomers converged on  $(S, aR)$ -**13** predominantly via epimerization [64]. The axial chirality was retained in cooled solution, and then it was effectively transferred to the products of the photochemical reaction with an anthracene derivative.

Quinolonamide **14** possessing a chiral auxiliary at the amide group also has axial chirality and exists as a mixture of two diastereomers of 45:65  $(S,aR:S,aS)$  in solution [65]. When the amide is solidified by evaporation from a solvent (THF) at 65 °C, the mixture converged on the crystalline minor diastereomer,  $(S,aR)$ -**14**, involving epimerization of axial chirality. The resolved optically active quinolonamide was transferred to cyclobutane-type products via 2 + 2 photocycloaddition reactions with electron-withdrawing alkenes with 100 % de.

Coumarincarboxamide **15** with a chiral prolyl function at the amide group also has both center and axial chirality and exists as a mixture of two diastereomers in solution. The diastereomers converged on  $(S,aR)$ -**15** by solidification from the melt

[39]. Although this substrate was gradually epimerized at room temperature, it has a stable axial chirality at  $-20\text{ }^{\circ}\text{C}$ , and in the irradiation in the presence of alkenes, the  $2 + 2$  addition product was afforded with 100 % de.

CIDT provides simple and effective resolution of chiral materials. Racemic materials do not always afford conglomerate crystals. However, optically active materials give chiral crystal systems in almost all cases that could be controlled by both intra- and intermolecular chiral auxiliaries, where the optical chirality can be controlled by effective epimerization.

## 22.5 Conclusion

Many valuable successful examples of CIET and CIDT have been developed in addition to the examples introduced in this chapter. Examples utilizing a new racemization process involving ring opening-closing reactions have also been developed [66]. Furthermore, combined methodologies to form achiral materials from chiral products using subsequent dynamic preferential crystallization have also been reported [67]. Crystallization-Induced Asymmetry Transformation involving CIET and CIDT is an excellent methodology for obtaining optically active materials by simple crystallization without complicated expensive reagents and resolution procedures. The most noteworthy phenomenon is that the desired enantiomer can be obtained without production of the undesired enantiomer. Many new systems will be developed in the future. In recent years, Viedma's ripening which involves dynamic crystallization by pulverizing crystals by stirring with glass beads provided excellent examples of chiral amplification [22–28]. We hope many new applications using organic crystals will be developed as they play an important role in organic chemistry.

## References

1. J. Jacques, A. Collet, S.H. Wilen, *Enantiomers, Racemates and Resolutions* (Krieger Publishing Company, Malabar, 1994)
2. R.A. Sheldon, *Chirotechnology: Industrial Synthesis of Optically Active Compounds* (CRC Press, New York, 1993)
3. A.N. Collins, G.N. Shelldrake, J. Crosby, *Chirality in Industry: The Commercial Manufacture and Applications of Optically Active Compounds* (Wiley, New York, 1992)
4. G. Coquerel, Preferential crystallization: In novel optical resolution technologies, in *Topics in Current Chemistry*, ed. by K. Sakai, N. Hirayama, R. Tamura, vol. 269 (Springer, New York, 2007)
5. D. Polenske, H. Lorenz, A. Seidel-Morgenstern, Potential of different techniques of preferential crystallization for enantioseparation of racemic compound forming systems. *Chirality* **21**(8), 728–737 (2009)
6. B.S. Green, M. Lahav, D. Rabinovich, Asymmetric synthesis via reactions in chiral crystals. *Acc. Chem. Res.* **12**, 191–197 (1979)

7. V. Ramamurthy, K. Venkatesan, Photochemical reactions of organic crystals. *Chem. Rev.* **87**, 433–481 (1987)
8. J.R. Scheffer, M. Garcia-Garibay, O. Nalamasu, The influence of the molecular crystalline environment on organic photorearrangements, in *Organic Photochemistry 8*, ed. by A. Padwa (Marcel Dekker, New York, 1987), pp. 249–347
9. M. Vaida, R. Popovitz-Biro, L. Leiserowitz, M. Lahav, Probing reaction pathways via asymmetric advances in crystallization processes 78 transformations in chiral and centrosymmetric crystals, in *Photochemistry in Organized and Constrained Media*, ed. by V. Ramamurthy (Wiley, New York, 1991), pp. 249–302
10. M. Sakamoto, Absolute asymmetric photochemistry using spontaneous chiral crystallization, in *Chiral Photochemistry*, ed. by V. Ramamurthy (Marcel Dekker, New York, 2004), pp. 415–446
11. M. Sakamoto, Absolute asymmetric synthesis from achiral molecules in the chiral crystalline environment. *Chem. Eur. J.* **3**, 684–689 (1997)
12. M. Sakamoto, T. Mino, Asymmetric reaction using molecular chirality controlled by spontaneous crystallization, in *Advances in Crystallization Processes*, ed. by Y. Mastai (InTech, Rijeka, 2012), pp. 59–80
13. M. Sakamoto, Spontaneous chiral crystallization of achiral materials and absolute asymmetric photochemical transformation using the chiral crystalline environment. *J. Photochem. Photobiol. C: Photochem. Rev.* **7**, 183–196 (2006)
14. R. Yoshioka, Racemization, optical resolution and crystallization-induced asymmetric transformation of amino acids and pharmaceutical intermediates. *Top. Curr. Chem.* **269**, 83–132 (2007)
15. W. Ostwald, Studies on the formation and inversion of solids: First paper: Supersaturation and supercooling. *Z. Phys. Chem. Stoehiom. Verwandtschafts.* **22**, 289 (1897)
16. K. Arai, Y. Obara, K. Takakuwa, T. Iizumi, Optical active esters of naphthylpropionic acid. US Patent US 4,417,070 (1983)
17. S. Miyahara, K. Nagahara, A. Sakaguchi, K. Nitta, Manufacture of D-valine from isopropylhydantoin. *Jpn. Kokai Tokkyo Koho.* JP61056094 (1986)
18. C. Hongo, S. Yamada, I. Chibata, Asymmetric transformation of N-acetyl-DL-leucine. *Bull. Chem. Soc. Jpn.* **54**, 3291–3295 (1981)
19. W.J. Boyle Jr., S. Sifniades, J.F. Van Peppen, Asymmetric transformation of  $\alpha$ -amino- $\epsilon$ -caprolactam, a lysine precursor. *J. Org. Chem.* **44**, 4841–4847 (1979)
20. S. Yamada, C. Hongo, R. Yoshioka, I. Chibata, Method for the racemization of optically active amino acids. *J. Org. Chem.* **48**, 843–846 (1983)
21. Y. Obara, H. Matsumoto, K. Arai, S. Tsuchiya, Optical resolution of N-(substituted phenylmethylidene)phenylalanine methyl esters. *Jpn. Kokai Tokkyo Koho.* JP6100165 (1986)
22. C. Viedma, Chiral symmetry breaking during crystallization: Complete chiral purity induced by nonlinear autocatalysis and recycling. *Phys. Rev. Lett.* **94**, 065504 (2005)
23. C. Viedma, Chiral symmetry breaking and complete chiral purity by thermodynamic-kinetic feedback near equilibrium: Implications for the origin of biochirality. *Astrobiology* **7**, 312–319 (2007)
24. W.L. Noorduin, E. Vlieg, R.M. Kellogg, B. Kaptein, From Ostwald ripening to single chirality. *Angew. Chem. Int. Ed.* **48**, 9600–9606 (2009)
25. W.L. Noorduin, P. van der Asdonk, H. Meekes, W.J.P. van Enckevort, B. Kaptein, M. Leeman, R.M. Kellogg, E. Vlieg, Complete chiral resolution using additive-induced crystal size bifurcation during grinding. *Angew. Chem. Int. Ed.* **48**, 3278–3280 (2009)
26. W.L. Noorduin, T. Izumi, A. Millemaggi, M. Leeman, H. Meekes, W.J.P. van Enckevort, R.M. Kellogg, B. Kaptein, E. Vlieg, D.G. Blackmond, Emergence of a single solid chiral state from a nearly racemic amino acid derivative. *J. Am. Chem. Soc.* **130**, 1158–1159 (2008)
27. W.L. Noorduin, A.A.C. Bode, M. van der Meiden, H. Meekes, A.F. van Etteger, W.J.P. van Enckevort, P.C.M. Christianen, B. Kaptein, R.M. Kellogg, T. Rasing, E. Vlieg, Complete chiral symmetry breaking of an amino acid derivative directed by circularly polarized light. *Nat. Chem.* **1**, 729–732 (2009)

28. W.L. Noorduin, B. Kaptein, H. Meekes, W.J.P. van Enckevort, R.M. Kellogg, E. Vlieg, Fast attrition-enhanced deracemization of naproxen by a gradual in situ feed. *Angew. Chem. Int. Ed.* **48**, 4581–4583 (2009)
29. R.E. Pincock, R.R. Perkins, A.S. Ma, K.R. Wilson, Probability distribution of enantiomorphous forms in spontaneous generation of optically active substances. *Science* **174**, 1018–1020 (1971)
30. A.S. Cooke, M.M. Harris, Ground-state strain and other factors influencing optical stability in the 1,1'-binaphthyl series. *J. Chem. Soc.* 2365–2373 (1963)
31. D.K. Kondepudi, J. Laudadio, K. Asakura, Chiral symmetry breaking in stirred crystallization of 1,1'-binaphthyl melt. *J. Am. Chem. Soc.* **121**, 1448–1451 (1999)
32. D.K. Kondepudi, K. Asakura, Chiral autocatalysis, spontaneous symmetry breaking, and stochastic behavior. *Acc. Chem. Res.* **34**, 946–954 (2001)
33. M. Sakamoto, N. Utsumi, M. Ando, M. Saeki, T. Mino, T. Fujita, A. Katoh, T. Nishio, C. Kashima, Breaking the symmetry of axially chiral N-Aryl-2(1H)-pyrimidinones by spontaneous crystallization. *Angew. Chem. Int. Ed.* **42**, 4360–4363 (2003)
34. M. Sakamoto, F. Yagishita, M. Ando, Y. Sasahara, N. Kamataki, M. Ohta, T. Mino, Y. Kasashima, T. Fujita, Generation and amplification of optical activity of axially chiral N-(1-Naphthyl)-2(1H)-pyrimidinethione by crystallization. *Org. Biomol. Chem.* **8**, 5418–5422 (2010)
35. M. Sakamoto, A. Unosawa, S. Kobaru, A. Saito, T. Mino, T. Fujita, Asymmetric photocycloaddition in solution of a chiral crystallized naphthamide. *Angew. Chem. Int. Ed.* **44**, 5523–5526 (2005)
36. M. Sakamoto, A. Unosawa, S. Kobaru, K. Fujita, T. Mino, T. Fujita, An asymmetric  $S_NAr$  reaction using the molecular chirality in a crystal. *Chem. Commun.* 3586–3587 (2007)
37. M. Sakamoto, K. Fujita, F. Yagishita, A. Unosawa, T. Mino, T. Fujita, Kinetic resolution of racemic amines using the provisional molecular chirality generated by spontaneous crystallization. *Chem. Commun.* **47**, 4267–4269 (2011)
38. M. Sakamoto, F. Yagishita, A. Saito, S. Kobaru, A. Unosawa, T. Mino, T. Fujita, Asymmetric photocycloaddition of naphthamide with a diene using the provisional molecular chirality in a chiral crystal. *Photochem. Photobiol. Sci.* **10**, 1387–1389 (2011)
39. M. Sakamoto, M. Kato, Y. Aida, K. Fujita, T. Mino, T. Fujita, Photosensitized 2 + 2 cycloaddition reaction using homochirality generated by spontaneous crystallization. *J. Am. Chem. Soc.* **130**, 1132–1133 (2008)
40. F. Yagishita, M. Sakamoto, T. Mino, T. Fujita, Asymmetric intramolecular cyclobutane formation via photochemical reaction of N, N-diallyl-2-quinolone-3-carboxamide using a chiral crystalline environment. *Org. Lett.* **13**, 6168–6171 (2011)
41. F. Yagishita, T. Mino, T. Fujita, M. Sakamoto, Two-step asymmetric reaction using the frozen chirality generated by spontaneous crystallization. *Org. Lett.* **14**, 2638–2641 (2012)
42. F. Yagishita, K. Okamoto, N. Kamataki, S. Kanno, T. Mino, Y. Kasashima, M. Sakamoto, Chiral symmetry breaking of axially chiral nicotinamide by crystallization from the melt. *Chem. Lett.* **42**, 1508–1510 (2013)
43. K.M.J. Brands, A.J. Davies, Crystallization-induced diastereomer transformations. *Chem. Rev.* **106**, 2711–2733 (2006)
44. J. Cooper, D.C. Humber, A.G. Long, Conversion of penicillin G into cephalixin employing a second-order asymmetric transformation. *Synth. Commun.* **16**, 1469–1477 (1986)
45. G.J. Kemperman, J. Zhu, A.J.H. Klunder, B. Zwanenburg, Clathration-induced asymmetric transformation of cefadroxil. *Org. Lett.* **2**, 2829–2831 (2000)
46. H. Leuchs, J. Wutke, Spiranes. IV. Stereochemical treatment of the keto-enol question. *Ber. Dtsch. Chem. Ges.* **46**, 2420–2435 (1913)
47. J.C. Clark, G.H. Phillipps, M.R. Steer, L. Stephenson, A.R. Cooksey, Resolution of esters of phenylglycine with (+)-tartaric acid. *J. Chem. Soc. Perkin Trans.* **1**, 471–474 (1976)
48. J.C. Clark, J. Elks, Process for the preparation of optically active. R-aminoacid esters. *Ger. Offe. DE 2309180*, *Chem. Abstr.* **79**, 126791 (1973)

49. J.C. Clark, G.H. Phillipps, M.R. Steer, A new asymmetric transformation of alpha-amino-acid esters with (+)-tartaric acid. *J. Chem. Soc. Perkin Trans.* **1**, 475–481 (1976)
50. R. Yoshioka, O. Ohtsuki, M. Senuma, T. Tosa, Efficient preparation of D-aspartic acid  $\beta$ -methyl ester as an aspoxicillin material by optical resolution, epimerization, and asymmetric transformation. *Chem. Pharm. Bull.* **37**, 883–886 (1989)
51. I. Chibata, S. Yamada, C. Hongo, R. Yoshioka, p-Hydroxyphenylglycine R-phenylethanesulfonate. Process for production thereof and utilization thereof in resolution of p-hydroxyphenylglycine. *Eur Pat Appl EP 75318 A2*, *Chem. Abstr.* **99**, 105702 (1983)
52. R. Yoshioka, M. Tohyama, O. Ohtsuki, C.I. Yamada, S., The optical resolution and asymmetric transformation of DL-p-hydroxyphenylglycine with (+)-1-phenylethanesulfonic acid. *Bull. Chem. Soc. Jpn.* **60**, 649–652 (1987)
53. R. Yoshioka, M. Tohyama, S. Yamada, O. Ohtsuki, I. Chibata, A facile method for the production of D-p-hydroxyphenylglycine: Asymmetric transformation of DL-p-hydroxyphenylglycine using (+)-1-phenylethanesulfonic acid. *Bull. Chem. Soc. Jpn.* **60**, 4321–4323 (1987)
54. V. Cannata, G. Tamerlani, A new process for the optical resolution of racemic mixtures of R-Naphtylpropionic acids. *Eur Pat Appl EP 143371 A1*, *Chem. Abstr.* **103**, 215015 (1985)
55. V. Cannata, G. Tamerlani, A new process for the optical resolution of racemic mixtures of R-Naphtylpropionic acids. *Eur Pat Appl EP 182279 A1*, *Chem. Abstr.* **1053**, 78693 (1986)
56. F.J. Lopez, S.A. Ferrino, M.S. Reyes, R. Roman, Asymmetric transformation of the second kind of racemic naproxen. *Tetrahedron Asymmetry* **8**, 2497–2500 (1997)
57. J. Brussee, J.L.G. Groenendijk, J.M. Koppele, A.C.A. Jansen, On the mechanism of the formation of *s*(-)-(1, 1'-binaphthalene)-2,2'-diol via copper(II)amine complexes. *Tetrahedron* **41**, 3313–3319 (1985)
58. M. Smrcina, M. Lorenc, S.P. Hanus, V. P. Kocovsky, Synthesis of enantiomerically pure 2,2'-dihydroxy-1,1'-binaphthyl, 2,2'-diamino-1,1'-binaphthyl, and 2-amino-2'-hydroxy-1,1'-binaphthyl. Comparison of processes operating as diastereoselective crystallization and as second order asymmetric transformation. *J. Org. Chem.* **57**, 1917–1920 (1992)
59. K. Tsubaki, M. Miura, M. Horikawa, H. Tanaka, T. Kawabata, T. Furuta, K. Tanaka, K. Fujii, Synthesis of optically active oligonaphthalenes via second-order asymmetric transformation. *J. Am. Chem. Soc.* **125**, 16200–16201 (2003)
60. R. Adams, W.J. Gross, Restricted rotation in aryl olefins. IV. Preparation and resolution of  $\beta$ -chloro- $\beta$ -(2-methoxy-4,6-dimethyl-5-chlorophenyl- $\alpha$ -methylacrylic and the corresponding acrylic acid. *J. Am. Chem. Soc.* **64**, 1786–1790 (1942)
61. M.S. Newman, A.S. Hussey, The synthesis and optical resolution of 4,5,8-trimethyl-1-phenanthrylacetic acid. *J. Am. Chem. Soc.* **69**, 3023–3027 (1947)
62. M.P. Coogan, E. Smart, D.E. Hibbs, Asymmetric transformation (deracemization) of an atropisomeric bisheterocyclic amine. *Chem. Commun.*, 1991–1992 (1999)
63. F. Yagishita, N. Kamataki, K. Okamoto, S. Kanno, T. Mino, H. Masu, M. Sakamoto, Deracemization of axially chiral nicotinamides by dynamic salt formation with Enantiopure Dibenzoyletartaric Acid (DBTA). *Molecules* **18**, 14430–14447 (2013)
64. M. Sakamoto, A. Unosawa, S. Kobaru, K. Fujita, T. Mino, T. Fujita, Diastereoselective photocycloaddition using memory effect of molecular chirality controlled by crystallization. *Chem. Commun.* 1632–1634 (2007)
65. M. Sakamoto, N. Sato, T. Mino, Y. Kasashima, T. TFujita, Crystallization-induced diastereomer transformation of 2-quinolone-4-carboxamide followed by stereoselective intermolecular photocycloaddition reaction. *Org. Biomol. Chem.* **6**, 848–850 (2008)
66. F. Yagishita, H. Ishikawa, T. Onuki, S. Hachiya, T. Mino, M. Sakamoto, Total spontaneous resolution by deracemization of isoindolinones. *Angew. Chem. Int. Ed.* **51**, 13023–13025 (2012)
67. S. Hachiya, Y. Kasashima, F. Yagishita, T. Mino, H. Masu, M. Sakamoto, Asymmetric transformation by dynamic crystallization of achiral succinimides. *Chem. Commun.* **49**, 4776–4779 (2013)

# Chapter 23

## Chiral Recognition by Inclusion Crystals of Amino-Acid Derivatives Having Trityl Groups

Motohiro Akazome

**Abstract** Enantioselective inclusion of racemic guests into chiral hosts can be used for enantiomeric resolution. We propose new crystalline host designs consisting of amino-acid derivatives having trityl groups. We first show that an *N,N'*-ditrityl amino amide host includes *N*-phenyl-2-halobutanamides (halogens: Cl and Br) in the host cavity to form inclusion crystals with high enantioselectivities (82–83 % ee, *S*-form). We then show that salts between *N*-trityl amino acids and *tert*-butylamine include several alcohols and that racemic 1-chloro-2-propanol is resolved to give the *S*-enriched sample of 69 % ee. In both of these kinds of hosts, trityl groups serve as crystal engineering tools for constructing inclusion crystals. The installation of trityl groups into amino-acid derivatives breaks their inherent hydrogen bonds, and the inclusion of guest molecules (amides or alcohols) compensates the loss of hydrogen bonds. Single-crystal X-ray analysis has elucidated these inclusion cavities and host-guest interactions.

**Keywords** Inclusion crystals • Chiral recognition • Amino acid • Trityl group

### 23.1 Introduction

Chiral compounds are very important owing to their biological activity, and of the several ways to obtain them, asymmetric synthesis is the most attractive but is not perfect. Enantiomeric resolution is still a reliable method in pharmaceutical process chemistry, where separation by diastereomeric salt formation is usually used [1]. On the other hand, the chemistry of inclusion crystals has a long history [2], and inclusion compounds are promising candidates for functional materials separating gases, structural isomers, enantiomers, and so on. When chiral hosts form inclusion

---

M. Akazome (✉)

Department of Applied Chemistry and Biotechnology, Graduate School of Engineering,  
Chiba University, 1-33 Yayoicho, Inageku, Chiba 263-8522, Japan  
e-mail: [akazome@faculty.chiba-u.jp](mailto:akazome@faculty.chiba-u.jp)

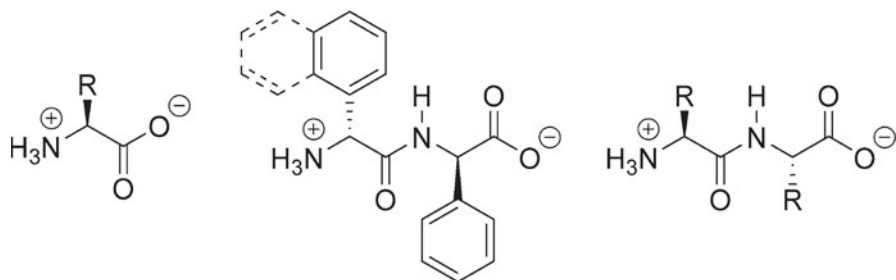


Fig. 23.1 Amino acids and dipeptides as hosts for inclusion crystals

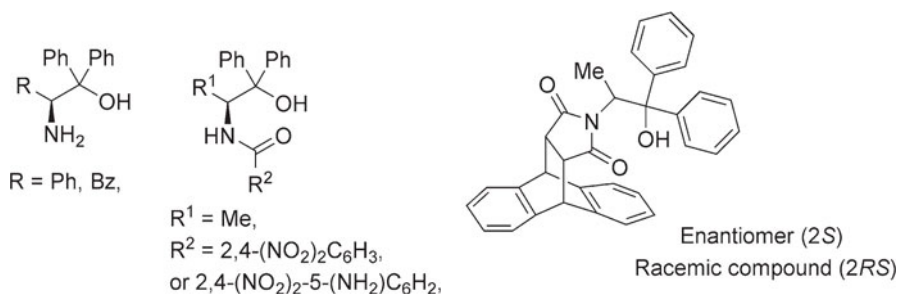


Fig. 23.2 2-Amino-1,1-diarylethanol hosts derived from amino acids

crystals including one enantiomer of a racemic guest selectively, these inclusion compounds are regarded as enantiomerically resolved [3, 4]. The design of such host molecules is consequently an area of great interest in host-guest chemistry.

Natural amino acids are plentiful and can serve as a chiral pool for constructing host molecules (Fig. 23.1), and during the past couple of decades, the use of crystalline dipeptides as organic host molecules has been well studied by us [5, 6] and other groups [7, 8]. Many reports have dealt with small achiral guests such as solvents, but there are several reported examples of chiral recognition in racemic samples; e.g., sulfoxides, hydroxyesters, and alcohols were enantioselectively included into simple dipeptides [6, 8]. One can predict from the accumulated candidate dipeptide data that their stacked sheet structures or tubal column structures can serve as inclusion cavities. Hosts using dipeptides, however, require two amino-acid molecules. A general design of hosts using one amino acid is awaited.

Enantiopure 2-amino-1,1-diarylethanol, which are easily prepared by the reaction of amino acids with Grignard reagents, have been used as chiral building blocks for crystalline hosts (Fig. 23.2). However, these host molecules consisting of amino-acid derivatives have yielded disappointing results with regard to the inclusion of alcohols [9].

We therefore proposed the following rational designs for inclusion crystals recognizing the chirality of racemic guests.

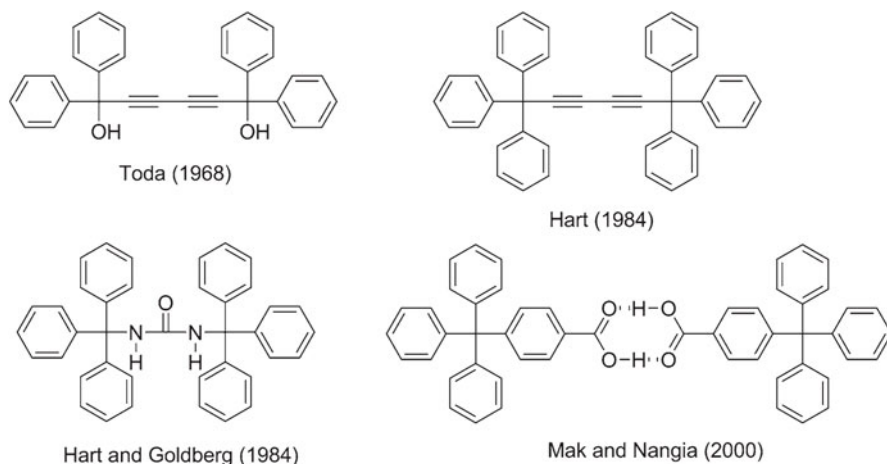


Fig. 23.3 Wheel-and-axle-type hosts having trityl and related groups

## 23.2 Trityl-Group Host Design as a Crystal Engineering Tool

Triphenylmethane has long been known to form inclusion crystals [10]. Toda first reported in 1968 that diacetylenic diols having four aryl groups on terminal carbons have good inclusion ability [11] and that wheel-and-axle design (Fig. 23.3) is still generally used today. Hart investigated wheel-and-axle molecules such as diacetylenes having two trityl groups [12] and Hart and Goldberg soon demonstrated the value of linear molecules having two trityl group and related *N,N'*-ditritylurea hosts [13]. Mak and Nangia reported that 4-tritylbenzoic acid assembled to form wheel-and-axle-type hosts with many kinds of organic guests [14].

The recent development of crystal engineering has shed new light on the trityl group as a powerful tool for constructing molecular compasses and gyroscopes [15] and supramolecular architecture [16]. Adding the trityl group into compounds not only facilitates their assembly by phenyl-phenyl interactions but also increases their crystallinity [17].

Although trityl group has the potential to make an inclusion cavity as mentioned above, there are few reports about chiral recognition. Here, we would like to introduce our new design using trityl groups on nitrogen functional groups such as amino or amide groups. In organic synthesis, the trityl group is a well-known protection group that is stable under basic conditions and is easily removed under acidic conditions [18].

Our host design illustrated in Fig. 23.4 is based on compensation of hydrogen bonds broken by bulky trityl groups. Since *N*-methyl acetamide has hydrogen-bond donor (H-N) and acceptor (CO) groups, a one-dimensional hydrogen-bond network is constructed [19]. Installation of two trityl groups on amino amides will break the hydrogen bonds between them. At the same time, the trityl groups

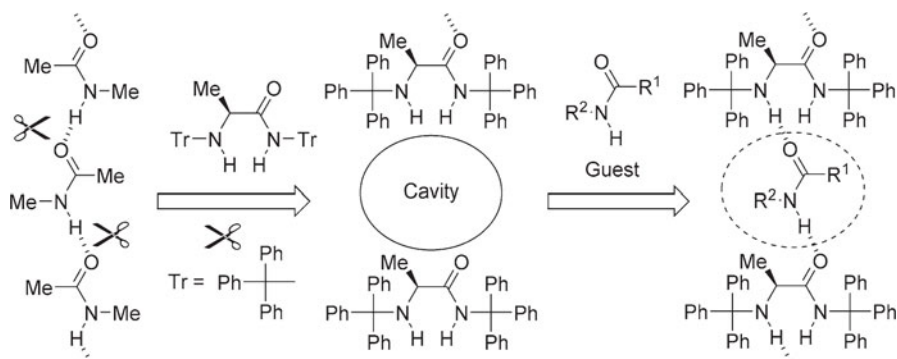


**Fig. 23.4** Host **1** designed to capture amide guests to compensate the loss of hydrogen bonds broken by trityl groups

form cavities in which guest molecules are captured. When a guest is suitable to compensate the loss of the inherent hydrogen bonds, the host-guest interaction will result in the formation of new inclusion crystals. To demonstrate how this concept can be used for enantiomeric separation, we focus on crystalline *N,N'*-ditrityl (*S*)-2-aminopropanamide (**1**) as one of the *N,N'*-ditrityl amino amides.

The salts between *N*-tritylamino acid and *tert*-butylamine are evaluated as another host design (Fig. 23.5). For example, *tert*-butylammonium acetate has a ladder-type hydrogen-bond network [20]. When a trityl group is installed in this network, its bulkiness will break the inherent hydrogen bond and form a cavity to include additional guest molecules. Miyata et al. reported the cluster structure of *tert*-butylammonium triphenylacetate, which has not only a pseudo-cubic hydrogen-bond network but also the ability to include organic guests such as benzene [16d]. On the other hand, we used *tert*-butylammonium salts of *N*-tritylamino acids (Tr-AA•tBuNH<sub>2</sub>) as chiral carboxylic acids and examined their inclusion properties with regard to racemic organic guests.

The amide approach and ammonium carboxylate approach are both based on the concept that bulky trityl groups will break inherent hydrogen-bond networks. Here, we will explain the details of chiral recognition by inclusion crystals of amino-acid derivatives having trityl groups.

### 23.2.1 *N,N'*-Ditrityl Amino Amides [21]

On the basis of the design in Fig. 23.4, we prepared crystalline host **1**, an alanine derivative from commercially available (*S*)-2-aminopropanamide, by *N*-tritylation of the amide group [22] and the amino group [23].

Crystallization of **1** from ethanol provided good quality of single crystals belonging to space group *P1*. In each asymmetric unit cell of the crystals were two

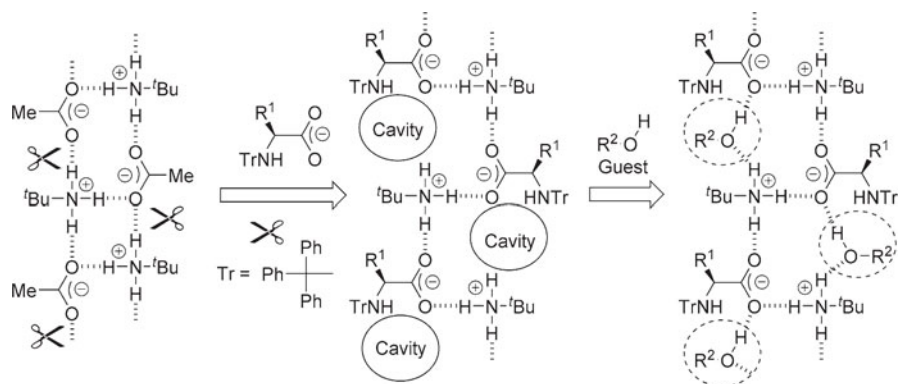


**Fig. 23.5** Host (Tr-AA•tBuNH<sub>2</sub>) designed to capture alcohol guests to compensate the loss of hydrogen bonds broken by trityl groups

molecules of **1** (Fig. 23.6). As expected, two bulky trityl groups broke the inherent one-dimensional hydrogen-bond network of the central amide groups. Between the carbonyl oxygen of one host **1** and an amino-group hydrogen of another host **1**, however, there was a hydrogen bond whose N•••O (H•••O) distance and angle (N-H•••O) were 3.344(4) Å (2.54 Å) and 165.0°. This hydrogen bond was thought to be very weak because it was longer than any of the other hydrogen bonds in the inclusion crystals (*vide infra*). We therefore thought that we could make inclusion crystals by forming stronger hydrogen bonds between host **1** and amide guests.

We examined whether *N,N'*-ditrityl (*S*)-2-aminopropanamide crystals did or did not include several amides. To obtain preliminary results, we tried with a micromole-scale crystallization of **1** (5.2 μmol) with a guest (1.2 equiv. for achiral guests or 2.5 equiv. for chiral guests) from ethanol solution (1 mL). Inclusion crystals of **1** with several amides (**2–7** in Fig. 23.7) were obtained. When racemic amides were used as the guest, highly enantioselective inclusion occurred.

Although esters such as phenyl acetate and methyl benzoate did not yield inclusion crystals, *N*-methyl benzamide (**2**) and *N*-phenyl acetamide (**3**) gave inclusion crystals in space group *P*<sub>2</sub><sub>1</sub><sub>2</sub><sub>1</sub>. Figure 23.8 shows that the crystal structures of **1•2** (CCDC 900257) and **1•3** (CCDC 900258) were quite similar to each other [24].

Both **2** and **3** settled into the host cavities, which were formed mainly by several of the phenyl groups of two trityl groups. Amide protons of guests **2** and **3** hydrogen bonded to the carbonyl oxygen atoms of host **1**, and these N•••O (H•••O) distances and angles (N-H•••O)—2.782 Å (1.99 Å) and 150° for **1•2** and 2.819 Å (1.96 Å) and 164° for **1•3**—were within the typical range of hydrogen-bond distances (mean N•••O 2.85 Å) [25]. The carbonyl oxygen atoms of these guests, however, were in contact not with the amide-group hydrogen of the host but with the amino-group hydrogen of the host. These N•••O (H•••O) distances and angles were 3.112 Å (2.25 Å) and 164° for **1•2** and 2.980 Å (2.14 Å) and 160° for **1•3**, and both of these

**Fig. 23.6** Crystal structure of **1** (a) arrangement of **1** in the crystal, (b) the schematic view of the loss of hydrogen bonds broken by two trityl groups

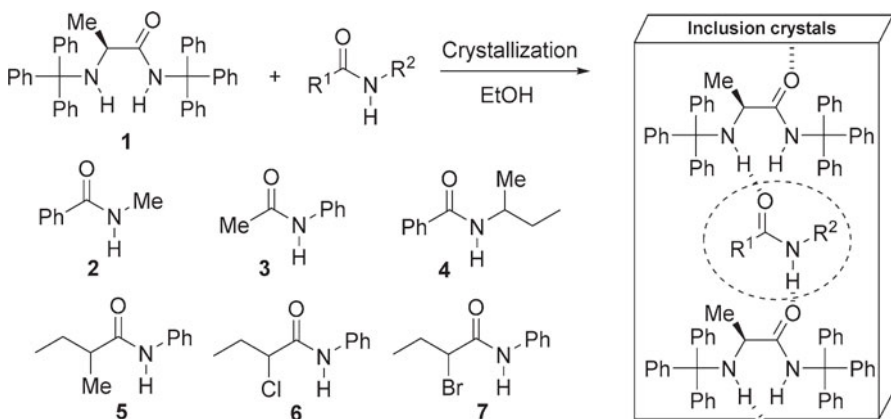
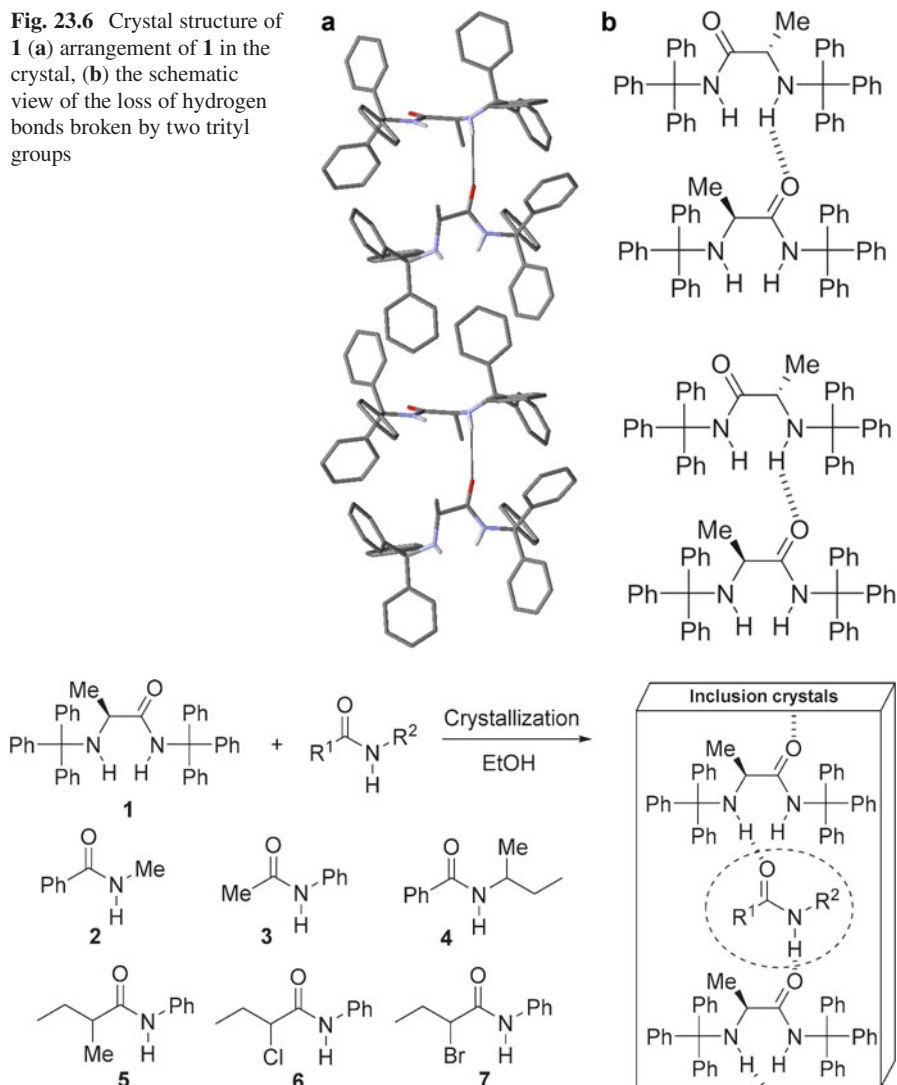


**Fig. 23.7** Crystallization of **1** with amides **2**–**7** to prepare inclusion crystals

distances are less than the sum of the van der Waals radii of hydrogen and oxygen atoms [ $2.72 \text{ \AA} = 1.20 \text{ \AA} (\text{H}) + 1.52 \text{ \AA} (\text{O})$ ] [26]. Thus, the guests compensated the loss of hydrogen bonds broken by the installation of trityl groups, and the result was that the one-dimensional hydrogen-bond network was reconstructed.

Since the host **1** is a chiral compound, we examined its ability to discriminate between the enantiomers in racemic mixtures of amides **4**–**7**. We used the 2-butyl group for this because the small asymmetric group is ubiquitous. Both *N*-2-butyl

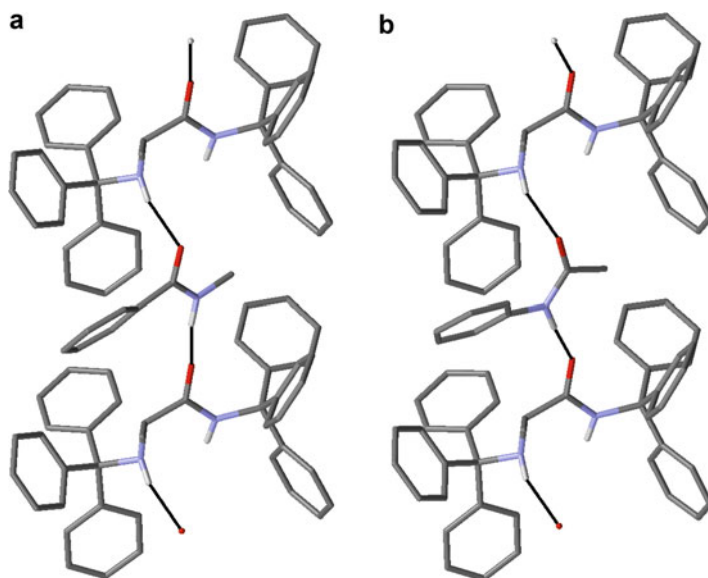
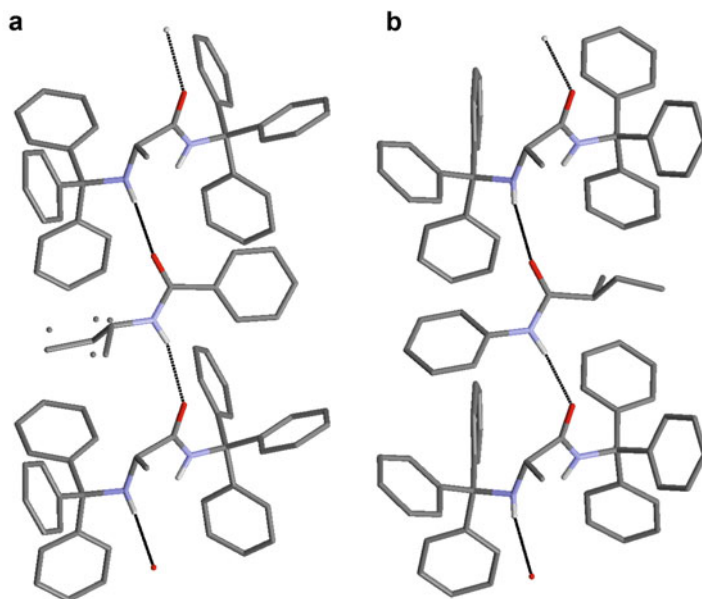


Fig. 23.8 Crystal structures of (a) **1•2** (CCDC 900257) and (b) **1•3** (CCDC 900258)

benzamide (**4**) and *N*-phenyl 2-methylbutanamide (**5**) yielded inclusion crystals (Fig. 23.9), and in those crystals the position of the 2-butyl group and phenyl group in the cavity of **1•4** (CCDC 900259) was opposite that of these groups in the cavity of **1•5** (CCDC 900260). More importantly, single-crystal X-ray analysis of **1•4** revealed that the inclusion crystal was a disordered structure in which the 2-butyl group was included at the ratio of 57(*R*):43(*S*) [total 14 % ee (*R*)], which meant the cavity included both enantiomers of **4** in the crystal. In fact, enantiomeric excess of recovered *N*-2-butyl benzamide from the bulk sample of inclusion crystals was confirmed as 10 % ee (*R*) by a chiral HPLC analysis. Single-crystal X-ray analysis of **1•5**, in contrast, revealed that only the *S*-form of **5** was settled in the cavity of **1**. This shows that the inclusion of **5** in the cavity of **1** occurred with high enantioselectivity.

Why does the cavity in **1•4** accommodate this disorder, while the cavity in **1•5** does not? We found the two crystals have different space groups ( $P2_12_12_1$  for **1•4** and  $C2$  for **1•5**), which means that their crystal-packing motifs are quite different. As seen in Fig. 23.10, the specific recognition site for the 2-butyl group is formed by one of the phenyl groups of the neighbor trityl moiety in a one-dimensional hydrogen-bonded column adjacent host-guest column. The differently oriented phenyl groups in **1•4** did not control the preferable enantiomer of **4** in the cavity, but the phenyl groups in **1•5** encountered the 2-butyl group of **5** at a tilt angle suitable to discriminate the *S*-form.

The crystal structure of **1•5** prompted us to examine the enantiomeric separation of not only **5** but also **6** and **7** because amides **5–7** are same-shaped molecules



**Fig. 23.9** Crystal structures: (a) **1•4** (CCDC 900259), (*R*)-**4** with four carbon atoms of (*S*)-2-butyl groups shown with four dots, (b) **1•5** (CCDC 900260)

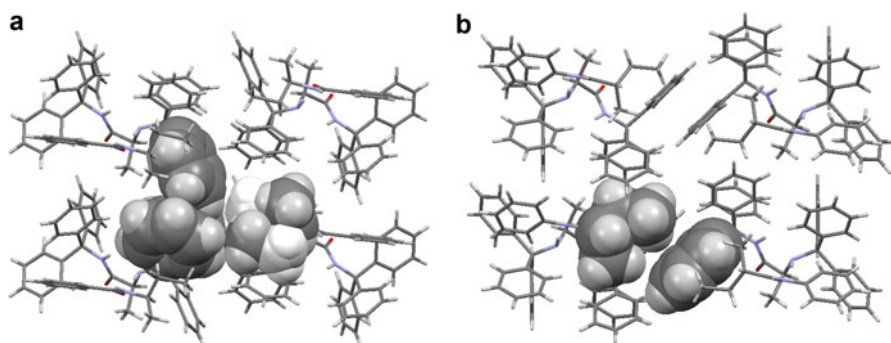


**Fig. 23.10** Crystal structures of adjacent phenyl groups in contact with 2-butyl groups: (a) disordered structure of (*R*)- and (*S*)-2-butyl groups in **1•4**, (b) **1•5**

whose substituent volumes of Cl, CH<sub>3</sub>, and Br are 11.62, 13.67, and 14.40 cm<sup>3</sup>/mol, respectively [26]. The enantiomeric separation of amides **5–7** was performed by crystallization from an ethanol solution of **1** (0.1 mmol, 57 mg) and the amide (2.2 equiv.). The scale of this crystallization was about 20-fold larger than that of preliminary crystallization. The enantiomeric excesses of recovered amides from bulk samples (not a crystal) were 67 % ee for **5**, 82 % ee for **6**, and 83 % ee for **7**, whose predominate enantiomers were *S*-form. At this stage, we could not explain the reason for the inconsistency of the ee between the bulk sample and a single

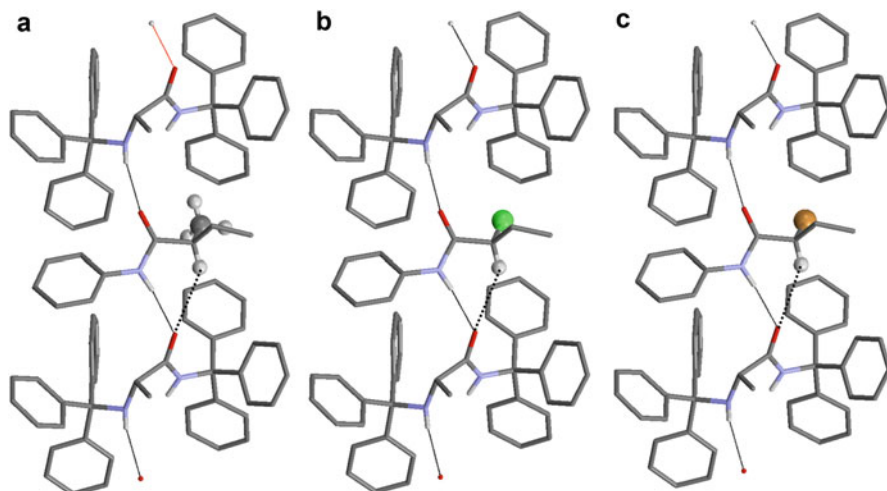
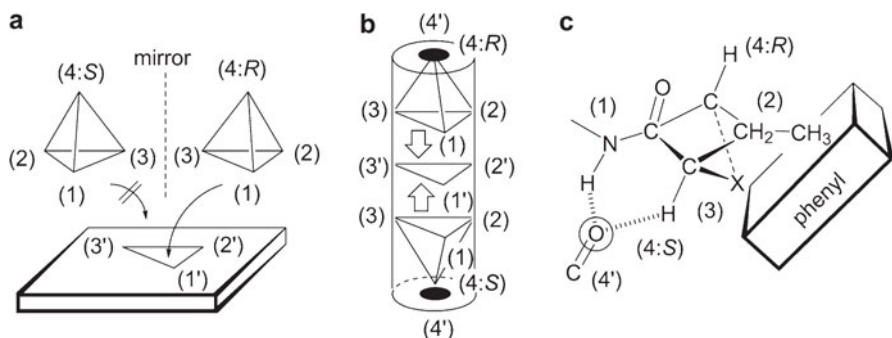


Fig. 23.11 Crystal structures: (a) **1**•**5**, (b) **1**•**6** (CCDC 900261), (c) **1**•**7** (CCDC 900262)

crystal. Figure 23.11 shows that the crystal structures of **1**•**6** (CCDC 900261) and **1**•**7** (CCDC 900262) were isostructural with **1**•**5**. As seen in **1**•**2** and **1**•**3** crystals, the major host-guest interactions were two kinds of hydrogen bonds between **1** and the guests. One is a hydrogen bond between an amide hydrogen of the guest and a carbonyl group of **1**, and for this bond the N•••O (H•••O) distances and angles (N-H•••O) are 2.939 Å (2.07 Å) and 169° for **1**•**5**, 2.904 Å (2.03 Å) and 173° for **1**•**6**, and 2.893 Å (2.02 Å) and 173° for **1**•**7**. The other is a hydrogen bond between an amino group of **1** and a carbonyl group of the guest, and for this bond the N•••O (H•••O) distances and angles (N-H•••O) are 3.074 Å (2.27 Å) and 167° for **1**•**5**, 3.072 Å (2.22 Å) and 171° for **1**•**6**, and 3.101 Å (2.33 Å) and 162° for **1**•**7**. As also seen in Figs. 23.8 and 23.9, these two kinds of hydrogen bonds restore the original one-dimensional hydrogen-bond network by compensating the loss of inherent hydrogen bonds that were broken by the installation of trityl groups.

To find out why *S*-amides (**5**, **6**, and **7**) were included preferentially over their *R*-forms, we inspected additional host-guest interactions in the cavity (Fig. 23.11). We found that the  $\alpha$ -hydrogen atoms of **6** and **7** were close to the carbonyl oxygen of **1**. The H•••O distances (2.84 Å for **1**•**5**, 2.75 Å for **1**•**6**, and 2.71 Å for **1**•**7**) suggested C-H•••O interactions [27]. Obviously, the H•••O distances of **1**•**7** and **1**•**6** are shorter than that of **1**•**5**, which is larger than the sum of the van der Waals radii [2.72 Å = 1.20 Å (H) + 1.52 Å (O)] [26]. Since Cl and Br have large electronegativity, the more acidic  $\alpha$ -hydrogen atoms of **6** and **7** are preferable hydrogen donors in a weak but important C-H•••O interaction. This preferable electrostatic interaction would be the reason the *S*-form of amides **6** and **7** settled in the cavity of **1** preferentially compared with the *R*-form.

Mesecar and Koshland pointed out the importance of the four-location model in enzyme-substrate recognition [28], and Miyata et al. used that model to explain the



**Fig. 23.12** (a) Three-location model for surface recognition. (b) Four-location model for a three-dimensional cavity. (c) Four-location model for the recognition site of **1•5–1•7**

chiral discrimination of inclusion crystals [29]. On the surface, the stereochemistry of guests can be determined by three-location recognition (Fig. 23.12a), but in the cavity a fourth interaction is required. As seen in Fig. 23.12c, the four-location model can also explain the high enantioselectivity seen with amides **6** and **7**. Although the positions of three groups of atoms in 2-halobutanamides—(1) carbonyl groups, (2) ethyl groups, and (3) the methyl group or halogen on the asymmetric carbon—are controlled by the hydrogen bonds and phenyl groups shown in Fig. 23.10b, this control is not enough to provide high enantioselectivity. For high performance of enantiomeric recognition in the cavity, an additional C–H•••O interaction [labeled 4 in Fig. 23.12c] is important. The acidic  $\alpha$ -hydrogen of 2-halobutanamides is small but acts as a preferable hydrogen-bond donor directed to a carbonyl oxygen of **1**. Thus, the highly enantioselective inclusion of **6** and **7** is explained by the four-location model.

### 23.2.2 *N*-Trityl Amino-Acid Salt [30]

Several organic salts have been reported to serve as inclusion host molecules for achiral alcohols [31], and highly enantiomeric inclusion of *racemic* alcohols has recently been achieved by two-component host systems with multiple chirality. In these designs, amino alcohols and diamines are used as chiral counterparts to construct an effective chiral recognition site [32]. Saigo et al. reported that salts between benzoic acid and 1,2-diphenylaminoethanol constructed a ladder-type hydrogen-bond network consisting of six non-hydrogen atoms (1L6), where (*S*)-alcohol was included enantioselectively through additional hydrogen bonds with hydroxy groups of 1,2-diphenylaminoethanol (Fig. 23.13).

Our host design in Fig. 23.14 is quite different in breaking the inherent hydrogen bonds, which constructs a ladder-type network. As shown in Fig. 23.5, trityl groups

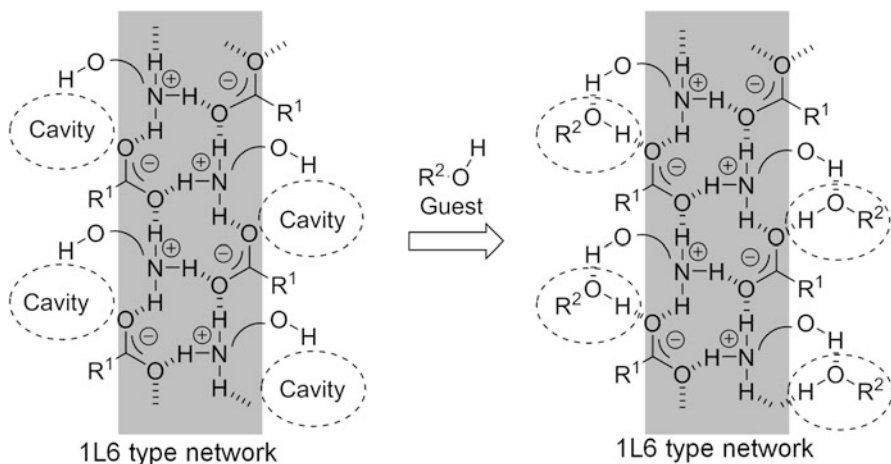


Fig. 23.13 Ammonium carboxylate to include alcohols with additional hydrogen bonds

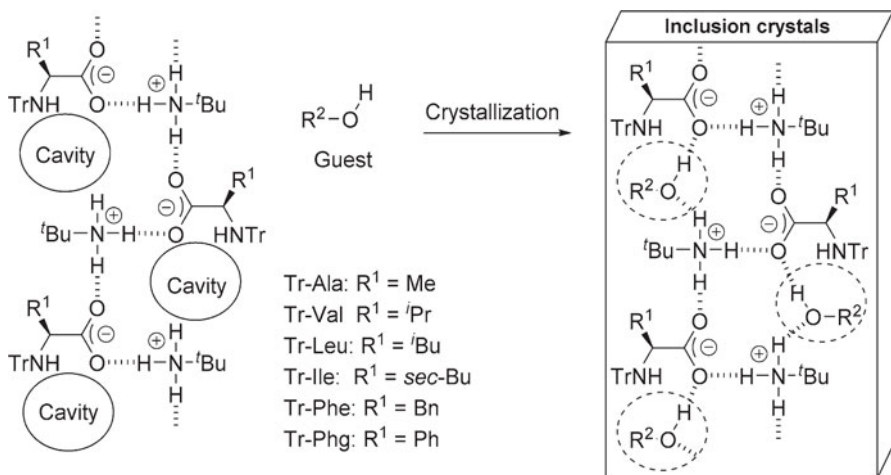
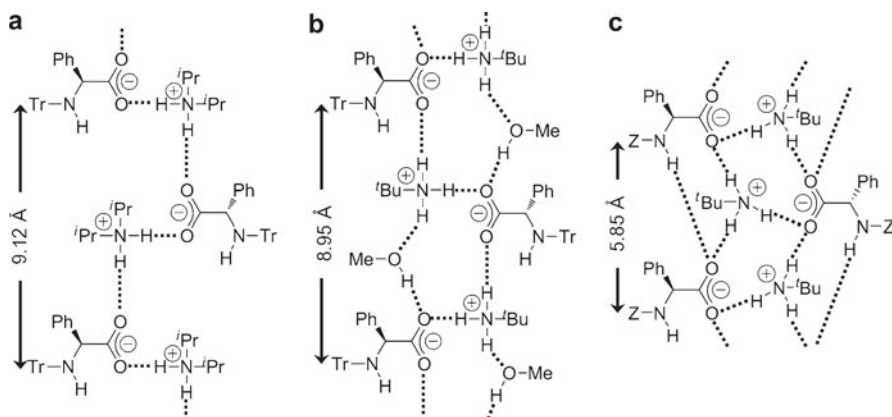


Fig. 23.14 Crystallization of Tr-AA•tBuNH<sub>2</sub> with alcohols to prepare inclusion crystals

on some amino-acid salts made a void to take guest alcohols. Simultaneously, the bulkiness of the trityl group disconnected original ladder hydrogen bonds to make additional space for binding a hydroxy group of a guest alcohol.

Six *N*-trityl (*S*)-amino acids (Tr-AAs)—Tr-Ala, Tr-Val, Tr-Leu, Tr-Ile, Tr-Phe, and Tr-Phg—were prepared in accordance with the literature [23], and these Tr-AAs formed 1:1 organic salts with alkylamines. These salts were evaluated as inclusion crystals as follows: A Tr-AA (0.1 mmol) was dissolved in alcohol (1 mL) and then amine (0.1 mmol) was added. Slow evaporation of the solvent over several days resulted in the deposition of single crystals. X-ray crystal structure analysis confirmed whether the salt included guest alcohols or not.



**Fig. 23.15** Typical hydrogen-bond networks of salts: (a) Tr-Phg•*i*Pr<sub>2</sub>NH (1D4) (CCDC-900798), (b) Tr-Phg•*t*BuNH<sub>2</sub>•MeOH (1L6S) (CCDC-900797), (c) Z-Phg•*t*BuNH<sub>2</sub> (1L6) (CCDC-900799)

In a preliminary experiment, we compared the inclusion abilities between two salts of Tr-Phg with primary amine (*tert*-butylamine) and secondary amine (*N,N*-diisopropylamine) by crystallization from a methanol solution. Although *tert*-butylammonium salts included methanol, *N,N*-diisopropylammonium salts did not. As shown in Fig. 23.15, both crystalline salts have similar columnar structures but different hydrogen-bond networks. Sada et al. recently reported the statistical classification of hydrogen-bond network of ammonium carboxylates using a survey based on the Cambridge Structural Database [33]. In the literature, two hydrogen atoms of a secondary amine combined the two oxygen atoms of carboxylate to form a one-dimensional hydrogen-bond network with four non-hydrogen atoms (1D4), which is the most common type (29 % of secondary ammonium carboxylate salts). In addition, *tert*-butylammonium salts captured a methanol guest, which was embedded in the original hydrogen-bond network. Just like 1D4 of *N,N*-diisopropylammonium salts, two hydrogen atoms of NH<sub>3</sub><sup>+</sup> bound to two oxygen atoms of the carboxylate. Therefore, the network is regarded as 1D4 with a solvent, namely, 1D4S (18 % of primary ammonium carboxylate salts). However, it was more important that one remaining hydrogen atom of NH<sub>3</sub><sup>+</sup> captured the oxygen atom of MeOH, and hydroxy hydrogen of MeOH was bound to the oxygen of carboxylate simultaneously. These hydrogen bonds are incorporated in a reconstructed ladder-type hydrogen-bond network (Fig. 23.15b). Since the hydroxy group of MeOH as a solvation molecule constitutes a one-dimensional ladder hydrogen-bond network with six non-hydrogen atoms and a solvent, it should be named 1L6S not 1D4S. This type of motif is very interesting, because primary ammonium carboxylates usually construct a one-dimensional ladder hydrogen-bond network consisting of six non-hydrogen atoms (1L6), which was pointed out by Sada et al. [32].

In addition, we examined the necessity of the trityl group by comparing it with the benzyloxycarbonyl group, the so-called Z group, which is also a common protecting group for amino acids [18]. Although a salt between Z-phenylglycine (Z-Phg) and  $t\text{BuNH}_2$  was crystallized from a methanol solution, the salt did not form inclusion crystals with methanol. As shown by dotted lines in Fig. 23.15c, a common ladder hydrogen-bond network (1L6 type) was also observed in this crystal structure. We also found that the *N*-bound hydrogen (N-H) of carbamates contributed to the hydrogen-bond network (dotted lines in Fig. 23.15c). In other words, the bulkiness of the trityl group isolated hydrogen atoms of N-H of Tr-AA from this hydrogen-bond network with the abovementioned solvent (1L6S).

Judging from these findings, our host design is rationalized: First, bulkiness of the trityl group expands repetition from 5.85 to 8.95 Å to break the 1L6 hydrogen-bond network and to generate inclusion cavity. Second, primary ammonium salts capture an alcohol guest by two hydrogen bonds to afford a new 1L6S hydrogen-bond network (Fig. 23.15b).

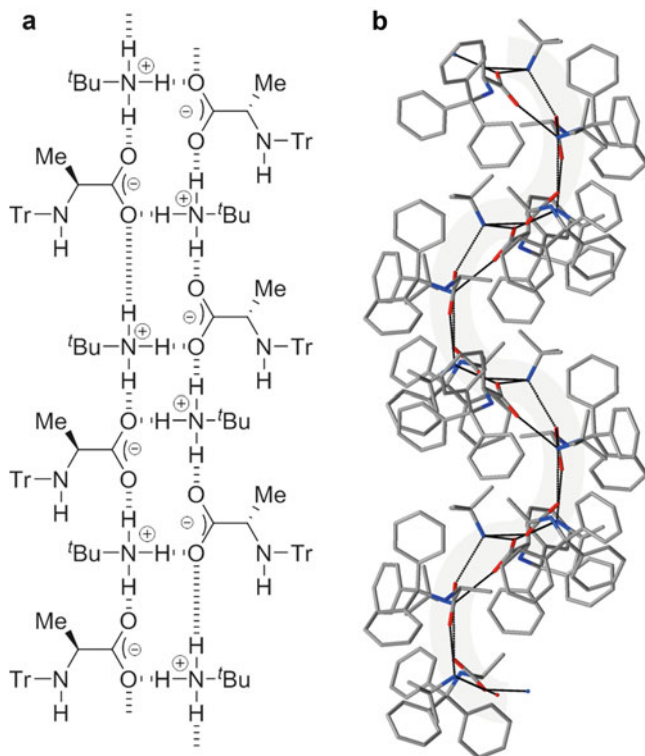
Other candidate *tert*-butylammonium *N*-trityl amino carboxylate (Tr-AA• $t\text{BuNH}_2$ ) salts were examined. Although a salt of Tr-Val did not give crystals to afford glassy residue, a salt of Tr-Ala gave crystals without methanol (Fig. 23.16, CCDC-900800). The crystal has a space group  $P2_12_12_1$  and  $Z = 12$ , which means three unique conformers were included in an asymmetric unit.

The hydrogen-bond network is the ladder motif. The methyl group as the side chain of Ala is too small to construct void space for guest alcohols. The methyl group was covered by the trityl group and buried in the curved columnar structure. It was also elucidated that not only trityl groups but also the side chains of Tr-AA play an important role in constructing an inclusion cavity for alcohols.

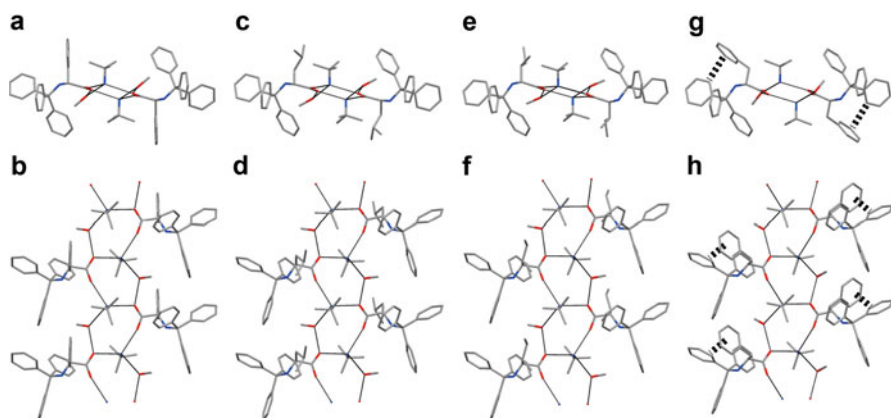
Salts of Tr-Leu, Tr-Ile, and Tr-Phe formed 1:1 inclusion crystals (CCDC-900801-900803) and their structures with the Tr-Phg salt are shown in Fig. 23.17. All three salts also included methanol, and the hydrogen-bond networks (1L6S) are very close to that of Tr-Phg depicted in Fig. 23.15. These results suggested the combination of a trityl group and the suitable side chain constructed a common host framework to capture alcohols in salts of Tr-AA. It is noteworthy that an edge-to-face interaction between the benzyl group of Phe and the phenyl group of the trityl group was observed. The phenyl-phenyl interaction (dotted line in Fig. 23.17g and h) tilted the benzyl group of Phe toward the edge of the trityl group to create a void space larger than those of other three Tr-AA amino acids.

When the bigger secondary alcohol 2-propanol was examined as a guest alcohol, only the Tr-Phe salt formed 1:1 inclusion crystals (see Table 23.1). Other Tr-AAs did not crystallize and remained amorphous residues. The crystals of the Tr-Phe salt with 2-propanol have a space group  $P2_1$  (CCDC-900804), and the columnar structure has a hydrogen-bond network (Fig. 23.18).

At a glance, the ladder hydrogen-bond network is similar to the 1L6S type seen in Fig. 23.15, but three components (Tr-Phe,  $t\text{BuNH}_2$ , and methanol) differed in position: the *t*-butylammonium cation and the guest alcohol replaced each other. The conformation of Tr-Phe resembles that of the methanol-inclusion compound, where the tilt of phenyl group of Phe toward the Tr group by phenyl-phenyl interaction also occurred.



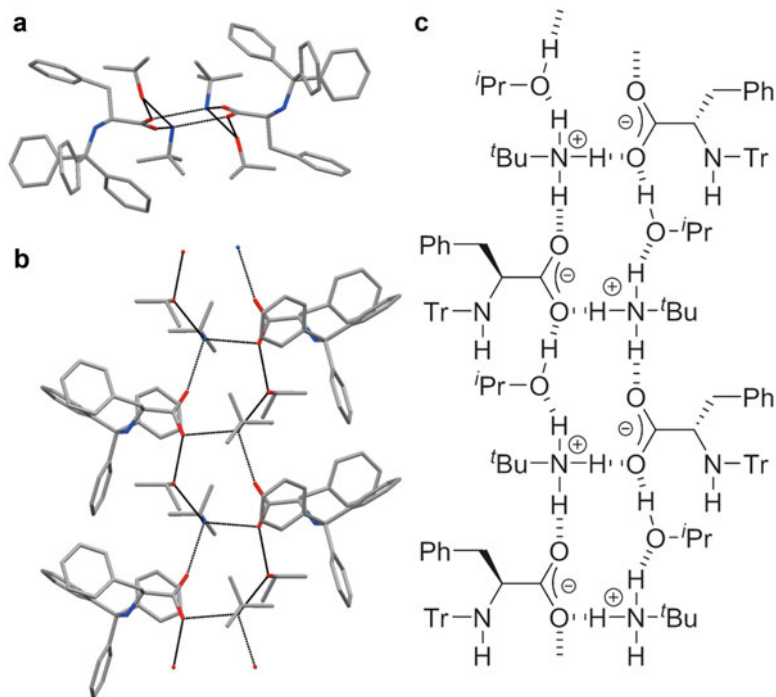
**Fig. 23.16** Crystal structure of Tr-Ala·tBuNH<sub>2</sub> (CCDC-900800): (a) ladder-type network, (b) curved column structure



**Fig. 23.17** Top and side views of crystal structures of Tr-AA·tBuNH<sub>2</sub> with methanol guest: (a and b) Tr-Phg (CCDC-900797), (c and d) Tr-Leu (CCDC-900801), (e and f) Tr-Ile (CCDC-900802), (g and h) Tr-Phe (CCDC-900803)

**Table 23.1** Included alcohols in salts of *tert*-butylammonium *N*-tritylphenylalanate

Entry	Alcohol guest	ee (%)	Predominant configuration
1	Methanol	–	–
2	2-Propanol	–	–
3	2-Butanol	7	<i>R</i>
4	2-Pentanol	27	<i>R</i>
5	1-Chloro-2-propanol	69	<i>S</i>

**Fig. 23.18** (a and b) *Top* and *side* views of crystal structures of Tr-Phe•tBuNH<sub>2</sub> with 2-propanol. (c) 1L6S hydrogen-bond network

As mentioned above, we found that Tr-Phe•tBuNH<sub>2</sub> salt is a good candidate for an inclusion host for alcohols. To evaluate its enantiomeric ability to recognize secondary alcohols, we chose 2-butanol, 2-pentanol, and 1-chloro-2-propanol as *racemic* alcohols. To our delight, the crystallization of Tr-Phe•tBuNH<sub>2</sub> with the alcohol gave 1:1 inclusion crystals. We confirmed the cavity of Tr-Phe•tBuNH<sub>2</sub> has enough void space for 2-butanol, 2-pentanol, and 1-chloro-2-propanol. After inclusion crystals were dissolved in chloroform, the included alcohol was transformed into the carbamates by reaction with phenylisocyanate. Enantiomeric excesses of alcohols were estimated by chiral HPLC (Daicel chiral cell OD) analysis of the isolated carbamates. The results are summarized in Table 23.1.

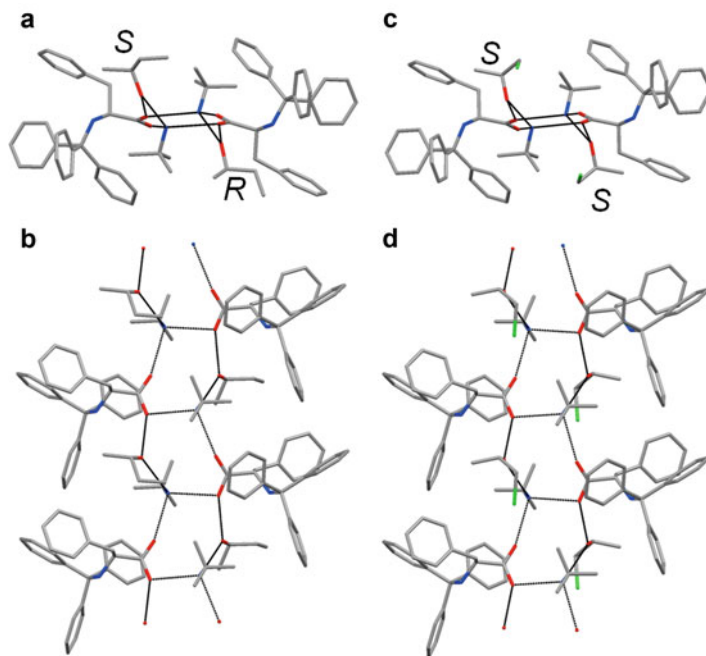


**Fig. 23.19** Top and side views of crystal structures of Tr-Phe•tBuNH<sub>2</sub> with alcohol guests, (a and b), with 2-butanol (CCDC-900805), and (c and d) with (*S*)-1-chloro-2-propanol (CCDC-900806)

The ee values for 2-butanol and 2-pentanol were only 7 and 27 %, but that for 1-chloro-2-propanol was 69 % ee (*S*-rich). We succeeded in single-crystal analyses of inclusion compounds with *racemic* 2-butanol and (*S*)-1-chloro-2-propanol (Fig. 23.19, CCDC-900805-900806). Both crystal structures are similar to that of 2-propanol-including column structure of Tr-Phe•tBuNH<sub>2</sub> (see Fig. 23.18). The crystals with (*S*)-1-chloro-2-propanol also have a space group of  $P2_1$  ( $Z = 2$ ), which corresponds to the hydrogen-bond network of 2-propanol (1L6S). *Racemic* 2-butanol-including crystals, however, has a space group  $P1$  and  $Z = 2$ , which means a diastereomeric pair of two host molecules and both enantiomeric 2-butanol molecules occupied a unit cell to construct a pseudo  $2_1$  helical column structure. Since one side of the pseudo  $2_1$  column consisted of the *R*-form of 2-butanol and the other side occupied the *S*-form of the guest (see also Fig. 23.20b, c), the enantiomeric excess is completely negligible. There is an element of inconsistency in the ee values of 1-chloro-2-propanol between the bulk sample and the single crystals. Judging from their powder XRD patterns, the bulk sample was contaminated by unidentified crystals including the opposite enantiomer.

To highlight the difference in ee between 2-butanol (7 % ee, *R*-rich) and 1-chloro-2-propanol (69 % ee, *S*-rich), we have to rationalize what kinds of interactions work for chiral discrimination in both their recognition sites. Figure 23.20a shows

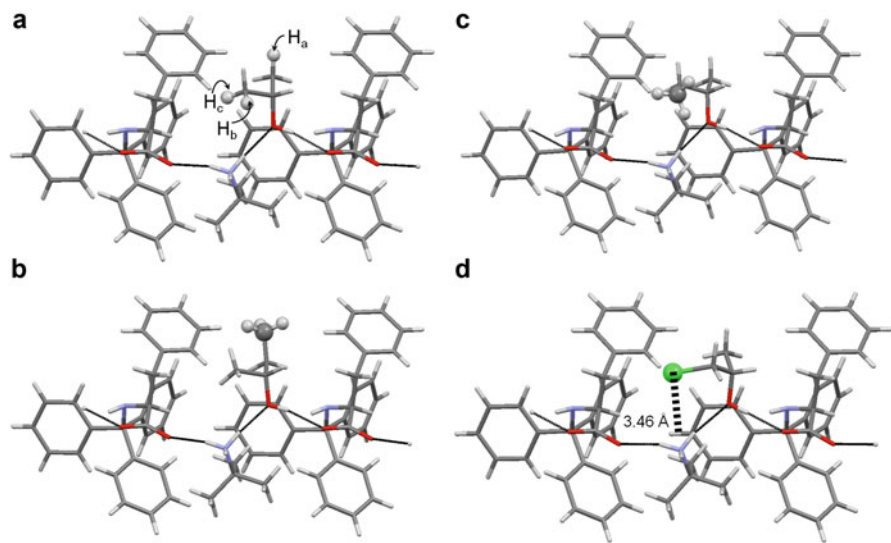


**Fig. 23.20** Side views of crystal structures of Tr-Phe•tBuNH<sub>2</sub> with alcohols: (a) with 2-propanol, (b) with (*R*)-2-butanol, (c) with (*S*)-2-butanol, (d) with (*S*)-1-chloro-2-propanol

an alternative drawing of included 2-propanol in the cavity of Tr-Phe•tBuNH<sub>2</sub> in Fig. 23.18. If H<sub>a</sub> of 2-propanol were a methyl group, the structure would become (*R*)-2-butanol, but the structure was actually found in the analyzed crystal structure (Fig. 23.20b). Similarly, the conformation of (*S*)-2-butanol observed in the crystal just like H<sub>b</sub> was replaced with a methyl group (Fig. 23.20c). On the other hand, 1-chloro-2-propanol was included with high enantioselectivity and only the (*S*)-form settled in the cavity as if H<sub>c</sub> of 2-propanol was substituted for the chlorine atom (Fig. 23.20d). As seen from Fig. 23.20, conformations of 2-butanol or 1-chloro-2-propanol in the cavity correspond to replacement of three hydrogen atoms (H<sub>a</sub>–H<sub>c</sub>) with a CH<sub>3</sub> or Cl group. Thus, settlements of 2-butanol and (*S*)-1-chloro-2-propanol in the similar cavity of Tr-Phe•tBuNH<sub>2</sub> occurred in three ways, which were regarded as analogous to the shape of 2-propanol in the cavity. Since the substituent volumes of CH<sub>3</sub> and Cl are 13.67 and 11.62 cm<sup>3</sup>/mol [26], both 2-butanol and (*S*)-1-chloro-2-propanol have almost the same volume. However, their degrees of enantioselectivities are quite different. As seen from the side view of the cavity in Fig. 23.20d, the chlorine atom is close to the ammonium cation (N•••Cl: 3.46 Å). The distance between chlorine atom and the closest hydrogen (N–H) is 2.93 Å, which is almost the same as the sum of van der Waals radii [2.95 Å = 1.20 Å (H) + 1.75 Å (Cl)] [26]. This preferable electrostatic interaction is the reason the chlorine atom was located at the position of H<sub>c</sub> of 2-propanol and the moderate enantioselectivity 69 % ee was achieved.

## 23.3 Summary

We demonstrated two kinds of inclusion crystal designs using amino-acid derivatives for chiral recognition of racemic molecules. Both are based on the use of bulky trityl groups, but they have quite different chemical functionalities.

First we demonstrated enantiomeric separation using a chiral *N,N'*-ditrityl amino amide host. We elucidated the structure of inclusion crystals and host-guest interactions based on four-location model, where a weak C-H...O interaction is important for high enantioselectivity of *N*-phenyl 2-halobutanamides.

We then showed that *tert*-butylammonium *N*-tritylphenylalanate (Tr-Phe•tBuNH<sub>2</sub>) was the best host system for including several alcohol guests. The bulkiness of the trityl group and the hydrogen-bond donor of primary ammonium cations were found to be essential for making the new host-guest ladder hydrogen-bond network. We could demonstrate that the trityl group was not only a protecting group for organic synthesis but also a crystal engineering tool for tuning simple salts of amino acids into new host materials. As an application for chiral recognition, enantioselective inclusion for *racemic* 1-chloro-2-propanol occurred to give *S*-enriched sample of 69 % ee. Unlike other multi-chiral systems, the present host is simple and has only one asymmetric amino-acid carbon atom.

We developed new amino-acid-based chiral hosts with trityl groups. These combinations of chiral source and trityl group could be a general design used to construct host molecules for other kinds of chiral recognition.

## References

1. R. Siedlecka, *Tetrahedron*. **69**, 6331–6363 (2013). (b) F. Faigel, E. Fogassy, M. Nógrádi, E. Pálóvics, J. Schindler, *Tetrahedron: Asymmetry*. **19**, 519–536 (2008). (c) E. Fogassy, M. Nógrádi, D. Kozma, G. Egri, E. Pálóvics, V. Kiss, *Org. Biomol. Chem.* **4**, 3011–3030 (2006)
2. E. Weber (ed.), *Molecular Inclusion and Molecular Recognition-Clathrates I and II*, vols. 140 and 149. (Springer, Berlin, 1987/1988)
3. F. Toda, R. Bishop (eds.), *Separations and Reactions in Organic Supramolecular Chemistry: Perspectives in Supramolecular Chemistry*, vol. 8 (Wiley, Chichester, 2004)
4. *Enantiomer Separation: Fundamentals and Practical Methods* (Kluwer Academic Publishers, Dordrecht Boston London, 2004), pp. 73–102
5. (a) M. Akazome, K. Senda, K. Ogura, *J. Org. Chem.* **67**, 8885–8889 (2002). (b) M. Akazome, T. Takahashi, R. Sonobe, K. Ogura, *Tetrahedron*. **58**, 8857–8861 (2002). (c) M. Akazome, T. Takahashi, R. Sonobe, K. Ogura, *Supramol. Chem.* **13**, 109–136 (2001). (d) M. Akazome, Y. Yanagita, R. Sonobe, K. Ogura, *Bull. Chem. Soc. Jp.* **70**, 2823–2827 (1997). (e) M. Akazome, A. Sumikawa, R. Sonobe, K. Ogura, *Chem. Lett.*, 995–996 (1996).
6. (a) M. Akazome, S. Toma, T. Horiguchi, K. Megumi, S. Matsumoto, *Tetrahedron*. **67**, 2844–2848 (2011). (b) M. Akazome, A. Doba, S. Matsumoto, K. Ogura, *J. Org. Chem.* **75**, 660–665 (2010). (c) M. Akazome, A. Hirabayashi, K. Senda, K. Ogura, *Tetrahedron*. **63**, 9933–9938 (2007). (d) M. Akazome, A. Hirabayashi, K. Takaoka, S. Nomura, K. Ogura, *Tetrahedron*. **61**, 1107–1113 (2005) (e) M. Akazome, A. Hirabayashi, K. Ogura, *Tetrahedron*. **60**, 12085–12093 (2004). (f) M. Akazome, Y. Ueno, H. Ooiso, K. Ogura, *J. Org. Chem.* **65**, 68–76 (2000). (g) M. Akazome, T. Takahashi, K. Ogura, *J. Org. Chem.* **64**, 2293–2300 (1999). (h) M. Akazome, M. Noguchi, O. Tanaka, A. Sumikawa, T. Uchida, K. Ogura, *Tetrahedron*. **53**, 8315–8322 (1997).

7. C.H. Görbitz, *Chem. Eur. J.* **13**, 1022–1031 (2007) and cited therein. (b) C.H. Görbitz, *Acta Crystallogr. Sect. C* **55**, 2171–2177 (1999). (c) C.H. Görbitz, *Acta Crystallogr. Sect. C* **55**, 670–672 (1999). (d) C.H. Görbitz, E. Torgersen, *Acta Crystallogr. Sect. B* **55**, 104–113 (1999). (e) C.H. Görbitz, *Acta Chem. Scand.* **52**, 1343–1349 (1998)
8. S. Muller, G.J.A. Ariaans, B. Kaptein, Q.B. Broxterman, F. Formaggio, E. Battan, M. Crisma, C. Toniolo, A. Bruggink, *Tetrahedron Asymmetry* **15**, 1919–1927 (2004)
9. (a) S. Müller, M.C. Afraz, R. de Gelder, G.J.A. Ariaans, B. Kaptein, Q.B. Broxterman, A. Bruggink, *Eur. J. Org. Chem.* 1082–1096 (2005). (b) E. Weber, C. Reutel, C. Foces-Foces, A.L. Llamas-Saiz, *J. Incl. Phenom. Macrocyc. Chem.* **33**, 47–68 (1999). (c) E. Weber, C. Reutel, C. Foces-Foces, A.L. Llamas-Saiz, *J. Phys. Org. Chem.* **8**, 159–170 (1995). (d) E. Weber, C. Reutel, C. Foces-Foces, A.L. Llamas-Saiz, *J. Chem. Soc. Perkin Trans. 2*, 1455–170 (1994).
10. P. Dastidar, I. Goldberg, Hydrocarbon hosts: Biaryl, polyaryls, allenes, spiranes, and cyclophanes. Solid-state supramolecular chemistry: Crystal engineering, in *Comprehensive Supramolecular Chemistry*, vol. 6, ed. by D.D. MacNicol, F. Toda, R. Bishop (Pergamon Press, Oxford, 1996), pp. 305–317 and references therein
11. F. Toda, K. Akagi, *Tetrahedron Lett.* **33**, 3695–3698 (1968)
12. H. Hart, L.-T.W. Lin, D.L.J. Ward, *Am. Chem. Soc.* **106**, 4043–4045 (1984)
13. (a) K.-K.D. Ng, H. Hart, *Tetrahedron.* **51**, 7883–7906 (1995). (b) Z. Stein, I. Golberg, *Acta Cryst.* **C48**, 1506–509 (1992). (c) Z. Stein, I. Golberg, *Acta Cryst.* **C48**, 1135–1136 (1992). (d) H. Hart, L.-T.W. Lin, D.L. Ward, *J. Chem. Soc. Chem. Commun.* 293–294 (1985). (e) I. Goldberg, L.-T.W. Lin, H. Hart, *J. Incl. Phenom.* **2**, 377–389 (1984)
14. (a) C.M. Reddy, L.S. Reddy, S. Aitipamula, A. Nangia, C.-K. Lam, T.C.W. Mak, *CrystEngComm.* **7**, 44–52 (2005). (b) C.M. Reddy, A. Nangia, C.-K. Lam, T.C.W. Mak, *CrystEngComm.* **4**, 323–325 (2002). (c) R.K.R. Jetti, F. Xue, T.C.W. Mak, A. Nangia, *J. Chem. Soc. Perkin Trans. 2*, 1223–1232 (2000)
15. (a) S.D. Karlen, S. Khan, M.A. Garcia-Garibay, *Cryst. Growth Des.* **1**, 53–55 (2005). (b) Z. Dominguez, T.-A.V. Khuong, H. Dang, C.N. Sanrame, J.E. Nuñez, M.A. Garcia-Garibay, *J. Am. Chem. Soc.* **125**, 8827–8837 (2003). (c) Z. Dominguez, H. Dang, M.J. Strouse, M.A. Garcia-Garibay, *J. Am. Chem. Soc.* **124**, 7719–7727 (2002). (d) Z. Dominguez, H. Dang, M.J. Strouse, M.A. Garcia-Garibay, *J. Am. Chem. Soc.* **124**, 2398–2399 (2002)
16. (a) T. Yuge, I. Hisaki, M. Miyata, N. Tohnai, *CrystEngComm.* **10**, 263–266 (2008). (b) T. Yuge, N. Tohnai, T. Fukuda, I. Hisaki, M. Miyata, *Chem. Eur. J.* **13**, 4163–4168 (2007). (c) N. Tohnai, Y. Mizobe, M. Doi, S.-I. Sukata, T. Hinoue, T. Yuge, I. Hisaki, Y. Matsukawa, M. Miyata, *Angew. Chem. Int. Ed.* **46**, 2220–2223 (2007). (d) A.D. Bond, W.H. Jørgensen, J.M. Pløger, *Chem. Commun.* 3273–3275 (2007). (e) K. Sada, T. Watanabe, J. Miyamoto, T. Fukuda, N. Tohnai, M. Miyata, T. Kitayama, K. Maehara, K. Ute, *Chem. Lett.* **33**, 160–161 (2004)
17. (a) Y.-Y. Zhu, H.-P. Yi, C. Li, X.-K. Jiang, Z.-T. Li, *Cryst. Growth Des.* **8**, 1294–1300 (2008). (b) P.S. Corbin, L.J. Lawless, Z. Li, Y. Ma, M.J. Witmer, S.C. Zimmerman, *Proc. Natl. Acad. Sci. U. S. A.* **99**, 5099–5104 (2002). (c) P.M. Petersen, W. Wu, E.E. Fenlon, S. Kim, S.C. Zimmerman, *Bioorg. Med. Chem.* **4**, 1107–1112 (1996)
18. T.W. Greene, P.G.M. Wuts, *Protective Groups in Organic Synthesis* (Wiley-Interscience, New York, 1991), pp. 366–367
19. (a) F. Hamzaoui, F. Baert, *Acta Cryst.* **C50**, 757–759 (1994). (b) D. André, R. Fourma, M. Renaud, *Acta Cryst.* **B27**, 2371–2380 (1971). (c) J.L. Katz, B. Post, *Acta Cryst.* **13**, 624–628 (1960)
20. J. Martí-Rujas, A. Morte-Ródenas, F. Guo, N. Thomas, K. Fujii, B.M. Kariuki, K.D.M. Harris, *Cryst. Growth Des.* **10**, 3176–3181 (2010)
21. K. Megumi, S. Yokota, S. Matsumoto, M. Akazome, *Tetrahedron Lett.* **54**, 707–710 (2013)
22. P. Sieber, B. Riniker, *Tetrahedron Lett.* **32**, 739–742 (1991)
23. (a) B.G. De la Torre, M.A. Marcos, R. Eritja, F. Albericio, *Let. Pept. Sci.* **8**, 331–338 (2002). (b) K. Barlos, D. Papaioannou, D. Theodoropoulos, *J. Org. Chem.* **47**, 1324–1326 (1982)
24. Crystallographic data for the structures in this review have been deposited with the Cambridge Crystallographic Centre as number CCDC 900257–900262 and 900797–900806

25. R. Taylor, O. Kennard, *Acc. Chem. Res.* **17**, 320–326 (1984)
26. A. Bond, *J. Phys. Chem.* **68**, 441–451 (1964)
27. (a) G. Desiraju, *Acc. Chem. Res.* **29**, 441–449 (1996). (b) G. Desiraju, *Acc. Chem. Res.* **24**, 290–296 (1991). (c) R. Taylor, O. Kennard, *J. Am. Chem. Soc.* **104**, 5063–5070 (1982)
28. (a) A.D. Mesecar, D.E. Jr. Koshland, *Nature* **403**, 614–615 (2000). (b) A.D. Mesecar, D.E. Jr. Koshland, *IUBMB Life* **49**, 457–466 (2000)
29. (a) K. Kato, Y. Aoki, M. Sugahara, N. Tohnai, K. Sada, M. Miyata, *Chirality* **15**, 53–59 (2003). (b) K. Kato, K. Aburaya, Y. Miyake, K. Sada, N. Tohnai, M. Miyata, *Chem. Commun.* 2872–2873 (2003)
30. K. Megumi, F. Nadiyah Binti Mohd Arif, S. Matsumoto, M. Akazome, *Cryst. Growth Des.* **12**, 5680–5685 (2012)
31. (a) Y. Imai, K. Kawaguchi, H. Matsuno, T. Sato, R. Kuroda, Y. Matsubara, *Tetrahedron* **64**, 4585–4589 (2008). (b) Y. Imai, K. Kawaguchi, K. Asai, T. Sato, R. Kuroda, Y. Matsubara, *CrystEngComm* **9**, 467–470 (2007). (i) K. Sada, N. Shiomi, M. Miyata, *J. Am. Chem. Soc.* **120**, 10543–10544 (1998)
32. (a) K. Kodama, Y. Kobayashi, K. Saigo, *Cryst. Growth Des.* **7**, 935–939 (2007). (b) K. Kodama, Y. Kobayashi, K. Saigo, *Chem. Eur. J.* **13**, 2144–2152 (2007). (c) Y. Imai, K. Kawaguchi, T. Sato, R. Kuroda, Y. Matsubara, *Tetrahedron Lett.* **47**, 7885–7888 (2006). (d) Y. Imai, M. Takeshita, T. Sato, R. Kuroda, *Chem. Commun.* 1070–1072 (2006). (e) Y. Imai, T. Sato, R. Kuroda, *Chem. Commun.* 3289–3291 (2005). (f) Y. Kobayashi, K. Kodama, K. Saigo, *Org. Lett.* **6**, 2941–2944 (2004)
33. K. Sada, T. Tani, S. Shinkai, *Synlett* **15**, 2364–2374 (2006)

**Part VI**  
**Solid-State Reaction**

# Chapter 24

## Reactions and Orientational Control of Organic Nanocrystals

Shuji Okada and Hidetoshi Oikawa

**Abstract** Organic nanocrystals can be prepared by the reprecipitation method. The solid-state reactions within the nanocrystals and the reactions on the nanocrystal surfaces were investigated. In the nanocrystals, strain accumulated during the solid-state reactions can be released by the deformation of the shape, and single-crystal-to-single-crystal transformation was achieved. In the solid-state polymerization, the size of monomer nanocrystals was closely related to the molecular weight of the resulting polymers. Radical attacks on crystal surfaces were found to stimulate the solid-state chain polymerization. By using excitation of the compound in the nanocrystals, metal cations can be selectively reduced on the crystal surfaces. Orientation control of nanocrystals using electric and magnetic fields was investigated. Nanocrystals were successfully oriented according to the crystal structures, in which molecules specifically interacted with the external fields. Degree of polar orientation by a DC electric field could be improved by assistance of a DC magnetic field. Solidification of the dispersion media realized fixation of nanocrystal orientation to generate permanent macroscopic anisotropy.

**Keywords** Organic nanocrystal • Solid-state reaction • Surface reaction • Field orientation

### 24.1 Introduction

Many kinds of inorganic single crystals have been grown and used in the fields of electronics and photonics. In contrast, utilization of organic single crystals is quite limited. Crystals for optical use, for example, should have an optically

---

S. Okada (✉)

Graduate School of Science and Engineering, Yamagata University, 4-3-16 Jonan,  
Yonezawa 992-8510, Japan

e-mail: [okadas@yz.yamagata-u.ac.jp](mailto:okadas@yz.yamagata-u.ac.jp)

H. Oikawa

Institute of Multidisciplinary Research for Advanced Materials, Tohoku University,  
2-1-1 Katahira, Aoba, Sendai 980-8577, Japan

e-mail: [oikawah@tagen.tohoku.ac.jp](mailto:oikawah@tagen.tohoku.ac.jp)

uniform area larger than the diameter of the input beam, i.e., a millimeter size. However, there are no general methods to prepare organic bulk crystals because diversity of organic molecules easily changes their properties even in the same series of compounds. Also, crystallization condition tuning for each compound is indispensable. Meanwhile, organic low-molecular-weight compounds in the solid state generally form microcrystals, whose sizes are comparable to or larger than the wavelengths of visible light or optical communication laser beams. These sizes result in light scattering. However, if the size of crystals reduced to a nanometer range, the light scattering is greatly diminished, while the material maintains the crystalline features. Thus, nanocrystallization is a versatile methodology to use organic crystalline materials.

More than two decades ago, the reprecipitation method was developed as a facile and general fabrication technique of organic nanocrystals [1]. The nanocrystal preparation procedure is as follows: A solution of an objective organic compound is just injected into a solvent, which cannot dissolve the compound but is miscible with the solvent of the compound. This method is useful especially for thermally unstable organic compounds because no heating process for their evaporation is required. By using this method, a variety of organic compounds have been nanocrystallized and their unique properties depending on the crystal sizes have been found [2, 3].

In this article, we review our nanocrystal studies from two aspects. One is the reaction control. Since the optical properties of organic nanocrystals of  $\pi$ -conjugated compounds have been found to be different from those of the corresponding bulk crystals [4–6], molecular conditions in the nanocrystals should not coincide with those of bulk crystals. Namely, molecular vibrational conditions, strength of intermolecular interactions, amount of accumulated strain during the reaction, and so on may vary. Differences in several types of reactions in the crystalline states were investigated between bulk crystals and nanocrystals.

The other is orientation control. One of the important features of organic crystals is anisotropy of physical properties due to ordered molecular orientation in the crystals. On the contrary, nanocrystals prepared by the reprecipitation method are obtained as the liquid dispersion. In this state, the crystals are randomly oriented to be macroscopically isotropic, and the physical properties are averaged in three dimensions. In order to maximize the physical properties like the corresponding single crystals, nanocrystal orientation and its fixation are necessary. If these two points are achieved, the materials obtained will show similar properties to those of the single crystals. For this purpose, application of external fields to nanocrystal dispersion was investigated.

## 24.2 Reactions of Nanocrystals

In 1960s, two types of topochemical polymerization were discovered, i.e., polymerization of so-called diolefin [7] and diacetylene derivatives [8]. The former and latter reaction mechanisms are step-growth polymerization and chain polymerization,

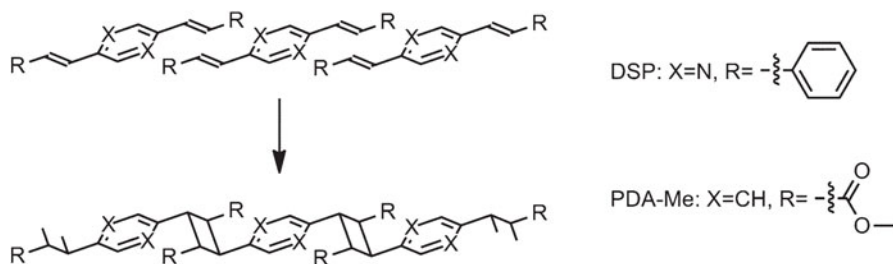


Fig. 24.1 Solid-state photopolymerization scheme and typical examples of diolefin derivatives

respectively, and both of them were examined in the nanocrystals. For the chain polymerization of diacetylene derivatives, its initiation using radical initiators like conventional radical polymerization reactions was confirmed, and the radical residues on the nanocrystal surfaces were applied to use for nanocrystal fixation on substrates. Solid-state valence isomerization reaction was also examined.

### 24.2.1 Polymerization of Diolefin Derivatives

1,4-Distyrylpyradine (DSP) and methyl *p*-phenylenediacrylate (PDA-Me) are typical examples of diolefin derivatives, which show intermolecular [2 + 2] photocycloaddition resulting in stepwise topochemical polymerization (Fig. 24.1). Their nanocrystal dispersions were prepared by injection of the THF solutions into water [9, 10]. When UV at 302 nm was irradiated to their bulk crystals with a size more than several hundreds of micrometers, fragmentation of the crystals occurred during photoirradiation. This is because changes in cell parameters of these compounds are relatively large and strain accumulated in the crystals during polymerization was mechanically released. On the other hand, their nanocrystals with a size of several hundreds of nanometers can maintain their single-crystalline features even after photoirradiation (Fig. 24.2). This indicates that the strain in nanocrystals can be released by deformation of the entire shape. Single-crystal-to-single-crystal transformation from a monomer to the corresponding polymer was found to be only achieved in a range less than submicrometer for these diolefin derivatives.

### 24.2.2 Polymerization of Diacetylene Derivatives

Chainpolymerization of some diacetylene derivatives in the crystals can be stimulated by UV or  $\gamma$ -ray irradiation or thermal annealing when the monomers are stacked in one direction with a proper alignment (Fig. 24.3). In this state, the translation distance  $d$  between adjacent monomers is approximately 0.5 nm and

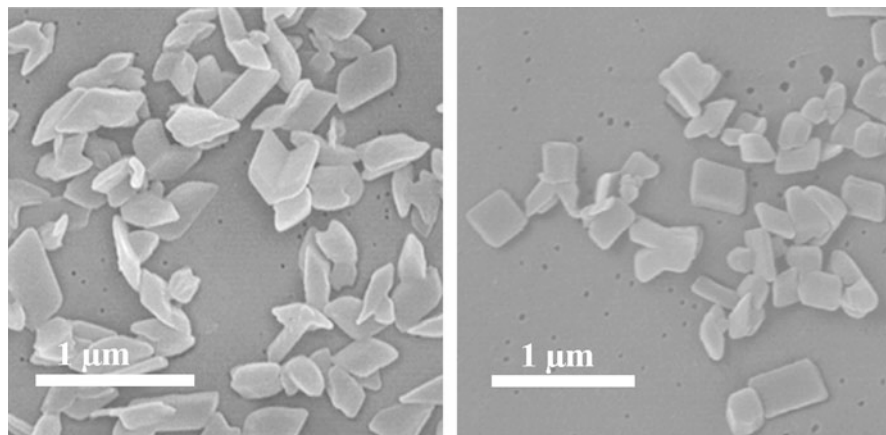


**Fig. 24.2** Morphology of PDA-Me nanocrystals before (*left*) and after (*right*) UV irradiation observed using a scanning electron microscope. Their single-crystalline feature was maintained even after polymerization and crystal shapes seem to be slightly changed by crystalline lattice deformation (Reprinted with permission from ref. [9]. Copyright 2002 American Chemical Society)

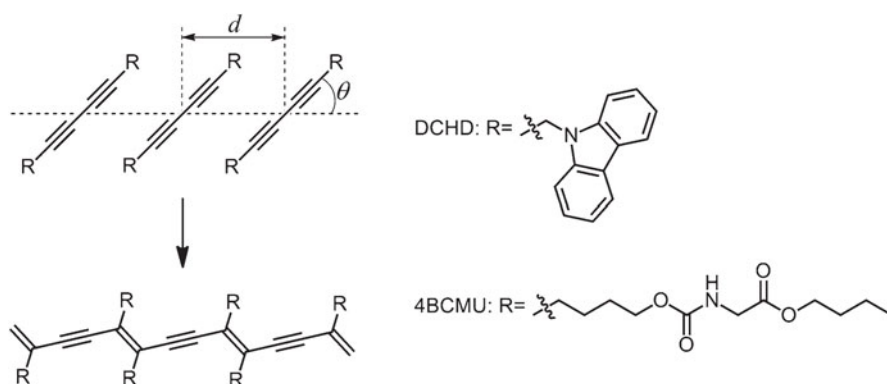


**Fig. 24.3** Solid-state polymerization scheme to form polydiacetylene and typical examples of diacetylene monomers

the angle  $\theta$  between translation axis and the diacetylene moiety is approximately  $45^\circ$  [11]. As an exception, 1,6-di(*N*-carbazolyl)hexa-2,4-diyne (DCHD) having  $d$  of 0.455 nm and  $\phi$  of  $60^\circ$  can polymerize with phase transition in the course of polymerization. The polymers obtained by the scheme in Fig. 24.3 are called polydiacetylenes, which have a  $\pi$ -conjugated backbone to show blue or red color originated from the characteristic excitonic absorption band. Nanocrystals of DCHD are easily prepared by the acetone solution injection into water. Therefore, DCHD is often used as a standard compound of nanocrystallization, and the crystal formation

mechanism has been clarified [12–14]. Interestingly, when UV was irradiated to the dispersion just after DCHD solution injection, characteristic blue color of polyDCHD did not appear. However, when the DCHD nanocrystal dispersion as prepared was kept for several tens of minutes at ambient temperature, the color turned blue by irradiation of UV at 254 nm. Morphological and structural studies clarified the following nanocrystallization mechanism. At first just after DCHD solution injection, DCHD amorphous nanoparticles with spherical shapes are formed in water. These particles do not show regular 1,4-addition photopolymerization because of random orientation of the monomers. Thermal crystallization takes place with time and the nanoparticle shapes change to rectangular. At this stage, the monomers in the nanocrystals can regularly polymerize to be the blue-colored polydiacetylene. Crystal sizes of DCHD can be controlled from several tens to several hundreds of nanometers mainly by varying solution concentration and volume for injection. When the DCHD nanocrystal dispersion containing sodium dodecyl sulfate (SDS) is heated up to 50–60 °C during the crystallization process, the anisotropic crystal growth along the polymerization direction occurs to form fibrous crystals. This crystal growth seems to be promoted by collision of crystalline and amorphous DCHD particles. Typical width and length of the fibrous crystals are about 50 nm and more than several micrometers, respectively.

### 24.2.3 *Molecular-Weight Control*

Two big issues in the polymer synthesis are stereoregularity and molecular-weight control. In the solid-state polymerization, stereoregularity of the polymers is guaranteed when the polymerization progresses topochemically. In this case, polymerization direction is strictly defined, and the crystal length along the polymerization direction can control the molecular weight if crystal defects are ignored. This fact was confirmed by using 5,7-dodecadiyn-1,12-diyl bis[*N*-(butoxycarbonylmethyl)carbamate] abbreviated as 4BCMU (Fig. 24.3), whose polymer is exceptionally soluble in chloroform among polydiacetylenes [15]. For crystals with sizes of 0.5–1.5 μm, the expected average molecular weight is between  $5.1 \times 10^5$  and  $1.5 \times 10^6$ . By gel permeation chromatography using polystyrene as a standard, the number-average and weight-average molecular weights, i.e.,  $M_n$  and  $M_w$ , were measured to be  $5.2 \times 10^5$  and  $1.6 \times 10^6$ , respectively. Meanwhile, for smaller crystal sizes of 0.2–0.4 μm corresponding to the expected molecular weight between  $2.0 \times 10^5$  and  $4.1 \times 10^5$ ,  $M_n$  and  $M_w$  were obtained to be  $1.6 \times 10^5$  and  $5.5 \times 10^5$ , respectively. Namely, the polymers with the smaller molecular weight were obtained from the nanocrystals with smaller sizes. These results suggested that polydiacetylene molecules obtained in nanocrystals extended from one crystal surface to the opposite crystal surface. Monodispersity of the polymers should be improved by precise control of the nanocrystal size and shape.

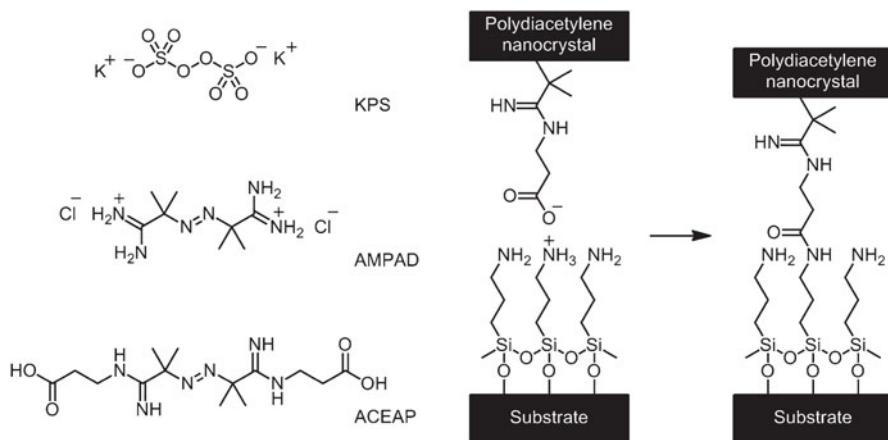


**Fig. 24.4** Chemical structures of water-soluble initiators used for radical-initiator-induced solid-state polymerization of diacetylene nanocrystals (*left*) and the fixation scheme of polydiacetylene nanocrystals modified by carboxyl groups onto a substrate covered with amino groups (*right*)

#### 24.2.4 Surface Functionalization

One of the specific features of nanocrystals is large surface areas relative to the volume. For example, catalytic performance of metal fine particles generally increases due to this reason. Thus, it is interesting to use the nanocrystal surfaces as a reaction field to modify the crystal surfaces. As mentioned above, the solid-state polymerization of diacetylene derivatives is a chain reaction stimulated usually by UV or  $\gamma$ -ray irradiation or thermal treatment. In order to use crystal surfaces for the reactions, the polymerization stimulated by radical initiators was investigated. To a DCHD nanocrystal water dispersion, water-soluble radical initiators such as potassium persulfate (KPS), 2,2'-azobis(2-methylpropionamidine) dihydrochloride (AMPAD), 2,2'-azobis{2-[N-(2-carboxyethyl)amidino]propane} (ACEAP), etc. (Fig. 24.4 (left)) were added and heated to start polymerization [16, 17]. SDS was also added to stabilize the dispersion through the reaction. Actually, radical polymerization was initiated by heating to give polyDCHD nanocrystals whose surfaces were modified by the radical-initiator residues. In the same heating conditions without the initiators, no polymerization occurred. This fact clearly indicated that the radicals generated from the initiators attacked the DCHD nanocrystal surfaces to start the solid-state polymerization. Since absorbance of the polymer nanocrystal dispersion obtained by the radical-initiator-induced polymerization is almost the same as that of the photopolymerized nanocrystal dispersion, its quantitative conversion was confirmed.

By using the functional groups on the nanocrystal surfaces, fixation of nanocrystals by covalent bonding became possible [18]. When ACEAP is used in the radical-

initiator-induced solid-state polymerization, nanocrystal surfaces are modified by carboxyl groups. On the other hand, amino groups can be introduced by reacting a hydrophilic surface of a glass substrate with 3-aminopropyltriethoxysilane. When the amino-modified substrates were soaked in DMF dispersion of polyDCHD nanocrystals modified by carboxyl groups, the nanocrystals were first attached on the substrate by the electrostatic manner, i.e., formation of ammonium carboxylate salts. Electrostatic attachment of nanocrystals with negative surface charges to the substrate coated by polycations has already been reported [19]. Covalent bonds between the nanocrystals and the substrate were formed by the condensation reaction as shown in Fig. 24.4 (right). This reaction was promoted by heating. Stronger adhesive property of the covalently bonded nanocrystals compared with the electrostatically attached nanocrystals was confirmed when sonication was performed. In order to obtain uniform spherical particles for photonic applications, encapsulation of polyDCHD with amorphous polymers such as polystyrene and poly(methyl methacrylate) was conducted by the soap-free emulsion polymerization [20–22]. Even in this case, the shell polymers may covalently bond to core polyDCHD although the cores were polymerized in advance.

### 24.2.5 *Metal-Shell Coating*

Core-shell-type hybrid nanocrystals are quite interesting from the point of view of material interactions, cooperative enhancement of physical properties, and so on [23, 24]. In the preparation process of polyDCHD nanocrystals coated with a silver layer, silver mirror reaction using formaldehyde or glucose as a reducing reagent was conducted [25]. Formaldehyde reduction gave polyDCHD whose surfaces were covered with colloidal silver particles with size of about 30 nm. When the polyDCHD crystal surfaces were treated with  $\text{Sn}^{2+}$  in advance and glucose was used as a reducing reagent, the morphology was different from the former case and thin silver layers were formed on the crystal surfaces.

In the next step, photocatalytic reduction was applied for silver-layer fabrication [26]. Ammoniac silver nitrate solution was added to the polyDCHD nanocrystal dispersion, and visible light was irradiated. Then, silver coating on polyDCHD nanocrystal surfaces occurred. Plausible explanation of this mechanism is as follows. First, electrons in the valence band of polyDCHD in nanocrystals are excited to the conduction band by the visible light irradiation. Then, the excited electrons are used to reduce  $\text{Ag}^+$  species, which are electrostatically attracted to the negatively charged nanocrystal surfaces. Without polyDCHD nanocrystals, the  $\text{Ag}^+$  species are not directly reduced by irradiation of visible light. Accordingly, reduction of  $\text{Ag}^+$  species selectively occurs on the nanocrystal surfaces to form a silver-coating layer. This type of metal-shell fabrication can be applied for other  $\pi$ -conjugated compounds' cores to form a variety of metal-coated organic nanocrystals.

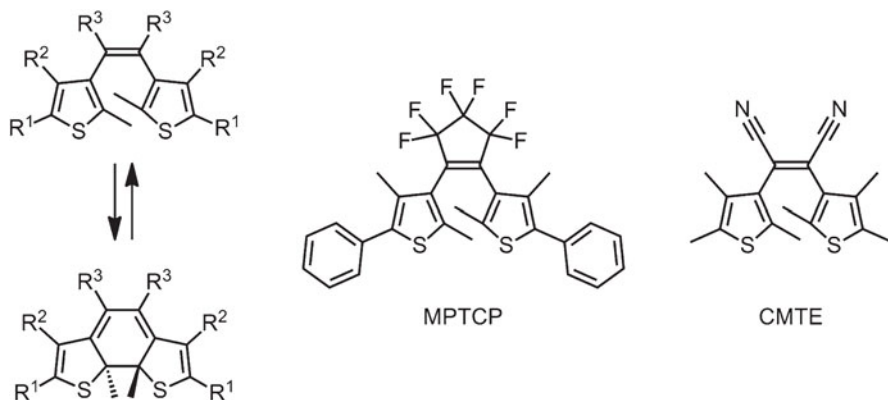


**Fig. 24.5** Solid-state photochromic reaction scheme and typical examples of diarylethene derivatives

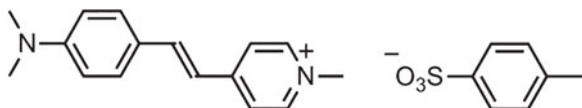
### 24.2.6 Valence Isomerization of Diarylethene Derivatives

Photochromic valence isomerization in nanocrystals was also investigated. Diarylethene derivatives show intramolecular ring-closure photoreaction [27] and some of them react even in the crystalline states. Nanocrystallization was performed for 1,2-bis(2,4-dimethyl-5-phenyl-3-thienyl) perfluorocyclopentene (MPTCP) and (*Z*)-1,2-dicyano-1,2-bis(2,4,5-trimethyl-3-thienyl) ethene (CMTE), whose structures are shown in Fig. 24.5. For nanocrystallization of MPTCP [28], microwave irradiation to the water just after the solution injection assisted its crystallization. Otherwise, the particles obtained were amorphous. Addition of a small amount of the ring-closed MPTCP to MPTCP in the solution for injection was also effective for the nanocrystallization because less-soluble ring-closed MPTCP worked as nuclei of the nanocrystals. The nanocrystal sizes could be changed between 60 and 120 nm by varying concentration of the injected solutions. For CMTE, the conventional reprecipitation method gave the nanocrystals [29], and the nanorods with the length more than 5  $\mu\text{m}$  were obtained when SDS was added [30]. In both compounds, the photochromic behaviors were confirmed by the color change due to alternate irradiation of UV and visible light, and it was repeated several times without serious deterioration.

## 24.3 Orientation Control of Nanocrystals

For an ionic dye with a polar space group, i.e., (*E*)-4-{2-[4-(dimethylamino)phenyl]ethenyl}pyridinium *p*-toluenesulfonate (DAST) in Fig. 24.6, generation of macroscopic polar or uniaxial order in the nanocrystal dispersion was investigated by using

**Fig. 24.6** Chemical structure of DAST



DC electric, AC electric, and DC magnetic fields. Meanwhile, macroscopic uniaxial order of polyDCHD nanocrystals having a centrosymmetric crystal structure was achieved by application of AC electric and DC magnetic fields.

### 24.3.1 Orientation and Fixation of Polar Nanocrystals

DAST is one of the most useful second-order nonlinear optical organic compounds [31, 32]. Its single crystals can generate broadband terahertz waves via optical rectification using femtosecond laser pulses and single-frequency terahertz waves via difference frequency generation. DAST was also investigated for nanocrystallization.

#### 24.3.1.1 Application of a Single External Field

Since DAST is dissolved in water and gives hydrated crystals with a centrosymmetric structure [33], the conventional reprecipitation method, in which a solution of water-soluble solvent is injected into water, cannot be applied. Thus, nanocrystallization of DAST was first prepared by injection of the ethanol solution into decahydronaphthalene (Decalin) as a nonsolvent. Some additives such as dodecyltrimethylammonium chloride and/or an acrylate polymer were added to stabilize the dispersion state [34–36].

DAST crystals belong to monoclinic polar space group  $Cc$ , and the crystal structure is shown in Fig. 24.7. Each crystal should have an electric permanent dipole moment, whose direction is parallel to the polar  $a$ -axis. Namely, the  $a$ -axis is apt to be parallel to the DC electric field. In the crystal, (dimethylamino)stilbazolium cations (hereafter DAST cations) stacked along the  $a$ -axis so as to pile up their long axis parallel each other on the  $bc$ -plane. The angle between the molecular long axis of the cation and the  $a$ -axis is about  $20^\circ$ . Accordingly, absorbance for the molecular long axis of the cation becomes large when the polarized light is irradiated parallel to the  $a$ -axis of the crystal. Thus, the DAST nanocrystal orientation can be evaluated by UV-visible spectra using polarized incident light.

DC electric field was applied to the DAST nanocrystals in Decalin. Under  $100 \text{ Vcm}^{-1}$ , nanocrystal orientation, in which the  $a$ -axis was aligned parallel to the electric field, was confirmed. Absorption changes between random and oriented states of the nanocrystals corresponding to off and on states of the electric field, respectively, were reversible. Degree of orientation linearly increases by

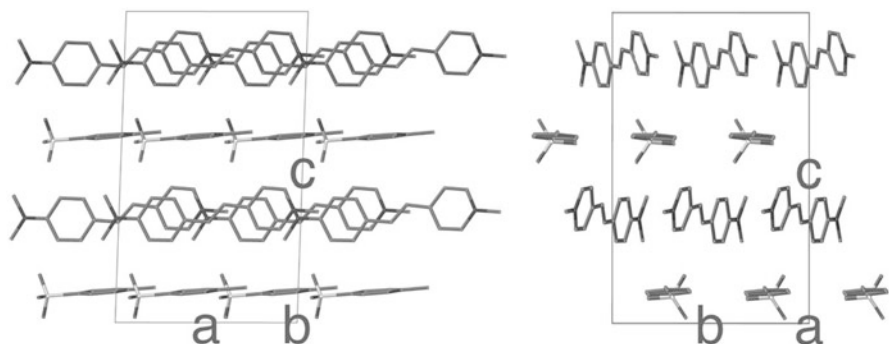


**Fig. 24.7** Crystal structure of DAST viewed along *b*-axis (left) and *a*-axis (right)

increasing the electric field up to  $300 \text{ Vcm}^{-1}$ . However, higher voltage or prolonged electric field application induced electrophoresis of the nanocrystals, which caused irreversible absorption changes. At the same electric field, the larger crystals showed more effective orientation [36] because the total dipole moment of a crystal is proportional to the number of the molecules in the crystal, which increases with the crystal size. Recently, the dipole moment of a DAST nanocrystal with a size of about 350 nm was successfully obtained to be  $4.5 \times 10^4 \text{ D}$  by using polarized electroabsorption spectroscopy [37].

Under an AC electric field, anisotropy of the induced dipole moment, in other words, anisotropy of the dielectric constant, is a driving force to orient the nanocrystals. Generally, larger induced dipole moments appear along longer  $\pi$ -conjugation systems. Accordingly, the *a*-axis of the DAST crystals, which is the principle dielectric axis, has a tendency to be parallel to the AC electric field. By using the AC field instead of the DC field, the problem on electrophoresis of the nanocrystals can be avoided when the frequency of the AC field is high enough to diminish the electric response like translational and rotational motions of the nanocrystals. At high frequencies, the crystal positions and orientation are maintained. Thus, higher electric fields can be applied up to approximately  $1 \text{ kVcm}^{-1}$  [38]. At low frequencies, temporal absorption oscillation was observed. From 10 to  $10^3 \text{ Hz}$ , absorption changes observed by polarized incident light became maximum and almost the same within this range. However, at frequencies more than  $10^3 \text{ Hz}$ , absorption changes dropped down.

DC magnetic fields are also effective to align nanocrystals in which aromatic rings are incorporated. When the magnetic field is applied to an aromatic compound in liquid, ring current of the aromatic ring induced by the external magnetic field generates an internal magnetic field with the opposite polarity, and the aromatic ring is apt to be parallel to the external magnetic field. Such magnetic repulsive forces of all molecules in a nanocrystal are summed up to determine the orientation of the crystal. According to this orientation mechanism of the aromatic compounds by the magnetic field, a plane with the smallest area of the projected aromatic rings is faced

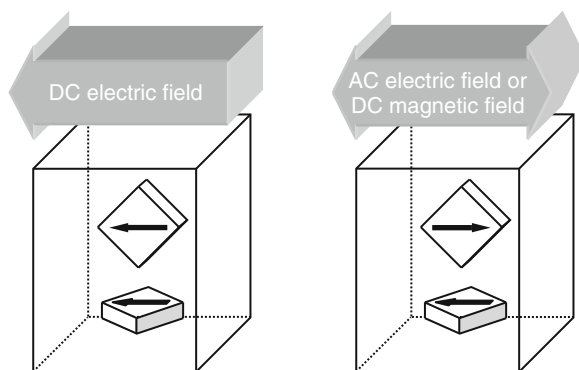


**Fig. 24.8** Favorable orientation of DAST nanocrystals under the DC electric field (*left*) and under the AC electric field or the DC magnetic field (*right*). Plates in *boxes* correspond to DAST nanocrystals in the dispersion medium and *arrows* drawn in the plates indicate the permanent dipole moment of the crystal along the *a*-axis. Although the *arrow* direction becomes the same under the DC electric field for all nanocrystals (*left*), a half of the *arrows* points the opposite direction under the AC electric and DC magnetic fields (*right*). Crystals may rotate around the *a*-axis, and the plane shown in Fig. 24.7 (*right*) is perpendicular to the external fields

perpendicular to the magnetic field. In the case of DAST nanocrystals, this plane corresponds to Fig. 24.7 (*right*) and the *a*-axis is apt to be parallel to the magnetic field [39]. DAST nanocrystal orientation under the external field is schematically shown in Fig. 24.8.

### 24.3.1.2 Application of Double External Fields and Orientation Fixation

As mentioned above, three external fields were applied to orient the DAST nanocrystals in liquid media, and the order of degree of orientation among three applied fields is summarized in Table 24.1 with their characteristics. Although all three cases result in uniaxial orientation of the nanocrystals, the polar orientation, which is useful for piezoelectricity, pyroelectricity, and second-order nonlinear optical properties, is only realized by the DC electric field. However, the degree of orientation is worst among the three. This is mainly due to the low applicable electric field to avoid electrophoresis of the nanocrystals. Then, combination of two external fields was investigated. Fortunately, uniaxial orientation directions of the DAST nanocrystals are the same along the *a*-axis for all. Thus, the DC electric field of  $0.5 \text{ kVcm}^{-1}$  was first applied to form the polar order with weak uniaxial orientation. Next, the DC magnetic field of 2.5 T was applied parallel to the electric field to intensify the uniaxial order and the electric field was switched off soon. According to this process, the strong polar orientation of the DAST nanocrystals was achieved [40]. Orientational changes during this process were clearly observed by the absorption spectra monitored by the polarized light parallel to the external fields (Fig. 24.9). By applying the first DC electric field and the second DC magnetic

**Table 24.1** Summary of the DAST nanocrystal orientation

Order of degree of orientation	External field for orientation (maximum field applied)	Driving force in nanocrystals	Orientation order
1	DC magnetic field ( 15 T)	Diamagnetic interaction	Uniaxial
2	AC electric field ( 3.0 kVcm <sup>-1</sup> )	Induced dipole moment	Uniaxial
3	DC electric field ( 0.3 kVcm <sup>-1</sup> )	Permanent dipole moment	Polar

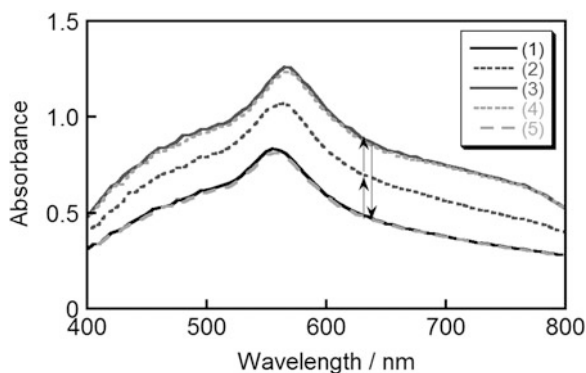


**Fig. 24.9** Absorption spectral changes of DAST nanocrystal dispersion: (1) the initial condition without external fields, (2) after applying the DC electric field, (3) after applying the additional DC magnetic field, (4) after removal of the electric field with continuous magnetic field application, and (5) after removal of the magnetic field. Curves (1) and (5) and curves (3) and (4) are almost overlapped, respectively

field, the absorption band of the DAST cations along  $a$ -axis in the crystals increased stepwise. This indicated that the  $a$ -axis of the crystals aligned parallel to the fields and degree of orientation increased stepwise. Since the absorption spectrum was unchanged even after removal of the electric field, the nanocrystal polar orientation must be maintained by the magnetic field. Spectrum recovery to the initial condition was also confirmed after turning off the magnetic field.

Even if the orientation of the nanocrystals was achieved in liquid dispersion, it is thermally randomized after removal of the external fields with ease. In order to maintain the properties for device applications induced by the field orientation, orientation fixation by solidification of the dispersion medium was also investigated [40, 41]. Namely, liquid monomers were used as the dispersion medium, which could polymerize after nanocrystal alignment. Since polar liquid dissolves DAST, less polar monomers like dodecyl acrylate were selected as dispersion medium. When the DAST ethanol solution was directly injected to dodecyl acrylate, the crystal size was approximately 700 nm. For preparation of smaller crystals to reduce optical scattering loss, the nanocrystals with average sizes of 120–160 nm were first obtained in volatile hydrocarbons such as cyclohexane and hexane. Then, the

dispersion medium was substituted to dodecyl acrylate, i.e., less volatile dodecyl acrylate was added to the nanocrystal dispersion and more volatile hydrocarbons were evaporated. A photoinitiator and a cross-linker were added to the dispersion, and the nanocrystals in the dispersion were oriented by the external fields. Solidification of the dispersion medium was stimulated by UV irradiation and completed before removal of the external fields. Since bleaching of the DAST nanocrystals occurred during photopolymerization, efficient combination of the monomer and the photoinitiator should be selected. Among the experiments so far, the fastest solidification rate was recorded for the combination of dodecyl acrylate and 2,2-dimethoxy-2-phenylacetophenone.

### 24.3.2 Orientation and Fixation of Nonpolar Nanocrystals

For nonpolar nanocrystals, the DC electric field is not useful for their orientation. However, the AC electric and the DC magnetic fields can interact with the nonpolar nanocrystals to orient them in the dispersion medium if there is a favorable molecular alignment in the crystal. Especially, the magnetic field has an advantage to orient nanocrystals compared with the electric field. When dispersion medium has a large dielectric constant, e.g., water, effective electric field applied for the nanocrystals reduced. Since the DAST nanocrystals have been prepared in media such as hydrocarbons with relatively low dielectric constants, reduction of the local field is not so serious. However, many of nanocrystal dispersions have been prepared in water and the reduced local field may cause insufficient orientation. On the other hand, the magnetic field can effectively interact with nanocrystals even in water. Actually, uniaxial orientation of perylene nanocrystals in water was confirmed [42]. Even in this case, the orientation principle is the same, i.e., a crystallographic plane with the smallest area of the projected aromatic rings became perpendicular to the magnetic field.

Orientation of polyDCHD nanocrystals was investigated by applying the AC electric and the DC magnetic fields [43]. Fibrous crystals were first obtained as the water dispersion and were polymerized. PolyDCHD crystals were collected by filtration. After drying, they were redispersed in dodecyl acrylate containing benzoin isopropyl ether as a photoinitiator and tricyclo[5.2.1.0<sup>2,6</sup>]decane-4,8-dimethanol diacrylate as a cross-linker. Typical AC electric and DC magnetic fields applied were 6 kVcm<sup>-1</sup> (50 Hz) and 15 T, respectively. Figure 24.10 shows crystal structure of polyDCHD [44], which belongs to monoclinic space group  $P2_1/c$ . From the molecular structure, the largest induced dipole moment seems to be generated along the  $\pi$ -conjugated polymer backbone direction, i.e., along the crystallographic  $b$ -axis. Namely, the  $b$ -axis is apt to be parallel to the AC electric field as shown in Fig. 24.11 (left). On the other hand, orientation under the magnetic field is mainly determined by the aromatic rings in the carbazole moieties. The crystallographic plane with the smallest area of the projected aromatic rings of polyDCHD is displayed in Fig. 24.10 (right), and this plane should be perpendicular to the magnetic field as shown in Fig. 24.11 (right). In the case of polyDCHD, orientation directions with

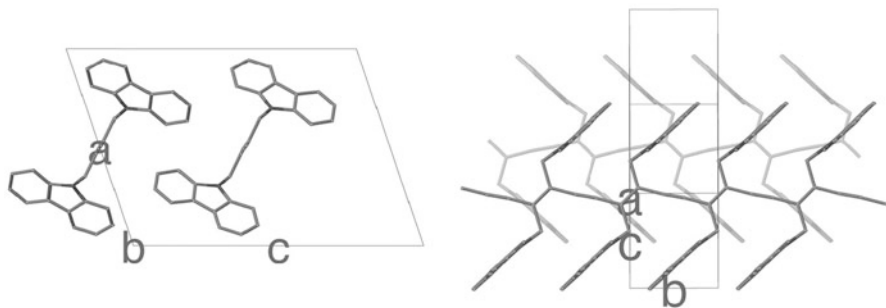


**Fig. 24.10** Crystal structure of polyDCHD viewed along  $b$ -axis (*left*) and projected on to the plane to which the carbazolyl moieties in the side groups are perpendicular (*right*)

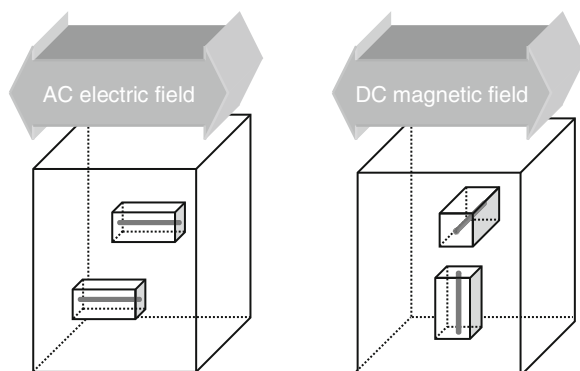


**Fig. 24.11** Favorable orientation of polyDCHD nanocrystals under the AC electric field (*left*) and the DC magnetic field (*right*). Cuboids in *boxes* correspond to polyDCHD nanocrystals in the dispersion medium and *bars* drawn in cuboids indicate  $\pi$ -conjugated polymer backbone direction along the  $b$ -axis. Under the AC electric field (*left*), the crystals may rotate around the  $b$ -axis. Namely, the plane shown in Fig. 24.10 (*left*) is perpendicular to the AC electric field. Meanwhile, under the DC magnetic field (*right*), the crystals may rotate to keep the plane shown in Fig. 24.10 (*right*) perpendicular to the magnetic field

respect to the external fields were different between electric and magnetic fields, and uniaxial orientation by the AC electric field may be strengthened by applying the DC magnetic field perpendicular to the electric field.

## 24.4 Conclusions

Several reactions of the organic nanocrystals such as topochemical polymerization of diolefin and diacetylene derivatives and solid-state photoisomerization of diarylethene derivatives were investigated. Their single-crystal-to-single-crystal transformation was found to progress by strain release based on the nanocrystal

shape deformation if the lattice parameter changes before and after the reaction are large. Molecular weight of the polymers obtained by topochemical polymerization could be managed by controlling the nanocrystal size. Radical-initiator-induced solid-state polymerization and photocatalytic reduction were studied as surface reactions of the nanocrystals. It was confirmed that radical attacks on the nanocrystal surfaces also stimulated solid-state chain reactions and the surface modification by the functional groups in the radical-initiator residues was performed. By using photoexcitation of the polydiacetylene nanocrystals and electron transfer from the nanocrystal to the metal cations on the surfaces, metal deposition selectively on the nanocrystal surfaces was achieved to form core-shell-type hybrid nanocrystals.

Anisotropy could be generated from isotropic nanocrystal dispersions by controlling nanocrystal orientation using DC and AC electric fields and DC magnetic field. Although polar orientation is only obtained by the DC electric field, electrophoresis of the nanocrystals avoids their efficient alignment. However, in the case of DAST, the polar alignment could be enhanced by the additional DC magnetic field. Controllability of the nanocrystal orientation in the dispersion exactly depends on molecular alignment in the nanocrystals and a different orientation depending on the external field was confirmed for polyDCHD. Temporal nanocrystal orientation in liquid could be successfully immobilized by polymerization of the dispersion media.

The basic technical issues related to reactions and orientation control of the nanocrystals have been improved though the studies mentioned above. However, we still have to consider reactivity and orientational controllability depending on compounds and the crystal structures. Another issue of the nanocrystals prepared by the reprecipitation method is relatively low concentration of the effective mass in the dispersion, and concentration or accumulation of the nanocrystals preferably with the orientational control is the next subject to be tackled.

**Acknowledgments** Most of the results summarized in this article have been attained by the active collaborators shown in the references. The authors especially thank to Emeritus Professor Hachiro Nakanishi, Dr. Hitoshi Kasai, Dr. Akito Masuhara, Dr. Tsunenobu Onodera, Dr. Hirohiko Miura, and Dr. Yuji Kaneko for their valuable discussions and scientific contributions.

## References

1. H. Kasai, H.S. Nalwa, H. Oikawa, S. Okada, H. Matsuda, N. Minami, A. Kakuta, K. Ono, A. Mukoh, H. Nakanishi, A novel preparation method of organic microcrystals. *Jpn. J. Appl. Phys.* **31**, L1132–L1134 (1992)
2. H. Kasai, H.S. Nalwa, S. Okada, H. Oikawa, H. Nakanishi, Fabrication and spectroscopic characterization of organic nanocrystals, in *Handbook of Nanostructured Materials and Nanotechnology*, ed. by H.S. Nalwa, vol. 5 (Academic, San Diego, 1999), pp. 433–473
3. H. Oikawa, A. Masuhara, H. Kasai, T. Mitsui, T. Sekiguchi, H. Nakanishi, Organic and polymer nanocrystals: their optical properties, in *Nanophotonics: Integrating Photochemistry, Optics, and Nano/Bio Materials*, ed. by H. Masuhara, S. Kawata, vol. 1 (Elsevier, Amsterdam, 2004), pp. 205–224
4. H. Kasai, H. Kamatani, S. Okada, H. Oikawa, H. Matsuda, H. Nakanishi, Size-dependent colors and luminescences of organic microcrystals. *Jpn. J. Appl. Phys.* **35**, L221–L223 (1996)

5. H. Kasai, H. Kamatani, Y. Yoshikawa, S. Okada, H. Oikawa, A. Watanabe, O. Ito, H. Nakanishi, Crystal size dependence of emission from perylene microcrystals. *Chem. Lett.* **26**, 1181–1182 (1977)
6. V.V. Volkov, T. Asahi, H. Masuhara, A. Masuhara, H. Kasai, H. Oikawa, H. Nakanishi, Size-dependent optical properties of polydiacetylene nanocrystal. *J. Phys. Chem. B* **108**, 7674–7680 (2004)
7. M. Hasegawa, Y. Suzuki, Four-center type photopolymerization in the solid state: poly-2,5-distrylpyrazine. *J. Polym. Sci. Part B: Polym. Lett.* **5**, 813–815 (1967)
8. G. Wegner, Topochemische Reaktionen von Monomeren mit konjugierten Dreifachbindungen I. Mitt.: Polymerisation von Derivaten des 2,4-Hexadiin-1,6-diols im kristallinen Zustand. *Z. Naturforsch.* **24b**, 824–832 (1969)
9. S. Takahashi, H. Miura, H. Kasai, S. Okada, H. Oikawa, H. Nakanishi, Single-crystal-to-single-crystal transformation of diolefin derivatives in nanocrystals. *J. Am. Chem. Soc.* **124**, 10944–10945 (2002)
10. H. Miura, S. Takahashi, H. Kasai, S. Okada, K. Yase, H. Oikawa, H. Nakanishi, Fabrication of nanocrystals from diolefin derivatives and their solid-state photoreaction behavior. *Cryst. Growth Des.* **10**, 510–517 (2010)
11. V. Enkelmann, Structural aspects of the topochemical polymerization of diacetylenes, in *Polydiacetylenes*, ed. by H.J. Cantow. *Advances in Polymer Science*, 63 (Springer, Berlin, 1984), pp. 91–136
12. H. Katagi, H. Kasai, S. Okada, H. Oikawa, K. Komatsu, H. Matsuda, Z. Liu, H. Nakanishi, Size control of polydiacetylene microcrystals. *Jpn. J. Appl. Phys.* **35**, L1364–L1366 (1996)
13. H. Katagi, H. Kasai, S. Okada, H. Oikawa, H. Matsuda, H. Nakanishi, Preparation and characterization of poly-diacetylene microcrystals. *J. Macromol. Sci. Part A: Pure Appl. Chem.* **A34**, 2013–2024 (1997)
14. H. Oikawa, T. Oshikiri, H. Kasai, S. Okada, S.K. Tripathy, H. Nakanishi, Various types of polydiacetylene microcrystals fabricated by reprecipitation technique and some applications. *Polym. Adv. Technol.* **11**, 783–790 (2000)
15. R. Iida, H. Kamatani, H. Kasai, S. Okada, H. Oikawa, H. Matsuda, A. Kakuta, H. Nakanishi, Solid-state polymerization of diacetylene microcrystals. *Mol. Cryst. Liq. Cryst.* **267**, 95–100 (1995)
16. M. Arai, S. Okada, Polymerization of a butadiyne derivative in crystalline state stimulated by radical initiators. *Chem. Lett.* **35**, 1012–1013 (2006)
17. S. Kato, T. Kinemuchi, Y. Tatewaki, S. Okada, A. Masuhara, H. Kasai, H. Oikawa, Radical-initiator-induced solid-state polymerization of butadiyne nanocrystals in water and their dispersion stabilization. *J. Nanosci. Nanotechnol.* **11**, 3340–3344 (2011)
18. T. Kinemuchi, Y. Moritani, Y. Tatewaki, S. Okada, Fixation of surface-modified polydiacetylene nano/microcrystals on substrates. *Jpn. J. Appl. Phys.* **50**, 095202-1–5 (2011)
19. S.K. Tripathy, H. Katagi, H. Kasai, S. Balasubramanian, H. Oshikiri, J. Kumar, H. Oikawa, S. Okada, H. Nakanishi, Self assembly of organic microcrystals I: electrostatic attachment of polydiacetylene microcrystals on a polyelectrolyte surface. *Jpn. J. Appl. Phys.* **37**, L343–L345 (1998)
20. Z. Wei, H. Miura, A. Masuhara, H. Kasai, S. Okada, H. Nakanishi, Monodispersed polydiacetylene-polystyrene composite particles. *Jpn. J. Appl. Phys.* **42**, L1213–L1215 (2003)
21. Z. Wei, K. Ujiye-Ishii, A. Masuhara, H. Kasai, S. Okada, H. Matsune, T. Asahi, H. Masuhara, H. Nakanishi, Synthesis and characterization of monodispersed polymer/polydiacetylene nanocrystals composite particles. *J. Nanosci. Nanotechnol.* **5**, 937–944 (2005)
22. T. Onodera, M. Nakamura, Y. Takaya, A. Masuhara, Y. Wakayama, N. Nemoto, H. Nakanishi, H. Oikawa, Encapsulation of  $\pi$ -conjugated polymer nanocrystals and their ordered array structure toward photonic nanomaterials. *J. Phys. Chem. C* **113**, 11647–11651 (2009)
23. H. Oikawa, T. Onodera, A. Masuhara, H. Kasai, H. Nakanishi, New class of materials of organic-inorganic hybridized nanocrystals/nanoparticles, and their assembled micro- and nanostructure toward photonics, in *Polymer Materials*, ed. by K.S. Lee, S. Kobayashi. *Advances in Polymer Science*, 231 (Springer, Berlin, 2010), pp. 147–190

24. H. Oikawa, Hybridized organic nanocrystals for optically functional materials. *Bull. Chem. Soc. Jpn.* **84**, 233–250 (2011)
25. H. Katagi, H. Kasai, S. Okada, H. Oikawa, H. Matsuda, H. Nakanishi, Fabrication of metal-coated organic microcrystals. *Polym. Adv. Technol.* **11**, 778–782 (2000)
26. T. Onodera, H. Oikawa, A. Masuhara, H. Kasai, T. Sekiguchi, H. Nakanishi, Silver-deposited polydiacetylene nanocrystals produced by visible-light-driven photocatalytic reduction. *Jpn. J. Appl. Phys.* **46**, L336–L338 (2007)
27. M. Irie, M. Mohri, Thermally irreversible photochromic systems: reversible photocyclization of diarylethene derivatives. *J. Org. Chem.* **53**, 803–808 (1988)
28. N. Tagawa, A. Masuhara, H. Kasai, H. Nakanishi, H. Oikawa, Nanocrystallization of diarylethene and photochromic properties. *Cryst. Growth Des.* **10**, 2857–2859 (2010)
29. N. Tagawa, A. Masuhara, T. Onodera, H. Kasai, H. Nakanishi, H. Oikawa, Nanocrystallization process of diarylethene. *Mol. Cryst. Liq. Cryst.* **539**, 45–49 (2011)
30. N. Tagawa, A. Masuhara, S. Okada, H. Katagiri, T. Onodera, H. Kasai, H. Oikawa, Diarylethene nanorods: preparation, crystal structure, and photochromic properties. *Chem. Lett.* **42**, 636–637 (2013)
31. S. Okada, H. Matsuda, H. Nakanishi, M. Kato, R. Muramatsu, Organic material for nonlinear optical use. Japan Patent Application 61–192404 (1986)
32. S.R. Marder, J.W. Perry, W.P. Schaefer, Synthesis of organic salts with large second-order optical nonlinearities. *Science* **245**, 626–628 (1989)
33. G.L. Bryant Jr., C.P. Yakymyshyn, K.R. Stewart, Structure of 4'-dimethylamino-4-methyl-4-azastilbenium *p*-toluenesulfonate hydrate. *Acta Crystallogr. C* **49**, 350–351 (1993)
34. S. Fujita, H. Kasai, S. Okada, H. Oikawa, T. Fukuda, H. Matsuda, S.K. Tripathy, H. Nakanishi, Electric-field-induced orientation of organic microcrystals with large dipole moment. *Jpn. J. Appl. Phys.* **38**, L659–L661 (1999)
35. H. Oikawa, S. Fujita, H. Kasai, S. Okada, S.K. Tripathy, H. Nakanishi, Electric field-induced orientation of organic microcrystals with large dipole moment in dispersion liquid. *Colloids Surf. A* **169**, 251–258 (2000)
36. S. Okazoe, S. Fujita, H. Kasai, S. Okada, H. Oikawa, H. Nakanishi, Electric-field-induced orientation of polar organic microcrystals with different crystal sizes dispersed in liquid as a novel optical device. *Mol. Cryst. Liq. Cryst.* **367**, 11–17 (2001)
37. H.C. Chiang, T. Iimori, T. Onodera, H. Oikawa, N. Ohta, Gigantic electric dipole moment of organic microcrystals evaluated in dispersion liquid with polarized electroabsorption spectra. *J. Phys. Chem. C* **116**, 8230–8235 (2012)
38. T. Onodera, M. Yoshida, S. Okazoe, S. Fujita, H. Kasai, S. Okada, H. Oikawa, H. Nakanishi, AC electric-field-induced orientation of polar organic nanocrystal in disperse system. *Int. J. Nanosci.* **1**, 737–741 (2002)
39. Y. Kaneko, T. Fukuda, T. Onodera, H. Kasai, S. Okada, H. Oikawa, H. Nakanishi, H. Matsuda, Orientation of suspended polar organic nanocrystals in magnetic fields: the effect of magnetic field configuration. *Jpn. J. Appl. Phys.* **42**, L1343–L1345 (2003)
40. T. Matsuura, T. Wada, Y. Tatewaki, S. Okada, Effective polar orientation of organic polar nanocrystals and their fixation in polymer matrices. *Jpn. J. Appl. Phys.* **53**, 061601-1–7 (2014)
41. Y. Kaneko, S. Shimada, T. Fukuda, T. Kimura, H. Yokoi, H. Matsuda, T. Onodera, H. Kasai, S. Okada, H. Oikawa, H. Nakanishi, A novel method for fixing the anisotropic orientation of dispersed organic nanocrystals in a magnetic field. *Adv. Mater.* **17**, 160–163 (2005)
42. Y. Kaneko, T. Onodera, H. Kasai, S. Okada, H. Oikawa, H. Nakanishi, T. Fukuda, H. Matsuda, Reversible and efficient anisotropic orientation of dispersed aromatic hydrocarbon nanocrystals in a magnetic field. *J. Mater. Chem.* **15**, 253–255 (2005)
43. Y. Kaneko, S. Shimada, T. Onodera, T. Kimura, H. Matsuda, S. Okada, H. Kasai, H. Oikawa, Y. Kakudate, H. Nakanishi, Anisotropic orientation control of nonpolar organic nanocrystal dispersion by external fields. *Jpn. J. Appl. Phys.* **46**, 6893–6897 (2007)
44. P.A. Apgar, K.C. Yee, Poly[1,6-di(*N*-carbazolyl)-2,4-hexadiene]. *Acta Crystallogr. B* **34**, 957–959 (1978)

# Chapter 25

## Topochemical Polymerization of Amino Acid *N*-Carboxy Anhydrides in Crystalline State

Hitoshi Kanazawa

**Abstract** Amino acid *N*-carboxy anhydrides (amino acid NCAs) can be polymerized using a butylamine initiator in dioxane or *N,N*-dimethylformamide solution or in heterogeneous acetonitrile systems in which the NCAs dissolve but the resulting polymers do not. NCAs can also be polymerized in the solid state, using the same initiator. The solid-state polymerization was carried out by dipping amino acid NCA crystals in hexane (an inactive solvent) and adding butylamine to the mixture. Each polymerization was carried out under strict conditions, preventing moisture contamination. Solid-state polymerization has the following features typical of topochemical polymerization. (1) Many amino acid NCAs are more reactive in the solid state than in solution or heterogeneous systems. (2) Many amino acid NCAs give polypeptides with molecular weights higher than those obtained in solution or heterogeneous systems. (3) Many amino acid NCAs give poly(amino acid)s with molecular conformations that are different from those obtained in solution or heterogeneous systems. The reaction is not topotactic, because the resulting polypeptides are not crystals. The solid-state polymerization of amino acid NCAs is useful for the preparation of any type of polypeptide, unlike solution reactions.

**Keywords** Amino acid NCA • Solid-state polymerization • Topochemical polymerization

### 25.1 Introduction

Amino acid *N*-carboxy anhydrides (NCAs) are obtained by the reaction of amino acids, amino acid esters, or other derivatives with compounds such as phosgene and phosgene derivatives (see Scheme 25.1). Amino acid NCAs are extensively used as monomers for preparing high-molecular-weight polypeptides [1].

---

H. Kanazawa (✉)

Department of Industrial Systems, Faculty of Symbiotic Systems Science, Fukushima University,  
Fukushima 960-1296, Japan

e-mail: [kana@sss.fukushima-u.ac.jp](mailto:kana@sss.fukushima-u.ac.jp)

© Springer Japan 2015

R. Tamura, M. Miyata (eds.), *Advances in Organic Crystal Chemistry*,

DOI 10.1007/978-4-431-55555-1\_25

503

**Scheme 25.1** L-Amino acid and L-amino acid NCA

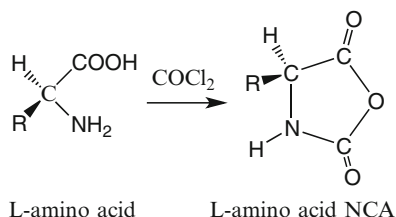
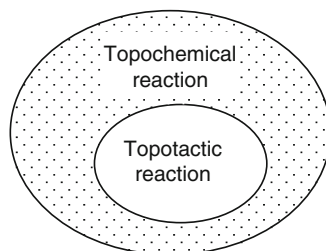


**Fig. 25.1** Relationship between topochemical and topotactic reactions



The first glycine NCA was reported by Leuchs in 1906 [2]. Three decades later, it was found that amino acid NCAs are polymerized by moisture or bases to give high-molecular-weight polypeptides. The compounds are very sensitive to moisture in the air. When a small amount of moisture is adsorbed by the compounds, they are polymerized in the solid state. These compounds are easily soluble in water and decompose to the original amino acids.

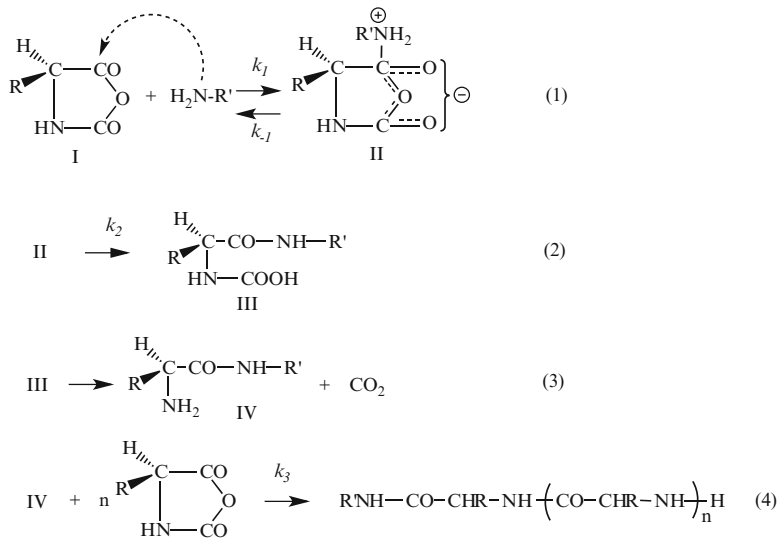
When lattice control occurs in solid-state reactions, the reactions are described as topochemical. The reaction rates or the molecular structures of the reaction products are controlled by the crystal structures of the starting materials in topochemical reactions [3]. When the reaction product forms crystals and the crystal structure is controlled or determined by those of the starting materials, the reaction is called a topotactic reaction. A topotactic reaction is a type of topochemical reaction, as shown in Fig. 25.1 [4]. If the reaction is a polymerization, the reaction is called topochemical or topotactic polymerization. Such polymerizations are summarized as follows.

**Topochemical polymerization:** the monomer crystal structure affects the reaction rate or the molecular structure of the polymer.

**Topotactic polymerization:** the monomer crystal structure affects the reaction rate, the molecular structure of the polymer, and the polymer crystal structure.

The centers of gravity of monomers after the topochemical polymerizations studied so far were unchanged: they were topotactic polymerizations [5, 6].

For a long time, polymerizations of amino acid NCAs have been performed in solution or heterogeneous systems. However, the authors found that the compounds were polymerized in the solid state, and the polymerizations had the typical features of topochemical polymerization.



**Scheme 25.2** Polymerization mechanism of amino acid NCA initiated by primary amine

## 25.2 Polymerization Mechanism of Amino Acid NCAs Initiated by Primary Amine

Bases such as primary, secondary, and tertiary amines and sodium methoxide are used as initiators for amino acid NCA polymerization. The mechanism of amino acid NCA polymerizations initiated by primary amines has been extensively studied and is considered to be as shown in Scheme 25.2. A primary amine,  $\text{R}'\text{-NH}_2$ , attacks 5-CO nucleophilically and intermediate II is formed. The five-membered ring opens and carbon dioxide is produced. The amino group of the resulting compound IV attacks another amino acid NCA, similarly to the primary amine, and the resulting polypeptide attacks other NCAs. The polymerization proceeds step by step. As there is no termination step in the polymerization, this mechanism is considered to be a living polymerization.

## 25.3 Three Amino Acid NCA Polymerization Systems

In general, amino acid NCAs are soluble in polar organic solvents, but most of the resulting polypeptides are insoluble in such solvents. The following polymerization systems have been investigated. In many cases, the polymerization of amino acid NCAs is greatly affected by their purity. It is important that the NCA purity is determined using accurate analytical methods. Ion chromatography is one of the best methods for determining the chlorine contents of NCAs, but traditional titration

methods or atomic analysis are not suitable for determining the exact contents. A series of NCA polymerizations should be carried out using NCA crystals obtained from the same recrystallization.

### **25.3.1 Solution Polymerization**

When the amino acid NCAs and the resulting polypeptides are both soluble in common organic solvents such as dioxane, tetrahydrofuran, and *N,N*-dimethylformamide (DMF), their polymerization in solution is possible. The polymerization of amino acid ester NCAs such as  $\gamma$ -benzyl L-glutamate NCA (BLG NCA),  $\gamma$ -methyl L-glutamate NCA (MLG NCA), and  $\beta$ -benzyl L-aspartate NCA (BLA NCA) are performed in solution, but the resulting polymers are poorly soluble. The solution polymerization of these amino acid NCAs becomes slow, and the molecular weights of the polypeptides do not increase much at a certain polymer conversion. The reason for this has been extensively studied and may be as follows. The resulting polypeptides form aggregates or gels when the polypeptide chains have grown to a certain extent in the solution. The amino groups at the polymer ends are involved in aggregation, and this hinders further polymer growth. This is supported by the finding that in solid-state polymerization, described below, the molecular weight is not limited.

### **25.3.2 Polymerization in Heterogeneous Systems**

When the polymerization of NCAs such as L-alanine NCA, L-valine NCA, L-leucine NCA, and L-phenylalanine NCA is performed in acetonitrile, the NCAs are easily soluble, but the resulting polypeptides are insoluble. The polymerization is considered to proceed at the interface between the dissolved amino acid NCAs and the precipitated polypeptides in the heterogeneous state. The polymerization of L-alanine NCA initiated by butylamine in acetonitrile has been studied in detail [7]. NCA polymerization initiated by a primary amine in acetonitrile was less active when well-purified amino acid NCA crystals were used under strict moisture-free conditions [8]. Polymerization in acetonitrile is useful for all types of amino acid NCAs, but contamination of the reaction systems by water must be avoided.

### **25.3.3 Solid-State Polymerization**

Amino acid NCA crystals can be polymerized by aqueous vapor in the solid state [9]. However, the reaction is difficult to control.

When amino acid NCA crystals are dipped in hexane (an inactive solvent) and butylamine is added to the mixture, polymerization takes place in the solid state.

This solid-state polymerization is easy to perform. Solid-state polymerization is very useful for the preparation of polypeptides using amino acid NCAs. Although the crystal structures of amino acid NCAs were not determined for a long time because of their instability to moisture, we have determined the crystal structures of several NCAs. NCA polymerization in hexane is considered to be a topochemical polymerization, as described below.

## 25.4 New Type of Topochemical Polymerization

The authors compared the solid-state polymerizations of amino acid NCAs initiated by butylamine in hexane with those in solution or heterogeneous systems in acetonitrile and discovered that the solid-state polymerization of amino acid NCAs had the following features, which are typical of topochemical polymerization:

1. Many amino acid NCAs are much more reactive in the solid state than in solution or heterogeneous systems.
2. Many amino acid NCAs give polypeptides with molecular weights higher than those obtained in solution or heterogeneous systems.
3. Many amino acid NCAs give polypeptides with molecular conformations different from those obtained in solution.

The reaction is not a topotactic polymerization, because the resulting polypeptides are not crystals.

### 25.4.1 *Comparison of Solid-State Polymerization and Solution Polymerization*

#### 25.4.1.1 BLG NCA, MLG NCA, and BLA NCA

The polypeptides obtained from BLG, MLG, and BLA NCAs are soluble in dioxane, so the polymerizations of these NCAs in hexane were compared with those in dioxane solution. The results are shown in Fig. 25.2. The chlorine contents of the NCAs were in the range 0.002–0.006 wt%. When the NCA purity is high, the solid-state polymerization becomes much more active than that in dioxane solution. Figure 25.2 shows that each NCA is more reactive in the solid state than in solution. The solid-state polymerizabilities of amino acid NCAs are very different from each other.

#### 25.4.1.2 Polymerizations of L-Alanine NCA, L-Valine NCA, L-Leucine NCA, and L-Phenylalanine NCA

Polymerizations of these NCAs were carried out in the solid state in hexane and in heterogeneous systems in acetonitrile, because the resulting polypeptides are

**Fig. 25.2** Polymerizations of BLG NCA, BLA NCA, and MLG NCA in solid state in hexane and in dioxane solution. Polymerization temperature, 30 °C; chlorine content of NCAs, 0.002–0.006 wt%

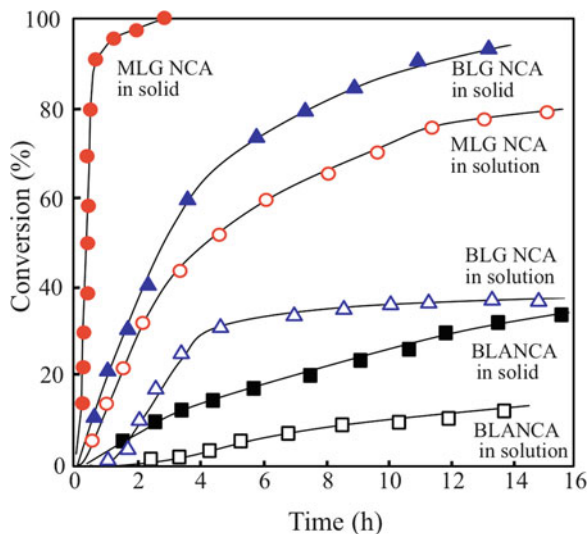


**Table 25.1** Polymer conversions (%) at 3 h

NCA	L-Leu	L-Phe	L-Ala	L-Val	Gly
Solid state	100	65	40	10	4.0
In acetonitrile	12	5.0	20	5.0	1.0

insoluble in organic solvents. Table 25.1 gives the polymer conversions (%) at 3 h after the start of polymerization in the solid state in hexane and in heterogeneous systems in acetonitrile. Each NCA is more reactive in the solid state than in acetonitrile, and large differences are seen among the solid-state polymerizations of different NCAs. L-Leucine NCA and L-phenylalanine NCA are very reactive in the solid state.

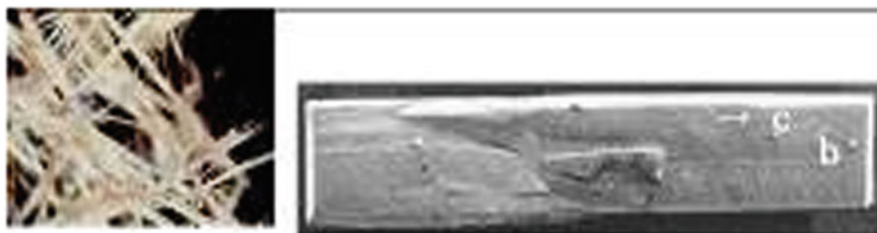
The results in Sects. 25.4.1.1 and 25.4.1.2 suggest that the solid-state polymerization of amino acid NCAs is greatly affected by their crystal structures.

### 25.4.1.3 Molecular Weights of Polypeptides

The polymerization of BLG NCA has been extensively studied, because determination of the molecular weight and molecular-weight distribution of the resulting polymer (PBLG) is possible. Table 25.2 gives the molecular weights and molecular-weight distributions,  $M_w/M_n$ , i.e., the ratio of the weight-average molecular weight ( $M_w$ ) to the number-average molecular weight ( $M_n$ ), of PBLG obtained in the solid state in hexane and in DMF solution. The molecular weight of PBLG obtained in the solid state was much higher than that in solution. Figure 25.3 shows BLG NCA crystals and a PBLG solid produced in the solid state. These results suggest that the solid-state polymerization of BLG NCA is topochemical.

**Table 25.2** Averaged molecular weights and molecular-weight distributions of PBLG

Molecular weight	$M_n$	$M_w$	$M_w/M_n$
Solid state	113,000	133,000	1.18
DMF solution	25,200	29,100	1.11

**Fig. 25.3** BLG NCA crystals (polarized photograph) (*left*) and a PBLG solid (scanning electron micrograph) obtained by solid-state polymerization**Table 25.3** Molecular conformations of polypeptides obtained in NCA polymerization in the solid state and in solution or heterogeneous systems

NCA	Gly	L-Ala	L-Val	L-Leu	L-Phe	BLG	BLA	MLG
Solution	$\beta$	$\alpha, p.\beta^a$	$\beta$	$\alpha$	$\alpha$	$\alpha$	$\beta$	$\alpha$
Solid	$\beta$	$\alpha, p.\beta^a$	$\beta$	$\alpha$	$\beta$	$\alpha$	$\beta$	$\beta$

<sup>a</sup> $p.\beta$ : partially  $\beta$ -structure

#### 25.4.1.4 Polymer Conformation

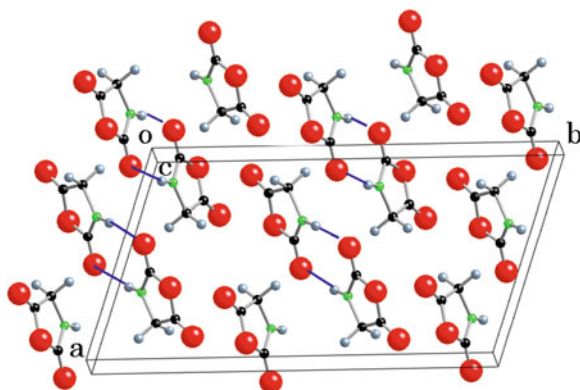
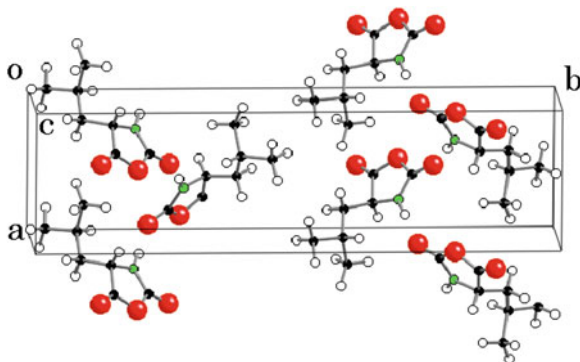
The preferred conformations of poly(amino acid)s and poly(amino acid ester)s are generally determined by the bulkiness of the side chains of the amino acid residues. The conformations of polymers obtained in the solid state and in solution or heterogeneous systems are given in Table 25.3. The polypeptides obtained by NCA polymerization in solution and heterogeneous systems have the normal molecular conformations. The conformations of PBLG and poly(L-leucine) obtained in both polymerization systems are  $\alpha$ -helices. These NCAs are highly reactive in the solid state. In contrast, L-phenylalanine NCA and MLG NCA are highly reactive in the solid state, but their polypeptides have  $\beta$ -structures, which was considered to be impossible. These results also suggest that the solid-state polymerization of amino acid NCAs is topochemical.

#### 25.4.1.5 Crystal Structure

The crystal structures of L-amino acid NCAs have been determined by the author et al. [10–16]. The crystal data are given in Table 25.4. Other crystal structures will be reported in the future.

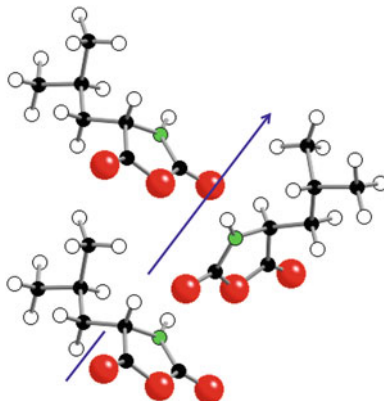
**Table 25.4** Crystallographic data for amino acid NCAs

NCA	M. W.	S. G.	a/Å	b/Å	c/Å	Z	$\beta/^\circ$
Glycine	101	C2/c	16.900(4)	5.156(2)	9.298(2)	8	107.9
L-Ala	115	P2 <sub>1</sub> 2 <sub>1</sub> 2 <sub>1</sub>	7.749(2)	10.699(3)	6.603(2)	4	
L-Val	143	P2 <sub>1</sub> 2 <sub>1</sub> 2 <sub>1</sub>	5.781(1)	22.740(3)	5.395(1)	4	
L-Leu	157	P2 <sub>1</sub> 2 <sub>1</sub> 2 <sub>1</sub>	6.518(4)	29.983(4)	5.531(5)	4	
L-Phe	191	P2 <sub>1</sub> 2 <sub>1</sub> 2 <sub>1</sub>	7.766(1)	22.470(4)	5.4823(9)	4	
BLG	263	P2 <sub>1</sub> 2 <sub>1</sub> 2 <sub>1</sub>	10.923(7)	15.783(3)	5.948(1)	4	
MLG	187	P2 <sub>1</sub>	6.0101(4)	7.176(5)	9.8528(6)	4	93.19
BLA	249	P2 <sub>1</sub> 2 <sub>1</sub> 2 <sub>1</sub>	7.995(3)	26.611(5)	5.348(7)	4	
DL-Val	143	Pca2 <sub>1</sub>	8.938(1)	10.207(2)	7.788(1)	4	
DL-Phe	191	Pna2 <sub>1</sub>	9.606(2)	6.376(2)	30.077(5)	4	
DL-Leu	157	P2 <sub>1</sub> /a	9.873(2)	5.641(3)	15.441(4)	4	105.4

**Fig. 25.4** Glycine NCA crystal**Fig. 25.5** L-Leucine NCA crystal

The molecular arrangements in the crystals of glycine NCA and L-leucine NCA are shown in Figs. 25.4 and 25.5. The factors determining the reactivity in the solid state were determined by comparing the crystal structures.

**Fig. 25.6** L-Leucine NCA molecular arrangement along *c*-axis in crystal



Glycine NCA was the most inactive NCA in the solid state. Figure 25.4 shows the crystal structure. Glycine NCA molecules form a dimer via two hydrogen bonds between  $-\text{NH}$  and  $-\text{C}=\text{O}$  groups; this structure suggests low reactivity. When glycine NCAs were polymerized in the solid state and in a heterogeneous system in acetonitrile, the  $\beta$ -structure of poly(glycine) was formed in both cases.

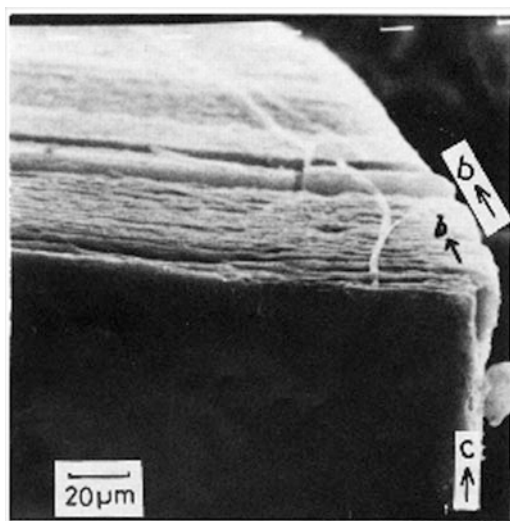
In the L-leucine NCA crystal, shown in Fig. 25.5, the NCA five-membered rings are in a layer and the side chains are in another layer. These layers are stacked alternately and form a sandwich structure. This sandwich structure is preferable for polymerization; the five-membered rings can react with each other in the layer. Infrared spectroscopy showed that the molecular conformations of poly(L-leucine) obtained in solid-state polymerization and acetonitrile are both  $\alpha$ -helices. Because of the bulky isobutyl group, poly(L-leucine) forms an  $\alpha$ -helix. The process of  $\alpha$ -helix formation in the crystal is considered to be as follows. L-Leucine NCA molecules rotate around an imaginary axis and react with each other to form an  $\alpha$ -helix along the *c*-axis, mainly in the crystal [17, 18]. Figure 25.6 shows the L-leucine NCA molecular arrangement along the *c*-axis in the crystal. The axis which the NCA molecules are considered to access is shown by a line with an arrow.

Figure 25.7 shows poly(L-leucine) obtained by the solid-state polymerization of an L-leucine NCA single crystal. The polymer lamellar plates are stacked perpendicular to the *b*-axis. This suggests that the polymerization proceeds at least in the *a*-*c* plane in the crystal. X-ray diffraction measurements showed that the polymerization proceeds mainly along the *c*-axis in the L-leucine NCA crystals before and after polymerization [17].

The crystal structures of L-alanine NCA and BLG NCA are shown in Figs. 25.8 and 25.9. A sandwich structure is not clearly seen in the L-alanine NCA, shown in Fig. 25.8. Formation of an  $\alpha$ -helix is less easy in this crystal. The crystal structure suggests that the reactivity of the L-alanine NCA crystal is lower than those of other reactive NCAs.

The sandwich structure is clearly seen in the BLG NCA crystal, shown in Fig. 25.9. The five-membered rings polymerize with each other in the layer

**Fig. 25.7** Poly(L-leucine)  
(scanning electron  
micrograph) obtained from  
NCA single crystal



**Fig. 25.8** L-Alanine NCA  
crystal

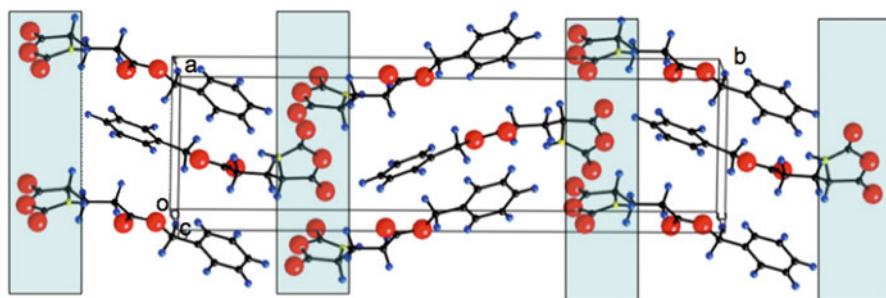
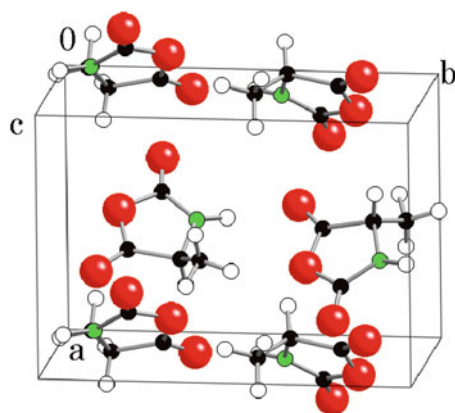


**Fig. 25.9** BLG NCA crystal

**Fig. 25.10** Model of PBLG  $\alpha$ -helix

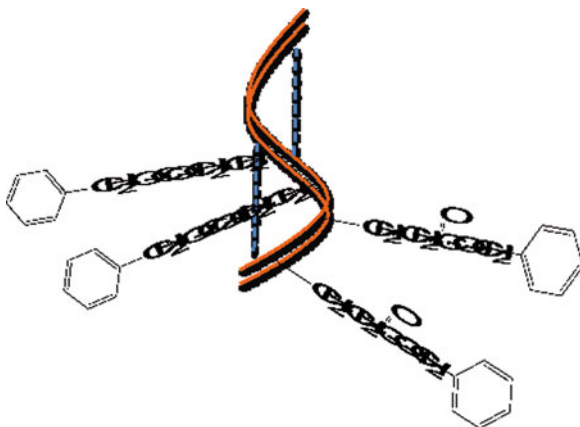
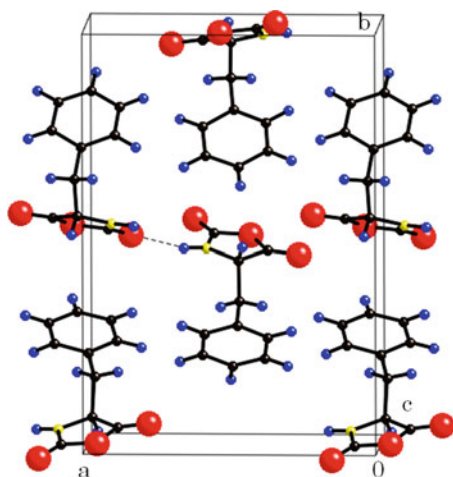


**Fig. 25.11** L-Phenylalanine NCA crystal



surrounded by squares in Fig. 25.9. BLG NCA is more reactive in the solid state than in solution, but PBLG forms an  $\alpha$ -helix in the crystal. The  $\alpha$ -helix should contain 3.6 amino acid residues in one pitch, 5.4 Å. When about ten BLG NCA molecules are polymerized stepwise, the resulting polymer makes an  $\alpha$ -helix [8, 19, 20]. BLG NCA molecules must move and rotate to form an  $\alpha$ -helix (see Fig. 25.10). Benzyl ester groups are bulky; therefore, this movement in the crystal is not easy. This suggests that the reactivity of BLG NCA in the solid state is lower than that of L-leucine.

The crystal structure of L-phenylalanine NCA is shown in Fig. 25.11. The sandwich structure is clearly seen in the phenylalanine NCA crystal, shown in Fig. 25.11. Although the stable conformation of poly(L-phenylalanine) is the  $\alpha$ -helix, poly(L-phenylalanine) obtained by NCA solid-state polymerization formed the  $\beta$ -structure. This conformation is considered to be dictated by the crystal structure.

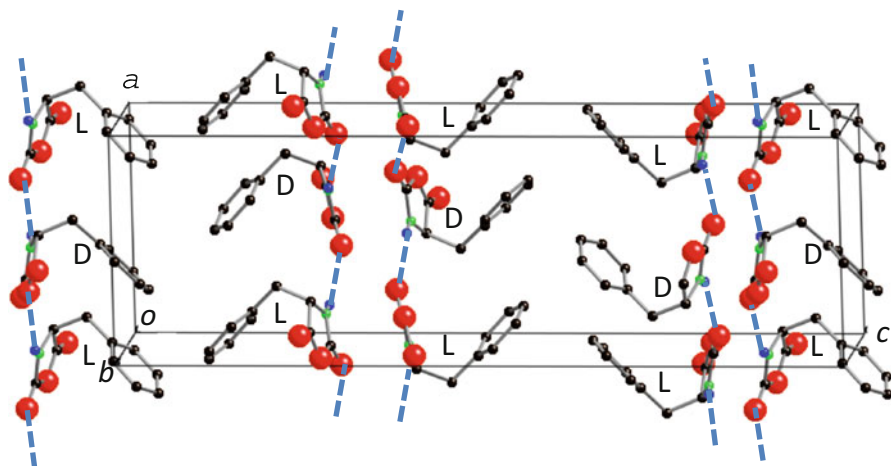


**Fig. 25.12** DL-Phenylalanine NCA crystal

The apparent activation energy ( $E_a$ ) of the solid-state polymerization of each L-amino acid NCA is larger than that in the solution or heterogeneous system, e.g.,  $E_a = 70.5$  kJ/mol in the solid-state polymerization of L-leucine NCA and  $E_a = 10.9$  kJ/mol in acetonitrile [17].

#### 25.4.1.6 Solid-State Polymerization of Racemic Amino Acid NCAs

In the crystallization of DL-amino acid NCAs, enantiomeric separation is often observed; for example, when the NCA prepared from DL-benzyl glutamate was crystallized, BLG NCA and BDG NCA crystallized separately. Single crystals of DL-phenylalanine, DL-valine, and DL-leucine NCAs were prepared and their crystal structures were determined [21–23].

Although DL-phenylalanine NCA polymerized very slowly in the heterogeneous state in acetonitrile, it polymerized very rapidly in the solid state [24, 25]. This suggests that the crystal structure is preferable for polymerization, and formation of the DL copolymer is expected. The polymerization of racemic amino acid NCAs will be studied in the future. Figure 25.12 shows the DL-phenylalanine NCA crystal.

## 25.5 Conclusion

The polymerization of amino acid NCAs initiated by a primary amine in hexane proceeds in the solid state. Many amino acid NCAs are more reactive in the solid state than in solutions. The high reactivity can be explained by the molecular arrangement in the crystal. Although some NCAs formed the  $\beta$ -structure polypeptide in the solid-state polymerization, they gave the  $\alpha$ -helix polypeptide in the polymerization in

solution or heterogeneous solution (in acetonitrile). The high reactivity in the solid state and the difference in the polymer conformation suggest a discovery of a new type topochemical polymerization. This solid-state polymerization is available for almost all of amino acid NCAs of which solution reactions are impossible. But, it is better to apply both of the solid state and solution or heterogeneous solution systems according to the purpose. When initiators are changed from primary amines to tertiary amines, the results become different.

## References

1. H.R. Kricheldorf, *Angew. Chem. Int. Ed.* **45**, 5752–5784 (2006)
2. H. Leuchs, *Chem. Ber.* **39**, 857–861 (1906)
3. M.D. Cohen, G.M. Schmidt, *J. Chem. Soc.* 1996–2000 (1964)
4. K. Kobayashi, N. Hayashi, *Kotai Yukikagaku (Solid State Organic Chemistry)* (Kagaku-dojin, Kyoto, 2009), pp. 172–176
5. G. Wegner, *J. Polym. Sci.* **B9**, 133 (1971)
6. G. Wegner, *Makromol. Chem. Phys.* **145**, 85 (1971)
7. Y. Iwakura, K. Uno, M. Oya, *J. Polym. Sci. A-1*(5), 2868 (1957)
8. H. Kanazawa, A. Inada, N. Kawana, *Polychar-14 World Forum Adv Mater* **242**, 104–112 (2006)
9. G. Kovacs, H. Morawetz, *J. Polym. Sci.* **A1**(4), 1553 (1966)
10. H. Kanazawa, Y. Matsura, N. Tanaka, M. Kakudo, T. Komoto, T. Kawai, *Bull. Chem. Soc. Jpn.* **49**, 954–956 (1976)
11. H. Kanazawa, Y. Matsura, N. Tanaka, M. Kakudo, T. Komoto, T. Kawai, *Acta Cryst.* **B32**, 3314–3315 (1976)
12. H. Kanazawa, Y. Ohashi, Y. Sasada, T. Kawai, *Bull. Chem. Soc. Jpn.* **51**, 2200–2204 (1978)
13. H. Kanazawa, Y. Ohashi, Y. Sasada, T. Kawai, *Bull. Chem. Soc. Jpn.* **51**, 2205–2208 (1978)
14. H. Kanazawa, Y. Ohashi, Y. Sasada, *Acta Cryst.* **C40**, 1094–1096 (1984)
15. H. Kanazawa, *Acta Cryst.* **C56**, 469–470 (2000)
16. H. Kanazawa, J. Magoshi, *Acta Cryst.* **C59**, 159–161 (2003)
17. H. Kanazawa, Y. Ohashi, Y. Sasada, T. Kawai, *J. Polym. Sci. Polym. Phys. Ed.* **20**, 1847–1862 (1982)
18. H. Kanazawa, *Mol. Cryst. Liq. Cryst.* **313**, 205–210 (1998)
19. H.J. Kanazawa, *Polymer* **33**, 2557–2566 (1992)
20. H. Kanazawa, A. Inada, *Joint Congress of ACTS-2014 and CGOM-2014*. Nara, Japan, *OC-CGOM11*, 2014, 17–20 June
21. Y. Takenaka, Y. Ohashi, H. Kanazawa, *Acta Cryst.* **C50**, 1950–1952 (1994)
22. H. Kanazawa, H. Uekusa, Y. Ohashi, *Acta Cryst.* **C53**, 1154–1156 (1997)
23. H. Kanazawa, *Acta Cryst.* **E59**, 1309–1311 (2003)
24. H. Kanazawa, *Mol. Cryst. Liq. Cryst.* **277**, 45–54 (1996)
25. H. Kanazawa, T. Kawai, *J. Polym. Sci. Polym. Chem. Ed.* **18**, 629–642 (1980)

# Chapter 26

## Topochemical Polymerizations and Crystal Cross-Linking of Metal Organic Frameworks

Kazuki Sada, Takumi Ishiwata, and Kenta Kokado

**Abstract** Topochemical polymerizations have been attracting continuous interest as one of the precise polymerizations in a confined space. However, it is still not easy for designing new monomers due to difficulty in designing and controlling the arrangement suitable for topochemical polymerization. In this chapter, we shortly review polymerization in a confined space and demonstrate recent advances in topochemical polymerizations, providing the molecular orientations for various topochemical polymerization monomers. Then, we propose a new type of topochemical polymerization by use of metal organic framework (MOF). MOF is nano-porous crystalline materials constructed by metal ions and rigid organic ligands equipped with two or more ligation sites to form robust 3D host framework with nano-pores. The void space between them is wide and stable, which prompted us to investigate cross-linking of the organic ligands as the host monomers by the external guest monomers by means of two chemical reactions: (1) azide-tagged MOF (**AzMOF**) cross-linked by multi-alkyne cross-linkers via click reaction and (2) cyclodextrin MOF (**CDMOF**) cross-linked by diglycidyl ethers. They should be new crystalline-state polymerization, because the cross-linking took place without any movement of the host monomers in the open-host framework.

**Keywords** Topochemical polymerization • Confined space • Metal organic framework (MOF) • Precise polymerization • Inclusion polymerization • Click reaction • Cyclodextrins • Crystal cross-linking method

---

K. Sada (✉) • T. Ishiwata • K. Kokado

Department of Chemistry, Graduate School of Science, Hokkaido University, Kita 10, Nishi 8, Kita-ku, Sapporo 060-0810, Japan

Graduate School of Chemical Sciences and Engineering, Hokkaido University, Kita 10, Nishi 8, Kita-ku, Sapporo 060-0810, Japan

e-mail: [sadatcm@mail.sci.hokudai.ac.jp](mailto:sadatcm@mail.sci.hokudai.ac.jp); [takumi@frontier.hokudai.ac.jp](mailto:takumi@frontier.hokudai.ac.jp); [kokado@sci.hokudai.ac.jp](mailto:kokado@sci.hokudai.ac.jp)

## 26.1 Introduction: Polymerization in a Confined Space

Development of preparative methods for polymers with highly controlled polymer structures including stereospecificity or stereoregularity has been extensively investigated and well documented as precise polymerizations [1]. One of the several approaches for them is the polymerizations in a confined space, where the propagating species and monomers are disrupted from free rotation and diffusion, taking restricted orientation and movement so that the stereochemistry of the resulting polymers is often controlled [2]. The specificity of the polymerization in the confined space could be generally understood from viewpoint of the “relativity” in size, i.e., size ratio of reaction space/monomer, and classified into the following three categories as shown in Fig. 26.1.

The first one is solution polymerization shown as (i) in Fig. 26.1, i.e., the size ratio is infinite, so that the reaction space have no effects on the propagating reaction. Namely, free rotation of the monomers and encountering direction of the monomer to the propagating species result in no selectivity or specificity. The versatility of the monomers is very wide due to no limitation for polymerization. Thus, the monomers generally provide the polymers without selectivity. Since the control around the propagating species should play a key role as the precise polymerizations, the vast number of the research have been concentrating for developing the new polymerization catalysts [1].

In the second type, called as inclusion polymerization and shown as (ii) in Fig. 26.1, which is the typical example of the confined polymerization and a kind of crystalline-state polymerization, the size ratio is more than one, but not too large [2–4]. The polymerization occurs in the one-dimensional cavity constructed by organic or inorganic host compounds in the crystalline state. The surface and the size of the cavity strongly affect the polymerization of the monomers, because the propagation occurs by movement of the monomers along the cavity. When size ratio is close to one, the monomers are arranged in one-dimensional array, and the polymerizations with high specificity are often achieved due to the restricted orientation of the monomers in the confined space. Increasing the size ratios lowers the selectivity of

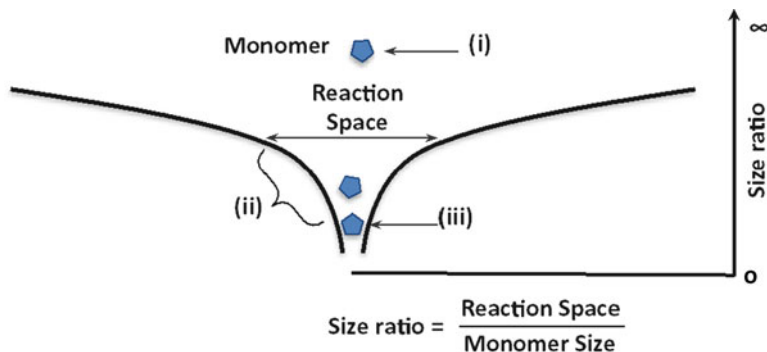


Fig. 26.1 Polymerization in a confined space

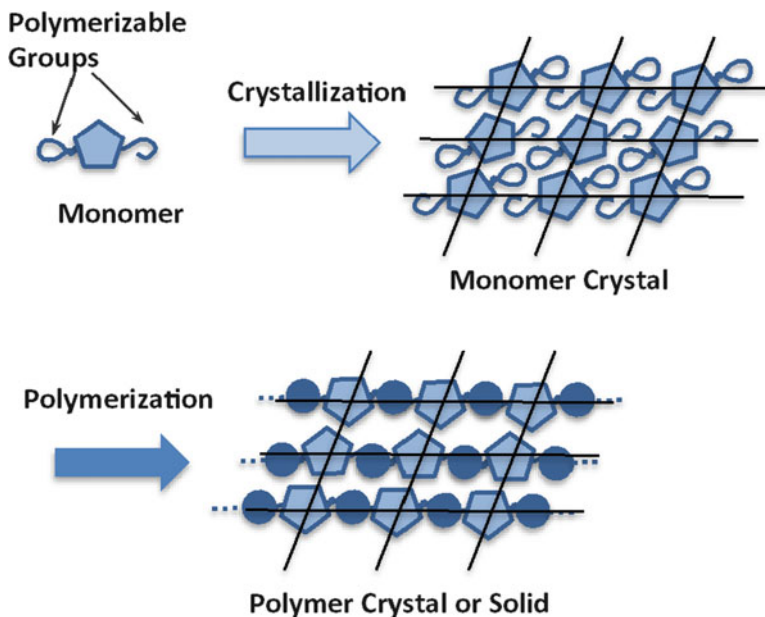


Fig. 26.2 Concept for topochemical polymerizations

the polymerization. With respect to versatility of monomers, increase of size ratio increases the numbers of the monomers that can be polymerized in the host cavity [2]. Enough large host cavity compared to the monomers provides the low selectivity, because most of the monomers are not affected by the surface of the host cavity. It should be similar to those of the solution polymerization without polymerization catalysts. Thus, size ratio plays a key role in designing the inclusion polymerization.

The third class is topochemical polymerization shown as (iii) in Fig. 26.1, where size ratio is substantially one. In this polymerization, the crystalline monomers transform to the polymers without change of crystallinity. As the confined polymerizations, the monomers themselves construct their own confined space. Movement of the monomers is highly restricted due to the crystalline state, and orientation and rotation of the monomers are perfectly fixed in the crystalline state as shown in Fig. 26.2. The polymerizations generally are triggered by the external stimuli such as light, heat, and  $\gamma$ -ray, and the propagating reaction occurs without movement of the center of gravity of the monomers. As expected, the polymerization selectivity is generally high due to the restricted orientations of the monomers. However, all the compounds with identical polymerizable group cannot always provide the topochemical polymerizations, because the polymerizations are governed by the crystal structures. Therefore, size ratio should play a key role in versatility and selectivity of the polymerization.

In this chapter, we discuss our new idea of “crystal cross-linking method” as a new type of topochemical polymerization, after reviewing briefly on the topochemical polymerizations.

## 26.2 Recent Advances of Topochemical Polymerizations

Figure 26.3 summarizes typical monomers for topochemical polymerizations. Concept of topochemical polymerization was first introduced in 1960s by Wegner in his research on the anisotropic polymerization of diacetylene monomers (Fig. 26.3a) in the crystalline state [5], followed by [2 + 2] photodimerization polymerization of 2,5-distyrylpyrazine (Fig. 26.3b) investigated by Hasegawa [6]. Definition of topochemical polymerization is a polymerization of monomer without movement of its center of gravity in the crystal lattice during polymerization process as shown in Fig. 26.2. Minimum movement is allowed only around the polymerizable group, and the rest remains static. In some cases, the change of the molecular structure from the monomer to the polymer can be monitored by X-ray crystallography in the atomic resolution. Accumulation of crystallographic data for the monomers and the unreactive related compounds having the same polymerizable group reveals specific steric requirement suitable for topochemical polymerizations, especially distance and orientation of the polymerizable group in the crystalline state. Clarification of the steric requirement in each topochemical polymerizable group should be the first step to understanding and designing topochemical polymerization. The following section (1) demonstrates the topochemical polymerization monomers and the steric requirements of some monomers appeared in the recent literature and (2) accounts for their topochemical polymerization abilities.

Diacetylene compounds are the most popular monomer that proceeds to topochemical polymerization and further are applied to polymerization in various supramolecular assemblies [7]. The steric requirement is one-dimensional stacking of the diacetylene groups in translational positions around 4.9 Å, and the inclination angles of the diacetylene axes to the packing axis are about 45° [5, 8]. In this structure, the diacetylene groups are packed closely in a rodlike assembly, and the polymerization occurs along this direction. The minimum movement of the reactive carbon atoms to poly(diacetylene) structure with alternation of double bond and triple and no movement of the non-polymerizable substituent group provide efficient polymerization even in the crystalline state. Studies on the topochemical polymerizations of diacetylenes have been already shifted from random screening to rational design with the aid of formation of host–guest cocrystals by crystal engineering [9]. Unique poly(diacetylene) that consists of only iodine atoms and carbon atoms was prepared [10]. Extension of the diacetylene monomers to triacetylenes was demonstrated successfully by Lauher and Fowler. They reported the elegant design of the 1,6-polymerization of a triacetylene by the formation of the host–guest crystals (Fig. 26.3c) [11]. The triacetylene moiety arranges in the translational distance (7.3 Å) by the one-dimensional hydrogen-bond network. This arrangement guarantees the full packing of the triacetylene groups by van der Waals interaction. The  $\gamma$ -ray irradiation yielded the poly(triacetylene) by selective 1,6-polymerizations.

The topochemical polymerizations of dienes (Fig. 26.3d) were explored by Matsumoto et al. in the 1990s [12]. The extensive X-ray crystallographic studies

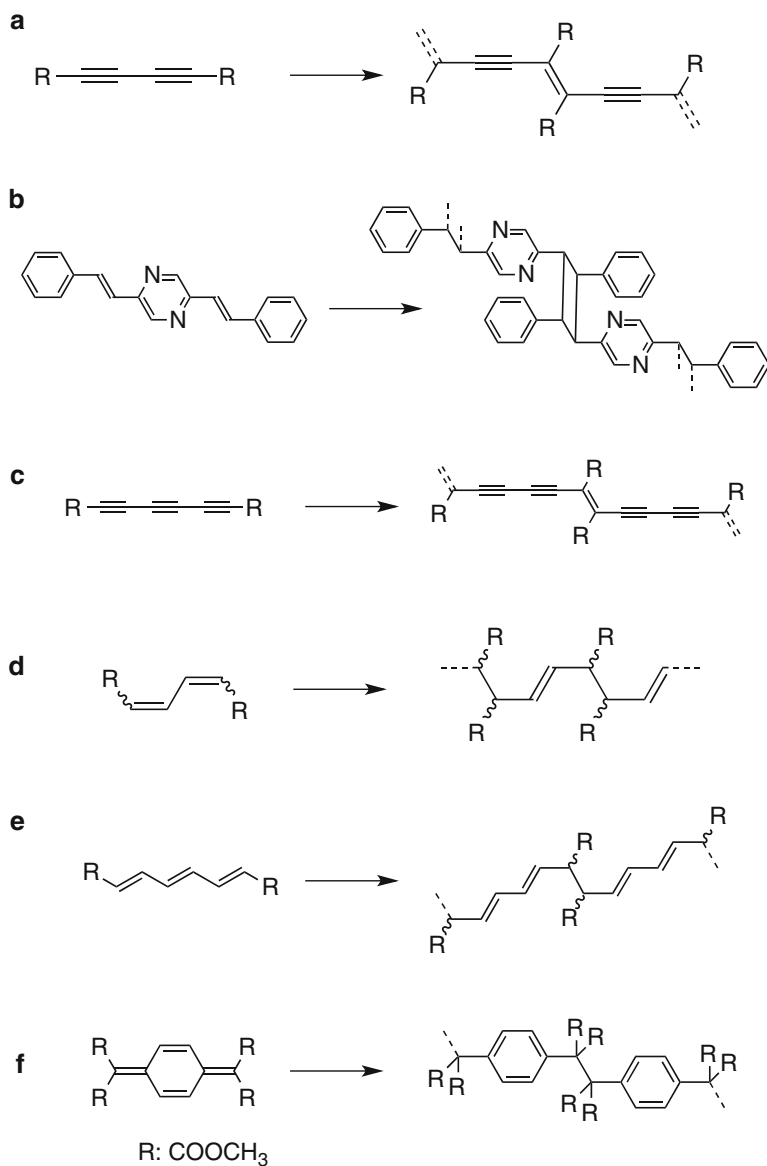


**Fig. 26.3** Monomers for topochemical polymerization and their polymers; **(a)** diacetylene, **(b)** 2,5-distyrylpyrazine, **(c)** triacetylene, **(d)** diene, **(e)** triene, **(f)** *p*-quinodimethane, **(g)** phenylacetylene, **(h)** diol compound, **(i)** clickable sugar compounds, **(j)** bis-thymine, and **(k)** trigonal prismatic monomer

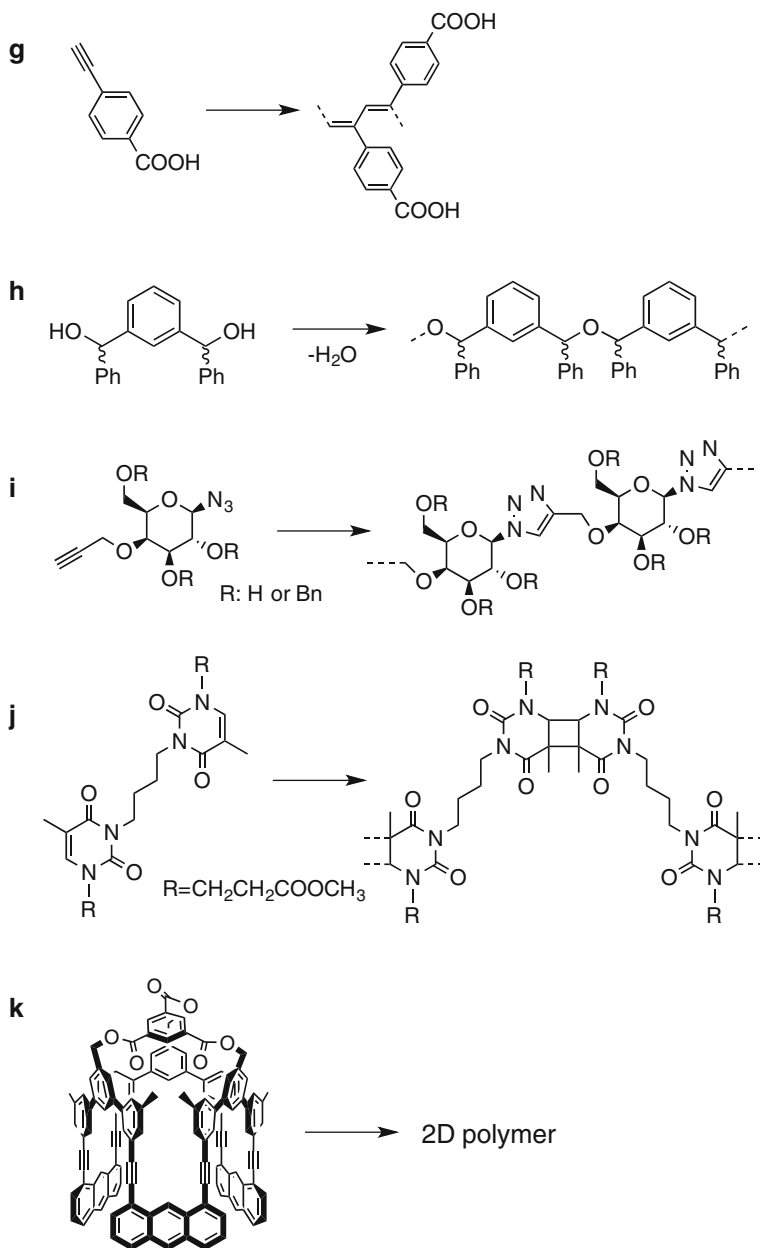


Fig. 26.3 (continued)

clearly revealed that the steric requirement of dienes is face-to-face stacking of the diene groups to form a one-dimensional array with the translational distance with 5 Å and the inclination angles with 30–60° [13]. In this orientation, the intermolecular closest distance between the diene carbon atoms is just 3.5 Å similar to those of diacetylene compounds. The steric requirement for the dienes is much more severe than that for the diacetylenes, because isotropic nature along the C–C triple bond would provide more stacking orientations than the face-to-face arrangement of the C–C double bond in the crystalline state. The most fruitful result is that geometrical isomerism (*cis* or *trans*) of the monomers and the controlled stacking fashion (translational or alternate) of the dienes moiety in the crystal structures perfectly control the stereoregularity of the resultant polymers [14]. Topochemical polymerization of bis-indene-dione derivatives was recently discovered. This system is quite similar to the diene topochemical polymerization, but the extension of p-conjugation of the monomer enabled polymerization triggered by visible light and quantitative depolymerization by thermal stimuli [15]. Lauher and Fowler demonstrated the 1,6-polymerization of triene monomer accidentally [16]. However, they revealed that the steric requirement for triene monomers is found to be close to that of the triacetylene monomers (Fig. 26.3e). The translational distance is 7.2 Å and the inclination angle is 34°, and additionally, the face-to-face stacking of the triene moieties was also required.

*p*-Quinodimethane was introduced as another topochemical polymerizable group by Itoh and coworkers (Fig. 26.3f). They reported the solid-state isomerization polymerization induced by photo, heat, and  $\gamma$ -ray irradiation [17, 18]. X-ray crystallographic studies revealed that the reactive monomer has face-to-face stacking with slight offset along the longer molecular axis. The translational stacking distance is around 7.0 Å, and the inclination angles of the quinodimethane axes to the packing axis are about 30°. This steric requirement needs much longer translational stacking distance than those of dienes and diacetylenes and slightly shorter than the triene and triacetylene. This is attributed to the quinodimethane moiety regarded as a kind of trans–trans fused triene monomer, which transforms to the phenyl group after isomerization polymerization.

Vinyl and acetylene monomers have not been so investigated with respect to crystalline-state polymerization, because the close packing of vinyl and acetylene monomers with shorter translation distances (ca. 2.8 Å) has been required for topochemical polymerization. However, Foxmann et al. reported the crystalline-state-controlled polymerization of a substituted phenylacetylene with high reactivity (Fig. 26.3g) [19]. In the crystalline state, the molecular packing of the acetylene groups is in parallel arrangement, and the orientation is suitable for the resultant poly(acetylene) structures. However, the distance between the monomers is longer than that of the expected repeating distances.

Some new polymerizable groups were introduced. Diol compounds treated with strong acid in the solid state induced the formation of poly(ether)s (Fig. 26.3h) [20]. High reactivity compared with that in the solution should be caused by the preorganized crystal structures and the high concentration of the monomers in the absence of solvents. This should be the crystalline lattice-controlled process.

Another recent important example for topochemical polymerization is based on click reaction of the sugar derivative with both acetylene and azide group (Fig. 26.3i) by Sureshan et al. [21, 22]. Intermolecular click reaction between the azide group and the acetylene group of the monomer took place to yield polymer crystals. This example is the first topochemical polymerization for polyaddition of the two different reactive groups. Sato et al. extensively reported topochemical polymerization of bis-thymine derivatives via crystalline state [2 + 2] photodimerization (Fig. 26.3j). The double bonds in the thymine groups are stacked each other within 4.0 Å in the crystalline state, which provides photodimerization polymerization [23]. More recently, elegantly designed new monomers for topochemical polymerization were reported by Sakamono et al. [24]. Their design is based on the trigonal prismatic molecular structure with three anthrance-acetylene moieties in each face [4 + 2]. Photochemical reaction between the anthrance and the acetylene provides well-defined two-dimensional polymers (Fig. 26.3k).

For understanding topochemical polymerization abilities, the steric requirements of the several new monomers have been demonstrated. In all the cases, the packings of the monomers in the crystalline state are quite similar to the expected packing of the resultant polymers. This similarity induces the minimum movement of the atoms during the polymerization, and this should be the first principle for topochemical polymerization systems. Moreover, the new trend of topochemical polymerization depends on the utility of cocrystals such as host–guest crystals or salts. This strategy has an advantage over screening of functional crystalline materials due to combinatorial approaches and easy preparations of the related molecules. This should provide an easy access to revealing the steric requirements of the polymerizable moieties and their crystal engineering. Especially, two recent unique topochemical polymerization systems, [4 + 2] or [2 + 2] photodimerization reactions and click reaction, clearly indicate that supramolecular control of the orientation of the reactive groups toward intermolecular direction in the crystalline state should play a crucial role in developing new topochemical polymerizations. They should expand the potential of topochemical polymerization from polyaddition of a single conventional polymerizable functional group such as diacetylene and diene to that of the chemical reaction between the two different reactive groups in the molecular structure, when these reactive groups have orientation suitable for polymerizations. However, the precise control of two or more reactive groups in the crystalline state is not so easy.

### 26.3 Crystal Cross-Linking as Topochemical Polymerization

Reviewing of the recent advances in topochemical polymerizations suggests that one of the most significant obstacles for designing topochemical polymerization is unpredictable crystal structure suitable for new monomers due to the severe restriction of the steric environments of the polymerizable groups in the crystalline state. In order to overcome this difficulty, we recently proposed a new type of crystalline-state polymerization, so-called crystal cross-linking method as schemat-

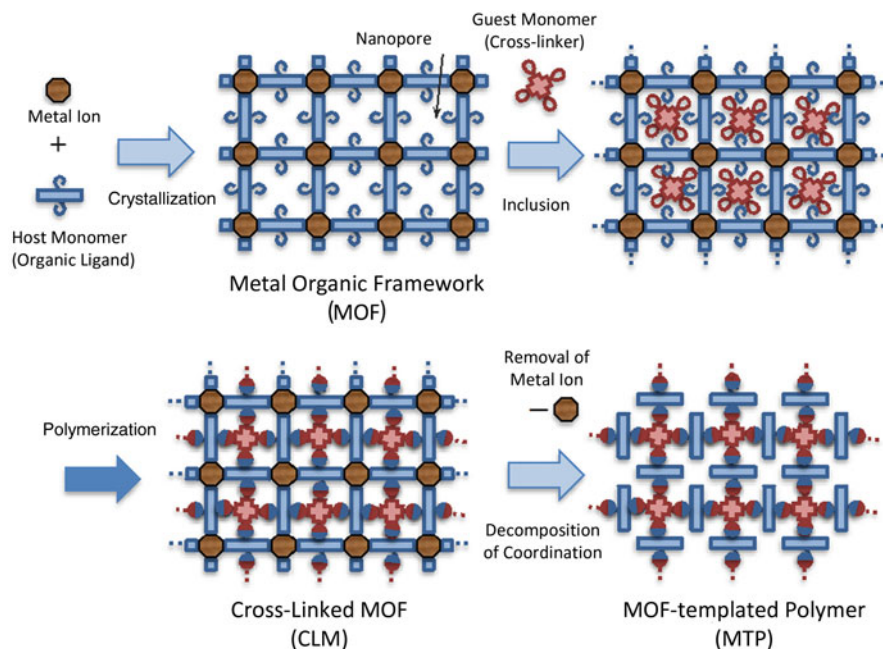
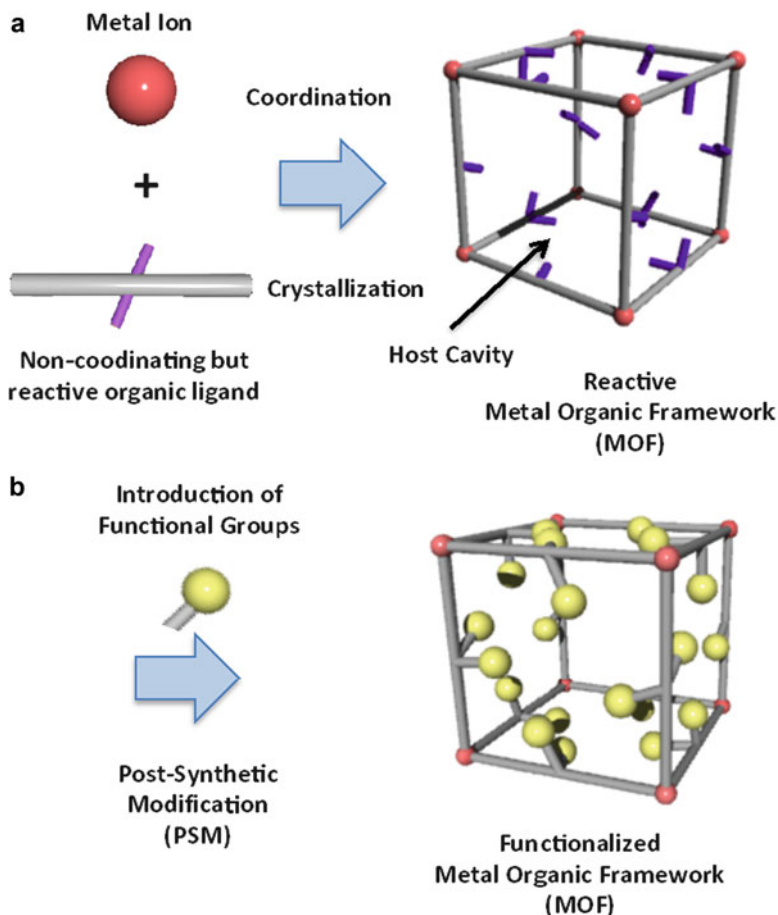


Fig. 26.4 Scheme of crystal cross-linking method

ically shown in Fig. 26.4. Our design for crystalline-state polymerization is based on polymerization between the host monomers that construct open three-dimensional frameworks and the guest monomers that are included in the open cavity of the host framework. In other words, for copolymerization between two monomers, one of them is fixed periodically along the crystal axes as the wall of the open framework, and the other is mobile in the host cavity and can react with the host monomers. When either of them contains bivalent or more reactive groups, they should form three-dimensional network structures by cross-linking of the whole molecules that construct the crystal. If the polymerization or cross-linking reactions takes place without decomposition of the open-host framework, it should be a new kind of topochemical polymerization, because the host monomers need not moving during the polymerization process.

Metal organic frameworks (MOF) or porous coordination polymers (PCP) are nanoporous crystalline materials constructed by metal ions and rigid organic ligands to form robust 3D network structures in the crystalline state [25]. It is well known that they have robust open frameworks. Extensive studies have been focused on molecular design of the open 3D network structures and their applications such as catalysis, storage, separation, and nanomaterials [26, 27]. Moreover, the chemical reaction takes place in the organic ligands without loss of the crystallinity of MOF, which are known as post-synthetic modification (PSM) of MOF shown in Fig. 26.5 [28]. With the aid of PSM, we recently reported cross-linking of the organic ligands in the MOF by the two different ways: (1) azide-tagged MOF (AzMOF) cross-



**Fig. 26.5** Concept for (a) reactive metal organic framework (MOF) and (b) post-synthetic modification (PSM) of MOF

linked by multi-alkyne cross-linkers via click reaction [29] and (2) cyclodextrin MOF (**CDMOF**) cross-linked by diglycidyl ethers via nucleophilic ring-opening reaction of epoxide [30].

The first example for crystal cross-linking method of MOF was click reaction between the terphenyl-type organic ligands with two azide groups in the azide-tagged MOF crystal (**AzMOF**) and the guest monomer (**CL4**) with four acetylene groups as shown in Fig. 26.6. **AzMOF** was subjected to reaction with **CL4** under standard click reaction conditions at 80 °C in the presence of Cu (I) as the catalyst. The cross-linked MOF (**CLM**) crystals were obtained. The scanning electron micrographic (SEM) and optical microscope observations of **CLM** revealed the cubic and transparent crystal with smooth surfaces and the sharp edges similar to those of **AzMOF** crystals, which suggest the preservation of shape of the crystals. Judging from the IR spectral change, all the azide groups on the organic linkers of

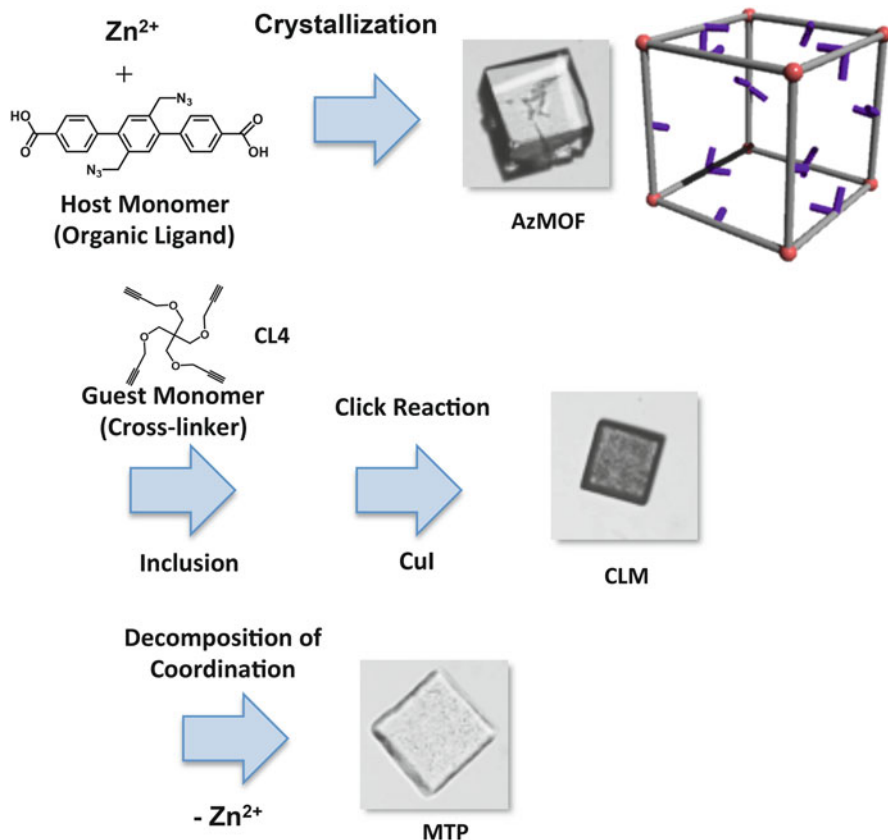


Fig. 26.6 Crystal cross-linking of azide-tagged MOF (AzM)

**AzMOF** crystals were consumed by the click reaction. X-ray diffraction (XRD) patterns of the crystals before (**AzMOF**) and after (**CLM**) the click reaction showed essentially identical peaks, which implies the topochemical polymerization of the organic ligands. In order to clarify the cross-linking of organic ligands, subsequently, the coordination of carboxylate anion to zinc(II) ion was decomposed by acidification. The cubic crystals of **CLM** turned to be cubic gels, MOF-templated polymer (**MTP**). **MTP** is practically insoluble in any solvents, and the shape as well as the surface morphology is preserved after the hydrolysis reaction. XPS analysis clearly illustrated the absence of the peaks assigned to Zn(II), indicating complete removal. No apparent diffraction peaks in XRD were observed after decomposition, indicating that **MTP** had no crystallinity. Therefore, the crystal cross-linking method provided the conversion of the crystalline material to amorphous soft matter without change of the shape. Moreover, Cu(II) and Zr(IV) ions provided colorless green truncated octahedral and colorless octahedral MOF crystals, respectively. They were successfully cross-linked under the same conditions by **CL4**. XRD

patterns of the cross-linked crystals showed essentially identical peaks to those of the starting MOF crystals. Moreover, after the acid treatment to transform to **MTP**, all the crystals became insoluble network polymers and had well-defined polyhedral shape originated from the MOF crystals.

Another example of the crystal cross-linking was achieved from cyclodextrin MOF (**CDMOF**) prepared from potassium hydroxide and  $\gamma$ -CD [31]. Cross-linking of  $\gamma$ -CDs as the monomer in **CDMOF** crystals was carried out by treatment of ethylene glycol diglycidyl ether (**L**) as the other monomers through nucleophilic ring-opening of epoxy groups induced by hydroxyl or alkoxy groups of  $\gamma$ -CD as shown in Fig. 26.7. After incubation of the cubic crystals of **CDMOF** in

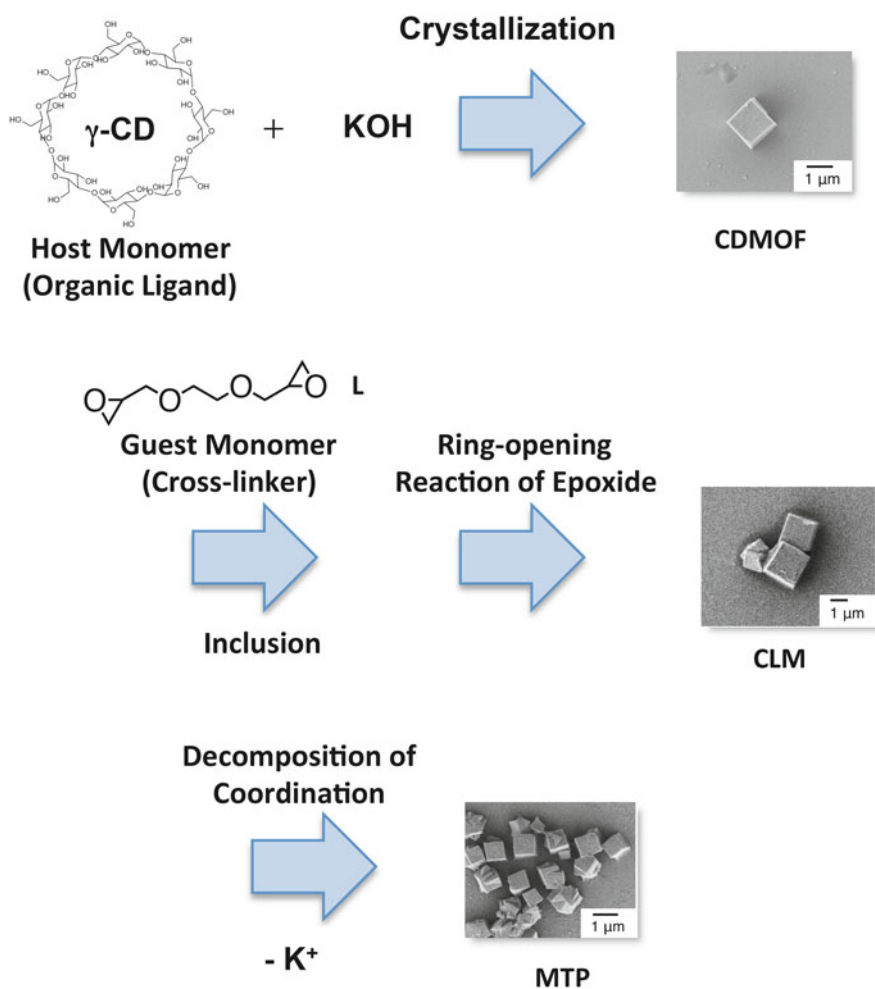


Fig. 26.7 Crystal cross-linking of cyclodextrin MOF (CDMOF)

ethanol solution of **L**, the cross-linked **CDMOF** was formed. XRD patterns of the crystals before and after the cross-linking reaction showed essentially identical peaks. Therefore, cross-linking reaction did not affect the MOF network structure, which also implies the topochemical polymerization of  $\gamma$ -CD. The cross-linking was confirmed by soaking in the solvent that decomposed **CDMOF** crystals. The resulting cubic material became practically insoluble and swollen in water, and the original cubic shape of the **CDMOF** maintained even after soaking. These results clearly indicated the cross-linking of the organic ligands by the guest monomers in the open-host framework, followed by degradation of coordination bonds to form network polymers with well-defined cubic shape. Further investigation for controlling the sizes of **CDMOF** successfully provides **CDMOF** from a few hundred nanometers to millimeters in size, which yielded the cubic polymer gels with a wide range of sizes. Therefore, the size variation of the **CDMOF** crystals enabled us to control the size of the cubic polymer gels.

## 26.4 Concluding Remark

In summary, using MOF crystals as templates enable us to prepare a wide variety of polyhedral network polymers with controlled polyhedral shapes. Therefore, this method can open a new horizon for the preparation of micro- and nanosized network polymers with well-defined shapes. They could provide mesoscopic building blocks with a soft interface for constructing complex architectures by self-organization or be used in biomedical applications such as drug carriers and cell-support materials. With respect to topochemical polymerization, these examples for crystal cross-linking should be a new type of topochemical polymerization, because the host monomers are fixed in the crystalline state with no movement. The possible chemical reactions between the host monomers and the guest monomers due to large three-dimensional cavities of MOF should provide various crystal cross-linking of MOFs and expand the versatility of topochemical polymerizations. Moreover, we believe that crystal cross-linking will be one of the most promising routes for creation of the polymer networks with well-defined repeating units in the network structure, i.e., “ideal network polymers,” which have never been prepared until now.

## References

1. K. Satoh, M. Kamigaito, *Chem. Rev.* **109**, 5120–5156 (2009)
2. M. Miyata, in *Polymerization in Organized Media*, ed. by C.M. Paleos (Gordon & Breach, New York); M. Miyata, in *Comprehensive Supramolecular Chemistry*, vol. 10, ed. by J.L. Atwood, J.E.D. Davies, D.D. MacNicol, F. Vögtle, J.-M. Lehen (Pergamon, Oxford, 1996), pp. 557–582
3. T. Uemura, S. Horiike, S. Kitagawa, *Chem. Asian. J.* **1**, 36–44 (2006)
4. K. Tajima, T. Aida, *Chem. Commun.* **42**, 2399–2414 (2000)

5. G. Wegner, *Z. Naturforsch. B.* **24b**, 824–832 (1969); G. Wegner, *Pure Appl. Chem.* **49**, 443–454 (1977)
6. M. Hasegawa, *Chem. Rev.* **83**, 507–518 (1983); M. Hasegawa, *Adv. Phys. Org. Chem.* **30**, 117–171 (1995)
7. R. Jelinek, M. Ritenberg, *RSC Adv.* **3**, 21192–21201 (2013)
8. V. Enkelmann, *Adv. Polym. Sci.* **63**, 91–136 (1984)
9. J.W. Lauher, F.W. Fowler, N.S. Goroff, *Acc. Chem. Res.* **41**, 1215–1229 (2008)
10. A. Sun, J.W. Lauher, N.S. Goroff, *Science*. **312**, 1030–1034 (2006); N.S. Goroff, S.M. Curtis, J.A. Webb, F.W. Fowler, J.W. Lauher, *Org. Lett.* **7**, 1891–1983 (2005)
11. J. Xiao, M. Yang, J.W. Lauher, F.W. Fowler, *Angew. Chem. Int. Ed.* **39**, 2132–2135 (2000)
12. A. Matsumoto, T. Matsuura, S. Aoki, *J. Chem. Soc. Chem. Commun.* **23**, 1389–1390 (1994)
13. A. Matsumoto, K. Sada, K. Tashiro, M. Miyata, T. Tsubouchi, T. Tanaka, T. Odani, S. Nagahama, T. Tanaka, K. Inoue, S. Saragai, S. Nakamoto, *Angew. Chem. Int. Ed.* **41**, 2502–2505 (2002); A. Matsumoto, *Top. Curr. Chem.* **254**, 263–305 (2005)
14. S. Nagahama, T. Tanaka, A. Matsumoto, *Angew. Chem. Int. Ed.* **43**, 3811–3814 (2004)
15. L. Dou, Y. Zheng, X. Shen, G. Wu, K. Fields, W.-C. Hsu, H. Zhou, Y. Yang, F. Wudl, *Science* **343**, 272–277 (2014)
16. T. Hoang, J.W. Lauher, F.W. Fowler, *J. Am. Chem. Soc.* **124**, 10656–10657 (2002)
17. T. Itoh, S. Nomura, T. Uno, M. Kubo, K. Sada, M. Miyata, *Angew. Chem. Int. Ed.* **41**, 4306–4309 (2002)
18. T. Itoh, T. Suzuki, T. Uno, M. Kubo, N. Tohnai, M. Miyata, *Angew. Chem. Int. Ed.* **50**, 2253–2256 (2011)
19. J.M. Njus, D.J. Sandman, L. Yang, B.M. Foxman, *Macromolecules* **38**, 7645–7652 (2005)
20. T. Sasaki, K. Hayashibara, M. Suzuki, *Macromolecules* **36**, 279–281 (2003)
21. A. Pathigoolla, R.G. Gonnade, K.M. Sureshan, *Angew. Chem. Int. Ed.* **51**, 4362–4366 (2012)
22. A. Pathigoolla, K.M. Sureshan, *Angew. Chem. Int. Ed.* **52**, 8671–8675 (2013)
23. P. Johnston, D. Wheldale, C. Braybrook, K. Sato, *Polym. Chem.* **5**, 4375–4384 (2014)
24. P. Kissel, R. Erni, W.B. Schweizer, M.D. Rossell, B.T. King, T. Bauer, S. Götzinger, A.D. Schlüter, J. Sakamoto, *Nat. Chem.* **4**, 287–291 (2012)
25. H. Furukawa, K.E. Cordova, M. O’Keeffe, O.M. Yaghi, *Science* **341**, 974 (2013). doi:[10.1126/science.1230444](https://doi.org/10.1126/science.1230444)
26. S. Kitagawa, R. Kitaura, S. Noro, *Angew. Chem. Int. Ed.* **43**, 2334–2375 (2004)
27. G. Ferey, *Chem. Soc. Rev.* **37**, 191–214 (2008)
28. K.K. Tanabe, S.M. Cohen, *Chem. Soc. Rev.* **40**, 498–519 (2011)
29. T. Ishiwata, Y. Furukawa, K. Sugikawa, K. Kokado, K. Sada, *J. Am. Chem. Soc.* **135**, 5427–5432 (2013)
30. Y. Furukawa, T. Ishiwata, K. Sugikawa, K. Kokado, K. Sada, *Angew. Chem. Int. Ed.* **51**, 10566–10569 (2012)
31. R.A. Smaldone, R.S. Forgan, H. Furukawa, J.J. Gassensmith, A.M.Z. Slawin, O.M. Yaghi, J.F. Stoddart, *Angew. Chem. Int. Ed.* **49**, 8630–8634 (2010)

**Part VII**  
**Photoinduced Behavior**

# Chapter 27

## Photoinduced Mechanical Motion of Photochromic Crystalline Materials

Seiya Kobatake and Daichi Kitagawa

**Abstract** Photochromic compounds undergo a photochemically reversible transformation reaction between two isomers. Such molecules in organic crystals, which are regularly oriented and fixed in the crystal lattice, may be potentially useful for optoelectronic devices, such as optical memory, photoswitchable color filter, photoswitchable polarizer, photomechanical actuator, and so on. This chapter has focused on photochromism of the diarylethene crystals and their photomechanical phenomena, such as crystal bending and twisting.

**Keywords** Photochromism • Photomechanical • Switching • Diarylethene • Bending

### 27.1 Introduction

A phenomenon of chromatic change upon photoirradiation is referred to as photochromism. Photochromic compounds, which show photochromism, have potential for application to ophthalmic lenses, optical memory, photooptical switching, displays, nonlinear optics, and so on. In most cases, compounds which show photochromism in the crystalline phase are rare because of their large geometrical change by photochromic reactions. For example, most of azobenzene and spiropyran derivatives cannot undergo photochromism in the crystalline phase. Typical photochromic compounds that show photochromism in the crystalline phase are known for paracyclophanes [1], triarylimidazole dimer [2, 3], diphenylmaleronitrile [4], aziridines [5], 2-(2,4-dinitrobenzyl)pyridine [6–9], *N*-salicylideneanilines [10–13], triazines [14], and diarylethenes [15–18]. In many cases, their photogenerated isomers are thermally unstable (T-type). Therefore, two states cannot be kept even at room temperature. On the other hand, the diarylethene derivatives show thermally stable (P-type) photochromic reactions even in the crystalline phase. The P-type photochromic compounds have potential for application to not only

---

S. Kobatake (✉) • D. Kitagawa  
Graduate School of Engineering, Osaka City University, Osaka, Japan  
e-mail: [kobatake@a-chem.eng.osaka-cu.ac.jp](mailto:kobatake@a-chem.eng.osaka-cu.ac.jp)

optical memory, photoswitching, and display but also photomechanical actuator. This chapter focuses on photochromism of the diarylethene crystals and their photomechanical phenomena, such as crystal bending and twisting.

## 27.2 Photochromism of Diarylethene Crystals

Some diarylethene derivatives undergo photochromic reactions in the crystalline phase as well as in solution. Upon irradiation with ultraviolet (UV) light, the colorless crystals change to yellow, red, blue, or green, depending on the molecular structure of diarylethenes [19–22]. The colors remain stable so far as being stored in the dark, but the colors disappear by irradiation with visible light. When diarylethene molecules are fixed in the antiparallel conformation and the distance between the reactive carbons is less than 4 Å, the photochromic reaction in the crystalline phase can proceed with the photocyclization quantum yield of unity [23, 24]. The photoinduced coloration/decoloration cycles of the crystals can be repeated more than  $10^4$  times while maintaining the shape of the crystals. A lot of researches on photochromism of diarylethene crystals have been reported so far such as multicolor photochromism [25–27], dichroism under polarized light [15, 16], fluorescence [28, 29], three-dimensional optical memory [28], diastereoselective cyclization [30, 31], selective photochromic reaction under polarized light [32, 33], theoretical study [34, 35], Raman spectroscopic study [36], nanostructures [37–42], and molecular motion observed by X-ray crystallography [43–45]. From the research on molecular motion observed by X-ray crystallography, it was revealed that the unit cell dimension was changed according to the photochromic reaction because of the decrease in the molecular volume by transformation from the opening isomers to the closed-ring isomers. In 2001, reversible surface morphology changes were reported as shown in Fig. 27.1 [46]. The surface morphology on single crystal of 1,2-bis(2,4-dimethyl-5-phenyl-3-thienyl)perfluorocyclopentene (**1**) was observed by atomic force microscope (AFM) before and after photoirradiation. Upon irradiation with UV light to the (100) crystalline surface, steps newly appeared as shown in Fig. 27.1a. The height of the steps is about 1 nm, which corresponds to one molecular layer. The steps can be erased by visible light irradiation. The surface morphology change is attributed to photoinduced contraction of the long axis of each molecule regularly packed in the single crystal. Moreover, when UV irradiation was carried out to the (010) crystalline surface, valleys were newly observed as shown in Fig. 27.1b. The valleys can be erased by irradiation with visible light. Such morphological changes can be explained by molecular structural changes of diarylethenes due to the photochromic reaction. These results indicated that the small molecular structural change may induce macroscopic crystal shape change and open the door of the research field on photomechanical crystals which can work without any direct contact or electrical wires.

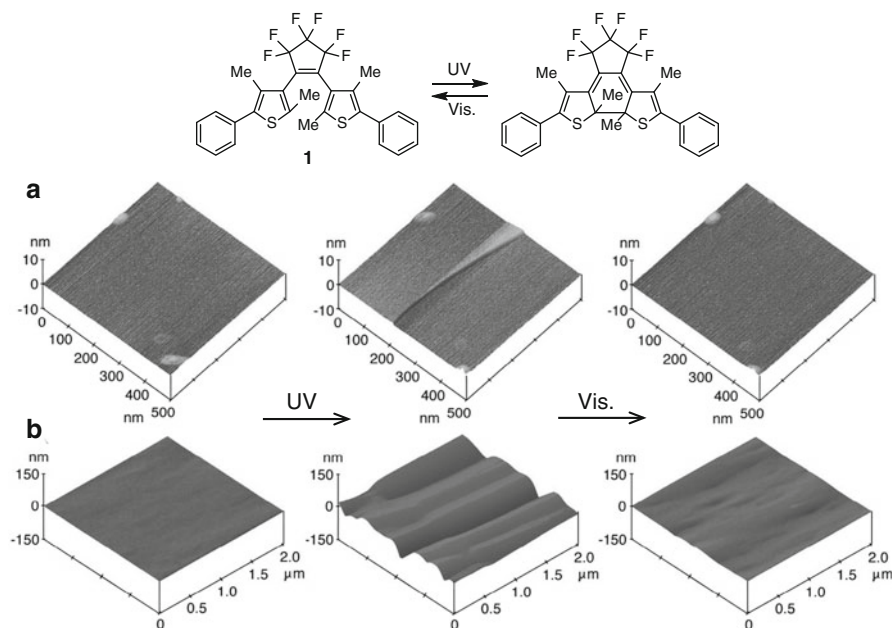


**Fig. 27.1** AMF images of photoinduced crystal surface morphology changes on (100) (a) and (010) crystal surfaces (b) of diarylethene **1** upon alternating irradiation with UV and visible light

### 27.3 Photoinduced Reversible Crystal Shape Changes

First example of photoinduced crystal shape changes using photochromic compounds was reported in 2007 [47]. It is the rapid and reversible crystal shape changes of photochromic diarylethenes upon alternating irradiation with UV and visible light. When irradiated with UV light, the photocyclization reaction of the diarylethene molecules from the open-ring isomer to the closed-ring isomer occurs in the crystalline phase. The twisted thiophene rings become coplanar and the thickness of each molecule is reduced. The closed-ring isomers in the photoirradiated crystal can stack each other accompanying the change in the cell dimensions. As a result, the contraction of platelike crystals of 1,2-bis(2-ethyl-5-phenyl-3-thienyl)perfluorocyclopentene (**2**) and 1,2-bis(5-methyl-2-phenyl-3-thiazolyl)perfluorocyclopentene (**3**), which were prepared by sublimation, can be observed upon UV irradiation, as shown in Fig. 27.2a, b. The contracted crystals can return to the original crystal shape due to the photocycloreversion reaction from the closed-ring isomer to the open-ring isomer by irradiation with visible

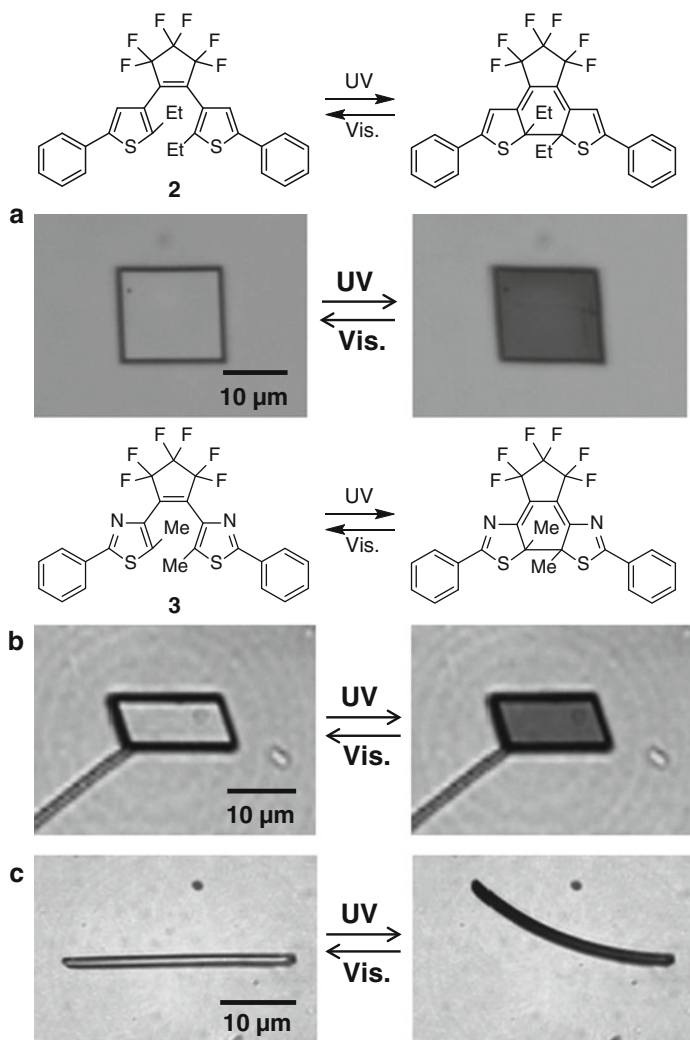


**Fig. 27.2** Photoinduced crystal shape changes of diarylethenes **2** (a) and **3** (b, c)

light. The rodlike crystals of **3** can also be prepared by recrystallization. When the rodlike crystal was irradiated with UV light from the side of the crystal, the crystal bends toward the direction of the incident light as shown in Fig. 27.2c because of contraction of the direction to the long axis of the crystal and a gradient in the extent of the photoisomerization reaction caused by high absorbance of the crystal surface, just like bimetal. The difference between the crystal contraction and bending is ascribed to the thickness of the crystal.

## 27.4 Various Types of Photomechanical Crystals

Since 2007, the photomechanical behavior of various photoreactive crystals has been reported for diarylethenes [47–55], furylfulgides [56], azobenzenes [57–60], salicylideneanilines [61, 62], anthracene derivatives [63–68], 4-chlorocinnamic acid [69], 1,2-bis(4-pyridyl)ethylene salt [70], benzylidenedimethylimidazolinone [71], and so on. Their structures and mechanical behaviors are shown in Fig. 27.3. There are various photoreactive motions such as contraction, expansion, bending, separation, twisting, curling, and so on. All of these motions are based on the geometry changes in the crystalline phase. The photomechanical behaviors are classified into (1) thermally stable and photoreversible P-type behavior such as diarylethenes and furylfulgides; (2) thermally unstable and photoreversible T-type behavior such as azobenzenes, salicylideneanilines, and anthracene derivatives; and (3) one-way photoreactive behavior.

Diarylethenes and furylfulgides undergo reversibly photocyclization and photocycloreversion reactions in the crystalline phase. The crystal of azobenzene having amino group can bend upon irradiation with UV light. However, the deformed crystal thermally returns to the initial crystal shape. Some salicylideneanilines can undergo photochromic reactions of keto-enol isomerization by photoinduced intramolecular proton transfer [10–13, 61, 62]. The salicylideneaniline derivatives undergo thermally unstable photochromic reactions. Introduction of two *tert*-butyl groups to salicylideneaniline suppresses the thermal back reaction, and the photoisomer becomes thermally stable (lifetime of 42 days at 25 °C) [10]. As a result, the microcrystals of the salicylideneaniline derivative with two *tert*-butyl groups show thermally stable and photoreversible bending during repeating cycles for a short time [61, 62]. The photomechanical motions of these compounds are induced by photoisomerization in single molecule. Intermolecular dimerization can also induce driving force of photomechanical motion. Anthracene carboxylates undergo [4 + 4] photodimerization in the crystalline phase and show photoinduced bending [63–68]. 4-Chlorocinnamic acid [69], 1,2-bis(4-pyridyl)ethylene salt [70], and benzylidenedimethylimidazolinone [71] show [2 + 2] photodimerization and photomechanical motions. These photomechanical motions occur in one way.

In both cases of intramolecular and intermolecular photochemical reactions, it is important for the photomechanical motions without fracturing to result from slight changes of cell dimensions in crystals upon photoirradiation.

## 27.5 Theoretical Analysis of Photoinduced Bending Behavior

Although there are various compounds which show photomechanical motion, the bending behavior is the most common motion. It is required for the development of the research field on photomechanical crystals to investigate the bending behavior in detail. 1,2-Bis(2-methyl-5-(4-(1-naphthoyloxymethyl)phenyl)-3-thienyl) perflu-



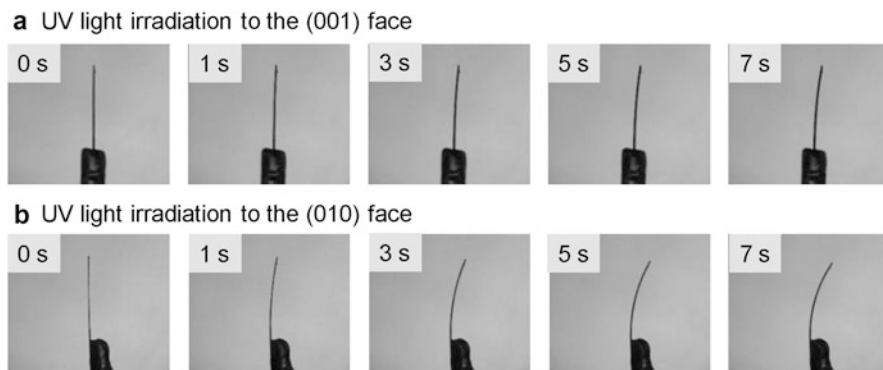


**Fig. 27.4** Photoinduced crystal bending of **4** upon irradiation with UV light to (001) face (a) and (010) face (b)

UV irradiation was performed to the (001) face, the movement of the crystal was slow and small. In contrast, when the crystal was irradiated from the (010) face, it was bent rapidly and largely. This is ascribed to the difference of the absorption coefficient and the photoreacted thickness. When viewed from the (001) face, the long axis of the diarylethene molecule is quite perpendicular to the face. In this case, the diarylethene molecules have a low absorption coefficient. In contrast, when viewed from the (010) face, the long axis of the diarylethene molecules is parallel to the face. The diarylethene molecules have a larger absorption coefficient. As a result, UV light irradiation to the (001) face leads to a relatively homogeneous photocoloration over the whole crystal. However, photoirradiation to the (010) face results in heterogeneous photocoloration in depth in the crystal. The heterogeneous photocoloration affects the speed of the bending. Furthermore, the speed of the bending depends on the crystal thickness.

The photoinduced bending behavior of different thickness samples was examined. When the crystal thickness is thin, the crystal is bent rapidly and largely. However, when the crystal thickness is  $0.62 \mu\text{m}$ , the crystal cannot be bent and can be expanded. In order to know the correlation between the crystal thickness and the initial speed of curvature change, Timoshenko's bimetal model was introduced. The illustration and equation of Timoshenko's bimetal model are shown in Fig. 27.5 and Eq. (27.1) [72]:

$$\text{Curvature} = \frac{1}{R} = \frac{\alpha_2 - \alpha_1}{h_2} \frac{6mn(1+m)}{1 + 4mn + 6m^2n + 4m^3n + m^4n^2} \quad (27.1)$$

$$= \frac{\alpha_2}{h_2} \frac{6m(1+m)}{1 + 4m + 6m^2 + 4m^3 + m^4} \quad (27.2)$$

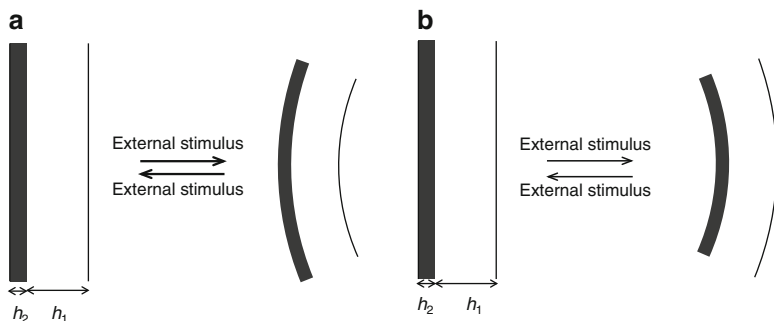


**Fig. 27.5** Illustration of Timoshenko's bimetal model: (a) expansion and (b) contraction in the left side layer

where  $R$  is the curvature radius;  $\alpha_i$  ( $i = 1, 2$ ) are the actuation strains;  $h_i$  ( $i = 1, 2$ ) are the layer thicknesses; and  $m = h_1/h_2$ ,  $n = E_1/E_2$ , and  $E_i$  ( $i = 1, 2$ ) are the Young's moduli. Actuation strain  $\alpha$  means the coefficient of expansion or contraction of the layer in the absence of the other layer upon UV irradiation. In the non-photoreacted layer, the value of actuation strain  $\alpha_1$  is always zero. Equation (27.1) can be simplified to Eq. (27.2).

In the case of diarylethene **4**, the  $\alpha_2$  value means the coefficient of expansion because the bending behavior takes place away from the incident UV light [54]. The initial speed ( $V_{\text{init}}$ ) of the curvature change against the crystal thickness was well fitted by Timoshenko's bimetal model equation, as shown in Fig. 27.6, with the assumption that Young's modulus  $E_1$  is the same as  $E_2$  because only a few percent of diarylethene molecules in the crystal are converted from the open-ring isomer to the closed-ring isomer in the discussed condition. As a result, it is clarified that when  $h_2$  is 1.0  $\mu\text{m}$ , the experimental data could be well explained, resulting in the  $\alpha_2$  value of 0.46  $\% \text{ s}^{-1}$ .

The photoinduced bending behavior of 1-(5-methyl-2-(4-(*p*-vinylbenzoyloxy-methyl)phenyl)-4-thiazolyl)-2-(5-methyl-2-phenyl-4-thiazolyl) perfluorocyclopentene (**5**) (Fig. 27.7) has been also investigated as the bending crystal toward the incident UV light [55]. The bending speed depends on the crystal thickness, and the curvature change on changing the crystal thickness agrees well with Timoshenko's bimetal model. In the case of diarylethene **5**, the value of actuation strain  $\alpha_2$  means the coefficient of the contraction because the bending behavior takes place toward the incident UV light. From the best fitting to the experimental data by Timoshenko's equation as shown in Fig. 27.7, the values of  $h_2$  and  $\alpha_2$  are obtained as 1.0  $\mu\text{m}$  and 0.56  $\% \text{ s}^{-1}$ , respectively. The  $h_2$  value is the same as that obtained for the crystal of diarylethene **4**. The difference in the values of  $\alpha_2$  indicates a difference in the initial speeds of the curvature change. This result means that the speed of the crystals of diarylethene **5** can bend 1.2 times as fast as that of diarylethene **4** when they are the same crystal thickness upon UV irradiation with the same power.

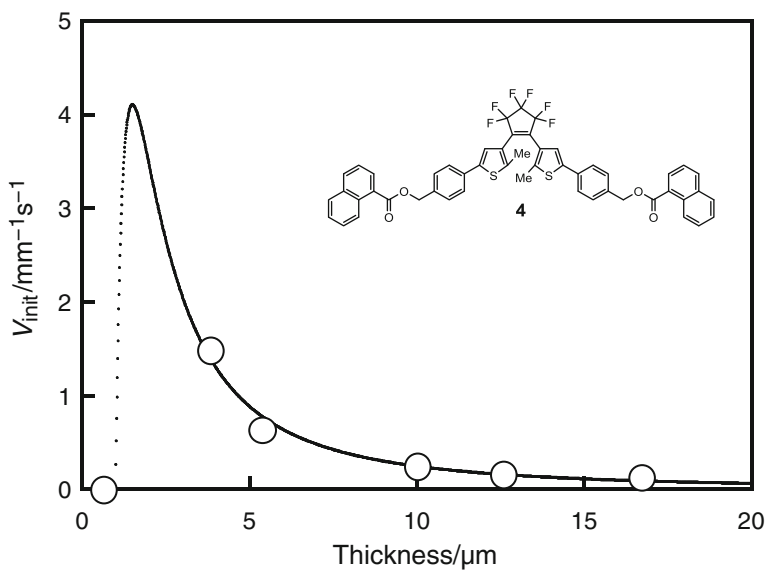


**Fig. 27.6** The initial speed ( $V_{\text{init}}$ ) of the curvature change to the crystal thickness of diarylethene crystal **4**. The fitting curve was calculated by Timoshenko's equation:  $h_2 = 1.0 \mu\text{m}$ ,  $\alpha_2 = 0.0046 \text{ s}^{-1}$

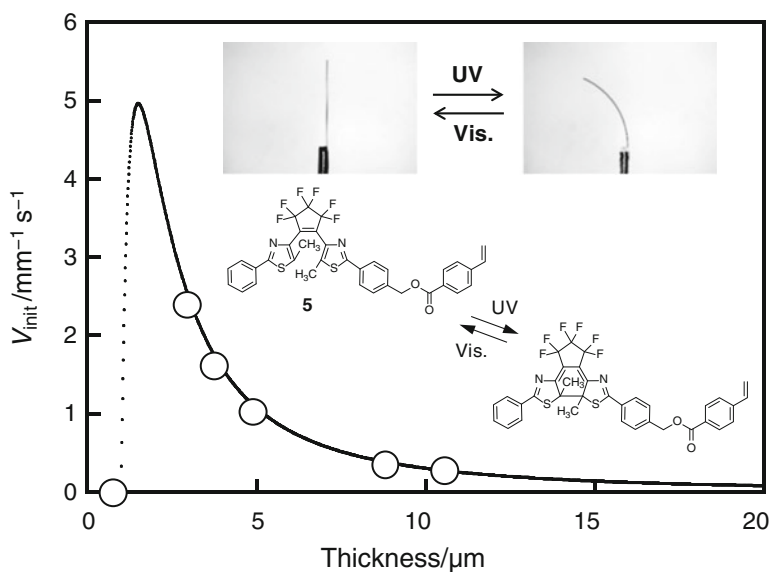


**Fig. 27.7** The initial speed ( $V_{\text{init}}$ ) of the curvature change to the crystal thickness of diarylethene crystal **5**. The fitting curve was calculated by Timoshenko's equation:  $h_2 = 1.0 \mu\text{m}$ ,  $\alpha_2 = 0.0056 \text{ s}^{-1}$

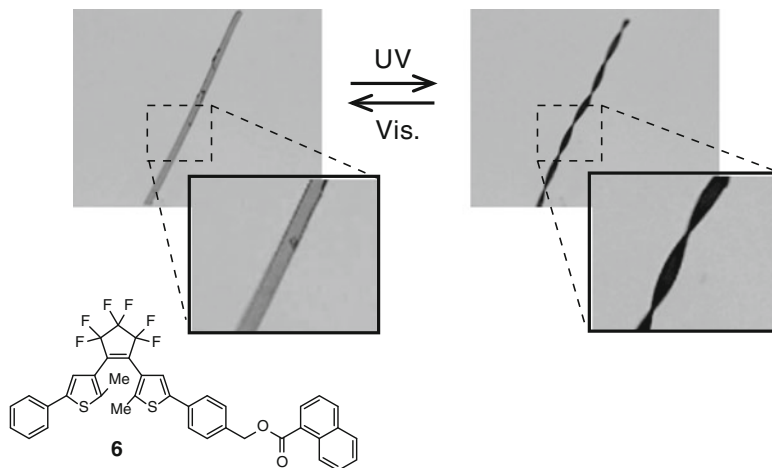


Fig. 27.8 Photoinduced twisting of a diarylethene crystal of **6**

## 27.6 New Photomechanical Motion: Photoreversible Twisting

A ribbonlike crystal of diarylethene (**6**) bearing naphthyl group at one side has been shown to twist photoreversibly [53]. Figure 27.8 shows photographs of the twisting crystal. Upon UV light irradiation to the crystal, the molecules in the crystal underwent the photocyclization reaction from the open-ring isomer to the closed-ring isomer, and the crystal rapidly twisted accompanying the color change of the crystal from colorless to blue. The twisting and color of the crystal can be maintained in the dark. By irradiation with visible light, the blue color disappeared by the back reaction to the initial open-ring isomer and the twisting of the crystal relaxed back to the original shape in a few seconds. This photoreversible twisting can be repeated over 30 cycles. The crystal twisting takes place in both a left-handed helix and a right-handed helix. When the (0–10) face was irradiated with UV light, the crystal twisted into a right-handed helix. In contrast, the crystal twisted into a left-handed helix when the (010) face was irradiated with UV light. This result indicates that the direction of the twisting depends upon the face irradiated with UV light. Furthermore, the direction of contraction in the unit cell was determined using the contracted crystal, which underwent a photocyclization reaction over the whole crystal by irradiation from both sides of the crystal surfaces. Comparing the crystal shape before and after irradiation with UV light clarified that the contraction in the unit cell occurred in the diagonal direction. As a result, a gradient of photocyclization conversion in the thickness direction and the contraction of the crystal in the diagonal direction can induce the crystal twisting. The similar twisting has been observed in a crystal of 9-anthracenecarboxylic acid, which undergoes a reversible [4 + 4] photocyclodimerization in the crystalline phase [66].

## 27.7 Applications of Photomechanical Motion

For practical applications, the photomechanical crystals should have sufficient durability and substantial mechanical properties. The mixed crystals composed of two diarylethene derivatives, 1-(5-methyl-2-phenyl-4-thiazolyl)-2-(5-methyl-2-*p*-tolyl-4-thiazolyl)perfluorocyclopentene (**7**) and 1,2-bis(5-methyl-2-*p*-tolyl-4-thiazolyl)perfluorocyclopentene (**8**), exhibit reversible bending upon alternating irradiation with UV and visible light [52]. The mixed crystals can be reversibly bent over 1,000 cycles without any crystal deformation and exhibit bending in wide temperature range from 4.6 to 370 K. Furthermore, the crystal can work the bending even in water. The bending takes place toward the incident UV light irrespective of the irradiation direction due to the contraction of the irradiated part of the crystal surface. When the light intensity of UV and visible light is controlled, the edge of the rodlike crystal exhibits rotation movement. This rotation movement has been used for actual photomechanical work to rotate gearwheel. Figure 27.9 shows gearwheel rotation by photoreversible bending. Upon irradiation with UV light, the crystal bends and hits the gear, resulting in rotation of the gear. Upon controlled irradiation with UV and visible light, the crystal can return to the initial position. Then, irradiation with UV light bends the crystal and again induces the rotation of the gearwheel.

The two-component co-crystals composed of 1,2-bis(2-methyl-5-(1-naphthyl)-3-thienyl)perfluorocyclopentene (**9**) and perfluoronaphthalene (**10**) with 1–5 mm size in length are also reversibly bent upon alternating irradiation with UV and visible light [50]. The photoinduced bending of such a large crystal is attractive for practical use. The bending occurred away from the incident UV light. From X-ray crystallographic analysis of the isolated open-ring isomer and closed-ring isomer, the length of short axis of diarylethene molecule in the closed-ring isomer is longer than that in the open-ring isomer. A similar change in the length of diarylethene molecule was also confirmed by *in situ* X-ray crystallographic analysis. This elongation in the length of short axis of diarylethene molecule results in the expansion of the direction to the crystal long axis. The bending away from the incident UV light is caused by the expansion of the crystal with a gradient in an extent of photoisomerization. Moreover, this crystal can lift a heavy metal ball which is 200–600 times heavier than the crystal. A rectangular plate crystal was fixed at the edge of a glass plate as a cantilever arm, and a 2-mm lead ball was loaded onto the crystal, as shown in Fig. 27.10. The crystal and the ball weigh 0.17 mg and 46.77 mg, respectively. The weight of the lead ball is 275 times heavier than that of the crystal. Upon irradiation with UV light from below, the heavy ball was lifted as high as 0.95 mm. A 3-mm steel ball (110.45 mg) was loaded onto a crystal plate (0.18 mg), and the crystal was irradiated with UV light. The weight of the ball is 614 times heavier than that of the crystal. The maximum stress generated by UV irradiation was estimated to be 44 MPa, which is 100 times larger than that of muscles (ca. 0.3 MPa). The modulus of the crystal was measured to be as large as 11 GPa. The large elastic modulus enables the crystal to generate a strong force and carry out large mechanical work.

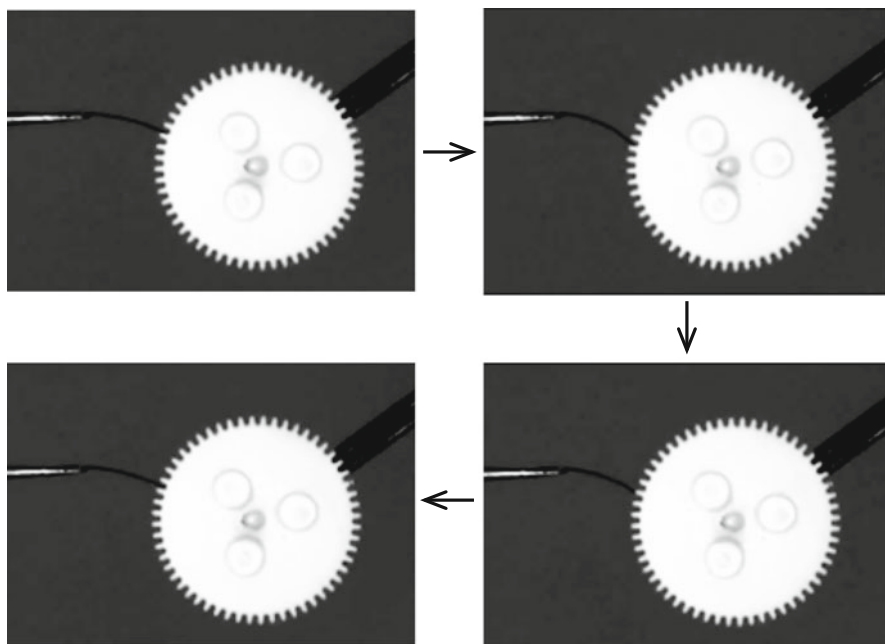
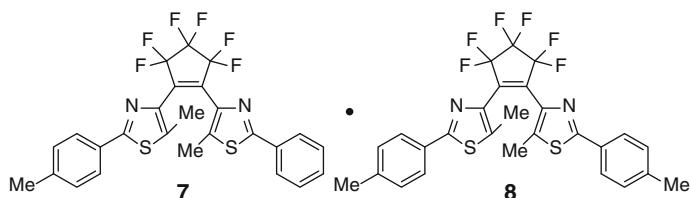


**Fig. 27.9** Gearwheel rotation operated by a light-driven molecular-crystal actuator. The two-component mixed crystal containing **7** and **8** (**7**:**8** = 63/37) (1.3 mm × 60 mm × 12 mm) was fixed on the tip of a metal needle. The gear (diameter: 3.2 mm) was rotated by the crystal, which showed reversible bending upon alternating irradiation with UV (365 nm) and visible (>500 nm) light

## 27.8 Summary

In this chapter, photoinduced mechanical motions of photochromic crystalline materials, especially diarylethene crystals, are introduced. Among photochromic compounds, diarylethenes have the most excellent properties such as thermal stability of both isomers, fatigue resistance, rapid response, and so on. Organic molecular crystals with such properties have a capability of photoinduced mechanical motions. In most cases of small-sized crystals, the crystals can be deformed without any cracking upon photoirradiation. There are various photoreactive motions such as contraction, expansion, bending, separation, twisting, curling, and so on. All of these motions are based on the geometry changes in the crystalline phase.

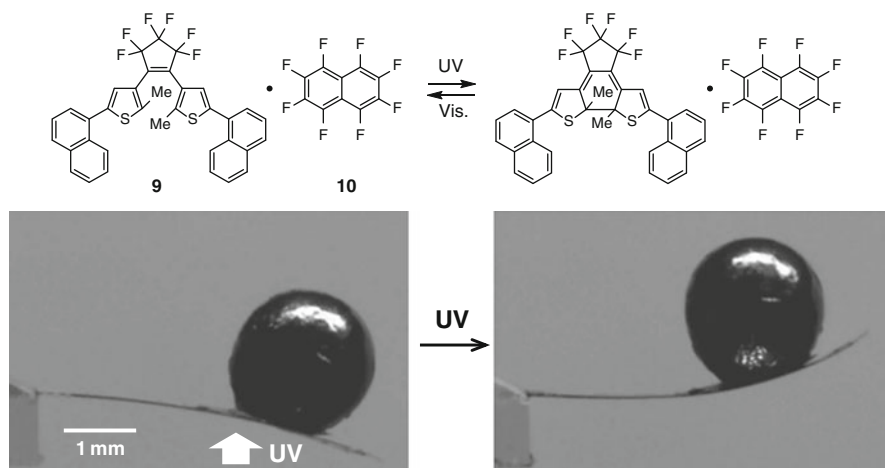


**Fig. 27.10** Photomechanical work of molecular-crystal cantilevers made of **9/10** co-crystal. UV light was irradiated from the lower side of the crystal: 2-mm lead ball, 46.77 mg; crystal cantilever, 0.17 mg

## References

1. J.H. Golden, *J. Chem. Soc.* 3741–3748 (1961)
2. K. Maeda, T. Hayashi, *Bull. Chem. Soc. Jpn.* **43**, 429–438 (1970)
3. M. Kawano, T. Sano, J. Abe, Y. Ohashi, *J. Am. Chem. Soc.* **121**, 8106–8107 (1999)
4. K. Ichimura, S. Watanabe, *Bull. Chem. Soc. Jpn.* **49**, 2220–2223 (1976)
5. A.M. Trozzolo, T.M. Leslie, A.S. Sarpotdar, R.D. Small, G.J. Ferraudi, T. Dominh, R.L. Hartless, *Pure Appl. Chem.* **51**, 261–270 (1979)
6. H. Sixl, R. Warta, *Chem. Phys.* **94**, 147–155 (1985)
7. Y. Eichen, J.M. Lehn, M. Scherl, D. Haarer, J. Fischer, A. Decian, A. Corval, H.P. Trommsdorff, *Angew. Chem. Int. Ed. Engl.* **34**, 2530–2533 (1995)
8. A. Schmidt, S. Kababya, M. Appel, S. Khatib, M. Botoshansky, Y. Eichen, *J. Am. Chem. Soc.* **121**, 11291–11299 (1999)
9. P. Naumov, A. Sekine, H. Uekusa, Y. Ohashi, *J. Am. Chem. Soc.* **124**, 8540–8541 (2002)
10. T. Kawato, H. Koyama, H. Kanatomi, M. Isshiki, *J. Photochem.* **28**, 103–110 (1985)
11. E. Hadjoudis, M. Vittorakis, I. Moustakalimavridis, *Tetrahedron* **43**, 1345–1360 (1987)
12. J. Harada, H. Uekusa, Y. Ohashi, *J. Am. Chem. Soc.* **121**, 5809–5810 (1999)
13. K. Amimoto, H. Kanatomi, A. Nagakari, H. Fukuda, H. Koyama, T. Kawato, *Chem. Commun.* 870–871 (2003)
14. Y. Mori, Y. Ohashi, K. Maeda, *Bull. Chem. Soc. Jpn.* **62**, 3171–3176 (1989)
15. S. Kobatake, M. Yamada, T. Yamada, M. Irie, *J. Am. Chem. Soc.* **121**, 8450–8456 (1999)
16. S. Kobatake, T. Yamada, K. Uchida, N. Kato, M. Irie, *J. Am. Chem. Soc.* **121**, 2380–2386 (1999)
17. M. Irie, T. Lifka, S. Kobatake, N. Kato, *J. Am. Chem. Soc.* **122**, 4871–4876 (2000)
18. S. Kobatake, K. Shibata, K. Uchida, M. Irie, *J. Am. Chem. Soc.* **122**, 12135–12141 (2000)
19. M. Irie, *Chem. Rev.* **100**, 1685–1716 (2000)
20. S. Kobatake, M. Irie, *Bull. Chem. Soc. Jpn.* **77**, 195–210 (2004)
21. M. Morimoto, M. Irie, *Chem. Commun.* 3895–3905 (2005)
22. M. Irie, T. Fukaminato, K. Matsuda, S. Kobatake, *Chem. Rev.* **114**, 12174–12277 (2014)

23. S. Kobatake, K. Uchida, E. Tsuchida, M. Irie, *Chem. Commun.* 2804–2805 (2002)
24. K. Shibata, K. Muto, S. Kobatake, M. Irie, *J. Phys. Chem. A* **106**, 209–214 (2002)
25. M. Morimoto, S. Kobatake, M. Irie, *Adv. Mater.* **14**, 1027–1029 (2002)
26. M. Morimoto, S. Kobatake, M. Irie, *J. Am. Chem. Soc.* **125**, 11080–11087 (2003)
27. S. Takami, L. Kuroki, M. Irie, *J. Am. Chem. Soc.* **129**, 7319–7326 (2007)
28. T. Fukaminato, S. Kobatake, T. Kawai, M. Irie, *Proc. Jpn. Acad., Ser. B* **77**, 30–35 (2001)
29. T. Fukaminato, T. Kawai, S. Kobatake, M. Irie, *J. Phys. Chem. B* **107**, 8372–8377 (2003)
30. T. Kodani, K. Matsuda, T. Yamada, S. Kobatake, M. Irie, *J. Am. Chem. Soc.* **122**, 9631–9637 (2000)
31. K. Uchida, M. Walko, J.J.D. de Jong, S. Sukata, S. Kobatake, A. Meetsma, J. van Esch, B.L. Feringa, *Org. Biomol. Chem.* **4**, 1002–1006 (2006)
32. M. Morimoto, S. Kobatake, M. Irie, *Chem. Eur. J.* **9**, 621–627 (2003)
33. S. Kobatake, S. Kuma, M. Irie, *Bull. Chem. Soc. Jpn.* **77**, 945–951 (2004)
34. Y. Asano, A. Murakami, T. Kobayashi, S. Kobatake, M. Irie, S. Yabushita, S. Nakamura, *J. Mol. Struct. (Theochem)* **625**, 227–234 (2003)
35. S. Kobatake, M. Morimoto, Y. Asano, A. Murakami, S. Nakamura, M. Irie, *Chem. Lett.* 1224–1225 (2002)
36. K. Saita, S. Kobatake, T. Fukaminato, S. Nanbu, M. Irie, H. Sekiya, *Chem. Phys. Lett.* **454**, 42–48 (2008)
37. M. Morimoto, S. Kobatake, M. Irie, *Cryst. Growth Des.* **3**, 847–854 (2003)
38. M. Morimoto, S. Kobatake, M. Irie, *Photochem. Photobiol. Sci.* **2**, 1088–1094 (2003)
39. M. Morimoto, S. Kobatake, M. Irie, *Chem. Rec.* **4**, 23–38 (2004)
40. S. Kobatake, Y. Matsumoto, M. Irie, *Angew. Chem. Int. Ed.* **44**, 2148–2151 (2005)
41. S. Kobatake, M. Morimoto, M. Irie, *Mol. Cryst. Liq. Cryst.* **431**, 523–527 (2005)
42. M. Morimoto, S. Kobatake, M. Irie, *Mol. Cryst. Liq. Cryst.* **431**, 529–534 (2005)
43. T. Yamada, S. Kobatake, K. Muto, M. Irie, *J. Am. Chem. Soc.* **122**, 1589–1592 (2000)
44. T. Yamada, S. Kobatake, M. Irie, *Bull. Chem. Soc. Jpn.* **73**, 2179–2184 (2000)
45. T. Hamazaki, K. Matsuda, S. Kobatake, M. Irie, *Bull. Chem. Soc. Jpn.* **80**, 365–370 (2007)
46. M. Irie, S. Kobatake, M. Horichi, *Science* **291**, 1769–1772 (2001)
47. S. Kobatake, S. Takami, H. Muto, T. Ishikawa, M. Irie, *Nature* **446**, 778–781 (2007)
48. K. Uchida, S. Sukata, Y. Matsuzawa, M. Akazawa, J.J.D. de Jong, N. Katsonis, Y. Kojima, S. Nakamura, J. Areephong, A. Meetsma, B.L. Feringa, *Chem. Commun.* 326–328 (2008)
49. L. Kuroki, S. Takami, K. Yoza, M. Morimoto, M. Irie, *Photochem. Photobiol. Sci.* **9**, 221–225 (2010)
50. M. Morimoto, M. Irie, *J. Am. Chem. Soc.* **132**, 14172–14178 (2010)
51. S. Kobatake, H. Hasegawa, K. Miyamura, *Cryst. Growth Des.* **11**, 1223–1229 (2011)
52. F. Terao, M. Morimoto, M. Irie, *Angew. Chem. Int. Ed.* **51**, 901–904 (2012)
53. D. Kitagawa, H. Nishi, S. Kobatake, *Angew. Chem. Int. Ed.* **52**, 9320–9322 (2013)
54. D. Kitagawa, S. Kobatake, *J. Phys. Chem. C* **117**, 20887–20892 (2013)
55. D. Kitagawa, S. Kobatake, *Photochem. Photobiol. Sci.* **13**, 764–769 (2014)
56. H. Koshima, H. Nakaya, H. Uchimoto, N. Ojima, *Chem. Lett.* **41**, 107–109 (2012)
57. H. Koshima, N. Ojima, H. Uchimoto, *J. Am. Chem. Soc.* **131**, 6890–6891 (2009)
58. H. Koshima, N. Ojima, *Dyes Pigment.* **92**, 798–801 (2012)
59. O.S. Bushuyev, T.A. Singleton, C. Barrett, *J. Adv. Mater.* **25**, 1796–1800 (2013)
60. O.S. Bushuyev, A. Tomberg, T. Friscic, C.J. Barrett, *J. Am. Chem. Soc.* **135**, 12556–12559 (2013)
61. H. Koshima, K. Takechi, H. Uchimoto, M. Shiro, D. Hashizume, *Chem. Commun.* **47**, 11423–11425 (2011)
62. H. Koshima, R. Matsuo, M. Matsudomi, Y. Uemura, M. Shiro, *Cryst. Growth Des.* **13**, 4330–4337 (2013)
63. R.O. Al-Kaysi, A.M. Mueller, C.J. Bardeen, *J. Am. Chem. Soc.* **128**, 15938–15939 (2006)
64. R.O. Al-Kaysi, C.J. Bardeen, *Adv. Mater.* **19**, 1276–1280 (2007)
65. L. Zhu, R.O. Al-Kaysi, R.J. Dillon, F.S. Tham, C.J. Bardeen, *Cryst. Growth Des.* **11**, 4975–4983 (2011)

66. L. Zhu, R.O. Al-Kaysi, C.J. Bardeen, *J. Am. Chem. Soc.* **133**, 12569–12575 (2011)
67. L. Zhu, A. Agarwal, J. Lai, R.O. Al-Kaysi, F.S. Tham, T. Ghaddar, L. Mueller, C.J. Bardeen, *J. Mater. Chem.* **21**, 6258–6268 (2011)
68. T. Kim, M.K. Al-Muhanna, S.D. Al-Suwaidan, R.O. Al-Kaysi, C.J. Bardeen, *Angew. Chem. Int. Ed.* **52**, 6889–6893 (2013)
69. T. Kim, L. Zhu, L.J. Mueller, C.J. Bardeen, *CrystEngComm* **14**, 7792–7799 (2012)
70. J.-K. Sun, W. Li, C. Chen, C.-X. Ren, D.-M. Pan, J. Zhang, *Angew. Chem. Int. Ed.* **52**, 6653–6657 (2013)
71. P. Naumov, J. Kowalik, K.M. Solntsev, A. Baldrige, J.-S. Moon, C. Kranz, L.M. Tolbert, *J. Am. Chem. Soc.* **132**, 5845–5857 (2010)
72. S. Timoshenko, *J. Opt. Soc. Am.* **11**, 233–255 (1925)

# Chapter 28

## Photoinduced Reversible Topographical Changes on Photochromic Microcrystalline Surfaces

Kingo Uchida

**Abstract** Diarylethenes are well known as thermally irreversible photochromic compounds, and some of their derivatives undergo the photochromic reactions even in the crystalline state. The reversible crystal growth of open- and closed-ring isomers of diarylethenes was discovered upon alternate irradiation with UV and visible light, accompanied with the topographical changes on the microcrystalline film surface. The photogenerated crystals form needle-shaped crystals for the closed-ring isomer, while cubic-shaped crystals for open-ring isomer for the initially discovered derivative. The former surfaces show a superhydrophobic wetting property, which is classified as a lotus or petal effect of wetting depending on the size of the needle-shaped crystals, while the latter does not show such superhydrophobicity. The needle crystals were randomly oriented. We tried epitaxial crystal growth to orient the needle-shaped crystals. The first epitaxial crystal growth was performed on a 110 surface of a strontium titanate single crystal whose lattice constant is similar to that of a diarylethene crystal. Then we found a self-epitaxial crystal growth of the needle-shaped crystals which grow on the lattice of the open-ring isomer and form well-ordered surface. Due to the orderings and submicron-sized crystals, the surface shows not only super water repellence but also antireflection moth-eye effect in near-infrared region.

**Keywords** Superhydrophobicity • Lotus effect • Moth-eye effect • Epitaxial crystal growth • Glass transition temperature

### 28.1 Introduction

Diarylethenes are well-known photochromic compounds which undergo a cyclization reaction to form colored closed-ring isomers by UV irradiation and revert to colorless open-ring isomers by visible light irradiation. The photochromic

---

K. Uchida (✉)

Department of Materials Chemistry, Ryukoku University, Seta, Otsu, Shiga 520-2194, Japan

e-mail: [uchida@rins.ryukoku.ac.jp](mailto:uchida@rins.ryukoku.ac.jp)

© Springer Japan 2015

R. Tamura, M. Miyata (eds.), *Advances in Organic Crystal Chemistry*,

DOI 10.1007/978-4-431-55555-1\_28

549

reactions show excellent performance: thermal stability of both isomers, a high fatigue resistance, rapid response, high quantum yield, and reactivity even in the crystalline state [1]. Such diarylethenes have been applied for memories, switches, and molecular devices [2]. However, before we have started our work, there was only one paper reported topographical changes of surfaces of a single crystal of a diarylethene derivative. In the paper, surface topographical changes introduced by irradiation with UV and visible lights were attributed to the changes of molecular volumes caused by the photoisomerization of diarylethene molecules [3].

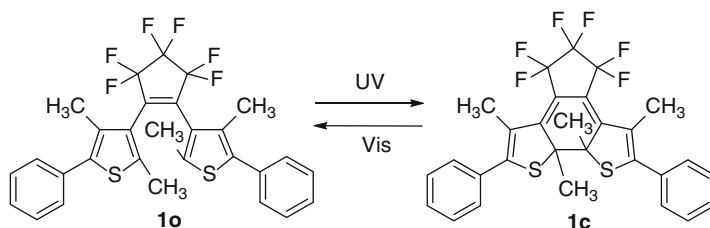
On the other hand, the polarity changes during the photochromism of azobenzene and spiropyran derivatives are much larger compared to those of diarylethenes. Consequently, those two derivatives have been used for photocontrol of the changes in surface wettability. For example, Garcia et al. reported the contact angle (CA) changes of a water droplet on a spiropyran-coated surface [4]. The CA before UV irradiation was 74°, but it dropped to 54° after UV irradiation. This is due to the enhanced polarity by photoisomerization, which converted nonpolar spiropyran to a polar merocyanine isomer. Such wettability changes have been extensively studied not only in organic materials but also in inorganic materials.

It is known that controlling surface wettability is much effective by changing the surface topography, and increasing surface roughness results in a superhydrophobic surface, which can be widely observed in natural plants such as lotus and taro leaves [5]. They have micrometer-scale rugged [6] or fractal [7, 8] structures and whose structures are also been artificially prepared by mimicking to make superhydrophobic surfaces. In 2006, we accidentally discovered reversible crystal growth of a diarylethene derivative, and this was accompanied by a reversible changes with superhydrophobic property [9–11]. Although the photogenerated needle-shaped crystals are randomly oriented, the finding became a breakthrough into a new surface science.

## 28.2 Photoinduced Reversible Topographical Changes on Diarylethene Surface

The topographical changes of diarylethene crystals were first reported by Irie et al, in 2001 [3]. Upon UV irradiation of a single-crystalline surface of a diarylethene derivative (**1o**), micrometer-sized steps and valleys were formed, and they were disappeared upon visible light irradiation. These phenomena were explained by the size difference between the open-ring isomer (**1o**) and the closed-ring isomer (**1c**) without changing the lattice structure of the crystals (Scheme 28.1).

A new type of photoinduced changes in morphology of a photochromic diarylethene crystalline thin film of 1,2-bis(2-methoxy-5-trimethylsilylthien-3-yl)perfluorocyclopentene (**2o**) as shown in Fig. 28.1 appeared, and it was accompanied with wettability changes [9, 10]. Upon UV irradiation (254 nm), the color became deep blue within 5 min, yet no change in surface morphology



**Scheme 28.1** Photochromic reaction of a diarylethene **1o**

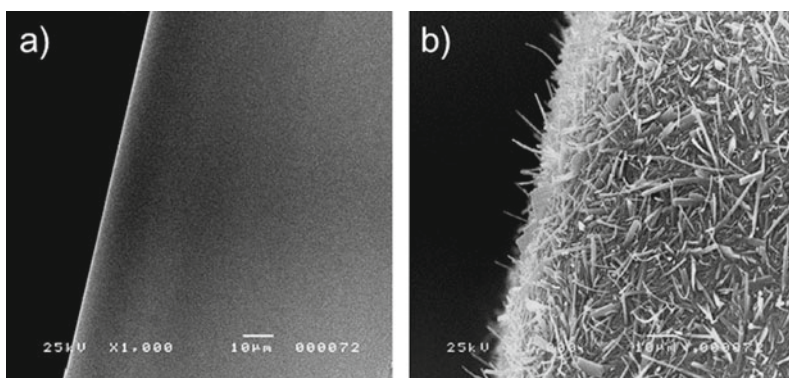
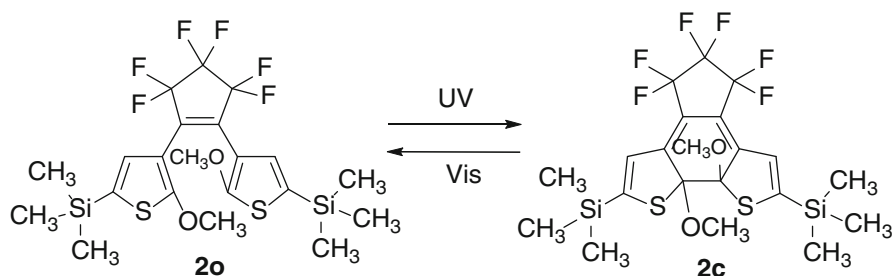


**Fig. 28.1** Photoinduced topographical changes on the surface of a single crystal of **2o**. (a) SEM image of a crystal surface from a side view before UV irradiation. (b) After UV (254 nm, 12 W) irradiation for 10 min followed by storing for 24 h at 30 °C in the dark. After visible light ( $\lambda > 500$  nm, 500 W, 20 min) irradiation to the (b) state, the surface reverts to the initial flat (a) state. (SEM images:  $\times 1,000$ )

is observed at this moment at room temperature. After irradiation for 10 min and then storing the crystal in the dark, microfibrils immediately started to grow. After storage for 24 h, the surface was covered with microfibrils as shown in Fig. 28.1b. Upon irradiation of the surface with visible light ( $\lambda > 500$  nm), the blue color and the microfibrils disappeared. Topographical changes were also observed on the surface of microcrystalline film prepared by coating the chloroform solution of **2o** on a glass substrate [9–11].

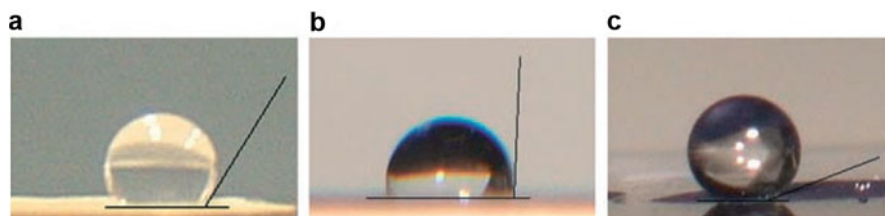


**Fig. 28.2** Contact angles (CAs) of a water droplet on the microcrystalline surface of diarylethene **2o** prepared on glass substrate by solution coating. **(a)** Water droplet (1.2 mm  $\Phi$ ) on the microcrystalline surface before irradiation with UV light (254 nm, 12 W). The contact angle was  $120^\circ$ . **(b)** Water droplet after UV irradiation for a short time (1–2 min). The contact angle changed to  $92^\circ$ . **(c)** Water droplet after UV irradiation (10 min) and stored in the dark at room temperature for 24 h. The contact angle increased to  $163^\circ$

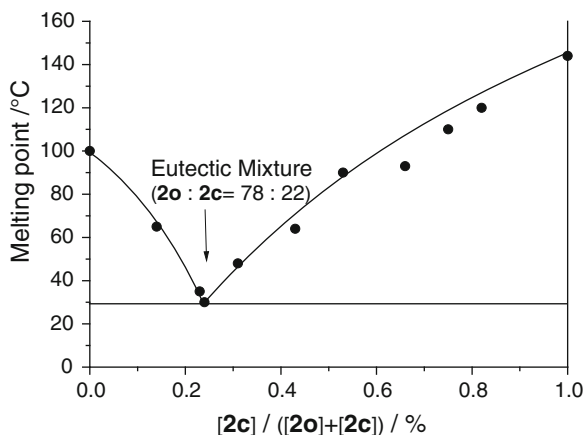
Measurement of the CA of a water droplet is a simple and direct method for evaluating wettability on a surface. The CA of the film surface before UV irradiation was  $120^\circ$  (Fig. 28.2a). Upon irradiation of the surface with UV light (254 nm), the color became blue and the angle decreased to around  $90^\circ$  (Fig. 28.2b) after a short irradiation time (1–2 min). After 24 h, the angle gradually increased to  $163^\circ$  (Fig. 28.2c). The colored surface was irradiated with visible light to regenerate the open-ring isomer. After 20 min, the blue color disappeared. The CA was also monitored during the fibril-disappearing process. It gradually decreased and finally recovered to the initial  $120^\circ$  [9–11].

Powder X-ray diffraction measurements were carried out to elucidate the composition of the microfibrils, and the results showed that the XRD pattern of the fibrils was in good agreement with that of the closed-ring isomer, whose pattern was estimated from single-crystal structure analysis of **2c**. Ordinarily, closed-ring isomers formed in the crystal of open-ring isomers are strained by the lattice and have different structures from closed-ring isomer crystals obtained by recrystallization in solution [12]. The above results indicate that the fibril crystal formed on the film grew freely from the crystal lattice of **2o** [9, 10].

The forming and disappearing mechanism of the needle-shaped crystals of **2c** by alternate irradiation with UV and visible light can be explained using a phase diagram (Fig. 28.3) [9, 10].

Melting points of **2o** and **2c** were 100 and  $140^\circ\text{C}$ , respectively. Furthermore, the shape of **2o** is cubic, while that of **2c** is a needle or fibril when obtained by recrystallization from the solutions of these isomers. The needle-shaped crystals tend to grow in one direction along the a-axis of the crystal [9–11]. Upon UV irradiation, **2o** is converted to **2c**. When the conversion exceeds 22 %, crystal growth of **2c** starts to form fibril structures on the film surface. To confirm this mechanism, samples were kept in air and in water at different temperatures. Below around  $0^\circ\text{C}$ , the fibril did not grow, while fibril formation was observed in air and in water around  $30^\circ\text{C}$ . These results also support the melt mechanism as depicted in the phase diagram. Fractal analysis was made by the box-counting method for

**Fig. 28.3** Phase diagram of mixtures of open- (**2o**) and closed-ring (**2c**) isomers formed by irradiation of diarylethene crystals with UV light (313 nm)



the photogenerated rough surface, and this revealed that the surface is also fractal [11]. The size of the roughness can be classified into three regions based on the fractal dimension: ca. 2.0 (roughness size smaller than 0.5  $\mu\text{m}$ ), 2.5 (roughness size of 0.5–20  $\mu\text{m}$ ), and ca. 2.0 (roughness size larger than 20  $\mu\text{m}$ ). The fractal dimension of ca. 2.5 is due to the fibril-like structures generated by UV irradiation on diarylethene surfaces accompanied by an increase in the contact angle. The surface structure with larger fractal dimension mainly contributes to the extremely high water repellency of the diarylethene surfaces. This mechanism of spontaneous formation of fractal surfaces is similar to that for triglyceride and alkyl ketene dimer waxes [7]. Furthermore, the needle shape is important for enhancing the CA of the surface, since diarylethene derivatives without needle-shaped crystals did not show remarkable CA enhancement from crystal growth on the surface [13].

Photoinduced fibril growth of **2c** was observed not only on glass and metal substrates but also on plastic and paper. Therefore, the compound is applicable to materials used in the photocontrol of surface-water repellency.

### 28.3 Measurement of the Activation Energies of Crystal Growth

The formation of needle-shaped crystals of **2c** was observed at different temperatures of the storage after UV irradiation. In the previous section, the rough surface formed at 30 °C was a fascinating geometrical fractal structure, characterized by self-similarity and non-integer dimensions [11]. Similar fractal surfaces have also been formed on several kinds of wax. For example, alkylketene dimer (AKD) forms fractal structures and provides super water repellency [7]. Tsujii et al. suggested that the spontaneous formation of fractal structures on the AKD surface originated in a phase transition from a metastable to a stable crystalline form [14]; it was

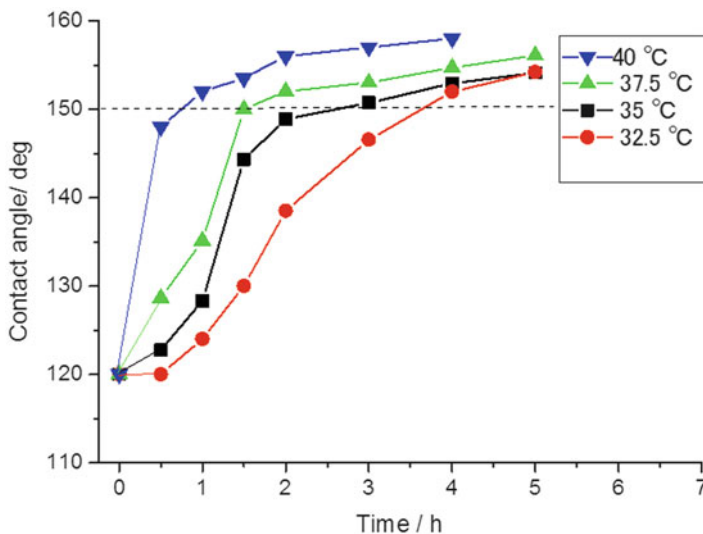


**Fig. 28.4** Time-dependent contact angles of water droplets on UV-irradiated diarylethene surface at different temperatures of a needle-shaped crystal (**2c**)-generation process

followed by the blooming theory, which was also proven by use of tristearin [15]. The surface after UV irradiation is considered to be a metastable state because the photogenerated closed-ring isomer has different crystal packing compared with that of the open-ring isomer [11]. In our system, diarylethene **2o** underwent a photoinduced cyclization reaction to form **2c** upon UV irradiation.

Because the photogenerated closed-ring isomer **2c** in the crystal lattice of the open-ring isomer has a distorted crystal packing rather than the most stable crystal structure of the closed-ring isomer **2c**. The photogenerated **2c** was strained. Due to the coexistence of the open- and closed-ring isomers, the system turned to be metastable state whose strains are released by forming the needle-shaped crystals of **2c** by self-assembling.

The activation energy to form a fractal surface of an alkylketene dimer or a triglyceride was obtained by measuring the periods required for the CA to reach 150° at different storage temperatures, followed by application of the Arrhenius equation [16]. In this system, the CAs of a water droplet increased with the growth of the needle-shaped crystals. We thus measured the periods required for the CA to reach 150° to obtain the activation energy for growing needle-shaped crystals. The time profiles of the CAs are shown in Fig. 28.4. From these data, the activation energies for the formation of needle-shaped crystals of **2c** on the surface were 143 kJ/mol [11]. Similar activation energies were obtained for the topographical changes of alkylketene dimer (158 kJ/mol) and trimyristin triglyceride (178 kJ/mol) [16].

## 28.4 Photoinduced Reversible Epitaxial Crystal Growth

So far we only discussed the photoinduced reversible crystal growth of the closed-ring isomer. In this section, we now discuss that of the open-ring isomer. In an earlier work, a new diarylethene derivative **3o** with an asymmetric structure was prepared in order to decrease the melting point of both isomers and eutectic temperature [17]. Additionally, a surface whose wettability changes are extended from hydrophilic, with CA of less than  $90^\circ$ , to superhydrophobic is desired. The photochromic reactions of **3o** were observed in a hexane solution, and the quantum yields of the cyclization and cycloreversion reactions of **3o** and **3c** in a hexane solution were 0.35 and  $4.2 \times 10^{-3}$ , respectively.

Although the compound showed polymorphism, only needle-shaped crystals were observed in the bulk film on the glass substrate. Recrystallization from the hexane solution gave platelet crystals, but the crystals from ether hexane mixtures were needles. The melting points of platelets and needles were  $92.9\text{--}93.5$  and  $95.2\text{--}95.8$  °C, respectively. Both crystals were monoclinic. In the crystalline states, the distances between the reactive carbon atoms of **3o** in the platelets and the needle-shaped crystals were 3.568 and 3.606 Å, respectively. It is well known that the cyclization reaction can proceed upon UV irradiation even in the crystalline state when the distance is less than 4 Å [18]. Therefore, the photocyclization can proceed in this system. To study the photoinduced topographical changes of the surface, the phase diagram of a mixture of **3o** and **3c** was prepared by DSC measurements of such mixtures with different components (Fig. 28.5). The melting points of **3o** and **3c** were  $95.2\text{--}95.8$  and  $134.5\text{--}135.0$  °C, respectively. The eutectic point was 67 °C, where the ratio of **3o** and **3c** was 61:39.

The microcrystalline surface was prepared by coating the chloroform solution of **3o** onto a glass plate and subsequent evaporation of the solvent. Through SEM observation of the microcrystalline film, the surface was covered only with rod-shaped crystals. The SEM image of the surface is shown in Fig. 28.6a. The surface was covered with microcrystals of **3o**, and the CA of a water droplet on the surface was  $150.4 \pm 0.3^\circ$ , showing a superhydrophobic property (Fig. 28.6d). Furthermore, a water droplet remained pinned on the surface even when the surface was turned over, showing the petal effect. Then the surface was irradiated with UV light (initially 10 min), and it became flat within 30 min as shown in Fig. 28.6b. The CA was drastically reduced to  $80.5 \pm 0.4^\circ$ , and a hydrophilic surface was generated as shown in Fig. 28.6e. Although the melting point of **3c** is high ( $134.5\text{--}135.0$  °C), **3c** crystal did not grow on the surface because the conversion to **3c** was not high enough to provide eutectic content (39 %). By scratching the surface after UV irradiation and measuring the absorption spectra in the hexane, the content of **3c** was found to be 31 % after 10 min of UV irradiation. No remarkable increment of the content was observed by prolonged UV irradiation of the surface. The flat surface reverted to a rough surface, accompanied by remarkable enhancement of the CA, by visible light irradiation within 1.5 h. During the visible light irradiation, the film was again maintained at the eutectic temperature. The SEM image of the surface is shown

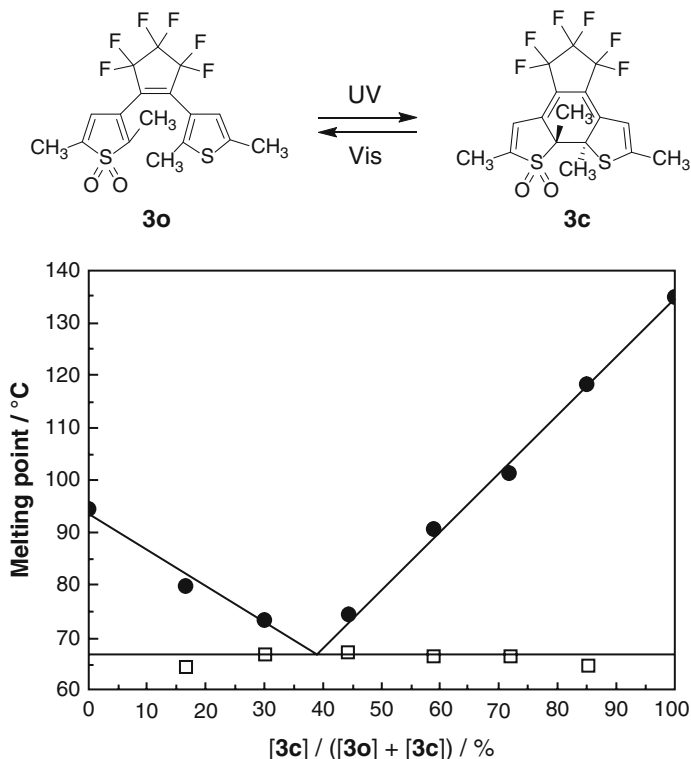


**Fig. 28.5** Phase diagram of mixtures of open-ring (**3o**) and closed-ring (**3c**) isomers formed by UV light (366 nm) irradiation

in Fig. 28.6c. The surface is covered with rod-shaped crystals whose diameters and lengths are around 2–5 and 20–30  $\mu\text{m}$ , respectively. The CA of a water droplet was  $150.9 \pm 0.6^\circ$  (Fig. 28.6f). Alternate formations of superhydrophobic and hydrophilic surfaces were also performed [17].

To understand the mechanism of the photoinduced crystal growth, the reversible crystal growing process was monitored by XRD. The diffraction angles of the **3o** film (Fig. 28.7) correspond to those of the **3o** powder [17]. The films were oriented to the 30-2 direction ( $2\theta = 20.5^\circ$ ). Some of the diffraction intensities of the films were different from those of the **3o** powder, because of the difference of the crystal size and orientation.

In the previous section, needle-shaped crystals of a closed-ring isomer grew on the subphase of the open-ring isomer upon UV light irradiation; therefore, the crystals of the subphase had no effect on the growth of needle-shaped crystals [9–11]. On the other hand, the current results showed the growth of open-ring isomer crystals because the eutectic ratio was not achieved; only the crystallization of open-ring isomer **3o** was possible. Indeed, maintaining the eutectic temperature at  $67^\circ\text{C}$  induced the rapid growth of the needle-shaped open-ring isomer crystals on the

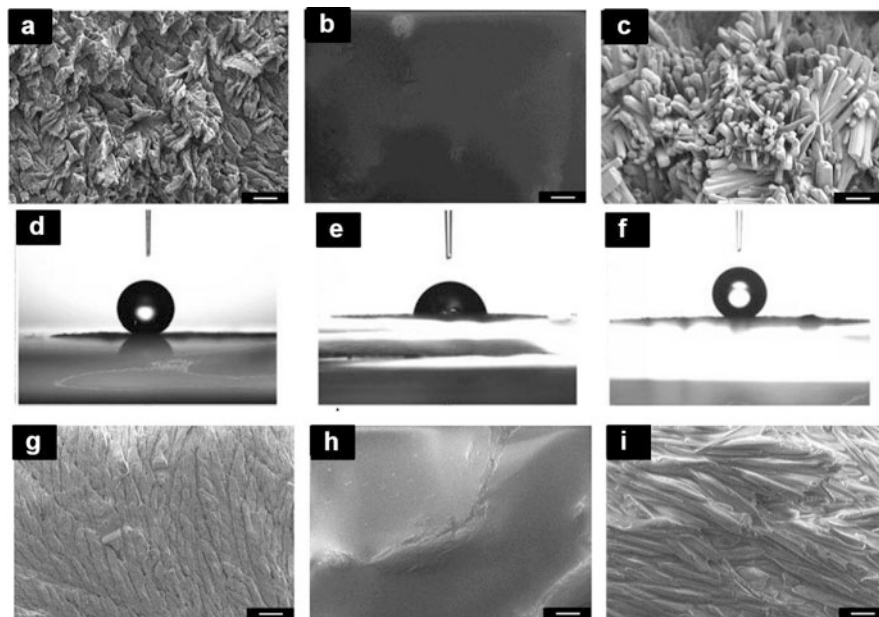
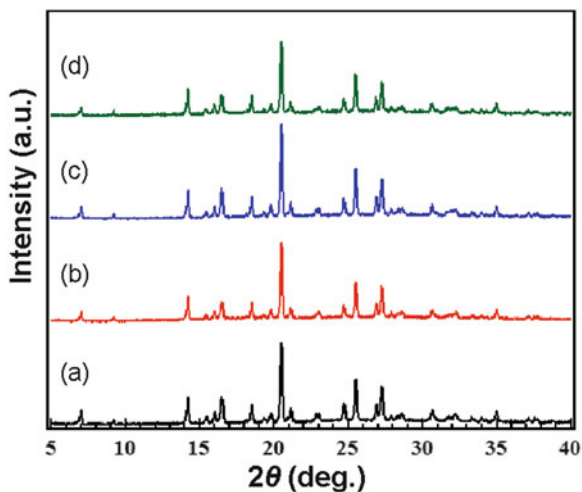


**Fig. 28.6** SEM images of the reversible topographical changes in the microcrystalline surface of **30** on a glass substrate (**a–c**) and SrTiO<sub>3</sub> (STO) (110) surface (**g–i**); water droplet shapes (**d–f**) on the surfaces of (**a–c**), respectively (scale bar: 10  $\mu\text{m}$ )

**Fig. 28.7** XRD pattern changes by alternate UV and visible light irradiation of microcrystalline surface of **30** on glass substrate: (**a**) Coated film before UV irradiation. (**b**) After UV irradiation at 67 °C for 30 min. (**c**) After next visible light irradiation while keeping at 67 °C for 1.5 h. (**d**) After second UV light irradiation for 10 min while keeping at 67 °C for 30 min



surface. The results demonstrated this rapid crystal growth and may explain the appearance of the petal effect. Furthermore, this inspired us to attempt epitaxial crystal growth of **30** on a suitable substrate whose lattice parameter resembles that of **30** [19]. For decades, the hetero-epitaxial growth of organic materials has received

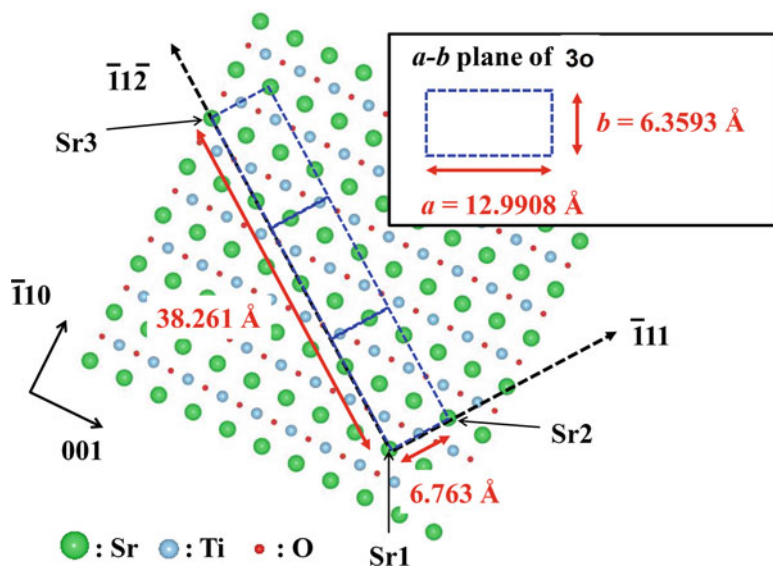


**Fig. 28.8** STO 110 plane with a space group of  $Pm\bar{3}m$  ( $a = 3.905 \text{ \AA}$ ). Distance between Sr atoms (Sr1–Sr2) on  $\bar{1}11$  axis is 6.763 Å, and this value is close to the length of the b axis of rod-shaped **3o**. The  $\bar{1}1\bar{2}$  axis of STO is perpendicular to the  $\bar{1}11$  axis. Distance between Sr1 and Sr3 on the  $\bar{1}1\bar{2}$  axis (38.261 Å) is close to three times the length of the a-axis (12.9908 Å) of rod-shaped **3o**. Therefore, the a-axis of rod-shaped **3o** fits the  $\bar{1}1\bar{2}$  axis on the 110 plane of STO

much attention because of its importance and unique characteristics. Organic hetero-epitaxial techniques are useful for the fabrication of electronic and photonic devices [20]. In device fields, single-crystal substrates of metal oxides, such as SrTiO<sub>3</sub> (STO), MgO, and sapphire, are used to obtain hetero-epitaxial thin films. Among single-crystal substrates, STO substrates are often used in the ferroelectric field. STO has a perovskite structure with a cubic phase (space group,  $Pm\bar{3}m$ ; lattice constant,  $a = 3.905 \text{ \AA}$ ; ICSD number, #23076). Figure 28.8 shows the 110 surface of STO, which has  $\bar{1}1\bar{2}$  and  $\bar{1}11$  axes on a plane, and the  $\bar{1}1\bar{2}$  axis is perpendicular to the  $\bar{1}11$  axis. The distance of Sr1–Sr2 is 6.763 Å in the  $\bar{1}11$  axis, and this value is close to lattice constant b (6.3593 Å) of rod-shaped **3o**. The Sr1–Sr3 distance on the  $\bar{1}1\bar{2}$  axis (38.261 Å) is close to three times the length of the a-axis (12.9908 Å) of the rod-shaped **3o**. Therefore, the a-axis of rod-shaped **3o** fits the  $\bar{1}1\bar{2}$  axis on the 110 plane of the STO. Thus, rod-shaped **3o** can grow on the 110 surface of the STO. We used an STO substrate with a 110 plane (110 STO) to epitaxially grow **3o** on the substrate.

The film was prepared by coating a chloroform solution containing **3o** (100 mg/mL) onto the substrate (10 × 10 mm, glass or STO crystal plates). The film was approximately 20 μm thickness. The photoinduced topographical changes were carried out in the same way as in the previous case on a glass substrate. Upon UV irradiation, crystals of **3o** were melted, and a flat eutectic surface

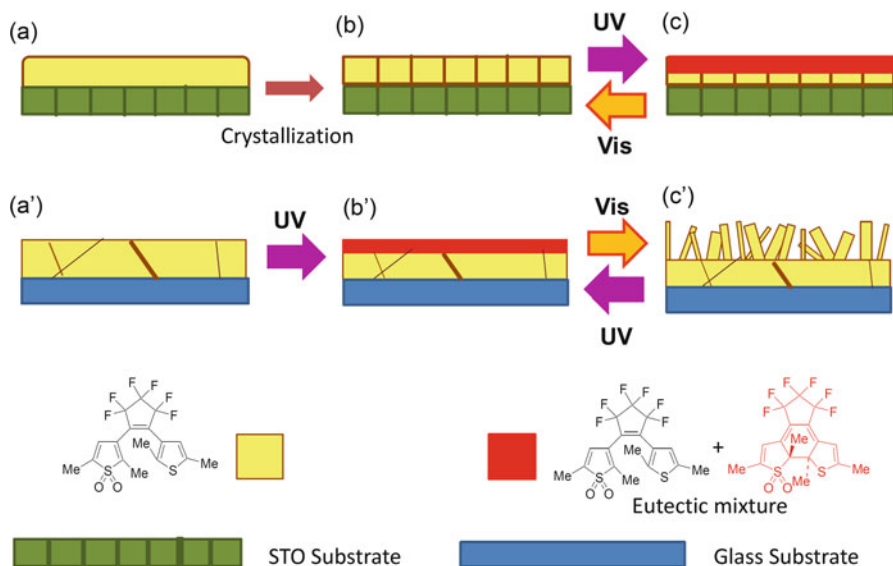


**Fig. 28.9** Schematic illustration of crystal growths of **3o**. (a–c) Photoinduced topographical changes of surface on STO substrate. (a'–c') Photoinduced topographical changes of surface on glass substrate

was generated within 30 min. Upon visible light irradiation of the surface, the microcrystals of **3o** regenerated and covered the entire surface of the bulk film within 1.5 h. Figure 28.6g–i represents the SEM images on the surface to compare the results obtained on glass substrate (Fig. 28.6a–c). Due to differences in the substrate, the shape of the microcrystalline surfaces was different. The surface on the STO was covered with prone rod-shaped microcrystals, while the surface on the glass substrate was covered with random standing rod-shaped microcrystals. The situations in Fig. 28.6h, i could be repeated by alternate UV and visible light irradiation. Here, the rapid crystal growth was due to the existence of seeds for the crystallization of regenerated **3o**. The results suggest that if the subphase crystals are generated by epitaxial growth on a crystal matrix, then photochemically reversible crystal growth can be performed (Fig. 28.9j).

The appropriate reversible reflection pattern profiles of **3o** on the STO substrate were monitored by XRD measurements (Fig. 28.10). Diffraction intensities were normalized using the diffraction intensity of the 110 diffraction of the STO substrate. The results were compared using glass (Fig. 28.7) as a control. The diffraction peaks at  $8.3^\circ$ ,  $16.6^\circ$ , and  $24.9^\circ$  correspond to the 002, 004, and 006 diffractions, respectively, of rod-shaped **3o**. Therefore, the **3o** film on the STO substrate with the 110 plane had the 001 orientation. In contrast, the **3o** films on (100) and (111) STO and glass had major orientations of 100, 100, and  $30\bar{2}$ , respectively, but minor orientations as well. The surface roughness of (100), (110),

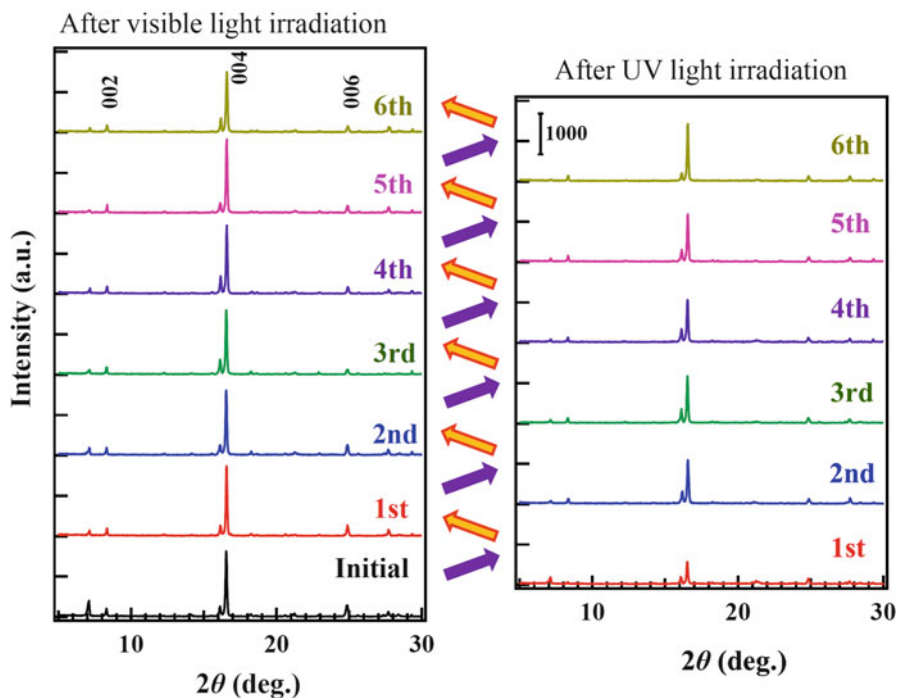


**Fig. 28.10** Photoinduced reversible XRD pattern changes of microcrystalline film of **3o** on (110) surface of STO single crystal upon alternate irradiation with UV ( $\lambda = 366$  nm) and visible ( $\lambda > 500$  nm) light. Purple and orange arrows indicate UV and visible light irradiations, respectively

and (111) STO substrates were examined by AFM, and all of them were ascertained to be flat [19]. This result clearly showed that the surface lattice structure of the substrates was important for the growth orientation of the films.

The microcrystalline film of **3o** on the glass substrate showed many reflection peaks (Fig. 28.7), while that on the STO substrate showed only one dominant reflection at  $16.6^\circ$  (Fig. 28.10). The purity of the reflections was maintained after several UV-induced crystal melting and visible light-induced crystal growing cycles of **3o**. To the best of our knowledge, such a photoswitchable crystal growing technique is novel and will be useful in controlling crystal growth for optoelectronic devices and controlling the crystal habit in a polymorphological system.

## 28.5 Photoinduced Reversible Self-Epitaxial Crystal Growth

As described in the previous section, photoinduced repetitive epitaxial crystal growth was performed by using a derivative **3o**. Although the finding is very

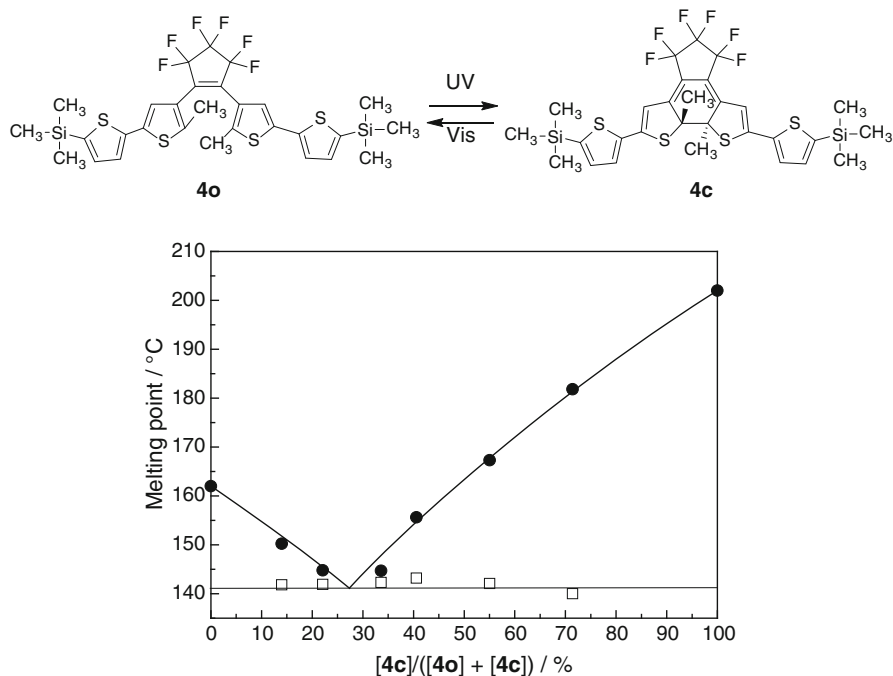


**Fig. 28.11** Phase diagram of mixtures of open-ring (**4o**) and closed-ring (**4c**) isomers formed by UV light (313 nm) irradiation

interesting, it is necessary to use very expensive STO crystal as a substrate. For the real applications, it is desirable to perform the epitaxial crystal growth on common substrates, i.e., glasses. We accidentally found the epitaxial crystal growth of needle-shaped crystals of **4c** even on the glass substrate.

Photoinduced isomerization between colorless **4o** and blue **4c** and the phase transition diagram of **4o** and **4c** obtained by DSC measurement are shown in Fig. 28.11. The melting points of **4o** (cubic-shaped crystals) and **4c** (needle-shaped crystals) were 162 and 202 °C, respectively. And the eutectic temperature was 141 °C. At the eutectic point, the ratio of **4o** and **4c** was 73: 27. Therefore, after prolonged UV irradiation to the surface the content of **4c** exceeded from 27 % near the surface, then the needle-shaped crystals of **4c** were expected to grow on the surface. The crystal growth of **4c** was observed at the eutectic temperature; however, the growth was observed even at 30 °C. The generated rough surface was shown in Fig. 28.12 which was well ordered and finer compared with that of **2c** in same magnifications of SEM images [21]. In the later experiments, such crystal growth was ascertained above glass transition temperature [22].

The sizes of the needle-shaped crystals of **4c** were 0.20–0.35  $\mu\text{m}$  in diameter and 2.2–2.5  $\mu\text{m}$  in length, while those of **2c** were 1.0–2.0  $\mu\text{m}$  in diameter and around 10  $\mu\text{m}$  in length. Additionally, the needles looked well ordered in **4c** compared with

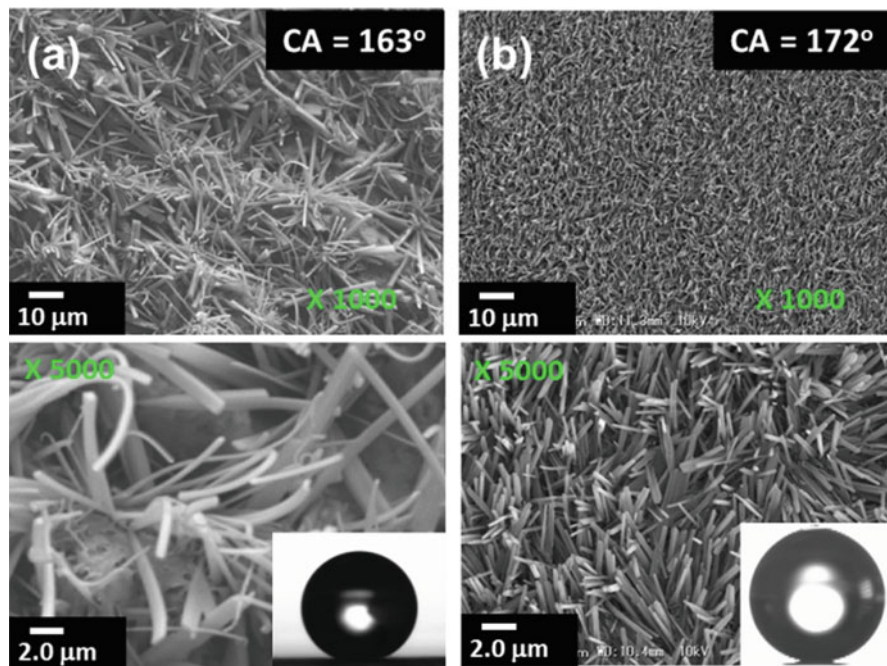


**Fig. 28.12** SEM images of (a) photoinduced rough surface covered with **2c** upon UV irradiation to the microcrystalline surface of **2o** and (b) photoinduced rough surface covered with **4c** upon UV irradiation to the microcrystalline surface of **4o** with same magnifications

those of **2c**. Due to the differences, CAs of a water droplet enhanced to 172° of **4c** from 163° of **2c**. The activation energy was measured for the crystal growth of **4c** according to the method used for **2c** (Sect. 28.2) and obtained to be 58 kJ/mol, which is much lower than that of **2c** (143 kJ/mol) [21].

To ascertain the epitaxy of the fine needle-shaped crystals **4c**, we carried out grazing incidence X-ray diffraction (GIXD) analysis for the film where **4c** crystals were standing on a **4o** subphase prepared by solution casting (Fig. 28.13) [3]. Due to the rough surface of **4o**, small peaks other than 110 and 220 reflections were observed. The largest peaks around 7.5° and 15° were attributed to the 110 and 220 peaks of **4o**, respectively (Fig. 28.14). The strong reflection attributed to the 013 peak of the **4c** crystals appeared only in the out-of-plane but not in the in-plane profiles (denoted by the arrow in Fig. 28.15a) among the diffraction peaks of **4o** after UV irradiation, in contrast to the out-of-plane profiles. This result indicated that the 013 surface (the sky blue surface in Fig. 28.15b) of **4c** was located almost parallel to the substrate; hence, the needle-shaped crystals stood all together at about 60° to the substrate. It was also expected that the alignment will effectively enhance

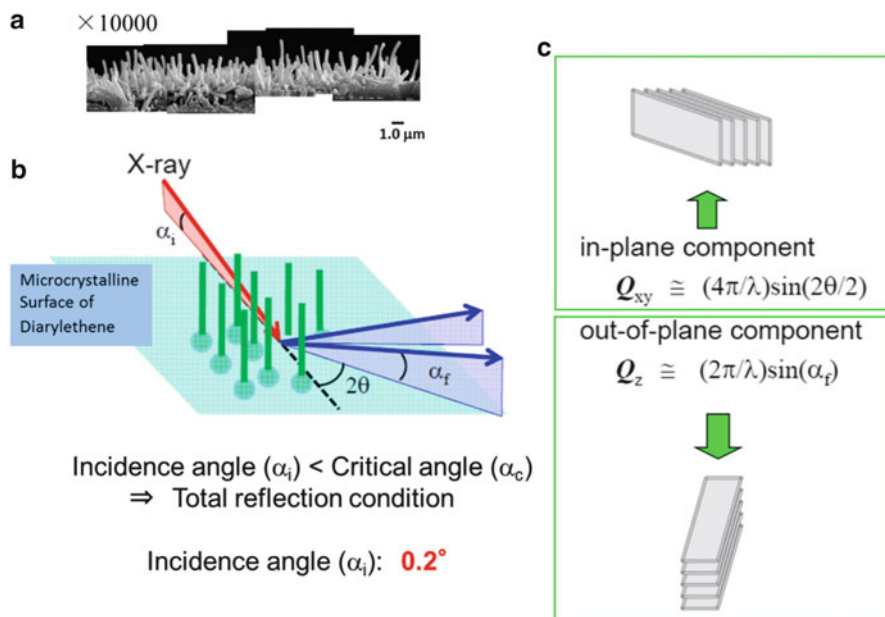


**Fig. 28.13** (a) SEM image of the cross section of a flat surface of crystalline surface of **4o** prepared by vacuum deposition on glass substrate (scale bar: 3.33 μm), (b) schematic illustration of the GIXD observation of the film, and (c) XRD diffraction of the crystalline film of **4o**: vertically repeating structure is detectable as in-plane component while horizontally repeating structure is detectable as out-of-plane component

the CA. The thin films of **4o** were also prepared on several kinds of substrates by solution coating, and generation of similar rough surfaces was observed. The as-prepared **4o** thin film had a 110 orientation from the X-ray diffraction (XRD) pattern (Fig. 28.14c). The 013-oriented needle-shaped **4c** grew on the surface of the 110-oriented **4o** thin film from the GIXD pattern (Fig. 28.15a). We compared the crystal lattice of **4o** and **4c**. The 110 plane of **4o** and 013 plane of **4c** are shown in Fig. 28.15b. The height and width of the 110 plane of **4o** are 23.609 and 11.956 Å, respectively, while those of the 013 plane of **4c** are 23.847 and 9.974 Å, respectively (Fig. 28.16). The height of the 013 plane of **4c** is in accordance with that of the 110 plane of **4o**. Although the width is different between them, 10 pieces of the 110 plane of **4o** and 12 pieces of the 013 plane of **4c** overlap similar regions (Fig. 28.16e). Therefore, the needle-shaped crystal of **4c** epitaxially grew on the crystal lattice of **4o**. In the above results, the nano crystals of **4c** always formed by UV irradiation standing at 60° regardless of which substrate was applied. The lower activation energy of formation of **4c** crystals (58 kJ/mol) [21] compared to that (143 kJ/mol) [11] of crystal growth of **2c** on the eutectic melted surface of the mixture of **2o** and **2c** was attributed to **4o** crystals acting as the seeds of formation of **4c** crystals.

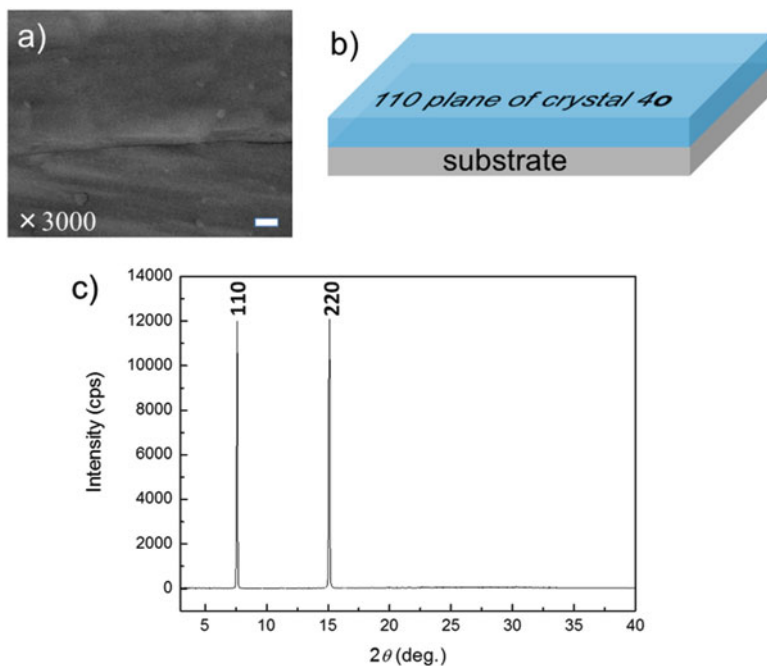


**Fig. 28.14** (a) SEM image of a flat surface of crystalline surface of **4o** prepared by vacuum deposition on glass substrate (scale bar: 3.33 μm), (b) schematic illustration of the film, and (c) XRD diffraction of the crystalline film of **4o**

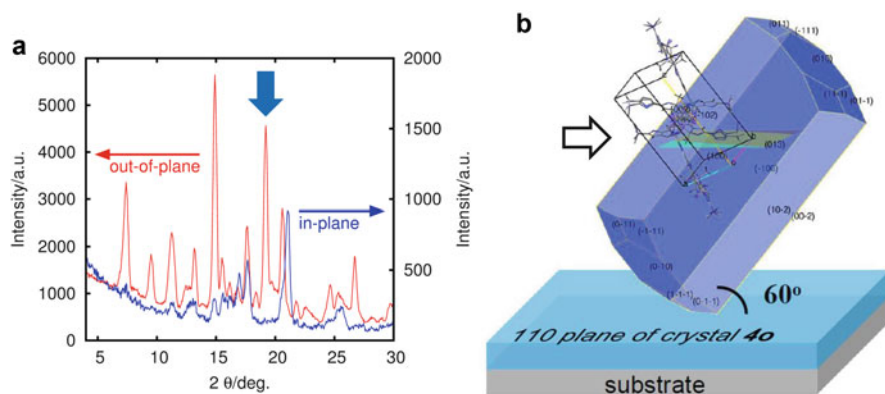


**Fig. 28.15** (a) In-plane and out-of-plane GIXD profiles. Reflection attributed to the 013 peak of the **4c** crystals appeared only in the out-of-plane profiles (denoted by the arrow). (b) Illustration of the **4c** crystal shape over the microcrystalline surface of a **4o** substrate unit cell of **4c** (black lines) and 013 plane of **4c** (sky blue plane in crystal **4c** denoted by the white arrow)

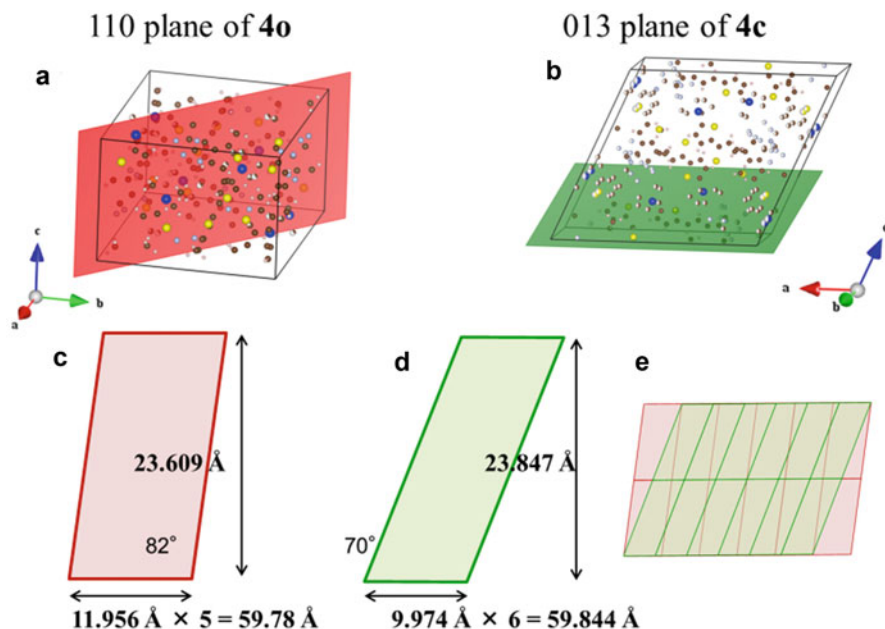


**Fig. 28.16** (a) The 110 plane of the **4o** crystal. (b) The 013 plane of the **4c** crystal. (c) The size and shape of the 110 plane of **4o**. (d) The size and shape of the 013 plane of **4c**. (e) The overlapping planes of 110 of **4o** and 013 of **4c**

## 28.6 Photoinduced Reversible-Appearance Moth-Eye Effect Near-IR Region

Due to the highly ordered structure, the rough surfaces are expected to show not only superhydrophobicity but also the moth-eye antireflection effect in the infrared region. The moth-eye effect is the antireflective capabilities of functional surfaces found in nature, especially in the eyes of moths [23]. The deep blue-colored closed-ring isomer **4c** formed by UV irradiation has an absorbance whose band tail extends to around 800 nm. Therefore, the antireflectance of the microcrystalline surface was monitored in a region larger than 800 nm wavelengths, where **4c** has no absorbance. The results are summarized in Fig. 28.17. The reflection spectrum of the initial microcrystalline surface of **4o** averages 3.5 % reflectance in the 800–1,800 nm wavelength region. By UV irradiation followed by maintaining the film in the dark at 30 °C for 3 days, the surface became covered with needle-shaped **4c** crystals whose diameters and lengths are around 0.2–0.3  $\mu\text{m}$  and 2.2–2.5  $\mu\text{m}$ , and almost no reflectance was observed (less than 0.5 %), thus demonstrating the moth-eye effect [24]. Reflectance was measured by a spectrophotometer via a mirror reflection arrangement of 5° incidence and 5° reflection in an 800–1,800 nm wavelength region. Incident light had 45° polarization to the plane of incidence. Reflectance

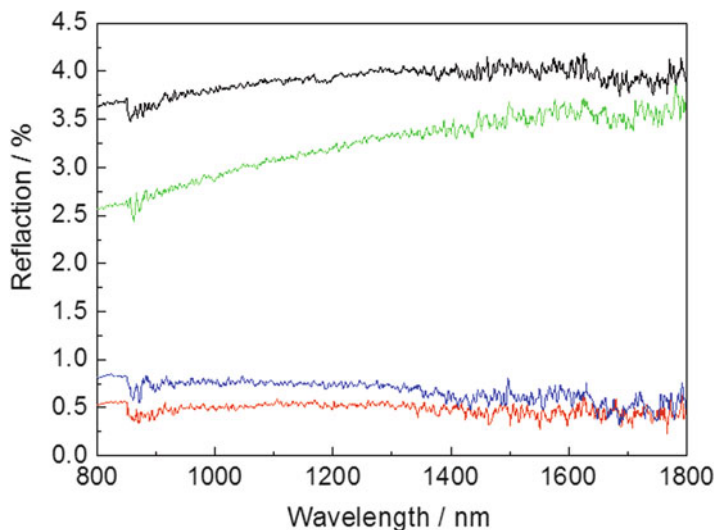


**Fig. 28.17** Reversible reflection changes accompanied by reversible topographical changes of the surface. *Black line*: Initial microcrystalline surface of **4o**, *red line*: UV-generated rough surface covered with needle-shaped **4c** crystals show in moth-eye effect, *green line*: Regenerated microcrystalline surface of **4o**, *blue line*: Regenerated rough surface of **4c**

of 3.97 % and 0.38 % were obtained for the **4o** and **4c** surfaces, respectively. In order to estimate the efficiency of the reflectance (observed reflectance/theoretical reflectance), the theoretical reflectance values were evaluated. The refractive indices of **4o** and **4c** were measured by changing the concentration of the polystyrene-**4o** or **4c** composite, and refractive indices at 1545 nm were estimated to be 1.572 for **4o** and 1.622 for **4c** by extrapolation of the concentration of **4o** or **4c** [25]. Using the measured values of refractive indices  $n$  and the incident angle  $\theta$  of reflectance measurement ( $\theta = 5^\circ$ ), the theoretical reflectance in P and S polarization for the ideal flat surfaces were calculated according to Eqs. 28.1 and 28.2 using Fresnel's coefficient.

$$R_s = \left( \frac{\cos \theta - \sqrt{n^2 - \sin^2 \theta}}{\cos \theta + \sqrt{n^2 - \sin^2 \theta}} \right)^2 \quad (28.1)$$

$$R_p = \left( \frac{n^2 \cos \theta - \sqrt{n^2 - \sin^2 \theta}}{n^2 \cos \theta + \sqrt{n^2 - \sin^2 \theta}} \right)^2 \quad (28.2)$$

The calculated average reflectance over S and P polarizations for the ideal flat surfaces were 4.94 and 5.63 for **4o** and **4c**, respectively. Therefore, the reductions of the reflectance due to the roughness of the surfaces, i.e., the moth-eye effect, were obtained to be 80.34 % for the relatively flat surface of **4o** but 6.68 % for the rough surface of **4c**.

Reflectance was recovered by regeneration of the **4o** surface by 2 h visible light ( $\lambda > 500$  nm) irradiation, maintaining the eutectic temperature (141 °C). As is expected from the previous observation of the reversible formation of a superhydrophobic surface by alternate irradiations with UV and visible light accompanied by temperature control, the surface showing the moth-eye effect was also switchable under the same conditions.

## 28.7 Conclusion

Diarylethenes show reversible topographical changes on the microcrystalline film surfaces via eutectic melted state. Initially, the randomly oriented needle-shaped crystals of **2c** generate upon UV irradiation. By using a suitable inorganic crystalline subphase, reversible epitaxial crystal growth is performed for rod-shaped crystals of **3o**. Ultimate epitaxial crystal growth is also obtained without using expensive inorganic crystals. One isomer itself act as the role of the subphase, hence the epitaxial crystal growth can be performed even on the glass plates. We call this Self-Epitaxial Crystal Growth (SECG), and crystal growth of **4c** undergo on the crystal lattice of **4o**. The epitaxial crystal growth can be repeated.

The mechanism requires two conditions:

1. The one (open-ring) isomer expands on the subphase showing only one crystal plane.
2. A lattice of the other (closed-ring) isomer matches the above lattice of the plane of the former (open-ring) isomer crystal. Then photoinduced SECG formation is expected.

Such stable formation of a hydrophobic surface is attributed to the submicron-scale needle-shaped crystals standing in a densely packed situation. Due to the ordered structure, the switchable moth-eye effect was also performed. These surface functions are due to the SECG mechanism. Such self-organized crystal growth will be a candidate for the formation of the photonic crystals.

## References

1. M. Irie, Diarylethenes for memories and switches. *Chem. Rev.* **100**, 1685–1716 (2000)
2. B.L. Feringa, W.B. Browne, *Molecular Switches* (Wiley-VCH, Weinheim, 2011)
3. M. Irie, S. Kobatake, M. Horichi, Reversible surface morphology changes of a photochromic diarylethene single crystal by photoirradiation. *Science* **291**, 1769–1772 (2001)
4. R. Rosario, D. Gust, M. Hayes, F. Jahnke, J. Springer, A.A. Garcia, Photon-modulated wettability changes on spiropyran-coated surfaces. *Langmuir* **18**, 8062–8069 (2002)
5. W. Barthlott, C. Neinhuis, Purity of the sacred lotus, or escape from contamination in biological surfaces. *Planta* **202**, 1–8 (1997)
6. H.Y. Erbil, A.L. Demirel, Y. Avci, O. Mert, Transformation of a simple plastic into a superhydrophobic surface. *Science* **299**, 1377–1380 (2003)

7. S. Shibuichi, T. Onda, N. Satoh, K. Tsujii, Super water-repellent surfaces resulting from fractal structure. *J. Phys. Chem.* **100**(50), 19512–19517 (1996)
8. T. Onda, S. Shibuichi, N. Satoh, K. Tsujii, Super-water-repellent fractal surfaces. *Langmuir* **12**(9), 2125–2127 (1996)
9. K. Uchida, N. Izumi, S. Sukata, Y. Kojima, S. Nakamura, M. Irie, Photoinduced reversible formation of microfibrils on a photochromic diarylethene microcrystalline surface. *Angew. Chem. Int. Ed.* **45**(39), 6470–6473 (2006)
10. K. Uchida, N. Nishikawa, N. Izumi, S. Yamazoe, H. Mayama, Y. Kojima, S. Yokojima, S. Nakamura, K. Tsujii, M. Irie, Phototunable diarylethene microcrystalline surfaces: lotus and petal effects upon wetting. *Angew. Chem. Int. Ed.* **49**(34), 5942–5944 (2010)
11. N. Nishikawa, A. Uyama, T. Kamitanaka, H. Mayama, Y. Kojima, S. Yokojima, S. Nakamura, K. Tsujii, K. Uchida, Photoinduced reversible topographical changes on diarylethene microcrystalline surfaces with bio-mimetic wetting properties. *Chem. Asian. J.* **6**(9), 2400–2406 (2011)
12. T. Yamada, S. Kobatake, K. Muto, M. Irie, X-ray crystallographic study on single-crystalline photochromism of bis(2,5-dimethyl-3-thienyl)perfluorocyclopentene. *J. Am. Chem. Soc.* **122**, 1589–1592 (2000)
13. N. Izumi, N. Nishikawa, S. Yokojima, Y. Kojima, S. Nakamura, S. Kobatake, M. Irie, K. Uchida, Photo-induced reversible topographical changes of photochromic dithienylethene microcrystalline surfaces. *New J. Chem.* **33**, 1324–1326 (2009)
14. S. Shibuichi, T. Onda, N. Satoh, K. Tsujii, Super water-repellent surfaces resulting from fractal structure II. *J. Jpn. Oil Chem. Soc.* **46**(6), 649–659 (1997) (in Japanese)
15. H. Mayama, Blooming theory of tristearin. *Soft Matter* **5**(4), 856–859 (2009)
16. W. Fang, H. Mayama, K. Tsujii, Spontaneous formation of fractal structures on triglyceride surfaces with reference to their super water-repellent properties. *J. Phys. Chem. B* **111**(3), 564–571 (2007)
17. A. Uyama, S. Yamazoe, S. Shigematsu, M. Morimoto, S. Yokojima, H. Mayama, Y. Kojima, S. Nakamura, K. Uchida, Reversible photocontrol of surface wettability between hydrophilic and superhydrophobic surfaces on an asymmetric diarylethene solid surface. *Langmuir* **27**(10), 6395–6400 (2011)
18. S. Kobatake, K. Uchida, E. Tsuchida, M. Irie, Single-crystalline photochromism of diarylethenes: reactivity–structure relationship. *Chem. Commun.* **38**, 2804–2805 (2002)
19. S. Sakiyama, S. Yamazoe, A. Uyama, M. Morimoto, S. Yokojima, Y. Kojima, S. Nakamura, K. Uchida, Photoinduced reversible heteroepitaxial microcrystal growth of a photochromic diarylethene on (110) surface of SrTiO<sub>3</sub>. *Cryst. Growth Des.* **12**, 1464–1468 (2012)
20. C. Simbrunner, F. Quochi, G. Hernandez-Sosa, M. Oehzelt, R. Resel, G. Hesser, M. Arndt, M. Saba, A. Mura, G. Bongiovanni, H. Sitter, Organic-organic heteroepitaxy of red-, green-, and blue-emitting nanofibers. *ACS Nano* **4**, 6244–6250 (2010)
21. N. Nishikawa, H. Kiyohara, S. Sakiyama, S. Yamazoe, H. Mayama, T. Tsujioka, Y. Kojima, S. Yokojima, S. Nakamura, K. Uchida, Photoinduced formation of superhydrophobic surface on which contact angle of a water droplet exceeds 170° by reversible topographical changes on a diarylethene microcrystalline surface. *Langmuir* **28**(51), 17817–17824 (2012)
22. N. Fujinaga, N. Nishikawa, S. Sakiyama, S. Yamazoe, Y. Kojima, T. Tsujioka, S. Yokojima, S. Nakamura, K. Uchida, Temperature dependence of the photoinduced micro-crystalline surface topography of a diarylethene. *CrystEngComm* **15**(42), 8416–8419 (2013)
23. M. Srinivasarao, Nano-optics in the biological world: beetles, butterflies, birds, and moths. *Chem. Rev.* **99**, 1935–1961 (1999)
24. P. Vukusic, J.R. Sambles, Photonic structures in biology. *Nature* **424**, 852–855 (2003)
25. N. Nishikawa, S. Sakiyama, S. Yamazoe, Y. Kojima, E. Nishihara, T. Tsujioka, H. Mayama, S. Yokojima, S. Nakamura, K. Uchida, Photoinduced self-epitaxial crystal growth of a diarylethene derivative with antireflection moth-eye and superhydrophobic lotus effects. *Langmuir* **29**(25), 8164–8169 (2013)

# Chapter 29

## Luminescence Modulation of Organic Crystals by a Supramolecular Approach

Norimitsu Tohnai

**Abstract** Solid-state fluorescence properties of organic compounds have attracted much attention due to their potential applications not only in organic light-emitting diodes and organic field-effect transistors but also in imaging tools and sensing devices. Solid-state fluorescence properties such as color, intensity, lifetime, and process of the organic compounds depend heavily on molecular arrangements, as well as molecular structures. However, it is difficult to create particular molecular arrangements easily and to modulate them as planned. An organic salt composed of an aromatic acid (functional part) and an alkylamine (arrangement-controlling part) is a potential strategy for creating functional organic solid materials. Organic salts of anthracene-2,6-disulfonic acid (ADS) with a wide variety of primary amines give various molecular arrangements, and their fluorescence properties depend on the amine. A suitable choice of the amine yields an outstanding fluorescent material that exceeds unmodified anthracene. Thus, a systematic investigation of this system reveals a library of arrangements and properties, which in turn leads to remarkable strategies for the development of organic solid materials.

**Keywords** Organic salt • Charge-assisted hydrogen bond • Solid-state fluorescence • Anthracene • Crystal engineering

### 29.1 Introduction

Solid-state fluorescence properties of organic compounds have attracted much interest due to their promising and widespread applications not only in organic light-emitting diodes and organic field-effect transistors but also in imaging tools and sensing devices [1–5]. Solid-state fluorescence properties such as color, intensity,

---

N. Tohnai (✉)

Department of Material and Life Science, Graduate School of Engineering, Osaka University,  
Yamadaoka 2-1, Suita, Osaka 565-0871, Japan

e-mail: [tohnai@mls.eng.osaka-u.ac.jp](mailto:tohnai@mls.eng.osaka-u.ac.jp)

© Springer Japan 2015

R. Tamura, M. Miyata (eds.), *Advances in Organic Crystal Chemistry*,

DOI 10.1007/978-4-431-55555-1\_29

569

lifetime, and process of the organic compounds depend heavily on molecular arrangements as well as molecular structures. In this context, the most serious problem in the development of solid-state fluorescence compounds and their applications is that many organic fluorophores that strongly fluoresce in solution lose this property in the solid state [6–9]. Namely, it is known that intermolecular interactions such as  $\pi/\pi$  interactions and hydrogen bonds and loose packing derived from molecular arrangements cause luminescence quenching in the solid state [10–13].

In order to solve these problems, one of the most useful strategies is to tune molecular arrangements in the solid state because the arrangements have a strong effect on the solid-state fluorescence properties. In previous studies on the tuning of fluorescence properties by changing the molecular arrangement, the changes were achieved by means of polymorphism, inclusion of guests, and introduction of substituents [14–27]. Control of the arrangement of fluorophores can regulate the solid-state fluorescence properties even though the same fluorophores are utilized. In addition, clarification of the effect of the arrangement on the solid-state fluorescence properties provides significant rules for regulation, i.e., for the development of organic solid materials. From these studies, it was found that the following affect the solid-state fluorescence properties: conformational changes of the fluorophore (e.g., dihedral angle), intermolecular interactions between fluorophores, and interactions between fluorophore and guest (e.g.,  $\pi/\pi$  interaction, CT interaction). However, the actual effect of the arrangements was not well understood, because the previous studies did not conduct systematic investigations in which various arrangements were constructed, and the corresponding properties were investigated for the same fluorophores. Namely, the methodologies of the changes in the previous studies were not suitable for systematic investigations of the relationship between fluorescence properties and molecular arrangements for the following reasons. Polymorphism does not always give different arrangements due to difficulty in control [28–33]. For example, anthracene, which is one of the simplest and most well-known fluorophores, exhibits only one type of arrangement and corresponding solid-state fluorescence property. However, twelve crystal structures of unmodified anthracene are deposited in the Cambridge Structural Database (CSD) as crystallographic information files (CIF). Their lattice parameters are slightly different due to the measurement conditions, but their arrangements of anthracene molecules are the same herringbone type. On the other hand, inclusion phenomena do not always afford co-crystals composed of fluorophore and guest molecules, because the fluorophore as host has certain limitations for the guest species [34]. Therefore, the resulting arrangements are also restricted in a narrow range. As a significant strategy for achieving various arrangements of fluorophores, the introduction of substituents by chemical modification has so far been utilized. However, the introduction of substituents may be time consuming to produce many fluorophore derivatives, and their syntheses are often troublesome. Moreover, such chemical modifications may change the inherent photophysical properties of the fluorophore.

## 29.2 Organic Salts Composed of Anthracenedisulfonic Acid and Alkyl Amines

### 29.2.1 Advantage of Organic Salts

Organic salts of anthracenedisulfonic acid (ADS) with various alkyl amines have been constructed as a tunable solid-state fluorescence system, in which the molecular arrangements of anthracene moieties and the corresponding solid-state fluorescence properties are easily regulated by alteration of the amines [35–39]. Consequently, these organic salts are suitable systems for systematic investigation due to their following advantages. First, the salts are formed by strong intermolecular interactions between the ion pairs, such as hydrogen bonds and electrostatic interactions, i.e., charge-assisted hydrogen bonds. These strong interactions yield a co-crystal between the acids and amines. Second, amines with various substituents are commercially available. Third, the salts are easily prepared by only mixing their components in organic solvents. These advantages of organic salts should provide diversity in arrangements of the same fluorophores. In fact, organic salts have been widely researched for screening of organic solid materials [40–48]. For instance, the salts have been employed for enantiomeric resolution of racemic acids or bases, for the creation of electronic or optical materials that have high conductivity or second harmonic generation, and for crystalline-state properties such as fluorescence emission maximum and quantum yield. Therefore, these systems serve as a useful strategy for efficient screening of arrangements and their corresponding properties.

### 29.2.2 Crystal Structures of Unmodified Anthracene

Many crystal structures of unmodified anthracene are deposited in the CSD. However, they are all nearly the same structure: there is only a slight difference in cell parameters depending on measurement conditions [49]. The typical packing manner of unmodified anthracene is classified as a herringbone-type structure according to structural motifs of polyaromatic hydrocarbons defined by G. Desiraju and A. Gavezzotti (Fig. 29.1). The herringbone-type structure is seen in many linear acene molecules, e.g., tetracene and pentacene.

### 29.2.3 Crystal Structures of ADS Salts

Scheme 29.1 shows chemical structures of the organic salts composed of anthracenedisulfonic acids and various primary amines. The organic salts were

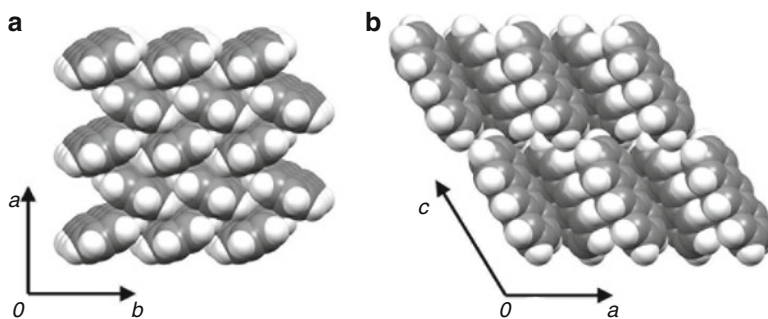
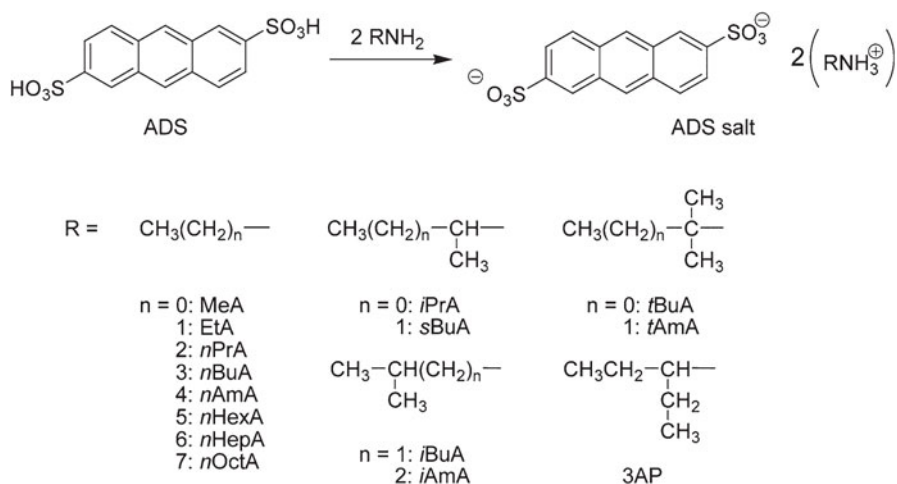


**Fig. 29.1** Molecular packing diagram of anthracene (a) viewed down the crystallographic  $c$  axis and (b) viewed down the crystallographic  $b$  axis



**Scheme 29.1** Chemical structures of the organic salts of ADS with various amines

recrystallized from a mixture of methanol and acetonitrile to give crystals. Figure 29.2 depicts the crystal structures of ADS salts with various primary amines, except for those with *n*-propylamine (*n*PrA), *n*-hexylamine (*n*HexA), and *n*-octylamine (*n*OctA), which did not give single crystals suitable for X-ray crystallographic study. Depending on the primary amines, the packing manners of anthracene in the crystal structures are different.

The crystal structures are composed of ADS and an amine in a molar ratio of 1:2 with charge-assisted hydrogen-bonding networks between sulfonate anions and the ammonium cations. The hydrogen-bonding networks are classified into three typical patterns as shown in Scheme 29.2: 6 + 6 sheet, 8 + 4 sheet, and 4 + 4 ladder. These networks depend on the bulkiness of the amines. According to the hydrogen-bonding network and the packing manners of the anthracene moieties, these crystal structures can be categorized into seven crystal forms (Forms I–VII, Table 29.1).

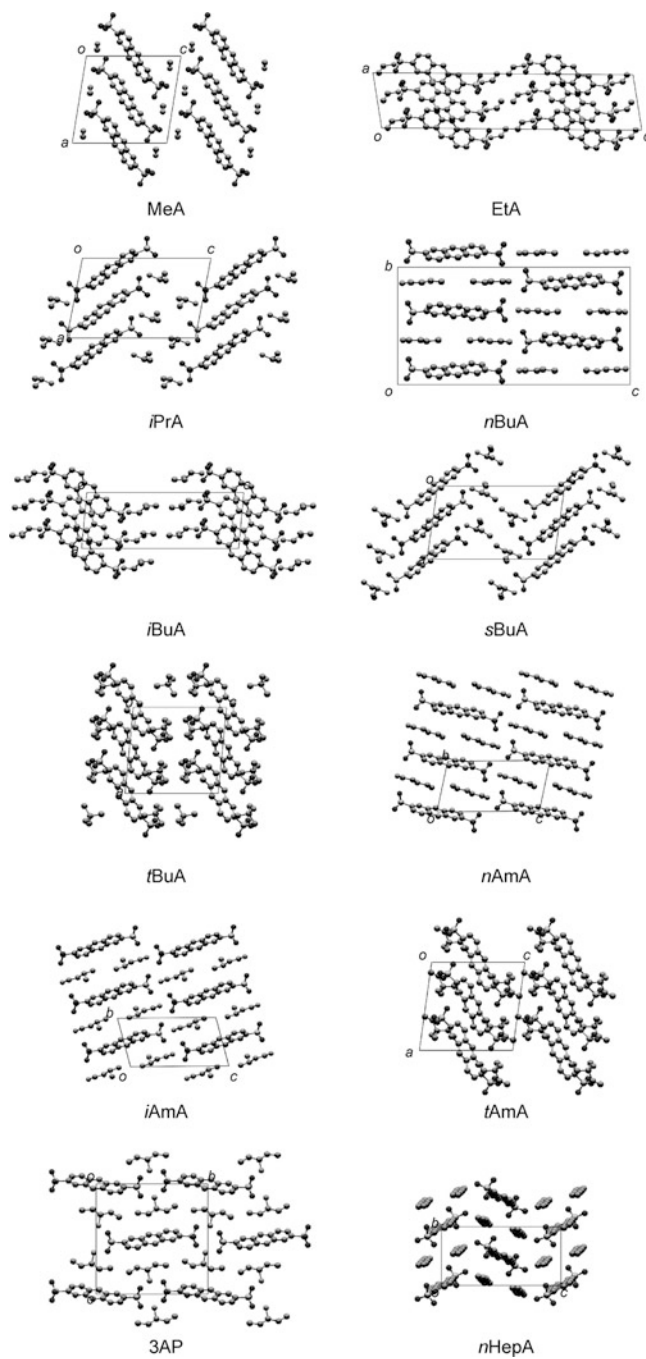


**Fig. 29.2** Crystal structures of the salts of ADS with various amines. Hydrogen atoms are omitted for clarity

**Scheme 29.2** Schematic representation of hydrogen-bonding networks between sulfonate anions and ammonium cations

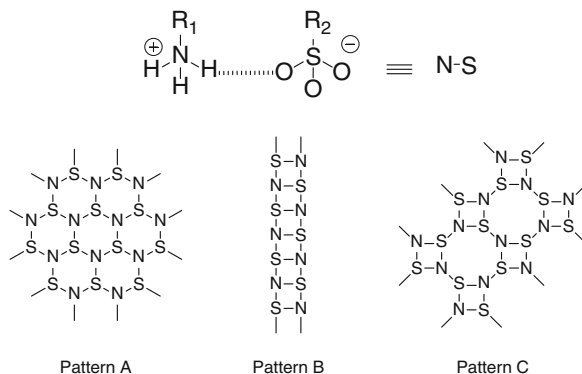
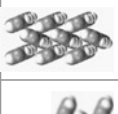


Table 29.1 shows the molecular arrangements, molecular packing diagrams, and hydrogen-bonding networks in the crystal structures of Forms I–VII. The ADS salts with short and/or branched alkyl amines give two-dimensional hydrogen-bonding networks (Patterns A and B in Scheme 29.2). Pattern A is formed by six-membered hydrogen-bonded rings consisting of three sulfonate anions and three ammonium cations, similar to those of alkanolate salts of 1-naphthylmethylammonium. Pattern B is composed of four- and eight-membered hydrogen-bonded rings, and this network is also seen in ammonium carboxylates composed of ammonium terephthalate. The ADS salts with long linear amines form a one-dimensional network composed of four-membered hydrogen-bonded rings (Pattern C in Scheme 29.2).

The hydrogen-bonding networks have an effect on the molecular arrangements. The ADS salts with two-dimensional networks (Patterns A and B) show layer-type arrangements of anthracene moieties. On the other hand, the salts with one-dimensional networks (Pattern C) have columnar or discrete-type arrangements of anthracene moieties, except for Form III. The one-dimensional network in Form III is close to neighboring networks. The distances between the networks are less than 3 Å, and thus the one-dimensional networks in Form III are regarded as pseudo-two-dimensional networks. According to the structural features and the structural parameters of their intermolecular interactions ( $\pi/\pi$  and  $\text{CH}/\pi$  interactions; Table 29.1), these arrangements can be additionally divided into layer 1 and layer 2. Layer 1 is the herringbone-type structure because of the similarity of its structural parameters to those of the anthracene crystal. In contrast, layer 2 shows longer distances between anthracene moieties than layer 1 (Table 29.1).

Layer 2 can be described as a T-shape because of its structural features. Moreover, Forms I and IV are different layer-type arrangements despite having the same hydrogen-bonding network pattern. The differences are due to the interdigitation between the alkyl groups of the amines and the anthracene moieties through their  $\text{CH}/\pi$  interactions; the alkyl groups in Form IV are interdigitated with the anthracene moieties more than those in Form I. The length and bulkiness of the alkyl groups have a significant effect on the interdigitation. Namely, bulky substituents of tert-butylamine and tert-amylamine expand the distance between anthracene moieties in the crystal structures of Form IV.

**Table 29.1** Structural features and solid-state fluorescence properties of unmodified anthracene and ADS salts

	Anthracene	Form I	Form II	Form III	Form IV	Form V	Form VI	Form VII
Amine	–	MeA	<i>t</i> PrA, <i>s</i> BuA	EtA, <i>t</i> BuA	<i>t</i> BuA, <i>t</i> AmA	<i>n</i> BuA, <i>n</i> AmA, <i>i</i> AmA	3AP	<i>n</i> HepA
Anthracene arrangement								
Molecular sequence	Layer 1	Layer 1	Layer 1	Layer 1	Layer 2	Column	Column	Column
Arrangement type	Herringbone	Herringbone	Herringbone	Slipped herringbone	T-shape	Slipped stack	Slipped stack	Discrete
H-bonding network								
$\lambda_{em}$ (nm)	–	422	433, 433	425, 427	412, 412	422, 421, 420	424	412
$\phi_F$ (%)	–	14.1	16.6, 16.2	28.2, 23.2	34.8, 35.0	5.94, 10.2, 11.3	17.8	46.1

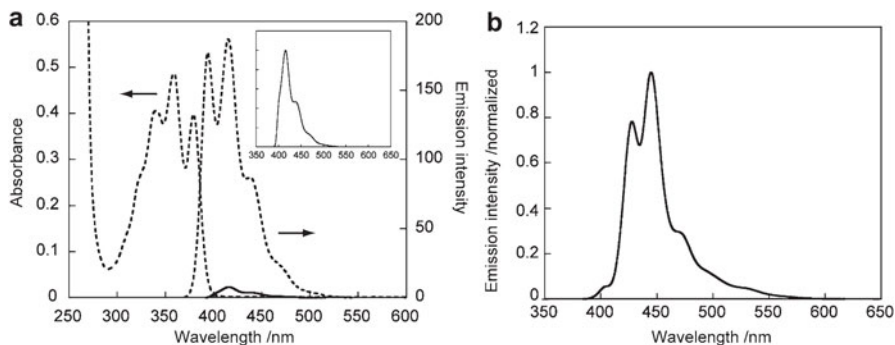


**Fig. 29.3** Fluorescence spectra in methanol solution. (a) Typical absorption and fluorescence emission spectra of  $10^{-4}$  M ADS salt solution (*dashed lines*) and the emission spectrum of  $10^{-2}$  M solution (*continuous line*) in methanol. *Inset*: magnified emission spectrum of  $10^{-2}$  M solution. (b) Fluorescence emission spectrum of  $10^{-4}$  M unmodified anthracene solution

Consequently, the arrangements of anthracene moieties in ADS salts can be modulated depending on the shapes and sizes of the amines, and this systematic method is convenient for novel aggregation of fluorophores in the solid state.

#### 29.2.4 Photophysical Properties in Isotropic Solution

Figure 29.3 shows UV/Vis absorption and fluorescence emission spectra of ADS salts with amines in methanol. All methanol solutions of the ADS salts exhibit exactly the same spectra (absorbance and emission spectra and emission intensity) independent of type of aliphatic primary amine. The emission spectrum is the mirror image of the absorption spectrum, and the Stokes shift of the emission is 15 nm. Even in concentrated solutions of ADS salts, all the salts show the same emission spectra, but the intensity of the spectrum dramatically decreases and the spectral profile broadens depending on concentration (Fig. 29.3). From these results, it is considered that the amines do not have an effect on the photophysical properties in isotropic solution.

#### 29.2.5 Solid-State Fluorescence Emission Spectra

Unmodified anthracene crystal shows a strong solid-state emission spectrum with several emission bands (Fig. 29.4a) derived from monomeric anthracene, which are assignable to the following clear vibrational structures of the anthracene molecule: the 0–0, 0–1, 0–2, 0–3, 0–4, and 0–5 emission bands at 403, 428, 445, 470, 500, and 527 nm, respectively [50]. In the emission of anthracene crystal, the 0–2 emission

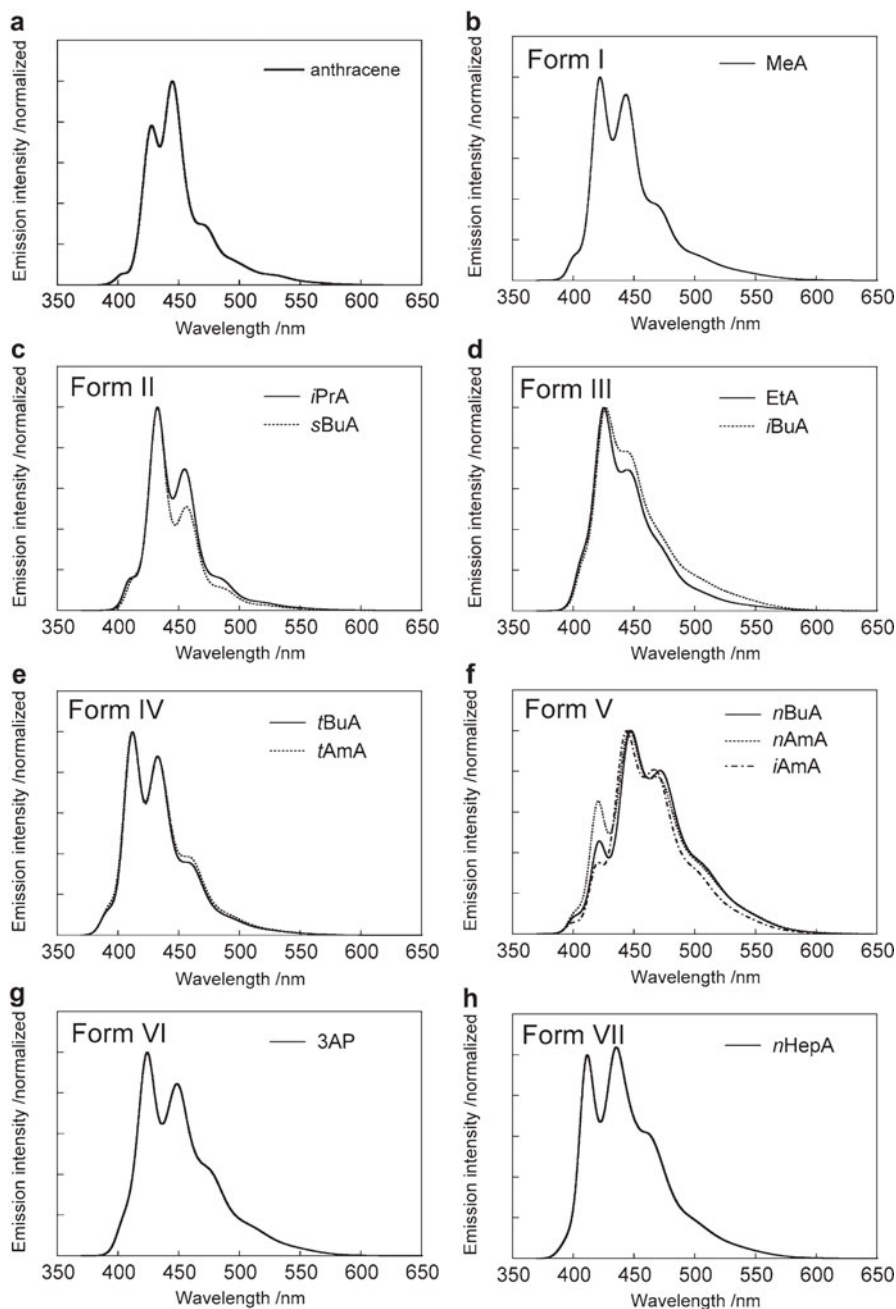


**Fig. 29.4** Solid-state fluorescence emission spectra of the crystals of unmodified anthracene (a) and of Forms I (b), II (c), III (d), IV (e), V (f), VI (g), and VII (h). The excitation wavelength is 350 nm

is observed as the emission maximum. Although all the ADS salts show the same emission spectrum in isotropic solution, the emission spectra in the crystalline state depend on the arrangements of anthracene moieties (Fig. 29.4).

The emission spectra of the ADS salts in the crystalline state also have several emission bands that can be assigned to vibrational structures. The emission spectra of the ADS salts are different from those of unmodified anthracene, and the same types of crystal forms exhibit similar emission spectra. On the other hand, Form VII with *n*-heptylamine shows a similar spectrum to methanol solutions of ADS salts (Fig. 29.4g). In the crystal structure of Form VII, the anthracene moieties are completely discrete. Specifically, they are separated by insertion of the long alkyl chain of the *n*-heptyl groups (Table 29.1). Therefore, the arrangement should be close to the disperse state in dilute solution. The solid-state spectra shift to shorter wavelength in the following order: Form VII = IV < V < I < VI < III < II. This result implies that the spectral shifts are derived from the degree of intermolecular interactions between anthracene moieties, i.e.,  $\pi/\pi$  interactions. In the arrangements of anthracene moieties, Form VII is completely discrete and Form IV gives a T-shape with CH/ $\pi$  interactions; therefore, they do not interact with each other. Forms V and VI (columnar type) arrange the anthracene moieties in a one-dimensional manner, and the resulting one-dimensional arrangements have only a small degree of  $\pi/\pi$  interaction. The arrangements of anthracene moieties in Forms I–III give the herringbone arrangement in which the anthracene moieties interact in a two-dimensional manner. The dimensions of the interactions almost correspond to the degree of  $\pi/\pi$  interaction between anthracene moieties. Namely, the dimensional expansion induces a red shift of the solid-state spectra. However, there is significant difference in the three herringbone-type arrangements. The herringbone arrangement in Form I is slipped to lead to the smallest  $\pi/\pi$  interaction in Forms I–III and a shorter wavelength emission. On the other hand, Form II has a smaller distance between anthracene moieties and stronger  $\pi/\pi$  interaction than Form III to give a larger red shift of emission. There have been reports on the relationship between the spectral shift and the intermolecular interaction between fluorophores, and strong  $\pi/\pi$  interactions lead to a dimer in the ground state and a concomitant spectral red shift [51]. In the case of ADS salts, similar events may be also induced by the intermolecular interaction between the anthracene moieties.

### 29.2.6 Solid-State Fluorescence Emission Quantum Yields

To evaluate the emission efficiency of the ADS salts in the solid state, their solid-state emission quantum yields were investigated (Table 29.1). The salts with herringbone arrangements (Forms I–III) exhibit much lower quantum yields than unmodified anthracene despite their similar herringbone arrangements (Table 29.1) and degree of  $\pi/\pi$  interaction. The lower yields are due to two features of ADS salts in the solid state. First, ADS has two electron-withdrawing sulfonic acid groups. Second, the ADS salts form charge-assisted hydrogen bonds between the sulfonate

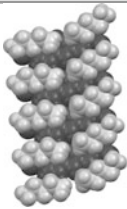
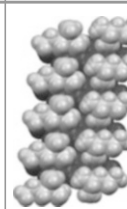
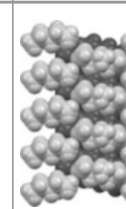
anions and ammonium cations. In fact, there have been several reports that hydrogen bonds close to a fluorophore reduce its emission efficiency in the solid state and solution [52–54].

Similar to the solid-state emission spectra, most reports mention the relationship between intermolecular interactions of fluorophores (mainly  $\pi/\pi$  interaction) and the solid-state fluorescence efficiency, i.e., the solid-state fluorescence efficiency is decreased by the intermolecular interaction of fluorophores. Therefore, the efficiency increases with a blue shift of the fluorescence spectra. In these ADS salts, the interaction between fluorophores corresponds to the number of neighbor anthracene moieties. According to this relationship, it seems that the quantum yields of the ADS salts basically increase in the reverse order of the spectral red shift as follows: two-dimensional types (herringbone: Forms I–III) < one-dimensional types (column: Forms V and VI) < discrete types (Forms IV and VII). However, the observed order of quantum yields of one-dimensional types disagrees with this expectation. The quantum yields of the one-dimensional types are lower than those of the two-dimensional types. Thus, even in the solid state, the quantum yields are dependent on not only the interactions but also on the immobilization of the anthracene moieties, which suppresses the distortion of the anthracene ring and the concomitant nonradiative decay process [36, 38, 39].

Crystallographic studies suggested that the anthracene moieties in the herringbone type are more rigid than those in the columnar type. There are two reasons for this. First, the herringbone type has a more expanded hydrogen-bonding network in the crystal structure than the columnar type; the columnar type displays one-dimensional hydrogen-bonding networks, whereas the herringbone type shows two-dimensional networks. Second, the herringbone type has intermolecular CH/ $\pi$  interactions between anthracene moieties in addition to  $\pi/\pi$  interactions. On the other hand, the anthracene moieties in the columnar type are not immobilized efficiently, because there are no well-defined intermolecular interactions between anthracene moieties except weak  $\pi/\pi$  interactions. Due to its efficient immobilization, the herringbone type leads to higher quantum yields than the columnar type, although the herringbone type has disadvantages in the number of neighbor anthracene moieties.

Moreover, in the columnar-type structures (Forms V and VI), there is a significant difference in immobilization of the anthracene moieties and concomitant quantum yields depending on the amine. In this case, void spaces in the crystals are a predominant factor in immobilization, because both hydrogen-bonding networks and arrangements are the same (Table 29.1). Table 29.2 shows the arrangements of alkyl chains in the anthracene moieties and indicates that the void spaces grow larger in the following order of salts: with 3AP < nAmA = iAmA < nBuA. The order of the void spaces is supported by the calculated free volumes in their crystals (Table 29.2; for graphics). In addition, the packing manner of the alkyl chains between the anthracene moieties also has an effect on the immobilization of anthracene moieties. In Form V, one anthracene ring is covered by two alkyl chains from the edge of the ring; however, the central ring is not covered well with alkyl chains. In contrast, one alkyl chain stacks on the central ring in Form VI. The packing manner in Form

**Table 29.2** Molecular packing diagrams and quantum yields of the ADS salts

	<i>n</i> BuA	<i>n</i> AmA	<i>i</i> AmA	3AP
Packing diagram				
Free volume (%)	9.8	7.8	8.1	6.1
Quantum yield (%)	5.9	10.2	11.3	17.8

VI immobilizes the anthracene moieties more effectively than that in Form V. This structural advantage of Form VI suppresses the distortion of the anthracene moieties more effectively than Form V.

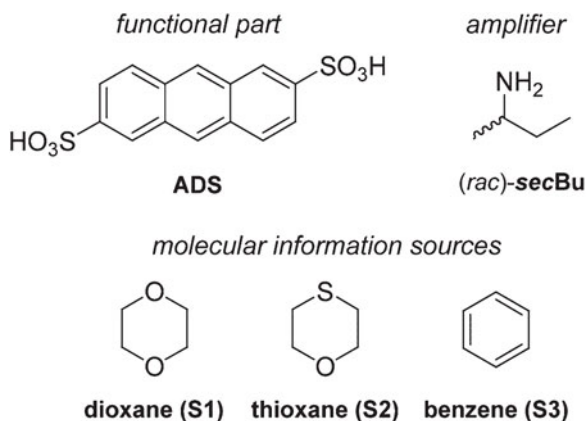
Consequently, two factors are essential for high fluorescence quantum yield in the solid state: prevention of excess contact between  $\pi$  planes of fluorophores and efficient immobilization of fluorophores. The ADS salt with *n*HepA (Form VII) is a satisfactory example of both factors. The salt exhibits the highest quantum yield ( $\Phi_F = 46.1 \pm 0.2 \%$ ) of all the ADS salts. Notably, the yield of the salt with *n*HepA is higher than that of unmodified anthracene crystal ( $\Phi_F = 42.9 \pm 0.2 \%$ ) despite the inherent disadvantages of the ADS salt. This high yield is caused by the structural features of the salt with *n*HepA. The anthracene moieties are dispersed to prevent contact between them, just like in a dilute solution (Fig. 29.2). The anthracene moieties and the alkyl chains of the amine are fully packed without any void spaces. Such an effective arrangement of Form VII is due to the linearity and appropriate length of *n*HepA to cover the anthracene ring. Indeed, the ADS salts with *n*HexA or *n*OctA do not form the discrete type but the herringbone type, similar to Forms I–III according to their X-ray diffraction patterns.

## 29.3 Ternary System Composed of ADS Salt and Guest Molecule

### 29.3.1 Construction of Ternary System

In Sect. 29.2, organic salts of anthracene-2,6-disulfonic acid (ADS) with aliphatic primary amines as a tunable solid-state fluorescence system are mentioned. The system provides various arrangements of anthracene moieties and concomitant solid-state fluorescence properties depending on the amines. Therefore, the alteration of the amines is one of the most convenient methods for the modulation of chemical structures and is suitable for the high-throughput screening of molecular arrangements and fluorescence properties.

**Scheme 29.3** Chemical structures of the functional and arrangement-controlling parts and molecular information sources



ADS and the amines act as a functional part and an arrangement-controlling part, respectively. The system must provide an appropriate method to investigate the structure-property relationship, which is a remarkable strategy to design materials. In order to produce further arrangements, another component as a source of molecular information (e.g., steric demand, noncovalent bonding capacity, and electrostatic property) [55] can be introduced to the system. Up to now, the inclusion phenomenon in steroidal crystals has been investigated for the systematic changes of molecular arrangements and assembly manners by replacement of adducts as the molecular information sources [56–58]. The utility of the inclusion phenomenon inspires a ternary system consisting of the salt and adducts as molecular information sources. Interestingly, the salt of ADS with racemic sec-butylamine [(rac)-s-BuA] includes adducts (dioxane, thioxane, and benzene), while the salts with enantiopure s-BuA [(R)- or (S)-] do not. The salts with enantiopure s-BuA give Form V. Fabrication methods of the system are quite convenient and easy. When the salt with racemic sec-butylamine is recrystallized from methanol, the corresponding solvents of adducts are added to the mixture to yield the ternary systems: ADS•(rac)-s-BuA•dioxane (S1), ADS•(rac)-s-BuA•thioxane (S2), and ADS•(rac)-s-BuA•benzene (S3) as shown in Scheme 29.3.

### 29.3.2 Crystal Structures of Ternary Systems

From X-ray crystallographic studies, total molecular packing manners of S1-3 are isostructural with each other: each adduct is incorporated in a one-dimensional channel cavity between ADS columns and (rac)-s-BuA columns as shown in Fig. 29.5a–c. The molecular arrangement of anthracene moieties in S1 is a zigzag type (Fig. 29.6a), while those in S2 and S3 are a slipped-stacked type (Fig. 29.6b, c). The zigzag type is a novel arrangement of anthracene derivatives in the crystalline state. On the other hand, the slipped-stacked types are commonly observed in the

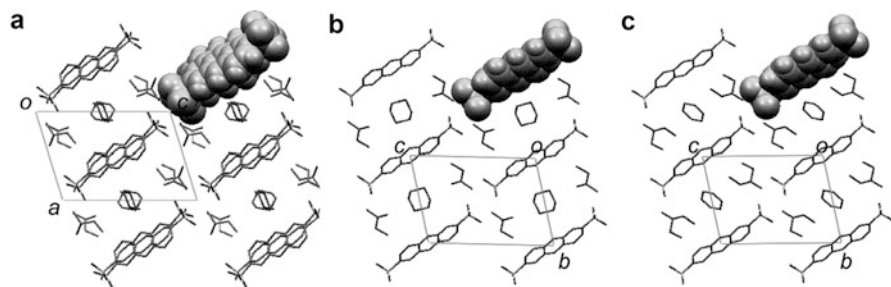


**Fig. 29.5** Molecular packing diagrams of S1 (a), S2 (b), and S3 (c) from X-ray crystallographic studies. The guest molecules thioxane and (rac)-s-BuA are disordered in the crystal structures of S2 and S3, respectively

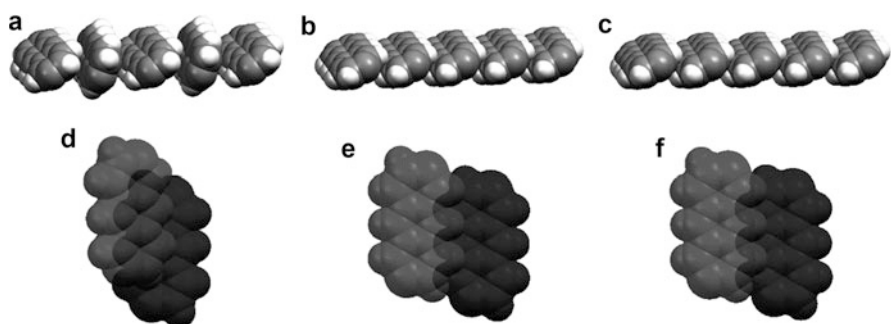


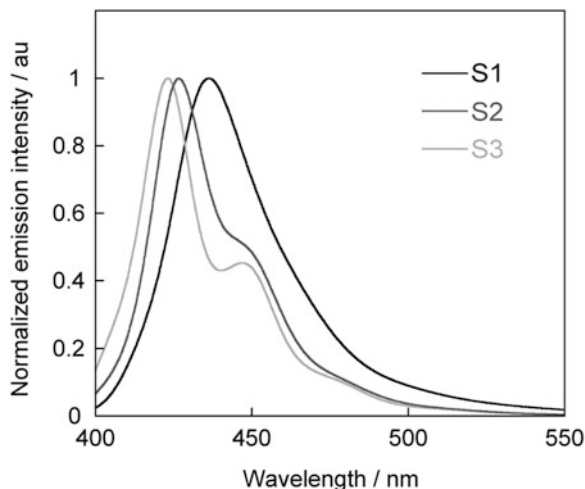
**Fig. 29.6** Arrangements of anthracene moieties (a–c) and stacking motifs of anthracene moieties (d–f): S1 (a) and (d), S2 (b) and (e), S3 (c) and (f)

crystal structures of anthracene derivatives. These differences in the arrangements have an effect on the degree of  $\pi$ -overlap of anthracene moieties as shown in Fig. 29.6d–f. The degree of  $\pi$ -overlap in S2 and S3 is clearly smaller than that in S1; therefore, the  $\pi/\pi$  interaction in S1 must be larger. From these results, the arrangement manner and the corresponding intermolecular interaction between anthracene moieties in S1 are clearly different from those in S2 and S3.

### 29.3.3 Fluorescence Properties of Ternary System Depending on Guest Molecules

Depending on the difference in the degree of  $\pi$ -overlap, the solid-state emission spectra are also distinct as shown in Fig. 29.7. The crystals of S2 and S3 exhibit emission maxima at 423 and 427 nm with vibrational bands at 448 and 451 nm, respectively. Both spectra are assigned to emission from the anthracene monomer compared to unmodified anthracene. S1 exhibits a structureless spectrum and

**Fig. 29.7** Emission spectra of S1, S2, and S3 in the solid state. The excitation wavelength is 340 nm in all samples



an emission maximum at 438 nm. This spectrum is assigned to emission from anthracene excimer because of a larger Stokes shift and conformity of the excitation spectrum, which suggest stronger electronic communication in the excited state. The emission maximum of S1 is at a shorter wavelength compared to those of common anthracene excimers [59, 60]. In this case, the shorter maximum is caused by the following: an electron-withdrawing group on anthracene, i.e., sulfonate group, and a smaller degree of  $\pi$ -overlap between anthracene moieties compared to common excimers. From these fluorescence results, the slipped-stacked type shows monomer emission, while the zigzag type exhibits excimer emission. Indeed, the excimer emission from anthracene at room temperature is quite rare compared to other polycyclic aromatic compounds (pyrene, perylene, etc.) due to very efficient photodimerization to dianthracene [61, 62]. Thus, there are only a few anthracene derivatives that show the excimer emission. This ternary system composed of the organic salt is of interest as a convenient method for the modulation of the emission mode depending on the adducts.

### 29.3.4 Relationship Between Fluorescence Properties and Molecular Arrangements

From detailed investigations of their crystal structures, the steric and the electronic features of the adducts determine the arrangements of the anthracene moieties and the corresponding emission mode. The dioxane molecule has a chair conformation and two oxygen atoms on both sides. These oxygen atoms interact with two neighboring dioxane molecules by CH/O interactions in the void space to give an alternating column of dioxane molecules. Moreover, these oxygen atoms interact

with anthracene moieties by CH/O interactions to lead to the zigzag type of anthracene moieties. Namely, the molecular information of dioxane is translated to give zigzag type and concomitant excimer emission. On the other hand, thioxane and benzene do not have effective interactions between themselves to give straight slipped-stacked types of anthracene moieties and monomeric emission.

## 29.4 Summary

Unmodified anthracene yields only one crystal form and corresponding solid-state fluorescence property. In contrast, the organic salts of anthracene-2,6-disulfonic acid (ADS) with primary amines show various crystal forms and corresponding arrangements of anthracene moieties. In these crystal structures, several hydrogen-bonding networks between sulfonate anions and ammonium cations are observed. According to the hydrogen-bonding networks and the substituents of the amines, these molecular packing manners of anthracene moieties can be classified into various forms. The solid-state fluorescence spectra of the ADS salts are shifted depending on molecular packing manners of anthracene moieties, although all the solutions of the ADS salts exhibit exactly the same fluorescence property. Namely, in the case of the ADS salts, strong  $\pi/\pi$  interaction between the anthracene moieties also leads to a dimer in the ground state and a concomitant spectral red shift.

Moreover, the ADS salts show suppression or enhancement of solid-state fluorescence intensity depending on the crystal structures, despite the same intensity of the solution fluorescence. According to this systematic investigation, the immobilization of fluorophores regulates the solid-state fluorescence intensity. Intermolecular CH/ $\pi$  interactions (not  $\pi/\pi$  interaction) of anthracene moieties and/or insertion of alkyl groups to reduce the void space around the anthracene moieties have an effect on the fluorescence intensity. The satisfactory combination of these two factors produces higher quantum yield than unmodified anthracene despite the disadvantage of the ADS salt. From these results, organic salts are suitable as a system to modulate the molecular arrangement of fluorophores and concomitant solid-state fluorescence properties.

Furthermore, a third component can also modulate the molecular arrangements and the concomitant fluorescence properties of the ADS salts. Specifically, inclusion phenomena of the ternary system composed of the ADS salts and organic solvents have strong potential to regulate fluorescence properties. Molecular arrangements of the host (the ADS salt) are regulated by the guest molecules (the adducts) to lead to a change in emission mode, i.e., monomer or excimer emission. Namely, molecular information of the adducts is translated to the molecular arrangements and concomitant emission properties.

Volatile organic compounds (VOCs) act as adducts to determine the emission mode; therefore, adsorption and desorption of the adducts enable dynamic switching from excimer to monomer emission in the solid state. This ternary system of organic salts should be applicable for sensing and imaging materials.

## References

1. A.W. Czarnik, *Acc. Chem. Res.* **27**, 302–308 (1994)
2. C.W. Tang, S.A. VanSlyke, *Appl. Phys. Lett.* **51**, 913–915 (1987)
3. C.W. Tang, S.A. VanSlyke, C.H. Chen, *J. Appl. Phys.* **65**, 3610–3616 (1989)
4. J. Shi, C.W. Tang, *Appl. Phys. Lett.* **70**, 1665–1667 (1997)
5. J. Shinar, *Organic Light-Emitting Devices* (Springer, New York, 2004)
6. R.H. Friend, R.W. Gymer, A.B. Holmes, J.H. Burroughes, R.N. Marks, C. Taliani, D.D.C. Bradley, D.A. Dos Santos, J.L. Bredas, M. Logdlund, W.R. Salaneck, *Nature (London)* **397**, 121–128 (1999)
7. H. Langhals, O. Krotz, K. Polborn, P. Mayer, *Angew. Chem. Int. Ed.* **44**, 2427–2428 (2005)
8. A. Dreuw, J. Ploetner, L. Lorenz, J. Wachtveitl, J.E. Djanhan, J. Bruening, T. Metz, M. Bolte, M.U. Schmidt, *Angew. Chem. Int. Ed.* **44**, 7783–7786 (2005)
9. J.N. Moorthy, P. Venkatakrishnan, P. Natarajan, D.-F. Huang, T.J. Chow, *J. Am. Chem. Soc.* **130**, 17320–17333 (2008)
10. G.R. Desiraju, A. Gavezzotti, *J. Chem. Soc. Chem. Commun.* 621–623 (1989)
11. G.R. Desiraju, *Crystal Engineering: The Design of Organic Solids* (Elsevier, Amsterdam, 1989)
12. G.R. Desiraju, *Nature* **412**, 397–400 (2001)
13. B. Moulton, M.J. Zaworotko, *Chem. Rev.* **101**, 1629–1658 (2001)
14. T. Mutai, H. Satou, K. Araki, *Nat. Mater.* **4**, 685–687 (2005)
15. H.G. Brittain, B.J. Elder, P.K. Isbester, A.H. Salerno, *Pharm. Res.* **22**, 999–1006 (2005)
16. M. Brinkmann, G. Gadret, M. Muccini, C. Taliani, N. Masciocchi, A. Sironi, *J. Am. Chem. Soc.* **122**, 5147–5157 (2000)
17. Y. Ooyama, Y. Harima, *Chem. Lett.* **35**, 902–903 (2006)
18. Y. Ooyama, T. Nakamura, K. Yoshida, *New J. Chem.* **29**, 447–456 (2005)
19. Y. Ooyama, K. Yoshida, *New J. Chem.* **29**, 1204–1212 (2005)
20. Y. Ooyama, S. Yoshikawa, S. Watanabe, K. Yoshida, *Org. Biomol. Chem.* **4**, 3406–3409 (2006)
21. J.L. Scott, T. Yamada, K. Tanaka, *Bull. Chem. Soc. Jpn.* **77**, 1697–1701 (2004)
22. J.L. Scott, T. Yamada, K. Tanaka, *New J. Chem.* **28**, 447–450 (2004)
23. E. Horiguchi, S. Matsumoto, K. Funabiki, M. Matsui, *Bull. Chem. Soc. Jpn.* **79**, 799–805 (2006)
24. Y. Sonoda, Y. Kawanishi, T. Ikeda, M. Goto, S. Hayashi, Y. Yoshida, N. Tanigaki, K. Yase, *J. Phys. Chem. B* **107**, 3376–3383 (2003)
25. K. Yoshida, Y. Ooyama, H. Miyazaki, S. Watanabe, *J. Chem. Soc. Perkin Trans.* **2**, 700–707 (2002)
26. K. Yoshida, Y. Ooyama, S. Tanikawa, S. Watanabe, *J. Chem. Soc. Perkin Trans.* **2**, 708–714 (2002)
27. H. Langhals, T. Potrawa, H. Noeth, G. Linti, *Angew. Chem. Int. Ed.* **28**, 478–499 (1989)
28. J. Bernstein, *Nat. Mater.* **4**, 427–428 (2005)
29. J.D. Dunitz, *J. Bernstein, Acc. Chem. Res.* **28**, 193–200 (1995)
30. A.R. Verma, P. Krishna, *Polymorphism and Polytypism in Crystals* (Wiley, New York, 1966)
31. J.D. Dunitz, *Chem. Commun. (Cambridge, UK)* 545–548 (2003)
32. G.M. Day, W.D.S. Motherwell, H.L. Ammon, S.X.M. Boerrigter, V.R.G. Della, E. Venuti, A. Dzyabchenko, J.D. Dunitz, B. Schweizer, B.P. van Eijck, P. Erk, J.C. Facelli, V.E. Bazterra, M.B. Ferraro, D.W.M. Hofmann, F.J.J. Leusen, C. Liang, C.C. Pantelides, P.G. Karamertzanis, S.L. Price, T.C. Lewis, H. Nowell, A. Torrisi, H.A. Scheraga, Y.A. Arnautova, M.U. Schmidt, P. Verwer, *Acta Crystallogr. B* **61**, 511–527 (2005)
33. A. Gavezzotti, *Acc. Chem. Res.* **27**, 309–314 (1994)
34. J.L. Atwood, J.E. Davies, D.D. MacNicol, F. Vcgtle, *Comprehensive Supramolecular Chemistry*, vol. 6 (Pergamon, Oxford, 1996)
35. Y. Mizobe, N. Tohnai, M. Miyata, Y. Hasegawa, *Chem. Commun. (Cambridge, UK)* 1839–1841 (2005)

36. Y. Mizobe, H. Ito, I. Hisaki, M. Miyata, Y. Hasegawa, N. Tohnai, *Chem. Commun.* (Cambridge, UK) 2126–2128 (2006)
37. T. Hinoue, Y. Mizobe, I. Hisaki, M. Miyata, N. Tohnai, *Chem. Lett.* **37**, 642–643 (2008)
38. Y. Mizobe, T. Hinoue, A. Yamamoto, I. Hisaki, M. Miyata, Y. Hasegawa, N. Tohnai, *Chem. Eur. J.* **15**, 8175–8184 (2009)
39. T. Hinoue, Y. Shigenoi, M. Sugino, Y. Mizobe, I. Hisaki, M. Miyata, N. Tohnai, *Chem. Eur. J.* **18**, 4634–4643 (2012)
40. A. Collet, in *Comprehensive Supramolecular Chemistry*, ed. by D.N. Reinhoudt, vol. 10 (Pergamon, Oxford, 1996), p. 113
41. E. Ebberts, G.J.A. Ariaans, B. Zwanenburg, A. Bruggink, *Tetrahedron Asymmetry* **9**, 2745–2753 (1998)
42. T. Vries, H. Wynberg, E. Van Echten, J. Koek, W. Ten Hoeve, R.M. Kellogg, Q.B. Broxterman, A. Minnaard, B. Kaptein, S. Van der Sluis, L. Hulshof, J. Kooistra, *Angew. Chem. Int. Ed.* **37**, 2349–2354 (1998)
43. D. Kozma, G. Pokol, M. Acs, *J. Chem. Soc. Perkin Trans.* **2**, 435–439 (1992)
44. K. Kinbara, K. Sakai, Y. Hashimoto, H. Nohira, K. Saigo, *J. Chem. Soc. Perkin Trans.* **2**, 2615–2622 (1996)
45. Y. Kobayashi, K. Kinbara, M. Sato, K. Saigo, *Chirality* **17**, 108–112 (2005)
46. Y. Kobayashi, K. Kodama, K. Saigo, *Org. Lett.* **6**, 2941–2944 (2004)
47. A. Tanaka, K. Inoue, I. Hisaki, N. Tohnai, M. Miyata, A. Matsumoto, *Angew. Chem. Int. Ed.* **45**, 4142–4145 (2006)
48. H. Koshima, M. Nagano, T. Asahi, *J. Am. Chem. Soc.* **127**, 2455–2463 (2005)
49. C.P. Brock, J.D. Dunitz, *Acta Crystallogr. Sect. B* **46**, 795–806 (1990)
50. N.J. Turro, *Modern Molecular Photochemistry* (The Benjamin/Cummings, Menlo Park, 1978)
51. J. Gierschner, M. Ehni, H.-J. Egelhaaf, B.M. Medina, D. Beljonne, H. Benmansour, G.C. Bazan, *J. Chem. Phys.* **123**, 144914–144919 (2005)
52. M.K. Singh, G.E. Walrafen, *J. Solut. Chem.* **34**, 579–583 (2005)
53. C.-F. Lin, Y.-H. Liu, C.-C. Lai, S.-M. Peng, S.-H. Chiu, *Chem. Eur. J.* **12**, 4594–4599 (2006)
54. J. Zhuang, W. Zhou, X. Li, Y. Li, N. Wang, X. He, H. Liu, Y. Li, L. Jiang, C. Huang, S. Cui, S. Wang, D. Zhu, *Tetrahedron* **61**, 8686–8693 (2005)
55. A.R. Hirst, D.K. Smith, *Chem. Eur. J.* **11**, 5496–5508 (2005)
56. N. Yoswathananont, K. Sada, K. Nakano, K. Aburaya, M. Shigesato, Y. Hishikawa, K. Tani, N. Tohnai, M. Miyata, *Eur. J. Org. Chem.* **2005**, 5330–5338 (2005)
57. K. Nakano, K. Sada, K. Nakagawa, K. Aburaya, N. Yoswathananont, N. Tohnai, M. Miyata, *Chem. Eur. J.* **11**, 1725–1733 (2005)
58. K. Sada, N. Shiomi, M. Miyata, *J. Am. Chem. Soc.* **120**, 10543–10544 (1998)
59. J.C. Amicangelo, W.R. Leenstra, *J. Am. Chem. Soc.* **125**, 14698–14699 (2003)
60. H. Ihmels, D. Leusser, M. Pfeiffer, D. Stalke, *Tetrahedron* **56**, 6867–6875 (2000)
61. H. Bouas-Laurent, J.-P. Desvergne, A. Castellan, R. Lapouyade, *Chem. Soc. Rev.* **29**, 43–55 (2000)
62. H. Bouas-Laurent, J.-P. Desvergne, A. Castellan, R. Lapouyade, *Chem. Soc. Rev.* **30**, 248–263 (2001)

# Chapter 30

## Solid-State Circularly Polarized Luminescence of Chiral Supramolecular Organic Fluorophore

Yoshitane Imai

**Abstract** Chiral supramolecular organic fluorophores were successfully developed using two organic components with different functionalities (namely, a chiral amine and an achiral fluorescent carboxylic acid (or sulfonic acid) or an achiral amine and achiral fluorescent carboxylic acid). The supramolecular organic fluorophores exhibited chiroptical properties in the solid state, as determined by circular dichroism (CD) or circularly polarized luminescence (CPL). The chiroptical properties could easily be tuned by changing the component molecules, without the need for synthetic modifications.

**Keywords** Circular dichroism (CD) • Circularly polarized luminescence (CPL) • Fluorophore • Supramolecule

### 30.1 Introduction

The solid-state optical properties of organic compounds are very important in the development of new functional materials. Specifically, the solid-state circularly polarized luminescence (CPL) of chiral organic compounds has recently attracted significant attention, such as in polarized 3D systems. However, there are few studies regarding the CPL of solid-state organic fluorophores. Most chiral organic fluorophores that possess solid-state fluorescence are composed of a single component, and there have only been a few reports concerning chiral, supramolecular organic fluorescent complexes containing two or more organic molecules. One of the key properties of chiral supramolecular fluorophores may be the ability to easily alter their chiroptical properties by varying the component molecules. In addition, the resultant chiral supramolecular fluorophores may exhibit effective functionalities due to the synergistic effects of packing and the properties of the component molecules in the solid state.

---

Y. Imai (✉)

Department of Applied Chemistry, Faculty of Science and Engineering,  
Kinki University, Osaka, Japan  
e-mail: [y-imai@apch.kindai.ac.jp](mailto:y-imai@apch.kindai.ac.jp)

In this chapter, the preparation of chiral supramolecular organic fluorophores derived from two different functional organic molecules and their solid-state chiroptical properties, as determined by circular dichroism (CD) and CPL, are reported.

## 30.2 Solid-State Circularly Polarized Luminescence (CPL) of a Chiral Supramolecular Organic Fluorophore Composed of a One-Dimensional (1D) Column Structure

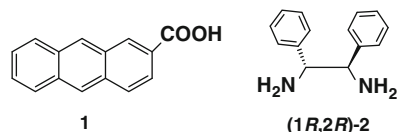
Chiral supramolecular organic fluorophores containing molecules with different characteristics (fluorescent and chiral molecules) have been reported. Two-component chiral supramolecular organic fluorophore **I** composed of the fluorescent component molecule 2-anthracenecarboxylic acid (**1**) and chiral amine molecule (1*R*,2*R*)-(+)-1,2-diphenylethylenediamine ((1*R*,2*R*)-**2**) was successfully prepared via crystallization from solution (Fig. 30.1) [1].

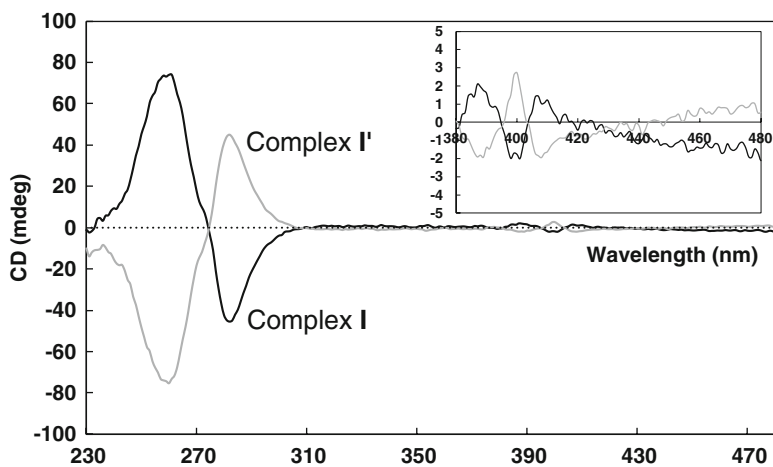
Complex **I** contains fluorescent and chiral units and therefore exhibits circular dichroism (CD) and circularly polarized luminescence (CPL). The solid-state CD of **I** was measured in a KBr pellet (Fig. 30.2). The KBr pellet samples were prepared according to the standard procedure for obtaining glassy KBr matrices [2].

Features in the CD spectrum originating from the fluorescent anthracene unit can be observed between 350 and 420 nm. The circular anisotropy ( $g_{CD} = \Delta OD/OD$ ) factor of the first Cotton CD band ( $\lambda^{CD} = 406$  nm) is approximately  $+0.5 \times 10^{-3}$ . In order to determine whether or not any artifacts contributed to the CD spectrum, the CD spectrum of complex **I'** composed of (1*S*,2*S*)-(-)-1,2-diphenylethylenediamine ((1*S*,2*S*)-**2**) instead of (1*R*,2*R*)-**2** was measured. A mirror image CD spectrum to that of **I** was observed. However, the observed CD spectrum of the supramolecular complex might represent the interactions between the complex and the KBr matrix, rather than the complex itself [3]. Therefore, the diffuse reflectance circular dichroism (DRCD) spectra of **I** and **I'** without the KBr matrix were measured (Fig. 30.3).

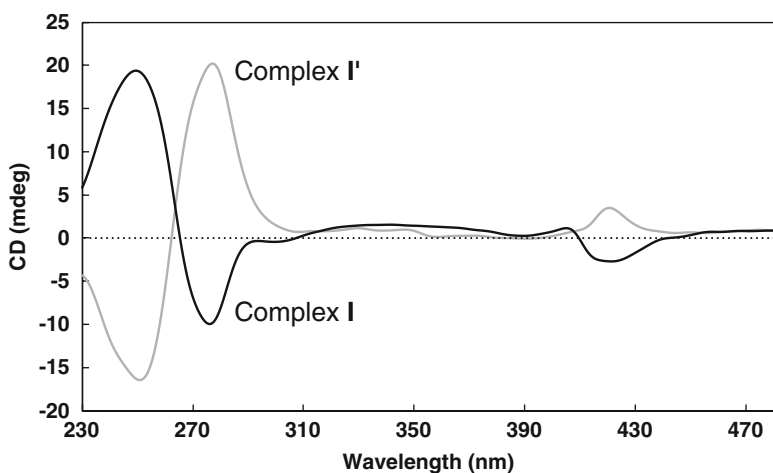
The DRCD spectrum was similar to the CD spectrum, suggesting that there was no influence of the KBr matrix on the CD measurements, and the effective chiral transfer from the chiral unit to fluorescent anthracene unit occurred during complexation.

Fig. 30.1 Supramolecular component molecules





**Fig. 30.2** Solid-state CD spectra of complexes **I** (black lines) and **I'** (gray lines) in the solid state (in KBr pellets)



**Fig. 30.3** Solid-state DRCD spectra of complexes **I** (black line) and **I'** (gray line) in the solid state

The solid-state CPL and PL spectra of complex **I** using KBr pellets are shown in Fig. 30.4.

Although fluorescence quenching in the condensed and crystalline states is a serious concern in the application of organic fluorophores in emitter materials, complex **I** exhibits solid-state fluorescence. The solid-state fluorescence maximum ( $\lambda_{em}$ ) of **I** is 432 nm, and a shift (27 nm) to a lower wavelength is observed relative to that of fluorescent component molecule **1**. Since the PL spectra of **I** with and

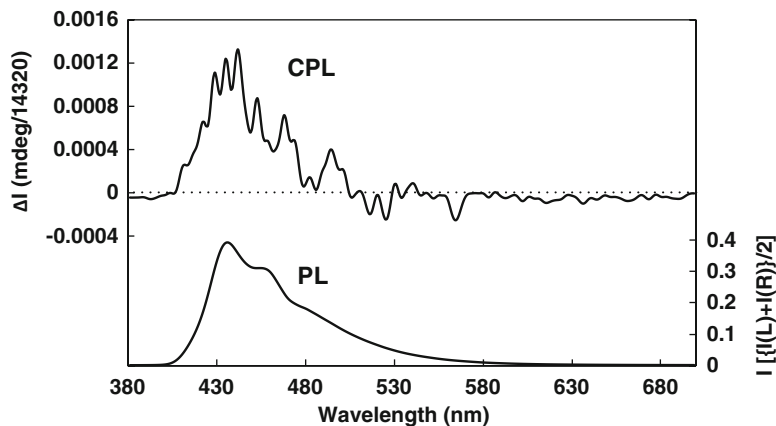


Fig. 30.4 Solid-state CPL and PL spectra of complex **I** in the solid state (in a KBr pellet)

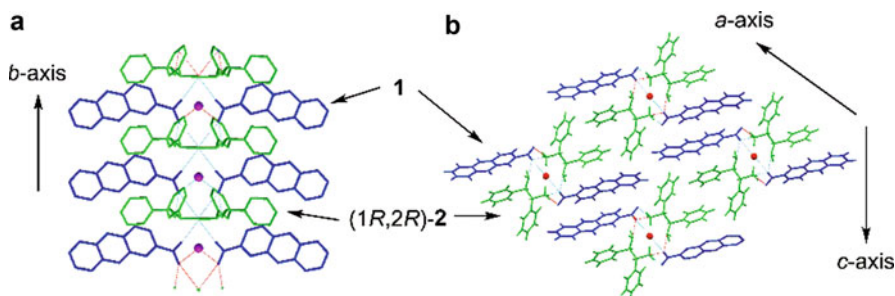


Fig. 30.5 Crystal structures of complex **I**. (a) Columnar hydrogen- and ionic-bonded network along the *b*-axis. (b) Packing structure observed along the *b*-axis. Balls indicate included water molecules

without KBr are similar, the KBr matrix did not influence the measurements of this supramolecular system. Complex **I** exhibits a positive (+) CPL. The circular anisotropy ( $g_{em} = 2(I_L - I_R) / (I_L + I_R)$ ) factor is approximately  $+7.74 \times 10^{-4}$ .

To determine the origin of CPL of complex **I**, the structure of **I** is shown in Fig. 30.5. Complex **I** has a one-dimensional (1D) columnar hydrogen- and ionic-bonded network along the *b*-axis (Fig. 30.5a). This network is primarily formed by the carboxylate oxygen of a carboxylic acid anion in **1** and the ammonium hydrogen of the protonated amine in (1*R*,2*R*)-**2**. Complex **I** is formed by the assembly of this 1D column (Fig. 30.5b). Regarding the origin of CD and CPL, the crystal structures and the oscillator coupling theory [4, 5] suggest that the features of the CD and CPL originating from the fluorescent anthracene unit were caused by interactions of the anthracene unit, between adjoining 1D columns.

### 30.3 Solid-State Circularly Polarized Luminescence (CPL) of a Chiral Supramolecular Organic Fluorophore Composed of a Two-Dimensional (2D) Layered Network Structure

The advantage of two-component supramolecular organic fluorophores is that the optical properties of these fluorophores can be easily controlled by changing the component molecules. Therefore, when suitable carboxylic acid or amine derivatives are used as component molecules, a chiral supramolecular organic fluorophore composed of a two-dimensional (2D) or 3D network structure can be formed.

By using chiral amine molecule (1*R*,2*S*)-(+)-1-amino-2-indanol ((1*R*,2*S*)-**3**) instead of (1*R*,2*R*)-(+)-**1**, 2D layered chiral supramolecular organic fluorophore **II** with fluorescent 2-anthracenecarboxylic acid [**1**] was successfully prepared (Fig. 30.6) [6].

The crystal structure of chiral complex **II** is shown in Fig. 30.7. Complex **II** has a supramolecular 2D layered hydrogen- and ionic-bonded network formed by the association of the carboxylate oxygen of a carboxylic acid anion in **1** and the ammonium hydrogen of the protonated amine in (1*R*,2*S*)-**3** along the *a*- and *b*-axes (indicated by dotted borders in Fig. 30.7). The stoichiometry of **II** is 1:(1*R*,2*S*)-**3**:H<sub>2</sub>O = 1:1:1 and its space group is *P*2<sub>1</sub>2<sub>1</sub>2<sub>1</sub>. The included water

Fig. 30.6 Supramolecular component molecules

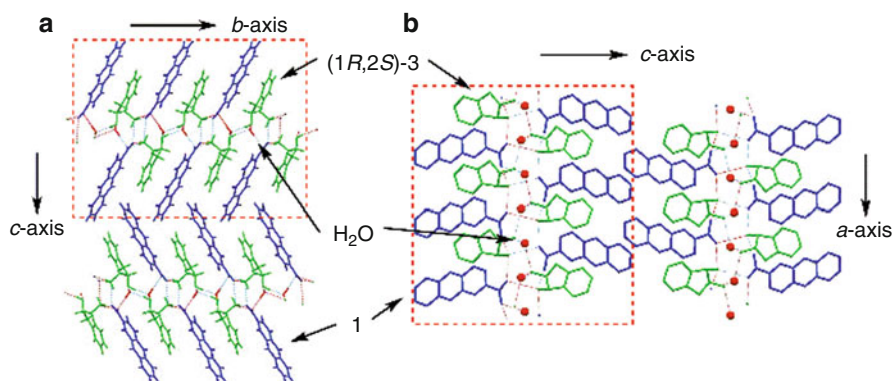
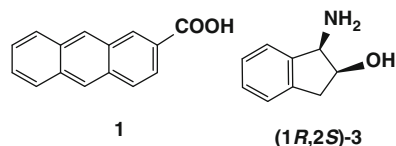
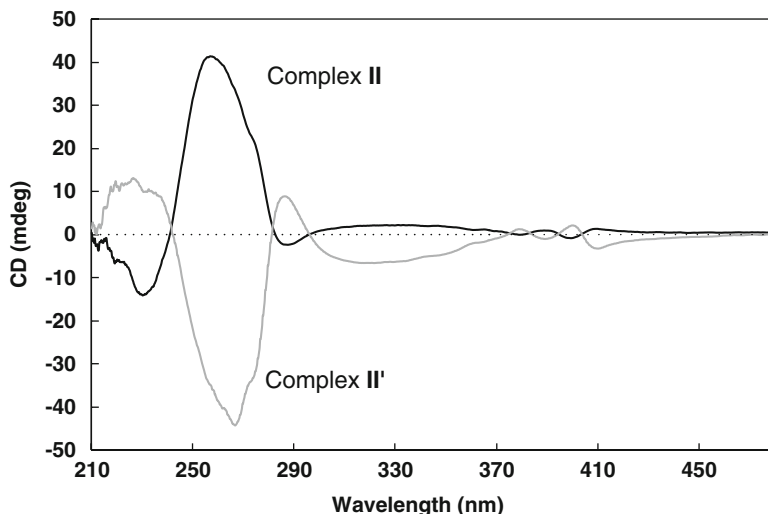


Fig. 30.7 Crystal structures of complex **II**. (a) Packing structure comprising 2D layered network structure observed along the *a*-axis. (b) View down the *b*-axis. The dotted borders indicate the 2D layered network structure



**Fig. 30.8** Solid-state CD spectra of complexes **II** (black line) and **II'** (gray line) in the solid state (in KBr pellets)

molecules link two hydroxyl groups of (1*R*,2*S*)-**3** via hydrogen bonds and contribute to the layered network structure. Moreover, this layered network structure is also maintained by CH- $\pi$  and benzene-anthracene edge-to-face interactions. The self-assembly of the 2D layered network structure with anthracene-anthracene edge-to-face interlayer interactions along the *c*-axis results in the formation of chiral complex **II** (Fig. 30.7a, b).

The solid-state CD spectrum of complex **II** (indicated by the black line) is shown in Fig. 30.8. Fluorescent anthracene unit peaks can be observed around 410 nm in the CD spectrum. The circular anisotropy factor ( $g_{\text{CD}}$ ) of the first Cotton CD band ( $\lambda^{\text{CD}} = 410 \text{ nm}$ ) is approximately  $+0.6 \times 10^{-3}$ . The CD spectrum of complex **II'** prepared using (1*S*,2*R*)-(-)-1-amino-2-indanol ((1*S*,2*R*)-**3**) was nearly a mirror image of that of **II** (indicated by the gray line in Fig. 30.8). These results confirmed the effective chirality transfer from the chiral unit to the fluorescent anthracene unit through complexation in the 2D layered network structure.

The solid-state fluorescence maximum ( $\lambda_{\text{em}}$ ) of complex **II** can be observed at 440 nm, and the absolute value of the photoluminescence quantum yield ( $\Phi_{\text{F}}$ ) is 0.16. Consequently, when the solid-state CPL spectrum of **II** was measured in a KBr pellet (Fig. 30.9), the PL spectrum of **II** was similar to the PL spectrum without KBr.

This result confirmed the lack of influence of the KBr matrix on the 2D layered complex. Complex **II** exhibits a negative (-) CPL, and the circular anisotropy factor ( $g_{\text{em}}$ ) is approximately  $-0.7 \times 10^{-3}$ .

Upon comparing 1D columnar anthracene supramolecular fluorophore **I** with 2D layered anthracene supramolecular fluorophore **II**, dramatic changes in  $\lambda_{\text{em}}$  and  $g_{\text{em}}$  are not observed. Interestingly, the sign of the CPL spectra are different (positive (+) for **I** and negative (-) for **II**), although the sign of optical rotation of chiral amine

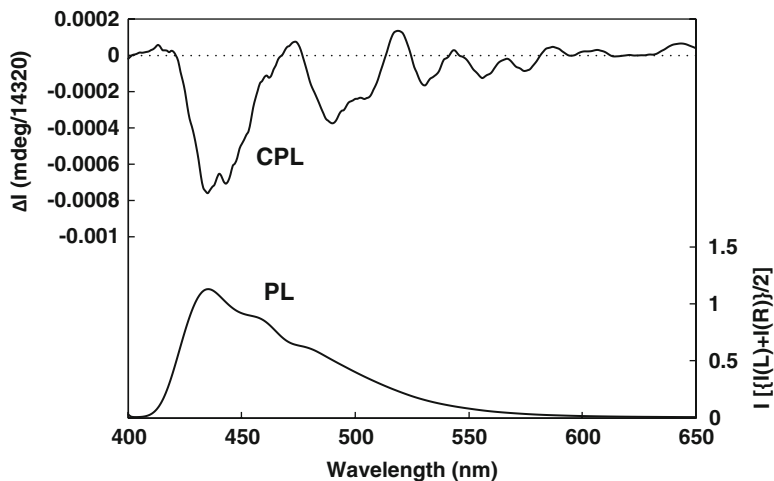
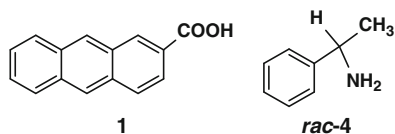


Fig. 30.9 Solid-state CPL and PL spectra of complex **II** in the solid state (in a KBr pellet)

Fig. 30.10 Supramolecular component molecules



molecules are the same. The reversal of the sign of the CPL spectra was caused by a local change in the packing arrangement of the fluorescent anthracene units.

### 30.4 Preparation of Spontaneously Resolved Chiral Supramolecular Organic Fluorophore

Generally, chiral organic materials are prepared using chiral molecules as starting compounds. Unfortunately, most chiral molecules are not readily available and are more expensive than achiral or racemic molecules. Therefore, chiral supramolecular organic fluorophores prepared via achiral or racemic molecules may be useful from economic and industrial viewpoints.

Chiral supramolecular organic fluorophore **III** can be obtained using achiral fluorescent molecule 2-anthracenecarboxylic acid (**1**) and *rac*-1-phenylethylamine (*rac*-**4**), where *rac*-**4** is an equimolar mixture of (*R*)- and (*S*)-1-phenylethylamine (Fig. 30.10) [7]. Notably, this is a spontaneously resolved chiral fluorescent system.

Chiral fluorophore **III** (or **III'**) composed of **1** and (*R*)-**4** (or (*S*)-**4**) can be easily obtained from the crystallization of a solution containing **1** and *rac*-**4**. Complexes **III** (indicated by black line) and **III'** (indicated by gray line) exhibit mirror image solid-state CD spectra (Fig. 30.11). The peaks in the CD spectrum originating from the fluorescent anthracene unit are observed between 330 and 450 nm. The

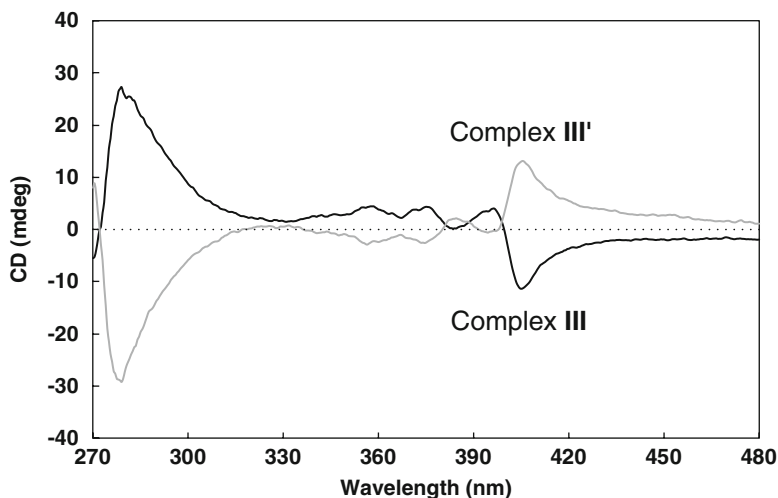


**Fig. 30.11** Solid-state CD spectra of complexes **III** (black line) and **III'** (gray line) in the solid state (in KBr pellets)

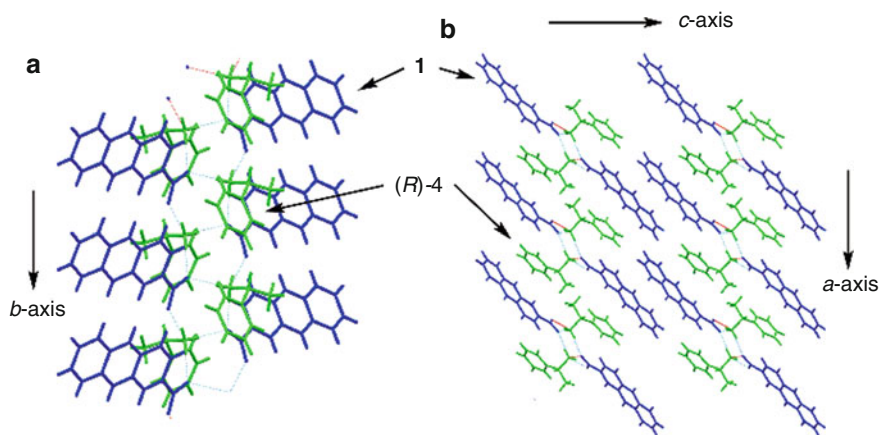


**Fig. 30.12** Crystal structures of complex **III**. (a)  $2_1$ -helical columnar network structure along the  $b$ -axis. (b) Packing structure observed along the  $b$ -axis

circular anisotropy ( $g_{CD}$ ) factor of the first Cotton CD band ( $\lambda^{CD} = 404$  nm) of **III** is approximately  $-0.6 \times 10^{-3}$ .

The solid-state fluorescence maximum ( $\lambda_{em}$ ) of complex **III** is 430 nm, and a hypsochromic shift (34 nm) is observed relative to the  $\lambda_{em}$  of **1**. The photoluminescence quantum yield ( $\Phi_F$ ) increases from 0.04 to 0.20 relative to that of **1**.

Interestingly, from the X-ray analysis, it is evident that complex **III** has a characteristic  $2_1$ -helical columnar network along the  $b$ -axis (Fig. 30.12a). This column is primarily formed by the carboxylate oxygen of the carboxylic acid anions

in **1** and the ammonium hydrogen of the protonated amine in **4**. Complex **III** is formed by the assembly of these  $2_1$ -columns by anthracene-anthracene edge-to-face, benzene-anthracene edge-to-face, and anthracene-benzene edge-to-face interactions (Fig. 30.12b). The stoichiometry of **III** is  $1:(R)\text{-4} = 1:1$ , and its space group is  $P2_1$ . This suggests that the combination that produces a  $2_1$ -column-like structure may produce the spontaneously resolved chiral supramolecular organic fluorophore.

### 30.5 Solid-State Circularly Polarized Luminescence (CPL) of a Chiral Supramolecular Organic Fluorophore Composed of Achiral Component Molecules

The origin and amplification of chirality that leads to an overwhelming enantioenrichment of organic molecules is a significant topic of interest in the field of chemistry. One proposed theory for the origin of chirality is the generation of chiral crystals from achiral molecules with each crystal exhibiting one of the two possible enantiomers [8–22]. In other words, enantioenriched organic molecules can be formed and augmented by asymmetric reactions using chiral crystals obtained from achiral molecules. Another theory involves the formation of enantioenriched molecules from racemic compounds by interstellar CPL [23–25].

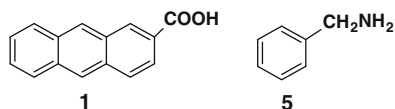
Chiral supramolecular organic fluorophore **IV** can be obtained from two achiral organic molecules, namely, fluorescent 2-anthracenecarboxylic acid (**1**) and benzylamine (**5**) (Fig. 30.13) [26].

When a mixture of **1** and **5** is dissolved in ethanol (EtOH) and left to stand at room temperature, two polymorphic colorless complexes **IV(A)** (or **IV(A)'** with opposite chirality to **IV(A)**) and **IV(B)** composed of **1** and **5** can be obtained. Complex **IV(A)** (or **IV(A)'**) shows a CD in the solid state and is a chiral crystal (Fig. 30.14). On the other hand, **IV(B)** shows no CD in the solid state and is a racemic complex.

Features in the CD spectrum of **IV(A)** originating from the fluorescent anthracene unit are observed around 416 nm (black line in Fig. 30.14). The circular anisotropy factor ( $g_{\text{CD}}$ ) of the first Cotton CD band ( $\lambda^{\text{CD}} = 416$  nm) is approximately  $-1.0 \times 10^{-3}$ .

Complex **IV(A)** exhibits fluorescence. The solid-state fluorescence maximum for **IV(A)** ( $\lambda_{\text{em}}$ ) is 446 nm, and the photoluminescence quantum yield ( $\Phi_{\text{F}}$ ) is 0.16, which is 4 times greater than that of **1** in the solid state.

Fig. 30.13 Supramolecular component molecules



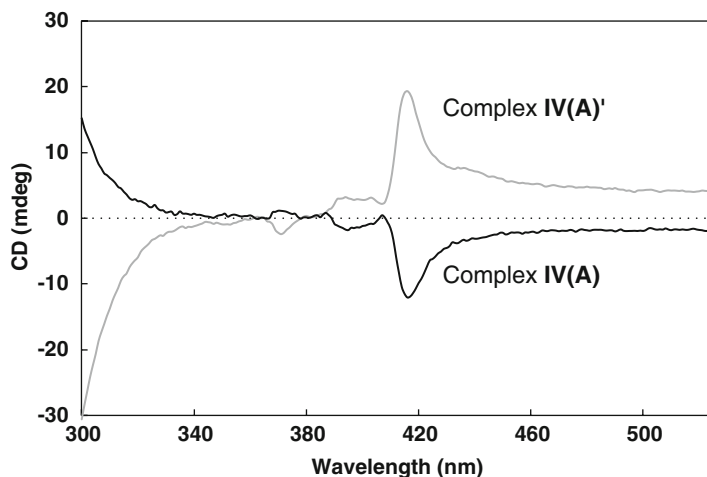


Fig. 30.14 Solid-state CD spectra of complexes **IV(A)** (black line) and **IV(A)'** (gray line) in the solid state (in KBr pellets)

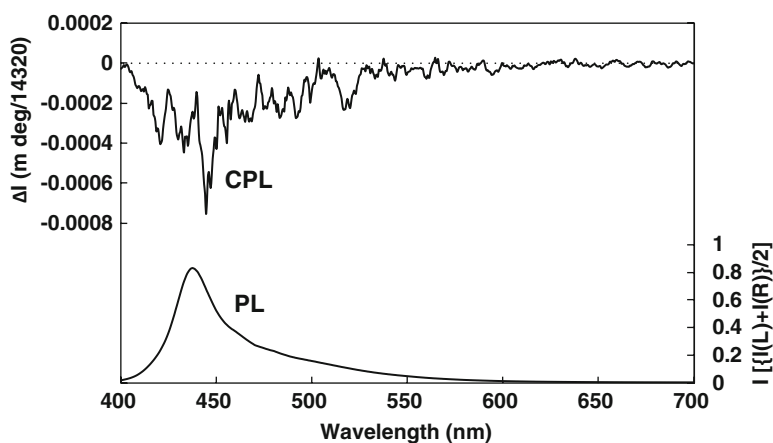
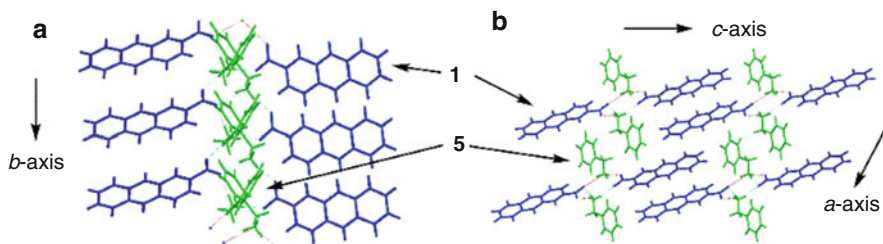


Fig. 30.15 Solid-state CPL and PL spectra of complex **IV(A)** in the solid state (KBr pellet)

Interestingly, **IV(A)** with a negative Cotton CD effect emits a negative (–) CPL with a circular anisotropy ( $g_{em}$ ) factor of approximately  $-1.1 \times 10^{-3}$ , despite the fact that it is composed of achiral component molecules (Fig. 30.15).

Expectedly, chiral **IV(A)** also has a  $2_1$ -helical columnar hydrogen- and ionic-bonded network along the  $b$ -axis, similar to spontaneously resolved chiral supramolecular fluorophore **III** (Fig. 30.16a).



**Fig. 30.16** Crystal structures of complex **IV(A)**. (a)  $2_1$ -helical columnar network along the  $b$ -axis. (b) Packing structure observed along the  $b$ -axis

The stoichiometry of **IV(A)** is **1:5** = 1:1 and the space group is  $P2_1$ . The complex is formed by the assembly of the  $2_1$ -column. Each column interacts *via* anthracene-anthracene edge-to-face and benzene-anthracene edge-to-face interactions (Fig. 30.16b).

The origin of the CPL can be explained by the crystal structure and by the theory of oscillator coupling, which suggest that the features of the CPL spectrum originating from the fluorescent anthracene unit are caused by the interactions of the anthracene units between adjoining  $2_1$ -helical columns.

In this system, crystal polymorphism (crystals **IV(A)** and **IV(B)**) creates an issue. This problem can be solved using unique crystallization methods, as opposed to the typical solution crystallization method. Interestingly, when fluorescent molecule **1** is left to stand at room temperature in the vapor of liquid molecule **5**, racemic **IV(B)** is obtained. On the other hand, when a mixture of **1** and **5** is directly ground in an agate mortar, chiral **IV(A)** can be obtained, suggesting that the polymorphism of the system can be controlled by the type of crystallization method.

### 30.6 Unclassical Control of Solid-State Circularly Polarized Luminescence (CPL) by Supramolecular Complexation–I

In order to control the sign of the optical properties of a given chiral compound, a chiral compound with the opposite chirality is typically used. However, chiral compounds with opposite chirality may not be readily available. Therefore, a way to tune the sign of the optical properties of a chiral fluorophore without using a counterpart with the opposite chirality is desired in the development of novel chiral fluorescent systems.

Interestingly, in two-component chiral supramolecular organic fluorophores, the sign of CPL can be controlled not only by using a chiral component molecule with opposite chirality but also by changing the bonding substituent of the achiral fluorescent component in the solid state [27].

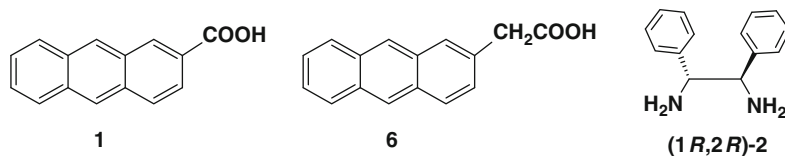


Fig. 30.17 Supramolecular component molecules

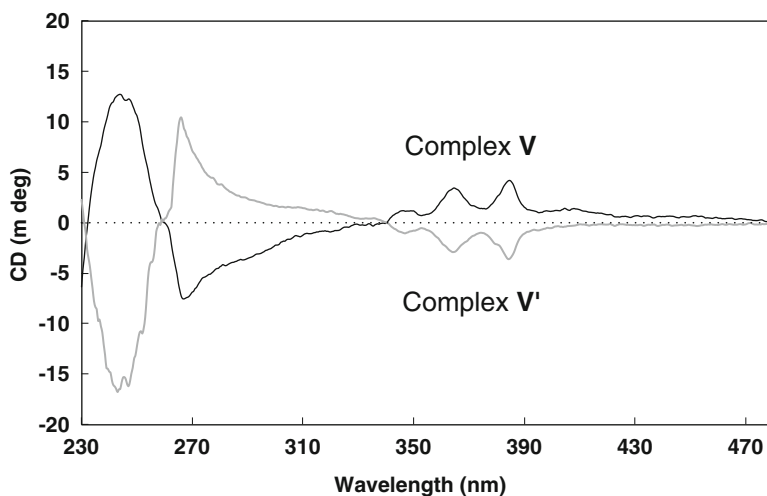
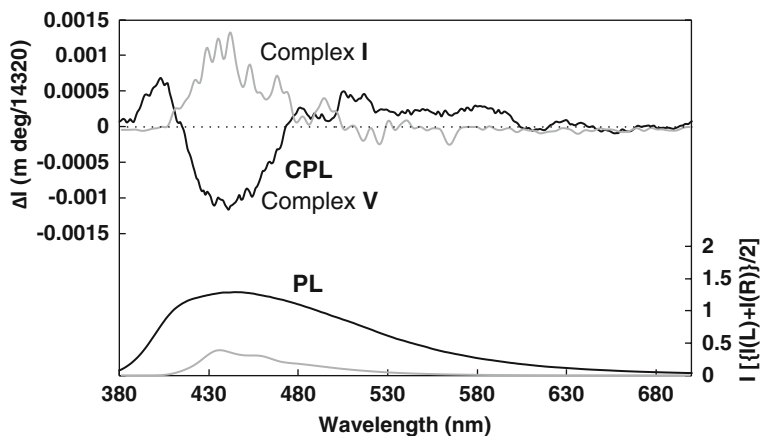


Fig. 30.18 Solid-state CD spectra of complexes **V** composed of (1*R*,2*R*)-**2** (black line) and **V'** composed of (1*S*,2*S*)-**2** (gray line) in the solid state (using KBr pellets)

Chiral complex **V** composed of (1*R*,2*R*)-**2** and 2-anthraceneacetic acid (**6**) exhibits fluorescence with a solid-state fluorescence maximum ( $\lambda_{em}$ ) at 435 nm and a photoluminescence quantum yield ( $\Phi_F$ ) of 0.06 (Fig. 30.17). Complex **V** shows a solid-state CD originating from a fluorescent anthracene unit between 330 and 420 nm (indicated by black line in Fig. 30.18). The circular anisotropy ( $g_{CD}$ ) factor of the first Cotton CD band ( $\lambda^{CD} = 405$  nm) is approximately  $+0.3 \times 10^{-3}$ . When the CD of **V** is compared to that of **I** composed of **1** and (1*R*,2*R*)-**2** (Fig. 30.2), the two spectra are similar. Specifically, the signs of the first Cotton CD bands ( $\lambda^{CD} = 405$  nm for **V** and 406 nm for **I**) are both positive (+), and the  $g_{CD}$  factor of **V** is close to that of **I**.

Interestingly, complex **V** exhibits a negative (−) CPL with a circular anisotropy ( $g_{em}$ ) factor at approximately  $-0.9 \times 10^{-3}$  in the solid state (indicated by black line in Fig. 30.19). However, the sign of the CPL spectrum of **I** is positive (+) (Fig. 30.19, indicated by gray line), despite the use of the same chiral component molecule, (1*R*,2*R*)-**2**. The  $g_{em}$  factor of **V** is close to that of **I**, and the sign of the CPL of the supramolecular fluorophore can clearly be controlled by simply changing a bonding substituent in the achiral fluorescent component molecule in the solid state.

The crystal structures of complexes **I** and **V** are shown in Fig. 30.20. The stoichiometry of **V** is (1*R*,2*R*)-**1**:**6**:H<sub>2</sub>O = 2:2:1 and the space group is  $P2_12_12$ .



**Fig. 30.19** Solid-state CPL and PL spectra of complexes **V** (black line) and **I** (gray line) in the solid state (using KBr pellets)

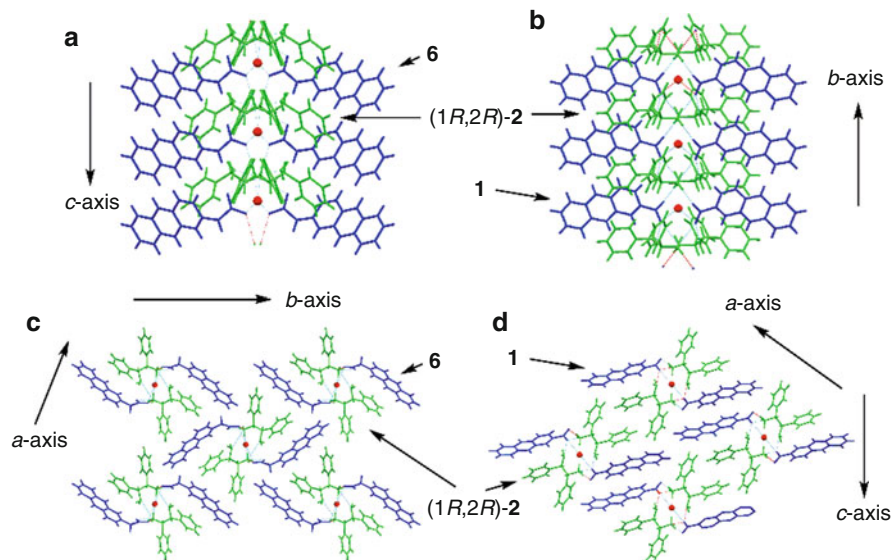


**Fig. 30.20** Crystal structures of complexes **I** and **V**. (a) 1D columnar network structure along the *c*-axis for **V**. (b) 1D columnar network structure along the *b*-axis for **I**. (c) Packing structure observed along the *c*-axis for **V**. (d) Packing structure observed along the *b*-axis for **I**

Complex **V** has a 1D columnar hydrogen- and ionic-bonded network along the *c*-axis, similar to **I** (Fig. 30.20a). The included water molecules (indicated by balls in Fig. 30.20) also contribute to the maintenance of the columnar frame, also similar to **I**. Complex **V** is formed by the assembly of the 1D column (Fig. 30.20c). Interestingly, although **V** and **I** have a similar chiral 1D columnar

structure (Fig. 30.20a, b), the packing structures of the 1D columns are different (Fig. 30.20c, d). Specifically, although the fluorescent anthracene units between the adjoining 1D columns are zigzag in **I**, the units in complex **V** lie vertically between the 1D columns.

Regarding the origin of CD and CPL, from the crystal structures and CD, it is evident that although the packing structure of the fluorescent anthracene unit in complexes **I** and **V** is different, the chirality of both complexes in the ground state is the same. The crystal structures and oscillator coupling theory suggest that the CD and CPL features originating from the fluorescent anthracene unit are caused by interactions between the adjoining 1D columns. Therefore, the reversal of the CPL sign between **I** and **V** may be caused by a local change in the excited-state packing arrangement of the fluorescent anthracene unit in **V**. Particularly, a local structural change in excited state of **V** may be induced in the crystalline state.

### 30.7 Unclassical Control of Solid-State Circularly Polarized Luminescence (CPL) by Supramolecular Complexation–II

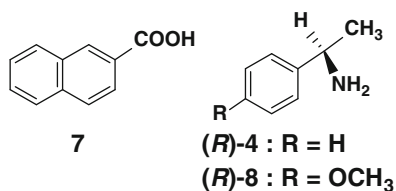
By changing the substituent in the chiral component molecule but not its chirality, the solid-state chiral optical properties of a two-component supramolecular organic fluorophore can be tuned [28].

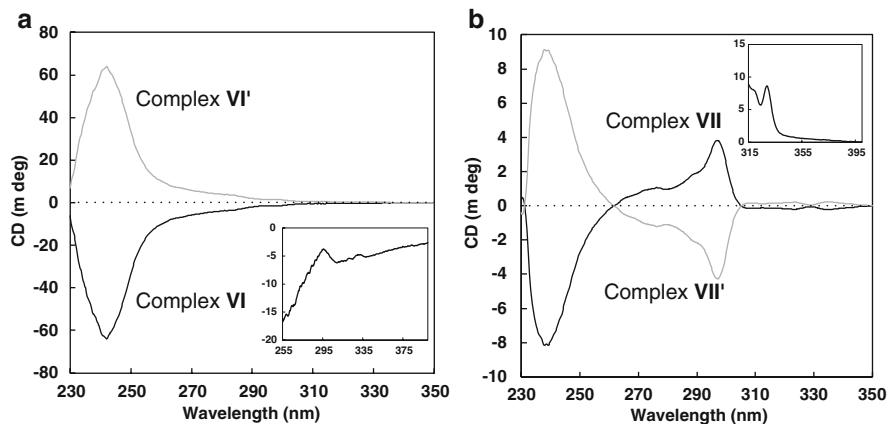
Complex **VI**, composed of **7** and (*R*)-(+)-1-phenylethylamine ((*R*)-**4**), and complex **VII**, composed of **7** and (*R*)-(+)-1-(4-methoxyphenyl)-ethylamine ((*R*)-**8**), can be easily prepared by crystallization from solution (Fig. 30.21). Chiral component molecules (*R*)-**4** and (*R*)-**8** possess different aryl units, yet the same chirality ((*R*)-(+)).

Complexes **VI** and **VII** exhibit fluorescence in the solid state. The solid-state fluorescence maximum ( $\lambda_{em}$ ) and photoluminescence quantum yields ( $\Phi_F$ ) of **VI** and **VII** are similar, despite the different aryl units on the 1-arylethylamine molecules. Solid-state  $\lambda_{em}$  for **VI** and **VII** are observed at 349 and 348 nm, and the  $\Phi_F$  for **VI** and **VII** are 0.09 and 0.08.

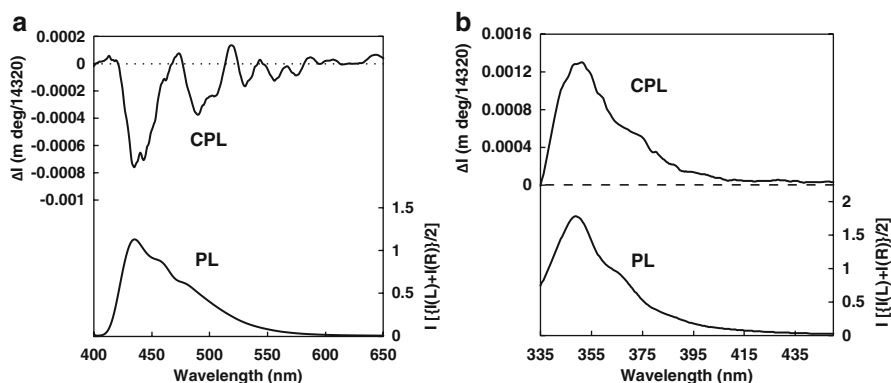
The shapes of the solid-state CD spectra of **VI** and **VII** are also similar (Fig. 30.22). Characteristic peaks of the naphthalene unit are observed between 260 and 350 nm. Effective chiral transfer occurs from the chiral unit to the fluorescent

Fig. 30.21 Supramolecular component molecules





**Fig. 30.22** Solid-state CD spectra of complex (a) **VI** composed of (*R*)-**4** (black line) and **VI'** composed of (*S*)-**4** (gray line) and (b) **VII** composed of (*R*)-**8** (black line) and **VII'** composed of (*S*)-**8** (gray line) in the solid state (in KBr pellets)



**Fig. 30.23** Solid-state CPL and PL spectra of complexes (a) **VI** and (b) **VII** in the solid state (in KBr pellets)

naphthalene unit through complexation. Interestingly, even though **VI** and **VII** are composed of amines with the same chirality, the signs of the CD spectra of **VI** and **VII** are opposite. Specifically, the sign is negative (−) for **VI** (indicated by black lines in Fig. 30.22a) and positive (+) for **VII** (indicated by black lines in Fig. 30.22b). The circular anisotropy factors ( $g_{CD}$ ) of the first Cotton CD band ( $\lambda^{CD} = 330$  nm for **VI** and 329 nm for **VII**) are approximately  $-5.6 \times 10^{-4}$  for **VI** and  $+3.7 \times 10^{-4}$  for **VII**.

The solid-state CPL of complexes **VI** and **VII** were measured in KBr pellets and compared (Fig. 30.23).

Expectedly, the sign of the CPL spectra changes from negative (−) for **VI** to positive (+) for **VII**. The circular anisotropy factor ( $g_{em}$ ) of complexes **VI** and

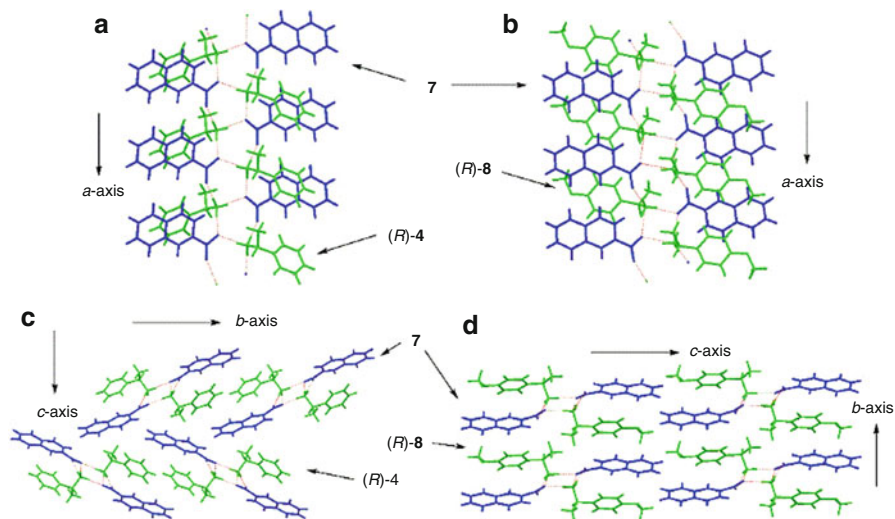


**Fig. 30.24** Crystal structures of **VI** and **VII**. (a)  $2_1$ -helical columnar network structure along the  $a$ -axis for **VI**. (b) Pseudo- $2_1$ -helical columnar network structure along the  $a$ -axis for **VII**. (c) Packing structure observed along the  $a$ -axis for **VI**. (d) Packing structure observed along the  $a$ -axis for **VII**

**VII** is approximately  $-4.0 \times 10^{-4}$  and  $7.6 \times 10^{-4}$ , respectively. The CPL sign of the chiral supramolecular organic fluorophore composed of 1-arylethylamine was controlled by changing the aryl unit in the chiral 1-arylethylamine component molecule, without changing its chirality.

The crystal structures of complexes **VI** and **VII** are quite different (Fig. 30.24). The stoichiometry of **VI** is  $7:(R)\text{-}4 = 1:1$ , and its space group is  $P2_12_12_1$ . On the other hand, the stoichiometry of **VII** is  $7:(R)\text{-}8 = 1:1$ , and its space group is  $P1$ . Complex **VI** has a characteristic  $2_1$ -helical columnar network structure along the  $a$ -axis (Fig. 30.24a). On the other hand, in complex **VII** the component molecules **7** and  $(R)\text{-}8$  form a pseudo- $2_1$ -helical columnar network along the  $a$ -axis (Fig. 30.24b).

**VI** is formed by the assembly of the  $2_1$ -helical columns (Fig. 30.24c) without major intercolumnar interactions (Fig. 30.24c). On the other hand, the packing structure of the pseudo- $2_1$ -helical column in **VII** is different from that of **VI** (Fig. 30.24d). In **VII**, there are three types of intercolumnar interactions: (a) CH- $\pi$  interactions, (b) naphthalene-benzene edge-to-face interactions, and (c) benzene-naphthalene edge-to-face interactions.

The origins of the chiroptical properties of **VI** and **VII** were studied on the basis of the crystal structures. The chiroptical properties of single molecules of **7** in the two complexes were examined theoretically. Figure 30.25 displays the calculated rotational strengths of **7** in **VI** and **VII**, where the rotational strengths at 300–350 nm correspond to the experimentally observed CD intensities in the longest wavelength

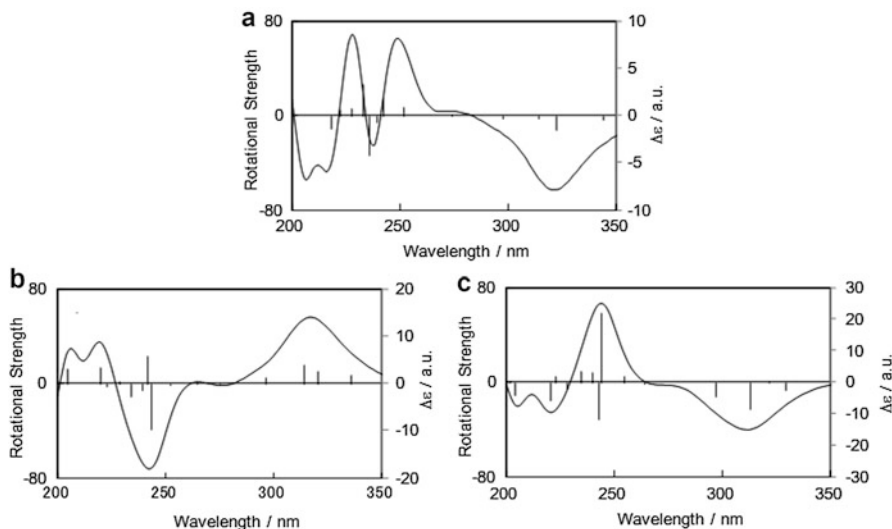


**Fig. 30.25** Calculated rotational strengths (in  $10^{-40}$  erg $\cdot$ esu $\cdot$ cm $\cdot$ Gauss $^{-1}$  unit) and electronic excitation wavelength for molecule **7**. (a) Molecules taking the geometries in complex **VI**. (b) and (c) Molecules taking the geometries in **VII** (two crystallographically independent molecules)

region 260–300 nm, although the correspondence to the experimentally observed wavelength is not good because of the calculation precision.

The data suggest a negative (–) intensity for **VI** (Fig. 30.25a) and a positive (+) intensity for **VII** (Fig. 30.25b). Complex **VII** has negative intensities as well (Fig. 30.25c), but the positive contribution overwhelms the negative contribution due to aggregation. These rotational strengths result from the distortions of **7** around the C–CO<sub>2</sub> bond; the OC–CC dihedral angles are  $-18.6^\circ$  ( $-15.7^\circ$ ) in **VI** and  $34.9^\circ$  ( $34.4^\circ$ ) and  $-42.0^\circ$  ( $-38.9^\circ$ ) in **VII**. The calculated data suggest that the fixation of the molecular structure of **7** may contribute to the experimentally observed CD intensities between 260 and 350 nm.

## 30.8 Conclusions

Chiral supramolecular organic fluorophores were successfully developed using two organic molecules with different functionalities, namely, a chiral amine and an achiral fluorescent carboxylic acid (or sulfonic acid) or an achiral amine molecule and achiral fluorescent acid. The supramolecular organic fluorophores exhibited circular dichroism (CD) or circularly polarized luminescence (CPL) in the solid state. The chiroptical properties of the fluorophores could be tuned by changing the component molecules. Specifically, the signs of the solid-state CD and CPL spectra could be reversed by altering the packing arrangement of the fluorescent unit, rather

than by reversing the chirality of the chiral component. Chiral supramolecular organic fluorophores with such functionalities are expected to be useful in the development of novel, solid-state chiral supramolecular fluorophores.

## References

1. Y. Imai, K. Kawaguchi, T. Harada, T. Sato, M. Ishikawa, M. Fujiki, R. Kuroda, Y. Matsubara, *Tetrahedron Lett.* **47**, 2927–2930 (2007)
2. R. Kuroda, Y. Saito, *Bull. Chem. Soc. Jpn.* **49**, 433–436 (1976)
3. D. Braga, L. Maini, M. Polito, F. Grepioni, *Chem. Commun.* **38**, 2302–2303 (2002)
4. N. Harada, K. Nakanishi, *Circular Dichroic Spectroscopy – Exciton Coupling in Organic Stereochemistry* (University Science Books, Mill Valley, 1983)
5. N. Berova, K. Nakanishi, in *Circular Dichroism: Principles and Applications*, ed. by N. Berova, K. Nakanishi, R.W. Woody, 2nd edn. (Wiley-VCH, New York, 2000), pp. 337–382
6. Y. Imai, N. Shiota, T. Kinuta, T. Okuno, Y. Nakano, T. Harada, T. Sato, M. Fujiki, R. Kuroda, Y. Matsubara, *Eur. J. Org. Chem.* **7**, 1353–1357 (2010)
7. Y. Imai, K. Kamon, K. Murata, T. Harada, Y. Nakano, T. Sato, M. Fujiki, R. Kuroda, Y. Matsubara, *Org. Biomol. Chem.* **6**, 3471–3475 (2008)
8. S. Mason, *Chem. Soc. Rev.* **17**, 347–359 (1988)
9. W.A. Bonner, *Orig. Life Evol. Biosph.* **25**, 175–190 (1995)
10. L. Keszthelyi, *Q. Rev. Biophys.* **28**, 473–507 (1995)
11. C.H. Girard, B. Kagan, *Angew. Chem. Int. Ed.* **37**, 2923–2959 (1998)
12. J.S. Siegel, *Chirality* **10**, 24–27 (1998)
13. B.L. Feringa, R.A. Delden, *Angew. Chem. Int. Ed.* **38**, 3418–3438 (1999)
14. M.M. Green, J.-W. Park, T. Sato, A. Teramoto, S. Lifson, R.L.B. Selinger, J.V. Selinger, *Angew. Chem. Int. Ed.* **38**, 3139–3154 (1999)
15. A. Eschenmoser, *Science* **284**, 2118–2124 (1999)
16. K. Soai, S. Osanai, K. Kadowaki, S. Yonekubo, T. Shibata, I. Sato, *J. Am. Chem. Soc.* **121**, 11235–11236 (1999)
17. M. Avalos, R. Babiano, P. Cintas, J.L. Jimenez, J.C. Palacios, *Tetrahedron Asymmetry* **11**, 2845–2874 (2000)
18. I. Sato, K. Kadowaki, K. Soai, *Angew. Chem. Int. Ed.* **39**, 1510–1512 (2000)
19. D.K. Kondepudi, K. Asakura, *Acc. Chem. Res.* **34**, 946–954 (2001)
20. H. Zepik, E. Shavit, M. Tang, T.R. Jensen, K. Kjaer, G. Bolbach, L. Leiserowitz, I. Weissbuch, M. Lahav, *Science* **295**, 1266–1269 (2002)
21. K. Mislow, *Collect. Czech. Chem. Commun.* **68**, 849–864 (2003)
22. I. Sato, K. Kadowaki, Y. Ohgo, K. Soai, *J. Mol. Catal. A Chem.* **216**, 209–214 (2004)
23. P. Bargeño, R. Pérez de Tudela, S. Miret-Artés, I. Gonzalo, *Phys. Chem. Chem. Phys.* **13**, 806–810 (2011)
24. E.K. Kodona, C. Alexopoulos, E. Panou-Pomonis, P.J. Pomonis, *J. Colloid Interface Sci.* **319**, 72–80 (2008)
25. C. Meinert, S.V. Hoffmann, P. Cassam-Chena, A.C. Evans, C. Giri, L. Nahon, U.J. Meierhenrich, *Angew. Chem. Int. Ed.* **2014**(53), 210–214 (2014)
26. Y. Imai, K. Murata, N. Asano, Y. Nakano, K. Kawaguchi, T. Harada, T. Sato, M. Fujiki, R. Kuroda, Y. Matsubara, *Cryst. Growth Des.* **8**, 3376–3379 (2008)
27. Y. Imai, K. Kawano, Y. Nakano, K. Kawaguchi, T. Harada, T. Sato, M. Fujiki, R. Kuroda, Y. Matsubara, *New J. Chem.* **32**, 1110–1112 (2008)
28. N. Nishiguchi, T. Kinuta, T. Sato, Y. Nakano, H. Tokutome, N. Tajima, M. Fujiki, R. Kuroda, Y. Matsubara, *Chem. Asian. J.* **7**, 360–366 (2012)

**Part VIII**  
**Electric and Magnetic Properties**

# Chapter 31

## Relationship Between the Crystal Structures and Transistor Performance of Organic Semiconductors

Yoshiro Yamashita

**Abstract** Organic field-effect transistors (OFETs) have several advantages such as low cost, flexibility, and large-area fabrication. High performance of transistor means high mobility, large on/off ratio, low threshold voltage, and high stability. To achieve the high performance, the development of new organic semiconductors is essential. The performance is dependent on the crystal structures of organic semiconductors. The relationship between them is described here, giving a guideline for molecular design. In thin-film transistors, polycrystalline films are necessary for strong intermolecular interactions leading to high mobility. Two-dimensional crystal structures are favorable for carrier transportation to reduce the grain boundary effects. Herringbone structures have an advantage of two-dimensional structures. In  $\pi$ -stacking structures, two-dimensional structures are achieved by the formation of two-dimensional columns or using interheteroatom interactions.

**Keywords** Organic semiconductors • Organic field-effect transistors • Electron donors • Electron acceptors

### 31.1 Introduction

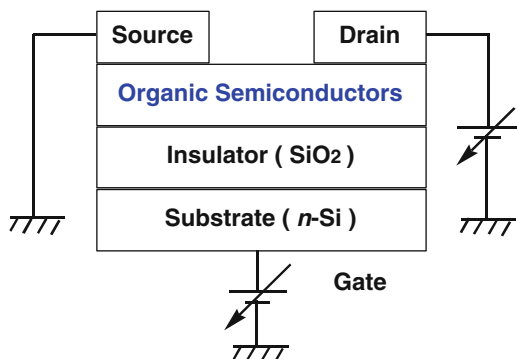
Organic field-effect transistors (OFETs) have attracted much attention for applications such as display drivers, identification tags, and smart cards because they have advantages of low cost, flexibility, and lightweight [1]. Organic semiconductors can be processed at low temperatures compatible with plastic substrates, whereas Si-based FETs require higher temperatures for processing. By using solution techniques such as spin coating, inkjet printing, and screen printing, large-area fabrication is possible at low costs. Modification of organic semiconductors can easily tune the characteristics of transistors.

---

Y. Yamashita (✉)

Department of Electronic Chemistry, Interdisciplinary Graduate School of Science and Engineering, Tokyo Institute of Technology, Nagatsuta, Midori-ku, Yokohama 226-8502, Japan  
e-mail: [yoshiro@echem.titech.ac.jp](mailto:yoshiro@echem.titech.ac.jp); [yoshiro@jcom.zaq.ne.jp](mailto:yoshiro@jcom.zaq.ne.jp)

**Fig. 31.1** Structure of OFET device



OFET devices have a simple structure. A typical bottom-contact structure is described in Fig. 31.1, which is composed of source, drain and gate electrodes, and an active layer of organic semiconductor. An insulator layer such as  $\text{SiO}_2$  exists between the gate electrode and organic semiconductor. The semiconductor layer affords carrier paths. FET characteristics are evaluated on carrier mobility, on/off current ratio, and threshold voltage. High performance of transistor means high mobility, large on/off ratio, and low threshold voltage. In addition, the high stability of device in air is essential for practical applications. To achieve such high performance, the development of new organic semiconductors is particularly important. Proper frontier orbital energy levels near the work functions of source/drain electrodes are necessary for injection of carriers. HOMO levels are important for p-type semiconductors, while LUMO levels are related to the n-type ones.  $\pi$ -Conjugated molecules with electron-donating properties have high HOMO levels and are candidates for p-type semiconductors. On the other hand, electron-accepting molecules with low LUMO levels become n-type semiconductors. Many p-type organic semiconductors have been reported so far and some semiconductors show higher mobilities than amorphous silicon ( $1 \text{ cm}^2/\text{Vs}$ ). Typical p-type semiconductors are acenes such as pentacene and heterocyclic oligomers such as oligothiophenes. These materials make OFETs more attractive and practical applications using them have been attempted. On the other hand, high-performance n-type semiconductors have been obtained by introducing electron-withdrawing groups such as fluoro or perfluoroalkyl substituents into p-type semiconductor cores.

In addition to the proper energy levels of molecules, efficient carrier paths should be constructed for high carrier mobilities in OFET devices. Strong intermolecular interactions lead to the high mobility in crystals. OFETs are a thin-film device, where polycrystalline thin films are necessary for high carrier mobilities and amorphous ones exhibit low mobility. The crystalline films are generally composed of grains. Since the grains are microcrystals, the single crystal structures can be used for discussion on carrier transport in the grains. However, the charge transport between the grains is hopping and less efficient compared with that in crystals. The grain boundary is a barrier to the carrier transportation. The efficiency of transport between the grains is considered to be dependent on the direction of

microcrystals. Since the control of the direction of crystals is difficult, molecules with two-dimensional crystal structures seem favorable for carrier transportation.

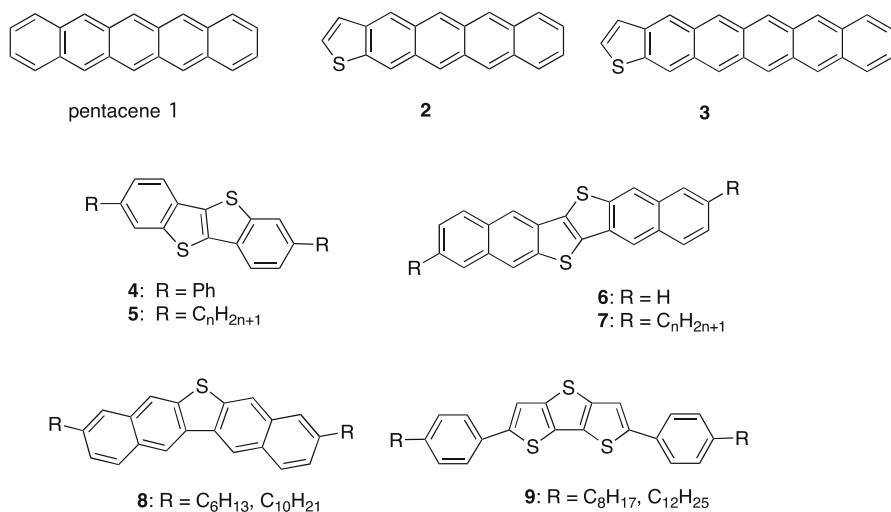
In this chapter organic semiconductors affording high-performance FET devices are described, and the relationship between the crystal structures and the transistor characteristics is discussed to show the strategies of molecular design for the high performance.

## 31.2 p-Type Organic Semiconductors

### 31.2.1 Acenes

Pentacene **1** has been most commonly used as a p-type semiconductor and shows the highest hole mobility of  $3.0 \text{ cm}^2/\text{Vs}$  in thin-film OFET devices [2]. Pentacene and the tetramethyl derivative have a herringbone structure in the crystals [3]. Such a structure is often observed in the structures of polycyclic aromatic compounds. Although the intermolecular interaction in the herringbone structure is weaker than that in the columnar  $\pi$ -stacking structure, the dimensionality of interaction is higher. As mentioned before, two-dimensional structures are favorable for carrier transportation in thin-film devices to reduce the boundary effect. The high mobility of pentacene is attributed to the structure as well as to the small reorientation energy (Scheme 31.1).

Pentacene has disadvantages such as instability in air and low solubility in solvents. Replacement of the benzene rings with thiophene ones enhances the air



**Scheme 31.1** Structures of 1–9

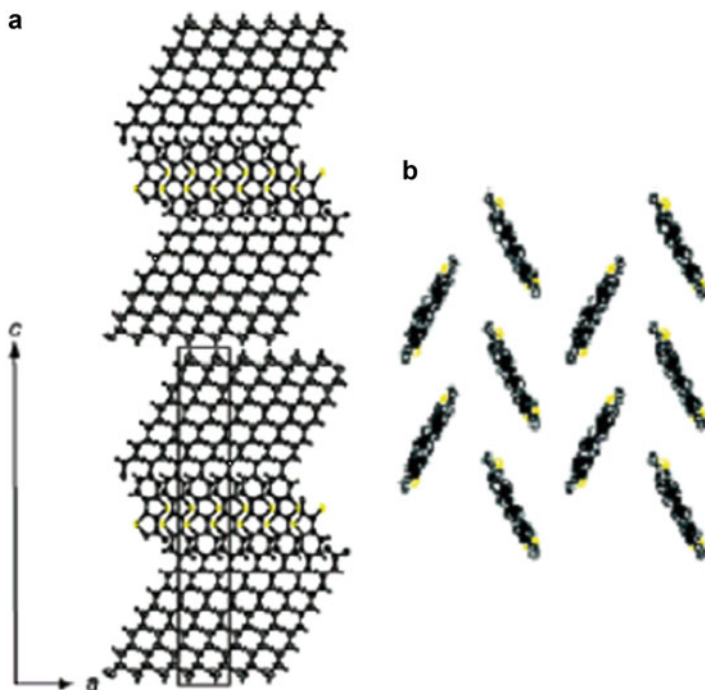


Fig. 31.2 (a) Crystal structure of **5** [7] and (b) that of **6** [8]

stability. For example, thiophene-containing compound **2** is stable in air and the hole mobility is  $0.31 \text{ cm}^2/\text{Vs}$  [4]. The pentacene derivative **3** exhibits higher mobility of  $0.39 \text{ cm}^2/\text{Vs}$  due to the more extended  $\pi$ -conjugation [5].

Takimiya et al. developed new semiconductors containing thienothiophene units **4** and **5**. The diphenyl derivative **4** showed excellent FET performance and the hole mobility reached to  $2.0 \text{ cm}^2/\text{Vs}$  [6]. The device was stable for several months on standing in air. Interestingly, the alkyl-substituted derivatives **5** afforded high-performance FETs using a solution method [7]. The mobility and solubility were dependent on the alkyl chain length. The highest solubility was observed at the C9 length and the solubility decreased in the derivatives with longer lengths due to the van der Waals attraction between the alkyl groups. The derivative with the C13 length showed the highest mobility of  $2.75 \text{ cm}^2/\text{Vs}$ . The single crystal structure of the C12 derivative revealed a layer by layer structure as shown in Fig. 31.2a, where the aliphatic layers and  $\pi$ -core layers are alternatively stacked. The stacking pattern of the  $\pi$ -core unit is herringbone. The naphthalene fused derivative **6** exhibited a higher mobility of  $2.9 \text{ cm}^2/\text{Vs}$  whose device was fabricated by a vacuum-deposition method and stable in air [8]. The single crystal structure of **6** is also herringbone as depicted in Fig. 31.2b.

The single crystal devices are expected to show higher mobilities than the conventional thin-film ones since no grain boundaries exist in the single crystals.

Very thin platelike crystals are suitable for the single crystal devices since they can be closely placed on the substrates. The alkyl-substituted thiophene-acenes with herringbone structures often afford such crystals because the crystals grow well along two-dimensional stacking directions and do not grow well along the alkyl groups. They show excellent mobility when they have strong intermolecular interactions. Sulfur-containing molecules have a possibility of strong intermolecular interactions owing to the intermolecular S $\cdots$ S contacts.

Recently, new fabrication methods for single crystal devices from the solutions have been developed. The device of alkyl substituted **5** fabricated by a double-shot inkjet method showed a very high mobility over 30 cm<sup>2</sup>/Vs [9]. Takeya et al. have developed a solution-crystallization method for single crystal devices. Using this method, they reported 11 cm<sup>2</sup>/Vs of alkyl-substituted **7** [10]. They also developed a new type of semiconductors **8** with a bent molecular and herringbone structure, which showed a high mobility of 12 cm<sup>2</sup>/Vs in the single crystal device [11]. The single crystal device of bithienothiophene **9** fabricated by a drop casting method showed 9.5 cm<sup>2</sup>/Vs [12]. The crystal structure is herringbone and intermolecular S $\cdots$ S contacts (3.34 Å) are observed. The heteroatom contacts are considered to increase intermolecular interactions leading to the high mobility.

As mentioned above, pentacene and its analogues with a herringbone structure in the crystal show high hole mobility. The herringbone structure has an advantage of two-dimensional structure, which is favorable for carrier transportation in thin films. On the other hand,  $\pi$ -stacking structures are expected to have stronger  $\pi$ - $\pi$  intermolecular interactions than in herringbone ones owing to the larger transfer integrals between molecules. Therefore, construction of  $\pi$ -stacking structures in acenes has been attempted to investigate the stacking effect.

A method for constructing a  $\pi$ -stacking structure is to use intermolecular charge-transfer interactions. Pentacene derivative **10** with an electron-accepting quinone unit takes a  $\pi$ -stacking columnar structure owing to the intermolecular electron donor-acceptor interaction, where the pentacene unit works as a donor part [13]. The mobility of **10** is 0.05 cm<sup>2</sup>/Vs, which is much lower than that of pentacene with a herringbone structure. This result can be attributed to the one-dimensional columnar structure of **10**, which is unfavorable for carrier transportation between grains in thin films.

However, formation of two-dimensional  $\pi$ -stacking structures is possible by molecular design using steric interactions. A pentacene derivative **11** containing acetylene units with a bulky substituent takes a  $\pi$ -stacking two-dimensional columnar structure to avoid steric interactions as shown in Fig. 31.3. The derivative containing isopropyl groups afforded an FET device with a high mobility of 0.4 cm<sup>2</sup>/Vs [14]. Another advantage of **11** is its good solubility, making a solution process for the device fabrication possible. This method of using bulky acetylene groups was applied to thiophene analogues **12**. The Et derivative takes a two-dimensional columnar structure and exhibited a high mobility of 1.0 cm<sup>2</sup>/Vs,

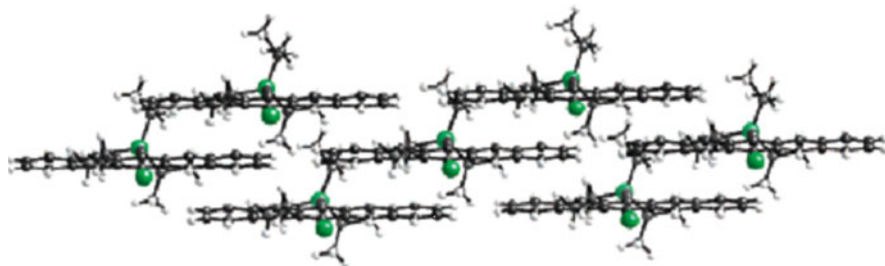
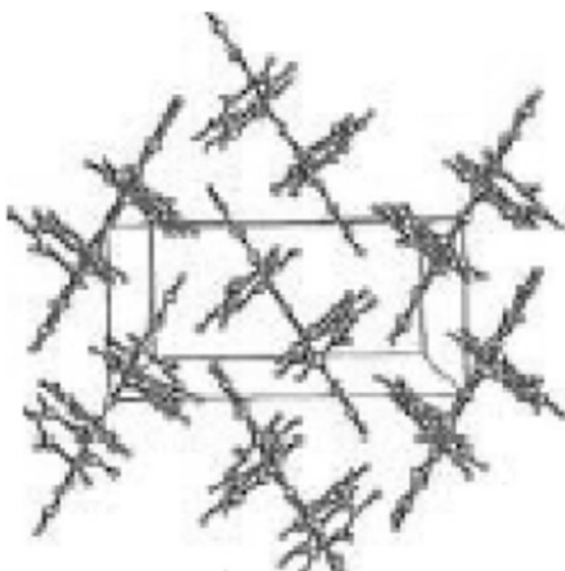


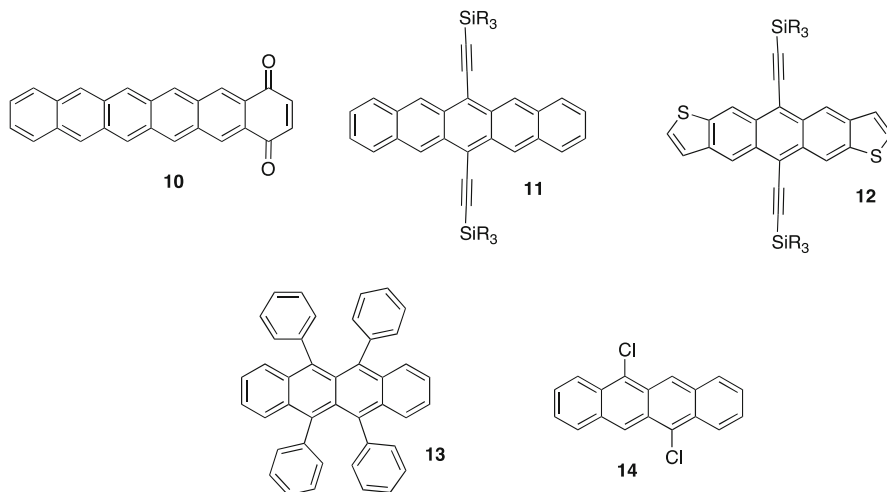
**Fig. 31.3** Two-dimensional columnar structure of **11** [15]

**Fig. 31.4** Crystal structure of rubrene **13** [16]



whereas the isopropyl derivative showed a lower mobility of  $10^{-4}$   $\text{cm}^2/\text{Vs}$  due to the one-dimensional columnar structure [15]. This result indicates that the bulk of substituents controls the crystal structures determining the carrier mobility.

On the other hand, in single crystal devices, molecules with  $\pi$ -stacking structures show high mobilities when thin crystals are obtained. Introduction of substituents to acene cores leads to  $\pi$ -stacking structures. Rubrene **13** with tetraphenyl groups has a  $\pi$ -stacking structure as shown in Fig. 31.4 [16]. The crystal does not grow well along the phenyl group direction, resulting in a very thin platelike crystal. The device shows a high mobility of  $15 \text{ cm}^2/\text{Vs}$ . A tetracene derivative **14** with dichloro groups forms a  $\pi$ -stacking structure and shows a high mobility of  $1.6 \text{ cm}^2/\text{Vs}$  in a single crystal device [17] (Scheme 31.2).



**Scheme 31.2** Structures of 10–14

### 31.2.2 Oligomers

Thiophene oligomers **15** have been extensively studied and the effects of ring numbers and alkyl chain lengths on FET characteristics have been investigated. In this study, 4–6 thiophene rings and 2–6 carbon numbers of alkyl chains were shown to be required for achieving good mobility [18]. Terthiophene does not show FET behavior and larger numbers of thiophene rings are necessary for efficient intermolecular interactions. Alkyl groups are considered to be favorable for arranging molecules on the substrate.

Thiophene-phenylene co-oligomers have higher air stability than thiophene oligomers owing to the lower HOMO levels. In co-oligomers **16**, an odd-even effect of the thiophene ring numbers on FET performance was found, where oligomers with even number of thiophene rings showed higher mobilities than oligomers with odd number of rings [19]. This is explained by considering that the molecular symmetry is higher in the former, which leads to better-ordered molecular arrangement.

Soluble polythiophenes have attracted much attention from application viewpoints because the uniform films of polymers can be obtained using solution methods. In polymers, high-performance FETs also require ordered structures with crystallinity, while amorphous films show low performance. To prepare crystalline polythiophenes with good solubility, long alkyl chains should be introduced at suitable positions of thiophene rings. Polythiophene **17** ( $R = C_{12}H_{25}$ ) showed liquid-crystal characteristics, and the ordered structure was confirmed by X-ray analysis as shown in Fig. 31.5 [20]. The mobility was 0.02–0.05 cm<sup>2</sup>/Vs and improved to 0.07–0.12 cm<sup>2</sup>/Vs after annealing which is helpful to order the

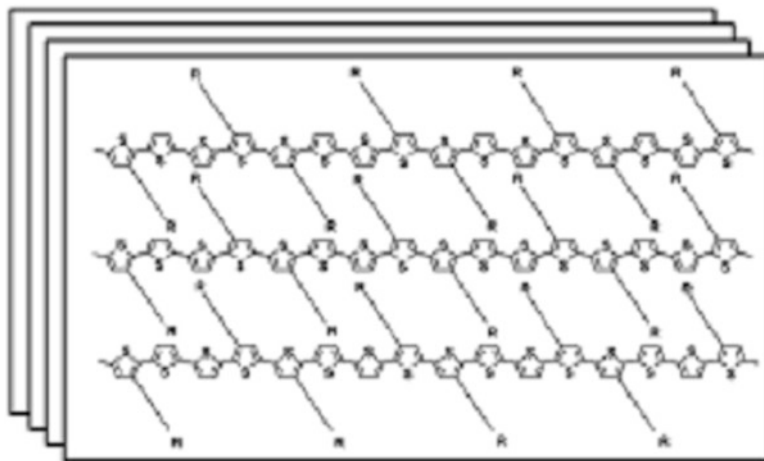
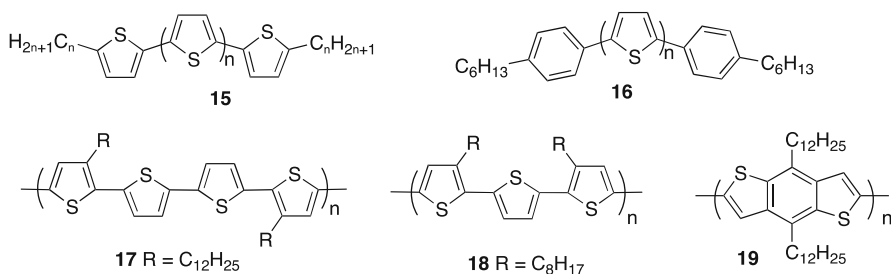


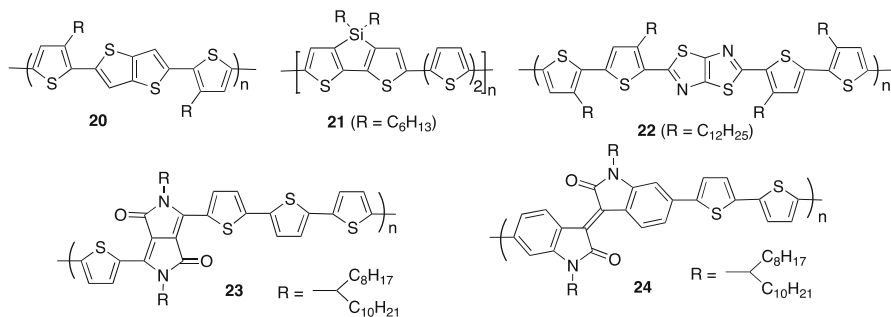
Fig. 31.5 Layer structure of polymer 17 [20]



Scheme 31.3 Structures of 15–19

polymer. Polythiophene **18** is also crystalline and showed a good mobility of 0.015–0.022  $\text{cm}^2/\text{Vs}$  [21]. The structure was investigated by XRD to reveal the  $\pi$ -stacked layer structure (Scheme 31.3).

Introduction of condensed heterocyclic units is considered to increase intermolecular interactions leading to high mobilities. Polymer **19** was designed according to this idea and the mobility was 0.012  $\text{cm}^2/\text{Vs}$  [22]. Thienothiophene-containing polymer **20** ( $\text{R} = \text{C}_{14}\text{H}_{29}$ ) showed an increased mobility of 0.6  $\text{cm}^2/\text{Vs}$  [23]. On the other hand, to enhance the air stability, introduction of electron-acceptor units is effective to lower the HOMO levels. Polymer **21** containing an electron-accepting silole part was found to be stable in air [24]. Furthermore, thiazolothiazole-containing polymer **22** was developed to show high air stability as well as high mobility of 0.14  $\text{cm}^2/\text{Vs}$  [25]. The thiazolothiazole ring is an electron-accepting one and the absence of hydrogen atoms leads to the planar structure. In addition, it can be easily prepared by one-step reaction from the corresponding aldehydes (Scheme 31.4).



**Scheme 31.4** Structures of **20–24**

Recently, very high-mobilities have been accomplished by using heterocycles with amide units, which have electron-withdrawing properties. Branched alkyl groups attached to the nitrogen atoms increase the solubility in organic solvents. The diketopyrrolopyrrole (DPP) derivative **23** afforded a mobility above 1 cm<sup>2</sup>/Vs [26]. The polymer **24** with an indigo unit also showed a high mobility of 0.79 cm<sup>2</sup>/Vs [27]. In these polymers, efficient  $\pi$ -conjugation with planar heterocyclic  $\pi$ -cores is accomplished. The alkyl parts occupy the space between the  $\pi$ -cores and do not bother  $\pi$ -interactions between the polymer chains.

### 31.2.3 Tetrathiafulvalenes (TTFs)

TTFs, which are famous for electron donors affording organic conductors and superconductors, are promising semiconductors for high-performance OFETs since they have properties of self-assembling. However, the electron-donating properties of TTFs are generally so strong that their thin films are easily oxidized, leading to the instability in air. Therefore, to use TTFs as semiconductors, the electron-donating properties should be reduced. For this purpose, we have used a TTF analogue **25** containing electron-accepting thiadiazole rings. The molecule forms a sheetlike network due to the short S $\cdots$ S contacts in the crystal. The FET device based on **25** showed a good mobility of 0.2 cm<sup>2</sup>/Vs with a very high on/off ratio of 10<sup>8</sup> [28]. Introduction of fused aromatic rings to the TTF is also useful to decrease the electron-donating property. Benzene- and thiophene-fused derivatives **26** and **27** exhibited high mobilities of 1.0 [29] and 1.4 cm<sup>2</sup>/Vs [30], respectively, in the single crystal devices. Although the dibenzoTTF has a herringbone structure, the mobility of **26** was 0.06 cm<sup>2</sup>/Vs in the thin-film device probably due to the lack of effective intermolecular interactions. The mobility was enhanced in **28** by replacing the benzene ring with a naphthalene ring to 0.42 cm<sup>2</sup>/Vs [31]. This is attributed to the extended  $\pi$ -conjugation resulting in stronger intermolecular interactions. However, the FET characteristics of **28** could not be observed in air owing to the still high HOMO level. In contrast, TTF derivative **29** containing electron-accepting

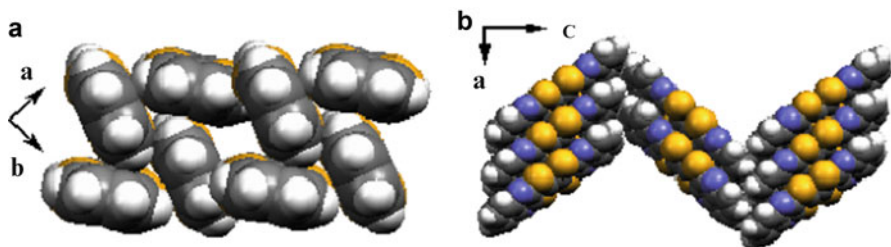
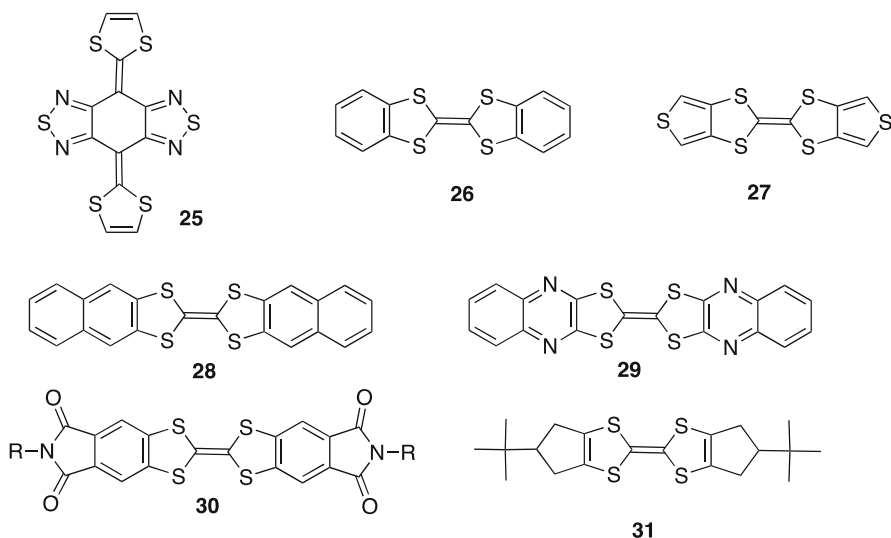


Fig. 31.6 Crystal structures of **28** (a) and **29** (b)



Scheme 31.5 Structures of **25**–**31**

quinoxaline rings showed enhanced stability to oxygen although the mobility was a little decreased to  $0.2 \text{ cm}^2/\text{Vs}$  [31]. TTF **29** has electron donor-acceptor parts leading to a  $\pi$ -stacking structure by an intermolecular charge-transfer interaction in the crystal as shown in Fig. 31.6b, whereas **28** takes a herringbone structure similarly to **26** as depicted in Fig. 31.6a. According to the similar idea, electron-accepting dimide groups were introduced to dibenzotTF to give **30**, which showed a high hole mobility of  $0.40 \text{ cm}^2/\text{Vs}$  [32] (Scheme 31.5).

The TTF derivative **31** containing *tert*-butyl groups has a columnar structure. The distance between the molecules in the column is long due to the steric interaction, and instead, the  $\text{S} \cdots \text{S}$  contacts between the columns are short, resulting in a two-dimensional structure [33]. The molecule showed high mobility of  $0.98 \text{ cm}^2/\text{Vs}$  in a thin-film device and  $2.3 \text{ cm}^2/\text{Vs}$  in a single crystal device. Although the HOMO level of **31** is high, the devices showed air stability probably due to the dense packing.

## 31.3 n-Type Organic Semiconductors

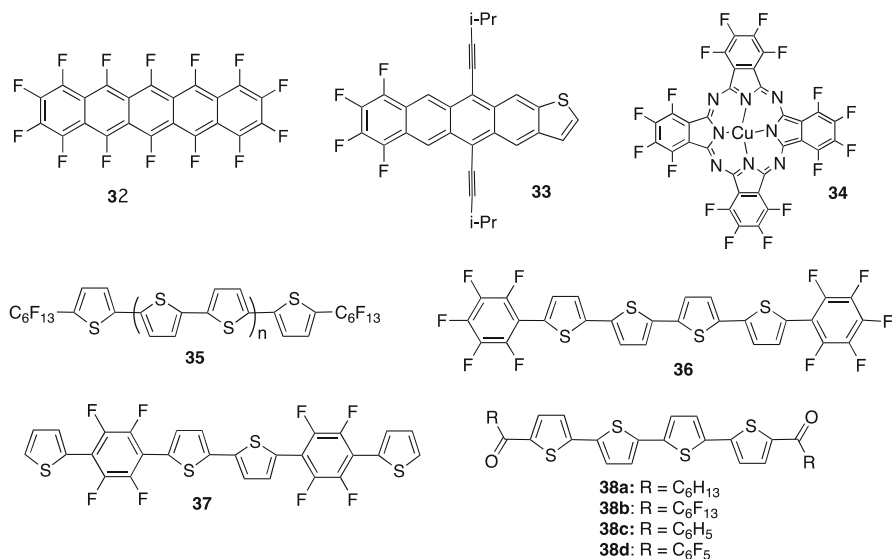
### 31.3.1 *Acenes*

Compared to p-type organic semiconductors, n-type semiconductors are not fully developed, and the FET performances are not satisfactory. Novel n-type organic semiconductors can be prepared by introducing electron-withdrawing substituents to p-type semiconductors. Perfluorinated pentacene **32** showed a high electron mobility of  $0.11 \text{ cm}^2/\text{Vs}$  under high vacuum conditions [34]. Tetrafluoro derivative **33** of the thiophene analogue with acetylene groups showed ambipolar behavior in vacuum [35]. The single crystal of **33** has a packing of two-dimensional columnar structure similar to the pentacene derivative **11**. The highest electron and hole mobilities were 0.2 and  $0.06 \text{ cm}^2/\text{Vs}$ , respectively. In air, the n-type behavior disappeared and the hole mobility increased to  $0.1 \text{ cm}^2/\text{Vs}$ , indicating that the n-type behavior is more sensitive to oxygen than the p-type one. On the other hand, perfluorophthalocyanine derivative **34** showed air stability although the electron mobility was not so high ( $0.03 \text{ cm}^2/\text{Vs}$ ) [36].

### 31.3.2 *Heterocyclic Oligomers*

Thiophene oligomers **35** with perfluorohexyl groups also exhibited n-type characteristics. The highest mobility of  $0.048 \text{ cm}^2/\text{Vs}$  was observed in the oligomer with a quaterthiophene core [37]. The oligomer **36** with pentafluorophenyl groups showed an electron mobility of  $0.08 \text{ cm}^2/\text{Vs}$  [38]. These findings could be rationalized in terms of LUMO levels since introduction of electron-withdrawing groups decreased the LUMO levels, leading to the n-type behavior. However, **37** possessing the similar HOMO and LUMO energies as **36** showed p-type behavior [38]. This result suggests the effect of the end groups on the FET polarity, and they might play an important role in accumulating carriers at the insulator-semiconductor interface. The single crystal of **36** has a kind of two-dimensional columnar structure, where one molecule overlaps two molecules in the stacking. This structure is considered to lead to the good electron mobility (Scheme 31.6).

Introduction of acyl groups to the thiophene-oligomer core also induces n-type characteristics. The electron mobilities of hexyl derivative **38a** and perfluorohexyl derivative **38b** were 0.1 and  $0.6 \text{ cm}^2/\text{Vs}$ , respectively [39]. They showed ambipolar behavior, where the hole mobility was better in the hexyl derivative **38a**. On the other hand, a benzoyl derivative **38c** showed only p-type behavior ( $0.043 \text{ cm}^2/\text{Vs}$ ), while a perfluorobenzoyl derivative **38d** showed only n-type behavior ( $0.45 \text{ cm}^2/\text{Vs}$ ) [40]. Their single-crystal structures are similar to each other and have a herringbone packing of the thiophene-oligomer core, suggesting that the difference in the electron-accepting property determines the polarity of FET.



**Scheme 31.6** Structures of 32–38

We have achieved high electron mobilities by using a trifluoromethylphenyl group as end substituent. Bithiophene derivative **39** with the substituent has a herringbone stacking and showed a good mobility of 0.18 cm<sup>2</sup>/Vs which is higher than that of the corresponding perfluorohexyl derivative [41]. The weak electron affinity of **39** makes the barrier of electron injection from the electrode large, resulting in a high threshold voltage of 70 V. Therefore, thiazolothiazole-containing compound **40** was designed to increase the electron affinity [41]. This bicyclic heterocycle is a rigid polarized ring which is expected to induce strong intermolecular  $\pi$ - $\pi$  interactions. Actually, **40** has a  $\pi$ - $\pi$  stacking structure and short S...S contact (3.25 Å) between the columns as shown in Fig. 31.7. The heteroatom contacts result in increasing the dimensionality and leading to the high mobility. The FET device based on **40** showed an electron mobility of 0.30 cm<sup>2</sup>/Vs with a threshold voltage of 60 V. The optimization of the device structure improved the mobility to 1.2 cm<sup>2</sup>/Vs [42].

Furthermore, higher mobilities were achieved by using bithiazole derivative **42** [43]. The molecule is completely planar and forms a two-dimensional columnar structure to avoid the steric interaction of the CF<sub>3</sub> group as shown in Fig. 31.8. The mobility was reached to 1.83 cm<sup>2</sup>/Vs by using an OTS (octadecyltrichlorosilane)-modified SiO<sub>2</sub> substrate. In contrast, the isomer **43** did not exhibit FET characteristics because the molecules of **43** are disordered in thin films due to the easy rotation around the central bond (Scheme 31.7).

Although high mobilities were achieved in oligomers with trifluoromethylphenyl groups as described above, the threshold voltages were above 60 V. To decrease these values, the LUMO levels of semiconductors should be lowered for ready

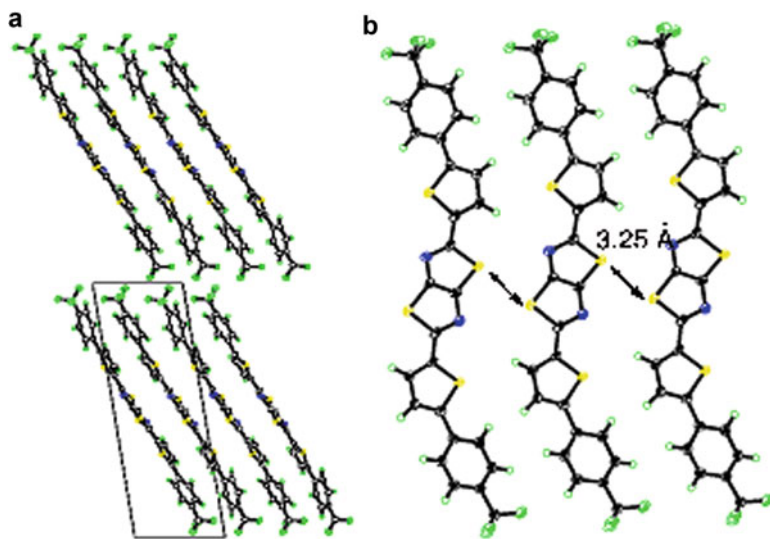
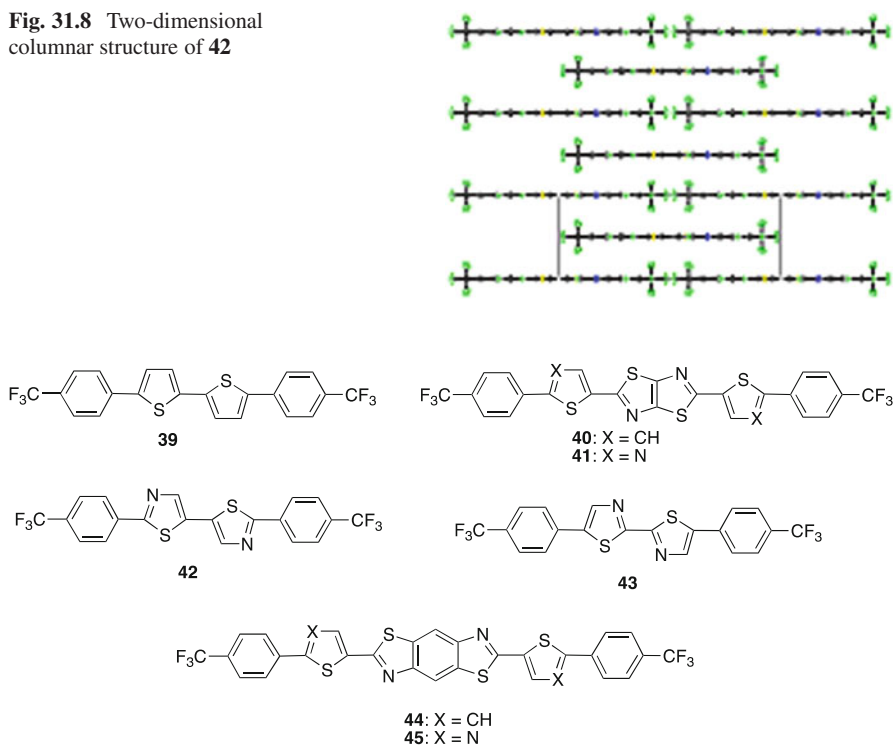


Fig. 31.7 Crystal structure of 40, (a) layer structure and (b) short S...S contact

Fig. 31.8 Two-dimensional columnar structure of 42



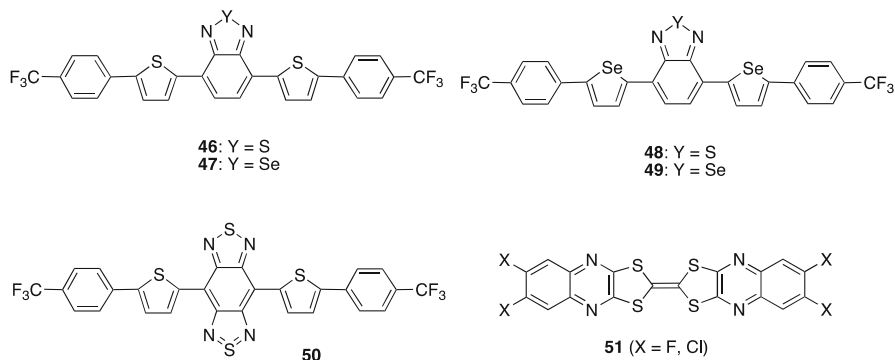
Scheme 31.7 Structures of 39–45

electron injection. Replacement of the thiophene rings of **40** by thiazole ones to give **41** increases the electron affinity [44]. The FET device based on compound **41** exhibited a lower threshold voltage of 24 V with a high mobility of  $0.64 \text{ cm}^2/\text{Vs}$ .

The extension of  $\pi$ -conjugation is considered to be useful for increase in intermolecular interactions as well as decrease in Coulomb repulsion. For this purpose, benzobisthiazole derivatives **44** and **45** were designed [45]. They were easily obtained by reaction of commercially available 2,5-diamino-1,4-benzenedithiol and the corresponding aldehydes. The packing structure in the single crystal of **44** is a herringbone type, which is in contrast to the  $\pi$ -stacking structure of **40**. This is probably due to the electron repulsion between the benzobisthiazole rings of **44**. Although the  $\pi$ - $\pi$  intermolecular interaction is weaker in the herringbone packing than in the  $\pi$ -stacked one, the former has an advantage of two-dimensional structure as seen in pentacene. The mobility of **44** is a little low compared to that of **40**. However, the threshold voltage is much reduced to 24 V although the electron affinity is similar. This result may be attributed to the herringbone structure of **44** leading to a better contact between the semiconductor and the electrodes. On the other hand, the thiazole analogue **45** exhibited a poor FET performance. This result was attributed to its amorphous-like morphology in the thin film since no peak was observed in the X-ray diffraction analysis.

As an electron-accepting heterocycle, 2,1,3-benzothiadiazole with a quinoid structure was also used for n-type semiconductors. Compound **46** containing this unit afforded high-performance n-type FETs, where a high mobility of  $0.19 \text{ cm}^2/\text{Vs}$  and a low threshold voltage of 3 V were observed [46]. On the other hand, introduction of selenium atoms is expected to increase intermolecular interactions owing to the more polarized nature of the selenium atom. In this context, selenium-containing compounds **47**–**49** were synthesized [46]. The comparison of **46** and **47** indicates that the selenadiazole ring has a higher electron affinity than the thiadiazole. The selenophene rings also decrease the LUMO energies compared with the corresponding thiophene rings because the reduction potentials of **48** and **49** are more positively shifted than those of **46** and **47**. The single crystal X-ray structure analysis of **48** reveals a multidimensional structure, where the molecules form a dimer pair which is arranged in a herringbone manner, and short S...Se contacts of 3.66 and 3.68 Å are observed. The mobilities of the bottom-contact FETs of **48** and **49** are higher than those of **46** and **47**. Particularly, the mobilities at the substrate temperature of 25 °C are greatly increased by the introduction of the selenophene rings. The threshold voltages of the selenophene-containing compounds **48** and **49** are lower than those of **46** and **47** because of the higher electron affinity of the former. The mobilities were improved by increasing the substrate temperature, and the highest mobilities of **48** and **49** in the bottom-contact devices reached to 0.19 and  $0.16 \text{ cm}^2/\text{Vs}$  at 100 °C, respectively.

Furthermore, bisthiadiazole derivative **50** was developed to increase the electron affinity and intermolecular interactions [47]. As expected, this molecule afforded air-stable high-performance FET devices with a mobility of  $0.77 \text{ cm}^2$ . This one



**Scheme 31.8** Structures of 46–51

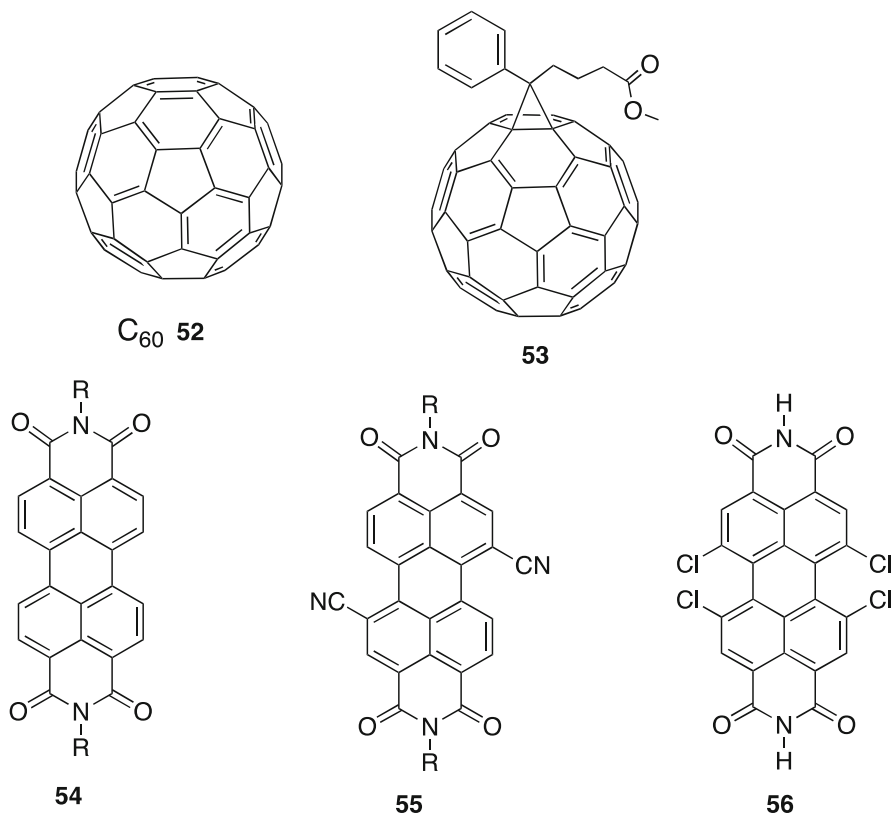
was applied as n-type semiconductor for an air-stable complementary inverter [48] (Scheme 31.8).

### 31.3.3 Other Electron-Accepting Compounds

Although quinoxaline-fused TTF derivatives **29** showed p-type behavior, the halogen-substituted derivatives **51** showed n-type behavior. The mobilities were  $0.1 \text{ cm}^2/\text{Vs}$  in both derivatives and they are the first examples of n-type FETs based on TTF derivatives [49]. The effect of halogen substituents is rationalized in terms of the lower LUMO levels. These TTF derivatives form  $\pi$ -stacking structures similarly to **29**. This result confirms that the FET polarity can be determined by the frontier orbital energies of semiconductors and end substituents can control the polarity.

$\text{C}_{60}$  **52**, which has a good electron affinity and a three-dimensional structure, also affords high-performance FET devices. The device fabricated by molecular-beam deposition showed a high mobility of  $0.56 \text{ cm}^2/\text{Vs}$  in vacuum [50]. The derivatives were developed to increase the solubility in solvents. The derivative **53** afforded ambipolar FET devices using a solution method, where the electron and hole mobilities were 0.01 and  $0.008 \text{ cm}^2/\text{Vs}$ , respectively [51]. This molecule is famous for an n-type semiconductor for thin-film solar cells. The high performance in the solar cells can be attributed to the three-dimensional structure as well as the small reorientation energy upon reduction (Scheme 31.9).

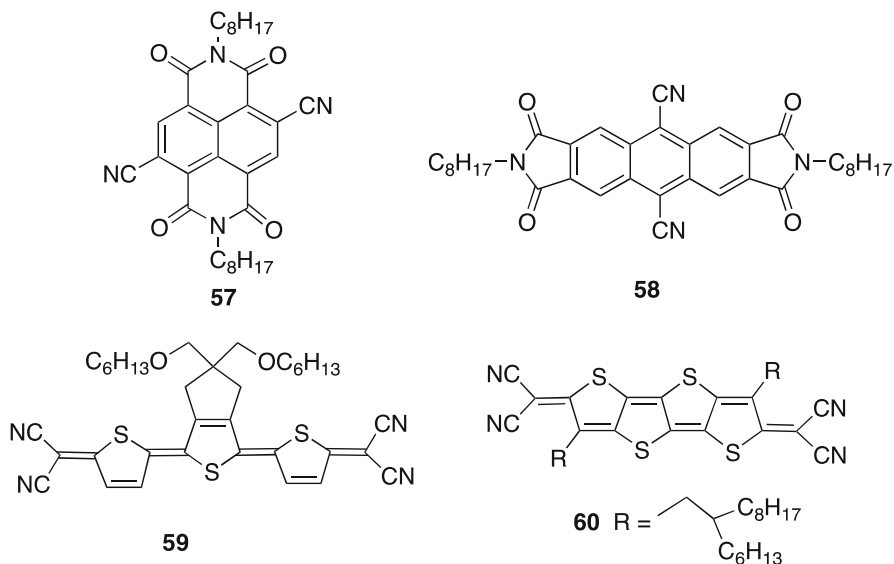
As typical n-type semiconductors, perylene diimides **54** are famous. The octyl derivative showed a high electron mobility of  $0.64 \text{ cm}^2/\text{Vs}$  [52], although the device was not stable in air. In the n-type organic semiconductors, radical anions are produced by electron injection. They are easily oxidized, resulting in the poor electron mobility in air. To enhance the stability of the radical anions, the electron-



**Scheme 31.9** Structures of **52**–**56**

accepting properties of semiconductors should be increased. For this purpose, cyano groups were introduced to give **55** with high electron affinity. As expected, **55** showed air stability as well as a high electron mobility of  $0.64 \text{ cm}^2/\text{Vs}$  [53]. Tetrachloro derivative **56** also showed a good mobility of  $0.18 \text{ cm}^2/\text{Vs}$  with air stability [54]. Similarly, naphthalene dimide **57** [55] and anthracene dimide **58** [56] containing cyano groups were developed. Their reduction potentials were  $+0.08$  and  $-0.33$  V vs. SCE, respectively, suggesting that the anion radicals are stable in air. Actually, their FET devices showed air stability and the mobilities were  $0.15$  and  $0.03 \text{ cm}^2/\text{Vs}$ , respectively (Scheme 31.10).

Tetracyanoquinodimethane (TCNQ) and their analogues are known as strong electron acceptors. The FET performances based on the TCNQ derivatives are usually low because the CN groups work as carrier trap when they are close to the substrate. However, the terthiophene TCNQ analogue with alkyl substituents afforded high-performance FET devices. Compound **59** has good solubility and the spin-coated thin film showed a good mobility of  $0.16 \text{ cm}^2/\text{Vs}$  after annealing at



**Scheme 31.10** Structures of **57–60**

150 °C [57]. Furthermore, the analogue **60** with a rigid tetracyclic thiophene ring afforded a higher mobility of 0.9 cm<sup>2</sup>/Vs in ambient conditions [58]. It is considered that in these heteroTCNQs, the alkyl groups are close to the substrate and the CN groups do not disturb the electron transportation.

## 31.4 Summary

As described here, a large number of novel organic semiconductors have recently been reported, which make great progress in OFETs. The relationship between the crystal structures of semiconductors and the FET performances has been investigated in these studies. Strong intermolecular interactions lead to the high mobility in crystals. In thin-film transistors, polycrystalline thin films are necessary for high carrier mobilities. Molecules with two-dimensional crystal structures are favorable for carrier transportation to reduce the grain boundary effects in the polycrystalline films. The herringbone stacking structures have an advantage of two-dimensional structures. In the  $\pi$ -stacking structures, however, two-dimensional structures are achieved by the formation of two-dimensional columns or using interheteroatom interactions, resulting in high carrier mobilities. In the future, new semiconductors affording higher-performance OFETs will be developed to bring about their practical applications.

## References

1. S. Allard, M. Forster, B. Souharce, H. Thiem, U. Scherf, *Angew. Chem. Int. Ed.* **47**, 4070 (2008)
2. H. Klauk, M. Halik, U. Zschieschang, F. Eder, G. Schmid, C. Dehm, *Appl. Phys. Lett.* **82**, 4175 (2003)
3. H. Meng, M. Bendlkov, G. Mitchell, R. Helgeson, F. Wudl, Z. Bao, T. Siegrist, C. Kloc, C.-H. Chen, *Adv. Mater.* **15**, 1090 (2003)
4. M.L. Tang, T. Okamoto, Z. Bao, *J. Am. Chem. Soc.* **128**, 16002 (2006)
5. M.L. Tang, S.C.B. Mannsfield, Y.-S. Sun, H.A. Becerril, Z. Bao, *J. Am. Chem. Soc.* **131**, 882 (2009)
6. K. Takimiya, H. Ebata, K. Sakamoto, T. Izawa, T. Otsubo, Y. Kunugi, *J. Am. Chem. Soc.* **128**, 12604 (2007)
7. H. Ebata, T. Izawa, E. Miyazaki, K. Takimiya, M. Ikeda, H. Kuwabara, T. Yui, *J. Am. Chem. Soc.* **129**, 15732 (2007)
8. T. Yamamoto, K. Takimiya, *J. Am. Chem. Soc.* **129**, 2224 (2007)
9. H. Minemarari, T. Yamada, H. Matsui, J. Tsutsumi, S. Haas, R. Chiba, R. Kumai, T. Hasegawa, *Nature* **475**, 364 (2011)
10. T. Uemura, Y. Hirose, M. Uno, K. Takimiya, J. Takeya, *Appl. Phys. Exp.* **2**, 111501 (2009)
11. T. Okamoto, C. Mitsui, M. Yamagishi, K. Nakahara, J. Soeda, Y. Hirose, K. Miwa, H. Sato, A. Yamano, T. Matsushita, T. Uemura, J. Takeya, *Adv. Mater.* **25**, 6392 (2003)
12. Y.S. Yang, T. Yasuda, H. Kakizoe, H. Mieno, H. Kido, Y. Tateyama, C. Adachi, *Chem. Commun.* **49**, 6483 (2013)
13. Q. Miao, M. Lefenfeld, T.-Q. Nguyen, T. Siegrist, C. Kloc, C. Nuckolls, *Adv. Mater.* **17**, 407 (2005)
14. C.D. Sheraw, T.N. Jackson, D.L. Eaton, J.E. Anthony, *Adv. Mater.* **15**, 2009 (2003)
15. M.P. Payne, S.R. Parkin, J.E. Anthony, C.-C. Kuo, T.N. Jackson, *J. Am. Chem. Soc.* **127**, 4986 (2005)
16. V.C. Sundar, J. Zaumseil, V. Podzorov, E. Menard, R.L. Willett, T. Someya, M.E. Gershenson, J.A. Rogers, *Science* **303**, 1644 (2004)
17. H. Moon, R. Zeis, E.-J. Borkent, C. Besnard, A.J. Lovinger, T. Siegrist, C. Kloc, Z. Bao, *J. Am. Chem. Soc.* **126**, 15322 (2004)
18. M. Halik, H. Klauk, U. Zschieschang, G. Schmid, S. Ponomarenko, S. Kirchmeyer, W. Weber, *Adv. Mater.* **15**, 917 (2003)
19. M. Musherush, A. Facchetti, M. Lefenfeld, H.E. Katz, T.J. Marks, *J. Am. Chem. Soc.* **125**, 9414 (2003)
20. B.S. Ong, Y. Wu, P. Liu, S. Gardner, *J. Am. Chem. Soc.* **126**, 3378 (2004)
21. Y. Wu, P. Liu, S. Gardner, B.S. Ong, *Chem. Mater.* **17**, 221 (2005)
22. H. Pan, Y. Li, Y. Wu, P. Liu, B.S. Ong, S. Zhu, G. Xu, *Chem. Mater.* **18**, 3237 (2006)
23. I. McCulloch, M. Heeney, C. Bailey, K. Genevicius, I. Macdonald, M. Shkunov, D. Sparrowe, S. Tierney, R. Wagner, W. Zhang, M.L. Chabynyc, R.J. Kline, M.D. McGehee, M.F. Toney, *Nat. Mater.* **5**, 328 (2006)
24. H. Usta, G. Lu, A. Facchetti, T.J. Marks, *J. Am. Chem. Soc.* **128**, 9034 (2006)
25. I. Osaka, G. Sauvé, R. Zhang, T. Kowalewski, R.D. McCullough, *Adv. Mater.* **19**, 4160 (2007)
26. J.S. Ha, K.H. Kim, D.H. Choi, *J. Am. Chem. Soc.* **133**, 10364 (2011)
27. T. Lei, Y. Cao, Y. Fan, C.-J. Liu, S.-C. Yuan, J. Pei, *J. Am. Chem. Soc.* **133**, 6099 (2011)
28. M. Takada, H. Graaf, Y. Yamashita, H. Tada, *Jpn. J. Appl. Phys.* **41**, L4 (2002)
29. M. Mas-Torrent, P. Hadley, S.T. Bromley, N. Crivillers, J. Veciana, C. Rovira, *Appl. Phys. Lett.* **86**, 012110 (2005)
30. M. Mas-Torrent, M. Durkut, P. Hadley, X. Ribas, C. Rovira, *J. Am. Chem. Soc.* **126**, 984 (2004)
31. Naraso, J. Nishida, H. Tada, Y. Inoue, S. Tokito, Y. Yamashita, *J. Am. Chem. Soc.* **127**, 10142 (2005)

32. X. Gao, Y. Wang, X. Yang, Y. Liu, W. Qiu, W. Wu, H. Zhang, T. Qi, Y. Liu, K. Lu, C. Du, Z. Shuai, G. Yu, D. Zhu, *Adv. Mater.* **19**, 3037 (2007)
33. Y. Kanno, Y. Bando, T. Shirahata, J. Inoue, T. Mori, *J. Mater. Chem.* **19**, 6548 (2009)
34. Y. Sakamoto, T. Suzuki, M. Kobayashi, Y. Gao, Y. Fukai, Y. Inoue, F. Sato, S. Tokito, *J. Am. Chem. Soc.* **126**, 8138 (2004)
35. M.L. Tang, A.D. Reichardt, N. Miyaki, R.M. Stoltenberg, Z. Bao, *J. Am. Chem. Soc.* **130**, 6064 (2008)
36. Z. Bao, A.J. Lovinger, J. Brown, *J. Am. Chem. Soc.* **120**, 207 (1998)
37. A. Facchetti, M. Mushrush, H.E. Katz, T. Marks, *J. Adv. Mater.* **15**, 33 (2003)
38. M.-H. Yoon, A. Facchetti, C.L. Stem, T.J. Marks, *J. Am. Chem. Soc.* **128**, 5792 (2006)
39. M.-H. Yoon, S.A. DiBenedetto, A. Facchetti, T.J. Marks, *J. Am. Chem. Soc.* **127**, 1348 (2005)
40. J.A. Letizia, A. Facchetti, C.L. Stem, M.A. Ratner, T.J. Marks, *J. Am. Chem. Soc.* **127**, 13476 (2005)
41. S. Ando, J. Nishida, H. Tada, Y. Inoue, S. Tokito, Y. Yamashita, *J. Am. Chem. Soc.* **127**, 5336 (2005)
42. D. Kumaki, S. Ando, S. Shimono, Y. Yamashita, T. Umeda, S. Tokito, *Appl. Phys. Lett.* **90**, 053506 (2007)
43. S. Ando, R. Murakami, J. Nishida, H. Tada, Y. Inoue, S. Tokito, Y. Yamashita, *J. Am. Chem. Soc.* **127**, 14996 (2005)
44. M. Mamada, J. Nishida, D. Kumaki, S. Tokito, Y. Yamashita, *Chem. Mater.* **19**, 5404 (2007)
45. M. Mamada, J. Nishida, S. Tokito, Y. Yamashita, *Chem. Lett.* **37**, 766 (2008)
46. T. Kono, D. Kumaki, J. Nishida, T. Sakanoue, M. Kakita, H. Tada, S. Tokito, Y. Yamashita, *Chem. Mater.* **19**, 1218 (2007)
47. T. Kono, D. Kumaki, J. Nishida, S. Tokito, Y. Yamashita, *Chem. Commun.* **46**, 3265 (2010)
48. Y. Fujisaki, Y. Nakajima, D. Kumaki, T. Yamamoto, S. Tokito, T. Kono, J. Nishida, Y. Yamashita, *Appl. Phys. Lett.* **97**, 133303 (2010)
49. H. Naraso, J. Nishida, D. Kumaki, S. Tokito, Y. Yamashita, *J. Am. Chem. Soc.* **128**, 9898 (2006)
50. S. Kobayashi, T. Takenobu, S. Mori, A. Fujiwara, Y. Iwasa, *Appl. Phys. Lett.* **82**, 4581 (2003)
51. T.D. Anthopoulos, C. Tanase, S. Setayesh, E.J. Meijer, J.C. Hummelen, P.W.M. Blom, D.M. de Leeuw, *Adv. Mater.* **16**, 2174 (2004)
52. P.R.L. Malenfant, C.D. Dimitrakopoulos, J.D. Gelorme, L.L. Kosbar, T.O. Graham, A. Curioni, W. Andreoni, *Appl. Phys. Lett.* **80**, 2517 (2002)
53. B.A. Jones, M.J. Ahrens, M.-H. Yoon, A. Facchetti, T.J. Marks, M.R. Wasielewski, *Angew. Chem. Int. Ed.* **43**, 6363 (2004)
54. M.-M. Ling, P. Erk, M. Gomez, M. Koenemann, J. Locklin, Z. Bao, *Adv. Mater.* **19**, 1123 (2007)
55. B.A. Jones, A. Facchetti, T.J. Marks, M.R. Wasielewski, *Chem. Mater.* **19**, 2703 (2007)
56. Z. Wang, C. Kim, A. Facchetti, T.J. Marks, *J. Am. Chem. Soc.* **129**, 13362 (2007)
57. S. Handa, E. Miyazaki, K. Takimiya, Y. Kunugi, *J. Am. Chem. Soc.* **129**, 11684 (2007)
58. Q. Wu, R. Li, H. Li, X. Gao, D. Zhu, *Chem. Mater.* **23**, 3138 (2011)

# Chapter 32

## Photocurrent Action Spectra of Organic Semiconductors

Richard Murdey and Naoki Sato

**Abstract** Photocurrents are reported for vacuum-deposited pentacene thin films as a function of incident photon energy, applied bias, photon flux, film thickness, and measurement temperature in order to develop a better understanding of the mechanisms underpinning photoinduced charge carrier generation, injection, and transport in molecular semiconductors. Intrinsic photocurrents caused by dissociation of photogenerated hole–electron geminate pairs in the bulk film are observed in the photocurrent action spectra at photon energies above a threshold value of 2.25 eV corresponding to the transport energy gap of the pentacene film,  $E_G$ . Aluminum electrodes form blocking contacts which substantially reduced extrinsic photocurrents attributed to exciton-enhanced charge injection and transport, enhancing the visibility of the intrinsic processes.

**Keywords** Organic semiconductor • Thin film • Photoconduction • Charge carrier • Transport energy gap

### 32.1 Introduction

It might surprise the modern reader to learn that, in what might be called the “golden age” of solid-state physics spanning WWII and the following decade leading up to the commercialization of the transistor, there was little distinction made between organic and inorganic materials. All kinds of conductive and photoconductive substances were subject to investigation on an equal footing, from cadmium sulfide to germanium to anthracene [1]. Of course germanium and, later, silicon and other inorganic semiconductors grew to ubiquity such that by the late 1970s, organic semiconductor research was generally limited to a much smaller niche mostly relating to xerography. The discovery [2] of organic light-emitting diodes (LEDs) in 1987, however, led to a resurgence of interest in molecular electronics that continues to the present day.

---

R. Murdey (✉) • N. Sato  
Institute for Chemical Research, Kyoto University, Uji, Kyoto 611-0011, Japan  
e-mail: [rmurdey@e.kuicr.kyoto-u.ac.jp](mailto:rmurdey@e.kuicr.kyoto-u.ac.jp); [naokis@e.kuicr.kyoto-u.ac.jp](mailto:naokis@e.kuicr.kyoto-u.ac.jp)

The published research on the subject of charge carrier generation and transport in organic semiconductors follows a similar arc, and the field is perhaps somewhat unusual in that such a large proportion of important work dates from before 1985. The general outline of photoconductivity – indiscriminately for organic and inorganic semiconductors – given by Albert Rose [3] in 1963 is still broadly applicable today, and most of the research of that era, exhaustively compiled in *Organic Semiconductors* by Gutmann and Lyons [4], is still relevant. These results, as well as those of the following decades, are fully covered in books by E.A. Silinsh [5], Pope and Swenberg [6], and Borsenburger and Weiss [7] and have already been concisely summarized in the important book chapter by Heinz Bässler [8].

It is a testament to the enduring physical complexity of organic and/or disordered systems, the experimental difficulties in obtaining data, and the ambiguity of the conclusions which can be drawn from those data, that despite over 60 years of continuous study, the simple question “How does an absorbed photon create electric charge?” is not satisfactorily resolved. In the following sections, we will first lay out an updated contextual framework for photoconductivity and photogeneration incorporating recent advances in our understanding of charge transport in organic solids before presenting and discussing our new *in situ* photocurrent measurements on thin films of the well-known acene molecule, pentacene.

## 32.2 Extrinsic and Intrinsic Photogeneration

To understand the mechanism of photoinduced charge generation requires, first of all, an appreciation for how charge transport is realized in organic materials. The transport and related states and their relative energies are illustrated schematically in Fig. 32.1. In the most general sense, these systems can be characterized as having electron-conducting states and hole-conducting states separated by an energy gap. For closed-shell molecular semiconductors, the HOMO and LUMO molecular orbitals remain largely unchanged in the solid state, though broadened into a nominally Gaussian distribution of energies due to a plurality of local environments [9]. For highly crystalline systems, relatively narrow dispersion effects can also be active, forming transport energy bands [10]. States having energies far above or below the average value of the distribution are isolated from the surrounding molecules and isolated states lying within the energy gap region form traps. Traps may additionally be created by impurities and defects sites which are not part of the main distribution of states in the bulk material. The gap energy region can also be host to charge-accepting or charge-donating species.

As a result of the large energy gap of organic semiconductors (typically 2–3 eV), the density of intrinsic charge carriers is exceedingly small. The materials are for all intents and purposes insulators and the role of the gap states, especially traps, becomes preeminent [11]. Trap states form a reservoir of charge that can be thermally excited to more mobile states. The distribution of these trap states

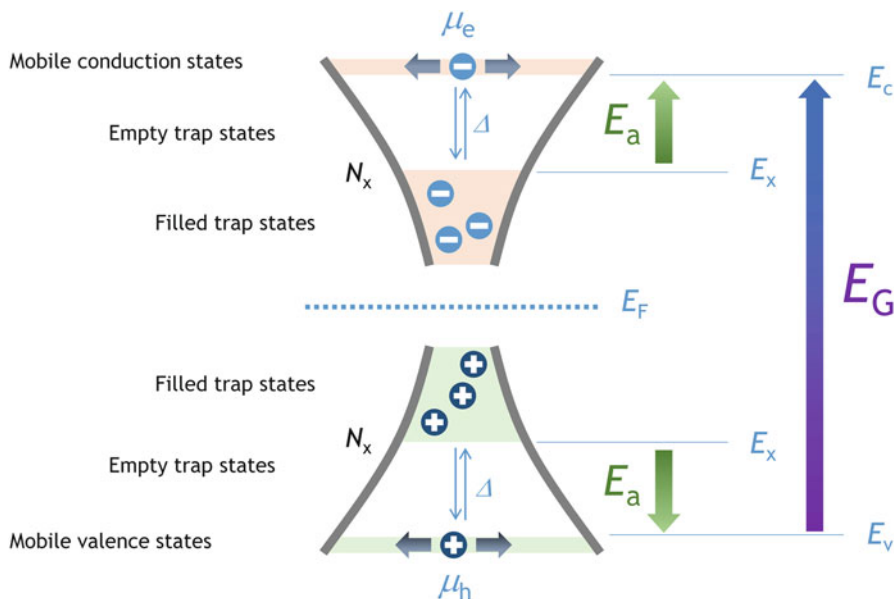


**Fig. 32.1** Schematic representation of the principle energy levels involved in the charge carrier generation and transport of organic semiconductors

is quasi-logarithmic and can be characterized by a pseudo-Fermi level defining the trap filling level in this distribution of states. The “pseudo” prefix is usually added as it is understood that while the system is never in true thermal equilibrium, the distribution of charge in the trap and mobile states can often be reasonably described by the Fermi distribution function [12]. If the hole–electron recombination is negligible over the observation time frame, the density of mobile charge carriers is constant and the dark conductivity,  $\sigma$ , of the material is described by

$$\sigma = N_x e \left( -\frac{E_a}{k_B T} \right) e (\mu_e + \mu_h), \quad (32.1)$$

where  $N_x$  is the density of states, taken as the molecular density. (Each molecule contributes one valence and one conduction state, whether trap or mobile.)  $E_a$  is the thermal activation energy of conduction,  $e$  is the unit of electrical charge, and  $\mu_e$  and  $\mu_h$  are the electron and hole mobility, respectively.

Most measurements are performed with electrodes which only provide ohmic contact for one sign of charge carrier, however. For monopolar transport, only the mobility of the relevant carrier is used. For the remainder of the text, we shall for concision assume injected currents are limited to hole transport. The treatment for electron transport is equivalent.

This model is overly simple, but on the understanding that filled trap states falling outside of the Gaussian tail as well as acceptor or donor states will have the same net effect of providing mobile charge carriers from a reservoir of gap states, it is sufficient here only to draw the fundamental distinction between extrinsic and intrinsic generation of charge carriers. Intrinsic generation requires overcoming the full energy gap,  $E_G = E_c - E_v$ , while extrinsic generation is governed instead by the position of the trap filling level,  $E_a = E_c - E_x$ , or  $E_a = E_x - E_v$ , or equivalently the energy separation of the dominant impurity/donor/acceptor gap state from the relevant mobile level.

It is worth mentioning at this point that there is a subtle but important distinction between the charge generation process, which can be classed as extrinsic or intrinsic as described above, and the charge transport, which can be described as either *injected* (charge carriers are injected from one electrode and retrieved at the other) or *harvested* (self-generated hole–electron pairs which are swept out to opposite electrodes). In the steady state, extrinsic charge generation can only contribute to injected photocurrent. Intrinsic charge generation, meanwhile, can in principle influence the current both from direct expulsion of dissociated hole–electron pairs and by increasing the injected currents by adding to the overall density of mobile charge carriers.

A generic energy-level diagram illustrating intrinsic (injected) and extrinsic (harvested) charge transport in a photocurrent measurement device is illustrated in Fig. 32.2. The conduction and valence states define the transport energy gap,  $E_G$ , with the Fermi levels of the two electrodes positioned at some arbitrary point within the gap. Charge injection into the device on application of an applied bias voltage,  $-eV$ , will occur provided the energy barrier,  $\phi_b$ , can be overcome. Large injection barriers result in small, non-ohmic dark currents, but under light irradiation, molecular excitons may diffuse to and – provided they retain sufficient energy – dissociate at electrode interface, effectively injecting charge. As the charge injection becomes more efficient, the likelihood increases that the injected photocurrents shift from injection limited to bulk limited and photocurrent will now depend on the density of mobile charge carriers in the bulk material. In organic semiconductors, a large proportion of the total charge carrier density is at any given time residing in trap states [11].

It has been proposed that molecular excitons can diffuse to the trapped charge and engage in an energy transfer process which excites the trapped charge back to the mobile states. This process is referred to as de-trapping [13]. The extrinsic photocurrent pathway is shown for holes in Fig. 32.2 by way of example; electron or hole currents are possible, the carrier having the lowest injection barriers being dominant.

Intrinsic photocurrents, in contrast, are created within the bulk material by photoinduced dissociation. Electrons are driven out to the anode, and holes swept to the cathode, by the applied electric field. No charge is injected *into* the organic semiconductor. While the mechanism for intrinsic photogeneration is still under debate [8] and will be discussed in detail in Sect. 32.4, it can be readily understood

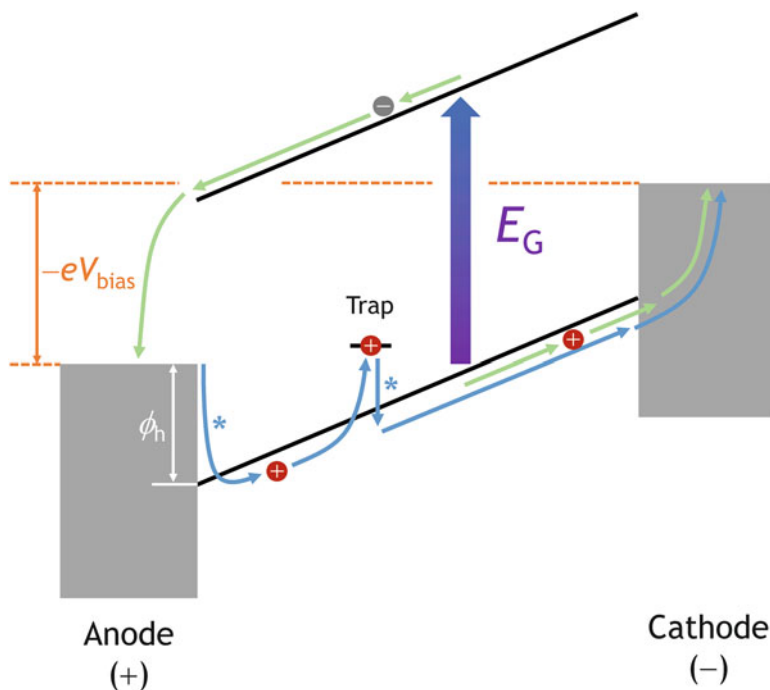


**Fig. 32.2** Schematic representation of the principle energy levels involved in the photoconduction, illustrated for the case where hole injection is the principal injected charge carrier. Intrinsic bulk photogeneration is defined as the photon-assisted formation of an independent hole–electron charge carrier pair, and the minimum required photon energy is indicated by the transport energy gap,  $E_G$ . Both electrons and holes exit the device. The injected, exciton-assisted photocurrents flow as holes between anode and cathode. Long-lived molecular excitons can promote hole transport by overcoming the injection barrier  $\phi_h$  and dissociating at the electrode interface and/or promoting trapped holes to the mobile valence states via an energy transfer mechanism. These exciton-enhanced steps are noted in the figure by the *asterisk* symbol

from Fig. 32.2 that for the single photon process, the photon energy must exceed the energy gap for the reaction to proceed efficiently.

There are only a small number of reliable reports of intrinsic photocurrent in molecular materials. The first observation was made by Castro and Hornig [14] on anthracene single crystals, and these initial findings were soon carefully elaborated by Chaikin and Kearns [15], Batt et al. [16], Geacintov and Pope [17], and Chance and Braun [18, 19]. The intrinsic photocurrent was observed in the photocurrent spectrum as a new peak midway between the first and second singlet absorption transitions, with an onset at about 3.85 eV. Similar behavior was observed for tetracene (naphthacene) [20] and for pentacene [13, 21]. Outside of these linear acene molecules, most of the published research is on conjugated polymers and charge-transfer complexes where the formation of a charge-transfer complex and/or

dissociation of the geminate pair is typically more facile. A very similar experiment to those on the acenes, above, with similar results, was performed on a conducting polymer thin film [22]. No reports of intrinsic photocurrents in phthalocyanine-based, perylene-based, or thiophene-based small molecules, either thin films or single crystals of the pure material, have – to our knowledge – been published.

It is reasonable to ask why intrinsic photocurrent is observed with relative ease in the linear acenes but not, for example, phthalocyanines. The answer is unfortunately not known. Our current, limited understanding of the photogeneration as a two-step process of geminate pair formation and dissociation [8, 23] does not suggest a reason why the efficiencies should be wildly different. It might be a simple technical issue involving, for example, sample purity, or it may instead reflect the different fundamental nature of the excited states of the molecules. The important thing is that these relevant and interesting issues remain unsolved. Despite its long and distinguished history, there is clearly much work left to do in the field.

### 32.3 A Mathematical Framework for Photocurrent Measurements

Any attempt to model the photocurrent requires an initial set of assumptions which may at any time become invalid under the experimental measurement conditions. An analysis of the photocurrent based on such a model must therefore be approached with great caution. With that in mind, the following treatment of photoconductivity assumes that the measurement system consists of a *homogeneous sample*, subjected to a *volume excitation*, under *steady-state conditions*, and remains *free from the effects of injected space charge*.

For a rectangular semiconducting block of dimensions  $wl$  and with electrodes forming ohmic contacts on opposite faces separated by the distance  $l$ , the injected monopolar photocurrent,  $I$ , can then be expressed as

$$I = V ne\mu \frac{wt}{l}. \quad (32.2)$$

Equation 32.2 is just a rearrangement of the standard definitions of conductance and conductivity,  $G = I/V$  and  $\sigma = ne\mu$ .  $n$  is the additional density of charge carriers present in the sample during exposure to light. The charge carrier density is controlled by the balance of the generation and extinction rates in the sample. The rate of charge generation is

$$\frac{dn}{dt} = \frac{F(1-T)\phi}{wtl}, \quad (32.3)$$

where  $F$  is the incident photon flux,  $T$  is the transmittance of the light through the photoactive material, and  $\Phi$  is the (internal) quantum yield – the probability that an absorption event results in the creation of a single unit of mobile charge.

The extinction rate depends on the process by which the charges are removed from the measurement sample. For injected, steady-state photocurrent, each unit of charge exiting the device is balanced by injection at the opposite electrode and the extinction rate is the just rate of internal charge recombination. This process may be monomolecular if the charge carrier encounters trapped charge of opposite sign or bimolecular if photogenerated charge carriers of opposite sign interact [15]. The sum of both recombination pathways is

$$-\frac{dn}{dt} = k_m n_T n + k_b n^2. \quad (32.4)$$

$n_T$  is the density of trapped charge, and the monomolecular and bimolecular rate constants are  $k_m$  and  $k_b$ , respectively. The rate constants are unlikely to be substantially different and are assumed hereafter to be equal and denoted  $k_r$ .

If  $n_T \gg n$ , monomolecular recombination kinetics dominate and

$$I = \frac{eV\mu}{l^2} \left( \frac{1}{k_r n_T} \right) F(1-T)\phi. \quad (32.5)$$

Equation 32.5 is just a modern restatement of the original derivation by Rose [4]. The photocurrent is proportional to the incident flux, absorption probability, and quantum yield, as well as the applied voltage. The current–voltage curves will be linear as long as the assumptions used in the derivation of the expression – particularly ohmic contacts and the absence to space charge effects – remain valid. There is no explicit temperature dependence, but both the quantum yield and the carrier mobility may be expected to be thermally activated processes.

If  $n_T \ll n$  recombination is regulated by bimolecular kinetics, the rate expression becomes slightly more complicated:

$$I = \frac{eV\mu}{l^2} \sqrt{\frac{wtl}{k_r}} \sqrt{F(1-T)\phi}. \quad (32.6)$$

While still linear with applied field, the photocurrent varies with the square root of the incident photon flux, absorption probability, and quantum yield. It is possible that both reaction channels are competitive, and it is likewise possible that the incident photon flux influences density and distribution of the trapped charge [24, 25]. Additionally, at high photon flux, exciton–exciton and multiphoton photogeneration reactions may have to be considered. In general,

$$I \propto eF^\gamma. \quad (32.7)$$

Nonlinear flux dependence has a substantive impact on the practical analysis of photocurrent data, specifically the normalization procedure to remove the dependencies of the photocurrent spectrum on the variation of the output intensity of the light source with photon energy. The coefficient,  $\gamma$ , must be determined accurately and checked for consistency over the parameter workspace of the measurement: temperature, incident photon flux, and photon energy. The normalization is no longer meaningful in cases where  $\gamma$  is found to vary significantly. The incident flux normalized photocurrent data is variously termed “external quantum yield,” “incident photon conversion efficiency,” “photocurrent yield,” or sometimes, rather ambiguously, “photocurrent.” The mathematical expression is

$$Y = \frac{1}{F} \frac{I_0}{e} \left( \frac{I}{I_0} \right)^{\frac{1}{\gamma}}, \quad (32.8)$$

where  $I_0$  is a required reference constant which, if it must be chosen arbitrarily, invalidates the absolute scale except when  $\gamma = 1$ . In the following discussion,  $Y$  will be referred to as the *photocurrent yield*. This parameter is the experimental point of entry for studying the photogeneration mechanism as it is expected to be proportional to the internal quantum yield. Before examining this point further, however, it is first necessary to revisit the model for intrinsic photocurrent.

Intrinsic photocurrent can contribute to the injected photocurrents by increasing the charge density, in which case the preceding derivation should apply. If, however, the current resulting from charge carriers swept out of the device – the harvested photocurrent – exceeds the injected photocurrent, the expressions must be modified. Neglecting the injected photocurrent for the moment, we begin by noting that the rate of charge carrier formation is unchanged from Eq. 32.3. (There is no factor of two needed since the electron is removed from one electrode and the hole removed from another, producing the same net current as a single injected hole or electron.) The rate of extinction must, however, now in addition to recombination, take into account holes and electrons swept out of the device by the electrodes. Expressed as a number density, this is equal to the charge carrier density,  $n$ , the drift velocity,  $v_d = \mu V/l$ , and the electrode area,  $wt$ , divided by the device volume:

$$-\frac{dn}{dt} = n \frac{\mu V}{l} (wt) \frac{1}{wtl} = \frac{\mu V}{l^2} n. \quad (32.9)$$

Setting the rates equal,

$$\frac{F(1-T)\phi}{wtl} = \frac{\mu V}{l^2} n + k_r n_T n + k_r n^2, \quad (32.10)$$

and solving the quadratic equation,

$$n = \frac{-\left(k_r n_T + \frac{\mu V}{l^2}\right) + \sqrt{\left(k_r n_T + \frac{\mu V}{l^2}\right)^2 + 4k_r \frac{F(1-T)\Phi}{wtl}}}{2k_r}. \quad (32.11)$$

The charge swept out of the device is of course the charge injected into the external circuit. Equation 32.8, expressed as an absolute number, on rearrangement returns Eq. 32.2:

$$I = e \frac{dn}{dt} wtl = e \frac{\mu V}{l^2} n wtl = Vne\mu \left(\frac{wt}{l}\right). \quad (32.12)$$

The final expression for intrinsic, harvested photocurrent is therefore

$$I = V \left[ \frac{-\left(k_r n_T + \frac{\mu V}{l^2}\right) + \sqrt{\left(k_r n_T + \frac{\mu V}{l^2}\right)^2 + 4k_r \frac{F(1-T)\phi}{wtl}}}{2k_r} \right] e\mu \left(\frac{wt}{l}\right). \quad (32.13)$$

This gives the photocurrent as a function of applied voltage and photon flux, together with the device dimensions and the spectral absorptance,  $1 - T$ . There are four unknown parameters:  $k_r$ ,  $\mu$ ,  $n_T$ , and the quantum efficiency  $\Phi$ .

Under the condition where there is no appreciable recombination and all the photogenerated charge is retrieved at the electrodes,

$$\frac{F(1-T)\phi}{wtl} = \frac{\mu V}{l^2} n, \quad (32.14)$$

allowing Eq. 32.13 to be simplified to

$$I = eF(1-T)\phi, \quad (32.15)$$

while the photocurrent yield becomes

$$Y = \frac{1}{eF} = (1-T)\phi. \quad (32.16)$$

Thus, we arrive finally at the expression for ballistic transport. With no recombination, the photocurrent is linear with the photon flux and the photocurrent yield becomes *equal* to the product of the spectral absorptance and the quantum yield.

The conditions favoring ballistic transport include high fields, low trap densities, and high charge mobilities. It is identified with current-voltage relationships that extrapolate to positive currents at zero field, behavior previously observed in anthracene single crystals [16, 18, 26].

There is no native dependence on the voltage or temperature; any observed dependences are instead attributed to changes in the photodissociation efficiency as a component of the quantum yield. The Onsager theory, originally derived to calculate the dissociation probability of ion pairs in solution [5], has often been used to model the field and temperature dependence of the photocurrent under the assumed condition of ballistic transport [6–9, 26]. While the fits are often exemplary, the theory allows for several free parameters, and the conclusions from the Onsager theory, especially where ballistic transport is not rigorously confirmed, are best treated with considerable caution.

## 32.4 Photogeneration, Quantum Yield, and the Energy Gap

The quantum yield is the probability that an absorbed photon creates a unit of mobile charge. It can itself be broken down into separate factors for whatever series of individual steps is postulated to comprise the photogeneration process.

As noted in Sect. 32.2, photocurrents can be extrinsic or intrinsic in origin. For the intrinsic photocurrent, a two-step process has been proposed [8, 23, 27] where a hole–electron (geminate) pair bound by Coulomb attraction is formed immediately after the absorption event, followed by the dissociation of the geminate pair into free charge carriers. The dissociation step is modeled as a thermally activated process and enhanced by the application of an external electric field. The dissociation probability also depends on the binding energy of the geminate pair: Where the hole and electron are separated by a large distance, the binding energy is small and dissociation becomes more likely. This is the essence of the rationalization for applying the Onsager theory to model the charge pair dissociation, though it should be pointed out that in this analysis, the charge separation distance is assumed rather than measured. The mechanism for the formation of the geminate pair has proven more elusive. The generation of the geminate pair depends solely on the photon energy; it is neither field nor temperature dependent leaving few experimental variables left with which to probe its behavior. Two mechanisms have been suggested, with experimental evidence offered in support of each. In the first, autoionization [23], the absorbed photon creates a singlet molecular exciton from which a high-energy electron is ejected into the surrounding medium and captured by a nearby molecule. The captured electron is quickly thermalized, forming the geminate pair. In the second explanation, the absorbed photon optically excites a pair of molecules to form a charge-transfer (CT) exciton state directly [13], which then thermalizes to form the geminate pair. The distinction lies primarily in whether the optical excitation is confined to a single molecule or a pair of molecules and the nature of the driving force which defines the starting separation radius of the geminate pair.

Intrinsic photogeneration produces as the final state a pair of free charge carriers created within the neutral solid. The minimum total energy for this process is the transport energy gap,  $E_G$ . Regardless of whether autoionization or CT exciton states

are invoked, in the two-step mechanism, most of that energy is obtained from the absorbed photon, with thermal energy expected to make up the remaining energy difference between the geminate pair and the free charges under the applied field. The dissociation probability for geminate pairs bound by more than  $3\text{--}4 k_B T$  being extremely small, at typical measurement temperatures up to 500 K, the minimum photon energy for the onset of intrinsic photocurrent can be anticipated to be no less than about 200 meV below the energy gap. The onset may, however, exceed the energy gap if (a) the relaxation energy of the optically excited state is large and (b) that excess energy cannot be efficiently used by the geminate pair to help offset the electrostatic attraction. The indeterminate nature of this “handoff” between the photogeneration and dissociation prevents a more precise correlation between the onset of intrinsic photocurrent and the energy gap of the semiconductor. Despite concern that the vertical and adiabatic energy gaps might differ by up to 0.4 eV [28, 29], for the existing work on acene molecules, the threshold onset value has been equated directly as the transport energy gap [13, 17, 21].

## 32.5 Experimental Determination of the Energy Gap

Here we present a short survey of the alternative experimental methods for estimating the transport energy gap of an organic semiconductor.

For a semiconductor, the variation of dark conductance,  $G$ , with temperature is found to follow the Arrhenius equation as

$$G = G_0 e^{-\frac{E_a}{k_B T}}. \quad (32.17)$$

$E_a$  is the activation energy,  $k_B$  is the Boltzmann constant, and  $T$  is the absolute temperature. For an intrinsic semiconductor, the thermal activation energy of conduction is directly related to the transport energy gap (commonly called the energy gap or bandgap when referring to covalently bonded solids) as

$$E_a = \frac{E_G}{2}. \quad (32.18)$$

In practice, though, the transport energy gap of organic semiconductors is rarely obtained from dark current measurements. While some early work obtained convincingly close values [13, 30], the measured activation energy is far more likely to be determined by extrinsic effects, principally traps. As there is no physical distinction between the activation energy for extrinsic and intrinsic dark currents, it is not possible to determine based on these measurements alone whether the activation energy correlates to the energy gap or not.

The transport energy gap has sometimes been estimated from the low-energy onset of the first peak of the low-energy electronic transition in the optical absorption spectra [31] and sometimes – under somewhat questionable reasoning – with

the second [32]. In the case where the absorption signal originates from a singlet exciton, the value estimated from the first singlet state underestimates the transport energy by a value equal to the exciton binding energy, estimates for which vary up to about 1 eV [8]. Direct optical methods therefore only give a very rough approximation of the transport energy gap, unless the exciton binding energies in the material are exceptionally small.

The transport energy gap can also be estimated by extrapolating the energy of charge-transfer (CT) states detected in electroabsorption experiments [28, 29, 33] to infinite separation. There is likely an energy difference between the vertical CT transitions observed in the electroabsorption spectra and a bound pair of thermally relaxed charge carriers at the same separation distance, and this energy shift has been invoked to explain the anomalously high estimates obtained by this method. This issue will be revisited in more depth in the discussion of the photocurrent data for pentacene, but here we note that the validity of the extrapolation is reliant on each observed signal being correctly identified as a CT rather than a singlet exciton state and, further, that the CT states are each correctly assigned to the excitation of a particular set of molecular ion pairs within the crystal lattice [33].

Finally the transport energy gap can also be measured from the onset of the HOMO- and LUMO-derived states observed by photoemission and inverse photoemission [34–37], from which, together with the determination of the vacuum level, the ionization energy,  $I$ , and electron affinity,  $A$ , are calculated. The energy gap is  $I-A$ . Recent improvements in the resolution of inverse photoemission instruments have enabled precise estimates for the energy gap in organic thin films [38]. The spectroscopic methods measure a density of states excited in typically adiabatic transitions and broadened by electronic polarization. There is no apparent distinction between a mobile state and a trap state and therefore no experimental indication of the mobility edge. For these reasons, the energy of the ionic state in thermal equilibrium which is the equivalent to a *free* hole or electron can only be indirectly inferred.

## 32.6 Practical Photoconductivity Measurements

Continuing to restrict the discussion to steady-state processes – while acknowledging that long response times and power law decay can make this very difficult to confirm experimentally – the aim of practical photoconductivity measurements is to obtain information about the underlying mechanisms, especially the intrinsic photogeneration and dissociation of charge carrier pairs. Extrinsic photocurrent involving trap states and distant interfaces is typically mediated by low-energy, long-lived excitons created after the initial absorption event. The mechanisms are therefore generally considered to be of secondary interest. If that is the case, the measurement system should be engineered to maximize the intrinsic photocurrent yield and minimize the extrinsic photocurrent. If the extrinsic photocurrent is created by interaction with trap states, steps can be taken with respect to the

sample purity and measurement environment to try and reduce the density of traps in the active material. If the intrinsic and extrinsic photocurrents have different temperature dependencies, the measurement temperature can be adjusted to favor the intrinsic mechanism. The electrode separation distance and magnitude of the applied field can also play a role, as these factors influence the transit time and may therefore influence the “harvested” yield of intrinsic photocurrent, facilitating ballistic transport. Lastly, taking advantage of the fact that extrinsic photocurrent is injected from an electrode, it can sometimes be possible to select electrodes which prevent charge injection into the measurement material, at least for one direction of the applied bias voltage, and by that route cut off the extrinsic current.

A literature survey on the subject of the photoconductivity of acenes reveals that while blocking electrodes have occasionally been used to suppress the extrinsic, injected photocurrent in anthracene and tetracene crystals [15, 17, 20], the technique does not seem to have been come into general practice. The idea was reintroduced several decades later for experiments on conducting polymers by Barth [22, 39]. In reports of intrinsic photocurrents in pentacene single crystals [21] and thick films [13] using titanium and aluminum contacts, respectively, the extrinsic effects appear to have fortuitously minimized as a result of the sample and measurement conditions, without explicitly choosing the electrodes to prevent charge injection. For other published works, it is likely that the observed photocurrents are largely if not wholly extrinsic when gold [40–42] or ITO [43] electrodes are used. Sorting the pentacene results by electrode material, a rough correlation with the electrode work function is noted: small-work-function metals like Al or Ti enable the observation of intrinsic photocurrent, while extrinsic photocurrents dominate for large-work-function electrodes like ITO or Au. Blocking electrodes can perhaps, therefore, be extended to a more general methodology based on the energy-level alignment between the electrode work function and either the valence or conduction states in the organic film.

Correctly identifying photocurrent as intrinsic or extrinsic is a far-from-trivial task. In principle, the quantum yield of the intrinsic photocurrent exhibits a step function at the transport energy gap. Under experimental conditions such that the photocurrent yield is proportional to the quantum yield, a sudden increase in yield indicates both the position of the energy gap and the onset of intrinsic photocurrent. On the other hand, if the quantum yields appear to be largely constant over a range of incident photon energies well below the anticipated value of the energy gap, this is usually taken to imply that the photocurrents are extrinsic in origin. This judgment can of course only be made if the photocurrent spectra are available. If the photon energy is fixed, it can sometimes be possible however to distinguish the photogeneration mechanisms from the temperature and field dependence of the photocurrent yields [15, 18, 19].

The data for anthracene single crystals is remarkably unambiguous. For many other systems, however, the photocurrent spectra show features which, while not conforming to the absorption peaks, do not originate from intrinsic photoconduction. These tend to occur when the assumption of volume excitation is unfounded and the photocurrent yield becomes sensitive to penetration depth,

which varies as the inverse of the absorption coefficient and is therefore strongly wavelength dependent. For devices where the photogeneration is strongly enhanced or quenched in a specific region, usually the surface or the electrode interfaces, the observed photocurrent spectrum may correlate with the absorption coefficient (sympatric), its inverse (anti-sympatric), or some intermediate value, even when the true photogeneration yield is fully independent of the incident photon energy.

Extrinsic photocurrents may obscure, or in the worst case be mistaken for, the intrinsic photocurrent signal. Care must be taken in the experiment to properly confirm that the photocurrents are, in fact, intrinsic in origin, before proceeding with further analysis.

## 32.7 Photocurrent Spectroscopy of Pentacene Thin Films

In the following experimental work, it will be demonstrated that the onset of intrinsic photocurrents can be reliably observed in vacuum-deposited pentacene thin films under 100 nm thick if the appropriate electrode material is selected. The influence of film thickness, measurement temperature, photon flux, and applied bias is examined to help characterize and differentiate between intrinsic photogeneration and extrinsic photocurrent. An estimate for the transport energy gap and information about the CT states is obtained from the intrinsic photocurrent yield spectra.

### 32.7.1 Details of the Experiment and Apparatus

Pentacene (Aldrich, sublimed, >99.9 %) was purified by four cycles of reduced-pressure sublimation under nitrogen and transferred immediately to the vacuum chamber where it was thoroughly degassed before use. The single-crystal sapphire [0001] substrate ( $10 \times 10 \times 0.5$  mm<sup>3</sup> Shinkosha) was annealed in air at 1,000 °C for 5 h to obtain an atomically flat, terraced surface and subsequently patterned with 35 nm thick aluminum or titanium electrodes formed by *ex situ* vacuum deposition through a stainless steel mask. Gold electrodes were formed by capping a 30 nm titanium electrode with a 5 nm layer of vacuum-deposited gold. The electrode spacing was in all cases 0.10 mm. Once mounted on the sample holder, the substrate was placed under ultrahigh vacuum and degassed at 175 °C for 2 h before use.

Pentacene thin films up to 100 nm thick were grown by stepwise thermal deposition through a 4 mm square shadow mask. The growth rate was 2 nm min<sup>-1</sup> and the substrate temperature was set at 30 °C. The base working pressure of the vacuum chamber was 10<sup>-7</sup> Pa and the sample was kept at 30 °C and in the dark between measurements. The general schematic of the measurement device in cross section is shown in Fig. 32.3, while the main features of the measurement chamber are shown in Fig. 32.4. All electrical measurements were made in situ.

**Fig. 32.3** Schematic diagram of the sample device

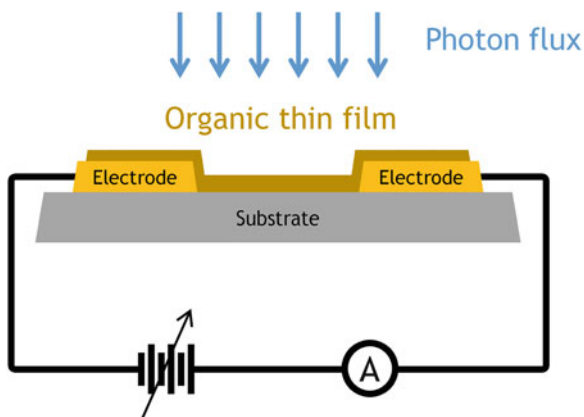
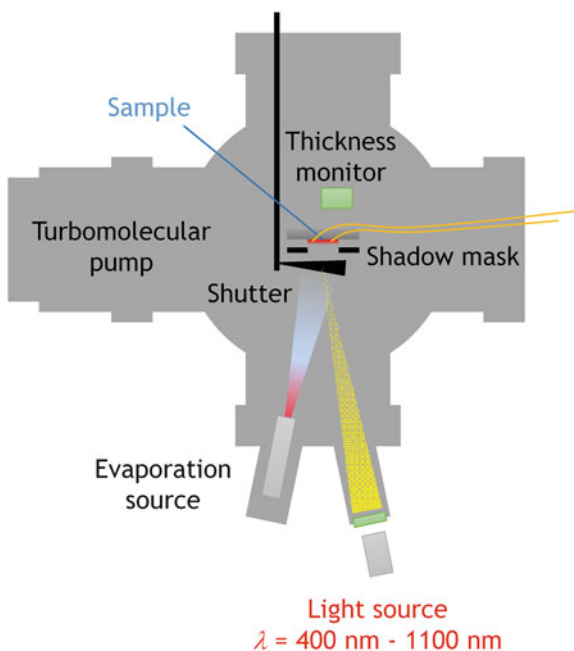


**Fig. 32.4** Schematic diagram of the ultrahigh vacuum chamber used for in situ film growth and electrical measurements



The photon flux was provided by a monochomatized 150 W Xe lamp light source (Bunkokeiki), while current measurements were performed using a picoammeter/sourcemeter (Keithley model 6487). The Keithley instrument also provided the sample bias. The average incident flux intensity was  $10^{19} \text{ photons m}^{-2}$  and the applied field was  $10^5 \text{ V m}^{-1}$ . Photocurrent action spectra were obtained by scanning over wavelengths between 400 nm and 1,100 nm at 5 nm intervals under a constant applied bias voltage. For each wavelength step, currents were taken with the shutter open and with it closed, the difference being recorded as the photocurrent. As

photocurrent action spectra over a range of temperature from 30 to 75 °C were measured, the stability of the samples was confirmed by comparing data from several cycles, from both the heating and cooling ramps.

Very slow responses in the order of 10 s or longer were attenuated by the high pass action of the shutter, which operated as a 0.1 Hz square wave. It was found however that when aluminum electrodes were used, the photocurrent response followed a clean square wave with rise and fall times under 1 s. The ratio of maximum photocurrent to dark current was in excess of 100:1. The dependence of the photocurrent on photon flux was confirmed to be linear, provided the applied bias was above  $10^4 \text{ V m}^{-1}$ . Ti and, particularly, Au electrodes resulted in substantially higher dark currents and photocurrents with longer rise and decay times, while a sublinear dependence of the photocurrent on the photon flux was observed.

For Al electrodes, the dark currents of the pentacene films were below the threshold of measurement. Photocurrent–voltage data could be obtained relatively easily, however, with no hysteresis and excellent reproducibility.  $I$ – $V$  data was recorded at 460 nm incident photon energy for different incident fluxes using wire mesh placed at the exit of the light source before the monochromator to attenuate the lamp intensity.

In situ absorption spectra were taken concurrently with the photocurrent data by placing a glass fiber behind the sample opposite the electrode gap and recording the light output at the fiber exit with a calibrated Hamamatsu silicon photodiode (S1227-1010BQ). The reference signal was taken with the substrate in position, before deposition of the organic film. The spectra were compared to the result of *ex situ* measurements obtained with a Hitachi U-4000 spectrophotometer and determined to be in very close agreement.

### 32.7.2 Film Thickness Dependence

Pentacene was deposited stepwise, with measurements made at film thicknesses of 20, 40, 60, 80, and 100 nm. The absorption spectra are shown in Fig. 32.5, while the photocurrent action spectra are shown in Fig. 32.6. Pentacene thin films often undergo structural change between around 20–40 nm [44], so it was of interest to see whether the photocurrent action spectra would reflect this.

The absorption spectra are typical of pentacene, with a manifold of peaks beginning at 1.75 eV attributed to the fundamental and higher vibrational excitations of the  $B_{1u}$  singlet exciton  $S_0 \rightarrow S_1$  transition, identified by time dependent density functional theory (TDDFT) as the HOMO–LUMO excitation. Davydov splitting in the polycrystalline pentacene film gives rise to the doublet comprising the first two visible peaks, at 1.83 and 1.95 eV [31, 45, 46], and this doublet signal is observed to change intensity and separate with film thickness, corresponding to small changes in the crystal structure and preferred orientation. Although there are no peaks visible above 2.5 eV, the absorption coefficient in this region increases in an irregular fashion with film thickness, possibly due to light scattering off the pentacene crystallites.

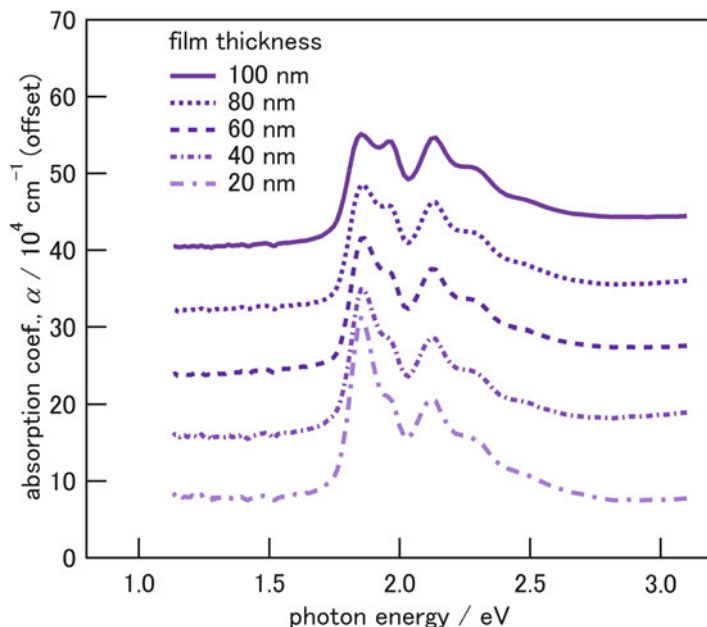


**Fig. 32.5** Optical absorption coefficient of pentacene thin films, from 20 to 100 nm thick. Measurements are made under UHV, in situ, obtained in conjunction with the photocurrents shown in Fig. 32.6

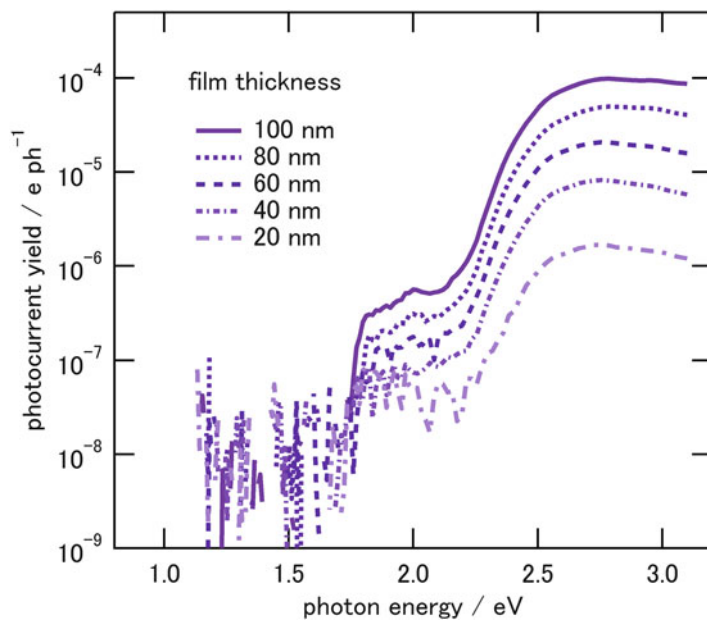


**Fig. 32.6** The photocurrent action spectra of pentacene thin films from 20 to 100 nm thick. Photocurrents are normalized to the incident photon flux. These results were obtained for the device with aluminum electrodes, at 10 V applied bias across the electrode spacing of 0.1 mm

The photocurrent action spectra, normalized to the incident photon flux, are shown in Fig. 32.6. These plots were data was obtained using aluminum electrodes. While there is a small component mirroring the absorption spectrum, starting at 1.75 eV, the dominant feature is instead a new peak or series of peaks with an onset starting at 2.25 eV and reaching a maximum about 2.8 eV. The action spectra have the same shape and position as the photocurrent signal previously observed in pentacene thick films [13] and single crystals [21]. In those papers, the photocurrent was considered to originate from the intrinsic photogeneration of hole–electron pairs, and given this remarkable consistency between single-crystal-, thick-, and thin-film measurements, it seems reasonable to assume that this distinctive, broad signal is indeed the intrinsic photocurrent of pentacene produced by photogeneration of hole–electron pairs induced by photon absorption above the transport energy.

At lower energy, the close correspondence between the singlet exciton absorption spectrum and the photocurrent points instead to a single, exciton-mediated, low-energy mechanism as the source of the photocurrent. As noted in Sect. 32.2, de-trapping and dissociation at the electrode are two possible ways whereby a long-lived, low-energy molecular exciton species may contribute to the measured photocurrent. The strong dependence of the magnitude of this current with electrode material, and its small value when aluminum is used, offers strong evidence that dissociation at the electrode interface dominates over bulk de-trapping effects.

The shape of action spectra is unchanged over the thickness range measured, but the intensity increases with film thickness. On closer inspection, it is found that the increase in photocurrent outstrips the increase in absorbed photons by a factor of ten. This indicates that the topmost layers of the film provide higher photocurrent yields than the bottommost layers.

As the same features are present for all the thicknesses measured, the analysis will concentrate on the data obtained for the 100 nm films where the signal-to-noise ratios were highest, noting in passing however that it was experimentally possible to clearly observe the intrinsic photocurrent in pentacene films as thin as 20 nm.

### 32.7.3 *Bias Voltage and Photon Flux Dependence*

At 10 V applied bias, the dark currents measured for 100 nm pentacene films depended on the electrode material. For titanium, the dark currents ranged from 10 to 50 pA, while for gold they ranged between 70 and 330 pA. For aluminum, they were below the threshold of measurement (10 fA). Where measurable, the dark current in these pentacene devices shows hysteresis and long-lived asymmetry caused by the injection of space charge at the electrode interfaces, which modified the local charge injection barrier [47, 48]. At all times, however, the dark currents were much lower for aluminum electrodes than for either titanium or gold. While it is possible that the oxide layer which covers the aluminum surface plays some role, it is noted in passing that substantial dark currents are observed between aluminum electrodes when metal phthalocyanine or perfluoropentacene thin films

are deposited (unpublished results) so it would seem that the particular details of the energy-level alignment between aluminum with pentacene are at least partially responsible for exceptionally good blocking behavior observed here.

For the 100 nm pentacene device with aluminum electrodes, the photocurrent measured at 2.7 eV incident photon energy was examined as a function of applied bias voltage and photon flux. The results are shown in Fig. 32.7. While the photocurrent yield increases slightly at reduced photon flux, the shape of the  $I$ - $V$  curve is nearly unchanged. There is a steep linear rise between  $-0.3$  and  $0.3$  V, while at higher applied field, the photocurrent quickly saturates. In the saturated regime, the photon flux approaches linearity with the incident photon flux, while at low field, the response is sublinear. The flux and field dependencies can be understood in terms of the recombination dynamics of the photogenerated charge carriers. Each charge carrier generated in the bulk requires a certain time to reach the electrodes. The likelihood of recombination depends on the probability that the mobile charge encounters (a) another mobile charge of opposite sign or (b) a trapped charge of opposite sign. The first process leads to bimolecular rate kinetics and a square root dependence of the photocurrent on photon flux; the latter process is a first-order reaction that results in a linear dependence of photocurrent on photon flux. At low field, the transit times are high, the density of mobile charge starts to exceed the density of trapped charge, and recombination is dominated by the bimolecular process. At high field, unimolecular recombination kinetics predominate.

Linear, saturated photocurrent at high field was observed previously in anthracene single crystals [18] where it was attributed to the increasing dissociation probability of the geminate hole–electron pair as a result of the stronger local electric fields. The similarity of the pentacene  $I$ - $V$  curves with the anthracene single crystal data is strong evidence that the photocurrent at 2.7 eV in pentacene thin films also originates from intrinsic photogeneration of geminate hole–electron pairs, in support of the assignment based on the shape of the photocurrent action spectra. Further evidence can be obtained from the temperature dependence of the photocurrents, discussed in the next section.

### 32.7.4 Temperature Dependence

Photocurrent spectra were measured at five temperatures ranging from 30 °C and 75 °C. The photocurrent was found to increase between 10 to 100 % over this temperature range depending on the photon energy. The narrow range of temperature and the small change in photocurrent make it difficult to accurately determine the mathematical form of the temperature dependence but a simple exponential dependence fits the data points within experimental error. The dependences are therefore expressed as activation energies based on the usual Arrhenius formula. The results are shown in Fig. 32.8.

The activation energies have previously been interpreted within the framework of the Onsager theory and the dissociation energy of the geminate pair [16]. Earlier still, however, it was proposed that the activation energies indicated the energy of

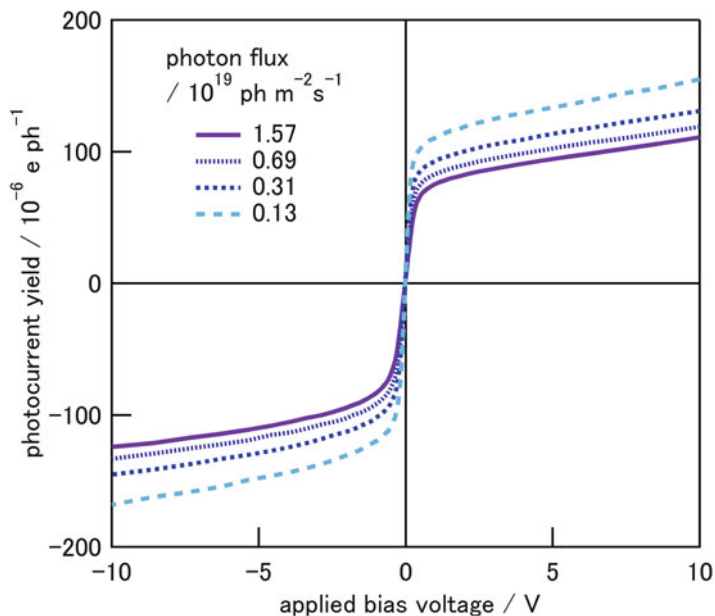


**Fig. 32.7** Photocurrent–voltage relationship for the 100 nm pentacene/Al electrode device measured at 2.7 eV incident photon energy. Photocurrent yields are normalized to the incident photon flux and the flux was attenuated over the range indicated using wire mesh. The curves are slightly asymmetrical in both shape and magnitude, and the current intercept has a  $-20$  mV offset. The bias voltage is applied across a gap of 0.1 mm

the trapping levels encountered by the free charge carriers [15]. As the activation energies in Fig. 32.8 vary approximately as the inverse of the magnitude of the photocurrent, i.e., the density of free charge carriers, it seems possible that the thermal dependence is indeed governed according to the filling of trap states. The activation energy obtained at photon energies where extrinsic photocurrent is dominant might also correspond to the energies required to dissociate charge pairs at the electrode interface, should this be the mechanism limiting the charge transport.

In short, the data is consistent with intrinsic photocurrent, but alternative interpretations are also valid.

### 32.7.5 Electrode Dependence

As noted in Sect. 32.7.3, the dark currents flowing through the pentacene film depended on the electrode metal used. The shape of the photocurrent action spectra also varied substantially on the electrode, as shown in Fig. 32.9. Aluminum electrodes, found to block charge injection into pentacene, resulted in low photocurrent below the threshold value of 2.25 eV. For titanium and gold, meanwhile, features

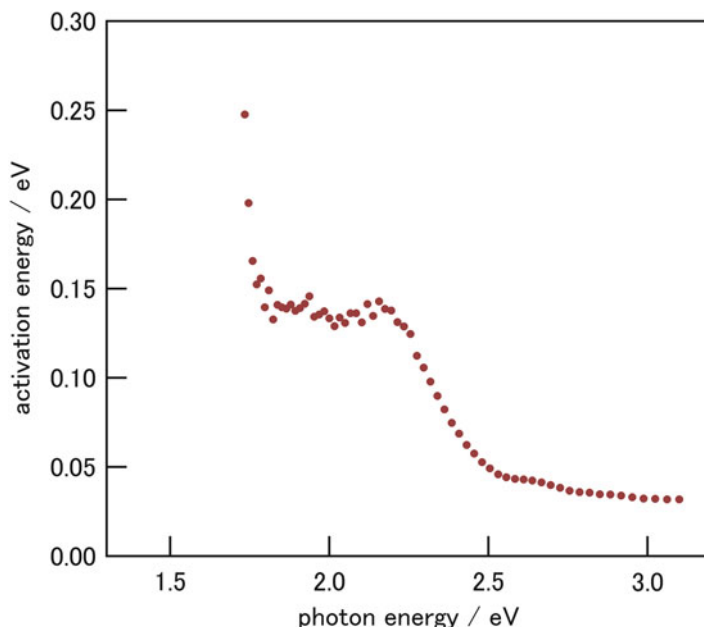


**Fig. 32.8** The activation energy of the photocurrent of the 100 nm pentacene/Al electrode device, measured over a temperature range of 30–75 °C. The activation energy in the energy region corresponding to singlet exciton absorption is about 140 meV, falling to about 35 meV for photon energies above 2.2 eV

in the photocurrent action spectra resembling the absorption spectrum of pentacene were superimposed over features attributed to the intrinsic photocurrent measured with the device with aluminum electrodes.

This result clearly demonstrates that the intrinsic and extrinsic photocurrent mechanisms can coexist and that the relative magnitudes are governed by the choice of electrode. As expected, the extrinsic photocurrent yield is almost independent of photon energy: all absorbed photons over the observed energy range are equally likely to contribute to the photocurrent, and the transport energy plays no role. Extrinsic photocurrent can be suppressed, however, by choosing an electrode such as aluminum which blocks the injection of dark current. It would seem that in the Al/pentacene/Al device the electrode work function is aligned near the middle of the transport energy gap of pentacene, whereas for Au the energy separation between the Fermi level and the HOMO-derived valence states of pentacene is substantially smaller. The larger work function of Au relative to Al supports this interpretation, but the density of trap states at the interface might also play a role and the influence of the metal surface on the morphology of pentacene [49] should also be considered. Ti presents an interesting intermediate case where the contribution of the intrinsic and extrinsic photocurrents is approximately equal.

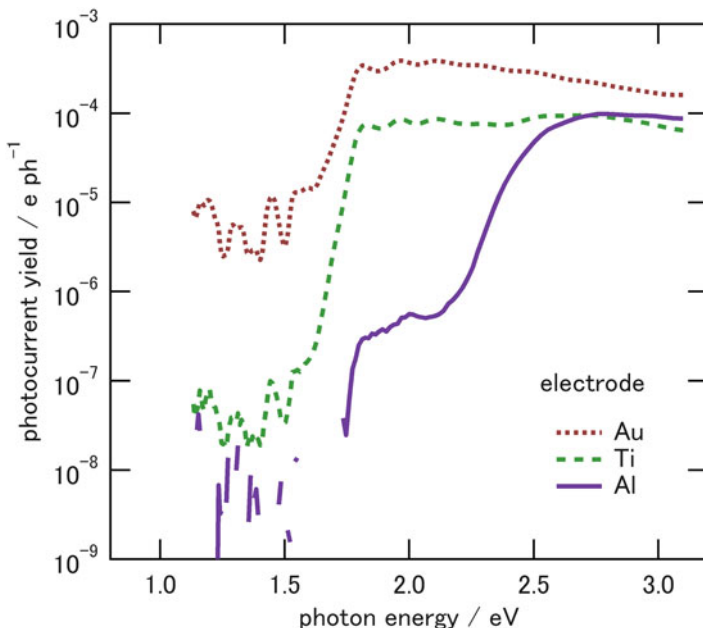


**Fig. 32.9** Action spectra of incident flux normalized photocurrent for 100 nm pentacene thin films for three different electrode materials. Only for aluminum electrodes is it possible to clearly observe the current from intrinsic photogeneration in pentacene. Injected photocurrents, approximately proportional to the exciton absorption spectrum, dominate the action spectra for both titanium and gold electrodes

### 32.7.6 Transport Energy

The photocurrent action spectrum of a 100 nm pentacene thin film together with the optical absorption spectrum, recorded in situ, is shown in Fig. 32.10. The results of the intensity, voltage, and temperature dependence all support the conclusion that the measured photocurrent recorded here using aluminum electrodes represents the intrinsic photogeneration, the result of the dissociation of geminate pairs created upon absorption of a photon.

The threshold value for the onset of photoconduction is 2.25 eV, in agreement with previous pentacene results on thick-film sandwich devices [13] and single crystals [21]. Following these previous studies, we therefore estimate the energy gap of the pentacene thin film directly from the onset at 2.25 eV. This is substantially higher than the onset of optical absorption at 1.75 eV [31], ascribed to the first singlet exciton. Meanwhile the extrapolation of the charge-transfer states of pentacene, observed by electroabsorption for a 300 nm thin film [28], leads to an estimate of 2.8 eV. Photoemission studies have suggested a value of 2.3 eV for a 10 nm pentacene film [50], estimated from the given peak–peak separation of 3.4 eV

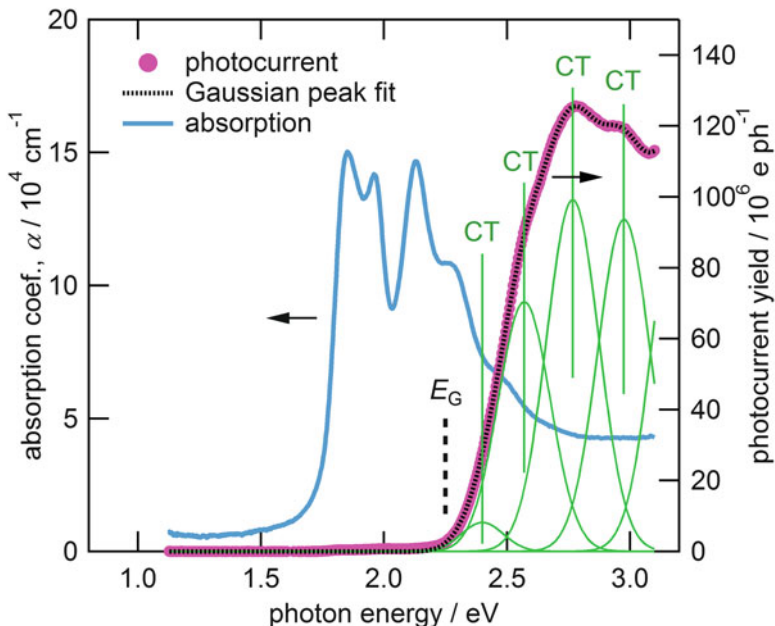


**Fig. 32.10** Photocurrent action spectra and absorption coefficient obtained for the 100 nm pentacene film/Al electrode device. Photocurrents are normalized to the incident photon flux. The transport energy gap is  $E_G = 2.25$  eV estimated from the threshold onset of the photocurrent yield

and assuming a peak width of 0.55 eV for the deconvoluted density of both occupied and unoccupied states.

The most basic conclusion that can be obtained from the photocurrent data is that photogeneration of charge carriers through geminate pair dissociation requires a minimum photon energy of 2.25 eV. The photocurrent yield rises to a maximum value at 2.8 eV and remains relatively constant at higher energies. Some fine structure can be discerned which can be fit as a sequence of Gaussian peaks at regularly spaced intervals of about 0.2 eV. This feature is assigned as a manifold of individual CT transitions. The spectral shape of the intrinsic photocurrent signal is notable for the broad initial rise which exceeds that predicted by a simple model of thermally assisted dissociation according to the energy difference between the CT state and the transport energy gap as the factor

$$\phi \propto e^{-\frac{E_G - E_{CT}}{k_B T}} \quad (32.19)$$

Equation 32.19 at 30 °C would cause the yield originating from excitation to a CT state 60 meV below the transport energy to be attenuated by a factor of ten. The threshold photocurrents can also be modeled as the convolution of valence and

conduction states [13, 51, 52], either as a calculated band edge or using optical densities, extending from a minimum value predefined as the energy gap.

It seems likely that the intrinsic photocurrent signal is a complex manifold of charge-transfer states, at least some of which represent higher-order vibronic transitions [28, 53]. These optically generated states are vertical transitions and may well extrapolate to 2.8 eV at infinite separation as estimated by Sebastian et al. [28] and later used by Petelenz et al. [33] in their energy assignment of the pentacene charge-transfer states. We agree with these authors that the transition energies are probably in excess of thermally relaxed ionic states identified as the charge carriers. The transport gap is therefore identified (within  $2\text{--}3 k_{\text{B}}T$ ) with the onset of intrinsic photocurrent signal, while the broad subsequent rise is attributed to the conversion of some fraction of the excess energy,  $h\nu - E_{\text{G}}$ , toward increasing the dissociation efficiency of the geminate pairs.

## 32.8 Final Thoughts

In summary, photocurrent action spectra were measured for vacuum-deposited pentacene thin films between 20 and 100 nm in thickness. A strong dependence on the electrode material was found, and, for aluminum electrodes, the measured photocurrent was determined to originate from an intrinsic mechanism, where hole–electron pairs are created in the bulk film. For gold or titanium electrodes, a substantial contribution to the photocurrent from extrinsic, or injected, photocurrents was observed.

The intrinsic photocurrent spectrum of pentacene thin film resembled the spectra obtained previously for thick films and single crystals. The onset of the intrinsic photocurrent, taken to indicate the transport energy,  $E_{\text{G}}$ , was determined to be 2.25 eV, the same value as the older studies.

The dependence of the intrinsic photocurrent with temperature, photon flux, and applied field is consistent with a mechanism in which optical generation of a charge-transfer state is followed by the thermally assisted dissociation of the geminate hole–electron pair into independent charge carriers.

**Acknowledgments** The referred research studies carried out by the authors were supported by JSPS KAKENHI Grant Numbers 25410093 in parts.

## References

1. P.R. Görlich, *Photoconductivity in Solids* (Routledge and Kegan Paul, London, 1967)
2. C.W. Tang, S.A. VanSlyke, *Appl. Phys. Lett.* **51**, 913 (1987)
3. A. Rose, *Concepts in Photoconductivity and Allied Problems* (Interscience, New York, 1963)
4. F. Gutmann, L.E. Lyons, *Organic Semiconductors*, vol. 4 (Wiley, New York, 1967)

5. E.A. Silinsh, *Organic Molecular Crystals* (Springer, Berlin, 1980)
6. M. Pope, C.E. Swenberg, *Annu. Rev. Phys. Chem.* **35**, 613 (1984)
7. P.M. Borsenberger, D.S. Weiss, *Organic Photoreceptors for Imaging Systems*, vol. 39 (Marcel Dekker, New York, 1993)
8. H. Bässler, *Organic Molecular Solids: Properties and Applications* (CRC Press, Boca Raton, 1997)
9. J.G. Simmons, *J. Phys. D* **4**, 613 (1971)
10. H. Yamane, D. Yoshimura, E. Kawabe, R. Sumii, K. Kanai, Y. Ouchi, N. Ueno, K. Seki, *Phys. Rev. B* **76** 165436 (2007)
11. P. Stallinga, *Electrical Characterization of Organic Electronic Materials and Devices* (Wiley, Chichester 2009)
12. J.G. Simmons, *Phys. Rev. B* **15**, 964 (1977)
13. E.A. Silinsh, A.I. Belkind, D.R. Balode, A.J. Biseniece, G.G. Grechov, L.F. Taure, M.V. Kurik, J.I. Vertzymacha, I. Bok, *Phys. Status Solidi A* **25**, 339 (1974)
14. G. Castro, J.F. Hornig, *J. Chem. Phys.* **42**, 1459 (1965)
15. R.F. Chaiken, D.R. Kearns, *J. Chem. Phys.* **45**, 3966 (1966)
16. R.H. Batt, C.L. Braun, J.F. Hornig, *Appl. Opt.* **8**, 20 (1969)
17. N. Geacintov, M. Pope, *J. Chem. Phys.* **45**, 3884 (1966)
18. R.R. Chance, C.L. Braun, *J. Chem. Phys.* **59**, 2269 (1973)
19. R.R. Chance, C.L. Braun, *J. Chem. Phys.* **64**, 3573 (1976)
20. N. Geacintov, M. Pope, H. Kallmann, *J. Chem. Phys.* **45**, 2639 (1966)
21. D.V. Lang, X. Chi, T. Siegrist, A.M. Sergent, A.P. Ramirez, *Phys. Rev. Lett.* **93** 086802 (2004)
22. S. Barth, H. Bässler, *Phys. Rev. Lett.* **79**, 4445 (1997)
23. E.A. Silinsh, H. Inokuchi, *Chem. Phys.* **149**, 373 (1991)
24. A. Rose, *Phys. Rev.* **97**, 322 (1955)
25. A. Rose, M.A. Lampert, *Phys. Rev.* **113**, 1227 (1959)
26. C.L. Braun, *J. Chem. Phys.* **80**, 4157 (1984)
27. E.A. Silinsh, V.A. Kolesnikov, I.J. Muzikante, D.R. Balode, *Phys. Status Solidi B* **113**, 379 (1982)
28. L. Sebastian, G. Weiser, H. Bässler, *Chem. Phys.* **61**, 125 (1981)
29. L. Sebastian, G. Weiser, G. Peter, H. Bässler, *Chem. Phys.* **75**, 103 (1983)
30. D.D. Eley, *Nature* **162**, 819 (1948)
31. K. Kim, Y.K. Yoon, M.O. Mun, S.P. Park, S.S. Kim, S. Im, J.H. Kim, *J. Supercond.* **15**, 595 (2002)
32. R.A. Collins, A. Krier, A.K. Abass, *Thin Solid Films* **229**, 113 (1993)
33. B. Petelenz, P. Petelenz, H.F. Shurvell, V.H. Smith Jr., *Chem. Phys.* **119**, 25 (1988)
34. D.R.T. Zahn, G.N. Gavrila, M. Gorgoi, *Chem. Phys.* **325**, 99 (2006)
35. N. Sato, H. Yoshida, K. Tsutsumi, *J. Electron. Spectrosc. Relat. Phenom.* **88–91**, 861 (1998)
36. I.G. Hill, A. Kahn, Z.G. Soos, Pascal, Jr., *Chem. Phys. Lett.* **327**, 181 (2000)
37. R. Murdey, N. Sato, M. Bouvet, *Mol. Cryst. Liq. Cryst.* **455**, 211 (2006)
38. H. Yoshida, *Chem. Phys. Lett.* **539–540**, 180 (2012)
39. S. Barth, H. Bässler, H. Rost, H.H. Hörhold, *Phys. Rev. B* **56**, 3844 (1997)
40. S. Gorgolis, A. Giannopoulou, D. Anastassopoulos, P. Kounavis, *J. Appl. Phys.* **112** 013101 (2012)
41. J. Gao, F.A. Hegmann, *Appl. Phys. Lett.* **93**, 223306 (2008)
42. I.H. Campbell, B.K. Crone, *J. Appl. Phys.* **106**, 113704 (2009)
43. A.E. Amrani, B. Lucas, F. Hijazi, A. Skaiky, T. Trigaud, M. Aldissi, *Eur. Phys. J. Appl. Phys.* **51**, 33207 (2010)
44. A.C. Mayer, A. Kazimirov, G.G. Malliaras, *Phys. Rev. Lett.* **97**, 105503 (2006)
45. H. Yamagata, J. Norton, E. Hontz, Y. Olivier, D. Beljonne, J.L. Brédas, R.J. Silbey, F.C. Spano, *J. Chem. Phys.* **134**, 204703 (2011)
46. R. Hesse, W. Hofberger, H. Bässler, *Chem. Phys.* **49**, 201 (1980)
47. R. Murdey, N. Sato, *J. Chem. Phys.* **137**, 234703 (2012)

48. R. Murdey, N. Sato, *Jpn. J. Appl. Phys.* **53**, 05FY04 (2014)
49. C.D. Dimitrakopoulos, P.R.L. Malenfant, *Adv. Mater.* **14**, 99 (2002)
50. F. Amy, C. Chan, A. Kahn, *Org. Electron.* **6**, 85 (2005)
51. A.I. Belkind, R.I. Kalendarev, *Phys. Status Solidi A* **14**, 681 (1972)
52. M. Silver, R. Sharma, *J. Chem. Phys.* **46**, 692 (1967)
53. P.J. Bounds, W. Siebrand, I. Eisenstein, R.W. Munn, P. Petelenz, *Chem. Phys.* **95**, 197 (1985)

# Chapter 33

## Electro-Responsive Columnar Liquid Crystal Phases Generated by Achiral Molecules

Keiki Kishikawa

**Abstract** Electro-responsive columnar liquid crystal (ER-CLC) materials were reviewed, especially ferroelectric columnar materials (FCLC). The history of polar columns are introduced with recent progress toward ER-CLC (electro-responsive columnar) materials. The final part of this review describes a recent study in our laboratory. The insertion of  $-C_6H_4-X-$  ( $X = OCH_2, OCO, NH_2CH_2, NHCO, N(CH_3)CH_2, SCH_2, CH_2CH_2,$  and  $CHCH$ ) into the Ar-N bonds of bis(*N,N'*-(3,4,5-trialkoxypheyl)ureas **4** ( $R = C_{12}H_{25}$ ) was performed, and the compounds with  $X = OCH_2, OCO, NH_2CH_2, NHCO, N(CH_3)CH_2,$  and  $SCH_2$  exhibited a CLC phase. The insertion greatly affected their responsiveness and temperature ranges. In the case of **14** ( $-C_6H_4-X-$  ( $X = OCH_2$ ),  $R = C_{12}H_{25}$ ), the responsiveness was highly improved in comparison with **4**. Broad temperature ranges of a CLC phase were achieved by mixing **14** and **19** ( $-C_6H_4-X-$  ( $X = SCH_2$ ),  $R = C_{12}H_{25}$ ).

**Keywords** Columnar phase • Electro-responsiveness • Ferroelectricity • Polarity

### 33.1 Introduction

The electro-responsiveness of the nematic and smectic liquid crystal (LC) phases has been well studied and used in LC displays (LCDs) and other devices. However, electro-responsive columnar LC (ER-CLC) phases are not well studied [1, 2]. In this review, we describe studies detailing ER-CLCs (especially ferroelectric CLCs (FCLCs)). A balance between the responsiveness and the polar columnar structure stability is important for obtaining the ER-CLC phase. In general, highly responsive materials do not exhibit stable polarizations, while stable one-directional columnar molecular aggregates do not exhibit a highly responsive switching behavior. In addition, a wide temperature range is necessary for the practical use of these phases.

---

K. Kishikawa (✉)

Department of Applied Chemistry and Biotechnology, Graduate School of Engineering,  
Chiba University, 1-33 Yayoi-cho, Inage-ku, Chiba 263-8522, Japan  
e-mail: [kishikawa@faculty.chiba-u.jp](mailto:kishikawa@faculty.chiba-u.jp)

© Springer Japan 2015

R. Tamura, M. Miyata (eds.), *Advances in Organic Crystal Chemistry*,  
DOI 10.1007/978-4-431-55555-1\_33

653

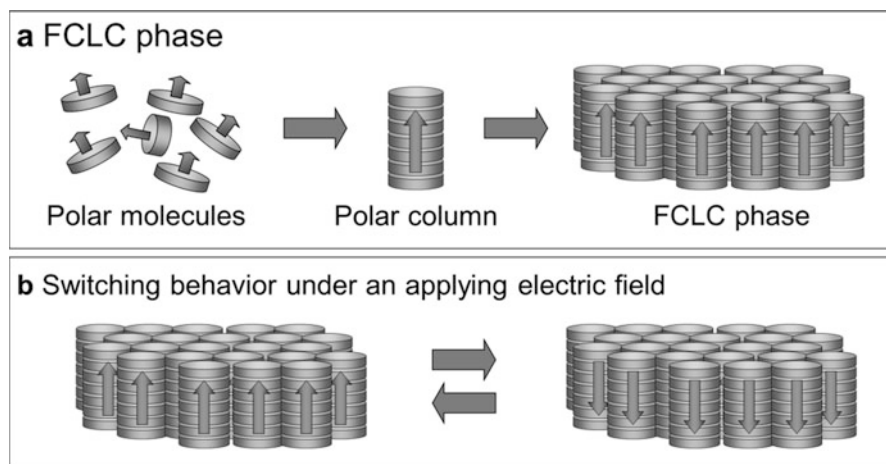


**Fig. 33.1** (a) Organization of polar molecules into an FCLC phase and (b) its switching behaviors

The polar FCLC phase molecules in Fig. 33.1a are organized into a polar column. Furthermore, the columns are organized in parallel to generate a CLC phase. Applying an electric field causes the polar direction of the columns to become uniform and generates a macroscopic polarity that switches their direction upon application of a triangular wave voltage, as shown in Fig. 33.1b. A clear threshold between the two polar states is necessary to achieve the FCLC phase. At this threshold voltage, the macroscopic polarities change their direction. Accordingly, the FCLC phase provides a sharp switching current peak at the threshold voltage upon the application of a triangular wave voltage.

Some polymers, such as polyvinylidene fluoride, also exhibit a ferroelectric behavior upon the application of a high voltage [3–6]. These polymers do not have a clear threshold voltage and do not exhibit a switching current peak upon reversal of the macroscopic polarities. These differences indicate that ferroelectric behavior does not originate from the cooperative behavior of polar polymer molecules.

Although the behaviors mentioned above are also considered ferroelectric, we prefer to distinguish ferroelectric switching from these behaviors in this review. Our ideal FCLC phases must possess a clear threshold voltage and sharp switching current peak.

### 33.1.1 First Stage of the History of ER-CLCs

#### 33.1.1.1 Laterally Polar Columns Using Chiral Oval Molecules

The first stage toward realizing ER-CLCs involves chiral oval disk-like molecules **1**, which were designed to generate laterally polar columns (Fig. 33.2) [7]. These

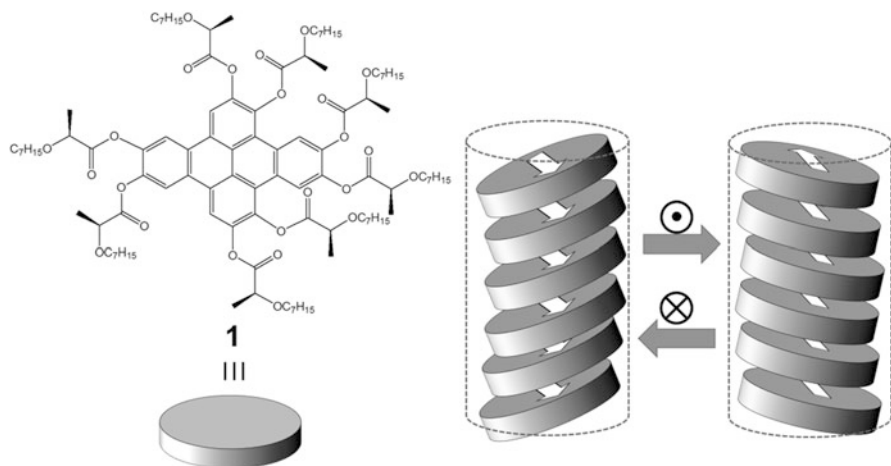


**Fig. 33.2** Molecular structure of **1** and the switching behavior for molecules in a column under applying an electric field

oval molecules were organized into columnar aggregates and exhibited a CLC phase. The molecules tilted into thickly packed cylinder-shaped columns. For  $C_2$  symmetric molecular packing, the peripheral chiral moieties in the molecule generate a macroscopic polarity perpendicular to the column axis. Switching the electric field direction changes the tilt directions for the molecules in each column, which is a movement similar to that of the chiral smectic C phases.

### 33.1.1.2 Molecular Shape Approaches for Realizing Polar Columns

Simultaneously, other scientists in the field of LC focused on obtaining a CLC phase with a macroscopic polarity in the direction of the column axis using achiral molecules. Molecules with bowl [8] and cone [9] shapes were designed for one-directional molecular packing. Despite these molecules organizing into one-directional molecular aggregates to minimize their free volume, adjacent columns are arranged in *anti*-parallel (Fig. 33.3 left) and not in *syn*-parallel (Fig. 33.3 right) to cancel out their polarities. These polarities did not switch upon the application of a voltage because the *anti*-parallel columns were highly stabilized with neighbors canceling each other's polarities.

## 33.1.2 Recent Studies of ER-CLCs

### 33.1.2.1 ER-CLCs of Benzene Triamides

To the best of our knowledge, the first ER-CLC phase with molecules aligned parallel to an electric field was reported by Nuckolls' group [10]. Trimecinamide **2**

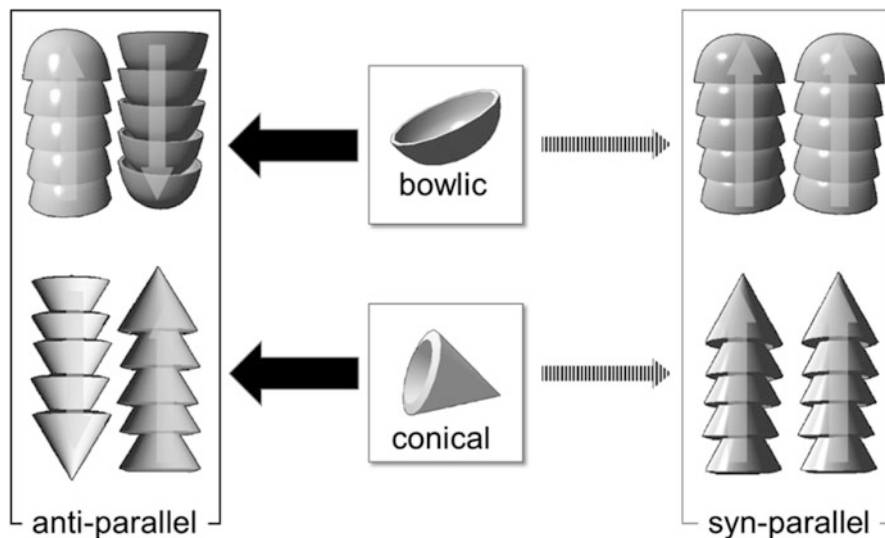


**Fig. 33.3** Organization of *anti-parallel* (left) and *syn-parallel* (right) arrangements of bowl- and cone-shaped molecules

(Fig. 33.4a) was self-organized into a columnar structure (Fig. 33.4b) that exhibited a CLC phase. The columnar axis directions were controlled by applying an electric field even though they did not exhibit switching current peak. Polarized light microscopy (POM) revealed that the focal conic textures were the CLC phase before applying a voltage, and these textures disappeared after applying a voltage. Furthermore, turning the voltage off caused the texture to reappear. This behavior was repeatable by continually switching on and off and is explained as follows. The molecules are self-organized into a columnar aggregate via intermolecular hydrogen bonding. Without an electric field, the columns are parallel to the ITO electrode surface, and the anisotropic textures are visible to POM. After applying an electric field, all of columns become perpendicular to the electrode surface, which makes the LC sample isotropic perpendicular to the column axes and thus invisible to POM using crossed polarizers. The direction of amide-carbonyl groups is presumably controlled by the applied electric field.

### 33.1.2.2 Stacking Large Aromatic Molecules via Intermolecular Hydrogen Bonds

The method to stack large aromatic molecules using intermolecular hydrogen bonds was reported by Ikeda et al. [11]. They synthesized compound **3** (Fig. 33.5a) with six *N*-alkyl amide moieties. While they did not determine its liquid crystallinity,

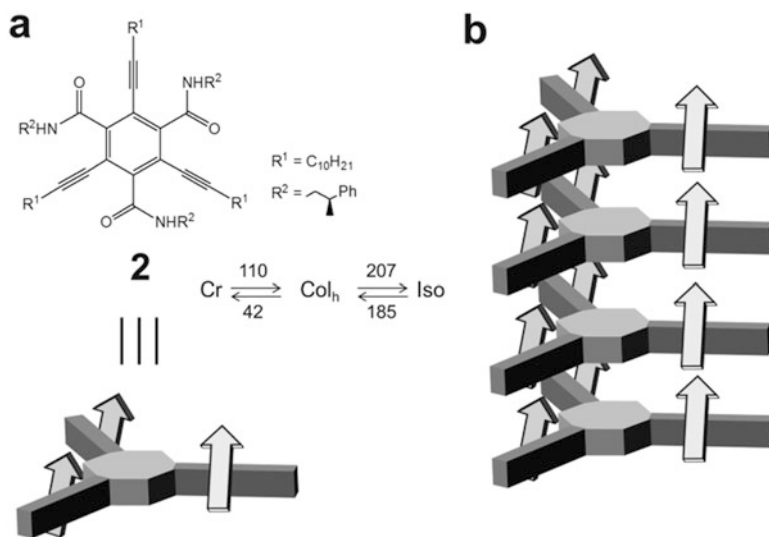


**Fig. 33.4** (a) Molecular structure for trimecinamides **2**. (b) Schematic model of hydrogen-bonded molecules after applying an electric field. The *arrows* indicate the intermolecular hydrogen-bonded direction

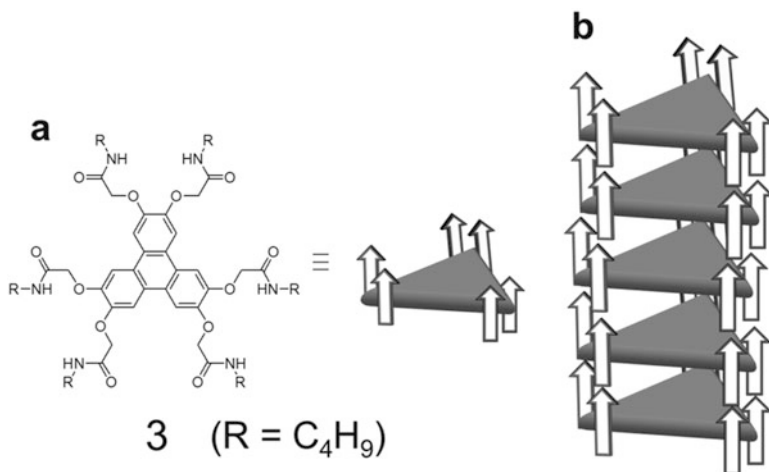


**Fig. 33.5** (a) Molecular structure of **3**. (b) Schematic presentation of the directional  $\pi$ -stacking of these molecules

its gelation was observed in some hydrocarbon solvents (*n*-hexane, *n*-octane, cyclohexane, and *p*-xylene). The triphenylenes presumably stack in one direction of the columnar structure due to the intermolecular amide hydrogen bonds, as shown in Fig. 33.5b.

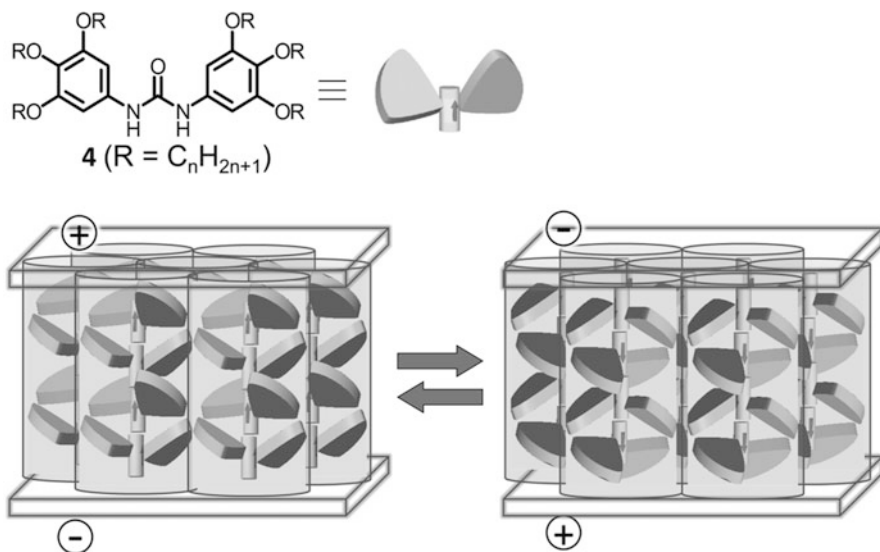


**Fig. 33.6** Schematic representation of the molecular packing structures for liquid crystalline urea **4** and the polar direction switching due to the applied electric field

### 33.1.2.3 Switchable FCLC Compounds

Over the last decade, a small number of ferroelectrically switchable CLC phases have been reported with observable switching current peaks. The first two examples are shown in Figs. 33.6 and 33.7. These examples were reported almost simultaneously. The liquid crystalline ureas, **4**, shown in Fig. 33.6 possessing 3,4,5-trialkoxyphenyl groups ( $n = 8-16$ ) as their *N*-substituents, were reported by our group [12, 13]. The urea molecules interact intermolecularly via hydrogen bonds to generate a linear and polar molecular aggregate and exhibited rectangular and hexagonal CLC phases. Applying a triangular wave voltage provided uniform column polarities that generated a macroscopic polarity, and reversing the electric field direction changed the macroscopic polar directions. During the switching process, the carbonyl group directions changed cooperatively and the intermolecular hydrogen bonds are recombined. In this study, the polar direction changed repeatedly after applying a triangular wave voltage even at 18 Hz. The spontaneous polarizations ( $P_s$ ) were calculated based on the switching current peak area ( $P_s$  is a half of the switching current peak area, and it indicates the degree of polarization per the area size of the electrode). The  $P_s$  was constant with the triangular wave voltage frequency. The polarity generated by applying this voltage was confirmed via second harmonic generation (SHG) measurements [14]. Their Kerr effects and other properties were measured [15, 16].

Gorecka et al. reported a ferroelectric behavior for long bent rod molecules ( $R = C_{12}H_{25}, C_{14}H_{29}$ ) (Fig. 33.7a) [17]. These switching behaviors were observed

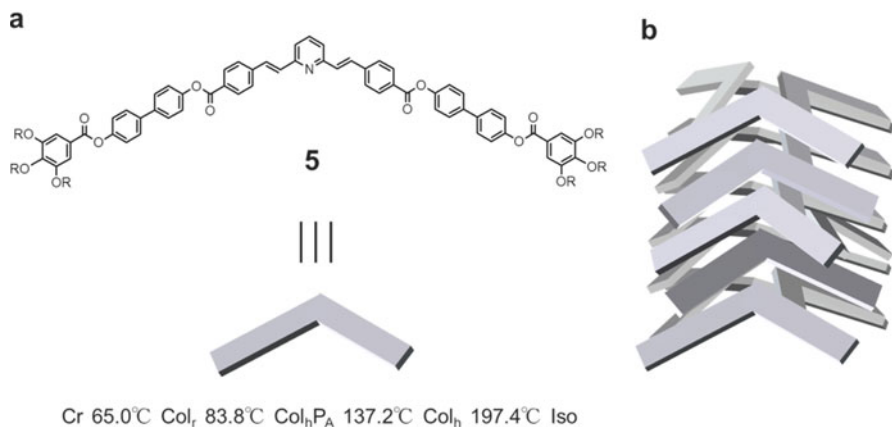


**Fig. 33.7** (a) Molecular structure of **5** and (b) its polar columnar aggregate

in the Col<sub>h</sub>P<sub>A</sub> phase. Three or four molecules are organized into cone-shaped structures, which stack to generate the polar columnar aggregates (Fig. 33.7b). In the Col<sub>h</sub>P<sub>A</sub> phase at 130 °C, the switching peaks (70 nC/cm<sup>2</sup>) were observed. However, such switching peaks were not observed in the Col<sub>h</sub> phase.

There are many examples of ferroelectrically switchable rectangular CLC phases composed of achiral bent molecules. Most of these CLC phases are generated by frustrations in the LC states. I believe that they should be classified into smectic phases with a columnar structure, because they contain smectic layer structures with all molecular long axes in each layer parallel (or slightly tilt) to the layer normal [18–20].

### 33.1.2.4 ER-CLCs of Various Amides

Recently, several liquid crystalline amides have been reported. These molecules have multiple *N*-alkylamide moieties around one central aromatic ring. The method is the same as those in sections 3.1 and 3.2.

Trimecinamide **6** (Fig. 33.8) has a simple *C*<sub>3</sub> symmetry consisting of one benzene ring and three amide groups [21, 22]. The molecules stack due to intermolecular hydrogen bonding. These aggregates are similar to those of **2**. The generated Ps value was 1.3–1.8 μC/cm<sup>2</sup>, and coercive field (*E*<sub>c</sub>) was 21–26 V/μm. The switching frequency is 0.1 Hz at 70 °C and 5.0 Hz at 150 °C, and the Ps was constant with the frequency.

Compound **7** (Fig. 33.9) contains a corannulene in its center and exhibited the CLC phase [23]. The ten amide groups interact intermolecularly to generate the columnar aggregate. Applying an electric field (15 V/μm) for 30 min at 125 °C aligns the column axes perpendicular to the electrode plane. Corannulene derivatives **7** did not show a ferroelectric switching peak in the CLC phase.

**Fig. 33.8** Molecular structure of **6**

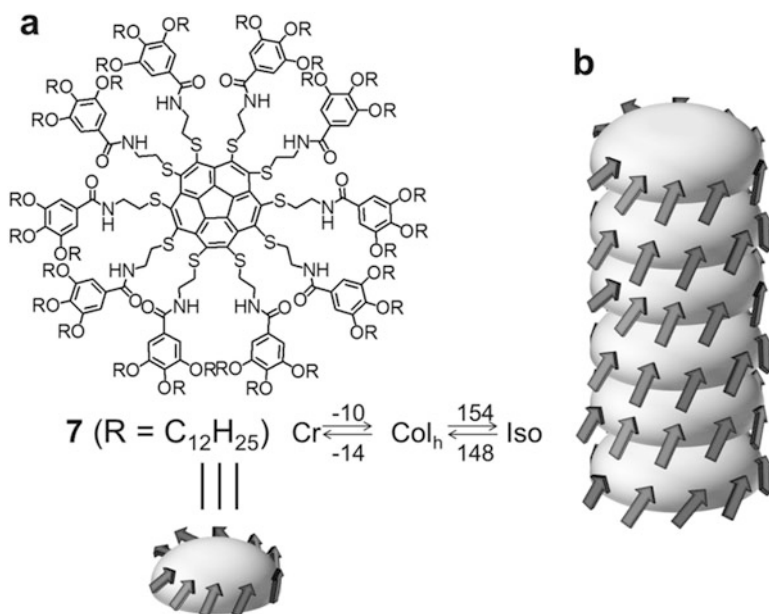


**Fig. 33.9** (a) Molecular structure of **7** and (b) its columnar aggregate

Thiafulvalen derivative **8** and triphenylene one **9** (Fig. 33.10) exhibited a highly responsive ER-CLC phase [24]. These compounds easily aligned homeotropically by applying an electric field. This method is useful for aligning aromatic molecules that may be used in organic electronic devices. The CLC phase of **9** exhibited SHG signals under applying an electric field. However, the SHG signal instantaneously vanished after switching it off. These results indicate that the polarity of **9** under the applied voltage is unstable in the LC phase.

Both the  $\pi$ -system and the cyclic tripeptide **10** (Fig. 33.11) can organize into columnar aggregates via the same method, even though the compounds did not show the switching current peak [25]. The aligned columns may be useful as selective membranes for transport of molecules and ions. The noncyclic dipeptide **11** exhibited an oblique CLC phase and the SHG signal was observed under applying an electric field [26].

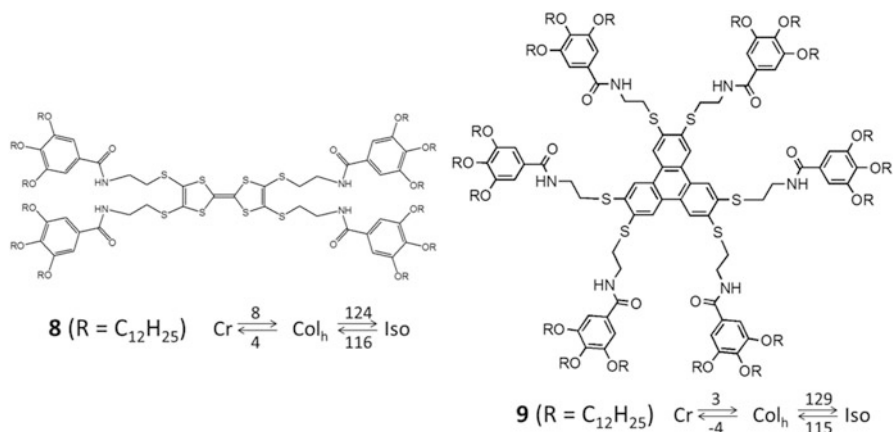


Fig. 33.10 Molecular structures of thiafulvalene derivative **8** and triphenylene one **9**

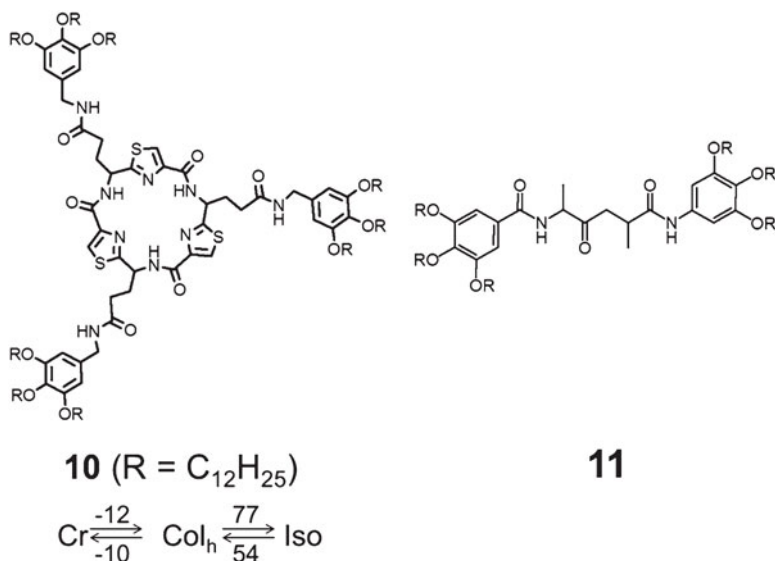
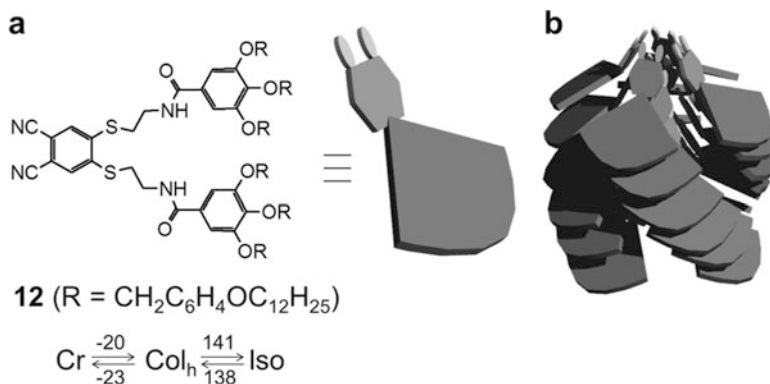


Fig. 33.11 Molecular structures for cyclic tripeptide **10** and noncyclic dipeptide **11**

Compound **12** (Fig. 33.12a) uses dicyanobenzene as the polar site and six terminal alkyl chains as the hydrophobic sites [27, 28]. The CLC phase for **12** was the first reported example of an FCLC phases. The molecules self-organized into core-shell columnar structures via their intermolecular hydrogen bonds as shown in Fig. 33.12b. They stacked in one direction. The central polar part of each column inverted during the switching process. Applying a square-shaped AC electric field (1.0 Hz, 20V<sub>pp</sub>/μm) at 120 °C aligned the columns perpendicularly to the electrode plane.



**Fig. 33.12** (a) Molecular structure of **12** and (b) its polar columnar molecular aggregate

In this paper, switching current peaks were observed when a slow triangular-shaped AC field (0.08 Hz,  $20 V_{pp}/\mu\text{m}$ ) was applied at  $120^\circ\text{C}$ . They claimed the peak resulted from the polarization inversion. However, it is assumed that the switching current peaks observed are originated in the movement of the amide groups (whose polarity is not ferroelectric) from the following two results which contradict each other. 1) In the application of triangular wave voltage, the switching peak was obtained at only 10–15 s after passing  $\pm 0 V_{pp}/\mu\text{m}$ , though the applied voltage was very low (the peak was observed at approximately  $\pm 5 V_{pp}/\mu\text{m}$ ). 2) In contrast, applying a DC electric field ( $10 V_{pp}/\mu\text{m}$ ) gradually increased the SHG signal and took over 2 min to reach saturation. Furthermore, slow decrease in the SHG signal was also observed ( $-21\%$  in a 1,000 min) with time period at  $120^\circ\text{C}$ . Presumably, these two experimental results are contradictory. It is thought that the inversion of polarization does not have bi-stability at least. The behaviors are similar to those of polyfluorovinylidene fluoride under applying a high voltage, for the reason that they do not have a clear threshold voltage and do not show the switching current peak during the inversion process of the macroscopic polarities.

### 33.1.2.5 Ionic CLCs

The mixtures of lithium triflate **6** and carbonate **7** reportedly exhibited CLCs (Fig. 33.13) [29]. The center of the column contained lithium triflate ions (**6**) and carbonate moieties of **7** surrounded by the alkoxy chains. Applying an electric field ( $2.5 \text{ V/mm}$ , 1 kHz,  $25^\circ\text{C}$ ) for 90 min aligned the columns parallel to the electric field. The electro-responsive molecular alignment is assumed to originate from the lithium triflate ion and/or the carbonate moiety movement.

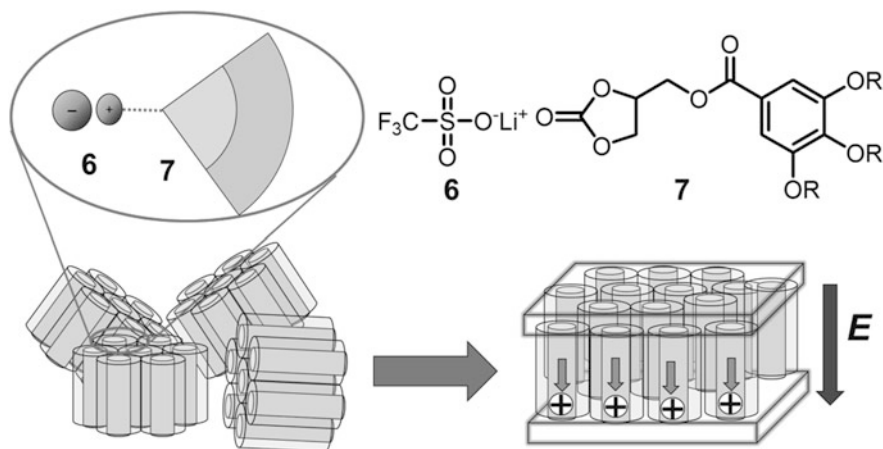


**Fig. 33.13** Molecular structures and columnar aggregates of **6** and **7** before and after applying an electric field

### 33.1.3 Recent Advances in Studies of Ferroelectrically Switchable Ureas

#### 33.1.3.1 Highly Responsive Switchable Ureas

Achieving a high responsiveness and wide temperature range is important for applicability. We attempted the following structural improvement to our urea molecules.

To increase the polar switching responsiveness, reducing the electrostatic interactions between adjacent columns is essential because the electrostatic interactions strongly stabilize the anti-parallel alignment of adjacent columns. We believe increasing the column diameter should effectively decrease the inter-columnar electrostatic interactions. Figure 33.14 shows the molecular structures for **4** ( $R = C_{12}H_{25}$ ) and **14** ( $R = C_{12}H_{25}$ ). Compound **4** ( $R = C_{12}H_{25}$ ) is our original molecular structure, while **14** ( $R = C_{12}H_{25}$ ) is an improvement. Their space-fill models of these compounds are shown in Fig. 33.14a and b. Introducing a  $-C_6H_4-O-CH_2-$  between the nitrogen and carbon atoms in the N-Ar bonds increased the molecule width and expanded the column diameter. Therefore, the switching peak became sharper. This change greatly improved the switching responsiveness [30].

Figure 33.15a shows the texture before applying a triangular wave voltage, and the broken black line indicates the border between the electric field applied (left side) and non-applied (right side) areas. Figure 33.15b shows the texture both after and while applying the triangular wave voltage. The ITO electrode textures immediately disappeared, whereas those for the non-ITO area did not change.

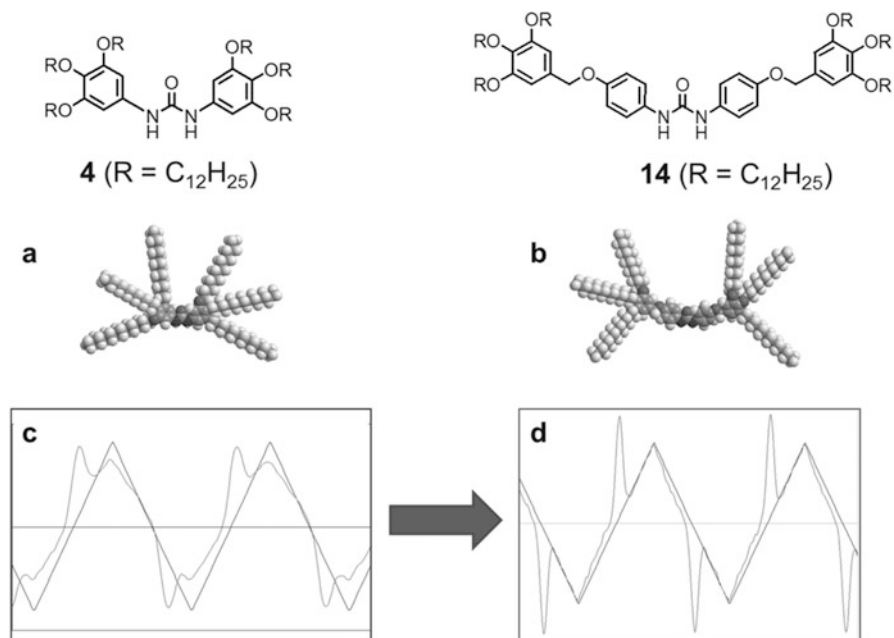


**Fig. 33.14** Comparison of **4** ( $R = C_{12}H_{25}$ ) and **14** ( $R = C_{12}H_{25}$ ): **(a, b)** space filling models, **(c)** **(d)** switching current peaks from the switching experiments (6 Hz–200 Vpp,  $T = 105^\circ\text{C}$ , ITO area  $1\text{ cm} \times 1\text{ cm}$ , cell gap  $5\ \mu\text{m}$ , ITO covered with polyimides)

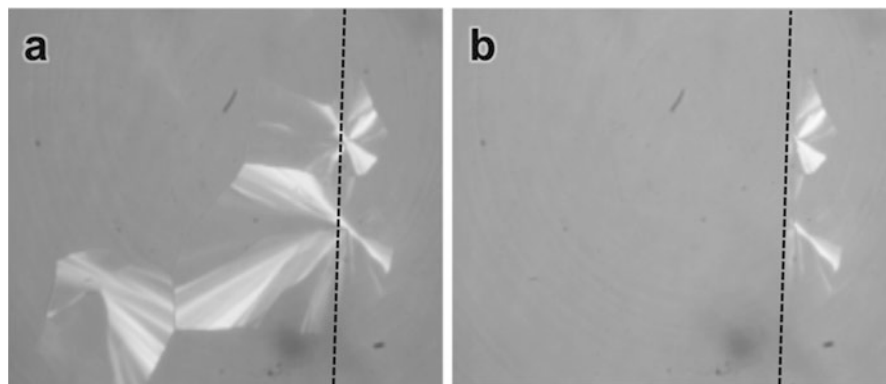


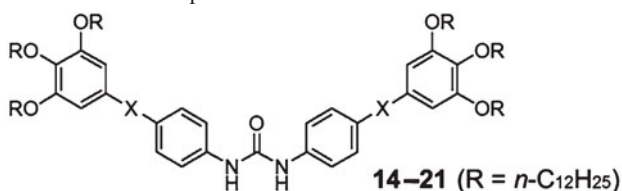
**Fig. 33.15** Switching experiment for **14** ( $R = C_{12}H_{25}$ ): **(a)** before the switching experiment (at 0 V) and **(b)** both after starting and during the switching experiment (triangular wave voltage at 6 Hz–200 Vpp,  $T = 105^\circ\text{C}$ , ITO area  $1\text{ cm} \times 1\text{ cm}$ , cell gap  $5\ \mu\text{m}$ , ITO covered with polyimides). The broken black line indicates the border between the electric field applied and non-applied areas

This result indicates the columns in the ITO areas oriented perpendicularly to the electrode. After applying the voltage, a sharp switching current peak was repeatedly observed. This result indicates the column axes remained perpendicular during the switching process even though the macroscopic polarities changed directions.

### 33.1.3.2 Substituent Effect on Liquid Crystallinity and Responsiveness in the Ureas

Various spacers were introduced between the nitrogen and carbon atoms in the N-Ar bonds of the urea molecule (**4**) to improve both its electro-responsiveness and polarization stability [31]. The result is shown in Table 33.1.

**Table 33.1** Transition phase behaviors of **14–21**



Compound	X	Phase transition behavior [ $^{\circ}\text{C}(\Delta H/\text{kJmol}^{-1})$ ]
<b>14</b>		Cr $\xrightleftharpoons[66.9(-3.1)]{94.4(3.5)}$ Col <sub>h</sub> $\xrightleftharpoons[116.9(-2.3)]{118.8(1.5)}$ Iso
<b>15</b>		Cr $\xrightleftharpoons[103]{118}$ Col <sub>h</sub> $\xrightleftharpoons[133]{135}$ Iso
<b>16</b>		Cr $\xrightleftharpoons[81.6(-4.2)]{90.9(4.9)}$ Col $\xrightleftharpoons[117]{119}$ Iso
<b>17</b>		Cr <sub>1</sub> $\xrightleftharpoons[50.4(-35.5)]{54.6(35.3)}$ Cr <sub>2</sub> $\xrightleftharpoons[175.7(-19.5)]{190.4(19.1)}$ Iso
<b>18</b>		Cr $\xrightleftharpoons[10.1(-24.7)]{41.9(41.5)}$ Col <sub>h</sub> $\xrightleftharpoons[42.0(-1.2)]{51.6(0.9)}$ Iso
<b>19</b>		Cr $\xrightleftharpoons[65.5(-1.8)]{83.2(1.2)}$ Col <sub>h</sub> $\xrightleftharpoons[80]{92}$ Iso
<b>20</b>		Cr $\xrightleftharpoons[62]{89}$ Iso
<b>21</b>		Cr $\xrightleftharpoons[110]{128}$ Iso

Cr, Cr<sub>1</sub>, and Cr<sub>2</sub> indicate the crystal phases. Col<sub>h</sub> and Col indicate a hexagonal CLC phase and an unidentified CLC phase. Iso indicates an isotropic liquid

A hexagonal CLC phase was observed for  $X = -O-CO-$  (**15**), and the transition temperatures were higher than those of **14**. An unidentified CLC phase was observed when  $X = -NH-CH_2-$  (**16**), and the transition temperatures were almost identical to **14**. No LC phase was found when  $X = -NH-CO-$  (**17**) because the melting point was high. The intermolecular hydrogen bonds between the amide molecules were too strong to generate an LC phase. A hexagonal CLC phase was observed when  $X = -N(CH_3)-CH_2-$  (**18**), and the transition temperatures were significantly below those of **14**. A hexagonal CLC phase was observed when  $X = -S-CH_2-$  (**19**), and the transition temperatures less than those of **14**.

No LC phase was observed when  $X = -CH_2-CH_2-$  (**20**) and  $X = -CH = CH-$  (**21**). This result indicates the heteroatom in  $X$  is required to generate a CLC phase.

Mixing experiments using **14** and **19** were performed to expand the temperature range for the switchable CLC phase (Fig. 33.16). The ratios 0:100, 25:75, 50:50, 75:25, and 100:0 were prepared by mixing **14** and **19**, respectively. A peak top of the  $P_s$  value for a ratio of 0:100 was observed at 77 °C. The switching was observed across a narrow temperature range (73–81 °C). The peak top for a ratio of 100:0 was observed at 107 °C. The switching was observed across narrow temperature range (96–108 °C). However, the 50:50 mixture exhibited the widest temperature range (66–110 °C) for all mixing experiments. These two compounds were freely miscible, and their mixture yielded a wide temperature range. The high miscibility originated from the molecular size of **19** matching that of **14**.

### 33.1.3.3 Strengthening the Intermolecular Interactions

To stabilize the polar structures, the intermolecular interactions were strengthened. Specifically, numerous hydrogen bonding sites were introduced into the molecule, and inversion of the N or P lone pair was used to stabilize the polarity (Fig. 33.17) [32]. Compound **22** contained a nitrogen atom in its center and three urea moieties were introduced. Compound **23** contained phosphorus atom in its center and three amide moieties were introduced. We expected a large threshold between the two ferroelectric polar states for these compounds with an observed ferroelectricity in their CLC phases. However, these compounds exhibited no LC phase between the crystal and liquid states. The intermolecular interactions were presumably too strong to generate an LC state.

### 33.1.4 Conclusion

I reviewed ER-CLCs in this chapter. Currently, many scientists in the LC field are studying ER-CLCs. However, creating ER-CLCs using achiral molecules is difficult. Especially, achieving the FCLC phases with both high responsiveness and polar stability is still a tough and fascinating scientific challenge. We have been studying the FCLCs exhibiting both high responsiveness and polar stability in this

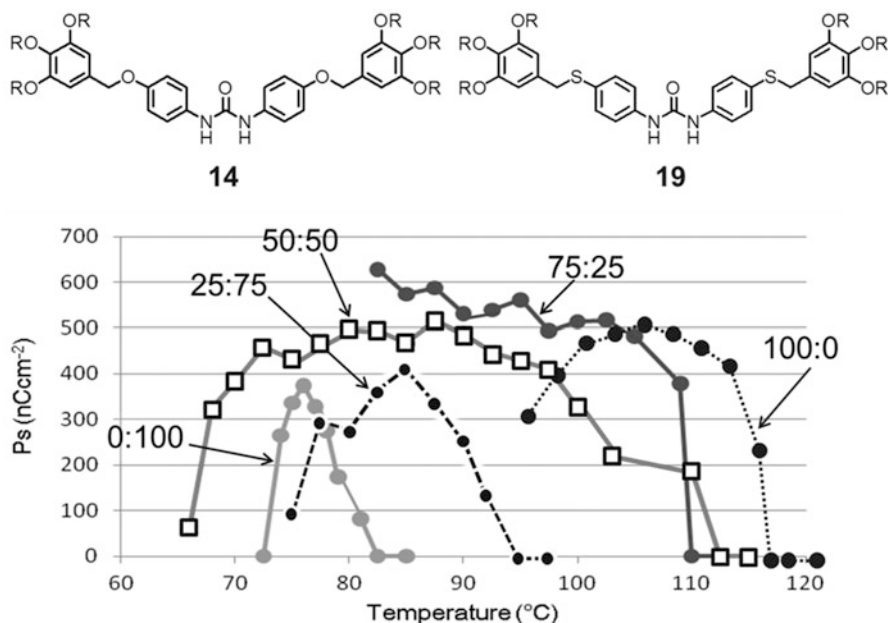


**Fig. 33.16**  $P_s$  values for the mixture of **14** and **19** (0:100, 75:25, 50:50, 25:75, and 0:100) versus temperature

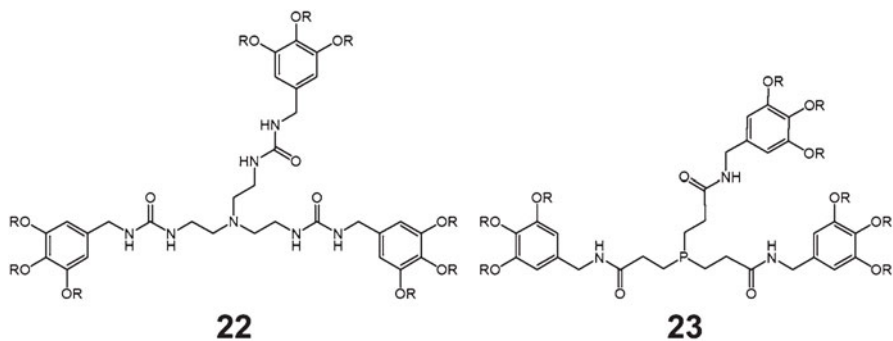


**Fig. 33.17** Molecular structures of **22** and **23**

decade. We believe that designing molecular shape and polarity is important to realize the FCLC phase.

Ferroelectric smectic phases opened a new large field in LC science and LC devices. Similarly, we believe that ER-CLCs will open a new world in LC materials and devices. For example, it can be used in electronic devices, such as high-density memory devices or molecular nano-wires. Further, controlling the surface polarities of the FCLC sheet allows other polar molecules to be arranged on the sheet.

## References

1. H. Takezoe, F. Araoka, *Liq. Cryst.* **41**, 393–401 (2014)
2. H. Takezoe, K. Kishikawa, E. Gorecka, *J. Mater. Chem.* **16**, 2412–2416 (2006)
3. H.M.G. Correia, M.M.D. Ramos, *Ferroelectrics* **338**, 179–184 (2006)
4. E. Fukada, *IEEE Trans. Ultrason. Ferroelectr. Freq. Control* **47**, 1277–1290 (2000)
5. M. Poulsen, S. Ducharme, *IEEE Trans. Dielectr. Electr. Insul.* **17**, 1028–1035 (2010)
6. A.J. Lovinger, *Science* **220**, 1115–1121 (1983)
7. H. Bock, W. Helfrich, *Liq. Cryst.* **12**, 697–703 (1992)
8. J. Malthéte, A. Collet, *J. Am. Chem. Soc.* **109**, 7544–7545 (1987)
9. B. Xu, T.M. Swager, *J. Am. Chem. Soc.* **115**, 1159–1160 (1993)
10. M.L. Bushey, T.Q. Nguyen, C. Nuckolls, *J. Am. Chem. Soc.* **125**, 8264–8269 (2003)
11. M. Ikeda, M. Takeuchi, S. Shinkai, *Chem. Commun.*, 1354–1355 (2003)
12. K. Kishikawa, S. Nakahara, M. Natsukawa, K. Suzuki, S. Kohmoto, *Mol. Cryst. Liq. Cryst.* **516**, 107–113 (2010)
13. K. Kishikawa, S. Nakahara, Y. Nishikawa, S. Kohmoto, M. Yamamoto, *J. Am. Chem. Soc.* **127**, 2565–2571 (2005)
14. Y. Okada, S. Matsumoto, Y. Takanishi, K. Ishikawa, S. Nakahara, K. Kishikawa, H. Takezoe, *Phys. Rev. E* **72**, 020701 (2005)
15. Y. Okada, F. Araoka, Y. Takanishi, K. Ishikawa, S. Nakahara, K. Kishikawa, H. Choi, J.W. Wu, H. Takezoe, *Phys. Rev. E* **75**, 050701 (2007)
16. Y. Okada, S. Matsumoto, F. Araoka, M. Goto, Y. Takanishi, K. Ishikawa, S. Nakahara, K. Kishikawa, H. Takezoe, *Phys. Rev. E* **76**, 041701 (2007)
17. E. Gorecka, D. Pocięcha, J. Mieczkowski, J. Matraszek, D. Guillon, B. Donnio, *J. Am. Chem. Soc.* **126**, 15946–15947 (2004)
18. C. Keith, G. Dantlgraber, R.A. Reddy, U. Baumeister, C. Tschierske, *Chem. Mater.* **19**, 694–710 (2007)
19. D. Kardas, M. Prehm, U. Baumeister, D. Pocięcha, R.A. Reddy, G.H. Mehl, C. Tschierske, *J. Mater. Chem.* **15**, 1722–1733 (2005)
20. R.A. Reddy, V.A. Raghunathan, B.K. Sadashiva, *Chem. Mater.* **17**, 274–283 (2005)
21. C.F.C. Fitié, W.S.C. Roelofs, M. Kemerink, R.P. Sijbesma, *J. Am. Chem. Soc.* **132**, 6892–6893 (2010)
22. T.F.A. de Greef, M.M.L. Nieuwenhuizen, P.J.M. Stals, C.F.C. Fitié, A.R.A. Palmans, R.P. Sijbesma, E.W. Meijer, *Chem. Commun.* **44**, 4306–4308 (2008)
23. D. Miyajima, K. Tashiro, F. Araoka, H. Takezoe, J. Kim, K. Kato, M. Takata, T. Aida, *J. Am. Chem. Soc.* **131**, 44–45 (2009)
24. D. Miyajima, F. Araoka, H. Takezoe, J. Kim, K. Kato, M. Takata, T. Aida, *Angew. Chem. Int. Ed.* **50**, 7865–7869 (2011)
25. K. Sato, Y. Itoh, T. Aida, *J. Am. Chem. Soc.* **133**, 13767–13769 (2011)
26. N. Koizumi, G. Shanker, F. Araoka, K. Ishikawa, C.V. Yelamagad, H. Takezoe, *NPG Asia Mater.* **4**, e11/1–e11/7 (2012)
27. D. Miyajima, F. Araoka, H. Takezoe, J. Kim, K. Kato, M. Takata, T. Aida, *J. Am. Chem. Soc.* **132**, 8530–8531 (2010)
28. D. Miyajima, F. Araoka, H. Takezoe, J. Kim, K. Kato, M. Takata, T. Aida, *Science* **336**, 209–213 (2012)
29. H. Shimura, M. Yoshio, A. Hamasaki, T. Mukai, H. Ohno, T. Kato, *Adv. Mater.* **21**, 1591–1594 (2009)
30. K. Kishikawa, M. Natsukawa, S. Moriyasu, unpublished work
31. K. Kishikawa, S. Moriyasu, unpublished work
32. K. Kishikawa, *Asahi Garasu Zaidan Josei Kenkyu Seika Hokoku*, 26/1–26/6 (2009)

# Chapter 34

## Crystal Engineering Approach Toward Molecule-Based Magnetic Materials

Naoki Yoshioka

**Abstract** The crystal engineering approach toward molecule-based magnetic materials by controlling the molecular arrangement of the stable radical based on the directionality of the hydrogen bonding is described in connection with the magnetic and orbital interactions between the radical units. Several derivatives of 4,4,5,5-tetramethyl-4,5-dihydro-1*H*-imidazole-1-oxyl-3-oxide (NN) carrying a heterocycle having an NH proton donor site at the 2-position were designed. The imidazole derivative, Im-NN, formed a hydrogen-bonded chain, and close contact between the NO bonds of the NN group were observed between the chains. The benzimidazole and naphthoimidazole derivatives, BIm-NN and NIm-NN, formed a 1D assembled structure induced by intra- and intermolecular hydrogen bonds. Magnetic measurements revealed that a strong ferromagnetic interaction existed in BIm-NN, while dimeric and 1D chained antiferromagnetic interactions were observed in Im-NN and NIm-NN, respectively. The magneto-structural correlation of the 4- and 5-azaindole derivatives (4NIn-NN, 5NIn-NN) is also described. In these crystals, the hydrogen bonds and  $\pi$ -stacking have an important role in the crystal scaffolding, and the occurrence of a magnetic interaction is explained by contact of the SOMOs. These results indicate that the NHCC(NO)NO moiety is a useful synthon for propagating intermolecular magnetic interactions.

**Keywords** Crystal engineering • Organic radical • Molecule-based magnetism

### 34.1 Introduction

Modern society is supported by various electronic materials and devices. Such materials and devices are mainly composed of inorganic compounds, such as metals, alloys, metal oxides, silicon, etc. More effort has been devoted to the development of these functional materials composed of molecule-based compounds. For example, the research regarding the molecular conductors and superconductors has achieved

---

N. Yoshioka (✉)

Department of Applied Chemistry, Keio University, Yokohama, Japan

e-mail: [yoshioka@applc.keio.ac.jp](mailto:yoshioka@applc.keio.ac.jp)

© Springer Japan 2015

R. Tamura, M. Miyata (eds.), *Advances in Organic Crystal Chemistry*,

DOI 10.1007/978-4-431-55555-1\_34

significant progress. The combination of organic compounds plus magnetism, on the other hand, is one of the most challenging topics of material science because the magnetic phase transition temperatures of purely organic-based ferromagnets that have been found are still limited to the cryogenic region. Under these circumstances, the research field of molecule-based magnetism has been rapidly developed as an interdisciplinary area involving organic chemistry, coordination chemistry, polymer chemistry, and solid-state physics [1, 2].

The essential condition of a magnetic material is the presence of the spins associated with unpaired electrons. Conventional inorganic magnetic materials are composed of atoms or ions of transition elements, such as iron, cobalt, and nickel, and rare earth elements. These magnets possess unpaired spins that contribute to the magnetic ordering in the atomic d- or f-orbital. Therefore, this magnetism is called atom-based magnetism. Molecule-based magnetism, on the other hand, originates with unpaired electron spins belonging to the p-orbital. Several properties unavailable in conventional inorganic magnets, such as a low density, low environmental contamination, and combination with other molecular functions, are also expected in molecule-based magnetic materials. In addition, the introduction of an unpaired electron into the  $\pi$ -orbital enables the modulation of their magnetic properties by means of synthetic chemistry, as has been applied in the fields of molecular conductors and superconductors.

As for purely organic systems, there are two kinds of approaches to the organic magnet; one is the through-bond approach, and the other is the through-space approach. The through-bond approach [3] is based on constructing a high-spin molecule by aligning spins parallel within the molecule using a magnetic coupler such as the *m*-phenylene unit or  $\pi$ -conjugated polymeric backbone. On the other hand, the essence of the through-space approach is to build a magnetic interaction between the molecules that are proposed by McConnell [4], which expands the possibility of the self-assemblies of radicals and charge-transfer complexes.

In a real system, the through-bond approach corresponds to polyradical macromolecules, and the through-space approach corresponds to organic radical crystals of low-molecular-weight substances (Fig. 34.1). The advantage of polyradical macromolecules is that magnetic interaction pathways within a chain can be controlled by molecular design taking advantage of various synthetic methods. In addition, the magnitude of the intramolecular magnetic interaction is usually more than ten times larger than that of the intermolecular magnetic interaction. A critical problem for polyradical macromolecules is difficulty in controlling the interchain magnetic coupling in the amorphous state. The crystal structures of low-molecular-weight organic radicals, on the other hand, are determined by X-ray crystallographic analyses, which make it possible to precisely and quantitatively examine the magneto-structural correlation. To develop the through-space interaction, we have to develop the technique for constructing molecular self-assemblies with desired magnetic interaction. Although a great progress has been achieved by synthetic chemistry in terms of planning the synthesis of open-shell molecules and the control of electronic properties, the crystal design using crystal engineering technique for that purpose still remains great challenges.

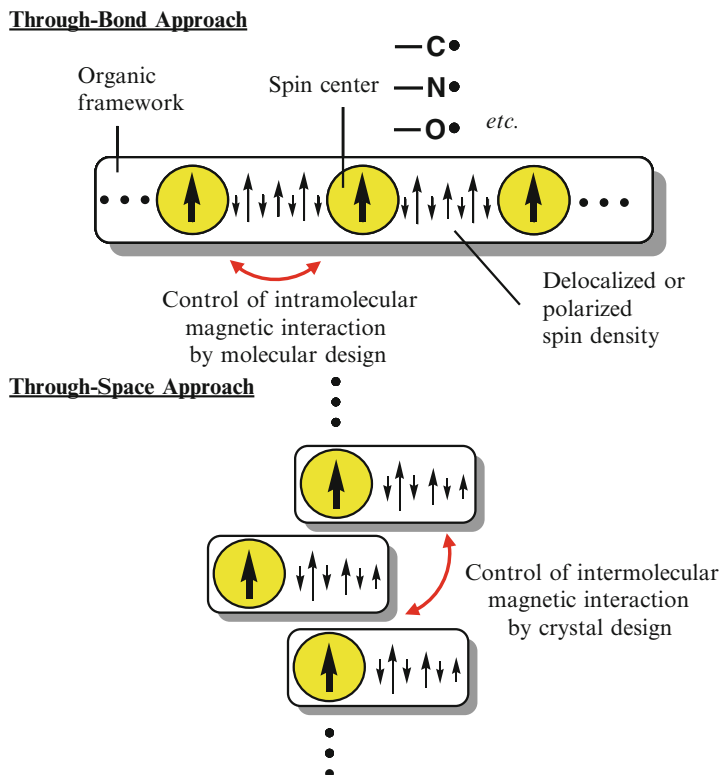


Fig. 34.1 Conceptual scheme for the construction of a molecule-based magnet

## 34.2 Magnetic Measurement of Organic Radical Solid

The magnetic properties of a paramagnetic material including organic radicals are described by the response to the applied magnetic field,  $H$ , and could be characterized by the temperature dependence of the molar magnetic susceptibility,  $\chi_m$ , and field dependence of the molar magnetization,  $M$ . These physical quantities are closely related to the spin quantum number,  $S$ , because the orbital quantum number,  $L$ , is quenched in organic radicals.  $M$  is proportional to  $H$ , and the proportionality constant is  $\chi_m$ .

$$M = \chi_m H \quad (34.1)$$

The temperature dependence of  $\chi_m$  follows the Curie-Weiss expression in Eq. (34.2).

$$\chi_m = \frac{C}{T - \theta} \quad (34.2)$$

$$C = \frac{N_A g^2 \mu_B^2 S(S+1)}{3k_B} \quad (34.3)$$

The Curie constant,  $C$ , is described by Eq. (34.3) in which  $N_A$  is Avogadro's number,  $g$  is the  $g$ -factor,  $\mu_B$  is the Bohr magneton, and  $k_B$  is the Boltzmann constant. The positive or negative value of the Weiss constant,  $\theta$ , corresponds to the ferromagnetic (parallel spin) or antiferromagnetic (antiparallel spin) alignment, respectively.  $\theta = 0$  denotes an independent (noninteracting) spin system. The Curie plot ( $\chi_m$  vs.  $T$ ) and inverse Curie plot ( $\chi_m^{-1}$  vs.  $T$ ) are shown in Fig. 34.2. The latter is convenient for determining  $\theta$  from the intercept. The temperature dependence of  $\chi_m T$  is also useful for estimating the energy gap or magnetic interaction parameter,  $J$ , by fitting the experimental data to the theoretical model as shown below. The temperature dependence of  $M$  is also described by Eq. (34.4).

$$M = N_A g \mu_B S B(x) \quad (34.4)$$

in which  $B(x)$  is the Brillouin function described by Eq. (34.5).

$$B(x) = \frac{2S+1}{2S} \coth\left(\frac{2S+1}{2S}x\right) - \frac{1}{2S} \coth\left(\frac{1}{2S}\right), x = \frac{g\mu_B SH}{k_B T} \quad (34.5)$$

At a high enough applied magnetic field and low temperature,  $x$  becomes very large, and then  $B(x)$  approaches unity. The saturation value of  $M$  is called saturation magnetization,  $M_s$ , as described by Eq. (34.6).

$$M_s = N_A g \mu_B S \quad (34.6)$$

The  $M/M_s$  vs.  $H/T$  plot can be used for estimating the average  $S$  of organic radicals in the solid state by fitting the experimental data to  $B(x)$ . The magnetization behavior is also important for classification of the magnetic state (Fig. 34.3).

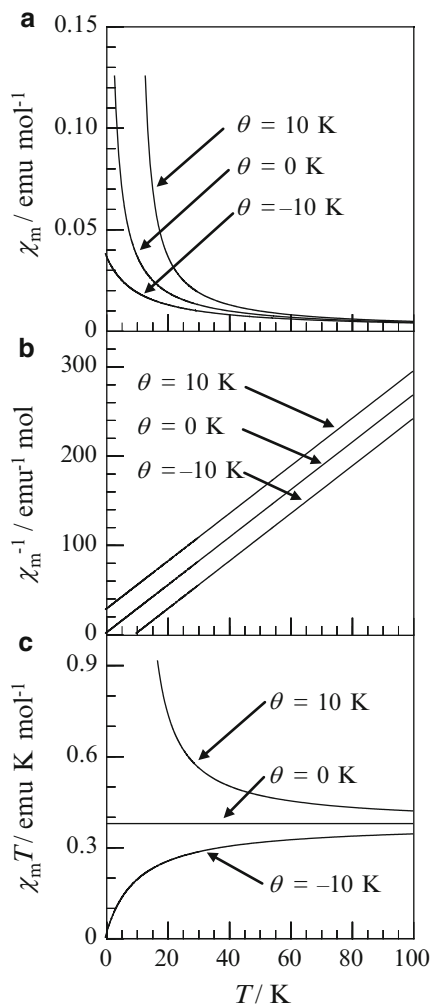
While isolable organic radicals are kinetically stabilized by a substituent, several derivatives might exhibit a magnetic interaction. The formation of a magnetically coupled dimer and chains also affects the temperature dependence of  $\chi_m$ .

If two monoradical molecules ( $S = 1/2$ ) interact in a crystal, the spin quantum numbers become  $S = 0$  and  $S = 1$ .  $E(S = 0)$  and  $E(S = 1)$  are defined as the energies of the two states with an energy gap,  $J$ , defined as

$$J = E(S = 0) - E(S = 1) \quad (34.7)$$

When  $S = 0$  is the ground state corresponding to a negative  $J$  value, the interaction is antiferromagnetic. When  $S = 1$  is the ground state corresponding to a positive  $J$  value, the interaction is ferromagnetic. The magnetic susceptibility of a dimer of a monoradical follows the Bleaney-Bowers equation [5] expressed by Eq. (34.8).

**Fig. 34.2**  $\chi_m$  vs.  $T$  plot (a),  $\chi_m^{-1}$  vs.  $T$  plot (b), and  $\chi_m T$  vs.  $T$  plot (c) for the systems obeying the Curie-Weiss law with a Curie constant  $C = 0.375 \text{ emu K mol}^{-1}$  ( $S = 1/2$ ,  $g = 2.00$ ) and Weiss constant  $\theta = 10, 0$ , and  $-10 \text{ K}$



$$\chi_m = \frac{N_A g^2 \mu_B^2}{k_B T [3 + \exp(-J/k_B T)]} \quad (34.8)$$

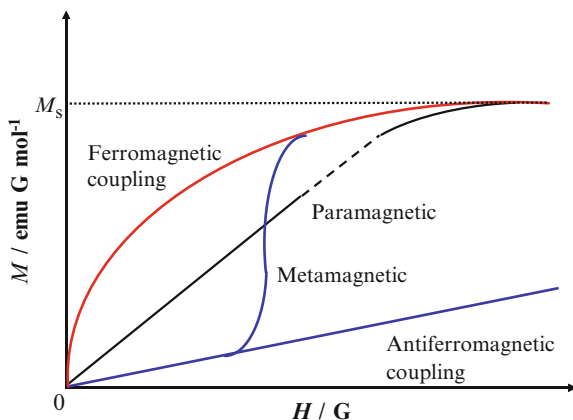
For the 1D chain of an antiferromagnetically coupled organic radical ( $J < 0$ ), its magnetic susceptibility follows the Bonner-Fisher model [6] of Eq. (34.9).

$$\chi_m = \frac{N_A g^2 \mu_B^2}{k_B T} \frac{0.25 + 0.074975x + 0.075235x^2}{1.0 + 0.9931x + 0.172135x^2 + 0.757825x^3}$$

with

$$x = |J|/k_B T \quad (34.9)$$

**Fig. 34.3** Relation between molar magnetization  $M$  and applied field  $H$



For the 1D chain of a ferromagnetically coupled organic radical ( $J > 0$ ), the magnetic susceptibility follows the Baker expression [7] of Eq. (34.10).

$$\chi_m = \frac{N_A g^2 \mu_B^2}{4k_B T} \left[ \frac{1.0 + Ax + Bx^2 + Cx^3 + Dx^4 + Ex^5}{1.0 + Fx + Gx^2 + Hx^3 + Ix^4} \right]^{2/3}$$

$A = 5.7979916, B = 16.902653, C = 29.376885, D = 29.832959, E = 14.036918,$   
 $F = 2.7979916, G = 7.0086780, H = 8.6538644, I = 4.5743114$

with

$$x = J/2k_B T \quad (34.10)$$

In 1963, McConnell proposed a mechanism that is frequently used to explain the magnetic interaction between aromatic radical molecules, which was later called the McConnell I mechanism [4a]. He suggested that magnetic interactions present between two aromatic radicals, A and B, could be described by the Heisenberg Hamiltonian of Eq. (34.11)

$$H^{AB} = - \sum_{ij} J_{ij}^{AB} S_i^A \cdot S_j^B \quad (34.11)$$

in which  $J_{ij}^{AB}$  are the two-center exchange integrals, and the Hamiltonian could be replaced by a simplified form

$$H^{AB} = -S^A \cdot S^B \sum_{ij} J_{ij}^{AB} \rho_i^A \rho_j^B \quad (34.12)$$

in which  $S^A$  and  $S^B$  are the total spin operators for fragments A and B, respectively,  $J_{ij}^{AB}$  are the two-center exchange integrals, and  $\rho_i^A \rho_j^B$  is the product of the atomic

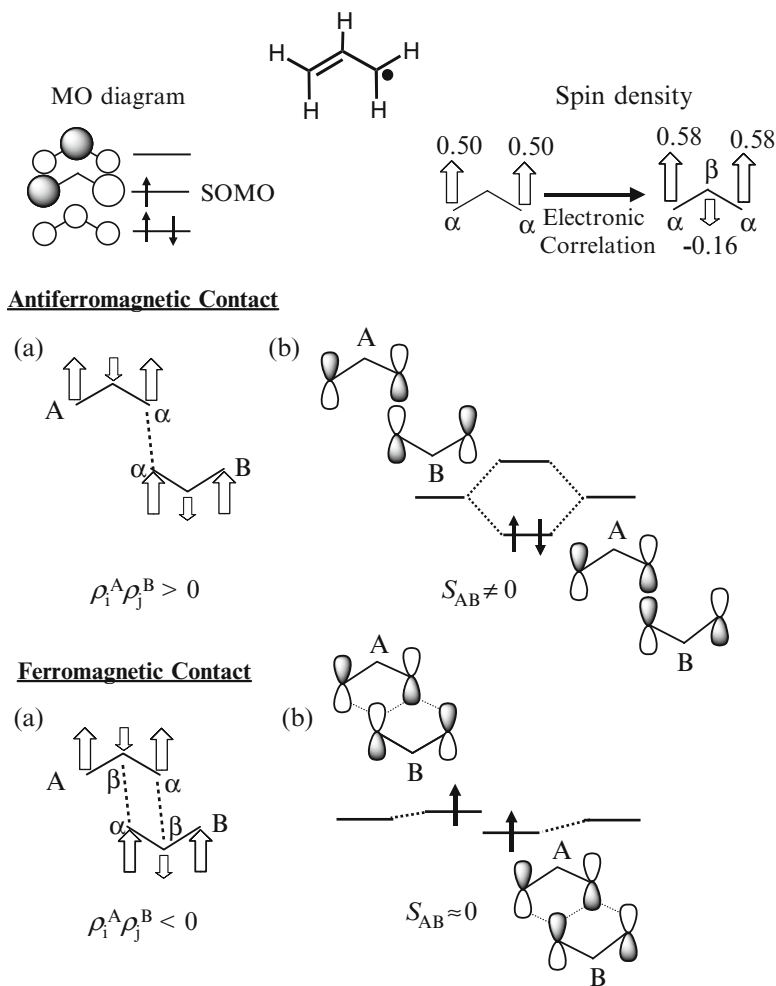


**Fig. 34.4** MO diagram and spin density distribution of allyl radical and interpretation of intermolecular interaction between two allyl radicals by McConnell I mechanism (a) and interaction between SOMOs (b)

spin densities on atoms  $i$  and  $j$  (the first from fragment A and the second from fragment B). The McConnell I mechanism states that a triplet ground state is obtained in the interaction between two doublet fragments when the atoms making the shortest contacts present atomic populations of opposite signs (Fig. 34.4a). Therefore, this mechanism relies on the construction of an organic radical crystal in such a way that atoms with opposite spin densities are aligned on each pair of radicals [8]. The effectiveness of the mechanism has been experimentally evaluated by Iwamura et al. using the cyclophane-type diphenylcarbene dimers [9].

Yoshizawa and Hoffmann explained the intermolecular magnetic interaction by interacting SOMOs [10]. This formulation indicates a ferromagnetic coupling between two radical molecules that can be expected if the two SOMOs are arranged in an orthogonal or nearly orthogonal fashion. This means that the ferromagnetic coupling is stabilized when molecules A and B are arranged in a way to cancel the overlap between the SOMOs ( $S_{AB} \approx 0$ ) (Fig. 34.4b). Based on the two mechanisms, the magnetic interaction of two allyl radicals is shown in Fig. 34.4.

### 34.3 Crystal Engineering Approach

While the possibility of an organic ferromagnet has been theoretically proposed, a magneto-structural correlation of a limited number organic radical crystal has been reported during the 1960s–1970s due to the inaccessibility to crystallographic data (Fig. 34.5). While the formation of a 1D antiferromagnetic chain was demonstrated in the crystal of DPPH [11] and TPV [12], a strong ferromagnetic interaction with a structural phase transition was discovered in the crystal of galvinoxyl [13]. A metamagnetic behavior was also observed in tanol suberate [14].

As mentioned in the previous section, the intermolecular magnetic interaction is very sensitive to molecular packing in the crystal. One presumable cause is that the magnetic properties change with the substituent introduced onto a radical molecule. For example, 1,5-diphenyl-3-(4-nitrophenyl)verdazyl consists of  $\pi$ -stacks between the tetraazapentadienyl moieties and exhibits an intermolecular antiferromagnetic interaction. In a crystal of the 1,5,6-triphenyl derivative, on the other hand, the stack is slid relative to another along the  $b$  direction, leading to an intermolecular

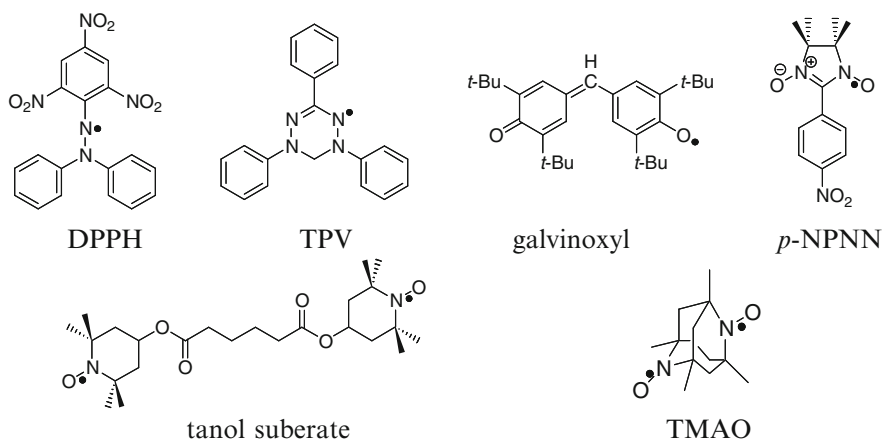


**Fig. 34.5** Chemical structures of typical stable organic radicals exhibiting characteristic magnetic properties

ferromagnetic interaction [15]. Moreover, the magnetic properties are changed when polymorphism is observed even though the molecular structure remains the same. For example, purely organic ferromagnets, *p*-NPNN [16] and TMAO [17], have the crystal polymorphism, and not all polymorphs show the bulk ferromagnetism. These results indicate that it is necessary not only to design organic open-shell molecules carrying unpaired electrons but also to establish the methodology of controlling the molecular arrangement by taking into account the magnetic interaction between the molecules. The problem of *p*-NPNN is that the crystal packing is governed by a van der Waals interaction. The rather weak bonding energy (less than  $1 \text{ kJ mol}^{-1}$ ) and no directionality make the crystal structure uncontrollable.

In order to stabilize the crystal packing, it is necessary to utilize rather strong intermolecular forces, which include a Coulombic force, hydrogen bond, and charge-transfer force. Among these intermolecular forces, the hydrogen bond [18] is suitable for building molecular assemblies because the direction is predictable, and their energies are comparable to thermal energies ( $20\text{--}40 \text{ kJ mol}^{-1}$ ). Such a design strategy for a new solid with the desired physical and chemical properties utilizing intermolecular forces defines crystal engineering [19].

### 34.4 Magnetism of Nitronyl Nitroxide Derivatives with NH Site

The nitronyl nitroxide radical has been recognized as a suitable spin center for organic magnetic materials. Its general structure is a five-membered ring in which two NO radicals are linked to an  $\text{sp}^2$  carbon bonding to a substituent group R (Fig. 34.6) [20]. The NO groups consist of a three-electron nitrogen-oxygen bond, which lead to the thermodynamic stability of the nitroxide groups. R can be a variety of groups including the simplest H to highly functionalized aromatic rings. Each NO group is also linked to an  $\text{sp}^3$  carbon that has two methyl groups, which play a role in the steric hindrance and lead to a kinetic stability. Because of the weak Lewis base character, the two O atoms of NN can be proton acceptor sites to form hydrogen bonds.

We focused our attention on the NN derivatives carrying a heterocycle with the NH site. The basic concept of the molecular design is shown in Fig. 34.7 [21–23].

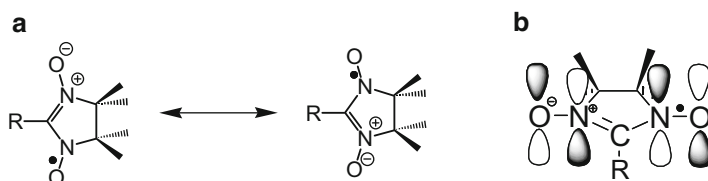
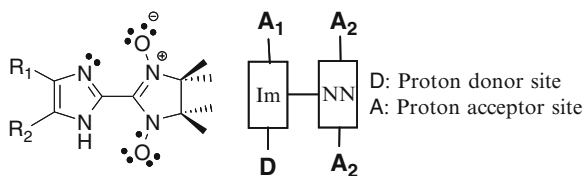


Fig. 34.6 Resonance structure (a) and SOMO distribution (b) of nitronyl nitroxide radical

**Fig. 34.7** Molecular design of nitronyl nitroxide derivative carrying NH site



The hydrogen-bonding pattern can be mainly controlled by the steric or electronic effects of substituents  $R_1$  and/or  $R_2$ . Im-NN derivatives are expected to have two basic hydrogen-bonding motifs due to the competition between the formations of  $A_1 \cdots D$  versus  $A_2 \cdots D$ .

In the first case, an intermolecular hydrogen bond between imidazole rings results in a polymeric chain structure linked by the  $NH \cdots N$  bond as found in Im-NN. The second case occurs when the intermolecular  $NH \cdots ON$  hydrogen bond is preferred [21].

In a crystal of BIm-NN [21], the imine N atom does not participate in the intermolecular hydrogen bonding. The hydrogen bonds are repeated to form a 1D columnar assembly in which close contact between the O atom of the nitroxide and  $sp^2$  C atom of the NN unit is observed. On the other hand, four-centered (trifurcated) intramolecular and intermolecular hydrogen bonds are observed between the NH proton (D), the imine N atom ( $A_1$ ), and nitroxide O atoms ( $A_2$ ) in a crystal of NIm-NN [23]. The hydrogen bonds are repeated to form a 1D chain with edge-to-edge linkage in which close contact between the O atoms of the nitroxide is observed (Fig. 34.8). Plausible mechanism for the formation of “columnar assembly” and “edge-to-edge assembly” is shown in Fig. 34.9.

The geometry of the intramolecular hydrogen bond between the NH site of heterocyclic ring and the O atom of the NO bond has a suitable geometry for the three-center or four-center hydrogen bond but not for the two-center hydrogen bond [24]. This site has further attractive force to other proton acceptor sites. If O atom of other molecule is hydrogen bonded at this site, the formation of self-assembly is realized. Depending on the position of  $sp^2$  C atom of the NN unit, “columnar assembly” or “edge-to-edge assembly” could be constructed.

The magnetic properties of Im-NN, BIm-NN, and NIm-NN are described by the  $\chi_m T$  vs.  $T$  plots in Fig. 34.10. The  $\chi_m T$  value of Im-NN rapidly decreased with a decreasing temperature. This behavior could be fit to the Bleaney-Bowers expression of the magnetic susceptibility for an antiferromagnetically coupled dimer with  $J = -123 \text{ cm}^{-1}$  in Eq. (34.8), taking into account of a fraction of the uncoupled monoradical (0.6 mol %) [21]. On the other hand, the  $\chi_m T$  value of BIm-NN steeply increases with the decreasing temperature. The magnetic data above 4 K fit the Curie-Weiss law, with a Curie constant of  $0.367 \text{ emu K mol}^{-1}$  and a Weiss constant of  $\theta = +8.2 \text{ K}$ . The temperature dependence of  $\chi_m T$  could be fit with a 1D Heisenberg ferromagnetic chain model.

A good fit was obtained for the coupling constant  $J = +12 \text{ cm}^{-1}$  in Eq. (34.10). The presence of a dominant ferromagnetic interaction is also confirmed by the

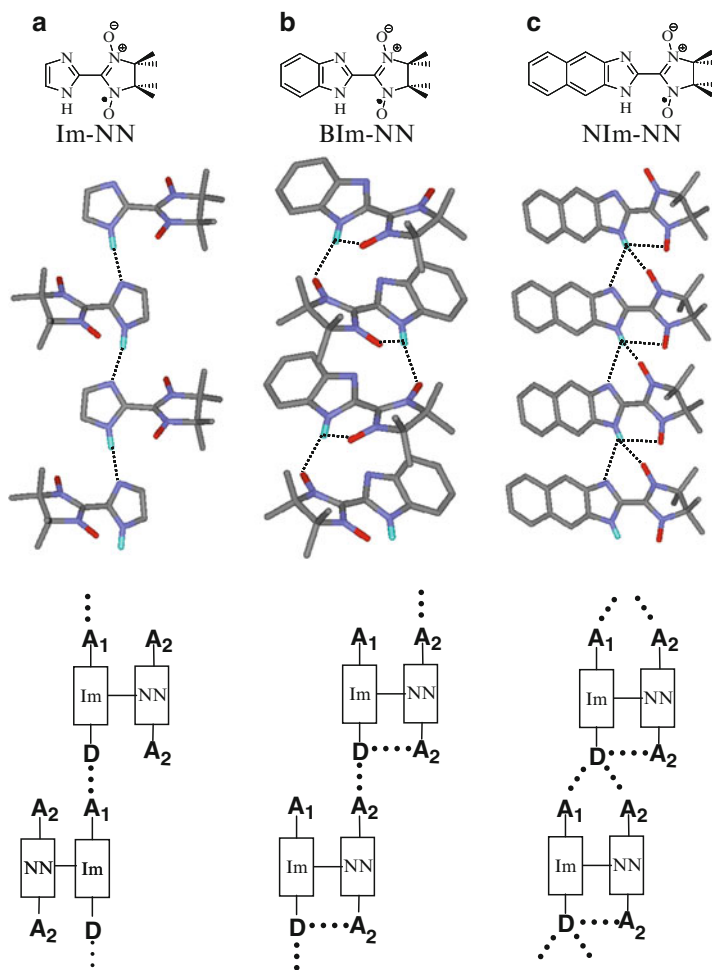


**Fig. 34.8** Crystal structure and hydrogen-bonding motifs of Im-NN (a), BIm-NN (b), and NIm-NN (c). Dashed lines show intramolecular and intermolecular hydrogen bonds

magnetization curve being significantly above the Brillouin function for  $S = 1/2$  (Fig. 34.10 inset) [21]. The magnetic susceptibility of NIm-NN gradually increases as the temperature decreases and has a broad maximum at 12 K. The magnetic data can be fit to the 1D Heisenberg antiferromagnetic chain model with the best fit parameter of  $J = -14 \text{ cm}^{-1}$  in Eq. (34.9) [23].

The magnetic character of Im-NN is reasonably explained by the close intermolecular contact of the ONCNO moieties between the hydrogen-bonded chains: a close contact between atoms, which have the same sign of spin densities, results in the occurrence of an antiferromagnetic interaction (Fig. 34.11a).

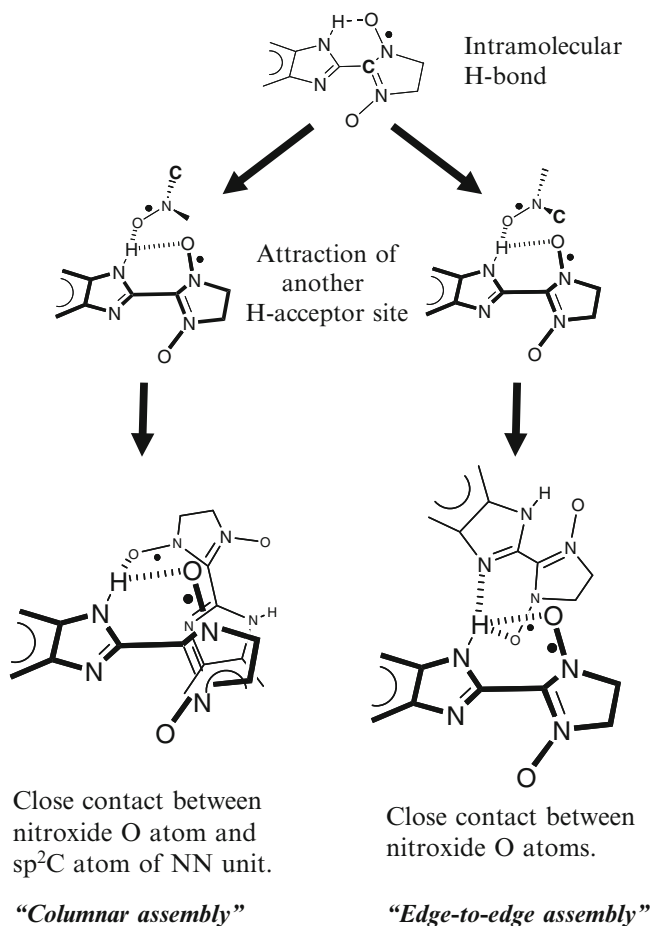


**Fig. 34.9** Plausible mechanisms of the formation of NN self-assembly induced by intra- and intermolecular hydrogen bondings

On the other hand, two magnetic interaction pathways were possible in the crystal of BIm-NN: (1) through the close contact between the nitroxide O atom and  $sp^2$  C atom of the ONCNO moieties (Fig. 34.11b) and (2) through the  $NH \cdots ON$  intermolecular hydrogen bonding [25]. To obtain an in-depth understanding of the magnetic interaction pathway of BIm-NN, the magnetic measurements of NH deuterated sample of BIm-NN and the computational study using the simplified model of BIm-NN were carried out [26, 27]. We have concluded that the  $NH \cdots ON$  hydrogen bonding contributes to stabilizing the molecular arrangement and realize the 1D chain structure. Not the  $NH \cdots ON$  hydrogen bonding but the in-between SOMO-SOMO contributes to the occurrence of the ferromagnetic interaction.

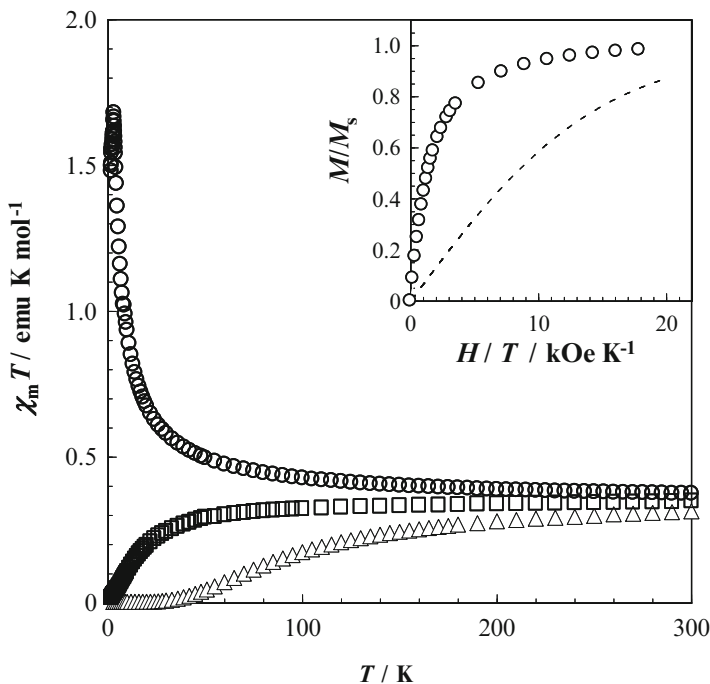


**Fig. 34.10**  $\chi_m T$  vs.  $T$  plots of Im-NN( $\Delta$ ), BiM-NN( $\circ$ ), and NiM-NN( $\square$ ) under the applied field of 5,000 G. The inset shows the magnetization isotherm of BiM-NN at 2.8 K. The broken line corresponds to the calculated curve using the Brillouin function for  $S = 1/2$

$A_1$  does not participate in the intermolecular hydrogen bond. In the crystal of NiM-NN, on the other hand,  $A_1$  does participate in the intermolecular hydrogen bond to form four-centered (trifurcated) intra- and intermolecular hydrogen bonds between D,  $A_1$ , and  $A_2$ . The hydrogen bonds lead to an edge-to-edge molecular arrangement, and the  $O \cdots C$  contact favorable for the occurrence of ferromagnetic interaction is collapsed. The  $O \cdots O$  distance of the nitroxide units along the hydrogen-bonded chain direction is 2.99 Å (Fig. 34.11c). Based on the  $O \cdots O$  distance and the spin densities carried by the nitroxide O atoms, an experimental  $J$  value of  $-14 \text{ cm}^{-1}$  is much smaller than expected. This can be explained by the canted overlap between the  $p_z$  orbitals. The one-dimensional hydrogen-bonded chain observed in the crystal of NiM-NN can be recognized as an ideal one-dimensional spin system because each chain is well isolated by the steric effects of the naphth[2,3-*d*]imidazole ring and four methyl groups.

Lahti et al. have also found that 4,5,6,7-tetrafluorobenzimidazole-nitronyl nitroxide (F4BiM-NN) forms a columnar assemblies similar to BiM-NN and reported ferromagnetic interaction with an intrachain exchange constant of  $J/k_B = +22 \text{ K}$  [28]. Very recently, Sugano, Blundell, et al. and Blundell, Lahti, et al. have reported

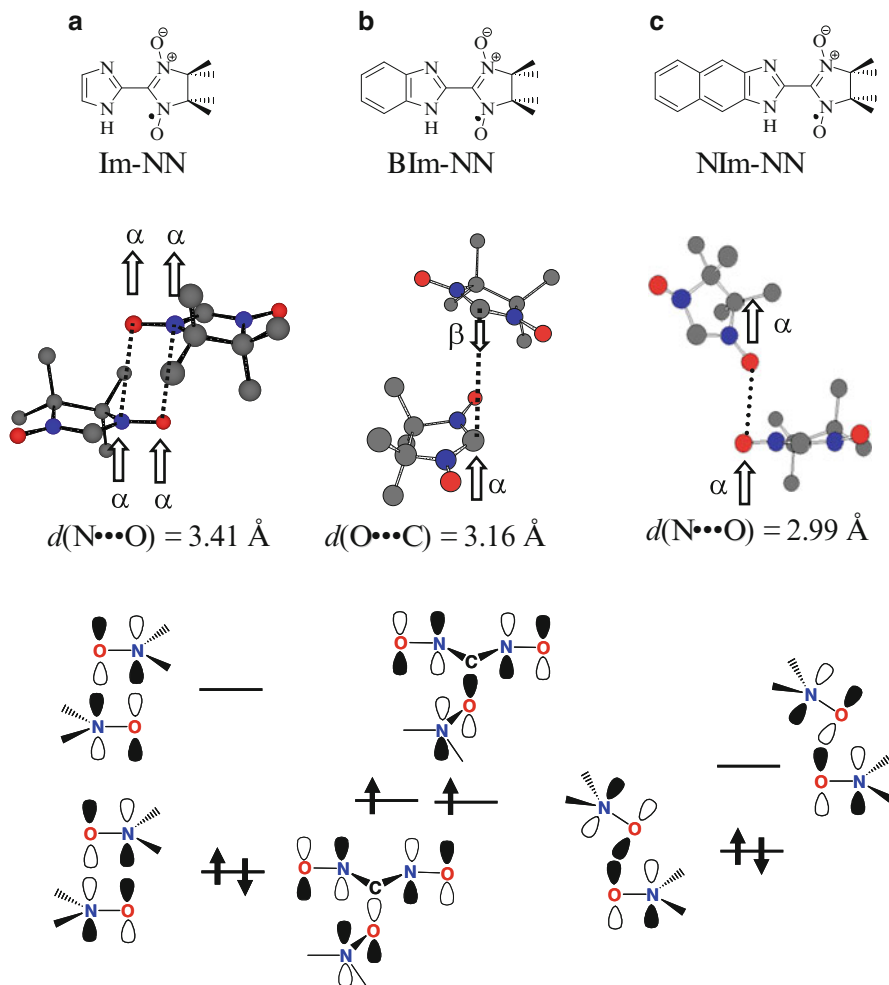


**Fig. 34.11** Magnetic interaction of Im-NN (a), BIm-NN (b), and NIm-NN (c) based on McConnell I mechanism and interaction between SOMOs

a bulk ferromagnetic phase transition of BIm-NN and F4BIm-NN using  $\mu$ SR measurements at  $T_c = 1.0 \text{ K}$  [28e] and  $0.72 \text{ K}$  [29], respectively.

### 34.5 Magnetism of Azaindole Nitronyl Nitroxide Derivatives

In the crystal of BIm-NN, the imine N atom did not participate in the intermolecular hydrogen bond. This fact prompted us to investigate other nitronyl nitroxide derivatives carrying other azaindole rings, which are the structural isomers of the

**Fig. 34.12** Chemical structures of 4NIn-NN and 5NIn-NN

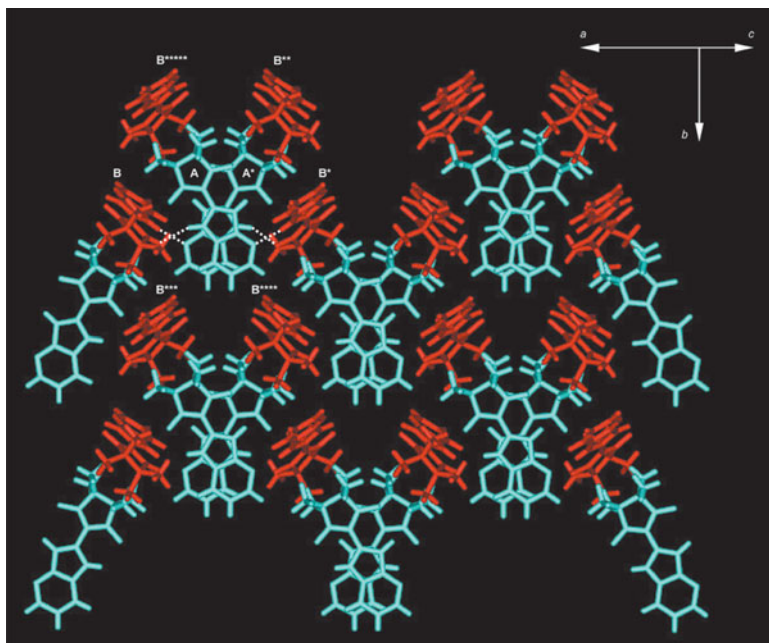
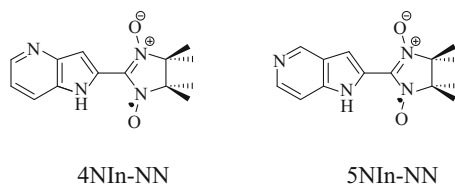


**Fig. 34.13** Crystal packing of 4NIn-NN projected onto the  $ab$  plane. Molecules A and B are colored blue and red, respectively (Ref. [30]; Reproduced by permission of The Royal Society of Chemistry)

benzimidazole ring. In this section, the magneto-structural correlation in the crystals of 4-azaindole nitronyl nitroxide (4NIn-NN) and 5-azaindole nitronyl nitroxide (5NIn-NN) is described [30, 31] (Fig. 34.12).

4NIn-NN crystallizes in the space group  $C2/c$  with two independent molecules (A and B) in the asymmetric unit, containing 16 independent molecules in one unit cell. Crystal packing of 4NIn-NN viewed on the  $ab$  plane and along the  $a$ -axis is shown in Fig. 34.13. A short intermolecular distance between  $N \cdots O$  of 2.87 Å is found, corresponding to an intermolecular hydrogen bond. The hydrogen-bonding motif is repeated to form a noticeable chain structure along the  $a$ -axis. These hydrogen bonds trigger rather short  $O \cdots O$  contacts of 3.27 Å. However, the orbital overlap between the SOMOs is expected to be small by taking into account the large dihedral angle between the neighboring ONCNO moieties of  $63.0^\circ$ .

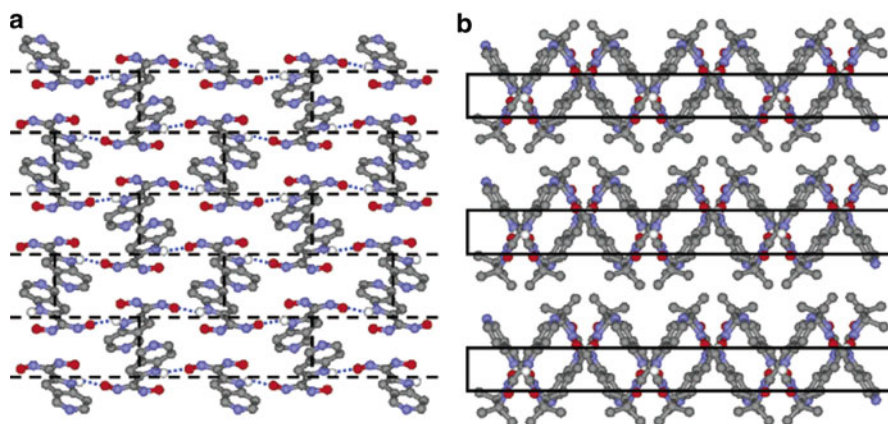
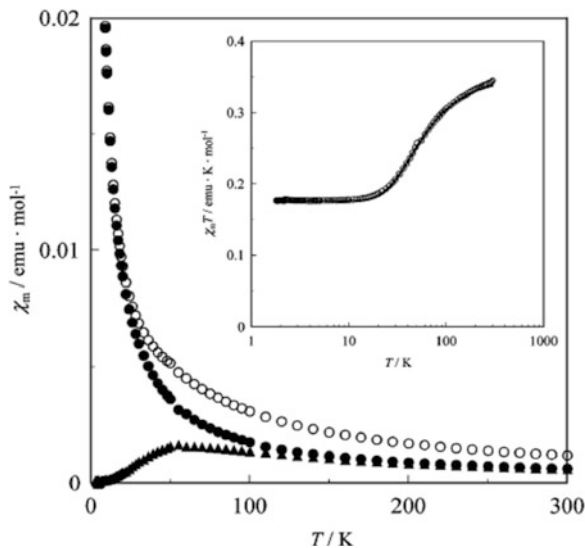


**Fig. 34.14** Crystal packing of 5NIn-NN viewed on the  $ab$  plane (a) and viewed along the  $a$ -axis (b). All the hydrogen atoms except for the NH site are omitted for clarity. The blue dotted lines represent intermolecular hydrogen bonding, and the black dotted lines highlight the brick-wall architecture. The black rectangle highlights the brick-wall stacking along the  $a$ -axis (Reprinted with permission from Ref. [31]. Copyright 2014 American Chemical Society)

5NIn-NN crystallizes in the space group  $P2_1/a$  with four molecules in a unit cell. The dihedral angle between the best planes of the pyrrole ring and the ONCNO moiety is  $7.0^\circ$ . When compared to the corresponding angle between the imidazole ring and the ONCNO moiety of  $24.3^\circ$  for BIm-NN, such a high coplanarity is the common characteristic for the azaindol-2-yl nitronyl nitroxide derivatives; e.g., the corresponding dihedral angles of 4NIn-NN are  $3.3^\circ$  and  $5.8^\circ$ . This characteristic is explained by the concomitance of the intramolecular hydrogen bonds at  $C-H \cdots O-N$  and  $N-H \cdots O-N$ . Between the hydrogen-bonded chains, a relatively close intermolecular contact is observed, corresponding to  $\pi$ -stacking between the 5-azaindole ring and ONCNO moieties. The calculated dipole moments for 4-, 5-, 6-, and 7-azaindoles are 4.15, 4.64, 3.81, and 1.64 debye, respectively, indicating that the 5-azaindole ring has the highest dipole moment among the azaindoles. This tendency has already been pointed out by Catalán et al. [32]. The introduction of an N atom at the 5-position of the indole ring seems to make 5NIn-NN easier to  $\pi$ -stack rather than form a hydrogen bond. The  $N(H) \cdots O$  hydrogen bond and  $\pi$ -stack form a two-dimensional brick-wall architecture on the  $ab$  plane (Fig. 34.14a) in the crystal. The layers pile along the  $a$ -axis while facing the four methyl groups of nitronyl nitroxide units (Fig. 34.14b). Because no contact between the ONCNO moieties within  $4.2 \text{ \AA}$  is observed between the layers, a strong interlayer magnetic interaction caused by direct orbital overlap of the SOMO would not be expected.

The  $\chi_m T$  vs.  $T$  plot of the polycrystalline sample of 4NIn-NN is shown in Fig. 34.15 inset. At 300 K,  $\chi_m T$  equals  $0.34 \text{ emu} \cdot \text{K} \cdot \text{mol}^{-1}$ , slightly less than what would be expected for an isolated monoradical ( $0.375 \text{ emu} \cdot \text{K} \cdot \text{mol}^{-1}$ ). This value decreases with the decreasing temperature down to *ca.* 10 K then becomes nearly constant ( $0.18 \text{ emu} \cdot \text{K} \cdot \text{mol}^{-1}$ ) below this temperature, corresponding to half the

**Fig. 34.15** Temperature dependence of  $\chi_m$  of 4NIn-NN ( $\circ$ ) and its deconvolution into paramagnetic ( $\bullet$ ) and antiferromagnetic ( $\blacktriangle$ ) components. The inset shows the  $\chi_m T$  vs.  $T$  plot. The solid line corresponds to the best-fit parameters (Ref. [30]; Reproduced by permission of The Royal Society of Chemistry)



value expected for an isolated monoradical ( $0.19 \text{ emu} \cdot \text{K} \cdot \text{mol}^{-1}$ ). These results suggest the existence of two magnetic sub-lattices, in which the radicals are magnetically independent or antiferromagnetically interact. In order to clarify the magnetic interaction, the paramagnetic component was subtracted from the experimental Curie plot as shown in Fig. 34.15. The residual component has a broad maximum at *ca.* 55 K and approaches  $0 \text{ emu} \cdot \text{K} \cdot \text{mol}^{-1}$  as the temperature decreases, suggesting a presence of antiferromagnetically coupled dimer system. The magnetic data can be nicely fit to a combined model with the Bleaney-Bowers expression in Eq. (34.8) and Curie's law as described in Eq. (34.2). The best-fit parameters are a singlet-triplet energy gap of  $J = -64 \text{ cm}^{-1}$  in Eq. (34.8). Calculation of the A-A\* dimer found a singlet ground state with  $J = -50.2 \text{ cm}^{-1}$ , thus providing good agreement with that obtained from the experimental results ( $J = -64 \text{ cm}^{-1}$ ). This calculation supports the discussion that the magnetic interaction expected from the correlation between the crystal structure and spin density distribution is reasonable. Calculations for the A-B and A-B\* (or A\*-B) dimers, on the other hand, found  $J = \pm 0.0 \text{ cm}^{-1}$  for both dimers, showing that these contacts do not contribute to the magnetic character. Even though small spin densities were observed for the N and H atoms of the 4-azaindole unit from the solution ESR spectrum and the result is supported by the DFT calculation, the densities were probably too low to affect the solid-state magnetic measurements.

Let us now consider the magnetic coupling mechanism of 4NIn-NN. According to the DFT calculations mentioned above,  $\alpha$  spin densities are induced on the N and O atoms of the nitronyl nitroxide unit. The close contact between atoms on which spin densities of the same sign are induced causes an antiferromagnetic interaction according to the McConnell I mechanism [4a]. When this mechanism is applied to the A-A\* dimer, an antiferromagnetic interaction seems plausible. However, the

magnitude of the magnetic interaction,  $J = -64 \text{ cm}^{-1}$  for 4NIn-NN, is smaller than that expected from the  $\text{N}\cdots\text{O}$  distance of  $3.58 \text{ \AA}$  of the nitronyl nitroxide units when compared to Im-NN for which  $J = -123 \text{ cm}^{-1}$  and the separation is  $3.41 \text{ \AA}$  [21];  $J$  for 4NIn-NN was only half the value found for Im-NN. In the magnetically interacting dimer observed in the crystal of Im-NN,  $\pi$ -stacking between imidazole units was not found, instead radical units approached in a head-to-head fashion. In the A-A\* dimer observed in the crystal of 4NIn-NN, on the other hand, the axis of symmetry enables the 4-azaindole units to  $\pi$ -stack as well as the nitronyl nitroxide units. These computational results support the notion that the magnetic interaction through the induced spin density on the 4-azaindole unit contributes to weakening the antiferromagnetic interaction on the A-A\* dimer.

The temperature dependence of the magnetic susceptibility was measured for a polycrystalline sample of 5NIn-NN in the temperature range of 1.8–300 K. Figure 34.15 shows the  $\chi_m T$  vs.  $T$  plot measured under the applied field of 5.0 kG. The  $\chi_m T$  value slightly increases when the temperature decreases to *ca.* 30 K, showing the occurrence of a very weak but noticeable ferromagnetic interaction. The magnetic data from 30 to 100 K obey the Curie-Weiss law with a Curie constant of  $0.367 \text{ emu} \cdot \text{K} \cdot \text{mol}^{-1}$  and a positive Weiss constant of  $+0.6 \text{ K}$ , indicating that the intralayer interaction is ferromagnetic. Below *ca.* 20 K, however, the  $\chi_m T$  value suddenly decreases and reaches  $0.102 \text{ emu} \cdot \text{K} \cdot \text{mol}^{-1}$  at 1.8 K with lowering temperature, suggesting an interlayer antiferromagnetic interaction. The  $\chi_m - T$  plot (Fig. 34.16a inset) shows a cusp around 3.0 K, which disappears under the high external magnetic field of 30 kG. This indicates that a transition from the antiferromagnetic to ferromagnetic state occurs under an adequately high applied field below 3.0 K. Figure 34.16b shows the low-temperature magnetization curves

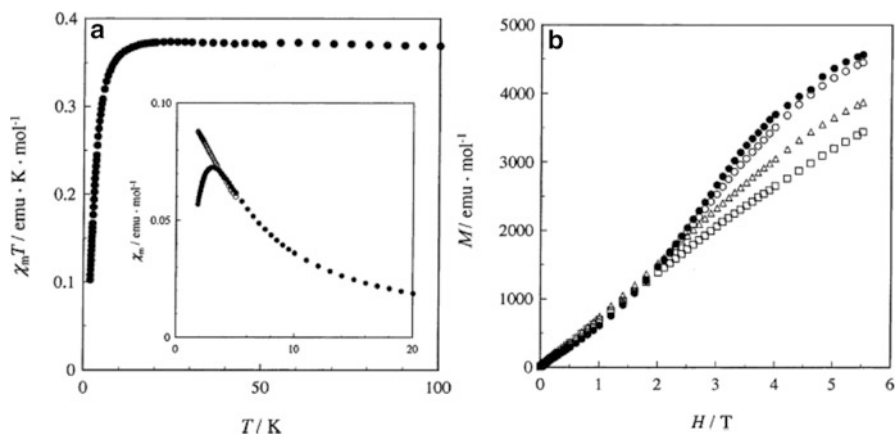


**Fig. 34.16** (a)  $\chi_m T$  vs.  $T$  plot of 5NIn-NN measured under the applied field of 5.0 kG. Inset shows  $\chi_m$  vs.  $T$  plots measured at 5.0 kG ( $\bullet$ ) and 30 kG ( $\circ$ ). (b) Low-temperature magnetization curves of measured at 1.8 K ( $\bullet$ ), 2.0 K ( $\circ$ ), 3.0 K ( $\Delta$ ), and 4.0 K ( $\square$ ) (Reprinted with permission from Ref. [31]. Copyright 2014 American Chemical Society)

at 1.8, 2.0, 3.0, and 4.0 K. At 1.8 K and 2.0 K, we can clearly confirm the S-shape dependence on the magnetic field characteristic for metamagnetic materials.

It is difficult to clearly discuss the nature of the intralayer ferromagnetic interaction because the magnitude of the ferromagnetic interaction is rather weak. The hydrogen bond between the NH proton and the nitroxide O atom might propagate the ferromagnetic interaction due to the close contact between the atoms on which the opposite sign of the spin densities is induced that causes the ferromagnetic interaction based on the McConnell I mechanism [4a]. On the other hand, each layer is separated by facing the four methyl groups of the nitronyl nitroxide unit. The occurrence of an interlayer antiferromagnetic interaction is understandable by taking into account the negative spins polarized on the H atoms of the methyl groups due to the close contact between the atoms on which the same sign of the spin densities is induced that causes the antiferromagnetic interaction.

## 34.6 Conclusions

We succeeded in finding NN derivatives carrying NH-heterocycles that exhibit interesting magnetic properties. These derivatives were crystallized to form a self-assembly exhibiting a strong intermolecular magnetic interaction. The correlation between crystal structure and magnetic property was rationalized. We also showed that the NHCC(NO)NO moiety including hydrogen-bonding sites works effectively as a “supramolecular synthon” for propagating intermolecular magnetic interaction.

**Acknowledgments** N.Y. thanks Professor S. Ohba (Keio University) for the collaboration on crystallographic study and Dr. H. Nagashima for his experimental support and productive comments. This work was partly supported by Grants-in-Aid for Scientific Research from the Ministry of Education, Culture, Sports, Science and Technology, Japan.

## References

1. For selected books: (a) O. Kahn, *Molecular Magnetism* (VCH, New York, 1993); (b) P.M. Lahti, *Magnetic Properties of Organic Materials* (Marcel-Dekker, New York, 1999); (c) K. Itoh, M. Kinoshita, *Molecular Magnetism New Magnetic Materials* (Kodansha Gordon and Breach Science Publishers, Tokyo, 2000); (d) J.S. Miller, M. Drillon, *Magnetism: Molecules to Materials*, vol. 1–5 (Wiley, Weinheim, 2001); (e) R. Hicks, *Stable Radicals: Fundamental and Applied Aspects of Odd-Electron Compounds* (Wiley, New York, 2010)
2. For selected reviews: (a) J.S. Miller, A.J. Epstein, W.M. Reiff, *Chem. Rev.* **88**, 201 (1988a); (b) J.S. Miller, A.J. Epstein, W.M. Reiff, *Acc. Chem. Res.* **21**, 114 (1988b); (c) H. Iwamura, *Adv. Phys. Org. Chem.* **26**, 179 (1990); (d) D.A. Dougherty, *Acc. Chem. Res.* **24**, 88 (1991); (e) H. Iwamura, N. Koga, *Acc. Chem. Res.* **26**, 346 (1993); (f) J.S. Miller, A.J. Epstein, *Angew. Chem. Int. Ed. Engl.* **33**, 385 (1994); (g) A. Rajca, *Chem. Rev.* **94**, 871 (1994); (h) M. Baumgarten, K. Müllen, *Top. Curr. Chem.* **169**, 1 (1994); (i) J.A. Crayston, J.N. Devine, J.C. Walton, *Tetrahedron* **56**, 7829 (2000); (j) P.M. Lahti, *Adv. Phys. Org. Chem.* **45**, 93–169 (2011); (k) P. Bujak, I. Kulszewicz-Bajer, M. Zagorska, V. Maurel, I. Weiglus, A. Pron, *Chem. Soc. Rev.* **42**, 8895 (2013)

3. (a) H.C. Longuet-Higgins, *J. Phys. Chem.* **18**, 265 (1950); N. Mataga, *Theor. Chim. Acta* **10**, 372 (1968); (b) W.T. Borden, E.R. Davidson, *J. Am. Chem. Soc.* **115**, 8928 (1977); (c) A.A. Ovchinnikov, *Theor. Chim. Acta* **47**, 297 (1978); (d) K. Itoh, *Pure Appl. Chem.* **50**, 1251 (1978); (e) N. Tyutyulkov, O.E. Polansky, P. Schuster, S. Karabunarliev, C.I. Ivanov, *Theor. Chim. Acta* **67**, 211 (1985)
4. (a) H.M.J. McConnell, *J. Chem. Phys.* **1963**, 39 (1910); (b) H.M. McConnell, *Proc. Robert A. Welch Found Conf. Chem. Res* **11**, 144 (1967)
5. B. Bleaney, K.D. Bowers, *Proc. R. Soc. Lond Ser. A* **214**, 451 (1952)
6. J.C. Bonner, M.E. Fishier, *Phys. Rev.* **135**, A640 (1964)
7. G.A. Baker Jr., G.S. Rushbrooke, H.E. Gilbert, *Phys. Rev.* **135**, A1272 (1964)
8. (a) K. Yamaguchi, H. Fukui, T. Fueno, *Chem. Lett.* **15**, 625 (1986); (b) K. Tanaka, T. Takeuchi, K. Yoshizawa, M. Toriumi, T. Yamabe, *Synth. Met.* **44**, 1 (1991); (c) J.J. Novoa, M. Deumal, *Struct. Bond.* **100**, 33 (2001)
9. T. Sugawara, H. Tsukada, A. Izuoka, H. Iwamura, *J. Am. Chem. Soc.* **107**, 1786 (1985)
10. K. Yoshizawa, R. Hoffmann, *J. Am. Chem. Soc.* **117**, 6921 (1995)
11. W. Duffy, D.L. Strandburg, *J. Chem. Phys.* **46**, 456 (1967)
12. N. Azuma, J. Yamauchi, K. Mukai, H. Ohya-Nishiguchi, *Bull. Chem. Soc. Jpn.* **46**, 2728 (1973)
13. (a) K. Mukai, *Bull. Chem. Soc. Jpn.* **42**, 40 (1969); (b) K. Awaga, T. Sugano, M. Kinoshita, *Solid State Commun.* **57**, 453 (1986); (c) K.M. Chi, J.C. Calabrese, J.S. Miller, S.I. Khan, *Mol. Cryst. Liq. Cryst.* **176**, 185 (1989)
14. C. Veyret, A. Blaise, *Mol. Phys.* **25**, 873 (1973)
15. P.M. Allemand, G. Srdanov, F. Wudl, *J. Am. Chem. Soc.* **112**, 9391 (1990)
16. M. Kinoshita, *Jpn. J. Appl. Phys.* **33**, 5718 (1994)
17. R. Chiarelli, M.A. Novak, A. Rassat, J.L. Tholence, *Nature* **363**, 147 (1993)
18. T. Steiner, *Angew. Chem. Int. Ed.* **41**, 48 (2002)
19. (a) G.R. Desiraju, *Angew. Chem. Int. Ed. Engl.* **34**, 2311 (1995); (b) B. Moulton, M. Zaworotko, *Chem. Rev.* **101**, 1629 (2001); (c) N. Blagden, R. Davey, *J. Cryst. Growth. Des.* **3**, 873 (2003); (d) G.R. Desiraju, *J. Am. Chem. Soc.* **135**, 9952 (2013)
20. (a) E.F. Ullman, J.H. Osiechi, D.G.B. Boocock, R. Darcy, *J. Am. Chem. Soc.* **94**, 7049 (1972); (b) A. Caneschi, D. Gatteschi, P. Rey, *Prog. Inorg. Chem.* **39**, 331 (1991)
21. N. Yoshioka, M. Irisawa, Y. Mochizuki, T. Kato, H. Inoue, S. Ohba, *Chem. Lett.* **26**, 251 (1997)
22. N. Yoshioka, N. Matsuoka, M. Irisawa, S. Ohba, H. Inoue, *Mol. Cryst. Liq. Cryst.* **334**, 239 (1999)
23. H. Nagashima, H. Inoue, N. Yoshioka, *J. Phys. Chem. B* **108**, 6144 (2004)
24. R. Taylor, W. Versichel, *J. Am. Chem. Soc.* **106**, 244 (1984)
25. (a) K. Yamaguchi, M. Okumura, J. Maki, T. Noro, H. Namimoto, M. Nakano, T. Fueno, K. Nakasuji, *Chem. Phys. Lett.* **190**, 353 (1992); (b) T. Kawakami, S. Takeda, W. Mori, K. Yamaguchi, *Chem. Phys. Lett.* **261**, 129 (1996)
26. H. Nagashima, M. Irisawa, N. Yoshioka, H. Inoue, *Mol. Cryst. Liq. Cryst.* **376**, 371 (2002)
27. H. Nagashima, H. Inoue, N. Yoshioka, *Synth. Met.* **137**, 1257 (2003)
28. (a) H. Murata, D. Zeynep, P.M. Lahti, *Chem. Mater.* **18**, 2625 (2006); (b) H. Murata, Y. Miyazaki, A. Inaba, A. Paduan-Filho, V. Bindilatti, N.F. Oliveira Jr., D. Zeynep, P.M. Lahti, *J. Am. Chem. Soc.* **130**, 186 (2008); (c) G. Seber, G.J. Halder, J.A. Schlueter, P.M. Lahti, *Cryst. Growth Des.* **11**, 4261 (2011); (d) G. Seber, R.S. Fretias, J.T. Mague, A. Paduan-Filho, X. Gratens, V. Bindilatti, N.F. Oliveira, N. Yoshioka, P.M. Lahti, *J. Am. Chem. Soc.* **134**, 3825 (2012); (e) S.J. Blundell, J.S. Moller, T. Lancaster, P.J. Baker, L. Pratt, G. Seber, P.M. Lahti, *Phys. Rev. B* **88**, 064423 (2013)
29. (a) S. Sharmin, S.J. Blundell, T. Sugano, A. Ardavan, *Polyhedron* **24**, 2360 (2005); (b) T. Sugano, S.J. Blundell, T. Lancaster, F.L. Pratt, H. Mori, *Phys. Rev. B* **82**, 180401 (2010)
30. H. Nagashima, N. Hashimoto, H. Inoue, N. Yoshioka, *New J. Chem.* **27**, 805 (2003)
31. H. Nagashima, S. Fujita, H. Inoue, N. Yoshioka, *Cryst. Growth Des.* **4**, 19 (2004)
32. J. Catalán, O. M6, P. Pérez, M. Yáñez, *Tetrahedron* **39**, 2851 (1983)

# Chapter 35

## Observation of Magnetoelectric Effect in All-Organic Ferromagnetic and Ferroelectric Liquid Crystals in an Applied Magnetic Field

Rui Tamura, Yoshiaki Uchida, and Katsuaki Suzuki

**Abstract** We successfully prepared the second generation of chiral rodlike all-organic liquid crystalline (LC) materials with a stable cyclic nitroxide radical unit in the central core position, which showed positive “magneto-LC effects,” a generation of a sort of spin glass-like ferromagnetic interactions (average spin–spin exchange interaction constant  $\bar{J} > 0$ ) induced by low magnetic fields in the various LC phases. By measuring the electric field dependence of EPR spectra of the ferroelectric LC phase which can simultaneously show the positive “magneto-LC effects,” two magnetic bistable states, anisotropy in spin–spin dipole interactions, and “magnetoelectric effect” were observed for the first time in a surface-stabilized liquid crystal cell.

**Keywords** Magnetoelectric effect • Magneto-LC effects • Organic radical liquid crystals • Ferromagnetic liquid crystals • Ferroelectric liquid crystals

### 35.1 Introduction

Liquid crystals (LCs), which are defined as a thermal mesophase between crystalline and isotropic phases and can also be regarded as high-temperature polymorphs of crystals, are unique soft materials that combine fluidity and anisotropy. From another viewpoint, liquid crystalline (LC) phases are considered to be a sort of “complexity” system consisting of nonequilibrium dynamic states due to the molecular motion and the coherent collective properties of molecules in the LC

---

R. Tamura (✉) • K. Suzuki  
Graduate School of Human and Environmental Studies, Kyoto University, Kyoto 606-8501, Japan  
e-mail: [tamura.rii.8c@kyoto-u.ac.jp](mailto:tamura.rii.8c@kyoto-u.ac.jp)

Y. Uchida  
Graduate School of Engineering Science, Osaka University, Toyonaka, Osaka 560-8531, Japan  
PRESTO, Japan Science and Technology Agency, Kawaguchi, Saitama 332-0012, Japan

state. Accordingly, they are so sensitive to external stimuli, such as heat, light, temperature, pressure, electric or magnetic field, and added chiral dopants, that LC superstructure can be easily altered [1–4].

Magnetic LC materials have attracted great interest as soft materials to enhance the effect of magnetic fields on the electric and optical properties of LCs [5–9]. For example, they were anticipated to exhibit unique magnetic interactions and thereby unconventional magnetoelectric [10–13] or magneto-optical [14–16] properties in the LC state. However, there had been no prominent study on this interesting topic, because the majority of magnetic LCs were highly viscous transition or lanthanide metal-containing metallomesogens which were not always appropriate for investigating the molecular alignment in the LC phases in applied magnetic fields [5, 6, 8, 9]. Therefore, we have investigated if metal-free magnetic LC materials with low viscosity can afford the following two possibilities: (i) formation of magnetic domains (or order) in applied magnetic fields and (ii) occurrence of coupling between magnetic dipole and electric dipole moments (magnetoelectric effect) in the LC phases [17–23].

As a consequence, we could discover that all-organic rodlike LC materials with a stable nitroxide radical unit in the central core portion [24, 25] exhibit unique intermolecular ferromagnetic interactions induced by low magnetic fields in the various LC phases, most likely owing to the swift coherent collective properties of organic molecules with structural anisotropy in the LC state [26, 27]. This observation was interpreted in terms of the generation of a sort of spin glass (SG)-like inhomogeneous ferromagnetic interactions (the average spin–spin exchange interaction constant  $\bar{J} > 0$ ) and proved to have nothing to do with the molecular reorientation effects arising from simple molecular magnetic anisotropy ( $\Delta\chi$ ) [27]. This unique magnetic phenomenon was referred to as positive “magneto-LC effects” ( $\bar{J} > 0$ ) [28].

Of various all-organic magnetic LC compounds synthesized, (2*S*,5*S*)-**1** (Fig. 35.1) exhibited a chiral smectic C (SmC\*) phase and showed both excellent ferroelectricity in a surface-stabilized liquid crystal cell and explicit ferromagnetic interactions (positive magneto-LC effects) in the bulk SmC\* phase [25, 27, 30]. Therefore, it was expected that the unique magnetoelectric coupling, which was only observed for inorganic multiferroic materials possessing both ferroelectricity and magnetic order (ferromagnetism or antiferromagnetism) at cryogenic temperatures [10–13], might occur in the ferroelectric LC (FLC) phase of (2*S*,5*S*)-**1** showing the positive magneto-LC effects at high temperatures. In this chapter, we introduce our works on the molecular design of (2*S*,5*S*)-**1** [24, 25] and their ferroelectricity [25, 29–31], magneto-LC effects [26–28, 33, 34], and magnetoelectric effect [34, 35].

## 35.2 Molecular Design and Synthesis [24, 25]

Only a few all-organic radical LC compounds were prepared before 2004, because the geometry and bulkiness of the radical-stabilizing substituents were believed to be detrimental to the stability of LCs which needs molecular linearity and

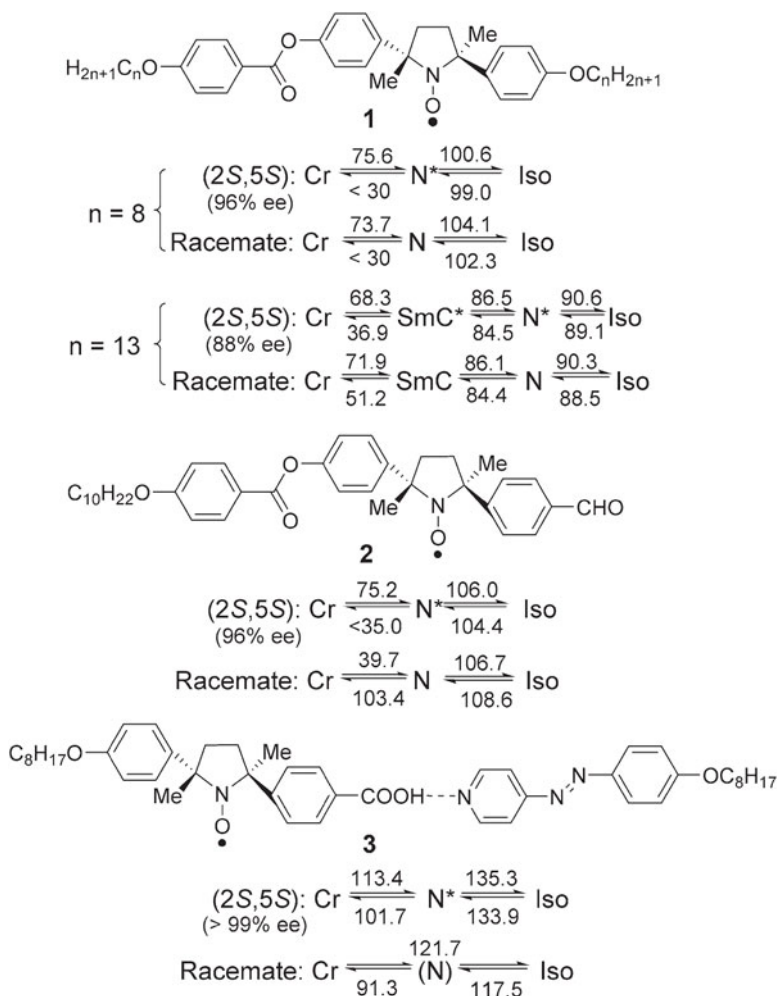


**Fig. 35.1** Molecular structures of compounds 1–3

planarity. Although several first generations of achiral rodlike all-organic LCs with a stable cyclic nitroxide radical unit (DOXYL or TEMPO group) as the spin source were prepared [36–41], their molecular structures were limited to those containing a nitroxyl group in the peripheral position, away from the rigid central core (Fig. 35.2), and thereby allowed the free rotation of the nitroxyl moiety inside the molecule, resulting in a considerable decrease in both paramagnetic anisotropy ( $\Delta\chi_{\text{para}}$ ) and dielectric anisotropy ( $\Delta\epsilon$ ) of the whole molecule.

With this situation in mind, we designed and synthesized the second generation of chiral rodlike all-organic radical LC compounds **1** as the prototype which could satisfy the following three mandatory requirements (Fig. 35.1):

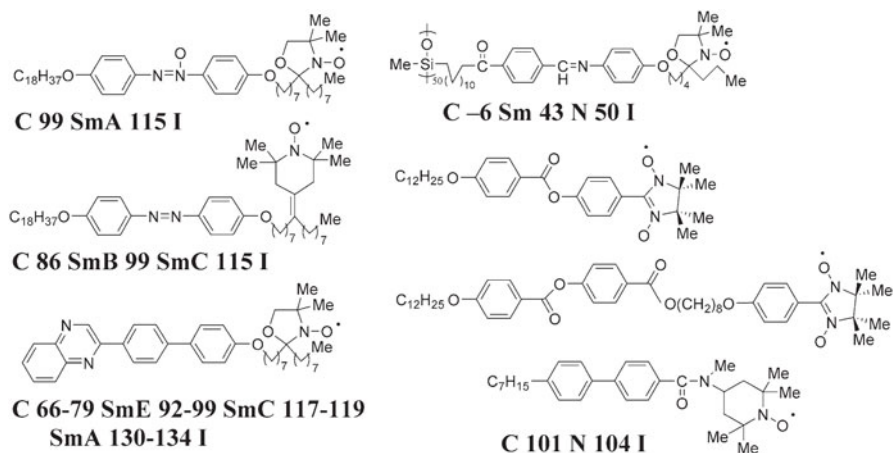


**Fig. 35.2** First generation of rodlike all-organic radical LC compounds

- (1) Spin source: a nitroxyl group with a large electric dipole moment (ca. 3 Debye) and known principal  $g$ -values ( $g_{xx}$ ,  $g_{yy}$ ,  $g_{zz}$ ) should be used as the spin source, because
  - i) the dipole moment is large enough for the source of spontaneous polarization ( $P_s$ ) and
  - ii) the principal  $g$ -values are useful to determine the direction of molecular alignment in the LC phase by EPR spectroscopy.
- (2) High thermal stability: a 2,2,5,5-tetraalkyl-substituted pyrrolidine-1-oxyl (PROXYL) radical structure, which is stable enough for repeated heating and cooling cycles below 150 °C in the air, is the most suitable.
- (3) Molecular structure:
  - i) to avoid the free rotation of the nitroxyl group inside the molecule so as to make use of the  $\Delta\chi_{\text{para}}$  and  $\Delta\varepsilon$ , a geometrically fixed chiral PROXYL radical unit should be incorporated into the rigid core of LC molecules, and
  - ii) to obtain a slightly zigzag molecular structure and a negative  $\Delta\varepsilon$  advantageous for the appearance of an SmC\* phase, a *trans*-2,5-dimethyl-2,5-diphenyl PROXYL radical skeleton in which the electric dipole moment orients to the molecular short axis is the best choice.

We could synthesize both optically active (2*S*,5*S*)-**1** and racemic [(2*S*,5*S*):(2*R*:5*R*) = 1:1] **1** which showed chiral and achiral nematic (N\* and N) phases and/or chiral and achiral smectic C (SmC\* and SmC) phases, respectively.

### 35.3 Ferroelectricity [25, 29–31]

It is well known that an  $\text{SmC}^*$  phase undergoes deformation of the helical superstructure in a thin sandwich cell to show ferroelectric switching by application of electric fields (Fig. 35.3). In fact, the optically active  $(2S,5S)\text{-1}$  ( $n = 11\text{--}15$ ) which showed an  $\text{SmC}^*$  phase indeed exhibited ferroelectricity in a planar anchoring thin sandwich cell ( $4\ \mu\text{m}$  thickness) (Table 35.1). Among them,  $(2S,5S)\text{-1}$  ( $n = 13$ ) showed the best ferroelectric properties with a  $P_s$  value of  $24\ \text{nCcm}^{-2}$ , an optical response time ( $\tau_{10-90}$ ) of  $213\ \mu\text{s}$ , and an ideal layer tilt angle ( $\theta$ ) of  $29^\circ$ . Furthermore, second-harmonic generation (SHG) was clearly observed by Kogo and Takezoe et al. under a phase-matching condition in the  $\text{SmC}^*$  phase of  $(2S,5S)\text{-1}$  ( $n = 13$ ) loaded into an LC cell ( $20\ \mu\text{m}$  thickness), validating the existence of ferroelectricity [42].

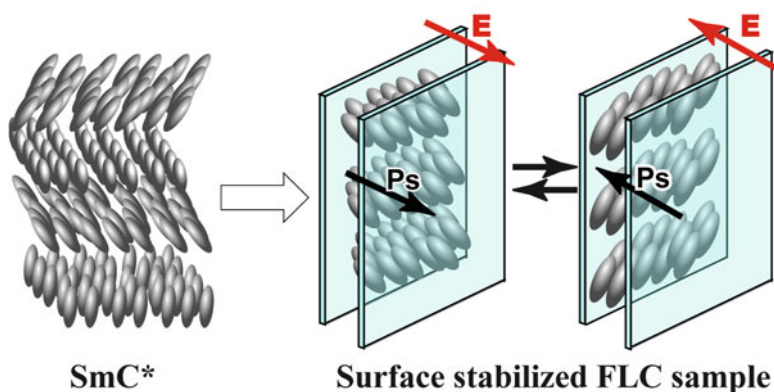


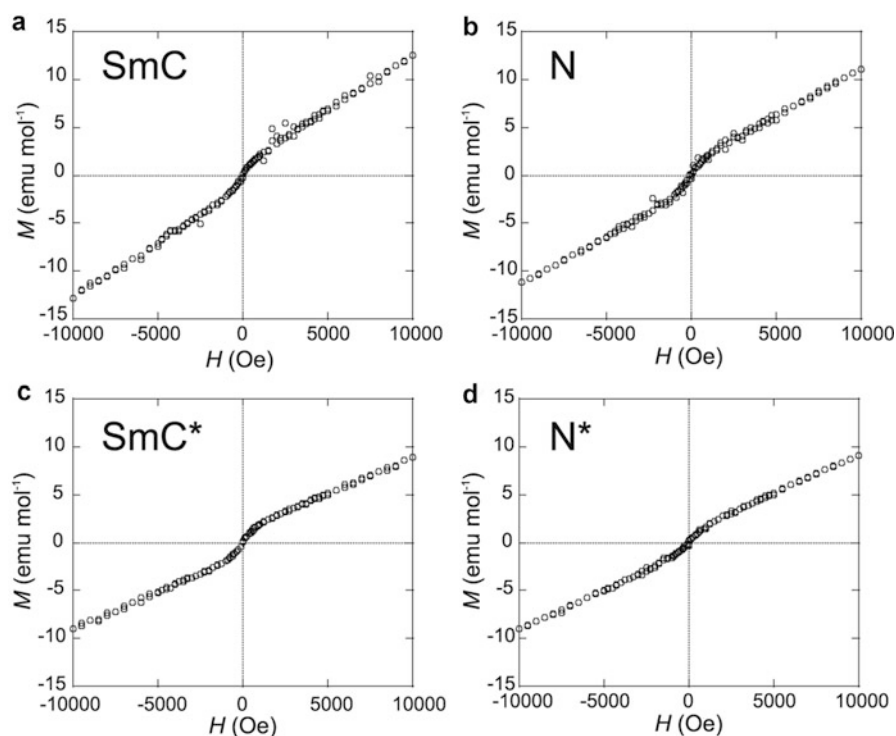
Fig. 35.3 Ferroelectric switching in a thin sandwich cell

Table 35.1 Ferroelectric properties of  $(S,S)\text{-1}$  ( $n = 11\text{--}15$ )

$(S,S)\text{-1}$	Spontaneous polarization	Response time	Viscosity	Tilt angle
$n$	$P_s (-10^\circ)$ [ $\text{nC cm}^{-2}$ ]	$\tau_{10-90} (-10^\circ)$ [ $\mu\text{s}$ ]	$\eta (-10^\circ)$ [ $\text{m Pa s}$ ]	$\theta (-10^\circ)$ [deg]
11	15 ( $74^\circ\text{C}$ )	850	182.1	41
12	18 ( $64^\circ\text{C}$ )	334	85.9	37
13	24 ( $74^\circ\text{C}$ )	213	73.0	29
14	16 ( $79^\circ\text{C}$ )	159	36.3	36
15	17 ( $79^\circ\text{C}$ )	146	35.5	34

### 35.4 Magneto-LC Effects [26–28, 32, 33]

The possibility of a ferromagnetic rodlike LC material had been considered unrealistic due to the inaccessibility of long-range spin–spin interactions between rotating molecules in the LC state [7]. Interestingly, however, a nonlinear relationship between the applied magnetic field ( $H$ ) and the observed magnetization ( $M$ ) in chiral and achiral LC phases of **1** (Fig. 35.4) implies the generation of unusual magnetic interactions in the LC phases under weak magnetic fields. Such a nonlinearity was not observed in the crystalline phases of the same compounds which showed a usual linear relationship indicating a paramagnetic behavior and no contamination of magnetic impurities in the sample. The Arrott–Belov–Kouvel plots ( $M^2$  vs  $H/M$ ) [43, 44] using the same data strongly suggested the generation of a sort of SG-like inhomogeneous magnetic interactions (the average spin–spin exchange interaction constant  $\bar{J} > 0$ ) induced by low magnetic fields in various LC phases of **1** (Fig. 35.5). In fact, these radical LC droplets floating on water were attracted by



**Fig. 35.4** Magnetic field ( $H$ ) dependence of molar magnetization ( $M$ ) at 77 °C for (a) the SmC phase of ( $\pm$ )-**1** ( $n = 13$ ), (b) the N phase of ( $\pm$ )-**1** ( $n = 8$ ), (c) the SmC\* phase of ( $2S,5S$ )-**1** ( $n = 13$ ), and (d) the N\* phase of ( $2S,5S$ )-**1** ( $n = 8$ ) (Reprinted with permission from Ref [27]; Copyright 2014 American Chemical Society)

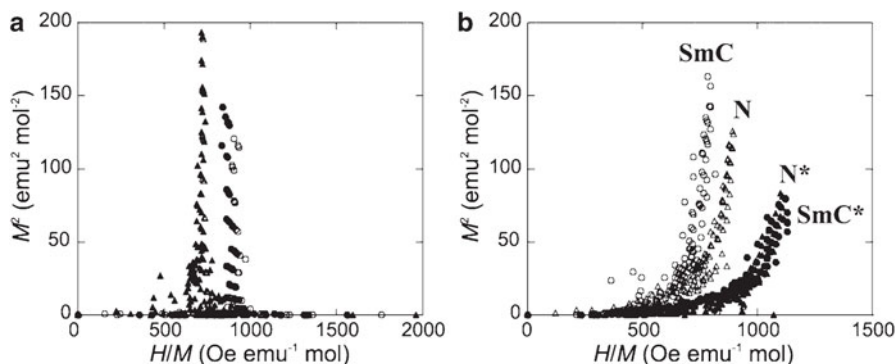


**Fig. 35.5** The Arrott–Belov–Kouvel plots ( $M^2$  vs  $HIM$ ) at 77 °C for (a) the crystalline phases and (b) the LC phases of **1** ( $n = 8, 13$ ) (Reprinted with permission from Ref [27]: Copyright 2014 American Chemical Society)

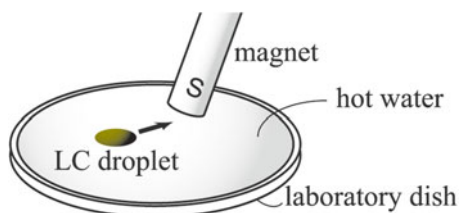


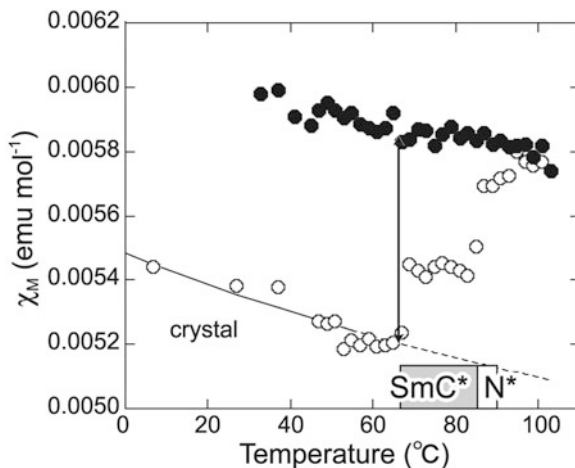
**Fig. 35.6** Schematic representation of the experimental setup for observing the attraction by a permanent magnet (<0.5 T) of a magnetic LC droplet on water in a shallow laboratory dish (Reprinted with permission from Ref [27]: Copyright 2014 American Chemical Society)

a permanent magnet and moved quickly and freely on water under the influence of this magnet (Fig. 35.6), whereas the crystallized particles of the same compounds did not respond to the same magnet.

To directly prove that the magnetic behavior in the LC phase is different from that in the crystalline phase, the temperature dependence of molar magnetic susceptibility ( $\chi_M$ ) was measured for (2*S*,5*S*)-**1** and racemic **1** ( $n = 8$  and 13 each) at a magnetic field of 0.05 T. The  $\chi_M$ – $T$  plots obeyed the Curie–Weiss law in the crystalline phase, while a considerable  $\chi_M$  increase at the Cr-to-LC phase transition was observed for all LC phases examined (Fig. 35.7). This unique magnetic phenomenon was referred to as positive “magneto-LC effects.”

We reported that EPR spectroscopy is much better means than SQUID magnetization measurement to analyze the temperature dependence of the  $\chi_{para}$  for organic nitroxide radical LC materials at high temperatures because of the following three reasons [27]: (1) Treatment of the  $\chi_{dia}$  term is unnecessary. (2) The experimental error is very small even at such high temperatures. (3) The analysis of microscopic magnetic interactions such as spin–spin dipole and exchange interactions is also feasible. For example, on the basis of the EPR spectra for (2*S*,5*S*)-**1** ( $n = 13$ )

**Fig. 35.7** Temperature dependence of molar magnetic susceptibility ( $\chi_M$ ) of (2*S*,5*S*)-**1** ( $n = 13$ , 88 % *ee*) at a field of 0.05 T in the temperature ranges of 0 to +105 °C. Open and filled circles represent the first heating and cooling runs, respectively. The solid lines show the Curie–Weiss fitting curves, while the dotted lines represent the extrapolated curves. An arrow indicates the difference in the  $\chi_M$  between the crystalline and LC states



measured between 25 and 115 °C at a magnetic field of 0.33 T by using a quartz tube, the temperature dependence of relative paramagnetic susceptibility ( $\chi_{rel}$ ), which is defined as

$$\chi_{rel} = \chi_{para} / \chi_0 \quad (35.1)$$

where  $\chi_0$  is the standard paramagnetic susceptibility at 30 °C in the heating run, is shown in Fig. 35.8. Again a considerable  $\chi_{rel}$  increase at the Cr-to-SmC\* phase transition was observed, indicating the generation of positive magneto-LC effects. Furthermore, to gain an insight into the origin of the positive magneto-LC effects operating in the SmC\* phase, the temperature dependence of line-width ( $\Delta H_{pp}$ ) was compared with that of  $\chi_{rel}$  (Fig. 35.9). As a consequence, the  $\chi_{rel}$  increase was accompanied by the large  $\Delta H_{pp}$  increase at the crystal-to-SmC\* phase transition in the heating run. Definitely, strong spin–spin dipole interactions as well as exchange interactions turned out to be responsible for the positive magneto-LC effects. Figure 35.10 shows the relative stability in spin–spin dipole interactions. There are two types; one is a head-to-tail type and the other is a side-by-side type. Since the ferromagnetic head-to-tail dipole interaction is energetically more stable than the antiferromagnetic side-by-side dipole interaction and other two interactions, the origin of positive magneto-LC effects can be interpreted in terms of the resulting ferromagnetic spin–spin dipole interactions induced by magnetic fields in the anisotropic LC superstructure.

To examine the relationship between the signs of  $\Delta\varepsilon$  and magneto-LC effects, (2*S*,5*S*)-**2** and racemic **2** with a terminal formyl group which have a positive  $\Delta\varepsilon$  were synthesized (Fig. 35.1) [28]. Under weak magnetic fields, positive magneto-LC effects ( $\bar{J} > 0$ ) were operated in the chiral N\* phase of (2*S*,5*S*)-**2**, whereas negative magneto-LC effects ( $\bar{J} < 0$ ) were observed in the achiral N phase. The origin of such negative magneto-LC effects operating in the N phase of racemic **2** was interpreted

**Fig. 35.8** Temperature dependence of relative paramagnetic susceptibility ( $\chi_{\text{rel}}$ ) for (2*S*,5*S*)-**1** ( $n = 13$ , 88 % ee) at a magnetic field of 0.33 T. *Open and filled circles* represent the first heating and cooling runs, respectively. The LC temperatures shown in a *box* refer to the first heating process (Reprinted with permission from Ref [27]: Copyright 2014 American Chemical Society)

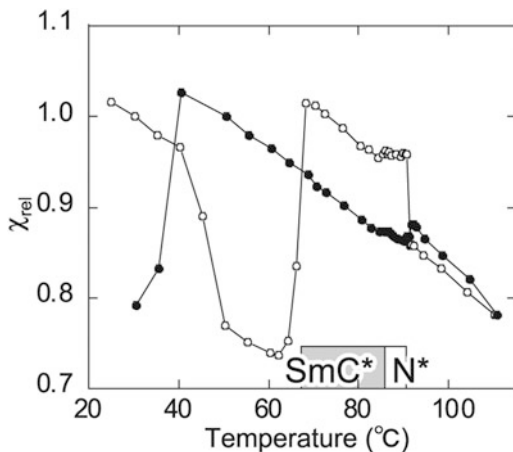
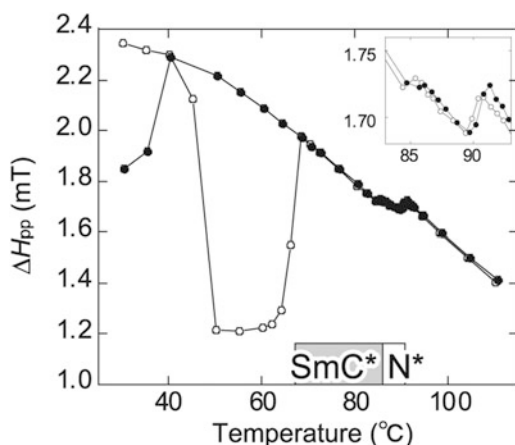


**Fig. 35.9** Temperature dependence of  $\Delta H_{\text{pp}}$  for (2*S*,5*S*)-**1** ( $n = 13$ , 88 % ee) at a magnetic field of 0.33 T. *Open and filled circles* represent the first heating and cooling runs, respectively. The LC temperatures shown in a *box* refer to the first heating process. The *inset* indicates the magnification in the temperature range of 83–93 °C (Reprinted with permission from Ref [27]: Copyright 2014 American Chemical Society)



in terms of the occurrence of antiferromagnetic interactions due to the local SOMO–SOMO overlapping and thereby the side-by-side spin–spin dipole interaction, which is associated with the strong racemic (2*R*,5*R*)/(2*S*,5*S*) dimer formation to cancel the electric dipole moments, while the energetically favored ferromagnetic head-to-tail spin–spin dipole interactions should operate in the N\* phase because the same enantiomers cannot form a strong dimer (Fig. 35.11). In contrast, only positive magneto-LC effects were observed for **1** with a negative  $\Delta\varepsilon$ , irrespective of the chirality of LC phases [27]. This result can be explained in terms of the occurrence of electric dipolar repulsion between the *R* and *S* enantiomers, which results in ferromagnetic head-to-tail spin–spin dipole interactions (Fig. 35.12).

Quite recently, by quantitative analysis of angular dependence of *g*-values and line-width of EPR spectra and DFT calculations of spin density distribution in the interacting molecules based on the crystal structure of an analogous compound, Vorobiev et al. revealed that an intermolecular spin polarization mechanism oper-

**Fig. 35.10** The origin of strong positive magneto-LC effects. (a) Relative stability of four possible spin–spin dipole interactions between two spins. (b) Spin–spin interaction between spins localized in radical moieties in the SmC or SmC\* phase of **1** ( $n = 13$ ) (Ref. [33] – Reproduced by permission of The Royal Society of Chemistry)

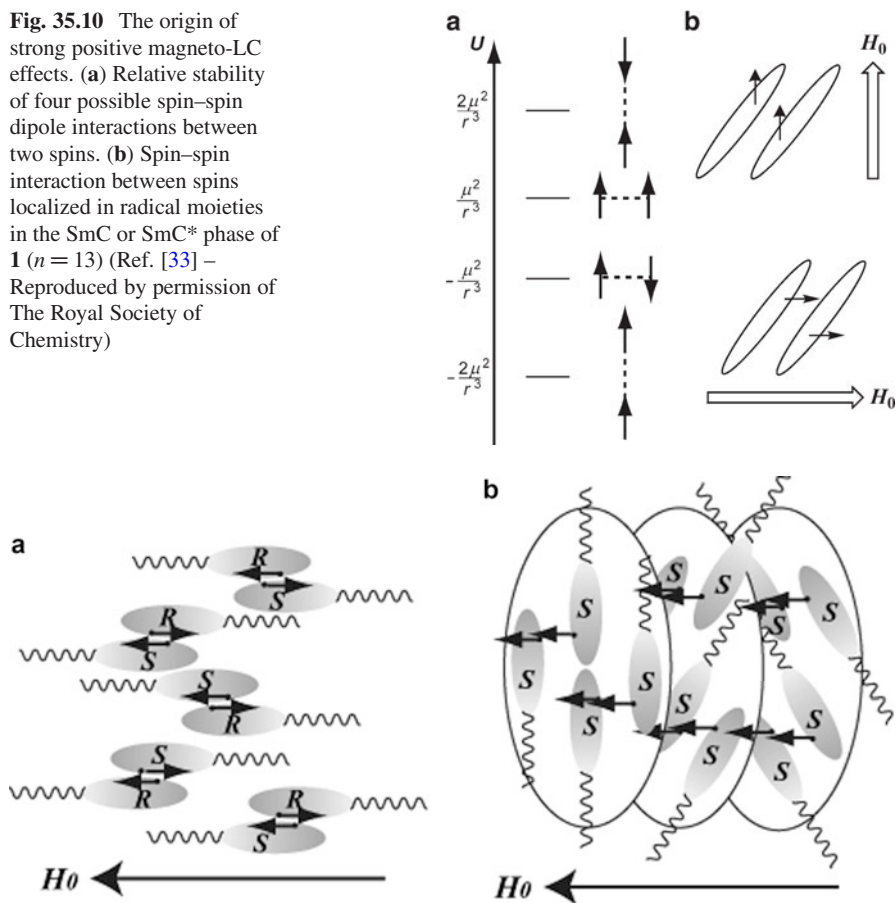
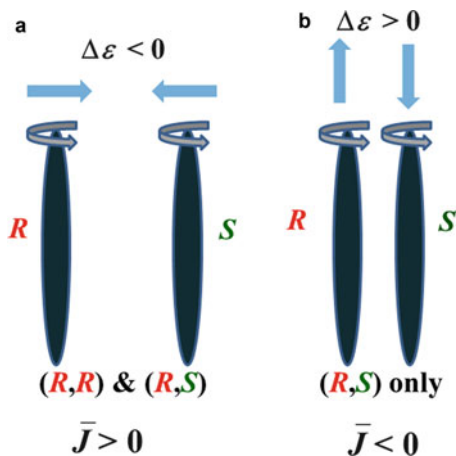


**Fig. 35.11** Schematic illustration of spin–spin dipole interactions in LC phases. (a) The N phase of ( $\pm$ )-**2** and (b) the N\* phase of (2*S*,5*S*)-**2** (96 % ee) (Ref. [28] – Reproduced by permission of The Royal Society of Chemistry)

ating between neighboring radical molecules rather than the direct through-space interactions between the paramagnetic centers contributes to the occurrence of the positive magneto-LC effects [32]. Meanwhile, we reported that hydrogen-bonded all-organic radical compound **3** (Fig. 35.1) showed (1) stronger positive magneto-LC effects in the LC phases than analogous covalent-bonded LC compounds and (2) the increase in the Gaussian component of  $\Delta H$  ( $\Delta H_{pp}^G$ ) and the decrease in the Lorentzian component of  $\Delta H$  ( $\Delta H_{pp}^L$ ) at the Cr-to-LC transition in the heating run, by variable-temperature EPR spectroscopic analysis of the N and N\* phases [33]. These results indicate that the positive magneto-LC effects arise from the inhomogeneous intermolecular contacts which give rise to inhomogeneous magnetic interactions.

**Fig. 35.12** Relationship between the signs of magneto-LC effects ( $\bar{J}$ ) and dielectric anisotropy ( $\Delta\varepsilon$ ). (a) Positive magneto-LC effects ( $\bar{J} > 0$ : ferromagnetic interactions) were exclusively observed in the case of  $\Delta\varepsilon < 0$ , irrespective of the chirality of LC phases. (b) Negative magneto-LC effects ( $\bar{J} < 0$ : antiferromagnetic interactions) were observed in the case of racemic samples with  $\Delta\varepsilon > 0$



### 35.5 Magnetolectric Effect [34, 35]

To clarify the relationship between the ferroelectric properties and positive magneto-LC effects, i.e., the existence of magnetolectric effect, we measured the electric field dependence of EPR spectra of (2*S*,5*S*)-**1** ( $n = 13$ ) confined in a surface-stabilized liquid crystal cell and thereby evaluated the EPR parameters such as  $g$ -value,  $\chi_{\text{rel}}$ , and  $\Delta H_{\text{pp}}$ .

The sample of (2*S*,5*S*)-**1** ( $n = 13$ ) of 65 % *ee* was introduced by capillary action into the lower tip of a handmade 4- $\mu\text{m}$ -thick sandwich cell (50 mm x 5 mm) in which the inner surface of two glass substrates with indium tin oxide (ITO) electrodes was coated with polyimide polymer and then only one inner surface in the cell was rubbed with a velvet roller (Fig. 35.13). Then the cell tip was inserted into the EPR cavity.

First, the generation of positive magneto-LC effects and ferroelectric switching in the liquid crystal cell were confirmed. By measuring the temperature dependence of  $\chi_{\text{rel}}$  under the conditions in which the applied magnetic field was parallel and perpendicular to the cell surface and the rubbing direction in the absence of an electric field, considerable increase (ca. 40 %) of  $\chi_{\text{rel}}$  was noted at the Cr-to-LC transition in both cases (Fig. 35.14). The ferroelectric switching at 25 V was confirmed in the absence of a magnetic field by polarized optical microscopy; the bright fan-shaped texture at  $-25$  V turned to the dark one at  $+25$  V (Fig. 35.15).

Next, the existence of ferroelectric bistable state was verified by evaluating the electric field dependence of  $g$ -value under the conditions in which the magnetic field (0.33 T) was applied perpendicular to the electric field and parallel to the rubbing direction (Fig. 35.16). The experimental  $g$ -values ( $g_{\text{exp}}$ ) exhibited a hysteresis loop between  $+25$  V and  $-25$  V. Since parallel and perpendicular  $g$ -values ( $g_{\parallel}$  and  $g_{\perp}$ ) of molecule **1** ( $n = 13$ ) were previously determined to be 2.0054 and 2.0068, respectively [45], the  $g_{\text{exp}}$  (2.0057) at  $-25$  V reflects a large contribution of  $g_{\parallel}$ ,

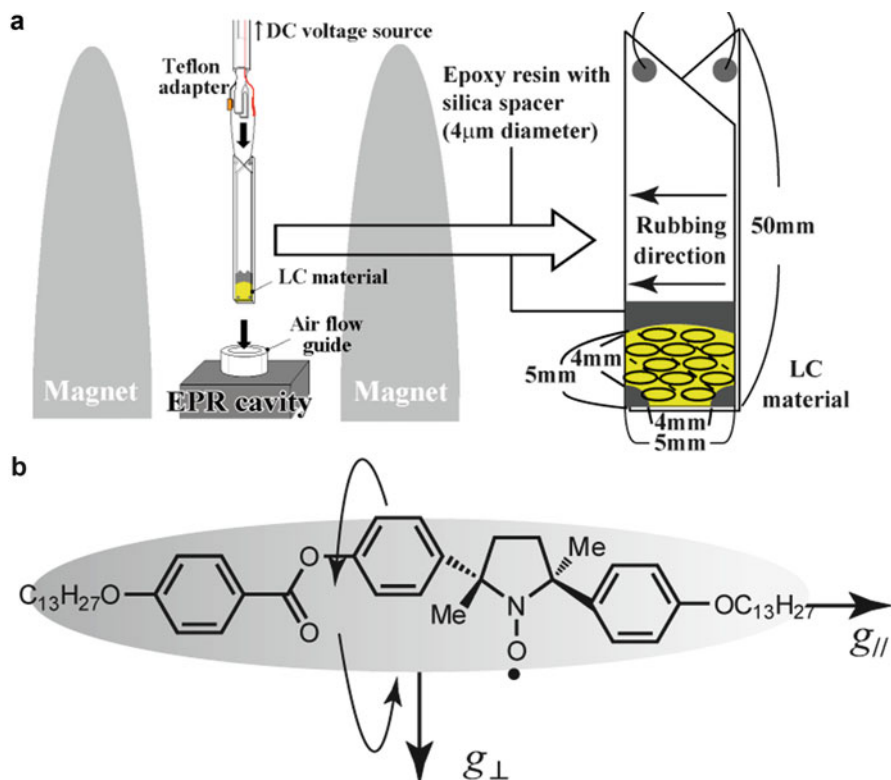


**Fig. 35.13** (a) Experimental setup to monitor the variable-temperature or electric field-dependent EPR spectra of (2*S*,5*S*)-**1** ( $n = 13$ ) confined in a long 4- $\mu$ m-thick sandwich cell. (b) Principal axes of inertia and  $g$ -values ( $g_{//}$  and  $g_{\perp}$ ) of **1** ( $n = 13$ ) (Ref. [34] – Reproduced by permission of The Royal Society of Chemistry)

suggesting that molecular long axis of (2*S*,5*S*)-**1** ( $n = 13$ ) aligns almost parallel to the magnetic field (Fig. 35.16a). On the other hand, the  $g_{\text{exp}}$  (2.0063) at +25 V indicates that the molecular long axis of (2*S*,5*S*)-**1** ( $n = 13$ ) is tilted by 58° ( $2\theta$ ) from the direction of the magnetic field. Thus, (2*S*,5*S*)-**1** ( $n = 13$ ) has proved to take a surface-stabilized ferroelectric bistable state between +25 V and –25 V.

The electric field dependence of  $\chi_{\text{rel,E}}$ , which is defined as

$$\chi_{\text{rel,E}} = \chi_{\text{para}}/\chi_1 \quad (35.2)$$

where  $\chi_1$  is the standard value at the initial potential of +25 V and at 75 °C, was plotted for (2*S*,5*S*)-**1** ( $n = 13$ ), showing a hysteresis loop between +25 V and –25 V (Fig. 35.16b). Since the molecular long axis is parallel to the magnetic field at –25 V, the spin easy axis in the ferroelectric LC phase of (2*S*,5*S*)-**1** ( $n = 13$ ) seemed to exist along the molecular long axis. Then, to gain an insight into the

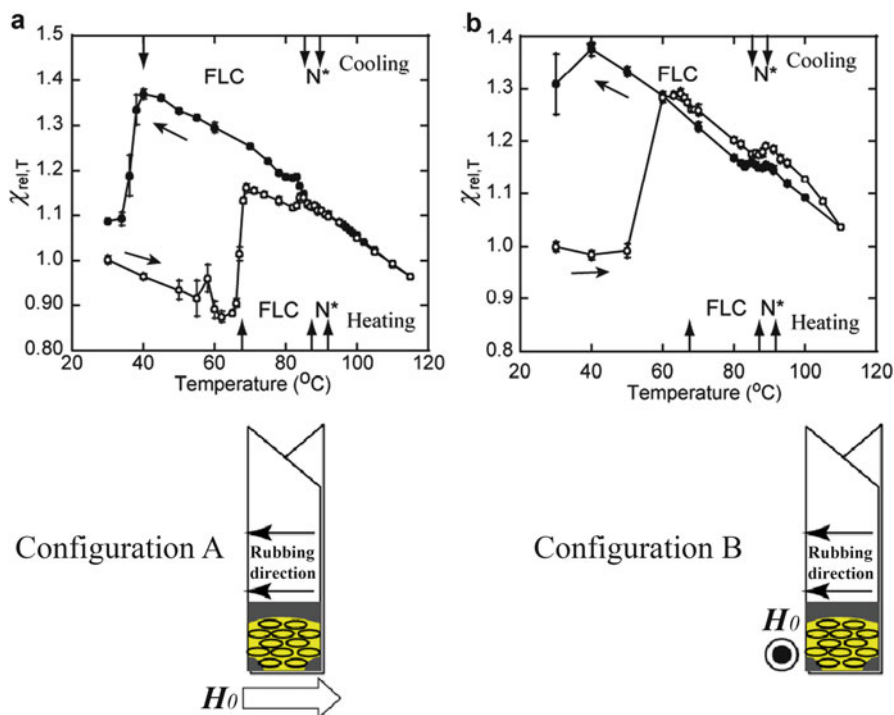


**Fig. 35.14** Temperature dependence of  $\chi_{rel}$  for (2*S*,5*S*)-1 ( $n = 13$ , 65 % ee) confined in a thin rubbed sandwich cell (4  $\mu\text{m}$ ) by EPR spectroscopy at a magnetic field of 0.33 T. The magnetic field was applied (a) parallel and (b) perpendicular to the rubbing direction. The LC temperatures determined by DSC analysis in the heating and cooling runs are shown in the *lower* and *upper* sides of the panels, respectively (Ref. [34] – Reproduced by permission of The Royal Society of Chemistry)

origin of the anisotropic positive magneto-LC effects operating in the ferroelectric LC phase, the electric field dependence of  $\Delta H_{pp}$  was compared with that of  $\chi_{rel,E}$  for (2*S*,5*S*)-1 ( $n = 13$ ) (Fig. 35.16c). The  $\Delta H_{pp}$  exhibited a hysteresis similar to that of  $\chi_{rel,E}$ . The  $\Delta H_{pp}$  is known to reflect the following two competing factors: (i) the spin–spin exchange interaction and (ii) the spin–spin dipole interaction. If the  $\chi_{rel,E}$  change results from the spin–spin exchange interaction, the experimental  $\Delta H_{pp}$  would decrease with increasing  $\chi_{rel,E}$ . However, the observed  $\Delta H_{pp}$  increased and decreased with increasing and decreasing  $\chi_{rel,E}$ , respectively, suggesting that the electric field dependence of  $\chi_{rel,E}$  should primarily arise from the change in the spin–spin dipole interaction. Thus, as the spin–spin dipole interactions contribute to the formation of the spin easy axis, these results proved the existence of a spin easy axis along the molecular long axis in the ferroelectric LC phase of (2*S*,5*S*)-1 ( $n = 13$ ).

Interestingly, however, the  $\chi_{rel,E}$  decreased from +10 V to 0 V and increased from 0 V to –8 V in Fig. 35.16b. This anomalous behavior cannot be explained

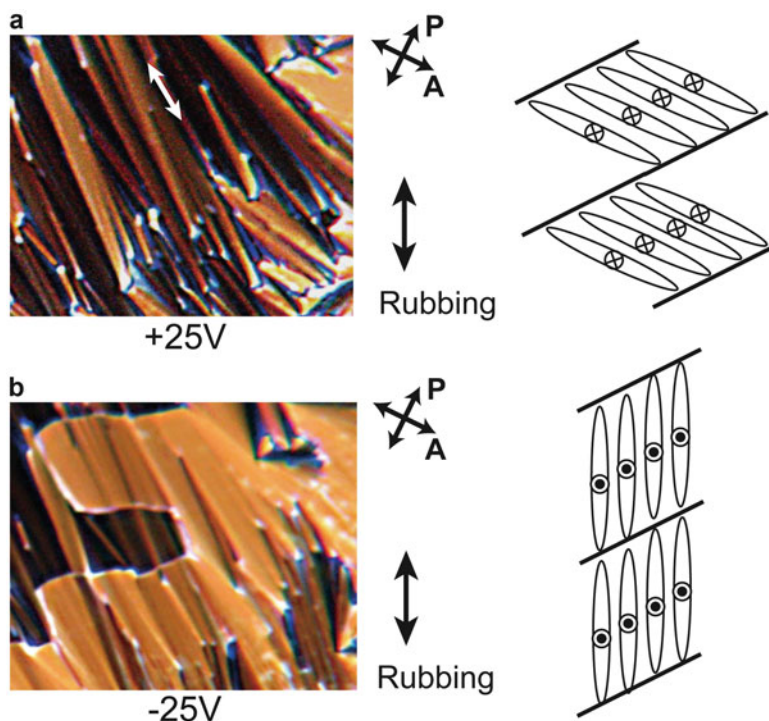


**Fig. 35.15** Polarized optical micrographs showing a broken fan-shaped texture in a surface-stabilized thin sandwich cell ( $4 \mu\text{m}$ ) under homogeneous planar boundary conditions for the ferroelectric LC phase of  $(2S,5S)\text{-1}$  ( $n = 13$ , 65 % ee) at  $75^\circ\text{C}$  in the electric fields of  $+25 \text{ V}$  and  $-25 \text{ V}$  and the corresponding schematic illustration of the direction of the molecular long axes. (a) A dark texture dominated at  $+25 \text{ V}$ . (b) A light texture dominated at  $-25 \text{ V}$ .  $P$  and  $A$  denote the directions of the crossed polarizer and the analyzer, respectively. White arrows in the panel (a) represent the direction of the layer normal (Ref. [34] – Reproduced by permission of The Royal Society of Chemistry)

simply by either the molecular reorientation or the spin–spin dipole interaction, because during the same electric field, the  $g$ -value was almost constant and the  $\Delta H_{\text{pp}}$  slightly increased (Fig. 35.16c). Accordingly this  $\Delta H_{\text{pp}}$  increase from  $+10 \text{ V}$  to  $0 \text{ V}$  should be ascribed to the decrease in the spin–spin exchange interaction and that from  $0 \text{ V}$  to  $-8 \text{ V}$  to the increase in both the spin–spin exchange and dipole interactions; we are most likely to observe magnetoelectric effect in the range from  $+10 \text{ V}$  to  $-8 \text{ V}$  in the ferromagnetic and ferroelectric liquid crystal at as high as  $75^\circ\text{C}$ .

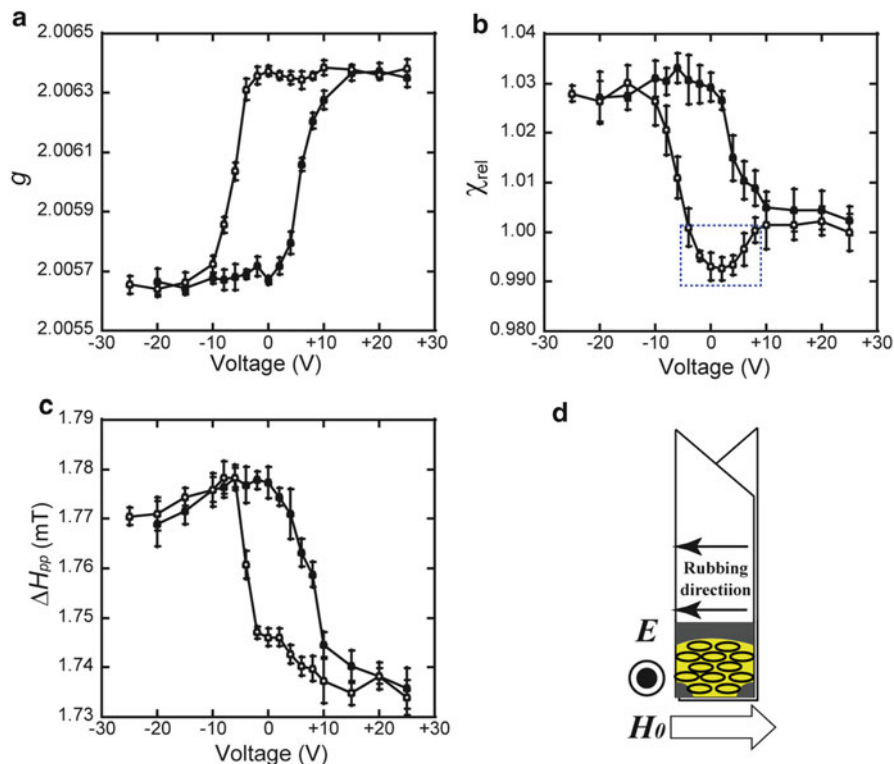


**Fig. 35.16** Electric field dependence of (a)  $g$ -value, (b)  $\chi_{rel,E}$ , and (c)  $\Delta H_{pp}$  for the ferroelectric phase of (2*S*,5*S*)-**1** ( $n = 13$ , 65 % ee) confined in a thin rubbed sandwich cell at 75 °C by EPR spectroscopy at a magnetic field of 0.33 T. (d) The magnetic field was applied perpendicular to the electric field and parallel to the rubbing direction. *Open and filled circles* represent the application of electric fields from +25 V to -25 V and from -25 V to +25 V, respectively. Magnetoelectric effect was observed in the range from +10 V to -8 V surrounded by a dotted square in the panel (b) (Ref. [34] – Reproduced by permission of The Royal Society of Chemistry)

## 35.6 Summary and Prospects

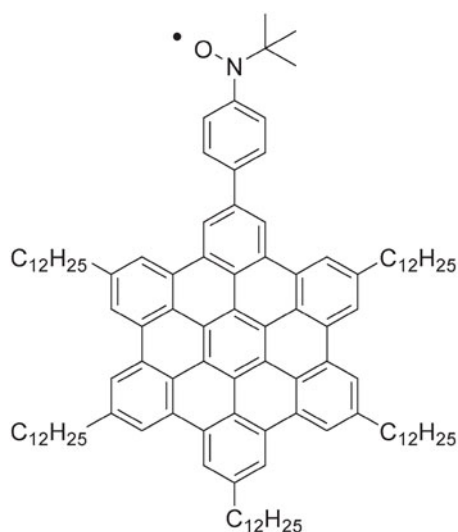
We observed the generation of spin glass-like inhomogeneous ferromagnetic interactions ( $\bar{J} > 0$ ) induced by applied magnetic fields at high temperatures in the various LC phases of the second generation of chiral rodlike all-organic radical LC compounds such as **1** and referred to this phenomenon as “magneto-LC effects.” The origin of this phenomenon was interpreted in terms of inhomogeneous intermolecular contacts to give ferromagnetic spin–spin dipole and exchange interactions. Furthermore, by EPR analysis and DFT calculations, an intermolecular spin polarization mechanism operating between the central paramagnetic center of one molecule and the aromatic ring of another molecule, rather than the direct through-

space interactions between the paramagnetic centers, turned out to contribute to the occurrence of the positive magneto-LC effects.

Then we evaluated the influence of electric fields on the positive magneto-LC effects in the FLC phase of (2*S*,5*S*)-**1** ( $n = 13$ ) confined in a surface-stabilized liquid crystal cell by measuring the electric field dependence of the EPR spectra. By application of electric fields between +25 V and -25 V under the conditions where the magnetic field (0.33 T) was applied perpendicular to the electric field and parallel to the cell surface and rubbing direction, for the first time we observed (1) two magnetic bistable states, (2) anisotropy in spin-spin dipole interactions, and (3) "magnetoelectric effect" in the range of +10 V to -8 V at as high as 75 °C in the ferromagnetic and ferroelectric liquid crystal. The electric field dependence of  $\Delta H_{pp}$  indicated that the anisotropy in spin-spin dipole interactions was responsible for the magnetic bistable states; strong spin-spin dipole interactions were observed when the magnetic field was applied parallel to the molecular long axis. Such unique magnetic properties may be applicable to the development of magnetic data storage materials operable at room temperature.

These experimental results strongly suggested that positive magneto-LC effects could be induced in columnar discotic magnetic LC phases, too, by introducing chirality or a bulky substituent into the molecule so as to avoid the strong  $\pi$ - $\pi$  dimer formation, although all three achiral all-organic radical columnar discotic LC compounds, which were reported before 2014, failed to show the positive magneto-LC effects [46–48]. In 2014, however, the columnar hexagonal LC (Col<sub>h</sub>) phase of achiral, paramagnetic hexa-*peri*-hexabenzocoronene derivative carrying a conjugated *tert*-butyl nitroxide moiety (Fig. 35.17), which is assumed to take a helical columnar structure in the LC state, has been reported to show the positive magneto-LC effects [49].

**Fig. 35.17** Hexa-*peri*-hexabenzocoronene derivative with a conjugated *tert*-butyl nitroxide group showing the positive magneto-LC effects



Meanwhile, quite recently, Kaszyński et al. have reported the bent-core mesogens containing 6-oxoverdazyl radical as the angular central unit exhibits a novel 3D tetragonal phase which shows gradual increase of antiferromagnetic interactions (negative magneto-LC effects) upon cooling [50]. In this case, it is also desirable to introduce chirality into the molecule for the observation of positive magneto-LC effects.

Thus, an in-depth understanding of positive magneto-LC effects would open up a new research field in the development of totally new metal-free all-organic magnetic LC and other soft materials.

## References

1. L.M. Bilinov, *Electro-Optical and Magneto-Optical Properties of Liquid Crystals* (Wiley, New York, 1983)
2. S. Chandrasekhar (ed.), *Liquid Crystal Second Edition* (Cambridge University Press, Cambridge, 1992)
3. D. Demus, J. Goodby, G.W. Gray, H.-W. Spiess, V. Vill (eds.), *Physical Properties of Liquid Crystals* (Wiley-VCH, Weinheim, 1999)
4. I. Dierking, *Textures of Liquid Crystals* (Wiley-VCH, Weinheim, 2003)
5. J.-L. Serrano, *Metallomesogens: Synthesis, Properties, and Applications* (Wiley-VCH, Weinheim, 1996)
6. D. Dunmur, K. Toriyama, in *Physical Properties of Liquid Crystals*, ed. by D. Demus, J. Gooby, G. W. Gray, H.-W. Spiess, V. Vill (Wiley-VCH-VCH, Weinheim, 1999), pp. 102–112
7. P. Kaszynski, in *Magnetic Properties of Organic Materials*, ed. by P.M. Lahti (Marcel Dekker, New York, 1999), pp. 305–324
8. K. Griesar, W. Haase, in *Magnetic Properties of Organic Materials*, ed. by P.M. Lahti (Marcel Dekker, New York, 1999), pp. 325–344
9. K. Binnemans, C. Gröller-Walrand, *Chem. Rev.* **102**, 2303–2345 (2002)
10. W. Eerenstein, N.D. Mathur, J.F. Scott, *Nature* **442**, 759–765 (2006)
11. C.N.R. Rao, C.R. Serrao, *J. Mater. Chem.* **17**, 4931–4938 (2007)
12. C. Felser, G.H. Fecher, B. Balke, *Angew. Chem. Int. Ed.* **46**, 668–699 (2007)
13. S. Seki, *Magnetolectric Response in Low-Dimensional Frustrated Spin Systems* (Springer, Tokyo, 2012)
14. G.L.J.A. Rikken, E. Raupach, *Nature* **390**, 493–494 (1997)
15. G.L.J.A. Rikken, E. Raupach, *Nature* **405**, 932–935 (2000)
16. C. Train, R. Gheorghe, V. Krstic, L.-M. Chamoreau, N.S. Ovanesyan, G.L.J.A. Rikken, M. Gruselle, M. Verdaguer, *Nat. Mater.* **7**, 729–734 (2008)
17. R. Tamura, in *Nitroxides: Application in Chemistry, Biomedicine, and Materials Science*, ed. G.I. Likhtenshtein, J. Yamauchi, S. Nakatsuji, A.I. Smirnov, R. Tamura (Wiley-VCH, Weinheim, 2008), pp. 303–329
18. R. Tamura, Y. Uchida, N. Ikuma, *J. Mater. Chem.* **18**, 2872–2876 (2008)
19. R. Tamura, N. Ikuma, S. Shimono, in *Soft Nanomaterials*, vol 1, ed. by H.S. Nalwa (American Scientific Publishers, Stevenson Ranch, 2009), pp. 257–277
20. R. Tamura, Y. Uchida, K. Suzuki, in *Liquid Crystals Beyond Display*, ed. by Q. Li (Wiley, Hoboken, 2012), pp. 83–110
21. R. Tamura, Y. Uchida, K. Suzuki, in *Nitroxides: Theory, Experiment and Application*, ed. by A.I. Kokorin (INTECH, Croatia, 2012), pp. 191–210
22. R. Tamura, K. Suzuki, Y. Uchida, Y. Noda, *Electron Paramag. Reson.* **23**, 1–21 (2013)

23. R. Tamura, Y. Uchida, K. Suzuki, in *Handbook of Liquid Crystals: Second Edition*, ed. J.W. Gooby, P.J. Collings, T. Kato, C. Tschierske, H.F. Gleeson, R. Raynes, vol 8 (Wiley-VCH, Weinheim, 2014), pp. 837–864
24. N. Ikuma, R. Tamura, S. Shimono, N. Kawame, O. Tamada, N. Sakai, J. Yamauchi, Y. Yamamoto, *Angew. Chem. Int. Ed.* **43**, 3677–3682 (2004)
25. N. Ikuma, R. Tamura, S. Shimono, Y. Uchida, K. Masaki, J. Yamauchi, Y. Aoki, H. Nohira, *Adv. Mater.* **8**, 477–480 (2006)
26. Y. Uchida, N. Ikuma, R. Tamura, S. Shimono, Y. Noda, J. Yamauchi, Y. Aoki, H. Nohira, *J. Mater. Chem.* **18**, 2950–2952 (2008)
27. Y. Uchida, K. Suzuki, R. Tamura, N. Ikuma, S. Shimono, Y. Noda, J. Yamauchi, *J. Am. Chem. Soc.* **132**, 9746–9752 (2010)
28. K. Suzuki, Y. Uchida, R. Tamura, S. Shimono, J. Yamauchi, *J. Mater. Chem.* **22**, 6799–6806 (2012)
29. N. Ikuma, R. Tamura, K. Masaki, Y. Uchida, S. Shimono, J. Yamauchi, Y. Aoki, H. Nohira, *Ferroelectrics* **343**, 119–125 (2006)
30. N. Ikuma, Y. Uchida, R. Tamura, K. Suzuki, J. Yamauchi, Y. Aoki, H. Nohira, *Mol. Cryst. Liq. Cryst.* **509**, 108–117 (2009)
31. Y. Uchida, R. Tamura, N. Ikuma, J. Yamauchi, Y. Aoki, H. Nohira, *Ferroelectrics* **365**, 158–169 (2008)
32. A.K. Vorobiev, N.A. Chumakova, D.A. Pompgailo, Y. Uchida, Y. Suzuki, Y. Noda, *J. Phys. Chem. B* **118**, 1932–1942 (2014)
33. Y. Uchida, K. Suzuki, R. Tamura, *J. Phys. Chem. B* **116**, 9791–9795 (2012)
34. K. Suzuki, Y. Uchida, R. Tamura, Y. Noda, N. Ikuma, S. Shimono, J. Yamauchi, *Soft Matter* **9**, 4687–4692 (2013)
35. K. Suzuki, Y. Uchida, R. Tamura, Y. Noda, N. Ikuma, S. Shimono, J. Yamauchi, *Adv. Sci. Tech.* **82**, 50–54 (2013)
36. M. Dvolaitzky, J. Billard, F. Polydy, *C. R. Acad. Sci. Paris, Ser. C* **279**, 533–535 (1974)
37. M. Dvolaitzky, C. Taupin, F. Polydy, *Tetrahedron Lett.* **18**, 1469–1472 (1976)
38. M. Dvolaitzky, J. Billard, F. Polydy, *Tetrahedron* **32**, 1835–1838 (1976)
39. J. Allgaier, H. Finkelmann, *Macromol. Chem. Phys.* **195**, 1017–1030 (1994)
40. S. Greve, V. Vill, W. Friedrichsen, *Z. Naturforsch.* **57b**, 677–684 (2002)
41. S. Nakatsuji, M. Mizumoto, H. Ikemoto, H. Akutsu, J. Yamada, *Eur. J. Org. Chem.* 1912–1918 (2002)
42. R. Kogo, F. Araoka, Y. Uchida, R. Tamura, K. Ishikawa, H. Takezoe, *Appl. Phys. Express* **3**, 041701 (2010)
43. S.K. Mandel, T.K. Nath, A. Das, R.K. Kremer, *Appl. Phys. Lett.* **89**, 162502 (2006)
44. J. Schneider, A. Handstein, K. Zaveta, *J. Magn. Magn. Mater.* **42**, 73–88 (1984)
45. Y. Uchida, R. Tamura, N. Ikuma, S. Shimono, J. Yamauchi, Y. Shimbo, H. Takezoe, Y. Aoki, H. Nohira, *J. Mater. Chem.* **19**, 415–418 (2009)
46. C.V. Yelamaggad, A.S. Achalkumar, D.D.S. Rao, M. Nobusawa, H. Akutsu, J. Yamada, S. Nakatsuji, *J. Mater. Chem.* **18**, 3433–3437 (2008)
47. S. Castellanos, F. Lopez-Calahorra, E. Brillas, L. Juliá, D. Velasco, *Angew. Chem. Int. Ed.* **48**, 6516–6519 (2009)
48. A. Jankowiak, D. Pocięcha, J. Szczytko, H. Monobe, P. Kaszynski, *J. Am. Chem. Soc.* **134**, 2465–2468 (2012)
49. P. Ravat, T. Marszałek, W. Pisula, K. Müllen, M. Baumgarten, *J. Am. Chem. Soc.* **136**, 12860–12863 (2014)
50. M. Jasiński, D. Pocięcha, H. Monobe, J. Szczytko, P. Kaszyński, *J. Am. Chem. Soc.* **136**, 14658–14661 (2014)

## ERRATUM

# Chapter 7 Metastability of Supersaturated Solution and Nucleation

Noriaki Kubota, Masanori Kobari, and Izumi Hirasawa

© Springer Japan 2015

R. Tamura, M. Miyata (eds.), *Advances in Organic Crystal Chemistry*,  
DOI 10.1007/978-4-431-55555-1

DOI 10.1007/978-4-431-55555-1\_36

In Chapter titled “Metastability of Supersaturated Solution and Nucleation”  
Figs. 7.1 and 7.2 were incorrect. The correct versions are given below:

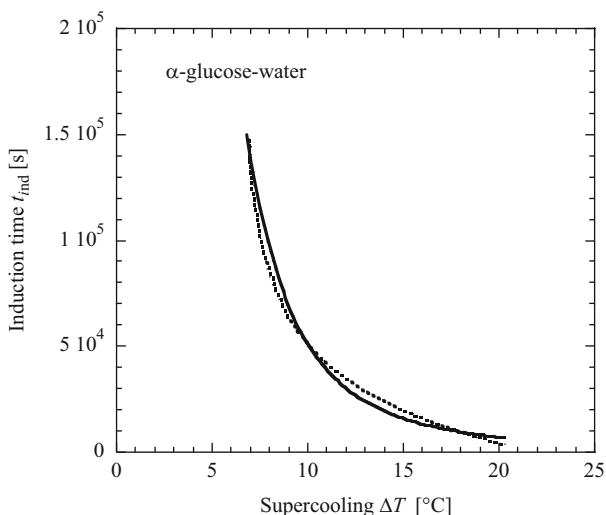


**Fig. 7.1** Induction time as a function of supercooling. The *solid line* is the experimental value reported by Srisa-nga et al. [27], and the *dotted line* is a best fit of a theoretical equation. This graph was taken from Kubota [32]

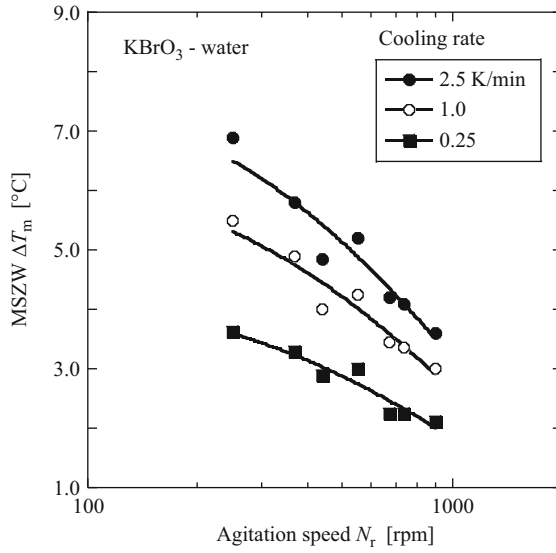


**Fig. 7.2** The effect of agitation speed on MSZW for the potassium bromate-water system (Data were taken from Matsui and Harano [35])